STATE OF THE CLIMATE IN 2020

Special Supplement to the
Bulletin of the American Meteorological Society
Vol. 102, No. 8, August 2021

Cover credits:

Cover graphic data from atmospheric CO_2 time series at Mauna Loa Dr. Pieter Tans, NOAA/GML (gml.noaa.gov/ccgg/trends/) and Dr. Ralph Keeling, Scripps Institution of Oceanography (scrippsco2.ucsd.edu/). See also Fig. 2.50a of this report.

Background graphic: Empty freeway streets in Los Angeles with almost no vehicles and people due to coronavirus (COVID-19) virus outbreak and stay at home order and mandatory quarantine. Credit: iStock/Getty Images Plus/vlvart.

How to cite this document:

Citing the complete report:
Blunden, J. and T. Boyer, Eds., 2020: "State of the Climate in 2020". *Bull. Amer. Meteor. Soc.*, **102** (8), Si–S475, doi:10.1175/2021BAMSStateoftheClimate.1.

Special Supplement to the *Bulletin of the American Meteorological Society,* Vol. 102, No. 8, August, 2021, https://doi.org/10.1175/2021BAMSStateoftheClimate.1

Corresponding author: Full report: Jessica Blunden / jessica.blunden@noaa.gov

STATE OF THE CLIMATE IN 2020

TABLE OF CONTENTS

ABSTRACT—J. BLUNDEN AND T. BOYER

In 2020, the dominant greenhouse gases stored in Earth's atmosphere continued to increase. The annual global average carbon dioxide (CO_2) concentration at Earth's surface was 412.5 ± 0.1 ppm, an increase of 2.5 ± 0.1 ppm over 2019, and the highest in the modern instrumental record and in ice core records dating back 800,000 years. While anthropogenic CO_2 emissions were estimated to decrease around 6%–7% globally during the year due to reduced human activities during the COVID-19 pandemic, the reduction did not materially affect atmospheric CO_2 accumulation as it is a relatively small change, less even than interannual variability driven by the terrestrial biosphere. The net global uptake of ~3.0 petagrams of anthropogenic carbon by oceans in 2020 was the highest in the 39-year record and almost 30% higher than the 1999–2019 average.

Weak El Niño-like conditions in the eastern equatorial Pacific Ocean in early 2020 cooled and transitioned to a moderate La Niña later in the year. Even so, the annual global surface temperature across land and oceans was among the three highest in records dating to the mid- to late 1800s. In Europe, 17 countries reported record high annual mean temperatures, contributing to the warmest year on record for the European continent. Elsewhere, Japan, Mexico, and Seychelles also experienced record high annual mean temperatures. In the Caribbean, Aruba, Martinique, and St. Lucia reported their all-time monthly maximum temperatures. In the United States, Furnace Creek in Death Valley, California, reached 54.4°C on 16 August—the hottest temperature measured on Earth since 1931, pending confirmation. North of 60°N, the annual mean temperature over Arctic land areas was 2.1°C above the 1981–2010 average, the highest in the 121-year record. On 20 June, a temperature of 38°C was observed at Verkhoyansk, Russia (67.6°N), provisionally the highest temperature ever measured within the Arctic Circle.

Near the opposite pole, an atmospheric river—a long, narrow region in the atmosphere that transports heat and moisture from sub-tropical and midlatitudes—brought extreme warmth from sub-tropical and midlatitudes to parts of Antarctica during austral summer. On 6 February, Esperanza Station recorded a temperature of 18.3°C, the highest temperature recorded on the continent, surpassing the previous record set in 2015 by 1.1°C. The warmth also led to the largest late-summer surface melt event in the 43-year record, affecting more than 50% of the Antarctic Peninsula. In August, daily sea ice extent in the waters surrounding Antarctica shifted from below to above average, marking the end of persistent below-average sea ice extent since austral spring 2016.

In the Arctic, when sea ice reached its annual maximum extent in March, thin, first-year ice comprised ~70% of the ice; the thickest ice, which is usually more than four years old, had declined by more than 86% since 1985 to make up just 2% of total ice in 2020. When the minimum sea ice extent was reached in September, it was the second smallest except for 2012 in the 42-year satellite record. The Northern Sea Route along the Siberian coast was open for about 2.5 months, from late July through mid-October, compared to less than a month typically.

Glaciers across the global cryosphere lost mass for the 33rd consecutive year, and permafrost temperatures continued to reach record highs at many high latitude and mountain locations. In the Northern Hemisphere, lakes froze three days later and thawed 5.5 days earlier on average. In Finland, the average duration of lake ice was 42 days shorter. Record high spring temperatures in central Siberia drove rapid snow melt that contributed to the lowest June snow cover extent across Eurasia in the 54-year record.

As is typical, some areas around the world were notably dry in 2020 and some were notably wet. The Middle East experienced an extreme drought during autumn, with most places reporting no precipitation in October. In South America, the Bolivian lowlands suffered one of its most severe droughts on record during autumn. Drought also spanned the Chaco and Pantanal in Bolivia, Paraguay, and southern Brazil. The Paraguay River shrank to its lowest levels in half a century. A decadal "mega drought" in south-central Chile continued through its 11th year, with extreme conditions in the most populated areas. Argentina reported its driest year since 1995. In North America, drought continued to prevail in the West.

The lack of moisture in drought-stricken regions often provide ideal conditions for fire. Total fire emissions in the western United States in 2020 were almost three times higher than the 2003–10 mean. The Arctic experienced its highest fire year in terms of carbon emitted into the atmosphere, surpassing the record set in 2019 by 34%, with most of the fires occurring in Arctic Asia. In the tropics, the Amazon saw its highest fire activity since 2012, while fire activity in tropical Asia—including Indonesia—was one of the lowest on record, related to wet conditions as La Niña evolved during the fire season.

The 2020 Southwest Asian Monsoon season (June–September) was the wettest since 1981, also coincident with the emergence of La Niña. The Meiyu rainy season, which usually occurs between July and August over the Yangtze and Huaihe River Valleys of China, was extended by two months in 2020. The

May–October total rainfall averaged over the area was the most since the start of the record in 1961. Associated severe flooding affected about 45.5 million people.

A widespread desert locust infestation during 2019–20 impacted equatorial and northern East Africa, as heavy rains and prevailing winds were favorable for breeding and movement of swarms across Kenya, Ethiopia, northeastern Somalia, Uganda, South Sudan, and northern Tanzania. The massive infestation destroyed thousands of square kilometers of cropland and pasture lands, resulting in one million people in need of food aid in Ethiopia alone. Extremely heavy rains in April also triggered widespread flooding and landslides in Ethiopia, Somalia, Rwanda, and Burundi. The Lake Victoria region was the wettest in its 40-year record.

Across the global oceans, the average ocean heat content reached a record high in 2020 and the sea surface temperature was the third highest on record, surpassed only by 2016 and 2019. Approximately 84% of the ocean surface experienced at least one marine heatwave (MHW) in 2020. For the second time in the past decade, a major MHW developed in the northeast Pacific, covering an area roughly six times the size of Alaska in September. Global mean sea level was record high for the ninth consecutive year, reaching 91.3 mm above the 1993 average when satellite measurements began, an increase of 3.5 mm over 2019. Melting of the Greenland Ice Sheet accounted for about 0.8 mm of the sea level rise, with an overall loss of 293 ± 66 gigatons of ice.

A total of 102 named tropical storms were observed during the Northern and Southern Hemisphere storm seasons, well above the 1981–2010 average of 85. In the North Atlantic, a record 30 tropical cyclones formed, surpassing the previous record of 28 in 2005. Major Hurricanes Eta and Iota made landfall along the eastern coast of Nicaragua in nearly the same location within a two-week period, impacting over seven million people across Central America. In the western North Pacific, Super Typhoon Goni was the strongest tropical cyclone to make landfall in the historical record and led to the evacuation of almost 1 million people in the Philippines. Very Severe Cyclonic Storm Gati was the strongest recorded cyclone to make landfall over Somalia. Bosaso, in northeast Somalia, received 128 mm of rainfall in a 24-hour period, exceeding the city's average annual total of 100 mm.

Above Earth's surface, the annual lower troposphere temperature equaled 2016 as the highest on record, while stratospheric temperatures continued to decline. In 2020, the stratospheric winter polar vortices in both hemispheres were unusually strong and stable. Between December 2019 and March 2020, the Arctic polar vortex was the strongest since the beginning of the satellite era, contributing to record low stratospheric ozone levels in the region that lasted into spring. The anomalously strong and persistent Antarctic polar vortex was linked to the longest-lived, and 12th-largest, ozone hole over the region, which lasted to the end of December.

STATE OF THE CLIMATE IN 2020

INTRODUCTION

Emissions from fossil fuel use in 2020 dropped by around 6% to 7% over 2019 due to decreased activity during the pandemic (section 2g1); however atmospheric concentration of carbon dioxide (CO_2), still reached the highest levels in the modern climate record.

Citing this chapter: Boyer, T., J. Blunden, and R. J. H. Dunn. 2021: Introduction [in "State of the Climate in 2020"]. *Bull. Amer. Meteor. Soc.,* **102** (8), S1–S10, https://doi.org/10.1175/2021BAMSStateoftheClimate_Intro.1.

Special Supplement to the *Bulletin of the American Meteorological Society* Vol.**102**, No. 8, August, 2021

The Introduction is one chapter from the *State of the Climate in 2020* annual report. Compiled by NOAA's National Centers for Environmental Information, *State of the Climate in 2020* is based on contributions from scientists from around the world. It provides a detailed update on global climate indicators, notable weather events, and other data collected by environmental monitoring stations and instruments located on land, water, ice, and in space. The full report is available from https://doi.org/10.1175/2021BAMSStateoftheClimate.1.
https://doi.org/10.1175/2021BAMSStateoftheClimate_Intro.1

Corresponding author, Introduction: Jessica Blunden / jessica.blunden@noaa.gov

STATE OF THE CLIMATE IN 2020

Introduction

Editors

Jessica Blunden
Tim Boyer

Chapter Editors

Freya Aldred
Peter Bissolli
Howard J. Diamond
Matthew L. Druckenmiller
Robert J. H. Dunn
Catherine Ganter
Nadine Gobron
Gregory C. Johnson
Tim Li
Rick Lumpkin
Ademe Mekonnen
John B. Miller
Twila A. Moon
Ahira Sánchez-Lugo
Ted A. Scambos
Carl J. Schreck III
Sharon Stammerjohn
Richard L. Thoman
Kate M. Willett

Technical Editor

Andrea Andersen

***BAMS* Special Editor for Climate**

Michael A. Alexander

American Meteorological Society

Editor and Author Affiliations (alphabetical by name)

Blunden, Jessica, NOAA/NESDIS National Centers for Environmental Information, Asheville, North Carolina
Boyer, T., NOAA/NESDIS National Centers for Environmental Information, Silver Spring, Maryland
Dunn, Robert, J. H., Met Office Hadley Centre, Exeter, United Kingdom

Editorial and Production Team

Allen, Jessicca, Graphics Support, Cooperative Institute for Satellite Earth System Studies, North Carolina State University, Asheville, North Carolina
Andersen, Andrea, Technical Editor, Innovative Consulting Management Services, LLC, NOAA/NESDIS National Centers for Environmental Information, Asheville, North Carolina
Hammer, Gregory, Content Team Lead, Communications and Outreach, NOAA/NESDIS National Centers for Environmental Information, Asheville, North Carolina
Love-Brotak, S. Elizabeth, Lead Graphics Production, NOAA/NESDIS National Centers for Environmental Information, Asheville, North Carolina
Misch, Deborah J., Graphics Support, Innovative Consulting Management Services, LLC, NOAA/NESDIS National Centers for Environmental Information, Asheville, North Carolina
Riddle, Deborah B., Graphics Support, NOAA/NESDIS National Centers for Environmental Information, Asheville, North Carolina
Veasey, Sara W., Visual Communications Team Lead, Communications and Outreach, NOAA/NESDIS National Centers for Environmental Information, Asheville, North Carolina

1. INTRODUCTION—T. Boyer, J. Blunden, and R. J. H. Dunn

The singular most significant event for humankind in 2020 was the COVID-19 pandemic, with the disruption of human activity and everyday life. As the cover of this year's *State of the Climate* report intimates, while the world's human population struggled with the pandemic, signs of a changing climate did not abate. Even though emissions from fossil fuel use in 2020 dropped by 6–7% over the previous year due to decreased activity during the pandemic (section 2g1), atmospheric concentration of the most important greenhouse gas, carbon dioxide (CO_2), still increased to the highest levels in the modern climate record (section 2g1). This is a stark reminder that factors leading to a changing climate are determined by time horizons far longer than a single year and have an inertia that will take a significant effort over a much longer period to halt, much less reverse. The effects of the drop in fossil fuel emissions are not discernable in atmospheric CO_2 in 2020 over 2019 due to the relative magnitude of interannual variability in natural CO_2 sources and sinks. Ocean carbon uptake (section 3j2), terrestrial photosynthetic activity (section 2h2) and, to a lesser extent, biomass burning (section 2h3) are some of the CO_2 sinks and/or sources whose collective year-to-year variability is larger than, and indistinguishable from, the 2020 drop in fossil fuel emissions.

The pandemic did have a definite effect on the monitoring of Earth's climate system. For example, some permafrost sites went without regular in situ monitoring (section 2c1) due to travel difficulties arising from pandemic restrictions. Annual data from significant sections of the northern Atlantic meridional overturning circulation monitoring arrays were not gathered because of a lack of research cruises due to pandemic cancellations or delays (section 3h). Still, given that much of our quantification of climate variables comes from satellite information and climate reanalyses, the catalogue of essential climate variables presented in the *State of the Climate in 2020* is as comprehensive as in prior years despite the difficulty of gathering in situ data related to the pandemic. The use of reanalyses, which incorporate (assimilate) observations into an underlying model of aspects of the climate system to numerically reproduce historic and recent climate conditions, helps to augment and extend the utility of satellite products and the sometimes scarce in situ observations. Ultimately bringing together all the observations, data and knowledge vital to the compilation of this report was accomplished through the continued and tireless efforts of more than 530 authors from 66 countries representing their colleagues and contributors from universities and agencies around the globe.

The *State of the Climate* in 2020 catalogues the two devastating hurricanes that hit Nicaragua and other Central American countries within two weeks of each other (section 4g2 and Sidebar 7.1), the hurricane with the strongest wind velocity to hit Louisiana in more than 150 years (Sidebar 4.1), and the strongest tropical cyclone to make landfall in the historic record (section 4g4), amongst many others tropical cyclones. The report also details the wet long-rain season in East Africa (sections 2d5, 7e4) that raised lake levels (section 2d6) and increased terrestrial water storage (section 4d9) enough to affect global ocean mass storage (section 3f). The 2020 report further catalogues, for surface temperature, the third-highest temperature ever recorded anywhere in the world (pending certification) occurring in Death Valley, California (54.4°C, sections 2b3, 7b2); Basra, Iraq, recording two successive days with maximum air temperature above 53°C (section 2b3); and the highest temperature ever recorded in Antarctica (sections 2b3, 6a, Sidebar 6.1). Moreover, the *State of the Climate* in 2020 notes the Antarctic temperature record occurred during a persistent period of abnormally high air temperatures and was accompanied by the largest ever satellite recorded late-summer ice melt on the Antarctic Peninsula affecting more than 50% of the area (section 6a, Sidebar 6.1).

It is this last juxtaposition of climate statistics which demonstrates the utility of cataloging singular or short duration events in this annual compendium in order to put these events in the context of our current and changing climate. One event on its own is noteworthy, numerous events of a similar nature in one year interesting, but many of these being record breaking in the context of past observations concerning. A heat wave is defined using the statistical analysis of climatic surface air temperature, giving perspective on abnormally high and long duration surface air temperatures experienced in Antarctica and elsewhere in 2020. Likewise, the abnormally high and long duration sea surface temperatures in the North Pacific meet the statistical definition for a marine heatwave, one of unprecedented duration (section 2b3, Sidebar 3.1). Statistical analysis of cyclone activity and intensity in different ocean basins (section 4g) give some perspective on the likelihood of hurricanes/typhoons of the location and intensity experienced in 2020.

It is here that this annual report goes further than a simple compendium of events and their relation to long-term climate statistics. Many of the causes of singular weather events are also catalogued herein. Cyclone generation and intensity are related to a complex set of circumstances, many of them detailed in the *State of the Climate* reports. For example, upper ocean heat content is a factor in hurricane generation and intensity. Attempting to relate cyclone activity and upper ocean heat content in the quantity tropical cyclone heat potential (section 4h) is an important step in understanding and monitoring the climatic factors responsible for cyclogenesis and cyclone intensity. For global, annual conditions, (as opposed to singular or short duration events), comparing 2020 averages to the previous year and to the long-term average provides information on the importance both of long-term trends and interannual to decadal variability. An attempt to differentiate the annual influence of the long-term trend and seasonal to interannual factors on surface air temperature (section 2b1) is a step to clarifying the relative influence of climate trends and interannual factors on annual means of the variables that define our climate.

Few factors aside from long-term trends come up as often in the *State of the Climate* as the El Niño–Southern Oscillation (ENSO). The 2020 conditions with a transition to moderate La Niña mid-year is an important driver of many of the cataloged conditions in the *State of the Climate*. Due to ENSO not in phase with seasonal cycles, global annual means of some essential climate variables do not provide sufficient granularity to fully quantify the variable—more regional and intra-annual description is provided. For example, lake water level changes (section 2d6) are not unidirectional globally but are highly dependent on regional factors related both to ENSO and other drivers, such as the Indian Ocean dipole (IOD; section 4f). These differences are discussed and contextualized herein. As an added complexity, the nature of ENSO, IOD, and other phenomena are themselves changing as the climate system itself changes.

Finally, while there is already a large body of variables to monitor and understand climate, new variables and means of monitoring existing variables are continually developing, improving, and maturing. Rock glacier kinematics provides a new means of understanding the effects of interannual and longer-term variability in ground temperature (Sidebar 2.2). Data from a single cruise provide a snapshot of ocean acidification in the North Pacific (Sidebar 3.2), showing both effective regional monitoring and possibly a need for a more global quantification of this essential climate variable on the annual time scales. The *State of the Climate* continually catalogs new methods for monitoring essential climate variables and details where the global observation system can provide enhanced monitoring.

It is, of course, somewhat difficult to compare singular events and even annual means to climatic statistics when the climate itself is changing. There is a clear trend in most climate variables (Plate 1.1), but the magnitude of the trend is not always larger than the interannual variability. The difference in Plate 1.1 of this report from last year's report is nearly indistinguishable. However, the long-term, clear, consistent trends over the last 10, 50, or 150 years tracing the ongoing warming of our planet are striking. While it is important to have a yearly snapshot of the essential climate variables as a quick reference, the real value of the annual *State of the Climate* report is in placing singular events and annual means in the context of climate—both the long-term mean

(climate) and the long-term trend (climate change). The *State of the Climate* report enables us to understand the year's events in terms of climate trends versus interannual factors. The report also showcases enhanced understanding and new means of measuring essential climate variables as well as illustrates further need for enhanced monitoring of these variables.

This year, the latest report from the Intergovernmental Panel on Climate Change (IPCC), The Physical Science Basis, will be released, representing a multi-year effort by scientists across the globe to quantify and qualify climate change. The IPCC report provides a definitive long view on climate change. The *State of the Climate* report augments the IPCC report with a higher frequency cataloging of climate information, contextualization of each individual year's singular events and collective state, and advances the current interim (between IPCC reports) state of the science for many essential climate variables.

The layout of the *State of the Climate in 2020* is similar to previous years. Following this introduction (Chapter 1), Chapter 2 catalogs global climate, Chapter 3 the oceans, Chapter 4 the tropics, Chapters 5 and 6 the high latitudes (Arctic and Antarctic, respectively), and Chapter 7 other specific regions of the globe (North America, Central America/Caribbean, South America, Africa, Europe, and Oceania). Expanding the breadth of regional coverage this year are the additions of sections on Central Africa (section 7e3) and Central Asia (section 7g6). The Central Africa section includes information specific to Cameroon, Chad, Central Africa Republic, Democratic Republic of the Congo, Congo, Gabon, Equatorial Guinea, and São Tomé and Príncipe. Central Asia is defined as the region encompassing the countries of Afghanistan to the south; from east to west, Turkmenistan, Uzbekistan, Tajikistan, and Kyrgyzstan in the central part of the region; and Kazakhstan to the north. Finally, Chapter 8 is a listing of many (though not all) datasets used in the various sections of the *State of the Climate in 2020* and a link to dataset access and further information. Datasets are listed by essential climate variables with a reference to chapter(s) in which the particular dataset was used. Most (though not all) datasets are readily downloadable by the reader who would like to reproduce the results found in the *State of the Climate* report or investigate further.

A large number of the datasets listed in Chapter 8 are from climate reanalyses and satellite products. However, the cover of Chapter 8 depicts the Atlantic Tradewinds Ocean-Atmosphere Interaction Campaign (ATOMIC; datasets detailed in Pincus et al., 2021; Quinn et al., 2021), an observational effort to measure all possible variables involved in air–sea interaction and cloud characteristics. It was conducted over an area near the island of Barbados from January to February 2020, mainly utilizing NOAA ocean and air platforms, a companion to the EUREC4A European field campaign in the same region. The importance of ATOMIC to the *State of the Climate* report is the expectation that research on the co-located observations will lead to better understanding of air–sea interaction and cloud characteristics, informing and improving future model iterations that underlay the reanalyses, which are used in the *State of the Climate* reports.

Time series of major climate indicators are again presented in this introductory chapter. Many of these indicators are essential climate variables, originally defined by the World Meteorological Organization's Global Climate Observing System (GCOS 2003) and updated again by GCOS (2010). As their name indicates, these variables are essential for a full understanding of the changing climate system. However, some of them are not available on the immediate timescales of this report, and others, particularly those dealing with the living world, are outside the scope of this report.

Essential Climate Variables—T. BOYER, J. BLUNDEN, AND R. J. H. DUNN

The following variables are considered fully monitored in this report, in that there are sufficient spatial and temporal data, with peer-reviewed documentation to characterize them on a global scale:

- Surface atmosphere: air pressure, precipitation, temperature, water vapor, wind speed and direction
- Upper atmosphere: Earth radiation budget, temperature, water vapor, wind speed and direction
- Atmospheric composition: carbon dioxide, methane and other greenhouse gases, ozone
- Ocean physics: ocean surface heat flux, sea ice, sea level, surface salinity, sea surface temperature, subsurface salinity, subsurface temperature, surface currents, surface stress
- Ocean biogeochemistry: ocean color
- Ocean biogeosystems: plankton
- Land: albedo, river discharge, snow, fire, fraction of absorbed photosynthetically active radiation, groundwater, ice sheets and ice shelves, lakes, soil moisture

The following variables are considered partially monitored, in that there is systematic, rigorous measurement found in this report, but some coverage of the variable in time and space is lacking due to observing limitations or availability of data or authors:

- Atmospheric composition: aerosols properties, cloud properties, precursors of aerosol and ozone
- Ocean physics: subsurface currents
- Ocean biogeochemistry: inorganic carbon
- Land: above-ground biomass, anthropogenic greenhouse gas fluxes, glaciers, permafrost
- Surface atmosphere: surface radiation budget

The following variables are not yet covered in this report, or are outside the scope of it.

- Upper atmosphere: lightning
- Ocean physics: sea state
- Ocean biogeochemistry: nitrous oxide, nutrients, oxygen, transient tracers
- Ocean biogeosystems: marine habitat properties
- Land: anthropogenic water use, land cover, land surface temperature, latent and sensible heat fluxes, leaf area index, soil carbon

Acknowledgments

The editors thank the *BAMS* editorial staff, in particular Bryan Hanssen, who provided technical guidance, oversaw publication of the report, and continues to help us shepherd the report into a digital publishing era; Hannah Kleppner, who provided peer review support; and Nicole Rietmann, who oversaw the hundreds of citations and references this year; and the NCEI Graphics team for facilitating the construction of the report and executing the countless number of technical edits needed. We thank our technical editor Andrea Andersen for her dedication and attention to detail. We also express our gratitude to Dr. Michael Alexander, who, for the first time, served as the AMS special editor for this report. Finally, we thank all of the authors and chapter editors who provide these valuable contributions each year, always with an aim to improve and expand their analyses for the readers.

Plate 1.1. Global (or representative) average time series for essential climate variables through 2020. Anomalies are shown relative to the base period in parentheses although base periods used in other sections of the report may differ. The numbers in the square brackets that follow in this caption indicate how many reanalysis (blue), satellite (red), and in situ (black) datasets are used to create each time series in that order. (a) NH polar stratospheric ozone (Mar) [0,0,6]; (b) SH polar stratospheric ozone (Oct) [0,0,6]; (c) apparent transmission (Mauna Loa) [0,0,1]; (d) surface temperature [2,0,4]; (e) lower tropospheric temperature [3,2,3]; (f) lower stratospheric temperature [3,3,0]; (g) extremes (warm days (solid) and cool days (dotted)) [0,0,1]; (h) Arctic sea ice extent (max [solid]) and min [dashed]; [0,0,1]); (i) Antarctic sea ice extent (max [solid] and min [dashed]; [0,0,1]); (j) glacier cumulative mean specific balance [0,0,1]; (k) NH snow cover extent [0,1,1]; (l) lower stratospheric water vapor [0,0,1]; (m) cloudiness [0,11,0]; (n) total column water vapor – land [3,1,1]; (o) total column water vapor – ocean [3,2,0]; (p) upper tropospheric humidity [1,2,0]; (q) specific humidity – land [3,0,1]; (r) specific humidity – ocean [3,0,1]; (s) relative humidity – land [2,0,1]; (t) relative humidity – ocean [2,0,1]; (u) precipitation – land [0,0,3]; (v) precipitation – ocean [0,0,1]; (w) ocean heat content (0–700 m) [0,0,6]; (x) sea level rise [0,0,1]; (y) tropospheric ozone [0,1,0]; (z) tropospheric wind speed at 850 hPa for 20°–40°N [4,0,0]; (aa) land wind speed [0,0,1]; (ab) ocean wind speed [3,3,0]; (ac) biomass burning [0,2,0]; (ad) soil moisture [0,1,0]; (ae) terrestrial groundwater storage [0,1,0]; (af) fraction of absorbed photosynthetically active radiation (FAPAR) [0,1,0]; (ag) land surface albedo – visible (solid) and infrared (dashed) [0,1,0].

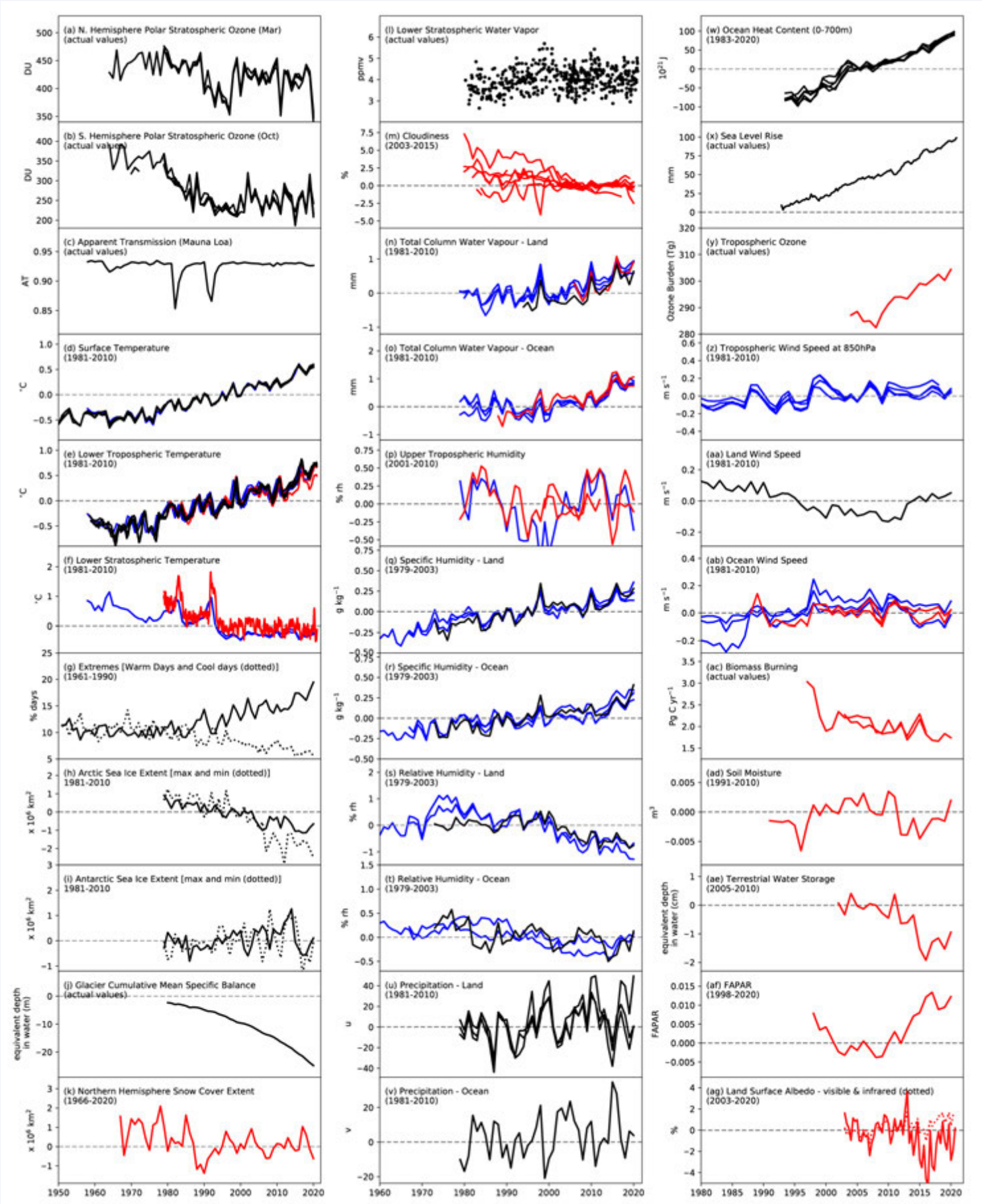
(a) N. Hemisphere Polar Stratospheric Ozone (Mar)
(actual values)
DU
(b) S. Hemisphere Polar Stratospheric Ozone (Oct)
(actual values)
DU
(c) Apparent Transmission (Mauna Loa)
(actual values)
AT
(d) Surface Temperature
(1981-2010)
°C
(e) Lower Tropospheric Temperature
(1981-2010)
°C
(f) Lower Stratospheric Temperature
(1981-2010)
°C
(g) Extremes [Warm Days and Cool days (dotted)]
(1961-1990)
% days
(h) Arctic Sea Ice Extent [max and min (dotted)]
1981-2010
x 10⁶ km²
(i) Antarctic Sea Ice Extent [max and min (dotted)]
1981-2010
x 10⁶ km²
(j) Glacier Cumulative Mean Specific Balance
(actual values)
equivalent depth in water (m)
(k) Northern Hemisphere Snow Cover Extent
(1966-2020)
x 10⁶ km²
(l) Lower Stratospheric Water Vapor
(actual values)
ppmv
(m) Cloudiness
(2003-2015)
%
(n) Total Column Water Vapour - Land
(1981-2010)
mm
(o) Total Column Water Vapour - Ocean
(1981-2010)
mm
(p) Upper Tropospheric Humidity
(2001-2010)
% rh
(q) Specific Humidity - Land
(1979-2003)
g kg⁻¹
(r) Specific Humidity - Ocean
(1979-2003)
g kg⁻¹
(s) Relative Humidity - Land
(1979-2003)
% rh
(t) Relative Humidity - Ocean
(1979-2003)
% rh
(u) Precipitation - Land
(1981-2010)
u
(v) Precipitation - Ocean
(1981-2010)
v
(w) Ocean Heat Content (0-700m)
(1983-2020)
10²¹ J
(x) Sea Level Rise
(actual values)
mm
(y) Tropospheric Ozone
(actual values)
Ozone Burden (Tg)
(z) Tropospheric Wind Speed at 850hPa
(1981-2010)
m s⁻¹
(aa) Land Wind Speed
(1981-2010)
m s⁻¹
(ab) Ocean Wind Speed
(1981-2010)
m s⁻¹
(ac) Biomass Burning
(actual values)
Pg C yr⁻¹
(ad) Soil Moisture
(1991-2010)
m³
(ae) Terrestrial Water Storage
(2005-2010)
equivalent depth in water (cm)
(af) FAPAR
(1998-2020)
FAPAR
(ag) Land Surface Albedo - visible & infrared (dotted)
(2003-2020)
%

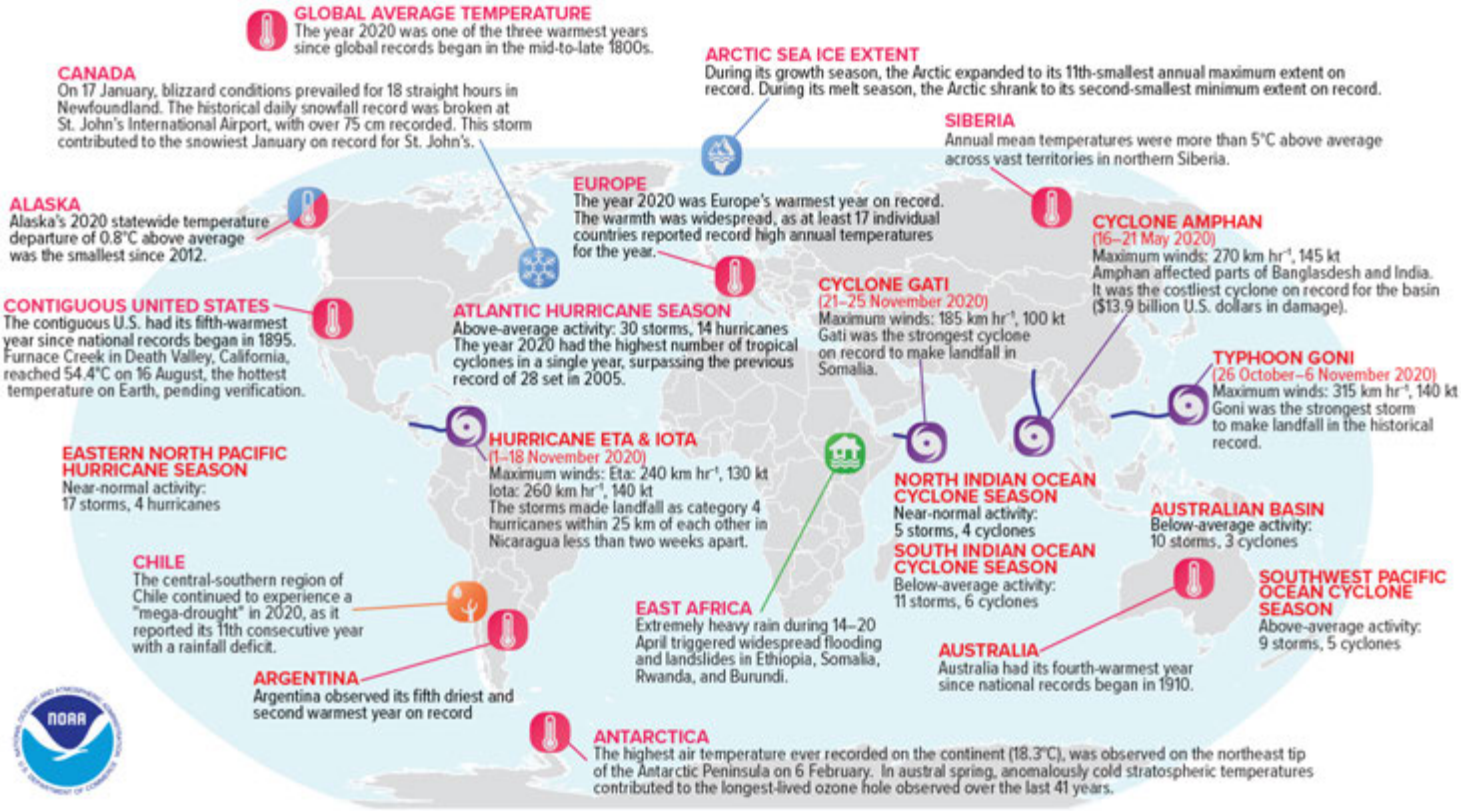

Fig. 1.1. Geographical distribution of selected notable climate anomalies and events in 2020.

STATE OF THE CLIMATE IN 2020

GLOBAL CLIMATE

R. J. H. Dunn, F. Aldred, N. Gobron, J. B Miller, and K. M. Willett, Eds.

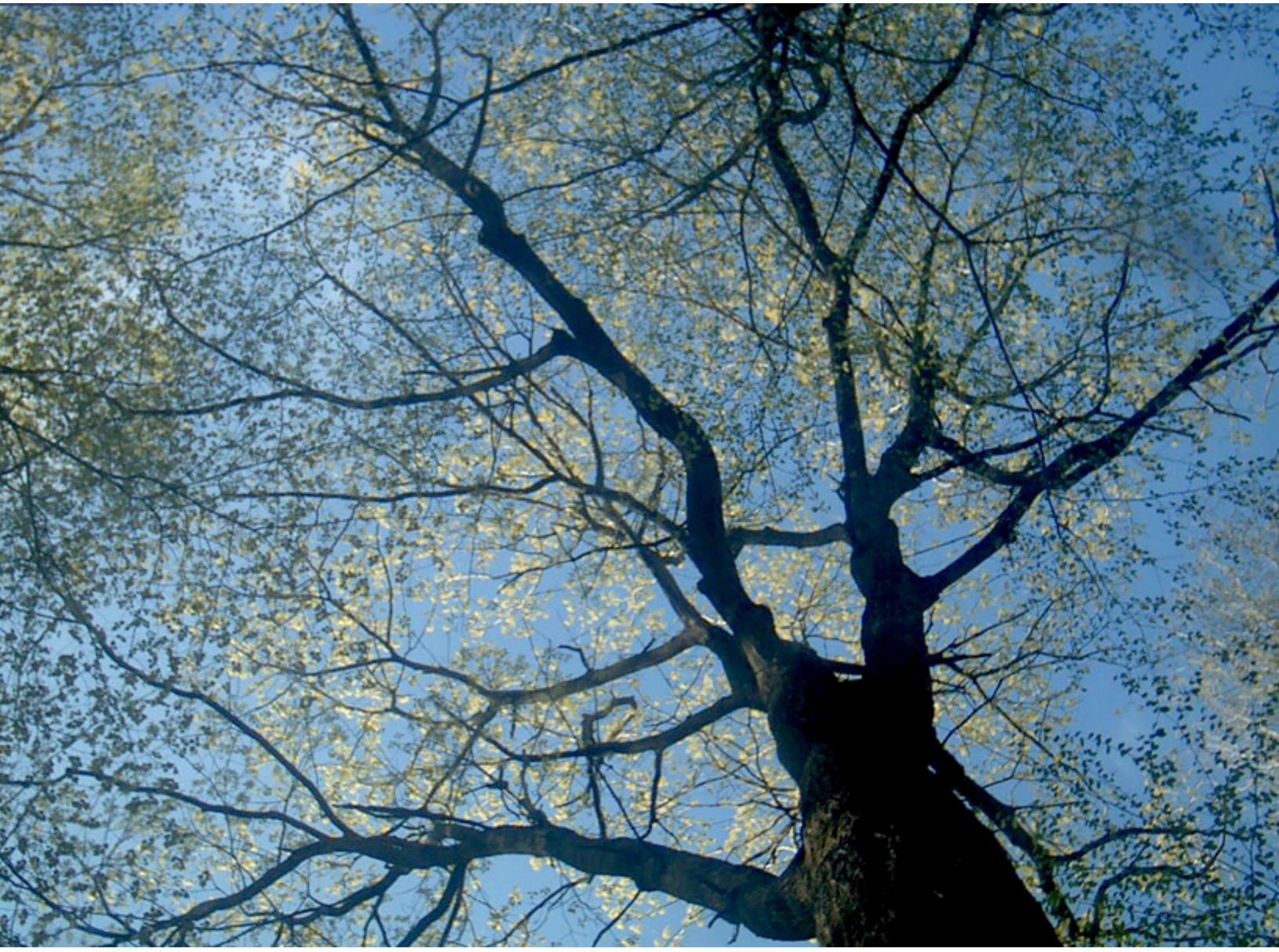

Special Online Supplement to the *Bulletin of the American Meteorological Society* Vol.102, No. 8, August, 2021

doi:10.1175/BAMS-D-21-0098.1

Corresponding author: Robert Dunn / robert.dunn@metoffice.gov.uk

STATE OF THE CLIMATE IN 2020
Global Climate

Editors

Jessica Blunden
Tim Boyer

Chapter Editors

Freya Aldred
Peter Bissolli
Howard J. Diamond
Matthew L. Druckenmiller
Robert J. H. Dunn
Catherine Ganter
Nadine Gobron
Gregory C. Johnson
Tim Li
Rick Lumpkin
Ademe Mekonnen
John B. Miller
Twila A. Moon
Ahira Sánchez-Lugo
Ted A. Scambos
Carl J. Schreck III
Sharon Stammerjohn
Richard L. Thoman
Kate M. Willett

Technical Editor

Andrea Andersen

***BAMS* Special Editor for Climate**

Michael A. Alexander

American Meteorological Society

Cover credit:
Caption: Spring leaf emergence at Harvard Forest, Petersham, MA, USA, exemplified by the Witness Tree (Mapes 2017), a century-old red oak (*Quercus rubra*). Image courtesy of the PhenoCam Network.

Mapes, L.M. *Witness Tree: Seasons of Change with a Century-Old Oak*. Bloomsbury USA, New York. 240 pp.

Global Climate is one chapter from the *State of the Climate in 2020* annual report and is available from https://doi.org/10.1175/BAMS-D-21-0098.1 Compiled by NOAA's National Centers for Environmental Information, *State of the Climate in 2020* is based on contributions from scientists from around the world. It provides a detailed update on global climate indicators, notable weather events, and other data collected by environmental monitoring stations and instruments located on land, water, ice, and in space.
The full report is available from https://doi.org/10.1175/2021BAMSStateoftheClimate.1.

How to cite this document:

Citing the complete report:
Blunden, J. and T. Boyer, Eds., 2021: "State of the Climate in 2020". *Bull. Amer. Meteor. Soc.*, **102** (8), Si–S475, https://doi.org/10.1175/2021BAMSStateoftheClimate.1.

Citing this chapter:
Dunn, R. J. H., F. Aldred, N. Gobron, J. B Miller, and K. M. Willett, Eds., 2021: Global Climate [in "State of the Climate in 2020"]. *Bull. Amer. Meteor. Soc.*, **102** (8), S11–S141, https://doi.org/10.1175/BAMS-D-21-0098.1.

Citing a section (example):
Tye, M. R., S. Blenkinsop, M. G. Bosilovich, M. G. Donat, I. Durre, A. J. Simmons, and M. Ziese, 2021: Land-based precipitation extremes [in "State of the Climate in 2020"]. *Bull. Amer. Meteor.*, **102** (8), S57–S60, https://doi.org/10.1175/BAMS-D-21-0098.1.

Editor and Author Affiliations (alphabetical by name)

Ades, M., European Centre for Medium-Range Weather Forecasts, Reading, United Kingdom
Adler, Robert, CMNS-Earth System Science Interdisciplinary Center, University of Maryland, College Park, Maryland
Aldred, F., Met Office Hadley Centre, Exeter, United Kingdom
Allan, Richard, P., Department of Meteorology and National Centre for Earth Observation, University of Reading, Reading, United Kingdom
Allan, Rob, Met Office Hadley Centre, Exeter, United Kingdom
Anderson, J., Department of Atmospheric and Planetary Science, Hampton University, Hampton, Virginia
Argüez, Anthony, NOAA/NESDIS National Centers for Environmental Information, Asheville, North Carolina
Arosio, C., University of Bremen, Bremen, Germany
Augustine, John A., NOAA/OAR Earth System Research Laboratory, Boulder, Colorado
Azorin-Molina, C., Centro de Investigaciones sobre Desertificación – Spanish National Research Council, Moncada (Valencia), Spain; and Regional Climate Group, Department of Earth Sciences, University of Gothenburg, Gothenburg, Sweden
Barichivich, J., Instituto de Geografía, Pontificia Universidad Católica de Valparaíso, Valparaíso, Chile
Beck, H. E., GloH2O, Almere, the Netherlands
Becker, Andreas, Global Precipitation Climatology Centre, Deutscher Wetterdienst, Offenbach, Germany
Bellouin, Nicolas, University of Reading, Reading, United Kingdom
Benedetti, Angela, European Centre for Medium-Range Weather Forecasts, Reading, United Kingdom
Berry, David I., National Oceanography Centre, Southampton, United Kingdom
Blenkinsop, Stephen, School of Engineering, Newcastle University, Newcastle-upon-Tyne, United Kingdom
Bock, Olivier, Université de Paris, Institut de physique du globe de Paris, CNRS, IGN, F-7500 Paris, France
Bodin, X., Laboratoire EDYTEM, CNRS/Université Savoie Mont-Blanc, Le Bourget-du-Lac, France
Bosilovich, Michael G., Global Modeling and Assimilation Office, NASA Goddard Space Flight Center, Greenbelt, Maryland
Boucher, Olivier, Sorbonne Université, Paris, France
Buehler, S. A., Meteorologisches Institut, Centrum für Erdsystem-und Nachhaltigkeitsforschung (CEN), Fachbereich Erdsystemwissenschaften, Universität Hamburg, Hamburg, Germany
Calmettes, B., Collecte Localisation Satellites (CLS), Ramonville Saint-Agne, France
Carrea, Laura, Department of Meteorology, University of Reading, Reading, United Kingdom
Castia, Laura, NOAA Climate Prediction Center, College Park, Maryland
Christiansen, Hanne H., Geology Department, University Centre in Svalbard, Longyearbyen, Norway
Christy, John R., The University of Alabama in Huntsville, Huntsville, Alabama
Chung, E.-S., Korea Polar Research Institute, Incheon, South Korea
Coldewey-Egbers, Melanie, DLR (German Aerospace Center) Oberpfaffenhofen, Wessling, Germany
Cooper, Owen R., Cooperative Institute for Research in Environmental Sciences, University of Colorado, Boulder, Colorado; NOAA Chemical Sciences Laboratory, Boulder, Colorado
Cornes, Richard C., National Oceanography Centre, Southampton, United Kingdom
Covey, Curt, Lawrence Livermore, National Laboratory, Livermore California
Cretaux, J.-F., CNES/LEGOS, UMR5566, Université de Toulouse, Toulouse, France
Crotwell, M., Cooperative Institute for Research in Environmental Sciences, University of Colorado, Boulder, Colorado; NOAA/OAR Global Monitoring Laboratory, Boulder, Colorado
Davis, Sean M., NOAA Chemical Sciences Laboratory, Boulder, Colorado
de Jeu, Richard A. M., VanderSat B.V., Haarlem, The Netherlands
Degenstein, Doug, University of Saskatchewan, Saskatoon, Saskatchewan, Canada
Delaloye, R., Department of Geosciences, University of Fribourg, Fribourg, Switzerland
Di Girolamo, Larry, University of Illinois at Urbana-Champaign, Illinois
Donat, Markus G., Barcelona Supercomputing Centre, Barcelona, Spain
Dorigo, Wouter A., TU Wien - Vienna University of Technology, Vienna, Austria
Dunn, Robert J. H., Met Office Hadley Centre, Exeter, United Kingdom
Durre, Imke, NOAA/NESDIS, National Center for Environmental Information, Asheville, North Carolina
Dutton, Geoff S., Cooperative Institute for Research in Environmental Sciences, University of Colorado, Boulder, Colorado; NOAA/OAR Global Monitoring Laboratory, Boulder, Colorado
Duveiller, Gregory, European Commission, Joint Research Centre, Ispra, Italy; currently at the Max Planck Institute for Biogeochemistry, Jena, Germany
Elkins, James W., NOAA/OAR Global Monitoring Laboratory, Boulder, Colorado
Fioletov, Vitali E., Environment and Climate Change Canada, Toronto, Canada
Flemming, Johannes, Copernicus Department, European Centre for Medium-Range Weather Forecasts, Reading, United Kingdom
Foster, Michael J., Cooperative Institute for Meteorological Satellite Studies, Space Science and Engineering Center, University of Wisconsin-Madison, Madison, Wisconsin
Frith, Stacey M., Science Systems and Applications, Inc., Lanham, Maryland; NASA Goddard Space Flight Center, Greenbelt, Maryland
Froidevaux, Lucien, Jet Propulsion Laboratory, California Institute of Technology, Pasadena, California
Garforth, J., Woodland Trust, Grantham, United Kingdom
Gentry, Matthew, Cooperative Institute for Research in Environmental Sciences, University of Colorado, Boulder, Colorado; NOAA/OAR Global Monitoring Laboratory, Boulder, Colorado
Gobron, Nadine, European Commission, Joint Research Centre, Ispra, Italy
Gupta, S. K., Science Systems and Applications, Inc. (SSAI), Hampton, Virginia
Hahn, S., TU Wien - Vienna University of Technology, Vienna, Austria
Haimberger, Leopold, Department of Meteorology and Geophysics, University of Vienna, Vienna, Austria
Hall, Brad D., NOAA/OAR Global Monitoring Laboratory, Boulder, Colorado
Harris, Ian, National Centre for Atmospheric Science (NCAS), University of East Anglia, Norwich, United Kingdom; Climatic Research Unit, School of Environmental Sciences, University of East Anglia, Norwich, United Kingdom
Hemming, D. L., Met Office Hadley Centre, Exeter, United Kingdom; Birmingham Institute of Forest Research, Birmingham University, Birmingham, United Kingdom
Hirschi, M., ETH Zürich, Zürich, Switzerland
Ho, Shu-pen (Ben), Center for Satellite Applications and Research, NOAA, College Park, Maryland
Hrbacek, F., Department of Geography, Masaryk University, Brno, Czechia
Hubert, Daan, Royal Belgian Institute for Space Aeronomy (BIRA-IASB), Brussels, Belgium

Editor and Author Affiliations (alphabetical by name)

Hurst, Dale F., Cooperative Institute for Research in Environmental Sciences, University of Colorado Boulder, Boulder, Colorado; NOAA/OAR Global Monitoring Laboratory, Boulder, Colorado
Inness, Antje, Copernicus Department, European Centre for Medium-Range Weather Forecasts, Reading, United Kingdom
Isaksen, K., Norwegian Meteorological Institute, Oslo, Norway
John, Viju O., EUMETSAT, Darmstadt, Germany
Jones, Philip D., Climatic Research Unit, School of Environmental Sciences, University of East Anglia, Norwich, United Kingdom
Junod, Robert, Earth System Science Center (ESSC), University of Alabama in Huntsville, Huntsville, Alabama
Kaiser, J. W., Satellite-based Climate Monitoring Unit, Deutscher Wetterdienst, Offenbach am Main, Germany
Kaufmann, V., Institute of Geodesy, Working Group Remote Sensing and Photogrammetry, Graz University of Technology, Graz, Austria
Kellerer-Pirklbauer, A., Institute of Geography and Regional Science, Cascade - The Mountain Processes and Mountain Hazards Group, University of Graz, Graz, Austria
Kent, Elizabeth C., National Oceanography Centre, Southampton, United Kingdom
Kidd, R., Earth Observation Data Centre (EODC), Vienna, Austria
Kim, Hyungiun, Moon Soul Graduate School of Future Strategy, Korea Advanced Institute of Science and Technology (KAIST), Daejeon, South Korea Institute of Industrial Science, The University of Tokyo, Tokyo, Japan
Kipling, Z., European Centre for Medium-Range Weather Forecasts, Reading, United Kingdom
Koppa, A., Hydro-Climate Extremes Lab (H-CEL), Ghent University, Ghent, Belgium
Kraemer, B. M., IGB Leibniz Institute for Freshwater Ecology and Inland Fisheries, Berlin, Germany
Kratz, D. P., NASA Langley Research Center, Hampton, Virginia
Lan, Xin, Cooperative Institute for Research in Environmental Sciences, University of Colorado, Boulder, Colorado; NOAA/OAR Global Monitoring Laboratory, Boulder, Colorado
Lantz, Kathleen O., NOAA/OAR Earth System Research Laboratory, Boulder, Colorado
Lavers, D., European Centre for Medium-Range Weather Forecasts, Reading, United Kingdom
Loeb, Norman G., NASA Langley Research Center, Hampton, Virginia
Loyola, Diego, DLR (German Aerospace Center) Oberpfaffenhofen, Wessling, Germany
Madelon, R., CESBIO (Université Toulouse 3, CNES, CNRS, INRAE, IRD), Toulouse, France
Mayer, Michael, University of Vienna, Vienna, Austria and European Centre for Medium-Range Weather Forecasts, Reading, United Kingdom
McCabe, M. F., Division of Biological and Environmental Sciences and Engineering, King Abdullah University of Science and Technology, Thuwal, Saudi Arabia
McVicar, Tim R., CSIRO Land and Water, Canberra, Australian Capital Territory; Australian Research Council Centre of Excellence for Climate Extremes, Sydney, New South Wales, Australia
Mears, Carl A., Remote Sensing Systems, Santa Rosa, California
Merchant, Christopher J., Department of Meteorology, University of Reading, Reading , United Kingdom
Miller, John B., NOAA/OAR Global Monitoring Laboratory, Boulder, Colorado,
Miralles, Diego G., Hydro-Climate Extremes Lab (H-CEL), Ghent University, Ghent, Belgium
Moesinger, L., TU Wien – University of Technology, Vienna, Austria
Montzka, Stephen A., NOAA/OAR Global Monitoring Laboratory, Boulder, Colorado
Morice, Colin, Met Office Hadley Centre, Exeter, United Kingdom
Mösinger, L., TU Wien – University of Technology, Vienna, Austria
Mühle, Jens, Scripps Institution of Oceanography, University of California, San Diego, La Jolla, California
Nicolas, Julien P., European Centre for Medium-Range Weather Forecasts, Reading, United Kingdom
Noetzli, Jeannette, WSL Institute for Snow and Avalanche Research SLF, Davos-Dorf, Switzerland
Noll, Ben, National Institute of Water and Atmospheric Research (NIWA), New Zealand
O'Keefe, J., The Harvard Forest, Harvard University, Petersham, Massachusetts
Osborn, Tim J., Climatic Research Unit, School of Environmental Sciences, University of East Anglia, Norwich, United Kingdom
Park, T., NASA Ames Research Center, Moffett Field, California; Bay Area Environmental Research Institute, Moffett Field, California
Pasik, A. J., TU Wien – Vienna University of Technology, Vienna, Austria
Pellet, C., Department of Geosciences, University of Fribourg, Fribourg, Switzerland
Pelto, Maury S., Nichols College, Dudley, Massachusetts
Perkins-Kirkpatrick, S. E., University of New South Wales, Canberra, Australia
Petron, G., Cooperative Institute for Research in Environmental Sciences, University of Colorado, Boulder, Colorado; NOAA/OAR Global Monitoring Laboratory, Boulder, Colorado
Phillips, Coda, Cooperative Institute for Meteorological Satellite Studies, Space Science and Engineering Center, University of Wisconsin-Madison, Madison, Wisconsin
Po-Chedley, S., Program for Climate Model Diagnosis and Intercomparison, Lawrence Livermore National Laboratory, Livermore, California
Polvani, L., Columbia University, New York, New York
Preimesberger, W., TU Wien – Vienna University of Technology, Vienna, Austria
Rains, D. G., Hydro-Climate Extremes Lab (H-CEL), Ghent University, Ghent, Belgium
Randel, W. J., National Center for Atmospheric Research, Boulder, Colorado
Rayner, Nick A., Met Office Hadley Centre, Exeter, United Kingdom
Rémy, Samuel, HYGEOS, Lille, France
Ricciardulli, L., Remote Sensing Systems, Santa Rosa, California
Richardson, A. D., School of Informatics, Computing, and Cyber Systems and Center for Ecosystem Science and Society, Northern Arizona University, Flagstaff, Arizona
Robinson, David A., Rutgers University, Piscataway, New Jersey
Rodell, Matthew, Hydrological Sciences Laboratory, NASA Goddard Space Flight Center, Greenbelt, Maryland
Rodríguez-Fernández, N. J., CESBIO (Université Toulouse 3, CNES, CNRS, INRAE, IRD), Toulouse, France
Rosenlof, K.H., NOAA Chemical Sciences Laboratory, Boulder, Colorado
Roth, C., University of Saskatchewan, Saskatoon, Canada
Rozanov, A., University of Bremen, Bremen, Germany
Rutishäuser, T., Institute of Geography and Oeschger Center, University of Berne, Berne, Switzerland
Sánchez-Lugo, Ahira, NOAA/NESDIS National Centers for Environmental Information, Asheville, North Carolina
Sawaengphokhai, P., Science Systems and Applications, Inc. (SSAI), Hampton, Virginia

Editor and Author Affiliations (alphabetical by name)

Scanlon, T., TU Wien – University of Technology, Vienna, Austria
Schenzinger, Verena, Medical University of Innsbruck, Innsbruck, Austria
Schlegel, R. W., Sorbonne Université, CNRS, Villefranche-sur-mer, France
Sharma, S., York University, Toronto, Ontario, Canada
Shi, Lei, NOAA/NESDIS, National Centers for Environmental Information, Asheville, North Carolina, United States
Simmons, Adrian J., European Centre for Medium-Range Weather Forecasts, Reading, United Kingdom
Siso, Carolina, Cooperative Institute for Research in Environmental Sciences, University of Colorado, Boulder, Colorado, USA, and NOAA/OAR Global Monitoring Laboratory, Boulder, Colorado
Smith, Sharon L., Geological Survey of Canada, Natural Resources Canada, Ottawa, Canada
Soden, B. J., University of Miami Rosenstiel School of Marine and Atmospheric Science (RSMAS), Key Biscayne, Florida, United States
Sofieva, Viktoria, Finnish Meteorological Institute (FMI), Helsinki, Finland
Sparks, T. H., Poznań University of Life Sciences, Poznań, Poland
Stackhouse, Jr., Paul W., NASA Langley Research Center, Hampton, Virginia
Steinbrecht, Wolfgang, German Weather Service (DWD), Hohenpeissenberg, Germany
Stengel, Martin, Deutscher Wetterdienst, Offenbach, Germany
Streletskiy, Dimitri A., George Washington University, Washington, D.C.
Sun-Mack, Sunny, Science Systems and Applications, Inc. (SSAI), Hampton, Virginia
Tans, P., NOAA/OAR Global Monitoring Laboratory, Boulder, Colorado
Thackeray, S. J., Centre for Ecology and Hydrology, Lancaster, United Kingdom
Thibert, E., Université Grenoble Alpes, INRAE, UR ETGR, Grenoble, France
Tokuda, D., Institute of Industrial Science, The University of Tokyo, Tokyo, Japan
Tourpali, Kleareti, Aristotle University, Thessaloniki, Greece
Tye, Mari R., National Center for Atmospheric Research, Boulder, Colorado
van der A, Ronald, Royal Netherlands Meteorological Institute (KNMI), DeBilt, The Netherlands
van der Schalie, Robin, VanderSat B.V., Haarlem, The Netherlands
van der Schrier, Gerard, Royal Netherlands Meteorological Institute, De Bilt, The Netherlands
van der Vliet, M., VanderSat B.V., Haarlem, The Netherlands
van der Werf, Guido R., Faculty of Science, Vrije Universiteit Amsterdam, Amsterdam, Netherlands
Vance, A., Met Office Hadley Centre, Exeter, United Kingdom
Vernier, Jean-Paul, National Institute of Aerospace/NASA Langley Research Center, Hampton, Virginia
Vimont, Isaac J., Cooperative Institute for Research in Environmental Sciences, University of Colorado Boulder, and NOAA/OAR Global Monitoring Laboratory, Boulder, Colorado
Vömel, Holger, Earth Observing Laboratory, National Center for Atmospheric Research, Boulder, Colorado
Vose, Russell S., NOAA/NESDIS, National Center for Environmental Information, Asheville, North Carolina
Wang, Ray, Georgia Institute of Technology, Atlanta, Georgia
Weber, Markus, University of Bremen, Bremen, Germany
Wiese, David, Jet Propulsion Laboratory, California Institute of Technology, Pasadena, California
Wilber, Anne C., Science Systems and Applications, Inc. (SSAI), Hampton, Virginia
Wild, Jeanette D., NOAA/NWS, Climate Prediction Center, College Park, Maryland; ESSIC/University of Maryland, College Park, Maryland
Willett, Kate M., Met Office Hadley Centre, Exeter, United Kingdom
Wong, Takmeng, NASA Langley Research Center, Hampton, Virginia
Woolway, R. Iestyn, European Space Agency Climate Office, ECSAT, Harwell Campus, Didcot, United Kingdom
Xinjia, Zhou, Global Science and Technology, Inc., Greenbelt, Maryland
Yin, Xungang, NOAA/NESDIS, NOAA National Centers for Environmental Information, Asheville, North Carolina
Zhao, Guangyu, University of Illinois at Urbana-Champaign, Illinois
Zhao, Lin, School of Geographical Sciences, Nanjing University of Information Science & Technology, Nanjing, China
Ziemke, Jerry R., Goddard Earth Sciences Technology and Research, Morgan State University, Baltimore, Maryland; NASA Goddard Space Flight Center, Greenbelt, Maryland
Ziese, Markus, Global Precipitation Climatology Centre, Deutscher Wetterdienst, Offenbach am Main, Germany
Zotta, R. M., TU Wien – University of Technology, Vienna, Austria

Editorial and Production Team

Allen, Jessicca, Graphics Support, Cooperative Institute for Satellite Earth System Studies, North Carolina State University, Asheville, North Carolina
Andersen, Andrea, Technical Editor, Innovative Consulting Management Services, LLC, NOAA/NESDIS National Centers for Environmental Information, Asheville, North Carolina
Hammer, Gregory, Content Team Lead, Communications and Outreach, NOAA/NESDIS National Centers for Environmental Information, Asheville, North Carolina
Love-Brotak, S. Elizabeth, Lead Graphics Production, NOAA/NESDIS National Centers for Environmental Information, Asheville, North Carolina
Misch, Deborah J., Graphics Support, Innovative Consulting Management Services, LLC, NOAA/NESDIS National Centers for Environmental Information, Asheville, North Carolina
Riddle, Deborah B., Graphics Support, NOAA/NESDIS National Centers for Environmental Information, Asheville, North Carolina
Veasey, Sara W., Visual Communications Team Lead, Communications and Outreach, NOAA/NESDIS National Centers for Environmental Information, Asheville, North Carolina

2. Table of Contents

2. Table of Contents

*Please refer to Chapter 8 (Relevant datasets and sources) for a list of all climate variables and datasets used in this chapter for analyses, along with their websites for more information and access to the data.

2. GLOBAL CLIMATE

R. J. H. Dunn, F. Aldred, N. Gobron, J. B Miller, and K. M. Willett, Eds.

a. Overview—R. J. H. Dunn, F. Aldred, N. Gobron, J. B Miller, and K. M. Willett

For reasons other than the climate, 2020 was an extraordinary year. The COVID-19 pandemic has affected almost all of us, changing the lives of many people around the globe. While the economic disruption associated with COVID-19 led to modest estimated reductions of 6–7% (e.g., le Quere et al. 2020; Friedlingstein et al. 2020; BP Statistical Review of the World Energy 2021) in global anthropogenic carbon dioxide (CO_2) emissions, atmospheric CO_2 levels continued to grow rapidly—a reminder of its very long residence time in the atmosphere and the challenge of reducing atmospheric CO_2. As we show in this chapter, the climate has continued to respond to the resulting warming from these increases in CO_2 and other greenhouse gases such as methane and nitrous oxide, which also experienced record increases in 2020.

The year 2020 was one of the three warmest since records began in the mid-to-late 1800s, with global surface temperatures around 0.6°C above the 1981–2010 average, despite the El Niño–Southern Oscillation progressing from neutral to La Niña conditions by August (see section 4b). Lower tropospheric temperatures matched those from 2016, the previous warmest year. Meanwhile, stratospheric temperatures continued to cool as a result of anthropogenic CO_2 increases. Along with the above-average surface temperatures, an unprecedented (since instrumental records began) geographic spread of heat waves and warm spells occurred. Antarctica observed its highest temperature on record (18.3°C) at Esperanza in February. In August, Death Valley, California, reported the highest temperature observed anywhere on Earth since 1931 (preliminary value of 54.4°C).

Consequently, many permafrost measurement sites experienced their highest temperatures on record; Northern Hemisphere (NH) snow cover was below the 51-year average and the fourth-least extensive on record. Glaciers in alpine regions experienced their 33rd consecutive year of negative mass balance and 12th year of average losses of more than 500 mm depth. On average, NH lakes froze over 3 days later and thawed 5.5 days earlier than the 1981–2010 average during the 2019/20 winter, which was the third-shortest ice cover season since 1979/80.

The atmosphere responded to higher temperatures accordingly by holding more water. Total column water vapor was high relative to the 1981–2010 average, ranging from 0.75 to 1.06 mm over ocean and 0.58 to 0.94 mm over land, but did not reach the record values of 2016. At the surface, specific humidity over oceans was at record high levels (0.23 to 0.41 g kg^{-1}) and was well above average over land (0.14 to 0.36 g kg^{-1}). Conversely, relative humidity was well below average over land (–1.28 to –0.68 %rh), continuing the long-term declining trend. Precipitation increased compared to 2019, driven largely by land values, but there were few exceptional extreme precipitation events, coupled with below-average cloudiness over most of the land. More lakes showed positive water level anomalies than 2019, and in East Africa, Lake Victoria's level rose by over a meter due to a wet long-rains season. Soil moisture and terrestrial water storage showed stronger regional variations than in previous years, with East Africa and India being especially moist. Global drought area continued to increase for most of the year, reaching a peak in October, with the third-highest global land area experiencing extreme drought according to the Palmer Drought

Severity Index (6.8%). Despite progression to a neutral Indian Ocean dipole (IOD) this year, from a strongly positive IOD in 2019 (see section 4h), the western Indian Ocean and East Africa showed above-average hydrological cycle anomalies generally, including upper tropospheric humidity.

Greenhouse gas levels continued to rise, with the three primary greenhouse gases, CO_2, CH_4, and N_2O, all reaching their highest levels in at least 800,000 years. Radiative forcing from the long-lived greenhouse gases also reached a new record level of 3.2 W m^{-2}, with CO_2 being responsible for a large majority of the total. Tropospheric ozone, another greenhouse gas (although shorter lived and not well-mixed throughout the atmosphere), continued a modest upward trend, which was dominated by trends over and downwind of Asia. Stratospheric ozone, on the other hand, exhibited unusually large negative anomalies, especially in the Arctic and Antarctic. These large ozone depletions resulted mainly from stable polar vortices despite continued reduction in equivalent effective stratospheric chlorine, as calculated from tropospheric values of ozone-depleting substances.

COVID-19 impacts on the troposphere, at least at large spatial scales, were not readily apparent in 2020 anomalies. Modest anthropogenic CO_2 emissions reductions of perhaps 6–7% were too small to be identified on a background of large interannual CO_2 variability driven by the terrestrial biosphere. Carbon monoxide (CO) and aerosol optical depth anomalies could also not be clearly tied to COVID-19-related emissions reductions. However, significant CO and aerosol anomalies related to large fires in southeastern Australia, the western United States, and Siberia were evident.

The warmer temperatures were also felt in the biosphere, with an earlier start of season, later end of season, and hence, longer growing season as measured by the normalized difference vegetation index, for example, the United Kingdom had the earliest "first leaf" of the Pedunculate oak in a 20-year series. Anomalies of vegetation productivity reached a record positive peak in the NH. Overall, 2020 saw one of the lowest fire years in the record but regionally some locations experienced extreme fire activity, notably southeastern Australia, the Siberian Arctic, and western United States, as noted above.

Three new measurements are included as sidebars in this year's report. Night marine air temperature (NMAT) provides a useful independent comparison against sea surface temperature datasets to explore ongoing warming over oceans. Available NMAT observations (and marine humidity) have declined from around 7000 Voluntary Observing Ships in the 1980s to around 1000 at present, severely endangering our monitoring ability. Extending our cryosphere coverage, rock glacier kinematics, which is linked to the state of the permafrost, shows speeds in 2020 in the European Alps close to the maximum recorded. Increasing our monitoring of the biosphere, the final sidebar outlines the use of passive microwave satellite measurements for determining the vegetation properties via the amount of attenuation (the vegetation optical depth).

Time series and anomaly maps for many of the variables in this chapter are shown in Plates 1.1 and 2.1, respectively.

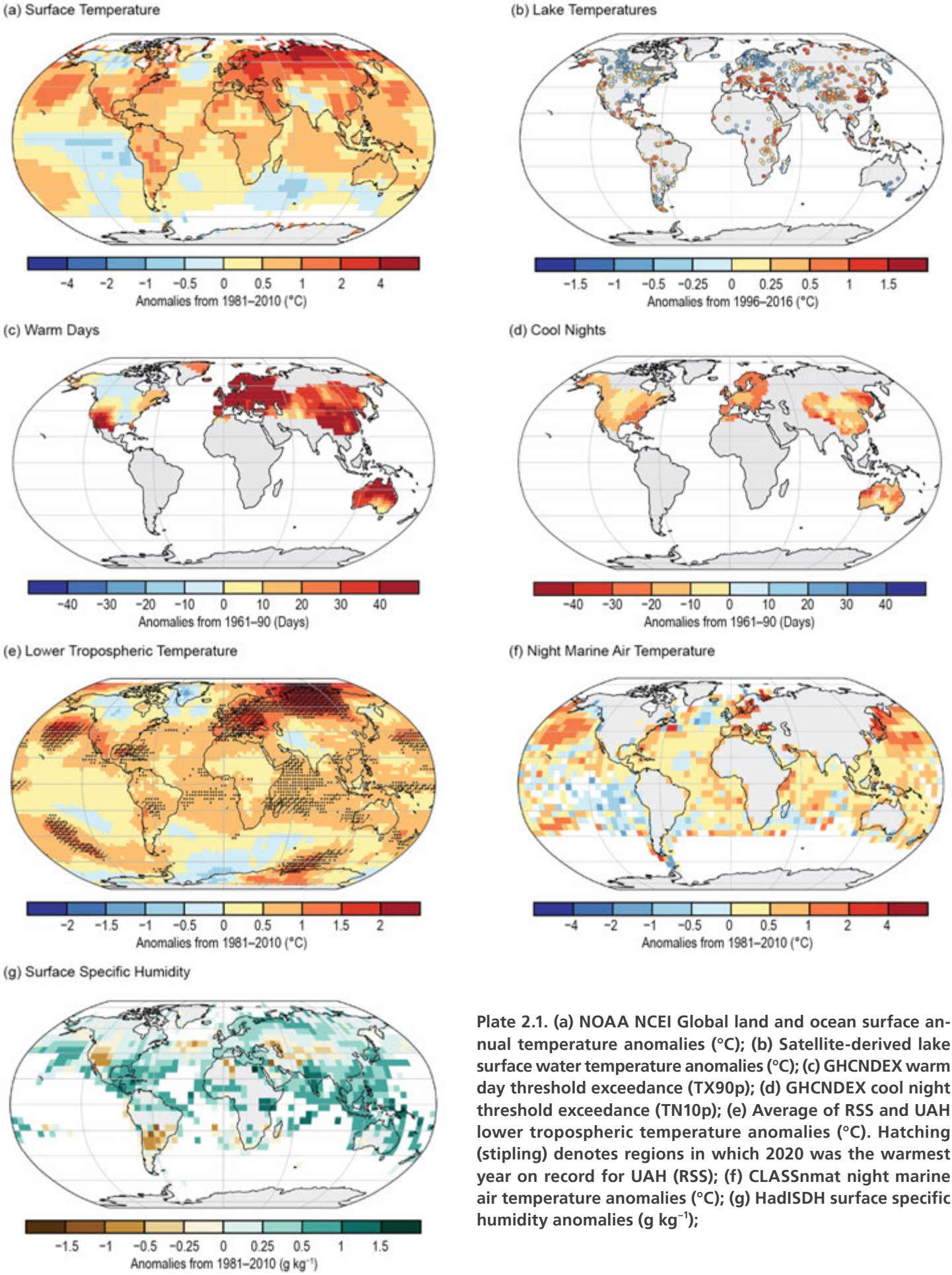

Plate 2.1. (a) NOAA NCEI Global land and ocean surface annual temperature anomalies (°C); (b) Satellite-derived lake surface water temperature anomalies (°C); (c) GHCNDEX warm day threshold exceedance (TX90p); (d) GHCNDEX cool night threshold exceedance (TN10p); (e) Average of RSS and UAH lower tropospheric temperature anomalies (°C). Hatching (stipling) denotes regions in which 2020 was the warmest year on record for UAH (RSS); (f) CLASSnmat night marine air temperature anomalies (°C); (g) HadISDH surface specific humidity anomalies (g kg^{-1});

(h) Surface Relative Humidity

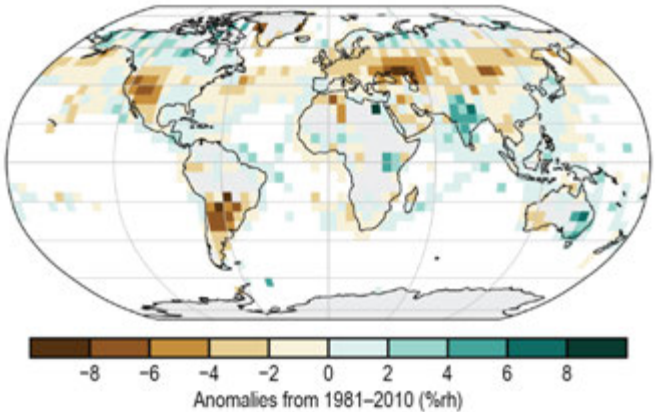

(i) Total Column Water Vapor

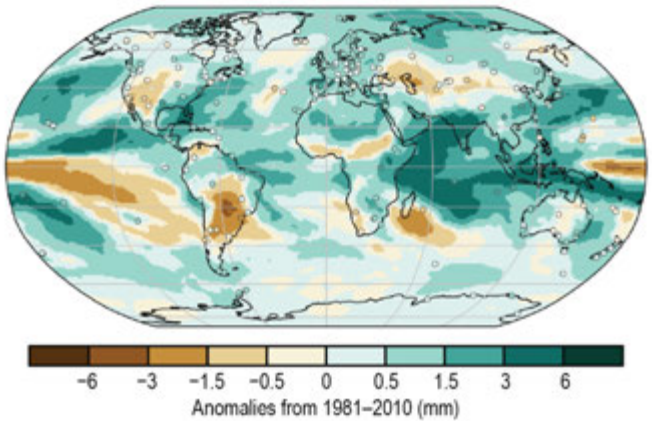

(j) Upper Tropospheric Humidity

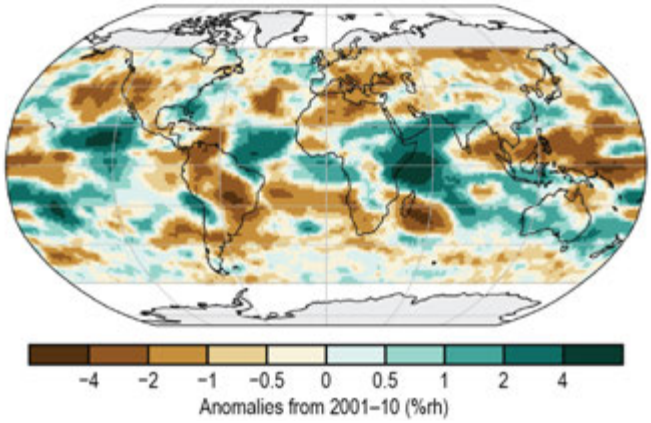

(k) Precipitation

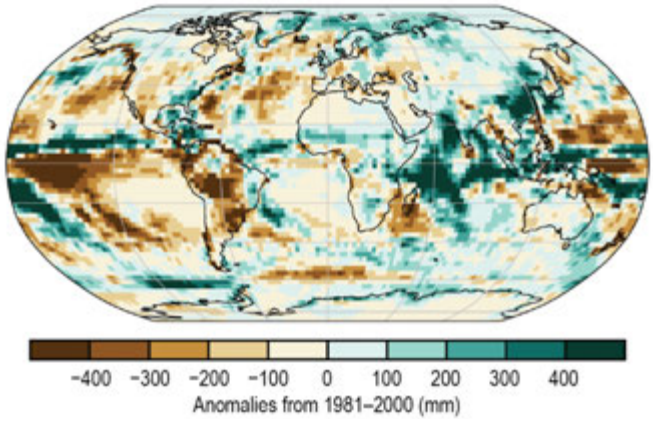

(l) Rx1day Anomalies

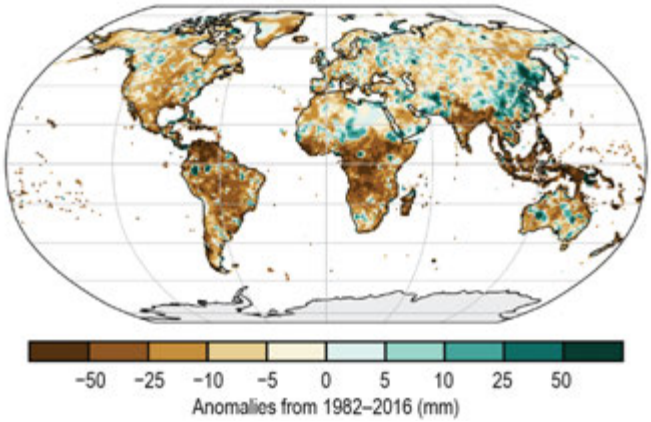

(m) Lake Water Level

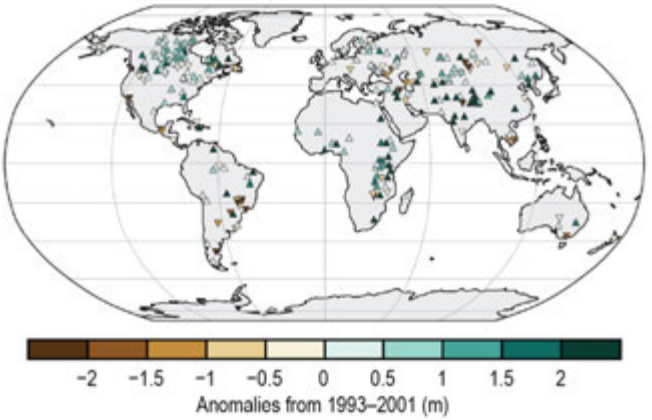

(n) Cloudiness

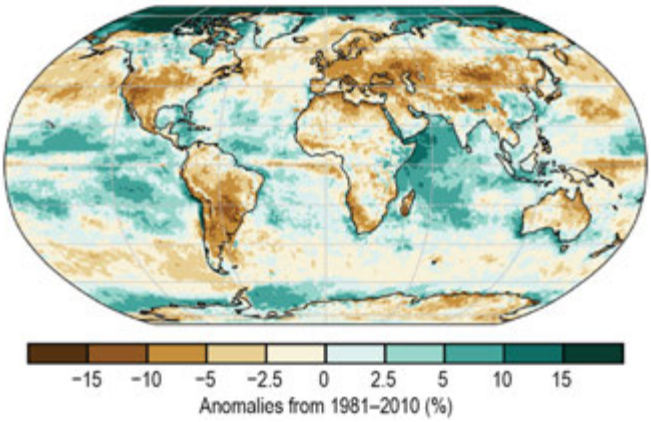

Plate 2.1. (cont.) (h) HadISDH surface relative humidity anomalies (%rh); (i) ERA5 TCWV anomalies (mm). Data from GNSS stations are plotted as filled circles; (j) "All sky" microwave-based UTH anomalies (%rh); (k) GPCP v2.3 annual mean precipitation anomalies (mm yr^{-1}); (l) GPCC maximum 1-day (Rx1day) annual precipitation anomalies (mm); (m) Lake water level anomalies (m); (n) PATMOS-x/AVHRR+HIRS global cloudiness anomalies (%);

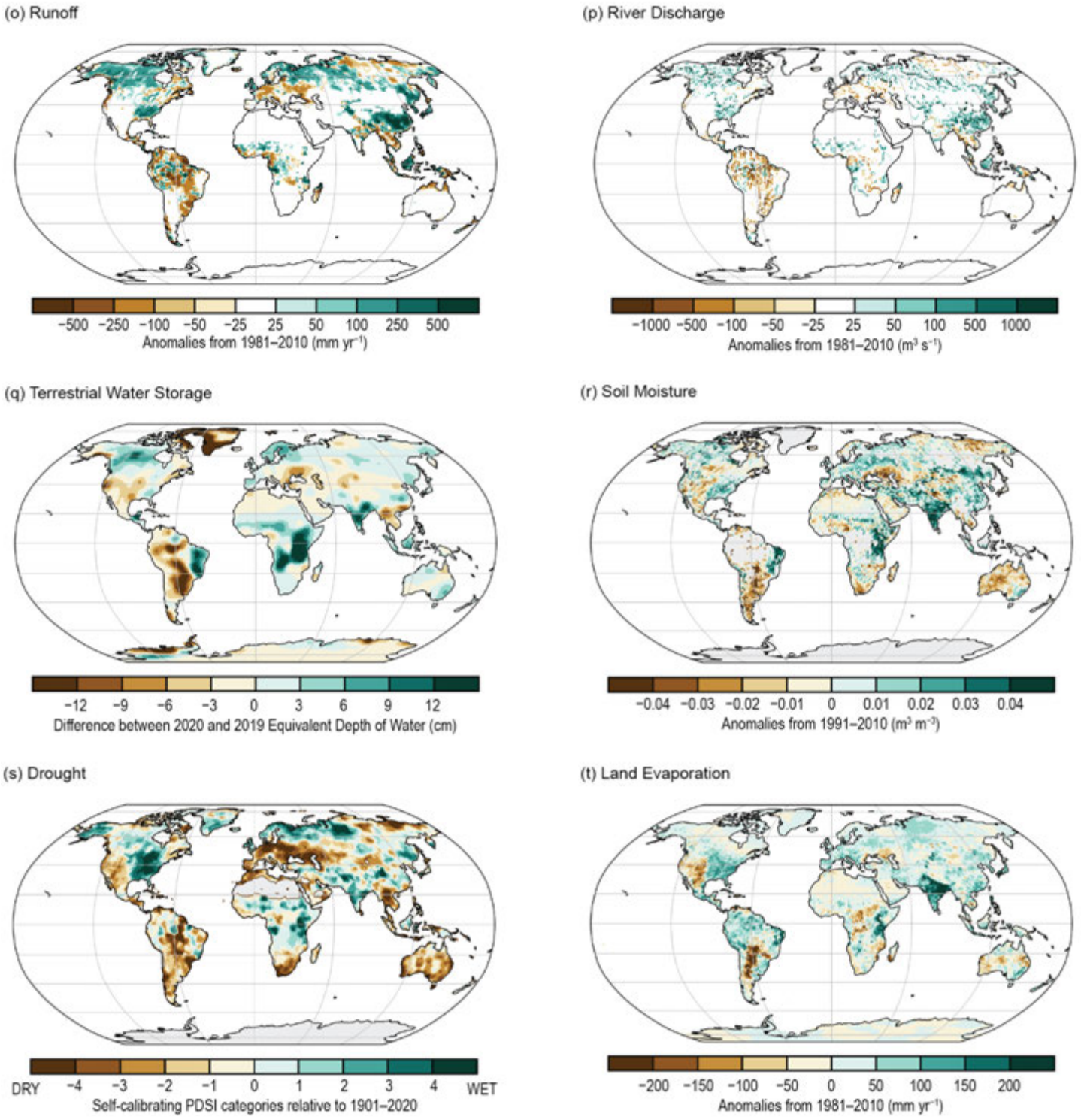

Plate 2.1. (cont.) (o) ELSE (Ensemble Land State Estimator) global distribution of runoff anomalies (mm yr^{-1}); (p) ELSE global distribution of river discharge anomalies (m^3 s^{-1}); (q) GRACE and GRACE-FO difference in annual-mean terrestrial water storage between 2019 and 2020 (cm); (r) ESA CCI average surface anomalies (m^3 m^{-3}); (s) Mean scPDSI for 2020. Droughts are indicated by negative values (brown), wet episodes by positive values (green); (t) GLEAM land evaporation anomalies (mm yr^{-1});

(u) Sea Level Pressure

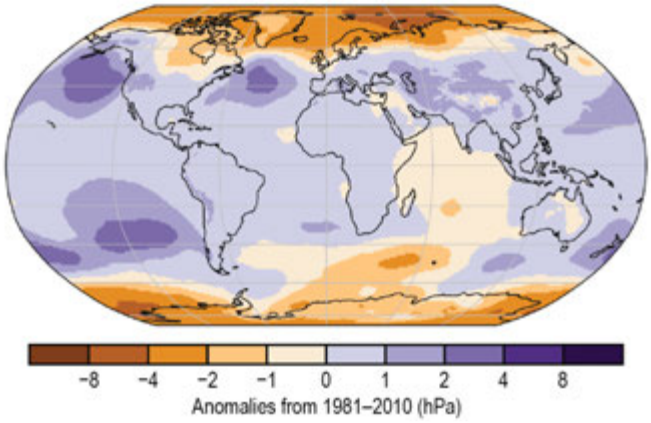

(v) Surface Winds

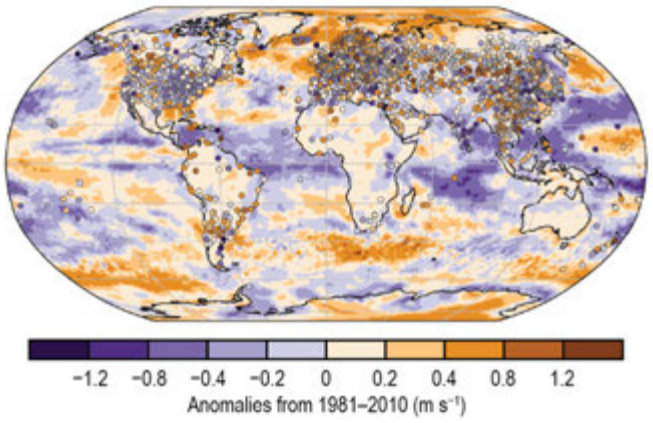

(w) Upper Air (850-hPa) Northward Winds (SOND)

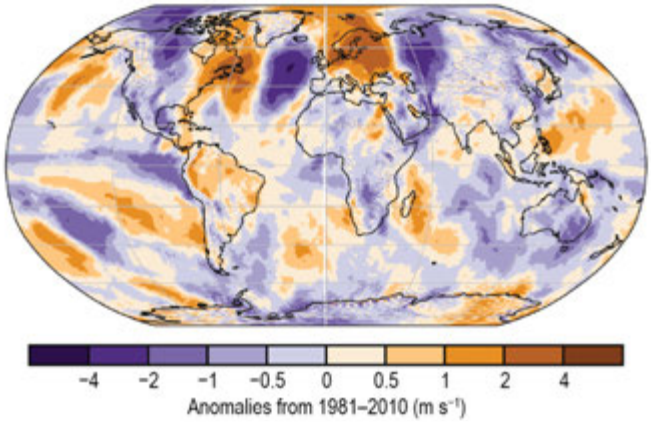

(x) Total Aerosol

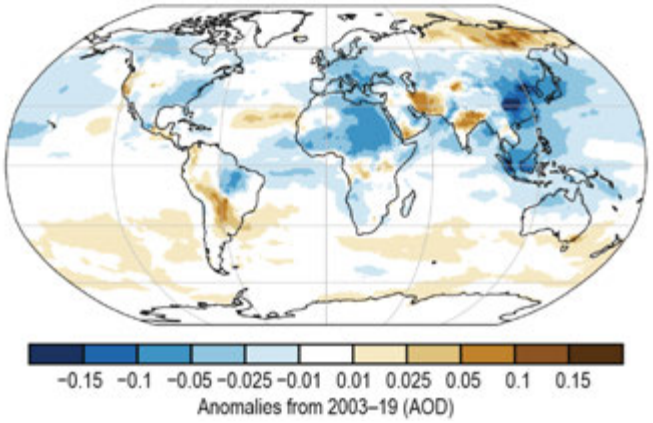

(y) AOD Ratio

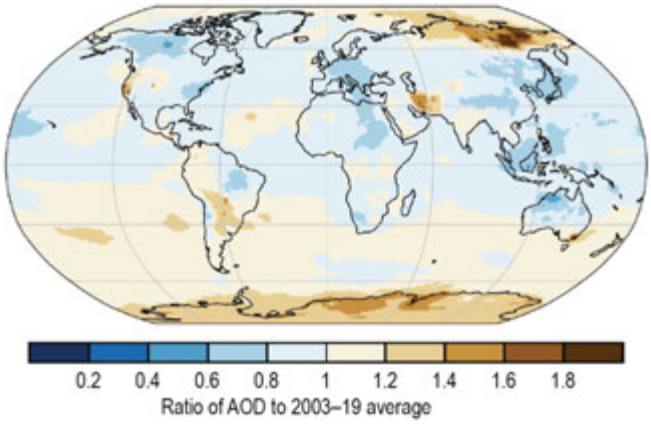

(z) Extreme Aerosol Days

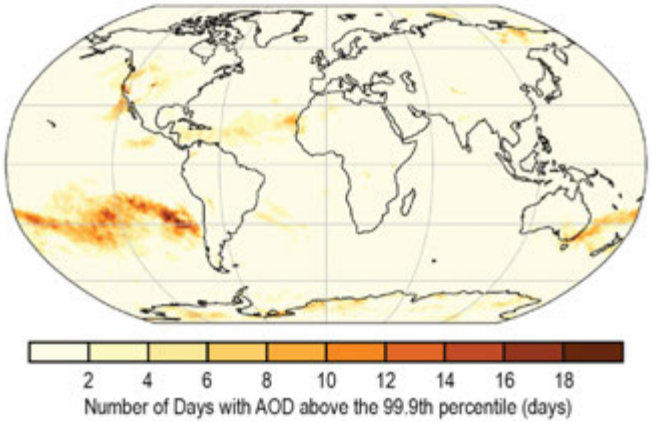

(aa) Stratospheric (Total Column) Ozone

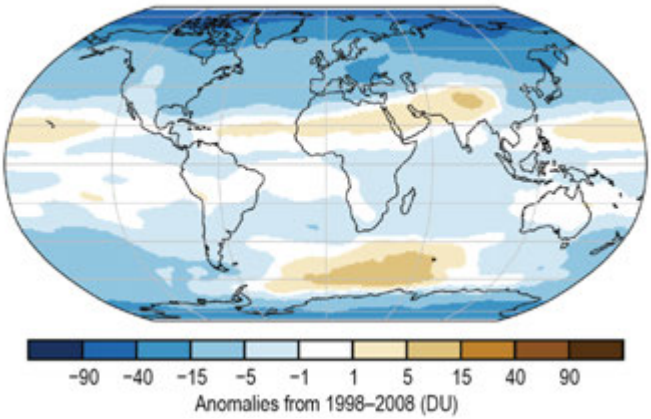

Plate 2.1. (cont.) (u) ERA5 surface pressure anomalies (hPa); (v) Surface wind speed anomalies (m s^{-1}) from the observational HadISD3 dataset (land, circles), the MERRA-2 reanalysis output (land, shaded areas), and RSS satellite observations (ocean, shaded areas); (w) ERA5 Sep–Dec average 850-hPa northward wind speed anomalies (m s^{-1}); (x) Total aerosol optical depth (AOD) anomalies at 550 nm; (y) Ratio of total AOD at 550 nm in 2020 relative to 2003–19; (z) Number of days with AOD above the 99.9th percentile; (aa) GOME2 total column ozone anomalies (DU; using GOME, SCIAMACHY, GOME-2A and -2B [GSG]);

(ab) OMI/MLS Tropospheric Column Ozone

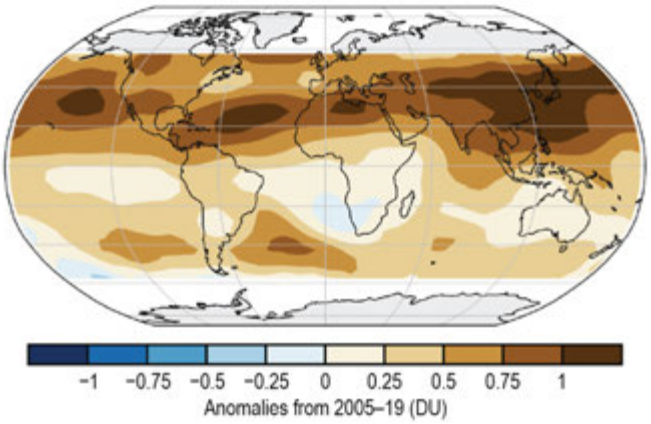

(ac) Carbon Monoxide

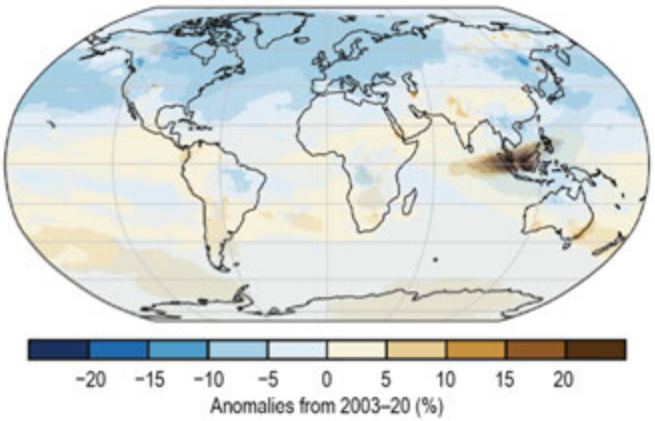

(ad) Land Surface Albedo in the Visible

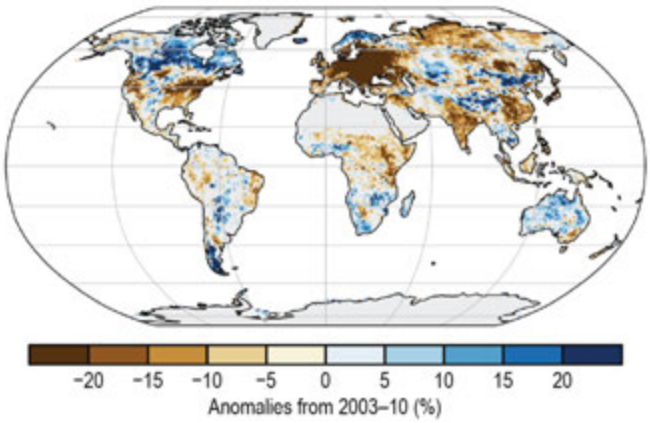

(ae) Land Surface Albedo in the Near-Infrared

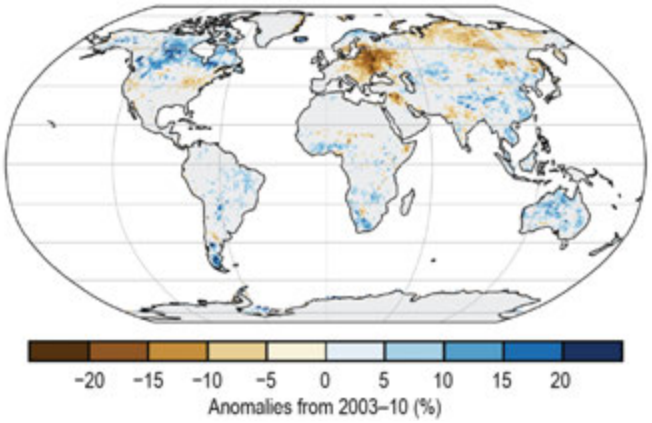

(af) Fraction of Absorbed Photosynthetically Active Radiation

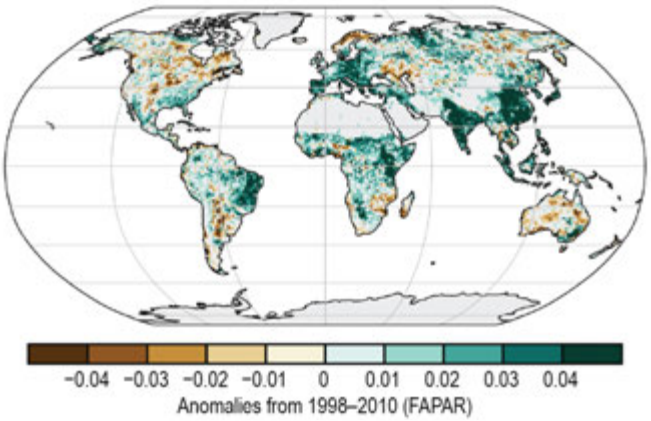

(ag) Carbon Emissions from Biomass Burning

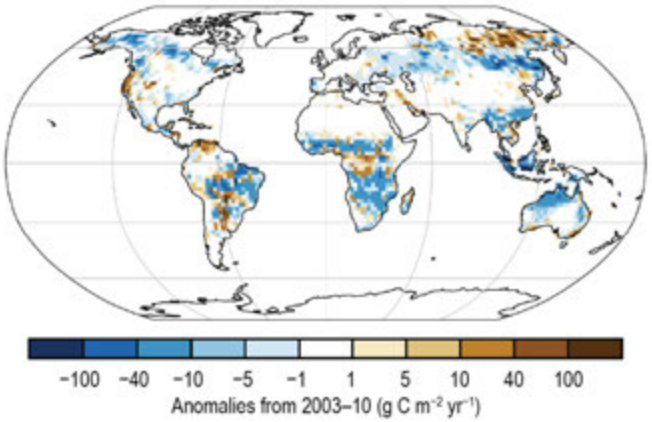

(ah) Vegetation Optical Depth

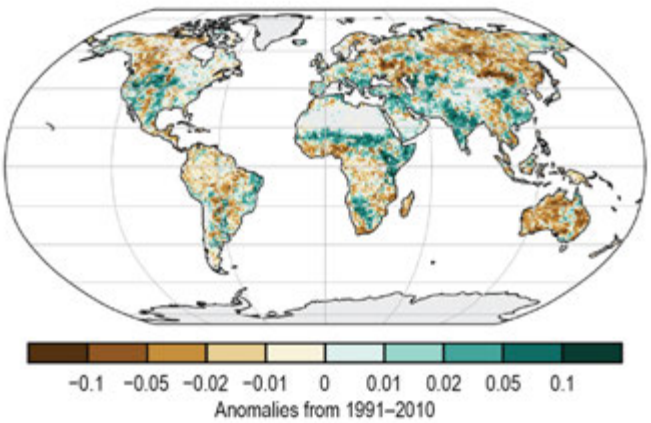

Plate 2.1. (cont.) (ab) OMI/MLS tropospheric ozone column anomalies for 60°S–60°N (DU); (ac) CAMS reanalysis total column CO anomalies (%); (ad) Land surface visible broad-band albedo anomalies (%); (ae) Land surface near-infrared albedo anomalies (%); (af) FAPAR anomalies; (ag) GFAS1.4 carbonaceous emission anomalies (g C m^{-2} yr^{-1}) from biomass burning; (ah) VODCA Ku-band VOD anomalies.

b. Temperature

1) Global surface temperature— A. Sánchez-Lugo, C. Morice, J. P. Nicolas, and A. Argüez

The year 2020 was one of the three warmest years since global records began in the mid-to-late 1800s, with a global land and ocean surface temperature 0.54°–0.62°C above the 1981–2010 average, according to five global temperature datasets (Table 2.1). These datasets consist of three independent global in situ surface temperature analyses (NASA-GISS, Lenssen et al. 2019; HadCRUT5, Morice et al. 2021; NOAAGlobalTemp, Zhang et al. 2019) and two global atmospheric reanalyses (ERA5, Hersbach et al. 2020; JRA-55, Kobayashi et al. 2015). Depending on the dataset, 2020 was either the warmest year on record, 2020 was tied with 2016 as the warmest on record, 2020 was the second-warmest year on record, or 2020 was the third-warmest (Fig. 2.1).

The year began in El Niño–Southern Oscillation (ENSO)-neutral conditions, transitioning to La Niña by August (see section 4b for details). The global monthly temperature anomalies were high throughout 2020, with each month from January through November ranking among the five warmest for each respective month across all datasets. December had the smallest temperature anomaly of the year. Despite the slightly cooler end to the year, this was the warmest non-El Niño year on record, surpassing 2017 by 0.07°–0.11°C. Furthermore, the five datasets agree that the last 7 years (2014–20) were the seven warmest years on record.

Even though each dataset might differ slightly on the yearly rankings and anomalies, it is worth noting that these differences are small and that, overall, temperature anomalies for each dataset are in close agreement. The three global in situ surface temperature analyses assessed here are derived from air temperatures observed at weather stations over land and sea surface temperatures (SSTs) observed from ships and buoys. The differences between each analysis are mainly due to how each methodology treats areas with little to no data and how each analysis accounts for changes in measurement methods (for more details see Kennedy et al. 2010; Hansen et al. 2010; Huang et al. 2015; Sánchez-Lugo et al. 2017). The global average surface temperature has increased at an average rate of 0.08°C decade^{-1} since 1880 with a rate more than twice as high since 1981 (0.19°–0.20°C decade^{-1}, depending on the dataset).

Unlike the global in situ surface temperature analyses, global atmospheric reanalyses use a weather prediction model to combine information from a range of satellite, radiosonde, aircraft, and other in situ observations to reconstruct historical weather and climate across the whole globe. These characteristics give reanalyses a unique ability to produce globally-complete temperature fields in a physically consistent manner; however, these datasets can also suffer from regional model biases and the effects of changes in the observation network over time (Simmons et al. 2017, 2021). Nonetheless, surface temperatures from reanalyses should be consistent with in situ analyses in regions of good observational coverage. One of the reanalyses used here, ERA5, provides data from 1950 onward, but because of lower confidence in its surface temperature data prior to 1967 (Simmons et al. 2021), only data from 1967 onward are shown. In addition, temperatures

Table 2.1. Temperature anomalies (°C) and uncertainties (where available) for 2020 with respect to the 1981–2010 base period. Where uncertainty ranges are provided, temperature anomalies correspond to the central values of a range of possible estimates. Uncertainty ranges represent a 95% confidence interval. Note that for HadCRUT5, land values were computed using the CRUTEM 5.0.1.0 dataset (Osborn et al. 2021), ocean values were computed using the HadSST4.0.0.0 dataset (Kennedy et al. 2019), and global land and ocean values used the HadCRUT5.0.1.0 dataset (Morice et al. 2021).

Global	NASA-GISS (°C)	HadCRUT5 (°C)	NOAA GlobalTemp (°C)	ERA5 (°C)	JRA-55 (°C)
Land	+0.97	+0.85 ± 0.13	+0.95 ± 0.14	+0.99	+0.88
Ocean	+0.37	+0.42 ± 0.07	+0.39 ± 0.16	+0.47	+0.41
Land and Ocean	+0.60 ±0.05	+0.57 ± 0.08	+0.54± 0.15	+0.62	+0.54

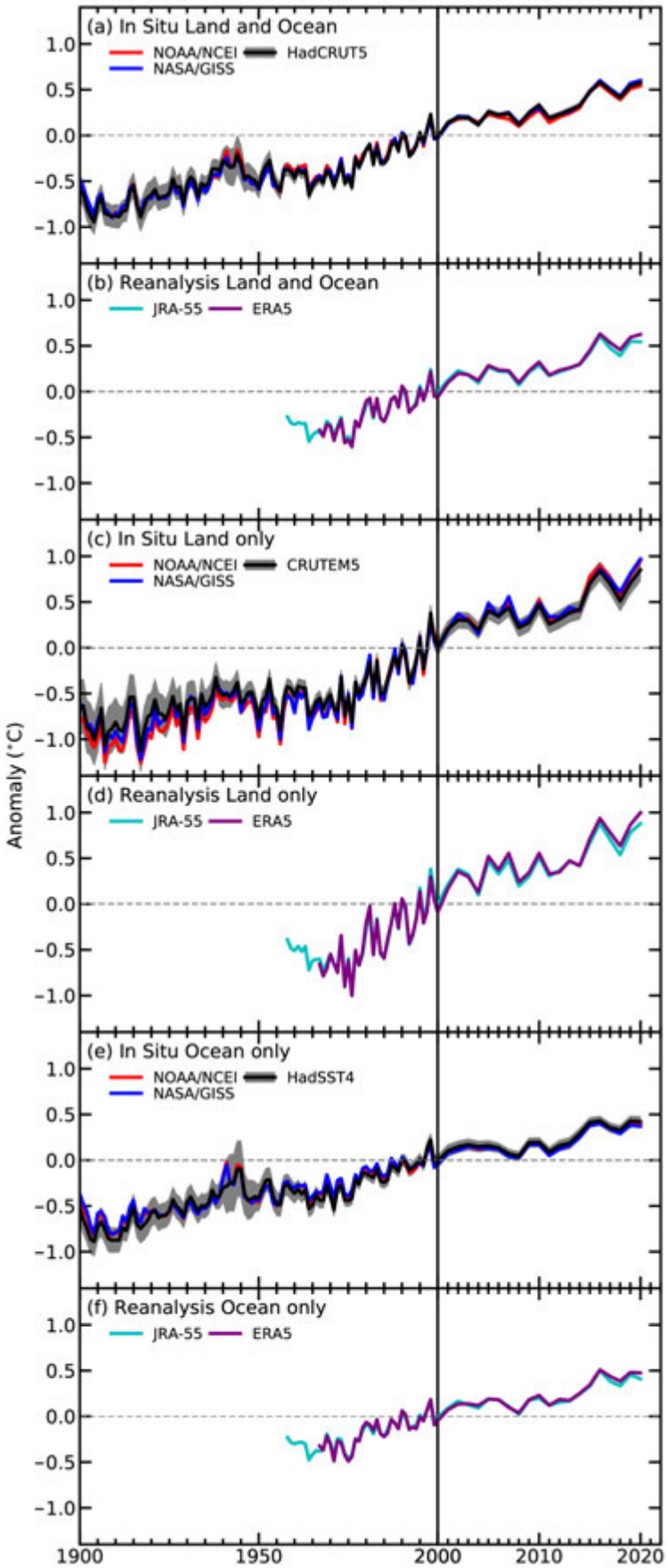

Fig. 2.1. Global average surface air temperature anomalies (°C; 1981–2010 base period). In situ estimates are shown from NOAA/NCEI (Zhang et al. 2019), NASA-GISS (Lenssen et al. 2019), HadCRUT5 (Morice et al. 2021), CRUTEM5 (Osborn et al. 2021), and HadSST4 (Kennedy et al. 2019). Reanalyses estimates are shown from ERA5 (Hersbach et al. 2020) and JRA-55 (Kobayashi et al. 2015). Please note change in *x*-axis scale pre/post 2000.

over the Great Lakes are adjusted as described in Simmons et al. (2021) to correct for a production error. This correction has a negligible impact on the global average temperature. The other reanalysis, JRA-55, provides data from 1958 onward. The JRA-55 global average temperature is computed as in Simmons et al. (2017, 2021), that is by using JRA-55 analysis temperature over land and its background temperature over ocean and other water bodies. For both reanalyses, the 2-m air temperature is used over both land and ocean whereas the global in situ analyses use SST over ocean. This difference is expected to have only a very small impact on the global averages assessed here (see Fig. 1 of Simmons et al. 2017).

While annual temperature rankings provide an intuitive measure of the state of global temperatures, a recently introduced global annual temperature score (Arguez et al. 2020) complements the annual temperature ranking by providing a basic characterization of the impacts of interannual variability on global temperature relative to the sustained upward trend since the mid-1970s. Scores range from 1 to 10, with a score of 1 (10) indicating the coldest (warmest) 10% of anomalies relative to the trend. In an era of seemingly perpetual near-record warm rankings, the annual temperature scores can help characterize whether the annual temperature ranking attained in a given year was due primarily to the secular trend, interannual variability, or both. For example, 2016 was not only the warmest year on record, but it also exhibited a temperature score of 10, whereas 2014 previously attained a ranking of warmest yet exhibited a temperature score of 4 (on the colder half of the scale). This indicates that, on top of the secular trend, interannual variability had a prominent contribution to the record temperature in 2016, whereas interannual variability did not synergistically contribute to 2014's previous record temperature. Using global annual time series from 1975 through 2020, the year 2020 registers a global annual temperature score of 9 (corresponding to the 80th–90th percentile) in the NASA-GISS and NOAAGlobalTemp datasets and a score of 8 (70th–80th percentile) in the HadCRUT5 dataset. This indicates that 2020, much like 2019, was moderately-to-considerably warmer than would be expected due to the secular trend alone, suggesting that its ranking of warmest or second warmest for the three in situ datasets was enhanced by the effects of the interannual variability.

Separately, the global land surface temperature for 2020 was the highest in four of the five datasets, surpassing the previous record set in 2016 by 0.05°–0.11°C. The fifth dataset (JRA-55) has the global land surface temperature tying with 2016 as the highest. The globally averaged SST was either third or fourth highest on record, depending on the dataset.

The year was characterized by higher-than-average temperatures across much of the globe (Plate 2.1a; Appendix Figs. A2.1–A2.4). The most notable feature of 2020 is the very large positive temperature anomalies (+4.0°C or higher above the 1981–2019 base period) over Arctic Siberia and the adjacent sector of the Arctic Ocean (Appendix Fig. A2.2). Large positive anomalies (+2.0°C or higher) are also found across northern Europe, northern Asia, and the North Pacific Ocean. In contrast, average to below-average conditions were limited to the central and eastern tropical Pacific Ocean and across parts of northern North America, subpolar North Atlantic, and the southern Indian Ocean.

2) Lake surface water temperature—L. Carrea, C. Merchant, B. Calmettes, and J.-F. Cretaux

In 2020, the worldwide averaged satellite-derived lake surface water temperature (LSWT) warm-season anomaly was +0.11°C with respect to the 1996–2016 baseline. The mean warming trend during 1996–2020 was 0.22 ± 0.01°C decade^{-1}, broadly consistent with previous analyses (Woolway et al. 2017; Woolway et al. 2018; Carrea et al. 2019, 2020). On average, anomalies in 2020 were only 0.01°C higher than in 2019. The warm-season anomalies for each lake are shown in Plate 2.1b. Lake mean temperature anomalies were positive for 55% of lakes and negative for 45%. Some lakes in eastern Africa recorded notable positive anomalies for both LSWT and lake water level (LWL; section 2d6). The LWL is defined as the height, in meters above the geoid (the shape that the surface would take under the influence of the gravity and rotation of Earth), of

the reflecting surface. Changes in lake water levels can be critical, as they affect water quantity and quality, food stocks, recreational opportunities, and transportation.

Globally, distinct regions of coherent warm and cool LSWT anomalies can be identified in 2020. Lakes in subtropical eastern China were markedly warm, with the three largest warm anomalies (+2.54°C, +2.39°C, +2.38°C) in this region. In northern Europe, Canada, the southeastern United States, and southeastern Australia, negative anomalies were observed for 70% or more of the water bodies, while southern Europe, Alaska, the Middle East, northern Russia, and eastern Africa had positive anomalies.

Four regions are considered here in more detail: Canada (number of lakes, n = 246, Fig. 2.2); Europe (n = 127, Fig. 2.2); Tibet (n = 104, Fig. 2.2); and Africa (n = 70). The boreal warm season (July–September) LSWT calculated from the satellite data shows a warming tendency of +0.39 ± 0.01°C decade^{-1} in Europe (Fig. 2.2a) and +0.18 ± 0.01 °C decade^{-1} in Canada (Fig. 2.2d). In Africa and Tibet, the tendency is closer to neutral (Figs. 2.2b,c). In Canada, 166 lakes had negative anomalies and 80 had positive in 2020, with an overall average of −0.22°C. In Tibet, 72% of the lakes had moderate-positive anomalies and 28% had negative anomalies, with an average of +0.20°C. In Europe, cool anomalies in northern Europe (67 lakes) balanced warmer anomalies in the south (60 lakes), producing +0.03°C on average. In Africa, positive anomalies were recorded for 80% of the 70 lakes over the considered period. Several of the warmest anomalies occurred in eastern Africa, where the LWL was also consistently higher than the 1996–2016 average. Therefore, for some of the eastern African lakes, LSWT was compared with their LWL anomalies, calculated using a time series of LWL changes obtained from satellite altimetry.

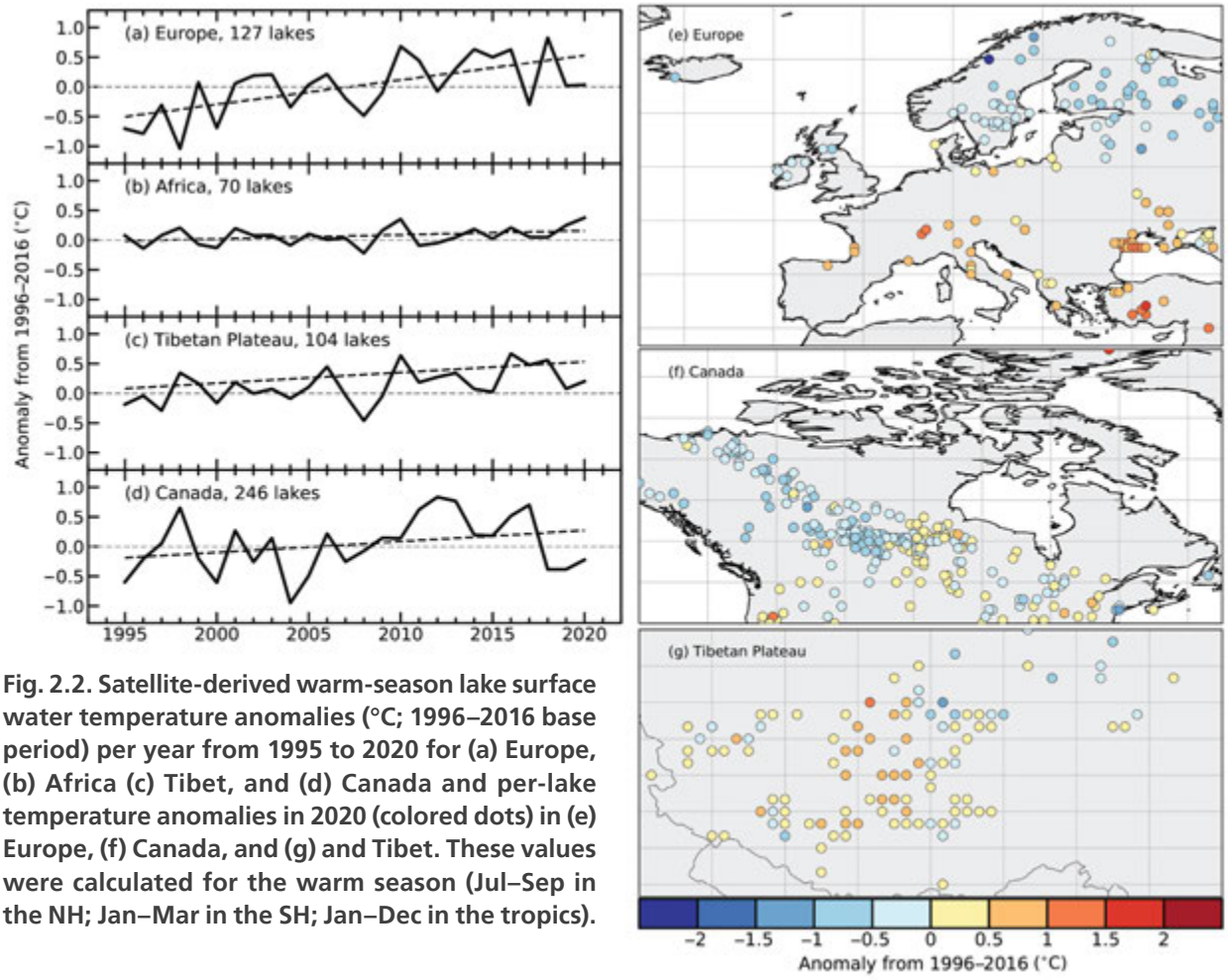

Fig. 2.2. Satellite-derived warm-season lake surface water temperature anomalies (°C; 1996–2016 base period) per year from 1995 to 2020 for (a) Europe, (b) Africa (c) Tibet, and (d) Canada and per-lake temperature anomalies in 2020 (colored dots) in (e) Europe, (f) Canada, and (g) and Tibet. These values were calculated for the warm season (Jul–Sep in the NH; Jan–Mar in the SH; Jan–Dec in the tropics).

Figure 2.3 presents a selection of African lakes (Victoria, Tanganyika, Malawi, Turkana, Rukwa, Albert, Kyoga, Edward, Mweru, Tana, and Bangweulu) for which the LSWT and the LWL normalized anomalies from 1996 to 2020 are reported for each of the lakes, together with the spatial distribution of the 2020 LSWT anomalies. All the lakes exhibit positive LWL anomalies in 2020, while Lakes Turkana, Edward, and Rukwa have notably high LSWT positive anomalies. For these lakes, the LSWT 2020 anomalies were consistently positive across their full spatial extent, while there was a mix of positive and negative anomalies spatially across other lakes. Most of the lakes exhibited an upward long-term trend for both the LSWT and LWL.

The LSWT warm-season averages for midlatitude lakes are computed for summers (July–September in the Northern Hemisphere [NH] and January–March in the Southern Hemisphere [SH]), and whole-year averages (January–December) are presented for tropical lakes (within 23.5° of the equator).

The LSWT time series were derived from satellite observations from the series of Along Track Scanning Radiometers (ATSRs), the Advanced Very High Resolution Radiometers (AVHRRs) on MetOp A and B, and the Sea and Land Surface Temperature Radiometers (SLSTRs) on Sentinel3A and 3B. The retrieval method of MacCallum and Merchant (2012) was applied on image pixels filled with water according to both the inland water dataset of Carrea et al. (2015) and a reflectance-based water detection scheme. The LWL observations for 11 African lakes were analyzed where long time series are available from radar altimetry (Cretaux et al. 2011). The LWL were validated using a set of in situ data over lakes in South America, North America, Russia, and Europe (Ričko et al. 2012). For lakes with sizes comparable to those in East Africa, the accuracy is generally within 0.1 m (Cretaux et al. 2018; Quartly et al. 2020).

The satellite-derived LSWT data are spatial averages for each of 947 lakes, for which high-quality temperature records were available in 2020. The satellite-derived LSWT data were validated with in situ measurements with an average satellite minus in situ temperature difference less than

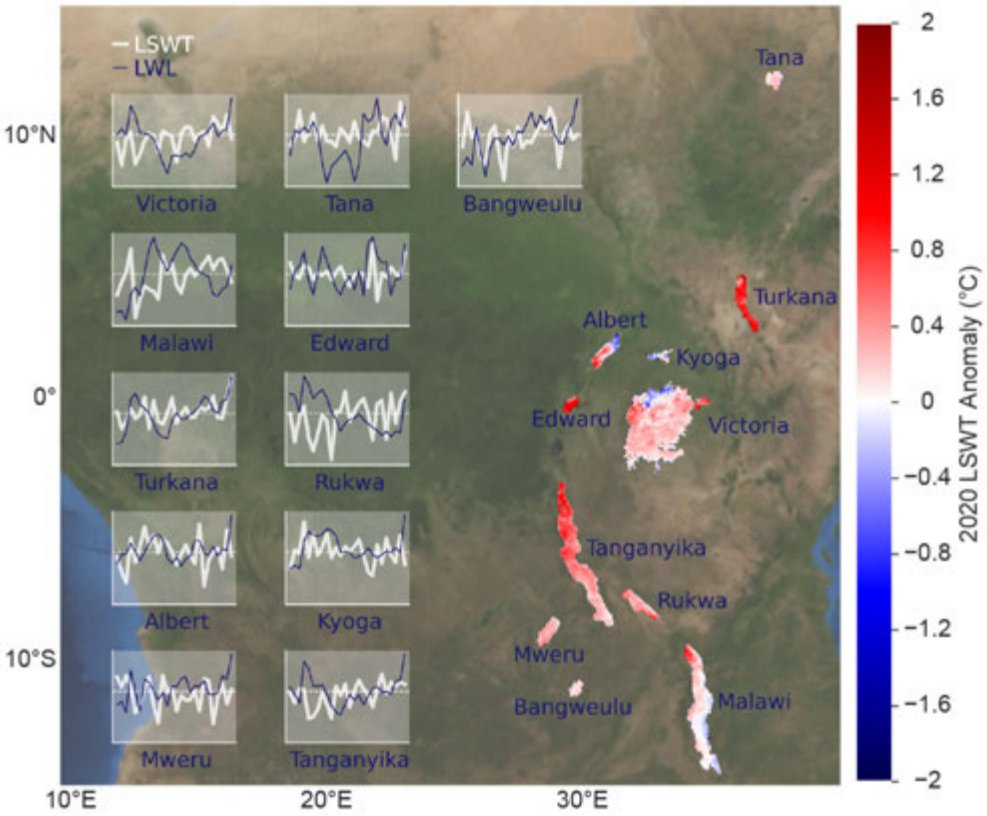

Fig. 2.3. Satellite-derived lake surface water temperature (LSWT) and lake water level (LWL) normalized anomalies relative to the 1996–2016 period from 1995 to 2020 for 11 lakes in East Africa, together with the spatial distribution of the 2020 LSWT anomalies (in °C) for the same lakes.

0.5°C and, consequently, a good agreement was found. Lake-wide average surface temperatures have been shown to provide a more representative picture of LSWT responses to climate change than single-point measurements (Woolway and Merchant 2018).

3) Land and marine temperature extremes—S. E. Perkins-Kirkpatrick, R. J. H. Dunn, R. W. Schlegel, M. G. Donat , and Michael G. Bosilovich.

Averaged over global land regions using the Global Historical Climatology Network-Daily dataset (GHCNDEX; Donat et al. 2013), 2020 recorded the highest number of days where the maximum temperature was above the climatological 90th percentile (TX90p, "warm days"; Fig. 2.4). There were over 70 days, which is almost double the average of 36.5 days during 1961–90, and 10 days more than 2019. The number of cool nights (TN10p, where the minimum temperature was below the 10th percentile) was lower than the 1961–90 average, at just over 20 nights throughout the year. This was below average compared to the last 70 years but comparable to the recent decade.

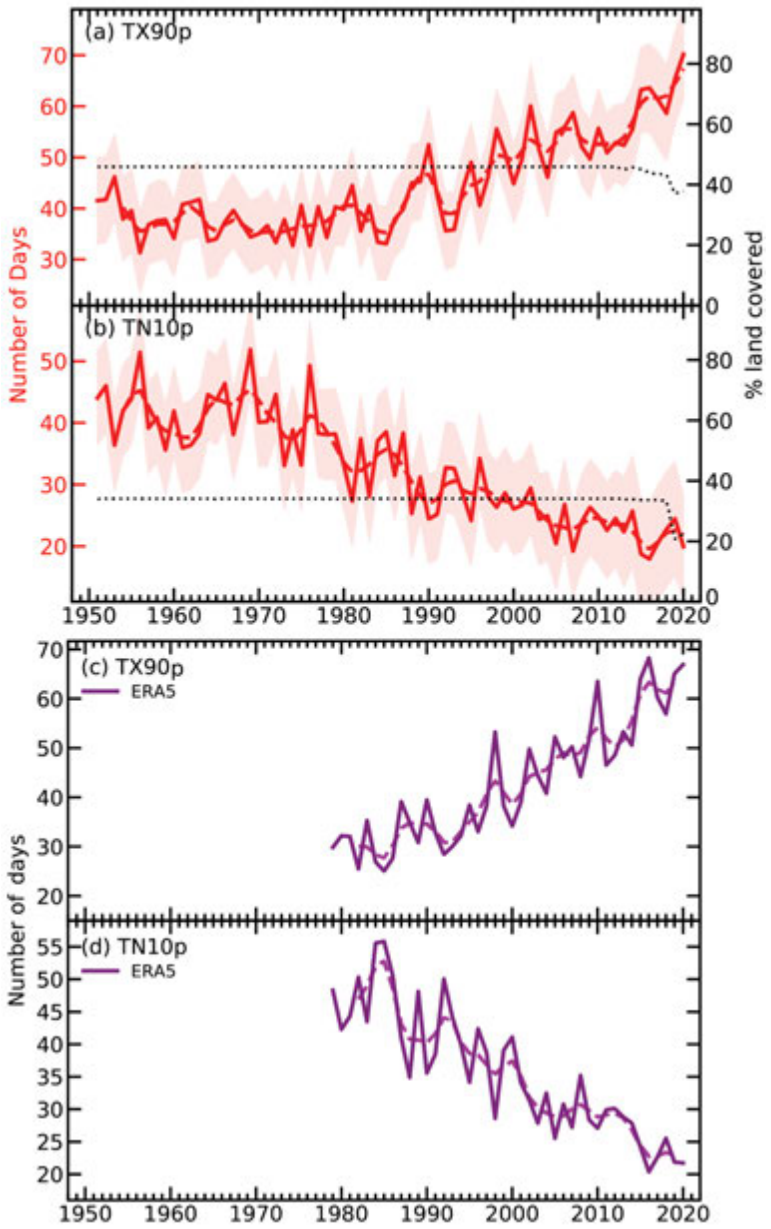

Fig. 2.4. Time series of (a) TX90p (warm days) and (b) TN10p (cool nights) from GHCNDEX relative to 1961–90. The red dashed line shows a binomial smoothed variation and red shading the coverage uncertainties estimated using ERA5 following Brohan et al. (2006). The dotted black line shows the percentage of land grid boxes with valid data in each year. Time series of (c) TX90p (warm days) and (d) TN10p (cool nights) from ERA5 relative to 1981–2010.

The behavior of the GHCNDEX time series is comparable to the more spatially complete ERA5 dataset (Fig. 2.4; Hersbach et al. 2019) for the last 40 years.

More detail on regional extreme temperature events is available in Chapter 7. There was a high number of warm days during 2020 in Europe, China, and northeast Australia compared to average (Plate 2.1c), and the number of warm days was larger than the number of cool nights almost everywhere (Plate 2.1d). Many extreme maximum temperatures were recorded (Table 2.2), several of which are described in the following text, and others discussed in Chapter 7 and the World Meteorological Organization (WMO) *State of the Global Climate* (2021).

Table 2.2. Examples of extreme maximum temperatures in 2020 described in this section.

Country	Location	Date	Value (°C)	Notes
UK	Heathrow	31 Jul	37.8	Third-hottest UK day
Spain	Around Seville	5 Mar	36	—
Russia	Verkhoyansk (Siberia)	20 Jun	38	Hottest regional day (Provisional Arctic Circle record)
United States	Furnace Creek, Death Valley, California	16 Aug	54.4	Globally third-hottest day on record
United States	Woodland Hills, Los Angeles	6 Sep	49.4	—
Canada	Montreal	27 May	36.6	Hottest May
Canada	Miramichi	19 Jun	37.2	New annual record
Iraq	Basra	27 and 28 Jul	53	—
Iraq	Baghdad	28 Jul	51.8	New record
Lebanon	Houch al-Oumara?	28 Jul	45.6	New record
Syria	Damascus	29 Jul	46	New record
Japan	Hamamatsu	18 Aug	41.4	Equal record
Australia	Sydney	29 Nov	25.4	Hottest November night
Antarctica	Casey	24 Jan	9.2	New record
Antarctica	Esperanza Base	6 Feb	18.3	New Antarctic record

In the United States, Furnace Creek in Death Valley (California) recorded a yet-to-be certified temperature of 54.4°C—the hottest temperature measured on Earth since 1931—on 16 August during a heat wave that affected the western and midwestern states. Another heat wave hit the southwest in early September where the extreme heat fueled wildfires (see sections 2h3, 7b2) and set new records. In Canada, Montreal and Burlington experienced six consecutive days at 32°C during a June heat wave. This heat wave lasted into July, enhancing conditions for wildfires in the Quebec province and seeing numerous daily maximum temperature records broken. Many locations in South America experienced extreme temperatures during September and October, with multiple records broken. Concepción, Paraguay, reached 42.6°C on 2 October; Sao José de Chiquitos, Bolivia, reached 43.4°C on 8 October, and Sao Paulo, Brazil, recorded four of its five highest daily maximum temperatures on record during this time (see sections 7d2, 7d3). Extreme heat also occurred over the Caribbean and Mexico during April. Daily maximum temperatures reached 39.7°C and 48.8°C at Veguitas, Cuba, and Gallinas, Mexico, respectively, on 12 April.

A protracted extreme temperature event occurred over Siberia during the first half of 2020. Heat wave frequency (HWF) and magnitude (HWM) indices for April–June over Siberia were the largest in the MERRA2 record (Collow et al. 2020; Fig. 2.5). The long-term and widespread heat helped

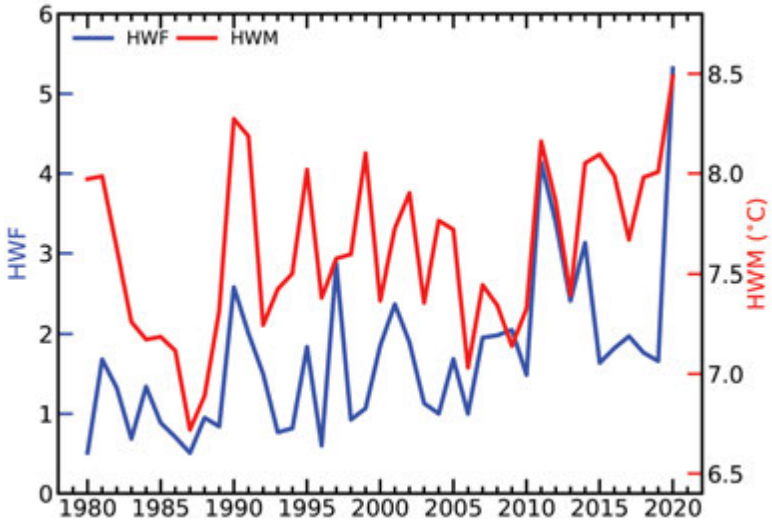

Fig. 2.5. MERRA-2 Apr–Jun seasonal heatwave frequency (HWF; count) and heatwave magnitude (HWM; °C; Callow et al. 2020) area averaged for the Siberian region affected by anomalous heat wave conditions (60°–160°E, 50°–80°N, land only).

fuel large wildfires in the region (see sections 2h3, 7g2, Sidebar 5.1). Verkhoyansk recorded 38.2°C on 22 June, provisionally the highest temperature ever measured within the Arctic Circle.

Antarctica experienced a period of record-breaking temperatures during 23–26 January 2020 at Casey, where minimum temperatures did not fall below 0°C and the highest ever daily maximum and minimum temperatures were recorded (9.2°C and 2.5°C, respectively). On 6 February, the highest Antarctic temperature on record was measured at Esperanza Base (18.3°C; see section 6b, Sidebar 6.1). This was part of a warm spell lasting from 5–13 February, causing widespread glacial melting.

During early August, record warm nights were widespread across the United Kingdom, with parts of the southeast experiencing five consecutive tropical nights (temperatures greater than 20°C) and 6 days with peak temperatures over 34°C (see section 7f2). A heat wave (defined as a period of three or more consecutive TX90p days [Perkins and Alexander 2013]) affected Spain and Portugal in May (see section 7f5).

An intense heat wave occurred over the Middle East during July, with daily maximum temperatures reaching over 53°C in Basra (Iraq) on both the 27th and 28th and widespread maximum temperatures over 45°C. During a heat wave in August, Tokyo experienced three consecutive days of maximum temperature above 35°C and multiple locations in central southwest Japan recorded temperatures above 39°C on 17 August. Numerous large-scale heat waves occurred over Vietnam, with maximum daily temperatures greater than 35°C over large parts of the country during June.

Australia had a warm start to 2020, with its second-warmest summer (December 2019–February 2020) on record for maximum and minimum temperature (2.11°C and 1.64°C above the 1961–90 average, respectively). On 4 January the Sydney suburb of Penrith recorded 48.9°C, the hottest temperature ever recorded across all Australian metropolitan areas. The country also experienced an anomalously warm spring, with records for nationally averaged minimum spring (September–November) and November temperatures (1.91°C and 2.9°C above average, respectively) . Numerous local maximum temperature records across the southeast were also broken during November (see section 7h4 for details).

Marine heatwaves (MHW) are defined as SST above the climatological 90th percentile for five or more days (Hobday et al. 2016). Categories of MHW are defined in Hobday et al. (2018). Using NOAA OISST v2 (Banzon et al. 2020), 84% of the surface of the ocean experienced at least one MHW in 2020 (Fig. 2.6). Category 2 – Strong events were the most common (45%), vastly exceeding Category 1 – Moderate events (28%), marking the seventh consecutive year that Category 2 – Strong MHWs have been the dominant category. The ocean experienced a global average of 77 MHW days, exceeding the 2019 average of 74 days, but fewer than the 2016 record of 83 days (Fig. 2.6). On average, 21% of the surface of the ocean in 2020 was experiencing a MHW on any given day (Fig. 2.6). This is slightly higher than the 2019 average of 20%, but lower than the 2016 record of 23%. Roughly the entire surface of the ocean experienced at least one MHW in 2020, with the exception of the equatorial Pacific Ocean. This is likely because heat anomalies in the equatorial Pacific Ocean are tightly linked with the ENSO, which was in a neutral or moderately

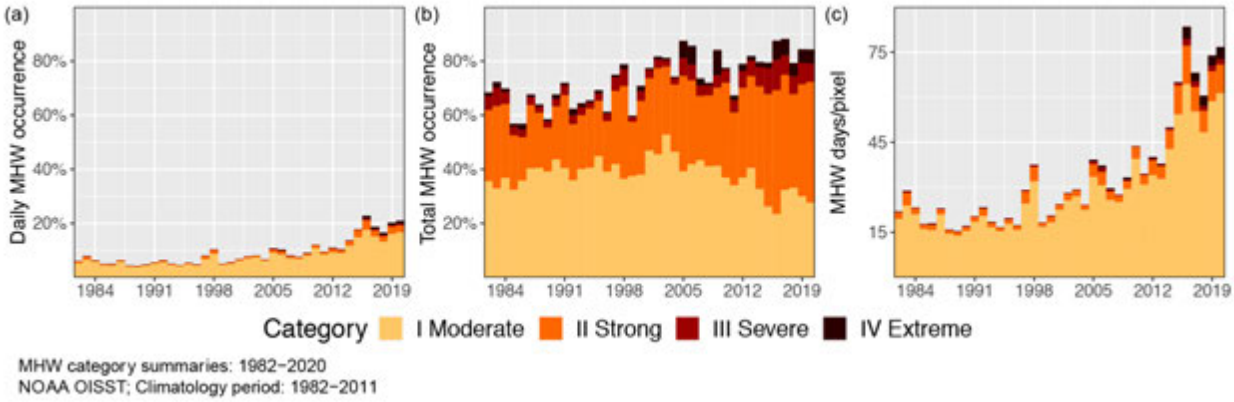

Fig. 2.6. Annual global marine heatwave (MHW) occurrence from NOAA OISST using a climatology base period of 1982–2011. (a) Daily average percent of the ocean that experienced an MHW. (b) Total percent of the ocean that experienced an MHW at some point during the year. The values shown are for the highest category of MHW experienced by each ocean grid cell during 2020. (c) Total average of daily MHW occurrence throughout the entire ocean.

negative phase in 2020 (see section 4b). The subpolar North Atlantic, southeast of Greenland, was another area that did not experience MHWs in 2020, a pattern persistent from 2014–18.

To show temperature extremes over land, we use a subset of the moderate extremes indices developed by the WMO Expert Team in Climate Change Detection and Indices (ETCCDI; Zhang et al. 2011). In the GHCNDEX dataset (Donat et al. 2013), daily temperature values from the GHCND (Menne et al. 2012) are interpolated onto a regular 2.5° grid. As in previous years, the spatial coverage is sparse (Plates 2.1c,d) and restricted to North America, parts of Eurasia, and Australia. To fill the gaps, we use the ERA5 reanalysis (Hersbach et al. 2019), though we have not included the preliminary release of the extension from 1950 to 1978. With the shorter temporal coverage, the reference period for the extremes indices is 1981–2010 (compared to 1961–90 for GHCNDEX), which can lead to differences when comparing recent trends (Dunn et al. 2020a; Yosef et al. 2021). Siberian heat waves were calculated from the MERRA-2 dataset (Gelaro et al. 2017; Collow et al. 2020). HWF frequency is the count of days satisfying heat wave conditions, where heat waves are defined as the MERRA-2 daily mean 2-m temperature exceeding the calendar day 90th percentile for at least three consecutive days. HWM magnitude is the average daily mean 2-m temperature anomaly over all heat wave days.

4) Tropospheric temperature—S. Po-Chedley, J. R. Christy, L. Haimberger, and C. A. Mears

The 2020 annual global lower tropospheric temperature (LTT) tied with 2016 as the highest on record. The annual average LTT was 0.49°–0.72°C above the 1981–2010 average, depending on dataset, and 10%–16% of Earth's surface experienced record high temperatures (Plate 2.1e). Such expansive and record warmth is notable because it occurred even though the ENSO exhibited neutral or La Niña conditions throughout the year (Fig. 2.7a) and is thus consistent with the background upward trend since 1958. In the past, record warm and cold tropospheric temperatures have typically followed El Niño and La Niña events, respectively (Figs. 2.7a,b). A La Niña pattern was established in August, which will likely depress the LTT in 2021 because tropospheric temperature lags ENSO by several months.

More than 90% of Earth's lower troposphere experienced above-average temperatures (Plate 2.1e). Regions experiencing record warmth included much of Europe and Russia, the Indian Ocean, the northeast and South Pacific, and a region off the coast of East Antarctica. Limited areas of below-average LTT included Canada, Greenland, and parts of Antarctica and the Southern Ocean.

Above-average lower tropospheric temperatures are consistent with long-term greenhouse gas warming and less-pronounced volcanic cooling over the past 3 decades (relative to significant cooling from the eruptions of Agung, El Chichón, and Pinatubo in 1963, 1982, and 1991, respectively;

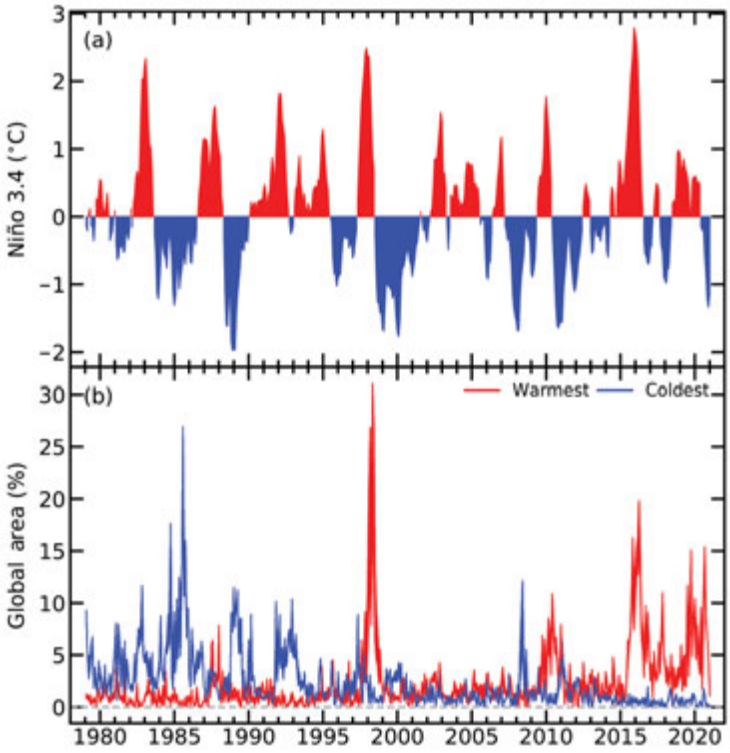

Fig. 2.7. (a) Sea surface temperature anomaly (°C) in the Niño 3.4 region in the central equatorial Pacific. (b) Fraction of Earth (%) with record warm (red) and cold (blue) monthly LTT values. The width of the line represents the difference between the UAH and RSS datasets.

e.g., Santer et al. 2014; Christy and McNider 2017). Recent warmth is recorded by in-situ radiosonde (balloon-borne), microwave (satellite), and reanalysis datasets (Fig. 2.8). Global and tropical tropospheric temperature (TTT) trends since 1958 and 1979 are approximately +0.18°C decade^{-1} (Table 2.3). While the individual tropospheric temperature datasets are broadly consistent, the temperature time series and trends vary across datasets, by altitude (TTT samples temperature at higher altitudes than LTT), and by region. As noted above, 2016 and 2020 are statistically tied for the warmest year on record; the average annual near-global LTT across all eight datasets was 0.68°C and 0.65°C above the climatological normal, respectively. In individual datasets, 2016 was the warmest year in the RATPACvA2, RICHv1.7, and RAOBCORE v1.7 radiosonde datasets (Free et al. 2004; Haimberger et al. 2012), the UAH v6.0 satellite product (Spencer et al. 2017), and JRA-55 reanalysis (Kobayashi et al. 2015). 2020 was the warmest year in the RSS v4.0 satellite product (Mears and Wentz 2016) and the ERA5 and MERRA-2 reanalyses (Hersbach et al. 2020; Gelaro et al. 2017). Structural uncertainty in satellite dataset construction can also affect the spatial pattern of record warm temperatures. RSS has a larger global surface area of record warm LTT values in 2020 compared to the UAH dataset (16% versus 10%, respectively; Plate 2.1e).

The tropical troposphere is expected to experience substantial warming in response to the increasing concentration of atmospheric carbon dioxide (CO_2; Flato et al. 2013). Simulations of satellite era tropical and global tropospheric warming in the most recent generation of climate models generally exhibit substantially greater warming than observations (McKitrick and Christy 2018, 2020). Over 1979–2014, the multimodel average TTT trend is +0.30°C decade^{-1}, while satellite-derived trends range from 0.09° to 0.20°C decade^{-1} (Po-Chedley et al. 2021). The difference in the rate of warming is partially attributable to Pacific decadal climate variability, which has reduced warming in the observed record (Po-Chedley et al. 2021). Such internal climate variability is random and is only captured by chance in climate model simulations. A number of individual model realizations simulate similar Pacific decadal climate variability and approximately 13% (24%) have tropical (global) tropospheric temperature trends that are within the range of satellite observations (Po-Chedley et al. 2021). Other possible drivers of this model-observational

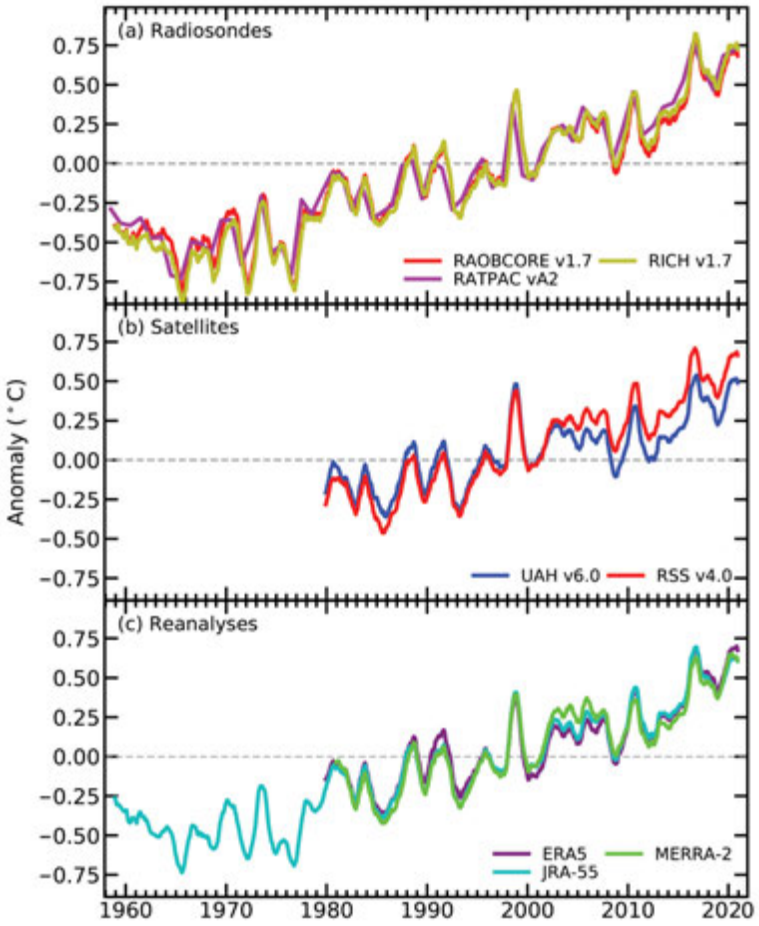

Fig. 2.8. Monthly average lower tropospheric temperature (LTT) anomalies (°C) for (a) radiosonde, (b) satellite, and (c) reanalysis datasets. Time series are smoothed using a 12-month running average. Annual averages are displayed for the RATPAC dataset.

Table 2.3. Temperature trends (°C decade^{-1}) for near-global lower tropospheric temperature (LTT) and tropical tropospheric temperature (TTT) over 1958–2020 and 1979–2020.

		LTT (90°S–90°N)		TTT (20°S–20°N)	
Start Year		**1958**	**1979**	**1958**	**1979**
Radiosonde	NOAA/RATPACvA2	0.19	0.21	0.16	0.17
	RAOBCOREv1.7	0.18	0.19	0.15	0.15
	RICHv1.7	0.20	0.21	0.17	0.19
Satellite	UAHv6.0	—	0.14*	—	0.13
	RSS v4.0	—	0.22	—	0.18
	UWv1.0	—	—	—	0.18
	NOAA STAR v4.1	—	—	—	0.23
Reanalyses	ERA5	—	0.18	—	0.16
	JRA-55	0.17	0.19	0.16	0.15
	NASA/MERRA-2	—	0.19	—	0.19
	Median	**0.19**	**0.19**	**0.16**	**0.18**

*The vertical sampling in UAH LTT is slightly different from other datasets and results in temperature trends that are approximately 0.01°C decade^{-1} smaller than other datasets.

discrepancy include model biases in their response to greenhouse gas forcing, deficiencies in the external forcing applied to models, and observational biases.

The 2σ trend error estimate for individual satellite datasets is approximately 0.04°C decade^{-1} (Mears et al. 2011; Po-Chedley et al. 2015; Spencer et al. 2017). Uncertainty in satellite datasets arise from instrument calibration and the removal of non-climatic artifacts, particularly between 2000 and 2005 (Christy et al. 2018). The conversion of level temperatures in radiosonde and reanalysis data to synthetic satellite brightness temperatures and incomplete spatial sampling in radiosonde data contribute to the trend error (Mears et al. 2011). The 2σ tropospheric trend error associated with these effects is approximately 0.01°C decade^{-1} and 0.02°C decade^{-1}, respectively, in both the tropical and global domain.

5) Stratospheric temperature and winds—W. J. Randel, C. Covey, and L. Polvani

Temperatures in the middle and upper stratosphere continued to exhibit strong decadal-scale cooling as a result of anthropogenic CO_2 increases. Lower stratospheric temperatures have been relatively constant since ~1998 as the Montreal Protocol stabilized ozone levels, but a transient temperature increase occurred in early 2020, likely related to enhanced stratospheric aerosols from extreme Australian bushfires. The Arctic and Antarctic stratospheric polar vortices were remarkably strong and undisturbed in 2020, with accompanying large polar ozone depletion in both hemispheres. Additionally, a new anomalous disruption of the stratospheric quasi-biennial oscillation (QBO) occurred in 2020, following a similar event in 2016.

Time series of global monthly temperature anomalies from the lower to upper stratosphere based on satellite measurements are shown in Fig. 2.9. The middle and upper stratosphere data (Stratospheric Sounding Unit [SSU] 1, 2, 3) represent ~20-km thick layers from infrared (SSU) data merged with more recent measurements (Zou and Qian 2016; Randel et al. 2016), while the lower stratospheric temperatures (TLS) represent the layer over ~13–22 km from microwave data. As shown in previous reports (Randel et al. 2020), the satellite TLS measurements agree well with radiosonde and reanalysis datasets. Middle- and upper-stratosphere temperatures show strong cooling since 1979 with larger negative trends at higher altitudes, a long-predicted response to increases in atmospheric CO_2 (Manabe and Wetherald 1967). The upper stratospheric cooling is modulated by stratospheric ozone changes, with weaker cooling after 1998 tied to observed increases in upper-stratospheric ozone (Maycock et al. 2018). The ozone is evolving as a response to changes in ozone-depleting substances linked to the Montreal Protocol (WMO 2018). In addition to long-term cooling, the upper-stratosphere time series show modulation by the 11-year solar cycle and transient warming from large volcanic eruptions in 1982 and 1991.

TLS have been relatively constant since the later 1990s with small year-to-year variability. Over most of the globe, the TLS layer spans the cross-over between tropospheric warming and stratospheric cooling associated with CO_2 increases; hence ozone variations strongly influence temperatures in this layer. TLS cooling prior to ~1998 is tied to ozone decreases in the lower stratosphere, while there are small ozone changes thereafter (WMO 2018). The TLS in Fig. 2.9 show an unusually large short-term warm anomaly in early 2020 that is probably related to enhanced stratospheric aerosols in the SH caused by extreme Australian bushfires and resulting smoke injection into the stratosphere (Kablick et al. 2020; Khaykin et al. 2020; Schwartz et al. 2020; Hirsch and Koren 2021; Yu et al. 2021).

The stratospheric winter polar vortices were uniquely strong and undisturbed in both hemispheres in 2020. The Arctic polar vortex was the strongest since the beginning of the satellite era and coincided with record-low stratospheric ozone levels in the Arctic that lasted into spring, together with a record-breaking positive Arctic Oscillation index in the troposphere during January–March (Lawrence et al. 2020). The Antarctic polar vortex in 2020 was also anomalously strong and persistent, with polar temperatures at record cold levels throughout spring (November–December). This strong vortex was linked to a large and persistent ozone hole over the Antarctic,

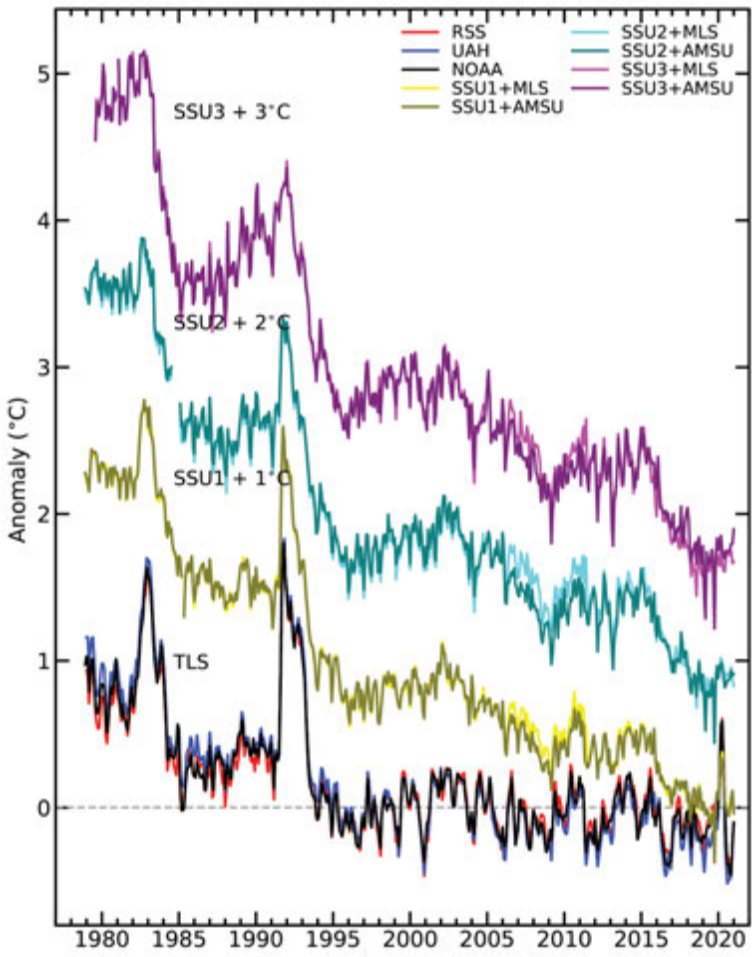

Fig. 2.9. Monthly global stratospheric temperature anomalies from the lower to upper stratosphere (bottom to top). Middle and upper stratosphere data are from the stratospheric sounding unit (SSU), representing thick-layer averages centered near 30, 38, and 45 km (SSU1, SSU2, and SSU3, respectively). Lower stratosphere temperatures (TLS) are ~13–22 km layer averages from satellite microwave measurements. Each time series has been normalized to zero for the period 1995–2005, and curves are offset for clarity.

which lasted to the end of December. While the polar vortices were anomalously cold, they have minimal influence on global average temperatures.

Another notable feature of stratospheric circulation in 2020 was a new disruption of the QBO, which is a repeating reversal of equatorial zonal winds, characterized by downward-propagating easterly and westerly wind regimes with a mean periodicity of ~28 months. While regular downward propagation from the upper to lower stratosphere had been observed continuously since its discovery in the early 1960s, a disruption occurred in 2016, when anomalous easterlies appeared in the lower stratosphere disconnected from upper levels, and a similar disruption occurred in 2020 (see Fig. 2.46). This behavior has been attributed to strong wave forcing from extratropical latitudes (e.g., Osprey et al. 2016; Coy et al. 2017; Anstey et al. 2021). With two disruptions over the last 5 years, there is now substantial uncertainty regarding QBO predictability and future evolution.

Sidebar 2.1: **Night marine air temperature**—R. C. CORNES, D. I. BERRY, R. JUNOD, E. C. KENT, AND N. A. RAYNER

Sea surface temperature (SST) is the principal variable for monitoring surface temperature change across ocean regions. Ship-based SST measurements provide the mainstay of the record, which extends back to the mid-nineteenth century, and these data have been supplemented with observations from moored and drifting buoys since the 1990s. In addition to recording SST, many ships also take measurements of air temperature but in general these marine air temperature (MAT) data are sparser than SST and the values are prone to daytime heating biases (Berry et al. 2004). To mitigate these biases and improve the accuracy of gridded anomaly datasets, only the nighttime values are selected. These night marine air temperature (NMAT) datasets provide a useful independent comparison against SST datasets.

NMAT readings require adjustment to account for variations in ship observation height, including an increase over time in the mean height of the bridge where the observations are typically taken (Kent et al. 2013). If this adjustment is not applied, a reduced trend would be apparent in the data series since temperature generally decreases with height. The temperature values are typically adjusted to the standard reference height of 10-m although the CLASSnmat dataset (Cornes et al. 2020) also provides values adjusted to 2 m and 20 m for comparison against other air temperature datasets.

Over long time periods and over sufficiently large spatial regions it has been assumed that anomalies of SST and NMAT anomalies show similar variability and trends (Kennedy et al. 2019). Climate model simulations indeed depict this relationship. Huang et al. (2015) demonstrate using the GFDL-coupled model that NMAT and SST display a consistent trend over the 1875–2000 period, and this evidence was used to justify the use of NMAT to bias-correct the SST data in the ERSST dataset. However, in situ NMAT and SST datasets indicate a divergent trend at the global scale, with NMAT anomalies increasing at a slower rate than SST (Cornes et al. 2020; Folland and Karl 2001; Kennedy et al. 2019). Initial analyses into this subject concluded that while it is difficult to ascertain the cause, the magnitude of the difference is small relative to the global warming trend (Folland and Karl 2001). However, the more up-to-date CLASSnmat and UAHNMAT (Junod and Christy 2020) datasets indicate an increase in this differential (Fig. SB2.1)—particularly in recent years—when compared against modern SST datasets, in this case HadSST4 (Kennedy et al. 2019).

The NMAT-SST discontinuity may appear as a step-like change in the early 1990s (Kennedy et al. 2019), although this may be a manifestation of a long-term divergence between SST and NMAT coupled with the use of a common 1961–90 base period for the calculation of the anomalies. In the evaluation of the long-term trends in NMAT and SST, differences in spatial coverage may have a large influence on the results (Jones 2020). In general, SST is more spatially complete than NMAT. This results from both the increase in drifting buoy observations and the considerable decline in voluntary observing ships (VOS; https://www.vos.noaa.gov/vos_scheme.shtml) from >7000 in the 1980s to ~1000 at present. Hence, only co-located grid-cell values across the three datasets are averaged in Fig. SB2.1. Note that differences in actual temperatures cannot be inferred from this figure because the time series are expressed as anomalies from climatological averages.

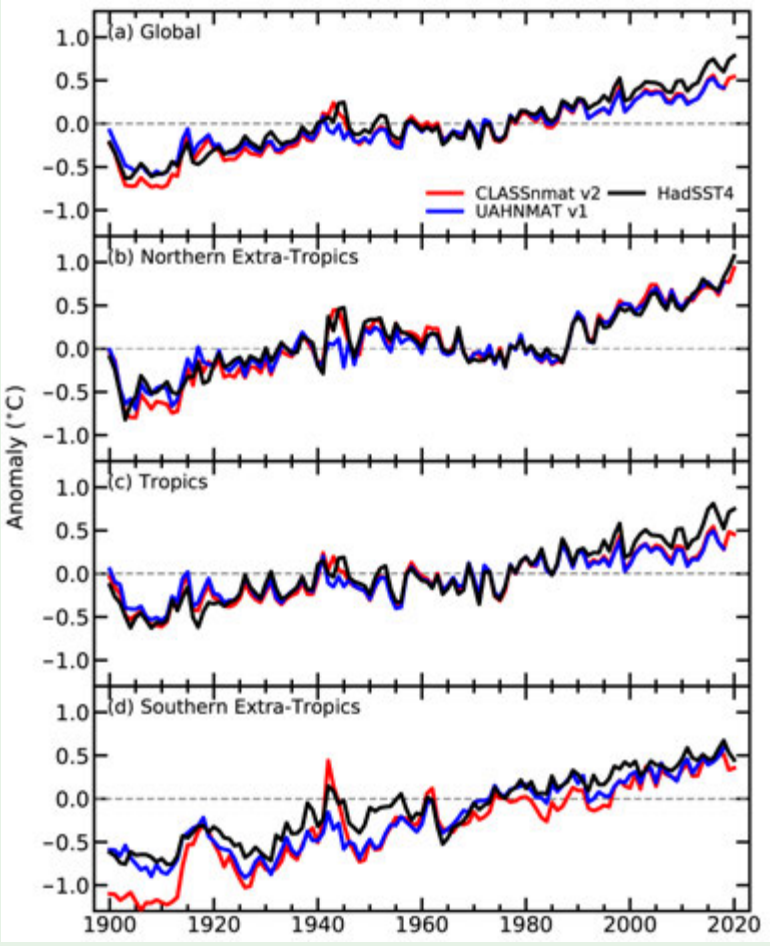

Fig. SB2.1. Large-scale average annual anomalies in the CLASSnmat (Cornes et al. 2020), UAHNMAT (Junod and Christy 2020), and HadSST4 (Kennedy et al. 2019) datasets relative to a 1961–90 base period over the period 1900–2020 (UAHNMAT to 2018).

The trend difference in NMAT and SST is strongest in the tropics (Fig. SB2.1), which may be attributable to changes in the atmospheric circulation across the region (Christy et al. 2001). Recent analyses by Rubino et al. (2020) examined the difference in MAT (day and night) and SST data recorded by moored tropical ocean atmosphere buoys in the tropical Pacific Ocean. The buoy data series are generally short in length (covering at most the period 1985–2010) relative to the century-long ship data, which inhibits definitive conclusions regarding long-term trends in MAT data relative to SST. However, the authors observed marked differences in these variables, particularly on sub-decadal timescales, which highlight the difficulty in assuming that MAT and SST are interchangeable.

Table SB2.1. Decadal trends (°C decade^{-1}) in large-scale average anomalies from 1979 to 2020 in the sea surface temperature (SST) and marine air temperature (MAT) data from ERA5 and in CLASSnmat and HadSST4. Note that ERA5 has complete coverage over ocean regions whereas CLASSnmat and HadSST4 are not complete. CLASSnmat and HadSST4 are masked to have the same spatial coverage.

	ERA5			
Region	SST	Air Temperature	CLASSnmat	HadSST4
Global	0.120	0.127	0.093	0.125
Northern extratropics	0.171	0.183	0.114	0.151
Tropics	0.116	0.123	0.039	0.101
Southern extratropics	0.081	0.084	0.069	0.098

Reanalysis datasets provide additional information about the (N)MAT-SST trend difference. Figure SB2.2 shows global and hemispheric annual average 2-m air temperature and SST anomalies (relative to 1981–2010) calculated from ERA5 over the period 1950–2020. This figure indicates a comparable trend in SST and co-located air temperature across all regions including the tropics (see also Table SB2.1), which is in contrast to the results in Figure SB2.1 using the gridded NMAT and SST datasets. Note that ERA5 is spatially complete (apart from the masking of sea ice regions) in Fig. SB2.2 whereas the in situ datasets have missing grid cells. Conversely, ERA5 data across the Arctic region, which are excluded in the Figure SB2.2 averages, show a much greater warming trend in air temperature relative to SST (Fig. SB2.3); however, SST is derived indirectly in these regions using sea ice concentration data (Hirahara et al. 2016).

It remains unclear if the trend difference seen in SST and NMAT datasets is due to physical processes or if it results from biases in either the SST or NMAT data or both. Understanding this feature is particularly important because global mean surface temperature (GMST) data products (Lenssen et al. 2019; Morice et al. 2021; Vose et al. 2012) combine anomalies of near-surface temperature over land with anomalies of SST rather than MAT. Resolving this question would also inform the debate about the suitability of comparing these merged GMST datasets against global climate model simulations of air temperature (Cowtan et al. 2015; Jones 2020), especially since simulated values using MAT for the marine component of global air temperature have been shown to warm at a slightly faster rate than a comparable dataset that used SST as the marine component (Richardson et al. 2018)

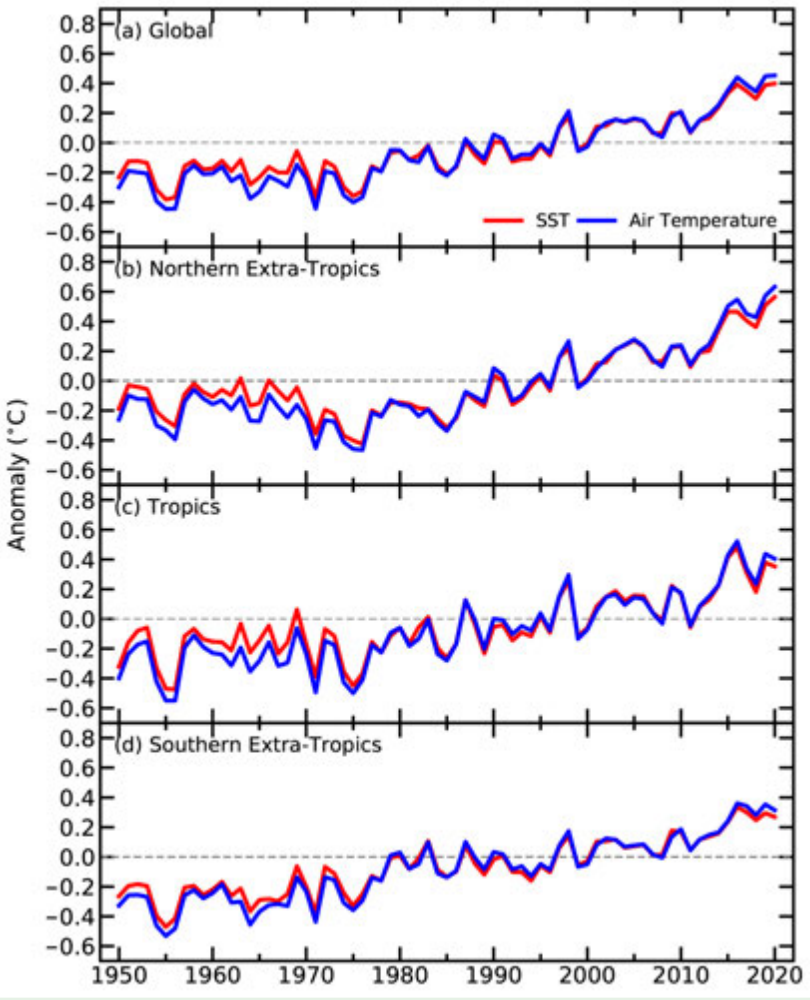

Fig. SB2.2. Large-scale average anomalies in 2-m air temperature across ocean regions and sea surface temperature from the ERA5 reanalysis dataset (Hersbach et al. 2020) from 1950 to 2020. Note that in contrast to Fig. SB2.1, the anomalies in this figure are expressed relative to 1981–2010 averages. The data prior to 1978 are currently considered experimental. Areas with sea ice are masked from the averaging.

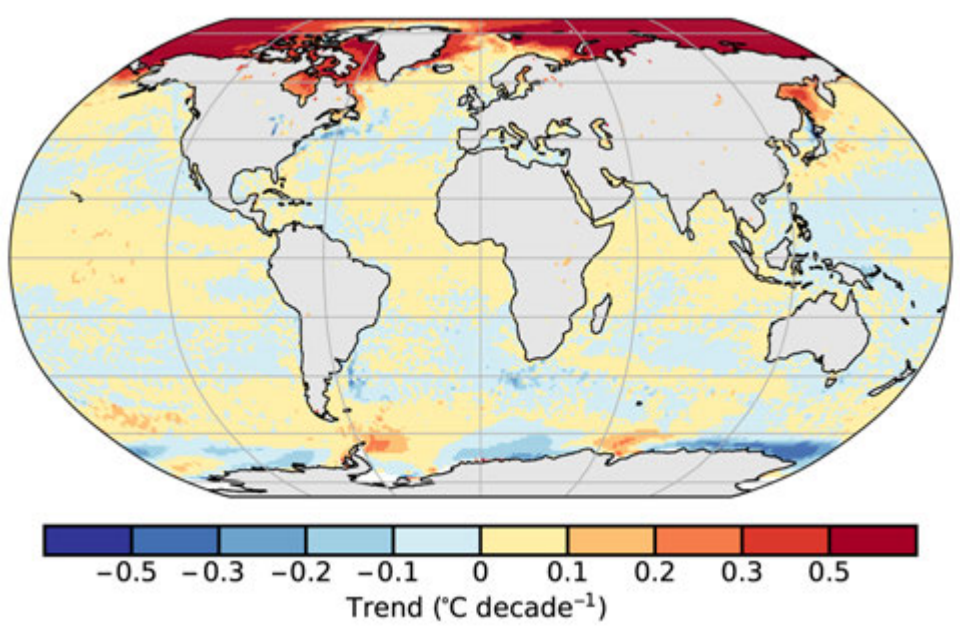

Fig. SB2.3. Linear trends in the difference between 2-m air temperature and sea surface temperature (SST) anomalies (°C decade^{-1}; relative to 1981–2010 averages) in the ERA5 dataset over the period 1980–2020. Red colors indicate where air temperature is warming faster than SST and blue colors where the reverse is true.

These analyses of NMAT and MAT illustrate the importance of exploring many different variables, using as many different methods as possible, and that some questions are yet unanswered. Despite the various issues discussed and differences in long-term trend, NMAT and MAT show similar year-to-year variability to spatially-matched SST in terms of the global average time series (Figs. SB2.1, SB2.2) and spatially for the annual average anomalies (Plate 2.1f). However, while 2020 was marginally the warmest year in globally average SST and reanalysis-derived MAT data (see section 2.b.1), this is not the case with CLASSnmat, which was cooler than 2016 and thus ranked 2020 as the second-warmest year in the record.

c. Cryosphere

1) Permafrost thermal state—J. Noetzli, H. H. Christiansen, F. Hrbacek, K. Isaksen, S. L. Smith, L. Zhao, and D. A. Streletskiy

Ongoing increases in global permafrost temperatures have occurred over the past several decades, with regional variability in magnitude. There have been short breaks in the warming trend due to shorter-term meteorological fluctuations, such as summer heat waves or snow-poor winters (e.g., Biskaborn et al. 2019; Romanovsky et al. 2007; Harris et al. 2009; Wu and Zhang 2008; PERMOS 2019; Etzelmueller et al. 2020). The largest increases were observed for sites with low permafrost temperatures, i.e., several degrees below 0°C, and low ground ice contents. Warmer and ice-rich permafrost warms up at a lower rate due to latent heat uptake during ice melt. This global picture continued in 2020. Record values were observed at many sites in polar and mountain regions. However, data could not be collected from all permafrost observation sites in 2020 (particularly in North America) due to pandemic-related travel restrictions.

Permafrost temperatures reported in 2020 for the Arctic regions were the highest on record at a majority of the observation sites. Warming rates for colder permafrost were as high as 0.8°C decade^{-1}, compared to less than 0.3°C decade^{-1} for permafrost at temperatures close to 0°C. Details on Arctic permafrost are given in section 5h. Increasing permafrost temperatures were reported from the Antarctic Peninsula and Victoria Land for the past decade up to 2018 (cf. Noetzli et al. 2019); however, deep boreholes and complete time series were scarce and the trend lacks statistical significance.

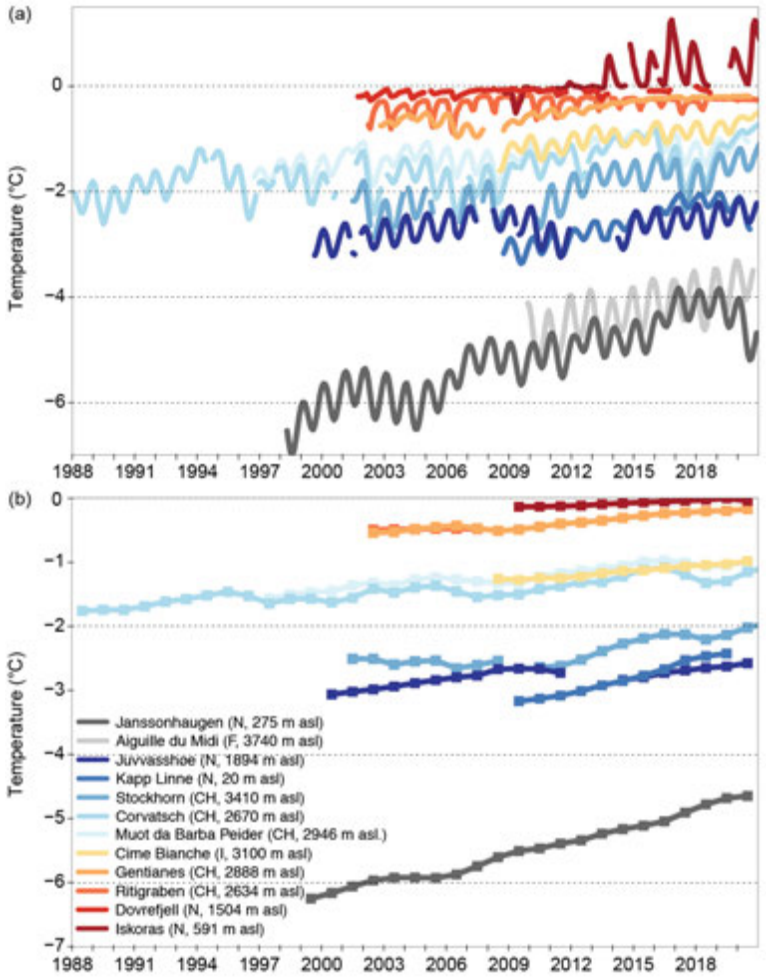

Fig. 2.10. Permafrost temperature measured in boreholes in the European Alps and the Nordic countries at a depth of approximately 10 m (monthly means, upper panel) and 20 m (annual means, lower panel). (Sources: Switzerland: Swiss Permafrost Monitoring Network PERMOS; Norway: Norwegian Meteorological Institute and the Norwegian Permafrost Database NORPERM; France: updated from Magnin et al. 2015; Italy: updated from Pogliotti et al. 2015.)

Mountain permafrost accounts for approximately 30% of the global area underlain by permafrost (Hock et al. 2019). Data are primarily available from the European Alps, the Nordic countries, and central Asia (Qinghai-Tibetan Plateau; QTP), but they are sparse for other mountain regions. A mean permafrost temperature increase of 0.19°C decade^{-1} was observed for 2007–16 (Biskaborn et al. 2019). Warming rates are heterogeneous due to the high spatial variability in thermal conditions resulting from complex topography, snow regime, and ground ice content. Highest rates are observed for bedrock with a low ice content and permafrost temperatures several degrees below 0°C and without a thicker winter snow cover. Permafrost temperatures recorded in 2020 in the European Alps were higher than in 2019 and close to or above the previous maximum observed in 2015 at the majority of sites (Fig. 2.10; Noetzli et al. 2020; updated from Pogliotti et al. 2015; PERMOS 2019) due to an early onset of the snow cover in autumn 2019 and the warmest year

recorded in Europe (Copernicus Climate Change Service 2021). Permafrost temperatures are thus higher or similar as before the temporary cooling in 2016 and 2017, which persisted in 2018 and only started to reverse in 2019. Temperatures at Murtèl-Corvatsch in the Engadin (Switzerland) increased by ~0.6°C at 20-m depth and by more than 1°C at 10-m depth over the past 3 decades. On Stockhorn above Zermatt (Switzerland), temperatures at 23-m depth increased by ~0.4°C over the past 2 decades. Surface velocities of rock glaciers generally follow the evolution of the permafrost temperatures. In the European Alps, rock glacier surface velocities for the year 2020 are at or above the previous maximum observed in 2015 (see Sidebar 2.1).

In the Nordic countries, permafrost temperatures measured in 2020 were the highest or second highest on record, continuing the reported warming trend (Fig. 2.10; Noetzli et al. 2020; Etzelmüller et al. 2020). In the cold mountain permafrost at Juvvasshøe in southern Norway, permafrost temperatures at 20-m depth increased by 0.5°C from 1999 to 2020. Permafrost temperatures decreased in Svalbard at 10-m depth compared to the previous extremely warm years due to the relatively cold winters in 2019 and 2020 (Christiansen et al. 2021). However, they are still above the long-term average; for example, at Kapp Linne they were 0.7°C higher in 2020 than at the start of the record in 2009.

Permafrost temperatures measured in the hinterland of the QTP in Central Asia continued to increase at all sites, with remarkable warming trends but variable rates: at 10-m depth they range between 0.45°C decade^{-1} (QTB15, Fig. 2.11) and 0.04°C decade^{-1} (QTB06), and at 20-m depth between 0.24 and 0.02 °C decade^{-1} (Zhao et al. 2020, 2021).

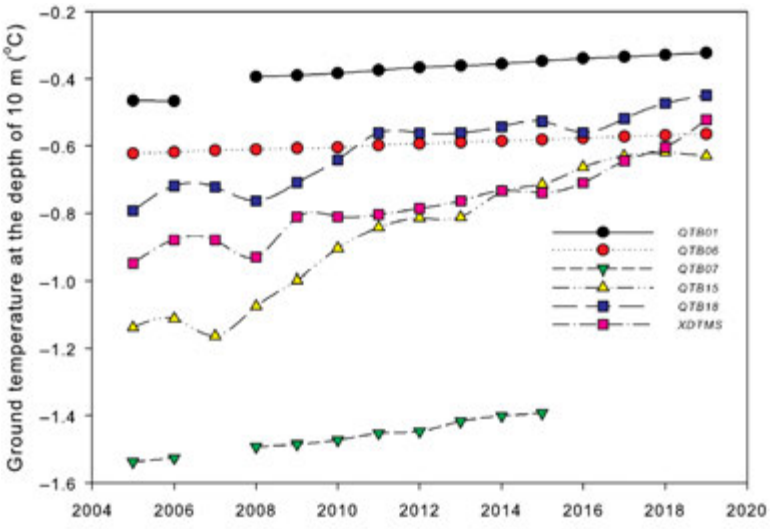

Fig. 2.11. Temperature measured in permafrost boreholes along the Qinghai-Xizang Highway on the Tibetan Plateau at 10-m depth from 2005 to 2019. (Source: Cryosphere Research Station on Qinghai-Xizang Plateau, CAS.)

The active layer thickness (ALT) is the ground layer that freezes and thaws annually and lies above the permafrost. Changes in ALT are a key indicator for changing permafrost conditions. ALT was not or only partly reported for some sites in Canada and Alaska due to COVID-19 travel restrictions. The ALT in northern Alaska was 6 cm thinner in 2020 than the decadal average (2008–17) and 8 cm thinner than in 2019. In the Alaska Interior, ALT was thicker than average, but 5 cm thinner than in 2019. ALT at the majority of sites in the Nordic region was similar to the previous year, at or close to record values. In Russia, ALT was thicker than average and thicker than in 2019 in all regions, except for Chukotka, where ALT was thinner than in 2019. The Siberian heat wave (see section 7g2, Sidebar 5.1) caused particularly thick ALT, with more than 10 cm larger values than in 2019 in West Siberia and neighboring sites in northwestern Russia. ALT in the regions of central and eastern Siberia was only 3 cm above previous regional averages. More details on ALT in Arctic regions are given in section 5h.

In the Scandinavian and European Alps, ALT values for 2020 were at or close to the previous maximum at most of the sites. In the Swiss Alps, record values were observed in 2020 for most sites, with values up to 10 m in extreme cases. Along the Qinghai-Tibet Highway (Kunlun mountain pass to Liangdaohe), an ALT increase was observed with a mean of 19.5 cm decade^{-1} from 1981 to 2019 (Fig. 2.12). In Antarctica, the February 2020 heat wave in the northwest Weddell Sea sector (section 2b3) accelerated active layer thickening. Thaw depth on James Ross Island reached 80 cm. This is comparable to observations in 2016/17 (Hrbáček et al. 2021), one of the warmest years so far measured in this sector (J. Turner et al. 2020).

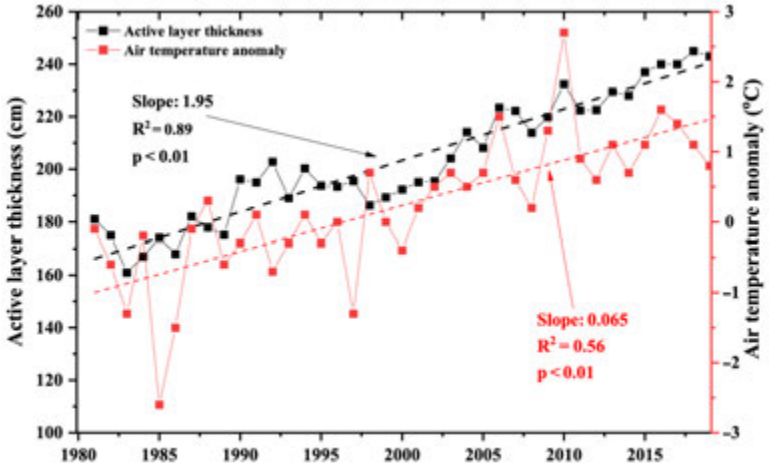

Fig. 2.12. The active layer thickness (cm) and air temperature anomaly (°C) in the permafrost zone along the Qinghai-Tibet Highway during the period 1981–2019. The air temperature anomaly is estimated relative to the climate baseline 1981–2010.

Long-term observation of permafrost relies on field observations of ALT and permafrost temperatures measured in boreholes. International data are collected by the Global Terrestrial Network for Permafrost (GTN-P) as part of the Global Climate Observing System (GCOS). Permafrost temperatures are logged manually or continuously using multi-sensor cables in boreholes reaching at least the depth of the zero annual amplitude. An assessment of the measurement accuracy of permafrost temperatures worldwide varied from 0.01° to 0.25°C, with an assumed overall accuracy of about 0.1°C (Biskaborn et al. 2019; Romanovsky et al. 2010). ALT is determined by mechanical probing where possible and has an accuracy of ~1 cm. Probing is not possible in bedrock or debris material, particularly in mountain regions. Here, ALT is interpolated from temperature sensors in boreholes. The current global coverage of permafrost monitoring sites is sparse; it is particularly limited in regions such as Siberia, central Canada, Antarctica, and the Himalayan and Andes Mountains.

Sidebar 2.2: Rock glacier kinematics—C. PELLET, X. BODIN, R. DELALOYE, V. KAUFMANN, J. NOETZLI, E. THIBERT, AND A. KELLERER-PIRKLBAUER

Rock glaciers are geomorphological indicators of permafrost occurrence in mountain areas and develop in most mountain ranges worldwide. Their kinematics derived from surface displacement measurements typically range from several centimeters up to several meters per year (Kääb and Vollmer 2000). Long-term studies from the European Alps have shown that the velocity of rock glaciers in a specific region responds sensitively and synchronously to interannual and decennial changes in ground temperature (e.g. Bodin et al. 2009; Delaloye et al. 2008, 2010; Kääb et al. 2007; Kellerer-Pirklbauer and Kaufmann 2012, 2018; Staub et al. 2016; Thibert et al. 2018; PERMOS 2019). Measurements of the surface velocity of rock glaciers based on aerial images and geodetic surveys first started in the 1960s in the European Alps (Haeberli 1985). Today, the majority of monitored rock glaciers are in the European Alps, and surface velocity measurements based on repeated terrestrial geodetic surveys have become part of operational permafrost monitoring in several European countries (Austria, France, Switzerland; see PERMOS 2019). In addition to their importance as climate indicators, rock glaciers are highly relevant for natural hazards risk management in mountain regions as well as for land use planning. Active rock glaciers are sediment conveyers and their increasing velocity can lead to a higher frequency of rock fall or debris flows from their frontal parts (e.g., Kummert et al. 2018).

The surface velocity of the majority of the observed rock glaciers in the European Alps behaved similarly during the past decades, despite variable size, morphology, and velocity range (Fig. SB2.4). The surface velocity increased by a factor of 2 to 10 from 1980s to 2015, and a maximum was reached in 2015. The acceleration was temporarily interrupted (i.e., velocity decrease was observed) for most of the landforms between 2004 and 2006, as well as between 2016 and 2018, coinciding with a decrease in ground temperatures (Noetzli et al. 2018; PERMOS 2019). The acceleration resumed in 2018. In 2020, the surface velocity of rock glaciers was close to or even higher than the maximum observed in 2015, which corresponds to the high ground temperatures observed (see section 2c1). Compared to the values of 2019, the surface velocity increase spans from +17% (Dösen [Austria] and Gemmi/Furggentälti [Switzerland]) to +45% (Grosses Gufer [Switzerland] and Hinteres Langtalkar [Austria]), which is in the same range as the acceleration observed between 2014 and 2015.

Long-term in situ measurements of rock glacier kinematics are scarcely available from other regions of the world. However,

the increasing emergence of open-access and high-resolution satellite data (e.g., optical and Synthetic Aperture Radar [SAR]) facilitates the setup of regional surveys worldwide (e.g., Strozzi et al. 2020). Recent studies in northern Norway (Eriksen et al. 2018) and in the Tien Shan Mountains (Kääb et al. 2020) found an overall increase of the rock glaciers' surface velocity from the 1950s on. These observations are consistent with the results obtained in the European Alps.

According to in situ measurement (e.g., Arenson et al. 2002; Buchli et al. 2018) and modeling approaches (e.g., Kannan and Rajagopal 2013), the displacement at the surface of rock glaciers mainly results from shearing within a layer of several decimeters to a few meters thickness, which typically lies between 15- and 30-m depth. The changes in rock glacier kinematics are mostly related to the evolution of ground temperature and liquid water content between the permafrost table and the main shearing horizon at depth: the closer to 0°C the temperature is, the faster the rock glacier is moving (Cicoira et al. 2019; Frauenfelder et al. 2003; Staub et al. 2016). A time lag of around 1 to 2 years has been observed between high air temperatures and the resulting acceleration (Kellerer-Pirklbauer and Kaufmann 2012; Staub et al. 2016).

The consistent regional evolution of rock glacier velocity and its sensitivity to changes in ground temperature, together with their global presence, make rock glaciers ideal climate indicators. An Action Group of the International Permafrost Association (IPA; see Delaloye et al. 2018) aims to internationally harmonize and coordinate measurements of rock glacier kinematics (RGK). Based on their recommendation, the Global Terrestrial Network for Permafrost (GTN-P) is proposing to include RGK as a new product of the GCOS essential climate variable (ECV) permafrost, in addition to the thermal state of permafrost and active layer thickness. RGK measurements are based on repeated terrestrial geodetic surveys or determined photogrammetrically using aerial images. Geodetic surveys are performed annually at the same time of the season (usually at the end of the summer). The coordinates and elevation are measured for a number of selected boulders (10–100 per landform) with an average accuracy in the range of millimeters to centimeters (Delaloye et al. 2008; PERMOS 2019). Multi-temporal aerial images are compared with each other to obtain rock glacier-wide movement information. Typically, horizontal displacement metrics are computed based on 2D ortho-image matching algorithms or digital elevation model matching. The accuracy of the photogrammetrically derived displacements strongly depends on the spatial resolution of the aerial images and on the image quality (e.g., sharpness, contrast, and so forth).

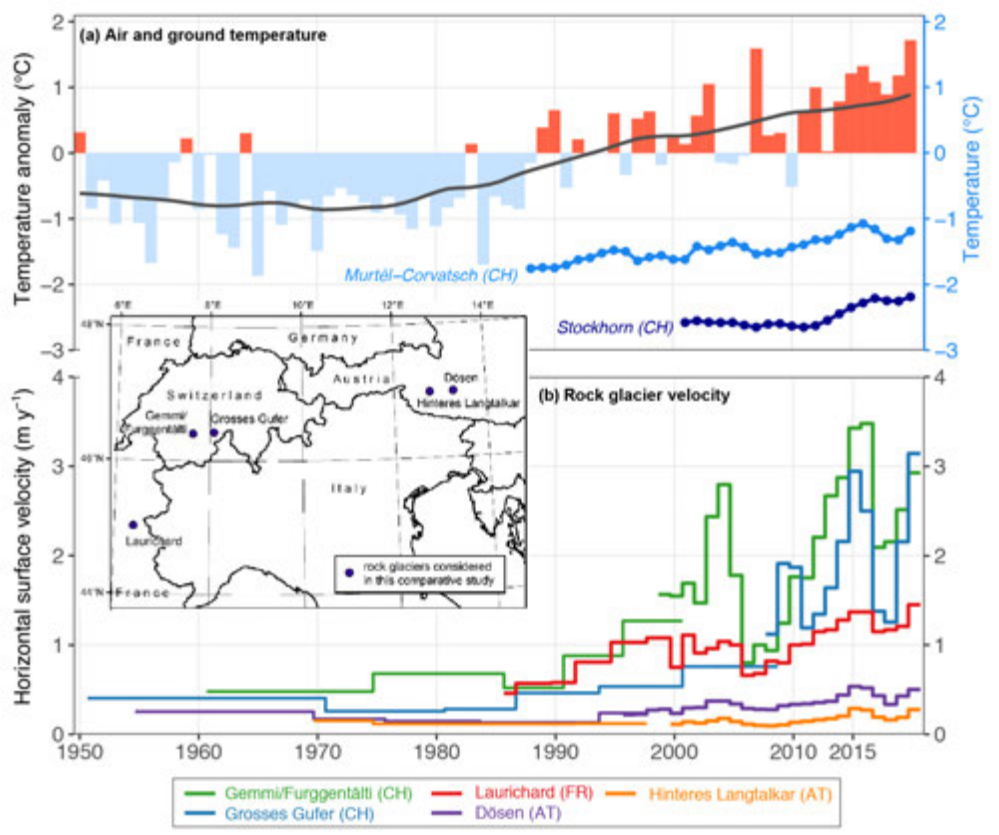

Fig. SB2.4. (a) Long-term in situ permafrost temperature measured at 20-m depth [blue lines]) and air temperature measurements (composite anomaly to the 1981–2010 norm [red and blue bars]) and composite 20-year running mean (solid line) at five selected sites in the European Alps (Switzerland, France, Austria): Besse France, Grand Saint-Bernard Switzerland, Sonnblick Austria and Zugspitze Germany. (b) Rock glacier surface velocities (m yr^{-1}) measured using in situ geodetic surveys and photogrammetrics. (Sources: Météo France, Deutscher Wetterdienst DWD, MeteoSwiss, Zentralanstalt für Meteorologie und Geodynamik ZAMG, Swiss Permafrost Monitoring Network, University of Fribourg, University of Graz, Graz University of Technology, Université Grenoble Alpes [INRAE].)

2) Northern Hemisphere continental snow cover extent—D. A. Robinson

Snow cover extent (SCE) displays considerable intra- and interannual variability. As such, variations in SCE impact surface albedo and thus, the overall surface energy balance. SCE also plays a role in atmospheric circulation and surface hydrology. Annual SCE over Northern Hemisphere (NH) lands averaged 24.1 million km^2 in 2020. This is 1.0 million km^2 less than the 51-year average (mapping extends back to late 1966, although three early years in the record are incomplete) and ranks 2020 as having the fourth-least extensive cover on record (Fig. 2.13; Table 2.4) and 0.7 million km^2 less than the 2019 mean extent. SCE over both NH continents, including the Greenland ice sheet, was considered in this analysis. Monthly SCE in 2020 ranged from 46.4 million km^2 in January to 2.3 million km^2 in August. The only years in the satellite record with less NH SCE than in 2020 were, from lowest upward, 1990, 1988, and 2007.

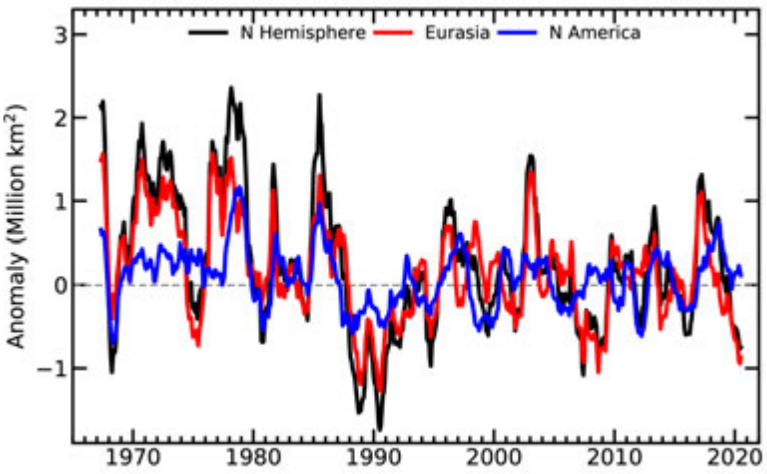

Fig. 2.13. Twelve-month running anomalies of monthly snow cover extent (million km^2 over NH lands as a whole, and Eurasia and North America separately, plotted on the seventh month using values from Nov 1966 to Dec 2020. Anomalies are calculated from NOAA snow maps. Mean hemispheric snow extent is 25.1 million km^2 for the full period of record. Monthly means for the period of record are used for nine missing months during 1968, 1969, and 1971 to create a continuous series of running means. Missing months fall between Jun and Oct, no winter months are missing.

Table 2.4. Monthly and annual climatological information on NH and continental snow extent between Nov 1966 and Dec 2020. Included are the numbers of years with data used in the calculations, NH means, standard deviations, 2020 values, and rankings. Areas are in million km^2. The years 1968, 1969, and 1971 have 1, 5, and 3 missing months, respectively, thus are not included in the annual calculations. N. Am. includes Greenland. Ranks are from most extensive (1) to least (ranges from 51 to 55 depending on the month).

	Years of data	Mean	Std. Dev.	2020	2020 NH rank	2020 Eurasia rank	2020 N Am. rank
Jan	54	47.2	1.5	46.4	37	39	33
Feb	54	46.0	1.8	43.5	52	52	39
Mar	54	40.4	1.9	37.7	50	51	32
Apr	54	30.5	1.7	29.1	42	52	14
May	54	19.2	2.0	16.7	49	52	28
Jun	53	9.4	2.5	6.0	49	52	43
Jul	51	3.9	1.2	2.4	50	51	50
Aug	52	3.0	0.7	2.3	50	52	42
Sep	52	5.4	0.9	4.5	42	50	22
Oct	53	18.6	2.7	21.2	10	19	1
Nov	55	34.3	2.1	36.0	12	17	13
Dec	55	43.7	1.8	43.7	32	26	37
Ann	**51**	**25.1**	**0.8**	**24.1**	**48**	**49**	**26**

During the first half of 2020, SCE was well below average across the NH. Monthly rankings ranged from below average for the 54-year record in January to third-least extensive in February. NH spring (March–May) SCE ranked fourth lowest on record, consistent with a generally persistent earlier snow melt in recent decades. Rankings of second- to fourth-least extensive cover occurred across Eurasia from February to June. North American snow cover was below average in five of the first six months of 2020, the exception being April, where a delayed melt resulted in above-average cover.

The NH SCE was above average in October and November, ranking 10th- and 12th-most extensive, respectively. The past nine autumns (September–November) have had average SCE exceeding 20 million km^2, while only eight of the prior 41 years exceeded that mark. December SCE was close to average. The excessive cover was primarily driven by conditions in North America, where October cover was the largest on record and November cover was 13th largest. December SCE was close to average in Eurasia, while a major turnaround occurred across North

America, with SCE below average. Research by Allchin and Dery (2020) supports the autumn increases, attributing this to atmospheric circulation patterns that have increased moisture fluxes into areas that are cold enough to sustain an autumn snow cover but previously were somewhat moisture deficient.

SCE over the contiguous United States during the first half of 2020 saw monthly rankings of third- to 20th-least extensive, with the exception of April which had above-average cover for the 54-year record. October 2020 was its most extensive SCE on record, with November above average and December below average.

SCE is calculated at the Rutgers Global Snow Lab from daily SCE maps produced by meteorologists at the National Ice Center (a United States joint NOAA, Navy, and Coast Guard facility), who rely primarily on visible satellite imagery to construct the maps (Estilow et al. 2015). Maps depicting daily, weekly, and monthly conditions, daily and monthly anomalies, and monthly climatologies for the entire period of record may be viewed at the Rutgers Global Snow Lab website (https://snowcover.org). Monthly SCE for the NH, Eurasia, North America, contiguous United States, Alaska, and Canada are also posted, along with information on how to acquire weekly areas and the weekly and monthly gridded products.

3) Alpine glaciers—M. Pelto

For 2019/20, the overall mean annual mass balance of 33 reporting reference glaciers, from 12 nations on four continents, was −621 mm and was −590 mm for all 79 reporting glaciers to date (World Glacier Monitoring Service [WGMS] 2020). This makes 2020 the 33rd consecutive year with a global alpine mass balance loss and the 12th consecutive year with a mean global mass balance below −500 mm, but it was less negative than the previous 2 years, which were the most negative of the entire 1950–2020 record. In the hydrological year 2017/18, reference glaciers experienced a mass balance loss of −1184 mm and in 2018/19 of −1177 mm.

Figure 2.14 illustrates glacier mass balance for the WGMS global reference glaciers with more than 30 continued observation years for the period 1950–2019. Global values were calculated using a single value (averaged) for each of 19 mountain regions in order to avoid a bias to well-observed regions. Zemp et al. (2019) indicated that the collective loss of alpine glaciers from 2006 to 2016 provided a global sea level contribution of 0.92 ± 0.39 mm yr^{-1} (see section 3f).

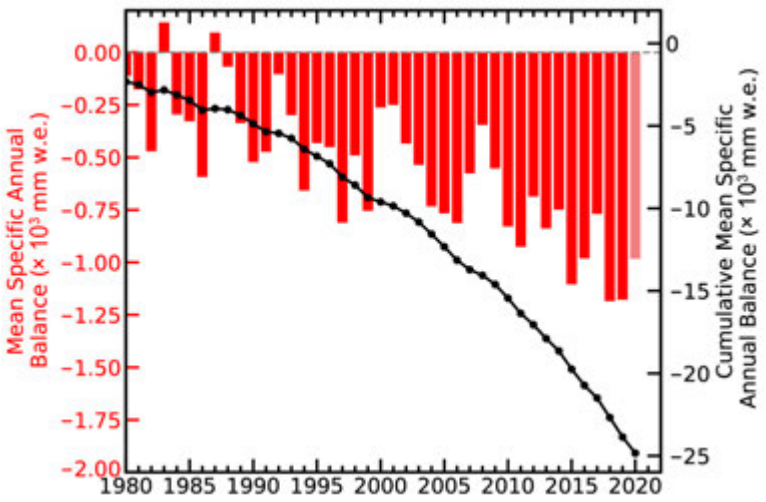

Fig. 2.14. Mass balance of alpine glaciers reporting to the World Glacier Monitoring Service in mm of water equivalent (mm w.e.). The values from 1980 to 2020 are based on average annual value determined for 19 different Alpine regions.

The decadal averaged annual mass balance was −214 mm in the 1980s, −499 mm in the 1990s, −527 mm in the 2000s, and −896 mm for the 2010s. The average mass loss reported by Slater et al (2021) identified a similar rise with a loss of 62 Gt yr^{-1} in the 1980s, 206 Gt yr^{-1} in the 1990s, 252 Gt yr^{-1} in the 2000s, and 327 Gt yr^{-1} in the 2010s. The increasing rate of glacier mass loss, with eight out of the 10 most negative mass balance years recorded after 2010 during a period of retreat, indicates that alpine glaciers are not approaching equilibrium and retreat will continue to be the dominant terminus response (WGMS 2020).

All 19 reporting glaciers in the Alps had a negative mass balance averaging −873 mm in 2020. In Austria in 2019, of the 92 glaciers with annual terminus observations, 86 (93.4%) withdrew, five remained stationary, and one advanced (Lieb and Kellerer-Pirklbauer 2020). This retreat trend continued in 2020.

In Sweden, all three glaciers reporting had a negative balance averaging −320 mm. In Norway, the eight reporting glaciers had a positive average mass balance of +365 mm in 2020. All 36 Norway glaciers surveyed in 2019 were retreating (Andreasson 2020). On Svalbard, the mean loss of three glaciers in 2020 was −1485 mm. Iceland completed surveys of nine glaciers, of which eight had negative balances with a mean mass balance of −442 mm.

In Alaska and Washington, all 14 glaciers observed in 2020 had a negative mass balance averaging −722 mm. This was significantly larger than the long-term average of four United States Geological Survey benchmark glaciers, which had a cumulative mass loss since the mid-twentieth century that averaged from −580 to −300 mm yr^{-1} (O'Neel et. al. 2019).

In South America, 2020 mass balance data were reported from two glaciers in Chile, one in Ecuador, and one in Argentina; all were negative with a mean of −1056 mm. This was greater than the 2000–18 average loss observed in the Andes of −720 ± 220 mm yr^{-1} (Dussaillant et. al. 2019).

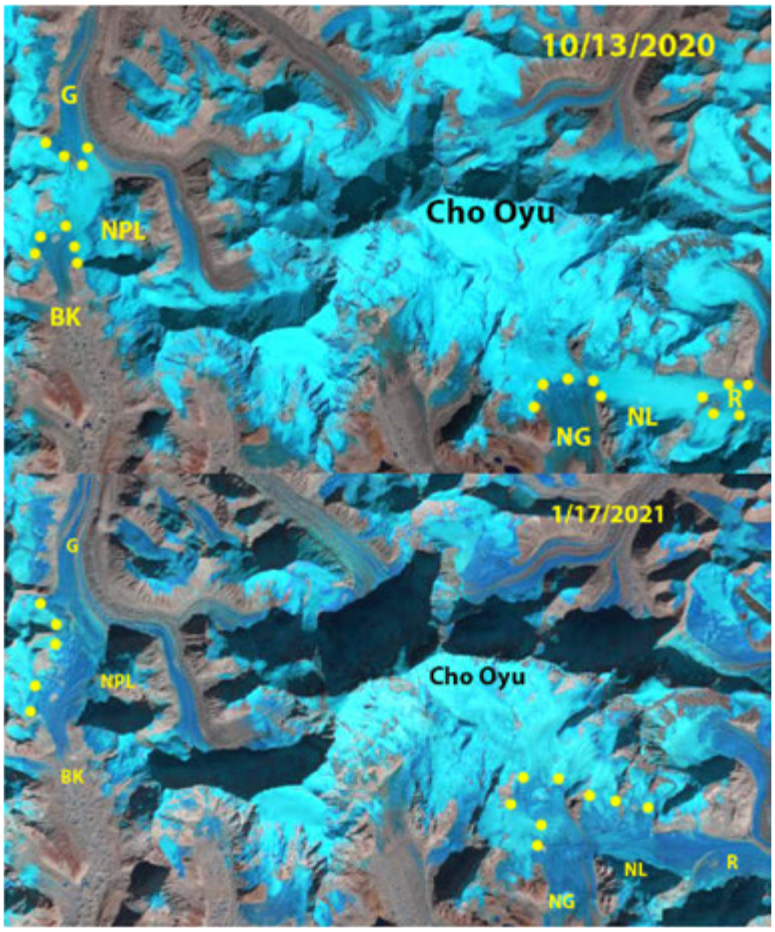

Fig. 2.15. LandSat imagery of Nangpa La (NPL-5806 m) and Nup La (NL-5850 m) 25–50 km west of Mount Everest, indicating the rise of the snow line from 13 Oct 2020 to 17 Jan 2021, leaving Nangpa La at the crest of the Gyabarg (G) and Bhote Koshi Glacier (BK) snow free. Nup La at the crest of Rongbuk (R) and Ngozumpa Glacier (NG) is also snow free on 17 Jan 2021.

In Kyrgyzstan and Kazakhstan, nine glaciers in the Tien Shan Range had near equilibrium balances. In the Himalayas, the two reporting reference glaciers had negative balances averaging −487 mm. King et al. (2019) identified that in the Mount Everest region mass loss has increased each of the last 6 decades. In 2020, the post-monsoon season and early winter were warm and dry in the Himalayas, leading to the ablation season extending into January with the snow line retreating over 100 m from October into January (Fig. 2.15; Patel 2021). This raises the question, when does the ablation season end in the region in our warmer climate?

The WGMS record of mass balance and terminus behavior (WGMS 2017, 2018) provides a global index for alpine glacier behavior. Glacier mass balance is the difference between accumulation and ablation, reported here in mm of water equivalent (mm w.e.).

4) Lake ice—S. Sharma and R. I. Woolway

In the 2019/20 winter, lake ice phenology (the timing of ice-on and ice-off) across the NH (calculated from Copernicus Climate Change Service [C3S] ERA5 [Hersbach et al. 2020]) continued to experience later ice-on dates, earlier ice-off dates, and shorter seasonal ice continuing the pattern seen over 1980–2020 (Magnuson et al. 2000; Benson et al. 2012; Woolway et al. 2020). The hemispheric average for ice-on was 1.5 days later $decade^{-1}$ and ice-off was 1.5 days earlier per $decade^{-1}$. In line with these calculated changes in ice phenology, the data suggest that the duration of lake ice cover was shortening at an average rate of 3 days $decade^{-1}$, albeit with considerable inter-annual variability ($R^2 = 0.44$). Relative to the 1981–2010 base period, NH lakes froze,

on average, 3 days later and thawed 5.5 days earlier during the 2019/20 winter season (Fig. 2.16). By ranking these ice phenology metrics according to the earliest and latest days in which they occurred since 1979/80 (the years in which these records began) we calculated that, in 2019/20, the hemispheric average ice-on was the eighth latest on record and ice-off was the third earliest. Relative to the 1981–2010 average, lake ice duration in 2019/20 was 8.5 days shorter across the NH. This was the third-shortest ice cover season since 1979/80. The regional variations in ice duration were consistent with the NH cold season (November–April) average surface air temperature anomalies (relative to 1981–2010) in 2019/20, similar to previous studies (Sharma and Woolway 2020). Most notably, some regions in North America, such as Canada, experienced below-average air temperatures, which resulted in longer-than-average ice duration. Conversely, many regions in Eurasia experienced warmer-than-average conditions that resulted in shorter-than-average ice duration (Figs. 2.16c,d).

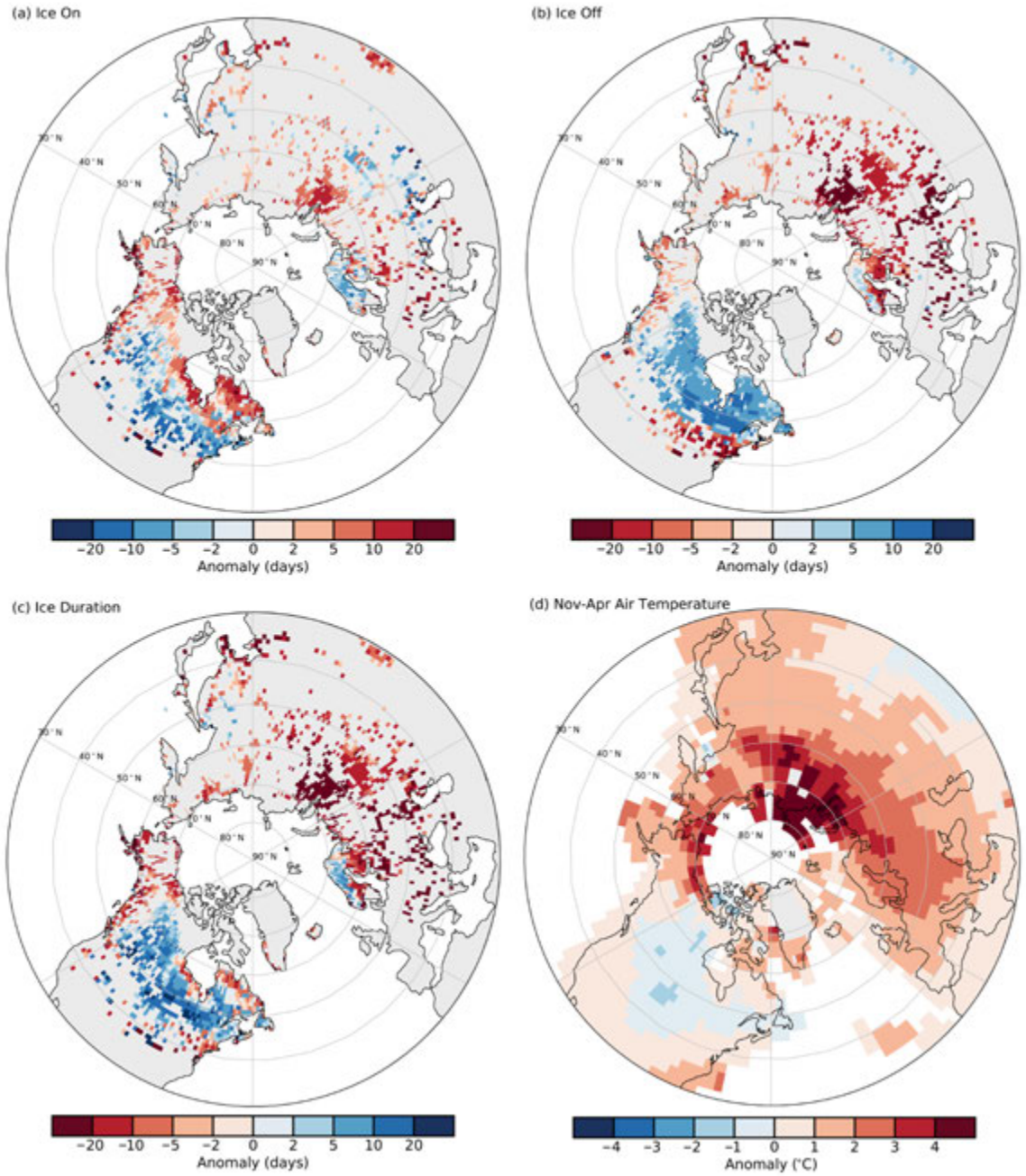

Fig. 2.16. Anomalies (days) in 2020 in (a) ice on, (b) ice off, and (c) ice duration for lakes across the NH, and (d) surface air temperature anomalies (°C) for the NH cold-season (Nov–Apr average), the time of year in which lakes typically freeze. The base period is 1981–2010. (Sources: ERA5, GISTEMP.)

In situ ice phenological records from 20 monitored lakes, situated mostly in Finland, the United States, Russia, and Canada, reveal that ice-on was 15 days later, ice-off was 11 days earlier, and there were 27 fewer days of ice cover over the winter season in 2020, on average, relative to 1981–2010 (Fig. 2.17). Lakes in Finland experienced remarkably warm conditions such that ice-on was 29 days later, ice-off was 13 days earlier, and ice duration was 42 days shorter. Typically, these Finnish lakes freeze in early December. However, during the 2020 winter, some of these same lakes froze as late as February (e.g., Lakes Nasijarvi and Visuvesi). Lakes in North America also experienced a warmer winter in 2020, with 16 fewer days of ice cover on average. Ice cover was especially anomalously low in the Finger Lakes region of New York state. For example, ice-on was 26 days later, ice-off was 16 days earlier, and ice duration was 43 days shorter for Cazenovia Lake. The winter of 2020 generally followed the long-term warming trend of 11 fewer days of ice cover for the 20 in situ lakes, on average.

In 2020, the Laurentian Great Lakes had substantially less ice cover, consistent with a warmer winter in the region. On average, the Laurentian Great Lakes had 33.9% less maximal ice coverage relative to 1981–2010. The smallest and most southern lake, Lake Erie, had the highest anomaly with a 65.4% reduction in ice coverage. Maximal ice coverage decreased by 38.1% in Lake Superior and 30.8% in Lake Huron, the two largest and most northern Great Lakes (Fig. 2.18).

To estimate the timing of ice-on and ice-off and, ultimately, the duration of winter ice cover across NH lakes, ice simulations from the ECMWFs ERA5 reanalysis product (Hersbach et al. 2020) were analyzed. Here, ice cover metrics were only calculated for pixels where lakes occupied greater than 1% of the land surface area. Lake ice conditions in 2020 were given as anomalies, calculated relative to the 1981–2010 average.

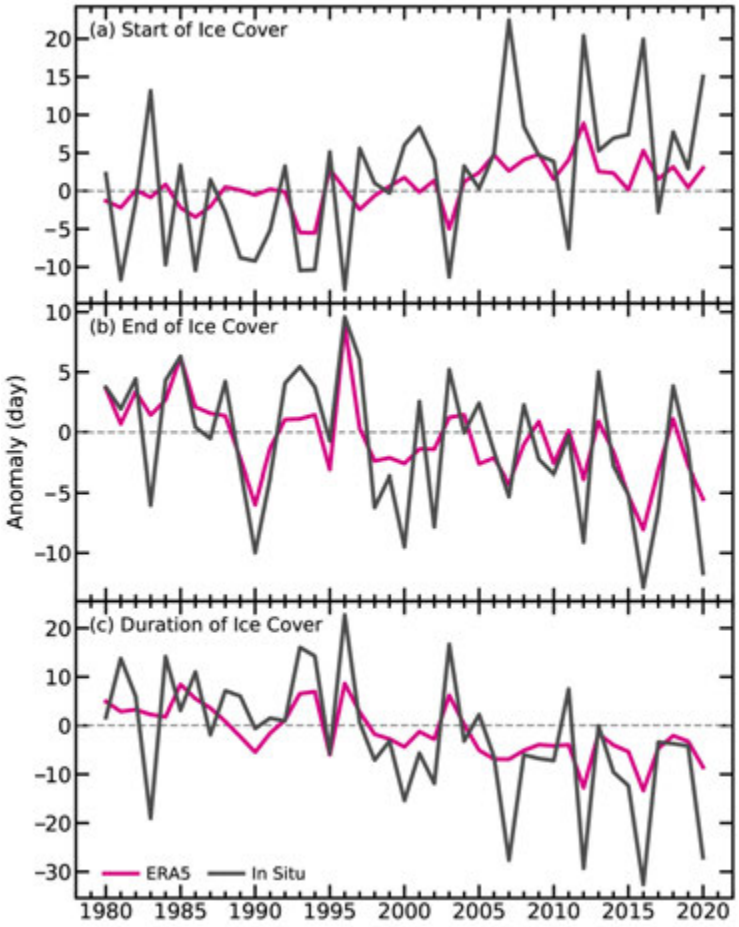

Fig. 2.17. (a) Lake ice on, (b) ice off, and (c) ice duration anomalies from 1980 to 2020 derived from in situ observations and ERA5. Base period is 1981–2010. In situ observations of ice on, ice off, and ice duration are derived from nine lakes monitored in Finland, one lake in Russia, nine lakes in the United States, and one lake in Canada.

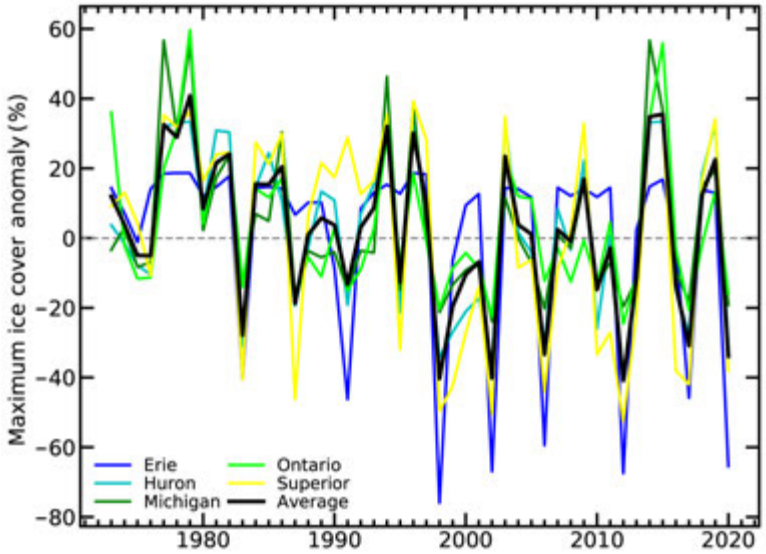

Fig. 2.18. Anomalies in Great Lakes maximum ice cover extent (%) for 1973–2020 (base period is 1981–2010). The black line shows the average anomaly for all of the Great Lakes, whereas the other lines show individual lakes (Erie, Michigan, Superior, Ontario, Huron).

Long-term in situ observations of ice-on, ice-off, and ice duration data were obtained for nine lakes in Finland, one lake in Russia, nine lakes in the United States, and one lake in Canada (Benson et al. 2000). Further, annual maximum ice cover (%) data for each of the Laurentian Great Lakes from 1973–2020 was obtained from the Great Lakes Environmental Research Laboratory. A combination of composite ice charts and observations from satellites, ships, and aircraft were used to quantify the maximum amount of ice coverage observed over the winter season in the Great Lakes (https://www.glerl.noaa.gov/data/ice/).

Surface air temperature data for the NH cold season (November–April average) were downloaded from the NASA GISS surface temperature analysis (Lenssen et al. 2019).

d. Hydrological cycle

1) Surface humidity—K. M. Willett, A. Vance, A. Simmons, M. Bosilovich, D. I. Berry, and D. Lavers

During 2020, the land surface specific humidity (q_{land})—a measure of atmospheric water vapor—remained well above average (0.14 to 0.36 g kg^{-1}), while relative humidity (RH_{land})—a measure of saturation—remained well below average (–1.28 to –0.68 %rh). Over oceans, q_{ocean} was a record high (0.23 to 0.41 g kg^{-1}) but RH_{ocean} was close to the 1981–2010 average (–0.14 to 0.13 %rh). Although the various estimates broadly agree there are differences in magnitudes and rankings (Fig. 2.19). In situ-based HadISDH and reanalyses MERRA-2 and JRA-55 show 2020 q_{land} as moister than 2019, ranking third, first, and fourth, respectively, within their records. ERA5 reanalysis shows 2020 tied with 2019, as sixth moistest on record. JRA-55 and HadISDH RH_{land} were also more saturated in 2020 but still low (third and fifth, respectively). ERA5 RH_{land} was slightly more arid than 2019, making it a record low for the second consecutive year. Over ocean, q_{ocean} was a record moist year by a large margin for HadISDH and ERA5. MERRA-2 and JRA-55 ranked q_{ocean} second and close to 2019. RH_{ocean} was more saturated in HadISDH and JRA-55 while marginally more arid in ERA5.

Taking HadISDH uncertainty into account, these rankings are less clear, but the 2020 q_{ocean} record lies outside the uncertainty range for all other years. HadISDH and ERA5 differ in input data, coverage, and processing, especially over ocean where no ship humidity data are assimilated (Simmons et al. 2021). The 2-sigma uncertainty for HadISDH broadly encompasses the ERA5 ocean values but not ERA5 land.

Surface humidity is driven by temperature and circulation patterns. The high q_{land} and record high q_{ocean} concur with the record/near-record high temperatures (section 2b1). Despite relatively neutral El Niño–Southern Oscillation (ENSO) conditions evolving to moderate La Niña conditions (section 4b), the q_{ocean} peak surpasses those of strong El Niño events (e.g., 1998, 2010, 2015–16); and the q_{land} peak is comparable for all datasets apart from ERA5.

Despite 2020 rankings differences, there is good agreement across estimates in long-term trends of increased q and decreased RH (Table 2.5). On average, the warmer air contains more water vapor, but not as much as it could, given its temperature. So, the air has become less saturated, even over oceans; ERA5, JRA-55, and HadISDH show small RH_{ocean} decreases. This is surprising given that several climate model studies show negligible or small increases in future RH_{ocean} (Held and Soden 2006; Schneider et al. 2010; Byrne and O'Gorman 2013, 2016, 2018).

HadISDH is affected by instrument and recording errors and biases along with changes in observation density, frequency, and precision (Willett et al. 2013, 2014, 2020). Reanalyses contain model and data biases and temporally changing data assimilation streams (Gelaro et al. 2017; Hersbach et al. 2020; Simmons et al. 2021). Unlike reanalyses, HadISDH is spatially incomplete, especially over the Southern Hemisphere oceans and many dry regions (where fewer people live and hence fewer weather stations). Spatially matching ERA5 to HadISDH slightly improves agreement (Fig. 2.19; Table 2.5). Over land, HadISDH reflects the well-observed regions and, hence, regions that are generally well constrained by observations in the reanalyses. Over oceans, ERA5 does not assimilate ship humidity or air temperature observations and thus poorer observational coverage has no effect, but various changes in satellite contributions do. Comparing trends over just the

Table 2.5. Global average decadal trends for specific humidity (q, g kg^{-1}) and relative humidity (RH; %rh) over 1979–2020 fitted using ordinary least squares regression. The 90th-percentile confidence intervals are shown in parentheses, fitted using AR(1) correction following Santer et al. (2008). Trends shown in bold are considered significantly different from a zero trend in that the confidence intervals do not cross the zero line.

Variable	HadISDH	ERA5	MERRA-2 (1980–2020)	JRA-55	HadISDH (continuous gridboxes)	ERA5 (continuous HadISDH gridboxes)	ERA5 (no HadISDH gridboxes)
Land q	**0.09 (0.02)**	**0.06 (0.01)**	**0.09 (0.02)**	**0.07 (0.01)**	**0.10 (0.02)**	**0.10 (0.02)**	**0.05 (0.01)**
Land RH	**−0.22 (0.07)**	**−0.44 (0.06)**	NA	**−0.32 (0.04)**	**−0.33 (0.07)**	**−0.46 (0.07)**	**−0.24 (0.03)**
Ocean q	**0.08 (0.01)**	**0.05 (0.02)**	**0.10 (0.02)**	**0.04 (0.01)**	**0.10 (0.02)**	**0.14 (0.03)**	**0.05 (0.02)**
Ocean RH	**−0.05 (0.05)**	**−0.18 (0.09)**	NA	**−0.05 (0.01)**	**−0.08 (0.05)**	**−0.17 (0.04)**	**−0.18 (0.02)**

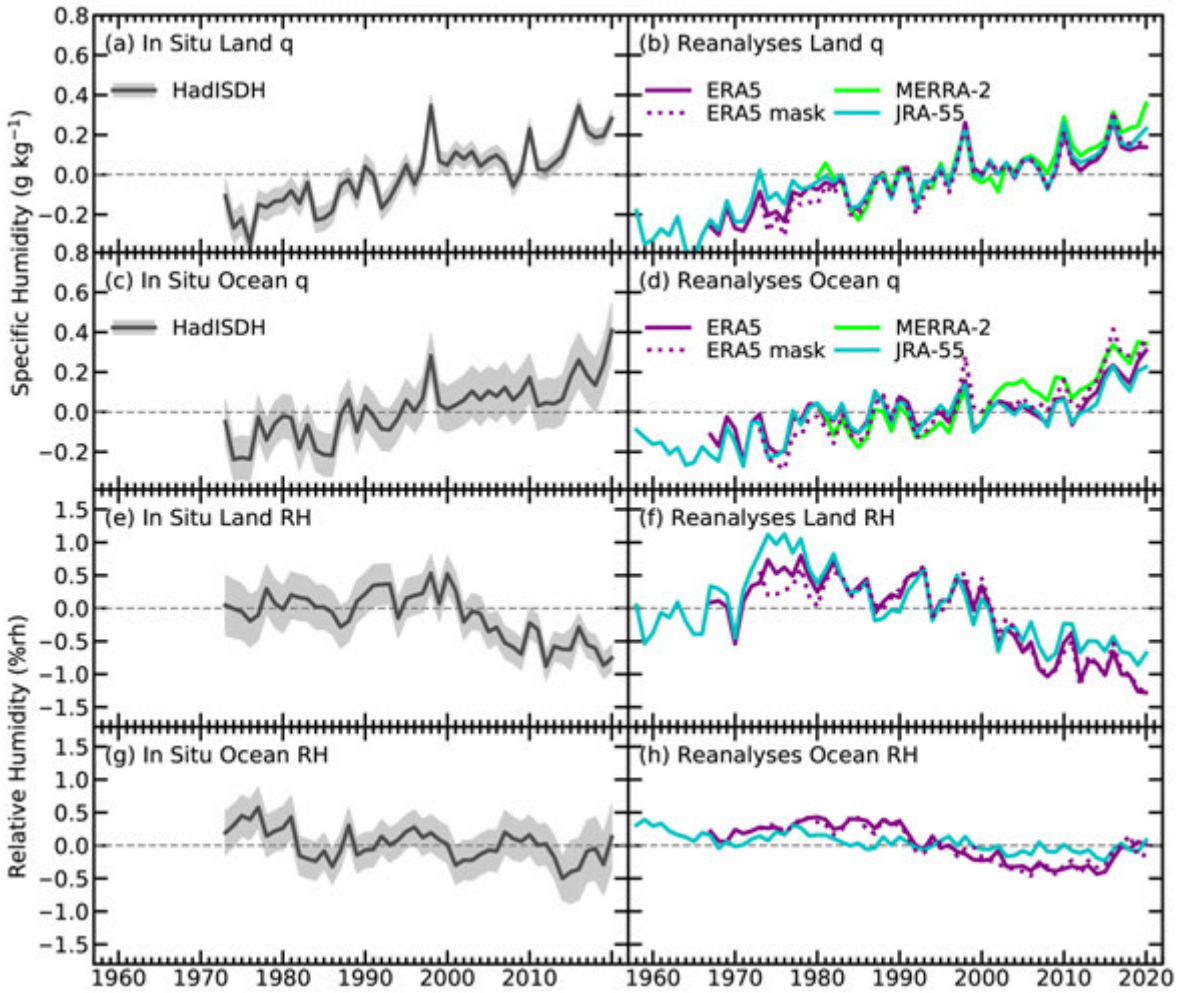

Fig. 2.19. (a)–(d) Global average land and ocean surface humidity annual anomalies of specific humidity (*q*; g kg^{-1}) and (e)–(h) relative humidity (RH; %rh) from in situ and reanalyses datasets relative to the 1981–2010 base period. For the in situ datasets 2-m surface humidity is used over land and ~10 m over the oceans. For the reanalysis, 2-m humidity is used over the whole globe. For ERA5, ocean series-only points over open sea are selected. 2-sigma uncertainty is shown for HadISDH capturing the observation, gridbox sampling, and spatial coverage uncertainty. (Sources: HadISDH [Willett et al. 2013, 2014, 2020]; ERA5 [C3S 2017, Hersbach et al. 2020]; JRA-55 [Kobayashi et al. 2015]; MERRA-2 [Gelaro et al. 2017].)

temporally complete HadISDH grid boxes with matched ERA5 grid boxes (Table 2.5) shows closer agreement. Compared to full coverage ERA5, HadISDH matched ERA5 shows stronger increasing *q* but near-identical decreasing RH, and HadISDH shows marginally stronger increasing *q* and slightly stronger decreasing RH. Trends over ERA5 where there are no HadISDH data are generally

weaker apart from RH_{ocean}. This suggests that HadISDH is biased towards regions with stronger moistening (q), especially over oceans. Possibly, ERA5 q is showing weaker moistening/stronger drying where it is unconstrained by surface observations. Further investigation is needed. Regardless, compared to the 1960–70s, when humidity monitoring records begin, in 2020, Earth contained more water vapor at the surface, while being less saturated.

2) Total column water vapor—C. A. Mears, S. P. Ho, O. Bock, X. Zhou, and J. P. Nicolas

In 2020, global land and ocean averages of total column water vapor (TCWV), the total amount of water vapor in the atmosphere, were well above the 1981–2010 climatology, ranging from 0.75 to 1.06 mm over ocean and 0.58 to 0.94 mm over land, yet did not approach the record levels observed in 2016 (Fig. 2.20). This is surprising at first because global temperatures in 2020 were essentially tied with those from 2016 in most surface and lower-tropospheric datasets (sections 2b1, 2b4). This discrepancy is likely explained by the highest temperature anomalies having occurred well away from the tropics (Plates 2.1a,e) where the sensitivity of TCWV to temperature changes is largest because of the Clausius-Clapeyron relationship.

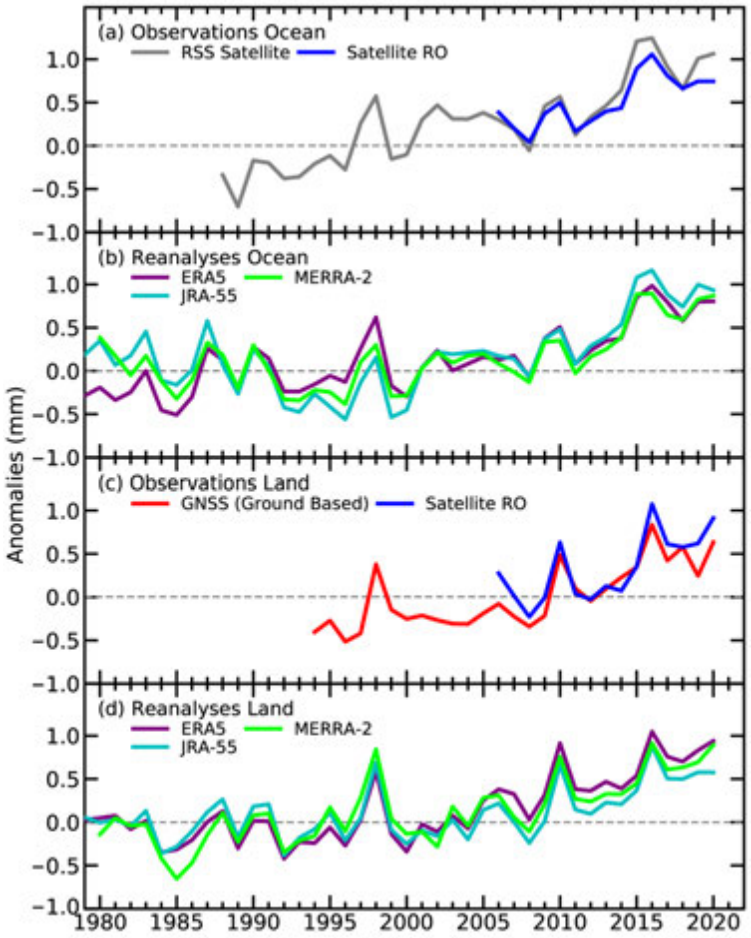

Fig. 2.20. Global mean total column water vapor annual anomalies (mm) over the oceans from (a) observations and (b) reanalyses, and over land from (c) observations and (d) reanalyses averaged over 60°S–60°N. The shorter time series from the observations have been adjusted so that there is zero mean difference relative to the ERA5 results during their respective periods of record.

Water vapor is an important part of the transport of energy in the atmosphere, and influences patterns of precipitation and evaporation, and thus drought and floods. Large-scale averages of TCWV are strongly correlated with atmospheric and surface temperature. Thus, as the planet warms, TCWV will also increase. TCWV estimates are derived from satellite-borne microwave radiometers over the ocean (RSS Satellite; Mears et al. 2018), from Global Positioning System–Radio Occultation (GPS-RO) observations from the COSMIC, Metop-A, -B, and -C and COSMIC-2 satellite missions over land and ocean (satellite RO; Ho et al. 2020a,b, 2010a,b; Teng et al. 2013; Huang et al. 2013), and from ground-based Global Navigation Satellite System (GNSS) stations over land (Bock 2020). In addition, three reanalysis products are also used here: ERA5 (Hersbach et al. 2020), MERRA-2 (Gelaro et al. 2017), and JRA-55 (Kobayashi et al. 2015). All three reanalyses assimilate satellite microwave radiometer and GPS-RO data and are therefore not independent from these two datasets. Ground-based GNSS measurements are not assimilated and are thus independent.

The most prominent TCWV anomaly features for 2020 (Plate 2.1i) were the strong north–south asymmetry over the tropical Pacific Ocean and the excess vapor anomaly over most of the tropical and subtropical Indian Ocean. Other regions showed a mix of smaller anomalies, with more regions showing positive anomalies than negative. The ocean patterns in TCWV from ERA5 (Plate 2.1i) are confirmed by the RSS satellite data (Appendix 2, Fig. A2.8), satellite RO ocean

measurements, and by the other two reanalyses. Over land, the patterns agree less well. There is good agreement in the dry anomalies over central South America and central Africa and in the wet anomalies over the Gulf of Mexico, Caribbean, North Africa, East Africa, and India. However, over the United States, satellite RO shows dry anomalies to the west and wet anomalies to the east, which is the opposite of ERA5 and ground-based GNSS. There are also opposing anomalies in western Europe, the southwest tip of Africa, eastern Asia, and central Australia. In ERA5, the Pacific Ocean wet–dry dipole and wetter-than-average Indian Ocean, in addition to many of the more regional features (e.g., dry western United States, wet East Africa), are consistent with those shown for surface specific humidity (section 2d1). Specific humidity should be broadly similar to TCWV in that the vast majority of water vapor lies close to the surface. The poorer agreement between ERA5 and RO over land may be partly due to different and incomplete temporal and spatial sampling from the satellite RO data. In 2020, only COSMIC-2, Metop-A, -B, and -C are used because COSMIC data are only available from January to April. COSMIC-2 mainly covers from 45°S to 45°N with about 4000 daily occultations and a relatively uniform local time coverage. The other RO missions (i.e., Metop-A, -B, and -C) cover both tropical and midlatitudes (60°S to 60°N) but with only about 1000 daily occultations and non-uniform local time coverage.

Ocean TCWV global average anomaly time series (Figs. 2.20a,b) from reanalyses and RSS satellite data show maxima in 1983–84, 1987–88, 1997–98, 2009–10, and 2015–16 associated with El Niño events. Both 2019 and 2020 approach, but do not exceed, the 2015–16 record levels due to the overall increasing trend. The RSS satellite data show a discernible increasing trend. On the other hand, the reanalysis products show different long-term trends up until the 1990s but agree well with each other and with the radiometer data after 2000. The satellite RO data are in good agreement with both the radiometer and reanalysis data but show a lower overall trend. TCWV is strongly driven by surface temperature and thus El Niño–Southern Oscillation conditions. After the 2015–16 El Niño peak, all datasets show a return to lower TCWV due to a generally neutral/weak La Niña in 2017–18, followed by larger TCWV anomalies associated with the weak El Niño in boreal winter-spring 2018–19. The positive anomaly continued into 2020. Although 2020 began with weak El Niño conditions, there was a shift by August, ending in moderate La Niña conditions in December (sections 2e1 and 4b).

Over land, the reanalyses, satellite RO missions, and ground-based GNSS agree well in terms of the global average anomaly time series (Figs. 2.20c,d). The small differences between ground-based GNSS and the other datasets are due to asymmetry in the spatial sampling, with more stations located in the Northern Hemisphere, but the general trend and interannual variability are consistent among all datasets. An ERA5 latitude–time Hövmuller plot of TCWV anomalies over land and ocean (Fig. 2.21) indicates that the long-term increase in TCWV occurs at all latitudes, with less variability outside the tropics. Following the most recent strong El Niño in 2015–16, elevated moisture has persisted in the tropics, mainly north of the equator.

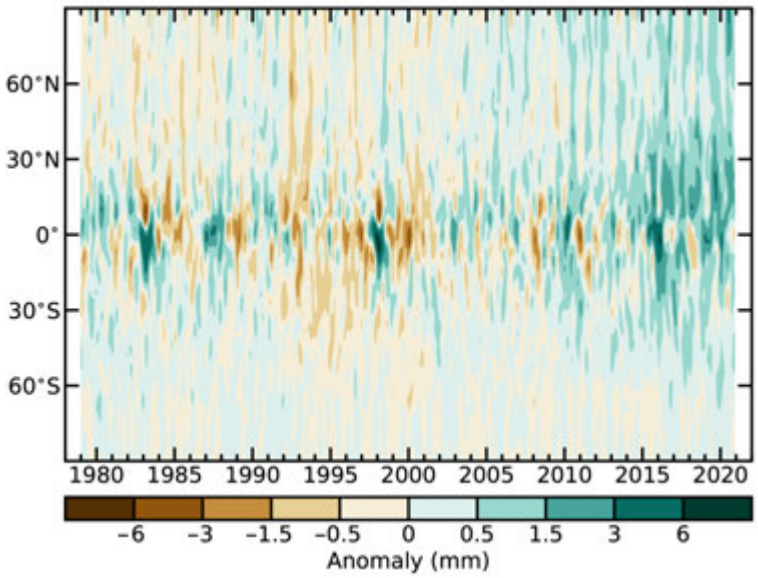

Fig. 2.21. Hövmuller plot of total column water vapor anomalies (mm; base period 1981–2010) derived from the ERA5 reanalysis.

3) Upper tropospheric humidity—V. O. John, L. Shi, E.-S. Chung, R. P. Allan, S. A. Buehler, and B. J. Soden

The 2020 near-global-average (60°S–60°N) upper tropospheric (relative) humidity (UTH) remained close to the 2001–10 average (0.04, −0.16, and −0.35 %rh for the three datasets shown in Fig. 2.22a). This implies a continued moistening of the upper troposphere with warming. A near-zero decadal trend (less than 0.01 %rh per decade for all datasets in Fig. 2.22) in the UTH indicates an increase in absolute (specific) humidity in line with the warming mid- and upper troposphere (about 0.2 K per decade as shown, for example, in Santer et al. 2017 and Christy et al. 2020), and hence is consistent with a positive (amplifying) water vapor feedback (Chung et al. 2016).

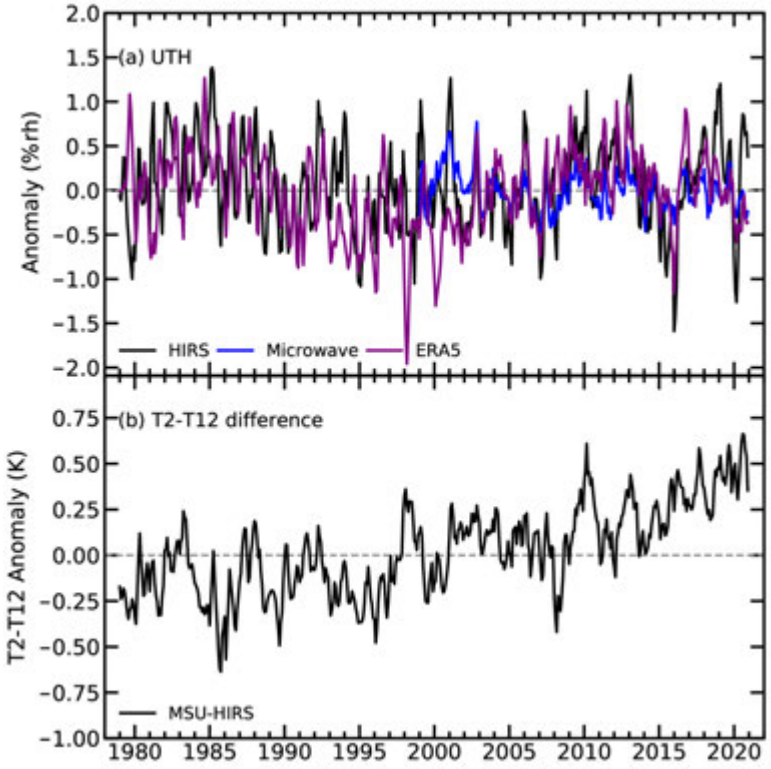

Fig. 2.22. (a) Global (60°S–60°N) average time series of upper tropospheric humidity anomalies (%rh) using HIRS (black), microwave (blue), and ERA5 (purple) datasets. (b) Anomalies of MSU/AMSU channel 2 brightness temperature (T2) minus HIRS channel 12 brightness temperature (T12) with increasing values indicative of higher absolute or specific humidity. The anomalies are computed with respect to the 2001–10 average, and the time series are smoothed to remove variability on time scales shorter than 3 months.

This moistening of the free troposphere is demonstrated in Fig. 2.22b, which shows the difference between the Microwave Sounding Unit/Advanced Microwave Sounding Unit (MSU/AMSU) channel 2 brightness temperature (T2; sensitive to upper-tropospheric temperature emissions from oxygen molecules) and High Resolution Infra Red Radiation Sounder (HIRS) upper tropospheric channel brightness temperature (T12). As shown in Chung et al. (2014), the difference, T2 minus T12, measures the divergence in emission levels between upper-tropospheric water vapor and oxygen. This divergence provides a direct measure of the extent of upper-tropospheric moistening as the emission level of T12 elevates with increasing concentrations of water vapor, while the T2 emission level remains the same because the oxygen concentration does not change over time. The positive trend in the T2 minus T12 time series thus indicates the moistening of the upper troposphere. The water vapor feedback is determined mainly by the mid- to upper troposphere though the concentration of water vapor is small there. This is because the radiative effect of absorption by water vapor is roughly proportional to the logarithm of its concentration, so it is the fractional change in water vapor concentration, not the absolute change, that governs its strength as a feedback mechanism (Allan et al. 1999; Held and Soden 2000; John and Soden 2007).

The microwave satellite data (Chung et al. 2013) and the ERA5 reanalysis (Hersbach et al. 2020) data show below-average UTH values throughout the year. However, the HIRS infrared satellite data (Shi and Bates 2011) show above-normal UTH values since summer 2020; the reason for this discrepancy is not yet understood. Despite this, there is broad agreement among the three datasets in interannual variability. During their common period, there is a correlation of 0.6 between the two satellite datasets and 0.5 between ERA5 and either of the satellite datasets. The mean and standard deviation of the anomaly time series are −0.01 ± 0.54, 0.08 ± 0.65, and −0.01 ± 0.33 %rh for the ERA5, HIRS, and microwave datasets, respectively, during their common period. HIRS and ERA5 show larger interannual variability compared to the microwave data, which can be

attributed in part to the clear-sky sampling of the infrared HIRS observations (e.g., Fig. 10 of John et al. 2011) and to the use of a single level (400 hPa) RH for the ERA5. Negative (dry) anomalies in all datasets can be observed during strong El Niño events (e.g., 2015–16).

Annual anomalies of UTH for 2020 are shown in Plate 2.1j and Appendix Fig. A2.9 for the microwave and HIRS datasets, respectively. Preconditioned in 2018–19 by a strong positive Indian Ocean dipole (IOD), the neutral to slightly positive phase of the IOD during 2020 led to widespread flooding in eastern Africa (Wainwright et al. 2020) and droughts in southeast Asia (Wang and Cai 2020). This is clearly reflected in the UTH data by positive anomalies over eastern Africa and surrounding oceans and negative anomalies over southeast Asia and eastern Australia. During the positive phase of IOD, sea surface temperature (SST) in the Indian Ocean near Africa's east coast is warmer than usual, while SST in the waters northwest of Australia is comparatively cooler. These conditions lead to above-average precipitation in the western equatorial Indian Ocean and surrounding areas and the opposite in southeast Asia (section 2d4). Severe drought conditions in Madagascar, South America, and the western United States are also reflected in the anomalies. Above-normal monsoon rainfall in central and southern India is indicated by the positive anomalies in UTH over those regions. Dry anomalies over Europe are associated with the high geopotential height associated with a blocking pattern that led to dry, sunny conditions, especially in spring 2020 (van Heerwaarden et al. 2021; section 7f). This close connection of UTH to convection makes it suitable for monitoring large-scale dynamics of the troposphere.

The inter-satellite calibrated and bias-corrected infrared and microwave satellite measurements sample a broad upper tropospheric region (roughly between 500 and 200 hPa, but this layer varies slightly depending upon the atmospheric humidity profile) twice per day, and infrared observations only sample clear-sky scenes (John et al. 2011). The ERA5 reanalysis is based on model runs constrained with in situ and satellite data including the HIRS and microwave radiances. ERA5 samples all regions every hour but here are only displayed at 400 hPa.

4) Precipitation—R. S. Vose, R. Adler, A. Becker, and X. Yin

Precipitation over global land areas in 2020, as estimated from three different monitoring products, was near to or above the 1981–2000 long-term average (Fig. 2.23a). All three products indicate that global average precipitation in 2020 was higher than 2019. The observational datasets with the most complete global coverage, that is, the gauge-based product from the Global Precipitation Climatology Centre (GPCC; Becker et al. 2013) and the blended gauge–satellite product from the Global Precipitation Climatology Project (GPCP; Adler et al. 2018), had near-normal precipitation for 2020 (area-average anomalies of +0.46 mm and +0.63 mm, respectively). In contrast, the gauge-based Global Historical Climatology Network (GHCN; Peterson and Vose 1997) dataset was well above the long-term normal, with an area-average anomaly of +49.38 mm. GHCN has had consistently higher precipitation estimates than the other products for the past 4 years. According to the GPCP dataset, the precipitation anomaly over the global ocean (Fig. 2.23b) was +3.93 mm, and the global (land and ocean) anomaly (Figure 2.23c) was +3.22 mm, the latter being a slight increase from the previous year.

Examining the geographic distribution of precipitation anomalies, there was substantial variability across the planet in 2020 (Plate 2.1k). Over global land areas, the largest positive anomalies were over eastern China, with much of central Asia and sub-Saharan Africa also well above average. The strongest positive anomaly over land was in eastern China, the scene of devastating and long-lasting floods primarily during the summer months (see Sidebar 7.3). The largest negative anomalies were over the continent of South America, with much of temperate North America also below average (see sections 7d and 7b, respectively). Over the global oceans, the largest positive anomalies were over the Maritime Continent and the Indian Ocean, as well as along the Intertropical Convergence Zone (ITCZ) and the South Pacific Convergence Zone (SPCZ) in the Pacific Ocean. Much of the rest of the Pacific Ocean, however, had negative anomalies, as did much of the North

Atlantic and part of the southern Indian Ocean. Rainfall excesses associated with tropical cyclones were evident in several areas, including the southeastern United States and in the Caribbean and South China Seas.

Precipitation patterns in 2020 reflect the transition from weak El Niño-like conditions early in the year to a moderate La Niña late in the year (see sections 2e1, 4b). During the first 3 months of 2020, there was excess rainfall in the central Pacific along the equator and generally below-average precipitation over the Maritime Continent associated with the El Niño-like conditions. During the last 3 months of the year, influenced by La Niña, the central Pacific reversed from a positive anomaly to an intense negative anomaly, and the Maritime Continent became positive. Outside the ENSO-affected regions, the large-scale patterns, e.g., over the subtropics of the Pacific and the Atlantic, stayed roughly the same during the year.

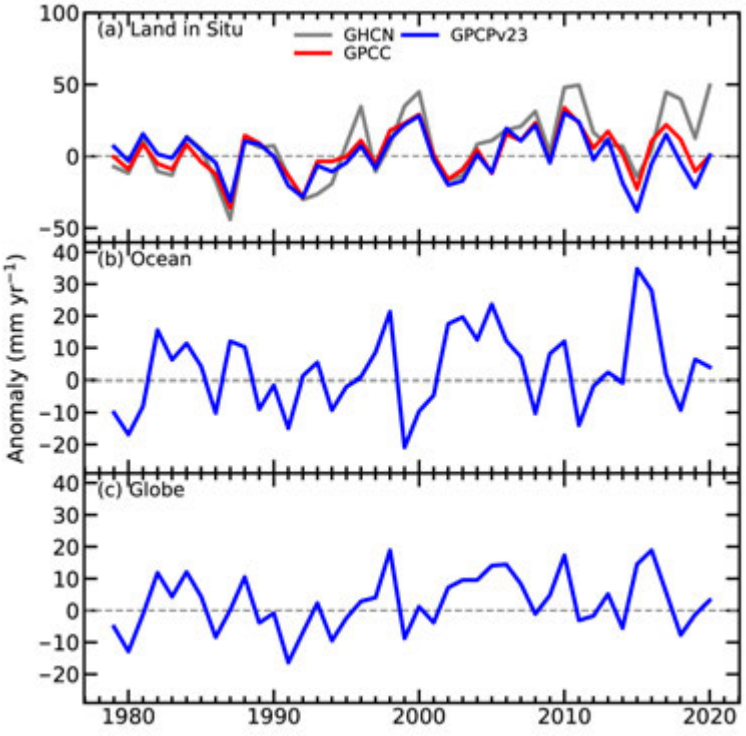

Fig. 2.23. Globally averaged precipitation anomalies (mm yr^{-1}) relative to the 1981–2000 base period over (a) land, (b) ocean, and (c) the globe. Land and ocean time series were created using a proportional land/sea mask at the 1°×1° scale.

5) Land-based precipitation extremes—M. R. Tye, S. Blenkinsop, M. G. Bosilovich, M. G. Donat, I. Durre, A. J. Simmons, and M. Ziese

Overall, extreme events during 2020 were less intense than normal across most of Eurasia and North America and more intense than normal over the tropics. The patterns of global mean and extreme anomalies illustrate the uneven spatial and temporal distribution of precipitation, whereby the heaviest events contribute disproportionately to the annual total volumes (PRCPTOT [see Table 2.6 for extremes index descriptions]; Pendergrass and Knutti 2018; see section 2d4, Plate 2.1k). Parts of Central America, Europe, and Asia reported very high PRCPTOT; and as illustrated by Plate 2.1l, Fig. 2.24 and Appendix Fig. A2.10, eastern China was influenced by very intense extremes (R95p, Rx1day, Rx5day) rather than frequent heavy rain days (R10mm, R20mm). Conversely, dryness in South America for instance, arose from the combined absence of heavy rain days and anomalous low intensity of extremes. In contrast with 2019, there was a far clearer pattern of exceptionally wet or dry regions (Blenkinsop et al. 2020), with global insured losses

Table 2.6. Precipitation indices used in this section and their definitions, as developed by the WMO ETCCDI (Zhang et al. 2011).

Index	Definition	FIgure/Plate
Rx1day	Highest 1-day precipitation amount (mm)	Plate 2.1l; Figs. 2.24c,d; 2.25
Rx5day	Highest 5-day precipitation amount (mm)	Appendix Figs. A2.10c,d
R10mm	Heavy precipitation days >10 mm (days)	Appendix Figs. A2.10c,d
R20mm	Very heavy precipitation days >20 mm (days)	Fig. 2.24
R95pTOT	Total precipitation on days exceeding the 95th percentile of wet days (mm)	Not shown
PRCPTOT	Annual total precipitation falling on wet (>1 mm) days (mm)	Not shown

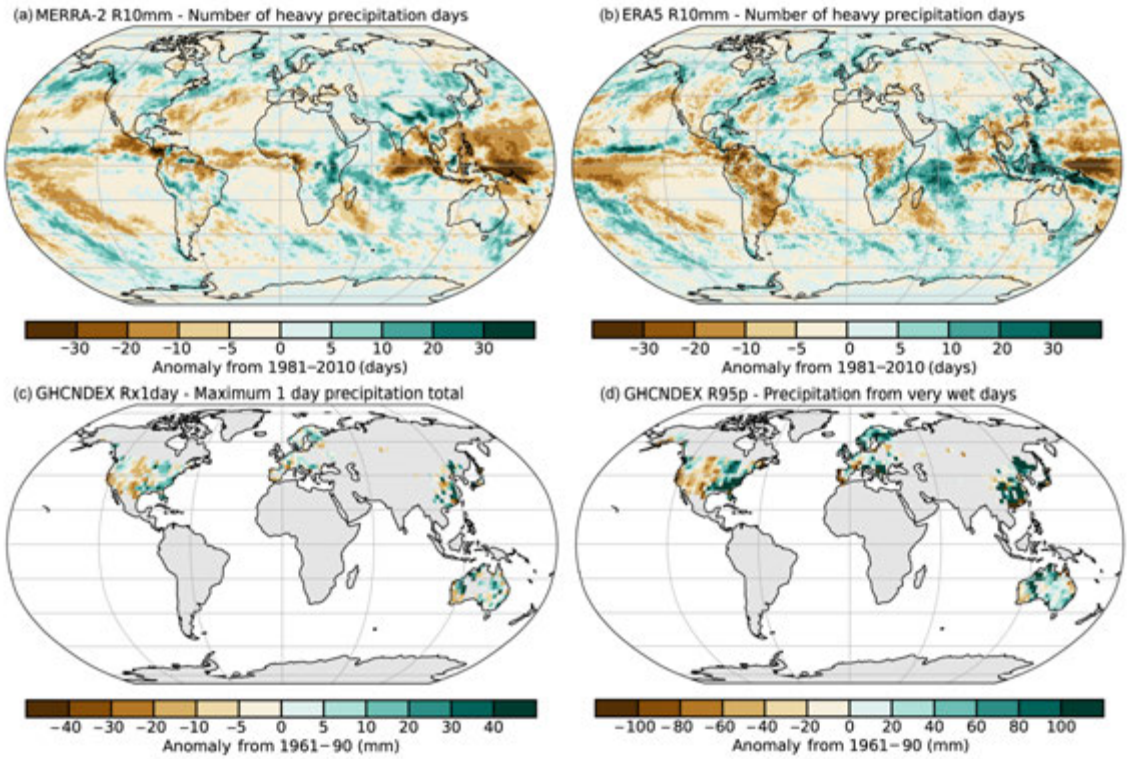

Fig. 2.24. Anomalies of 2020 indices relative to a 1981–2010 baseline for: R20mm (days) derived from (a) MERRA-2 (Gelaro et al. 2017) and (b) ERA5 (Hersbach et al. 2020) reanalyses, (c) Rx1day (mm), and (d) R95p (mm) derived from the in situ-based GHCNDEX relative to a 1961–90 baseline (Donat et al. 2013).

of $76 billion U.S. from natural hazards largely driven by floods from severe convective storms and drought-influenced fires (Swiss Re 2020).

Several notable events stand out in relation to the long-term mean of extreme precipitation indices (Table 2.6). Reanalysis products (MERRA-2, Gelaro et al. 2017; ERA5, Hersbach et al. 2020) and gridded observations (GPCC, Schamm et al. 2013; GHCNDEX, Donat et al. 2013) generally show similar patterns, with the exception of the tropics, parts of central and southern Africa, and South America for extreme indices (e.g., R10mm, Rx1day) as noted in recent publications (Alexander et al. 2020; Hersbach et al. 2020). Rx1day and Rx5day highlight storm tracks and anomalous events over the Middle East, southeast Asia, southeastern United States, and northern and eastern Australia (Fig. 2.24, Appendix Fig. A2.10b, Table 2.7).

The "Dragon Storm" over the Middle East/North Africa on 12 March was an unusually powerful midlatitude cyclone for early boreal spring, bringing ~70 mm of precipitation in 24 hours to the north coast and Nile Delta in Egypt (NESDIS 2020; The Watchers 2020). Above-average SSTs in the Indian Ocean (see section 3b), coupled with favorable atmospheric conditions over East Africa, resulted in a particularly wet long-rains season (March–June), with several prolonged duration events contributing to floods (see section 7e4). These events follow a pattern of increased duration and total volume in persistent extremes (Du et al. 2019). Exceptionally wet monsoon conditions led to the highest Rx1day on record in Karachi-Faisal, Pakistan (see section 7g4; WMO 2021; Table 2.7), compounding the effects of Super Cyclonic Storm Amphan over India and Bangladesh (Floodlist 2020a). The Indian Ocean conditions also contributed to the first known landfalling tropical cyclone in Somalia, with accompanying precipitation extremes (Floodlist 2020b).

Few records were broken over Australia during 2020, the exception being the Northern Territory during January where the highest Rx1day totals on record accompanied Cyclone Claudia (see section 4g7; BoM 2020; Table 2.7). Eastern Australia was wetter than average, reversing drought conditions in the southeast. New Zealand experienced a drier-than-normal year over the northern and eastern North Island, and near-normal conditions in most other locations.

Table 2.7. Notable events and new precipitation maxima.

Location	Duration	Amount	Comment	Reference
Wagait Beach and Dum in Mirrie, Australia	24 hours	515.2 mm 562 mm	10 Jan pre-cyclone Claudia (Wagait Beach—new January record, Dum in Mirrie—new record for Northern Territory)	BoM 2021
Belo Horizonte, Brazil	24 hours	172 mm	24 Jan (new record)	WMO 2021
Kolkata, India Ishwardi, Bangladesh	24 hours	250 mm 155 mm	20 May Super Cyclonic Storm Amphan	Floodlist 2020a
Karachi-Faisal, Pakistan	24 hours	231 mm	28 Aug (new record for Karachi area)	WMO 2021
Khombole, Senegal	24 hours	225.8 mm	5 Sep (new record)	WMO 2021
Jeju Island, South Korea	48 hours	963.5 mm	7 Sep Tropical Cyclone Julian (Mayask)	WMO 2021
Hué, Vietnam	7 days	1500 mm	7–13 Oct	WMO 2021
Napier, New Zealand	1 hour 24 hours	54 mm 242.4 mm	9 Nov (new hourly record)	Floodlist 2020d
Ciro Marina, Calabria Italy	48 hours	456.8 mm	20–22 Nov	Floodlist 2020c
Bosaso Somalia	24 hours	128 mm	22 NovTropical Cyclone Gati	Floodlist 2020b

A longer-term perspective using near-complete series of extreme indices (≥50 years) from ~6000 gauges over Europe (Klein Tank et al. 2002) indicates new Rx1day (Rx5day) records at 70 (40) gauges. These are fewer than normally expected and suggestive of an inactive year for European rainfall extremes. Many record-breakers were in Germany (Fig. 2.25), which accounted for 43 Rx1day records, but also included a total of 200.2 mm in Dimitrovgrad, Serbia, exceeding the previous record of 123.3 mm. In total, 11.6% (7.5%) of the Rx1day (Rx5day) values ranked in the top 10% of annual values for an individual gauge in 2020. Comparing these data on upper decile events for each year in the period 1980–2020 shows that 2020 ranked 15th (34th) out of the 41 years for which at least ~4500 gauges contribute. The R10mm (R20mm) indices for 2020 were around average with 8.8% (10.6%) of gauges in the top decile for the location, ranking 24th (19th) with new records at 82 (84) gauges, particularly across Scandinavia.

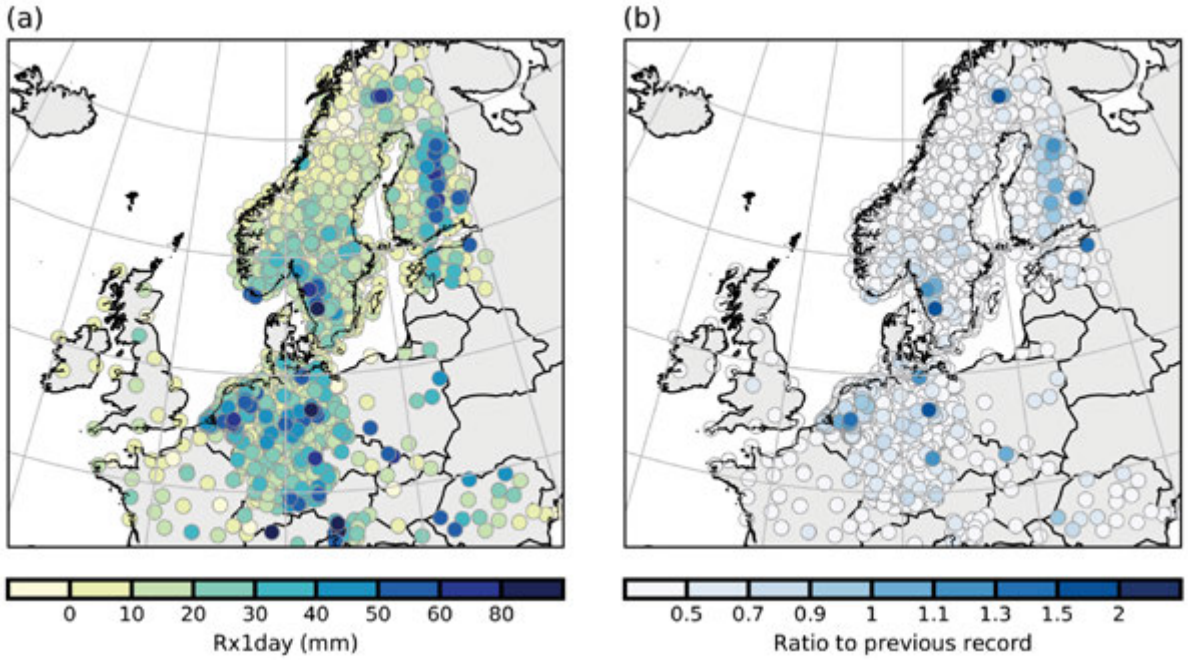

Fig. 2.25. Comparison of absolute Rx1day values (mm) and their ratio to the previous record from GHCN-Daily (Menne et al. 2012) over Germany.

Component 4 of the U.S. NOAA Climate Extremes Index (CEI4, area of the United States that experienced 1-day precipitation totals exceeding the 90th percentile; Gleason et al. 2008; NOAA 2021) was low for 2020, ranking 75th in the 111-year record. Of the seasonal indices, only autumn ranked in the top tercile at 34th. From a regional perspective, the western United States registered CEI4 = 0% in all seasons, or no areas of heavy precipitation. CEI4 registered in the top decile during spring and summer in the upper midwest and autumn in the southeast, also illustrated by the location of Rx1day events (Plate 2.11; Fig. 2.24c). Despite the very active Atlantic hurricane season (see section 4g2), CEI4 values along the eastern seaboard were at or below average.

6) Lake water levels—B. M. Kraemer

In 2020, the average water level anomaly across 249 of Earth's largest lakes was +1.05 m (range: −9.16 m to +44.45 m) compared to their mean lake water levels from 1993–2001 (Fig. 2.26). Water level anomalies were positive in 73% of the lakes (183 out of the 249) compared to 68% in the previous year. Measurements of lake water level variation provide an important indicator of global hydrological change, water availability, drought, and human hydrological influence. Publicly available satellite altimetry data are used to assess changes in surface water storage. This year there are an additional 51 monitored lakes compared to 2019.

The 2020 water level anomalies differed widely both between and within regions. Lakes in southern Brazil and the Caucasus region had consistent negative water level anomalies while

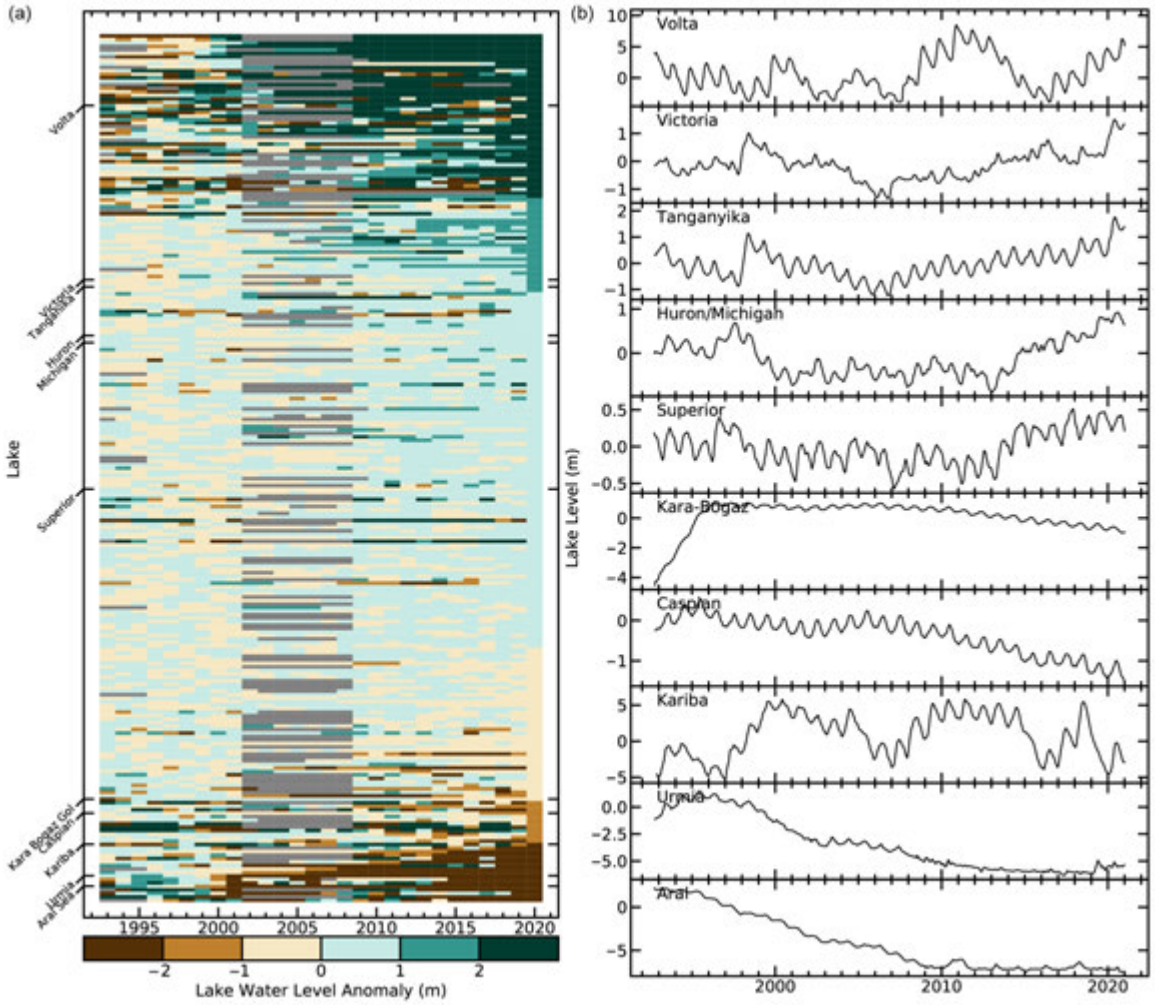

Fig. 2.26. (a) Lake water level time series for 249 globally distributed lakes ranked by their 2020 anomaly (m) relative to the 1993–2001 mean. Ninety-five of the 249 water level time series had substantial data gaps from 2002 to 2008. The subset of lakes that are named on the y-axis of (a) and plotted in (b) are those with the five largest positive anomalies and five largest negative anomalies when water levels anomalies were weighted by the surface area of each lake.

Canada, equatorial Africa, and western China had consistent positive water level anomalies (Plate 2.1m). The Tibetan-Qinghai Plateau experienced positive water level anomalies in most lakes (Plate 2.1m), consistent with the expected effects of climate change on regional rainfall and glacier melt (Woolway et al. 2020). Aside from broadscale and consistent regional variability, lake water level anomalies in nearby lakes within regions also varied. For example, Cahora Bassa and Kariba, two large, nearby reservoirs on the Zambezi River in southern Africa (within 185 km), had strongly diverging water levels (+4.38 m and –2.28 m, respectively), potentially due to differences in their water level management as reservoirs. The Middle East, Australia, and northern Asia all included lakes with both strong positive water level anomalies and strong negative anomalies, often in close proximity.

When lake level anomalies were multiplied by the lake surface area, the resulting approximate volumetric anomalies were most negative for the Caspian Sea (–433 km^3), Aral Sea (–47 km^3), Kara-Bogaz-Gol (–32 km^3), Urmia (–22 km^3), and Kariba (–19 km^3). The largest positive volumetric anomalies were found in Tanganyika (+26 km^3), Volta (+28 km^3), Superior (+45 km^3), Victoria (+76 km^3), and Huron/Michigan (+105 km^3). These lakes are highlighted in the time series shown in Fig. 2.26. The largest volumetric water level anomalies matched global patterns in terrestrial water storage assessed using data from the Gravity Recovery and Climate Experiment (GRACE) satellite mission (see Fig. 2.31).

Water level data were acquired from the NASA/CNES Topex/Poseidon and Jason satellite missions via the Global Reservoir and Lake Monitoring (G-REALM) project version 2.4 and via Theia's Hydroweb database. The 2020 water level anomalies in 80 lakes that had data from both sources were averaged across the two sources. One hundred and sixty lakes were unique to the G-REALM dataset and nine lakes were unique to the Hydroweb dataset. Satellite altimeters were originally developed to map ocean surface height. A small subset of the world's lakes are monitored in this way because the space-borne sensors must pass directly over the lake with sufficient regularity to produce accurate and complete time series. The lakes in this study comprise the 249 lakes with the longest (>29 years) and highest temporal resolution time series which are updated in near real time. Comparing the satellite altimeter measurements to in situ measurements, the root mean squared error of elevation variations is ~5 cm for large lakes such as those analyzed here. Water levels are typically measured every 10 days, but the exact dates on which water levels are measured vary from lake to lake. To make water level data temporally consistent, we have linearly interpolated each lake's time series to the daily scale so that all lakes had time series of the same interval. Of the 249 water level time series, 95 had substantial data gaps from 2002 to 2008, so we used a period prior to these gaps (1993–2001) as the baseline for calculating 2020 water level anomalies.

In situ monitoring of lake water levels is vital for cross-validating and calibrating altimeter-based estimates of long-term water level variation in lakes. However, our capacity to monitor changes in a global population of lakes with in situ data alone is currently limited due to the scarcity of publicly available near-real time data from key regions. Impediments to data sharing need to be overcome, and data delivery needs to be more timely in order to monitor water cycle variation with in situ data. Landsat-based surface water extent datasets, such as those produced by the Copernicus Programme (Pekel et al. 2016), could be used for near real-time monitoring of water storage in many thousands of lakes but to date, no near real-time data products exist to support such efforts.

7) Cloudiness—M. J. Foster, L. Di Girolamo, C. Phillips, M. Stengel, S. Sun-Mack, and G. Zhao

Global cloudiness in 2020 increased by 0.31% (±0.14%) relative to 2019, based on several satellite records (Fig. 2.27). Mean global cloudiness tends to stay reasonably stable, but regional distribution of cloud changes year-to-year. Some of this is due to normal variation in synoptic-scale weather events, but cloudiness can also be driven by modes of variability, the best-known being the El Niño–Southern Oscillation (ENSO). ENSO is characterized by a shifting gradient of SST and

low-level winds between the eastern and central equatorial Pacific and Indonesia. This gradient can in turn enhance or suppress convection, which drives the formation of clouds. This means that different phases of ENSO (and other modes) are frequently accompanied by characteristic patterns of cloudiness, which typically have a seasonal dependence. These large-scale patterns are important for several reasons. Clouds cool Earth by reflecting incoming solar radiation and warm it by trapping outgoing terrestrial radiation. Whether the overall effect is one of cooling or warming depends on many factors including the geographic distribution, height, and opacity of clouds (Bony et al. 2015). Clouds are also a gauge for moisture, and their presence may increase or decrease the risk of hydrological hazards like droughts, flooding, and wildfires.

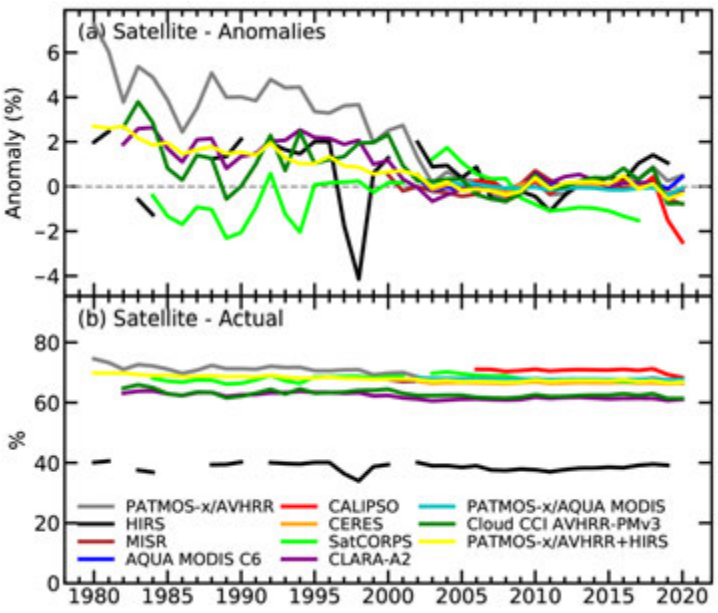

Fig. 2.27. Annual global cloudiness (a) anomalies and (b) actual (%) for 1980–2020. The anomaly is defined as the annual value minus the mean, derived between 2003 and 2015, a period common to the satellite records excluding CALIPSO, where the entire record was used instead. The datasets include (1) PATMOS-x/AVHRR (Pathfinder Atmospheres Extended; Heidinger et al. 2013), (2) HIRS High Cloud (Wylie et al. 2005, Menzel et al. 2016), (3) MISR (Multi-angle Imaging SpectroRadiometer; Di Girolamo et al. 2010), (4) Aqua + Terra MODIS C6 (Moderate Resolution Imaging Spectroradiometer Collection 6; Platnick et al. 2015), (5) CALIPSO (Cloud-Aerosol Lidar and Infrared Pathfinder Satellite Observation; Winker et al. 2007), (6) CERES Aqua MODIS (Clouds and the Earth's Radiant Energy System; Trepte et al. 2010; Minnis et al. 2008), (7) SatCORPS (satellite cloud and radiative property retrieval system; Minnis et al. 2016), (8) CLARA-A2 (cloud, albedo, and radiation dataset; Karlsson et al. 2017), (9) PATMOS-x/AQUA MODIS (created specifically for this report), (10) CLOUD_CCI (Cloud Climate Change Initiative AVHRR-PM v3.0; Stengel et al. 2017), and (11) PATMOS-x/AVHRR+HIRS (Foster et al. 2018).

The Indian Ocean dipole (IOD) can also be characterized by a shifting gradient in SST but affects the Indian Ocean, and a positive phase typically means fewer clouds and drier-than-normal conditions over much of Australia (BoM 2021). After being strongly positive and the most notable mode of variability present in 2019, the IOD returned to neutral conditions in 2020 (see section 4f). Meanwhile, ENSO shifted from neutral conditions to a moderate La Niña phase, which began in the boreal summer and persisted through the rest of the year (see section 4b). These features are apparent in the cloudiness anomalies across the four typical seasons of 2020 (Fig. 2.28). Positive cloudiness anomalies and wet conditions in the tropical central and eastern Pacific are indicative of weak El Niño-like conditions during December 2019–February 2020, while negative anomalies over the western tropical Pacific paired with positive anomalies over Indonesia are characteristic of La Niña during June–August 2020.

Plate 2.1n shows global cloudiness anomalies for 2020. Large and/or persistent changes over a specific region can result in a statistically significant cloudiness anomaly. This is an anomaly that, when averaged over the entire year, falls more than 2 standard deviations outside the mean as determined from the PATMOS-x/AVHRR climatology base period (1981–2010). In 2020 there were several such anomalies, and, in particular, there were large numbers of negative continental anomalies. Significant maritime anomalies include increased cloudiness in the eastern tropical Pacific and northern Indian ocean, particularly the Arabian Sea and Gulf of Aden, and decreased cloudiness in the northern Pacific. The increased cloudiness in the tropical Pacific is on either side of the ITCZ, the equatorial belt where northern and southern trade winds converge to produce precipitating convective clouds, and suggests a poleward shift of convective activity. Continental

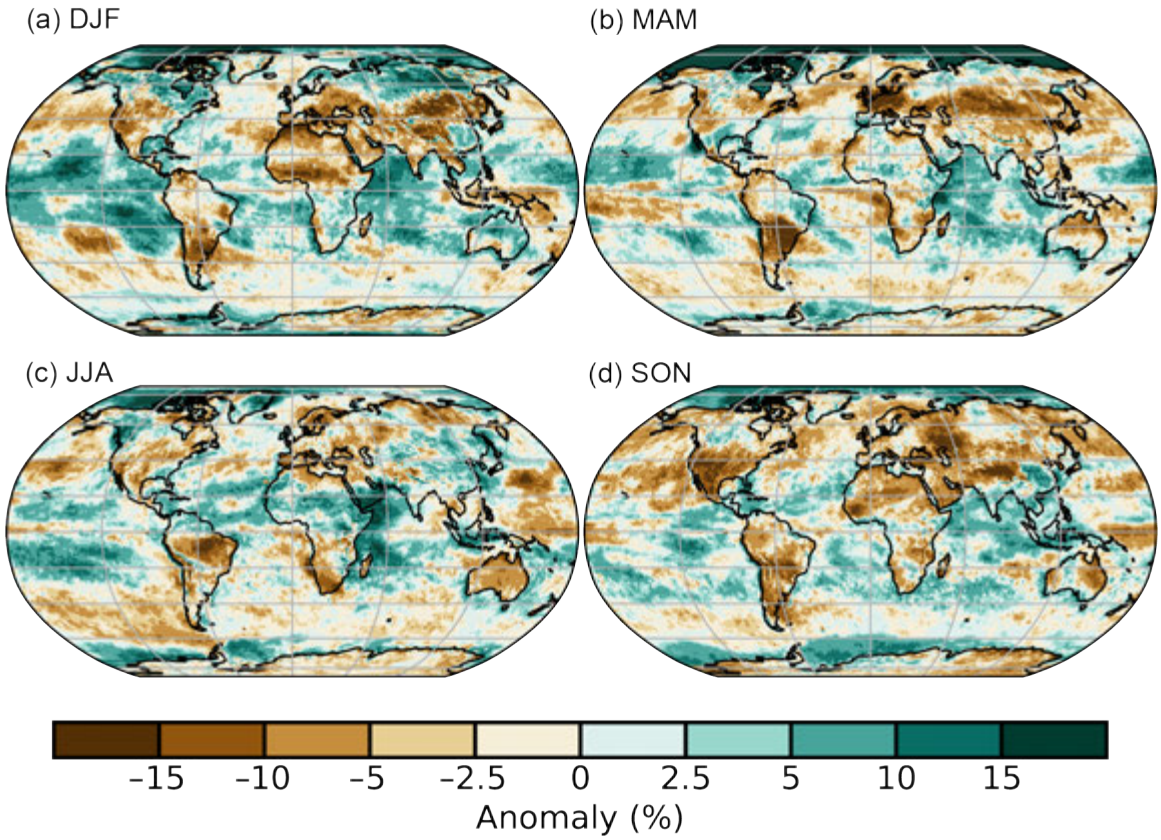

Fig. 2.28. Global seasonal cloudiness anomaly (%; 1981–2010 base period) for (a) Dec–Feb (DJF), (b) Mar–May (MAM), (c) Jun–Aug (JJA), and Sep–Nov (SON) generated from the 30-year PATMOS-x/AVHRR+HIRS cloud climatology.

anomalies include decreased cloudiness in the Americas over the western United States and portions of Brazil, Paraguay, Uruguay, and Argentina. Africa experienced decreased cloudiness in the south over Namibia and South Africa and in the north over Libya, Tunisia, and Algeria. Europe experienced negative anomalies driven by decreased cloudiness during March–May (Fig. 2.28). Decreased cloudiness also occurred in Asia over Turkey, southern Russia, Kazakhstan, Mongolia, and parts of western China. The continental anomalies frequently coincided with regions that experienced below-average precipitation and/or severe wildfires (Plates 2.1k,x,z,ag).

8) River discharge and runoff—H. Kim and D. Tokuda

Since 2017, global land has been overall slightly wetter than average, and the anomalies of runoff (Plate 2.1o) and discharge (Plate 2.1p) make clear that the distribution of wet and dry regions were similar to those of 2019. In many regions, the deviations intensified during 2020. A wet state of runoff prevailed in a large area of the United States (except the west), Canada (except the southeast), and the Eurasian continent. In particular, a strong wet signal has been discerned in East Asia (i.e., China, Japan, and Korea) in contrast to the strong dry spell of the previous year. During summer, anomalous runoff was generated by a disastrous amount of rainfall fostered by the enhanced Changma (also known as Meiyu in China and Baiu in Japan; see Sidebar 7.3 for details). According to recent studies, the East Asia Summer Monsoon lifecycle has intensified (Park et al. 2020; Wang et al. 2019). The United Kingdom also observed an anomalous wet year due to an exceptionally wet 2019/20 winter, and all the seasons of 2020 except for the record-breaking sunny spring (see section 7f2; Met Office 2020). Most regions of the European continent suffered anomalous dry spells, while the climate state of Scandinavian countries shifted to become wetter. Also, a large area of South America experienced a drier hydroclimate. Such anomalous states of climate were reflected in the global distributions of runoff and river discharge.

It has been well-known that ENSO and Pacific Decadal Oscillation (PDO; Zhang et al. 1997) are key drivers modulating global freshwater discharge (e.g., Kim 2020). The long-term variability of total runoff and those climate modes are shown in Fig. 2.29. This indicates that a positive (negative) phase inherent to ENSO and PDO tends to be associated with a drier (wetter) state of the global freshwater discharge by which about 46% of total variance is explained by the combined contribution of ENSO and PDO. Globally, a continuous wet state since 2017 was prolonged and then further intensified during 2020 due to the emergence of La Niña in the second half of the year. 2020 saw the third-highest (~95th percentile) runoff of the 63-year period (1958–2020).

Figure 2.30 displays the inter-annual variability and climatology of freshwater discharge into the Atlantic, Pacific, Indian, and Arctic basins, which comprise approximately 75% and 85% of the entire terrestrial land area and river discharge, respectively. For the Atlantic Ocean, it was nearly neutral during 2020, while river runoff was above normal for much of the past decade. The seasonality was relatively weaker due to the excess and deficit of discharge during the dry and wet season, respectively. The Pacific Ocean received significantly greater volumes of water from rivers during the wet season (May–July) and over the rest of the year. In terms of long-term variability, there is a strong upward trend since the 1990s. Therefore, it was significantly wet during 2020. A similar upward trend is seen in the Indian Ocean as well, following a long-term decline since the mid-twentieth century. During the entire analysis period, the freshwater discharge into the Arctic Ocean has been increasing, and the wet season of 2020 was significantly anomalous (see section 5g for details).

The 63-year series of runoff and freshwater discharge were provided from off-line hydrologic simulations of the Ensemble Land State Estimator (ELSE; Kim et al. 2009) and a global-scale river routing model, Catchment-based Macro-scale Floodplain (CaMa-Flood; Yamazaki et al. 2011) over 1° and 0.5° global grids, respectively. To keep uniformity with the other estimates, river networks information was prepared in a regular grid system, 30-min drainage direction map (DDM30; Döll and Lehner 2002), and sub-grid-scale parameters (e.g., river length and floodplain shape) were derived accordingly. To distinguish the freshwater discharge to each oceanic basin, the World Ocean Atlas 2018 (Garcia et al. 2019) was referenced. The Japanese global atmospheric reanalysis (JRA-55; Kobayashi et al. 2015) and the GPCC Monitoring Product version 2020 (Schneider et al. 2020) were combined to produce the atmospheric boundary conditions.

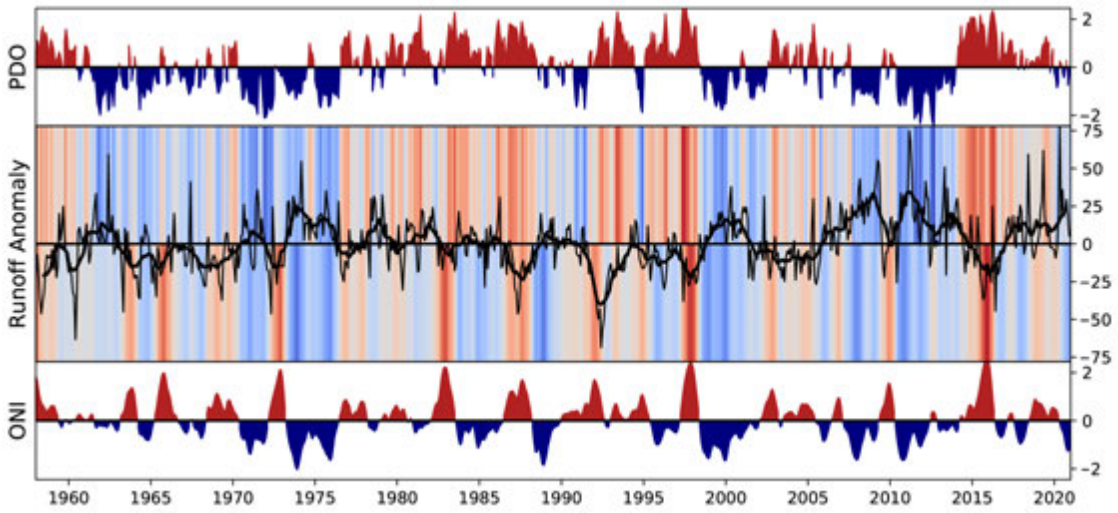

Fig. 2.29. Interannual variability of Ocean Nino Index (ONI; lower), Pacific Decadal Oscillation (PDO) index (upper), and global runoff (middle; mm; thick black line is 12-month moving average). ONI and PDO index are shaded red (positive phase) or blue (negative phase). Shading above and below the zero-line of global runoff is proportional to PDO and ONI, respectively.

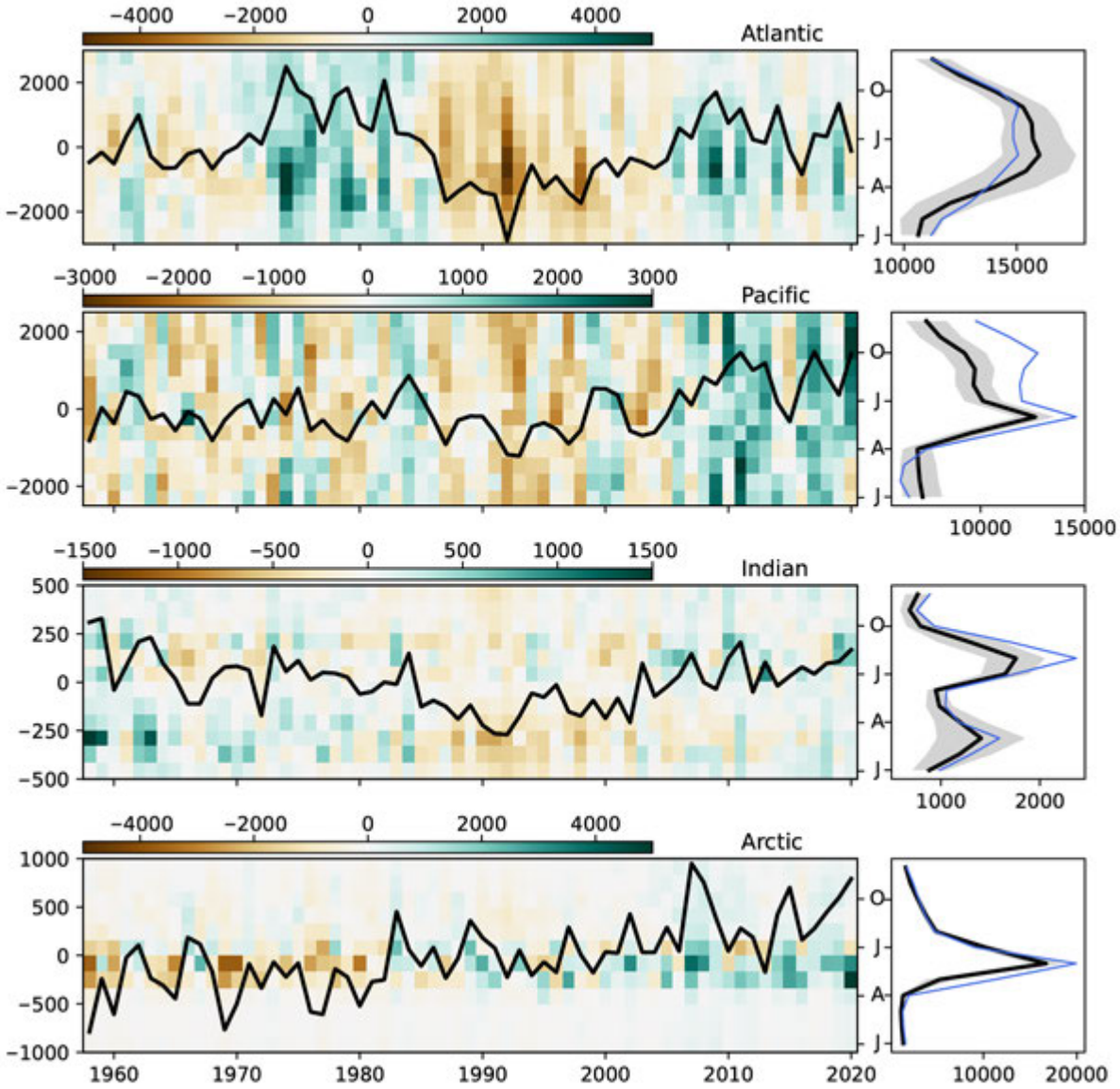

Fig. 2.30. Interannual variability of freshwater discharge to global ocean basins (km^3 yr^{-1}). Line and shades indicate annual mean and monthly anomaly, respectively. (Left) Seasonality of freshwater discharge to global ocean basins (km^3 yr^{-1}). Thick black line, thin blue line, and gray shade indicate long-term climatology, seasonal variation during 2020, and 1σ of long-term variability. J, A, J, O for the tick labels of the shared-ordinate between left and right panels indicate Jan, Apr, Jul, and Oct, respectively (right).

9) Groundwater and terrestrial water storage—M. Rodell and D. Wiese

Terrestrial water storage (TWS) comprises all the water on and below the land surface: groundwater, soil moisture, surface water, snow, and ice. In general, snow and ice dominate interannual TWS variability at high latitudes and in alpine regions, surface water dominates in the wet tropics, and groundwater dominates elsewhere (Getirana et al. 2017).

Changes in mean annual TWS between 2019 and 2020 as measured by the GRACE (Tapley et al. 2004) and GRACE-FO (Landerer et al. 2020) satellite missions, shown in Plate 2.1q as equivalent heights of water in centimeters (cm), integrate the effects of multiple hydroclimatic variables (see Plates 2.1k,p,t). Of note in 2020, heavy rains raised TWS in a large region of south-central and eastern Africa by 12–25 cm equivalent height of water. Exacerbated by increased runoff due to environmental degradation and urbanization (Mafaranga 2020), Lake Victoria consequently gained more than a meter of water (see sections 2d6, 7e4), with flooding in the surrounding region. Groundwater and TWS remained depressed over most of Europe, excluding Scandinavia, following losses in 2019. Much of India experienced large TWS gains, but, directly to the east, drought worsened in the Indochina Peninsula. Above-normal precipitation increased TWS in

much of the rest of far eastern Asia as well as north-central Asia. TWS changes in Australia were of mixed sign and generally mild. In North America, the most notable changes were considerable increases in TWS in central Canada and the southeastern United States and drying that stretched from the coast of California to eastern Texas, all of which were driven by precipitation anomalies (see section 7b2). Consistent with past years (Tapley et al. 2004), some of the most massive TWS changes occurred in South America, including large increases in eastern Brazil and a north–south swath of large decreases down the center of the continent (see section 7d).

Figures 2.31 and 2.32 depict time series of zonal mean and global mean monthly TWS anomalies after removing the seasonal cycle. Ice sheet and glacier ablation continued to produce large TWS declines in Antarctica, Greenland, the Gulf Coast of Alaska, and polar islands, hence we excluded these regions from the data used in Figs. 2.31 and 2.32, but additional ice mass loss is still apparent at high latitudes in Fig. 2.31. The large TWS increase in south-central and eastern Africa was apparent near the equator in Fig. 2.31. TWS decreases near 40°N can be attributed to four factors (Plate 2.1q): droughts in California, the central United States, and the land adjacent to the Aegean Sea and Black Seas; glacier ablation in the Alay Mountains of Tajikistan; persistent water level decline in the Caspian Sea; and groundwater depletion to support irrigated agriculture in the North China Plain. At the global scale (Fig. 2.32), mean TWS decreased by about 7 mm equivalent height of water from the start of 2020 through June and then quickly gained nearly 12 mm, much of that in central Africa, causing a temporary 4 mm decline in sea level (see section 3f).

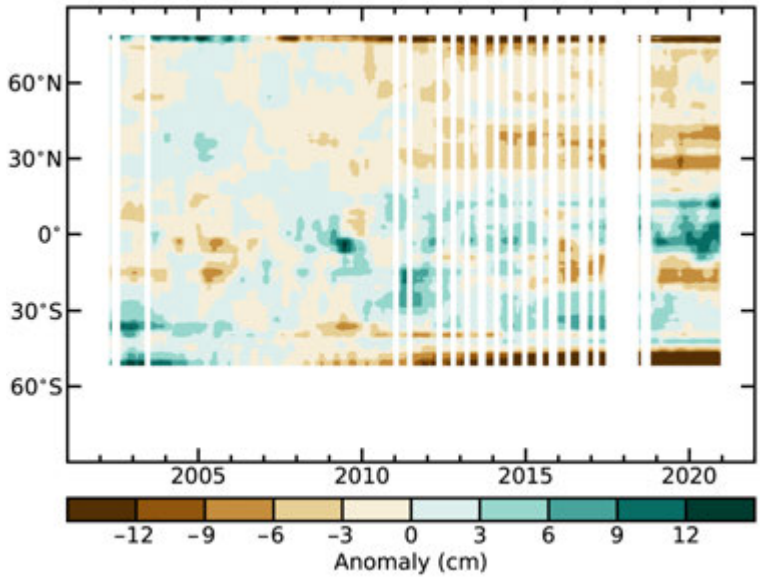

Fig. 2.31. Zonal means of terrestrial water storage anomalies, excluding those in Antarctica, Greenland, the Gulf Coast of Alaska, and polar islands, in cm equivalent height of water, based on gravity observations from GRACE and GRACE-FO. The anomalies are relative to a base period of 2004–09.

In situ measurement records of the TWS components are rarely available outside of the United States and parts of Europe and Australia; however, GRACE and GRACE-FO have provided monthly, global maps of TWS anomalies based on precise measurements of Earth's time-varying gravity field. The GRACE and GRACE-FO data were the basis for this analysis. Uncertainty in the derived TWS anomalies varies depending on the latitude (higher near the equator), size of the region of interest (higher at small scales), TWS anomaly averaging period (higher for short periods), and orientation (higher for north–south oriented regions near substantially different gravity change signals). At scales greater than about 500,000 km^2, uncertainty in monthly TWS anomalies is typically around 1–2 cm equivalent height of water (Wiese et al. 2016).

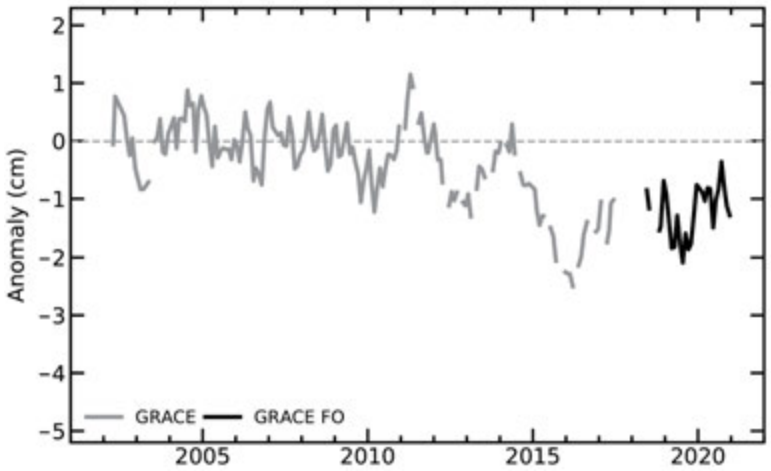

Fig. 2.32. Global average terrestrial water storage anomalies from GRACE (gray) and GRACE-FO (black), in cm equivalent height of water, relative to a 2004–09 mean baseline.

10) Soil moisture—R. van der Schalie, T. Scanlon, W. Preimesberger, A. J. Pasik, M. van der Vliet, L. Mösinger, N. J. Rodríguez-Fernández, R. Madelon, S. Hahn, M. Hirschi, R. Kidd, R. A. M. de Jeu, and W. A. Dorigo

Monitoring global soil moisture conditions is key for our understanding of the climate system, as soil moisture has a defining role in the energy and water fluxes at the land–atmosphere boundary. The global surface soil moisture conditions in 2020, as measured by satellite, were on average close to the climatology derived from historical data of the 1991–2010 period (Fig. 2.33), being slightly wetter than normal at the start of the year. Although still present, the large discrepancy between the Northern Hemisphere (NH) and Southern Hemisphere (SH) observed at the end of 2019 became slightly less pronounced in 2020 (Fig. 2.34). Drier-than-usual conditions persisted in the SH throughout 2020, and while the record wet peak of the NH at the end of 2019 weakened, it remained historically high in 2020. Plate 2.1r and Appendix Fig. A2.11a show the yearly and monthly soil moisture anomalies for 2020, respectively. There are strong spatial anomalies, which are discussed per individual continent.

In North America the year started with mostly wet conditions, but from the spring onward a strong deviation started to develop between the eastern United States, northwest Canada, and Alaska, with wet anomalies, and the Great Plains, southwestern United States, and Mexico, with strong dry anomalies. In the United States, this was linked to the precipitation anomalies (NOAA 2021), which show a similar pattern, with Nevada and Utah posting record lows. The peak in dry anomalies occurred in autumn and coincided with the record-breaking 2020 western United States wildfire season (see section 7b2 for details about the U.S. drought and wildfires). Consistent with the La Niña forming in the second half of the year (see section 4b), these dry conditions remained in place until the end of 2020.

For Europe an overall wet anomaly was recorded, with the only exception being the region around the Black Sea, which experienced drier-than-normal conditions. April diverted from this, with high-pressure systems dominating the weather in Europe, causing extraordinary warm, sunny, and dry conditions, and consequently led to a sharp decline in soil moisture conditions. The eastern part

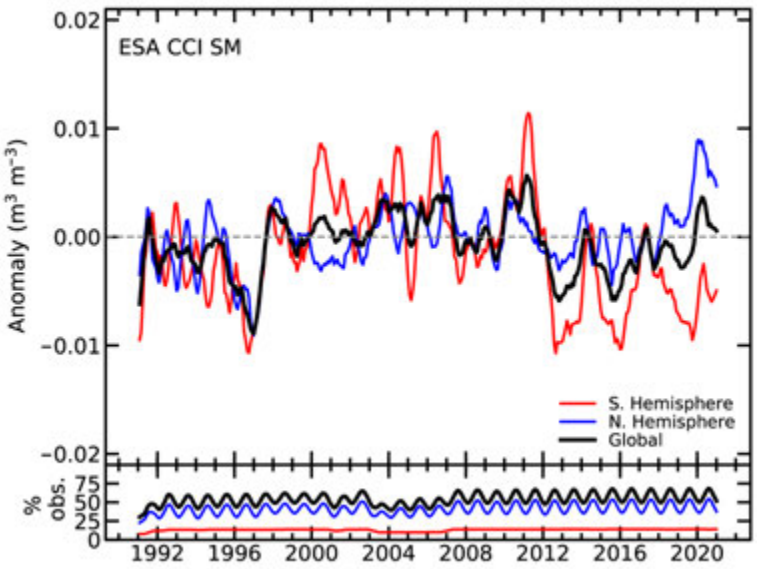

Fig. 2.33. Time series of global, NH, and SH surface soil moisture anomalies for 1991–2020 (upper, $m^3\ m^{-3}$; 1991–2010 base period) and the percentage of valid retrievals over land (lower, %). Data are masked where no retrieval is possible or where the quality is not assured and flagged due to dense vegetation, frozen soil, radio frequency, interference, and so forth. (Source: ESA CCI Soil Moisture.)

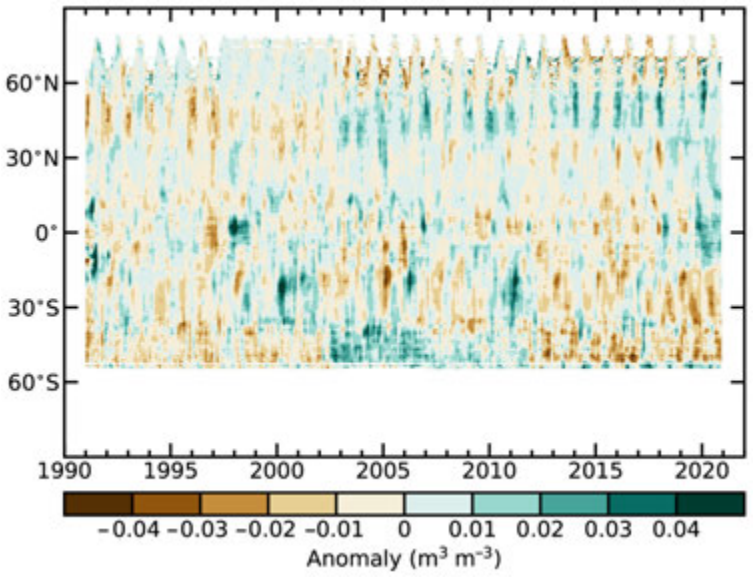

Fig. 2.34. Time–latitude diagram of surface soil moisture anomalies ($m^3\ m^{-3}$; 1991–2010 base period). Data are masked where no retrieval is possible or where the quality is not assured and flagged due to dense vegetation, frozen soil, radio frequency, interference, and so forth. (Source: ESA CCI Soil Moisture.)

of Europe was the most affected, and related early season wildfires were recorded in multiple countries, including Germany, Poland, and Ukraine. From the second half of May onward, the moisture deficiencies returned to wetter-than-usual conditions for most of Europe (see section 7f).

South America experienced a widespread drought (see section 7d), which is clearly visible in the strong dry anomalies found over central Brazil, Bolivia, Paraguay, Uruguay, and Argentina. This situation was amplified by the emergence of La Niña (section 4b) in the second half of the year (Penalba and Rivera 2016). One region that clearly stands out with a severe dry anomaly is Brazil's Pantanal, known as the world's largest wetland, which endured its worst drought in almost 50 years and saw more than a quarter of its area burned. Eastern Brazil is the only major exception to this, with an opposite strong wet anomaly caused by heavy rains early on in the year. Wetter-than-usual conditions in this region generally coincide with La Niña events (see section 7d for details).

In eastern Africa an intensification of the already above-average wet conditions was observed. In the second half of 2019 above-average rainfall was recorded in this region, caused by a strong positive Indian Ocean dipole (Preimesberger et al. 2020), leading to above-average conditions in early 2020. This wet anomaly remained intact due to exceptionally heavy seasonal rains. The dry conditions in southern Africa alleviated in 2020, while southern Madagascar became much drier. The Sahel saw strong wet anomalies developing from August onwards, caused by heavy rainfall (see section 7e for details).

Asia mainly experienced wetter-than-normal soil moisture conditions throughout 2020, especially in India, China, Mongolia, North Korea, and South Korea, where unusually long and strong monsoon rains were reported (see section 7g). The countries in the Lower Mekong Basin continued to experience dry conditions, according to the Mekong River Commission, with below-average annual rainfall in 2019 and a shorter-than-normal monsoon season in 2020. In eastern Siberia, a widespread dry anomaly was observed in the region that experienced massive wildfires and a record heat wave (Overland and Wang 2020; see section 7g2).

While most of Australia still recorded below-average soil moisture conditions in 2020, it shifted considerably toward the long-term mean following the extraordinary low values seen in 2019 (Preimesberger et al. 2020). The only exception to this was southeastern Australia, where soil moisture increased to above-average conditions, providing some much needed relief from the multi-year drought (see section 7h4 for details).

The soil moisture anomalies used in this analysis were derived from the COMBINED product of ESA's Climate Change Initiative for Soil Moisture v05.3 (ESA CCI SM; Dorigo et al., 2017), which is a product that merges satellite soil moisture retrievals from multiple active (Wagner et al. 2013) and passive microwave (Van der Schalie et al. 2017) sensors to achieve the most accurate and consistent climate data record of soil moisture (representing the top ~5 cm of the soil). Merging is done based on both the quality and the temporal and spatial availability of observations, in order to achieve both an improved coverage and quality as compared to any single sensor dataset (Gruber et al. 2017, 2019).

11) Monitoring global drought using the self-calibrating Palmer Drought Severity Index—

J. Barichivich, T. J. Osborn, I. Harris, G. van der Schrier, and P. D. Jones

The sharp increase in global drought area based on different severities of the self-calibrating Palmer Drought Severity Index (scPDSI) that began in mid-2019 (Barichivich et al. 2020), continued in 2020, and reached a historical peak in October, with a small decrease afterward (Fig. 2.35). Around 6.8% of the global land area experienced extreme drought conditions in October, marking the third historical peak since 1950 after earlier peaks in October 1984 (7.7%) and October 1983 (7.3%). The extent of severe plus extreme drought conditions peaked at 15% of the global land area in October and November, matching the largest historical peaks of this drought severity in September 1983. Moderate or worse drought conditions peaked in August at 27.8% of the global

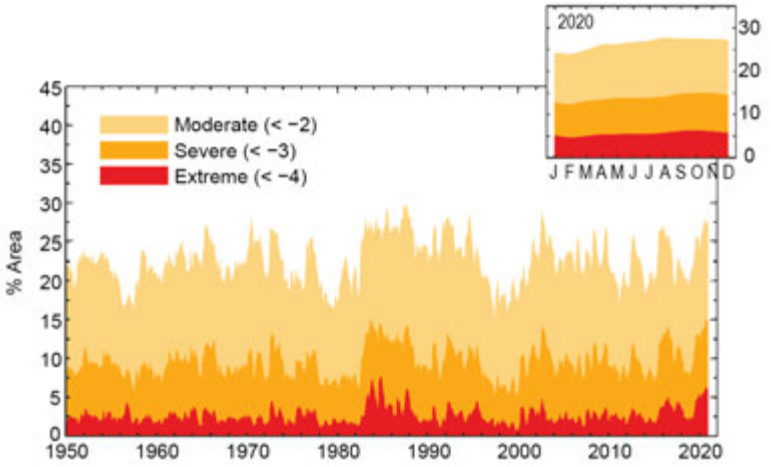

Fig. 2.35. Percentage of global land area (excluding ice sheets and deserts) with scPDSI indicating moderate (< –2), severe (< –3) and extreme (< –4) drought for each month of 1950–2020. Inset: Each month of 2020, denoted by first letter.

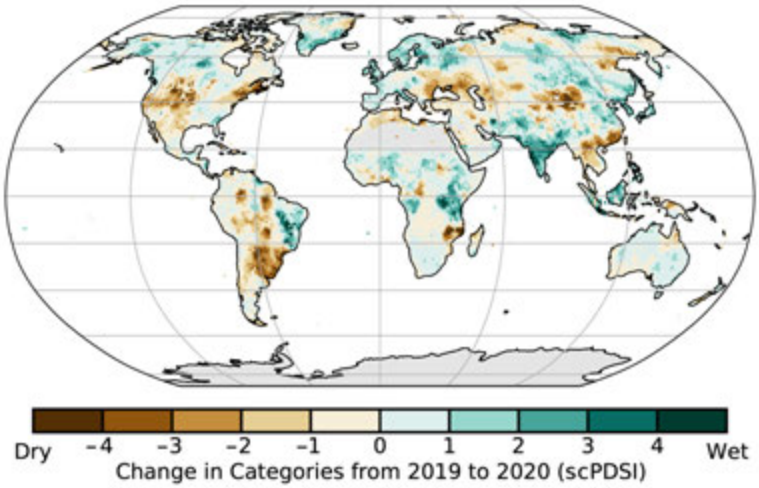

Fig. 2.36. Change in drought from 2019 to 2020 (mean scPDSI for 2020 minus mean scPDSI for 2019). Increases in drought severity are indicated by negative values (brown), decreases by positive values (green). No calculation is made where a drought index is meaningless (gray areas: ice sheets or deserts with approximately zero mean precipitation).

land area, marking the fifth historical peak after June 1987 (29.6%) and the largest peak since August 2002 (29%).

Extensive severe-to-extreme drought conditions during 2020 affected most of the SH, southern and central Europe, the Middle East, and Southeast Asia (Plate 2.1s). Compared to 2019 (Barichivich et al. 2020), drought severity worsened to extreme in central South America (Fig. 2.36). Worsening drought during the dry season (austral winter and spring) contributed to ravaging fires across the Chaco floodplains and Pantanal wetland in northern Argentina and southern Brazil (Rodríguez 2020; see section 7d). The decadal drought in north-central Chile (Garreaud et al. 2017; Alvarez-Garreton et al. 2021) continued through its 11th year in 2020, with extreme conditions in the central and most populated region of the country (Plate 2.1s). In North America, the east–west moisture contrast observed across the United States since 2017 (Osborn et al. 2018; Barichivich et al. 2020) also persisted during 2020 (Plate 2.1s). Extensive wet conditions extended over the whole eastern half of the country and moderate but protracted drought prevailed in the west. Under these persistent drought conditions, California saw another extreme season of wildfires (Goss et al. 2020).

Previous drought conditions in southern Africa eased slightly in general, but worsened in northern Mozambique (Fig. 2.36). South Africa declared a state of disaster as many parts of the country had remained under extreme drought since 2018. Wet conditions from 2019 in most of Central and East Africa persisted in 2020 (Plate 2.1s), though moisture anomalies in these regions were uncertain due to sparse coverage of station data. Previous drought conditions also eased in Australia (Fig. 2.36) but most of the country remained under drought during 2020 (Plate 2.1s).

In Southeast Asia, extreme drought because of a weak monsoon season affected Malaysia, Myanmar, Thailand, Cambodia, Vietnam, and particularly Laos (Plate 2.1s), contributing to record low levels of the Mekong River. Extreme drought affected a vast region of northeastern Siberia. Dry conditions through the Sakha Republic, Russia, were associated with anomalously extensive wildfires that burned around 6 million ha. Most of the midlatitude belt from Mongolia in central Asia to western Europe and the Mediterranean saw moderate to extreme drought severity during 2020 (Plate 2.1s). Extreme drought in Europe was once again exacerbated by increasingly recurrent spring and summer heat waves combined with below-average spring precipitation and

antecedent soil moisture deficit. In the midst of two heat waves, France experienced its driest July on record. As in 2019, the most intense annual drought persisted across northern Germany and Poland, where a strong soil moisture deficit has developed since 2018 (Fig. 2.36). In contrast to central and southern Europe, wet conditions occurred across northern Europe from the British Isles to Fennoscandia and the Ural Mountains.

Hydrological drought results from a period of abnormally low precipitation, sometimes exacerbated by a concurrent increase in evapotranspiration (ET). Its occurrence can be apparent in reduced river discharge, soil moisture, and/or groundwater storage, depending on season and duration of the event. Here, a simple estimate of drought as measured by the scPDSI (Wells et al. 2004; van der Schrier et al. 2013) is presented, using global precipitation and Penman-Monteith Potential ET from an early update of the Climatic Research Unit gridded Time Series (CRU TS 4.05 dataset; Harris et al. 2020). Moisture categories are calibrated over the complete 1901–2020 period to ensure that "extreme" droughts and pluvials (wet periods) relate to events that do not occur more frequently than in approximately 2% of the months. This calibration affects direct comparison with other hydrological cycle variables in Plate 2.1 that use a different baseline period.

12) Land evaporation—D. G. Miralles, A. Koppa, D. Rains, H. E. Beck, and M. F. McCabe

The geographical patterns of land evaporation anomalies for the year 2020 are illustrated in Plate 2.1t. Several regions experienced anomalously low evaporation, including most of the west and central United States and parts of Russia and central Africa. Moreover, a strong negative anomaly was recorded in central South America, comprising Bolivia, Paraguay, and large parts of Brazil and Argentina. This anomaly reflected severe meteorological drought conditions in autumn, which propagated as agricultural and hydrological drought as the year progressed, leading to the unprecedented dry-out of the Parana River (see sections 2d11, 7d3). Likewise, the drought conditions in the west and central United States led to lower-than-usual evaporation across vast areas of the country. On the other side of the spectrum, regions of positive anomalies included the eastern half of the United States, western Europe, the Amazon basin, the Greater Horn of Africa, and India. In the first three instances, these anomalies related to higher-than-usual surface net radiation and air temperature (see sections 2b1, 2b3). In the case of Amazonia, they occurred despite the widespread meteorological drought conditions in South America, highlighting the positive influence that mild droughts can have on rainforest productivity and transpiration due to associated anomalies of incoming solar radiation (see e.g., Liu et al. 2017). In India, the seasonal monsoon was exceptionally wet in 2020 (see sections 4e, 7g4), which explains the large positive anomaly in evaporation over the region.

The global mean land evaporation in 2020 was the highest on record, exceeding the values of the 2010 La Niña year (Fig. 2.37). The trend of approximately 0.3 mm year^{-1}, according to the Global Land Evaporation Amsterdam Model (GLEAM) v3.5, falls within the range reported in recent literature (Zhang et al. 2016a; Brutsaert et al. 2017; Anabalón and Sharma 2017). This multi-decadal tendency to higher evaporation has been attributed to increasing global temperatures (Miralles et al. 2014) and greening (Cheng et al. 2017). The overall positive

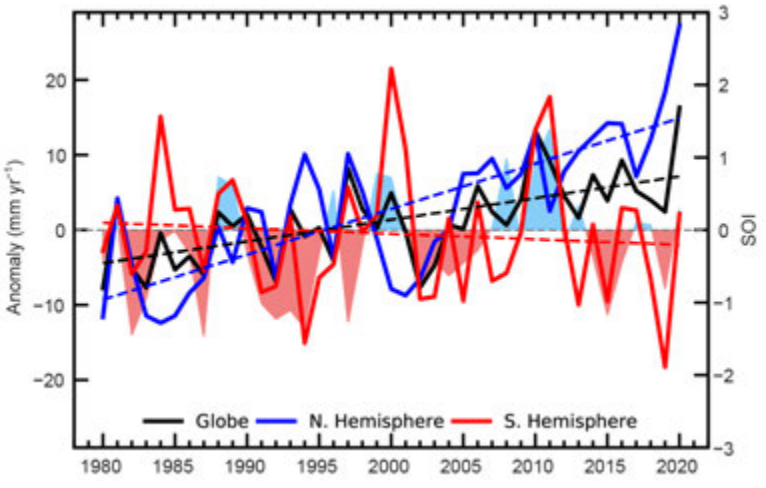

Fig. 2.37. Land evaporation anomaly (mm yr^{-1}; 1981–2010 base period) for the NH, SH, and the entire globe (blue, red, and black solid lines, respectively). Linear trends in evaporation (dashed lines) and the Southern Oscillation Index (SOI) from CRU (right axis, shaded area) are also shown. (Source: GLEAM.)

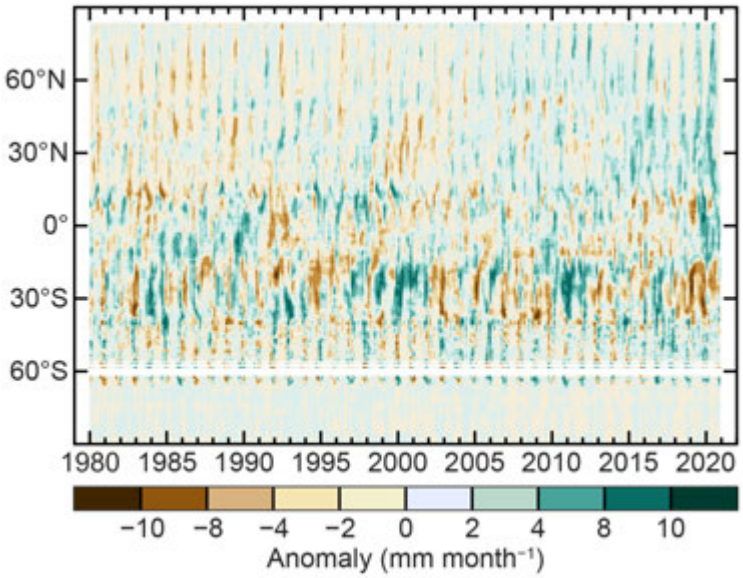

Fig. 2.38. Zonal mean terrestrial evaporation anomalies (mm month^{-1}; 1981–2010 base period). (Source: GLEAM.)

global evaporation anomaly in 2020 resulted from the mean positive anomaly in the NH (Figs. 2.37, 2.38), likely associated to the unusually high temperatures across Eurasia (see sections 2b1, 2b3, 7f). The characteristic negative anomalies in land evaporation in the SH during El Niño years (Miralles et al. 2014; Martens et al. 2018) dissipated as the atmosphere returned to a neutral ENSO state during early 2020 and then shifted toward La Niña later in the year (see Southern Oscillation Index; SOI in Fig. 2.37). Nonetheless, evaporation in the SH remained below average, particularly during the first half of the year, and especially over the latitudes where the South American drought occurred (Fig. 2.38).

Evaporation is the phase change of liquid water into vapor. On average, two-thirds of the precipitation over land is evaporated (Dorigo et al. 2021). The ability to monitor its spatial and temporal dynamics is critical for agriculture and water management, as well as to diagnose climate changes. Its crucial climatic role, combined with an increased monitoring ability, has led to the recent consideration of land evaporation as an essential climate variable (ECV) by the World Meteorological Organization (WMO). This consideration was enabled by the proliferation, over the past 2 decades, of approaches dedicated to quantifying this flux at regional to continental scales based on satellite data (McCabe et al. 2016; Miralles et al. 2016). A handful of such approaches regularly update their simulations, including the Land Surface Analysis Satellite Applications Facility (LSA-SAF; Ghilain et al. 2011), the Atmosphere–Land Exchange Inverse (ALEXI; Anderson et al. 2011), and GLEAM (Miralles et al. 2011). The latter provides global-scale estimates and serves as the basis for the results presented in this section.

The accuracy of GLEAM v3 has been reported to be on the order of 0.7 mm day^{-1} (unbiased root mean square error), and its correlation against in situ eddy covariance measurements is around 0.8 on average (Martens et al. 2017). Some climate zones are known to be challenging for models of terrestrial evaporation such as GLEAM (McCabe et al. 2017a; Fisher et al. 2017; Talsma et al. 2018): in semiarid regions, difficulties in capturing the response of evaporation to drought stress affect the accuracy, while for tropical forests, interception loss remains a key source of uncertainty. Moreover, reported global trends are affected by the poor representation of the effects of carbon dioxide (CO_2) and atmospheric aridity on stomatal conductance in current evaporation models (Zhang et al. 2016a). Further advances in the field of global terrestrial evaporation monitoring need to be realized in order to reduce these uncertainties. These may include developments in high-resolution optical platforms (McCabe et al. 2017b) and thermal missions such as ECOSTRESS (Fisher et al. 2020) or TRISHNA (Lagouarde et al. 2018).

e. Atmospheric Circulation

1) Mean sea level pressure and related modes of variability—R. Allan and B. Noll

Global atmospheric circulation patterns are dominated by the El Niño–Southern Oscillation (ENSO), measured in the atmosphere by the Southern Oscillation Index (SOI), and in the Northern Hemisphere (NH) by the Arctic Oscillation (AO) and the North Atlantic Oscillation (NAO); ENSO is measured in the Southern Hemisphere (SH) by the Antarctic Oscillation (AAO), also known as

the Southern Annular Mode (SAM; see Fig. 2.39). A detailed summary of all the above modes, their definitions, and so forth, are given in Kaplan (2011).

In section 4b, 2019 to mid-2020 conditions are denoted as being ENSO-neutral, with evidence for the development of a La Niña by August–September 2020. However, from March–April 2018 until July–August 2020, monthly Niño-4 sea surface temperature (SST) anomalies (https://www.cpc.ncep.noaa.gov/data/indices/sstoi.indices) remained positive and thus passed one criterion for this period being indicative of a protracted El Niño episode (Allan et al. 2019). Different "flavors" of ENSO have been addressed in the literature (Capotondi et al. 2015; L'Heureux et al. 2017; Wang et al. 2017; Timmermann et al. 2018; Santoso et al. 2019), including protracted El Niño and La Niña episodes (Allan and D'Arrigo 1999; Allan et al. 2019). The latter are distinguished by periods of both sustained above-average SST anomalies in the Niño-4 region in the western equatorial Pacific (5°S–5°N, 160°E–150°W) and a persistent negative SOI. This pattern is similar to El Niño and La Niña episodes known as Modoki (Ashok et al. 2007; Weng et al. 2007; Ashok and Yamagata 2009) and they could be argued to be the same phenomenon (Allan et al. 2019; see also section 4b).

The second criteria, for the SOI to have acted similarly by being consistently negative (allowing for at most two consecutive months to have gone positive), occurred from June 2018 to August 2020 (Fig. 2.39). This period of continuously warm Niño-4 SST anomalies led to enhanced atmospheric convection over that region and the generation of a teleconnection that caused large-scale subsidence across eastern Australia in the early 2018 to mid-to-late 2020 period (Allan et al. 2021). Together with the continued impact of a positive Indian Ocean dipole (IOD) from late 2019, the warm Niño-4 SST teleconnection suppressed rainfall across southern and eastern Australia and New Zealand (Zhang et. al. 2021; see also sections 2d5, 7h).

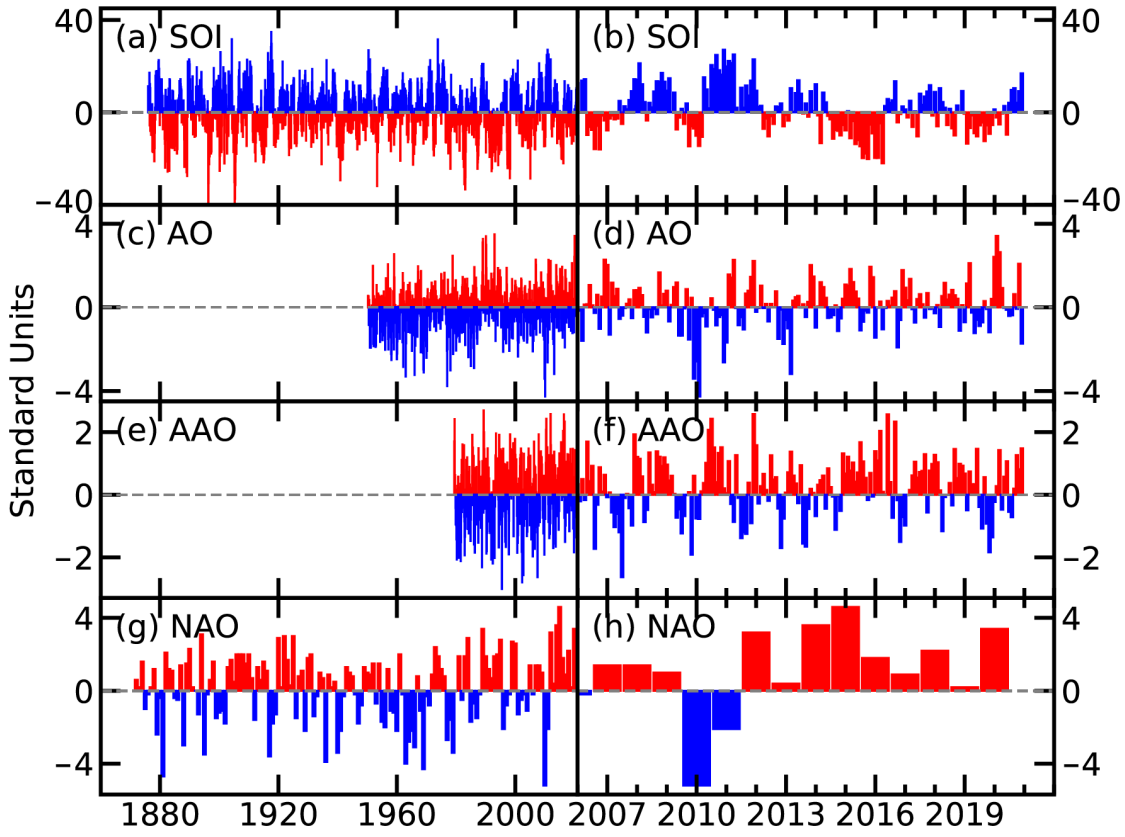

Fig. 2.39. Time series for modes of variability described using sea level pressure for the (left) complete period of record and (right) 2006–20. (a),(b) Southern Oscillation Index (SOI; provided by the Australian Bureau of Meteorology); (c),(d) Arctic Oscillation (AO; NOAA NCEP Climate Prediction Center); (e),(f) Antarctic Oscillation (AAO; NOAA NCEP Climate Prediction Center); (g),(h) winter (Dec–Feb) North Atlantic Oscillation (NAO) average (NCAR; presented for winter at the beginning of each year so winter 2020/21 is not shown).

In the NH, the last several boreal winters have displayed a variety of AO and NAO conditions (Figs. 2.39, 2.40). The 2019/20 boreal winter (Figs. 2.40b,e) was characterized by a persistent, mainly positive NAO, which led to mild conditions across the entire European region (see section 7f). This NAO phase contributed to heavy rainfall leading to flooding and a series of deep Atlantic cyclones, culminating in large storms in February 2020 (e.g., Storms Ciara and Dennis that impacted the United Kingdom; see section 7f2 for details). A strong stratospheric polar vortex dominated the winter, extending down through the troposphere and leading to abnormally cold air temperatures extending eastward from Alaska to Greenland and Svalbard (see section 5b).

During the 2020/21 boreal winter (Figs. 2.40c,f), the NAO was near average in December but shifted to negative throughout January, becoming the most negative observed in 11 years, and this extended through the first half of February 2021. In December 2020, Europe experienced its fourth-warmest December on record, with such conditions most pronounced over Scandinavia. Above-average precipitation occurred over most of western, northern, and southern Europe, with localized damage and flooding. This extended into January and February for western and central Europe, while temperatures were generally close to average across the continent, though colder in the west and north.

In the SH, the AAO was positive over 60% of the time during 2020, associated with a wide swath of higher-than-normal air pressure in the southwest Pacific (Figs. 2.40b,e), both early and again late in the year. This, along with the continued impact of a positive IOD event from late 2019, was associated with one of the worst droughts on record for northern New Zealand (NIWA 2020; see section 7h5). Slightly higher-than-normal air pressure in the Great Australian Bight also occurred as Australia recorded its fourth-warmest year on record (BoM 2020a; see section 7h4). Pressures were also above normal across South America, leading to Argentina's second-warmest year on record (see section 7d3). Influenced by the aforementioned IOD and the Pacific Niño-4 teleconnection, tropical cyclone activity was near or slightly above normal in the South Indian Ocean and southwest Pacific but below normal in the Australian region (see section 4g).

The frequently positive AAO also meant that pressures were below normal across Antarctica, which in September 2020 experienced an above-average maximum sea ice extent of 19.06×10^6 km^2 (NOAA 2021; see section 6f). Frequent patterns of lower-than-normal pressure near South Africa caused a wetter-than-normal winter during 2020 (see section 7e5), leading to the full recharge of Cape Town's dams for the first time in about 6 years (City of Cape Town 2021), following the severe drought of 2015–18 (Otto et al. 2018; section 2d9; SOTC 2018)

The AAO remained mostly positive during the 2020/21 austral summer (Figs. 2.40c,f), contributing to a drier-than-normal summer across New Zealand for the second consecutive year (NIWA 2021; see section 7h5). During December, Severe Tropical Cyclone Yasa formed as a pulse of enhanced convection crossed the tropical Pacific, becoming the South Pacific's strongest tropical cyclone since Winston in 2016 and making landfall in Fiji. Above-average sea surface temperatures to the north of Australia, as is typical during La Niña, led to above-normal rainfall totals in the tropical north and southeast, a marked change compared to the previous year (BoM 2021).

2) Land and ocean surface winds—C. Azorin-Molina, R. J. H. Dunn, L. Ricciardulli, C. A. Mears, T. R. McVicar, and J. P. Nicolas

The strengthening in global average surface wind speed over land (i.e., ~10 m above the ground) persisted in 2020, consistent with the reversal in global terrestrial winds observed since around 2010 (e.g., Azorin-Molina et al. 2020; Zeng et al. 2019; Fig. 2.41a). Prior to ~2010, a slowdown of terrestrial surface winds (termed stilling; Roderick et al. 2007) had dominated globally and regionally since the 1960s (e.g., Kim and Paik 2015; Azorin-Molina 2018a; Zeng et al. 2019). The global land average wind speed anomaly in 2020 with respect to the 1981–2010 climatology (Table 2.8) showed a positive value (+0.052 m s^{-1}), which was the highest over the last 2 decades. Europe (+0.082 m s^{-1}), Central Asia (+0.178 m s^{-1}), and East Asia (+0.051 m s^{-1}) continued with the recovery of

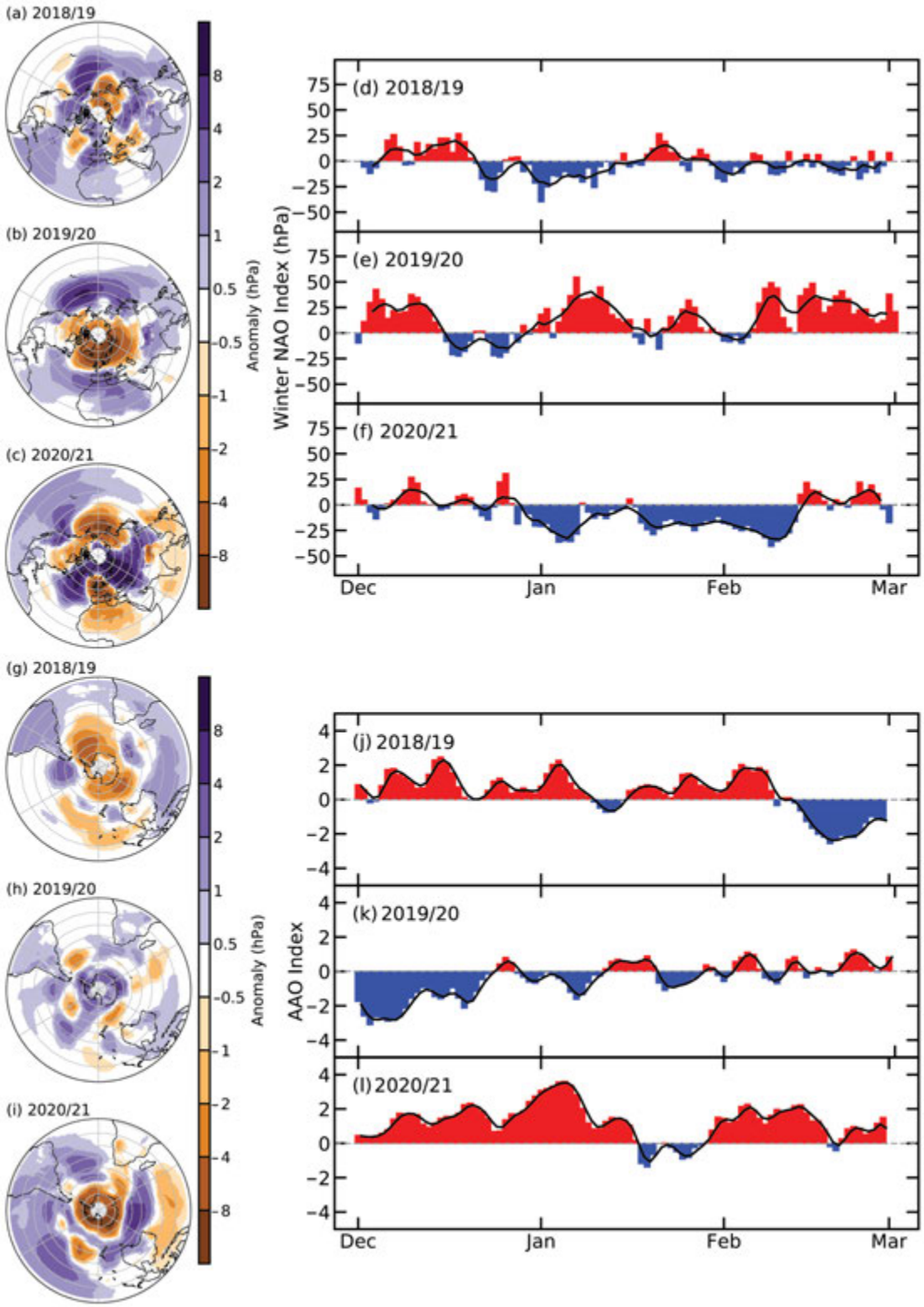

Fig. 2.40. Boreal winter sea level pressure anomalies (hPa; 1981–2010 base period) around the NH averaged over Dec–Feb for (a) 2018/19, (b) 2019/20, and (c) 2020/21 (constructed using ERA5, Hersbach et al. 2019). North Atlantic Oscillation (NAO) daily time series (hPa) for boreal winter (d) 2018/19, (e) 2019/20, and (f) 2020/21. The 5-day running mean is shown by the solid black line (constructed using Met Office MIDAS data). Austral summer sea level pressure anomalies (hPa; 1981–2010 base period) around the Southern Hemisphere (hPa; 1981–2010 base period) averaged over Dec–Feb for (g) 2018/19, (h) 2019/20, and (i) 2020/21 (constructed using ERA5). Antarctic Oscillation (AAO) daily time series (hPa) for austral summer (j) 2018/19, (k) 2019/20, and (l) 2020/21 (NOAA NCEP Climate Prediction Center).

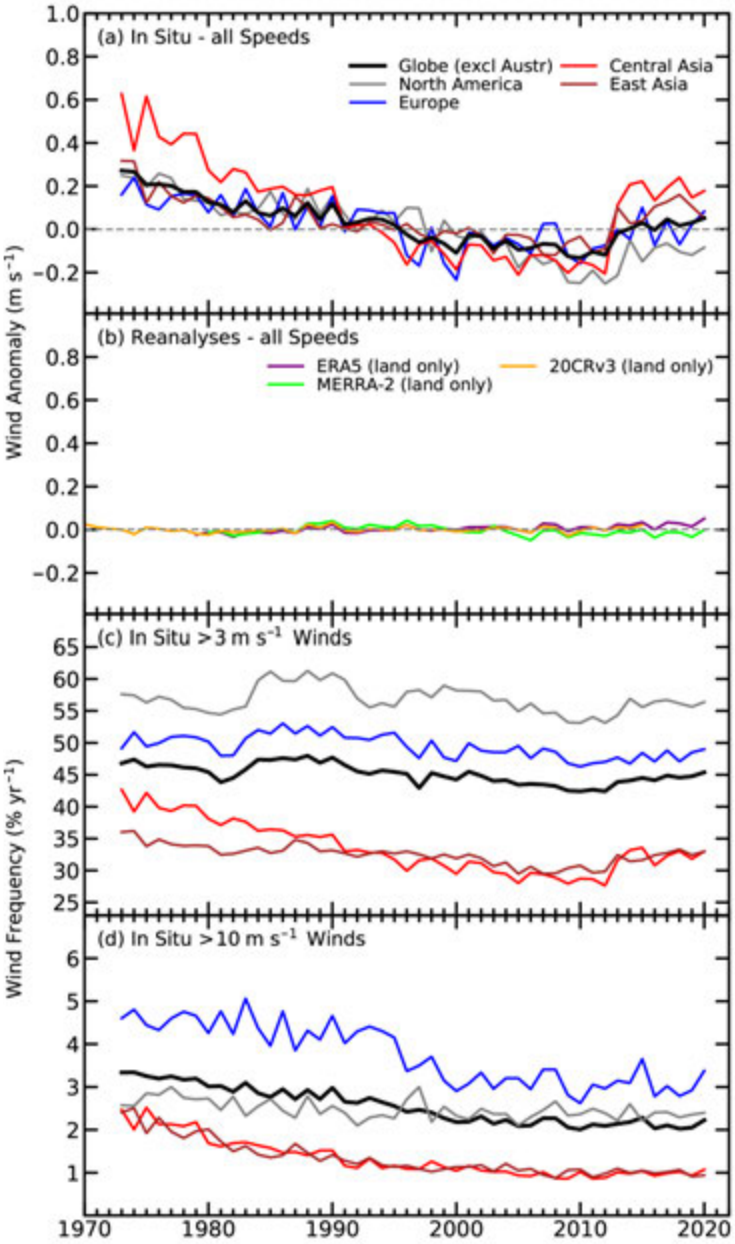

Fig. 2.41. Global (excluding Australia in panels [a], [c] and [d]) and regional annual time series of land surface wind speed anomaly (m s^{-1}; 1981–2010 base period) using (a) HadISD3 (1973–2020) and (b) ERA5 (1979–2020), MERRA-2 (1980–2020), and 20CRv3 (1836–2015, only 1970–2015 shown here). HadISD3 occurrence frequencies (in %) for wind speeds (c) >3 m s^{-1} and (d) >10 m s^{-1}.

winds, while North America showed less negative anomalies (–0.084 m s^{-1}) compared to the lowest value (–0.253 m s^{-1}), which occurred in 2012. Wind speed frequencies above a moderate threshold (>3 m s^{-1}; Fig. 2.41c) exhibited a weak recovery in the last decade, with no trend for stronger wind speeds over land (>10 m s^{-1}; Fig. 2.41d).

The assessment of wind speed changes across land and ocean surfaces for the 1979–2020 period is based on two types of products. First, global in situ anemometer observations were obtained from the quality-controlled HadISD3 dataset (v3.1.1.2020f; 1973–2020; Dunn et al. 2012, 2016, 2019) for 2554 stations that had sufficient coverage during the 1981–2010 climatology period. Second, wind speed estimates from three gridded reanalysis products were used to cover Earth's surface evenly: (i) ERA5 (1979–2020; Hersbach et al. 2020); (ii) MERRA-2 (1980–2020; Gelaro et al. 2017); and (iii) 20CRv3 (1836–2015; Slivinski et al. 2019). A major shortcoming of these products is their inability to capture the stilling and reversal phenomena shown by observations (Fig. 2.41b; Torralba et al. 2017; Ramon et al. 2019; Wohland et al. 2019); therefore, trends should be interpreted with caution.

Despite the rebound of surface winds observed since 2012, the sign of the long-term 1979–2020 trends of terrestrial wind speed remained negative. Globally, land surface winds weakened at a rate of –0.056 m s^{-1} $decade^{-1}$ (Table 2.8). This slowdown is of lesser magnitude compared to previous reports (Azorin-Molina et al. 2020) and especially when compared to the global average trend in observed terrestrial near-surface wind speeds of –0.140 m s^{-1} $decade^{-1}$ reviewed by McVicar et al. (2012) Regions also exhibited a weakening of negative trends and in the magnitudes of the 5th to 95th percentile confidence ranges because of the reversal of winds in the 2010s, with Central Asia and North America showing the strongest changes, and Europe and East Asia the weakest. As shown in Fig. 2.42, negative trends mostly occur across midlatitude regions of the NH, where most land-based observations exist. In the SH, ERA5 shows a greater dominance of weak positive trends over continents, particularly for Antarctica. In fact, the percentage of positive trends for stations and grid-points increased from 37% in 2019 to 42% because of the recovery of terrestrial winds, especially in Asia.

Table 2.8. Global and regional statistics for land surface wind speed (m s^{-1}) using the observational HadISD3 dataset for 1979–2020.

Region	Mean 1981–2010 (m s^{-1})	Anomaly 2020 (m s^{-1})	Trend 1979–2020 (m s^{-1} $decade^{-1}$) and 5th–95th percentile confidence range	Number of stations
Globe (excluding Australia)	3.324	+0.052	−0.056 (−0.065 → −0.040)	2554
North America	3.709	−0.084	−0.080 (−0.092 → −0.069)	578
Europe	3.677	+0.082	−0.042 (−0.053 → −0.032)	765
Central Asia	2.890	+0.178	−0.089 (−0.116 → −0.060)	258
East Asia	2.726	+0.051	−0.028 (−0.037 → −0.015)	459

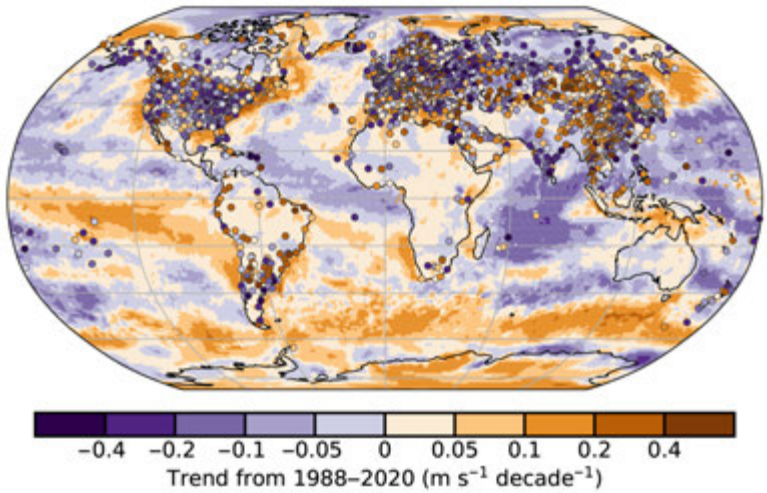

Fig. 2.42. Wind speed trends (m s^{-1} $decade^{-1}$) for the observational HadISD3 dataset (circles) over land, and ERA5 reanalysis output over land/ice and RSS satellite radiometers (SSM/I, SSMIS, TMI, GMI, AMSR2, AMSR-E, and WindSat) over ocean for 1988–2020 (shaded areas).

Ocean surface winds for 1988–2020 were assessed using: (i) reanalyses (MERRA-2, ERA5, and 20CRv3) and (ii) satellite-based products including the Special Sensor Microwave/Imager (SSM/I), the Special Sensor Microwave Imager/Sounder (SSMIS), the Advanced Microwave Scanning Radiometer (AMSR-E and AMSR2), and microwave imagers TMI, GMI, WindSat, QuikSCAT, and ASCAT (Wentz 1997; Wentz et al. 2007, 2015; Ricciardulli and Wentz 2015; Ricciardulli 2016). For 2020, satellite radiometers showed a near-zero global mean wind speed anomaly over ocean (−0.013 m s^{-1}; Fig. 2.43), consistent with the satellite scatterometers (ASCAT) and with MERRA-2; whereas ERA5 shows a positive anomaly and biases compared to the other products. In general, the magnitudes of any positive wind speed anomalies in 2020 were weak (Plate 2.1v), except in the Arctic Ocean, the North Atlantic Ocean, the southern fringe of both the South Pacific and South Atlantic Oceans, and the Bering Sea. In contrast, negative wind speed anomalies dominated tropical and subtropical ocean surfaces in 2020, particularly in the Atlantic and Indian Oceans. The ocean wind speed trend from satellite radiometers is nearly zero (+0.002 m s^{-1} $decade^{-1}$) for 1988–2020 (Fig. 2.42), with a dominance of negative regional trends (moderate ones in the Indian Ocean and western Pacific Ocean), except for the positive trends found in the Southern Ocean, and the Pacific and Atlantic trade winds south of the equator (Young and Ribal 2019)

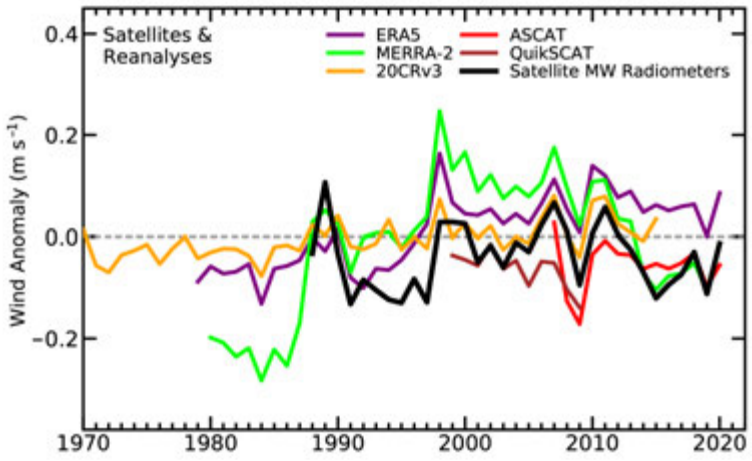

Fig. 2.43. Annual global mean wind speed anomalies (m s^{-1}; 1981–2010 base period) over the ocean from satellite radiometers and scatterometers, and reanalysis outputs. The values for the first year of both ASCAT and QuikSCAT are based on 6 months of deseasonalized data (monthly anomaly compared to monthly climatology).

Decadal-scale variations and trends of land and ocean surface winds are likely driven by internal decadal ocean–atmosphere oscillations (Zeng et al. 2019) and anthropogenic greenhouse gas forcing (Deng et al. 2021), respectively, with vegetation growth (Vautard et al. 2010), urbanization (Chen et al. 2020), and instrumentation issues (Azorin-Molina et al. 2018b) having a lesser impact. After decades of a slowdown of winds over land, the recent reversal, which continued in 2020, is increasing potential wind energy across the world (Zeng et al. 2019). The most challenging research questions now are to predict how long the positive anomalies will last and to estimate future wind projections given a changing climate with a direct impact on the wind energy sector.

3) Upper air winds—L. Haimberger, M. Mayer, and V. Schenzinger

The 2020 global mean wind speed anomaly at 850 hPa has slightly recovered from a minimum in late 2019 to values close to the long term (1981–2010) average (Fig. 2.44). However, the clear positive trend over the past 40 years remains in all four included reanalyses. The wind time series start now in 1950, thanks to the backward extension of ERA5 (Bell et al. 2021). In the NH extratropics, there is no evidence of wind stilling at 850 hPa, in contrast to surface winds (section 2e2).

Plate 2.1w shows the meridional (positive northward) wind anomaly averaged over September–December 2020 at 850 hPa. That period showed a pronounced wave train with wavenumber 4 around 55°N, with particularly strong southerly winds of up to 4 m s^{-1} in the 4-month average over northeastern Europe and far eastern Newfoundland. This pattern, together with ongoing climate change, led to the highest autumn temperatures on record in this region (Copernicus 2021). The dynamics that led to this pattern need to be fully investigated but are likely an example of enhanced resonance of Rossby waves in a warming climate (Petoukhov et al. 2013; Mann et al. 2019; Wills et al. 2019).

Turning to higher altitudes, we first assess the impact of tropical climate anomalies on upper-tropospheric circulation through inspection of 200-hPa

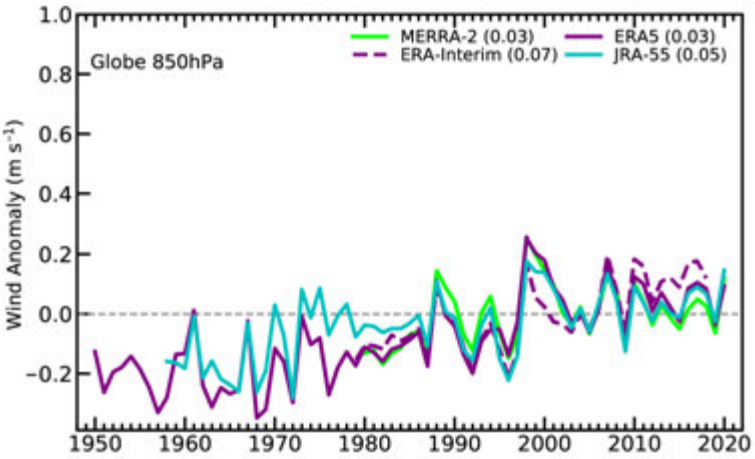

Fig. 2.44. Annual anomalies of global mean wind speed (m s^{-1}; 1981–2010 base period) at 850 hPa from four reanalyses (ERA5, ERA-Interim, MERRA-2, JRA-55). The numbers in parentheses are linear trends in m s^{-1} $decade^{-1}$ for the period 1980–2020. The *y*-axis range matches that for the land surface winds (Fig. 2.41).

velocity potential. After a strong positive IOD event in 2019, IOD conditions returned to neutral in 2020 (section 4f). In the Pacific, cold equatorial sea surface temperature (SST) anomalies appeared from early boreal summer 2020 and developed into a moderate La Niña event had formed by the end of the year (if defined by ONI index as >- 1.0 value, see section 4b).

Figure 2.45 depicts the imprint of these major tropical climate anomalies on upper air circulation. In August–September (Fig. 2.45a), negative velocity potential anomalies were present over the tropical Indian Ocean, with local minima over the northwestern and southeastern parts of the basin, indicating widespread, positive upper-air divergence anomalies. This differs from 2019 when there was a clear east–west dipole in the Indian Ocean velocity potential anomalies. An explanation for this difference is that SSTs were above normal both in the western and eastern equatorial Indian Ocean in 2020 (suggestive of a positive state of the Indian Ocean Basin Mode; Yang et al. 2007) but with more pronounced anomalies in the east (see also section 4f). The generally positive SST anomalies were favorable for enhanced upper-air divergence. At the same time, positive velocity potential anomalies were present over the western Pacific, consistent with reduced atmospheric convection associated with the developing La Niña event.

Velocity potential anomalies shifted eastward in October–November (Fig. 2.45b). Negative anomalies were centered over the Indo-Pacific Warm Pool. This is consistent with enhanced atmospheric convection over the eastern Indian Ocean associated with positive SST anomalies in this region. Moreover, in October–November changes to the Pacific Walker Circulation related to the negative SST anomalies of the now more mature La Niña event were centered farther eastward in the Pacific. This is reflected in positive velocity potential anomalies centered east of the date line arising from suppressed convection and likely contributed to the negative anomaly over the Indo-Pacific Warm Pool.

La Niña years provide more favorable conditions for Atlantic hurricanes, and indeed the late 2020 hurricane season was exceptionally intense (see section 4g). The imprint of the strong

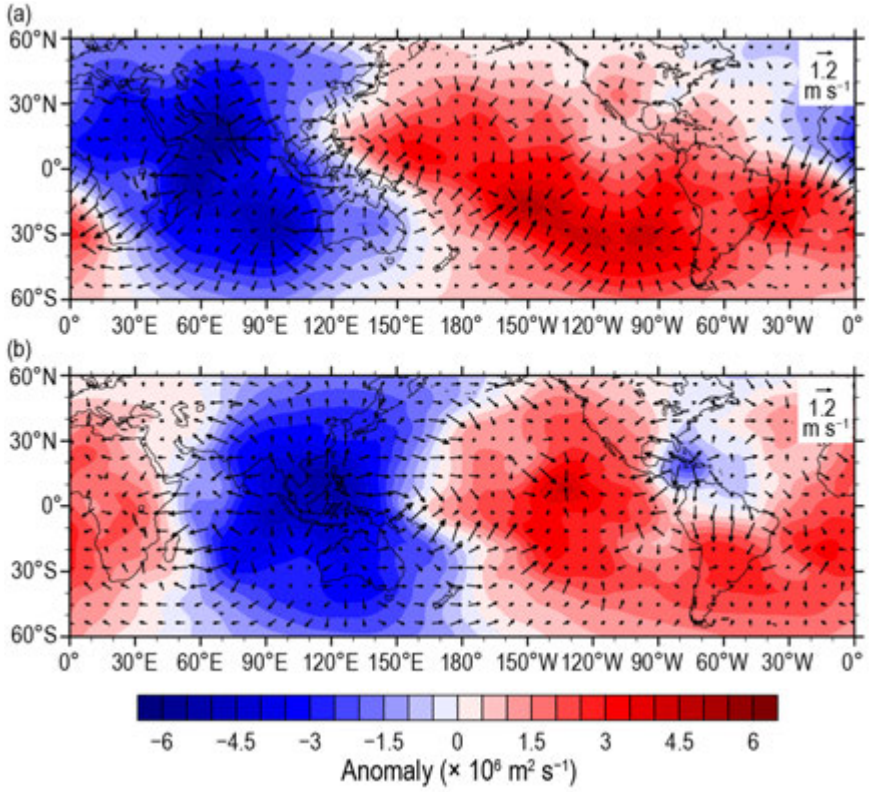

Fig. 2.45. Anomalous 200-hPa velocity potential (× 10^6 m^2 s^{-1}) and divergent winds (m s^{-1}) averaged over (a) Aug–Sep and (b) Oct–Nov 2020 (1981–2010 base period) based on ERA5 data.

hurricane activity can also be seen in Fig. 2.45b, with a prominent negative anomaly over the Caribbean. Such a pattern favored hurricane activity, but likely was also enhanced by the strong upper-air divergence in the hurricanes once they had formed.

After the anomaly around the 2015/16 year transition (Osprey et al. 2016), the quasi-biennial oscillation (QBO) saw its second disruption in 2019/20. In both cases, a thin layer of westerlies appeared to be split off the descending westerly phase around 40 hPa and propagated upward through the stratosphere (Fig. 2.46). While these winds were overall weaker in the recent anomaly, the disruption, as measured by the explained variance of the first two empirical orthogonal functions (EOFs), was much stronger (Anstey et al. 2020). Typically, the first two EOFs explain around 90% of the vertical wind variance. In the 2015/16 disruption, this value dropped to around 60% and in 2019/20 down to 20%.

While the anomaly in 2015/16 was associated with unusually high wave-momentum fluxes from the NH (Osprey et al. 2016), the 2019/20 anomaly was probably caused by meridional momentum fluxes from the SH (Anstey et al. 2020). The QBO pattern stabilized again around May 2020. The combination of the QBO phase shifts following the disruptions results in the phase again aligning with the expectation from the historical record (Anstey et al. 2020). However, with long-term changes in the tropical circulation like increased upwelling, it remains to be seen whether the QBO returns to its regular cycle for a longer period of time.

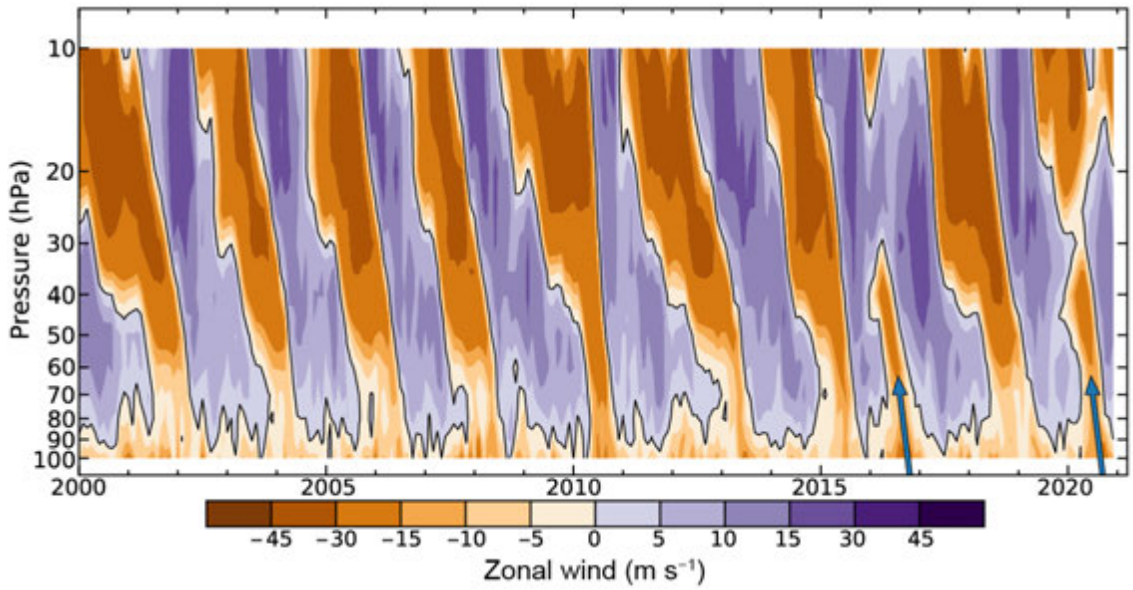

Fig. 2.46. Monthly mean stratospheric zonal winds (m s^{-1}) at Singapore with 2016 and 2020 highlighted by arrows (FU Berlin, 2021). Purple shades show westerly winds; orange colors show easterly winds.

f. Earth radiation budget

1) Earth radiation budget at top-of-atmosphere—P. W. Stackhouse Jr., T. Wong, P. Sawaengphokhai, A. C. Wilber, S. K. Gupta, D. P. Kratz, and N. G. Loeb

The energetic state of the Earth–atmosphere system is defined by the balance of the incoming total solar irradiance (TSI), the reflected shortwave (RSW), and the outgoing longwave radiation (OLR) from Earth. This balance defines Earth's radiation budget (ERB) at the top of the atmosphere (TOA) and its regional distribution drives atmosphere and ocean circulations.

An analysis of all Clouds and the Earth's Radiant Energy System (CERES) ERB measurements (Table 2.9) shows that 2020 global annual mean OLR increased by ~0.20 W m^{-2} and RSW increased by ~0.40 W m^{-2} relative to their corresponding values in 2019 (rounded to nearest 0.05 W m^{-2}).

Table 2.9. Global annual mean top of atmosphere (TOA) radiative flux changes (W m^{-2}) between 2019 and 2020, the 2020 global annual mean radiative flux anomalies relative to their corresponding 2001–19 mean climatological values (also shown), and the 2-sigma interannual variabilities of the 2001–19 global annual mean fluxes for the outgoing longwave radiation (OLR), total solar irradiance (TSI), reflected shortwave (RSW), absorbed shortwave (SW; TSI minus RSW), absorbed SW (TSI – RSW), and total net fluxes (TSI minus RSW minus OLR)). All flux values have been rounded to the nearest 0.05 W m^{-2} and only balance to that level of significance.

	One-Year Change (2020 minus 2019) (W m^{-2})	2020 Anomaly (Relative to Climatology) (W m^{-2})	Climatological Mean (2001–19) (W m^{-2})	Interannual Variability (2001–19) (W m^{-2})
OLR	0.20	+0.65	240.20	±0.65
TSI	0.05	–0.05	340.00	±0.15
RSW	0.40	–0.70	99.00	±1.00
TSI – RSW	–0.40	+0.65	241.00	±0.95
Net	**–0.60**	**0.00**	**0.80**	**±0.80**

Over the same timeframe, the global annual mean TSI increased by 0.05 W m^{-2}, showing a steady increase, possibly toward the next solar maximum. The sum of these components amounts to a decrease of ~0.60 W m^{-2} in the global annual mean total net radiation relative to 2019. Figure 2.47 shows the annual mean regional difference maps in the OLR and RSW between 2019 and 2020. The largest reductions in OLR and increases in RSW are observed over the tropical Indian Ocean extending over Indonesia and southeastward over and east of Australia (a recovery from a 2019 Indian Ocean dipole event; see sections 2a1, 2d7, 4f), as well as a feature in the tropical Atlantic. The largest increases in OLR and reductions in RSW were observed in the tropical western and south-central Pacific regions. These regional differences appear associated with the change from near-neutral ENSO conditions at the end of 2019 to La Niña conditions by August 2020 that persisted through the end of the year (see section 2e1, 4b). Also noted are broad areas of moderate OLR increase and RSW decrease over both North and South America corresponding to reduced cloudiness and increased surface warmth in these regions (see sections 2d4, 2d7, 2d11 and 2b1). Relative to the 2001–19 climatological average, the 2020 global annual mean flux anomalies are +0.65, –0.05, –0.70, and +0.00 W m^{-2}

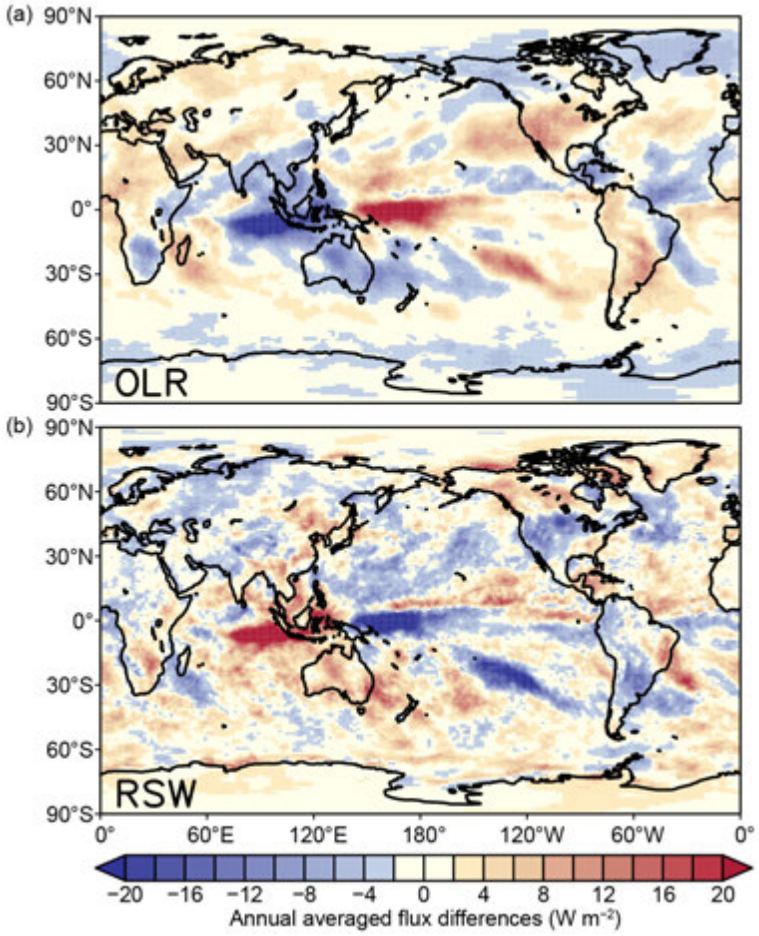

Fig. 2.47. Annual average top of atmosphere (TOA) flux differences between 2020 and 2019 (W m^{-2}) for the (top panel) OLR and (bottom panel) TOA reflected shortwave (RSW). The annual mean maps for 2020 were derived after adjusting December 2020 FLASHFlux v4A using the difference between EBAF and FF v4A in 2019. The pattern of differences shows several significant features including changes over the Indian and tropical western and south-central Pacific Oceans. The tropical Indian/Pacific Ocean pattern is dominated by an atmospheric shift from neutral ENSO conditions during the latter half of 2019 and early 2020 to La Niña conditions that persisted from Aug through Dec 2020 and also includes a transition from an IOD event in 2019 (see section 4f).

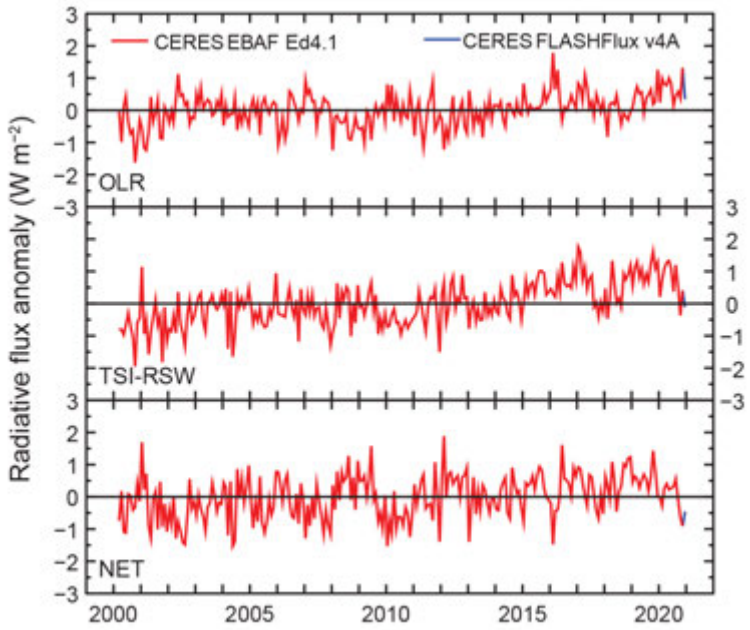

Fig. 2.48. Time series of global monthly mean deseasonalized anomalies (W m^{-2}) of top-of-atmosphere (TOA) Earth radiation budget for outgoing longwave radiation (OLR; upper); absorbed shortwave (total solar irradiance [TSI] minus reflected shortwave [RSW]; middle); and total net (TSI minus RSW minus OLR; lower) from Mar 2000 to Dec 2020. Anomalies are relative to their calendar month climatology (2001–19). Time series shows the CERES EBAF Ed4.1 1-Deg data (Mar 2000–Nov2020) in red and the CERES FLASHFlux version 4A data (Dec 2020) in blue; see text for merging procedure. (Sources: https://ceres-tool.larc.nasa.gov/ord-tool/jsp/EBAF41Selection.jsp and https://ceres-tool.larc.nasa.gov/ord-tool/jsp/FLASH_TISASelection.jsp.)

for OLR, TSI, RSW, and total net flux, respectively (Table 2.9), all at or within their corresponding 2-sigma interannual variability (Table 2.9).

The global monthly mean anomaly time series of TOA fluxes (Fig. 2.48) reveal that the global monthly mean OLR anomaly remained positive throughout the first half of 2020 at a level of about +1.00 W m^{-2}. During the second half of 2020, the OLR anomalies remained positive, but decreased to less than +0.50 W m^{-2} except for November, which spiked to +1.30 W m^{-2}. This large November OLR anomaly is consistent with the values obtained from the NOAA HIRS OLR (Lee and NOAA CDR Program 2011) and NASA AIRS OLR (Susskind et al. 2012) datasets (not shown). The global monthly mean absorbed shortwave (SW; TSI minus RSW) anomaly began 2020 at +0.20 W m^{-2}, peaked in May at around +1.35 W m^{-2}, and then decreased sharply after August, ending the year with a value of −0.10 W m^{-2}. For the year as a whole, the 2020 global annual mean absorbed SW anomaly was +0.65 W m^{-2}. The global monthly mean total net anomaly, which is calculated from the absorbed SW anomaly minus the OLR anomaly, began 2020 with a value of −0.05 W m^{-2}, reached a maximum value of +0.75 W m^{-2} in August, then decreased rapidly to about −0.90 W m^{-2} in November, ending the year at −0.45 W m^{-2}. The positive OLR anomalies approximately balanced the positive absorbed SW anomalies in 2020, resulting in a global annual mean total net anomaly of 0.0 W m^{-2}. The total net anomaly decreased by ~1.65 W m^{-2} between August and November 2020. Although this corresponds to the onset of the 2020 La Niña, more analysis is required for definitive attribution. Long-term trend analyses that include the last month of the merged dataset are discouraged because of the natural fluctuation in ERB components, uncertainty from the data-merging process, and potential for drift in the FLASHFlux product.

The TSI data used in this study are provided by the Total Irradiance Monitor aboard the Solar Radiation and Climate Experiment (SORCE) mission (Kopp and Lean 2011) and the Royal Meteorological Institute of Belgium composite dataset (Dewitte et al. 2004), both renormalized to the SORCE Version 15. Starting in February 2020, data from the Total Solar and Spectral Irradiance Sensor-1 (TSIS-1, Coddington, 2017) mission on board the International Space Station is normalized to SORCE Version 15. The RSW and OLR data were obtained from the CERES instruments (Wielicki et al. 1996, 1998) aboard *Terra* and *Aqua* spacecraft. The time series (Fig. 2.48) were constructed from the CERES EBAF (Energy Balanced And Filled) Ed4.1 product (Loeb et al. 2009, 2012, 2018) for March 2000–November 2020 and from the CERES Fast Longwave and Shortwave Radiative Fluxes (FLASHFlux) version 4A product (Kratz et al. 2014) for December 2020. The normalization of the FLASHFlux data (Stackhouse et al. 2016) results in 2-sigma monthly uncertainties of ±0.47, ±0.07, ±0.24, and ±0.58 W m^{-2} for the OLR, TSI, RSW, and total net radiation, respectively.

2) Mauna Loa apparent transmission—J. A. Augustine, K. O. Lantz, and J.-P. Vernier

Initiated in 1958 as part of the International Geophysical Year, one of the longest records of atmospheric transmission, i.e., the percent of top of atmosphere (TOA) solar radiation that reaches the surface, has been recorded on the island of Hawaii at 3397 m above mean sea level, just below the summit of the Mauna Loa volcano. Because of the clean nature of the atmosphere over Mauna Loa, its elevation and vertical separation from the marine boundary layer, atmospheric transmission there is considered a proxy of stratospheric aerosol loading. One exception is the effect from the annual transport of Asian dust over Hawaii at high-tropospheric levels in springtime (Bodhaine et al. 1981).

The updated time series of "apparent" transmission (see definition below) through 2020 is presented in Fig. 2.49. Plotted are monthly averages and a 6-month-smoothed fit that reveals intra-annual variability caused mainly by springtime Asian dust. The most pronounced features are deviations caused by three major volcanic eruptions: Agung, Indonesia, in 1963; El Chichon, Mexico, in 1982; and Pinatubo, Philippines, in 1991. Resultant deep reductions in transmission are followed by slow recoveries that last up to 8 years and reflect the long residence time of aerosols in the stratosphere. For reference, the horizontal dashed line in Fig. 2.49 represents the average transmission prior to Agung (0.934) when the stratosphere was exceptionally clean. That level of stratospheric purity has been achieved only briefly over the 62-year time series, most notably in the late 1970s and from the late 1990s into the early 2000s. A steady decrease from 2002 to 2010 is associated with a series of tropical and high-latitude volcanic eruptions (Andersson et al. 2015; Vernier et al. 2011), each of which affected the stratosphere for a year or less (Augustine et al. 2020). Apparent transmission over Mauna Loa increases after 2010 and remains relatively stable through 2018. A slow decline is apparent through 2019 from the eruptions of Mt. Raikoke on the Kuril Islands north of Japan in June 2019 and Mt. Ulawun in Papua New Guinea in June and August 2019.

The only major volcanic event in 2020 was the explosive eruption of Mt. Taal in the Philippines on 12 January, but there is no indication from the Cloud-Aerosol Lidar with Orthogonal Polarization (CALIOP) space-borne lidar that it significantly affected the stratosphere. The most notable aerosol events of 2020 were wildfires in Australia from December 2019 to early 2020 (Kablick et al. 2020) and the record-setting Saharan dust event in June (Francis et al. 2020). However, neither affected Mauna Loa. Stratospheric aerosols from Australian wildfire pyrocumulus had limited cross-equatorial transport, and Saharan dust reached just ~3–7 km in altitude and only affected the troposphere in the low-latitude North Atlantic Ocean, the Caribbean, and eastern North America (Francis et al. 2020). Aerosols from wildfire pyrocumulus in the western United States that began in August 2020, especially in central California, were observed in the lower stratosphere in September by CALIOP and in September and October by SAGE III aboard the International Space Station (see https://appliedsciences.nasa.gov/our-impact/news/californias-creek-fire-blasts-smoke-stratosphere). Satellite visualization shows a relatively small amount of that smoke reaching Hawaii in late August and September 2020 and is probably partially responsible for the transmission decrease in September

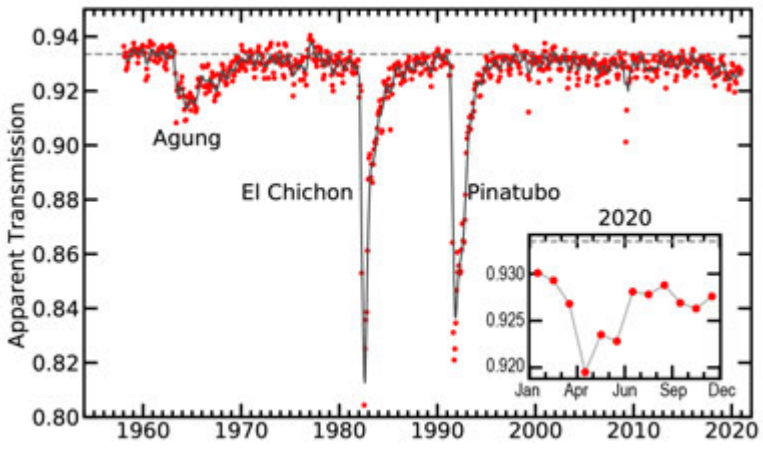

Fig. 2.49. Apparent transmission at Mauna Loa, Hawaii, from 1958 through 2020. Red dots are monthly average morning transmissions, the gray curve is a fit with a 6-month smoother applied, and the dashed horizontal line is the average transmission for the clean period before the eruption of Agung. Insert is an enlargement of the newest data for 2020.

apparent in the inset of Fig. 2.49. Residual effects from the 2019 eruptions of Raikoke and, to a lesser extent Ulawun, were likely responsible for maintaining a relatively low transmission of 0.9265 ± 0.0029 in 2020. CALIOP shows those stratospheric volcanic plumes much reduced from 2019 levels but still present at the latitude of Mauna Loa through October 2020, which is the extent of CALIOP data analyzed. Transmission reached the annual minimum of 0.919 in April, presumably from the addition of springtime Asian dust.

Atmospheric transmission is defined as the ratio of the solar beam intensity at the surface to that at the top of the atmosphere over a vertical path. Given the impracticality of that calculation, Ellis and Pueschel (1971) showed mathematically equivalency of vertical transmission to the ratio of surface solar beam measurements at two distinct integer path lengths. However, because broadband transmission is influenced by path length, that calculation is referred to as "apparent" transmission. Here, a representative daily apparent transmission is the mean of three successive ratios of pyrheliometer measurements at 2, 3, 4, and 5 atmospheric path lengths. Only morning data are considered because upslope winds typically contaminate afternoon measurements with marine-layer aerosols. Individual points in Fig. 2.49 represent the average of all acceptable morning transmissions within a particular month. Neither the radiometer calibration factor nor the solar intensity at TOA are needed, resulting in a precise time series back to 1958.

g. Atmospheric composition

1) Long-lived greenhouse gases—X. Lan, P. Tans, B. D. Hall, G. Dutton, J. Mühle, J. W. Elkins, and I. Vimont

Increased atmospheric burdens of long-lived greenhouse gases (LLGHGs) are the dominant driver of warming climate (IPCC AR5 2013). Carbon dioxide (CO_2), methane (CH_4), and nitrous oxide (N_2O) are naturally present in the atmosphere but have been greatly increased by human activity in the industrial era.

Systematic measurements of atmospheric CO_2 began at Mauna Loa, Hawaii (MLO), in 1958, when CO_2 was approximately 315 ppm (parts per million by moles in dry air). In 2020, annually averaged CO_2 at MLO reached 414.2 ± 0.1 ppm (all uncertainties are reported as 1 sigma [σ] in this section), while globally averaged CO_2 derived from remote marine boundary layer (MBL) measurements from NOAA's Global Greenhouse Gas Reference Network (GGGRN) was 412.5 ± 0.1 ppm (Fig. 2.50a; gml.noaa.gov/ccgg/trends). Both levels were the highest since the systematic measurements of CO_2 started. The globally averaged level represents an increase of 48% over pre-industrial values of 278 ppm (Etheridge et al. 1996). Annual growth in global mean CO_2 has accelerated from 0.8 ± 0.3 ppm yr^{-1} (± 1 σ for interannual variability) in the 1960s to an average of 2.4 ± 0.4 ppm yr^{-1} during 2010–19 (Fig. 2.50a). The annual increase in global mean CO_2 in 2020 was 2.5 ± 0.1 ppm. In 2020, the radiative forcing due to anthropogenic CO_2 increased to 2.11 W m^{-2} relative to pre-industrial times (1750 CE; Table 2.10; gml.noaa.gov/gmd/aggi/; Hofmann et al. 2006).

The main driver of increasing atmospheric CO_2 is fossil fuel (FF) burning, with emissions (including a minor amount from cement production) between 2010 and 2019 averaging 9.4 ± 0.5 Pg C yr^{-1} (Friedlingstein et al. 2020). If all of this CO_2 remained in the atmosphere, the average 2010–19 increase would have been 4.4 ppm yr^{-1} instead of 2.4 ppm yr^{-1}. Thus, only about 55% of FF-emitted CO_2 in 2010–19 has remained in the atmosphere, while the rest has been stored by the ocean and the terrestrial biosphere. While emissions of CO_2 from FF combustion drive its increasing atmospheric burden, the large interannual variability in the CO_2 growth rate is mostly driven by terrestrial biospheric exchange of CO_2, which is confirmed by stable carbon isotope (^{13}C) measurements (e.g., Keeling et al. 1985; Alden et al. 2010). Terrestrial biosphere flux variability is influenced by both temperature and moisture anomalies (Cox et al. 2013; Hu et al. 2019; Humphrey et al. 2018). For example, the terrestrial impacts of the strong El Niño that peaked in late-2015 contributed to a strong global CO_2 increase of 3.0 ppm yr^{-1} (Betts et al. 2016). Because El Niño–Southern Oscillation (ENSO) changed from neutral to La Niña during 2020, it is not surprising that the observed CO_2 increase was near the 2010–19 mean.

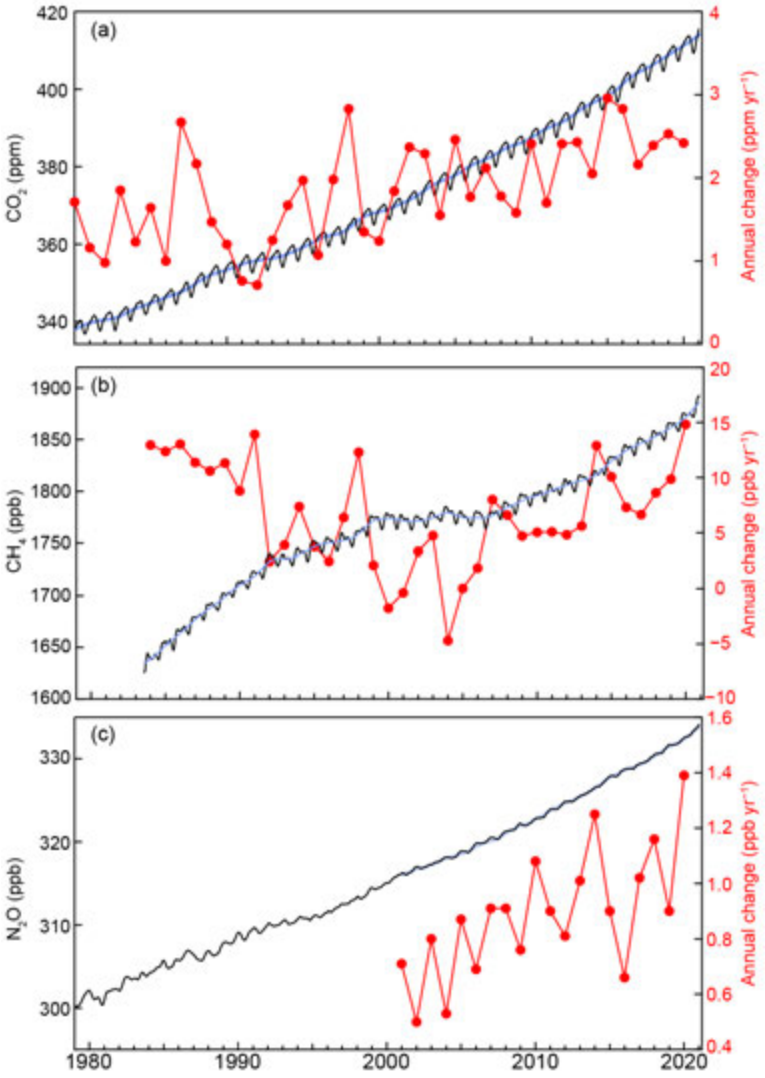

Fig. 2.50. Global monthly mean dry-air surface mole fractions (black, left axis) and annual increases (red, right axis) of (a) carbon dioxide (CO_2), (b) methane (CH_4), and nitrous oxide (N_2O) derived from NOAA Global Greenhouse Gases Reference Network marine boundary layer measurement sites. Deseasonalized trend curves (see Dlugokencky et al. 1994 for methods) are shown in blue; annual increases are defined as 1 Jan minus 1 Jan of consecutive years from the trend line. N_2O data prior to 1995 are insufficient and noisy, thus hindering the calculation of a growth rate.

Anthropogenic CO_2 emissions are estimated to have decreased by about 6%–7% due to reduced human activities during the COVID-19 pandemic (Friedlingstein et al. 2020; Le Quere et al. 2020; BP Statistical Review of the World Energy 2021). However, this reduction is not obvious in observed global atmospheric CO_2 signals, because it is a relatively small signal compared with natural variability that is driven by the large fluxes from photosynthesis and respiration of ecosystems on land. The estimated ~6%–7% reduction in global CO_2 emissions of ~10 Pg C yr^{-1} would result in a ~0.3 ppm decrease in global CO_2 (given a conversion factor of 2.12 Pg C ppm^{-1}; Ballantyne et al. 2012), which is within the 1-σ interannual variability of CO_2 annual growth in 2010–19 (0.4 ± 0.1 ppm yr^{-1}). The impact of emission changes during COVID-19 may be more discernible in urban atmospheric CO_2 measurements because most of the emission reductions come from urban areas (A. J. Turner et al. 2020).

Methane is the second-most important anthropogenic greenhouse gas after CO_2. Its abundance in the atmosphere increased to 1879.2 ± 1.0 ppb (parts per billion by moles in dry air) in 2020, a 160% increase compared to its pre-industrial level of 722 ± 15 ppb. Since the beginning of NOAA's systematic CH_4 measurements in 1983, the global CH_4 annual increase has varied between −4.9 and 14.8 ppb yr^{-1} (red line in Fig. 2.50b) as a result of the changing balance between emissions and chemical destruction. The CH_4 annual increase averaged 11.4 ± 1.4 ppb yr^{-1} from 1983 to 1992, followed by a strong decrease to 4.4 ± 1.8 ppb yr^{-1} between 1992 and 1998, and further reduced to near zero (0.5 ± 3.0 ppb yr^{-1}) during 1999–2006. The rise and then flattening of the global methane abundance is consistent with an approach to steady state if there was no trend in its lifetime (Dlugokencky et al. 2003). Atmospheric CH_4 growth restarted again in 2007 and the average growth rate after 2014 was higher than 2007–14 (red line in Fig. 2.50b). The annual increase in 2020 was 14.8 ± 0.5 ppb, which is by far the largest annual increase since systematic atmospheric CH_4 measurements began. There is no obvious explanation at this time for this large anomaly. CH_4 now contributes 0.52 W m^{-2} in direct radiative forcing (Table 2.10) relative to pre-industrial times, while the CH_4-related production of tropospheric ozone (O_3) and stratospheric water vapor (H_2O) contributes ~0.3 W m^{-2} in indirect radiative forcing (Myhre et al. 2013).

Table 2.10. Summary table of long-lived greenhouse gases for 2020 (Carbon dioxide [CO_2] abundances [mole fractions] are in ppm, nitrous oxide [N_2O] and methane [CH_4] in ppb, and all others in ppt).

Industrial Designation or Common Name	Chemical Formula	Included in the AGGI[a]? (Yes/No)	Radiative Efficiency (W m^{-2} ppb^{-1})[b]	Rad. Forcing (W m^{-2})	Mean surface mole fraction, 2020 (change from 2019)[c]	Lifetime (years)
Carbon Dioxide	CO_2	Y	1.37×10^{-5}	2.11	412.5 (2.5)	—
Methane	CH_4	Y	3.63×10^{-4}	0.52	1879.2 (12.7)	9.1
Nitrous Oxide	N_2O	Y	3.00×10^{-3}	0.21	333.0 (1.2)[d]	123
Chlorofluorocarbons						
CFC-11	CCl_3F	Y	0.26	0.058	224.5 (–1.8)[c]	52
CFC-12	CCl_2F_2	Y	0.32	0.159	497.3 (–3.9)[c]	102
CFC-113	CCl_2FCCl	Y	0.30	0.021	69.0 (–0.7)[c]	93
Hydrochlorofluorocarbons						
HCFC-22	$CHClF_2$	Y	0.21	0.052	246.4 (1.4)	11.9
HCFC-141b	CH_3CCl_2	Y	0.16	0.004	24.2 (0.03)	9.4
HCFC-142b	CH_3CClF	Y	0.19	0.004	21.6 (–0.2)	18
Hydrofluorocarbons						
HFC-134a	CH_2FCF_3	Y	0.16	0.018	111.5 (5.1)	14
HFC-152a	CH_3CHF_2	Y	0.10	<0.001	6.2 (–0.03)	1.6
HFC-143a	CH_3CF_3	Y	0.16	0.004	24.9 (1.5)	51
HFC-125	CHF_2CF_3	Y	0.23	0.007	33.0 (3.0)	30
HFC-32	CH_2F_2	N	0.11	0.002	21.1 (2.9)	5.4
HFC-23	CHF_3	Y	0.18	0.006	33.7 (1.3)	228
HFC-365mfc	CH_3CF_2C	N	0.22	< 0.001	1.0 (0.02)	8.9
HFC-227ea	CF_3CHFC	N	—	< 0.001	1.70 (0.15)	36
Chlorocarbons						
Methyl Chloroform	CH_3CCl_3	Y	0.07	< 0.001	1.4 (–0.2)	5.0
Carbon Tetrachloride	CCl_4	Y	0.17	0.013	86.8 (–0.9)[c]	32
Methyl Chloride	CH_3Cl	N	0.01	< 0.001	546.6 (8.7)	0.9
Bromocarbons						
Methyl Bromide	CH_3Br	N	0.004	< 0.001	6.70 (0.15)	0.8
Halon 1211	$CBrClF_2$	Y	0.29	0.001	3.11 (–0.10)	16
Halon 1301	$CBrF_3$	Y	0.30	0.001	3.31 (0.0)	72
Halon 2402	$CBrF_2CB$	Y	0.31	< 0.001	0.40 (0.0)	28
Fully fluorinated species						
Sulfur Hexafluoride	SF_6	Y	0.57	0.006	10.3 (0.3)	> 600
PFC-14	CF_4	N	0.09	0.005	86.4 (0.9)	~ 50000
PFC-116	C_2F_6	N	0.25	0.001	4.94 (0.09)	~ 10000
PFC-218	C_3F_8	N	0.28	< 0.001	0.70 (0.02)	~ 2600
PFC-318	c-C_4F_8	N	0.32	< 0.001	1.82 (0.06)	~ 3200

[a] Annual Greenhouse Gas Index (AGGI). See https://gml.noaa.gov/aggi/ for more information

[b] Radiative efficiencies and lifetimes were taken from Appendix A in WMO (2018), except for SF_6 lifetime from Ray et al. (2017) and CH_4 lifetime from Prather et al. (2012). For CO_2, numerous removal processes complicate the derivation of a global lifetime. For more on radiative forcing, see https://www.esrl.noaa.gov/gmd/aggi/

[c] Mole fractions are global, annual surface means for the 2020 determined from the NOAA Global Greenhouse Gas Reference Network, except for PFC-14, PFC-116, PFC-218, PFC-318, and HFC-23, which were measured by AGAGE (Mühle et al. 2010; Miller et al. 2010). Changes indicated in brackets are the differences between the 2020 and 2019 means, the relevant quantities for calculating radiative forcing. These changes are somewhat different from the 2020 annual increases reported in 2.g.1, which are determined as the difference between Jan. 1, 2021 and Jan. 1, 2020. All values are preliminary and subject to minor updates.

[d] Global mean estimates derived from multiple NOAA measurement programs ("Combined Dataset").

Given the complexity of the CH_4 budget and the uncertainty in CH_4 source partitioning, the magnitudes and long-term trends of many CH_4 sources are still uncertain. FF exploitation is estimated to account for ~19% of total global CH_4 emissions since 2000 based on top-down approaches that use atmospheric CH_4 measurements and inverse models (Saunois et al. 2020). However, studies including the radiocarbon (^{14}C) or stable carbon (^{13}C) isotopes of CH_4 suggest a much larger fraction of FF emissions (~30%; Lassey et al. 2007; Schwietzke et al. 2016). Measurements of $\delta^{13}C\text{-}CH_4$ also suggest that increased emissions from biogenic sources, from natural and/or anthropogenic origins, are the dominant drivers for the post-2006 growth (Chang et al. 2019; Nisbet et al. 2019; Schaefer et al. 2016; Schwietzke et al. 2016). Global atmospheric $\delta^{13}C\text{-}CH_4$ has become more depleted since 2008, which is consistent with an increased contribution from biogenic sources with more negative $\delta^{13}C\text{-}CH_4$ signatures. Increased wetland emissions may play a role in the post-2006 renewed increase (Yin et al. 2020), but further investigation is required to better quantify wetland emissions given the large uncertainties associated with wetland emission areas and processes controlling wetland CH_4 emissions (Bloom et al. 2017). A decrease in biomass burning and a small increase in FF emissions (Worden et al, 2017) may also play a smaller role in post-2006 global CH_4 change (Lan et al. 2021).

Methane is removed from the atmosphere mainly by reaction with hydroxyl radical (OH); OH has a very short lifetime (~1 s), which makes it difficult to constrain by direct observations. While recent studies suggest that a decreasing OH sink may not be the dominant driver for the post-2006 renewed increase in global atmospheric CH_4 (Fujita et al. 2020), uncertainties remain in the temporal variations of the OH sink and other CH_4 sinks such as oxidation by tropospheric chlorine (Cl; Hossaini et al. 2016; Gromov et al. 2018) and soils. The global soil CH_4 sink is estimated to be ~30 Tg yr^{-1}; however, up to a 77% decrease was reported for 1988–2015 based on long-term measurements and data reviews (Ni and Groffman 2018). A decrease in the soil CH_4 sink is consistent with an observed global decrease in $\delta^{13}C\text{-}CH_4$ (Lan et al. 2021).

Nitrous oxide (N_2O) is an important LLGHG that also depletes stratospheric ozone (Ravishankara et al. 2009). Atmospheric N_2O has been increasing steadily throughout the industrial era except for a brief period in the 1940s (MacFarling Meure et al. 2006; Thompson et al. 2019). The mean global atmospheric N_2O abundance in 2020 was 333.0 ± 0.1 ppb, while the annual increase in 2020 was 1.4 ± 0.1 ppb (Fig. 2.50c), and a 23% increase over pre-industrial levels of 270 ppb. The 1.4 ppb increase in the annual mean is similar to average rate of increase of 1.0 ± 0.2 ppb yr^{-1} over the past decade (2010–19), but slightly larger than the average rate in previous decade (2000–09) of 0.7 ± 0.2 ppb yr^{-1}. The observed increase in atmospheric N_2O over preindustrial levels is mostly caused by nitrogen-containing fertilizers and manure used for agriculture (Davidson 2009). A recent study found that anthropogenic N_2O emissions have increased by 30% since 1980, with significant contributions from developing countries such as Brazil, China, and India (Tian et al. 2020). Radiative forcing from N_2O in 2020 is now 0.21 W m^{-2} relative to pre-industrial times (Table 2.10).

The combined radiative forcing in 2020 from major and minor LLGHGs was 3.2 W m^{-2} (Fig. 2.51). Annual increases in radiative forcing correspond roughly with variability in CO_2, since CO_2 is responsible for about 65% of radiative forcing by LLGHGs and its increase during 2015–20 accounts for 82% of total increase in radiative forcing.

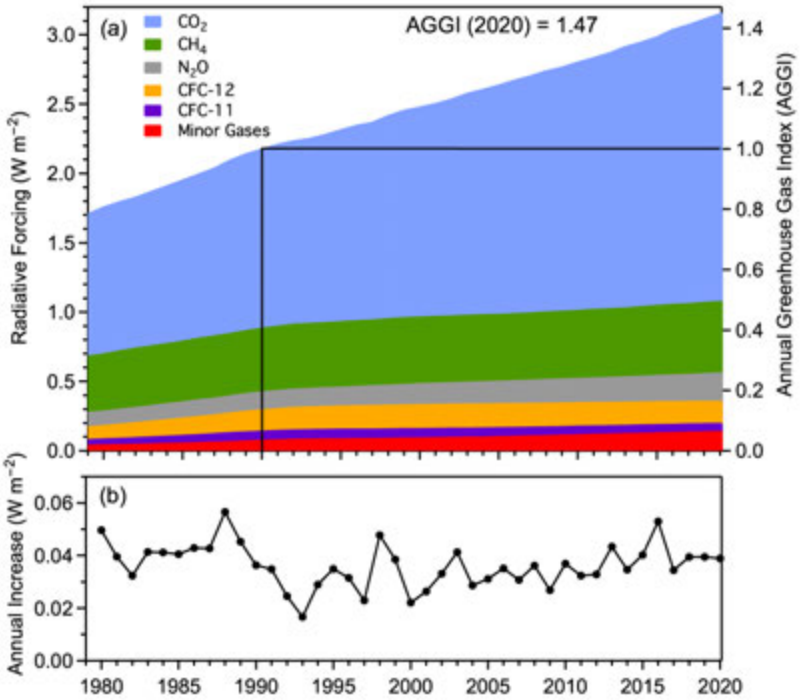

Fig. 2.51. (a) Direct radiative forcing (W m^{-2}) due to five major long-lived greenhouse gases (LLGHG) and 15 minor gases (left axis) and the associated values of the NOAA AGGI (right axis). The Annual Greenhouse Gas Index (AGGI) is defined to have a value of one in 1990. (b) Annual increase in direct radiative forcing (W m^{-2}).

2) Ozone-depleting substances—I. J. Vimont, B. D. Hall, S. A. Montzka, G. Dutton, C. Siso, M. Crotwell, and M. Gentry

Our climate is affected by the presence of halogenated trace gases in the atmosphere. This group of compounds includes, but is not limited to, chlorofluorocarbons (CFCs), hydrochlorofluorocarbons (HCFCs), hydrofluorocarbons (HFCs), chlorinated hydrocarbons, and halons. These compounds both directly (via radiative forcing) and indirectly (via ozone depletion in the stratosphere) influence the radiative balance of the atmosphere (Karpechko and Maycock 2018).

The Montreal Protocol (1987) and its subsequent amendments regulate the production and consumption of these ozone-depleting substances (ODS) and other compounds. These controls started in the late 1980s by phasing out production of CFCs and were followed by the reduction and phaseout of halons in the 1990s and early 2000s. The year 2020 marks the near-complete phaseout of HCFCs in developed countries. These controls have resulted in declines in atmospheric abundance for many of these gases (Engel and Rigby, 2018). CFC-11 and CFC-12 declined 16% ± 1% and 8% ± 0.3%, respectively, from their maximum values by 2020 (Fig. 2.52). Additionally, while the reduction of CFC-11 in the atmosphere slowed after 2012 owing to an unexpected increase in emissions that were likely linked to unreported production of CFC-11 (Montzka et al. 2018; Rigby et al.

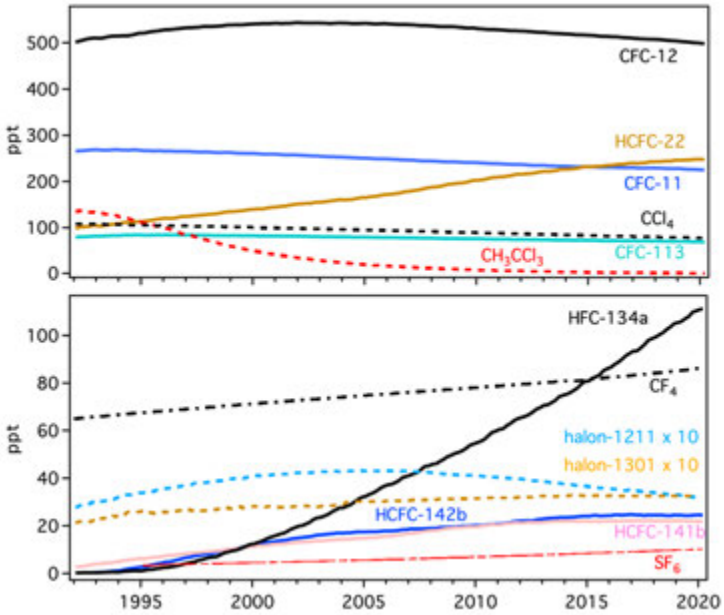

Fig. 2.52. Global mean abundances (mole fractions) at Earth's surface (ppt = nmol mol^{-1} in dry air) for several halogenated gases, many of which also deplete stratospheric ozone. See Table 2.10 for the 2020 global mean mole fractions of these and other gases.

2019), continued monitoring has shown an accelerated decline from 2018 to 2019, signaling a decline in these emissions (Montzka et al. 2021; Park et al. 2021).

As HCFCs replaced CFCs, their abundances increased in the atmosphere. More recently, however, as the phaseout of HCFC production nears completion, growth rates of atmospheric HCFC-22, HCFC-141b, and HCFC-142b have slowed (Fig. 2.52). Notably, atmospheric abundances of both HCFC-141b and HCFC-142b have remained nearly constant since 2018 (Table 2.10; Fig. 2.52). With the near-complete phaseout of HCFCs in developed nations scheduled for 2020, and significant reductions in production and consumption occurring in developing countries, the atmospheric abundances of these compounds may soon begin to decline. The Kigali Amendment to the Montreal Protocol has mandated the phase-down of HFCs, which are substitutes for ODS. While these compounds do not contribute to ozone destruction, they contribute to radiative forcing, and atmospheric abundances for most have been increasing in the atmosphere (Table 2.10, Fig. 2.52). HFC-134a is the largest contributor to radiative forcing among the HFCs, and its global abundance increased by 5.3 ppt (4.7%) from 2019 to 2020, similar to the mean yearly increase over the last decade (~5.5 ppt yr^{-1}; Fig. 2.52).

In order to quantify the overall efficacy of ozone-destroying halogen in the stratosphere, equivalent effective stratospheric chlorine (EESC) is calculated from the weighted global average surface abundance of ozone-depleting gases (Daniel et al. 1995). The weights represent the ozone-destruction efficiency of the halogens contained in each ODS, the destruction rates of each ODS in the stratosphere, and transport and mixing processes within the stratosphere (Montzka et al. 1996; Newman et al. 2007). EESC is calculated for the Antarctic (EESC-A) and the midlatitude (EESC-M) stratosphere. The abundance of reactive halogen in the Antarctic stratosphere is higher than in midlatitudes because air reaching the Antarctic stratosphere has been in the stratosphere longer and has been transported to higher altitudes, factors that lead to both ODS destruction and release of reactive halogen (Montzka and Reimann et al. 2011). CFCs, despite their decreasing global abundance, contribute strongly to EESC (Fig. 2.53), because they account for most of the reactive halogen present in the atmosphere today.

At the beginning of 2020, EESC-A was 3685 ppt, and EESC-M was 1562 ppt, decreases of 25 ppt and 12 ppt, respectively, relative to 2019. To put these values into context of stratospheric reactive halogen reduction, the Ozone Depleting Gas Index (Hoffmann and Montzka, 2009, gml.noaa.gov/odgi/) is defined for both the Antarctic and midlatitude stratosphere (ODGI-A and ODGI-M). This index is defined as 100 for the peak EESC and 0 at the 1980 level of EESC, for both the Antarctic and midlatitude stratosphere. Even though ozone destruction was occurring

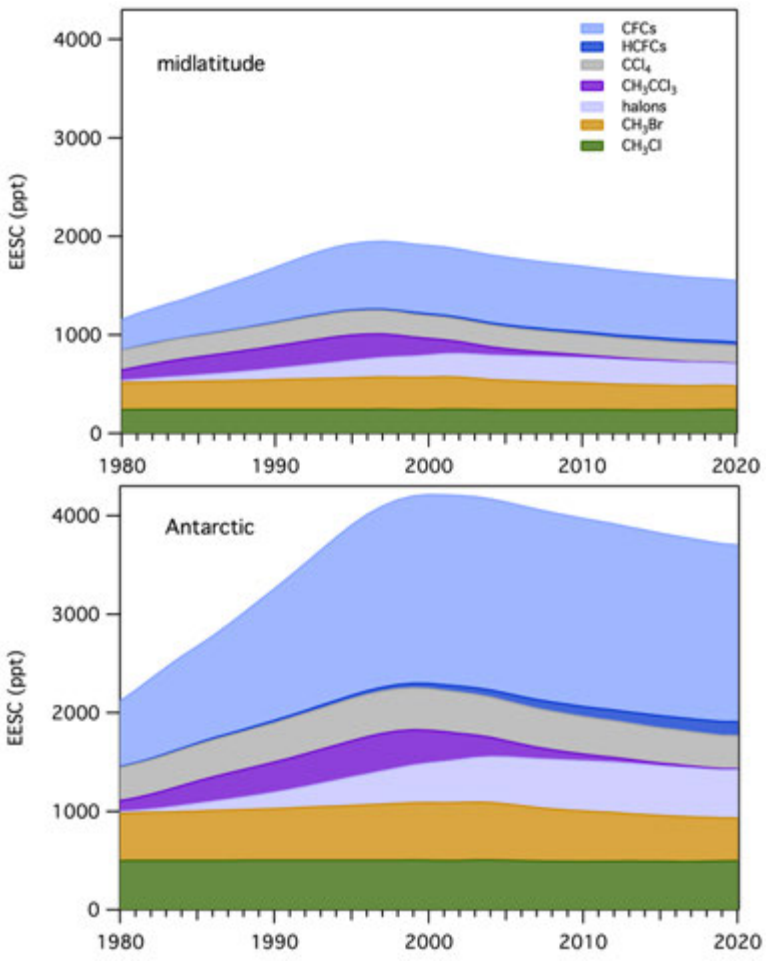

Fig. 2.53. Equivalent effective stratospheric chlorine (EESC, ppt) for the midlatitude and Antarctic stratosphere derived from surface measurements. The EESC values represent EESC on 1 Jan of each year.

in 1980, returning the stratosphere to 1980 levels of reactive halogen would represent a major accomplishment for the Montreal Protocol and the global community. At the beginning of 2020, the ODGI-A was 77, and the ODGI-M was 52, representing progress of 23% and 48% toward the 1980 benchmarks, respectively. Carpenter et al. (2018) estimate that ODGI-A will reach zero around 2070, and ODGI-M will reach zero around 2045, assuming all other factors remain constant.

3) Aerosols—S. Rémy, N. Bellouin, Z. Kipling, M. Ades, A. Benedetti, and O. Boucher

Atmospheric aerosols play an important role in the climate system by scattering and absorbing radiation, and by affecting the life cycle, optical properties, and precipitation activity of clouds (Boucher et al. 2013). Aerosols also represent a serious public health issue in many countries, and hence are subject to monitoring and forecasting as part of air quality policies. There is also growing evidence that aerosols influence ecosystems through changes in the quality and quantity of light (over land) and deposition flux of nutrients (over land and ocean) such as iron (e.g., Hamilton et al. 2019).

The Copernicus Atmosphere Monitoring Service (CAMS; http://atmosphere.copernicus.eu) runs a near-real time global analysis of aerosols and trace gases. The CAMS project also produced a reanalysis of global aerosols and trace gases that covers the years 2003–20, named the CAMS reanalysis (CAMSRA; Inness et al. 2019) by combining state-of-the-art numerical modeling and aerosol remote-sensing retrievals from MODIS (Levy et al. 2013) and the Advanced Along Track Scanning Radiometer (AATSR) (Popp et al. 2016). Verification of aerosol optical depth (AOD) at 550 nm against independent AERONET observations shows that the CAMS reanalysis has a smaller bias and error than its predecessors, the CAMS interim reanalysis (Flemming et al. 2017) and the Monitoring Atmospheric Composition and Climate (MACC) reanalysis (Inness et al. 2013). This section uses data exclusively from the CAMS reanalysis. Here, we assess aerosols in terms of the AOD at 550 nm because this wavelength corresponds to the middle of the visible part of the spectrum, and because many remote-sensing products provide retrievals at this wavelength.

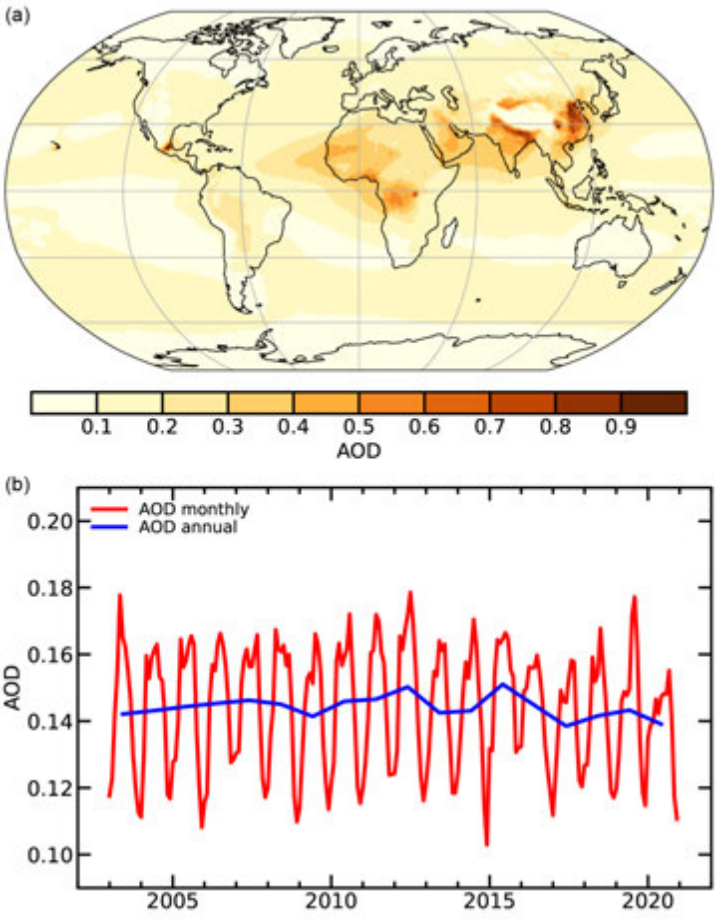

Fig. 2.54. (a) Global aerosol optical depth (AOD) at 550 nm in 2020 from CAMSRA. (b) Global average of total AOD at 550 nm for monthly (red) and annual (blue) periods for 2003–20.

The time series of monthly and yearly globally-averaged total AOD during 2003–20 are depicted in Fig. 2.54b, showing strong seasonality, driven mainly by dust episodes between March and July in the Sahara, Middle East, and the Taklimakan/Gobi Desert and seasonal biomass burning in Africa, South America, and Indonesia. There is no significant trend over the period, but extreme events such as the July–October 2015 fires over Indonesia associated with El Niño can have an impact on the global mean. Globally averaged AOD in 2020 was on average lower than in 2019, with a less pronounced summer maximum, mostly because of less intense biomass burning in the Northern Hemisphere summer and autumn over Indonesia and parts of equatorial Africa as well as Canada. Figure 2.54a shows the geographical distribution of AOD in

2020, with maxima from anthropogenic aerosols over India and China, as well as less pronounced maxima over the Arabian Peninsula and parts of the Sahara from dust, and over equatorial Africa from biomass burning aerosols.

Average AOD between 2003 and 2020 (Fig. 2.55a) is marked by high values over the highly populated regions of India and China, mainly caused by anthropogenic emissions. High AOD values over the Sahara and Middle East are from dust, while the maxima over central Africa, Indonesia, the Amazon Basin, and parts of Siberia are caused by biomass burning. The high values over Hawaii and close to Mexico City are a known artifact of the CAMS reanalysis related to volcanic outgassing.

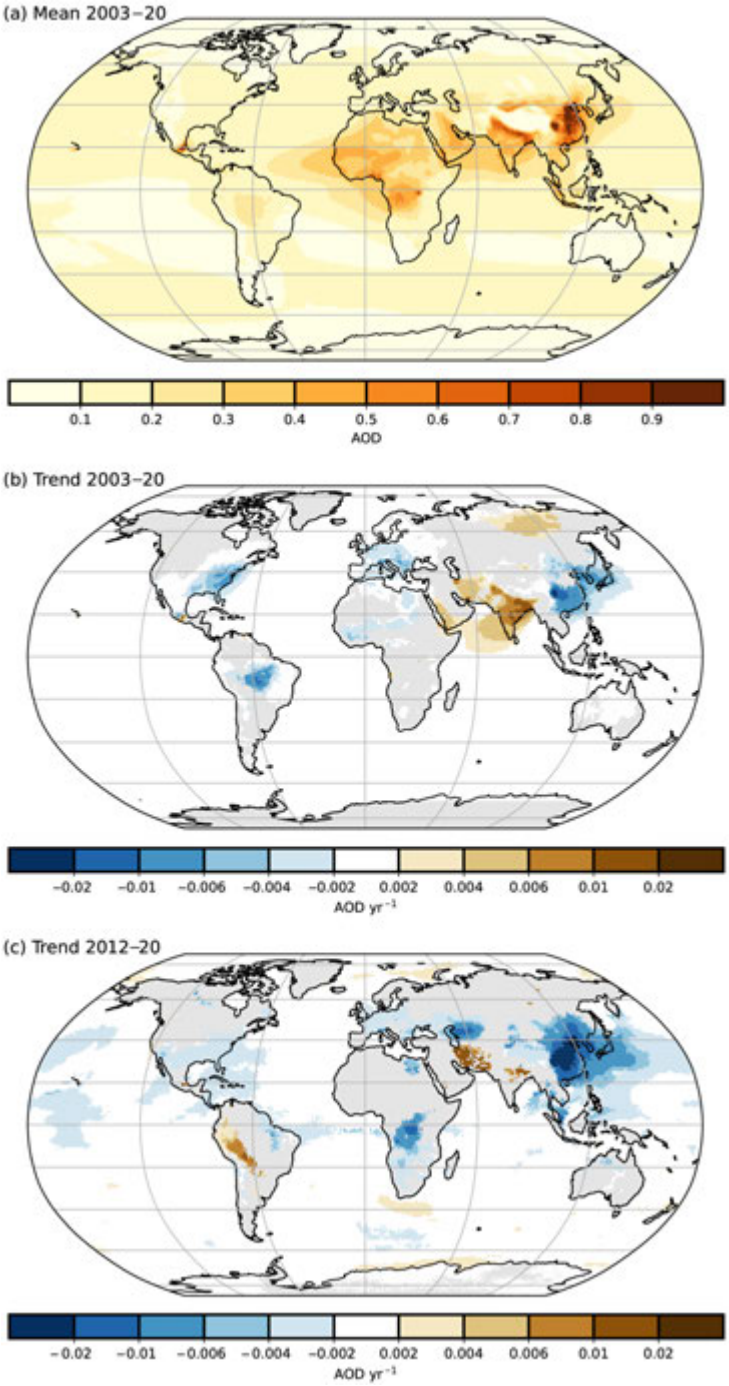

Fig. 2.55. (a) Total aerosol optical depth (AOD) at 550 nm averaged over the period 2003–20 from CAMSRA. Note the regional differences, with much greater total AOD values over parts of northern Africa, the Arabian Peninsula, southern Asia, and eastern China. (b) Linear trends of total AOD (AOD unit yr^{-1}) for 2003–20 and 2012-20. (c) Only trends that are statistically significant (95% confidence level) are shown. Regions with decreasing trends include the eastern United States, most of Europe, parts of Brazil and China, as well as the Korean peninsula and Japan.

As compared to the 2003–19 average from the CAMS reanalysis, total AOD in 2020 shows negative anomalies over most of Europe, Africa, and East Asia, as well as parts of the Amazon basin, United States, and Canada (Plate 2.1x). The negative anomalies over the eastern United States, Europe, and China/Japan are part of a longer trend over these regions (Fig. 2.55b). As shown by Fig. 2.55c, the trend is more negative over China for 2012–20 than for 2003–20, which is consistent with the observed decrease of anthropogenic aerosol emissions there since around 2012 (Li et al. 2017). The 2012–20 trends are positive or not significant over much of the Amazon basin, while the 2003–20 trends are mostly negative over the same area, showing that most of the decrease in AOD occurred before 2012. Reduced anthropogenic emissions because of COVID-19 lockdowns may have contributed to local AOD anomalies, although the impact was probably more important for surface particulate matter ($PM_{2.5}$).

Positive anomalies of total AOD in 2020 (Plate 2.1x) were found over parts of Brazil and Bolivia, Siberia, and the western United States. These positive anomalies are associated with large fire events. The positive anomaly over southeast Australia and large parts of the southern Pacific Ocean were caused by the extreme fires over New South Wales in late 2019 and early 2020. The positive anomalies over parts of western Africa and the Atlantic Ocean were caused by an extreme dust event in June 2020, while the positive anomaly over Iran was caused by meteorological conditions that favored severe pollution events (Broomandi et al. 2020). The positive anomaly over the Indian subcontinent corresponds to a long-term trend of increasing anthropogenic aerosol emissions (Satheesh et al. 2017), as shown in Figs. 2.55b,c. Plate 2.1y shows the ratio of AOD at 550 nm in 2020 to the 2003–19 average, which gives a measure of the relative importance of the anomalies as compared to climatological values. The highest relative anomalies in 2020 are almost all associated with fire events (Siberia, southeastern Australia, western United States, southwestern Brazil), except over Iran. The exceptional severity of the Australian fires of early 2020 and of the associated plume over the southern Pacific is highlighted in Plate 2.1z, which shows the number of days in 2020 with daily AOD at 550 nm above the 99.9th percentile of the 2003–19 daily values. The same plot also shows the exceptional nature of the fires that affected the western United States in August and September 2020, as well as the dust plume that crossed the Atlantic from western Africa to the Caribbean Sea in June 2020.

Anthropogenic AOD and radiative forcing resulting from aerosol–radiation (RFari) and aerosol–cloud interactions (RFaci) are shown in Fig. 2.56 for the period 2003–20. They are estimated using the methods described in Bellouin et al. (2020). 2020 was characterized by a small anthropogenic AOD and a weak RFari and RFaci in the context of the past 18 years. This may be partly due to regional decreases in aerosol primary and precursor emissions caused by the response to the COVID-19 pandemic. Such decreases have, for example, reduced aerosol radiative effects off the coast of China, at least in cloud-free conditions (Ming et al. 2020), which would weaken RFari. The data suggest a weakening trend in aerosol radiative forcing starting around 2015, but the trend would need to be sustained over a longer period to become statistically significant.

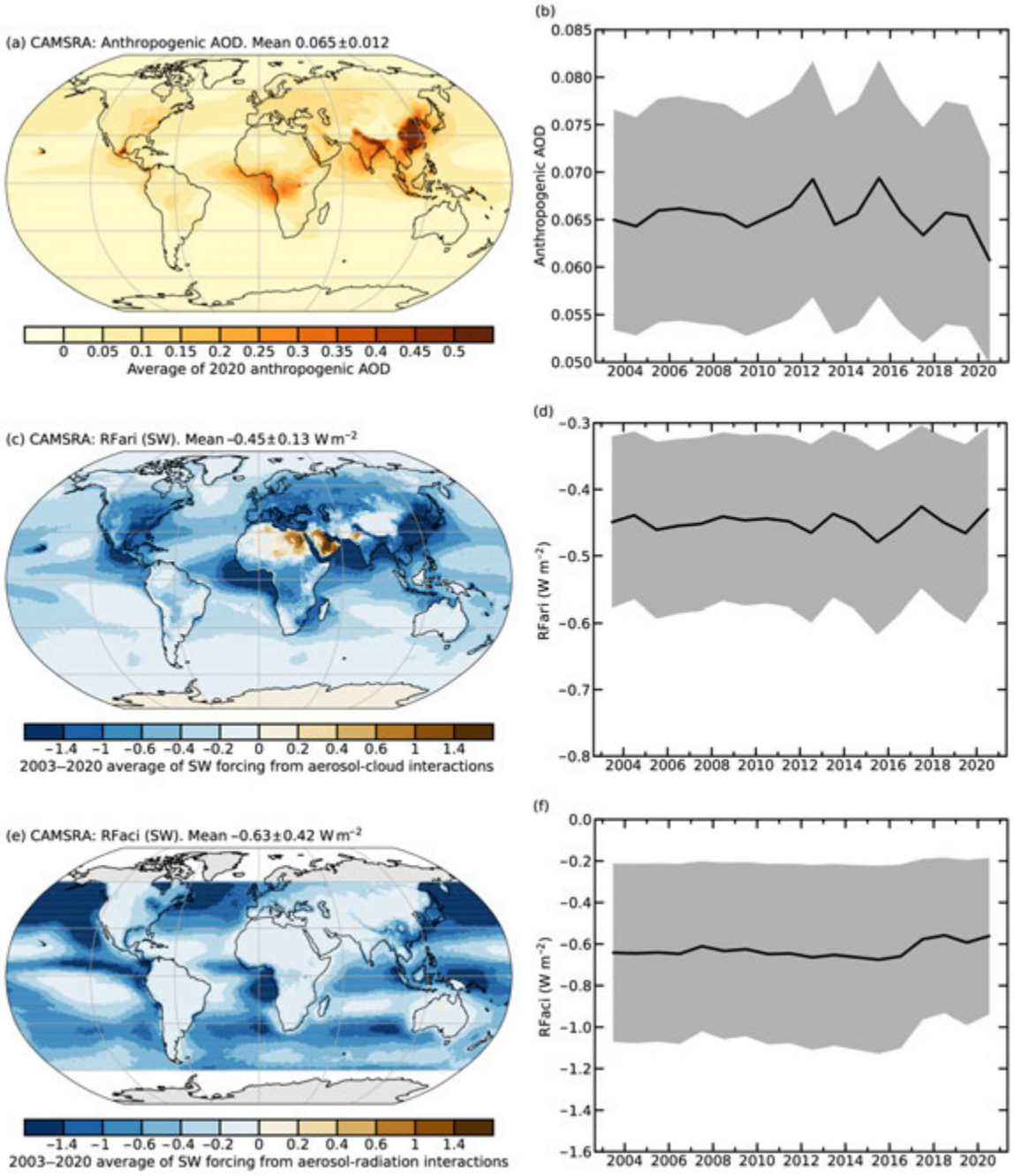

Fig. 2.56. CAMSRA (a) 2020 average of anthropogenic aerosol optical depth (AOD); (b) global annual average of anthropogenic AOD from 2003 to 2020. Radiative forcing in the shortwave (SW) spectrum due to (c),(d) aerosol-radiation (RFari) and (e),(f) aerosol-cloud interactions (RFaci). The left column shows the average distribution for the period 2003–20. The right column shows time series of global averages for the same period, with the 1-σ uncertainties of these estimates shown in gray.

4) Stratospheric ozone—M. Weber, W. Steinbrecht, C. Arosio, R. van der A, S. M. Frith, J. Anderson, L.Castia, M. Coldewey-Egbers, S. Davis, D. Degenstein, V. E. Fioletov, L. Froidevaux, D. Hubert, D. Loyola, C. Roth, A. Rozanov, V. Sofieva, K. Tourpali, R. Wang, and J. D. Wild

Stratospheric ozone protects Earth's biosphere from harmful ultraviolet (UV) solar radiation. The total ozone column determines how much UV reaches the surface. Most of the ozone resides in the lower stratosphere ("ozone layer"), where it is recovering slowly from anthropogenic Ocean Depleting Substances (ODS). Clearer signs of ozone recovery, due to the phase-out of ODSs mandated by the Montreal Protocol in the late 1980s (section 2g2), are seen in the upper stratosphere (WMO 2018).

The year 2020 was remarkable because the annual mean anomaly of total column ozone was negative for most of the globe (Plate 2.1aa). This negative anomaly was due to the combination of

very low polar ozone during Arctic winter/spring (Manney et al. 2020; Inness et al. 2020; Dameris et al. 2021) and a large and unusually long-lasting Antarctic ozone hole (see sections 5j and 6h, respectively). Low winter/spring polar ozone is a consequence of stable and cold stratospheric winter vortices with very low temperatures that permit wide-spread formation of polar stratospheric clouds (PSC), chlorine activation, and large polar ozone depletion (Solomon et al. 1999, 2015).

Figure 2.57 shows time series of Arctic and Antarctic daily minimum total column ozone. Generally, Arctic minimum total ozone increases from early winter (November) to spring (April). However, in cold Arctic winters, with stratospheric temperatures sufficiently low for persistent PSC formation (~195 K), minimum total ozone decreases over the winter, due to both chemical loss and reduced poleward ozone transport related to a weak Brewer-Dobson circulation (BDC; Lawrence et al. 2020). In March 2020 record low column values slightly below 220 Dobson unit (DU) were reached (Inness et al. 2020, Dameris et al. 2021), less than in previous cold winters (e.g., 2010/11). Even these record minimum values are, however, higher than values observed in the Southern Hemisphere (SH) ozone hole. Chemical ozone losses of up to 2.8 ppm near 18 km altitude and 88 DU (vortex average) by the end of March 2020 were similar to losses observed in March 2011, but due to the larger polar vortex area, the ozone mass loss was higher in 2020 and reached a new record after the previous record in 2011 (Manney et al. 2020; Weber et al. 2021). Without the Montreal Protocol phaseout of ODS, this chemical ozone loss would have been even higher (Feng et al. 2021). Above Antarctica, minimum total column ozone remained extremely low in 2020 and only rose rapidly at the end of November about 2 months later than in 2016, which had a winter with an average size ozone hole.

The low total ozone levels during winter/spring in both hemispheres contributed significantly to the annual mean low ozone anomaly (Plate 2.1aa). Zonally averaged annual mean total column ozone was as much as 20 and 60 DU below the long-term mean of 1998–2008 at northern middle and Arctic latitudes, respectively. The band of positive anomalies in the outer tropics along with

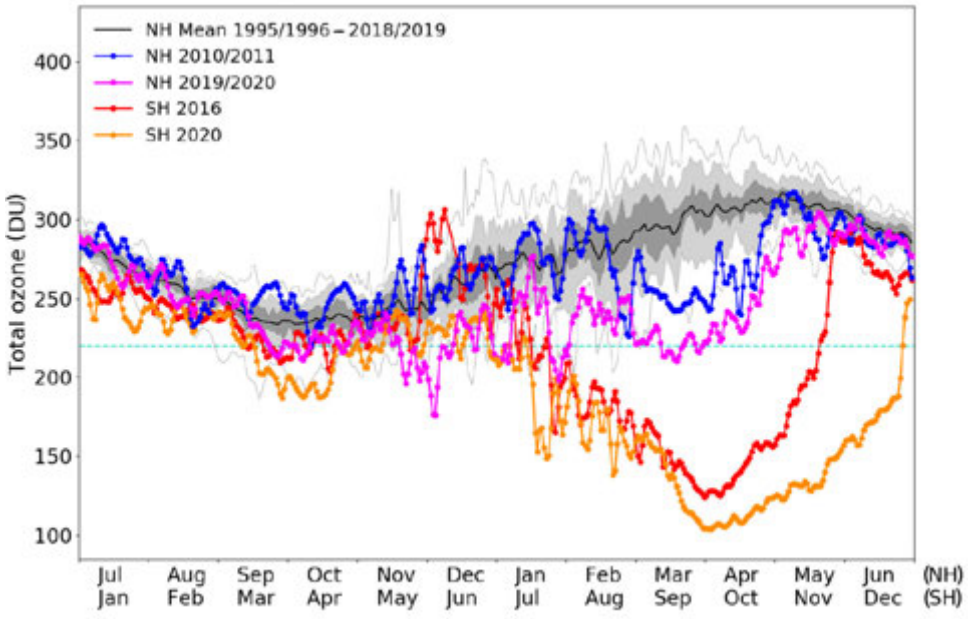

Fig. 2.57. Annual cycle of daily minimum total column ozone values (Dobson Units [DU]) in the polar regions between 50° and 90° in both hemispheres derived from the European GOME-type Total Ozone Essential Climate Variable (GTO) satellite record from Jul 1995 to Jun 2019 and TROPOMI data thereafter. The black line shows the GTO mean annual cycle in the north polar region. The thin gray lines indicate the maximum and minimum values of the observed daily minima from Jul 1995 to Jun 2019. The light gray shading denotes the 10th percentile and 90th percentile, the dark gray shading the 30th percentile and 70th percentile, respectively. The cyan dashed line shows the upper limit of 220 DU that defines the edge of the Antarctic ozone hole. Total ozone minimum time series are shown for winter/spring 2010/11 (blue) and 2019/20 (magenta) in the Northern Hemisphere (Jul–Jun) and in Antarctic winter/spring 2016 (red) and 2020 (orange) in the Southern Hemisphere (Jan–Dec). Updated from Dameris et al. (2021).

the negative anomalies at high latitudes are a typical pattern during quasi-biennial oscillation (QBO) westerly phases, as explained in previous reports. The Arctic Oscillation (AO) index was at a record high during Northern Hemisphere (NH) winter/spring and contributed to the very low ozone observed in the NH extratropics resulting from a very weak meridional circulation (Lawrence et al. 2020).

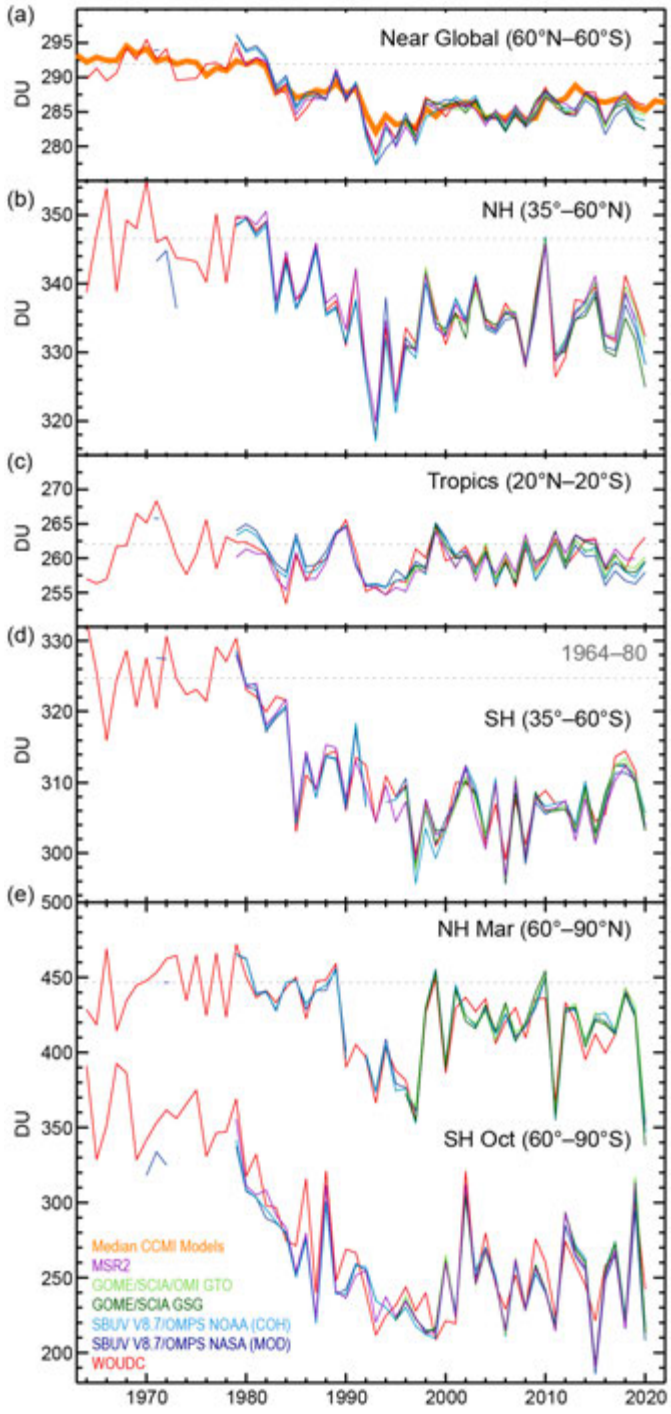

Figure 2.58 shows the long-term evolution of total column ozone for different zonal bands. Except for the polar region (NH: March mean; SH: October mean) annual mean total column ozone is shown. Following the decline until the middle 1990s due to ODS increases, total column ozone has remained at a steady level with substantial year-to-year variability during the last 2 decades, but still well below the 1964–80 mean (indicated by the dashed line). Near-global mean total column ozone (Fig. 2.58a) is on average still about 2% below the 1964–80 mean. The median ozone from the Chemistry Climate Model Initiative (CCMI) model simulations (SPARC/IO3C/GAW 2019), accounting for ODS and greenhouse gas changes, is in good agreement with observations. This shows that ozone observations are consistent with the expected slow ozone recovery due to the phasing out of certain ODSs (section 2g2). In 2020, the annual means in all latitude bands, as well as the Arctic March and Antarctic October mean (Fig. 2.58), were all below the decadal average of 1998–2008, but were within the variability observed in recent years (except March 2020).

Figure 2.59 shows the ozone evolution at different altitudes in the stratosphere. Ozone in the upper stratosphere showed a large decline in the 1980s caused by ODS increases, which was stopped in the late 1990s, thanks to the ODS phase-out mandated by the Montreal Protocol. Since about 2000, upper stratospheric ozone has been in a phase of slow recovery. In

Fig. 2.58. Time series of annual mean total column ozone (Dobson Units [DU]) in (a)–(d) four zonal bands, and (e) polar (60°–90°) total column ozone in Mar (Northern Hemisphere) and Oct (Southern Hemisphere), the months when polar ozone losses usually are largest. Red: WOUDC ground-based measurements combining Brewer, Dobson, SAOZ, and filter spectrometer data (Fioletov et al. 2002, 2008). Dark blue and light blue: BUV/SBUV/SBUV2 V8.6/OMPS merged products from NASA (MOD V8.6, Frith et al. 2014, 2017) and NOAA (Wild and Long, personal communication, 2019), respectively. Dark green and light green: GOME/SCIAMACHY/GOME-2 products GSG from University of Bremen (Weber et al. 2018) and GTO (additionally includes OMI and TROPOMI) from ESA/DLR (Coldewey-Egbers et al. 2015; Garane et al. 2018). Purple: MSR-2, which assimilates nearly all available ozone datasets after corrections based on the ground-based data (van der A et al. 2015). All datasets have been bias-corrected by subtracting averages for the reference period 1998–2008 and adding back the mean of these averages. The dashed gray lines in each panel show the average ozone level for 1964–1980 calculated from the WOUDC data. The thick orange line shows the median from CCMI model runs (SPARC/IO3C/GAW, 2019). Most of the observational data for 2020 are preliminary.

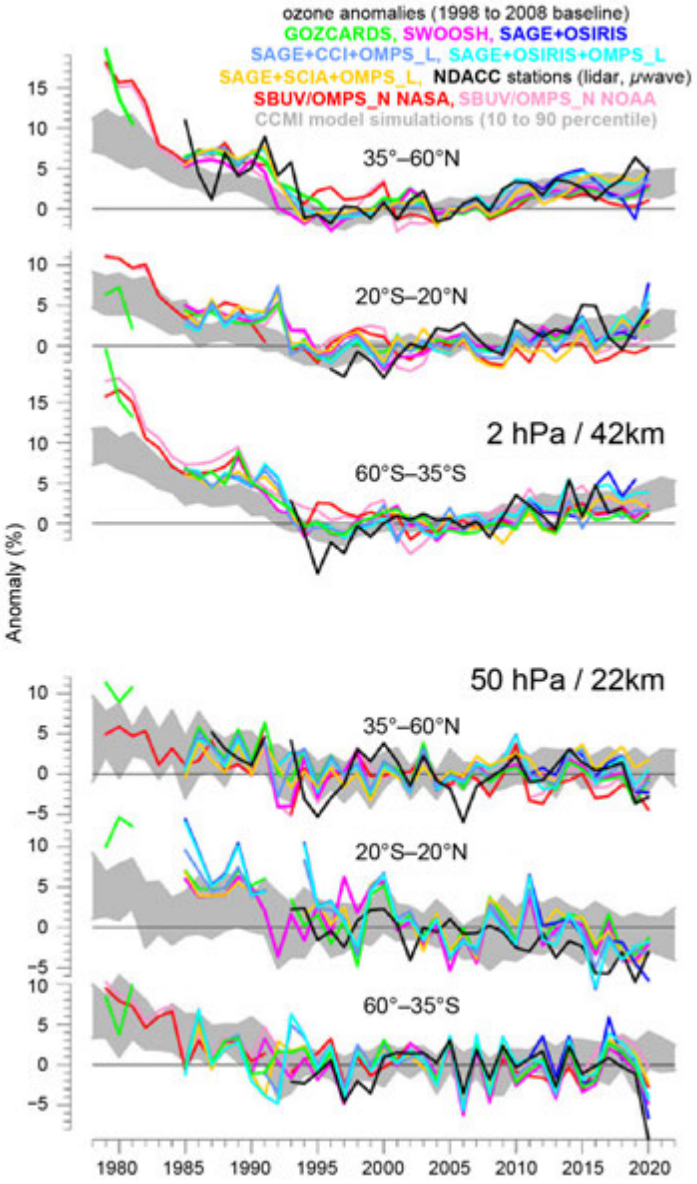

Fig. 2.59. Annual mean anomalies of ozone in the upper stratosphere (top three panels) near 42-km altitude or 2-hPa pressure, and in the lower stratosphere (bottom three panels, near 22 km or 50 hPa for three zonal bands: 35°–60°N, 20°S–20°N (tropics), 35°–60°S respectively. Anomalies are referenced to the 1998–2008 baseline. Colored lines are long-term records obtained by merging different limb (GOZCARDS, SWOOSH, SAGE+OSIRIS, SAGE+CCI+OMPS-L, SAGE+SCIAMACHY+OMPS-L, SAGE+OSIRIS+OMPS-L) or nadir-viewing (SBUV, OMPS-N) satellite instruments. The nadir-viewing instruments have much coarser altitude resolution than the limb-instruments. This can cause differences in some years, especially at 50 hPa. The black line is from merging ground-based ozone records at seven NDACC stations employing differential absorption lidars and microwave radiometers. See Steinbrecht et al. (2017), WMO (2018), and Arosio et al. (2018) for details on the various datasets. Gray-shaded area shows the range of simulations from CCMI (SPARC/IO3C/GAW 2019). At the time of publication, ozone data for 2020 were not yet complete for all instruments and were still preliminary.

all recent years, including 2020, ozone values in the upper stratosphere from most datasets were above the 1998–2008 average, consistent with expectations from the CCMI simulations (gray shaded range in Fig. 2.59; SPARC/IO3C/GAW 2019). In the lower stratosphere, however, long-term ozone variations are dominated by meteorological and transport variations (e.g., Chipperfield et al. 2018), and Fig. 2.59 shows no clear sign of ozone increases in this region over the last 20 or so years. This is consistent with total column ozone in Fig. 2.58. In 2020, lower stratospheric values were at the low end of recent years, and also at the low end of the model predictions. The tropical (20°S–20°N) long-term ozone decline is linked to the acceleration of the meridional Brewer-Dobson circulation (Ball et al. 2018; Chipperfield et al. 2018; WMO 2018). The low annual mean 2020 values of lower stratospheric ozone in the northern and southern extratropical 35°–60° latitude bands, however, similar to the generally low total column ozone (Plate 2.1aa; Fig. 2.58), are the result of the weak meridional Brewer-Dobson circulation in winter in both hemispheres.

5) Stratospheric water vapor—S. M. Davis, K. H. Rosenlof, D. F. Hurst, and H. Vömel

Variations in stratospheric water vapor (WV) occur over a wide range of timescales and can impact stratospheric ozone (Dvortsov and Solomon 2001) and surface climate (Solomon et al. 2010). Such variations are forced by prominent modes of seasonal and interannual dynamical variability that influence temperatures in the tropical tropopause layer (TTL; ~14–19 km). In general, the amount of WV entering the stratosphere is controlled by the lowest temperature encountered by an ascending air mass (i.e., through the Clausius-Clapeyron relationship), with more WV entering the stratosphere when TTL temperatures are warmer. As a result, processes that cause temporal variability in TTL temperatures also lead to global-scale variability in stratospheric WV.

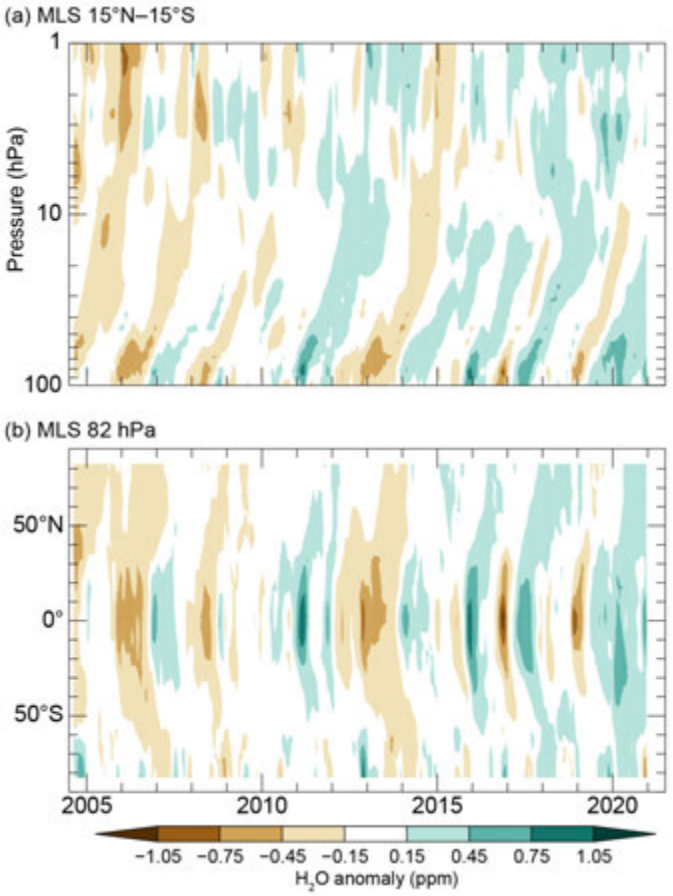

Fig. 2.60. (a) Time series of vertical profiles of tropical (15°S–15°N) lower stratospheric water vapor (WV) anomalies and (b) latitudinal distributions of WV anomalies at 82 hPa. Both are based on version 4.2 *Aura* MLS data from the SWOOSH v2.6 5° zonal mean product (Davis et al. 2016). Anomalies are differences from the mean 2004–20 water vapor mixing ratios (ppm) for each month. (b) shows the propagation of tropical lower stratospheric WV anomalies to higher latitudes in both hemispheres as well as the influences of dehydrated air masses from the Antarctic polar vortex as they are transported toward the SH midlatitudes at the end of each year. Tick marks denote the beginning of each year.

In 2020, WV anomalies in the tropical lower stratosphere were positive (wet). Figure 2.60 shows the vertical–time cross section of tropical-averaged WV anomalies from the *Aura* satellite Microwave Limb Sounder (MLS; Fig. 2.60a), as well as the latitudinal distribution of WV anomalies as a function of time in the base of the stratosphere at 82 hPa (~17 km; Fig. 2.60b). The vertical–time plot shows a substantial region (in time and space) of positive water vapor anomalies ascending into the stratosphere starting in mid-2019 and continuing throughout 2020.

The 2020 *Aura* MLS (version 4.2) annual tropical average (15°S–15°N) WV anomaly at 82 hPa was 0.4 ppm (parts per million, i.e., μmol mol^{-1}), or 11% above the annual average since 2005. Monthly WV anomalies ranged from +0.1 ppm (+2%) in October to +0.8 ppm (+22%) in December, which was the fifth-wettest anomaly in the *Aura* MLS record dating back to August 2004. The tropical WV anomaly time series in 2020 is U-shaped, with strong positive anomalies at the beginning and end of the year and weak positive anomalies in the middle (Fig. 2.60b). The qualitative behavior of lowermost stratospheric WV observed by *Aura* MLS is consistent with balloon-borne frost-point hygrometer soundings at five locations, as shown in Fig. 2.61.

In 2020, tropical cold-point tropopause (CPT) temperature anomalies were positive (warm) from January through April, negative from May through August, and positive from September through the end of the year (blue line, Figs. 2.61c,d). The annual mean tropical cold-point anomaly was +0.48 K.

In general, interannual variations in CPTs are correlated with interannual variability in modes of climate variability such as the ENSO and QBO in equatorial stratospheric winds. These phenomena partly impact CPTs through their modulation of upwelling of air in the tropical lower stratosphere and the associated temperature response. Although we do not attempt formal attribution of the CPT and lower stratospheric WV variability to QBO and ENSO, below we discuss the changes in the phases of QBO and ENSO during 2020 as they pertain to WV variability.

The QBO westerly shear phase is associated with a negative upwelling anomaly and cold temperatures, whereas the reverse is true for easterly shear. Equatorial winds from the Singapore radiosonde wind data, which are a commonly used proxy for the QBO phase, were westerly at 70 hPa at the beginning of 2020, but transitioned to easterly from May through September, before returning back to westerly for the final 3 months of 2020 (sections 2b5, 2e3; see Fig. 2.46). The wind shear between 70 hPa and 100 hPa was positive (westerly over easterly) for all of 2020, with the exception of July and August. It is possible that these anomalies impacted tropical CPTs, as the most negative CPT anomaly of the year (−0.4 K) occurred in August (Fig. 2.61d).

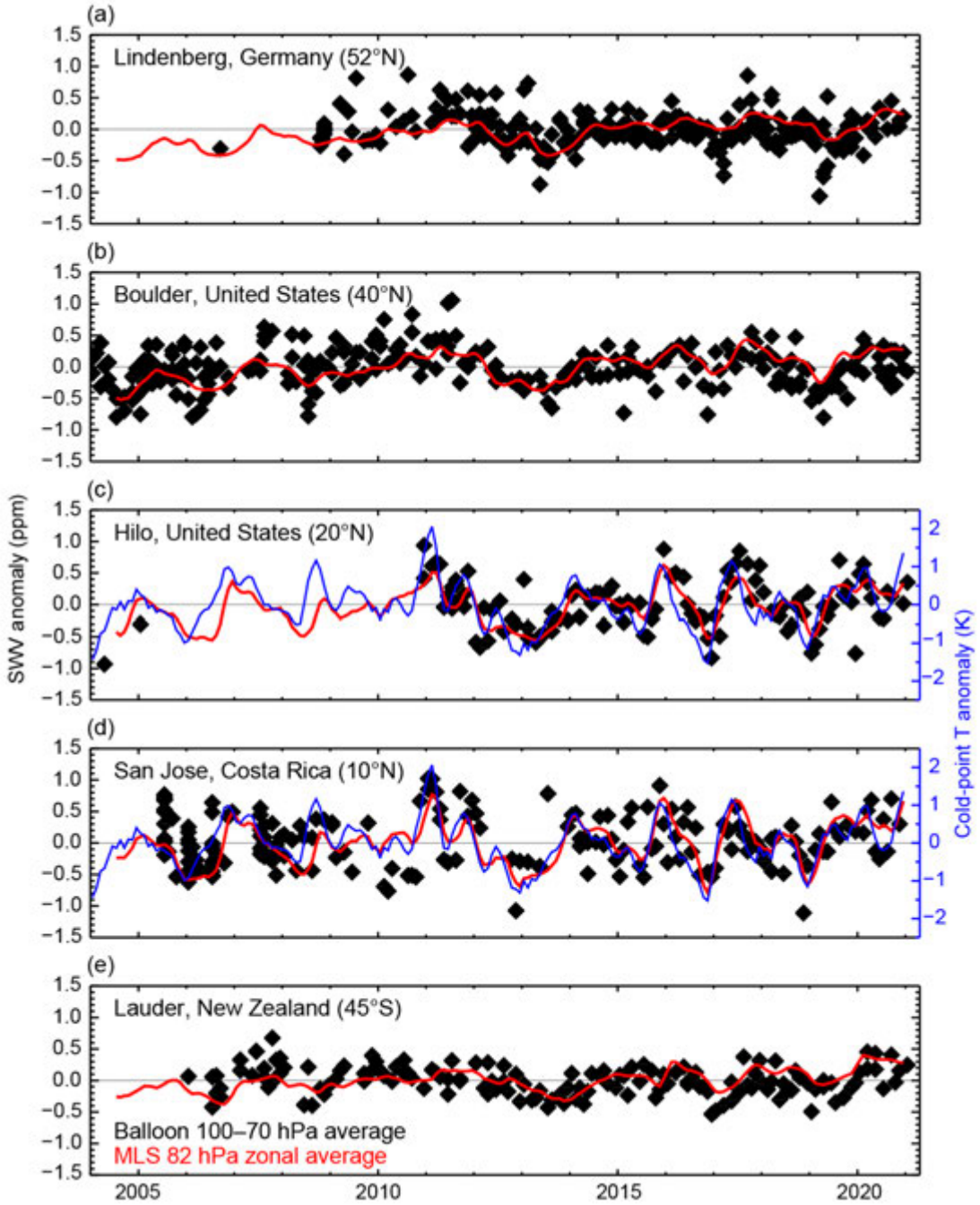

Fig. 2.61. Lower stratospheric water vapor (SWV) anomalies over five balloon-borne frost point (FP) hygrometer stations. Each panel shows the lower stratospheric anomalies of individual FP soundings (black) and of monthly zonal averages of Microwave Limb Sounder (MLS) retrievals at 82 hPa in the 5° latitude band containing the FP station (red). High-resolution FP vertical profile data were averaged between 70 hPa and 100 hPa to emulate the MLS averaging kernel for 82 hPa. Each MLS monthly zonal mean was determined from 2000–3000 profiles. Anomalies for MLS and FP data are calculated relative to the 2004–20 period for sites except for Lindenberg (2009–20) and Hilo (2011–20). Tropical CPT anomalies based on the MERRA-2 reanalysis (d, blue curve), which are generally well correlated with the tropical lower stratospheric WV anomalies, are the driving force behind the variations in tropical WV during 2020.

ENSO was in a neutral phase in the first half of 2020 before transitioning to La Niña in August and remaining in that phase through the end of the year (see sections 2e1, 4b). In boreal winter, La Niña is known to result in weaker tropical lower stratospheric upwelling, anomalously higher cold-point temperatures, and enhanced water vapor in the tropical lower stratosphere (Calvo et al. 2010; Garfinkel et al. 2018; Simpson et al. 2011). The large positive tropical anomalies in the lower stratospheric WV observed at the end of 2020 are consistent with the known behavior associated with a La Niña. This narrow band of positive anomalies in December 2020 is shown in contrast

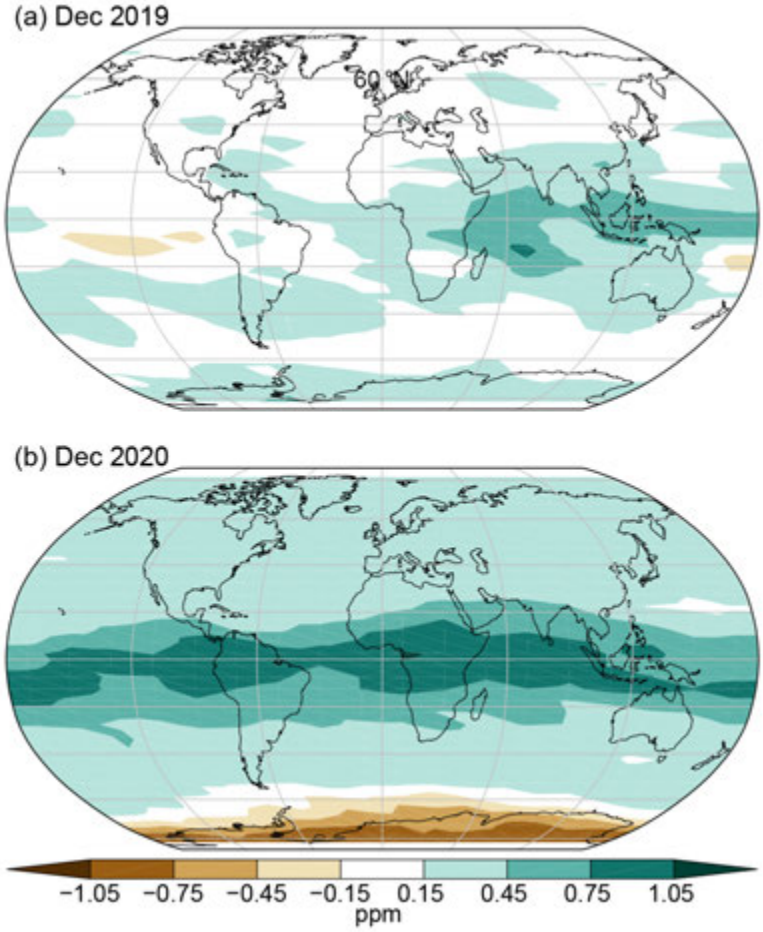

Fig. 2.62. Deseasonalized monthly lower stratospheric Microwave Limb Sounder (MLS) anomalies (ppm; 2004–20 base period) centered on 82 hPa in (a) Dec 2019 and (b) Dec 2020 from the *Aura* MLS.

to the same month of the previous year in Fig. 2.62.

In addition to the tropical stratospheric WV features in 2020, there are several notable higher latitude features. First, strong negative WV anomalies at high southern latitudes at 82 hPa in the last several months of 2020 (Figs. 2.60b, 2.62b) are likely the signal of anomalously strong dehydration associated with the very strong and persistent Antarctic vortex (see sections 2b5, 6h). The remarkably long-lived and stable Antarctic vortex likely explains why the dry anomaly is most noticeable at the very end of the year rather than earlier in austral spring.

Additionally, the positive tropical lower stratospheric WV anomaly discussed previously appears to be somewhat shifted toward the SH in the early part of the year (Fig. 2.60b). This anomaly may be related to the rapid injection of wet tropospheric air into the stratosphere by Australian bushfires of record-breaking intensity at the beginning of 2020 (Kablick et al. 2020; Khaykin et al. 2020). Of course, this anomaly occurs in concert with widespread positive WV anomalies in the tropics, so it is not possible to quantitatively determine the contribution of the fires to stratospheric WV with the analysis presented here. Further modeling and analysis should be able to shed light on the contribution of the Australian bushfires to stratospheric WV levels in 2020 in the context of other sources of variability such as QBO and ENSO.

6) Tropospheric ozone—J. R. Ziemke and O. R. Cooper

Tropospheric ozone is the third-most effective climate-forcing greenhouse gas following CO_2 and CH_4 (IPCC 2013). Average global radiative forcing due to tropospheric ozone is $+0.4 \pm 0.2$ W m^{-2} and thus contributes to net warming of the atmosphere. In addition, tropospheric ozone is a surface pollutant damaging to vegetation and human health (Fleming et al. 2018; Mills et al. 2018), and it is the primary producer of OH radical (OH), which is the main oxidant of tropospheric pollutants. The sources for tropospheric ozone include transport from the stratosphere, non-combustive, non-biogenic volatile organic compound (VOC) sources such as solvents or fuel evaporation, photochemical production from precursors that include non-methane biogenic hydrocarbons, CH_4, lightning NO_x, and also emissions generated from the combustion of fossil fuels and biomass burning (Young et al. 2013, 2018; Monks et al. 2015; McDonald et al. 2018; Archibald et al. 2020). The main drivers of planetary-scale variability of tropospheric ozone include dynamical forcing from the ENSO and Walker circulation in the tropics, and "weather system" baroclinic waves in midlatitudes (Chandra et al. 1998, 2009; Sun et al. 2014; Ziemke et al. 2015). The main drivers of small-scale patterns in tropospheric ozone are local emissions of ozone precursors, both anthropogenic and natural, and ozone surface deposition driven mainly by vegetation

(Archibald et al. 2020). The large temporal variability of tropospheric ozone from diurnal to interannual timescales makes it difficult to determine decadal trends from regional to global scales (Neu et al. 2014; Cooper et al. 2014; Lin et al. 2014; Barnes et al. 2016; Strode et al. 2019; Tarasick et al. 2019).

Since 2012, all *State of the Climate* reports have provided updates on global tropospheric ozone based on independent measurements from ground- and satellite-based instruments (Ziemke and Cooper 2019, and references therein). Due to limited annual updates of ground-based observations, these reports have relied primarily on combined *Aura* Ozone Monitoring Instrument (OMI) and MLS satellite ozone measurements (Ziemke et al. 2019). Vertical resolution of OMI/MLS monthly tropospheric column ozone is 2–3 km about the tropopause with ~2 DU (7%) precision in regional measurements; uncertainties in calculated trends are about 0.5 DU decade^{-1} (1.5% decade^{-1}). OMI/MLS data show broad regions of positive 2020 tropospheric ozone column anomalies (relative to the 2005–19 average) of ~1.2 DU (4%) in the NH midlatitudes, with smaller anomalies of ~1 DU or less elsewhere (Plate 2.1ab). Hemispheric and global average tropospheric ozone burdens and their 95% confidence levels for 2020 were 160 ± 7 Tg (0°–60°N), 145 ± 8 Tg (0°–60°S), and 304 ± 8 Tg (60°S–60°N; Fig. 2.63). Trends and their 95% confidence levels (in units Tg yr^{-1}) in hemispheric and 60°S–60°N burdens from October 2004 through December 2020 are shown in Fig. 2.63; these trends correspond to increases of about 0.50 ± 0.15% yr^{-1} for all three curves. Spatially, the trends are overwhelmingly positive, the strongest of which are ~ +3.2 DU decade^{-1} (~ +1% yr^{-1}) above India and East/Southeast Asia, extending eastward over the North Pacific Ocean (Fig. 2.64). These trends are consistent with model estimates based on strengthening emissions of ozone precursors from Southeast, East, and South Asia, primarily due to fossil fuel combustion (Zhang et al. 2016b; Lin et al. 2014; Ziemke et al. 2019) and with NH ozone trends (1994–2016) as observed by instrumented commercial aircraft (Gaudel et al. 2020).

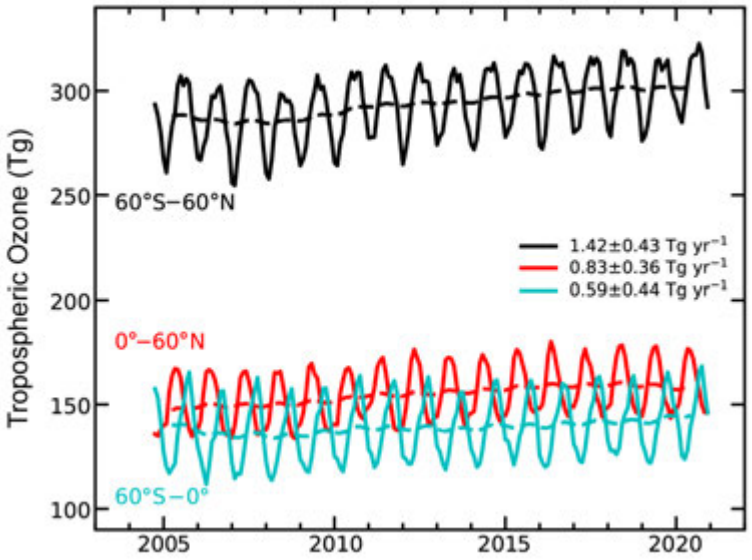

Fig. 2.63. Monthly averages of Ozone Monitoring Instrument / Microwave Limb Sounder (OMI/MLS) tropospheric ozone burdens (Tg) from Oct 2004 through Dec 2020. The top curve (black) shows 60°S–60°N monthly averages (solid) with 12-month running mean (dashed). The bottom two curves show monthly averages (solid) and running means (dashed) for the Northern Hemisphere (red) and Southern Hemisphere (blue). Slopes of linear fits to the data are presented with their 95% confidence-level uncertainties.

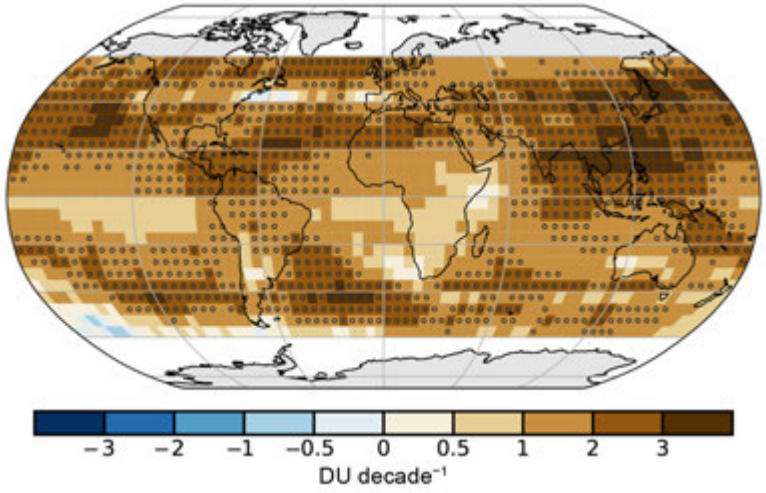

Fig. 2.64. Linear trends in Ozone Monitoring Instrument / Microwave Limb Sounder (OMI/MLS) tropospheric column ozone (DU decade^{-1}) on a 5° × 5° grid from Oct 2004 through Dec 2020. Asterisks denote trends with *p*-values less than 0.05. Trends were calculated using a multivariate linear regression model (e.g., Randel and Cobb 1994, and references therein) that included a seasonal cycle fit and the Niño-3.4 index as an ENSO proxy; trend uncertainties included autoregressive adjustment via Weatherhead et al. (1998).

Models indicate that ozone produced in these areas is transported northward and eastward in the free troposphere over the North Pacific Ocean (Zhang et al. 2020), as supported by the trend patterns in Fig. 2.64. Positive trends in the SH extra-tropics have been linked to a broadening of the Hadley circulation (Lu et al. 2018a).

Three long-term baseline monitoring sites with quality assured data are available for updating surface ozone trends through 2020: 1) Mauna Loa Observatory (MLO), Hawaii (19.5°N, 155.6°W, 3397 m a.s.l.); 2) South Pole Observatory (SPO), Antarctica (90°S, 59°E, 2840 m a.s.l.); and 3) Barrow Atmospheric Baseline Observatory (BRW), near Utqiaġvik, Alaska (71.3°N, 156.6°W, 11 m a.s.l.). Continuous ozone measurements began at MLO in September 1973, at SPO in January 1975, and at BRW in March 1973, with reliable observations available at SPO for the years 1961–63 and at MLO for the years 1957–59 (Tarasick et al. 2019). Observations at remote baseline sites are important for understanding long-term ozone trends in the boundary layer, but they do not necessarily match the trends in the free troposphere, which have been overwhelmingly positive since the mid-1990s, as measured by ozonesondes, lidars, and commercial aircraft (Cooper et al. 2020).

Ozone levels at BRW in the Arctic increased by 3 ppbv (11%) since 1973. The limited data at MLO and SPO from the 1950s and 1960s indicate that ozone levels at these remote high-elevation sites were similar in the mid-twentieth century despite being located in different hemispheres. Ozone levels at SPO have changed little since the 1960s, with only a slight increase of ~2 ppbv (6%) from 1975 to 2020 (Fig. 2.65). In contrast, ozone levels at MLO increased at the rate of 0.14 ± 0.05 ppbv yr^{-1}, resulting in a 17% increase since 1973. MLO experiences high inter-annual ozone level variability due to its location in the transition region between tropical and extratropical air masses. The ozone level trend in the extratropical air masses can be isolated by focusing on the dry air masses, which tend to originate at higher altitudes and latitudes to the west and northwest of MLO (Gaudel et al. 2018). The trend in the dry air masses is 50% greater compared to the trend using all air masses (10.1 ppbv total increase since 1974, or 24%), which implies that the site is influenced by ozone level increases in upwind regions to the west and northwest, most likely Asia where surface and free tropospheric ozone levels have generally increased over the past 2 decades due to increased anthropogenic emissions of ozone precursor gases (Zhang et al. 2016b; Cohen et al. 2018; Lu et al. 2018b; Gaudel et al. 2018, 2020).

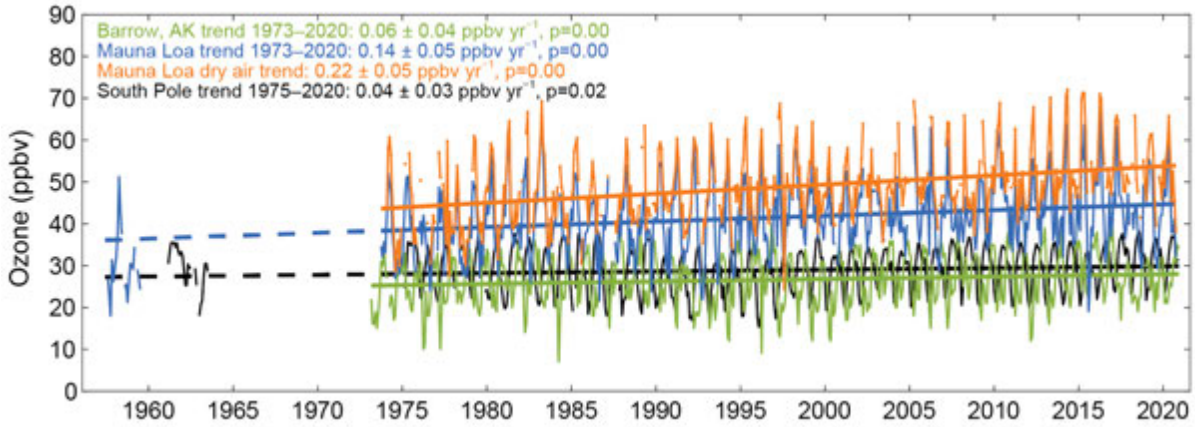

Fig. 2.65. Monthly median ozone (ppbv) at Barrow Observatory (Mar 1973–Dec 2020, green) and South Pole (Jan 1975–Dec 2020, black) using data from all hours of the day. Additional data from South Pole are shown for the early 1960s. Also shown are nighttime monthly median ozone values at Mauna Loa (MLO) calculated with all available data for months with at least 50% data availability, Oct 1973–Oct 2020 (blue), with early observations from the late 1950s. In addition, the monthly median values associated with dry air masses (orange) at MLO are included (dewpoint < the climatological monthly 40th percentile, and a sample size of at least 24 individual hourly nighttime observations). Trends (solid straight lines) are based on least-squares linear regression fit through the monthly values (1970s–2020), and reported with 95% confidence intervals and *p*-values. The MLO and South Pole trend lines are extrapolated back in time to the late 1950s (dashed lines).

7) Carbon monoxide—J. Flemming and A. Inness

Carbon monoxide (CO) plays a significant role in determining the abundance of climate-forcing gases like CH_4 and tropospheric ozone through OH chemistry (Hartmann et al. 2013). CO is therefore regarded as an indirect climate-forcing agent. Sources of CO include incomplete fossil fuel and biomass combustion and in situ production via the oxidation of CH_4, isoprene, and other organic trace gases. Combustion and atmospheric chemical sources typically produce similar amounts of CO on the global scale but vary in space and time because of the varying distribution of anthropogenic and biomass burning CO emissions as well as biogenic isoprene emissions.

CAMS (https://atmosphere.copernicus.eu) produced a retrospective analysis of CO, aerosols, and ozone for the period 2003–20 by assimilating satellite retrievals of atmospheric composition with the ECMWF model (Inness et al. 2019). This CAMS reanalysis assimilated thermal infrared (TIR) column CO retrievals of the Measurement of Pollution in the Troposphere (MOPITT) instrument (Deeter et al. 2014) globally, only excluding observations polewards of 65°N/S using the ECMWF 4D-VAR data assimilation system. The anthropogenic CO emissions used in the ECMWF model were taken from the MACC/CityZEN EU projects (MACCity) inventory (Granier et al. 2011), which estimates emission trends according to the IPCC RCP 8.5 scenario. No COVID-19 pandemic-related emissions modifications for 2020 were applied in the assimilation. Anthropogenic biomass burning emissions were taken from the Global Fire Assimilation System (GFAS) v1.2 (Kaiser et al. 2012; see section 2h3).

Figure 2.66 shows the time series of the monthly mean global burden of CO from the CAMS reanalysis for the period 2003–20. The total burden in 2020 was similar to the burden in the previous years, with the exception of the year 2015 when the global CO burden was dominated by emissions from fires in Indonesia (Huijnen et al. 2016). Approximated with a linear trend over the whole period, the total global CO burden has declined by –1.5 Tg CO yr^{-1}, and as piecewise trends by –3.1, –14.0, and +0.1 Tg CO yr^{-1} for 2003–07, 2008, and 2009–20, respectively, following Flemming and Inness (2019). Figure 2.67 shows clean marine boundary layer (MBL) mean surface CO for five zonal bands based on measurements of weekly air samples collected at MBL sites in the NOAA Global Greenhouse Gas Reference Network (Novelli et al. 2003; Pétron et al. 2020). The global negative trend seen in both surface and satellite records is dominated by the decrease of the CO burden in the mid- and high-latitudes of the NH, likely as a result of reductions in vehicle emissions (Wang et al. 2012). The tropics and the SH exhibit no trends or a small positive trend.

The spatial patterns of the 2020 annual CO total column anomalies (Plate 2.1ac) agree with the multi-year trends and show about 0%–5% higher values throughout the SH and most of the tropics and negative values for most of the NH mid- and high-latitudes. The most noticeable negative

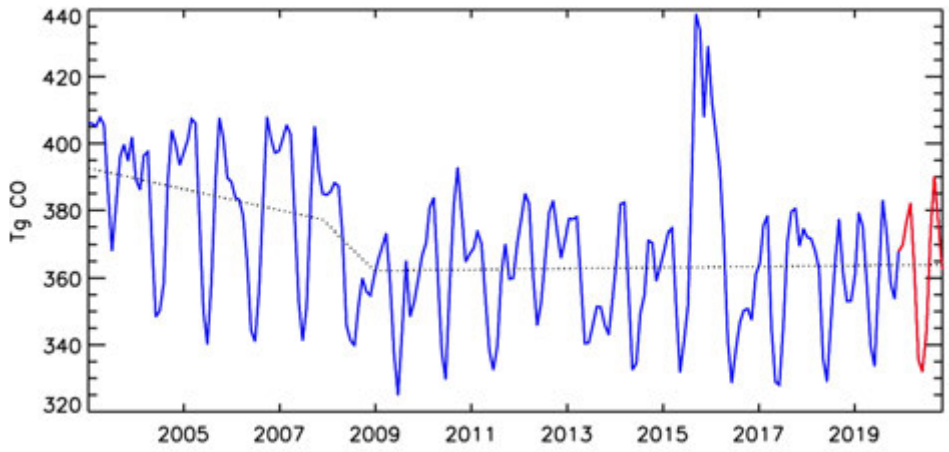

Fig. 2.66. Time series of monthly global carbon monoxide (CO) burdens (Tg CO) from the total column CO output from the CAMSRA (TCCO CAMSRA) and a piecewise linear trend for the periods 2003–07, 2008, and 2009–20. The red line indicates the year 2020.

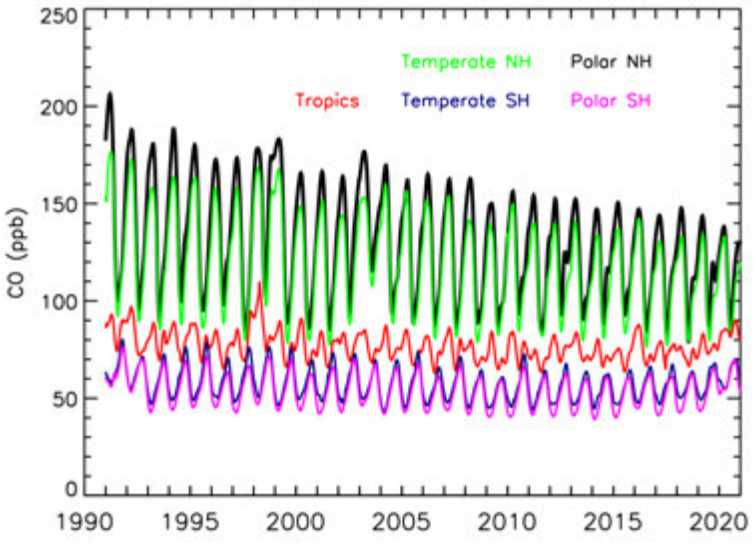

Fig. 2.67. Time series of carbon monoxide (CO) over the clean marine boundary layer for the polar NH (53.1°–90°N, black), temperate NH (17.5°–53.1°N, green), tropics (17.5°S–17.5°N, red), temperate SH (17.5°–53.1°S, dark blue), and SH (53.1°–90°S, magenta) for the period 1991–2020.

anomaly in 2020 appeared over maritime Southeast Asia (Indonesia) and was caused by low fire activity in the region, because La Niña conditions were starting to evolve in (austral) spring 2020. Positive anomalies occurred over the western United States and over northeast Siberia (Yakutia), caused by intense biomass burning in boreal summer and early autumn 2020 (see also sections 2g3, 2h3). The widespread positive anomaly over the southern South Pacific Ocean was the result of long-range transport of CO plumes originating from intense fires in southwestern Australia between December 2019 and January 2020. The observed increase in tropical and SH MBL CO in 2020 was also most likely caused by the Australian fires.

The reduction in anthropogenic CO emission during the COVID-19 pandemic has been estimated to be up to 30% in North America and Europe and 10%–20% over China during the height of the lockdown measures (Foster et al. 2020; Doumbia et al. 2021). The CAMSRA CO total columns over Europe and North America were the lowest since 2003 for the period February–April (Fig. 2.68). However, the attribution of these anomalies to COVID-19-related emission reduction is complicated by the multi-year negative CO trends in the regions and the unquantified influence of other factors such as meteorological conditions.

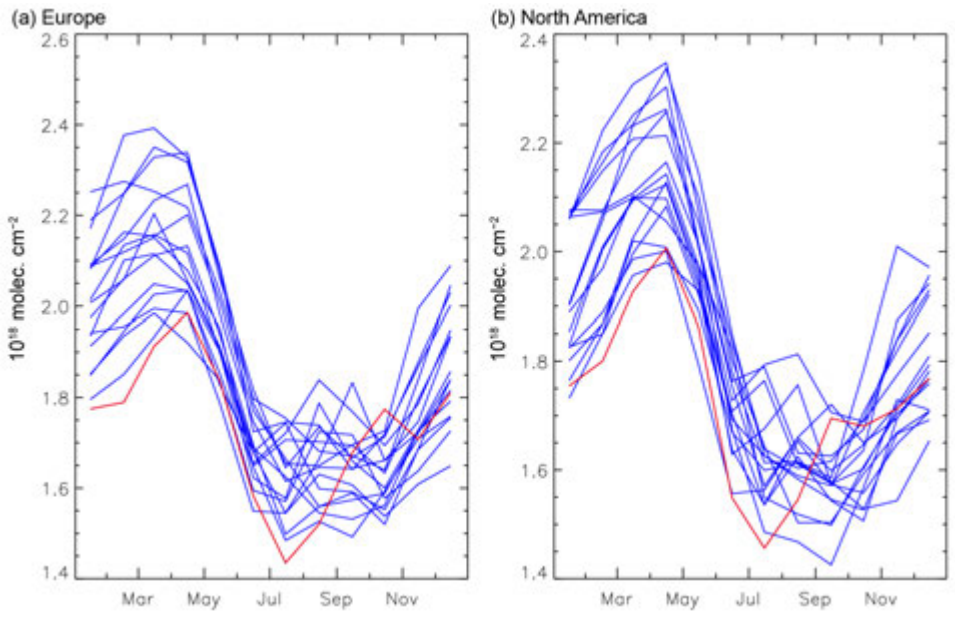

Fig. 2.68. Seasonal cycle of monthly global carbon monoxide (CO; ppb) total column (10^{18} molec. cm^{-2}) over (a) Europe and (b) North America for all years in the 2003–19 period (blue) and for 2020 (red) from the CO total column output from the CAMSRA (TCCOsfc CAMSRA).

h. Land surface properties

1) Land surface albedo dynamics—G. Duveiller and N. Gobron

The presence and absence of snow cover dominates the large-scale spatial patterns of the land surface albedo for 2020 (Plates 2.1ad, ae). The most prominent feature was a strong reduction in albedo in Europe from western Germany to Moscow, and from southern Scandinavia to the Balkans, corresponding to a large deficit in snow cover over this area, particularly during the January–March 2020 period (see sections 2c2, 7f), when temperatures were particularly high (see section 2b1). This same effect occurred to a lesser extent in the eastern half of the United States. Reductions in the snow cover extent during spring over large parts of Siberia also contributed to reducing the overall albedo of the Northern Hemisphere (NH). Conversely, an anomalously high duration of snow cover resulted in a rise in albedo in several parts of the world. For northeastern China, the Tibetan plateau, and central parts of North America, excess snow cover duration occurred in boreal winter (January–March), for Canada and northern Scandinavia in boreal spring (April–June), and for Patagonia in austral winter (July–September). All left a clear mark in the annual maps of albedo, both in the visible and near infrared parts of the spectrum (Plates 2.1ad, ae).

Beyond the strong effect of snow, the land surface albedo dynamics were affected by vegetation growth, which darkens the surface, and by dry climatic conditions, which typically lighten the surface due to either the hastening of leaf senescence or the drying up of bare soil. In 2020, warm conditions across most of the globe and during considerable portions of the year contributed to the development of greener surfaces (see section. 2h2), which translated to lower visible albedo. This was particularly evident over India, northern East Africa, and southeastern Australia, all of which had higher-than-average soil moisture during large parts of the year (see section 2d10). On the other hand, drought conditions increased visible albedo in southern Africa (mostly in Mozambique) and in central South America (around the Gran Chaco but also extending eastward and northward, see section 2d11). Rain deficits attributable to the development of La Niña in late 2020 further exacerbated the dry conditions in these regions of South America (see section 7d). However, drier conditions in the later part of the year over various parts of the NH did not considerably alter the albedo patterns that were mostly dominated by spring snow cover.

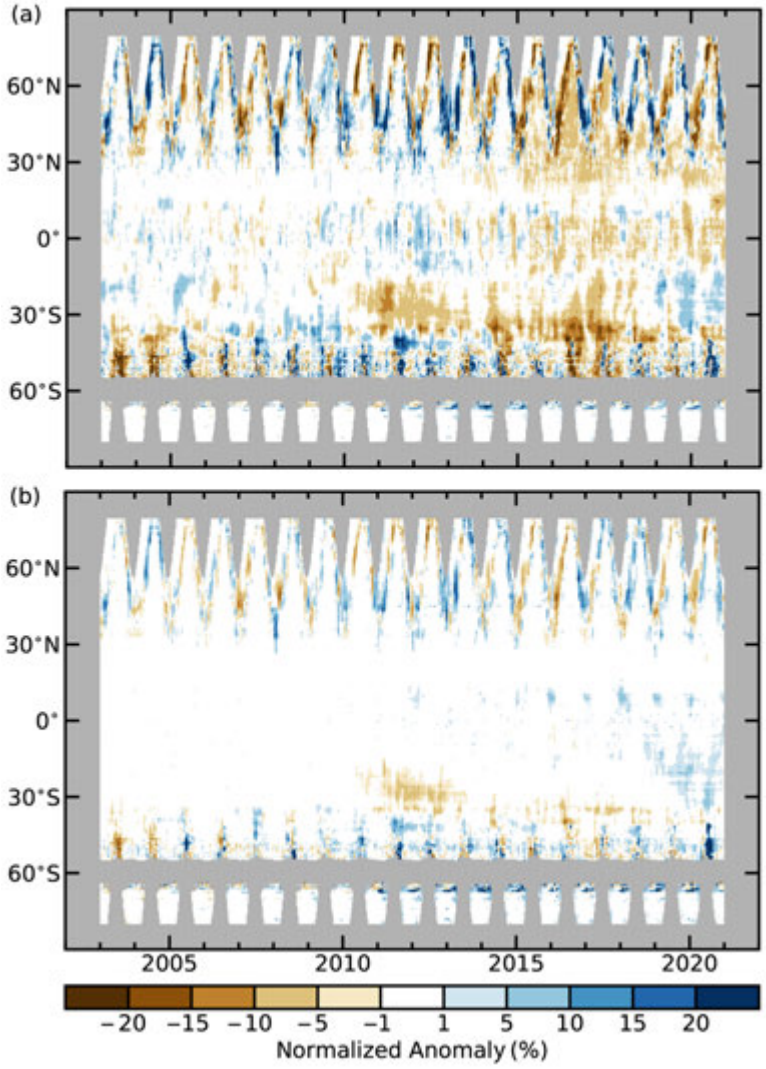

Fig. 2.69. Zonally averaged (a) white sky visible and (b) near infrared albedo anomalies (%) for the period 2003–20 using a 2003–10 baseline period.

Overall, 2020 contributed to the general darkening trend of the land surface with respect to visible albedo (Figs. 2.69, 2.70). There was, however, a clear separation between NH and Southern Hemisphere (SH), with the SH seeing its second consecutive brighter year than the 2003–10 baseline, and following a steady

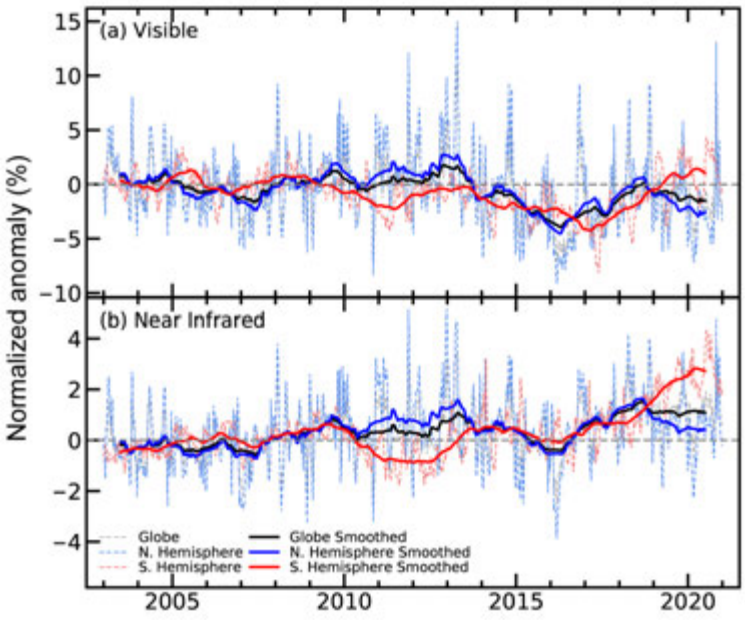

Fig. 2.70. Global (black/gray lines), NH (blue), and SH (red) land surface (a) visible and (b) near infrared albedo anomalies for the period 2003–20 using a 2003–10 baseline period. Dotted lines denote each monthly period; solid lines indicate the 6-month running averaged mean.

brightening trend since its lowest point on the satellite record in 2017. With respect to the albedo in the near infrared part of the spectrum, the overall trend was toward a slight brightening, which was more pronounced in the SH than in the NH.

This analysis of the land surface albedo relied exclusively on satellite information. Surface albedo was retrieved from multispectral surface reflectance measured by the Moderate Resolution Imaging Spectroradiometer (MODIS) instrument on-board the *Aqua* and *Terra* satellite platforms (Schaaf et al. 2002). Satellite retrievals are probably the most accurate way to assess surface albedo at the global level as they rely on a limited set of assumptions. They have been shown to provide sufficiently accurate estimates when compared to ground measurements both on ice sheets (Stroeve et al. 2013) and over different types of vegetation (Cescatti et al. 2012). The MODIS albedo products provide separate estimations for different parts of the shortwave electromagnetic spectrum, allowing this analysis to focus separately on the visible and the near infrared parts of the spectrum. Furthermore, the analysis was based on estimation of white-sky albedo (bi-hemispherical reflectance), which is defined as albedo in the absence of a direct radiation component and when the diffuse radiation component is isotropic.

2) Terrestrial vegetation dynamics—N. Gobron

The Fraction of Absorbed Photosynthetically Active Radiation (FAPAR) plays a critical role in assessing the primary productivity of canopies, the associated fixation of atmospheric CO_2, and the energy balance of the surface. FAPAR anomalies from the 1998–2010 average show significant regional variations in the vegetation productivity conditions worldwide in 2020 (Plate 2.1af). The SH appeared similar to typical La Niña conditions, with largest negative anomalies (brown) occurring over Argentina, Paraguay, and Chile and largest positive (dark blue) in eastern Brazil, Malaysia, and Indonesia (see section 2e1). However, there were negative anomalies in regions such as Mozambique, southern Madagascar, and most of Australia, except the southeast. To a lesser extent, negative regional anomalies were observed near the northwest coast of the South American continent.

In the NH, the largest negative anomalies were observed over herbaceous vegetation in Norway, northern Sweden, and Canada. Local negative occurrences were notable in the north-central United States (Colorado, Iowa, North Dakota, and Wisconsin), but also in California, as well as in the Russian Far East, including Kamchatka. The biggest positive anomalies occurred in eastern China and India and north Pakistan, South Sudan, and Kenya, followed by southern and central Europe. Similar to 2016, some arctic regions in Russia and Canada also showed strong positive anomalies.

La Niña had an impact on vegetation health by contributing heavy rains over Indonesia, India, and western Brazil. In contrast, Argentina, Paraguay, and Chile recorded a strong negative anomaly that increased from June to December due to the dry conditions caused by La Niña coupled with above-normal temperatures (see section 2d4). At the start of the dry season in April,

northern Mozambique and western Madagascar suffered from rainfall deficits that induced the negative annual anomalies. Strong negative anomalies were also observed over some regions of Australia that suffered from the devastating 2019/20 summer bushfires, although vegetation partially recovered locally with adequate rains.

The European summer heat wave (see sections 2b3, 7f) significantly impacted the vegetation productivity, as can be seen in the annual anomaly of herbaceous vegetation in Sweden and Norway. The rest of Europe was also strongly affected during spring and summer, but this was not apparent per se in the annual analysis. During spring, Canadian vegetation suffered from very cold temperatures that affected the annual value. The western and central United States experienced both high temperatures and dry conditions in much of the year, and the impacts on central states were perceived in the annual study. Terrestrial photosynthesis was enhanced over eastern China, with vegetation growth noticeable since 2015 due to important changes in the main land use, with a net increase in leaf area mainly from croplands (Gobron 2019; Chen et al. 2019). The strong positive anomalies over some northern latitudes were largely due to the warm spring that was ideal for vegetation growth. Furthermore, heavy rains enhanced the positive anomalies in China and East Africa.

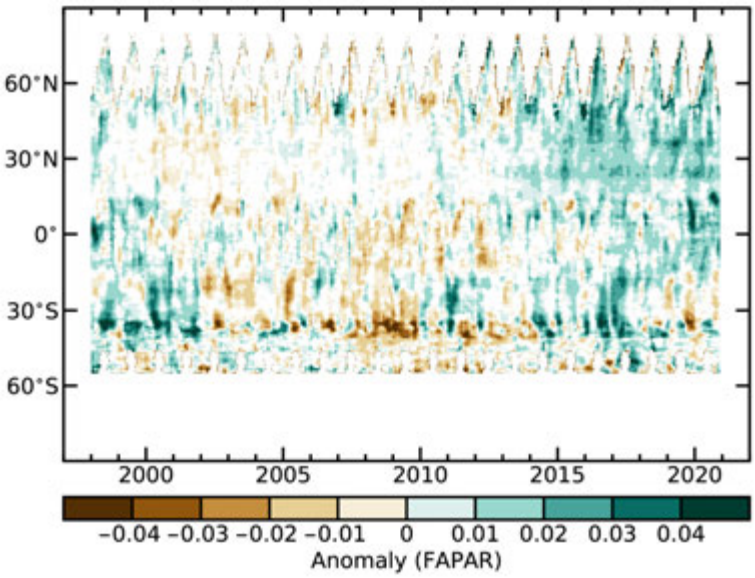

Fig. 2.71. Zonally averaged Fraction of Absorbed Photosynthetically Active Radiation (FAPAR) anomalies for 1998–2020 (1998–2010 base period).

Figure 2.71 shows the latitudinal anomalies average from 1998 to 2020 compared to the base period 1998–2010. The strong seasonal deviations mainly include positive anomalies north of 20°N after 2014. In 2020, this positive behavior extended south of the equator. Negative anomalies from 2002 to 2014 affected the SH, except in 2010–12. Around 30°S, 2019/20 anomalies again became again negative.

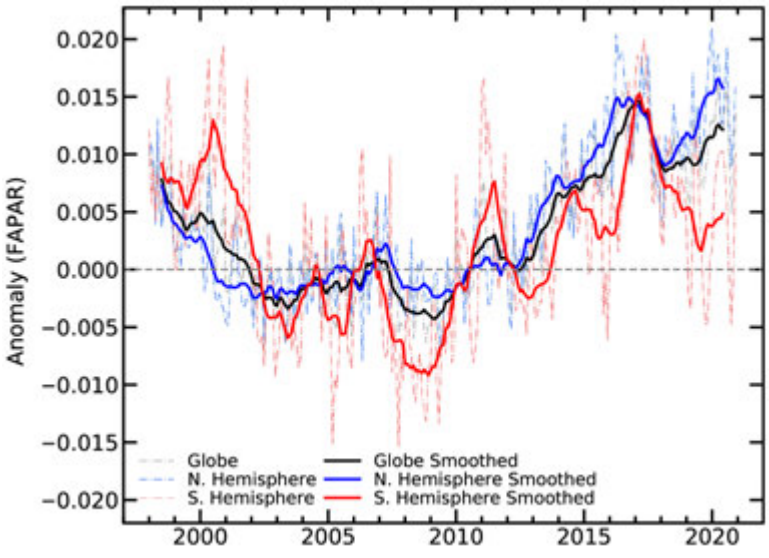

Fig. 2.72. Global (black/gray lines), Northern Hemisphere (blue), and Southern Hemisphere (red) Fraction of Absorbed Photosynthetically Active Radiation (FAPAR) anomalies for 1998–2020 (1998–2010 base period). Dotted lines denote each monthly period; solid lines indicate the 6-month running averaged mean.

Figure 2.72 draws the global and bihemispherical anomalies, revealing more seasonal oscillations in the SH than in the NH. Analysis of SH data reveals two positive extreme peaks in 2000 and 2017, while extreme minima events occurred in 2008–09. Afterwards, SH anomalies increased with interannual variations and were positive since 2014. The NH experienced fewer extreme negative events compared to the SH, and its photosynthetic activity increased from 2010 to 2017 and, after a brief decline in late 2017/early 2018, increased again to a high value in 2020. The global average has been positive since 2010 with a positive trend.

Earth observations measurements are fundamental for monitoring the activity of vegetation worldwide. These observations are used to infer FAPAR,

an essential climate variable (as defined by GCOS [2016]). The 2020 analysis merged 23 years of global FAPAR monthly products based on three optical sensors from 1998 to 2020 (Gobron et al. 2010; Pinty et al. 2011; Gobron and Robustelli 2013; the base period is 1998–2010). Comparisons between each dataset and with multiple proxies using ground measurements provide an estimate of the uncertainties and biases. This long-term global FAPAR dataset presents an estimated average uncertainty close to 5%–10%.

3) Biomass burning—J. W. Kaiser and G. R. van der Werf

The year 2020 illustrates how two distinct trends that have emerged in global biomass burning over the last decade shape current pyrogeography: a declining trend in many savanna regions related to agricultural expansion and an increasing trend in many forested regions where climate change increases the flammability of the landscape. It was one of the lowest fire years in the Global Fire Assimilation System (GFAS) record (13% below the 2003–10 average), but there was also extreme regional fire activity (Table 2.11). This activity included the continuation of fires in southeastern Australia early in the year that had started in late 2019, fires above the Arctic circle in Russia, and in the western United States.

Table 2.11. Annual continental-scale biomass burning budgets in terms of carbon emission (Tg C yr^{-1}) from Global Fire Assimilation System (GFASv1.4).

Time period		2003–10	2020	
Quantity in Tg C yr^{-1}	Latitude/ longitude	Mean value (range)	Value	Anomaly (percent)
Global		2010 (1828–2272)	1741	–269 (–13%)
North America	30°–75°N 190°–330°E	79 (63–109)	65	–14 (–18%)
Central America	13°–30°N 190°–330°E	42 (31–58)	42	0 (0%)
South America	13°–60°S 190°–330°E	427 (255–524)	418	–9 (–2%)
Europe and Mediterranean	30°–75°N 330°–60°E	37 (29–62)	30	–7 (–17%)
N. Hem. Africa	0°–30°N 330°–60°E	419 (353–453)	374	–45 (–11%)
S. Hem. Africa	0°–35°S 330°–60°E	484 (444–528)	426	–58 (–12%)
Northern Asia	30°–75°N 60°–190°E	176 (99–418)	193	+17 (+10%)
South-East Asia	10°–30°N 60°–190°E	128 (107–150)	104	–24 (–18%)
Tropical Asia	10°S–10°N 60°–190°E	118 (38–228)	23	–95 (–80%)
Australia	10°–50°S 60°–190°E	99 (47–137)	64	–34 (–35%)
Arctic	67°–90°N 0°–60°E	4 (0–11)	37	+32 (+724%)
Western United States	30°–49°N 230°–260°E	15 (7–25)	42	+27 (+183%)

Global fire emissions are generally dominated by savanna burning (Fig, 2.73). For example, African fire emissions comprise roughly half of total global fire carbon emissions; but fires here and in many other savanna regions have decreased over the past decade (Andela et al. 2017). This trend continued in 2020 with Africa north (south) of the equator seeing emissions 11% (12%) below the 2003–10 average. Given the dominance of these regions, this reduction was reflected in the global total of 1741 Tg C emissions from biomass burning in 2020, which was the fourth lowest of the past 18 years. The lowest fire year in this period was 2018 with 1661 Tg C, followed by 2017 and 2013 with 1683 Tg C and 1690 Tg C, respectively. While the long-term trend is partly driven by agricultural expansion into savanna ecosystems and associated fragmentation of the landscape, anomalous rainfall years also influence interannual variability on top of the declining trend.

Tropical forests in the Amazon saw the highest fire activity since 2012, surpassing the year 2019, which attracted more media attention at that time. The emerging upward trend is also supported by independent VIIRS observations (https://globalfiredata.org/pages/2020/09/22/amazon-fire-activity-in-2020-surpasses-2019; Schroeder et al. 2014). In contrast, fire activity in tropical

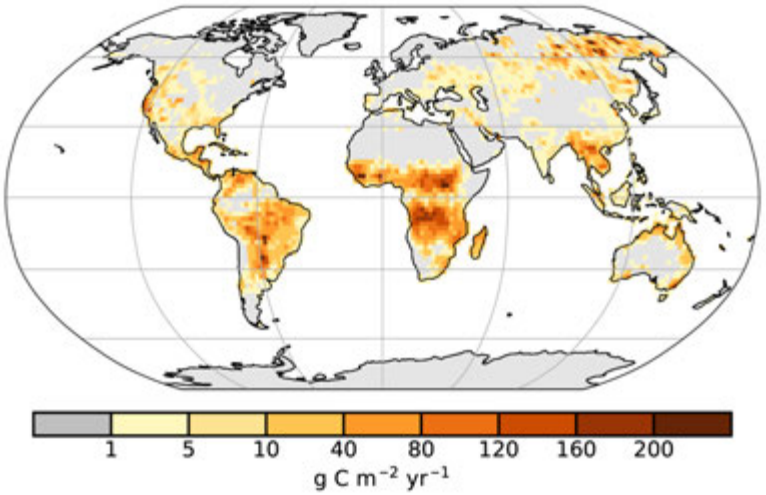

Fig. 2.73. Global map of fire activity in 2020 in terms of carbon consumption (g C m^{-2} yr^{-1}). (Source: Global Fire Assimilation System GFASv1.4.)

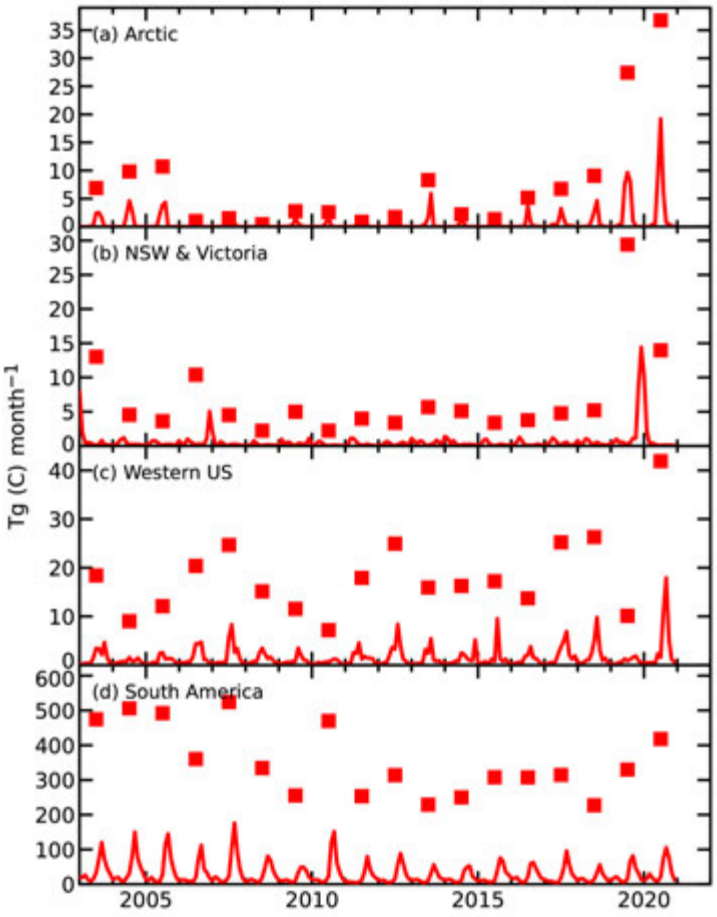

Fig. 2.74. Time series of annual (squares) and monthly (lines) regional fire activity in terms of carbon consumption: (a) Arctic, (b) New South Wales and Victoria, (c) western United States, and (d) South America. (Source: Global Fire Assimilation System GFASv1.4.)

Asia—including Indonesia—was one of the lowest on record, related to relatively wet conditions as La Niña started to evolve during the fire season.

At higher latitudes, 2020 was record breaking in both southeastern Australia and the western United States, where extreme heat and drought contributed to unprecedented fire conditions (Van Oldenborgh et al. 2020). While Australia as a whole did not exhibit anomalies (Table 2.11) due to the dominance of savanna fires in the northern part of the country and because the fire season in southeastern Australia started in 2019, the combined 2019–20 southeastern Australian fire season was unprecedented. For example, emissions were the highest since at least 2003 (Fig. 2.74), burnt area in New South Wales was the largest since at least 1968 with more than 5 million ha, and ~43% of the total Australian coverage of Eucalyptus forests and woodlands burned (Bowman et al. 2021). In the western United States, total fire emissions almost tripled compared to the 2003–10 mean and thus continued the recent upward trend (Fig. 2.74).

The Arctic experienced its highest fire year in 2020, surpassing the record set in 2019 (Kaiser et al. 2020; Sidebar 5.1) by 34%. Each of the last 5 years have thus seen more Arctic fires than the preceding year (Fig. 2.74). Most of the fires occurred in Arctic Asia, with Arctic America, and also all of Canada plus Alaska, experiencing their lowest fire year on record in 2020. While the fires burned within the Arctic circle and partly affected thawed permafrost, the largest fire complex was still in thinly forested regions and not in tundra, which leaves the long-term possibility of a partial uptake of the emitted carbon through re-growth.

The time series in Plate 1.1ac puts GFAS in the context of the Global Fire Emissions Database, version 4 with small fires (GFED4s), which is mostly based on burnt area observation and dates back to 1997 (van der Werf et al. 2017). It shows that the global fire emissions during the 1997–98 El Niño remain unsurpassed.

GFAS produces global fire emission estimates in near real-time for the Copernicus Atmosphere Monitoring Service (Kaiser et al. 2012). Here, we used a consistent reprocessing of 2003–20 based on Collection 6 of the MODIS Fire Radiative Power product (Giglio et al. 2016). The 14% bias with respect to Collection 5 has been corrected and the satellite- and observation time-specific bias correction factors from Hüser et al. (2018) were applied for 17 August–2 September 2020 in order to compensate for the outage of observations from MODIS onboard the *Aqua* satellite.

4) Phenology of primary producers—D. L. Hemming, J. Garforth, J. O'Keefe, T. Park, A. D. Richardson, T. Rutishauser, T. H. Sparks, and S. J. Thackeray

During 2020, the satellite-derived (MODIS) normalized difference vegetation index (NDVI; Park et al. 2016) across the NH landmass (>30°N) revealed an earlier mean start of season (SOS_M), later end of season (EOS_M), and 1.8 days longer growing season, compared to the 2000–10 baseline (Fig. 2.75). These coincided with the second-warmest spring and warmest autumn on record across the NH (NOAA 2020). Regional differences resulted in 2.1 days earlier and 0.9 days later SOS_M in Eurasia (EA) and North America (NA), respectively. No clear signal in EOS_M was observed across NA, whereas, later EOS_M was dominant across EA (Fig. 2.75d). Overall, about 55% and 65% of the NH showed earlier SOS_M and later EOS_M in 2020. These spatial variations also correlate with spring and autumn surface temperature (section 2b1; NASA MERRA-2, Gelaro et al. 2017), which were 0.5°C (+1.2°C for EA, −0.95°C for NA) and 0.7°C (+1.0°C for EA, −0.05°C for NA) warmer in 2020 compared to the baseline. NH trends of earlier SOS_M and later (less significant) EOS_M over the last 21 years were noted in MODIS NDVI (SOS_M = −2.3 ± 0.7 days decade^{-1}, p = 0.01; EOSM = 1.3 ± 0.9 days decade^{-1}, p = 0.18) while significant differences in magnitude were observed between

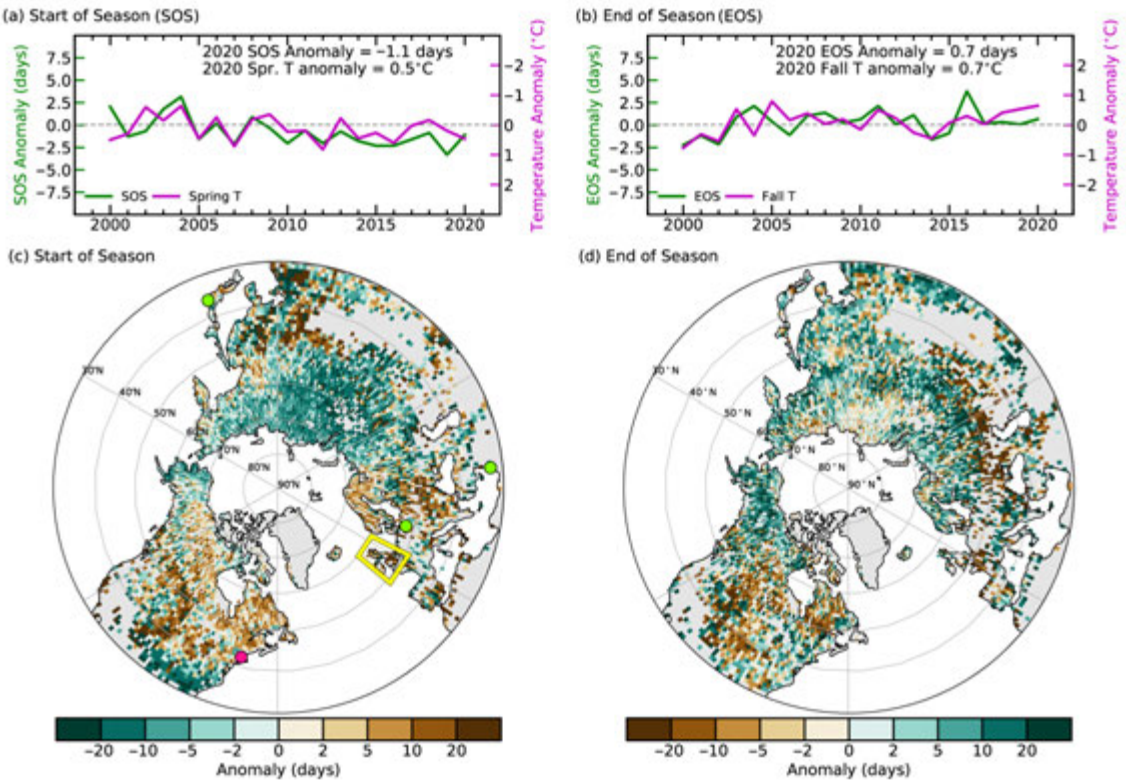

Fig. 2.75. (a) Time series of area-mean anomalies (days; base period 2000–10) in MODIS NDVI-based start of season (SOS) (green) and MERRA-2 spring (Mar–May, pink) temperature (°C) for Northern Hemisphere (>30°N). (b) Same as (a) but for end of season (EOS) (green) and autumn (Sep–Nov, pink) temperature. Note temperature scale reversal for (a). 2020 spatial pattern of (c) SOS and (d) EOS anomaly with respect to the baseline. Highlighted points and box identify the location of phenology sites shown in Fig. 2.76. (United States Harvard Forest, Massachusetts PhenoCam and Red oak [pink point]; United Kingdom mean Pedunculate oak [yellow box]; Lake Kasumigaura, Japan, Lake Kinneret, Israel and Müggelsee, Germany [green points]).

NA (SOSM = −0.05 ± 0.5 days decade^{-1}, p = 0.24; EOS_M = 2.0 ± 0.6 days decade^{-1}, p = 0.01) and EA (SOS_M = −1.7 ± 0.6 days decade^{-1}, p = 0.02; EOS_M = 0.1 ± 0.8 days decade^{-1}, p = 0.89), indicating asymmetric extension of the growing season at the continental scale.

PhenoCam data across NA (Seyednasrollah et al. 2019) provide a link between the coarse and fine resolutions of satellite monitoring and site-level observations on individual organisms (Richardson et al. 2019). We compared PhenoCam-derived estimates (2008–20, n = 13) of start of season (SOS_{PC}) and end of season (EOS_{PC}) at Harvard Forest, a deciduous forest in Massachusetts, United States, with ground observations of Red oak (*Quercus rubra*) phenology (SOSRO = 50% budburst and EOS_{RO} = 50% autumn color; Richardson and O'Keefe 2009, 2019), and MODIS SOS_M and EOS_M for the associated pixel (Figs. 2.76a,b). SOS_{PC} and EOS_{PC} were strongly correlated with SOS_{RO} and EOS_{RO} (r = 0.90 and 0.81, respectively) and their timings were similar. Although SOS_{PC} and SOS_M were strongly correlated (r = 0.79), SOS_{PC} was later by 12 ± 3 days (Fig. 2.76a). The correlation between EOS_{PC} and EOS_M was weaker (r = 0.48), and EOS_{PC} was earlier on average by 48 ± 12 days (Fig. 2.76b). These differences may be explained in part by a mix of land cover types covered by the MODIS 5-km pixel. In 2020, SOS_{PC} (day 137, 16 May, ± 2 days) was 6 days later than in 2019, and consistent with the change for SOS_{RO}, which was 9 days later in 2020 than 2019. EOS_{PC} in 2020 (day 293, 19 October, ± 1 day) was unchanged, while EOS_{RO} was 4 days later than 2019. In comparison, SOS_M was 3 days earlier than 2019 and EOS_M remained unchanged (Figs. 2.76a,b). Later SOS_{PC} in 2020 was related to relatively cold spring temperatures and resulted in a growing season 5 days shorter than in 2019. 2020 had the shortest growing season observed at Harvard Forest in the last 13 years.

Dates of Pedunculate oak (*Quercus robur*) "first leaf" (SOS_{PO}) and "bare tree" (EOS_{PO}) recorded by citizen scientists across the United Kingdom have been collated by the Woodland Trust since 1999 (Collinson and Sparks 2008). The mean SOS_{PO} for the 2000–09 baseline was 26 April (day 116), and EOS_{PO} was 30 November (day 334), giving a 218-day growing season length (Figs. 2.76c,d). Both events were strongly influenced by temperature; SOS_{PO} advances by approximately 6 days for every 1°C increase in mean February–April temperature, and EOS_{PO} is delayed by approximately 3 days for every 1°C increase in October temperature. The year 2020, like 2019, had a very warm spring, and this resulted in the earliest United Kingdom SOS_{PO} in the 20-year series (10 days earlier than the in-situ baseline). October temperature was similar to recent years, and the EOS_{PO} date

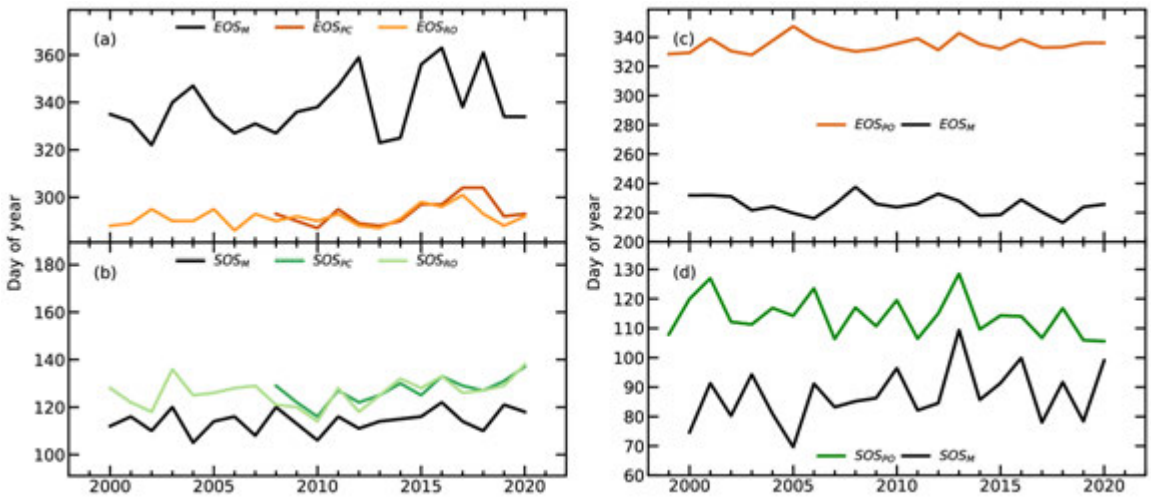

Fig. 2.76. Start of season (SOS) and end of season (EOS) phenology indicators derived from (a),(b) Harvard Forest, Massachusetts, United States, PhenoCam (SOS_{PC} and EOS_{PC}), Red oak ground observations (SOS_{RO} and EOS_{RO}), and MODIS remote sensing (SOS_M and EOS_M), and (c),(d) United Kingdom mean Pedunculate oak (SOS_{PO} and EOS_{PO}) and MODIS.

(note these were predicted from the temperature relationship due to COVID-19 monitoring restrictions) was approximately 2 days later than the baseline. The net result was a United Kingdom "oak season" 12 days longer than the baseline.

In 2020, monitoring data on lake water concentrations of the photosynthetic pigment chlorophyll-*a* were available to estimate the spring phytoplankton peak in three NH lake basins (Lake Kasumigaura in Japan, Lake Kinneret in Israel, and Müggelsee in Germany). Some in situ lake monitoring schemes were inactive in 2020 due to COVID-19 restrictions. The mean start of spring bloom during the 2000–10 baseline in these lakes ranged from 22 March (day 81, Lake Kasumigaura) to 21 April (day 111, Lake Kinneret). Spring peak was earlier in 2020 than the baseline in two lake basins (by 15 to 38 days), but later for Müggelsee (by 4 days). This variation between sites may relate to differences in climate or other factors that interact with climate to influence seasonal ecosystem behavior.

Sidebar 2.3. **Long-term monitoring of vegetation state through passive microwave satellites**—W. DORIGO, L. MOESINGER, R. VAN DER SCHALIE, R. M. ZOTTA, T. SCANLON, AND R. A. M. DE JEU

Microwave radiation emitted or reflected by the land surface is strongly affected by available water, including that stored in living biomass. The all-weather, sunlight-independent observing capacity of microwave satellites makes them complementary to satellites in the optical domain traditionally used to observe vegetation characteristics (Becker and Choudhury 1988; see section 2h2.). Particularly for areas with frequent cloud cover, such as the humid tropics, microwave satellites provide novel insights into vegetation dynamics, although with lower spatial detail (Rodriguez-Fernandez et al. 2018).

The portion of the radiance attenuated by the canopy is expressed by its vegetation optical depth (VOD), a parameter used in radiative transfer models to describe radiance interaction with vegetation. Long seen as a by-product of soil moisture retrievals (see section 2d10), VOD is increasingly proven to be a valuable indicator of land surface conditions itself. While VOD is not a biogeophysical variable per se, various studies have shown its close relationship to vegetation above-ground biomass (Mialon et al. 2020, Rodriguez-Fernandez et al. 2018), leaf area index (Vreugdenhil et al. 2017), gross primary production (Teubner et al. 2019), or canopy water content (Konings et al. 2017). Since VOD is wavelength-dependent and, with increasing frequency, increasingly sensitive to the upper vegetation layer (Li et al. 2021), VOD estimates at low frequencies (L-band) are more closely related to forest biomass (Chaparro et al. 2019), while higher frequency observations (C-, X-, and Ku-band) show closer agreement with seasonal leaf dynamics and photosynthetic activity (Teubner et al. 2018; Fig. SB2.5) and, hence, are valuable phenological indicators (see section 2h4; Pfeil et al. 2020).

VOD products from various frequencies have been used to monitor global terrestrial carbon dynamics (Liu et al. 2015), assess the severity of agricultural droughts (Van Dijk et al. 2013; Crocetti et al. 2020), assess crop yield (Chaparro et al. 2018), model fire occurrence (Forkel et al. 2017, 2019) and terrestrial evaporation (Martens et al. 2017), and monitor land degradation (Liu et al. 2013) and deforestation (van Marle et al. 2015).

VOD observations from several available meteorological and Earth observation satellites, including SSM/I, TRMM, AMSR-E, and AMSR2, have been retrieved with the Land Parameter Retrieval Model (Meesters et al. 2005; Van der Schalie et al. 2018) and amalgamated into the long-term VOD Climate Archive (VODCA), which allows for studying variability and change at climatic time scales (Moesinger et al. 2020). VODCA contains individual

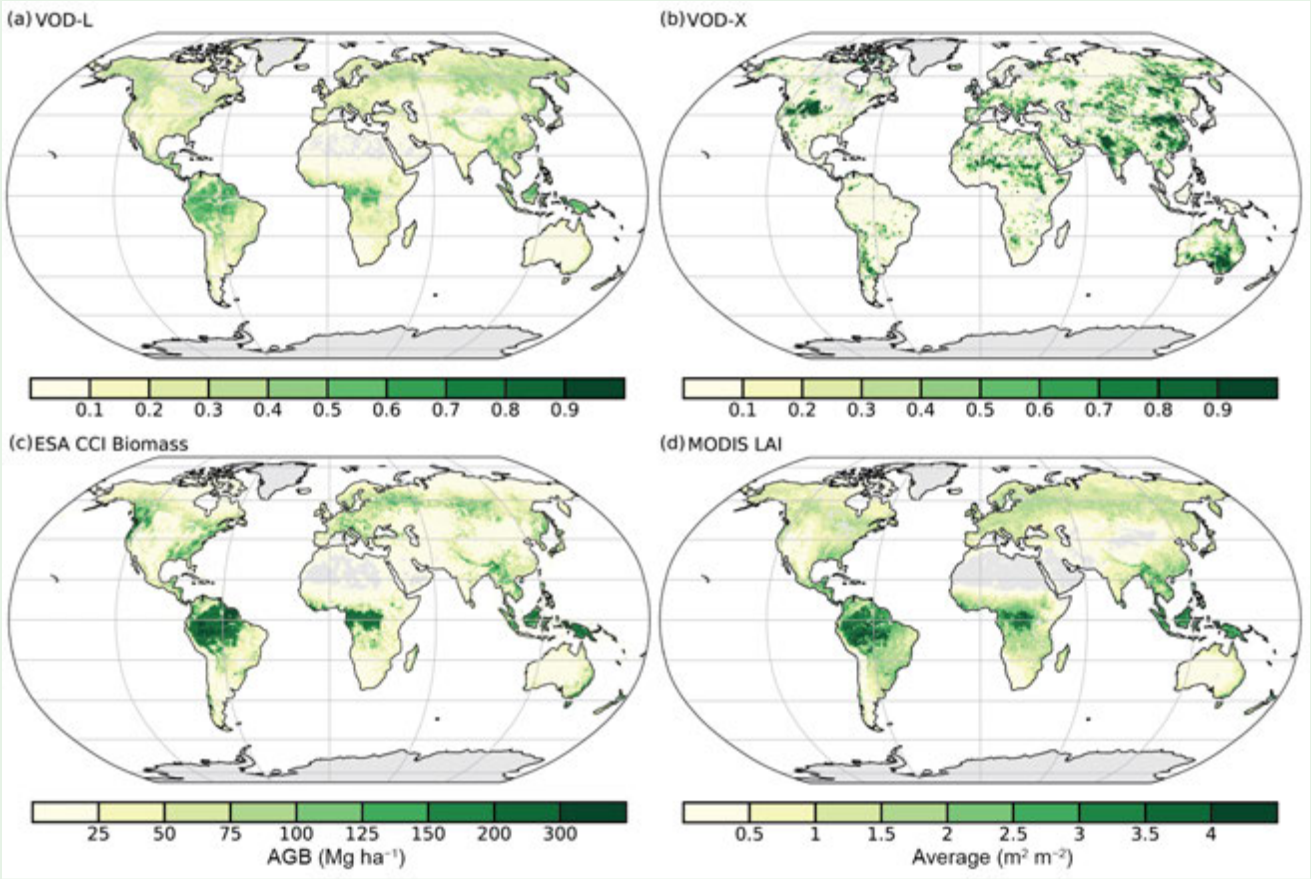

Fig. SB2.5. (a),(b) Global maps of average vertical optical depth (VOD; unitless) for the period 2010–20 for L- and X-band, respectively. Note that VOD is wavelength-dependent and hence has a different range for different bands. (c) ESA CCI above-ground biomass (Mg ha^{-1}) for 2017, (d) Average LAI (m^2 m^{-2}) from MODIS for 2010–20.

datasets for Ku-band (covering the period 1987–2020), X-band (1997–2020), and C-band (2002–20) at 0.25° spatial and daily temporal resolutions. Because of the superior length of the data record, we used the VODCA Ku-band dataset to compute anomalies from the long-term (1991–2010) mean seasonal cycle. This frequency has a noted higher sensitivity to the upper canopy than the other frequencies and is thus a suitable indicator of foliage biomass and water content dynamics over space and time.

The year 2020 saw lower-than-usual VOD values (Appendix Fig. A2.12 in large parts of North and South America, central and southern Africa, most of Australia, and in a wide belt from eastern Europe, through Russia and Mongolia, to northern China and Korea. Some of these regions had to cope with strong agricultural droughts and crop yield losses, e.g., Argentina and Ukraine (see sections 7d3, 7f6). In early 2021, in southern Madagascar over one million people were at the brink of famine because of yield losses, according to the UN Global Disaster Alert and Coordination System. Above-normal vegetation activity was observed in the central United States, northeastern Brazil, the Sahel, eastern and central southern Africa, India, and large parts of Eurasia. Many of these regions were much wetter than usual in 2020 (section 2d10). For example, eastern Africa was repeatedly struck by torrential rainfall, flooding, and landslides throughout the first half of the year (see sections 2d5, 7e4), while India received 109% of its typical rainfall during its monsoon season (see section 7g4).

Vegetation dynamics are not only driven by water availability, as they are the result of complex interactions of multiple drivers (e.g., precipitation, temperature, radiation, carbon dioxide fertilization), weather extremes, lagged effects due to deep rooting systems, and land management (Nemani et al. 2003; Reichstein et al. 2013). For example, in regions or seasons where plant growth is traditionally limited by low temperatures or radiation, plant growth may be anti-correlated with precipitation, as precipitation events are characterized by more cloud cover and, hence, lower temperatures. A good example is the dry, warm, and sunny April in Europe in 2019 (see section 7f; Appendix Fig. A.SB2.1d), which clearly boosted vegetation development in the same month. In May, while soil moisture conditions had returned to normal, VOD showed a lagged drought response to the soil water depletion in early spring for several consecutive months (Appendix Figs. A.SB2.1e,f).

Worldwide, but particularly in the global south, interannual VOD conditions can be linked to variations in the El Niño–Southern Oscillation (ENSO; Fig. SB2.6), which is characterized by predominantly dry conditions during El Niño and mostly wet conditions during La Niña episodes (see sections 2d4, 2d10). This connection between VOD and ENSO confirms previous studies based on optical data (e.g., Poulter et al. 2014) that, at the global scale, interannual vegetation activity is largely controlled by moisture supply. Although 2020 saw a transition from weak El Niño-like conditions at the start of the year to a moderate La Niña toward the end (see sections 2e1, 4b), this is not clearly reflected by the yearly and monthly VOD anomaly patterns (Appendix Fig. A.SB2.1), which show a mixture of typical El Niño-like patterns (e.g., wet and, hence, green conditions in eastern Africa and dry conditions in southern Africa and Australia) and patterns typically observed during La Niña episodes (e.g., wetter conditions in northeastern Brazil and drier conditions in Argentina; see section 2e1).

Global long-term VOD trends are slightly positive (Fig. SB2.6; Moesinger et al. 2020) and in line with greening trends derived from observations in the optical domain (e.g., Forzieri et al. 2017; see section 2h2), thus affirming the usability of VOD for detecting and attributing long-term changes in vegetation activity (Liu et al. 2013). Through its multiple facets, long-term VOD observations perfectly complement the available suite of Earth observation tools to solve the complex puzzle of the effects of climate change on our biosphere.

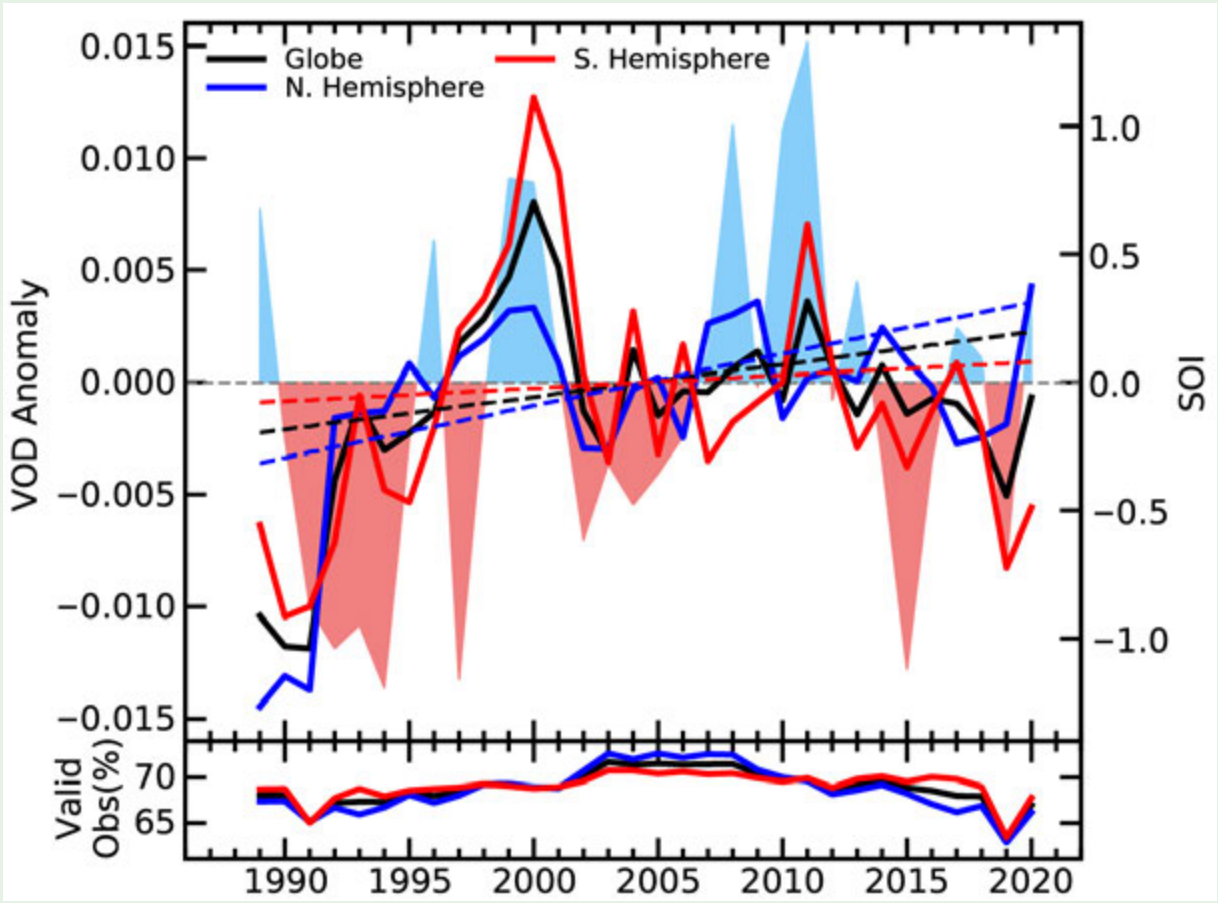

Fig. SB2.6. Yearly Ku-band virtual optical depth (VOD) anomalies juxtaposed with the Southern Oscillation Index Lines indicate the global and hemispheric VOD while the shading is the southern oscillation index (SOI) (red: La Niña, negative; blue: El Niño, positive). (Source: VODCA, http://www.bom.gov.au/climate/current/soi2.shtml.) The bottom plot shows the percentage of land pixels that provides valid data for each year.

Acknowledgments

2a1 (Overview)

Freya Aldred, Robert Dunn, and Kate Willett were supported by the Met Office Hadley Centre Climate Programme funded by BEIS and Defra.

We thank Rob Chadwick and David Parker, the five anonymous reviewers, and the BAMS Editor for their detailed comments when reviewing the chapter. We also thank Atsushi Goto (JMA), Julien Nicolas (ECMWF) and Mike Bosilovich (NASA) for the provision of the reanalysis data used in this chapter.

2b2 (Lake surface water temperature)

Lake surface water temperatures from satellite data have been generated within the GloboLakes project funded by the UK National Environment Research Council (NE/J023345/2) with extensions funded by the EU Copernicus Climate Change Service (C3S) programme. The in situ measurements used to validate the LSWT dataset have been kindly shared by Eugene Silow (Irkutsk State University, Russia); Merja Pulkkanen (SYKE, Helsinki, Finland); Antii Raike (SYKE, Helsinki, Finland); Eric Leibensperger (Department of Physics and Astronomy, Ithaca College, Ithaca, New York); Alo Laas (Estonian University of Life Sciences, Tartu, Estonia); Michela Rogora (CNR Institute for Water Research, Italy); Martin Dokulil (Austria); Shin-ichiro Matsuzaki (National Institute for Environmental Studies, Japan); Claudia Giardino (CNR IREA, Italy); Curtis DeGasperi (King County Water and Land Resources Division, Department of Natural Resources and Parks, Seattle, Washington); Martin Schmid (Eawag, Switzerland); and Don Pierson (Uppsala University, Sweden).

Lake Water Level timeseries are generated by LEGOS/CLS as part of the Theia Land programme supported by CNES with extensions funded by the EU Copernicus Climate Change Service (C3S) programme and by ESA through the Climate Change Initiative (CCI+) project. Valery Vuglinskii (SHI, Russia) provided water level in situ time series on 16 lakes in Russia allowing to validate the LWL products.

2b3 (Land and marine temperature extremes)

Robert J. H. Dunn was supported by the Hadley Centre Climate Programme funded by BEIS and Defra.

2b4 (Tropospheric temperature)

Work performed by Stephen Po-Chedley at Lawrence Livermore National Laboratory (LLNL) was performed under the auspices of the U.S. Department of Energy under Contract DE-AC52-07NA27344 with support from the Regional and Global Model Analysis Program of the Office of Science at the DOE.

2b5 (Stratospheric temperature and winds)

The National Center for Atmospheric Research is sponsored by the U.S. National Science Foundation.

Sidebar 2.1 (Night marine air temperature)

Richard Cornes, David Berry, and Elizabeth Kent were funded by the NERC CLASS programme (NE/R015953/1), the NERC GloSAT project (NE/S015647/2), and the Copernicus Climate Change Service (C3S_311a_Lot2). The UAHNMATv1 work was supported by the U.S. Department of Energy (DE-SC0005330 and DE-SC0019296. Nick Rayner was supported by the Met Office Hadley Centre Climate Programme funded by BEIS and Defra.

2c1 (Permafrost thermal state)

PERMOS is financially supported by MeteoSwiss in the framework of GCOS Switzerland, the Federal Office for the Environment, and the Swiss Academy of Sciences and acknowledges the important contribution of the partner institutions and principal investigators. The French Network PermaFRANCE is financially supported by OSUG (Observatoire des Sciences de l'Univers Grenoble) and the French Research Infrastructure OZCAR. Czech Antarctic Research Programme is supported by Czech Ministry of Education, Youth and Sport project VAN2020/1.

2c2 (Northern Hemisphere continental snow cover extent)

This work is funded in part by NOAA's Climate Data Record (CDR) Program located in Asheville, North Carolina, at the National Centers for Environmental Information.

2c4 (Lake ice)

We thank Kevin Blagrave, Nikolay Granin, Lars Rudstam, and Merja Pulkanen for providing updates to in situ lake ice phenology records.

Sidebar 2.2 (Rock glacier kinematics)

Rock glacier monitoring at Hinteres Langtalkar and Dösen rock glaciers (AT) was supported by different national and international projects during the last decades. The authority of the Hohe Tauern National Park is one of the most important supporters of this monitoring. Laurichard (FR) survey is supported by CryobsClim "long-term Observation and Experimentation System for Environmental Research" (SOERE/All'envi-OZCAR Research Infrastructure) and the PermaFrance observatory "monitoring the mountain permafrost in the French Alps." The Ecrins National Park helps field surveys since the early 2000's. The Swiss Permafrost Monitoring Network PERMOS is financially supported by MeteoSwiss in the framework of GCOS Switzerland, the Federal Office for the Environment and the Swiss Academy of Sciences. PERMOS acknowledges the important contribution of the partner institutions and principal investigators.

2d1 (Surface humidity)

Kate Willett and Alan Vance were supported by the Met Office Hadley Centre Climate Programme funded by BEIS and Defra. Adrian Simmons was supported by the Copernicus Climate Change Service implemented by ECMWF on behalf of the European Commission.

2d5 (Land-based precipitation extremes)

Mari Tye was supported by the National Center for Atmospheric Research, which is a major facility sponsored by the National Science Foundation under Cooperative Agreement No. 1852977.

2d6 (Lake water levels)

B. M. Kraemer received support from the 2017–2018 Belmont Forum and BiodivERsA joint call for research proposals, under the BiodivScen ERA-Net COFUND program, and with the funding organizations German Science Foundation (AD 91/22-1). This work benefited from B. M. Kraemer's participation in the Global Lake Ecological Observatory Network (GLEON).

2d8 (River discharge and runoff)

Hyungjun Kim was supported by the Japan Society for the Promotion of Science KAKENHI (16H06291 and 18KK0117) for this contribution.

2d10 (Soil moisture)

The ESA CCI SM datasets and the authors were supported by ESA's Climate Change Initiative for Soil Moisture (Contract No. 4000104814/11/I-NB and 4000112226/14/I-NB) and in addition the authors were supported by activities under provision of services to Copernicus Climate Change Service (Contract No. ECMWF/COPERNICUS/2018/C3S_312b_Lot4_EODC/SC2).

2d11 (Monitoring global drought using the self-calibrating Palmer Drought Severity Index)

J. Barichivich acknowledges the FONDECYT Grant 1181956. Tim Osborn received funding from UK NERC (NE/S015582/1). Ian Harris received funding from UK National Centre for Atmospheric Science (NCAS). The research presented in the drought section was carried out on the High Performance Computing Cluster supported by the Research and Specialist Computing Support service at the University of East Anglia.

2d12 (Land evaporation)

Diego G. Miralles acknowledges support from the European Research Council (ERC) under grant agreement no. 715254 (DRY–2–DRY). A. Koppa and D. Rains acknowledge support from the Belgian Science Policy Office (BELSPO) in the frame of the STEREO III program projects ALBERI (SR/00/373) and ET–Sense (SR/02/377). M. F. McCabe is supported by the King Abdullah University of Science and Technology.

2e2 (Land and ocean surface winds)

Robert J. H. Dunn was supported by the Hadley Centre Climate Programme funded by BEIS and Defra. L. Ricciardulli and Carl A. Mears are supported by the NASA Ocean Vector Wind Science Team (OVWST) program.

2f1 (Earth radiation budget at top-of-atmosphere)

This research has been supported by the NASA CERES project. The NASA Langley Atmospheric Sciences Data Center processed the instantaneous Single Scanner Footprint (SSF) data used as input to EBAF Ed4.1 and processes the FLASHFlux TISA version 4A.

2g4 (Stratospheric ozone)

Carlo Arosio, Melanie Coldewey-Egbers, Daan Hubert, Diego Loyola, Victoria Sofieva, Alexei Rozanov, and Mark Weber are grateful to ESA's Climate Change Initiative Ozone project and to the EU Copernicus Climate Change Service 312b Lot4 Ozone project for supporting the generation and extension of the GTO-ECV total ozone and SAGE-CCI-OMPS data records. Stacey M. Frith is supported by the NASA Long Term Measurement of Ozone program WBS 479717. Lucien Froidevaux's contribution, with the assistance of Ryan Fuller, was performed at the Jet Propulsion Laboratory, California Institute of Technology, under contract with NASA. Daan Hubert acknowledges the partial support by the EU/ERC Horizon 2020 project GAIA-CLIM.

2h1 (Land surface albedo dynamics)

The authors thanks Monica Robustelli for her technical support and NASA's Land Processes Distributed Active Archive Center (LP DAAC) for providing access to the remote sensing data.

2h2 (Terrestrial vegetation dynamics)

The author thanks Monica Robustelli for her technical support and the providers of the remote sensing dataset needed to perform this research, i.e., the SeaWiFS Project (Code 970.2) and the Goddard Earth Sciences Data and Information Services Center/Distributed Active Archive Center (Code 902) at the Goddard Space Flight Center, Greenbelt, Maryland 20771. MERIS products were processed at the Grid On Demand facility of European Space Agency (ESA/ESRIN) using JRC software code.

2h4 (Phenology of primary producers)

Debbie Hemming acknowledges support from the Met Office Hadley Centre Climate Programme funded by BEIS and Defra, and thanks Robert Dunn for his expertise finalizing the figures. Taejin Park acknowledges support from the NASA Earth Science Directorate (grants NNX16AO34H and 80NSSC18K0173-CMS). Andrew Richardson acknowledges support from the National Science Foundation through the Macrosystems Biology (award 1702697) and LTER (award 1832210) programs. Nature's Calendar thanks all its volunteer recorders, without whom it could not function. Stephen Thackeray thanks Rita Adrian, Tamar Zohary, Kazuhiro Komatsu and Shin-Ichiro Matsuzaki for collecting and providing lake chlorophyll-*a* data.

Sidebar 2.3 (Long-term monitoring of vegetation state through passive microwave satellites)

Wouter A. Dorigo, L. Moesinger, and R. M. Zotta acknowledge the TU Wien Wissenschaftspreis 2015, a personal grant awarded to Wouter Dorigo.

Chapter 2 – Acronyms

AAO	Antarctic Oscillation
AATSR	Advanced Along Track Scanning Radiometer
ALEXI	Atmosphere–Land Exchange Inverse
ALT	active layer thickness
AMSRE-E	Advanced Microwave Scanning Radiometer
AO	Arctic Oscillation
AOD	aerosol optical depth
ATSR	Along Track Scanning Radiometer
AVHRR	Advanced Very High Resolution Radiometer
BDC	Brewer-Dobson circulation
BRW	Barrow Atmospheric Baseline Observatory
C3S	Copernicus Climate Change Service
CALIOP	Cloud-Aerosol Lidar with Orthogonal Polarization
CAMS	Copernicus Atmosphere Monitoring Service
CAMSRA	Copernicus Atmosphere Monitoring Service Reanalysis
CCMI	Chemistry Climate Model Initiative
CEI	Climate Extremes Index
CERES	Clouds and the Earth's Radiant Energy System
CFC	chlorofluorocarbon
CH_4	methane
Cl	chlorine
CO	carbon monoxide
CO_2	carbon dioxide
CPT	cold-point tropopause
CRU TS	Climatic Research Unit gridded Time Series
DDM	drainage direction map
DU	Dobson unit
EA	Eurasia
ECV	essential climate variable
EESC	equivalent effective stratospheric chlorine
EESC-A	equivalent effective stratospheric chlorine-Antarctic
EESC-M	equivalent effective stratospheric chlorine-Midlatitude
ENSO	El Niño–Southern Oscillation
EOFs	empirical orthogonal functions
EOS	end of season
ERB	Earth's radiation budget
ESA CCI SM	European Space Agency's Climate Change Initiative for Soil Moisture
ET	evapotranspiration
ETCCDI	WMO Expert Team in Climate Change Detection and Indices
FAPAR	Fraction of Absorbed Photosynthetically Active Radiation
FF	fossil fuel
GCOS	Global Climate Observing System
GFAS	Global Fire Assimilation System
GFED	Global Fire Emissions Database
GGGRN	NOAA's Global Greenhouse Gas ReferenceNetwork

GHCN	Global Historical Climatology Nework
GHCNDEX	Global Historical Climatology Network-Daily database
GIN-P	Global Terrestrial Network for Permafrost
GLEAM	Global Land Evaporation Amsterdam Model
GMST	global mean surface temperature
GNSS	Global Navigation Satellite System
GPCC	Global Precipitation Climatology Centre
GPCP	Global Precipitation Climatology Project
GPS-RO	Global Positioning System-Radio Occultation
GRACE	Gravity Recovery and Climate Experiment
GRACE-FO	Gravity Recovery and Climate Experiment - Follow On
GTN-P	Global Terrestrial Network for Permafrost
HFCF	hydrochlorofluorocarbon
HFC	hydrofluorocarbon
HIRS	High Resolution Infra Red Radiation Sounder
HWF	heat wave frequency
HWM	heat wave magnitude
IOD	Indian Ocean dipole
IPA	International Permafrost Association
ITCZ	Intertropical Convergence Zone
LLGHG	long-lived greenhouse gases
LSA-SAF	Land Surface Analysis Satellite Applications Facility
LSWT	lake surface water temperature
LTT	lower tropospheric temperature
LWL	lake water level
MACC	Monitoring Atmospheric Composition and Climate
MAT	marine air temperature
MBL	marine boundary layer
MHW	marine heatwave
MLO	Mauna Loa, Hawaii
MLS	Microwave Limb Sounder
MODIS	Moderate Resolution Imaging Spectroradiometer
MOPITT	Measurement of Pollution in the Troposphere
MSU/AMSU	Microwave Sounding Unit/Advanced Microwave Sounding Unit
N_2O	nitrous oxide
NA	North America
NAO	North Atlantic Oscillation
NDVI	normalized difference vegetation index
NH	Northern Hemisphere
NMAT	night marine air temperature
O_3	ozone
ODGI	Ozone Depleting Gas Index
ODGI-A	Ozone Depleting Gas Index-Antarctic
ODGI-M	Ozone Depleting Gas Index-Midlatitude
ODS	ozone-depleting substances
OH	hydroxyl radical
OLR	outgoing longwave radiation
OMI	Ozone Monitoring Instrument

PDO	Pacific Decadal Oscillation
PSC	polar stratospheric cloud
QBO	quasi-biennial oscillation
QTP	Qinghai-Tibetan Plateau
RFaci	radiative forcing resulting from aerosol–cloud interactions
RFari	radiative forcing resulting from aerosol–radiation
RGK	rock glacier kinematics
RH	relative humidity
RO	radio occultation
RSW	reflected shortwave
SAM	Southern Annular Mode
SAR	Synthetic Aperture Radar
SCE	snow cover extent
scPDSI	self-calibrating Palmer Drought Severity Index
SH	Southern Hemisphere
SLSTR	Sea and Land Surface Temperature Radiometer
SOI	Southern Oscillation Index
SORCE	Solar Radiation and Climate Experiment
SOS	start of season
SPO	South Pole Observatory
SSM/I	Special Sensor Microwave/Imager
SSMIS	Special Sensor Microwave Imager/Sounder
SSMIS	Special Sensor Microwave Imager/Sounder
SST	sea surface temperature
SSU	Stratospheric Sounding Unit
SW	shortwave
TCWV	total column water vapor
TIR	thermal infrared
TLS	lower stratospheric temperature
TOA	top of the atmosphere
TSI	total solar irradiance
TSIS-1	Total Solar and Spectral Irradiance Sensor-1
TTL	tropical tropopause layer
TTT	tropical tropospheric temperature
TWS	terrestrial water storage
UTH	upper tropospheric (relative) humidity
UV	ultraviolet
VOC	volatile organic compound
VOD	vegetation optical depth
VODCA	vegetation optical depth Climate Archive
WGMS	World Glacier Monitoring Service
WMO	World Meteorological Organization
WV	water vapor

APPENDIX 2: Supplemental Material

2b1 Surface air temperature

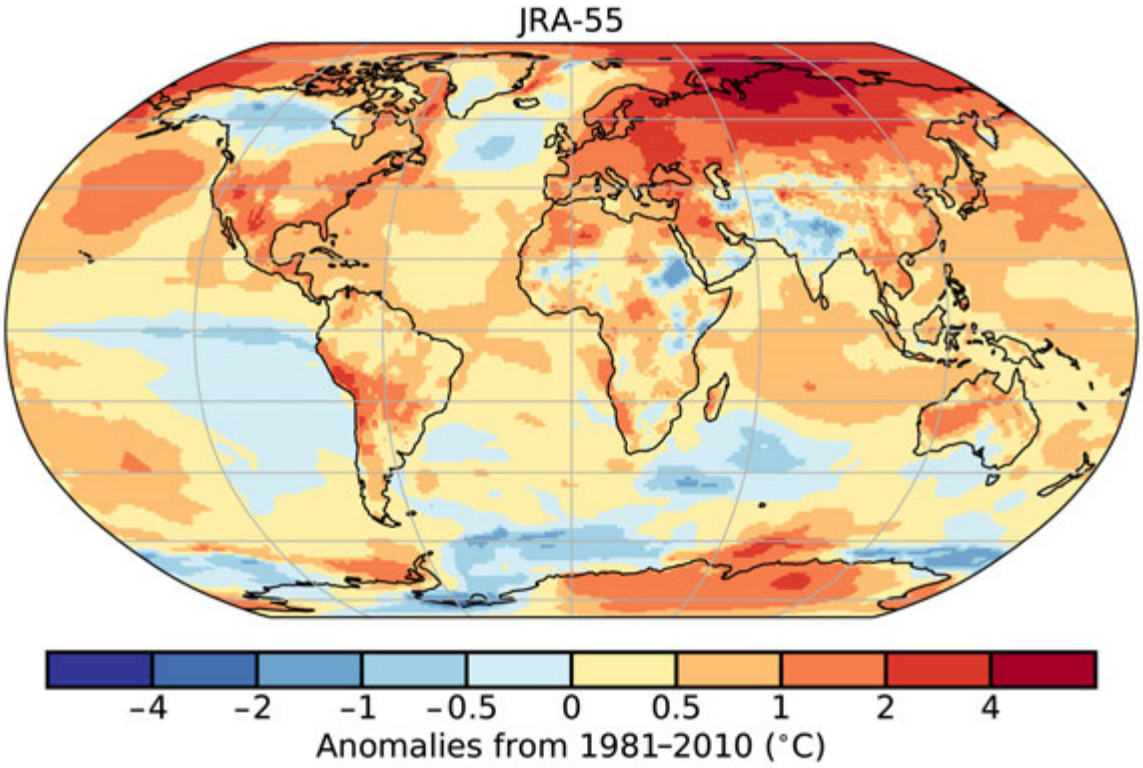

Fig. A2.1. Global 2-m surface temperature anomalies (°C; 1981–2010 base period). (Source: JRA-55.)

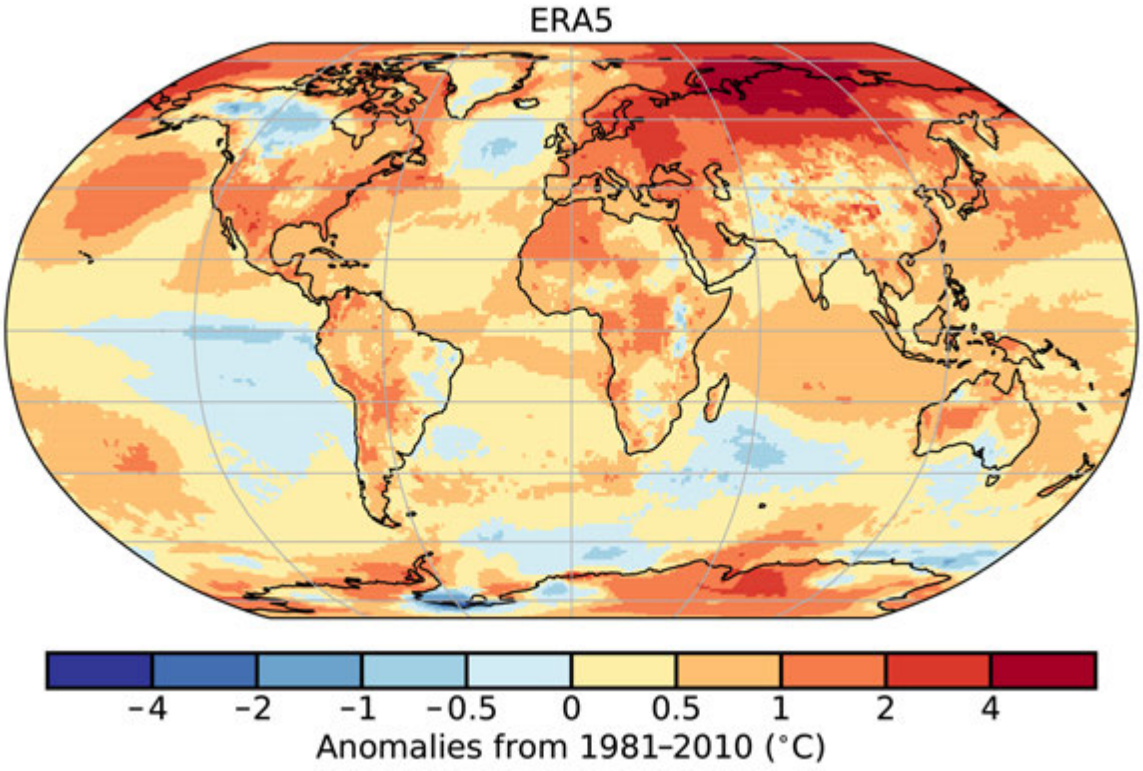

Fig. A2.2. Global 2-m surface temperature anomalies (°C; 1981–2010 base period). (Source: ERA5.)

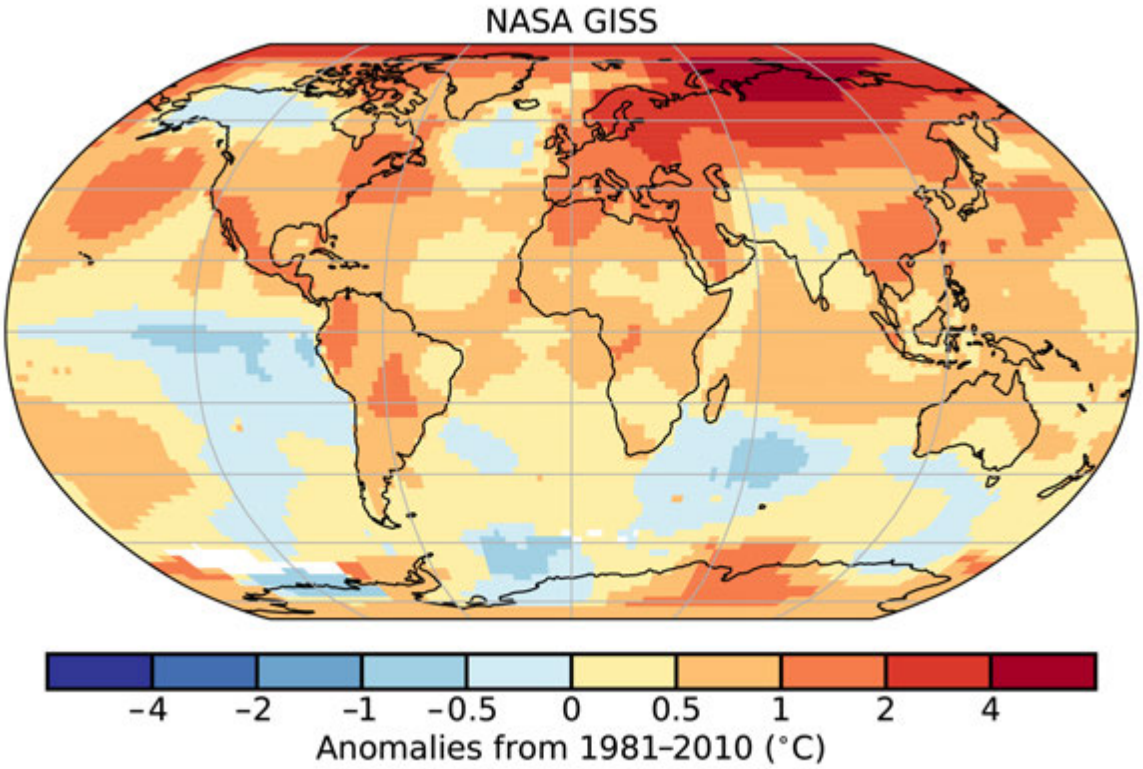

Fig. A2.3. Global surface temperature anomalies (°C; 1981–2010 base period). (Source: NASA GISS.)

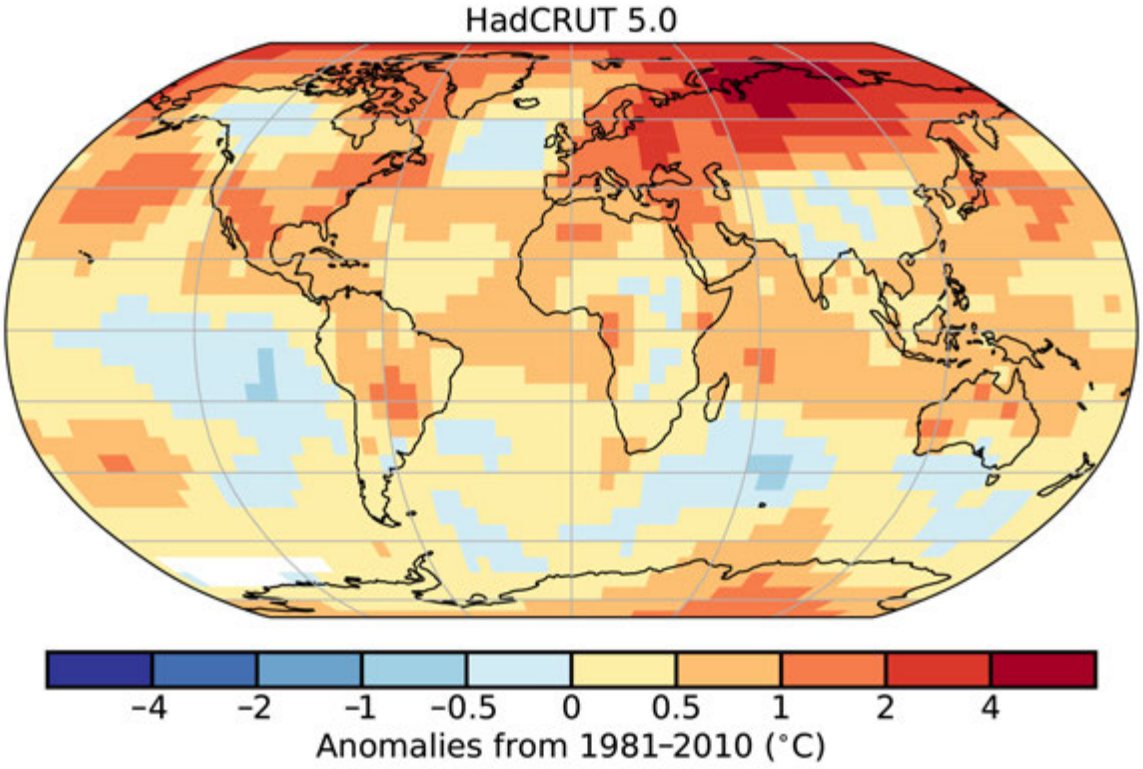

Fig. A2.4. Global surface temperature anomalies (°C; 1981–2010 base period). (Source: HadCRUT5.)

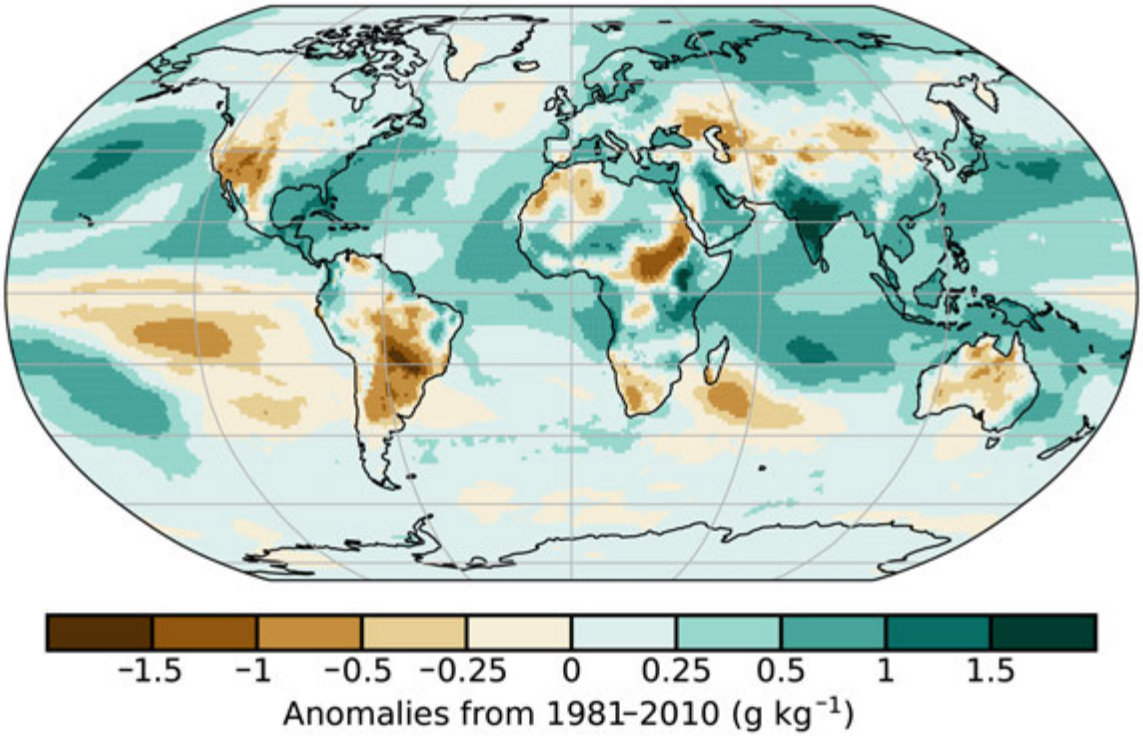

Fig. A2.5. Specific humidity annual average anomaly (g kg^{-1}; base period 1981–2010) (Source: ERA5.)

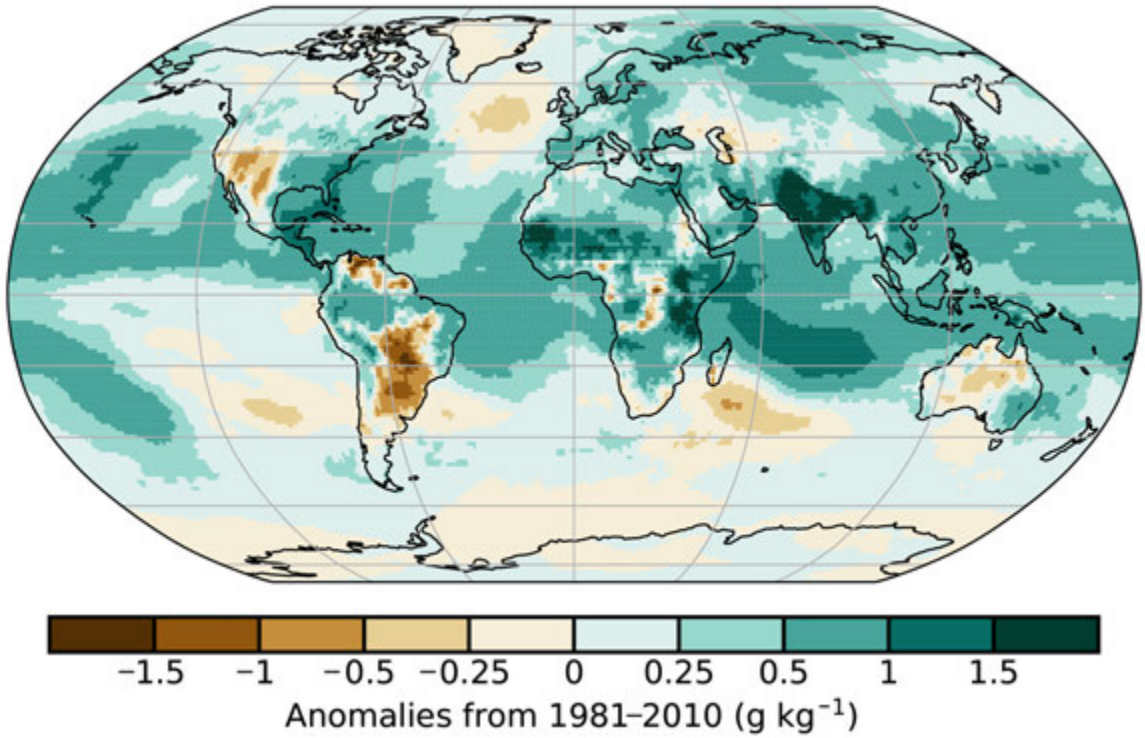

Fig. A2.6. Specific humidity annual average anomaly (g kg^{-1}; base period 1981–2010) (Source: MERRA-2.)

Section 2d2 Total column water vapor

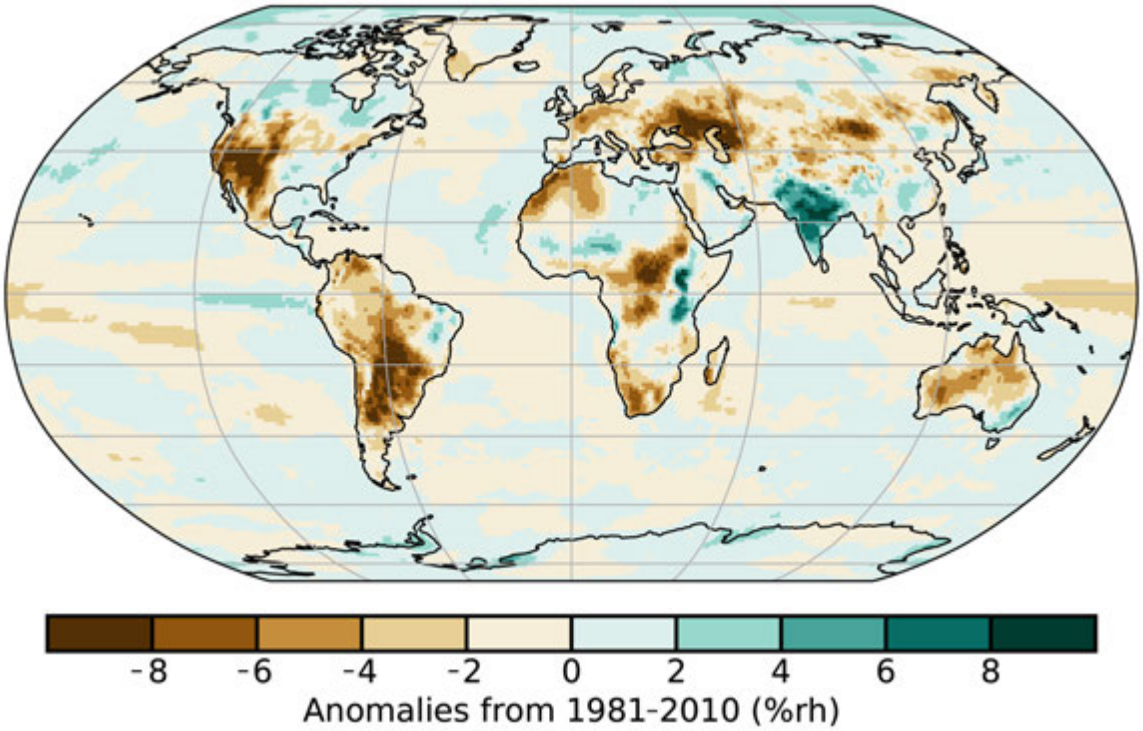

Fig. A2.7. Relative humidity annual average anomaly (%rh; base period 1981–2010) (Source: ERA5.)

Section 2d3 Upper tropospheric humidity

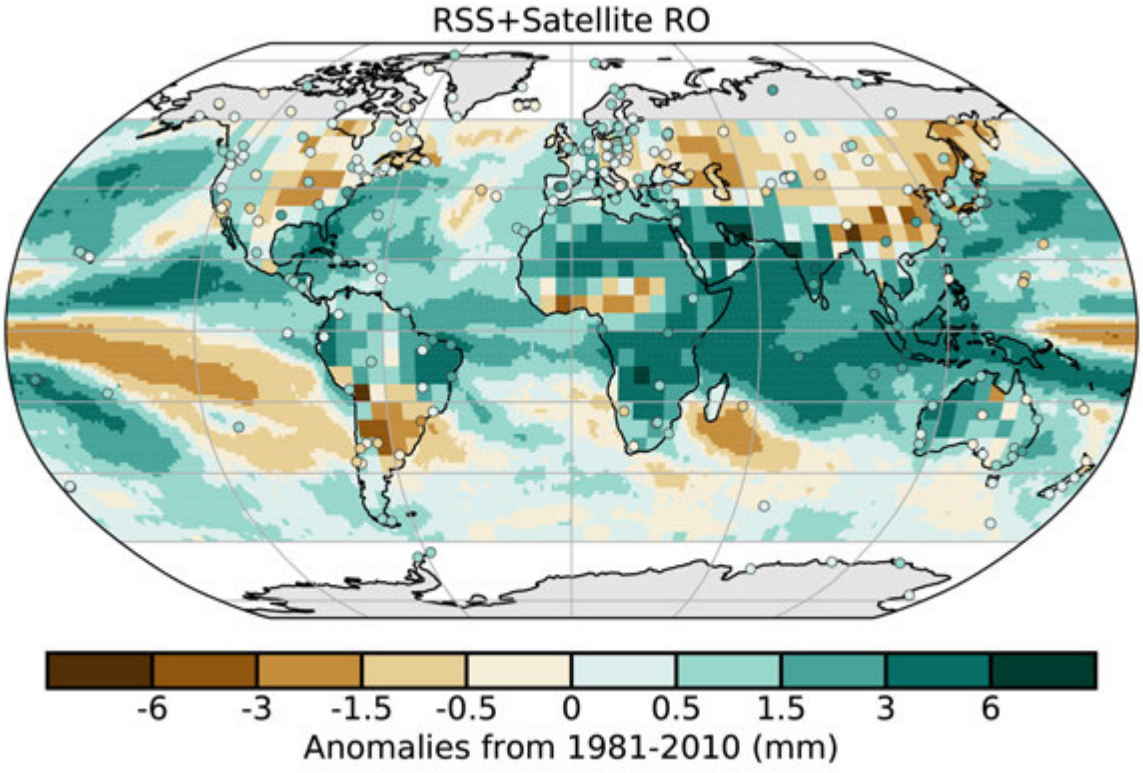

Fig. A2.8. Annual average TCWV anomalies (mm; 1981–2010 base period). The data are from satellite radiometers over the oceans (RSS) and from satellite RO over land. Data from GNSS stations are plotted as filled circles.

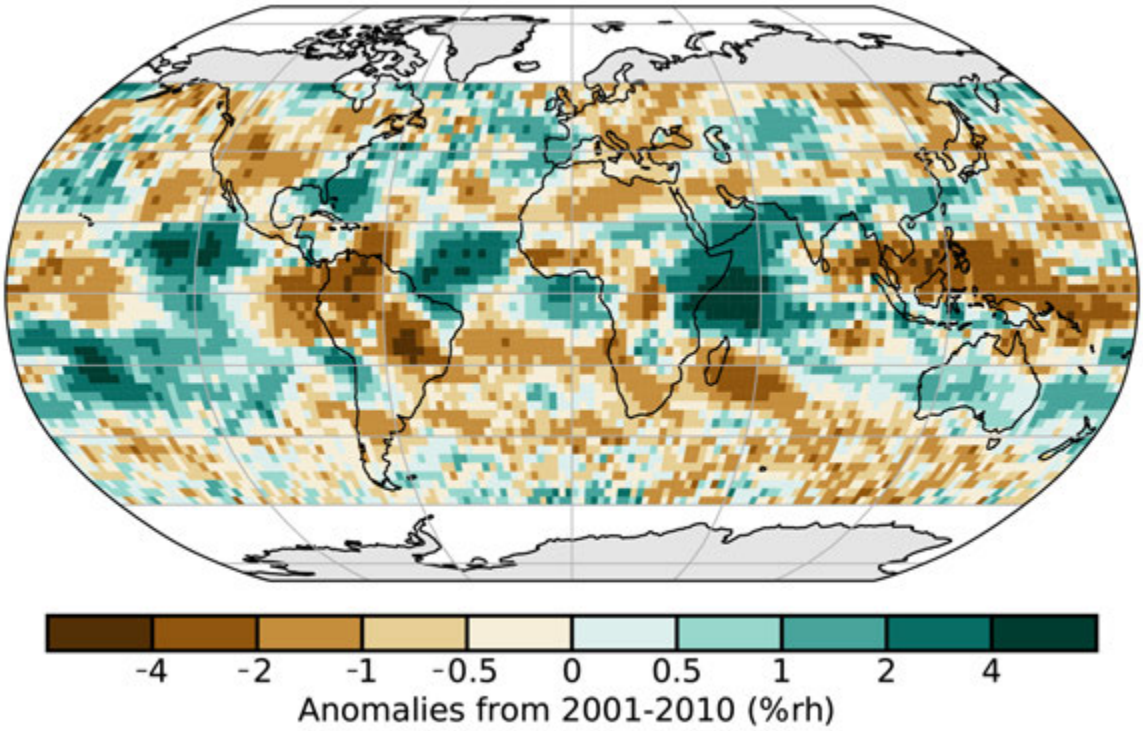

Fig. A2.9. Annual average UTH anomalies (%rh; 2001–10 base period) (Source: HIRS UTH dataset.)

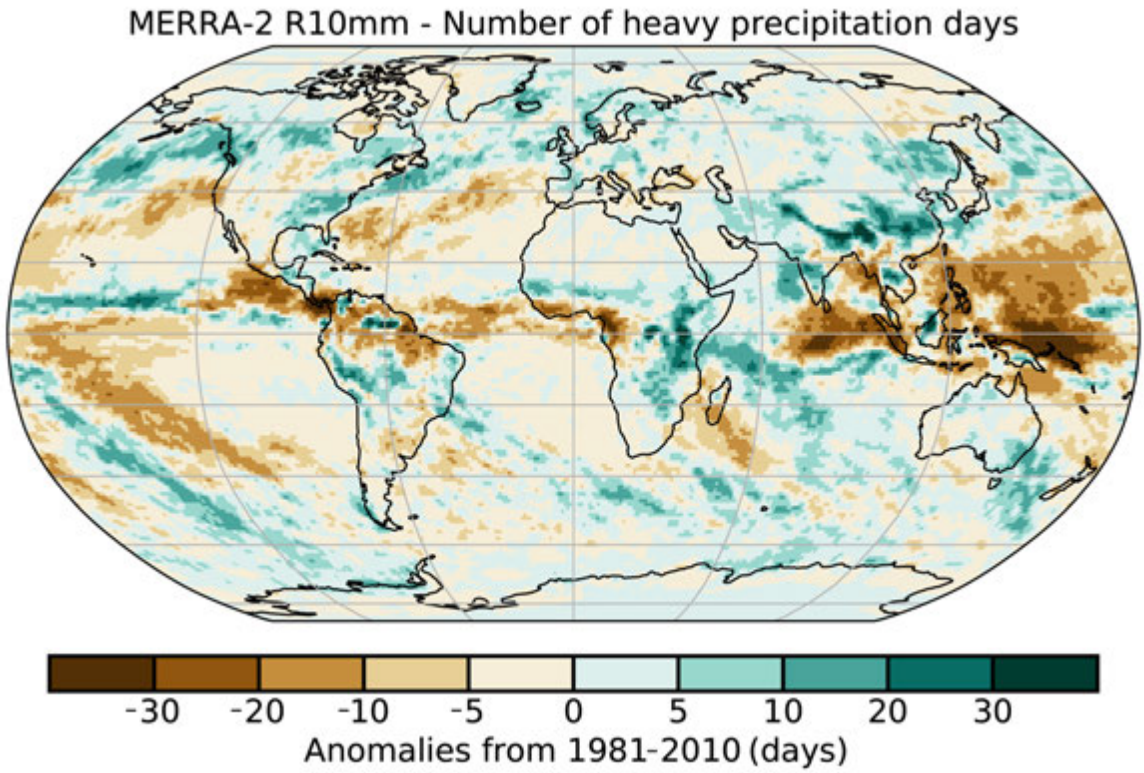

Fig. A2.10a.

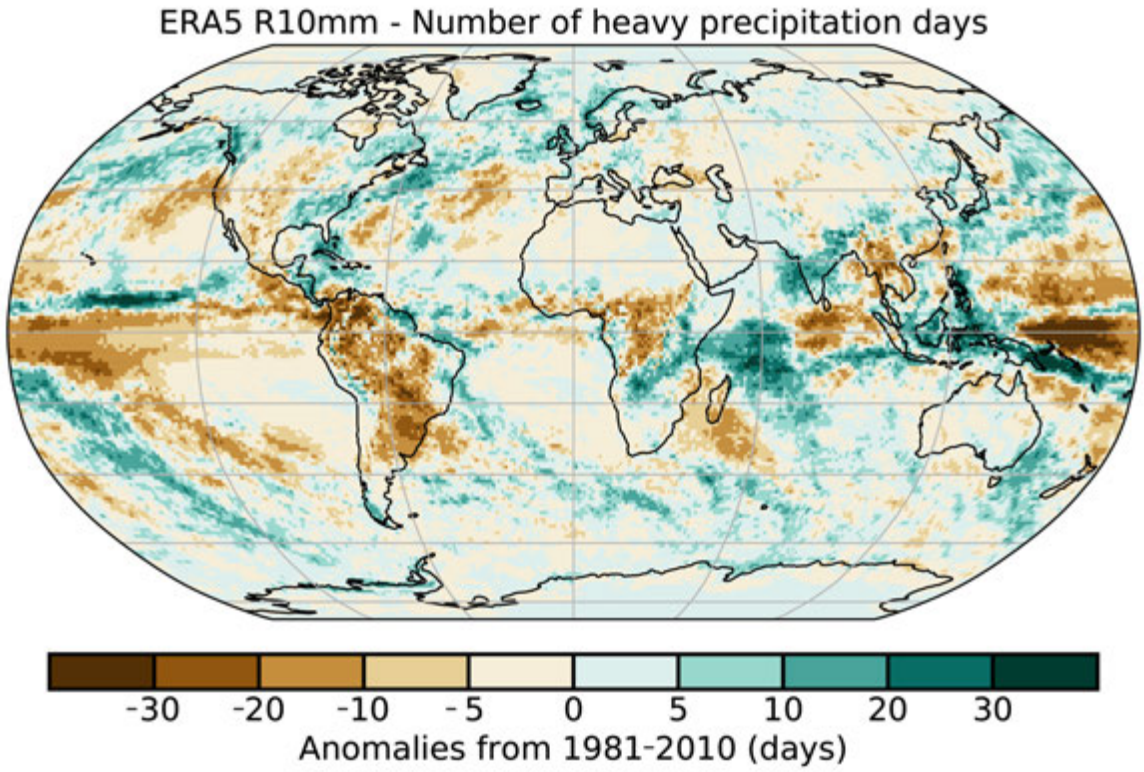

Fig. A2.10b.

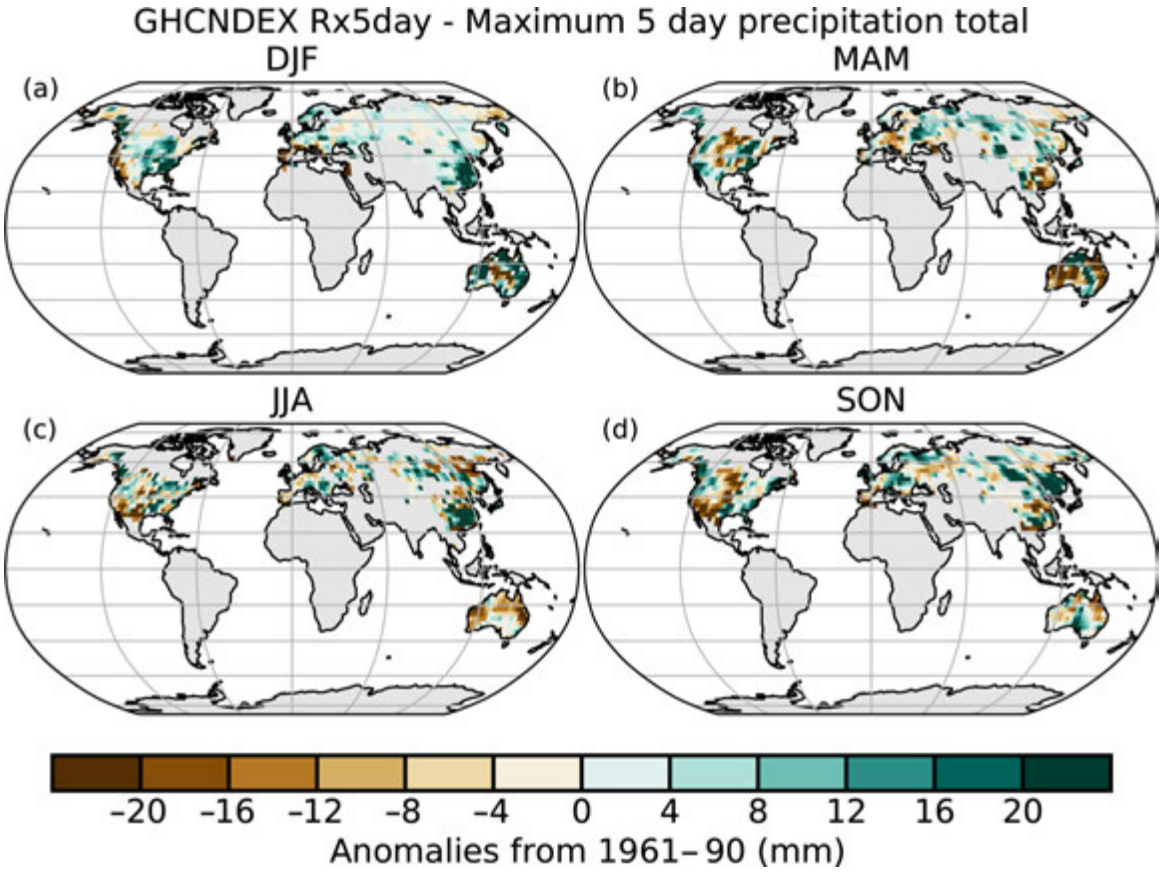

Fig. A2.10c.

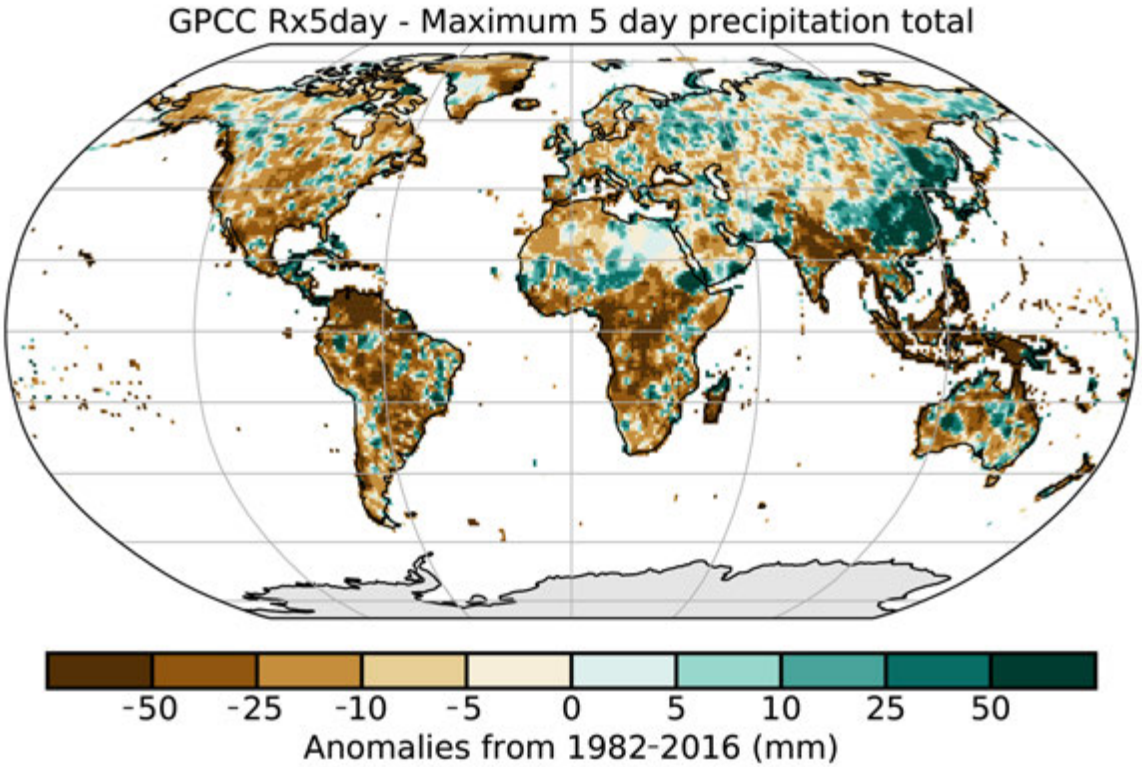

Fig. A2.10d. Anomalies of 2020 indices relative to a 1981–2010 base period for R10mm (days) derived from (a) MERRA-2 (Gelaro et al. 2017) and (b) ERA5 (Hersbach et al. 2020); Rx5day (mm) derived (c[a–d]) seasonally relative to a 1961–1990 base period from GHCNDEX (Donat et al. 2013) and (d) annually relative to a 1982–2016 base period from GPCC (Schamm et al. 2013).

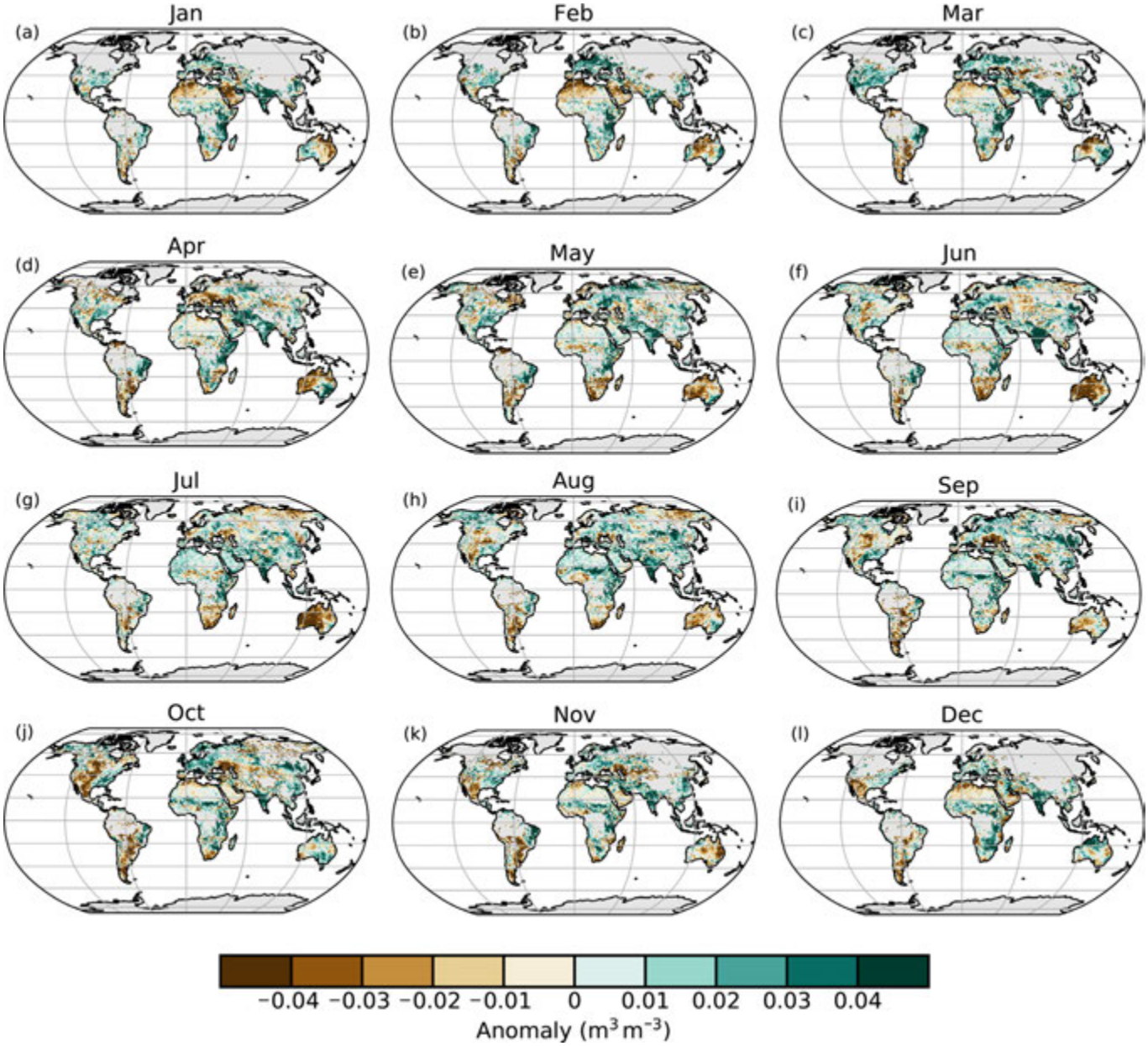

Fig. A2.11. (a–l) Monthly average soil moisture anomalies for 2020 ($m^3\ m^{-3}$; 1991–2010 base period). Data are masked where no retrieval is possible or where the quality is not assured and flagged due to dense vegetation, frozen soil, radio frequency interference, etc. (Source: ESA CCI Soil Moisture.)

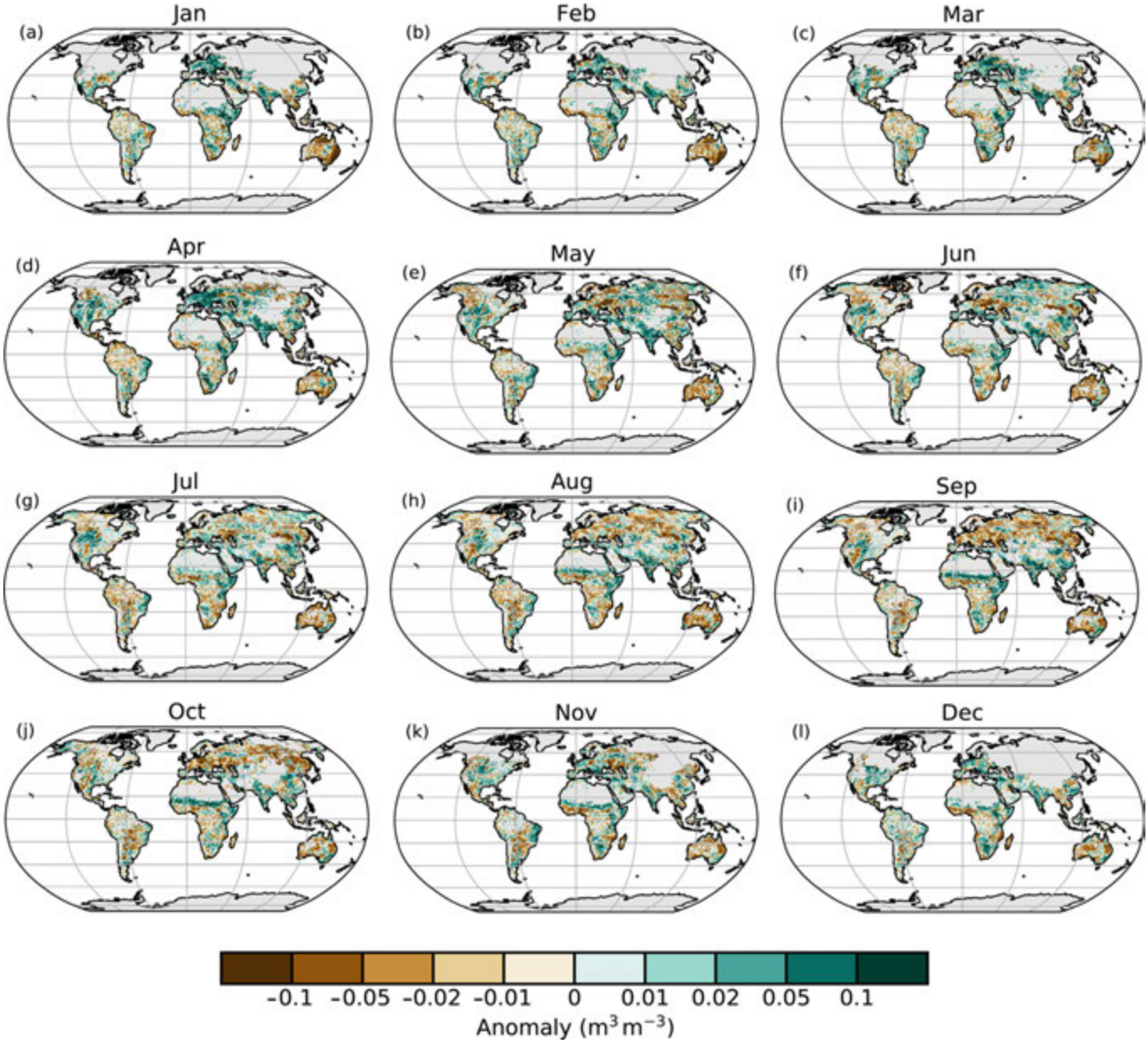

Fig. A2.12. (a–l) Monthly global Ku-band VOD anomalies (unitless; 1991–2010 reference period). High values indicate favorable vegetation conditions, and low values indicate lower vegetation activity than normal. Data are masked where no retrieval is possible due to sparse vegetation or frozen soils/snow cover. (Source: VODCA.)

References

Adler, R., and Coauthors, 2018: The Global Precipitation Climatology Project (GPCP) monthly analysis (new version 2.3) and a review of 2017 global precipitation. *Atmosphere*, **9**, 138, https://doi.org/10.3390/atmos9040138.

Alden, C. B., J. B. Miller, and J. W. C. White, 2010: Can bottom-up ocean CO_2 fluxes be reconciled with atmospheric ^{13}C observations? *Tellus*, **62B**, 369–388, https://doi.org/10.1111/j.1600-0889.2010.00481.x.

Alexander, L. V., M. Bador, R. Roca, S. Contractor, M. G. Donat, and P. L. Nguyen, 2020: Intercomparison of annual precipitation indices and extremes over global land areas from in situ, space-based and reanalysis products. *Environ. Res. Lett.*, **15**, 055002, https://doi.org/10.1088/1748-9326/ab79e2.

Allan, R. J., and R. D. D'Arrigo, 1999: 'Persistent' ENSO sequences: How unusual was the 1990-1995 El Niño? *Holocene*, **9**, 101–118, https://doi.org/10.1191/095968399669125102.

——, J. Gergis, and R. D. D'Arrigo, 2019: Placing the 2014–2016 'protracted' El Niño episode into a long-term context. *Holocene*, **30**, 90–105, https://doi.org/10.1177/0959683619875788.

Allan, R. P., K. P. Shine, A. Slingo, and J. A. Pamment, 1999: The dependence of clear-sky outgoing longwave radiation on surface temperature and relative humidity. *Quart. J. Roy. Meteor. Soc.*, **125**, 2103–2126, https://doi.org/10.1002/qj.49712555809.

Allchin, M. I., and S. J. Dery, 2020: The climatolgic context of trends in the onset of Northern Hemisphere seasonal snow cover, 1972–2017. *J. Geophys. Res. Atmos.*, **125**, e2019JD032367, https://doi.org/10.1029/2019JD032367.

Alvarez-Garreton, C., J. P. Boisier, R. Garreaud, J. Seibert, and M. Vis, 2021: Progressive water deficits during multiyear droughts in basins with long hydrological memory in Chile. Hydrol. *Earth Syst. Sci.*, **25**, 429–446, https://doi.org/10.5194/hess-25-429-2021.

Anabalón, A., and A. Sharma, 2017: On the divergence of potential and actual evapotranspiration trends: An assessment across alternate global datasets. *Earth's Future*, **5**, 905–917, https://doi.org/10.1002/2016EF000499.

Andela, N., and Coauthors, 2017: A human-driven decline in global burned area. *Science*, **356**, 1356–1362, https://doi.org/10.1126/science.aal4108.

Anderson, M. C., and Coauthors, 2011: Mapping daily evapotranspiration at field to continental scales using geostationary and polar orbiting satellite imagery. *Hydrol. Earth Syst. Sci.*, **15**, 223–239, https://doi.org/10.5194/hess-15-223-2011.

Andersson, S. M., and Coauthors, 2015: Significant radiative impact of volcanic aerosol in the lowermost stratosphere. *Nat. Commun.*, **6**, 7692, https://doi.org/10.1038/ncomms8692.

Andreassen, L., 2020: Glaciological investigations in Norway 2019. NVE Fakta 2/2020, 4 pp., http://publikasjoner.nve.no/faktaark/2020/faktaark2020_02.pdf.

Anstey, J., T. Banyard, N. Butchart, L. Coy, P. Newman, S. Osprey, and C. Wright, 2020: Quasi-biennial oscillation disrupted by abnormal Southern Hemisphere stratosphere. Research Square, accessed 19 January 2021, https://doi.org/10.21203/rs.3.rs-86860/v1.

——, ——, ——, ——, ——, ——, and ——, 2021: Prospect of increased disruption to the QBO in a changing climate. *Geophys. Res. Lett.*, https://doi.org/10.1029/2021GL093058, in press.

Archibald, A. T., and Coauthors, 2020: Tropospheric Ozone Assessment Report: A critical review of changes in the tropospheric ozone burden and budget from 1850 to 2100. *Elem. Sci. Anthropocene*, **8**, 034, https://doi.org/10.1525/elementa.2020.034.

Arenson, L., M. Hoelzle, and S. Springman, 2002: Borehole deformation measurements and internal structure of some rock glaciers in Switzerland. *Permafrost Periglacial Processes*, **13**, 117–135, https://doi.org/10.1002/ppp.414.

Arguez, A., and Coauthors, 2020: Should we expect each year in the next decade (2019–28) to be ranked among the top 10 warmest years globally? *Bull. Amer. Meteor. Soc.*, **101**, E655–E663, https://doi.org/10.1175/BAMS-D-19-0215.1.

Arosio, C., A. Rozanov, E. Malinina, M. Weber, and J. P. Burrows, 2019: Merging of ozone profiles from SCIAMACHY, OMPS and SAGE II observations to study stratospheric ozone changes. *Atmos. Meas. Tech.*, **12**, 2423–2444, https://doi.org/10.5194/amt-12-2423-2019.

Ashok, K., and T. Yamagata, 2009: The El Niño with a difference. *Nature*, **461**, 481–484, https://doi.org/10.1038/461481a.

——, S. K. Behera, S. A. Rao, H. Weng, and T. Yamagata, 2007: El Niño Modoki and its possible teleconnection. *J. Geophys. Res.*, **112**, C11007, https://doi.org/10.1029/2006JC003798.

Augustine, J. A., K. O. Lantz, J.-P. Vernier, and H. Telg, 2020: Mauna Loa clear-sky "apparent" solar transmission [in "State of the Climate in 2019"]. *Bull. Amer. Meteor. Soc.*, **101** (8), S61–S62, https://doi.org/10.1175/BAMS-D-20-0104.1.

Azorin-Molina, C., S. Rehman, J. A. Guijarro, T. R. McVicar, L. Minola, D. Chen, and S. M. Vicente-Serrano, 2018a: Recent trends in wind speed across Saudi Arabia, 1978-2013: A break in the stilling. *Int. J. Climatol.*, **38**, e966–e984, https://doi.org/10.1002/joc.5423.

——, J. Asin, T. R. McVicar, L. Minola, J. I. Lopez-Moreno, S. M. Vicente-Serrano, and D. Chen, 2018b: Evaluating anemometer drift: A statistical approach to correct biases in wind speed measurement. *Atmos. Res.*, **203**, 175–188, https://doi.org/10.1016/j.atmosres.2017.12.010.

——, R. J. H. Dunn, L. Ricciardulli, C. A. Mears, T. R. McVicar, J. P. Nicolas, G. P. Compo, and C. A. Smith, 2020: [Land and ocean surface winds [in "State of the Climate in 2019"]. *Bull. Amer. Meteor. Soc.*, **101** (8), S63–S65, https://doi.org/10.1175/BAMS-D-20-0104.1.

Ball, W. T., and Coauthors, 2018: Evidence for a continuous decline in lower stratospheric ozone offsetting ozone layer recovery. *Atmos. Chem. Phys.*, **18**, 1379–1394, https://doi.org/10.5194/acp-18-1379-2018.

Ballantyne, A. P., C. B. Alden, J. B. Miller, P. P. Tans, and J. W. C. White, 2012: Increase in observed net carbon dioxide uptake by land and oceans during the past 50 years. *Nature*, **488**, 70–72, https://doi.org/10.1038/nature11299.

Banzon, V., T. M. Smith, M. Steele, B. Huang, and H.-M. Zhang, 2020: Improved estimation of proxy sea surface temperature in the arctic. *J. Atmos. Oceanic Technol.*, **37**, 341–349, https://doi.org/10.1175/JTECH-D-19-0177.1.

Barichivich, J., T. J. Osborn, I. Harris, G. van der Schrier, and P. D. Jones, 2020: Global climate: Drought [in "State of the Climate in 2019"]. *Bull. Amer. Meteor. Soc.*, **101**, S59–S60, https://doi.org/10.1175/BAMS-D-20-0104.1.

Barnes, E. A., A. M. Fiore, and L. W. Horowitz, 2016: Detection of trends in surface ozone in the presence of climate variability. *J. Geophys. Res. Atmos.*, **121**, 6112–6129, https://doi.org/10.1002/2015JD024397.

Becker, A., P. Finger, A. Meyer-Christoffer, B. Rudolf, K. Schamm, U. Schneider, and M. Ziese, 2013: A description of the global land-surface precipitation data products of the Global Precipitation Climatology Centre with sample applications including centennial (trend) analysis from 1901–present. *Earth Syst. Sci. Data*, **5**, 71–99, https://doi.org/10.5194/essd-5-71-2013.

Becker, F., and B. J. Choudhury, 1988: Relative sensitivity of normalized difference vegetation index (NDVI) and microwave polarization difference Index (MPDI) for vegetation and desertification monitoring. *Remote Sens. Environ.*, **24**, 297–311, https://doi.org/10.1016/0034-4257(88)90031-4.

Bell, B., and Coauthors, 2020: ERA5 hourly data on pressure levels from 1950 to 1978 (preliminary version). Copernicus Climate Change Service (C3S) Climate Data Store (CDS), accessed 2 February 2021, https://cds.climate.copernicus.eu/cdsapp#!/dataset/reanalysis-era5-pressure-levels-preliminary-back-extension?tab=overview.

Bellouin, N., and Coauthors, 2020: Radiative forcing of climate change from the Copernicus reanalysis of atmospheric composition. *Earth Syst. Sci. Data*, **12**, 1649–1677, https://doi.org/10.5194/essd-12-1649-2020.

Benson, B., J. Magnuson, and S. Sharma, 2000: Global Lake and River Ice Phenology Database, Version 1. National Snow and Ice Data Center, accessed 8 January 2021, https://doi.org/10.7265/N5W66HP8.

——, and Coauthors, 2012: Extreme events, trends, and variability in Northern Hemisphere lake-ice phenology (1855–2005). *Climatic Change*, **112**, 299–323, https://doi.org/10.1007/s10584-011-0212-8.

Berry, D. I., E. C. Kent, and P. K. Taylor, 2004: An analytical model of heating errors in marine air temperatures from ships. *J. Atmos. Oceanic Technol.*, **21**, 1198–1215, https://doi.org/10.1175/1520-0426(2004)021<1198:AAMOHE>2.0.CO;2.

Betts, R. A., C. D. Jones, J. R. Knight, R. F. Keeling, and J. J. Kennedy, 2016: El Niño and a record CO_2 rise. *Nat. Climate Change*, **6**, 806–810, https://doi.org/10.1038/nclimate3063.

Biskaborn, B. K., and Coauthors, 2019: Permafrost is warming at a global scale. *Nat. Commun.*, **10**, 264, https://doi.org/10.1038/s41467-018-08240-4.

Blenkinsop, S., M. R. Tye, M. Bosilovich, M. G. Donat, I. Durre, A. J. Simmons, and M. Ziese, 2020: Land surface precipitation extremes [in "State of the Climate in 2019"]. *Bull. Amer. Meteor. Soc.*, **101** (8), S47–S49, https://doi.org/10.1175/BAMS-D-20-0104.1.

Bloom, A. A., and Coauthors, 2017: A global wetland methane emissions and uncertainty dataset for atmospheric chemical transport models (WetCHARTs version 1.0). *Geosci. Model Dev.*, **10**, 2141–2156, https://doi.org/10.5194/gmd-10-2141-2017.

Blunden, J., and D. S. Arndt, 2019: State of the Climate in 2018. *Bull. Amer. Meteor. Soc.*, **100** (9), Si–S306, https://doi.org/10.1175/2019BAMSStateoftheClimate.1.

Bock, O., 2020: Global GNSS integrated water vapour data, 1994-2020 [Data set]. AERIS, accessed 21 July 2021, https://doi.org/10.25326/68.

Bodhaine, B. A., B. G. Mendonca, J. M. Harris, and J. M. Miller, 1981: Seasonal variations in aerosols and atmospheric transmission at Mauna Loa Observatory. *J. Geophys. Res.*, **86**, 7395–7398, https://doi.org/10.1029/JC086iC08p07395.

Bodin, X., E. Thibert, D. Fabre, A. Ribolini, P. Schoeneich, B. Francou, and M. Fort, 2009: Two decades of responses (1986–2006) to climate by the Laurichard rock glacier, French Alps. *Permafrost Periglacial Processes*, **20**, 331–344, https://doi.org/10.1002/ppp.665.

BoM, 2020a: Monthly Weather Review Australia. Bureau of Meteorology, www.bom.gov.au/climate/mwr/aus/mwr-aus-202001.pdf.

——, 2020b: Annual climate statement 2020. Bureau of Meteorology, 27 pp., www.bom.gov.au/climate/current/annual/aus/.

——, 2021a: Climate monitoring graphs. Bureau of Meteorology, www.bom.gov.au/climate/enso/indices.shtml?bookmark=iod.

——, 2021b: Recent and historical rainfall maps. Bureau of Meteorology, www.bom.gov.au/climate/maps/rainfall/?variable=rainfall&map=anomaly&period=3month&region=nat&year=2020&month=12&day=31.

Bony, S., and Coauthors, 2015: Clouds, circulation and climate sensitivity. *Nat. Geosci.*, **8**, 261–268, https://doi.org/10.1038/ngeo2398.

Boucher, O., and Coauthors: Clouds and aerosols. *Climate Change 2013: The Physical Science Basis*, T. F. Stocker et al., Eds., Cambridge University Press, 571–657, https://doi.org/10.1017/CBO9781107415324.016.

Bowman, D. M. J. S., G. J. Williamson, O. F. Price, M. N. Ndalila, and R. A. Bradstock, 2021: Australian forests, megafires and the risk of dwindling carbon stocks. *Plant Cell Environ.*, **44**, 347–355, https://doi.org/10.1111/pce.13916.

BP Statistical Review of the World Energy, 2021:https://www.bp.com/content/dam/bp/business-sites/en/global/corporate/pdfs/energy-economics/statistical-review/bp-stats-review-2021-co2-emissions.pdf

Brohan, P., J. J. Kennedy, I. Harris, S. F. Tett, and P. D. Jones, 2006: Uncertainty estimates in regional and global observed temperature changes: A new data set from 1850. *J. Geophys. Res.*, **111**, D12106, https://doi.org/10.1029/2005JD006548.

Broomandi, P., F. Karaca, A. Nikfal, A. Jahanbakhshi, M. Tamjidi, and J. R. Kim, 2020: Impact of COVID-19 event on the air quality in Iran. *Aerosol Air Qual. Res.*, **20**, 1793–1804, https://doi.org/10.4209/aaqr.2020.05.0205.

Brutsaert, W., 2017: Global land surface evaporation trend during the past half century: Corroboration by Clausius-Clapeyron scaling. *Adv. Water Resour.*, **106**, 3–5, https://doi.org/10.1016/j.advwatres.2016.08.014.

Buchli, T., A. Kos, P. Limpach, K. Merz, X. Zhou, and S. M. Springman, 2018: Kinematic investigations on the Furggwanghorn Rock Glacier, Switzerland. *Permafrost Periglacial Processes*, **29**, 3–20, https://doi.org/10.1002/ppp.1968.

Byrne, M. P., and P. A. O'Gorman, 2013: Link between land-ocean warming contrast and surface relative humidities in simulations with coupled climate models. *Geophys. Res. Lett.*, **40**, 5223–5227, https://doi.org/10.1002/grl.50971.

——, and ——, 2016: Understanding decreases in land relative humidity with global warming: Conceptual model and GCM simulations. *J. Climate*, **29**, 9045–9061, https://doi.org/10.1175/JCLI-D-16-0351.1.

——, and ——, 2018: Trends in continental temperature and humidity directly linked to ocean warming. *Proc. Natl. Acad. Sci. USA*, **115**, 4863–4868, https://doi.org/10.1073/pnas.1722312115.

Calvo, N., R. R. Garcia, W. J. Randel, and D. R. Marsh, 2010: Dynamical mechanism for the increase in tropical upwelling in the lowermost tropical stratosphere during warm ENSO events. *J. Atmos. Sci.*, **67**, 2331–2340, https://doi.org/10.1175/2010JAS3433.1.

Capotondi, A., and Coauthors, 2015: Understanding ENSO diversity. *Bull. Amer. Meteor. Soc.*, **96**, 921–938, https://doi.org/10.1175/BAMS-D-13-00117.1.

Carpenter, L. J., and Coauthors, 2018: Scenarios and information for policy makers. Scientific Assessment of Ozone Depletion: 2018, Global Ozone Research and Monitoring Project Rep. 58, 6.1–6.69, https://ozone.unep.org/sites/default/files/2019-05/SAP-2018-Assessment-report.pdf.

Carrea, L., O. Embury, and C. J. Merchant, 2015: Datasets related to in-land water for limnology and remote sensing applications: Distance-to-land, distance-to-water, water-body identifier and lake-centre co-ordinates. *Geosci. Data J.*, **2**, 83–97, https://doi.org/10.1002/gdj3.32.

——, and Coauthors, 2019: Lake surface temperature [in "State of the Climate in 2018"]. *Bull. Amer. Meteor. Soc.*, **100**, S13–S14, https://doi.org/10.1175/2019BAMSStateoftheClimate.1.

——, and Coauthors, 2020: Lake surface temperature [in "State of the Climate in 2019"]. *Bull. Amer. Meteor. Soc.*, **101** (8), S26–S28, https://doi.org/10.1175/BAMS-D-20-0104.1.

Cescatti, A., and Coauthors, 2012: Intercomparison of MODIS albedo retrievals and in situ measurements across the global FLUXNET network. *Remote Sens. Environ.*, **121**, 323–334, https://doi.org/10.1016/j.rse.2012.02.019.

Chandra, S., J. R. Ziemke, W. Min, and W. G. Read, 1998: Effects of 1997-1998 El Niño on tropospheric ozone and water vapor. *Geophys. Res. Lett.*, **25**, 3867–3870, https://doi.org/10.1029/98GL02695.

——, ——, B. N. Duncan, T. L. Diehl, N. Livesey, and L. Froidevaux, 2009: Effects of the 2006 El Niño on tropospheric ozone and carbon monoxide: Implications for dynamics and biomass burning. *Atmos. Chem. Phys.*, **9**, 4239–4249, https://doi.org/10.5194/acp-9-4239-2009.

Chang, J., and Coauthors, 2019: Revisiting enteric methane emissions from domestic ruminants and their $\delta^{13}C_{CH4}$ source signature. *Nat. Commun.*, **10**, 3420, https://doi.org/10.1038/s41467-019-11066-3.

Chaparro, D., M. Piles, M. Vall-llossera, A. Camps, A. G. Konings, and D. Entekhabi, 2018: L-band vegetation optical depth seasonal metrics for crop yield assessment. *Remote Sens. Environ.*, **212**, 249–259, https://doi.org/10.1016/j.rse.2018.04.049.

——, G. Duveiller, M. Piles, A. Cescatti, M. Vall-llossera, A. Camps, and D. Entekhabi, 2019: Sensitivity of L-band vegetation optical depth to carbon stocks in tropical forests: A comparison to higher frequencies and optical indices. *Remote Sens. Environ.*, **232**, 111303, https://doi.org/10.1016/j.rse.2019.111303.

Chen, C., and Coauthors, 2019: China and India lead in greening of the world through land-use management. *Nat. Sustainability*, **2**, 122–129, https://doi.org/10.1038/s41893-019-0220-7.

Chen, X., S. Jeong, H. Park, J. Kim, and C.-R. Park, 2020: Urbanization has stronger impacts than regional climate change on wind stilling: A lesson from South Korea. *Environ. Res. Lett.*, **15**, 054016, https://doi.org/10.1088/1748-9326/ab7e51.

Cheng, L., and Coauthors, 2017: Recent increases in terrestrial carbon uptake at little cost to the water cycle. *Nat. Commun.*, **8**, 110, https://doi.org/10.1038/s41467-017-00114-5.

Chipperfield, M. P., and Coauthors, 2018: On the cause of recent variations in lower stratospheric ozone. *Geophys. Res. Lett.*, **45**, 5718–5726, https://doi.org/10.1029/2018GL078071.

Christiansen, H. H., G. L. Gilbert, U. Neumann, N. Demidov, M. Guglielmin, K. Isaksen, M. Osuch, and J. Boike, 2021: Ground ice content, drilling methods and equipment and permafrost dynamics in Svalbard 2016–2019 (PermaSval). SESS Report 2020, M. Moreno-Ibáñez et al., Eds., Svalbard Integrated Arctic Earth Observing System, 259–275.

Christy, J. R., and R. T. McNider, 2017: Satellite bulk tropospheric temperatures as a metric for climate sensitivity. Asia-Pacific *J. Atmos. Sci.*, **53**, 511–518, https://doi.org/10.1007/s13143-017-0070-z.

——, D. E. Parker, S. J. Brown, I. Macadam, M. Stendel, and W. B. Norris, 2001: Differential trends in tropical sea surface and atmospheric temperatures since 1979. *Geophys. Res. Lett.*, **28**, 183–186, https://doi.org/10.1029/2000GL011167.

——, R. W. Spencer, W. D. Braswell, and R. Junod, 2018: Examination of space-based bulk atmospheric temperatures for climate research. *Yaogan Xuebao*, **39**, 3580–3607, https://doi.org/10.1080/01431161.2018.1444293.

——, C. A. Mears, S. Po-Chedley, and L. Haimberger, 2020: Tropospheric temperature [in "State of the Climate in 2019"]. *Bull. Amer. Meteor. Soc.*, **101** (8), S30–S31, https://doi.org/10.1175/BAMS-D-20-0104.1.

Chung, E.-S., B. Soden, and V. O. John, 2013: Intercalibrating microwave satellite observations for monitoring long-term variations in upper- and midtropospheric water vapor. *J. Atmos. Oceanic Technol.*, **30**, 2303–2319, https://doi.org/10.1175/JTECH-D-13-00001.1.

——, B. J. Soden, B. J. Sohn, and L. Shi, 2014: Upper-tropospheric moistening in response to anthropogenic warming. *Proc. Natl. Acad. Sci. USA*, **111**, 11 636–11 641, https://doi.org/10.1073/pnas.1409659111.

——, ——, X. Huang, L. Shi, and V. O. John, 2016: An assessment of the consistency between satellite measurements of upper tropospheric water vapor. *J. Geophys. Res. Atmos.*, **121**, 2874–2887, https://doi.org/10.1002/2015JD024496.

Cicoira, A., J. Beutel, J. Faillettaz, and A. Vieli, 2019: Water controls the seasonal rhythm of rock glacier flow. *Earth Planet. Sci. Lett.*, **528**, 115844, https://doi.org/10.1016/j.epsl.2019.115844.

City of Cape Town, 2021: Weekly water dashboard, 12 July 2021. 5 pp., https://resource.capetown.gov.za/documentcentre/Documents/City%20research%20reports%20and%20review/damlevels.pdf.

Coddington, O. M., 2017: TSIS Algorithm Theoretical Basis Document. Laboratory for Atmospheres and Space Physcis (LASP) Doc. No. 151430 RevA, 108 pp., https://docserver.gesdisc.eosdis.nasa.gov/public/project/TSIS/TSIS_Algorithm_Theoretical_Basis_Document_151430RevA.pdf.

Cohen, Y., and Coauthors, 2018: Climatology and long-term evolution of ozone and carbon monoxide in the upper troposphere–lower stratosphere (UTLS) at northern midlatitudes, as seen by IAGOS from 1995 to 2013. *Atmos. Chem. Phys.*, **18**, 5415–5453, https://doi.org/10.5194/acp-18-5415-2018.

Coldewey-Egbers, M., and Coauthors, 2015: The GOME-type Total Ozone Essential Climate Variable (GTO-ECV) data record from the ESA Climate Change Initiative. *Atmos. Meas. Tech.*, **8**, 3923–3940, https://doi.org/10.5194/amt-8-3923-2015.

Collinson, N., and T. Sparks, 2008: Phenology – nature's calendar: An overview of results from the UK phenology network. *Arboric. J.*, **30**, 271–278, https://doi.org/10.1080/03071375.2008.9747506.

Collow, A., M. Bosilovich, A. Dezfuli, and R. Lucchesi, 2020: File specification for MERRA-2 climate statistics products. GMAO Office Note 19 (Version 1.0), 15 pp., http://gmao.gsfc.nasa.gov/pubs/office_notes.

Cooper, O. R., and Coauthors, 2014: Global distribution and trends of tropospheric ozone: An observation-based review. *Elementa*, **2**, 000029, https://doi.org/10.12952/journal.elementa.000029.

——, and Coauthors, 2020: Multi-decadal surface ozone trends at globally distributed remote locations. *Elem. Sci. Anthropocene*, **8**, 23, https://doi.org/10.1525/elementa.420.

Copernicus Climate Change Service, 2021: Copernicus: 2020 warmest year on record for Europe; globally, 2020 ties with 2016 for warmest year recorded. 8 January, https://climate.copernicus.eu/2020-warmest-year-record-europe-globally-2020-ties-2016-warmest-year-recorded.

Cornes, R. C., E. C. Kent, D. I. Berry, and J. J. Kennedy, 2020: CLASSnmat: A global night marine air temperature data set, 1880–2019. *Geosci. Data J.*, **7**, 170–184, https://doi.org/10.1002/gdj3.100.

Cowtan, K., and Coauthors, 2015: Robust comparison of climate models with observations using blended land air and ocean sea surface temperatures. *Geophys. Res. Lett.*, **42**, 6526–6534, https://doi.org/10.1002/2015GL064888.

Cox, P. M., D. Pearson, B. B. Booth, P. Friedlingstein, C. Huntingford, C. D. Jones, and C. M. Luke, 2013: Sensitivity of tropical carbon to climate change constrained by carbon dioxide variability. *Nature*, **494**, 341–344, https://doi.org/10.1038/nature11882.

Coy, L., P. A. Newman, S. Pawson, and L. R. Lait, 2017: Dynamics of the disrupted 2015/16 Quasi-biennial oscillation. *J. Climate*, **30**, 5661–5674, https://doi.org/10.1175/JCLI-D-16-0663.1.

Crétaux, J.-F., and Coauthors, 2011: SOLS: A Lake database to monitor in Near Real Time water level and storage variations from remote sensing data. *J. Adv. Space Res.*, **47**, 1497–1507, https://doi.org/10.1016/j.asr.2011.01.004.

——, and Coauthors, 2018: Absolute calibration/validation of the altimeters on Sentinel-3A and Jason-3 over the Lake Issykkul. *Remote Sens.*, **10**, 1679, https://doi.org/10.3390/rs10111679.

Crocetti, L., and Coauthors, 2020: Earth observation for agricultural drought monitoring in the Pannonian Basin (southeastern Europe): Current state and future directions. *Reg. Environ. Change*, **20**, 123, https://doi.org/10.1007/s10113-020-01710-w.

Dameris, M., D. G. Loyola, M. Nützel, M. Coldewey-Egbers, C. Lerot, F. Romahn, and M. van Roozendael, 2021: Record low ozone values over the Arctic in boreal spring 2020. *Atmos. Chem. Phys.*, **21**, 617–633, https://doi.org/10.5194/acp-21-617-2021.

Daniel, J. S., S. Solomon, and D. L. Albritton, 1995: On the evaluation of halocarbon radiative forcing and global warming potentials. *J. Geophys. Res.*, **100**, 1271–1285, https://doi.org/10.1029/94JD02516.

Davidson, E. A., 2009: The contribution of manure and fertilizer nitrogen to atmospheric nitrous oxide since 1860. *Nat. Geosci.*, **2**, 659–662, https://doi.org/10.1038/ngeo608.

Davis, S. M., and Coauthors, 2016: The Stratospheric Water and Ozone Satellite Homogenized (SWOOSH) database: A long-term database for climate studies. *Earth Syst. Sci. Data*, **8**, 461–490, https://doi.org/10.5194/essd-8-461-2016.

Deeter, M. N., and Coauthors, 2014: The MOPITT Version 6 product: Algorithm enhancements and validation. *Atmos. Meas. Tech.*, **7**, 3623–3632, https://doi.org/10.5194/amt-7-3623-2014.

Delaloye, R., and Coauthors, 2008: Recent interannual variations of rock glacier creep in the European Alps. *Proc. of the 9th Int. Conf. on Permafrost*, Fairbanks, AK, University of Alaska Fairbanks, 343–348.

——, C. Lambiel, and I. Gärtner-Roer, 2010: Overview of rock glacier kinematics research in the Swiss Alps. *Geogr. Helv.*, **65**, 135–145, https://doi.org/10.5194/gh-65-135-2010.

——, C. Barboux, X. Bodin, A. Brenning, L. Hartl, Y. Hu, and A. Ikeda, 2018: Rock glacier inventories and kinematics: A new IPA Action Group. *5th European Conf. on Permafrost, Book of Abstracts*, Chamonix, France, Laboratoire EDYTEM, 392–393.

Deng, K., C. Azorin-Molina, L. Minola, G. Zhang, and D. Chen, 2021: Global near-surface wind speed changes over the last decades revealed by reanalyses and CMIP6 model simulations. *J. Climate*, **34**, 2219–2234, https://doi.org/10.1175/JCLI-D-20-0310.1.

Dewitte, S., D. Crommelynck, and A. Joukof, 2004: Total solar irradiance observations from DIARAD/VIRGO. *J. Geophys. Res.*, **109**, A02102, https://doi.org/10.1029/2002JA009694.

Di Girolamo, L., A. Menzies, G. Zhao, K. Mueller, C. Moroney, and D. J. Diner, 2010: Multi-angle imaging SpectroRadiometer level 3 cloud fraction by altitude algorithm theoretical basis document. JPL Publ., D-62358, 23 pp., https://eospso.nasa.gov/sites/default/files/atbd/MISR_CFBA_ATBD.pdf.

Dlugokencky, E. J., L. P. Steele, P. M. Lang, and K. A. Masarie, 1994: The growth rate and distribution of atmospheric methane. *J. Geophys. Res.*, **99**, 17 021–17 043, https://doi.org/10.1029/94JD01245.

——, S. Houweling, L. Bruhwiler, K. A. Masarie, P. M. Lang, J. B. Miller, and P. P. Tans, 2003: Atmospheric methane levels off: Temporary pause or a new steady-state? *Geophys. Res. Lett.*, **30**, 1992, https://doi.org/10.1029/2003GL018126.

Döll, P., and B. Lehner, 2002: Validation of a new global 30-min drainage direction map. *J. Hydrol.*, **258**, 214–231, https://doi.org/10.1016/S0022-1694(01)00565-0.

Donat, M., L. Alexander, H. Yang, I. Durre, R. Vose, and J. Caesar, 2013: Global land-based datasets for monitoring climatic extremes. *Bull. Amer. Meteor. Soc.*, **94**, 997–1006, https://doi.org/10.1175/BAMS-D-12-00109.1.

Dorigo, W. A., and Coauthors, 2017: ESA CCI Soil Moisture for improved Earth system understanding: State-of-the art and future directions. *Remote Sens. Environ.*, **203**, 185–215, https://doi.org/10.1016/j.rse.2017.07.001.

——, and Coauthors, 2021: Closing the water cycle from observations across scales: Where do we stand? *Bull. Amer. Meteor. Soc.*, https://doi.org/10.1175/BAMS-D-19-0316.1, in press.

Doumbia, T., and Coauthors, 2021: Changes in global air pollutant emissions during the COVID-19 pandemic: A dataset for atmospheric chemistry modeling. *Earth Syst. Sci. Data Discuss.*, https://doi.org/10.5194/essd-2020-348.

Du, H., and Coauthors, 2019: Precipitation from persistent extremes is increasing in most regions and globally. *Geophys. Res. Lett.*, **46**, 6041–6049, https://doi.org/10.1029/2019GL081898.

Dunn, R. J. H., 2019: HadISD version 3: Monthly updates. Hadley Centre Tech. Note 103, 10 pp., www.metoffice.gov.uk/research/library-and-archive/publications/science/climate-science-technical-notes.

——, K. M. Willett, P. W. Thorne, E. V. Woolley, I. Durre, A. Dai, D. E. Parker, and R. S. Vose, 2012: HadISD: A quality-controlled global synoptic report database for selected variables at long-term stations from 1973–2011. *Climate Past*, **8**, 1649–1679, https://doi.org/10.5194/cp-8-1649-2012.

——, ——, D. E. Parker, and L. Mitchell, 2016: Expanding HadISD: Quality-controlled, sub-daily station data from 1931. *Geosci. Instrum. Methods Data Syst.*, **5**, 473–491, https://doi.org/10.5194/gi-5-473-2016.

——, and Coauthors, 2020a: Development of an updated global land in-situ-based data set of temperature and precipitation extremes: HadEX3. *J. Geophys. Res. Atmos.*, **125**, e2019JD032263, https://doi.org/10.1029/2019JD032263.

Dussaillant, I., and Coauthors, 2019: Two decades of glacier mass loss along the Andes. *Nat. Geosci.*, **12**, 802–808, https://doi.org/10.1038/s41561-019-0432-5.

Dvortsov, V., and S. Solomon, 2001: Response of the stratospheric temperatures and ozone to past and future increases in stratospheric humidity. *J. Geophys. Res.*, **106**, 7505–7514, https://doi.org/10.1029/2000JD900637.

Ellis, H. T., and R. F. Pueschel, 1971: Solar radiation: Absence of air pollution trends at Mauna Loa. *Science*, **172**, 845–846, https://doi.org/10.1126/science.172.3985.845.

Engel, A., and M. Rigby, 2018: Update on ozone-depleting substances (ODSs) and other gases of interest to the Montreal protocol. Scientific Assessment of Ozone Depletion: 2018, Global Ozone Research and Monitoring Project Rep. 58, 1.1–1.66, https://ozone.unep.org/sites/default/files/2019-05/SAP-2018-Assessment-report.pdf.

Eriksen, H. Ø., L. Rouyet, T. R. Lauknes, I. Berthling, K. Isaksen, H. Hindberg, Y. Larsen, and G. D. Corner, 2018: Recent acceleration of a rock glacier complex, Ádjet, Norway, Documented by 62 years of remote sensing observations. *Geophys. Res. Lett.*, **45**, 8314–8323, https://doi.org/10.1029/2018GL077605.

Estilow, T. W., A. H. Young, and D. A. Robinson, 2015: A long-term Northern Hemisphere snow cover extent data record for climate studies and monitoring. *Earth Syst. Sci. Data*, **7**, 137–142, https://doi.org/10.5194/essd-7-137-2015.

Etheridge, D. M., L. P. Steele, R. L. Langenfelds, R. J. Francey, J. M. Barnola, and V. I. Morgan, 1996: Natural and anthropogenic changes in atmospheric CO_2 over the last 1000 years from air in Antarctic ice and firn. *J. Geophys. Res.*, **101**, 4115–4128, https://doi.org/10.1029/95JD03410.

Etzelmüller, B., and Coauthors, 2020: Twenty years of European mountain permafrost dynamics – The PACE legacy. *Environ. Res. Lett.*, **15**, 104070, https://doi.org/10.1088/1748-9326/abae9d.

Feng, W., S. Dhomse, C. Arosio, M. Weber, J. P. Burrows, M. L. Santee, and M. P. Chipperfield, 2021: Arctic ozone depletion in 2019/20: Roles of chemistry, dynamics and the Montreal Protocol. *Geophys. Res. Lett.*, **48**, e2020GL091911, https://doi.org/10.1029/2020GL091911.

Fioletov, V. E., G. E. Bodeker, A. J. Miller, R. D. McPeters, and R. Stolarski, 2002: Global and zonal total ozone variations estimated from ground-based and satellite measurements: 1964–2000. *J. Geophys. Res.*, **107**, 4647, https://doi.org/10.1029/2001JD001350.

——, and Coauthors, 2008: The performance of the ground-based total ozone network assessed using satellite data. *J. Geophys. Res.*, **113**, D14313, https://doi.org/10.1029/2008JD009809.

Fisher, J. B., and Coauthors, 2017: The future of evapotranspiration: Global requirements for ecosystem functioning, carbon and climate feedbacks, agricultural management, and water resources. *Water Resour. Res.*, **53**, 2618–2626, https://doi.org/10.1002/2016WR020175.

——, and Coauthors, 2020: ECOSTRESS: NASA's next generation mission to measure evapotranspiration from the international space station. *Water Resour. Res.*, **56**, https://doi.org/10.1029/2019WR026058.

Flato, G., and Coauthors, 2013: Evaluation of climate models. *Climate Change 2013: The Physical Science Basis*, T. F. Stocker et al., Eds., Cambridge University Press, 741–866.

Fleming, Z. L., and Coauthors, 2018: Tropospheric Ozone Assessment Report: Present-day ozone distribution and trends relevant to human health. *Elem. Sci. Anthropocene*, **6**, 12, https://doi.org/10.1525/elementa.273.

Flemming, J., and A. Inness, 2019: Carbon monoxide [in "State of the Climate in 2018"]. *Bull. Amer. Meteor. Soc.*, **100**, S181–S185, https://doi.org/10.1175/2019BAMSStateoftheClimate.1.

——, and Coauthors, 2017: The CAMS interim reanalysis of carbon monoxide, ozone and aerosol for 2003–2015. *Atmos. Chem. Phys.*, **17**, 1945–1983, https://doi.org/10.5194/acp-17-1945-2017.

Floodlist, 2020a: India and Bangladesh – Torrential rain from Cyclone Amphan triggers flooding. 21 May, accessed 11 February 2021, http://floodlist.com/asia/india-bangladesh-cyclone-amphan-floods-may-2020.

——, 2020b: Somalia – Floods after Tropical Storm Gati dumps year's worth of rain. 24 November, accessed 8 February 2021, http://floodlist.com/africa/somalia-floods-storm-gati-november-2020.

——, 2020c: Italy - 200 rescued from floods in Calabria after 450mm in 48 hours. 23 November, accessed 11 February 2021, http://floodlist.com/europe/italy-floods-calabria-november-2020.

——, 2020d: New Zealand – Record rainfall causes flooding in Napier. 10 November, accessed 11 February 2021, http://floodlist.com/australia/new-zealand-flood-napier-november-2020.

Folland, C. K., and T. R. Karl, 2001: Recent rates of warming in marine environment meet controversy. *Eos, Trans. Amer. Geophys. Union*, **82**, 453–461, https://doi.org/10.1029/01EO00270.

Forkel, M., W. Dorigo, G. Lasslop, I. Teubner, E. Chuvieco, and K. Thonicke, 2017: A data-driven approach to identify controls on global fire activity from satellite and climate observations (SOFIA V1). *Geosci. Model Dev.*, **10**, 4443–4476, https://doi.org/10.5194/gmd-10-4443-2017.

——, and Coauthors, 2019: Recent global and regional trends in burned area and their compensating environmental controls. *Environ. Res. Commun.*, **1**, 051005, https://doi.org/10.1088/2515-7620/ab25d2.

Forster, P. M., and Coauthors, 2020: Current and future global climate impacts resulting from COVID-19. *Nat. Climate Change*, **10**, 913–919, https://doi.org/10.1038/s41558-020-0883-0.

Forzieri, G., R. Alkama, D. G. Miralles, and A. Cescatti, 2017: Satellites reveal contrasting responses of regional climate to the widespread greening of Earth. *Science*, **356**, 1180–1184, https://doi.org/10.1126/science.aal1727.

Francis, D., R. Fonseca, N. Nelli, J. Cuesta, M. Weston, A. Evan, and M. Temimi, 2020: The atmospheric drivers of the major Saharan dust storm in June 2020. *Geophys. Res. Lett.*, **47**, e2020GL090102, https://doi.org/10.1029/2020GL090102.

Frauenfelder, R., W. Haeberli, and M. Hoelzle, 2003: Rock glacier occurrence and related terrain parameters in a study area of the Eastern Swiss Alps. *Permafrost: Proceedings of the 8th International Conference on Permafrost*, M. Phillips, S. M. Springman, and L. U. Arenson, Eds., A. A. Balkema, 253–258.

Free, M., D. J. Seidel, J. K. Angel, J. Lanzante, I. Durre, and T. C. Peterson, 2005: Radiosonde Atmospheric Temperature Products for Assessing Climate (RATPAC): A new dataset of large-area anomaly time series. *J. Geophys. Res.*, **110**, D22101, https://doi.org/10.1029/2005JD006169.

Freie Universität Berlin, 2021: Die Quasi-Biennial-Oszillation (QBO) Datenreihe. Accessed 19 January 2021, www.geo.fu-berlin.de/met/ag/strat/produkte/qbo/index.html.

Friedlingstein, P., and Coauthors, 2020: Global carbon budget 2020. *Earth Syst. Sci. Data*, **12**, 3269–3340, https://doi.org/10.5194/essd-12-3269-2020.

Frith, S. M., N. A. Kramarova, R. S. Stolarski, R. D. McPeters, P. K. Bhartia, and G. J. Labow, 2014: Recent changes in total column ozone based on the SBUV Version 8.6 Merged Ozone Data Set. *J. Geophys. Res.*, **119**, 9735–9751, https://doi.org/10.1002/2014JD021889.

——, R. S. Stolarski, N. A. Kramarova, and R. D. McPeters, 2017: Estimating uncertainties in the SBUV Version 8.6 merged profile ozone data set. *Atmos. Chem. Phys.*, **17**, 14695–14707, https://doi.org/10.5194/acp-17-14695-2017.

Fujita, R., S. Morimoto, S. Maksyutov, H. S. Kim, M. Arshinov, G. Brailsford, S. Aoki, and T. Nakazawa, 2020: Global and regional CH_4 emissions for 1995–2013 derived from atmospheric CH_4, $\delta^{13}C\text{-}CH_4$, and $\delta D\text{-}CH_4$ observations and a chemical transport model. *J. Geophys. Res. Atmos.*, **125**, e2020JD032903, https://doi.org/10.1029/2020JD032903.

Garane, K., and Coauthors, 2018: Quality assessment of the Ozone_cci Climate Research Data Package (release 2017): 1. Ground-based validation of total ozone column data products. *Atmos. Meas. Tech.*, **11**, 1385–1402, https://doi.org/10.5194/amt-11-1385-2018.

Garcia, H. E., and Coauthors 2019: World Ocean Atlas 2018: Product documentation. NOAA, 20 pp., www.ncei.noaa.gov/sites/default/files/2020-04/woa18documentation.pdf.

Garfinkel, C. I., A. Gordon, L. D. Oman, F. Li, S. Davis, and S. Pawson, 2018: Nonlinear response of tropical lower-stratospheric temperature and water vapor to ENSO. *Atmos. Chem. Phys.*, **18**, 4597–4615, https://doi.org/10.5194/acp-18-4597-2018.

Garreaud, R. D., and Coauthors, 2017: The 2010–2015 megadrought in central Chile: Impacts on regional hydroclimate and vegetation. *Hydrol. Earth Syst. Sci.*, **21**, 6307–6327, https://doi.org/10.5194/hess-21-6307-2017.

Gaudel, A., and Coauthors, 2018: Tropospheric Ozone Assessment Report: Present-day distribution and trends of tropospheric ozone relevant to climate and global atmospheric chemistry model evaluation. *Elementa*, **6**, 39, https://doi.org/10.1525/elementa.291.

——, and Coauthors, 2020: Aircraft observations since the 1990s reveal increases of tropospheric ozone at multiple locations across the Northern Hemisphere. *Sci. Adv.*, **6**, eaba8272, https://doi.org/10.1126/sciadv.aba8272.

GCOS, 2016: The Global Observing System for Climate: Implementation needs. Tech. Rep. GCOS-200, World Meteorological Organization, 315 pp., https://library.wmo.int/doc_num.php?explnum_id=3417.

Gelaro, R., and Coauthors, 2017: The Modern-Era Retrospective Analysis for Research and Applications, Version 2 (MERRA-2). *J. Climate*, **30**, 5419–5454, https://doi.org/10.1175/JCLI-D-16-0758.1.

Getirana, A., S. Kumar, M. Girotto, and M. Rodell, 2017: Rivers and floodplains as key components of global terrestrial water storage variability. *Geophys. Res. Lett.*, **44**, 10359–10368, https://doi.org/10.1002/2017GL074684.

Ghilain, N., A. Arboleda, and F. Gellens-Meulenberghs, 2011: Evapotranspiration modelling at large scale using near-real time MSG SEVIRI derived data. *Hydrol. Earth Syst. Sci.*, **15**, 771–786, https://doi.org/10.5194/hess-15-771-2011.

Giglio, L., W. Schroeder, and C. O. Justice, 2016: The collection 6 MODIS active fire detection algorithm and fire products. *Remote Sens. Environ.*, **178**, 31–41, https://doi.org/10.1016/j.rse.2016.02.054.

Gleason, K. L., J. H. Lawrimore, D. H. Levinson, T. R. Karl, and D. J. Karoly, 2008: A revised U.S. Climate Extremes Index. *J. Climate*, **21**, 2124–2137, https://doi.org/10.1175/2007JCLI1883.1.

Gobron, N., 2019: Terrestrial vegetation activity [in "State of the Climate in 2018"]. *Bull. Amer. Meteor. Soc.*, **100** (9), S63–S64, https://doi.org/10.1175/2019BAMSStateoftheClimate.1.

——, and M. Robustelli, 2013: Monitoring the state of the global terrestrial surfaces. *Proc. 2013 ESA Living Planet Symp.*, Edinburgh, United Kingdom, European Space Agency, JRC84937, https://publications.jrc.ec.europa.eu/repository/handle/JRC84937.

——, A. S. Belward, B. Pinty, and W. Knorr, 2010: Monitoring biosphere vegetation 1998-2009. *Geophys. Res. Lett.*, **37**, L15402, https://doi.org/10.1029/2010GL043870.

Goss, M., D. L. Swain, J. T. Abatzoglou, A. Sarhadi, C. A. Kolden, A. P. Williams, and N. S. Diffenbaugh, 2020: Climate change is increasing the likelihood of extreme autumn wildfire conditions across California. *Environ. Res. Lett.*, **15**, 094016, https://doi.org/10.1088/1748-9326/ab83a7.

Granier, C., and Coauthors, 2011: Evolution of anthropogenic and biomass burning emissions of air pollutants at global and regional scales during the 1980–2010 period. *Climatic Change*, **109**, 163–190, https://doi.org/10.1007/s10584-011-0154-1.

Gromov, S., C. A. Brenninkmeijer, and P. Jöckel, 2018: A very limited role of tropospheric chlorine as a sink of the greenhouse gas methane. *Atmos. Chem. Phys.*, **18**, 9831–9843, https://doi.org/10.5194/acp-18-9831-2018.

Gruber, A., W. A. Dorigo, W. Crow, and W. Wagner, 2017: Triple collocation-based merging of satellite soil moisture retrievals. *IEEE Trans. Geosci. Remote Sens.*, **55**, 6780–6792, https://doi.org/10.1109/TGRS.2017.2734070.

——, T. Scanlon, R. van der Schalie, W. Wagner, and W. Dorigo, 2019: Evolution of the ESA CCI Soil Moisture Climate Data Records and their underlying merging methodology. *Earth Syst. Sci. Data*, **11**, 717–739, https://doi.org/10.5194/essd-11-717-2019.

Haeberli, W., 1985: Creep of mountain permafrost: Internal structure and flow of alpine rock glaciers. Mitteilungen der Versuchsanstalt für Wasserbau, Hydrologie und Glaziologie 77, 142 pp., https://ethz.ch/content/dam/ethz/special-interest/baug/vaw/vaw-dam/documents/das-institut/mitteilungen/1980-1989/077.pdf.

Haimberger, L., C. Tavolato, and S. Sperka, 2012: Homogenization of the Global Radiosonde Temperature dataset through combined comparison with reanalysis background series and neighboring stations. *J. Climate*, **25**, 8108–8131, https://doi.org/10.1175/JCLI-D-11-00668.1.

Hamilton, D. S., and Coauthors, 2019: Improved methodologies for Earth system modelling of atmospheric soluble iron and observation comparisons using the Mechanism of Intermediate complexity for Modelling Iron (MIMI v1.0). *Geosci. Model Dev.*, **12**, 3835–3862, https://doi.org/10.5194/gmd-12-3835-2019.

Hansen, J., R. Ruedy, M. Sato, and K. Lo, 2010: Global surface temperature change. *Rev. Geophys.*, **48**, RG4004, https://doi.org/10.1029/2010RG000345.

Harris, C., and Coauthors, 2009: Permafrost and climate in Europe: Monitoring and modelling thermal, geomorphological and geotechnical responses. *Earth-Sci. Rev.*, **92**, 117–171, https://doi.org/10.1016/j.earscirev.2008.12.002.

Harris, I., T. J. Osborn, P. D. Jones, and D. H. Lister, 2020: Version 4 of the CRU TS monthly high-resolution gridded multivariate climate dataset. *Sci. Data*, **7**, 109, https://doi.org/10.1038/s41597-020-0453-3.

Hartmann, D. L., and Coauthors, 2013: Observations: Atmosphere and surface. *Climate Change 2013: The Physical Science Basis*, T. F. Stocker et al., Eds., Cambridge University Press, 159–254.

Heidinger, A. K., M. J. Foster, A. Walther, and X. Zhao, 2013: The pathfinder atmospheres extended AVHRR climate dataset. *Bull. Amer. Meteor. Soc.*, **95**, 909–922, https://doi.org/10.1175/BAMS-D-12-00246.1.

Held, I. M., and B. J. Soden, 2000: Water vapor feedback and global warming. *Annu. Rev. Energy Environ.*, **25**, 441–475, https://doi.org/10.1146/annurev.energy.25.1.441.

——, and ——, 2006: Robust responses of the hydrological cycle to global warming. *J. Climate*, **19**, 5686–5699, https://doi.org/10.1175/JCLI3990.1.

Hersbach, H., and Coauthors, 2019: Global reanalysis: Goodbye ERA-Interim, hello ERA5. ECMWF Newsletter, No. 159, ECMWF, Reading, United Kingdom, 17–24, https://doi.org/10.21957/vf291hehd7.

——, and Coauthors, 2020: The ERA5 global reanalysis. *Quart. J. Roy. Meteor. Soc.*, **146**, 1999–2049, https://doi.org/10.1002/qj.3803.

Hirahara, S., M. A. Balmaseda, E. de Boisseson, and H. Hersbach, 2016: Sea surface temperature and sea ice concentration for ERA5. ERA Rep. Series 26, 25 pp, www.ecmwf.int/node/16555.

Hirsch, E., and I. Koren, 2021: Record-breaking aerosol levels explained by smoke injection into the stratosphere. *Science*, **371**, 1269–1274, https://doi.org/10.1126/science.abe1415.

Ho, S.-P., X. Zhou, Y.-H. Kuo, D. Hunt, and J.-H. Wang, 2010a: Global evaluation of radiosonde water vapor systematic biases using GPS radio occultation from COSMIC and ECMWF analysis. *Remote Sens.*, **2**, 1320–1330, https://doi.org/10.3390/rs2051320.

——, Y.-H. Kuo, W. Schreiner, and X. Zhou, 2010b: Using SI-traceable global positioning system radio occultation measurements for climate monitoring [in "State of the Climate in 2009"]. *Bull. Amer. Meteor. Soc.*, **91** (7), S36–S37, https://doi.org/10.1175/BAMS-91-7-StateoftheClimate.

——, and Coauthors, 2020a: The COSMIC/FORMOSAT-3 radio occultation mission after 12 years: Accomplishments, remaining challenges, and potential impacts of COSMIC-2. *Bull. Amer. Meteor. Sci.*, **101**, E1107–E1136, https://doi.org/10.1175/BAMS-D-18-0290.1.

——, and Coauthors, 2020b: Initial assessment of the COSMIC-2/FORMOSAT-7 neutral atmosphere data quality in NESDIS/STAR using in situ and satellite data. *Remote Sens.*, **12**, 4099, https://doi.org/10.3390/rs12244099.

Hobday, A.J., and Coauthors, 2016: A hierarchical approach to defining marine heatwaves. *Prog. Oceanogr.*, **141**, 227–238, https://doi.org/10.1016/j.pocean.2015.12.014.

——, and Coauthors, 2018: Categorizing and naming marine heatwaves. *Oceanography*, **31**, 162–173, https://doi.org/10.5670/oceanog.2018.205.

Hock, R., and Coauthors, 2019: High mountain areas. *IPCC Special Report on the Ocean and Cryosphere in a Changing Climate*, H.-O. Pörtner, Eds., IPCC, 131–202, www.ipcc.ch/srocc/.

Hofmann, D. J., and S. A. Montzka, 2009: Recovery of the ozone layer: The ozone depleting gas index. *Eos, Trans. Amer. Geophys. Union*, **90**, 1–2, https://doi.org/10.1029/2009EO010001.

——, J. H. Butler, E. J. Dlugokencky, J. W. Elkins, K. Masarie, S. A. Montzka, and P. Tans, 2006: The role of carbon dioxide in climate forcing from 1979 to 2004: Introduction of the annual greenhouse gas index. *Tellus*, **58B**, 614–619, https://doi.org/10.1111/j.1600-0889.2006.00201.x.

Hossaini, R., and Coauthors, 2016: A global model of tropospheric chlorine chemistry: Organic versus inorganic sources and impact on methane oxidation. *J. Geophys. Res. Atmos.*, **121**, 14271–14297, https://doi.org/10.1002/2016JD025756.

Hrbáček, F., Z. Engel, M. Kňažková, and J. Smolíková, 2021: Effect of summer snow cover on the active layer thermal regime and thickness on CALM-S JGM site, James Ross Island, eastern Antarctic Peninsula. *Catena*, https://doi.org/10.1016/j.catena.2021.105608.

Hu, L., and Coauthors, 2019: Enhanced North American carbon uptake associated with El Niño. *Sci. Adv.*, **5**, eaaw0076, https://doi.org/10.1126/sciadv.aaw0076.

Huang, B., and Coauthors, 2015: Extended reconstructed sea surface temperature version 4 (ERSST.v4). Part I: Upgrades and intercomparisons. *J. Climate*, **28**, 911–930, https://doi.org/10.1175/JCLI-D-14-00006.1.

Huang, C.-Y., W.-H. Teng, S.-P. Ho, and Y. H. Kuo, 2013: Global variation of COSMIC precipitable water over land: Comparisons with ground-based GPS measurements and NCEP reanalyses. *Geophys. Res. Lett.*, **40**, 5327–5331, https://doi.org/10.1002/grl.50885.

Huijnen, V., and Coauthors, 2016: Fire carbon emissions over maritime southeast Asia in 2015 largest since 1997. *Sci. Rep.*, **6**, 26886, https://doi.org/10.1038/srep26886.

Humphrey, V., J. Zscheischler, P. Ciais, L. Gudmundsson, S. Sitch, and S. I. Seneviratne, 2018: Sensitivity of atmospheric CO_2 growth rate to observed changes in terrestrial water storage. *Nature*, **560**, 628–631, https://doi.org/10.1038/s41586-018-0424-4.

Hüser, I., B. Gehrke, and J. W. Kaiser, 2018: Methodology to correct biases in individual satellite FRP products. CAMS Rep. CAMS44-2016SC3-D44.3.3.1-2018-20187, ECMWF, Reading, United Kingdom, 20 pp., Available upon request from http://support.ecmwf.int.

Inness, A., and Coauthors, 2013: The MACC reanalysis: An 8-year data set of atmospheric composition. *Atmos. Chem. Phys.*, **13**, 4073–4109, https://doi.org/10.5194/acp-13-4073-2013.

——, and Coauthors, 2019: The CAMS reanalysis of atmospheric composition. *Atmos. Chem. Phys.*, **19**, 3515–3556, https://doi.org/10.5194/acp-19-3515-2019.

——, S. Chabrillat, J. Flemming, V. Huijnen, B. Langenrock, J. Nicolas, I. Polichtchouk, and M. Razinger, 2020: Exceptionally low Arctic stratospheric ozone in Spring 2020 as seen in the CAMS reanalysis. *J. Geophys. Res.*, **125**, e2020JD033563, https://doi.org/10.1029/2020JD033563.

IPCC, 2013: *Climate Change 2013: The Physical Science Basis*. Cambridge University Press, 1535 pp., https://doi.org/10.1017/CBO9781107415324.

John, V. O., and B. J. Soden, 2007: Temperature and humidity biases in global climate models and their impact on climate feedbacks. *Geophys. Res. Lett.*, **34**, L18704, https://doi.org/10.1029/2007GL030429.

——, G. Holl, R. P. Allan, S. A. Buehler, D. E. Parker, and B. J. Soden, 2011: Clear-sky biases in satellite infra-red estimates of upper tropospheric humidity and its trends. *J. Geophys. Res.*, **116**, D14108, https://doi.org/10.1029/2010JD015355.

Jones, G. S., 2020: "Apples and oranges": On comparing simulated historic near-surface temperature changes with observations. *Quart. J. Roy. Meteor. Soc.*, **146**, 3747–3771, https://doi.org/10.1002/qj.3871.

Junod, R. A., and J. R. Christy, 2020: A new compilation of globally gridded nighttime marine air temperatures: The UAHNMATv1 dataset. *Int. J. Climatol.*, **40**, 2609–2623, https://doi.org/10.1002/joc.6354.

Kääb, A., and M. Vollmer, 2000: Surface geometry, thickness changes and flow fields on creeping mountain permafrost: Automatic extraction by digital image analysis. *Permafrost Periglacial Processes*, **11**, 315–326, https://doi.org/10.1002/1099-1530(200012)11:4<315::AID-PPP365>3.0.CO;2-J.

——, R. Frauenfelder, and I. Roer, 2007: On the response of rockglacier creep to surface temperature increase. *Global Planet. Change*, **56**, 172–187, https://doi.org/10.1016/j.gloplacha.2006.07.005.

——, T. Strozzi, T. Bolch, R. Caduff, H. Trefall, M. Stoffel, and A. Kokarev, 2021: Inventory and changes of rock glacier creep speeds in Ile Alatau and Kungöy Ala-Too, northern Tien Shan, since the 1950s. *Cryosphere*, 15, 927–949, https://doi.org/10.5194/tc-15-927-2021.

Kablick, G. P., D. R. Allen, M. D. Fromm, and G. E. Nedoluha, 2020: Australian PyroCb smoke generates synoptic-scale stratospheric anticyclones. *Geophys. Res. Lett.*, **47**, e2020GL088101, https://doi.org/10.1029/2020GL088101.

Kaiser, J. W., and Coauthors, 2012: Biomass burning emissions estimated with a global fire assimilation system based on observed fire radiative power. *Biogeosciences*, **9**, 527–554, https://doi.org/10.5194/bg-9-527-2012.

——, G. R. van der Werf, and I. Hüser, 2020: Biomass burning [in "State of the Climate in 2019"]. *Bull. Amer. Meteor. Soc.*, **101** (8), S93–S95, https://doi.org/10.1175/BAMS-D-20-0104.1.

Kannan, K., and K. R. Rajagopal, 2013: A model for the flow of rock glaciers. *Int. J. Non-linear Mech.*, **48**, 59–64, https://doi.org/10.1016/j.ijnonlinmec.2012.06.002.

Kaplan, A., 2011: Patterns and indices of climate variability [in "State of the Climate in 2010"]. *Bull. Amer. Meteor. Soc.*, **92** (6), S20–S25, https://doi.org/10.1175/1520-0477-92.6.S1.

Karlsson, K.-G., and Coauthors, 2017: CLARA-A2: The second edition of the CM SAF cloud and radiation data record from 34 years of global AVHRR data. *Atmos. Chem. Phys.*, **17**, 5809–5828, https://doi.org/10.5194/ACP-17-5809-2017.

Karpechko, A. Y., and A. C. Maycock, 2018: Stratospheric ozone changes and climate. Scientific Assessment of Ozone Depletion: 2018, Global Ozone Research and Monitoring Project Rep. 58, 5.1–5.50, https://ozone.unep.org/sites/default/files/2019-05/SAP-2018-Assessment-report.pdf.

Keeling, C. D., and R. Revelle, 1985: Effects of El-Nino Southern Oscillation on the atmospheric content of carbon-dioxide. *Meteoritics*, **20**, 437–450.

Kellerer-Pirklbauer, A., and V. Kaufmann, 2012: About the relationship between rock glacier velocity and climate parameters in central Austria. *Aust. J. Earth Sci.*, **105**, 94–112.

——, and ——, 2018: Deglaciation and its impact on permafrost and rock glacier evolution: New insight from two adjacent cirques in Austria. *Sci. Total Environ.*, **621**, 1397–1414, https://doi.org/10.1016/j.scitotenv.2017.10.087.

Kennedy, J. J., and Coauthors, 2010: How do we know the world has warmed? [in "State of the Climate in 2009"]. *Bull. Amer. Meteor. Soc.*, **91** (7), S26–S27, https://doi.org/10.1175/BAMS-91-7-StateoftheClimate.

——, N. A. Rayner, C. P. Atkinson, and R. E. Killick, 2019: An ensemble data set of sea surface temperature change from 1850: The Met Office Hadley Centre HadSST.4.0.0.0 data set. *J. Geophys. Res. Atmos.*, **124**, 7719–7763, https://doi.org/10.1029/2018JD029867.

Kent, E. C., N. A. Rayner, D. I. Berry, M. Saunby, B. I. Moat, J. J. Kennedy, and D. E. Parker, 2013: Global analysis of night marine air temperature and its uncertainty since 1880: The HadNMAT2 data set. *J. Geophys. Res. Atmos.*, **118**, 1281–1298, https://doi.org/10.1002/jgrd.50152.

Khaykin, S., and Coauthors, 2020: The 2019/20 Australian wildfires generated a persistent smoke-charged vortex rising up to 352km altitude. *Commun. Earth Environ.*, **1**, 22, https://doi.org/10.1038/s43247-020-00022-5.

Kim, H., 2020: River discharge and runoff [in "State of the Climate in 2019"]. *Bull. Amer. Meteor.*, **101**, S53–S55, https://doi.org/10.1175/BAMS-D-20-0104.1.

——, P. J.-F. Yeh, T. Oki, and S. Kanae, 2009: Role of rivers in the seasonal variations of terrestrial water storage over global basins. *Geophys. Res. Lett.*, **36**, L17402, https://doi.org/10.1029/2009GL039006.

Kim, J., and K. Paik, 2015: Recent recovery of surface wind speed after decadal decrease: A focus on South Korea. *Climate Dyn.*, **45**, 1699–1712, https://doi.org/10.1007/s00382-015-2546-9.

King, O., and Coauthors, 2019: Six decades of glacier mass changes around mount everest are revealed by historical and contemporary images. *One Earth*, **3**, 608–620, https://doi.org/10.1016/j.oneear.2020.10.019.

Klein Tank, A. M. G., and Coauthors, 2002: Daily dataset of 20th-century surface air temperature and precipitation series for the European Climate Assessment. *Int. J. Climatol.*, **22**, 1441–1453, https://doi.org/10.1002/joc.773.

Kobayashi, S., and Coauthors, 2015: The JRA-55 reanalysis: General specifications and basic characteristics. J. *Meteorol. Soc. Japan*, **93**, 5–48, https://doi.org/10.2151/jmsj.2015-001.

Konings, A. G., Y. Yu, L. Xu, Y. Yang, D. S. Schimel, and S. S. Saatchi, 2017: Active microwave observations of diurnal and seasonal variations of canopy water content across the humid African tropical forests. *Geophys. Res. Lett.*, **44**, 2290–2299, https://doi.org/10.1002/2016GL072388.

Kopp, G., and J. L. Lean, 2011: A new, lower value of total solar irradiance: Evidence and climate significance. *Geophys. Res. Lett.*, **38**, L01706, https://doi.org/10.1029/2010GL045777.

Kratz, D. P., P. W. Stackhouse Jr., S. K. Gupta, A. C. Wilber, P. Sawaengphokhai, and G. R. McGarragh, 2014: The Fast Longwave and Shortwave Flux (FLASHFlux) data product: Single scanner footprint fluxes. *J. Appl. Meteor. Climatol.*, **53**, 1059–1079, https://doi.org/10.1175/JAMC-D-13-061.1.

Kummert, M., R. Delaloye, and L. Braillard, 2018: Erosion and sediment transfer processes at the front of rapidly moving rock glaciers: Systematic observations with automatic cameras in the western Swiss Alps. *Permafrost Periglacial Processes*, **29**, 21–33, https://doi.org/10.1002/ppp.1960.

Lagouarde, J.-P., and Coauthors, 2018: The Indian-French Trishna Mission: Earth observation in the thermal infrared with high spatio-temporal resolution. *IGARSS 2018—2018 IEEE Int. Geoscience and Remote Sensing Symp.*, Valencia, Spain, IEEE, 4078–4081, https://doi.org/10.1109/IGARSS.2018.8518720.

Lan, X., and Coauthors, 2021: Improved constraints on global methane emissions and sinks using $\delta^{13}C\text{-}CH_4$. *Global Biogeochem. Cycles*, **35**, e2021GB007000, https://doi.org/10.1029/2021GB007000.

Landerer, F. W., and Coauthors, 2020: Extending the global mass change data record: GRACE follow-on instrument and science data performance. *Geophys. Res. Lett.*, **47**, e2020GL088306, https://doi.org/10.1029/2020GL088306.

Lassey, K. R., D. M. Etheridge, D. C. Lowe, A. M. Smith, and D. F. Ferretti, 2007: Centennial evolution of the atmospheric methane budget: What do the carbon isotopes tell us? *Atmos. Chem. Phys.*, **7**, 2119–2139, https://doi.org/10.5194/acp-7-2119-2007.

Lawrence, Z. D., J. Perlwitz, A. H. Butler, G. L. Manney, P. A. Newman, S. H. Lee, and E. R. Nash, 2020: The remarkably strong Arctic stratospheric polar vortex of winter 2020: Links to record-breaking Arctic oscillation and ozone loss. *J. Geophys. Res. Atmos.*, **125**, e2020JD033271, https://doi.org/10.1029/2020JD033271.

Lee, H.-T., and NOAA CDR Program, 2011: NOAA Climate Data Record (CDR) of Monthly Outgoing Longwave Radiation (OLR), Version 2.2-1. NOAA National Climatic Data Center, accessed 2 February 2021, https://doi.org/10.7289/V5222RQP.

Lenssen, N. J. L., G. A. Schmidt, J. E. Hansen, M. J. Menne, A. Persin, R. Ruedy, and D. Zyss, 2019: Improvements in the GISTEMP uncertainty model. *J. Geophys. Res. Atmos.*, **124**, 6307–6326, https://doi.org/10.1029/2018JD029522.

Le Quéré, C., and Coauthors, 2020: Temporary reduction in daily global CO_2 emissions during the COVID-19 forced confinement. *Nat. Climate Change*, **10**, 647–653, https://doi.org/10.1038/s41558-020-0797-x.

Levy, R. C., and Coauthors, 2013: The collection 6 MODIS aerosol products over land and ocean. *Atmos. Meas. Tech.*, **6**, 2989–3034, https://doi.org/10.5194/amt-6-2989-2013.

L'Heureux, M. L., and Coauthors, 2016: Observing and predicting the 2015/16 El Niño. *Bull. Amer. Meteor. Soc.*, **98**, 1363–1382, https://doi.org/10.1175/BAMS-D-16-0009.1.

Li, M., and Coauthors, 2017: Anthropogenic emission inventories in China: A review. *Nat. Sci. Rev.*, **4**, 834–866, https://doi.org/10.1093/nsr/nwx150.

Li, X., and Coauthors, 2021: Global-scale assessment and inter-comparison of recently developed/reprocessed microwave satellite vegetation optical depth products. *Remote Sens. Environ.*, **253**, 112208, https://doi.org/10.1016/j.rse.2020.112208.

Lieb, G. K., and A. Kellerer-Pirklbauer, 2020: Sammelbericht über die Gletschermessungen des Österreichischen Alpenvereins im Jahr 2019. Letzter Bericht: Bergauf 2/2019, Jg. 74 (144), S. 20–29, www.alpenverein.at/portal_wAssets/docs/service/bergauf/Lieb_Kellerer_Gletscherbericht_2_20.pdf.

Lin, M., L. W. Horowitz, S. J. Oltmans, A. M. Fiore, and S. Fan, 2014: Tropospheric ozone trends at Mauna Loa Observatory tied to decadal climate variability. *Nat. Geosci.*, **7**, 136–143, https://doi.org/10.1038/ngeo2066.

Liu, Y. Y., A. I. J. M. van Dijk, M. F. McCabe, J. P. Evans, and R. A. M. de Jeu, 2013: Global vegetation biomass change (1988–2008) and attribution to environmental and human drivers. *Global Ecol. Biogeogr.*, **22**, 692–705, https://doi.org/10.1111/geb.12024.

——, and Coauthors, 2015: Recent reversal in loss of global terrestrial biomass. *Nat. Climate Change*, **5**, 470–474, https://doi.org/10.1038/nclimate2581.

——, and Coauthors, 2017: Enhanced canopy growth precedes senescence in 2005 and 2010 Amazonian droughts. *Remote Sens. Environ.*, **211**, 26–37, https://doi.org/10.1016/j.rse.2018.03.035.

Loeb, N. G., B. A. Wielicki, D. R. Doelling, G. L. Smith, D. F. Keyes, S. Kato, N. Manalo-Smith, and T. Wong, 2009: Toward optimal closure of the Earth's top-of-atmosphere radiation budget. *J. Climate*, **22**, 748–766, https://doi.org/10.1175/2008JCLI2637.1.

——, S. Kato, W. Su, T. Wong, F. Rose, D. R. Doelling, and J. Norris, 2012: Advances in understanding top-of-atmosphere radiation variability from satellite observations. *Surv. Geophys.*, **33**, 359–385, https://doi.org/10.1007/s10712-012-9175-1.

——, and Coauthors, 2018: Clouds and the Earth's Radiant Energy System (CERES) Energy Balanced and Filled (EBAF) Top-of-Atmosphere (TOA) Edition-4.0 data product. *J. Climate*, **31**, 895–918, https://doi.org/10.1175/JCLI-D-17-0208.1.

Lu, X., and Coauthors, 2018a: Surface and tropospheric ozone trends in the Southern Hemisphere since 1990: Possible linkages to poleward expansion of the Hadley circulation. *Sci. Bull.*, **64**, 400–409, https://doi.org/10.1016/j.scib.2018.12.021.

——, and Coauthors, 2018b: Severe surface ozone pollution in China: A global perspective. *Environ. Sci. Technol. Lett.*, **5**, 487–494, https://doi.org/10.1021/acs.estlett.8b00366.

MacCallum, S. N., and C. J. Merchant, 2012: Surface water temperature observations of large lakes by optimal estimation. *Can. J. Remote Sens.*, **38**, 25–45, https://doi.org/10.5589/m12-010.

MacFarling Meure, C., and Coauthors, 2006: Law dome CO_2, CH_4 and N_2O ice core records extended to 2000 years BP. *Geophys. Res. Lett.*, **33**, L14810, https://doi.org/10.1029/2006GL026152.

Mafaranga, H., 2020: Heavy rains, human activity, and rising waters at Lake Victoria. *Eos, Trans. Amer. Geophys. Union*, **101**, https://doi.org/10.1029/2020EO146582.

Magnin, F., P. Deline, L. Ravanel, J. Noetzli, and P. Pogliotti, 2015: Thermal characteristics of permafrost in the steep alpine rock walls of the Aiguille du Midi (Mont Blanc Massif, 3842 m a.s.l). *Cryosphere*, **9**, 109–121, https://doi.org/10.5194/tc-9-109-2015.

Magnuson, J. J., and Coauthors, 2000: Historical trends in lake and river ice cover in the Northern Hemisphere. *Science*, **289**, 1743–1746, https://doi.org/10.1126/science.289.5485.

Manabe, S., and R. Wetherald, 1967: Thermal equilibrium of the atmosphere with a given distribution of relative humidity. *J. Atmos. Sci.*, **24**, 241–259, https://doi.org/10.1175/1520-0469(1967)024<0241:TEOTAW>2.0.CO;2.

Mann, M., and Coauthors, 2017: Influence of anthropogenic climate change on planetary wave resonance and extreme weather events. *Sci. Rep.*, **7**, 452242, https://doi.org/10.1038/srep45242.

Manney, G. L., and Coauthors, 2020: Record-low Arctic stratospheric ozone in 2020: MLS observations of chemical processes and comparisons with previous extreme winters. *Geophys. Res. Lett.*, **47**, e2020GL089063, https://doi.org/10.1029/2020GL089063.

Martens, B., and Coauthors, 2017: GLEAM v3: Satellite-based land evaporation and root-zone soil moisture. *Geosci. Model Dev.*, **10**, 1903–1925, https://doi.org/10.5194/gmd-10-1903-2017.

——, W. Waegeman, W. A. Dorigo, N. E. C. Verhoest, and D. G. Miralles, 2018: Terrestrial evaporation response to modes of climate variability. *npj Climate Atmos. Sci.*, **1**, 43, https://doi.org/10.1038/s41612-018-0053-5.

Maycock, A. C., and Coauthors, 2018: Revisiting the mystery of recent stratospheric temperature trends. *Geophys. Res. Lett.*, **45**, 9919–9933, https://doi.org/10.1029/2018GL078035.

McCabe, M. F., A. Ershadi, C. Jiménez, D. G. Miralles, D. Michel, and E. F. Wood, 2016: The GEWEX LandFlux project: Evaluation of model evaporation using tower-based and globally-gridded forcing data. *Geosci. Model Dev.*, **9**, 283–305, https://doi.org/10.5194/gmd-9-283-2016.

——, and Coauthors, 2017a: The future of Earth observation in hydrology. *Hydrol. Earth Syst. Sci.*, **21**, 3879–3914, https://doi.org/10.5194/hess-21-3879-2017.

——, B. Aragon, R. Houborg, and J. Mascaro, 2017b: CubeSats in hydrology: Ultrahigh-resolution insights into vegetation dynamics and terrestrial evaporation. *Water Resour. Res.*, **53**, 10 017–10 024, https://doi.org/10.1002/2017WR022240.

McDonald, B. C., and Coauthors, 2018: Volatile chemical products emerging as largest petrochemical source of urban organic emissions. *Science*, **359**, 760–764, https://doi.org/10.1126/science.aaq0524.

McKitrick, R., and J. Christy, 2018: A test of the tropical 200- to 300-hPa warming rate in climate models. *Earth Space Sci.*, **5**, 529–536, https://doi.org/10.1029/2018EA000401.

——, and J. Christy, 2020: Pervasive warming bias in CMIP6 tropospheric layers. *Earth Space Sci.*, **7**, e2020EA001281, https://doi.org/10.1029/2020EA001281.

McVicar, T. R., and Coauthors, 2012: Global review and synthesis of trends in observed terrestrial near-surface wind speeds: Implications for evaporation. *J. Hydrol.*, **416–417**, 182–205, https://doi.org/10.1016/j.jhydrol.2011.10.024.

Mears, C. A., and F. J. Wentz, 2016: Sensitivity of satellite-derived tropospheric temperature trends to the diurnal cycle adjustment. *J. Climate*, **29**, 3629–3646, https://doi.org/10.1175/JCLI-D-15-0744.1.

——, ——, P. Thorne, and D. Bernie, 2011: Assessing uncertainty in estimates of atmospheric temperature changes from MSU and AMSU using a Monte-Carlo estimation technique. *J. Geophys. Res.*, **116**, D08112, https://doi.org/10.1029/2010JD014954.

——, D. K. Smith, L. Ricciardulli, J. Wang, H. Huelsing, and F. J. Wentz, 2018: Construction and uncertainty estimation of a satellite-derived total precipitable water data record over the world's oceans. *Earth Space Sci.*, **5**, 197–210, https://doi.org/10.1002/2018EA000363.

Meesters, A. G. C. A., R. A. M. De Jeu, and M. Owe, 2005: Analytical derivation of the vegetation optical depth from the microwave polarization difference index. *IEEE Trans. Geosci. Remote Sens.*, **2**, 121–123, https://doi.org/10.1109/LGRS.2005.843983.

Menne, M. J., I. Durre, R. S. Vose, B. E. Gleason, and T. G. Houston, 2012: An overview of the global historical climatology network-daily database. *J. Atmos. Oceanic Technol.*, **29**, 897–910, https://doi.org/10.1175/JTECH-D-11-00103.1.

Menzel, W. P., R. A. Frey, E. E. Borbas, B. A. Baum, G. Cureton, and N. Bearson, 2016: Reprocessing of HIRS satellite measurements from 1980-2015: Development towards a consistent decadal cloud record. *J. Appl. Meteor. Climatol.*, **55**, 2397–2410, https://doi.org/10.1175/JAMC-D-16-0129.1.

Met Office, 2020: A look back at 2020. 30 December, www.metoffice.gov.uk/about-us/press-office/news/weather-and-climate/2020/2020-round-up.

Mialon, A., N. Rodriguez-Fernandez, M. Santoro, S. Saatchi, S. Mermoz, E. Bousquet, and Y. Kerr, 2020: Evaluation of the sensitivity of SMOS L-VOD to forest above-ground biomass at global scale. *Remote Sens.*, **12**, 1450, https://doi.org/10.3390/rs12091450.

Miller, B. R., and Coauthors, 2010: HFC-23 (CHF3) emission trend response to HCFC-22 (CHClF2) production and recent HFC-23 emission abatement measures. *Atmos. Chem. Phys.*, **10**, 7875–7890, https://doi.org/10.5194/acp-10-7875-2010.

Mills, G., and Coauthors, 2018: Tropospheric Ozone Assessment Report: Present-day tropospheric ozone distribution and trends relevant to vegetation. *Elem. Sci. Anthropocene*, **6**, 47, https://doi.org/10.1525/elementa.302.

Ming, Y., and Coauthors, 2020: Assessing the influence of COVID-19 on the shortwave radiative fluxes over the East Asian marginal seas. *Geophys. Res. Lett.*, **48**, e2020GL091699, https://doi.org/10.1029/2020GL091699.

Minnis, P., and Coauthors, 2008: Cloud detection in nonpolar regions for CERES using TRMM VIRS and Terra and Aqua MODIS data. *IEEE Trans. Geosci. Remote Sens.*, **46**, 3857–3884, https://doi.org/10.1109/TGRS.2008.2001351.

——, K. Bedka, Q. Trepte, C. R. Yost, S. T. Bedka, B. Scarino, K. Khlopenkov, and M. M. Khaiyer, 2016: A consistent long-term cloud and clear-sky radiation property dataset from the Advanced Very High Resolution Radiometer (AVHRR). Climate Algorithm Theoretical Basis Document (C-ATBD), CDRP-ATBD-0826 Rev 1, 159 pp., www.ncdc.noaa.gov/sites/default/files/cdr-documentation/CDRP-ATBD-0826%20AVHRR%20Cloud%20Properties%20-%20NASA%20C-ATBD%20(01B-30b)%20(DSR-1051).pdf.

Miralles, D. G., T. R. H. Holmes, R. A. M. De Jeu, J. H. Gash, A. G. C. A. Meesters, and A. J. Dolman, 2011: Global land-surface evaporation estimated from satellite-based observations. *Hydrol. Earth Syst. Sci.*, **15**, 453–469, https://doi.org/10.5194/hess-15-453-2011.

——, and Coauthors, 2014: El Niño–La Niña cycle and recent trends in continental evaporation. *Nat. Climate Change*, **4**, 122–126, https://doi.org/10.1038/nclimate2068.

——, and Coauthors, 2016: The WACMOS-ET project – Part 2: Evaluation of global terrestrial evaporation data sets. *Hydrol. Earth Syst. Sci.*, **20**, 823–842, https://doi.org/10.5194/hess-20-823-2016.

Moesinger, L., W. Dorigo, R. de Jeu, R. van der Schalie, T. Scanlon, I. Teubner, and M. Forkel, 2020: The global long-term microwave Vegetation Optical Depth Climate Archive (VODCA). *Earth Syst. Sci. Data*, **12**, 177–196, https://doi.org/10.5194/essd-12-177-2020.

Monks, P. S., and Coauthors, 2015: Tropospheric ozone and its precursors from the urban to the global scale from air quality to short-lived climate forcer. *Atmos. Chem. Phys.*, **15**, 8889–8973, https://doi.org/10.5194/acp-15-8889-2015.

Montzka, S. A., and Coauthors, 1996: Decline in the tropospheric abundance of halogen from halocarbons: Implications for stratospheric ozone depletion. *Science*, **272**, 1318–1322, https://doi.org/10.1126/science.272.5266.1318.

——, and Coauthors, 2011: Ozone-depleting substances (ODSs) and related chemicals. Scientific Assessment of Ozone Depletion: 2010, Global Ozone Research and Monitoring Project Rep.. 52, World Meteorological Organization, Ch. 1, https://tsapps.nist.gov/publication/get_pdf.cfm?pub_id=909747.

——, and Coauthors, 2018: An unexpected and persistent increase in global emissions of ozone-depleting CFC-11. *Nature*, **557**, 413–417, https://doi.org/10.1038/s41586-018-0106-2.

——, and Coauthors, 2021: A decline in global CFC-11 emissions during 2018–2019. *Nature*, **590**, 428–432, https://doi.org/10.1038/s41586-021-03260-5.

Morice, C. P., and Coauthors, 2021: An updated assessment of near-surface temperature change from 1850: The HadCRUT5 data set. *J. Geophys. Res. Atmos.*, **126**, e2019JD032361, https://doi.org/10.1029/2019JD032361.

Mühle, J., and Coauthors, 2010: Perfluorocarbons in the global atmosphere: Tetrafluoromethane, hexafluoroethane, and octafluoropropane. *Atmos. Chem. Phys.*, **10**, 5145–5164, https://doi.org/10.5194/acp-10-5145-2010.

Myhre, G., and Coauthors, 2013: Anthropogenic and natural radiative forcing. *Climate Change 2013: The Physical Science Basis*, T. F. Stocker et al., Eds., Cambridge University Press, 659–740.

Nemani, R. R., C. D. Keeling, H. Hashimoto, W. M. Jolly, S. C. Piper, C. Tucker, R. B. Myneni, and S. W. Running, 2003: Climate-driven increases in global terrestrial net primary production from 1982 to 1999. *Science*, **300**, 1560–1563, https://doi.org/10.1126/science.1082750.

NESDIS, 2020: Powerful "dragon" storm hits Egypt while Israel prepares for Impact. 13 March, accessed 11 February 2021, www.nesdis.noaa.gov/content/powerful-%E2%80%9Cdragon%E2%80%9D-storm-hits-egypt-while-israel-prepares-impact.

Neu, J., and Coauthors, 2014: Tropospheric ozone variations governed by changes in stratospheric circulation. *Nat. Geosci.*, **7**, 340–344, https://doi.org/10.1038/ngeo2138.

Newman, P. A., J. S. Daniel, D. W. Waugh, and E. R. Nash, 2007: A new formulation of equivalent effective stratospheric chlorine (EESC). *Atmos. Chem. Phys.*, **7**, 4537–4552, https://doi.org/10.5194/acp-7-4537-2007.

Ni, X., and P. M. Groffman, 2018: Declines in methane uptake in forest soils. *Proc. Natl. Acad. Sci. USA*, **115**, 8587–8590, https://doi.org/10.1073/pnas.1807377115.

Nisbet, E. G., and Coauthors, 2019: Very strong atmospheric methane growth in the 4 years 2014-2017: Implications for the Paris Agreement. *Global Biogeochem. Cycles*, **33**, 318–342, https://doi.org/10.1029/2018GB006009.

NIWA, 2020: Auckland's drought most extreme in modern times. https://niwa.co.nz/news/aucklands-drought-most-extreme-in-modern-times.

——, 2021: Aotearoa New Zealand Climate Summary: Summer 2020-21. https://niwa.co.nz/climate/summaries/seasonal/summer-2020-21.

NOAA, 2020: State of the Climate. www.ncdc.noaa.gov/sotc/.

——, 2021a: State of the Climate: National Climate Report for Annual 2020. Accessed 5 February 2021, www.ncdc.noaa.gov/sotc/national/202013.

——, 2021b: State of the Climate: Global Climate Report for Annual 2020. Accessed 21 March 2021, www.ncdc.noaa.gov/sotc/global/202013.

——, 2021c: US Climate Extremes Index (CEI). Accessed 25 February 2021, www.ncdc.noaa.gov/extremes/cei/graph/us/01-12/4.

Noetzli, J., and Coauthors, 2018: Permafrost thermal state [in "State of the Climate in 2017"]. *Bull. Amer. Meteor. Soc.*, **99** (8), S20–S22, https://doi.org/10.1175/2018BAMSStateoftheClimate.1.

——, and Coauthors, 2019: Permafrost thermal state [in "State of the Climate in 2018"]. *Bull. Amer. Meteor. Soc.*, **100** (9), S21–S22, https://doi.org/10.1175/2019BAMSStateoftheClimate.1.

——, H. H. Christiansen, K. Isaksen, S. Smith, L. Zhao, and D. A. Streletskiy, 2020: Permafrost thermal state [in "State of the Climate in 2019"]. *Bull. Amer. Meteor. Soc.*, **101** (8), S34–S36, https://doi.org/10.1175/BAMS-D-20-0104.1.

Novelli, P. C., K. A. Masarie, P. M. Lang, B. D. Hall, R. C. Myers, and J. W. Elkins, 2003: Reanalysis of tropospheric CO trends: Effects of the 1997–1998 wildfires. J. Geophys. Res., 108, 4464, https://doi.org/10.1029/2002JD003031.

O'Keefe, J., 2019: Phenology of Woody Species at Harvard Forest since 1990. Harvard Forest Data Archive: HF003, Environmental Data Initiative: https://doi.org/10.6073/pasta/6b0a6e266e06ab52148af3e5cd942159.

O'Neel, S., and Coauthors, 2019: Reanalysis of the US Geological Survey Benchmark Glaciers: Long-term insight into climate forcing of glacier mass balance. *J. Glaciol.*, **65**, 850–866, https://doi.org/10.1017/jog.2019.66.

Osborn, T. J., J. Barichivich, I. Harris, G. van der Schrier, and P. D. Jones, 2018: Monitoring global drought using the self-calibrating Palmer Drought Severity Index [in "State of the Climate in 2017"]. *Bull. Amer. Meteor. Soc.*, **99**, S36–S37, https://doi.org/10.1175/2018BAMSStateoftheClimate.1.

——, and Coauthors, 2021: Land surface air temperature variations across the globe updated to 2019: The CRUTEM5 dataset. *J. Geophys. Res. Atmos.*, **126**, e2019JD032352, https://doi.org/10.1029/2019JD032352.

Osprey, S. M., and Coauthors, 2016: An unexpected disruption of the atmospheric quasi-biennial oscillation. *Science*, **353**, 1424–1427, https://doi.org/10.1126/science.aah4156.

Otto, F. E. L., and Coauthors, 2018: Anthropogenic influence on the drivers of the Western Cape drought 2015–2017. *Environ. Res. Lett.*, **13**, 124010, https://doi.org/10.1088/1748-9326/aae9f9.

Overland, J. E., and M. Wang, 2020: The 2020 Siberian heat wave. *Int. J. Climatol.*, 41, E2341–E2346, https://doi.org/10.1002/joc.6850.

Park, J., and H. Kim, S-.Y. Wang, J-.H. Jeong, K-.S. Lim, and J-.H. Yoon, 2020: Intensification of the East Asian summer monsoon lifecycle based on observation and CMIP6. *Environ. Res. Lett.*, 15, 0940b9, https://doi.org/10.1088/1748-9326/ab9b3f.

Park, S., and Coauthors, 2021: A decline in emissions of CFC-11 and related chemicals from eastern China. *Nature*, **590**, 433–437, https://doi.org/10.1038/s41586-021-03277-w.

Park, T., and Coauthors, 2016: Changes in growing season duration and productivity of northern vegetation inferred from long-term remote sensing data. *Environ. Res. Lett.*, **11**, 084001, https://doi.org/10.1088/1748-9326/11/8/084001.

Patel, K., 2021: Snow free glaciers in winter. NASA Earth Observatory, https://earthobservatory.nasa.gov/images/147840/snow-free-glaciers-in-winter.

Pekel, J.-F., A. Cottam, N. Gorelick, and A. S. Belward, 2016: High-resolution mapping of global surface water and its long-term changes. *Nature*, **540**, 418–422, https://doi.org/10.1038/nature20584.

Penalba, O. C., and J. A. Rivera, 2016: Precipitation response to El Niño/La Niña events in Southern South America – Emphasis in regional drought occurrences. *Adv. Geosci.*, **42**, 1–14, https://doi.org/10.5194/adgeo-42-1-2016.

Pendergrass, A. G., and R. Knutti, 2018: The uneven nature of daily precipitation and its change. *Geophys. Res. Lett.*, **45**, 11 980–11 988, https://doi.org/10.1029/2018GL080298.

Perkins, S. E., and L. V. Alexander, 2013: On the measurement of heat waves. *J. Climate*, **26**, 4500-4517, https://doi.org/10.1175/JCLI-D-12-00383.1.

PERMOS, 2019: Permafrost in Switzerland 2014/2015 to 2017/2018. Glaciological Rep. (Permafrost) 16–19, Cryospheric Commission of the Swiss Academy of Sciences, 104 pp., https://doi.org/10.13093/permos-rep-2019-16-19.

Peterson, T. C., and R. S. Vose, 1997: An overview of the global historical climatology network temperature database. *Bull. Amer. Meteor. Soc.*, **78**, 2837–2849, https://doi.org/10.1175/1520-0477(1997)078<2837:AOOTGH>2.0.CO;2.

Petoukhov, V., S. Rahmstorf, S. Petri, and H. J. Schellnhuber, 2013: Quasiresonant amplification of planetary waves and recent Northern Hemisphere weather extremes. *Proc. Natl. Acad. Sci. USA*, **110**, 5336–5341, https://doi.org/10.1073/pnas.1222000110.

Pétron, G., and Coauthors, 2020: Atmospheric Carbon Monoxide dry air mole fractions from the NOAA GML Carbon Cycle Cooperative Global Air Sampling Network, 1988-2020, Version: 2020-08. NOAA, https://doi.org/10.15138/33bv-s284.

Pfeil, I., W. Wagner, M. Forkel, W. Dorigo, and M. Vreugdenhil, 2020: Does ASCAT observe the spring reactivation in temperate deciduous broadleaf forests? *Remote Sens. Environ.*, **250**, 112042, https://doi.org/10.1016/j.rse.2020.112042.

Pinty, B., and Coauthors, 2011: Exploiting the MODIS albedos with the Two-stream Inversion Package (JRC-TIP): 2. Fractions of transmitted and absorbed fluxes in the vegetation and soil layers. *J. Geophys. Res.*, **116**, D09106, https://doi.org/10.1029/2010JD015373.

Platnick, S., P. Hubanks, K. Meyer, and M. D. King, 2015: MODIS Atmosphere L3 Monthly Product (08_L3). NASA MODIS Adaptive Processing System, Goddard Space Flight Center, accessed 21 January 2021, https://doi.org/10.5067/MODIS/MOD08_M3.006 (Terra), https://doi.org/10.5067/MODIS/MYD08_M3.006 (Aqua).

Po-Chedley, S., T. J. Thorsen, and Q. Fu, 2015: Removing diurnal cycle contamination in satellite-derived tropospheric temperatures: Understanding tropical tropospheric trend discrepancies. *J. Climate*, **28**, 2274–2290, https://doi.org/10.1175/JCLI-D-13-00767.1.

——, B. D. Santer, S. Fueglistaler, M. D. Zelinka, P. J. Cameron-Smith, J. Painter, and Q. Fu, 2021: Natural variability contributes to model-satellite differences in tropical tropospheric warming. *Proc. Natl. Acad. Sci. USA*, **118**, e2020962118, https://doi.org/10.1073/pnas.2020962118.

Pogliotti, P., M. Guglielmin, E. Cremonese, U. M. di Cella, G. Filippa, C. Pellet, and C. Hauck, 2015: Warming permafrost and active layer variability at Cime Bianche, Western European Alps. *Cryosphere*, **9**, 647–661, https://doi.org/10.5194/tc-9-647-2015.

Popp, T., and Coauthors, 2016: Development, production and evaluation of aerosol climate data records from European satellite observations (Aerosol_cci). *Remote Sens.*, **8**, 421, https://doi.org/10.3390/rs8050421.

Poulter, B., and Coauthors, 2014: Contribution of semi-arid ecosystems to interannual variability of the global carbon cycle. *Nature*, **509**, 600–603, https://doi.org/10.1038/nature13376.

Prather, M. J., C. D. Holmes, and J. Hsu, 2012: Reactive greenhouse gas scenarios: Systematic exploration of uncertainties and the role of atmospheric chemistry. *Geophys. Res. Lett.*, **39**, L09803, https://doi.org/10.1029/2012GL051440.

Preimesberger, W., A. Pasik, R. van der Schalie, T. Scanlon, R. Kidd, R. A. M. De Jeu, and W. A. Dorigo, 2020: Soil moisture [in "State of the Climate in 2019"]. *Bull. Amer. Meteor.*, **101** (8), S81–S83, https://doi.org/10.1175/BAMS-D-20-0104.1.

Quartly, G. D., and Coauthors, 2020: The roles of the S3MPC: Monitoring, validation and evolution of Sentinel-3 altimetry observations. *Remote Sens.*, **12**, 1763, https://doi.org/10.3390/rs12111763.

Ramon, J., L. Lledó, V. Torralba, A. Soret, and F. J. Doblas-Reyes, 2019: What global reanalysis best represents near-surface winds? *Quart. J. Roy. Meteor. Soc.*, **145**, 3236–3251, https://doi.org/10.1002/qj.3616.

Randel, W. J., and J. B. Cobb, 1994: Coherent variations of monthly mean total ozone and lower stratospheric temperature. *J. Atmos. Sci.*, **99**, 5433–5447, https://doi.org/10.1029/93JD03454.

——, A. K. Smith, F. Wu, C.-Z. Zou, and H. Qian, 2016: Stratospheric temperature trends over 1979–2015 derived from combined SSU, MLS and SABER satellite observations. *J. Climate*, **29**, 4843–4859, https://doi.org/10.1175/JCLI-D-15-0629.1.

——, C. Covey, and L. Polvani, 2020: Stratospheric temperature [in "State of the Climate in 2019"]. *Bull. Amer. Meteor. Soc.*, **101** (8) S32–S34, https://doi.org/10.1175/BAMS-D-20-0104.1.

Ravishankara, A. R., J. S. Daniel, and R. W. Portmann, 2009: Nitrous oxide (N_2O): The dominant ozone-depleting substance emitted in the 21st century. *Science*, **326**, 123–125, https://doi.org/10.1126/science.1176985.

Ray, E. A., and Coauthors, 2017: Quantification of the SF6 lifetime based on mesospheric loss measured in the stratospheric polar vortex. *J. Geophys. Res. Atmos.*, **122**, 4626–4638, https://doi.org/10.1002/2016JD026198.

Reichstein, M., and Coauthors, 2013: Climate extremes and the carbon cycle. *Nature*, **500**, 287–295, https://doi.org/10.1038/nature12350.

Ricciardulli, L., 2016: ASCAT on MetOp-A data product update notes: V2.1 Data Release. Tech. Rep. 040416, Remote Sensing Systems, Santa Rosa, CA, 5 pp., http://images.remss.com/papers/rsstech/2016_040416_RSS_ASCAT_V2_update.pdf.

——, and F. J. Wentz, 2015: A scatterometer geophysical model function for climate-quality winds: QuikSCAT Ku-2011. *J. Atmos. Oceanic Technol.*, **32**, 1829–1846, https://doi.org/10.1175/JTECH-D-15-0008.1.

Richardson, A. D., 2018: Tracking seasonal rhythms of plants in diverse ecosystems with digital camera imagery. *New Phytol.*, **222**, 1742–1750, https://doi.org/10.1111/nph.15591.

——, and J. O'Keefe, 2009: Phenological differences between understory and overstory. *Phenology of Ecosystem Processes*, A. Noormets, Eds., Springer, 87–117, https://doi.org/10.1007/978-1-4419-0026-5_4.

Richardson, M., K. Cowtan, and R. J. Millar, 2018: Global temperature definition affects achievement of long-term climate goals. *Environ. Res. Lett.*, **13**, 054004, https://doi.org/10.1088/1748-9326/aab305.

Ričko, M., and Coauthors, 2012: Intercomparison and validation of continental water level products derived from satellite radar altimetry. *J. Appl. Remote Sens.*, **6**, 061710, https://doi.org/10.1117/1.JRS.6.061710.

Rigby, M., and Coauthors, 2019: Increase in CFC-11 emissions from eastern China based on atmospheric observations. *Nature*, **569**, 546–550, https://doi.org/10.1038/s41586-019-1193-4.

Roderick, M. L., L. D. Rotstayn, G. D. Farquhar, and M. T. Hobbins, 2007: On the attribution of changing pan evaporation. *Geophys. Res. Lett.*, **34**, L17403, https://doi.org/10.1029/2007GL031166.

Rodríguez, E., 2020: 'Apocalyptic' fires are ravaging the world's largest tropical wetland. *Nature*, 586, 20–21, https://doi.org/10.1038/d41586-020-02716-4.

Rodríguez-Fernández, N. J., and Coauthors, 2018: An evaluation of SMOS L-band vegetation optical depth (L-VOD) data sets: High sensitivity of L-VOD to above-ground biomass in Africa. *Biogeosciences*, **15**, 4627–4645, https://doi.org/10.5194/bg-15-4627-2018.

Romanovsky, V. E., T. S. Sazonova, V. T. Balobaev, N. I. Shender, and D. O. Sergueev, 2007: Past and recent changes in air and permafrost temperatures in eastern. Siberia *Global Planet. Change*, **56**, 399-413, https://10.1016/j.gloplacha.2006.07.022.

Romanovsky, V. E., and Coauthors, 2010: Thermal state of permafrost in Russia. *Permafrost Periglacial Processes*, **21**, 136–155, https://doi.org/10.1002/ppp.683.

Rubino, A., D. Zanchettin, F. De Rovere, and M. J. McPhaden, 2020: On the interchangeability of sea-surface and near-surface air temperature anomalies in climatologies. *Sci. Rep.*, **10**, 7433, https://doi.org/10.1038/s41598-020-64167-1.

Sanchez-Lugo, A., C. Morice, P. Berrisford, and A. Arguez, 2017: Global surface temperatures [in "State of the Climate in 2016"]. *Bull. Amer. Meteor. Soc.*, **90** (8), S11–S13, https://doi.org/10.1175/2017BAMSStateoftheClimate.1.

Santer, B. D., and Coauthors, 2008: Consistency of modelled and observed temperature trends in the tropical troposphere. *Int. J. Climatol.*, **28**, 1703–1722, https://doi.org/10.1002/joc.1756.

——, and Coauthors, 2014: Volcanic contribution to decadal changes in tropospheric temperature. *Nat. Geosci.*, **7**, 185–189, https://doi.org/10.1038/ngeo2098.

——, and Coauthors, 2017: Tropospheric warming over the past two decades. *Sci. Rep.*, **7**, 2336, https://doi.org/10.1038/s41598-017-02520-7.

Santoso, A., and Coauthors, 2019: Dynamics and predictability of the El Nino-Southern Oscillation: An Australian perspective on progress and challenges. *Bull. Amer. Meteor. Soc.*, **100**, 403–420, https://doi.org/10.1175/BAMS-D-18-0057.1.

Satheesh, S. K., and Coauthors, 2017: Variability of atmospheric aerosols over India. Observed Climate Variability and Change over the Indian Region, M. Rajeevan and S. Nayak, Springer, 221–248, https://doi.org/10.1007/978-981-10-2531-0_13.

Saunois, M., and Coauthors, 2020: The global methane budget 2000–2017. *Earth Syst. Sci. Data*, **12**, 1561–1623, https://doi.org/10.5194/essd-12-1561-2020.

Schaaf, C. B., and Coauthors, 2002: First operational BRDF, albedo nadir reflectance products from MODIS. *Remote Sens. Environ.*, **83**, 135–148, https://doi.org/10.1016/S0034-4257(02)00091-3.

Schaefer, H., and Coauthors, 2016: A 21st-century shift from fossil-fuel to biogenic methane emissions indicated by $^{13}CH_4$. *Science*, **352**, 80–84, https://doi.org/10.1126/science.aad2705.

Schamm, K., M. Ziese, A. Becker, P. Finger, A. Meyer-Christoffer, B. Rudolf, and U. Schneider, 2013: GPCC First Guess Daily Product at 1.0°: Near Real-Time First Guess Daily Land-Surface Precipitation from Rain-Gauges Based on SYNOP Data. Global Precipitation Climatology Centre, accessed 18 January 2021, https://doi.org/10.5676/DWD_GPCC/FG_D_100.

Schneider, T., P. A. O'Gorman, and X. J. Levine, 2010: Water vapor and the dynamics of climate changes. *Rev. Geophys.*, **48**, RG3001, https://doi.org/10.1029/2009RG000302.

Schneider, U., A. Becker, P. Finger, R. Elke, and M. Ziese, 2020: GPCC Monitoring Product: Near Real-Time Monthly Land-Surface Precipitation from Rain-Gauges based on SYNOP and CLIMAT Data, Global Precipitation Climatology Centre Global Precipitation Climatology Centre, accessed 2 March 2021, https://doi.org/10.5676/DWD_GPCC/MP_M_V2020_100.

Schroeder, W., P. Oliva, L. Giglio, and I. A. Csiszar, 2014: The new VIIRS 375m active fire detection data product: Algorithm description and initial assessment. *Remote Sens. Environ.*, 143, 85–96, https://doi.org/10.1016/j.rse.2013.12.008.

Schwartz, M. J., and Coauthors, 2020: Australian New Year's PyroCb impact on stratospheric composition. *Geophys. Res. Lett.*, **47**, e2020GL090831, https://doi.org/10.1029/2020GL090831.

Schwietzke, S., and Coauthors, 2016: Upward revision of global fossil fuel methane emissions based on isotope database. *Nature*, **538**, 88–91, https://doi.org/10.1038/nature19797.

Seyednasrollah, B., and Coauthors, 2019: Tracking vegetation phenology across diverse biomes using Version 2.0 of the PhenoCam Dataset. *Sci. Data*, **6**, 261, https://doi.org/10.1038/s41597-019-0270-8.

Sharma, S., and R. I. Woolway, 2020: Lake ice [in "State of the Climate in 2019"]. *Bull. Amer. Meteor. Soc.*, **101** (8), S39–S41, https://doi.org/10.1175/BAMS-D-20-0104.1.

Shi, L., and J. J. Bates, 2011: Three decades of intersatellite-calibrated high-resolution infrared radiation sounder upper tropospheric water vapor. *J. Geophys. Res.*, **116**, D04108, https://doi.org/10.1029/2010JD014847.

Simmons, A., and Coauthors, 2021: Low frequency variability and trends in surface air temperature and humidity from ERA5 and other datasets. ECMWF Tech. Memo. 881, 97 pp., https://doi.org/10.21957/ly5vbtbfd.

Simmons, A. J., P. Berrisford, D. P. Dee, H. Hersbach, S. Hirahara, and J. N. Thepaut, 2017: A reassessment of temperature variations and trends from global reanalyses and monthly surface climatological datasets. *Quart. J. Roy. Meteor. Soc.*, **143**, 101–119, https://doi.org/10.1002/qj.2949.

Simpson, I. R., T. G. Shepherd, and M. Sigmond, 2011: Dynamics of the lower stratospheric circulation response to ENSO. *J. Atmos. Sci.*, **68**, 2537–2556, https://doi.org/10.1175/JAS-D-11-05.1.

Slater, T., and Coauthors, 2021: Review article: Earth's ice imbalance. *Cryosphere*, **15**, 233–246, https://doi.org/10.5194/tc-15-233-2021.

Slivinski, L. C., and Coauthors, 2019: Towards a more reliable historical reanalysis: Improvements for version 3 of the twentieth century reanalysis system. *Quart. J. Roy. Meteor. Soc.*, **145**, 2876–2908, https://doi.org/10.1002/qj.3598.

Solomon, S., 1999: Stratospheric ozone depletion: A review of concepts and history. *Rev. Geophys.*, **37**, 275–316, https://doi.org/10.1029/1999RG900008.

——, K. H. Rosenlof, R. W. Portmann, J. S. Daniel, S. M. Davis, T. J. Sanford, and G.-K. Plattner, 2010: Contributions of stratospheric water vapor to decadal changes in the rate of global warming. *Science*, **327**, 1219–1223, https://doi.org/10.1126/science.1182488.

——, D. Kinnison, J. Bandoro, and R. Garcia, 2015: Simulation of polar ozone depletion: An update. *J. Geophys. Res.*, **120**, 7958–7974, https://doi.org/10.1002/2015JD023365.

SPARC/IO3C/GAW, 2019: SPARC/IO3C/GAW report on long-term ozone trends and uncertainties in the stratosphere. SPARC Rep. No. 9, WCRP-17/2018, GAW Rep. 241, 99 pp., https://doi.org/10.17874/f899e57a20b.

Spencer, R. W., J. R. Christy, and W. D. Braswell, 2017: UAH Version 6 global satellite temperature products: Methodology and results. *Asia-Pac. J. Atmos. Sci.*, **53**, 121–130, https://doi.org/10.1007/s13143-017-0010-y.

Stackhouse, P. W., T. Wong, D. P. Kratz, P. Sawaengphokhai, A. C. Wiber, S. K. Gupta, and N. G. Loeb, 2016: Earth radiation budget at top-of-atmosphere [in "State of the Climate in 2015"]. *Bull. Amer. Meteor. Soc.*, **97** (8), S41–S43, https://doi.org/10.1175/2016BAMSStateoftheClimate.1.

Staub, B., C. Lambiel, and R. Delaloye, 2016: Rock glacier creep as a thermally-driven phenomenon: A decade of inter-annual observation from the Swiss Alps. XI Int. Conf. on Permafrost, Potsdam, Germany, Alfred Wegener Institute Helmholtz Center for Polar and Marine Research, 96–97, https://doi.org/10.2312/GFZ.LIS.2016.001.

Steinbrecht, W., and Coauthors, 2017: An update on ozone profile trends for the period 2000 to 2016. *Atmos. Chem. Phys.*, **17**, 10675–10690, https://doi.org/10.5194/acp-17-10675-2017.

Stengel, M., and Coauthors, 2017: Cloud property datasets retrieved from AVHRR, MODIS, AATSR and MERIS in the framework of the Cloud_cci project. *Earth Syst. Sci. Data*, **9**, 881–904, https://doi.org/10.5194/essd-9-881-2017.

Strode, S. A., J. R. Ziemke, L. D. Oman, L. N. Lamsal, M. A. Olsen, and J. Liu, 2019: Global changes in the diurnal cycle of surface ozone. *Atmos. Environ.*, **199**, 323–333, https://doi.org/10.1016/j.atmosenv.2018.11.028.

Stroeve, J., J. E. Box, Z. Wang, C. Schaaf, and A. Barrett, 2013: Re-evaluation of MODIS MCD43 Greenland albedo accuracy and trends. *Remote Sens. Environ.*, **138**, 199–214, https://doi.org/10.1016/j.rse.2013.07.023.

Strozzi, T., and Coauthors, 2020: Monitoring rock glacier kinematics with satellite synthetic aperture radar. *Remote Sens.*, **12**, 559, https://doi.org/10.3390/rs12030559.

Sun, W., P. Hess, and B. Tian, 2014: The response of the equatorial tropospheric ozone to the Madden-Julian Oscillation in TES satellite observations and CAM-chem model simulation. *Atmos. Chem. Phys.*, **14**, 11775–11790, https://doi.org/10.5194/acp-14-11775-2014.

Susskind, J., G. Molnar, L. Iredell, and N. G. Loeb, 2012: Interannual variability of outgoing longwave radiation as observed by AIRS and CERES. *J. Geophys. Res.*, **117**, D23107, https://doi.org/10.1029/2012JD017997.

Swiss Re, 2020: Swiss Re Institute estimates USD 83 billion global insured catastrophe losses in 2020, the fifth-costliest on record. 15 December, accessed 9 February 2021, www.swissre.com/media/news-releases/nr-20201215-sigma-full-year-2020-preliminary-natcat-loss-estimates.html.

Takaya, Y., I. Ishikawa, C. Kobayashi, H. Endo, and T. Ose, 2020: Enhanced Meiyu-Baiu rainfall in early summer 2020: Aftermath of the 2019 super IOD event. *Geophys. Res. Lett.*, **47**, e2020GL090671, https://doi.org/10.1029/2020GL090671.

Talsma, C. J., S. P. Good, C. Jiménez, B. Martens, J. B. Fisher, D. G. Miralles, M. F. McCabe, and A. J. Purdy, 2018: Partitioning of evapotranspiration in remote sensing-based models. *Agric. For. Meteor.*, **260–261**, 131–143, https://doi.org/10.1016/j.agrformet.2018.05.010.

Tapley, B. D., S. Bettadpur, J. C. Ries, P. F. Thompson, and M. M. Watkins, 2004: GRACE measurements of mass variability in the Earth system. *Science*, **305**, 503–505, https://doi.org/10.1126/science.1099192.

Tarasick, D. W., and Coauthors, 2019: Tropospheric Ozone Assessment Report: Tropospheric ozone from 1877 to 2016, observed levels, trends and uncertainties. *Elem. Sci. Anthropocene*, **7**, 39, https://doi.org/10.1525/elementa.376.

Teng, W.-H., C.-Y. Huang, S.-P. Ho, Y.-H. Kuo, and X.-J. Zhou, 2013: Characteristics of global precipitable water in ENSO events revealed by COSMIC measurements. *J. Geophys. Res. Atmos.*, **118**, 8411–8425, https://doi.org/10.1002/jgrd.50371.

Teubner, I. E., and Coauthors, 2018: Assessing the relationship between microwave vegetation optical depth and gross primary production. *Int. J. Appl. Earth Obs. Geoinf.*, **65**, 79–91, https://doi.org/10.1016/j.jag.2017.10.006.

——, and Coauthors, 2019: A carbon sink-driven approach to estimate gross primary production from microwave satellite observations. *Remote Sens. Environ.*, **229**, 100–113, https://doi.org/10.1016/j.rse.2019.04.022.

The Watchers, 2020: Very rare cyclone over the Middle East, state of emergency declared in Egypt. 12 March, accessed 11 February 2021, https://watchers.news/2020/03/12/very-rare-cyclone-over-the-middle-east-state-of-emergency-declared-in-egypt/.

Thibert, E., M. Bonnefoy-Demongeot, F. Finance, and X. Bodin, 2018. Extracting the time signal in surface velocity changes along 3 decades at Laurichard rock glacier (French Alps). *5th European Conf. Permafrost, Book of Abstracts*, Chamonix, France, Laboratoire EDYTEM, 615–616.

Thompson, R. L., and Coauthors, 2019: Acceleration of global N_2O emissions seenfrom two decades of atmospheric inversion. *Nat. Climate Change*, **9**, 993–998, https://doi.org/10.1038/s41558-019-0613-7.

Tian, H., and Coauthors, 2020: A comprehensive quantification of global nitrous oxide sources and sinks. *Nature*, **586**, 248–256, https://doi.org/10.1038/s41586-020-2780-0.

Timmermann, A., and Coauthors, 2018: El Niño–Southern Oscillation complexity. *Nature*, **559**, 535–545, https://doi.org/10.1038/s41586-018-0252-6.

Torralba, V., F. J. Doblas-Reyes, and N. Gonzalez-Reviriegol, 2017: Uncertainty in recent near-surface wind speed trends: A global reanalysis intercomparison. *Environ. Res. Lett.*, **12**, 114019, https://doi.org/10.1088/1748-9326/aa8a58.

Trepte, Q. Z., P. Minnis, C. R. Trepte, S. Sun-Mack, and R. Brown, 2010: Improved cloud detection in CERES Edition 3 algorithm and comparison with the CALIPSO Vertical Feature Mask. *13th Conf. on Atmospheric Radiation and Cloud Physics*, Portland, OR, Amer. Meteor. Soc., JP1.32, https://ams.confex.com/ams/13CldPhy13AtRad/webprogram/Paper171785.html.

Turner, A. J., and Coauthors, 2020: Observed impacts of COVID-19 on urban CO_2 emissions. *Geophys. Res. Lett.*, **47**, e2020GL090037, https://doi.org/10.1029/2020GL090037.

Turner, J., G. J. Marshall, K. Clem, S. Colwell, T. Phillips, and H. Lu, 2020: Antarctic temperature variability and change from station data. *Int. J. Climatol.*, **40**, 2986–3007, https://doi.org/10.1002/joc.6378.

van der A, R. J., M. A. F. Allaart, and H. J. Eskes, 2015: Extended and refined multi sensor reanalysis of total ozone for the period 1970–2012. *Atmos. Meas. Tech.*, **8**, 3021–3035, https://doi.org/10.5194/amt-8-3021-2015.

van der Schalie, R., and Coauthors, 2017: The merging of radiative transfer based surface soil moisture data from SMOS and AMSR-E. *Remote Sens. Environ.*, **189**, 180–193, https://doi.org/10.1016/j.rse.2016.11.026.

——, R. De Jeu, R. Parinussa, N. Rodríguez-Fernández, Y. Kerr, A. Al-Yaari, J.-P. Wigneron, and M. Drusch, 2018: The effect of three different data fusion approaches on the quality of soil moisture retrievals from multiple passive microwave sensors. *Remote Sens.*, **10**, 107, https://doi.org/10.3390/rs10010107.

van der Schrier, G., J. Barichivich, K. R. Briffa, and P. D. Jones, 2013: A scPDSI-based global dataset of dry and wet spells for 1901-2009. *J. Geophys. Res. Atmos.*, **118**, 4025–4048, https://doi.org/10.1002/jgrd.50355.

van der Werf, G. R., and Coauthors, 2017: Global fire emissions estimates during 1997–2016. *Earth Syst. Sci. Data*, **9**, 697–720, https://doi.org/10.5194/essd-9-697-2017.

van Dijk, A. I. J. M., H. E. Beck, R. S. Crosbie, R. A. M. de Jeu, Y. Y. Liu, G. M. Podger, B. Timbal, and N. R. Viney, 2013: The Millennium Drought in southeast Australia (2001–2009): Natural and human causes and implications for water resources, ecosystems, economy, and society. *Water Resour. Res.*, **49**, 1040–1057, https://doi.org/10.1002/wrcr.20123.

van Heerwaarden, C. C., and Coauthors, 2021: Record high solar irradiance in Western Europe during first COVID-19 lockdown largely due to unusual weather. *Commun. Earth Environ.*, **2**, 37, https://doi.org/10.1038/s43247-021-00110-0.

van Marle, M. J. E., R. D. Field, G. R. van der Werf, I. A. Estrada de Wagt, R. A. Houghton, L. V. Rizzo, P. Artaxo, and K. Tsigaridis, 2016: Fire and deforestation dynamics in Amazonia (1973–2014). *Global Biogeochem. Cycles*, **31**, 24–38, https://doi.org/10.1002/2016GB005445.

van Oldenborgh, G. J., and Coauthors, 2020: Attribution of the Australian bushfire risk to anthropogenic climate change. *Nat. Hazards Earth Syst. Sci.*, **21**, 941–960, https://doi.org/10.5194/nhess-2020-69.

Vautard, R., J. Cattiaux, P. Yiou, J. N. Thépaut, and P. Ciais, 2010: Northern Hemisphere atmospheric stilling partly attributed to an increase in surface roughness. *Nat. Geosci.*, **3**, 756–761, https://doi.org/10.1038/ngeo979.

Vernier, J.-P., and Coauthors, 2011: Major influence of tropical volcanic eruptions on the stratospheric aerosol layer during the last decade. *Geophys. Res. Lett.*, **38**, L12807, https://doi.org/10.1029/2011GL047563.

Vose, R. S., and Coauthors, 2012: NOAA's merged land–ocean surface temperature analysis. *Bull. Amer. Meteor. Soc.*, **93**, 1677–1685, https://doi.org/10.1175/BAMS-D-11-00241.1.

Vreugdenhil, M., S. Hahn, T. Melzer, B. Bauer-Marschallinger, C. Reimer, W. Dorigo, and W. Wagner, 2017: Assessing vegetation dynamics over Mainland Australia with Metop ASCAT. *IEEE J. Sel. Top. Appl. Earth Obs. Remote Sens.*, **10**, 2240–2248, https://doi.org/10.1109/JSTARS.2016.2618838.

Wagner, W., and Coauthors, 2013: The ASCAT soil moisture product: A review of its specifications, validation results, and emerging applications. *Meteor. Z.*, **22**, 5–33, https://doi.org/10.1127/0941-2948/2013/0399.

Wainwright, C. M., D. L. Finney, M. Kilavi, E. Black, and J. H. Marsham, 2020: Extreme rainfall in East Africa October 2019–January 2020 and context under future climate change. *Weather*, **76**, 26–31, https://doi.org/10.1002/wea.3824.

Wang, C., C. Deser, J. Y. Yu, P. DiNezio, and A. Clement, 2017: El Niño and Southern Oscillation (ENSO): A Review. *Coral Reefs of the Eastern Tropical Pacific*, P. Glynn, D. Manzello, and I. Enochs, Eds., Coral Reefs of the World, Vol. 8, Springer, 85–106, https://doi.org/10.1007/978-94-017-7499-4_4.

Wang, G., and W. Cai, 2020: Two-year consecutive concurrences of positive Indian Ocean Dipole and Central Pacific El Niño preconditioned the 2019/2020 Australian "black summer" bushfires. *Geosci. Lett.*, **7**, 19, https://doi.org/10.1186/s40562-020-00168-2.

Wang, S.-Y., H. Kim, D. Coumou, J-.H. Yoon, L. Zhao and R. Gillies, 2019: Consecutive extreme flood and heat wave events in Japan: Are they becoming a norm? *Atmos. Sci. Lett.*, 20, e933, https://doi.org/10.1002/asl.933.

Wang, Z., and Coauthors, 2012: The isotopic record of Northern Hemisphere atmospheric carbon monoxide since 1950: Implications for the CO budget. *Atmos. Chem. Phys.*, **12**, 4365–4377, https://doi.org/10.5194/acp-12-4365-2012.

Weatherhead, E. C., and Coauthors, 1998: Factors affecting the detection of trends: Statistical considerations and applications to environmental data. *J. Geophys. Res.*, **103**, 17149–17161, https://doi.org/10.1029/98JD00995.

Weber, M., and Coauthors, 2018: Total ozone trends from 1979 to 2016 derived from five merged observational datasets – The emergence into ozone recovery. *Atmos. Chem. Phys.*, **18**, 2097–2117, https://doi.org/10.5194/acp-18-2097-2018.

——, and Coauthors, 2021: The unusual stratospheric Arctic winter 2019/20: Chemical ozone loss from satellite observations and TOMCAT chemical transport model. *J. Geophys. Res. Atmos.*, **126**, e2020JD034386, https://doi.org/10.1029/2020JD034386.

Wells, N., S. Goddard, and M. J. Hayes, 2004: A self-calibrating palmer drought severity index. *J. Climate*, **17**, 2335–2351, https://doi.org/10.1175/1520-0442(2004)017<2335:ASPDSI>2.0.CO;2.

Weng, H. Y., K. Ashok, S. Behera, A. S. Rao, and T. Yamagata, 2007: Impacts of recent El Niño Modoki on dry/wet conditions in the Pacific rim during boreal summer. *Climate Dyn.*, **29**, 113–129, https://doi.org/10.1007/s00382-007-0234-0.

Wentz, F. J., 1997: A well calibrated ocean algorithm for Special Sensor Microwave/Imager. *J. Geophys. Res.*, **102**, 8703–8718, https://doi.org/10.1029/96JC01751.

——, 2015: A 17-year climate record of environmental parameters derived from the Tropical Rainfall Measuring Mission (TRMM) microwave imager. *J. Climate*, **28**, 6882–6902, https://doi.org/10.1175/JCLI-D-15-0155.1.

——, L. Ricciardulli, K. Hilburn, and C. Mears, 2007: How much more rain will global warming bring? *Science*, **317**, 233–235, https://doi.org/10.1126/science.1140746.

WGMS, 2017: Global Glacier Change Bulletin No. 2 (2014-2015). M. Zemp et al., Eds., World Glacier Monitoring Service, 244 pp., https://wgms.ch/ggcb/.

——, 2018: Glacier Map Collection (GMC), World Glacier Monitoring Service, https://doi.org/10.5904/wgms-maps-2018-02

——, 2020: Global Glacier Change Bulletin No. 3 (2016-2017). M. Zemp et al., Eds., World Glacier Monitoring Service, 274 pp., https://wgms.ch/ggcb/.

Wielicki, B. A., B. R. Barkstrom, E. F. Harrison, R. B. Lee III., G. L. Smith, and J. E. Cooper, 1996: Clouds and the Earth's Radiant Energy System (CERES): An Earth observing system experiment. *Bull. Amer. Meteor. Soc.*, **77**, 853–868, https://doi.org/10.1175/1520-0477(1996)077<0853:CATERE>2.0.CO;2.

——, and Coauthors, 1998: Clouds and the Earth's Radiant Energy System (CERES): Algorithm overview. *IEEE Trans. Geosci. Remote Sens.*, **36**, 1127–1141, https://doi.org/10.1109/36.701020.

Wiese, D. N., F. W. Landerer, and M. M. Watkins, 2016: Quantifying and reducing leakage errors in the JPL RL05M GRACE mascon solution. *Water Resour. Res.*, **52**, 7490–7502, https://doi.org/10.1002/2016WR019344.

Willett, K. M., C. N. Williams Jr., R. J. H. Dunn, P. W. Thorne, S. Bell, M. de Podesta, P. D. Jones, and D. E. Parker, 2013: HadISDH: An updated land surface specific humidity product for climate monitoring. *Climate Past*, **9**, 657–677, https://doi.org/10.5194/cp-9-657-2013.

——, R. J. H. Dunn, P. W. Thorne, S. Bell, M. de Podesta, D. E. Parker, P. D. Jones, and C. N. Williams Jr., 2014: HadISDH land surface multi-variable humidity and temperature record for climate monitoring. *Climate Past*, **10**, 1983–2006, https://doi.org/10.5194/cp-10-1983-2014.

——, R. J. H. Dunn, J. Kennedy, and D. Berry, 2020: Development of the HadISDH marine humidity climate monitoring dataset. *Earth Syst. Sci. Data*, **12**, 2853–2880, https://doi.org/10.5194/essd-12-2853-2020.

Wills, R. C. J., R. H. White, and X. J. Levine, 2019: Northern Hemisphere stationary waves in a changing climate. *Curr. Climate Change Rep.*, **5**, 372–389, https://doi.org/10.1007/s40641-019-00147-6.

Winker, D. M., W. Hunt, and M. J. McGill, 2007: Initial performance assessment of CALIOP. *Geophys. Res. Lett.*, **34**, L19803, https://doi.org/10.1029/2007GL030135.

WMO, 2018: Scientific assessment of ozone depletion, 2018. Global Ozone Research and Monitoring Project Rep. 58, 588 pp., https://csl.noaa.gov/assessments/ozone/2018/.

——, 2021: State of the Global Climate 2020. Provisional Rep., 38 pp., accessed 11 February 2021, https://library.wmo.int/doc_num.php?explnum_id=10444.

Wohland, J., N.-E. Omrani, D. Witthaut, and N.-S. Keenlyside, 2019: Inconsistent wind speed trends in current twentieth century reanalyses. *J. Geophys. Res. Atmos.*, **124**, 1931–1940, https://doi.org/10.1029/2018JD030083.

Woolway, R. I., and C. J. Merchant, 2018: Intralake heterogeneity of thermal responses to climate change: A study of large Northern Hemisphere lakes. *J. Geophys. Res. Atmos.*, **123**, 3087–3098, https://doi.org/10.1002/2017JD027661.

——, and Coauthors, 2017: Lake surface temperature [in "State of the Climate in 2016"]. *Bull. Amer. Meteor. Soc.*, **98** (8), S13–S14, https://doi.org/10.1175/2017BAMSStateoftheClimate.1.

——, and Coauthors, 2018: Lake surface temperature [in "State of the Climate in 2017"]. *Bull. Amer. Meteor. Soc.*, **99** (8), S13–S15, https://doi.org/10.1175/2018BAMSStateoftheClimate.1.

——, B. M. Kraemer, J. D. Lenters, C. J. Merchant, C. M. O'Reilly, and S. Sharma, 2020: Global lake responses to climate change. *Nat. Rev. Earth Environ.*, **1**, 388–403, https://doi.org/10.1038/s43017-020-0067-5.

Worden, J. R., and Coauthors, 2017: Reduced biomass burning emissions reconcile conflicting estimates of the post-2006 atmospheric methane budget. *Nat. Commun.*, **8**, 2227, https://doi.org/10.1038/s41467-017-02246-0.

Wu, Q., and T. Zhang, 2008: Recent permafrost warming on the Qinghai—Tibetan Plateau. *J. Geophys. Res. Atmos.*, **113**, 1–22, https://doi.org/10.1029/2007JD009539.

Wylie, D. P., D. L. Jackson, W. P. Menzel, and J. J. Bates, 2005: Trends in Global cloud cover in two decades of HIRS observations. *J. Climate*, **18**, 3021–3031, https://doi.org/10.1175/JCLI3461.1.

Yamazaki, D., S. Kanae, H. Kim, and T. Oki, 2011: A physically-based description of floodplain elevation dynamics in a global river routing model. *Water Resour. Res.*, **47**, W04501, https://doi.org/10.1029/2010WR009726.

Yang, J., Q. Liu, S.-P. Xie, Z. Liu, and L. Wu, 2007: Impact of the Indian Ocean SST basin mode on the Asian summer monsoon. *Geophys. Res. Lett.*, **34**, L02708, https://doi.org/10.1029/2006GL028571.

Yin, Y., and Coauthors, 2020: Accelerating methane growth rate from 2010 to 2017: Leading contributions from the tropics and East Asia. *Atmos. Chem. Phys. Discuss.*, https://doi.org/10.5194/acp-2020-649.

Yosef, Y., E. Aguilar, and P. Alpert, 2021: Is it possible to fit extreme climate change indices together seamlessly in the era of accelerated warming? *Int. J. Climatol.*, **41**, E952–E963, https://doi.org/10.1002/joc.6740.

Young, I., and A. Ribal, 2019: Multiplatform evaluation of global trends in wind speed and wave height. *Science*, **364**, 548–552, https://doi.org/10.1126/science.aav9527.

Young, P. J., and Coauthors, 2013: Pre-industrial to end 21st century projections of tropospheric ozone from the Atmospheric Chemistry and Climate Model Inter-comparison Project (ACCMIP). *Atmos. Chem. Phys.*, **13**, 2063–2090, https://doi.org/10.5194/acp-13-2063-2013.

——, and Coauthors, 2018: Tropospheric Ozone Assessment Report: Assessment of global-scale model performance for global and regional ozone distributions, variability, and trends. *Elem. Sci. Anthropocene*, **6**, 10, https://doi.org/10.1525/elementa.265.

Yu, P., and Coauthors, 2021: Persistent stratospheric warming due to 2019-2020 Australian wildfire smoke. *Geophys. Res. Lett.*, **48**, e2021GL092609, https://doi.org/10.1029/2021GL092609.

Zemp, M., and Coauthors, 2019: Global glacier mass changes and their contributions to sea-level rise from 1961 to 2016. *Nature*, **568**, 382–386, https://doi.org/10.1038/s41586-019-1071-0.

Zeng, Z., and Coauthors, 2019: A reversal in global terrestrial stilling and its implications for wind energy production. *Nat. Climate Change*, **9**, 979–985, https://doi.org/10.1038/s41558-019-0622-6.

Zhang, H.-M., and Coauthors, 2019: Updated temperature data give a sharper view of climate trends, *Eos*, **100**, https://doi.org/10.1029/2019EO012822.

Zhang, X., and Coauthors, 2011: Indices for monitoring changes in extremes based on daily temperature and precipitation data. *Wiley Interdiscip. Rev.: Climate Change*, **2**, 851–870, https://doi.org/10.1002/wcc.147.

Zhang, Y., J. M. Wallace, and D. S. Battisti, 1997: ENSO-like interdecadal variability: 1900-93. *J. Climate*, **10**, 1004–1020, https://doi.org/10.1175/1520-0442(1997)010<1004:ELIV>2.0.CO;2.

Zhang, Y., and Coauthors, 2016a: Multi-decadal trends in global terrestrial evapotranspiration and its components. *Sci. Rep.*, **6**, 19124, https://doi.org/10.1038/srep19124.

——, O. R. Cooper, A. Gaudel, A. M. Thompson, P. Nédélec, S.-Y. Ogino, and J. J. West, 2016b: Tropospheric ozone change from 1980 to 2010 dominated by equatorward redistribution of emissions. *Nat. Geosci.*, **9**, 875–879, https://doi.org/10.1038/ngeo2827.

Zhang, Y., and Coauthors, 2020: Contributions of world regions to the global tropospheric ozone burden change from 1980 to 2010. *Geophys. Res. Lett.*, **47**, e2020GL089184, https://doi.org/10.1029/2020GL089184.

Zhang, W., W. Mao, F. Jiang, M. F. Stuecker, F-F. Jin, and L. Qi, 2021: Tropical Indo-Pacific compounding thermal conditions drive the 2019 Australian extreme drought. *Geophys. Res. Lett.*, **48**, e2020GL090323. https://doi.org/10.1029/2020GL090323.

Zhao, L., and Coauthors, 2020: Changing climate and the permafrost environment on the Qinghai–Tibet (Xizang) plateau. *Permafrost Periglacial Processes*, **31**, 396–405, https://doi.org/10.1002/ppp.2056.

——, and Coauthors, 2021: A synthesis dataset of permafrost thermal state for the Qinghai-Xizang (Tibet) plateau, China. *Earth Syst. Sci. Data Discuss.*, https://doi.org/10.5194/essd-2021-1.

Ziemke, J. R., and O. R. Cooper, 2019: Tropospheric ozone [in "State of the Climate in 2019"]. *Bull. Amer. Meteor. Soc.*, **101** (8), S83–S85, https://doi.org/10.1175/BAMS-D-20-0104.1.

——, A. R. Douglass, L. D. Oman, S. E. Strahan, and B. N. Duncan, 2015: Tropospheric ozone variability in the tropical Pacific from ENSO to MJO and shorter timescales. *Atmos. Chem. Phys.*, **15**, 8037–8049, https://doi.org/10.5194/acp-15-8037-2015.

——, and Coauthors, 2019: Trends in global tropospheric ozone inferred from a composite record of TOMS/OMI/MLS/OMPS satellite measurements and the MERRA-2 GMI simulation. *Atmos. Chem. Phys.*, **19**, 3257–3269, https://doi.org/10.5194/acp-19-3257-2019.

Zou, C.-Z., and H. Qian, 2016: Stratospheric temperature climate data record from merged SSU and AMSU-A observations. *J. Atmos. Oceanic Technol.*, **33**, 1967–1984, https://doi.org/10.1175/JTECH-D-16-0018.1.

STATE OF THE CLIMATE IN 2020

GLOBAL OCEANS

G. C. Johnson and R. Lumpkin, Eds.

Special Online Supplement to the *Bulletin of the American Meteorological Society* Vol.102, No. 8, August, 2021

https://doi.org/10.1175/ BAMS-D-21-0083.1
Corresponding author: Rick Lumpkin / rick.lumpkin@noaa.gov

STATE OF THE CLIMATE IN 2020
Global Oceans

Editors

Jessica Blunden
Tim Boyer

Chapter Editors

Freya Aldred
Peter Bissolli
Howard J. Diamond
Matthew L. Druckenmiller
Robert J. H. Dunn
Catherine Ganter
Nadine Gobron
Gregory C. Johnson
Tim Li
Rick Lumpkin
Ademe Mekonnen
John B. Miller
Twila A. Moon
Ahira Sánchez-Lugo
Ted A. Scambos
Carl J. Schreck III
Sharon Stammerjohn
Richard L. Thoman
Kate M. Willett

Technical Editor

Andrea Andersen

***BAMS* Special Editor for Climate**

Michael A. Alexander

American Meteorological Society

Cover credit:
Oil bar and pencil on mat board

Original artwork by Gregory C. Johnson–chapter co-editor

Global Oceans is a chapter from the *State of the Climate in 2020* annual report. This chapter is available from https://doi.org/10.1175/ BAMS-D-21-0083.1. Compiled by NOAA's National Centers for Environmental Information, *State of the Climate in 2020* is based on contributions from scientists from around the world. It provides a detailed update on global climate indicators, notable weather events, and other data collected by environmental monitoring stations and instruments located on land, water, ice, and in space. The full report is available from: https://doi.org/10.1175/2021BAMSStateoftheClimate.1.

How to cite this document:

Citing the complete report:
Blunden, J. and T. Boyer, Eds., 2021: "State of the Climate in 2020". *Bull. Amer. Meteor. Soc.*, **102** (8), Si–S475, https://doi.org/10.1175/2021BAMSStateoftheClimate.1.

Citing this chapter:
Johnson, G. C. and R. L. Lumpkin, Eds., 2021: Global Oceans [in "State of the Climate in 2020"]. *Bull. Amer. Meteor. Soc.*, **102** (8), S143–S198, https://doi.org/10.1175/ BAMS-D-21-0083.1.

Citing a section (example):
Yu, L., P. W. Stackhouse, A. C. Wilber, C. Wen, and R. A. Weller, 2021: Global ocean heat, freshwater, and momentum fluxes [in "State of the Climate in 2020"]. *Bull. Amer. Meteor. Soc.*, **102** (8), S164–S169, https://doi.org/10.1175/ BAMS-D-21-0083.1.

Editor and Author Affiliations (alphabetical by name)

Alin, Simone R., NOAA/OAR Pacific Marine Environmental Laboratory, Seattle, Washington
Amaya, Dillon J., Cooperative Institute for Research in Environmental Sciences, University of Colorado, Boulder, Colorado
Baringer, Molly O., NOAA/OAR Atlantic Oceanographic and Meteorological Laboratory, Miami, Florida
Boyer, Tim, NOAA/NESDIS National Centers for Environmental Information, Silver Spring, Maryland
Brandt, Peter, GEOMAR Helmholtz Centre for Ocean Research Kiel, Kiel, Germany
Carter, Brendan R., Cooperative Institute for Climate, Ocean, and Ecosystem Studies, University of Washington, Seattle, Washington; NOAA/OAR Pacific Marine Environmental Laboratory, Seattle, Washington
Cetinić, Ivona, NASA Goddard Space Flight Center, Greenbelt, Maryland; Universities Space Research Association, Columbia, Maryland
Chambers, Don P., College of Marine Science, University of South Florida, St. Petersburg, Florida
Cheng, Lijing, International Center for Climate and Environment Sciences, Institute of Atmospheric Physics, Chinese Academy of Sciences, Beijing, China
Collins, Andrew U., Cooperative Institute for Climate, Ocean, and Ecosystem Studies, Seattle, Washington, University of Washington,
Cosca, Cathy, NOAA/OAR Pacific Marine Environmental Laboratory, Seattle, Washington
Domingues, Ricardo, Cooperative Institute for Marine and Atmospheric Studies, University of Miami, Miami, Florida; NOAA/OAR Atlantic Oceanographic and Meteorological Laboratory, Miami, Florida
Dong, Shenfu, NOAA/OAR Atlantic Oceanographic and Meteorological Laboratory, Miami, Florida
Feely, Richard A., NOAA/OAR Pacific Marine Environmental Laboratory, Seattle, Washington
Frajka-Williams, Eleanor, National Oceanography Centre, United Kingdom
Franz, Bryan A., NASA Goddard Space Flight Center, Greenbelt, Maryland
Gilson, John, Scripps Institution of Oceanography, University of California San Diego, La Jolla, California
Goni, Gustavo, NOAA/OAR Atlantic Oceanographic and Meteorological Laboratory, Miami, Florida
Hamlington, Benjamin D., Center for Coastal Physical Oceanography, Old Dominion University, Norfolk, Virginia
Herrford, Josefine, GEOMAR Helmholtz Centre for Ocean Research Kiel, Kiel, Germany
Hu, Zeng-Zhen, NOAA/NWS NCEP Climate Prediction Center, College Park, Maryland
Huang, Boyin, NOAA/NESDIS National Centers for Environmental Information, Asheville, North Carolina
Ishii, Masayoshi, Department of Atmosphere, Ocean and Earth System Modeling Research, Meteorological Research Institute, Japan Meteorological Agency, Tsukuba, Japan
Jevrejeva, Svetlana, National Oceanography Centre, Liverpool, United Kingdom
Johnson, Gregory C., NOAA/OAR Pacific Marine Environmental Laboratory, Seattle, Washington
Kennedy, John J., Met Office Hadley Centre, Exeter, United Kingdom
Kersalé, Marion, Cooperative Institute for Marine and Atmospheric Studies, University of Miami, Miami, Florida; NOAA/OAR Atlantic Oceanographic and Meteorological Laboratory, Miami, Florida
Killick, Rachel E., Met Office Hadley Centre, Exeter, United Kingdom
Landschützer, Peter, Max Planck Institute for Meteorology, Hamburg, Germany
Lankhorst, Matthias, Scripps Institution of Oceanography, University of California San Diego, La Jolla, California
Leuliette, Eric, NOAA/NWS NCWCP Laboratory for Satellite Altimetry, College Park, Maryland
Locarnini, Ricardo, NOAA/NESDIS National Centers for Environmental Information, Silver Spring, Maryland
Lumpkin, Rick, NOAA/OAR Atlantic Oceanographic and Meteorological Laboratory, Miami, Florida
Lyman, John M., Joint Institute for Marine and Atmospheric Research, University of Hawaii, Honolulu, Hawaii; NOAA/OAR Pacific Marine Environmental Laboratory, Seattle, Washington
Marra, John J., NOAA/NESDIS National Centers for Environmental Information, Honolulu, Hawaii
Meinen, Christopher S., NOAA/OAR Atlantic Oceanographic and Meteorological Laboratory, Miami, Florida
Merrifield, Mark A., Joint Institute for Marine and Atmospheric Research, University of Hawaii, Honolulu, Hawaii
Mitchum, Gary T., College of Marine Science, University of South Florida, St. Petersburg, Florida
Moat, Ben I., National Oceanography Centre, United Kingdom
Nerem, R. Steven, Colorado Center for Astrodynamics Research, Cooperative Institute for Research in Environmental Sciences, University of Colorado Boulder, Boulder, Colorado
Perez, Renellys C., NOAA/OAR Atlantic Oceanographic and Meteorological Laboratory, Miami, Florida
Purkey, Sarah G., Scripps Institution of Oceanography, University of California San Diego, La Jolla, California
Reagan, James, Earth System Science Interdisciplinary Center/Cooperative Institute for Satellite Earth System Studies–Maryland, University of Maryland, College Park, Maryland; NOAA/NESDIS National Centers for Environmental Information, Silver Spring, Maryland
Sanchez-Franks, Alejandra, National Oceanography Centre, United Kingdom
Scannell, Hillary A., Lamont-Doherty Earth Observatory, Columbia University, Palisades, New York
Schmid, Claudia, NOAA/OAR Atlantic Oceanographic and Meteorological Laboratory, Miami, Florida
Scott, Joel P., NASA Goddard Space Flight Center, Greenbelt, Maryland; Science Application International Corporation, Reston, Virginia
Siegel, David A., University of California–Santa Barbara, Santa Barbara, California
Smeed, David A., National Oceanography Centre, United Kingdom
Stackhouse, Paul W., NASA Langley Research Center, Hampton, Virginia
Sweet, William, NOAA/NOS Center for Operational Oceanographic Products and Services, Silver Spring, Maryland
Thompson, Philip R., Joint Institute for Marine and Atmospheric Research, University of Hawaii, Honolulu, Hawaii
Triñanes, Joaquin A., Laboratory of Systems, Technological Research Institute, Universidad de Santiago de Compostela, Santiago de Compostela, Spain; Cooperative Institute for Marine and Atmospheric Studies, University of Miami; NOAA/OAR Atlantic Oceanographic and Meteorological Laboratory, Miami, Florida
Volkov, Denis L., Cooperative Institute for Marine and Atmospheric Studies, University of Miami, Miami, Florida; NOAA/OAR Atlantic Oceanographic and Meteorological Laboratory, Miami, Florida
Wanninkhof, Rik, NOAA/OAR Atlantic Oceanographic and Meteorological Laboratory, Miami, Florida
Weller, Robert A., Woods Hole Oceanographic Institution, Woods Hole, Massachusetts

Editor and Author Affiliations (alphabetical by name)

Wen, Caihong, NOAA/NWS NCEP Climate Prediction Center, College Park, Maryland
Westberry, Toby K., Oregon State University, Corvallis, Oregon
Widlansky, Matthew J., Joint Institute for Marine and Atmospheric Research, University of Hawaii, Honolulu, Hawaii
Wilber, Anne C., Science Systems and Applications, Inc., Hampton, Virginia
Yu, Lisan, Woods Hole Oceanographic Institution, Woods Hole, Massachusetts
Zhang, Huai-Min, NOAA/NESDIS National Centers for Environmental Information, Asheville, North Carolina

Editorial and Production Team

Allen, Jessicca, Graphics Support, Cooperative Institute for Satellite Earth System Studies, North Carolina State University, Asheville, North Carolina
Andersen, Andrea, Technical Editor, TeleSolv Consulting LLC, NOAA/NESDIS National Centers for Environmental Information, Asheville, North Carolina
Hammer, Gregory, Content Team Lead, Communications and Outreach, NOAA/NESDIS National Centers for Environmental Information, Asheville, North Carolina
Love-Brotak, S. Elizabeth, Lead Graphics Production, NOAA/NESDIS National Centers for Environmental Information, Asheville, North Carolina
Misch, Deborah J., Graphics Support, Innovative Consulting & Management Services, LLC, NOAA/NESDIS National Centers for Environmental Information, Asheville, North Carolina
Riddle, Deborah B., Graphics Support, NOAA/NESDIS National Centers for Environmental Information, Asheville, North Carolina
Veasey, Sara W., Visual Communications Team Lead, Communications and Outreach, NOAA/NESDIS National Centers for Environmental Information, Asheville, North Carolina

3. Table of Contents

*Please refer to Chapter 8 (Relevant datasets and sources) for a list of all climate variables and datasets used in this chapter for analyses, along with their websites for more information and access to the data.

3. GLOBAL OCEANS

G. C. Johnson and R. Lumpkin, Eds.

a. Overview—G. C. Johnson and R. Lumpkin

This chapter details 2020 global patterns in select observed oceanic physical, chemical, and biological variables relative to long-term climatologies, their differences between 2020 and 2019, and puts 2020 observations in the context of the historical record. In this overview we address a few of the highlights, first in haiku, then paragraph form:

La Niña arrives,
shifts winds, rain, heat, salt, carbon:
Pacific—beyond.

Global ocean conditions in 2020 reflected a transition from an El Niño in 2018–19 to a La Niña in late 2020. Pacific trade winds strengthened in 2020 relative to 2019, driving anomalously westward Pacific equatorial surface currents. Sea surface temperatures (SSTs), upper ocean heat content, and sea surface height all fell in the eastern tropical Pacific and rose in the western tropical Pacific. Efflux of carbon dioxide from ocean to atmosphere was larger than average across much of the equatorial Pacific, and both chlorophyll-a and phytoplankton carbon concentrations were elevated across the tropical Pacific. Less rain fell and more water evaporated in the western equatorial Pacific, consonant with increased sea surface salinity (SSS) there. SSS may also have increased as a result of anomalously westward surface currents advecting salty water from the east. El Niño–Southern Oscillation conditions have global ramifications that reverberate throughout the report.

Marine heatwave strikes
northeast Pacific again,
twice in past decade

Anomalously warm SSTs were especially prominent and persistent in the northeast Pacific, coincident with relatively fresh SSS anomalies, both increasing surface buoyancy and strengthening upper-ocean stratification in the remarkable 2019–20 northeast Pacific marine heatwave (MHW; see Sidebar 3.1). The warm SSTs there were over 2 standard deviations above normal in the second half of 2020, on par with the Blob's peak magnitudes of 2013–15, and were associated with ocean heat loss to the atmosphere in 2020. As SSTs rise, MHWs are likely to increase in size, magnitude, and duration, which brings us to long-term context.

Over the decades,
seas rise, warm, acidify,
Earth's climate changes.

Global average SST was 0.39°C above the 1981–2010 average and the third-warmest year on record behind 2016 and 2019, consistent with El Niño years being anomalously warm and La Niña years being anomalously cool, relative to an overall warming trend of 0.10 ± 0.01°C decade^{-1} from 1950 to 2020. Global ocean heat content trends are generally steadier than those of SST, with four out of five analyses indicating a record high for 2020 in the 0–700-m and all five indicating a record high in the 700–2000-m layers, and a total heat increase from 2019 to 2020 in those two layers of 9.3 ± 6.2 ZJ (10^{21} Joules), entirely consistent with the long-term (1993–2020) trend of 0.58 to 0.78 W m^{-2} of excess heat energy applied to the surface area of Earth. While the strength of the Atlantic meridional overturning circulation exhibits no significant trends in the North Atlantic,

a blended satellite/in situ analysis suggests a long-term (1993–2020) strengthening of the South Atlantic subtropical gyre since 1993, consistent with warming in that basin. Global mean sea level was also at a record high in 2020, 91.3 mm above the 1993 mean, with a linear trend of 3.3 ± 0.4 mm yr^{-1}, and a statistically significant acceleration from 1993 to 2020. Anthropogenic carbon storage in the ocean was estimated at 3.0 Pg C yr^{-1} in 2020, somewhat above the 1999–2019 average of 2.33 (±0.52) Pg C yr^{-1}.

b. Sea surface temperatures—B. Huang, Z.-Z. Hu, J. J. Kennedy, and H.-M. Zhang

Sea surface temperature (SST) and its uncertainty over the global oceans (all water surfaces including seas and lakes) in 2020 are assessed using four updated products of SST. These products are the Extended Reconstruction Sea Surface Temperature version 5 (ERSSTv5; Huang et al. 2017, 2020), Daily Optimum Interpolation SST version 2.1 (DOISST; Huang et al. 2021), and two U. K. Met Office Hadley Centre SST products (HadSST.3.1.1.0 and HadSST.4.0.0.0; Kennedy et al. 2011a,b, 2019). SST anomalies (SSTAs) are calculated for each product relative to its own 1981–2010 climatology. ERSSTv5 uses averages of 500-member ensembles at monthly 2° × 2° resolution; HadSST.3.1.1.0 and HadSST.4.0.0.0 use medians of 100-member ensembles at monthly 5° × 5° resolution; and DOISST has daily 0.25° × 0.25° resolution. Magnitudes of SSTAs are compared against SST standard deviations over 1981–2010.

Averaged over the global oceans, ERSSTv5 analysis shows that SSTAs decreased slightly, but not statistically significantly, by 0.02° ± 0.02°C, from 0.41° ± 0.02°C in 2019 to 0.39° ± 0.01°C in 2020. ERSSTv5 uncertainties are determined by a Student's t-test using a 500-member ensemble with randomly drawn parameter values within reasonable ranges in the SST reconstructions (Huang et al. 2015, 2020).

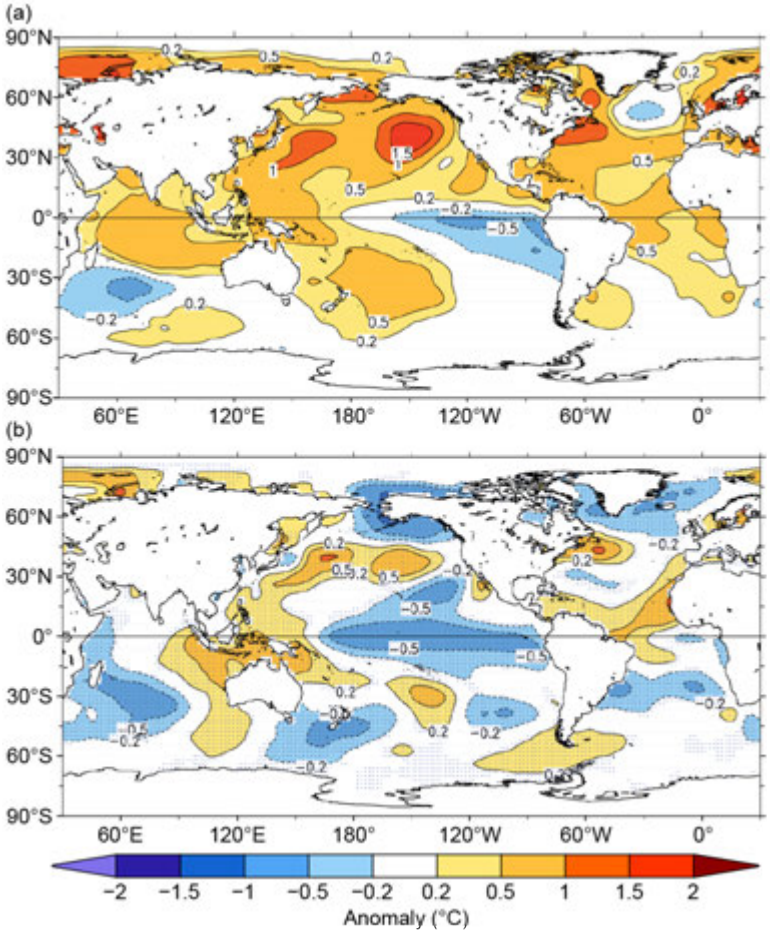

Fig. 3.1. (a) Annually averaged SSTAs (°C) in 2020 and (b) difference of annually averaged SSTAs between 2020 and 2019. Values are relative to a 1981–2010 climatology and SST differences are significant at 95% level in stippled areas.

Annually averaged SSTAs in 2020 (Fig. 3.1a) were mostly above average, between +0.5°C and +1.5°C across much of the North Pacific, between +0.2°C and +0.5°C in the western South Pacific, and between −0.2°C and −0.5°C in the eastern tropical Pacific. In the Atlantic, SSTAs were between +0.2°C and +1.0°C except south of Greenland (−0.2°C), a pattern linked to a slowdown in the Atlantic meridional overturning circulation (AMOC; Caesar et al. 2018). In the Indian Ocean, SSTAs were +0.5°C north of 25°S and between −0.2°C and −0.5°C in the western South Indian Ocean. Along the Arctic coasts, SSTAs were between +0.5°C to +1.0°C.

In comparison with averaged SST in 2019 (Fig. 3.1b), the averaged SST in 2020 increased by approximately +0.5°C in the North Pacific between 30°N and 45°N, the Indo-Pacific surrounding the Maritime Continent, the central South Pacific near 30°S, the western equatorial and tropical North Atlantic, the western North Atlantic near 45°N, and the coasts of the Arctic in the Euro-Asia sector. In

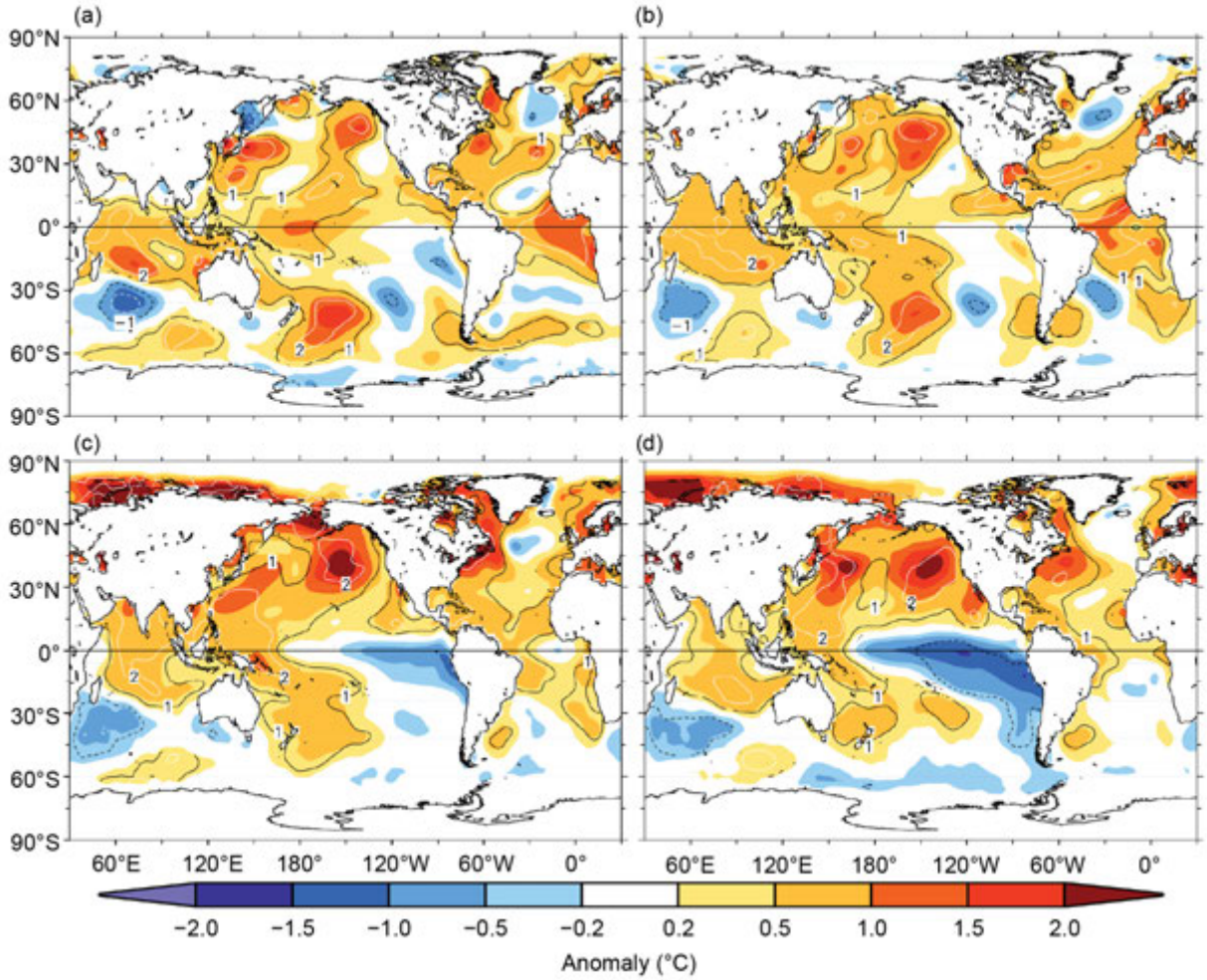

Fig. 3.2. Seasonally averaged SSTAs of ERSSTv5 (°C; shading) for (a) DJF 2019/20, (b) MAM 2020, (c) JJA 2020, and (d) SON 2020. Normalized seasonal mean SSTA based on seasonal mean std. dev. over 1981–2010 are contoured at values of –2 (dashed white), –1 (dashed black), 1 (solid black), and 2 (solid white).

contrast, the SST decreased by approximately −0.5°C in the equatorial tropical Pacific, the western and eastern South Pacific, the North Pacific and the Arctic regions surrounding Alaska, the western Indian Ocean, the North Atlantic regions surrounding Greenland, and the South Atlantic near 30°S. These SST changes are statistically significant at the 95% confidence level based on an ensemble analysis of 500 members.

The cooling in the tropical Pacific is associated with the transition from a weak El Niño in 2018–19 to a moderate La Niña in 2020–21 (see section 4b). The La Niña cooling started to be visible in June–August (JJA; Fig. 3.2c) and continued strengthening throughout September–November (SON; Fig. 3.2d). The near-uniform SSTAs in the Indian Ocean resulted in a near-neutral Indian Ocean dipole (IOD; Saji et al. 1999; see section 4f), in contrast to the strongly positive IOD index seen in late 2019. The Atlantic Niño index (Zebiak 1993) dropped dramatically from +1.5°C in 2018–19 to +0.2°C in the latter half of 2020, indicating a transition from a strong Atlantic Niño in 2018–19 to more neutral conditions.

For the seasonal mean SSTAs in 2020, in most of the North Pacific, SSTAs were +0.2° to +1.0°C (+1 to +2 std. dev.) in December–February (DJF) and March–May (MAM) (Figs. 3.2a,b). The anomalies increased to as high as +2.0°C (+2 std. dev.) in JJA and SON (Figs. 3.2c, d). In contrast, in the tropical and eastern South Pacific, SSTAs were small in DJF and MAM, and decreased to −0.5° to −1.0°C (–1 std. dev.) in JJA and SON. In the western South Pacific, SSTAs decreased from +1.5°C (+2 std. dev.) in DJF to +1.0°C in MAM and +0.5°C in JJA and SON. The pronounced SSTAs in the North Pacific in JJA and SON (Sidebar 3.1; Scannell et al. 2020) and in the western South Pacific east of New Zealand

Table 3.1. Linear trends of annually and regionally averaged SSTAs (°C decade^{-1}) from ERSSTv5, HadSST, and DOISST. Uncertainties at 95% confidence level are estimated by accounting for the effective sampling number quantified by lag-1 autocorrelation on the degrees of freedom of annually averaged SST series.

Product	Region	2000–2020 (°C decade^{-1})	1950–2020 (°C decade^{-1})
HadSST.3.1.1.0	Global	0.14 ± 0.06	0.09 ± 0.02
HadSST.4.0.0.0	Global	0.18 ± 0.06	0.112 ± 0.02
DOISST	Global	0.20 ± 0.05	N/A
ERSSTv5	Global	0.17 ± 0.07	0.10 ± 0.01
ERSSTv5	Tropical Pacific (30°S–30°N)	0.18 ± 0.17	0.10 ± 0.03
ERSSTv5	North Pacific (30°–60°N)	0.36 ± 0.14	0.08 ± 0.04
ERSSTv5	Tropical Indian Ocean (30°S–30°N)	0.21 ± 0.09	0.14 ± 0.02
ERSSTv5	North Atlantic (30°–60°N)	0.14 ± 0.09	0.11 ± 0.05
ERSSTv5	Tropical Atlantic (30°S–30°N)	0.15 ± 0.09	0.11 ± 0.02
ERSSTv5	Southern Ocean (30°–60°S)	0.12 ± 0.06	0.10 ± 0.02

were associated with marine heatwaves (Hu et al. 2011; Oliver et al. 2017; Perkins-Kirkpatrick et al. 2019; Babcock et al. 2019; see also section 2b3).

In the Euro-Asian coasts of the Arctic, SSTAs were neutral in DJF and MAM due to sea ice holding SSTs at the freezing point, but reached more than +2.0°C (+2 std. dev.) in JJA and SON (Figs. 3.2c,d). In the Indian Ocean and Maritime Continent, SSTAs of approximately +0.5°C (+2 std. dev.) were sustained throughout 2020 (Figs. 3.2a–d). In the tropical Atlantic, SSTAs were approximately +1.0°C (+2 std. dev.) in DJF and MAM and decreased to between +0.2°C and 0.5°C (+1 std. dev.) in JJA and SON. In contrast, in the western North Atlantic, SSTAs increased from between +0.5°C and 1.0°C (+1 std. dev.) in DJF and MAM to between +1.0°C and 1.5°C (+2 std. dev.). In the South Atlantic, SSTAs were near neutral in DJF, became below normal (−0.5°C) in the west and above normal (+0.5°C) in the east in MAM, and became near neutral again in JJA and SON.

The global oceans have exhibited an overall warming trend since the 1950s (Figs. 3.3a,b; Table 3.1), albeit with slightly lower SSTAs in 2020 (+0.39° ± 0.01°C) than in 2019 (+0.41° ± 0.02°C), due in part to La Niña. The year 2020 was the third warmest after the record high of 2016 (+0.44° ± 0.01°C) and 2019, but their separation may not be statistically significant. Linear trends of globally annually averaged SSTAs were 0.10° ± 0.01°C decade^{-1} over 1950–2020 (Table 3.1). Spatially, the warming was largest in the tropical Indian Ocean (Fig. 3.3e; 0.14° ± 0.02°C decade^{-1}) and smallest in the North Pacific (Fig. 3.3d; 0.08° ± 0.04°C decade^{-1}). Here, the uncertainty of the trends represents the 95% confidence level of the linear fitting uncertainty and 500-member data uncertainty.

In addition, interannual to interdecadal variabilities of SSTAs can be seen in all ocean basins. The variation amplitudes are large in the North Atlantic (Fig. 3.3f), which may be associated with the Atlantic Multidecadal Variability (Schlesinger and Ramankutty 1994) that may have in turn resulted from many internal and external factors such as aerosols and the AMOC (Zhang et al. 2019; Wang and Yang 2017), with warm periods in the early 1950s and from the late 1990s to the 2010s, and a cold period from the 1960s to the early 1990s. Similarly, SSTAs in the North Pacific (Fig. 3.3d) decreased from the 1960s to the late 1980s, followed by an increase from the late 1980s to the 2010s.

We compare SSTAs in ERSSTv5 with those in DOISST, HadSST.3.1.1.0, and HadSST.4.0.0.0, averaging all annually on a 2° × 2° grid (Fig. 3.3). SSTA departures of DOISST, HadSST.3.1.1.0, and HadSST.4.0.0.0 from ERSSTv5 are largely within 2 standard deviations (gray shading, Fig. 3.3). Overall, HadSST.4.0.0.0 is more consistent with ERSSTv5 than HadSST.3.1.1.0 before 1980, owing to its updated corrections to the SST observations from ships (e.g., ship engine room intakes, ship bucket) that had been used in both HadSST.4.0.0.0 and ERSSTv5. In the 2000s–10s, SSTAs were slightly higher in DOISST than in ERSSTv5 in the Southern Ocean, tropical Atlantic Ocean, and tropical Indian Ocean, and therefore

SST trends were slightly higher in DOISST over 2000–20 (Table 3.1). These SSTA differences have been mostly attributed to the differences in bias corrections to ship observations in those products (Huang et al. 2015; Kent et al. 2017), and have resulted in a slightly weaker SSTA trend in HadSST.3.1.1.0 but a stronger SSTA trend in HadSST.4.0.0.0 over both 1950–2020 and 2000–20 (Table 3.1).

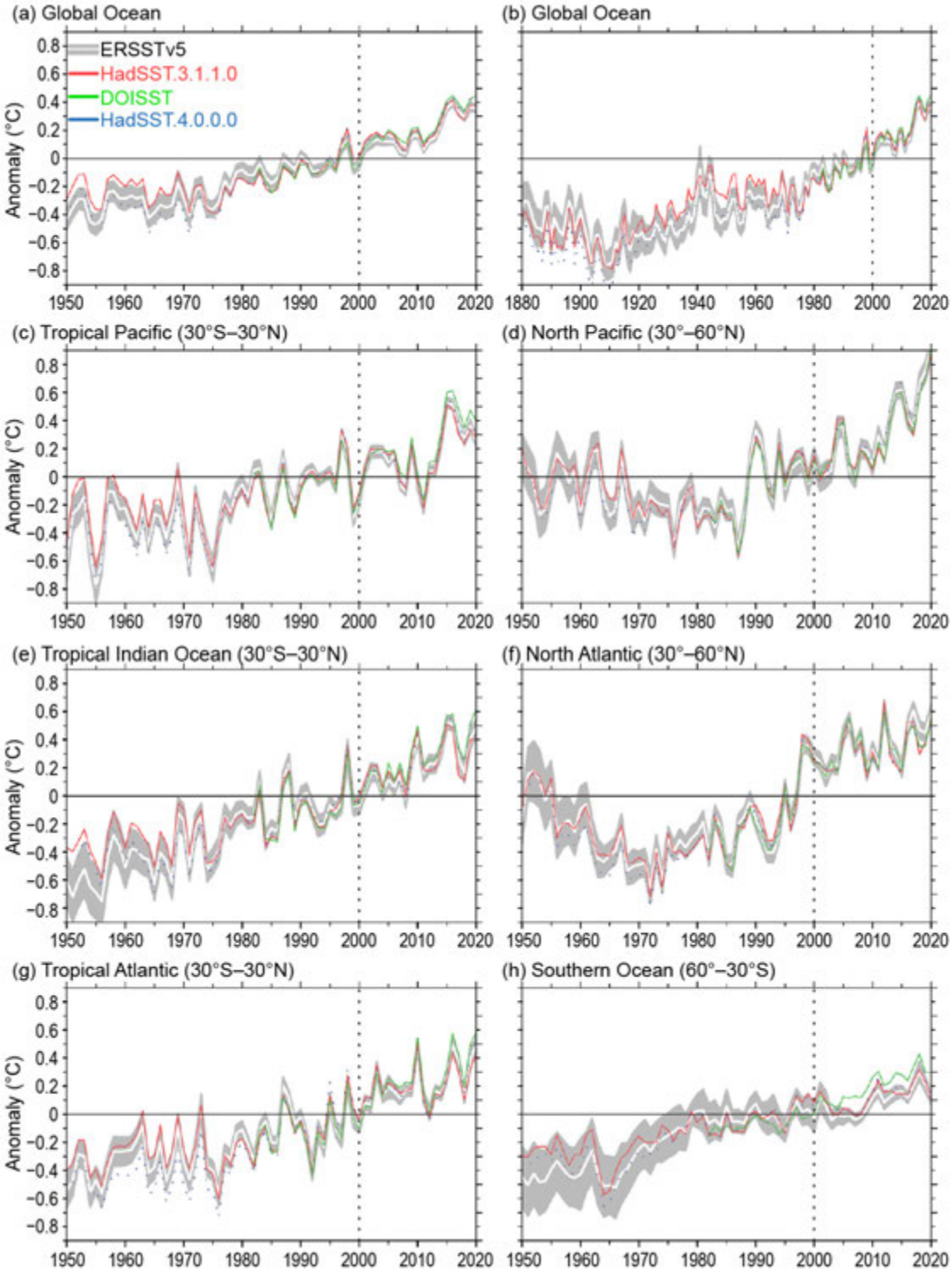

Fig. 3.3. Annually-averaged SSTAs of ERSSTv5 (solid white) and 2 std. dev. (gray shading) of ERSSTv5, SSTAs of DOISST (solid green), and SSTAs of HadSST.3.1.1.0 (solid red) and HadSST.4.0.0.0 (dotted blue) during 1950–2020 except for (b). (a) Global oceans, (b) global oceans in 1880–2020, (c) tropical Pacific, (d) North Pacific, (e) tropical Indian, (f) North Atlantic, (g) tropical Atlantic, and (h) Southern Oceans. The 2 std. dev. envelope was derived from a 500-member ensemble analysis based on ERSSTv5 (Huang et al. 2020) and centered to SSTAs of ERSSTv5. The year 2000 is indicated by a vertical black dotted line.

Sidebar 3.1: **The 2019–20 northeast Pacific marine heatwave**—H. A. SCANNELL AND D. J. AMAYA

Following the warm years of the 2013–15 marine heatwave (MHW) known as "the Blob" (Bond et al. 2015), the northeast Pacific Ocean experienced another devastating MHW, which formed during the summer of 2019 and persisted through 2020 (Amaya et al. 2020; Scannell et al. 2020). An MHW is defined when sea surface temperatures (SSTs) exceed an extremely warm threshold (e.g., the 90th percentile) for an extended period of time (e.g., at least five days; Hobday et al. 2016). In June 2019, an MHW developed in the northeast Pacific Ocean and by August it grew to encompass an ocean area spanning the Gulf of Alaska to the Hawaiian Islands (Fig. SB3.1a). The event was so unusual that the June–August SST anomalies (SSTA), which were >2.5°C above normal, broke a 40-year (1980–2019) summertime record (Amaya et al. 2020). Like the Blob, this event had local and regional impacts on marine ecosystems and fish redistributions (NOAA 2019). During 2019, the MHW along the U.S. West Coast initiated harmful algal blooms and coral reefs near Hawaii started to bleach under high thermal stress (Cornwall 2019). Off Oregon, warmer waters brought albacore tuna closer to shore, making them more accessible to recreational anglers, leading to record-breaking landings in September (Lambert 2019). Although many speculated that this summertime MHW would not last due to its shallow depth, its persistence into 2020 was unrelenting (Fig. SB3.1c)

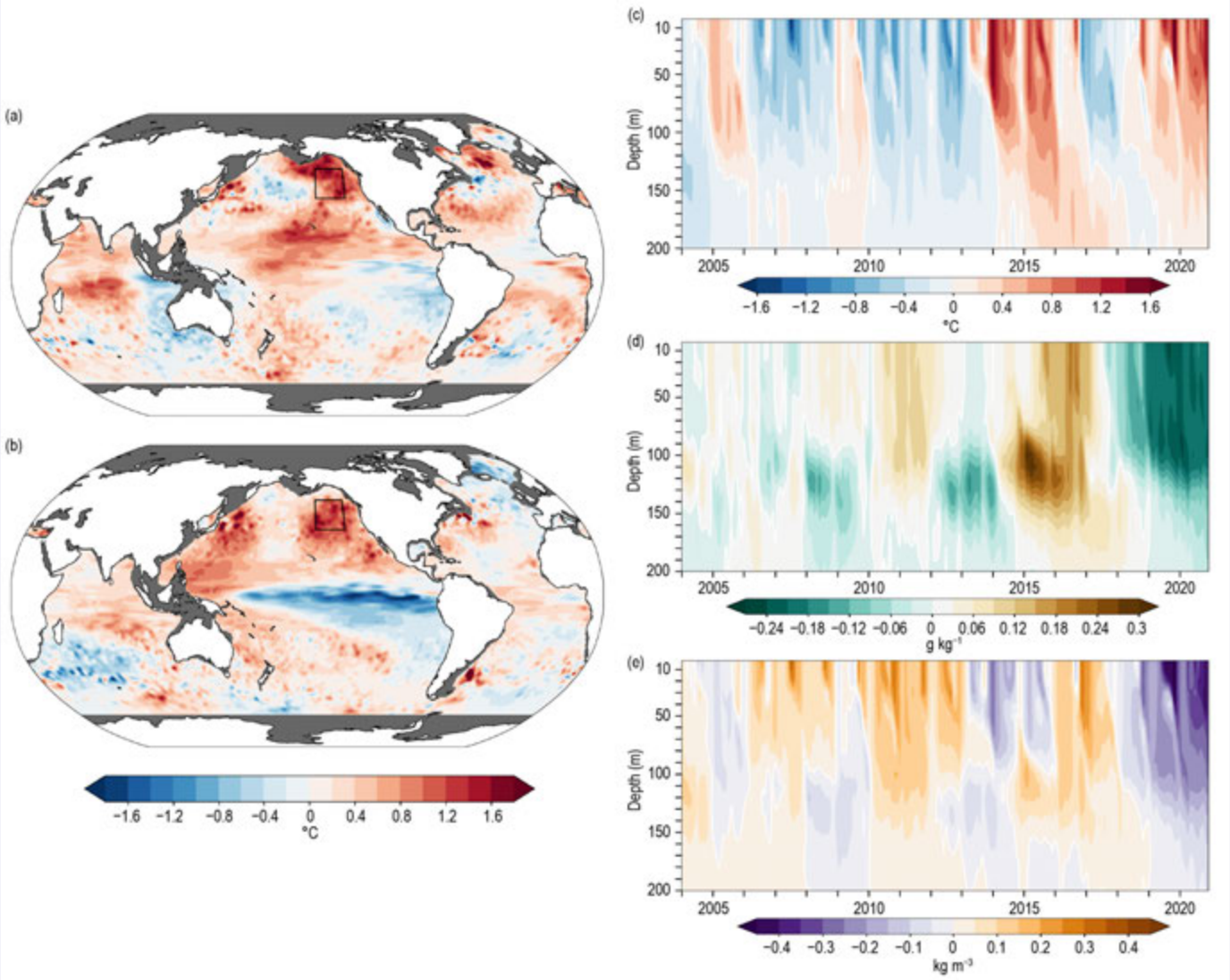

Fig. SB3.1. Seasonal 2.5-m temperature anomaly average (°C) over (a) JJA in 2019 and (b) SON in 2020. Time–depth plots of subsurface (c) temperature (°C), (d) salinity (g kg^{-1}), and (e) density (kg^{-3}) anomalies averaged within the northeast Pacific (35.5°–51.5°N, 135.5°–154.5°W; black box in (a) and (b) from Jan 2004 through Dec 2020. Subsurface observations were taken from the updated Roemmich-Gilson Argo Climatology (Roemmich and Gilson 2009) and monthly anomalies were computed with respect to the 2004–20 monthly means.

and its spatial scale rivaled its predecessor—the Blob (Bond et al. 2015).

The factors contributing to the onset of the 2019–20 northeast Pacific MHW are described by Amaya et al. (2020) and are summarized here. SSTAs that formed during summer 2019 were atmospherically forced. Remote influence from warm SSTAs near the central equatorial Pacific contributed to a weakening of the North Pacific (atmospheric pressure) High and associated surface winds from April through August. A reduction in wind-driven, upper-ocean mixing resulted in a record shallow mixed layer depth. Summertime surface heat fluxes more efficiently warmed the anomalously thin mixed layer, contributing to the rapid rise in SST. Downward heat fluxes were dominated by a reduction in latent heat loss from weakened surface winds and an increase in downwelling shortwave radiation due to diminished low-level clouds. In particular, the reduction in low cloud cover initiated a positive low-cloud-SST feedback, which amplified the intensity of the 2019 summer MHW and contributed to its overall persistence.

The spatial pattern of surface warming evolved in the northeast Pacific over the course of 2019 and 2020. This evolution was facilitated by remote influences from the tropics and extratropics. As described previously, warm anomalies in the central equatorial and subtropical Pacific in 2019 (Fig. SB3.1a) helped weaken the mean state of the atmosphere over northern latitudes, leading to the MHW onset. A positive Pacific Meridional Mode also likely helped modulate the surface heat fluxes over the North Pacific by shifting the Intertropical Convergence Zone farther north and further weakening the North Pacific High (Amaya et al. 2020). The transition to La Niña conditions in 2020 reversed the sign of anomalies near the equator. However, the northeast Pacific remained in a MHW-like state (Fig. SB3.1b). La Niña can disrupt weather patterns in the Northern Hemisphere midlatitudes through a teleconnection associated with the negative phase of the Pacific/North American (PNA) pattern (Wallace and Gutzler 1981). The negative PNA can establish more atmospheric ridging over the northeast Pacific Ocean, which diverts normal upper-level flow and is conducive to warming SSTs during boreal winter.

Once the surface mixed layer is heated from the atmosphere, those temperature anomalies can be redistributed within the ocean and begin to propagate horizontally or downward (Scannell et al. 2020). The upper 200 m of the water column was anomalously warm throughout 2020, with maximum intensities contained within the upper 70 m (Fig. SB3.1c). An unusual fresh anomaly that extended to 120 m (Fig. SB3.1d) accompanied the near-surface warming and likely originated from a net freshwater input from precipitation in the Gulf of Alaska in 2018 (Reagan et al. 2019; Yu et al. 2019). The salinity anomaly from 2018 through 2020 was the longest lasting, most intense, and deepest reaching fresh event observed since at least 2004. In contrast, the Blob in 2013–15 had the warmest and most salty near-surface anomalies since at least 2004. The subsurface freshwater anomaly in 2019–20 increased the buoyancy of the surface layer (Fig. SB3.1e). The decrease in surface density and resulting increase in stratification prevented the warm surface anomalies from penetrating as deeply as the Blob in 2013–15. However, the surface MHW anomalies in 2019–20 mixed into the subsurface across both isobars and isopycnals (Scannell et al. 2020). The subsurface burial and storage of surface MHW anomalies contributes to the long-lived persistence and memory of these events in the northeast Pacific Ocean, and their possible seasonal reemergence.

The northeast Pacific Ocean has warmed significantly over the past half-century due to anthropogenic climate change (Bulgin et al. 2020). Increased ocean temperatures not only make MHWs more likely to occur in the North Pacific (Scannell et al. 2016), they also increase the intensity and duration of these events over time (Oliver 2019; Laufkötter et al. 2020). Ocean warming has significantly contributed to a shoaling trend in North Pacific summertime mixed layers (~15% decrease) from 1980 to 2015 (Amaya et al. 2021). Shallower mixed layers reduce the effectiveness of detraining surface MHW anomalies into the subsurface and trap them near the surface (Amaya et al. 2020; Scannell et al. 2020). As a result, it is expected that MHWs will intensify in the coming decades as surface stratification increases and summertime mixed layers continue to shoal (Amaya et al. 2021; Li et al. 2020; Alexander et al. 2018).

The 2019–20 MHW was the latest event in a recent trend of increasing temperature extremes that has dominated the northeast Pacific. Second to the Blob in 2013–15, this event was the most expansive MHW since 1982, covering an ocean area roughly six times the size of Alaska in September 2020 (NWFSC 2020). However, the 2019–20 event really stands out for developing during the summer, when mixed layers were anomalously shallow and the subsurface was extremely fresh (Amaya et al. 2020; Scannell et al. 2020). The combination of these factors likely helped to amplify the intensification of this event. It is an open question whether the physical mechanisms responsible for this MHW are broadly applicable to summer-initiated events. The northeast Pacific Ocean has remained anomalously warm and fresh heading into 2021, and the subsurface has warmed substantially, likely as a result (Fig. SB3.1). This event's persistence is being closely monitored as La Niña conditions continue to dominate the tropics.

c. Ocean heat content—G. C. Johnson, J. M. Lyman, T. Boyer, L. Cheng, J. Gilson, M. Ishii, R. E. Killick, and S. G. Purkey

The oceans have been warming for decades owing to increases in greenhouse gasses in the atmosphere (Rhein et al. 2013), storing massive amounts of heat energy and expanding as they warm to contribute about 40% of the increase in global average sea level (WCRP Global Sea Level Budget Group 2018). This warming, while surface intensified, is not limited to the upper ocean, having been widely observed from 4000 to 6000 m in the coldest, densest bottom waters (Purkey and Johnson 2010). The El Niño–Southern Oscillation effects strong regional variations in ocean temperature and also modulates the rate of global ocean heat uptake (Johnson and Birnbaum 2017). The overall warming trend has increased the frequency and intensity of marine heatwaves (Laufkötter et al. 2020; see section 3b and Sidebar 3.1), which in turn have substantial effects on ecosystems (Smale et al. 2019). Additionally, warmer upper ocean waters can drive stronger hurricanes (Goni et al. 2009). Ocean warming has also been shown to increase melting rates of ice sheet outlet glaciers around Greenland (Castro de la Guardia et al. 2015) and Antarctica (Schmidtko et al. 2014).

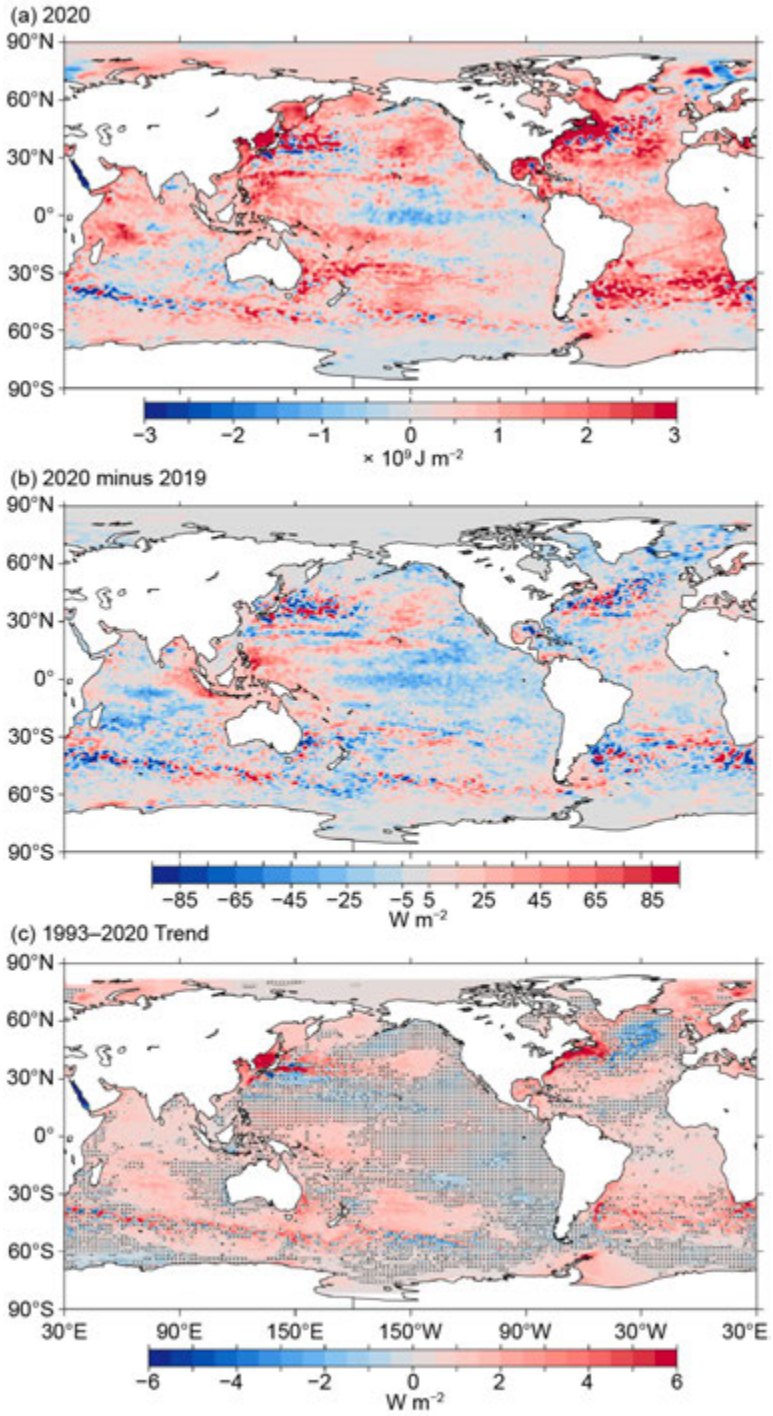

Fig. 3.4. (a) Combined satellite altimeter and in situ ocean temperature data estimate of upper (0–700 m) OHCA (× 10^9 J m^{-2}) for 2020 analyzed following Willis et al. (2004) but using an Argo monthly climatology and displayed relative to the 1993–2020 baseline. (b) 2020 minus 2019 combined estimates of OHCA expressed as a local surface heat flux equivalent (W m^{-2}). For (a) and (b) comparisons, note that 95 W m^{-2} applied over one year results in a 3 × 10^9 J m^{-2} change of OHCA. (c) Linear trend from 1993–2020 of the combined estimates of upper (0–700 m) annual OHCA (W m^{-2}). Areas with statistically insignificant trends are stippled.

Maps of annual (Fig. 3.4) upper (0–700 m) ocean heat content anomaly (OHCA) relative to a 1993–2020 baseline mean are generated from a combination of in situ ocean temperature data and satellite altimetry data following Willis et al. (2004), but using Argo (Riser et al. 2016) data downloaded from an Argo Global Data Assembly Centre in January 2021. Near-global average monthly temperature anomalies (Fig. 3.5) versus pressure from Argo data (Roemmich and Gilson 2009, updated) since 2004 and in situ global estimates of OHCA (Fig. 3.6) for three pressure layers (0–700 m, 700–2000 m, and 2000–6000 m) from five different research groups are also discussed.

The 2020 minus 2019 difference of 0–700-m OHCA (Fig. 3.4b) in the Pacific shows an increase in the western tropical Pacific and a decrease in the central to eastern equatorial Pacific, consistent

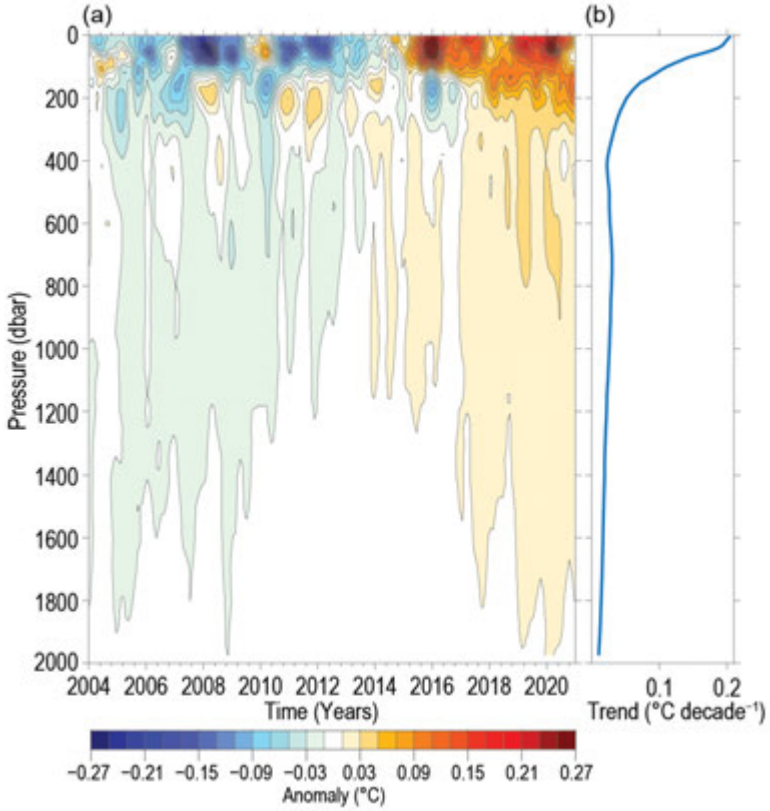

Fig. 3.5. (a) Near-global (65°S–80°N, excluding continental shelves, the Indonesian seas, and the Sea of Okhostk) average monthly ocean temperature anomalies (°C; updated from Roemmich and Gilson [2009]) relative to record-length average monthly values, smoothed with a 5-month Hanning filter and contoured at odd 0.02°C intervals (see colorbar) versus pressure and time. (b) Linear trend of temperature anomalies over time for the length of the record in (a) plotted versus pressure in °C decade^{-1} (blue line).

with the onset of a La Niña in 2020. La Niña induces this pattern with a shoaling of the equatorial thermocline in the central and eastern equatorial Pacific and a deepening of the western tropical Pacific warm pool as a response to strengthened easterly trade winds (see Fig. 3.13a), which also generate anomalous westerly surface currents on the equator (see Figs. 3.18, 3.19b–d). As a result, in the equatorial Pacific, the 2020 anomalies (Fig. 3.4a) are negative in the east and positive in the west. Outside of the tropics, the 2020 minus 2019 difference is toward higher values in the centers of the North and South Pacific basins, with some lower values in the eastern portions of the basin, consistent with an intensified cool (negative) phase of the Pacific Decadal Oscillation index in 2020 (see Fig. 3.1). Upper OHCA in the Pacific in 2020 is generally above the long-term average (Fig. 3.4a), with the most prominent negative values limited to the central tropical Pacific and the Southern Ocean south of 60°S.

In the Indian Ocean, the 2020 minus 2019 difference of 0–700-m OHCA

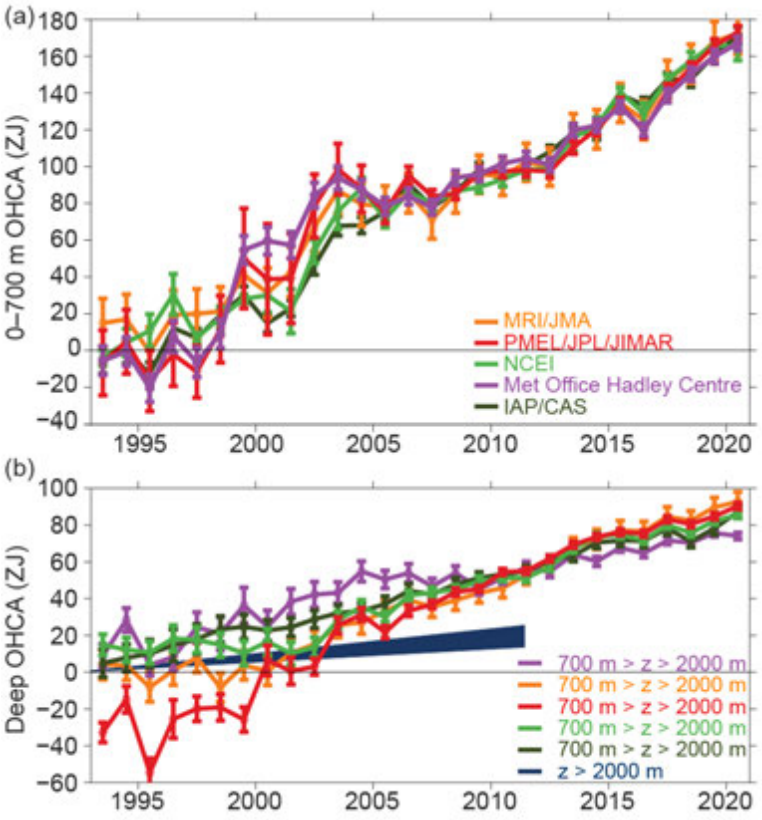

Fig. 3.6. (a) Annual average global integrals of in situ estimates of upper (0–700 m) OHCA (ZJ; 1 ZJ = 10^{21} J) for 1993–2020 with standard errors of the mean. The MRI/JMA estimate is an update of Ishii et al. (2017). The PMEL/JPL/JIMAR estimate is an update and refinement of Lyman and Johnson (2014). The NCEI estimate follows Levitus et al. (2012). The Met Office Hadley Centre estimate is computed from gridded monthly temperature anomalies (relative to 1950–2019) following Palmer et al. (2007). The IAP/CAS estimate is reported in Cheng et al. (2020). See Johnson et al. (2014) for details on uncertainties, methods, and datasets. For comparison, all estimates have been individually offset (vertically on the plot), first to their individual 2005–20 means (the best sampled time period), and then to their collective 1993 mean. (b) Annual average global integrals of in situ estimates of intermediate (700–2000 m) OHCA for 1993–2020 with standard errors of the mean, and a long-term trend with one standard error uncertainty shown from 1992.4–2011.6 for deep and abyssal (z > 2000 m) OHCA following Purkey and Johnson (2010) but updated using all repeat hydrographic section data available from https://cchdo.ucsd.edu/ as of Jan 2021.

(Fig. 3.4b) exhibits increases in the eastern third of the basin, from the Bay of Bengal to the Antarctic Circumpolar Current (ACC) and decreases in the center of the basin from the equator to the ACC. Upper OHCA values for 2020 were above the 1993–2020 mean over almost all of the Indian Ocean (Fig. 3.4a), with the higher values in the western half of the basin. The low 2020 upper OHCA values in the vicinity of the ACC in the west and the high values in the east suggest a northward excursion of that current in the west and a southward excursion in the east in 2020. The 2020 minus 2019 differences of 0–700-m OHCA (Fig. 3.4b) in the Atlantic Ocean are toward cooling around the Caribbean Islands and Florida, offshore of some of the east coast of North America, and in the Greenland–Iceland–Norwegian Seas. In much of the rest of the ocean, the tendency is weakly, but generally toward, warming. In 2020, almost the entire Atlantic Ocean exhibited upper OHCA above the 1993–2020 average (Fig. 3.4a) with especially warm conditions in the Gulf of Mexico, off the east coast of North America, and across the southern subtropical South Atlantic.

The large-scale statistically significant (Fig. 3.4c) regional patterns in the 1993–2020 local linear trends of upper OHCA are quite similar to those from 1993–2019 (Johnson et al. 2020). The longer the period over which these trends are evaluated, the more of the ocean surface area is covered by warming trends, either statistically significant or not, and the less it is covered by cooling trends (Johnson and Lyman 2020). The most prominent area with statistically significant negative trends is found mostly south of Greenland in the North Atlantic, a pattern that has been linked, together with the very strong warming trend off the east coast of North America, to a decrease in the Atlantic meridional overturning circulation (Dima and Lohmannn 2010; Caesar et al. 2018), although there are contributions from variations in local air–sea exchange (strong winter cooling in the years around 2015) and shortwave cloud feedbacks as well (Josey et al. 2018). Another cooling trend is found near the ACC in the central South Pacific. As noted in previous *State of the Climate* reports, the warming trends in the western boundary currents and extensions (Gulf Stream, Kuroshio, Agulhas, East Australia Current, and Brazil Current) are all quite prominent and may be associated with poleward shifts of these currents driven by changes in surface winds (Wu et al. 2012). Much of the Atlantic Ocean, the Indian Ocean, and the western and central Pacific Ocean exhibit statistically significant warming trends as well.

Near-global average seasonal temperature anomalies (Fig. 3.5a) from the start of 2004 through the end of 2020 exhibit a clear surface-intensified, record-length warming trend (Fig. 3.5b) that exceeds 0.2°C decade^{-1} at the surface. The reduction of warm anomalies during 2020 in the upper 100 dbar, with increases in warming from 100 to 400 dbar, is consistent with the transition to a La Niña in 2020. This pattern in the global average reflects a prominent large-scale regional change, as the equatorial Pacific thermocline shoals in the east and deepens in the west (e.g., Roemmich and Gilson 2011; Johnson and Birnbaum 2017). The pattern can be seen in other La Niña periods (e.g., 2007–08 and 2010–12). The opposite pattern is evident during El Niño years (e.g., 2009–10 and 2015–16) when the east–west tilt of the equatorial Pacific thermocline reduces as easterly trade winds subside, and even reverse at times.

As noted in previous reports, the analysis is extended back in time from the Argo period to 1993, and expanded to examine greater depths, using sparser, more heterogeneous historical data collected mostly from ships (e.g., Abraham et al. 2013). The different estimates of annual globally integrated 0–700-m OHCA (Fig. 3.6a) all reveal a large increase since 1993, with four of the five analyses reporting 2020 as a record high. The globally integrated 700–2000-m OHCA annual values (Fig. 3.6b) vary somewhat among analyses, but all five analyses report 2020 as a record high, and the long-term warming trend in this layer is also clear. Globally integrated OHCA values in both layers vary more both from year-to-year for individual years and from estimate-to-estimate in any given year prior to the achievement of a near-global Argo array around 2005. The water column from 0–700 and 700–2000 m gained 5.4 (±4.8) and 3.9 (±3.9) ZJ, respectively

Table 3.2. Trends of ocean heat content increase (in W m^{-2} applied over the 5.1 × 10^{14} m^2 surface area of Earth) from seven different research groups over three depth ranges (see Fig. 3.6 for details). For the 0–700- and 700–2000-m depth ranges, estimates cover 1993–2020, with 5%–95% uncertainties based on the residuals taking their temporal correlation into account when estimating degrees of freedom (Von Storch and Zwiers 1999). The 2000–6000-m depth range estimate, an update of Purkey and Johnson (2010), uses data from 1981 to 2020, while the global average is from May 1992 to Aug 2011, again with 5%–95% uncertainty.

	Global ocean heat content trends (W m^{-2}) for three depth ranges		
Research Group	0–700 m	700–2000 m	2000–6000 m
MRI/JMA	0.37 ± 0.05	0.24 ± 0.05	
PMEL/JPL/JIMAR	0.39 ± 0.12	0.31 ± 0.05	
NCEI	0.39 ± 0.05	0.19 ± 0.05	
Met Office Hadley Centre	0.38 ± 0.12	0.15 ± 0.04	
IAP/CAS	0.41 ± 0.04	0.18 ± 0.01	
Purkey and Johnson			0.06 ± 0.03

(means and standard deviations given) from 2019 to 2020. Causes of differences among estimates are discussed in Johnson et al. (2015).

The estimated linear rates of heat gain for each of the five global integral estimates of 0–700-m OHCA from 1993 through 2020 (Fig. 3.6a) range from 0.37 (±0.05) to 0.41 (±0.04) W m^{-2} applied over the surface area of Earth, as is customary in climate science (Table 3.2). These results are not much different from those in previous reports, although with an increasing record length trend uncertainties tend to decrease and differences among analyses tend to grow smaller. Linear trends from 700 to 2000 m over the same time period range from 0.15 (±0.04) to 0.31 (±0.05) W m^{-2}. Trends in the 0–700-m layer all agree within their 5%–95% confidence intervals. However, as noted in previous reports, one of the trends in the 700–2000-m layer, which is quite sparsely sampled prior to the start of the Argo era (circa 2005), does not. Different methods for dealing with under-sampled regions likely cause this disagreement. Using repeat hydrographic section data collected from 1981 to 2020 to update the estimate of Purkey and Johnson (2010) for 2000–6000 m, the linear trend is 0.06 (±0.03) W m^{-2} from May 1992 to August 2011 (these dates are global average times of first and last sampling of the sections). Summing the three layers (despite their slightly different time periods as given above), the full-depth ocean heat gain rate ranges from 0.58 to 0.78 W m^{-2} applied to Earth's entire surface.

d. Salinity—G. C. Johnson, J. Reagan, J. M. Lyman, T. Boyer, C. Schmid, and R. Locarnini

1) Introduction

Salinity is the measure of the mass of dissolved salts in a unit mass of seawater. Temperature and salinity vary spatially and temporally in the ocean. Atmospheric freshwater fluxes (namely evaporation and precipitation), advection, mixing, entrainment, sea ice melt/freeze, and river runoff all modify salinity (e.g., Qu et al. 2011; Ren et al. 2011). Sea surface salinity (SSS) and evaporation minus precipitation ($E-P$) have long been known to be highly correlated (Wüst 1936). SSS patterns are maintained through a balance among advection, mixing, and $E-P$ fluxes (Durack 2015). Roughly 86% of global evaporation and 78% of global precipitation occurs over the ocean (Baumgartner and Reichel 1975; Schmitt 1995), making the ocean Earth's largest rain gauge (Schmitt 2008). Evaporation-dominated regions, such as the subtropical North Atlantic, are generally saltier, whereas precipitation-dominated regions like the Intertropical Convergence Zone (ITCZ) are generally fresher. Furthermore, changes in the hydrological cycle can be estimated by salinity changes (e.g., Durack and Wijffels 2010; Durack et al. 2012; Skliris et al. 2014).

Seawater density at a given pressure is a function of temperature and salinity. In cold water, salinity variations tend to dominate density (Pond and Pickard 1983). Therefore, changes in salinity at high latitudes can have large impacts on ocean stratification and even alter the global thermohaline circulation (e.g., Gordon 1986; Broecker 1991). For example, the Atlantic meridional overturning circulation (section 3h) is vulnerable to changes in salinity (e.g., Liu et al. 2017). Ocean stratification (i.e., the vertical density gradient) has been found to be increasing over the past 50 years (Li et al. 2020), which has likely reduced ocean ventilation. Thus, diagnosing changes in surface and subsurface salinity is critical for monitoring potential changes in the hydrological cycle and ocean dynamics.

To investigate interannual changes of subsurface salinity, all available salinity profile data are quality controlled following Boyer et al. (2018) and then used to derive 1° monthly mean gridded salinity anomalies relative to a long-term monthly mean for years 1955–2012 (World Ocean Atlas 2013 version 2 [WOA13v2]; Zweng et al. 2013) at standard depths from the surface to 2000 m (Boyer et al. 2013). In recent years, the largest source of salinity profiles is the profiling floats of the Argo program (Riser et al. 2016). These data are a mix of real-time (preliminary) and delayed-mode (scientific quality controlled) observations. Hence, the estimates presented here may be subject to instrument biases such as Argo conductivity, temperature, depth devices with "fast salty drift," and could change after all data are subjected to scientific quality control. The SSS analysis relies on Argo data downloaded in January 2021, with annual anomaly maps relative to a seasonal climatology generated following Johnson and Lyman (2012) as well as monthly maps of bulk (as opposed to skin) SSS data from the Blended Analysis of Surface Salinity (BASS; Xie et al. 2014). BASS blends in situ SSS data with data from the *Aquarius* (Le Vine et al. 2014; mission ended in June 2015), Soil Moisture and Ocean Salinity (Font et al. 2013), and the Soil Moisture Active Passive (Fore et al. 2016) satellite missions. Despite the larger uncertainties of satellite data relative to Argo data, their higher spatial and temporal sampling allows higher spatial and temporal resolution maps than are possible using in situ data alone at present. All salinity values used in this section are dimensionless and reported on the Practical Salinity Scale-78 (PSS-78; Fofonoff and Lewis 1979).

2) Sea surface salinity—G. C. Johnson and J. M. Lyman

As noted in previous reports, since salinity has no direct feedback to the atmosphere, large-scale SSS anomalies can be quite persistent. This persistence contrasts with sea surface temperature (SST) anomalies, which are often damped by air–sea heat exchange (e.g., an anomalously warm ocean loses heat to the atmosphere, so SST cools). For example, one of the largest fresh SSS anomalies in 2020, located in the northeastern Pacific (Fig. 3.7a), began around 2016 in the central North Pacific (near 40°N between Hawaii and the Aleutian Islands), shifting eastward over time and strengthening overall (see previous *State of the Climate* reports). This upper ocean fresh anomaly increased density stratification and stabilized the upper ocean, which, together with surface-intensified warming of marine heat waves in the area that occurred in 2013–15 (e.g., Gentemann et al. 2017) and again in 2019–20 (Scannell et al. 2020), perhaps prolonging and amplifying especially the second event (Scannell et al. 2020; Sidebar 3.1).

Elsewhere in the Pacific Ocean, the fresh 2020 SSS anomaly (Fig. 3.7a) observed over much of the ITCZ and South Pacific Convergence Zone and extending north of Hawaii in the Central Pacific began around 2015 (see previous *State of the Climate* reports). In contrast, the more recent strong increase in salinity along the equator from 150°E to the dateline from 2019 to 2020 (Fig. 3.7b) is owing to the westward migration of the fresh pool with the advent of La Niña in 2020 (section 4b), linked to the anomalous westward currents across the equator in 2020 (see Fig. 3.18a), as well as westward shifts in precipitation in the region (see Fig. 3.12d).

There was mostly freshening of SSS from 2019 to 2020 in the tropical Atlantic ITCZ (punctuated by areas of strong salinification north of Brazil and Colombia) and in the Gulf of Guinea (Fig. 3.7b). Elsewhere in the Atlantic in 2020, as in many previous years, the relatively fresh regions

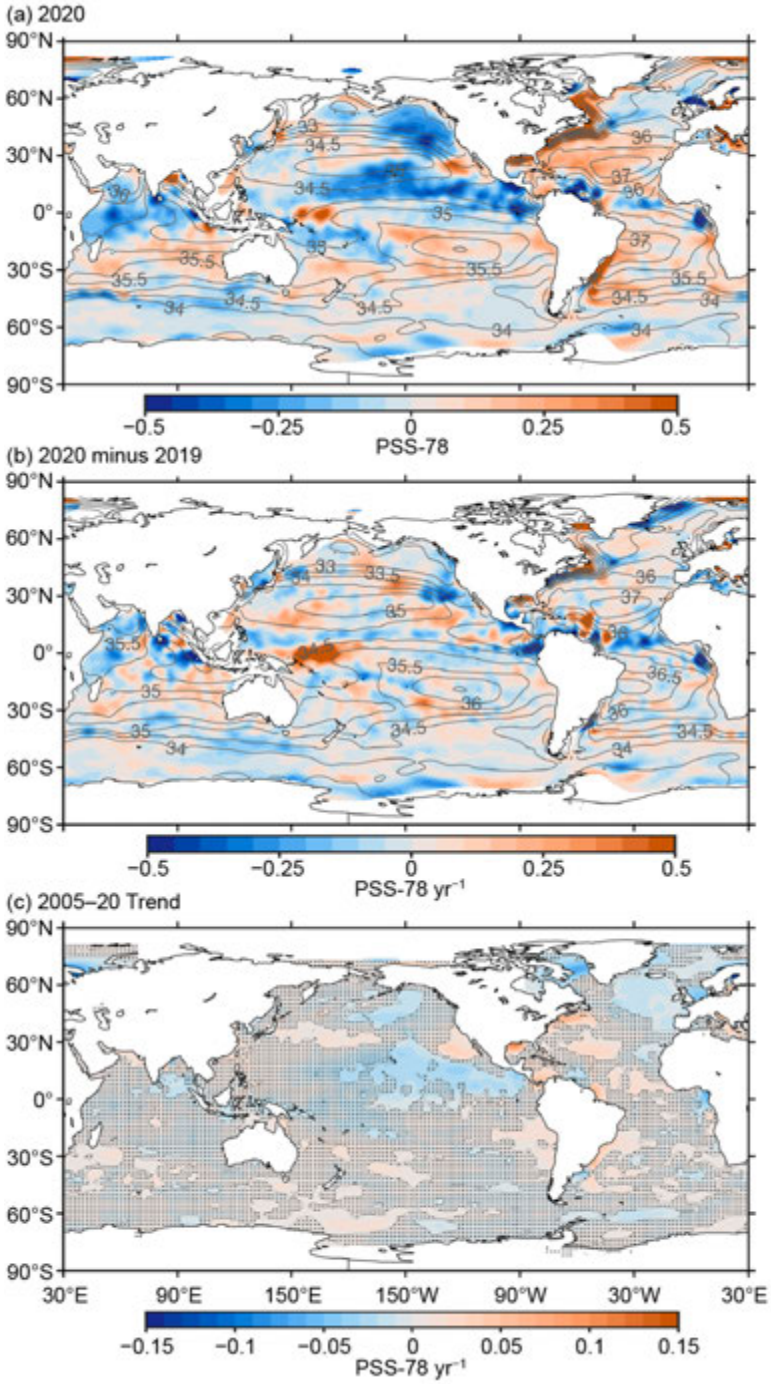

Fig. 3.7. (a) Map of the 2020 annual surface salinity anomaly (colors, PSS-78) with respect to monthly climatological 1955–2012 salinity fields from WOA13v2 (yearly average—gray contours at 0.5 intervals, PSS-78). (b) Difference of 2020 and 2019 surface salinity maps (colors, PSS-78 yr^{-1}). White ocean areas are too data-poor (retaining <80% of a large-scale signal) to map. (c) Map of local linear trends estimated from annual surface salinity anomalies for 2005–20 (colors, PSS-78 yr^{-1}). Areas with statistically insignificant trends at 5%–95% confidence are stippled. All maps are made using Argo data.

(subpolar North Atlantic and under the ITCZ) were fresher than climatology, and the relatively saltier regions (the subtropics) were saltier than climatology (Fig. 3.7a) These salty signals appear to be especially strong just off the east coasts of North and South America.

Freshening in much of the tropical Indian Ocean from 2019 to 2020 (Fig. 3.7b) left most of that region fresher than climatology in 2020 (Fig. 3.7a). In a warming climate, the atmosphere can hold more water, leading to expectations of more evaporation in regions where evaporation is dominant over precipitation and more precipitation where precipitation exceeds evaporation (Held and Soden 2006; Durack and Wijffels 2010). In the ocean this translates to "Salty gets saltier and fresh gets fresher." This pattern has been evident in *State of the Climate* reports going back as far as 2006, the first year of the SSS section. In 2020, salty SSS anomalies are associated with the subtropical salinity maxima in the South Indian, the South Pacific, and the North and South Atlantic Oceans (Fig. 3.7a), with fresh SSS anomalies in the subpolar North Pacific, the eastern subpolar North Atlantic, and the ITCZs of the Pacific and Atlantic. The 2005–20 SSS trends (Fig. 3.7c) reflect this pattern to some extent as well, although the portions with trends statistically different from zero at the 5%–95% confidence limits (Fig. 3.7c, unstippled areas) are somewhat limited. Still, there are statistically significant freshening trends evident in the subpolar North Pacific and North Atlantic, the Bay of Bengal, and the Pacific ITCZ. There are also statistically significant salty trends in parts of the subtropics in all basins. The salty trends in the stratocumulus deck regions west of California and Chile are interesting, as they are, to the best of our knowledge, unexplained.

In 2020, the seasonal BASS (Xie et al. 2014) SSS anomalies (Fig. 3.8) show the year-round persistence of fresh SSS anomalies in the North Pacific subpolar and tropical regions and salty SSS anomalies in the subtropics of all the other basins. The western equatorial Pacific starts

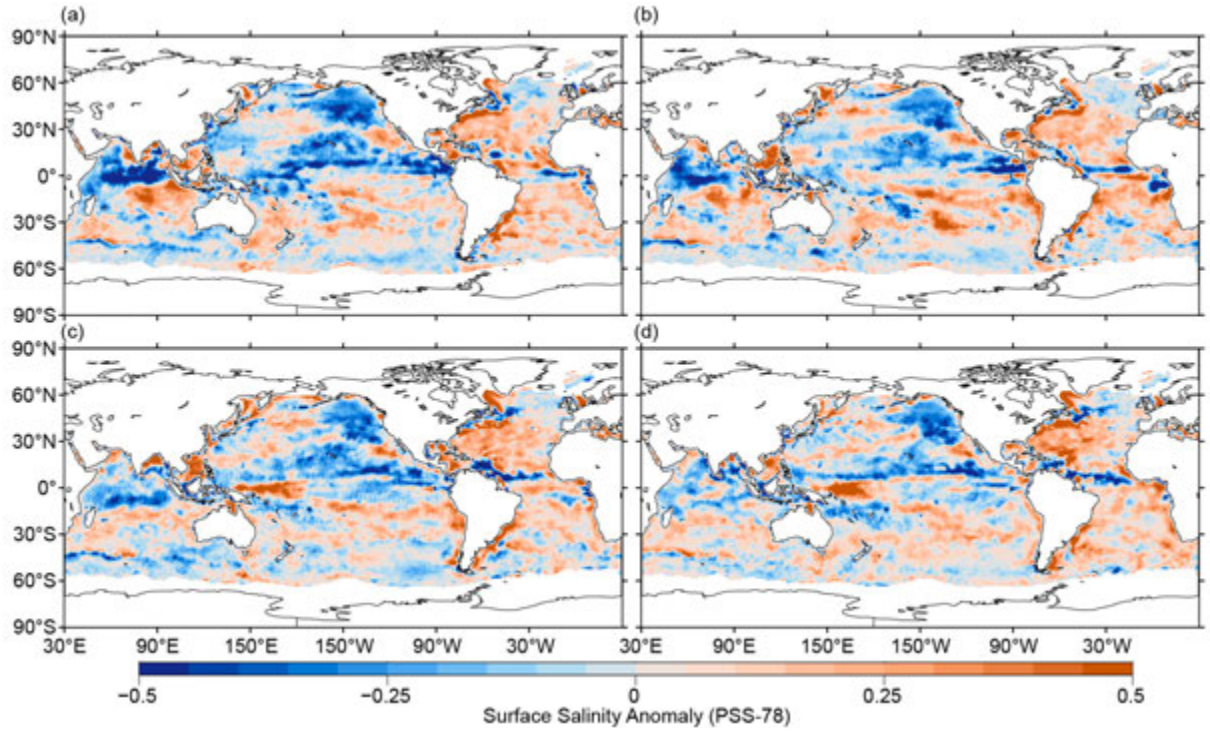

Fig. 3.8. Seasonal maps of SSS anomalies (PSS-78; colors) from monthly blended maps of satellite and in situ salinity data (BASS; Xie et al. 2014) relative to monthly climatological 1955–2012 salinity fields from WOA13v2 for (a) DJF 2019/20, (b) MAM 2020, (c) JJA 2020, and (d) SON 2020. Areas with maximum monthly errors exceeding 10 PSS-78 are left white.

out anomalously fresh, but becomes increasingly anomalously salty throughout the year with the advent of La Niña. Similarly, much of the tropical Indian Ocean becomes progressively less anomalously fresh during 2020. In the tropical Atlantic, fresh anomalies build in the Gulf of Guinea in boreal spring 2020 and north and east of the Orinoco and Amazon Rivers in boreal summer and autumn 2020. With their higher spatial and temporal resolution, BASS data also reveal some features like the fresh anomaly near the North Atlantic Current that are not as readily apparent in the Argo maps.

3) Subsurface salinity—J. Reagan, T. Boyer, C. Schmid, and R. Locarnini

Salinity anomalies originating near the surface of the ocean often propagate into the ocean's interior through mixing or through the sinking of water masses along isopycnals. Thus, subsurface salinity anomalies can often be used as a tracer for what has happened at the surface. Here we analyze salinity in the three main ocean basins (Atlantic, Pacific, and Indian) from 64.5°S to 65.5°N with definitions following World Ocean Atlas 2018 conventions (https://www.ncei.noaa.gov/data/oceans/woa/WOA18/MASKS/basinmask_01.msk).

The 0–1000-m Atlantic basin-average monthly salinity anomalies for 2011–20 exhibit large positive anomalies (>0.05) near the surface that weaken with depth to ~0.01 at 600 m (Fig. 3.9a), a pattern that has persisted for over a decade and continued in 2020. From 2019 to 2020 there was salinification (≥0.015) from 50 to 125 m (Fig. 3.9b), with little change above and below. Thus, the surface salinification between 2018 and 2019 (Reagan et al. 2020) appears to have deepened to ~100 m between 2019 and 2020. Statistically significant (>1 std. dev.) changes in zonally averaged salinity anomalies in the Atlantic (Fig. 3.9c) between 2019 and 2020 reveal large freshening (<−0.15) around 8°N in the upper 30 m and weaker freshening (~−0.03) in the upper 100 m near 35°S. Significant salinification (>0.03) is centered at 40°S and extends from the surface to 500 m. Additional salinification (>0.06) extends from the surface to 100-m depth centered at 45°N with subsurface pockets of salinification (>0.03) from 50 to 150 m between 5°N and 30°N.

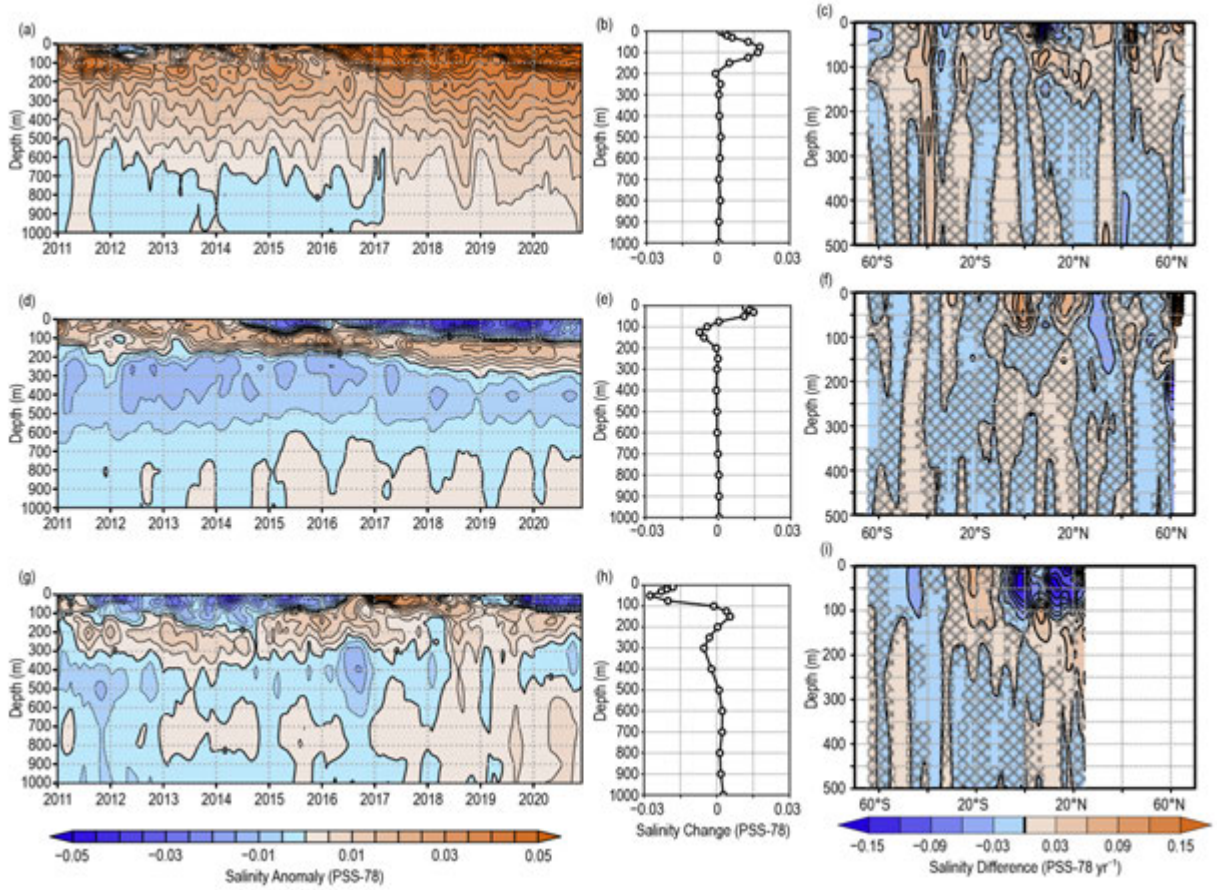

Fig. 3.9. Average monthly salinity anomalies from 0–1000-m depth for 2011–20 for the (a) Atlantic, (d) Pacific, and (g) Indian Ocean basins. Change in salinity from 2019 to 2020 for the (b) Atlantic, (e) Pacific, and (h) Indian Ocean basins. Change in the 0–500-m zonal-average salinity from 2019 to 2020 in the (c) Atlantic, (f) Pacific, and (i) Indian Ocean basins with areas of statistically insignificant change, defined as <±1 std. dev. and calculated from all year-to-year changes between 2005 and 2020, stippled in dark gray. Data were smoothed using a 3-month running mean. Anomalies are relative to the long-term (1955–2012) WOA13v2 monthly salinity climatology (Zweng et al. 2013).

The 2020 basin-average monthly salinity anomalies for the Pacific continued the persistent pattern that has been evident since mid-2014 (Fig. 3.9d). In 2020, fresh anomalies (<−0.01) dominated the upper 100 m, with salty anomalies (>0.01) between 125 and 250 m, and fresh anomalies (<−0.01) between 350 and 550 m. Changes from 2019 to 2020 (Fig. 3.9e) reveal salinification in the upper 75 m (peak of ~0.015 at 30 m) with freshening from 75 to 200 m (peak of ~−0.0075 at 125 m). The zonally averaged salinity changes from 2019 to 2020 (Fig. 3.9f) in the Pacific reveal significant salinification (>0.06) in the upper 100 m centered at three latitudes: 0°, 15°N, and 62°N. Significant freshening (<−0.03) occurred between the surface and 175 m between 27°N and 37°N and in a subsurface pocket between 175- and 275-m depths at 60°N.

Throughout 2020 in the Indian basin there were large (<−0.025) fresh anomalies in the upper 75 m with salty anomalies (>0.005) between 100- and 200-m depths (Fig. 3.9g). Similar to the salinity tendency exhibited from 2018 to 2019 (Reagan et al. 2020), there was strong freshening in the upper 100 m (peak of ~−0.028 at 50 m) from 2019 to 2020 (Fig. 3.9h). Additionally, there was salinification between 100- and 200-m depths (peak ~0.0065 at 150 m) and more freshening between 200- and 500-m depths (peak ~−0.0065 at 300 m). The 2019 to 2020 changes in zonally averaged salinity anomalies in the Indian basin reveal significant freshening (<−0.06) in the upper 100 m from ~6°S to 23°N, which was likely the result of enhanced precipitation over the eastern Indian basin associated with the 2020 La Niña event (see Fig. 3.12). Additional significant freshening (<−0.03) near 45°S from the surface to 100 m is also evident. Significant salinification (>0.03) occurred between 0 and 125-m depths between 25°S and 15°S and in two subsurface

pockets centered at 100 m and ~7°N and at 200 m and 22°N, respectively.

Figure 3.10 shows the 2005–20 basin average salinity trends for the three oceans. The Atlantic reveals significant salinification trends throughout the 0–1000-m water column, with maximum values of 0.04 decade^{-1} at the surface. The Pacific experienced significant freshening trends from 0 to 50 m (peak of ~–0.02 decade^{-1} at 20 m), with salinification trends between 75 and 250 m (peak of ~0.018 decade^{-1} at 150 m). The Indian Ocean experienced significant subsurface salinification trends with a peak at 125 m (0.01 decade^{-1}). The near-surface freshening in the Pacific (precipitation-dominated basin) and salinification in the Atlantic (evaporation-dominated basin) supports the idea that the hydrological cycle is amplifying in a warming world (Held and Soden 2006) and can be traced by changes in salinity (Durack 2015). Furthermore, a recent study by Li et al. (2020) shows that the ocean has become increasingly stratified over the last half century, which has been primarily due to ocean temperatures rising faster at the surface than below, creating less dense surface water. Based on the 2005–20 trend analysis, the Atlantic salinity trends have worked to destabilize the water column as salinity (and therefore density) increases the most at the surface, whereas the Pacific and Indian salinity trends have worked in conjunction with the temperature trends to stabilize the water column as there is freshening at the surface (decreasing density) and salinification below (increasing density).

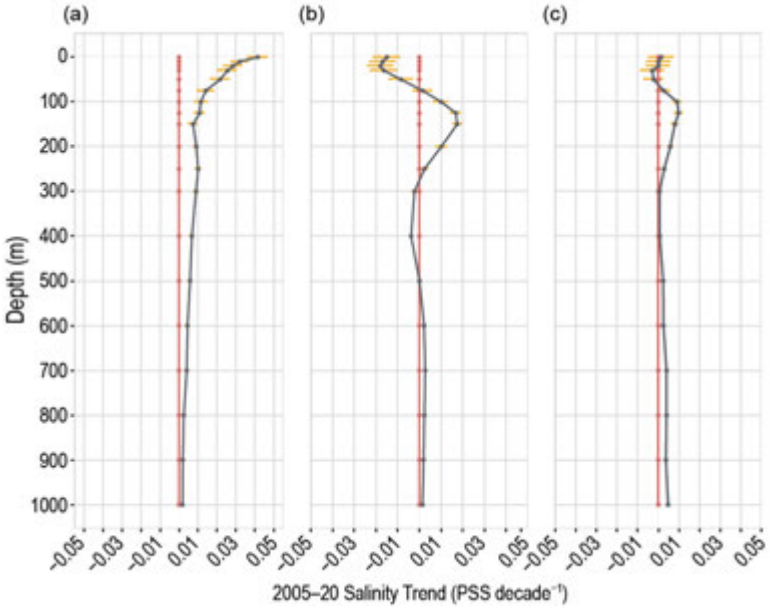

Fig. 3.10. Basin-average salinity trends from 2005 to 2020 (black line, PSS-78 decade^{-1}) with 95% confidence intervals (orange bars) at standard depths for (a) Atlantic, (b) Pacific, and (c) Indian Ocean basins. Red line is the zero-trend line.

e. Global ocean heat, freshwater, and momentum fluxes—L. Yu, P. W. Stackhouse, A. C. Wilber, C. Wen, and R. A. Weller

The ocean and atmosphere exchange heat, freshwater, and momentum at the surface. These air–sea fluxes are the primary mechanisms for keeping the global climate system in balance with the incoming insolation at Earth's surface. Most of the shortwave radiation (SW) absorbed by the ocean's surface is vented into the atmosphere by three processes: longwave radiation (LW), turbulent heat loss by evaporation (latent heat flux, or LH), and conduction (sensible heat flux, or SH). Heat is stored in the ocean and transported by the ocean circulation, forced primarily by wind stress. Evaporation connects heat and moisture transfers, and the latter, together with precipitation, determines the local surface freshwater flux. Identifying changes in air–sea fluxes is essential in deciphering observed changes in ocean water properties and transport of mass, freshwater, and heat.

We examined air–sea heat flux, freshwater flux, and wind stress in 2020 and their relationships with ocean surface variables. The net surface heat flux is: Qnet = SW+LW+LH+SH. The net surface freshwater flux into the ocean (neglecting riverine and glacial fluxes from land) is precipitation (P) minus evaporation (E). Wind stress is computed from satellite wind retrievals using the bulk parameterization Coupled Ocean-Atmosphere Response Experiment (COARE) version 3.5 (Fairall et al. 2003). We produce global maps of Qnet, $P-E$, and wind stress (Figs. 3.11–3.13) and the long-term perspective of the change of the forcing functions (Fig. 3.14) by integrating efforts of multiple groups. Ocean-surface LH, SH, E, and wind stress are from the Objectively Analyzed air-sea Fluxes (OAFlux) project's high-resolution products (Yu and Weller 2007). Surface SW and LW radiative fluxes are from the Clouds and the Earth's Radiant Energy Systems (CERES) Fast Longwave And Shortwave Radiative Fluxes (FLASHFlux) version

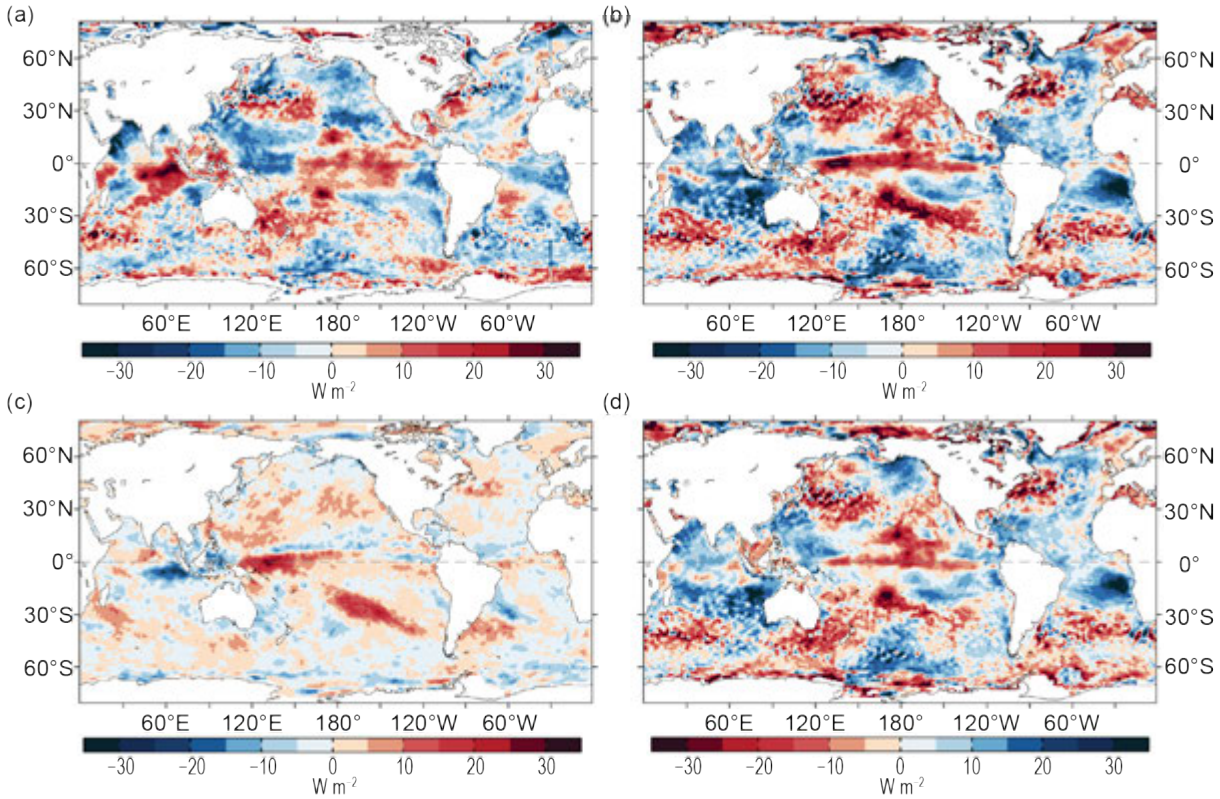

Fig. 3.11. (a) Surface heat flux (Qnet) anomalies for 2020 relative to the 2001–15 climatology. Positive values denote ocean heat gain. (b) 2020 minus 2019 difference for Qnet, (c) surface radiation (SW+LW), and (d) turbulent heat fluxes (LH+SH), respectively. Positive changes denote more ocean heat gain in 2020 than in 2019, consistent with the reversal of the color scheme in (d). All units are given in W m^{-2}. LH+SH are from OAFlux, and SW+LW is the NASA FLASHFlux version 4A.

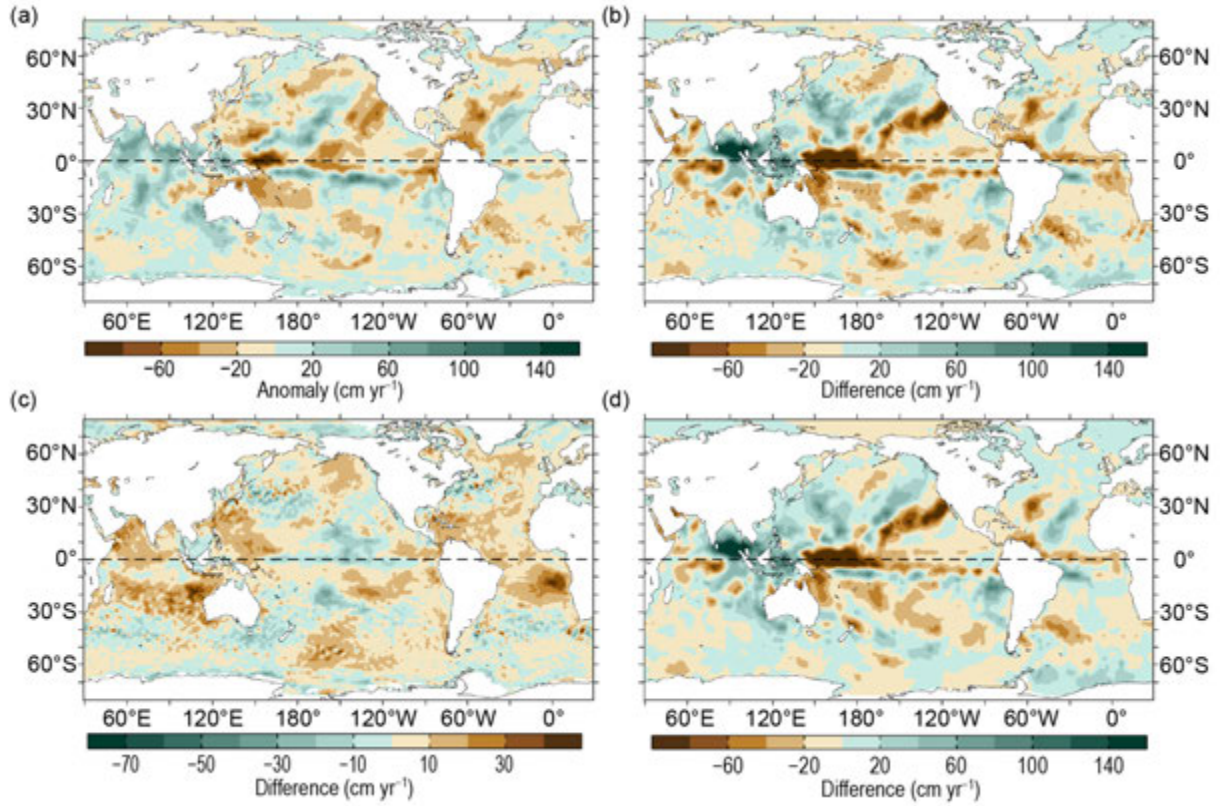

Fig. 3.12. (a) Surface freshwater *(P−E)* flux anomalies for 2020 relative to the 1988–2015 climatology. 2020 minus 2019 difference for (b) *P−E*, (c) evaporation (*E*), and (d) precipitation (*P*). Green colors denote anomalous ocean moisture gain, and browns denote loss, consistent with the reversal of the color scheme in (c). All units are given in cm yr^{-1}. *P* is the GPCP version 2.3rB1 product, and *E* is from OAFlux.

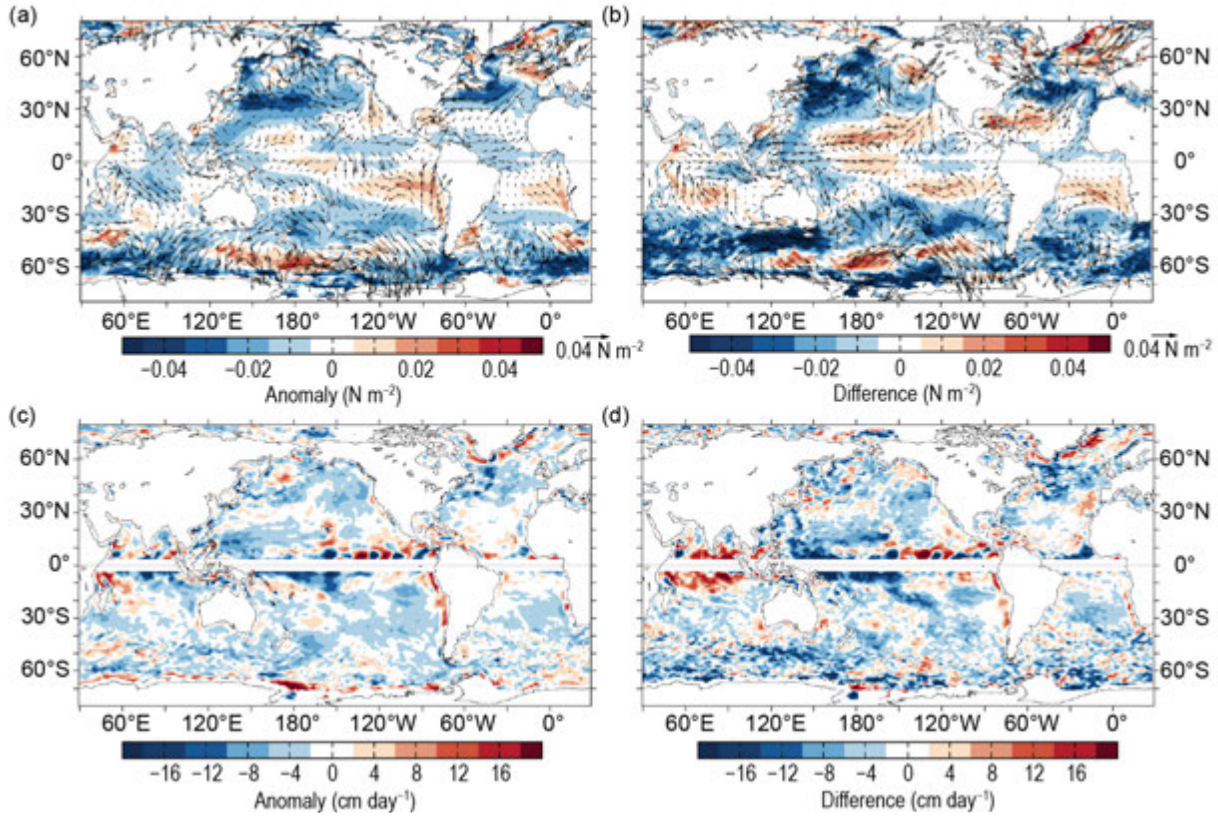

Fig. 3.13. (a) Wind stress magnitude (colors) and vector anomalies for 2020 relative to the 1988–2015 climatology, (b) 2020 minus 2019 difference in wind stress (N m^{-2}), (c) Ekman vertical velocity anomalies (W_{EK}; cm day^{-1}) for 2020 relative to the 1988–2015 climatology, and (d) 2020 minus 2019 difference in W_{EK} (cm day^{-1}). In (c) and (d), positive values denote upwelling tendency and negative downwelling tendency. Winds are computed from the OAFlux.

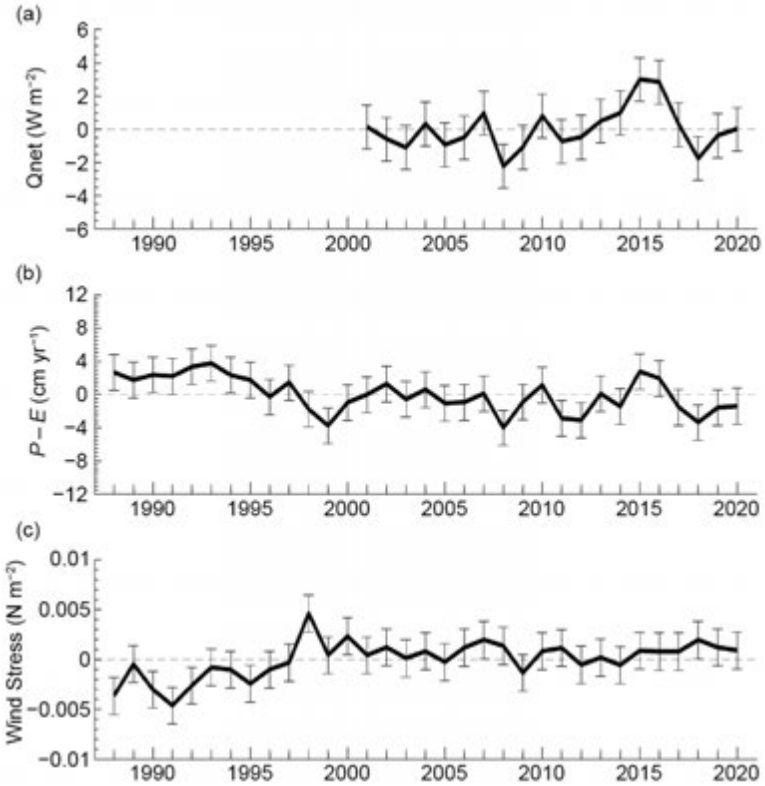

4A product (Stackhouse et al. 2006). Global P is from the Global Precipitation Climatology Project (GPCP) version 2.3 products (Adler et al. 2018). The CERES Energy Balanced and Filled (EBAF) surface SW and LW version 4.1 products (Loeb et al. 2018; Kato et al. 2018) are used in the time series analysis.

1) Surface heat fluxes

The ocean received anomalous net heat (Qnet anomalies) in 2020 (Fig. 3.11a) from the atmosphere (positive anomalies) in the eastern equatorial Indian Ocean (>30 W m^{-2}), the central and eastern equatorial Pacific (~10 W m^{-2}), the western North Pacific around 30°N (~10 W m^{-2}), the northwest subtropical Atlantic (~10 Wm^{-2}), and the midlatitude Southern Ocean 30°–50°S (~10 W m^{-2}). The regions where the ocean had pronounced anomalous heat loss to

Fig. 3.14. Annual-mean time series of global averages of (a) net surface heat flux (Qnet; W m^{-2}) from the combination of CERES EBAF4.1 SW+LW and OAFlux LH+SH. The 2020 Qnet estimate is based on FLASHFlux and OAFlux. (b) net freshwater flux ($P-E$; cm yr^{-1}) from the combination of GPCP P and OAFlux E, and (c) wind stress magnitude (N m^{-2}) from OAFlux. Shaded area denotes 1 std. dev. of annual mean variability.

the atmosphere include the Arabian Sea (<–25 W m^{-2}), the western tropical Pacific (~–20 W m^{-2}), the subtropical eastern North Pacific (~–20 W m^{-2}), and the tropical South Atlantic Ocean (~–15 W m^{-2}).

The 2020 minus 2019 Qnet differences (Fig. 3.11b) in the tropical Pacific reflect the transition from a weak El Niño in 2019 to a moderate La Niña in 2020 (see section 4b; compare Fig. 3.11b to sea surface temperature [SST] differences in Fig. 3.1b). Cool SST anomalies were damped by increased ocean heat uptake. In general, Qnet differences were dominated by the LH+SH difference (Fig. 3.11d), though both LH+SH and SW+LW (Fig. 3.11c) showed similar structures over most of the global ocean. Furthermore, SW+LW increases were dominant in the western equatorial Pacific and the central South Pacific, with increases in the region extending from the western equatorial Pacific to the southeastern Pacific, but maximum magnitude (~10 W m^{-2}) confined in a northwest-southeast tilted band between the dateline and 120°W. LH+SH showed a similar warming tendency in the central equatorial Pacific and the center of the South Pacific, induced primarily by a weakened LH heat loss (–10 Wm^{-2}).

Outside of the equatorial Pacific, both SW+LW and LH+SH 2020 minus 2019 differences produced an anomalous warming along 40°–50°S in the Southern Ocean, in the vicinity of the Kuroshio–Oyashio Extension in the North Pacific, and in a large area in the eastern North Pacific (170°E–150°W, 20°–40°N). In the latter, the band of SW+LW warming tendencies (~5 W m^{-2}) was likely caused by a reduction of clouds in 2020 relative to 2019. This location was on the southern edge of the 2019–20 northeast Pacific marine heatwave (MHW; Fig. 3.1; Sidebar 3.1), where LH+SH also showed warming tendencies (~10 W m^{-2}) due to the weakened LH loss.

In the tropical Indian Ocean, the 2020 minus 2019 Qnet differences revealed anomalous ocean cooling. As the 2020 minus 2019 SST differences (Fig. 3.1b) were mostly negative in the western half of the Indian Ocean, there seems to be a causality relationship between the Qnet forcing and SST. On the other hand, the SST differences in the eastern Indian Ocean did not have the same sign as Qnet.

In the Atlantic Ocean, there was a tripole-like difference pattern of Qnet featuring Qnet increases in the Gulf Stream and extension and Qnet decreases elsewhere between 30°S and 60°N (Fig. 3.11d). The subpolar North Atlantic (north of 60°N) and the South Atlantic (south of 30°S) gained heat (~10–15 W m^{-2}) from the atmosphere in 2020. The source of heating was attributable primarily to the reduced LH+SH and secondly to the net radiative heating (<5 W m^{-2}) in these regions.

2) Surface freshwater fluxes

The 2020 $P-E$ anomalies (Fig. 3.12a) reflect a basin-wide increase in the net freshwater input (~20 cm yr^{-1} on average) to the tropical Indian Ocean (positive anomalies with green colors; a freshening effect on the ocean), consonant with a local reduction of sea surface salinity (SSS; see Fig. 3.7a). The net freshwater input reduced (negative anomalies with brown colors; salinification effect on the ocean) in the eastern North Pacific and the western North Atlantic and increased in a few other regions, such as the zonal freshening band just south of the equator in the Pacific and the tilted southwest-northeast freshening bands in the central North Pacific and North Atlantic. The maximum $P-E$ reduction (~80 cm yr^{-1}) occurred in the western equatorial Pacific where SSS increased dramatically (see Fig. 3.7b).

The 2020 minus 2019 $P-E$ difference pattern in the tropical Pacific (Fig. 3.12b) resembles that of the net surface radiation (SW+LW) difference pattern (Fig. 3.11b), with the bands of the reduced $P-E$ value coinciding with the bands of increased SW+LW values. The $P-E$ tendencies are attributable to the P tendencies (Fig. 3.12d), showing that SW+LW increased in areas of reduced rainfall and conversely, SW+LW reduced in areas of increased rainfall. Outside of the tropics, the largest evaporative tendencies occurred in the eastern subtropical North Pacific (~80 cm yr^{-1}), resulting from the reduction of P. This freshwater deficit was concurrent with increased SW+LW tendencies (Fig. 3.11c).

3) Wind stress

Midlatitude westerly winds became weaker (negative wind stress anomalies; Fig. 3.13a) in 2020 in both Northern and Southern Hemispheres (NH and SH). In the North Pacific and North Atlantic Oceans, marked reduction of westerly winds occurred along 30°–40°N and the magnitude of negative anomalies was <0.04 N m^{-2}. In the SH, negative wind anomalies developed on the southern edge of the westerly winds along 50°–60°S in the eastern Pacific, and the Atlantic and Indian sectors (from 120°W to 120°E), with anomalies reaching −0.04 N m^{-2} in several locations. However, the change of the westerly winds was not uniform across the circumpolar region; for instance, the westerly winds actually became stronger in the western Pacific sector. Winds also became stronger in the subpolar North Atlantic Ocean, where winds are predominantly easterlies.

The trade winds in 2020 strengthened (<0.025 N m^{-2}) in the central tropical Pacific as expected with the transition to La Niña (see section 4b), as well as the southern tropical Pacific and Atlantic. In the North Indian Ocean, winds over the Arabian Sea accelerated while winds over the Bay of Bengal slowed down.

The 2020 minus 2019 wind stress difference map (Fig. 3.13b) further shows that the most noted changes in winds are the strengthening of the trade winds in the three tropical basins, the weakening of the westerly winds in the midlatitude NH and SH, and the strengthening of the easterly winds in the subpolar North Atlantic. Surface winds were stronger in the Gulf of Alaska associated with the evolving MHW (Sidebar 3.1).

Winds vary considerably in space. The spatial variations of winds cause divergence and convergence of the Ekman transport, leading to a vertical velocity, denoted by Ekman pumping (downward) or suction (upward) velocity W_{EK}, at the base of the Ekman layer. Computation of W_{EK} follows the equation: $W_{EK} = 1/\rho\nabla\cdot(\tau/f)$, where ρ is the water density and f the Coriolis force. The 2020 W_{EK} anomaly pattern (Fig. 3.13c) is dominated by large downwelling (negative) anomalies in the tropical South Indian Ocean and tropical South Pacific Ocean, with maximum magnitude of ~−16 cm yr^{-1}. The change indicates a weakening of the typical upwelling conditions in the former and a strengthening of the typical downwelling conditions in the latter. Outside of the tropical region, the 2020 W_{EK} anomalies were generally weak and less organized. The 2020 minus 2019 W_{EK} difference pattern (Fig. 3.13d) suggests the resuming of the typical upwelling conditions in the equatorial Indian Ocean after the end of the major 2019 positive Indian Ocean dipole event (see Fig. 3.1b), with its anomalously warm waters in the western Indian Ocean, and cool waters in the east.

4) Long-term perspective

A long-term perspective on the change of ocean surface forcing functions in 2020 is examined in the context of multi-decade annual mean time series of Qnet, $P-E$, and wind stress averaged over the global ice-free oceans (Figs. 3.14a–c). The Qnet time series commences in 2001, when CERES EBAF4.1 surface radiation products begin. The $P-E$ and wind stress time series are each 33 years long, starting from 1988 when higher quality global flux fields can be constructed from Special Sensor Microwave/Imager (SSM/I) satellite retrievals. Qnet anomalies are relative to the 2001–15 climatology, and positive anomalies denote increased net downward heat flux into the ocean that has a warming effect on the ocean. $P-E$ anomalies are relative to the 1988–2015 climatology, and positive anomalies denote increased freshwater flux into the ocean that causes sea surface freshening. Wind stress anomalies are relative to the 1988–2015 climatology, and positive anomalies denote increased wind stress magnitude over the ocean.

Qnet did not change significantly between 2001 and 2007 but had large interannual fluctuations thereafter. The total downward heat flux into the global ocean increased by about 3 W m^{-2} during 2011–16, when the tropical Pacific switched from a strong La Niña event in 2011 to a strong El Niño event in 2015–16. This period of increasing oceanic heat gain coincided with an increase of the global mean SST by about 0.35°C (Fig. 3.3a). Qnet went up slightly in 2019 after a

sharp reduction of about 4 W m^{-2} during the 2017–18 La Niña, and the 2020 Qnet remained at a similar level to its 2019 value. The $P - E$ time series shows similar interannual variability to that of the Qnet time series, with the 2020 level more or less the same as the 2019 level. The time series of wind stress was flat in the recent two decades after a regime shift around 1999, and the 2020 winds were slightly but not significantly down from the 2019 level. The error bars in the time series represent one standard deviation of year-to-year variability.

f. Sea level variability and change—P. R. Thompson, M. J. Widlansky, E. Leuliette, W. Sweet, D. P. Chambers, B. D. Hamlington, S. Jevrejeva, J. J. Marra, M. A. Merrifield, G. T. Mitchum, and R. S. Nerem

Global mean sea level (GMSL) during 2020 had the highest annual average in the satellite altimetry record (1993–2020), 91.3 mm above 1993 (Fig. 3.15a). This marks the ninth consecutive year (and 25th out of the last 27) that GMSL increased relative to the previous year. The new high reflects an ongoing multi-decadal trend of 3.3 ± 0.4 mm yr^{-1} in GMSL during the satellite altimetry era (Fig. 3.15a). A quadratic fit with corrections for the eruption of Mt. Pinatubo (Fasullo et al. 2016) and El Niño-Southern Oscillation effects (Hamlington et al. 2020) yields an average (1993–2020) climate-driven trend of 3.0 ± 0.4 mm yr^{-1} and acceleration of 0.081 ± 0.025 mm yr^{-2} (updated from Nerem et al. 2018).

Variations in GMSL (Fig. 3.15a) result from changes in both the mass and density of the global ocean (Leuliette and Willis 2011; Chambers et al. 2017). The steric (i.e., density-related) sea level rise rate observed by the Argo profiling float array during 2005–20, 1.4 ± 0.2 mm yr^{-1}, which is mostly due to ocean warming, accounted for about one-third of the GMSL trend of 3.7 ± 0.4 mm yr^{-1} since 2005. Increasing global ocean mass observed by the NASA Gravity Recovery and Climate Experiment (GRACE) and GRACE Follow-On (GRACE-FO) missions, contributed the remaining two-thirds, 2.6 ± 0.4 mm yr^{-1}, of the GMSL trend during 2005–20. The positive trend in ocean mass primarily resulted from melting of glaciers and ice sheets (see sections 5e, 6d, 6e) with a small contribution, 0.3 ± 0.1 mm yr^{-1}, from terrestrial water storage (Frederikse et al. 2020; a decrease in terrestrial storage will cause an increase in sea level).

Annually averaged GMSL from satellite altimetry increased by 3.5 mm from

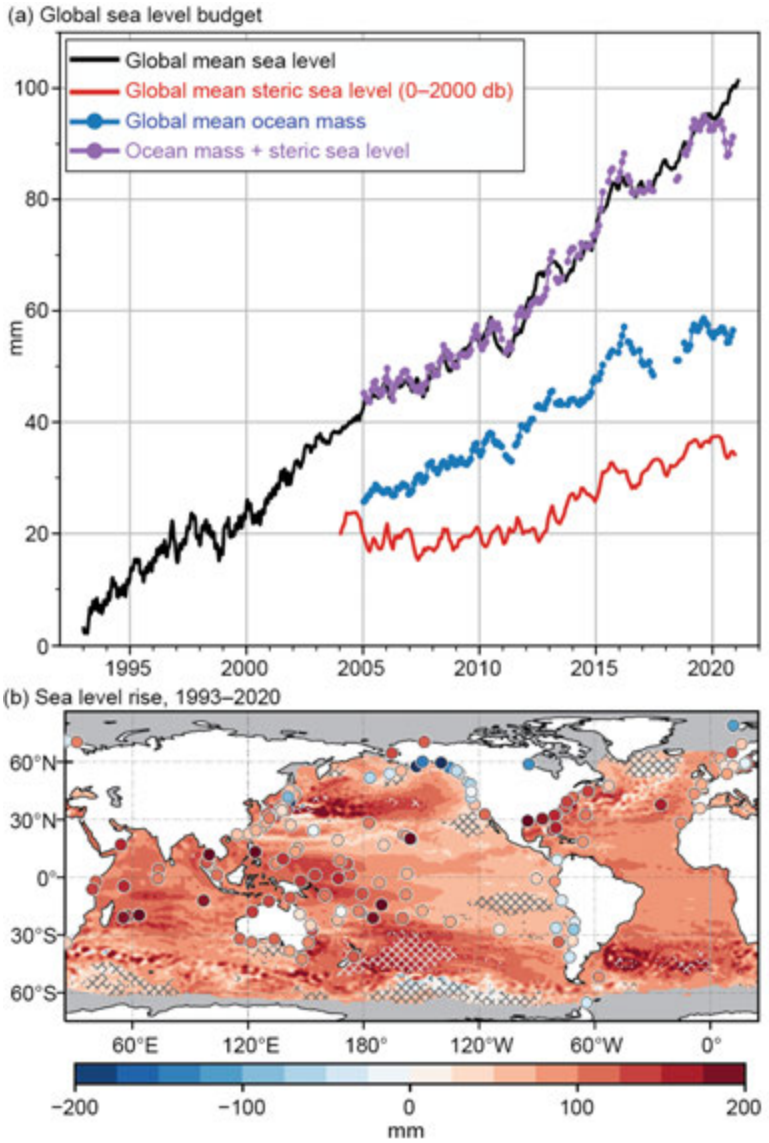

Fig. 3.15. (a) Monthly averaged GMSL (mm) observed by satellite altimeters (black, 1993–2020 from the NOAA Laboratory for Satellite Altimetry), global ocean mass (blue, 2005–20 from GRACE and GRACE-FO), global mean steric sea level (red, 2004–20 from the Argo profiling float array), mass plus steric (purple), and inferred global ocean mass (blue) calculated by subtracting global mean steric sea level from global mean sea level. All time series have been smoothed with a 3-month filter. (b) Total local sea level change during 1993–2020 as measured by satellite altimetry (contours) and tide gauges (circles). Hatching indicates local changes that are significantly different from the change in GMSL.

2019 to 2020 (Fig. 3.15a) while annual global mean steric sea level observed by Argo (0–2000 m) decreased by 0.75 mm from 2019 to 2020 (Fig. 3.15a). The decrease in global mean steric sea level contrasts with the estimated year-over-year increase in the globally integrated ocean heat content anomaly (OHCA; 0–2000 m) from an ensemble of OHCA products (see section 3c). One of the five estimates (e.g., the NCEI estimate, Fig. 3.6) shows little globally integrated OHCA change from 2019 to 2020 and is not inconsistent with the year-over-year reduction in total steric sea level given a modest salinification of the global ocean. Annual global ocean mass from GRACE-FO decreased by 1.0 mm from 2019 to 2020, which was primarily due to anomalous precipitation in eastern Africa during 2020 and associated terrestrial water storage there (see sections 2d4, 2d9, 7e4).

The sea level budget based on observations from altimetry, Argo, and GRACE-FO did not close during 2020 as annually averaged GMSL measured by satellite altimeters diverged from the sum of the independently estimated steric and mass contributions by more than 5 mm (Fig. 3.15a). Previous discrepancies in the global sea level budget coincided with the failure of an accelerometer onboard the original GRACE mission (Chen et al. 2020). A similar issue may be affecting recent observations from GRACE-FO, because one accelerometer has not functioned properly since launch. However, the reduction in global ocean mass during 2020 can be directly attributed to terrestrial water storage, which is known to produce fluctuations in global ocean mass (Boening et al. 2012). For 2020 specifically, the reduction in global ocean mass is linked to increased water storage in eastern Africa (see sections 2d, 7e4). Given this link, errors in altimetry and/or salty drift in Argo observations cannot be ruled out in accounting for recent discrepancies in the global sea level budget (Chen et al. 2020).

Spatial structure in sea level change over the 28-year altimeter record (Fig. 3.15b) is due to a combination of natural fluctuations in coupled modes of atmosphere–ocean variability (Han et al. 2017) and spatial structure in the response of the ocean to anthropogenic radiative forcing (Fasullo and Nerem 2018). It is difficult to disentangle these contributions to regional differences in sea level change (Hamlington et al. 2019), but salient features can be attributed to specific processes. For example, the east–west difference in sea level change across the Pacific (e.g., the more than 100 mm difference between Palau and Los Angeles) is associated with multidecadal variability in the strength of Pacific trade winds (e.g., Merrifield 2011). The region of enhanced sea level change in the high-latitude South Pacific can be attributed to regional warming of the ocean above 2000 m (Llovel and Terray 2016) and below 2000 m (Volkov et al. 2017). Sea level change relative to land (i.e., relative sea level, the quantity measured by tide gauges; red circles, Fig. 3.15b) is most relevant for societal impacts and can differ substantially from satellite-derived changes in tectonically active regions (e.g., Japan) and areas strongly affected by glacial isostatic adjustment (e.g., Alaska; Fig. 3.15b).

Due to long-term trends in GMSL (Fig. 3.15), annual sea level anomalies during 2020 were positive nearly everywhere (Fig. 3.16a). In the global tropics, the highest sea level anomalies were in the western Indian Ocean (10–15 cm above normal), whereas the lowest anomalies were in the central equatorial Pacific Ocean (0–5 cm). Sea level anomalies were positive across most of the subtropics (i.e., approximately within 20°–30° of the equator), except for small areas in the subtropical southern Indian Ocean, northwestern Pacific, and Gulf of Mexico Loop Current System where the 2020 sea levels were below normal. Each region of negative anomalies was near where some of the highest positive anomalies occurred in the tropical and subtropical latitudes (e.g., northeast of Madagascar, around Hawaii, and along the entire Gulf of Mexico Coast; anomalies 10–15 cm above normal). The 2020 annual mean anomalies were even higher in parts of the midlatitudes, such as in the extension regions of the Kuroshio and Gulf Stream Currents, although upwelling mesoscale eddy activity also contributed to small-scale areas of negative sea level anomalies.

Development of La Niña conditions during 2020 (see section 4b) explains most of the large-scale changes in the sea level compared to 2019 (Fig. 3.16b). Year-to-year sea level increases exceeding 15 cm occurred around parts of Indonesia and the Philippines (i.e., in the equatorial eastern

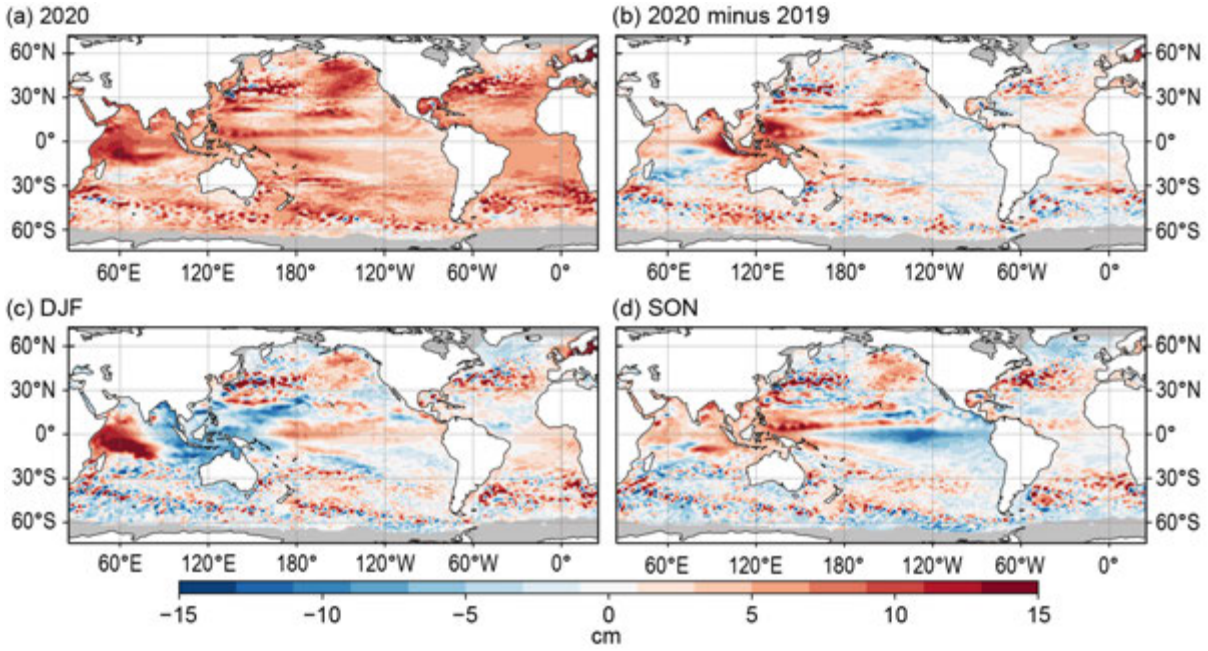

Fig. 3.16. (a) Annual average sea level anomaly during 2020 relative to average sea level at each location during 1993–2020. (b) Average 2020 minus 2019 sea level anomaly. (c) Average sea level anomaly during DJF 2020 relative to 1993–2020 average. (d) Same as (c), but for SON. All units are given in cm. GMSL was subtracted from panels (c),(d) to emphasize regional, non-secular change. Altimetry data were obtained from the gridded, multi-mission product maintained by Copernicus Marine and Environment Monitoring Service.

Indian Ocean and tropical northwestern Pacific Ocean, respectively), whereas in the central and eastern tropical Pacific, sea levels during 2020 were 5–10 cm lower relative to 2019. Elsewhere in the North Pacific Ocean, tendencies from 2019 to 2020 were for higher sea levels in a broad region centered around Hawaii (15 cm year-over-year increase) that extended both southwestward toward the Philippines and northeastward to near the U.S. West Coast. The shape of high sea level anomalies around Hawaii resembles the SST pattern associated with a positive Pacific Meridional Mode (Chiang and Vimont 2004), which is also indicative of weaker-than-normal trade winds in the region (Long et al. 2020), consistent with 2020 observations of wind stress (Fig. 3.13b). The 2020 minus 2019 sea level difference was also positive in the southwestern and south-central Pacific Ocean (greatest near 30°S), throughout most of the Atlantic Ocean including along almost the entire U.S. Gulf and East Coasts, and in the northern Indian Ocean (especially in the Bay of Bengal). Overall, these sea level changes from 2019 to 2020 (Fig. 3.16b) are representative of the underlying OHCA changes in these locations (Fig. 3.4b) but also incorporate the sea level response to year-to-year variability of oceanic warming (Widlansky et al. 2020).

Besides development of La Niña and the associated falling sea levels that occurred in the eastern half of the equatorial Pacific during 2020, the largest intra-seasonal changes (Figs. 3.16c,d) occurred in the tropical Indian Ocean. The year began with well above-normal sea levels in the western Indian Ocean and well below-normal sea levels to the east (a gradient of almost 30 cm during the December–February [DJF] season; Fig. 3.16c). By the September–November (SON) season, the zonal gradient of sea level anomalies in the Indian Ocean had mostly disappeared (Fig. 3.16d). This relaxation of the Indian Ocean sea level anomalies was concurrent with the transition of the Indian Ocean dipole (IOD) index from positive at the beginning of 2020 to near neutral for the remainder of the year (see section 4f). The 2020 minus 2019 sea level difference (Fig. 3.16b) in the tropical Indo-Pacific more closely resembles the end-of-year pattern (Fig. 3.16d; SON), compared to the early-year pattern (Fig. 3.16c; DJF), which is consistent with the abrupt termination of the positive IOD.

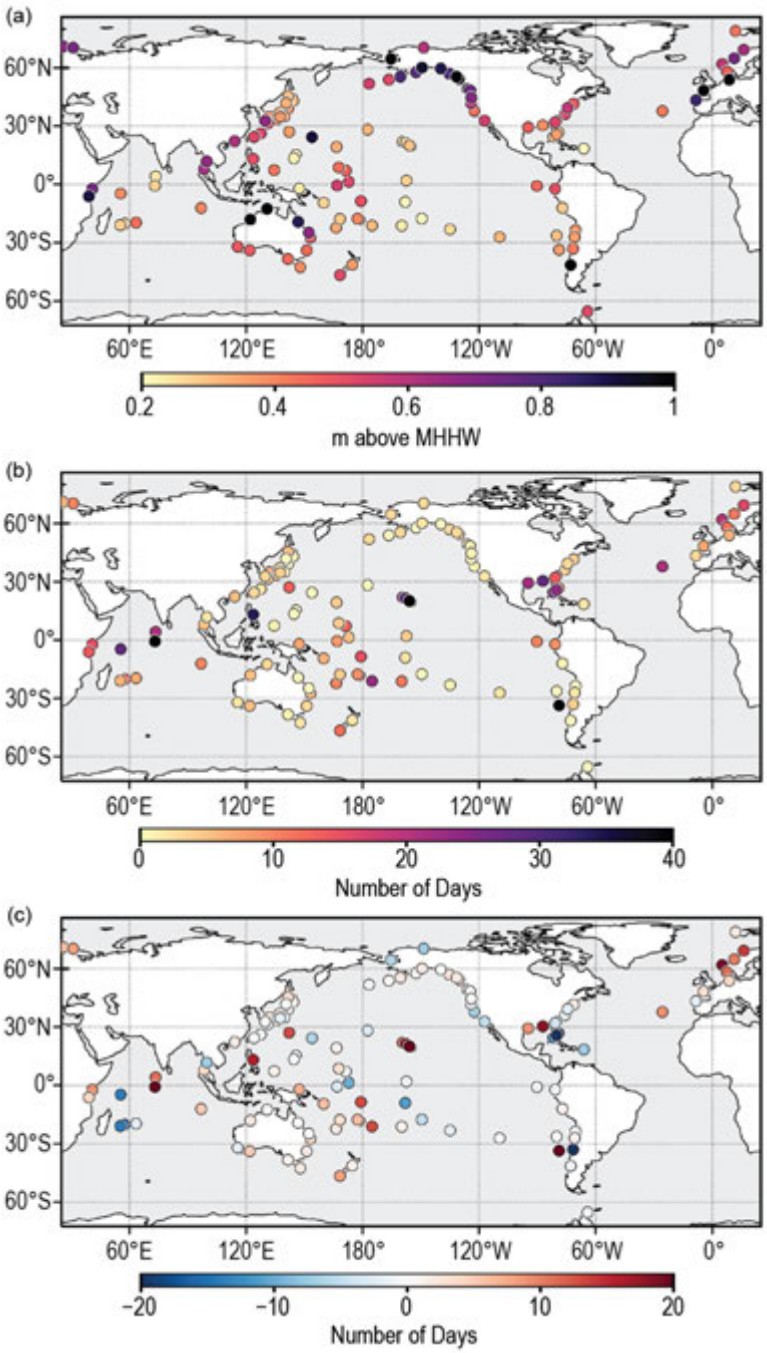

Fig. 3.17. (a) Nuisance-level flooding thresholds defined by the level of the top 1% of observed daily maxima during 2000–18 from tide gauge records. Units are in meters above mean higher high water (MHHW) calculated over 2000–18. (b) Number of daily maximum water levels exceeding the thresholds in (a) during 2020. (c) Same as in (b), but for 2020 minus 2019. Daily maximum water levels were calculated from hourly tide gauge observations obtained from the University of Hawaii Sea Level Center Fast Delivery database. Only records with at least 80% completeness during 2000–18 and 80% completeness during 2020 were analyzed.

Ongoing trends and year-to-year changes in sea level impact coastal communities by increasing the magnitude and frequency of positive sea level extremes that cause flooding and erosion. In many areas, coastal infrastructure is exposed to minor high-tide flooding when water levels exceed a threshold defined by the top 1% of observed daily maxima (Sweet et al. 2014). Such thresholds are expected to be exceeded three to four times per year but the heights of the thresholds vary geographically (Fig. 3.17a). The greatest numbers of 1%-threshold exceedances during 2020 occurred in regions that experienced the highest sea level anomalies (Fig. 3.17b): the equatorial and northern Indian Ocean and coasts along the western Pacific, the Hawaiian Islands, along the Gulf of Mexico, the southeast United States, and northern Europe. The number of threshold exceedances decreased by more than five days from 2019 to 2020 at 17 of the 122 locations analyzed and increased by more than five days at 31 locations (Fig. 3.16c). The largest year-over-year increases occurred in the equatorial Indian Ocean, Hawaii, and northern Europe, while elevated numbers of exceedances in the eastern Gulf of Mexico and southeast United States mostly represented a continuation of (or decrease from) elevated exceedances during 2019.

g. Surface currents—R. Lumpkin, R. Domingues, and G. Goni

This section describes ocean surface current changes, transports derived from ocean surface currents, and features such as rings inferred from surface currents. Surface currents are obtained from in situ (global arrays of drogued drifters and moorings) and satellite (altimetry and wind stress) observations. Transports are derived from a combination of sea surface height anomalies (from altimetry) and hydrographic climatologies. See Lumpkin et al. (2011) for details of these calculations. Zonal surface current anomalies are calculated with respect to a 1993–2007 climatology and are discussed for individual ocean basins as follows.

1) Pacific Ocean

In 2020, the Pacific exhibited basin-wide annual mean zonal westward (negative) current anomalies of 14–16 cm s^{-1} from 150°E to 100°W (Fig. 3.18a) and the equator to 1°N, associated with the 2020 La Niña (see sections 3b, 4b). These were driven by strengthened easterly trade winds (Fig. 3.13a) and produced equatorial upper ocean heat anomalies that were negative in the east and positive in the west (Fig. 3.4a). To the north, eastward anomalies of 5 cm s^{-1} at 150°E–120°W, 8°–10°N indicated a stronger and northward-shifted North Equatorial Countercurrent (NECC; e.g., Johnson et al. 2002), which had a maximum eastward speed of 28 cm s^{-1} (total, not anomaly) at 6.6°N. This northward shift has been seen since 2018, when the NECC was similar in strength to 2020; because it was slightly weaker in 2019, the 2020 minus 2019 anomaly difference (Fig. 3.18b) indicates weaker eastward anomalies along this band.

Eastward anomalies of ~25 cm s^{-1} were present in the western equatorial Pacific in December–February (DJF), but reversed to strong (25 cm s^{-1}) westward anomalies across the basin by March–May (MAM; Fig. 3.19), leading sea surface temperature anomalies (see Fig. 3.2) by a season.

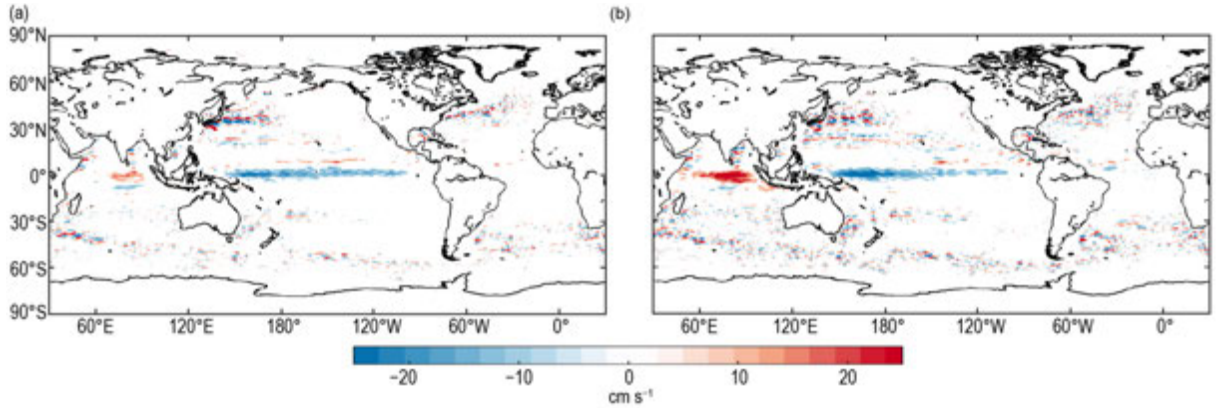

Fig. 3.18. Annually averaged geostrophic zonal current anomalies (cm s^{-1}) for (a) 2020 and (b) 2020 minus 2019 difference derived from a synthesis of drifters, altimetry, and winds. Values not shown where they are not significantly from zero.

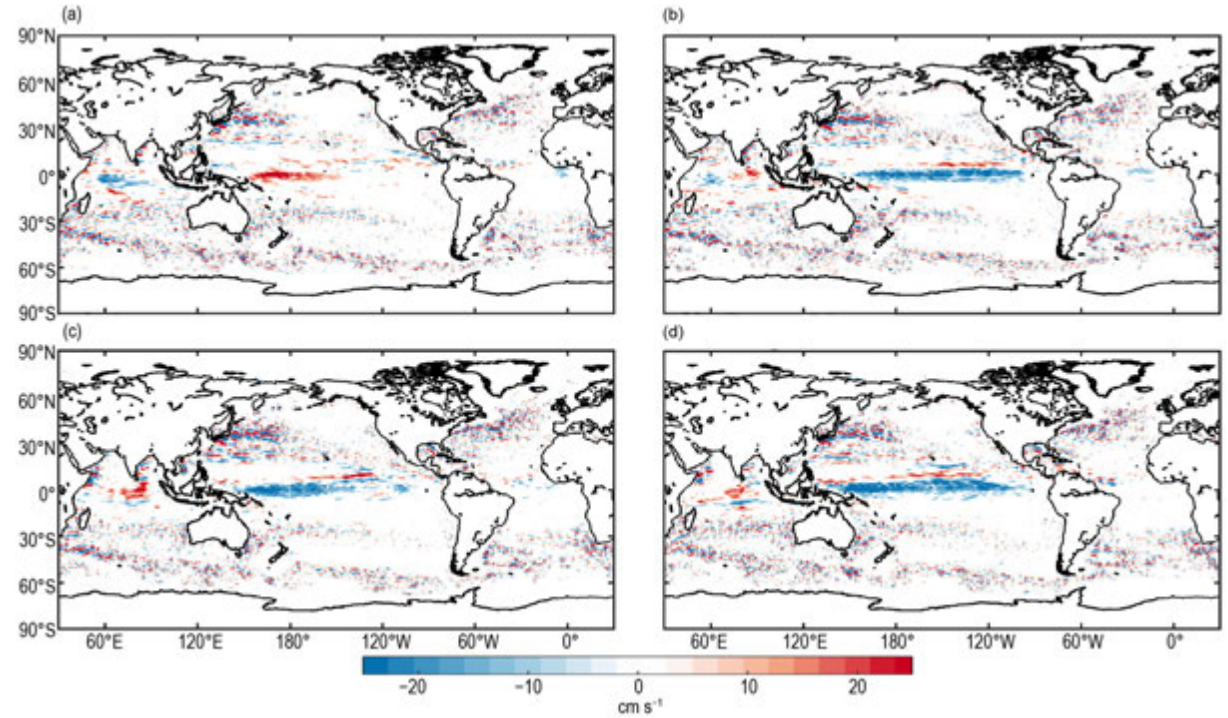

Fig. 3.19. Seasonally averaged zonal geostrophic anomalies (cm s^{-1}) with respect to seasonal climatology, for (a) DJF 2019/20, (b) MAM 2020, (c) JJA 2020, and (d) SON 2020. Values not shown where they are not significantly different from zero.

These zonal surface current anomalies were strongest (25 cm s^{-1}) on the equator but were present from 6°S–4°N. Also in MAM, the NECC accelerated and exhibited eastward anomalies of ~10 cm s^{-1} along 6°–7°N. By June–August (JJA), the equatorial westward anomalies were primarily confined to the western third of the basin, while NECC anomalies weakened except in a narrow longitude range 125°–150°W. During these months, the core of the NECC was shifted north from its climatological location of 6.6°N to 8°N. As the year waned (September–November [SON]), westward anomalies reappeared west of 100°W from 6°N to 5°S, with maxima of ~25 cm s^{-1} on the equator.

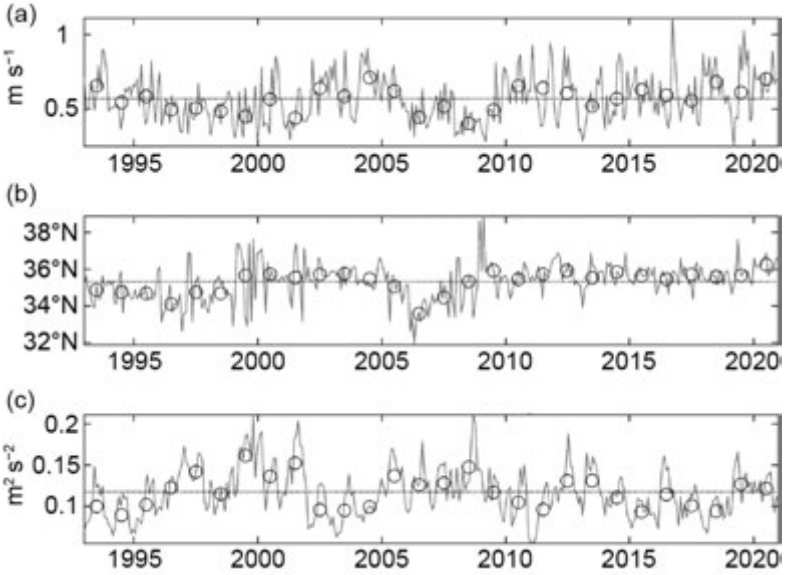

Fig. 3.20. (a) Maximum zonally averaged value of total geostrophic zonal velocity (U; m s^{-1}) versus time in the Kuroshio Extension region (141°–153°E, 32°–38°N; Qiu and Chen 2005). (b) Latitude (°N) of the maximum velocity shown in (a). (c) Eddy kintetic energy (EKE; m^2 s^{-2}) averaged in the Kuroshio Extension region. In all plots, monthly values are shown in gray, annual averages as black circles, and the time-mean is shown as a horizontal gray line.

In 2020, the global anomaly map (Fig. 3.18a) featured strong positive anomalies north of and strong negative anomalies south of the mean Kuroshio Extension location, indicating a shift to the north of 1.3° latitude (from 35.3°N to 36.6°N; Figs. 3.20a,b), the most northern annually-averaged location since 1993 (the start of satellite altimeter records). Long-term shifts in the location of the Kuroshio Extension are associated with a decadal stable/unstable oscillation (Qiu and Chen 2005). The Kuroshio Extension shifts to the north when it intensifies and becomes stable thus lowering eddy kinetic energy (EKE). Averaged in the downstream Kuroshio Extension region (141°–153°E, 32°–38°N; Qiu and Chen 2005), EKE was low in 1993–95, elevated in 1999–2001, low in 2002–04, high in 2005–08, and low in 2015–18 (Fig. 3.20c). EKE was close to its long-term average during 2019 and 2020. As noted in the *State of the Climate in 2019* report, the northern location of the Kuroshio Extension and near-climatological levels of EKE are so far inconsistent with a phase shift of the decadal mode described by Qiu and Chen (2005).

2) Indian Ocean

Annually-averaged zonal currents in the Indian Ocean exhibited 10–20 cm s^{-1} eastward anomalies at 6°S–2°N, 70°–95°E and, in the same longitude range, westward anomalies of 10–15 cm s^{-1} at 8°–14°S (Fig. 3.18a). The eastward anomalies are consistent with strong La Niña conditions and a southward migration of the South Equatorial Current (SEC; Lumpkin and Johnson 2013), while the westward anomalies indicate a strengthening of the SEC in that latitude band. Differences from 2019 (Fig. 3.18b) reflect the strong westward anomalies at 55°–95°E, 2°S–1°N seen in 2019 (and hence are positive anomalies in the 2020 minus 2019 difference map). The 2020 eastward anomalies indicate an acceleration of the seasonally varying eastward Wyrtki Jet, which climatologically is most prominent in May and November (e.g., Nagura and McPhaden 2010). These anomalies developed in JJA after the westward La Niña-related Pacific anomalies were established (Fig. 3.19c), when the Wyrtki Jet typically weakens to a weakly reversed state (Lumpkin and Johnson 2013). They persisted through SON (Fig. 3.19d) consistent with La Niña conditions (Lumpkin and Johnson 2013).

3) Atlantic Ocean

Annual mean zonal currents in the tropical Atlantic Ocean in 2020 exhibited a similar pattern to those in the Pacific, but zonal velocity anomalies were much weaker (Fig. 3.18a). Averaged across the basin, eastward anomalies of 3–4 cm s^{-1} at 6°–7°N indicate a slightly accelerated and northward-shifted NECC, while westward anomalies of 3–5 cm s^{-1} from the equator to 4°N indicate an acceleration of the westward northern core of the SEC. These westward anomalies rapidly developed in March–May (Fig. 3.19b) to maxima of ~10 cm s^{-1}, weakened through JJA (Fig. 3.19c), and were gone by SON (Fig. 3.19d).

The variability of key Atlantic Ocean currents is continuously monitored in near-real time by leveraging relationships between in situ and satellite altimetry observations (https://www.aoml.noaa.gov/phod/indexes/index.php). In the South Atlantic, the Agulhas Current shed five rings, within the 1993–2020 average of four to six rings in a given year. The annual transport of the Agulhas Current was slightly below the average by –1.4 Sv in a cross section at ~28°E and between 34°S and 40°S. In the southwestern Atlantic, the Brazil–Malvinas Confluence was for the fourth consecutive year displaced to the south with respect to its mean location during 1993–2020. Since 1993, the Brazil–Malvinas Confluence has shifted southward at decadal time scales (cf., Lumpkin and Garzoli 2011; Goni et al. 2011). During 2020, the confluence was on average 0.5 degrees of latitude south of its 1993–2019 mean location, and over 1.5 degrees of latitude south of its average location in the early 1990s. This is important because the Brazil Current is the mechanism by which waters of subtropical origin are transported into subpolar regions.

In the North Atlantic, the 2020 volume transports of the North Brazil Current, Yucatan Current, and Florida Current (FC) were all below their 1993–2020 averages. The North Brazil Current serves as an interhemispheric conduit for water masses and heat from the South Atlantic into the North Atlantic. It also often sheds rings (Goni and Johns 2003) that can enter the Caribbean Sea while carrying low-salinity Amazon River waters (Ffield 2007), which are known for creating barrier layer conditions that can often contribute to hurricane intensification (e.g., Balaguru et al. 2012; Domingues et al. 2015). The North Brazil Current exhibited a mean negative transport anomaly of –1.4 Sv in 2020, which is within the lowest 25th percentile in terms of its annual mean transport, with anomalies as low as –5 Sv observed mostly during the first half of 2020. Farther to the north, the Yucatan Current and FC exhibited mean negative anomalies of –0.3 Sv and –0.7 Sv, respectively, with positive anomalies reaching ~2 Sv in the first half of 2020 and negative anomalies as low as –4 Sv during the second half of the year. Interestingly, the negative anomalies observed in the North Brazil Current during the first quarter of 2020 are of similar magnitude to the negative anomalies observed both in the Yucatan Current and FC in the latter half of the year. Because these currents are a critical part of the Atlantic meridional overturning circulation's surface pathway (section 3h), negative transport anomalies first seen in the North Brazil Current may have subsequently propagated westward through the Caribbean Sea, were then transported into the Gulf of Mexico by the Yucatan Current, and then into the Florida Straits by the FC in the latter half of 2020. A lower-than-usual FC transport is closely tied to higher coastal sea level and "sunny day" flooding events along the southeast U.S. coast (Ezer and Atkinson 2014; Domingues et al. 2016; Volkov et al. 2020a) , which may partly explain the 2020 increased number of high-tide flooding days in the Gulf of Mexico and southeast U.S. (Fig. 3.16b). Further studies addressing the delayed North Brazil Current to FC connection may help develop early warnings for such flooding events.

h. Meridional overturning circulation and heat transport in the Atlantic Ocean—D. L. Volkov, S. Dong, M. Lankhorst, M. Kersalé, A. Sanchez-Franks, C. Schmid, J. Herrford, R. C. Perez, B. I. Moat, P. Brandt, C. S. Meinen, M. O. Baringer, E. Frajka-Williams, and D. A. Smeed

The zonally integrated component of surface and deep currents, known as the meridional overturning circulation (MOC), plays an important role in Earth's climate because it provides a mechanism for ocean meridional heat transport (MHT). The observing system for the Atlantic MOC/MHT consists of several basin-wide moored arrays as well as the combination of satellite altimetry and in situ (mainly Argo and eXpendable BathyThermograph [XBT]) measurements (Fig. 3.21a; e.g., Frajka-Williams et al. 2019). The currently active basin-wide moored arrays are the Rapid Climate Change/MOC and Heatflux Array/Western Boundary Time Series (RAPID/MOCHA/WBTS) array at 26.5°N (Moat et al. 2020a), the South Atlantic MOC Basin-wide Array (SAMBA) at 34.5°S (Meinen et al. 2013, 2018), the Overturning in the Subpolar North Atlantic Program (OSNAP) array between about 55° and 60°N (Lozier et al. 2017, 2019), and the Tropical Atlantic Circulation and Overturning array at 11°S (TRACOS; Herrford et al. 2021).

The *State of the Climate in 2019* report included MOC/MHT estimates derived from mooring measurements up to 2018 (Volkov et al. 2020b). The COVID-19 pandemic negatively impacted the servicing of moorings, because most research cruises scheduled in 2020 were either postponed or canceled. Therefore, no updates are available as of this writing for the basin-wide arrays in the North Atlantic (Figs. 3.21b,c). In this report, however, we present novel MOC upper- and lower- ("abyssal") cell transport estimates from the extended number of SAMBA moorings (Fig. 3.21e; Kersalé et al. 2020) and new results for the TRACOS array (Fig. 3.21d; Herrford et al. 2021). Then we discuss the state of the Florida Current (FC) at 27°N (Fig. 3.22a) and provide the new estimates of the North Atlantic Current (NAC) volume transport (Fig. 3.22b; Lankhorst and Send 2020), which

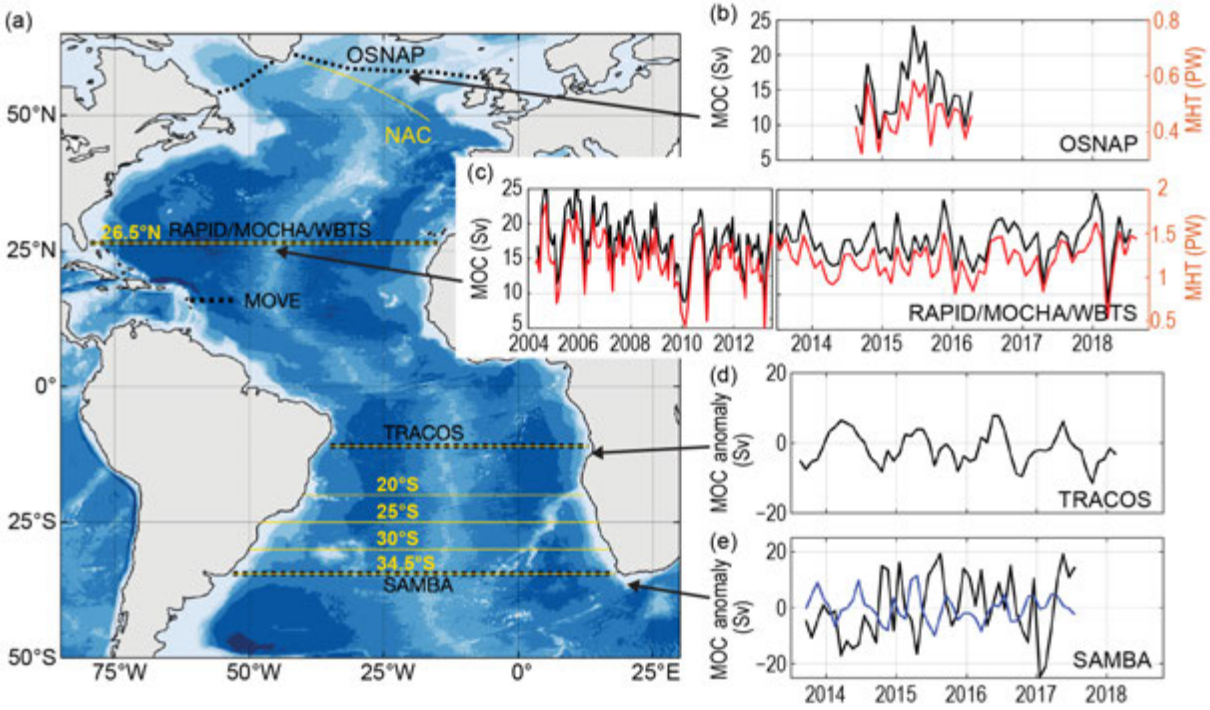

Fig. 3.21. (a) The Atlantic Ocean meridional overturning circulation (MOC) observing system: moored arrays (dashed black lines) and sections (yellow lines) across which the MOC is estimated by combining in situ measurements (Argo, XBT, bottom pressure) with satellite altimetry data. (b) Monthly time series of the MOC northward volume transport (black) and meridional heat transport (MHT; red) across the OSNAP array (Lozier et al. 2019). (c) Monthly time series of the MOC northward volume transport (black) and MHT (red) across the RAPID/MOCHA/WBTS array (Moat et al. 2020b). (d) Monthly time series of the MOC northward volume transport anomaly across the TRACOS array (Herrford et al. 2021). (e) Monthly time series of the MOC northward upper (black) and abyssal cell (blue) volume transport anomalies across the SAMBA (Kersalé et al. 2020). Units for (b)–(e) are given in Sv.

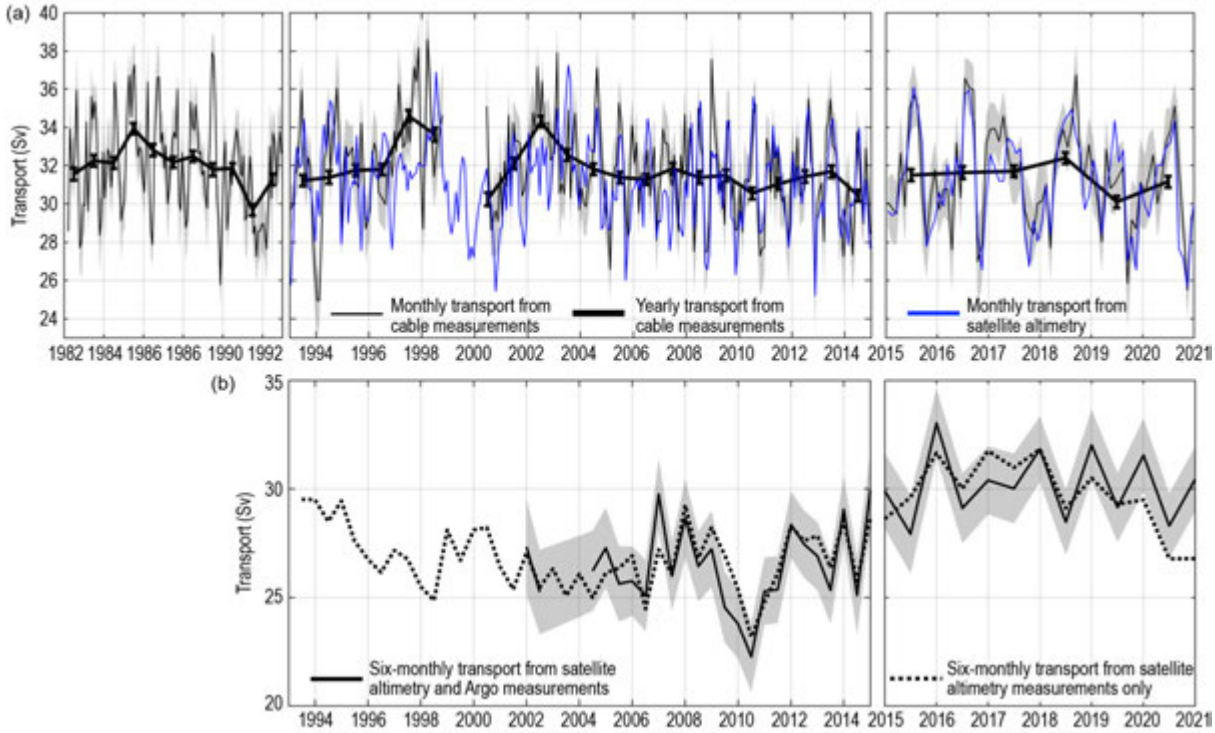

Fig. 3.22. (a) Monthly (thin black curve) and yearly (thick black curve) averages of the Florida Current (FC) volume transport (Sv) derived from the cable measurements at 27°N with associated uncertainties (gray shading and black error bars, respectively). Uncertainties include the measurement error and the standard error of the mean. Monthly averaged FC volume transport (Sv) derived from satellite altimetry (blue) following Volkov et al. (2020b). (b) Six-monthly North Atlantic Current (NAC) volume transport across the NAC section (see Fig. 3.21a for location) following Lankhorst and Send (2020): transport derived from satellite altimetry and Argo measurements (solid curve) with uncertainties (gray shading) and transport derived from satellite altimetry measurements only (dotted curve).

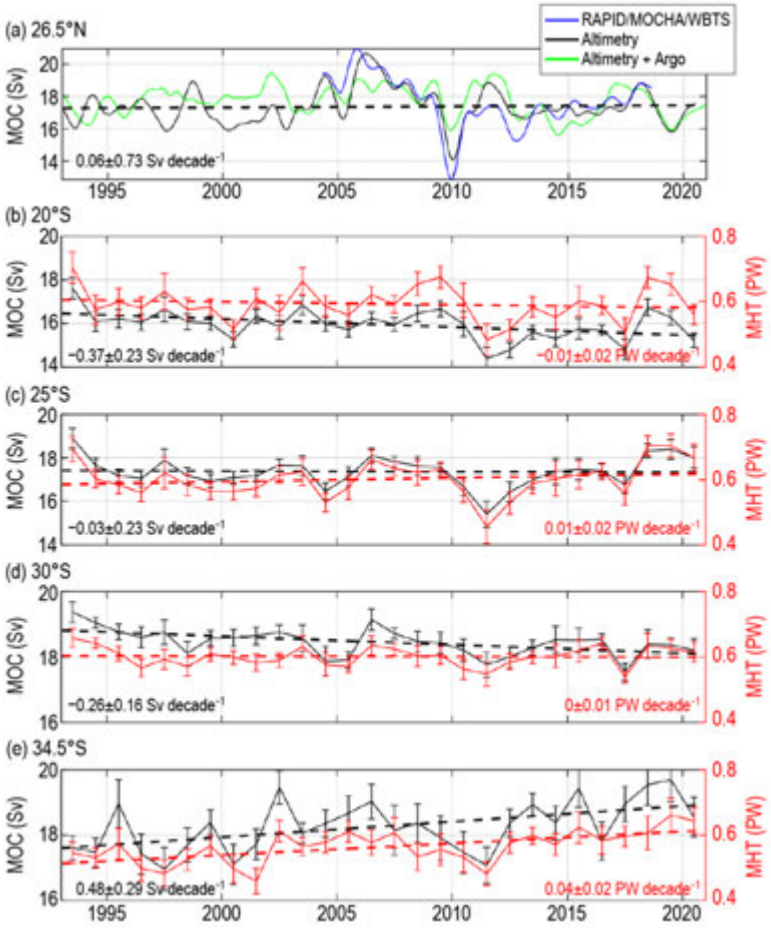

Fig. 3.23. Blended meridional overturning circulation (MOC) estimates (Sv) based on combinations of satellite altimetry and in situ hydrography data. (a) The MOC at 26.5°N derived from RAPID/MOCHA/WBTS observing array (blue), satellite altimetry (black), and satellite altimetry and Argo (green). (b–e) The yearly MOC Sv; (black) and meridional heat transport (MHT) (PW, red) averages at various latitudes in the South Atlantic. Error bars in (b)–(e) show standard errors of the yearly means. Dashed lines show linear trends over the observational period.

both constitute the bulk of the upper limb northward MOC transport in the subtropical and subpolar North Atlantic, respectively. Finally, we present updated MOC/MHT estimates derived from blended in situ and satellite observations at different locations through 2020 (Fig. 3.23).

The Atlantic MOC consists of an upper cell and an abyssal cell. Preliminary SAMBA efforts focused solely on the upper cell using two pressure-equipped inverted echo sounder (PIES) moorings at 1350-dbar isobath on either side of the basin (Meinen et al. 2013, 2018). Recently,

both the upper and abyssal cell volume transports at 35.5°S from September 2013 to July 2017 were obtained using nine PIES (Fig. 3.21e; Kersalé et al. 2020). Both the upper and abyssal cells exhibit a high degree of variability at time scales ranging from a few days to a few weeks. The upper-cell transport variability obtained from nine PIES is about twice as strong as the variability observed with only two PIES (std. devs. are 15.5 and 8.2 Sv, respectively), due to a better representation of barotropic flows and mesoscale eddies. The rather low (−0.4) correlation between the upper and abyssal cell daily transports suggests that transport variability in the abyssal cell is largely independent of the variations in the upper cell. Both cells exhibit positive, but statistically insignificant, transport trends.

TRACOS array data at 11°S were analyzed in Herrford et al. (2021). This array consists of a western boundary current transport array (Hummels et al. 2015), an eastern boundary current meter mooring (Kopte et al. 2017), and two sets of pressure gauges deployed at 300-m and 500-m depth across the Brazilian continental slope and at the eastern boundary off Angola. The MOC transport estimate is based on the combination of bottom pressure measurements with satellite altimetry and wind stress data, and covers 2013–18 (Fig. 3.21d). Given the limitations of instruments and the shortness of time series, only the seasonal variability of the MOC at 11°S was investigated. The seasonal peak-to-peak amplitude of the MOC transport is 14 Sv, which is contributed by the upper-ocean geostrophic and Ekman transport fluctuations with peak-to-peak amplitudes of 12 Sv and 7 Sv, respectively. The seasonal variability of the geostrophic contribution to the MOC at 11°S is mainly modulated by oceanic adjustment to local and remote wind forcing.

The oldest MOC trans-basin array at 26.5°N (RAPID/MOCHA/WBTS) consists of tall moorings between the Bahamas and Africa and measurements of the FC volume transport with a submarine cable. Although the COVID-19 pandemic made it impossible to retrieve the mooring data and update the MOC estimates in 2020, cable measurements of the FC (Fig. 3.22a) were not affected. In 2020, the annual mean FC transport (31.2 ± 0.3 Sv) was stronger than in 2019 (30.1 ± 0.3 Sv), and close to the record mean transport (31.8 ± 0.2 Sv). The FC transport has been rather stable over the entire observational record, exhibiting only a small, statistically insignificant, negative trend (−0.03 ± 0.03 Sv yr^{-1}). Given the extremely high value of the FC measurements for monitoring the Atlantic MOC at 26.5°N, backup observing systems have been investigated in case the cable someday becomes inoperable. Transports estimated from bottom pressure measurements (8 July 2008–17 September 2014) on both sides of the Straits of Florida at 27°N explain roughly 55% of the daily cable transport variability (Meinen et al. 2020). Similarly, FC transports derived from cross-stream sea level differences measured by satellite altimetry (blue curve in Fig. 3.22a) account for up to 60% of the cable transport subsampled at the days of satellite overpasses (Volkov et al. 2020a). Although pressure gauges provide unrivaled temporal resolution, satellite altimetry yields a longer homogeneous data record (back to 1993) filling in the existing gaps in cable data (e.g., 1998–2000).

While no updates are available for the OSNAP array in the subpolar North Atlantic since the past year's report (Fig. 3.21b), an estimate of the NAC volume transport across a section between the central Irminger Sea and the Porcupine Abyssal Plain (NAC section in Fig. 3.21a) was computed from in situ density profiles and satellite altimetry sea level anomalies (Lankhorst and Send 2020). Similar to the FC in the subtropical gyre, the NAC is an important contributor to the upper-ocean MOC transport in the subpolar gyre. The six-monthly NAC transport estimates (Fig. 3.22b) suggest that there is a likely multi-decadal oscillation exhibiting high values in the early 1990s, lower values throughout the 2000s, and higher transports again in recent years (2015–20). Values in recent years are below the recent maximum and may indicate the beginning of a downward tendency.

The only basin-integrated transports that were updated through 2020 are the blended estimates derived from the combination of satellite altimetry and in situ hydrography (XBT, Argo, etc.; Sanchez-Franks et al. 2021; McCarthy et al. 2020; Majumder et al. 2016; Dong et al. 2015). An MOC time series at 26.5°N, generated from the combination of altimetry and Argo data using the

method of Majumder et al. (2016), has been updated through 2020 (McCarthy et al. 2020; green curve in Fig. 3.23a). Another dynamically based method was recently developed for estimating the MOC at 26.5°N using satellite altimetry, in situ density profiles, and the ERA5 zonal wind stress (Sanchez-Franks et al. 2021). This latter MOC estimate (black curve in Fig. 3.23a) captures 69% of the interannual MOC variability observed by the RAPID/MOCHA/WBTS array (blue curve in Fig. 3.23a). The two satellite-based estimates reasonably agree only after the advent of Argo data in 2004, which indicates sensitivity to the amount of in situ data available for calibration and methodology used to derive them. Both estimates suggest that the MOC in 2020 was 1–2 Sv stronger than in 2019, but weaker than in 2018. It is too early to draw conclusions about the longer MOC tendencies, in particular in relation to a possible MOC strengthening since 2010 reported in Moat et al. (2020a).

Yearly blended MOC/MHT estimates at 20°S, 25°S, 30°S, and 34.5°S (Figs. 3.23b–e) obtained following Dong et al. (2015) estimate that in 2020, the MOC and MHT were somewhat lower than in 2019 at all latitudes. However, this change was statistically significant only at 34.5°S and 20°S for the MOC and at 20°S for the MHT. Significant positive trends in both the MOC and MHT over the entire observational period are observed at 34.5°S (0.48 ± 0.29 Sv decade^{-1} and 0.04 ± 0.02 PW decade^{-1}, respectively). Significant negative trends in the MOC are observed at 30°S (−0.26 ± 0.16 Sv decade^{-1}) and 20°S (−0.37 ± 0.23 Sv decade^{-1}), with no significant trends in the MHT at other latitudes. These trends suggest that there has been a strengthening of the South Atlantic subtropical gyre and associated heat convergence in 1993–2020, consistent with the warming trend observed in the region (e.g., Dong et al. 2020; Fasullo and Gent 2017; Fig. 3.4c).

Comparisons of the various blended satellite/in situ MOC estimates among each other and the results from moored arrays (at 26.5°N and 34.5°S) usually yield low correlations and different variances (not shown), suggesting that the estimates are sensitive to the methodology used to derive them. In addition, differences between the MOC estimates from the pilot (two PIES) and extended (nine PIES) SAMBA moorings suggest sensitivity to the design of the observing array. To better determine the state of the MOC and understand its variability, it is necessary to reconcile different estimates and investigate the sources of uncertainties.

i. Global ocean phytoplankton—B. A. Franz, I. Cetinić, J.P. Scott, D. A. Siegel, and T.K. Westberry

Photosynthetic production of carbon by marine phytoplankton fuels oceanic ecosystems and drives biogeochemical cycles (e.g., Falkowski et al. 1998; Field et al. 1998), contributing roughly 50% of global net primary production (NPP). Phytoplankton distribution, growth, and diversity are governed by the availability of light and nutrients (e.g., nitrogen, phosphorous, and iron) in the upper ocean euphotic zone, which in turn are influenced by physical factors such as ocean temperature and circulation processes (e.g., Behrenfeld et al. 2006). Satellite ocean color sensors such as Sea-viewing Wide Field-of-view-Sensor (SeaWiFS; McClain 2009) and Moderate Resolution Imaging Spectroradiometer (MODIS; Esaias et al. 1998) allow detection of spatial and temporal changes in the distribution of phytoplankton through measurements of near-surface concentrations of the phytoplankton pigment chlorophyll-*a* (Chl*a*; mg m^{-3}) or phytoplankton carbon (C_{phy}, mg m^{-3}). While C_{phy} is a direct measure of phytoplankton biomass, Chl*a* is an indicator of variability in both biomass and phytoplankton physiology. Discrepancies between their distributions (shifts in Chl*a*:C_{phy} ratios) thus provide valuable insight into physiological variability within the cells (due to the changes in light and nutrient conditions) or variability in species composition (Westberry et al. 2016; Siegel et al. 2013; Dierssen 2010; Geider et al. 1997). Taken together, these measurements provide a synoptic view of phytoplankton biomass, composition, and health in the ocean, as well as its response to climate-driven changes in the marine environment.

Here we evaluate global Chl*a* and C_{phy} distributions for the one-year period from October 2019 through September 2020 (the analysis year), within the context of the continuous 23-year record provided through the combined observations of SeaWiFS (1997–2010) and MODIS on *Aqua*

(MODIS-A, 2002–present). The MODIS-A daytime sea surface temperature (SST; °C) is also assessed for the same time period to provide context on the physical state of the oceans. The Chl*a* product was derived using the Ocean Color Index algorithm of Hu et al. (2012), while C_{phy} was derived from the particle backscattering coefficient, b_{bp}, at 443 nm (Generalized Inherent Optical Properties algorithm; Werdell et al. 2013) and a linear relationship between b_{bp} and C_{phy} as described in Graff et al. (2015). In combining the ocean color records, the overlapping period from 2003 through 2010 was used to assess and correct for residual bias between the two mission datasets.

Changes in phytoplankton distribution were evaluated by subtracting monthly climatological means for MODIS-A (October 2002–September 2019) from their monthly mean values for MODIS-A Chl*a* and C_{phy} in the analysis year. These monthly anomalies were then averaged to produce the global Chl*a* and C_{phy} annual mean anomaly maps (Figs. 3.24a,b). Similar calculations were performed on MODIS-A SST data to produce an equivalent SST annual mean anomaly for the same time period (Fig. 3.24c). The permanently stratified ocean (PSO) is defined as the region, spanning the tropical and subtropical oceans, where annual average SST is greater than 15°C and surface mixed layers are typically low in nutrients and shallower than the nutricline (black lines near 40°N and 40°S in Fig. 3.24; Behrenfeld et al. 2006).

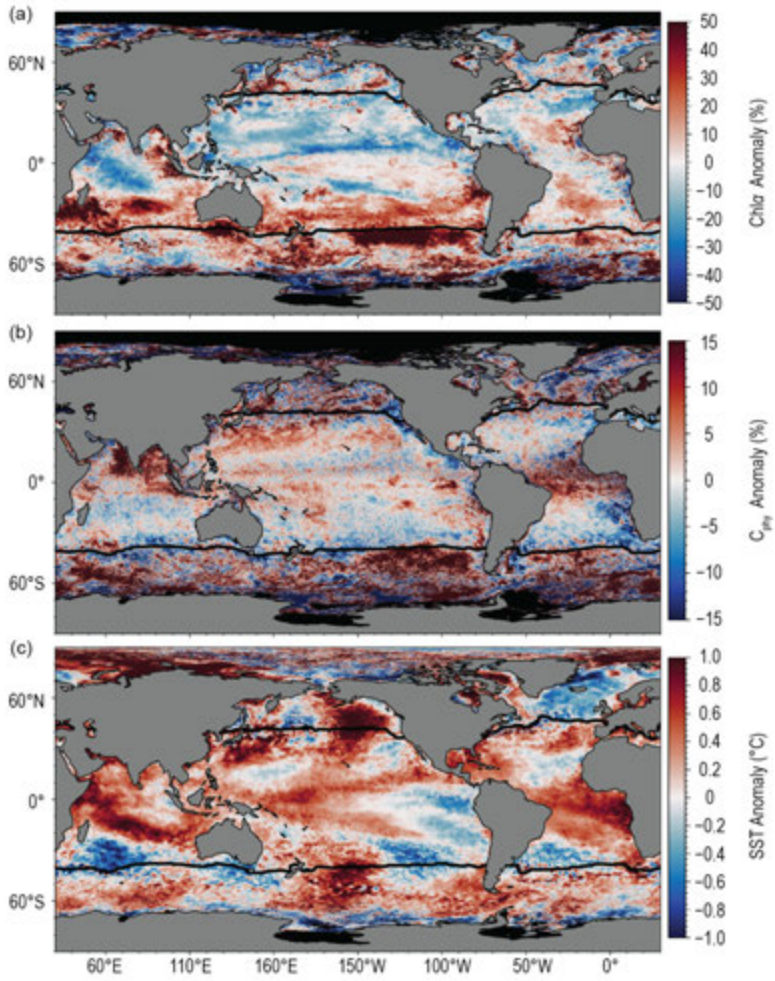

Fig. 3.24. Spatial distribution of average monthly (a) MODIS-A Chl*a* anomalies, (b) MODIS-A C_{phy} anomalies, and (c) MODIS-A SST anomalies, where monthly differences were derived relative to a MODIS-A 17-year climatological record (Oct 2002–Sep 2019). Chl*a* and C_{phy} are stated as % difference from climatology, while SST is shown as an absolute difference. Also shown in each panel is the location of the mean 15°C SST isotherm (black lines) delineating the permanently stratified ocean (PSO). Differences in the SST anomalies here versus in Fig. 3.1a are owing to differences in climatological periods, smoothing, and data sources.

A striking feature of the phytoplankton Chl*a* anomaly distributions for this year is a strong hemispherical difference, with elevated concentrations in the south and depressed concentrations in the north, and with C_{phy} distributions showing a weaker but inverse hemispherical difference (Figs. 3.24a,b). Within the PSO, Chl*a* concentrations (Fig. 3.24a) were consistently elevated 20%–40% throughout much of the subtropical Southern Hemisphere (SH), with the largest positive anomalies in the southern Indian Ocean followed by the subtropical South Pacific and South Atlantic. These regions were generally characterized by anomalously cold water conditions, characteristic of the La Niña phase of the El Niño-Southern Oscillation ([ENSO] with SST depressed −0.6° to −0.8°C; Fig. 3.24c). Negative SST anomalies in these stratified ocean regions typically correspond with a deepening of the surface mixed layer (Deser et al. 2010), which decreases the effective light exposure per unit of phytoplankton biomass within that mixed layer. The response of the phytoplankton to this decreased insolation is to increase cellular chlorophyll concentration and thus light-use efficiency (Behrenfeld et al. 2015). In combination with the physiological response to low-nutrient conditions in the PSO, this leads to increased cellular chlorophyll-to-carbon ratios (Westberry et al. 2016) and thus a decoupling of the Chl*a* and C_{phy} anomalies. The C_{phy}

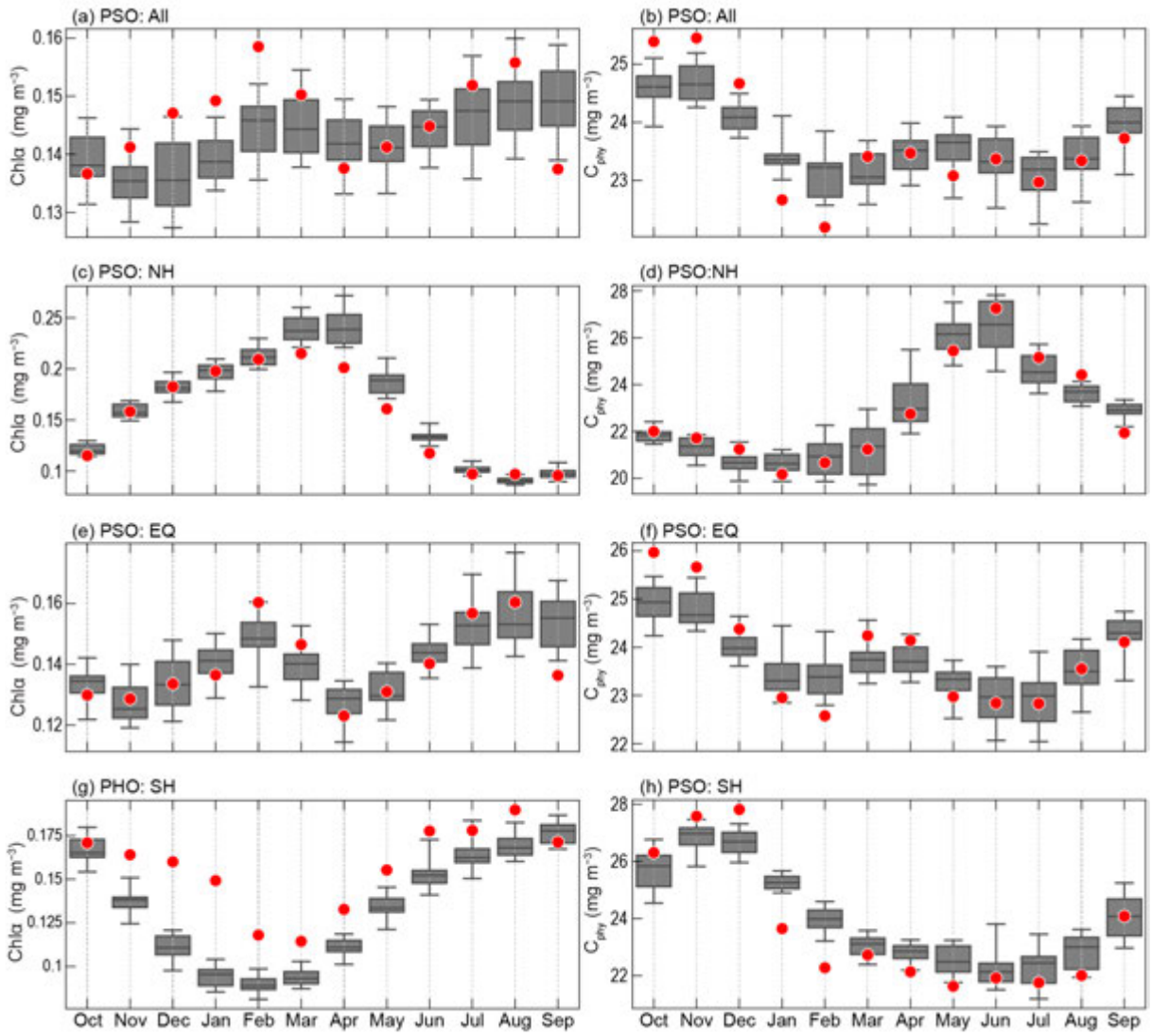

Fig. 3.25. Distribution of Oct 2019–Sep 2020 monthly means (red circles) for (a) MODIS-A Chl*a* and (b) MODIS-A C_{phy} for the PSO region, superimposed on the climatological values as derived from the combined time series of SeaWiFS and MODIS-A over the 22-year period 1998–2019. Gray boxes show the interquartile range of the climatology, with a black line for the median value and whiskers extending to the 5th and 95th percentiles. Subsequent panels show latitudinally segregated subsets of the PSO for the (c),(d), Northern Hemisphere, (e),(f), tropical ±23.5° latitude subregion, EQ, and (g),(h), Southern Hemisphere.

anomalies (Fig. 3.24b) show a reduction in phytoplankton biomass of 5%–10% in these elevated Chl*a* (Fig. 3.24a) regions of the subtropical southern PSO, supporting this hypothesis. A weaker but opposite change in Chl*a* and C_{phy} is observed in the subtropical North Pacific PSO region, with Chl*a* generally depressed (0%–10%) and C_{phy} concentrations neutral to elevated (0%–5%) within anomalously warmer ocean waters (Fig. 3.24c; Sidebar 3.1). Large increases in C_{phy} were also observed in the Arabian Sea and Bay of Bengal, as well as the tropical Atlantic. In the tropical Pacific, both Chl*a* and C_{phy} were weakly elevated, consistent with a transition to La Niña conditions. Outside the PSO, phytoplankton anomalies (Figs. 3.24a,b) showed larger spatial variability and patchiness, including some large patches of highly elevated (>50%) phytoplankton biomass anomalies in the Southern Ocean, but with Chl*a* and C_{phy} generally covarying in these well-mixed waters, consistent with previous studies (e.g., Franz et al. 2020). The higher spatial variability typically observed poleward of the PSO is indicative of the episodic and intense nature of phytoplankton blooms in these regions, but the relatively poor sampling at high latitudes due to clouds and polar night also contributes to higher noise in the ocean color signal, thus limiting confidence in the interpretation of interannual changes.

Seasonal changes in phytoplankton biomass in the PSO typically display two pronounced peaks, reflecting vernal increases in biomass in the Northern Hemisphere (NH) and SH (Fig. 3.25). Peaks in monthly climatological C_{phy} tend to lag peaks in Chl*a* by roughly two to three months, reflecting a reduction in phytoplankton chlorophyll-to-carbon ratios as the seasonal bloom progresses (e.g., Westberry et al. 2016). During 2020, the NH peak in Chl*a* (Fig. 3.25c) occurred in March, followed by C_{phy} maximum in June (Fig. 3.25d), consistent with previous observations (Franz et al. 2020). Generally, monthly mean values of Chl*a* and C_{phy} fell within the range of climatological norms, with the exception of depressed Chl*a* concentrations observed during March–June. In the SH, however, Chl*a* concentrations were well above the climatological norms for much of the analysis period, with a delayed transition from the austral spring peak in October (2019) to the autumn minimum in March, while a weaker but inverse deviation from the climatology was observed in the C_{phy} seasonal cycle. These SH seasonal trend deviations from the climatology are consistent with the

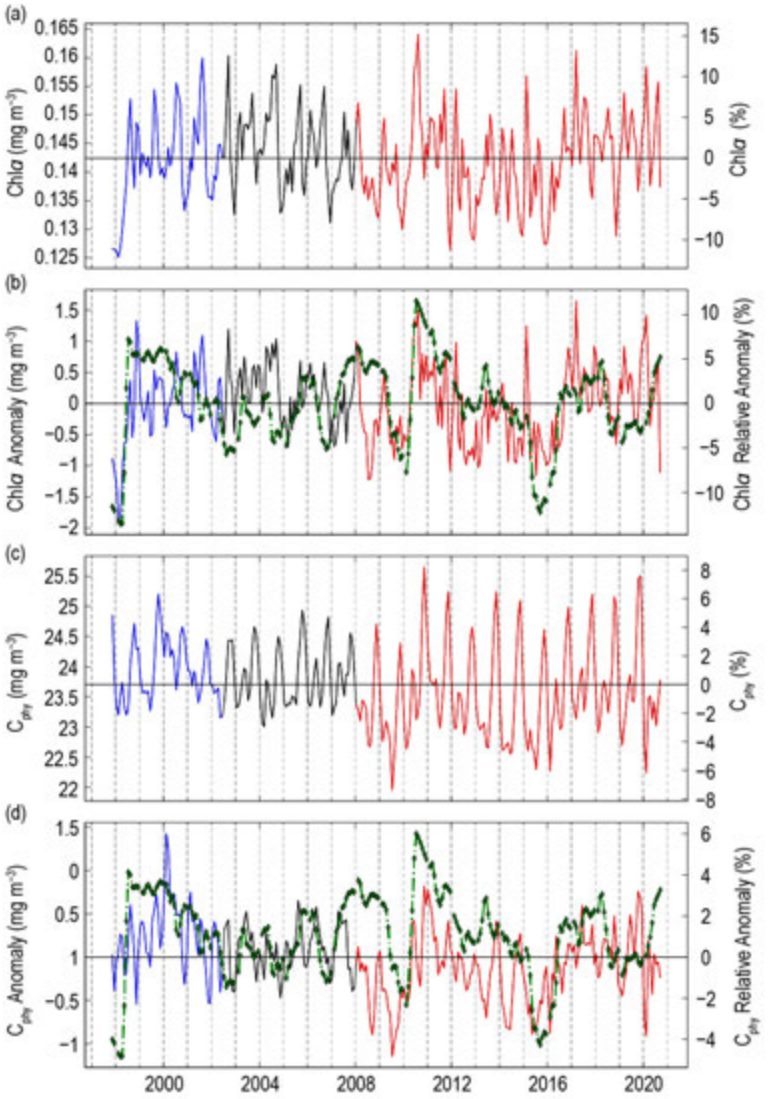

Fig. 3.26. 23-year, multi-mission record of Chl*a* (mg m^{-3}) and C_{phy} (%) averaged over the PSO for SeaWiFS (blue), MODIS-A (red), and combined (black). (a) Chl*a* from each mission, with the horizontal line indicating the multi-mission mean Chl*a* concentration for the region. (b) Monthly Chl*a* anomalies from SeaWiFS and MODIS-A after subtraction of the 22-year multi-mission climatological mean (Fig. 3.25). (c),(d) Same as (a),(b), respectively, but for C_{phy}. Green diamonds show the Multivariate ENSO Index, inverted and scaled to match the range of the Chl*a* and C_{phy} anomalies.

mean anomalies observed in Fig. 3.24, and provide additional context for the progression of the anomaly through the year.

Over the 23-year time series of spatially integrated monthly mean Chl*a* within the PSO (Fig. 3.26a), concentrations vary by ~15% (±0.02 mg m^{-3}) around a long-term average of 0.142 mg m^{-3} (Fig. 3.26a). This variability includes significant seasonal cycles in Chl*a* distributions and responses to climatic events, as has been observed previously (e.g., Behrenfeld et al. 2006; Franz et al. 2020). C_{phy} over the same 23-year period varies by ~7% (±1.5 mg m^{-3}) around an average of 23.7 mg m^{-3} (Fig. 3.26c). Seasonal cycles in C_{phy} are more clearly defined than those of Chl*a*, consistent with the assertion that C_{phy} better represents variability of phytoplankton biomass, independent of the confounding influence of physiology.

Chl*a* monthly anomalies within the PSO (Fig. 3.26b) vary by ±10% (±0.015 mg m^{-3}) over the multi-mission time series, with the largest deviations generally associated with ENSO events, as demonstrated by the correspondence of Chl*a* anomaly variations with the Multivariate ENSO Index (MEI; Wolter and Timlin 1998; presented in the inverse to illustrate the covariation). Pearson correlation coefficients between MEI and the Chl*a* and C_{phy} monthly anomalies calculated for the 23-year record were 0.36 and 0.30, respectively. Over the last year, variability in monthly Chl*a* anomalies was modest (–2% to +10%) and generally elevated, consistent with weak La Niña conditions (Fig. 3.26b). Similar observations cannot be made of the C_{phy} anomalies, which were more constrained than the Chl*a* anomalies and generally do not follow the MEI over the last year (Fig. 3.26d). Our findings suggest that the effect of the 2020 La Niña on phytoplankton populations within the PSO was generally to increase Chl*a*:C_{phy} ratios while leaving phytoplankton biomass largely unchanged.

Observed trends and variability in C_{phy} reflect changes in phytoplankton biomass, while Chl*a* variability can indicate changes in biomass, physiology, and community composition (e.g., Dierssen 2010). These properties are mechanistically linked to physical conditions of the upper ocean, as well as to ecological interactions between phytoplankton and their zooplankton predators. Our ability to track subtle variations in the distribution of Chl*a* and C_{phy} on the global scale can help unravel the diversity and covariation of climate-driven changes in phytoplankton distributions. Future satellite missions, such as the upcoming hyperspectral Plankton, Aerosol, Cloud, ocean Ecosystem (PACE) mission, will enable a more precise identification of phytoplankton absorption features (Werdell et al. 2019) and separation of those features from non-algal optical contributions (Siegel et al. 2005), and thereby facilitate the assessment of changes in phytoplankton species or community composition. Such data will further advance our ability to disentangle the impacts of climate forcing on global phytoplankton communities that drive biogeochemical processes, govern the role of the oceans in the global carbon cycle, and through their productivity exert a controlling influence on marine ecosystems, food webs, and fisheries.

Sidebar 3.2: **Ocean acidification status in Pacific Ocean surface seawater in 2020**—S. R. ALIN, A. U. COLLINS, B. R. CARTER, AND R. A. FEELY

While the Pacific Ocean north of ~20°S has the lowest column inventory of anthropogenic carbon dioxide (CO_2) outside of the Southern Ocean (Gruber et al. 2019), background dissolved inorganic carbon content is high as a result of respiration that occurs in the ocean's interior and old "ages" of deep Pacific waters. Consequently, the northern Pacific Ocean, where deep water resurfaces, has naturally steep vertical gradients in buffering capacity (Egleston et al. 2010; Jiang et al. 2019), CO_2 fugacity (fCO_2; see section 3j), pH—a measure of acidity (Jiang et al. 2019), and calcium carbonate saturation states (Jiang et al. 2015) with many Pacific marine ecosystems vulnerable to ocean acidification impacts (Christian and Ono 2019). In combination with projected deoxygenation, sea surface temperature (SST) change, and a recent propensity for strong, lasting, large-scale marine heatwaves (Bopp et al. 2013; Sidebar 3.1), ocean acidification in the northern Pacific Ocean poses an accelerating threat to marine species and ecosystems that underpin economically important industries from fishing to tourism.

Underway CO_2 observations collected by M/V *Bluefin* provide a synoptic look at carbonate chemistry and pH status in surface waters of the Pacific Ocean north of 15°S during 2020 (Alin et al. 2021). Here we combined the underway fCO_2, temperature, and salinity measurements with total alkalinity estimates generated using the locally interpolated alkalinity regression (LIARv2) method to calculate pH on the total scale (pH_{total}) using CO_2SYS (Carter et al. 2018; van Heuven et al. 2011), creating a 2020 snapshot of ocean acidification status in Pacific surface waters (Fig. SB3.2b). We compared calculated values with published climatological average fCO_2 and pH_{total} values to 2020 observations to determine how 2020 acidification conditions around the Pacific compared to climatological conditions and variability typical of each region.

Because it is an upwelling system, the California Current System (CCS) has high spatial variability in biogeochemical parameters. The Strait of Juan de Fuca (SJDF) is a major source of freshwater to the northern CCS. Winter, spring, and autumn 2020 observations in CCS and SJDF regions revealed average surface fCO_2 values in the CCS below atmospheric values, with relatively high variability, and SJDF fCO_2 averages and variability both higher than in the CCS due to strong mixing of the water column (Feely et al. 2010). Average winter SJDF fCO_2 and pH_{total} values were higher and lower, respectively, than climatological averages but just within seasonal amplitudes for the region; spring observations agreed with climatological averages for both parameters; and autumn average values were substantially

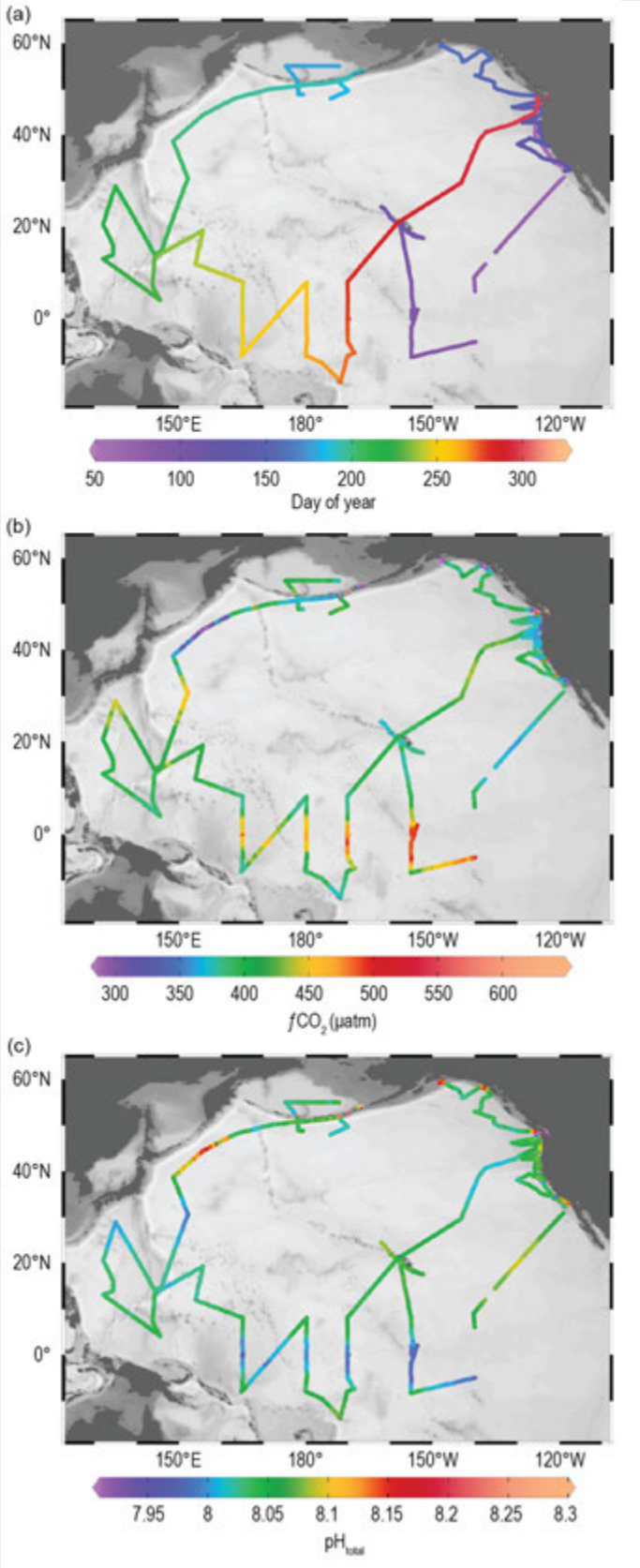

Fig. SB3.2. Pacific Ocean maps for 2020 of (a) day of year, (b) CO_2 fugacity (fCO_2, µatm), and (c) pH_{total}.

higher for fCO_2 and lower for pH_{total} than monthly averages (Fassbender et al. 2018). Seasonal CCS observations for fCO_2 and pH_{total} variability fell within historical bounds as calculated by Fassbender et al. (2018) and Sutton et al. (2019). Most of the highest highs and lowest lows in this 2020 dataset occurred in the CCS or SJDF.

In the subarctic waters (>48°N) of the Gulf of Alaska and south of the Aleutian Archipelago (to 165°E), summer 2020 observations showed moderate to high variability in carbonate chemistry, with average fCO_2 values below atmospheric levels and average pH_{total} values >8.0. Outside of the CCS and SJDF, the lowest and highest fCO_2 and pH_{total} values were recorded near the Aleutians, which reflect strong physical mixing of the water column and resulting biological productivity as water masses pass from the North Pacific into the Bering Sea. Regional average values of fCO_2 and pH_{total} were on the high and low ends, respectively, of published climatological values for summer (Takahashi et al. 2014; Jiang et al. 2019; Sutton et al. 2019).

During mid-summer, the Oyashio Current was a region of strong undersaturation of CO_2 relative to the atmosphere, with the lowest average fCO_2 and highest average pH_{total} values during this synoptic 2020 survey. However, these values were relatively high for fCO_2 and low for pH_{total} compared to climatological values for this region, which is known for strong primary production (Jiang et al. 2019; Midorikawa et al. 2010; Ono et al. 2019), suggesting that the positive 2020 SST anomalies of the northwestern Pacific (cf. Figs. 3.2 and SB3.1) may have resulted in either earlier phytoplankton bloom timing than normal and/or an increase of fCO_2 driven by thermodynamics. The reduced drawdown during these mid-summer observations is consistent with the slightly reduced air–sea CO_2 flux anomaly for 2020 relative to 2019 in this region (cf. Fig. 3.28b).

In the western tropical–subtropical Pacific, relatively low variability in fCO_2 and pH_{total} values were typical of the region, with average values above and below annual climatological values, respectively (Jiang et al. 2019). However, on central equatorial Pacific transects (10°S–10°N, 165°E–140°W), steep meridional gradients in surface carbonate chemistry due to equatorial upwelling resulted in moderately high variability in both fCO_2 and pH_{total}. Peak fCO_2 and minimum pH_{total} were centered near or just south of the equator on each transect. The equatorial upwelling of high-CO_2, low-pH water during La Niña conditions that developed late in 2020 extended farther westward than normal (see section 4b).

In the oligotrophic subtropical North Pacific Gyre (NPG), the lowest fCO_2 and pH variability was recorded during all 2020 cruises. Waters surrounding Hawaii (10°–30°N) and in the northeastern subtropical to temperate Pacific had fCO_2 cruise averages mostly below or near atmospheric values, and pH_{total} averages >8.0. While spring NPG fCO_2 and pH_{total} were within range of climatological values, autumn values of fCO_2 and pH_{total} were somewhat elevated and depressed, respectively, relative to climatological values, likely also reflecting the late 2020 onset of La Niña conditions (Takahashi et al. 2014; Jiang et al. 2019; Sutton et al. 2019).

Overall, 2020 fCO_2 and pH_{total} observations around the northern Pacific Ocean were consistent with historical observations in showing the highest variability and averages in northeastern Pacific ecosystems, followed by the central and eastern equatorial Pacific, and the lowest variability and moderate averages in the western Pacific low latitudes and the subtropical NPG. These differences in mean conditions and variability largely reflect the buffering effects of higher alkalinity in the southwestern Pacific compared to the northeastern North Pacific. Moderately anomalous ocean acidification conditions associated with SST anomalies and La Niña conditions were observed during the second half of 2020.

j. Global ocean carbon cycle—R. A. Feely, R. Wanninkhof, P. Landschützer, B. R. Carter, J. A. Triñanes, and C. Cosca

1) Introduction

The oceans play major roles in the global carbon cycle, including taking up a substantial fraction of the excess carbon dioxide (CO_2) that humans release into the atmosphere. As a consequence of humankind's collective CO_2 emissions into the atmosphere, referred to as "anthropogenic CO_2" (C_{anth}) emissions, atmospheric CO_2 concentrations have risen from pre-industrial levels of about 278 ppm (parts per million) to 412 ppm in 2020. Marine C_{anth} is the major cause of anthropogenic ocean acidification, with riverine C_{anth} and other atmospheric trace gases (e.g., nitrogen and sulfur gases) being other sources. Over the last decade, the global ocean has continued taking up a substantial fraction of the C_{anth} emissions and therefore is a major mediator of global climate change. Of the 11.5 (±0.9) Pg C yr^{-1} C_{anth} released from 2010 to 2019, about 2.5 (±0.6) Pg C yr^{-1} (23%) accumulated in the ocean, 3.4 (±0.6) Pg C yr^{-1} (29%) accumulated on land, and 5.1 (±0.02) Pg C yr^{-1} (44%) remained in the atmosphere with an imbalance of −0.1 Pg C yr^{-1} (4%; Table 6 in Friedlingstein

et al. 2020). This decadal ocean carbon uptake consensus estimate combines measured decadal CO_2 inventory changes, models, and global air–sea CO_2 flux estimates based on surface ocean fugacity of CO_2 (fCO_{2w}) measurements[1] from ships and moorings. The oceanic anthropogenic carbon sink has grown from 1.0 (±0.3) Pg C yr^{-1} in the decade of the 1960s to 2.6 (±0.6) Pg C yr^{-1} in 2019 (Friedlingstein et al. 2020).

2) Air–sea carbon dioxide fluxes

Ocean uptake of CO_2 is estimated from the net air–sea CO_2 flux derived from the bulk flux formula with air (a) minus surface seawater (w) differences in CO_2 fugacity ($\Delta fCO_2 = fCO_{2w} - fCO_{2a}$) and gas transfer coefficients as input. Gas transfer is parameterized with wind as described in Wanninkhof (2014). This provides a net flux estimate. To determine the C_{anth} fluxes into the ocean, several other processes need to be considered. A steady contribution of carbon from riverine runoff, originating from organic and inorganic detritus from land, with estimates ranging from 0.45 to 0.78 Pg C yr^{-1} (Resplandy et al. 2018) needs to be included. We use 0.6 Pg C yr^{-1} as the riverine adjustment. We assume other factors such as natural carbon deposition into the sea floor and margins are small. C_{anth} flux is therefore defined here as the sum of the net flux minus the riverine adjustment. The data sources for fCO_{2w} are annual updates of observations from the Surface Ocean CO_2 Atlas (SOCAT) composed of mooring, uncrewed surface vehicle, and ship-based observations (Bakker et al. 2016), and the database with ship-based observations (Takahashi et al. 2020). The increased observations and improved mapping techniques, including neural network methods summarized in Rödenbeck et al. (2015), now provide global fCO_{2w} fields on a 1° latitude × 1° longitude grid at monthly time scales. This allows investigation of variability on monthly to decadal time scales.

The monthly 2020 ΔfCO_2 maps are based on the observation-trained neural network (NN; artificial intelligence) approach of Landschützer et al. (2013, 2014). The 2020 values are projections using the NN predictor variables based on sea surface temperatures (SST), sea surface salinity (SSS), satellite chlorophyll-a (Chl*a*), and atmospheric CO_2 for 2020; a climatological mixed layer depth product (de Boyer Montegut et al. 2004); and an NN approach for fCO_{2w} developed using SOCAT data from 1982 through December 2019. The 2020 estimate uses the monthly ERA5 wind fields for the fluxes, as the cross-calibrated multi-platform winds (Atlas et al. 2011) used for previous years are not available (Fig. 3.27).

The NN results show an increasing ocean sink in the first part of the record from 1982 to 1994, followed by a period of rapidly decreasing uptake from 1995 to 2000 with no definite attribution. Thereafter, the NN results show a strong

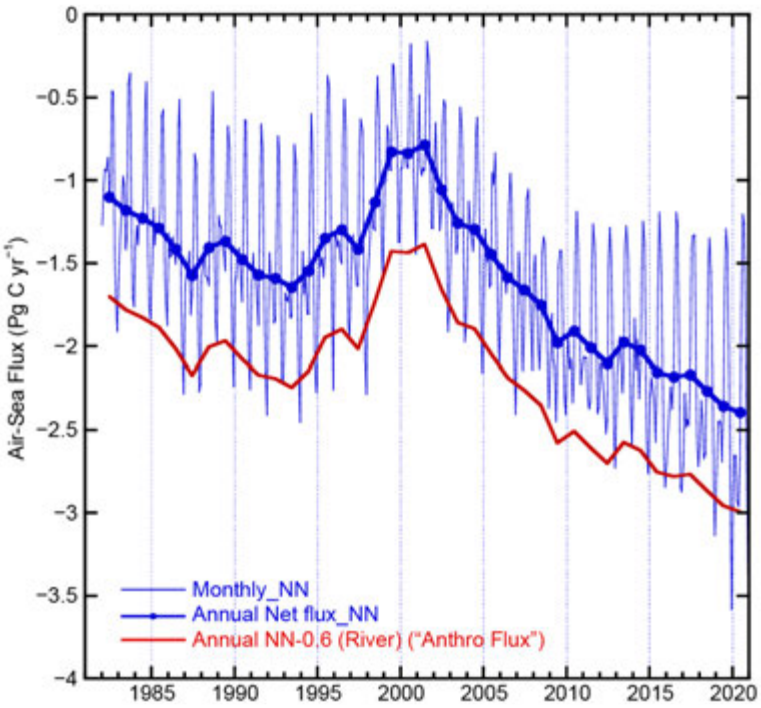

Fig. 3.27. Global annual (thick blue line) and monthly (thin blue line) net CO_2 fluxes (Pg C yr^{-1}) for 1982–2020 using a Neural Network (NN) approach. The red line is the anthropogenic CO_2 flux, that is the net flux including a riverine adjustment of −0.6 Pg C. Negative values indicate CO_2 uptake by the ocean.

[1] The fugacity is the partial pressure of CO_2 (pCO_2) corrected for non-ideality. They are numerically similar for surface waters with $fCO_2 \approx 0.997\ pCO_2$.

increase in the ocean sink from 2001 onward that continues through 2020 with a 0.03 Pg C yr^{-1} increase for the NN in 2020 over 2019. The amplitude of seasonal variability for the NN approach is ≈1 Pg C with minimum uptake from June to September, with a seasonal cycle amplitude exceeding interannual uptake variations. The C_{anth} flux of 3.0 Pg C yr^{-1} for 2020 from the NN approach in 2020 is 29% above the 1999–2019 average of 2.33 (±0.52) Pg C yr^{-1}.

The annual average flux map for 2020 (Fig. 3.28a) shows the characteristic pattern of effluxes (ocean-to-air CO_2 fluxes) in the tropics as well as coastal and open ocean upwelling zones. Coastal upwelling regions include the Arabian Sea and off the west coasts of North and South America. The western Bering Sea in the northwest Pacific was a strong CO_2 source as well in 2020. The region with the largest efflux is the upwelling region of the eastern and central equatorial Pacific. Cumulatively, the regions of effluxes are significant CO_2 sources to the atmosphere (≈ 1 Pg C). The primary uptake regions are in the subtropical and subpolar regions. The largest sinks are observed poleward of the subtropical fronts. The frontal positions determine the location of the maximum uptake. This sink is weaker in the Pacific sector of the Southern Ocean compared to the other basins.

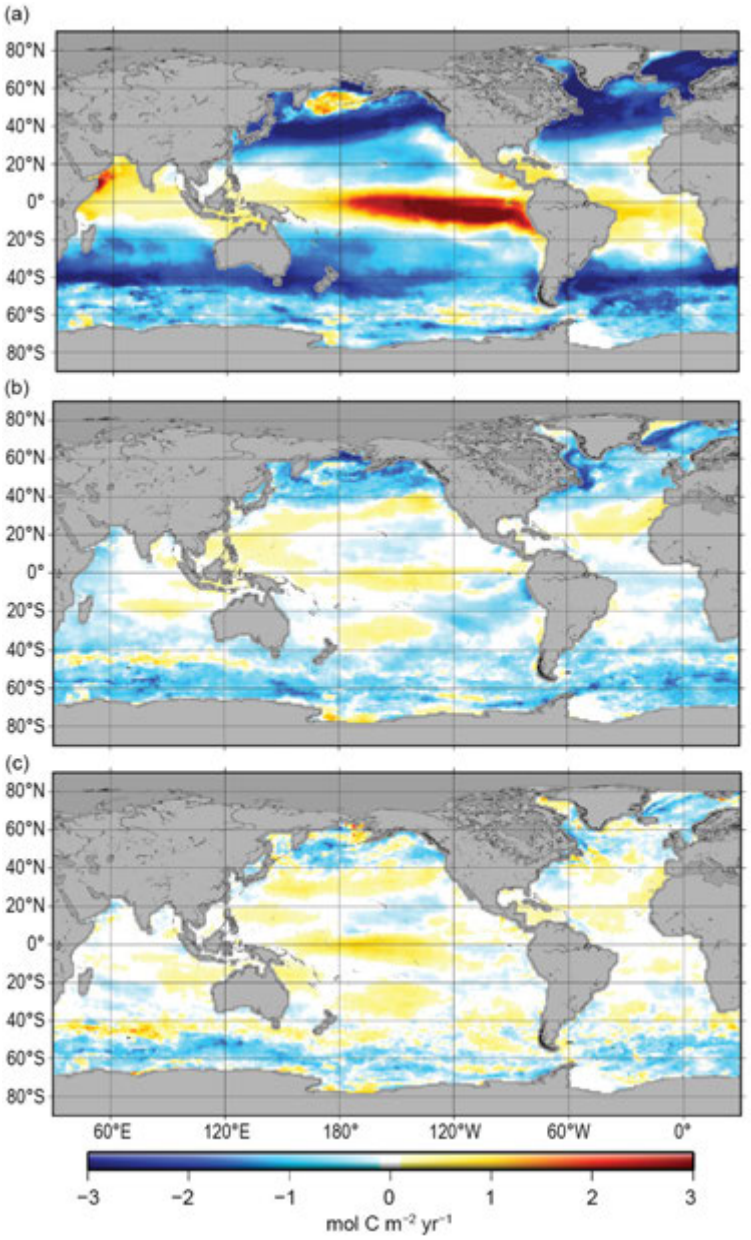

Fig. 3.28. Global map of (a) net air–sea CO_2 fluxes for 2020, with ocean CO_2 uptake regions shown in blue. (b) Net air–sea CO_2 flux anomalies for 2020 relative to the 1997–2018 average using the NN approach of Landschützer et al. (2013), and (c) net air–sea CO_2 flux anomalies for 2020 minus 2019. All maps have units of mol C m^{-2} yr^{-1}.

In the Northern Hemisphere, there is a significant asymmetry in fluxes in the sub-Arctic gyres, with the North Atlantic being a large CO_2 sink while the North Pacific's Bering Sea is a CO_2 source. This difference is partly due to the position of the western boundary currents whose cooling waters are known to contribute to CO_2 sinks at high latitudes: the Gulf Stream/North Atlantic Drift in the Atlantic extends farther north than the Kuroshio in the Pacific (Takahashi et al. 2009).

The ocean carbon uptake anomalies (Fig. 3.28b) in 2020 relative to the 1997–2018 average are attributed to the increasing ocean CO_2 uptake with time due to atmospheric CO_2 increases (Fig. 3.27) and to variations in large-scale climate modes. The long-term air–sea flux trend since the minimum uptake in 2000 is −0.72 Pg C $decade^{-1}$ (blue shading in Fig. 3.28c). Despite this trend, there are several large regions showing positive anomalies for 2020. Notably large positive anomalies are seen in the central equatorial Pacific; in a broad band running northwest across the subtropical northwest Pacific (from ≈20° to 40°N) attributed in the northeastern edge of the band to the North Pacific marine heat wave (Sidebar 3.1, see section 2b3); and in the western central to eastern subtropical Atlantic. The increased effluxes in the central equatorial Pacific are related to

the Oceanic Niño Index (ONI) turning negative in 2020, indicating La Niña conditions following a period of predominantly positive ONI (i.e., more El Niño-like conditions) in the preceding two years. The negative SST anomalies (Fig. 3.1a) indicate increased upwelling of waters with high CO_2 content in the central Pacific returning after a period of lower-than-normal upwelling. Of note, the eastern equatorial Pacific southeast of the Galapagos shows a negative CO_2 flux anomaly. The positive anomalies in fluxes (i.e., more efflux/less influx in 2020 compared to the long-term mean) in the subtropics closely correspond to positive temperature anomalies (Fig. 3.1), showing that the flux anomalies in these regions are temperature driven. The difference in fluxes between 2020 and 2019 (Fig. 3.28c) are similar to the anomalies (Fig. 3.28b).

The oceanic variability of the air–sea exchange fluxes in the tropical Pacific are largely controlled by the surface ocean variability and wind forcing influenced by the type and phasing of the El Niño-Southern Oscillation events (e.g., Feely et al. 1999, 2002, 2006, 2019; Ishii et al. 2009, 2014, 2020; Takahashi et al. 2009; Wanninkhof et al. 2013; Landschützer et al. 2014, 2016). The central and eastern equatorial Pacific is a major source of CO_2 to the atmosphere during neutral and La Niña periods, a weak source during weak El Niño periods, and near-neutral during strong El Niño periods. El Niño is characterized by a large-scale weakening of the trade winds, a decrease in upwelling of CO_2 and nutrient-rich subsurface waters, and a corresponding warming of SST in the eastern and central equatorial Pacific. La Niña is characterized by strong trade winds, cold tropical SSTs, and enhanced upwelling along the equator. During the strong eastern Pacific El Niño events of 1982–83, 1997–98, and 2015–16, the cold waters of the eastern equatorial Pacific disappear and fCO_2 values are close to equilibrium with the atmosphere (FIG. 3.29), whereas during the weaker central Pacific El Niños of 1991–94, 2002–05, 2006–07, and 2009–10, the equatorial

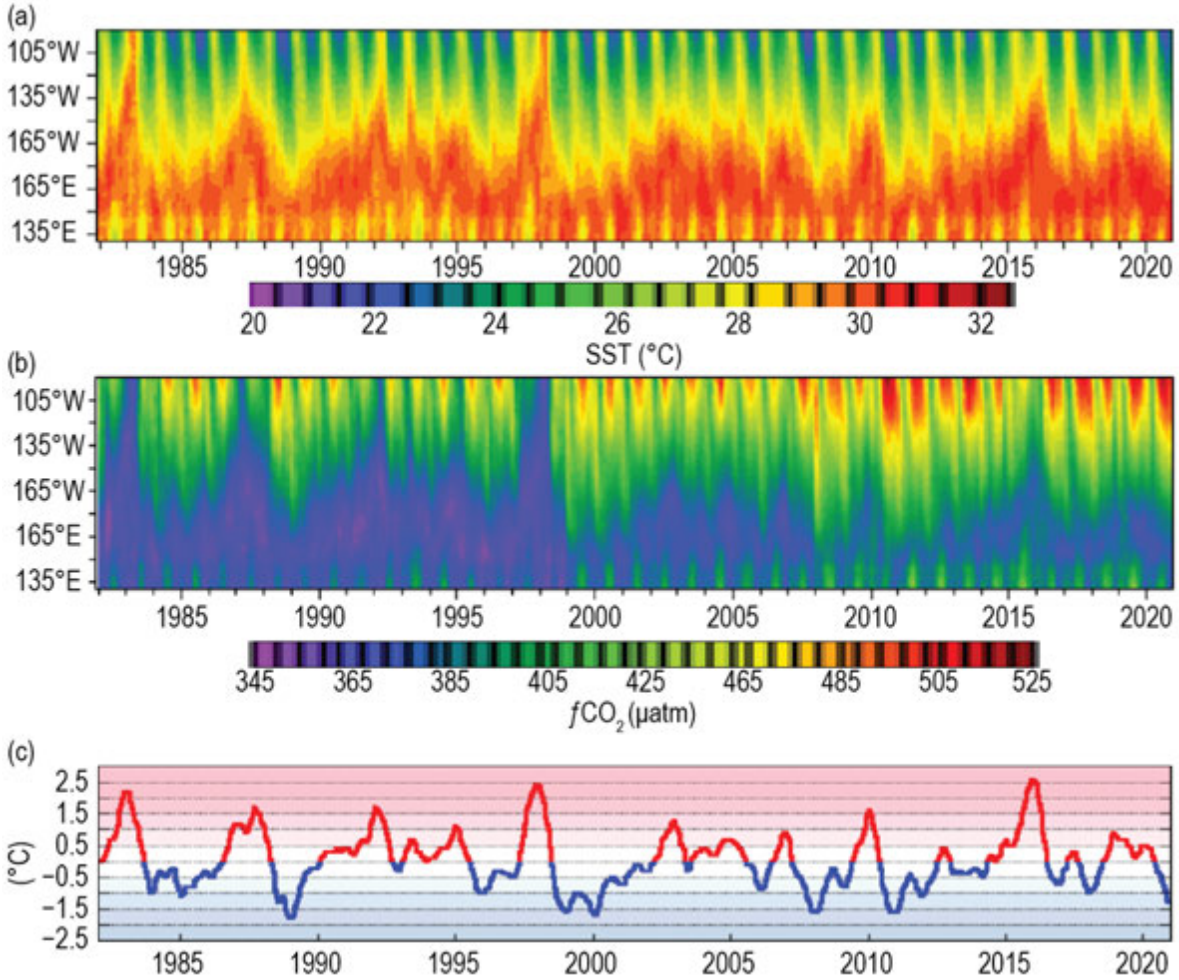

Fig. 3.29. Time–longitude plots of (a) SST (°C), (b) fCO_2 (µatm) from 1982–2020 in the equatorial Pacific, and (c) the Oceanic Niño Index (°C).

cold tongue is present but less pronounced, and fCO_2 values are higher than atmospheric values but lower than corresponding values for non-El Niño periods. The strong 1997–98 El Niño has SST anomalies exceeding 4°C and the lowest fCO_2 values throughout most of the equatorial Pacific. In contrast, the 2015–16 El Niño has SST anomalies that are similar to those seen during the 1997–98 event, yet the fCO_2 values were significantly higher because the upwelling-favorable winds were stronger in the easternmost and westernmost parts of the region. La Niña conditions returned in summer and autumn of 2020 (see section 4b) and were characterized by low SST and high fCO_2 levels throughout the entire tropical Pacific, but were mostly enriched in the central portion of the equatorial belt relative to previous years.

3) Large-scale carbon changes in the ocean interior

Global-scale CO_2 emissions from human activities are causing ocean interior C_{anth} increases and acidification. Delineating how the biogeochemical processes in the ocean interior will be affected by the changing heat content and C_{anth} uptake is essential for developing future mitigation and adaptation responses to climate change. Anthropogenic carbon accumulation occurs against a backdrop of vigorous natural marine carbon cycling. In the well-lit surface ocean, photosynthesizing organisms take up dissolved inorganic carbon to form organic matter, and some organisms form their shells and hard parts out of carbonate minerals. A portion of the organic matter and carbonate mineral matter that is formed or precipitated sinks into the interior ocean where it is remineralized, releasing the carbon back into the interior ocean. This biological transport of dissolved inorganic carbon from the surface ocean into the interior ocean is called the "soft" and "hard" tissue pumps. Several recently produced data products—i.e., interior ocean data products (Olsen et al. 2016, 2020), seawater property estimation algorithms (Carter et al. 2017), and circulation fields based on model simulations that assimilate interior-ocean observations (DeVries et al. 2017)—were combined to produce a new carbon data product containing estimates of the properties that seawater would have in the absence of this natural interior ocean biogeochemical cycling (Fig. 3.30; Carter et al. 2021). The dissolved inorganic carbon accumulated from the hard and soft tissue pumps can be quantified as the difference between the observed values and those estimated from several seawater properties. These estimates suggest the ocean holds 1300 Pg C of carbon from remineralized organic matter and 560 Pg C from dissolution of carbonate mineral phases. This is ~500 Pg C less carbon from organic matter than would be calculated using the assumption that all interior ocean water masses were initially 100% saturated with oxygen. The carbonate mineral dissolution accumulations found in this study are more evenly spread across the water column than those from previous estimates, suggesting a more uniform carbonate mineral dissolution rate with depth than was previously found.

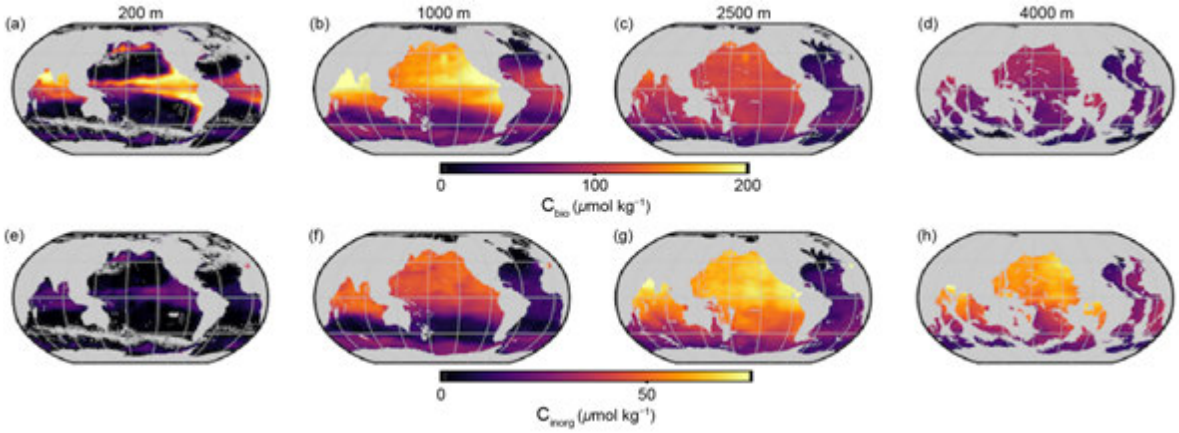

Fig. 3.30. Maps of the accumulation of dissolved inorganic carbon (μmol kg^{-1}) from (a–d) remineralized organic matter (C_{bio}) and from (e–h) dissolution of carbonate minerals (C_{inorg}) at (a,e) 200 m, (b,f) 1000 m, (c,g) 2500 m, and (d,h) 4000 m.

Acknowledgments

- Sandra Bigley provided invaluable editorial support for Chapter 3. Internal reviewers, external reviews, and report editors all provided comments that helped to improve the chapter.
- Argo data used in the chapter were collected and made freely available by the International Argo Program and the national programs that contribute to it. (https://argo.ucsd.edu, https://www.ocean-ops.org). The Argo Program is part of the Global Ocean Observing System. Many authors of the chapter are supported by NOAA Research, the NOAA Global Ocean Monitoring and Observing Program, or the NOAA Ocean Acidification Program.
- L. Cheng is supported by National Natural Science Foundation of China (42076202) and Strategic Priority Research Program of the Chinese Academy of Sciences (XDB42040402.
- R. E. Killick is supported by the Met Office Hadley Centre Climate Programme funded by BEIS and Defra. PMEL contribution numbers 5214, 5215, 5216, 5217, and 5247.

Chapter 3 – Acronyms

ACC	Antarctic Circumpolar Current
AMOC	Atlantic meridional overturning circulation
BASS	Blended Analysis of Surface Salinity
C_{anth}	anthropogenic CO_2
CCS	California Current System
CERES	Clouds and the Earth's Radiant Energy System
Chl*a*	chlorophyll-*a*
CO_2	carbon dioxide
COARE	Coupled Ocean-Atmosphere Response Experiment
C_{phy}	phytoplankton carbon
DJF	December–February
DOISST	Daily Optimum Interpolation ST version 2.1
E	evaporation
E–*P*	evaporation minus precipitation
EBAF	Energy Balanced and Filled
EKE	eddy kinetic energy
ENSO	El Niño–Southern Oscillation
ERSSTv5	Extended Reconstruction Sea Surface Temperature version 5
FC	Florida Current
FLASHFlux	Fast Longwave And Shortwave Radiative Fluxes
GMSL	global mean sea level
GPCP	Global Precipitation Climatology Project
GRACE	Gravity Recovery and Climate Experiment
GRACE-FO	Gravity Recovery and Climate Experiment Follow-On
HadSST	Hadley Centre SST
IO	Indian Ocean
IOD	Indian Ocean dipole
ITCZ	Intertropical Convergence Zone
JJA	June–August
LH	latent heat
LIARv2	Locally Interpolated Alkalinity Regression
LW	longwave
MAM	March–May
MEI	Multivariate ENSO Index
MHHW	mean higher high water
MHT	meridional heat transport
MHW	marine heat wave
MOC	meridional overturning circulation
MODIS	Moderate Resolution Imaging Spectroradiometer
MODIS-A	MODIS on *Aqua*
NAC	North Atlantic Current
NECC	North Equatorial Countercurrent
NH	Northern Hemisphere
NN	Neural Network
NPG	North Pacific Gyre
NPP	net primary production
OAFlux	Objectively Analyzed air-sea Fluxes

OHCA	ocean heat content anomaly
ONI	Oceanic Niño Index
OSNAP	Overturning in the Subpolar North Atlantic Program
P	precipitation
PACE	Plankton, Aerosol, Cloud, ocean Ecosystem
P – *E*	precipitation minus evaporation
PIES	Pressure-equipped inverted echo sounder
PNA	Pacific/North American
ppm	parts per million
PSO	permanently stratified ocean
RAPID/MOCHA/WBTS	Rapid Climate Change/MOC and Heatflux Array/Western Boundary Time Series
RF	Random Forest
SAMBA	South Atlantic MOC Basin-wide Array
Sea-WiFS	Sea-viewing Wide Field-of-view Sensor
SEC	South Equatorial Current
SH	sensible heat flux
SH	Southern Hemisphere
SJDF	Strait of Juan de Fuca
SMAP	Soil Moisture Active Passive
SMOS	Soil Moisture and Ocean Salinity
SOCAT	Surface Ocean CO_2 Atlas
SON	September–November
SPCZ	South Pacific Convergence Zone
SSM/I	Special Sensor Microwave/Imager
SSS	sea surface salinity
SST	sea surface temperature
SSTA	sea surface temperature anomaly
std. dev.	standard deviation
SW	shortwave
TRACOS	Tropical Atlantic Circulation and Overturning at 11°S
XBT	eXpendable BathyThermograph

References

Abraham, J. P., and Coauthors, 2013: A review of global ocean temperature observations: Implications for ocean heat content estimates and climate change. *Rev. Geophys.*, **51**, 450–483, https://doi.org/10.1002/rog.20022.

Adler, R. F., and Coauthors, 2018: The Global Precipitation Climatology Project (GPCP) monthly analysis (new version 2.3) and a review of 2017 global precipitation. *Atmosphere*, **9**, 138, https://doi.org/10.3390/atmos9040138.

Alexander, M. A., J. D. Scott, K. D. Friedland, K. E. Mills, J. A. Nye, A. J. Pershing, and A. C. Thomas, 2018: Projected sea surface temperatures over the 21st century: Changes in the mean, variability and extremes for large marine ecosystem regions of northern oceans. *Elementa*, **6**, 9, https://doi.org/10.1525/elementa.191.

Alin, S. R., R. A. Feely, A. Collins, and C.E. Cosca, 2021: Fugacity of carbon dioxide (fCO2), temperature, salinity and other variables collected from surface underway observations using shower head equilibrator, carbon dioxide gas detector and other instruments from the M/V Bluefin cruises in the Tropical and North Pacific Ocean from 2020-02-26 to 2020-10-26 (NCEI Accession 0225428). NOAA National Centers for Environmental Information, accessed 24 April 2021, https://doi.org/10.25921/kk66-zz33.

Amaya, D. J., A. J. Miller, S. P. Xie, and Y. Kusaka, 2020: Physical drivers of the summer 2019 North Pacific marine heatwave. *Nat. Commun.*, **11**, 1903, https://doi.org/10.1038/s41467-020-15820-w.

——, M. A. Alexander, A. Capotondi, C. Deser, K. B. Karnauskas, A. J. Miller, and N. J. Mantua, 2021: Are long-term changes in mixed layer depth influencing North Pacific marine heatwaves? [in "Explaining Extremes of 2019 from a Climate Perspective"]. *Bull. Amer. Meteor. Soc.*, **102** (1), S59–S66, https://doi.org/10.1175/BAMS-D-20-0144.1.

Atlas, R., R. N. Hoffman, J. Ardizzone, S. M. Leidner, J. C. Jusem, D. K. Smith, and D. Gombos, 2011: A cross-calibrated multiplatform ocean surface wind velocity product for meteorological and oceanographic applications. *Bull. Amer. Meteor. Soc.*, **92**, 157–174, https://doi.org/10.1175/2010BAMS2946.1.

Babcock, R. C., and Coauthors, 2019: Severe continental-scale impacts of climate change are happening now: Extreme climate events impact marine habitat forming communities along 45% of Australia's coast. *Front. Mar. Sci.*, **6**, 411, https://doi.org/10.3389/fmars.2019.00411.

Bakker, D. C. E., and Coauthors, 2016: A multi-decade record of high quality fCO2 data in version 3 of the surface ocean CO2 Atlas (SOCAT). *Earth Syst. Sci. Data*, **8**, 383–413, https://doi.org/10.5194/essd-8-383-2016.

Balaguru, K., P. Chang, R. Saravanan, L. R. Leung, Z. Xu, M. Li, and J. S. Hsieh, 2012: Ocean barrier layers' effect on tropical cyclone intensification. *Proc. Natl. Acad. Sci. USA*, **109**, 14343–14347, https://doi.org/10.1073/pnas.1201364109.

Baumgartner, A., and E. Reichel, 1975: *The World Water Balance*. Elsevier, 179 pp.

Behrenfeld, M. J., and Coauthors, 2006: Climate-driven trends in contemporary ocean productivity. *Nature*, **444**, 752–755, https://doi.org/10.1038/nature05317.

——, and Coauthors, 2015: Revaluating ocean warming impacts on global phytoplankton. *Nat. Climate Change*, **6**, 323–330, https://doi.org/10.1038/nclimate2838.

Boening, C., J. K. Willis, F. W. Landerer, R. S. Nerem, and J. Fasullo, 2012: The 2011 La Niña: So strong, the oceans fell. *Geophys. Res. Lett.*, **39**, L19602, https://doi.org/10.1029/2012GL053055.

Bond, N. A., M. F. Cronin, H. Freeland, and N. Mantua, 2015: Causes and impacts of the 2014 warm anomaly in the NE Pacific. *Geophys. Res. Lett.*, **42**, 3414–3420, https://doi.org/10.1002/2015GL063306.

Bopp, L., and Coauthors, 2013: Multiple stressors of ocean ecosystems in the 21st century: projections with CMIP5 models. *Biogeosciences*, **10**, 6225–6245, https://doi.org/10.5194/bg-10-6225-2013.

Boyer, T. P., and Coauthors, 2013: *World Ocean Database 2013*. S. Levitus, Ed., NOAA Atlas NESDIS 72, 209 pp.

——, and Coauthors, 2018: *World Ocean Database 2018*. A.V. Mishonov, Ed., NOAA Atlas NESDIS 87, 207 pp.

Broecker, W. S., 1991: The Great Ocean Conveyor. *Oceanography*, **4**, 79–89, https://doi.org/10.5670/oceanog.1991.07.

Bulgin, C. E., C. J. Merchant, and D. Ferreira, 2020: Tendencies, variability and persistence of sea surface temperature anomalies. *Sci. Rep.*, **10**, 7986, https://doi.org/10.1038/s41598-020-64785-9.

Caesar, L., S. Rahmstorf, A. Robinson, G. Feulner, and V. Saba, 2018: Observed fingerprint of a weakening Atlantic Ocean overturning circulation. *Nature*, **556**, 191–196, https://doi.org/10.1038/s41586-018-0006-5.

Carter, B. R., and Coauthors, 2017: Two decades of Pacific anthropogenic carbon storage and ocean acidification along GO-SHIP Sections P16 and P02. *Global Biogeochem. Cycles*, **31**, 306–327, https://doi.org/10.1002/2016GB005485.

——, R. A. Feely, N. L. Williams, A. G. Dickson, M. B. Fong, and Y. Takeshita, 2018: Updated methods for global locally interpolated estimation of alkalinity, pH, and nitrate. *Limnol. Oceanogr. Methods*, **16**, 119–131, https://doi.org/10.1002/lom3.10232.

——, ——, S. K. Lauvset, A. Olsen, T. DeVries, and R. Sonnerup, 2021: Preformed properties for marine organic matter and carbonate mineral cycling quantification. *Global Biogeochem. Cycles*, **35**, e2020GB006623, https://doi.org/10.1029/2020GB006623.

Castro de la Guardia, L., X. Hu, and P. G. Myers, 2015: Potential positive feedback between Greenland Ice Sheet melt and Baffin Bay heat content on the west Greenland shelf. *Geophys. Res. Lett.*, **42**, 4922–4930, https://doi.org/10.1002/2015GL064626.

Chambers, D. P., A. Cazenave, N. Champollion, H. Dieng, W. Llovel, R. Forsberg, K. von Schuckmann, and Y. Wada, 2017: Evaluation of the global mean sea level budget between 1993 and 2014. *Surv. Geophys.*, **38**, 309–327, https://doi.org/10.1007/s10712-016-9381-3.

Chen, J., B. Tapley, C. Wilson, A. Cazenave, K. W. Seo, and J. S. Kim, 2020: Global ocean mass change from GRACE and GRACE follow-on and altimeter and Argo measurements. *Geophys. Res. Lett.*, **47**, e2020GL090656, https://doi.org/10.1029/2020GL090656.

Cheng, L., and Coauthors, 2020: Record-setting ocean warmth continued in 2019. *Adv. Atmos. Sci.*, **37**, 137–142, https://doi.org/10.1007/s00376-020-9283-7.

Chiang, J. C. H., and D. J. Vimont, 2004: Analagous meridional modes of atmosphere-ocean variability in the tropical Pacific and tropical Atlantic. *J. Climate*, **17**, 4143–4158, https://doi.org/10.1175/JCLI4953.1.

Christian, J. R., and T. Ono, Eds., 2019: Ocean acidification and deoxygenation in the North Pacific Ocean. PICES Special Publication 5, 116 pp.

Cornwall, W., 2019: A new 'Blob' menaces Pacific ecosystems. *Science*, **365**, 1233, https://doi.org/10.1126/science.365.6459.1233.

de Boyer Montegut, C., G. Madec, A. S. Fischer, A. Lazar, and D. Iudicone, 2004: Mixed layer depth over the global ocean: An examination of profile data and a profile-based climatology. *J. Geophys. Res.*, **109**, C12003, https://doi.org/10.1029/2004JC002378.

Deser, C., M. A. Alexander, S. P. Xie, and A. S. Phillips, 2010: Sea surface temperature variability: Patterns and mechanisms. *Annu. Rev. Mar. Sci.*, **2**, 115–143, https://doi.org/10.1146/annurev-marine-120408-151453.

DeVries, T., M. Holzer, and F. Primeau, 2017: Recent increase in oceanic carbon uptake driven by weaker upper-ocean overturning. *Nature*, **542**, 215–218, https://doi.org/10.1038/nature21068.

Dierssen, H. M., 2010: Perspectives on empirical approaches for ocean color remote sensing of chlorophyll in a changing climate. *Proc. Natl. Acad. Sci. USA*, **107**, 17073–17078, https://doi.org/10.1073/pnas.0913800107.

Dima, M., and G. Lohmann, 2010: Evidence for two distinct modes of large-scale ocean circulation changes over the last century. *J. Climate*, **23**, 5–16, https://doi.org/10.1175/2009JCLI2867.1

Domingues, R., and Coauthors, 2015: Upper ocean response to Hurricane Gonzalo (2014): Salinity effects revealed by sustained and targeted observations from underwater gliders. *Geophys. Res. Lett.*, **42**, 7131–7138, https://doi.org/10.1002/2015GL065378.

——, M. Baringer, and G. Goni, 2016: Remote sources for year-to-year changes in the seasonality of the Florida Current transport. *J. Geophys. Res. Oceans*, **121**, 7547–7559, https://doi.org/10.1002/2016JC012070.

Dong, S., G. Goni, and F. Bringas, 2015: Temporal variability of the meridional overturning circulation in the South Atlantic between 20°S and 35°S. *Geophys. Res. Lett.*, **42**, 7655–7662, https://doi.org/10.1002/2015GL065603.

——, H. Lopez, S.-K. Lee, C. S. Meinen, G. J. Goni, and M. O. Baringer, 2020: What caused the large-scale heat deficit in the subtropical South Atlantic Ocean during 2009-2012? *Geophys. Res. Lett.*, **47**, e2020GL088206, https://doi.org/10.1029/2020GL088206.

Durack, P. J., 2015: Ocean salinity and the global water cycle. *Oceanography*, **28**, 20–31, https://doi.org/10.5670/oceanog.2015.03.

——, and S. E. Wijffels, 2010: Fifty-year trends in global ocean salinities and their relationship to broad-scale warming. *J. Climate*, **23**, 4342–4362, https://doi.org/10.1175/2010JCLI3377.1.

——, ——, and R. J. Matear, 2012: Ocean salinities reveal strong global water cycle intensification during 1950 to 2000. *Science*, **336**, 455–458, https://doi.org/10.1126/science.1212222.

Egleston, E. S., C. L. Sabine, and F. M. M. Morel, 2010: Revelle revisited: Buffer factors that quantify the response of ocean chemistry to changes in DIC and alkalinity. *Global Biogeochem. Cycles*, **24**, GB1002, https://doi.org/10.1029/2008GB003407.

Esaias, W. E., and Coauthors, 1998: An overview of MODIS capabilities for ocean science observations. *IEEE Trans. Geosci. Remote Sens.*, **36**, 1250–1265, https://doi.org/10.1109/36.701076.

Ezer, T., and L. P. Atkinson, 2014: Accelerated flooding along the U.S. East Coast: On the impact of sea-level rise, tides, storms, the Gulf Stream, and the North Atlantic Oscillations. *Earth's Future*, **2**, 362–382, https://doi.org/10.1002/2014EF000252.

Fairall, C. W., E. F. Bradley, J. E. Hare, A. A. Grachev, and J. B. Edson, 2003: Bulk parameterization of air–sea fluxes: Updates and verification for the COARE algorithm. *J. Climate*, **16**, 571–591, https://doi.org/10.1175/1520-0442(2003)016<0571:BPOASF>2.0.CO;2.

Falkowski, P. G., R. T. Barber, and V. Smetacek, 1998: Biogeochemical controls and feedbacks on ocean primary production. *Science*, **281**, 200–206, https://doi.org/10.1126/science.281.5374.200.

Fassbender, A. J., and Coauthors, 2018: Seasonal carbonate chemistry variability in marine surface waters of the Pacific Northwest. *Earth Syst. Sci. Data*, **10**, 1367–1401, https://doi.org/10.5194/essd-10-1367-2018.

Fasullo, J. T., and P. R. Gent, 2017: On the relationship between regional ocean heat content and sea surface height. *J. Climate*, **30**, 9195–9211, https://doi.org/10.1175/JCLI-D-16-0920.1.

——, and R. S. Nerem, 2018: Altimeter-era emergence of the patterns of forced sea-level rise in climate models and implications for the future. *Proc. Natl. Acad. Sci. USA*, **115**, 12 944–12 949, https://doi.org/10.1073/pnas.1813233115.

——, R. S. Nerem, and B. Hamlington, 2016: Is the detection of accelerated sea level rise imminent? *Sci. Rep.*, **6**, 31245, https://doi.org/10.1038/srep31245.

Feely, R. A., R. Wanninkhof, T. Takahashi, and P. Tans, 1999: Influence of El Niño on the equatorial Pacific contribution of atmospheric CO2 accumulation. *Nature*, **398**, 597–601, https://doi.org/10.1038/19273.

——, and Coauthors, 2002: Seasonal and interannual variability of CO2 in the equatorial Pacific. *Deep-Sea Res. II*, **49**, 2443–2469, https://doi.org/10.1016/S0967-0645(02)00044-9.

——, T. Takahashi, R. Wanninkhof, M. J. McPhaden, C. E. Cosca, S. C. Sutherland, and M.-E. Carr, 2006: Decadal variability of the air-sea CO2 fluxes in the equatorial Pacific Ocean. *J. Geophys. Res.*, **111**, C08S90, https://doi.org/10.1029/2005JC003129.

——, S. R. Alin, J. Newton, C. L. Sabine, M. Warner, A. Devol, C. Krembs, and C. Maloy, 2010: The combined effects of ocean acidification, mixing, and respiration on pH and carbonate saturation in an urbanized estuary. *Estuarine Coastal Shelf Sci.*, **88**, 442–449, https://doi.org/10.1016/j.ecss.2010.05.004.

——, R. Wanninkhof, B. R. Carter, P. Landschützer, A. J. Sutton, C. Cosca, and J. A. Triñanes, 2019: Global ocean carbon cycle [in "State of the Climate in 2018"]. *Bull. Amer. Meteor. Soc.*, **100** (9), S94–S99, https://doi.org/10.1175/2019BAMSStateoftheClimate.1.

Ffield, A., 2007: Amazon and Orinoco River plumes and NBC rings: Bystanders or participants in hurricane events? *J. Climate*, **20**, 316–333, https://doi.org/10.1175/JCLI3985.1.

Field, C. B., M. J. Behrenfeld, J. T. Randerson, and P. Falkowski, 1998: Primary production of the biosphere: Integrating terrestrial and oceanic components. *Science*, **281**, 237–240, https://doi.org/10.1126/science.281.5374.237.

Fofonoff, N. P., and E. L. Lewis, 1979: A practical salinity scale. *J. Oceanogr. Soc. Japan*, **35**, 63–64, https://doi.org/10.1007/BF02108283.

Font, J., and Coauthors, 2013: SMOS first data analysis for sea surface salinity determination. *Int. J. Remote Sens.*, **34**, 3654–3670, https://doi.org/10.1080/01431161.2012.716541.

Fore, A. G., S. H. Yueh, W. Q. Tang, B. W. Stiles, and A. K. Hayashi, 2016: Combined active/passive retrievals of ocean vector wind and sea surface salinity with SMAP. *IEEE Trans. Geosci. Remote Sens.*, **54**, 7396–7404, https://doi.org/10.1109/TGRS.2016.2601486.

Frajka-Williams, E., and Coauthors, 2019: Atlantic meridional overturning circulation: Observed transports and variability. *Front. Mar. Sci.*, **6**, 260, https://doi.org/10.3389/fmars.2019.00260.

Franz, B. A., I. Cetinić, J. P. Scott, D. A. Siegel, and T. K. Westberry, 2020: Global ocean phytoplankton [in "State of the Climate in 2019"]. *Bull. Amer. Meteor. Soc.*, **101** (8), S163–S169, https://doi.org/10.1175/BAMS-D-20-0105.1.

Frederikse, T., and Coauthors, 2020: The causes of sea-level rise since 1900. *Nature*, **584**, 393–397, https://doi.org/10.1038/s41586-020-2591-3.

Friedlingstein, P., and Coauthors, 2020: Global carbon budget 2020. *Earth Syst. Sci. Data*, **12**, 3269–3340, https://doi.org/10.5194/essd-12-3269-2020.

Geider, R. J., H. L. MacIntyre, and T. M. Kana, 1997: Dynamic model of phytoplankton growth and acclimation: Responses of the balanced growth rate and the chlorophyll a:carbon ratio to light, nutrient limitation and temperature. *Mar. Ecol. Prog. Ser.*, **148**, 187–200, https://doi.org/10.3354/meps148187.

Gentemann, C. L., M. R. Fewings, and M. García-Reyes, 2017: Satellite sea surface temperatures along the West Coast of the United States during the 2014–2016 northeast Pacific marine heat wave. *Geophys. Res. Lett.*, **44**, 312–319, https://doi.org/10.1002/2016GL071039.

Goni, G. J., and W. E. Johns, 2003: Synoptic study of warm rings in the North Brazil Current retroflection region using satellite altimetry. *Interhemispheric Water Exchange in the Atlantic Ocean*, G. J. Goni, and P. Malanotte-Rizzoli, Eds., Elsevier Oceanography Series, Vol. 68, Elsevier, 335–356, https://doi.org/10.1016/S0422-9894(03)80153-8.

——, and Coauthors, 2009: Applications of satellite-derived ocean measurements to tropical cyclone intensity forecasting. *Oceanography*, **22**, 190–197, https://doi.org/10.5670/oceanog.2009.78.

——, F. Bringas, and P. N. Di Nezio, 2011: Observed low frequency variability of the Brazil Current front. *J. Geophys. Res.*, **116**, C10037, https://doi.org/10.1029/2011JC007198.

Gordon, A. L., 1986: Interocean exchange of thermocline water. *J. Geophys. Res.*, **91**, 5037–5046, https://doi.org/10.1029/JC091iC04p05037.

Graff, J. R., and Coauthors, 2015: Analytical phytoplankton carbon measurements spanning diverse ecosystems. *Deep-Sea Res. I*, **102**, 16–25, https://doi.org/10.1016/j.dsr.2015.04.006.

Gruber, N., and Coauthors, 2019: The oceanic sink for anthropogenic CO2 from 1994 to 2007. *Science*, **363**, 1193–1199, https://doi.org/10.1126/science.aau5153.

Hamlington, B. D., J. T. Fasullo, R. S. Nerem, K. Kim, and F. W. Landerer, 2019: Uncovering the pattern of forced sea level rise in the satellite altimeter record. *Geophys. Res. Lett.*, **46**, 4844–4853, https://doi.org/10.1029/2018GL081386.

——, C. G. Piecuch, J. T. Reager, H. Chandanpurkar, T. Frederikse, R. S. Nerem, J. T. Fasullo, and S.-H. Cheon, 2020: Origin of interannual variability in global mean sea level. *Proc. Natl. Acad. Sci. USA*, **117**, 13983–13990, https://doi.org/10.1073/pnas.1922190117.

Han, W., G. A. Meehl, D. Stammer, A. Hu, B. Hamlington, J. Kenigson, H. Palanisamy, and P. Thompson, 2017: Spatial patterns of sea level variability associated with natural internal climate modes. *Surv. Geophys.*, **38**, 217–250, https://doi.org/10.1007/s10712-016-9386-y.

Held, I. M., and B. J. Soden, 2006: Robust responses of the hydrological cycle to global warming. *J. Climate*, **19**, 5686–5699, https://doi.org/10.1175/JCLI3990.1.

Herrford, J., P. Brandt, T. Kanzow, R. Hummels, M. Araujo, and J. V. Durgadoo, 2021: Seasonal variability of the Atlantic Meridional Overturning Circulation at 11°S inferred from bottom pressure measurements. *Ocean Sci.*, **17**, 265–284, https://doi.org/10.5194/os-17-265-2021.

Hobday, A. J., and Coauthors, 2016: A hierarchical approach to defining marine heatwaves. *Prog. Oceanogr.*, **141**, 227–238, https://doi.org/10.1016/j.pocean.2015.12.014.

Hu, C., Z. Lee, and B. A. Franz, 2012: Chlorophyll a algorithms for oligotrophic oceans: A novel approach based on three-band reflectance difference. *J. Geophys. Res.*, **117**, C01011, https://doi.org/10.1029/2011JC007395.

Hu, Z.-Z., A. Kumar, B. Huang, Y. Xue, W. Wang, and B. Jha, 2011: Persistent atmospheric and oceanic anomalies in the North Atlantic from summer 2009 to summer 2010. *J. Climate*, **24**, 5812–5830, https://doi.org/10.1175/2011JCLI4213.1.

Huang, B., and Coauthors, 2015: Extended reconstructed sea surface temperature version 4 (ERSST.v4). Part I: Upgrades and intercomparisons. *J. Climate*, **28**, 911–930, https://doi.org/10.1175/JCLI-D-14-00006.1.

——, and Coauthors, 2017: Extended reconstructed sea surface temperature version 5 (ERSSTv5): Upgrades, validations, and intercomparisons. *J. Climate*, **30**, 8179–8205, https://doi.org/10.1175/JCLI-D-16-0836.1.

——, and Coauthors, 2020: Uncertainty estimates for sea surface temperature and land surface air temperature in NOAAGlobalTemp version 5. *J. Climate*, **33**, 1351–1379, https://doi.org/10.1175/JCLI-D-19-0395.1.

——, C. Liu, V. Banzon, E. Freeman, G. Graham, B. Hankins, T. Smith, and H.-M. Zhang, 2021: Improvements of the Daily Optimum Interpolation Sea Surface Temperature (DOISST) version 2.1. *J. Climate*, **34**, 2923–2939, https://doi.org/10.1175/JCLI-D-20-0166.1.

Hummels, R., P. Brandt, M. Dengler, J. Fischer, M. Araujo, D. Veleda, and J. V. Durgadoo, 2015: Interannual to decadal changes in the western boundary circulation in the Atlantic at 11°S. *Geophys. Res. Lett.*, **42**, 7615–7622, https://doi.org/10.1002/2015GL065254.

Ishii, M., and Coauthors, 2009: Spatial variability and decadal trend of the oceanic CO2 in the western equatorial Pacific warm/fresh water. *Deep-Sea Res. II*, **56**, 591–606, https://doi.org/10.1016/j.dsr2.2009.01.002.

——, and Coauthors, 2014: Air-sea CO2 flux in the Pacific Ocean for the period 1990-2009. *Biogeosciences*, **11**, 709–734, https://doi.org/10.5194/bg-11-709-2014.

——, Y. Fukuda, S. Hirahara, S. Yasui, T. Suzuki, and K. Sato, 2017: Accuracy of global upper ocean heat content estimation expected from present observational datasets. *SOLA*, **13**, 163–167, https://doi.org/10.2151/sola.2017-030.

——, and Coauthors, 2020: Ocean acidification from below in the tropical Pacific. *Global Biogeochem. Cycles*, **34**, e2019GB006368, https://doi.org/10.1029/2019GB006368.

Jiang, L.-Q., R. A. Feely, B. R. Carter, D. J. Greeley, D. K. Gledhill, and K. M. Arzayus, 2015: Climatological distribution of aragonite saturation state in the global oceans. *Global Biogeochem. Cycles*, **29**, 1656–1673, https://doi.org/10.1002/2015GB005198.

——, B. R. Carter, R. A. Feely, S. K. Lauvset, and A. Olsen, 2019: Surface ocean pH and buffer capacity: Past, present and future. *Sci. Rep.*, **9**, 18624, https://doi.org/10.1038/s41598-019-55039-4.

Johnson, G. C., and J. M. Lyman, 2012: Sea surface salinity [in "State of the Climate in 2011"]. *Bull. Amer. Meteor. Soc.*, **93**, S68–S69, S72, https://doi.org/10.1175/2012BAMSStateoftheClimate.1

——, and A. N. Birnbaum, 2017: During El Niño, Pacific Warm Pool expands, ocean gains more heat. *Geophys. Res. Lett.*, **44**, 438–445, https://doi.org/10.1002/2016GL071767.

——, and J. M. Lyman, 2020: Warming trends increasingly dominate global ocean. *Nat. Climate Change*, **10**, 757–761, https://doi.org/10.1038/s41558-020-0822-0.

——, B. M. Sloyan, W. S. Kessler, and K. E. McTaggart, 2002: Direct measurements of upper ocean currents and water properties across the tropical Pacific Ocean during the 1990s. *Prog. Oceanogr.*, **52**, 31–61, https://doi.org/10.1016/S0079-6611(02)00021-6.

——, J. M. Lyman, J. K. Willis, T. Boyer, J. Antonov, S. A. Good, C. M. Domingues, and N. Bindoff, 2014: Ocean heat content [in "State of the Climate in 2013"]. *Bull. Amer. Meteor. Soc.*, **95** (7), S54–S57, https://doi.org/10.1175/2014BAMSStateoftheClimate.1.

——, and Coauthors, 2015: Ocean heat content [in "State of the Climate in 2014"]. *Bull. Amer. Meteor. Soc.*, **96** (7) , ES64–ES66, ES68, https://doi.org/10.1175/2015BAMSStateoftheClimate.1.

——, and Coauthors, 2020: Ocean heat content [in "State of the Climate in 2019"]. *Bull. Amer. Meteor. Soc.*, **101** (8), S140–S144, https://doi.org/10.1175/2020BAMSStateoftheClimate.1.

Josey, S. A., and Coauthors, 2018: The recent Atlantic cold anomaly: Causes, consequences, and related phenomena. *Annu. Rev. Mar. Sci.*, **10**, 475–501, https://doi.org/10.1146/annurev-marine-121916-063102.

Kato, S., and Coauthors, 2018: Surface irradiances of edition 4.0 Clouds and the Earth's Radiant Energy System (CERES) Energy Balanced and Filled (EBAF) data product. *J. Climate*, **31**, 4501–4527, https://doi.org/10.1175/JCLI-D-17-0523.1.

Kennedy, J. J., N. A. Rayner, R. O. Smith, D. E. Parker, and M. Saunby, 2011a: Reassessing biases and other uncertainties in sea surface temperature observations measured in situ since 1850: 1. Measurement and sampling errors. *J. Geophys. Res.*, **116**, D14103, https://doi.org/10.1029/2010JD015218.

——, ——, ——, ——, and ——, 2011b: Reassessing biases and other uncertainties in sea surface temperature observations measured in situ since 1850: 2: Biases and homogenization. *J. Geophys. Res.*, **116**, D14104, https://doi.org/10.1029/2010JD015220.

——, ——, C. P. Atkinson, and R. E. Killick, 2019: An ensemble data set of sea surface temperature change from 1850: The Met Office Hadley Centre HadSST.4.0.0.0 data set. *J. Geophys. Res. Atmos.*, **124**, 7719–7763, https://doi.org/10.1029/2018JD029867.

Kent, E. C., and Coauthors, 2017: A call for new approaches to quantifying biases in observations of sea surface temperature. *Bull. Amer. Meteor. Soc.*, **98**, 1601–1616, https://doi.org/10.1175/BAMS-D-15-00251.1.

Kersalé, M., and Coauthors, 2020: Highly variable upper and abyssal overturning cells in the South Atlantic. *Sci. Adv.*, **6**, eaba7573, https://doi.org/10.1126/sciadv.aba7573.

Kopte, R., P. Brandt, M. Dengler, P. C. M. Tchipalanga, M. Macuéria, and M. Ostrowski, 2017: The Angola Current: Flow and hydrographic characteristics as observed at 11°S. *J. Geophys. Res. Oceans*, **122**, 1177–1189, https://doi.org/10.1002/2016JC012374.

Lambert, H. R., 2019: 2019 albacore catch blows old record out of the water. KOIN.com, Accessed 11 February 2021, www.koin.com/news/oregon/2019-albacore-catch-blows-old-record-out-of-the-water/.

Landschützer, P., N. Gruber, D. C. E. Bakker, U. Schuster, S. Nakaoka, M. R. Payne, T. P. Sasse, and J. Zeng, 2013: A neural network-based estimate of the seasonal to inter-annual variability of the Atlantic Ocean carbon sink. *Biogeosciences*, **10**, 7793–7815, https://doi.org/10.5194/bg-10-7793-2013.

Landschützer, P., N. Gruber, D. C. E. Bakker, and U. Schuster, 2014: Recent variability of the global ocean carbon sink. *Global Biogeochem. Cycles*, **28**, 927–949, https://doi.org/10.1002/2014GB004853.

——, ——, and ——, 2016: Decadal variations and trends of the global ocean carbon sink. *Global Biogeochem. Cycles*, **30**, 1396–1417, https://doi.org/10.1002/2015GB005359.

Lankhorst, M., and U. Send, 2020: Uncertainty of North Atlantic Current observations from altimetry, floats, moorings, and XBT. *Prog. Oceanogr.*, **187**, 102402, https://doi.org/10.1016/j.pocean.2020.102402.

Laufkötter, C., J. Zscheischler, and T. L. Frölicher, 2020: High-impact marine heatwaves attributable to human-induced global warming. *Science*, **369**, 1621–1625, https://doi.org/10.1126/science.aba0690.

Leuliette, E. W., and J. K. Willis, 2011: Balancing the sea level budget. *Oceanography*, **24**, 122–129, https://doi.org/10.5670/oceanog.2011.32.

Le Vine, D. M., E. P. Dinnat, G. S. E. Lagerloef, P. de Matthaeis, S. Abraham, C. Utku, and H. Kao, 2014: Aquarius: Status and recent results. *Radio Sci.*, **49**, 709–720, https://doi.org/10.1002/2014RS005505.

Levitus, S., and Coauthors, 2012: World ocean heat content and thermosteric sea level change (0–2000 m), 1955–2010. *Geophys. Res. Lett.*, **39**, L10603, https://doi.org/10.1029/2012GL051106.

Li, G., L. Cheng, J. Zhu, K. Trenberth, M. Mann, and J. Abraham, 2020: Increasing ocean stratification over the past half-century. *Nat. Climate Change*, **10**, 1116–1123, https://doi.org/10.1038/s41558-020-00918-2.

Liu, W., S.-P. Xie, Z. Liu, and J. Zhu, 2017: Overlooked possibility of a collapsed Atlantic Meridional Overturning Circulation in warming climate. *Sci. Adv.*, **3**, e1601666, https://doi.org/10.1126/sciadv.1601666.

Llovel, W., and L. Terray, 2016: Observed southern upper-ocean warming over 2005–2014 and associated mechanisms. *Environ. Res. Lett.*, **11**, 124023, https://doi.org/10.1088/1748-9326/11/12/124023.

Loeb, N. G., and Coauthors, 2018: Clouds and the Earth's Radiant Energy System (CERES) Energy Balanced and Filled (EBAF) Top-of-Atmosphere (TOA) edition-4.0 data product. *J. Climate*, **31**, 895–918, https://doi.org/10.1175/JCLI-D-17-0208.1.

Long, X., M. J. Widlansky, F. Schloesser, P. R. Thompson, H. Annamalai, M. A. Merrifield, and H. Yoon, 2020: Higher sea levels at Hawaii caused by strong El Niño and weak trade winds. *J. Climate*, **33**, 3037–3059, https://doi.org/10.1175/JCLI-D-19-0221.1.

Lozier, M. S., and Coauthors, 2017: Overturning in the Subpolar North Atlantic Program: A new international ocean observing system. *Bull. Amer. Meteor. Soc.*, **98**, 737–752, https://doi.org/10.1175/BAMS-D-16-0057.1.

——, and Coauthors, 2019: Meridional overturning circulation and the associated heat and freshwater transports observed by the OSNAP (Overturning in the Subpolar North Atlantic Program) Array from 2014 to 2016. Duke Digital Repository, accessed 29 January 2021, https://doi.org/10.7924/r4z60gf0f.

Lumpkin, R., and S. Garzoli, 2011: Interannual to decadal changes in the western South Atlantic's surface circulation. *J. Geophys. Res.*, **116**, C01014, https://doi.org/10.1029/2010JC006285.

——, and G. C. Johnson, 2013: Global ocean surface velocities from drifters: Mean, variance, El Nino–Southern Oscillation response, and seasonal cycle. *J. Geophys. Res. Oceans*, **118**, 2992–3006, https://doi.org/10.1002/jgrc.20210.

——, G. Goni, and K. Dohan, 2011: State of the ocean in 2010: Surface currents [in "State of the Climate in 2010"]. *Bull. Amer. Meteor. Soc.*, **92** (6), S92–S95, https://doi.org/10.1175/1520-0477-92.6.S1.

Lyman, J. M., and G. C. Johnson, 2014: Estimating global ocean heat content changes in the upper 1800 m since 1950 and the influence of climatology choice. *J. Climate*, **27**, 1946–1958, https://doi.org/10.1175/JCLI-D-12-00752.1.

Majumder, S., C. Schmid, and G. Halliwell, 2016: An observations and model-based analysis of meridional transports in the South Atlantic. *J. Geophys. Res. Oceans*, **121**, 5622–5638, https://doi.org/10.1002/2016JC011693.

McCarthy, G. D., and Coauthors, 2020: Sustainable observations of the AMOC: Methodology and technology. *Rev. Geophys.*, **58**, e2019RG000654, https://doi.org/10.1029/2019RG000654.

McClain, C. R., 2009: A decade of satellite ocean color observations. *Annu. Rev. Mar. Sci.*, **1**, 19–42, https://doi.org/10.1146/annurev.marine.010908.163650.

Meinen, C. S., and Coauthors, 2013: Temporal variability of the meridional overturning circulation at 34.5°S: Results from two pilot boundary arrays in the South Atlantic. *J. Geophys. Res. Oceans*, **118**, 6461–6478, https://doi.org/10.1002/2013JC009228.

——, and Coauthors, 2018: Meridional overturning circulation transport variability at 34.5°S during 2009–2017: Baroclinic and barotropic flows and the dueling influence of the boundaries. *Geophys. Res. Lett.*, **45**, 4180–4188, https://doi.org/10.1029/2018GL077408.

——, R. H. Smith, and R. F. Garcia, 2021: Evaluating pressure gauges as a potential future replacement for electromagnetic cable observations of the Florida Current transport at 27°N. *J. Oper. Oceanogr.*, 14, 166–176, https://doi.org/10.1080/1755876X.2020.1780757.

Merrifield, M., 2011: A shift in western tropical Pacific sea level trends during the 1990s. *J. Climate*, **24**, 4126–4138, https://doi.org/10.1175/2011JCLI3932.1.

Midorikawa, T., and Coauthors, 2010: Decreasing pH trend estimated from 25-yr time-series of carbonate parameters in the western North Pacific. *Tellus*, **62B**, 649–659, https://doi.org/10.1111/j.1600-0889.2010.00474.x.

Moat, B. I., and Coauthors, 2020a: Pending recovery in the strength of the meridional overturning circulation at 26°N. *Ocean Sci.*, **16**, 863–874, https://doi.org/10.5194/os-16-863-2020.

——, and Coauthors, 2020b: Atlantic meridional overturning circulation observed by the RAPID-MOCHA-WBTS (RAPID-Meridional Overturning Circulation and Heatflux Array-Western Boundary Time Series) array at 26N from 2004 to 2018 (v2018.2). British Oceanographic Data Centre, National Oceanography Centre, accessed 29 January 2021, https://doi.org/10/d3z4.

Nagura, M., and M. J. McPhaden, 2010: Wyrtki jet dynamics: Seasonal variability. *J. Geophys. Res.*, **115**, C07009, https://doi.org/10.1029/2009JC005922.

Nerem, R. S., B. D. Beckley, J. T. Fasullo, B. D. Hamlington, D. Masters, and G. T. Mitchum, 2018: Climate-change-driven accelerated sea-level rise detected in the altimeter era. *Proc. Natl. Acad. Sci. USA*, **115**, 2022–2025, https://doi.org/10.1073/pnas.1717312115.

NOAA, 2019: New marine heatwave emerges off West Coast, resembles "the Blob." NOAA, accessed 11 February 2021, www.fisheries.noaa.gov/feature-story/new-marine-heatwave-emerges-west-coast-resembles-blob.

——, 2020: String of marine heatwaves continues to dominate Northeast Pacific. NOAA, accessed 11 February 2021, www.fisheries.noaa.gov/feature-story/string-marine-heatwaves-continues-dominate-northeast-pacific.

Oliver, E. C. J., 2019: Mean warming not variability drives marine heatwave trends. *Climate Dyn.*, **53**, 1653–1659, https://doi.org/10.1007/s00382-019-04707-2.

——, J. A. Benthuysen, N. L. Bindoff, A. J. Hobday, N. J. Holbrook, C. N. Mundy, and S. E. Perkins-Kirkpatrick, 2017: The unprecedented 2015/16 Tasman Sea marine heatwave. *Nat. Commun.*, **8**, 16101 https://doi.org/10.1038/ncomms16101.

Olsen, A., and Coauthors, 2016: The Global Ocean Data Analysis Project version 2 (GLODAPv2) – An internally consistent data product for the world ocean. *Earth Syst. Sci. Data*, **8**, 297–323, https://doi.org/10.5194/essd-8-297-2016.

——, and Coauthors, 2020: An updated version of the global interior ocean biogeochemical data product, GLODAPv2.2020. *Earth Syst. Sci. Data*, **12**, 3653–3678, https://doi.org/10.5194/essd-12-3653-2020.

Ono, H., and Coauthors, 2019: Acceleration of ocean acidification in the western North Pacific. *Geophys. Res. Lett.*, **46**, 13 161–13 169, https://doi.org/10.1029/2019GL085121.

Palmer, M. D., K. Haines, S. F. B. Tett, and T. J. Ansell, 2007: Isolating the signal of ocean global warming. *Geophys. Res. Lett.*, **34**, L23610, https://doi.org/10.1029/2007GL031712.

Perkins-Kirkpatrick, S. E., A. D. King, E. A. Cougnon, N. J. Holbrook, M. R. Grose, E. C. J. Oliver, S. C. Lewis, and F. Pourasghar, 2019: The role of natural variability and anthropogenic climate change in the 2017/18 Tasman Sea marine heatwave. *Bull. Amer. Meteor. Soc.*, **100**, S105–S110, https://doi.org/10.1175/BAMS-D-18-0116.1.

Pond, S., and G. L. Pickard, 1983: *Introductory Dynamical Oceanography*. 2nd ed. Pergamon Press, 349 pp.

Purkey, S. G., and G. C. Johnson, 2010: Warming of global abyssal and deep Southern Ocean waters between the 1990s and 2000s: Contributions to global heat and sea level rise budgets. *J. Climate*, **23**, 6336–6351, https://doi.org/10.1175/2010JCLI3682.1.

Qiu, B., and S. Chen, 2005: Variability of the Kuroshio extension jet, recirculation gyre, and mesoscale eddies on decadal time scales. *J. Phys. Oceanogr.*, **35**, 2090–2103, https://doi.org/10.1175/JPO2807.1.

Qu, T., S. Gao, and I. Fukumori, 2011: What governs the sea surface salinity maximum in the North Atlantic? *Geophys. Res. Lett.*, **38**, L07602, https://doi.org/10.1029/2011GL046757.

Reagan, J., T. Boyer, C. Schmid, and R. Locarnini, 2019: Subsurface salinity [in "State of the Climate in 2018"]. *Bull. Amer. Meteor. Soc.*, **100** (9), S79–S81, https://doi.org/10.1175/2019BAMSStateoftheClimate.1.

——, ——, ——, and ——, 2020: Subsurface salinity [in "State of the Climate in 2019"] . *Bull. Amer. Meteor. Soc.*, **101** (8), S144–S148, https://doi.org/10.1175/2020BAMSStateoftheClimate.1.

Ren, L., K. Speer, and E. P. Chassignet, 2011: The mixed layer salinity budget and sea ice in the Southern Ocean. *J. Geophys. Res.*, **116**, C08031, https://doi.org/10.1029/2010JC006634.

Resplandy, L., and Coauthors, 2018: Revision of global carbon fluxes based on a reassessment of oceanic and riverine carbon transport. *Nat. Geosci.*, **11**, 504–509, https://doi.org/10.1038/s41561-018-0151-3.

Rhein, M., and Coauthors, 2013: Observations: Ocean. *Climate Change 2013: The Physical Science Basis*, T. F. Stocker et al., Eds., Cambridge University Press, 255–315

Riser, S. C., and Coauthors, 2016: Fifteen years of ocean observations with the global Argo array. *Nat. Climate Change*, **6**, 145–153, https://doi.org/10.1038/nclimate2872.

Rödenbeck, C., and Coauthors, 2015: Data-based estimates of the ocean carbon sink variability—First results of the Surface Ocean pCO2 Mapping intercomparison (SOCOM). *Biogeosciences*, **12**, 7251–7278, https://doi.org/10.5194/bg-12-7251-2015.

Roemmich, D., and J. Gilson, 2009: The 2004–2008 mean and annual cycle of temperature, salinity, and steric height in the global ocean from the Argo Program. *Prog. Oceanogr.*, **82**, 81–100, https://doi.org/10.1016/j.pocean.2009.03.004.

——, and ——, 2011: The global ocean imprint of ENSO. *Geophys. Res. Lett.*, **38**, L13606, https://doi.org/10.1029/2011GL047992.

Saji, N. H., B. N. Goswami, P. N. Vinayachandran, and T. Yamagata, 1999: A dipole mode in the tropical Indian Ocean. *Nature*, **401**, 360–363, https://doi.org/10.1038/43854.

Sanchez-Franks, A., E. Frajka-Williams, B. I. Moat, and D. A. Smeed, 2021: A dynamically based method for estimating the Atlantic overturning circulation at 26° N from satellite altimetry. *Ocean Sci. Discuss*, https://doi.org/10.5194/os-2021-10.

Scannell, H. A., A. J. Pershing, M. A. Alexander, A. C. Thomas, and K. E. Mills, 2016: Frequency of marine heatwaves in the North Atlantic and North Pacific since 1950. *Geophys. Res. Lett.*, **43**, 2069–2076, https://doi.org/10.1002/2015GL067308.

——, G. C. Johnson, L. Thompson, J. M. Lyman, and S. C. Riser, 2020: Subsurface evolution and persistence of marine heatwaves in the Northeast Pacific. *Geophys. Res. Lett.*, **47**, e2020GL090548, https://doi.org/10.1029/2020GL090548.

Schlesinger, M. E., and N. Ramankutty, 1994: An oscillation in the global climate system of period 65–70 years. *Nature*, **367**, 723–726, https://doi.org/10.1038/367723a0.

Schmidtko, S., K. J. Heywood, A. F. Thompson, and S. Aoki, 2014: Multidecadal warming of Antarctic waters. *Science*, **346**, 1227–1231, https://doi.org/10.1126/science.1256117.

Schmitt, R. W., 1995: The ocean component of the global water cycle. *Rev. Geophys.*, **33**, 1395–1409, https://doi.org/10.1029/95RG00184.

——, 2008: Salinity and the global water cycle. *Oceanography*, **21**, 12–19, https://doi.org/10.5670/oceanog.2008.63.

Siegel, D. A., S. Maritorena, N. B. Nelson, M. J. Behrenfeld, and C. R. McClain, 2005: Colored dissolved organic matter and its influence on the satellite-based characterization of the ocean biosphere. *Geophys. Res. Lett.*, **32**, L20605, https://doi.org/10.1029/2005GL024310.

——, and Coauthors, 2013: Regional to global assessments of phytoplankton dynamics from the SeaWiFS mission. *Remote Sens. Environ.*, **135**, 77–91, https://doi.org/10.1016/j.rse.2013.03.025.

Skliris, N., R. Marsh, S. A. Josey, S. A. Good, C. Liu, and R. P. Allan, 2014: Salinity changes in the World Ocean since 1950 in relation to changing surface freshwater flux. *Climate Dyn.*, **43**, 709–736, https://doi.org/10.1007/s00382-014-2131-7.

Smale, D. A., and Coauthors, 2019: Marine heatwaves threaten global biodiversity and the provision of ecosystem services. *Nat. Climate Change*, **9**, 302–312, https://doi.org/10.1038/s41558-019-0412-1.

Stackhouse, P. W., D. P. Kratz, G. R. McGarragh, S. K. Gupta, and E. B. Geier, 2006: Fast longwave and shortwave radiative flux (FLASHFlux) products from CERES and MODIS measurements. 12th Conf. on Atmospheric Radiation, Amer. Meteor. Soc., Madison, WI, P1.10, https://ams.confex.com/ams/Madison2006/techprogram/paper_113479.htm.

Sutton, A. J., and Coauthors, 2019: Autonomous seawater pCO2 and pH time series from 40 surface buoys and the emergence of anthropogenic trends. *Earth Syst. Sci. Data*, **11**, 421–439, https://doi.org/10.5194/essd-11-421-2019.

Sweet, W.V., J. Park, J. J. Marra, C. Zervas, and S. Gill, 2014: Sea level rise and nuisance flood frequency changes around the United States. NOAA Tech. Rep. NOS CO-OPS 073, 58 pp., https://tidesandcurrents.noaa.gov/publications/NOAA_Technical_Report_NOS_COOPS_073.pdf.

Takahashi, T., and Coauthors, 2009: Climatological mean and decadal change in surface ocean pCO2, and net sea-air CO2 flux over the global oceans. *Deep-Sea Res. II*, **56**, 554–577, https://doi.org/10.1016/j.dsr2.2008.12.009.

——, S. C. Sutherland, D. W. Chipman, J. G. Goddard, C. Ho, T. Newberger, C. Sweeney, and D. R. Munro, 2014: Climatological distributions of pH, pCO2, total CO2, alkalinity, and CaCO3 saturation in the global surface ocean, and temporal changes at selected locations. *Mar. Chem.*, **164**, 95–125, https://doi.org/10.1016/j.marchem.2014.06.004.

——, ——, and A. Kozyr, 2020: Global ocean surface water partial pressure of CO2 database: Measurements performed during 1957–2019 (LDEO database version 2019) (NCEI accession 0160492). Version 9.9, NOAA National Centers for Environmental Information, accessed 17 December 2020, https://doi.org/10.3334/CDIAC/OTG.NDP088(V2015).

van Heuven, S., D. Pierrot, J. W. B. Rae, E. Lewis, and D. W. R. Wallace, 2011: MATLAB program developed for CO2 system calculations. ORNL/CDIAC-105b. Carbon dioxide Information Analysis Center, Oak Ridge National Laboratory, accessed 25 September 2014, https://doi.org/10.3334/CDIAC/otg.CO2SYS_MATLAB_v1.1.

Volkov, D. L., S.-K. Lee, F. W. Landerer, and R. Lumpkin, 2017: Decade-long deep-ocean warming detected in the subtropical South Pacific. *Geophys. Res. Lett.*, **44**, 927–936, https://doi.org/10.1002/2016GL071661.

——, R. Domingues, C. S. Meinen, R. Garcia, M. Baringer, G. Goni, and R. H. Smith, 2020a: Inferring Florida current volume transport from satellite altimetry. *J. Geophys. Res. Oceans*, **125**, e2020JC016763, https://doi.org/10.1029/2020JC016763.

——, and Coauthors, 2020b: Atlantic meridional overturning circulation and associated heat transport [in "State of the Climate 2019"]. *Bull. Amer. Meteor. Soc.*, **101** (8), S159–S163, https://doi.org/10.1175/2020BAMSStateoftheClimate.1.

Von Storch, H., and F. W. Zwiers, 1999: *Statistical Analysis in Climate Research*. Cambridge University Press, 484 pp.

Wallace, J. M., and D. S. Gutzler, 1981: Teleconnections in the geopotential height field during the Northern Hemisphere Winter. *Mon. Wea. Rev.*, **109**, 784–812, https://doi.org/10.1175/1520-0493(1981)109<0784:TITGHF>2.0.CO;2.

Wang, J., and B. Yang, 2017: Internal and external forcing of multidecadal Atlantic climate variability over the past 1,200 years. *Nat. Geosci.*, **10**, 512–517, https://doi.org/10.1038/ngeo2962.

Wanninkhof, R., 2014: Relationship between wind speed and gas exchange over the ocean revisited. *Limnol. Oceanogr. Methods*, **12**, 351–362, https://doi.org/10.4319/lom.2014.12.351.

——, and Coauthors, 2013: Global ocean carbon uptake: Magnitude, variability, and trends. *Biogeosciences*, **10**, 1983–2000, https://doi.org/10.5194/bg-10-1983-2013.

WCRP Global Sea Level Budget Group, 2018: Global sea-level budget 1993–present. *Earth Syst. Sci. Data*, **10**, 1551–1590, https://doi.org/10.5194/essd-10-1551-2018.

Werdell, P. J., and Coauthors, 2013: Generalized ocean color inversion model for retrieving marine inherent optical properties. *Appl. Opt.*, **52**, 2019–2037, https://doi.org/10.1364/AO.52.002019.

——, and Coauthors, 2019: The Plankton, Aerosol, Cloud, Ocean Ecosystem mission: Status, science, advances. *Bull. Amer. Meteor. Soc.*, **100**, 1775–1794, https://doi.org/10.1175/BAMS-D-18-0056.1.

Westberry, T. K., and Coauthors, 2016: Annual cycles of phytoplankton biomass in the subarctic Atlantic and Pacific Ocean. *Global Biogeochem. Cycles*, **30**, 175–190, https://doi.org/10.1002/2015GB005276.

Widlansky, M. J., X. Long, and F. Schloesser, 2020: Increase in sea level variability with ocean warming associated with the nonlinear thermal expansion of seawater. *Commun. Earth Environ.*, **1**, 9, https://doi.org/10.1038/s43247-020-0008-8.

Willis, J. K., D. Roemmich, and B. Cornuelle, 2004: Interannual variability in upper ocean heat content, temperature, and thermosteric expansion on global scales. *J. Geophys. Res.*, **109**, C12036, https://doi.org/10.1029/2003JC002260.

Wolter, K., and M. S. Timlin, 1998: Measuring the strength of ENSO events: How does 1997/98 rank? *Weather*, **53**, 315–324, https://doi.org/10.1002/j.1477-8696.1998.tb06408.x.

Wu, L. X., and Coauthors, 2012: Enhanced warming over the global subtropical western boundary currents. *Nat. Climate Change*, **2**, 161–166, https://doi.org/10.1038/nclimate1353.

Wüst, G., 1936: Oberflächensalzgehalt, Verdunstung und Niederschlag auf dem Weltmeere. Länderkundliche Forschung: Festschrift zur Vollendung des sechzigsten Lebensjahres Norbert Krebs, J. Engelhorns Nachfahren, 347–359.

Xie, P., and Coauthors, 2014: An in situ-satellite blended analysis of global sea surface salinity. *J. Geophys. Res. Oceans*, **119**, 6140–6160, https://doi.org/10.1002/2014JC010046.

Yu, L., and R. A. Weller, 2007: Objectively analyzed air–sea heat fluxes for the global ice-free oceans (1981–2005). *Bull. Amer. Meteor. Soc.*, **88**, 527–540, https://doi.org/10.1175/BAMS-88-4-527.

——, X. Jin, P. W. Stackhouse, A. C. Wilber, S. Kato, N. G. Loeb, and R. A. Weller, 2019: Global ocean heat, freshwater, and momentum fluxes [in "State of the Climate in 2018"]. *Bull. Amer. Meteor. Soc.*, **100** (9), S81–S84, https://doi.org/10.1175/2019BAMSStateoftheClimate.1.

Zebiak, S. E., 1993: Air–sea interaction in the Equatorial Atlantic region. *J. Climate*, **6**, 1567–1568, https://doi.org/10.1175/1520-0442(1993)006<1567:AIITEA>2.0.CO;2.

Zhang, R., and Coauthors, 2019: A review of the role of the Atlantic meridional overturning circulation in Atlantic multidecadal variability and associated climate impacts. *Rev. Geophys.*, **57**, 316–375, https://doi.org/10.1029/2019RG000644.

Zweng, M. M., and Coauthors, 2013: Salinity. Vol. 2, World Ocean Atlas 2013, NOAA Atlas NESDIS 74, 39 pp., http://data.nodc.noaa.gov/woa/WOA13/DOC/woa13_vol2.pdf.

STATE OF THE CLIMATE IN 2020

THE TROPICS

H. J. Diamond and C. J. Schreck, Eds.

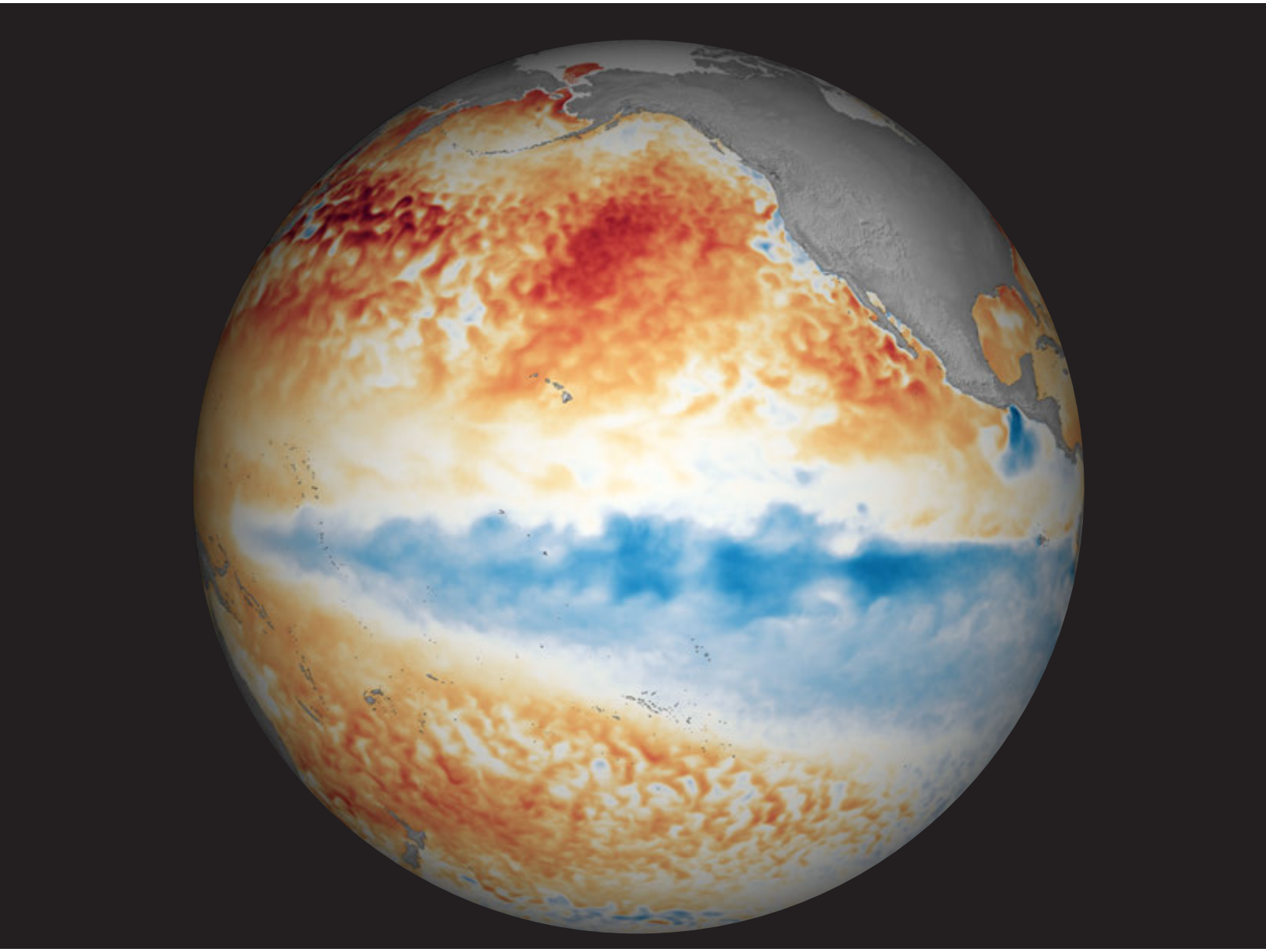

Special Online Supplement to the *Bulletin of the American Meteorological Society* Vol.102, No. 8, August, 2021

https://doi.org/10.1175/BAMS-D-21-0080.1

Corresponding author: Howard J. Diamond / howard.diamond@noaa.gov

STATE OF THE CLIMATE IN 2020
THE TROPICS

Editors

Jessica Blunden
Tim Boyer

Chapter Editors

Freya Aldred
Peter Bissolli
Howard J. Diamond
Matthew L. Druckenmiller
Robert J. H. Dunn
Catherine Ganter
Nadine Gobron
Gregory C. Johnson
Tim Li
Rick Lumpkin
Ademe Mekonnen
John B. Miller
Twila A. Moon
Ahira Sánchez-Lugo
Ted A. Scambos
Carl J. Schreck III
Sharon Stammerjohn
Richard L. Thoman
Kate M. Willett

Technical Editor

Andrea Andersen

***BAMS* Special Editor for Climate**

Michael A. Alexander

American Meteorological Society

Cover credit:
Sea surface temperature (SST) anomalies along the equatorial Pacific in November 2020 compared to the long-term 30-year average from 1981–2010; the blue colors across the equatorial Pacific Ocean indicate below-normal SSTs that are a key and canonical feature associated with the La Niña conditions in place at the time.

The Tropics is one chapter from the *State of the Climate in 2020* annual report and is available from https://doi.org/10.1175/BAMS-D-21-0080.1. Compiled by NOAA's National Centers for Environmental Information, *State of the Climate in 2020* is based on contributions from scientists from around the world. It provides a detailed update on global climate indicators, notable weather events, and other data collected by environmental monitoring stations and instruments located on land, water, ice, and in space. The full report is available from https://doi.org/10.1175/2021BAMSStateoftheClimate.1.

How to cite this document:

Citing the complete report:
Blunden, J. and T. Boyer, Eds., 2021: "State of the Climate in 2020". *Bull. Amer. Meteor. Soc.*, **102** (8), Si–S475, https://doi.org/10.1175/2021BAMSStateoftheClimate.1.

Citing this chapter:
Diamond, H.J. and C. J. Schreck, Eds., 2021: The Tropics [in "State of the Climate in 2020"]. *Bull. Amer. Meteor. Soc.*, **102** (8), S199–S261, https://doi.org/10.1175/BAMS-D-21-0080.1.

Citing a section (example):
Domingues, R., G. J. Goni, J. A. Knaff, I-I Lin, and F. Bringas, 2021: Tropical cyclone heat potential [in "State of the Climate in 2020"]. *Bull. Amer. Meteor. Soc.*, **102** (8), S252–S255, https://doi.org/10.1175/BAMS-D-21-0080.1.

Editor and Author Affiliations (alphabetical by name)

Becker, Emily, J., University of Miami Rosenstiel School of Marine & Atmospheric Science, Miami, Florida
Bell, Gerald D., NOAA/NWS Climate Prediction Center, College Park, Maryland
Blake, Eric S., NOAA/NWS National Hurricane Center, Miami, Florida
Bond, Stephanie, Australian Bureau of Meteorology, Perth, Australia
Bringas, Francis G., NOAA/OAR Atlantic Oceanographic and Meteorological Laboratory, Miami, Florida
Camargo, Suzana J., Lamont-Doherty Earth Observatory, Columbia University, Palisades, New York
Chen, Lin, Institute for Climate and Application Research (ICAR)/KLME/ILCEC/CIC-FEMD, Nanjing University of Information Science and Technology, Nanjing, China
Coelho, Caio A. S., CPTEC/INPE Center for Weather Forecast and Climate Studies, National Institute for Space Research, Cachoeira Paulista, Brazil
Diamond, Howard J., NOAA/OAR Air Resources Laboratory, College Park, Maryland
Domingues, Ricardo, Cooperative Institute for Marine and Atmospheric Studies, University of Miami, Miami, Florida
Goldenberg, Stanley B., NOAA/OAR/AOML Hurricane Research Division, Miami, Florida
Goni, Gustavo, NOAA/OAR/AOML Hurricane Research Division, Miami, Florida
Fauchereau, Nicolas, National Institute of Water and Atmospheric Research, Ltd., Auckland, New Zealand
Halpert, Michael S., NOAA/NWS Climate Prediction Center, College Park, Maryland
He, Qiong, Earth System Modeling Center, Nanjing University of Information Science and Technology, Nanjing, China
Klotzbach, Philip J., Department of Atmospheric Science, Colorado State University, Fort Collins, Colorado
Knaff, John A., NOAA/NESDIS Center for Satellite Applications and Research, Fort Collins, Colorado
L'Heureux, Michelle, NOAA/NWS Climate Prediction Center, College Park, Maryland
Landsea, Chris W., NOAA/NWS National Hurricane Center, Miami, Florida
Lin, I.-I., National Taiwan University, Taipei, Taiwan
Lorrey, Andrew M., National Institute of Water and Atmospheric Research, Ltd., Auckland, New Zealand
Luo, Jing-Jia, Institute for Climate and Application Research (ICAR)/KLME/ILCEC/CIC-FEMD, Nanjing University of Information Science and Technology, Nanjing, China
MacRitchie, Kyle, NOAA/NWS Climate Prediction Center, College Park, Maryland
Magee, Andrew D., Centre for Water, Climate and Land, School of Environmental and Life Sciences, University of Newcastle, Callaghan, NSW, Australia
Noll, Ben, National Institute of Water and Atmospheric Research, Ltd., Auckland, New Zealand
Pasch, Richard J., NOAA/NWS National Hurricane Center, Miami, Florida
Pezza, Alexandre B., Greater Wellington Regional Council, Wellington, New Zealand
Rosencrans, Matthew, NOAA/NWS Climate Prediction Center, College Park, Maryland
Schreck III, Carl J., North Carolina State University, Cooperative Institute for Climate and Satellites–North Carolina (CICS-NC), Asheville, North Carolina
Tippet, Michael K., Department of Applied Physics and Applied Mathematics, Columbia University, New York, New York
Trewin, Blair C., Australian Bureau of Meteorology, Melbourne, Victoria, Australia
Truchelut, Ryan E., "WeatherTiger," Tallahassee, Florida
Wang, Bin, Department of Atmospheric Science and IPRC, University of Hawaii, Honolulu, Hawaii
Wang, Hui, NOAA/NWS Climate Prediction Center, College Park, Maryland
Wood, Kimberly M., Department of Geosciences, Mississippi State University, Mississippi State, Mississippi
Woolley, John-Mark, National Institute of Water and Atmospheric Research, Ltd., Auckland, New Zealand
Young, Steven, H., Independent Researcher, Long Beach, California

Editoral and Production Team

Allen, Jessicca, Graphics Support, Cooperative Institute for Satellite Earth System Studies, North Carolina State University, Asheville, North Carolina
Andersen, Andrea, Technical Editor, Innovative Consulting and Management Services, LLC, NOAA/NESDIS National Centers for Environmental Information, Asheville, North Carolina
Hammer, Gregory, Content Team Lead, Communications and Outreach, NOAA/NESDIS National Centers for Environmental Information, Asheville, North Carolina
Love-Brotak, S. Elizabeth, Lead Graphics Production, NOAA/NESDIS National Centers for Environmental Information, Asheville, North Carolina
Misch, Deborah J., Graphics Support, Innovative Consulting and Management Services, LLC, NOAA/NESDIS National Centers for Environmental Information, Asheville, North Carolina
Riddle, Deborah B., Graphics Support, NOAA/NESDIS National Centers for Environmental Information, Asheville, North Carolina
Veasey, Sara W., Visual Communications Team Lead, Communications and Outreach, NOAA/NESDIS National Centers for Environmental Information, Asheville, North Carolina

4. Table of Contents

*Please refer to Chapter 8 (Relevant datasets and sources) for a list of all climate variables and datasets used in this chapter for analyses, along with their websites for more information and access to the data.

4. THE TROPICS

H. J. Diamond and C. J. Schreck, Eds.

a. Overview—H. J. Diamond and C. J. Schreck

The tropics in 2020 reflected El Niño–Southern Oscillation neutral conditions through June–August, with the index decreasing from positive values during boreal spring to negative values during boreal summer. Starting in July–September (JAS), La Niña thresholds were met, with Oceanic Niño Index (ONI) values decreasing through October–December (OND). In OND 2020, the ONI reached a minimum of –1.3°C, which is considered informally to be a La Niña of moderate strength (ONI values between –1.0°C and –1.4°C). The ONI reached and slightly exceeded the +0.5°C threshold in several seasons during the Northern Hemisphere (NH) winter of 2019/20, but the anomalies were weak and did not last long enough to be considered an El Niño episode.

For the global tropics, combined land and ocean surface temperatures (measured at 20°S–20°N) registered +0.43°C above the 1981–2010 average. This makes 2020 the fourth-warmest year for the tropics since records began in 1880. The five warmest years have all occurred since 2015. Data from the Global Precipitation Climatology Project indicate a mean annual total precipitation value of 1317 mm across the 20°S–20°N latitude band over land. This is 11 mm above the 1981–2010 average and ranks 11th in the 1979–2020 period of record.

Globally, 102 named tropical cyclones (TCs; ≥34 kt; or ≥17 m s^{-1}) were observed during the 2020 NH season (January–December 2020) and the 2019/20 Southern Hemisphere season (July–June 2019/20; Table 4.2), as documented in IBTrACSv4 (Knapp et al. 2010). Overall, this number was well above the 1981–2010 global average of 85 TCs, slightly greater than the 96 TCs reported during 2019 (Diamond and Schreck 2020), and was three storms shy of the record 104 named storms in 1992. The 30 named storms in the North Atlantic during 2020 surpassed the previous record of 28 set in 2005. For the North Atlantic, the 14 hurricanes during 2020 were the second most on record behind the 15 observed in 2005, and the seven major hurricanes were the most on record, tying the seven observed in 2005.

In terms of Accumulated Cyclone Energy (ACE; Bell et al. 2000), all basins were below their 1981–2010 averages except for the North Atlantic and North Indian Ocean basins. The 2020 seasonal ACE value in the North Atlantic was 191.5% of the 1981–2010 median. This value is the sixth highest since 1970 and is above NOAA's threshold (Bell et al 2011) for both an above-normal (120%) and an extremely active (165%) season. There have now been a record five consecutive above-normal seasons, which surpasses the previous record of four set in 1998–2001. In the western North Pacific, Super Typhoons Goni and Haishen and Typhoon Maisak contributed 45% of the seasonal ACE for that basin. The Australian and South Indian Ocean basins were comparatively quiet; each had an ACE that was below normal. The global total ACE was below the average for 1981–2010 at 574×10^4 kt^2 and well below the 795×10^4 kt^2 value recorded in 2019. Three TCs across the globe reached Saffir–Simpson Hurricane Wind Scale (https://www.nhc.noaa.gov/aboutsshws.php) Category 5 intensity level, one in the western North Pacific (Goni), one in the North Indian Ocean (Amphan), and one in the southwest Pacific (Harold).

b. ENSO and the tropical Pacific—M. L'Heureux, E. Becker, M. S. Halpert, Z.-Z. Hu, K. MacRitchie, and M. Tippett

The El Niño–Southern Oscillation (ENSO) is a coupled ocean–atmosphere climate phenomenon across the tropical Pacific Ocean, with opposite phases called El Niño and La Niña. For historical purposes, NOAA's Climate Prediction Center (CPC) classifies and assesses the strength and duration of El Niño and La Niña events using the Oceanic Niño Index (ONI, shown for mid-2019 through 2020 in Fig. 4.1). The ONI is the 3-month (seasonal) running average of sea surface temperature (SST) anomalies in the Niño-3.4 region (5°S–5°N, 170°–120°W), currently calculated as the departure from the 1991–2020 base period mean.[1] El Niño is classified when the ONI is at or greater than +0.5°C for at least five consecutive and overlapping seasons, while La Niña occurs when the ONI is at or less than −0.5°C for at least five consecutive and overlapping seasons.

The ONI reached and slightly exceeded the +0.5°C threshold in several seasons during the Northern Hemisphere winter of 2019/20, but the anomalies were weak and did not last long enough to be considered an El Niño episode. Consequently, NOAA CPC and other agencies (e.g., Australian Bureau of Meteorology and World Meteorological Organization) did not post El Niño advisories or alerts during the boreal winter of 2019/20. At times, intraseasonal variability also contributed to El Niño-like atmospheric anomalies across the tropical Pacific Ocean, especially during mid-January and mid-February (see section 4c).

The ONI reflected ENSO-neutral conditions through June–August (JJA) 2020, with the index decreasing from positive values during boreal spring to negative values during boreal summer. Starting in July–September (JAS), La Niña thresholds were met, with ONI values decreasing through October–December.[2] During this period, the ONI reached a minimum of –1.3°C, which is considered informally to be a La Niña of moderate strength (ONI values between –1.0°C and –1.4°C).

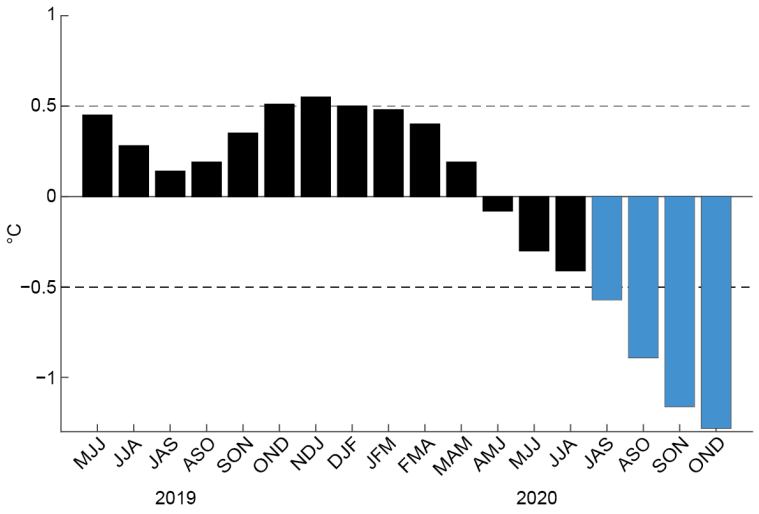

Fig. 4.1. Time series of the ONI (°C) from mid-2019 through 2020. Overlapping 3-month seasons are labeled on the *x*-axis, with initials indicating the first letter of each month in the season. Blue bars indicate negative values that are below –0.5°C. The ONI values are derived from the ERSSTv5 dataset and are based on departures from the 1991–2020 period monthly means (Huang et al. 2017).

1) Oceanic conditions

Figure 4.2 displays the mean SST (left column) and SST anomalies (right column) for four, 3-month periods from December–February (DJF) 2019/20 through September–November (SON) 2020. SST anomalies on the equator during DJF (Fig. 4.2, top row) exceeded +1.0°C near the date line, extending from 170°W to 160°E. The western Pacific warm pool extended farther east than its mean position, with the 30°C isotherm reaching the date line. However, the east-central and eastern equatorial Pacific remained near average during DJF 2019/20.

[1] The ONI is an index measuring a climate phenomenon, ENSO, and for that reason, the base period is updated every 5 years with a rolling 30-year climatology. The rolling climatology is used in part to remove those secular SST trends and focus on the state of ENSO. The 1986–2015 normal was used operationally for 2020, but it was updated to 1991–2020 at the completion of the year.

[2] While the season November 2020–January 2021 (NDJ) is not covered by this review, the NDJ value of the ONI was –1.2°C. Therefore, the period beginning in JAS 2020 is part of an official La Niña episode.

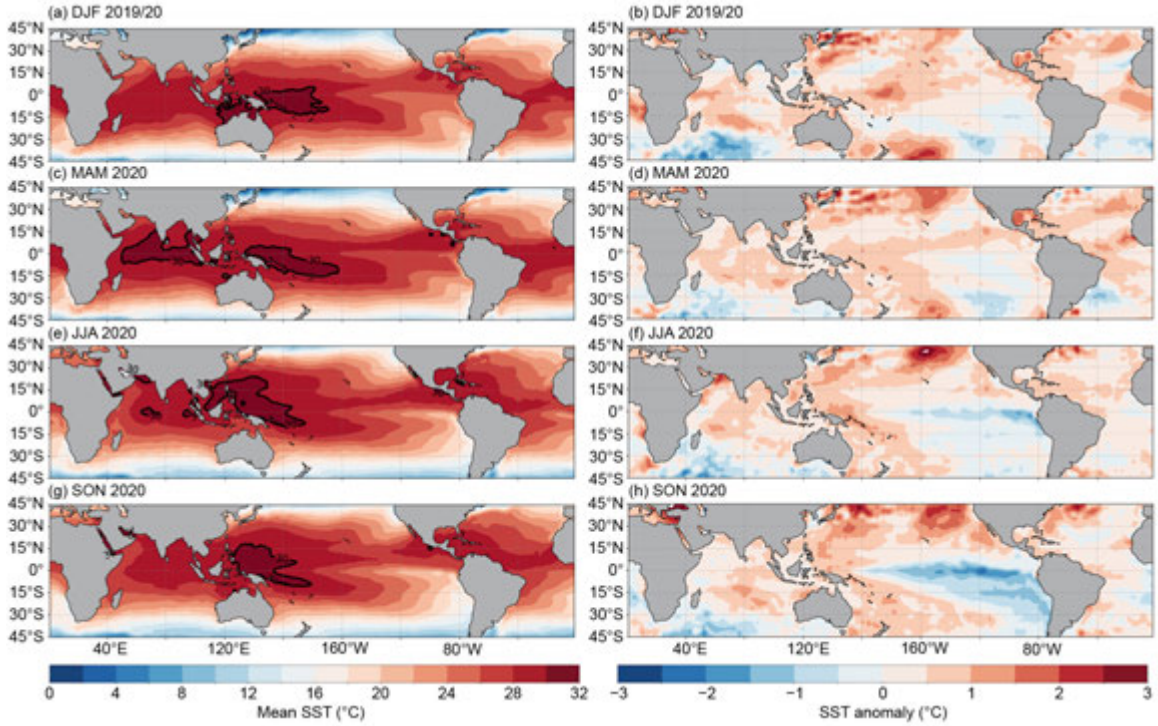

Fig. 4.2. (left) Mean SST and (right) SST anomaly for (°C) (a), (b) DJF 2019/20, (c), (d) MAM 2020, (e), (f) JJA 2020, and (g), (h) SON 2020. The bold contour for total SST is located at 30°C. Anomalies are departures from the 1981–2010 seasonal adjusted OI climatology (Reynolds et al. 2002).

The duration of positive SST anomalies was too short to be considered an El Niño episode, and by March–May (MAM) 2020, anomalies weakened across the equatorial Pacific Ocean (Figs. 4.2a–d). However, SSTs remained elevated in the western equatorial Pacific and extended east-northeast to coastal Central America. While this band of positive SST anomalies projects onto the optimal SST growth pattern that can precede the development of El Niño the following winter (Penland and Sardeshmukh 1995), by SON 2020 the Pacific had instead transitioned to La Niña.

By JJA 2020 (Figs. 4.2e,f), the western Pacific warm pool had retracted farther west and the cold tongue was stronger than average. Negative SST anomalies became more prominent on the equator from ~160°W to the South American coast. During SON 2020 (Figs. 4.2g,h), these negative SST anomalies strengthened and expanded even farther west to the date line. By this season, SST anomalies exceeded –1.0°C across the east-central and eastern equatorial Pacific Ocean. Below-average SSTs were also quite prominent in the southeastern Pacific Ocean, reaching coastal Chile. These subtropical SST anomalies were asymmetric across the hemispheres. Below-average SSTs did not extend into the northeastern Pacific Ocean, which was instead above average.

Consistent with the SST evolution, subsurface temperatures during DJF 2019/20 were above average in the central and eastern equatorial Pacific Ocean (Fig. 4.3a). Near the date line, temperature anomalies in excess of +1.5°C extended from ~150-m depth to the surface. Like those at the surface, the positive subsurface temperature anomalies weakened by MAM (Fig. 4.3b), and, by JJA, negative subsurface temperature anomalies dominated the eastern equatorial Pacific Ocean (Fig. 4.3c). This cooling reflected the shallower oceanic thermocline and increased upwelling that accompanies a developing La Niña. During SON 2020 (Fig. 4.3b), the shoaling of the equatorial thermocline in the eastern Pacific was most apparent relative to earlier in the year, and subsurface temperature anomalies were –4.5°C or cooler at a depth of ~50–100 m. Late in the year, positive temperature anomalies remained weak and confined at depth near the date line and in the western Pacific. The east–west contrast in subsurface temperature anomalies is consistent with the tilt mode of ENSO (Clarke 2010; Kumar and Hu 2014).

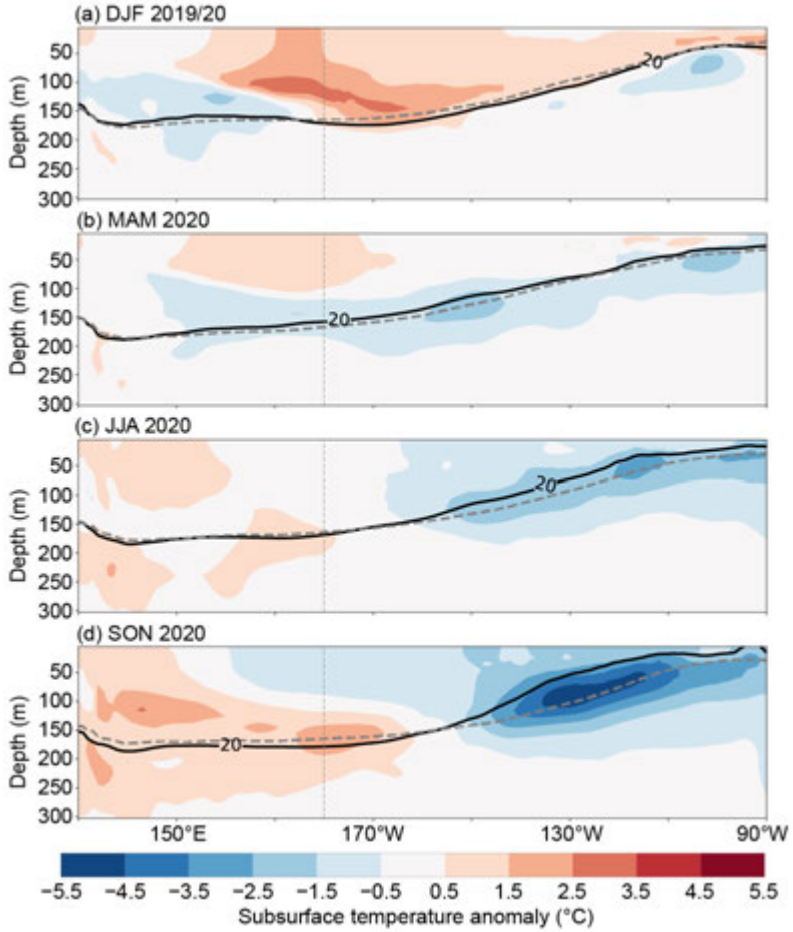

Fig. 4.3. Equatorial depth–longitude section of Pacific Ocean temperature anomalies (°C) averaged between 5°S and 5°N during (a) DJF 2019/20, (b) MAM 2020, (c) JJA 2020, and (d) SON 2020. The 20°C isotherm (thick solid line) approximates the center of the oceanic thermocline. The gray, dashed line shows the climatology of the 20°C isotherm based on 1982–2010. The data are derived from a reanalysis system that assimilates oceanic observations into an oceanic general circulation model (Behringer et al. 1998). Anomalies are departures from the 1982–2010 period monthly means.

2) Atmospheric circulation and precipitation anomalies from December–February 2019/20 to June–August 2020

The pattern of tropical convection and low-level winds during DJF 2019/20 was associated with weak warm SST anomalies (Figs. 4.4–4.6). Specifically, tropical convection (as measured by outgoing longwave radiation [OLR]) was enhanced around the date line (green shading) and suppressed over Indonesia (brown shading; Fig. 4.4a). Low-level (850-hPa) tropical wind anomalies were westerly over the western Pacific Ocean during DJF (Fig. 4.5a). Upper-level (200-hPa) tropical winds were westerly across the central to eastern Pacific Ocean, and were strongest over the eastern Pacific (Fig. 4.6a). Despite the enhanced convection around the date line, the upper-level zonal wind anomalies were not divergent on the equator (though meridional wind anomalies were divergent over the western Pacific, highlighting the lack of a robust circulation response through the entire atmosphere to the underlying SST anomaly pattern). Because the climatological 200-hPa winds are westerly from ~160°W to coastal South America during this season, the upper-branch of the Pacific Walker circulation was stronger than average. The lack of a weak Walker circulation at upper levels, the mild, westward shifted SST anomalies, and the short duration of warming precluded the designation of El Niño conditions during DJF 2019/20. Furthermore, several pulses of enhanced convection occurred near the date line, concurrent with the passage of eastward-propagating intraseasonal disturbances that can be seen in the 200-hPa velocity potential anomalies in early 2020 (see Fig. 4.7).

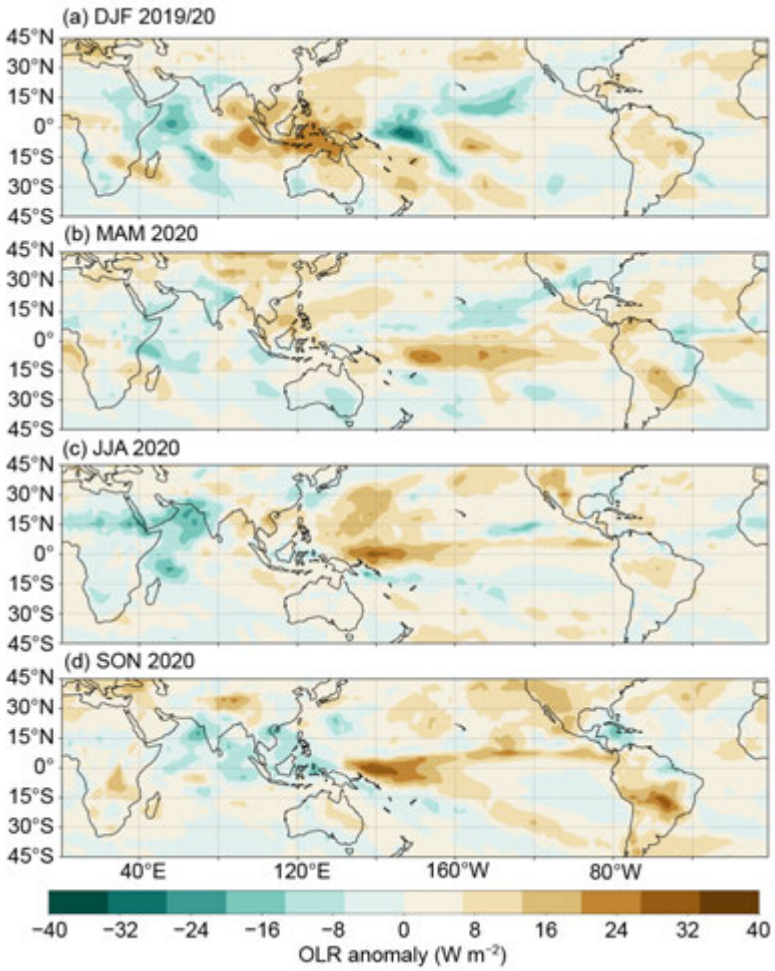

Fig. 4.4. OLR anomalies (shaded, W m^{-2}), during (a) DJF 2019/20, (b) MAM 2020, (c) JJA 2020, and (d) SON 2020. Anomalies are departures from the 1981–2010 period monthly means. Data are from the NCEP/NCAR Reanalysis (Kalnay et al. 1996).

ENSO-neutral conditions continued through JJA though signs of a developing La Niña were evident in anomalies of OLR and winds during the boreal spring and summer. In particular, below-average convection was observed near the date line starting in MAM (Fig. 4.4b). These suppressed OLR anomalies were initially focused south of the equator and became more equatorially confined to the western and central Pacific during JJA (Fig. 4.4c). Low-level trade winds were enhanced, with easterly wind anomalies observed on the equator starting in MAM and continuing through the remainder of 2020 (Figs. 4.5b–d). The strengthening of the upper-level branch of the Walker circulation, first seen in the 200-hPa wind anomalies in DJF 2019/20, also persisted throughout the remainder of the year, with the brief exception of near-average winds in the central Pacific during JJA 2020 (Fig. 4.6c). The upper-level branch of the Walker Circulation became stronger again with the onset of La Niña in SON (Fig. 4.6d).

3) Atmospheric circulation and precipitation anomalies during La Niña (September–November 2020)

As La Niña formed in JAS 2020, its signal increasingly dominated the atmospheric circulation over the tropical Pacific Ocean. A convective anomaly dipole became evident as the Pacific Walker circulation strengthened. Suppressed convection became even more noticeable in the western and central equatorial Pacific during SON (Fig. 4.4d). Enhanced convection appeared around Indonesia, extending northwestward into Southeast Asia and India. Anomalous low-level easterlies were prominent across most of the equatorial Pacific Ocean (Fig. 4.5d) along with anomalous upper-level westerlies overlying them (Fig. 4.6d). These wind anomalies also reflect the further strengthening of the Walker circulation as per Bjerknes (1969).

While global teleconnections are typically strongest following the peak of La Niña in the boreal winter, there were extratropical circulation anomalies that resembled La Niña during SON 2020. In particular, over the North Pacific Ocean, the retraction of the East Asia–North Pacific jet stream was evident in the easterly wind anomalies from ~20°N to 40°N (Fig. 4.6d). This signal was hemispherically symmetric, with a weakened jet stream also apparent across the middle latitudes of the South Pacific Ocean. A wave train with positive height anomalies around New Zealand, negative height anomalies near West Antarctica, and positive height anomalies east of Argentina is reminiscent of the Pacific–South America pattern (Mo and Higgins 1998).

In addition to suppressed precipitation over Indonesia and Southeast Asia, La Niña is typically associated with below-average precipitation anomalies over parts of the southwestern United States and coastal southern Alaska, which indeed emerged during SON. Southern Brazil, Chile, and Argentina, experienced below-average precipitation in SON, which has been shown to be influenced by La Niña conditions (Ropelewski and Halpert 1989).

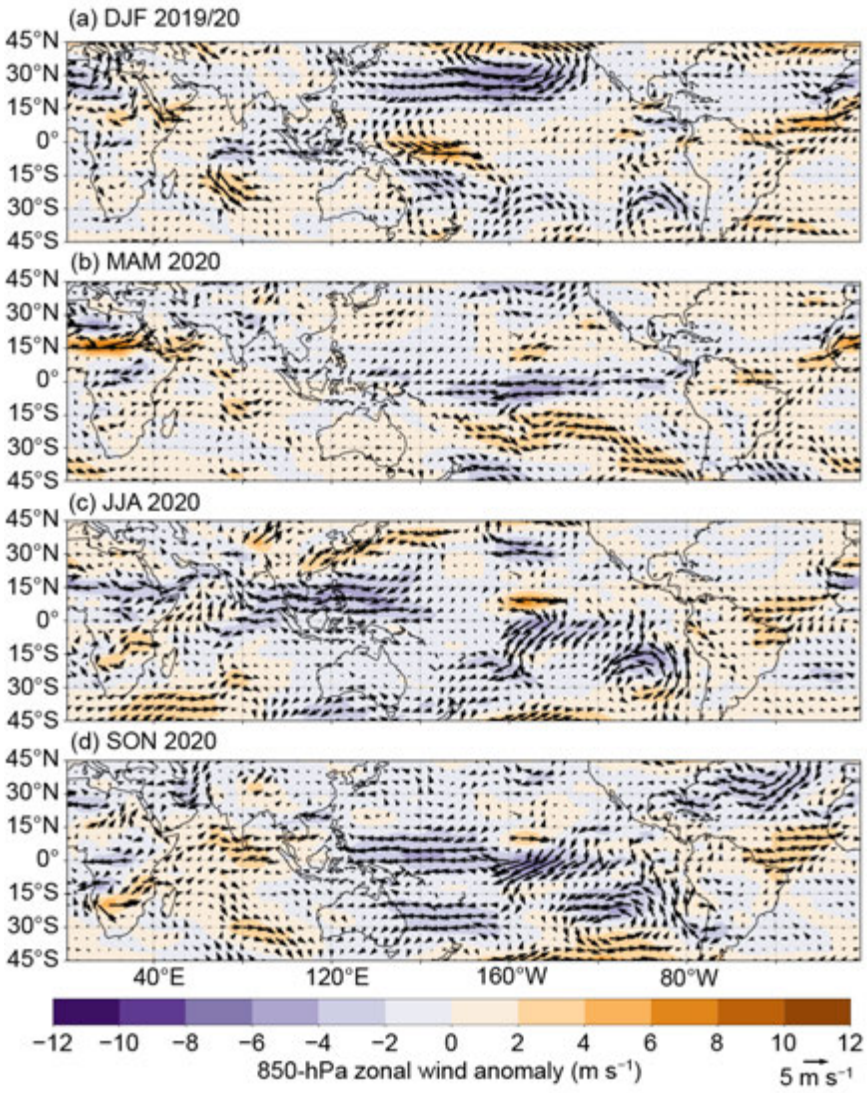

Fig. 4.5. Anomalous 850-hPa wind vectors and zonal wind speed during (a) DJF 2019/20, (b) MAM 2020, (c) JJA 2020, and (d) SON 2020. The reference wind vector is located at the bottom right. Anomalies are departures from the 1981–2010 period monthly means. Data are from the NCEP/NCAR Reanalysis (Kalnay et al. 1996).

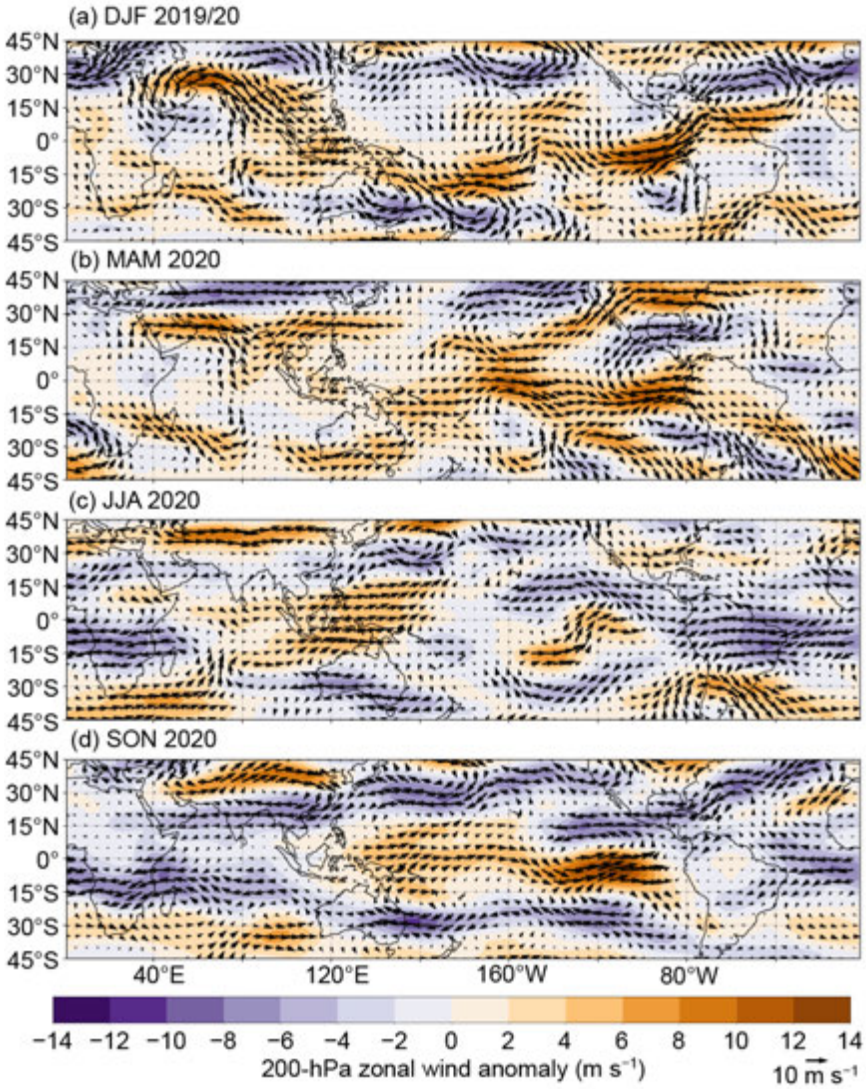

Fig. 4.6. Anomalous 200-hPa wind vectors and zonal wind speed during (a) DJF 2019/20, (b) MAM 2020, (c) JJA 2020, and (d) SON 2020. The reference wind vector is located at the bottom right. Anomalies are departures from the 1981–2010 period monthly means. Data are from the NCEP/NCAR Reanalysis (Kalnay et al. 1996).

c. Tropical intraseasonal activity—K. MacRitchie and C. Schreck

The Madden-Julian Oscillation (MJO; Madden and Julian 1971, 1972, 1994; Zhang 2005) and convectively coupled equatorial wave activity (Wheeler and Kiladis 1999; Kiladis et al. 2009) are the primary modes of tropical intraseasonal variability. The MJO is the leading mode of intraseasonal variability in the tropics and is characterized by an eastward-propagating convective envelope generally traverses the globe in 30–60 days. Other convectively coupled equatorial waves, such as atmospheric Kelvin and equatorial Rossby waves, are typically zonally narrower and faster than the MJO. All of these waves affect weather patterns around the globe, though the MJO has the most robust connections with midlatitude synoptic circulations (Knutson and Weickmann 1987; Kiladis and Weickmann 1992; Mo and Kousky 1993; Kousky and Kayano 1994; Kayano and Kousky 1999; Cassou 2008; Lin et al. 2009; Riddle et al. 2012; Schreck et al. 2013; Baxter et al. 2014) and can impact monsoons (Krishnamurti and Subrahmanyam 1982; Lau and Waliser 2012) and tropical cyclones (Mo 2000; Frank and Roundy 2006; Camargo et al. 2009; Schreck et al. 2012; Diamond and Renwick 2015).

The MJO is often episodic, with periods of moderate-to-strong activity followed by little or no activity (e.g., Matthews 2008). Common metrics for identifying the MJO include time–longitude plots of anomalous 200-hPa velocity potential and outgoing longwave radiation (OLR; Fig. 4.7) and the Wheeler-Hendon (2004) Real-time Multivariate MJO (RMM) index (Fig. 4.8). In the time–longitude

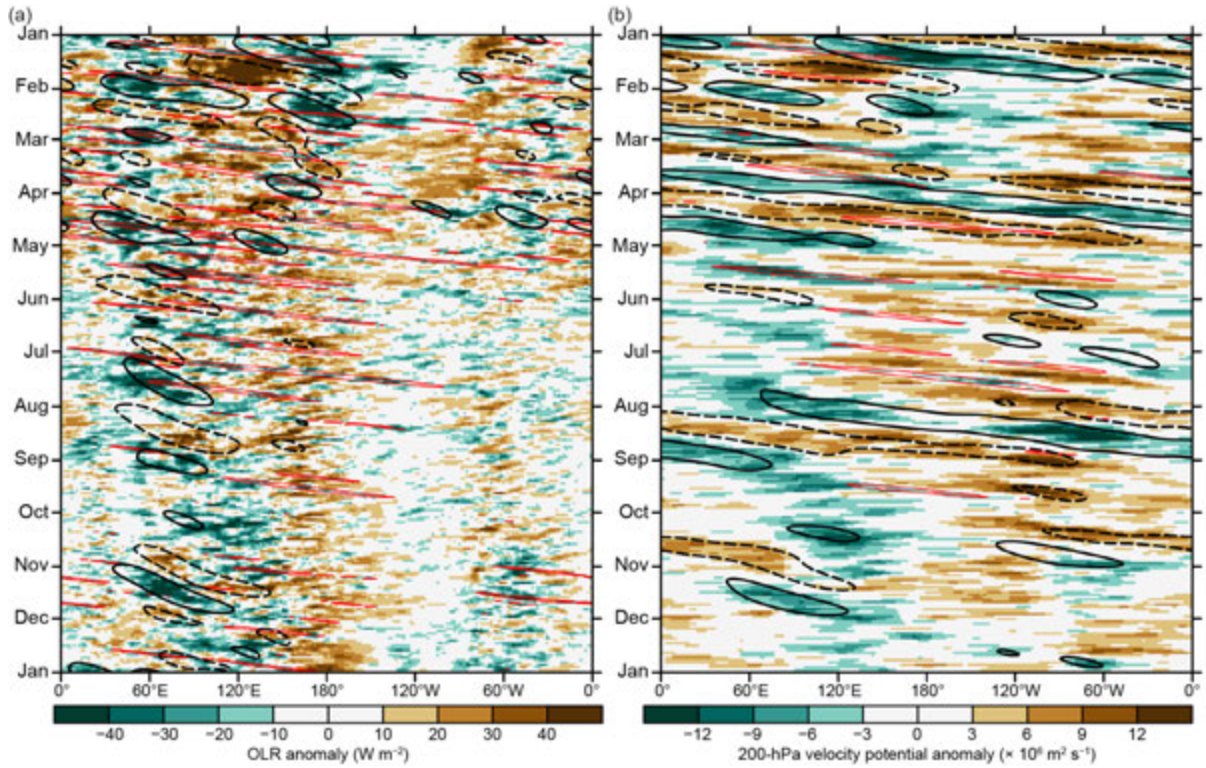

Fig. 4.7. Time–longitude section of (a) OLR (Schreck et al. 2018) anomalies (W m^{-2}) and (b) 200-hPa velocity potential anomalies (× 10^6 m^2 s^{-1}) from the CFSR (Saha et al. 2014). Both variables are averaged over 10°S–10°N. Time increases downward on this graph, beginning with Jan 2020 at the top and ending with Jan 2021 at the bottom. Negative anomalies (green) indicate enhanced convection, and positive anomalies (brown) indicate suppressed convection. Contours identify anomalies filtered for the MJO (black) and atmospheric Kelvin waves (red). Contours are drawn at ±12 W m^{-2} and ±4 × 10^6 m^2 s^{-1} with the enhanced (suppressed) convective phase of these phenomena indicated by solid (dashed) contours. Anomalies are departures from the 1981–2010 base period daily means.

plots, the MJO exhibits eastward propagation from upper-left to lower-right. In the RMM plots, the MJO propagation and intensity are seen as large, counter-clockwise circles around the origin.

The MJO was more active during the first 5 months of 2020 than it was during the remainder of the year (Fig. 4.7, black contours). The strongest MJO activity occurred during January (Fig. 4.8), with a zonal wave number 1 pattern across the tropical strip. The RMM index showed an especially prominent signal over the Maritime Continent during mid-January (Fig. 4.8a), which then weakened during February before strengthening again over the Indian Ocean during March. This period of MJO activity projected more strongly onto the 200-hPa velocity potential anomaly field (Fig. 4.7b) than the OLR anomaly field (Fig. 4.7a) or the 850-hPa zonal wind anomaly field (Fig. 4.9a), which is a common characteristic of MJO events (Straub 2013).

The high-amplitude MJO activity coincided with a period of anomalously high sea surface temperatures (SSTs) in the central and eastern Pacific (Fig. 4.2), resulting in positive Oceanic Nino Index values (Fig. 4.1) and El Niño-like OLR anomalies (Fig. 4.7a). Strong MJO activity often precedes El Niño events, but is often weak during La Niña events (Hendon et al. 1999; Zhang and Gottschalck 2002; Zhang 2005). Zonal wind anomalies at 850-hPa were also enhanced during this period (Fig. 4.9a), with westerly wind bursts (WWBs) evident in January and April across the western and central Pacific. The WWB activity likely aided development of an oceanic Kelvin wave, which began in January and continued through the April (Fig. 4.9a).

SST anomalies trended negative beginning in April (Fig. 4.1) and eventually developed La Niña criteria during the July–September period. MJO activity also weakened substantially around this time (Fig. 4.7). The primary intraseasonal convective variability during this period was a series of prominent atmospheric Kelvin waves (Fig. 4.7, red contours), which move eastward with a smaller scale and faster phase speed than the MJO.

There were only two distinct MJO events in the second half of 2020: one in mid-July to early September and one in late October through November. These types of events have been shown to be particularly impactful for modulating tropical cyclone (TC) activity (Klotzbach 2010). They likely contributed to the most active periods for TC activity over the North Pacific and North Atlantic. The suppressed phase in late September–early October also contributed to a relative lack of TC activity in the North Atlantic during that time.

The typical MJO structure features anomalous easterlies throughout the low levels of the suppressed region of the convective envelope (Rui and Wang 1990), resulting in a surge of trade winds throughout the Pacific. Indeed, trade wind surges are evident in the 850-hPa zonal wind anomaly plot (Fig. 4.9a) during late August and November. Such trade wind surges are consistent with La Niña conditions (see section 4b).

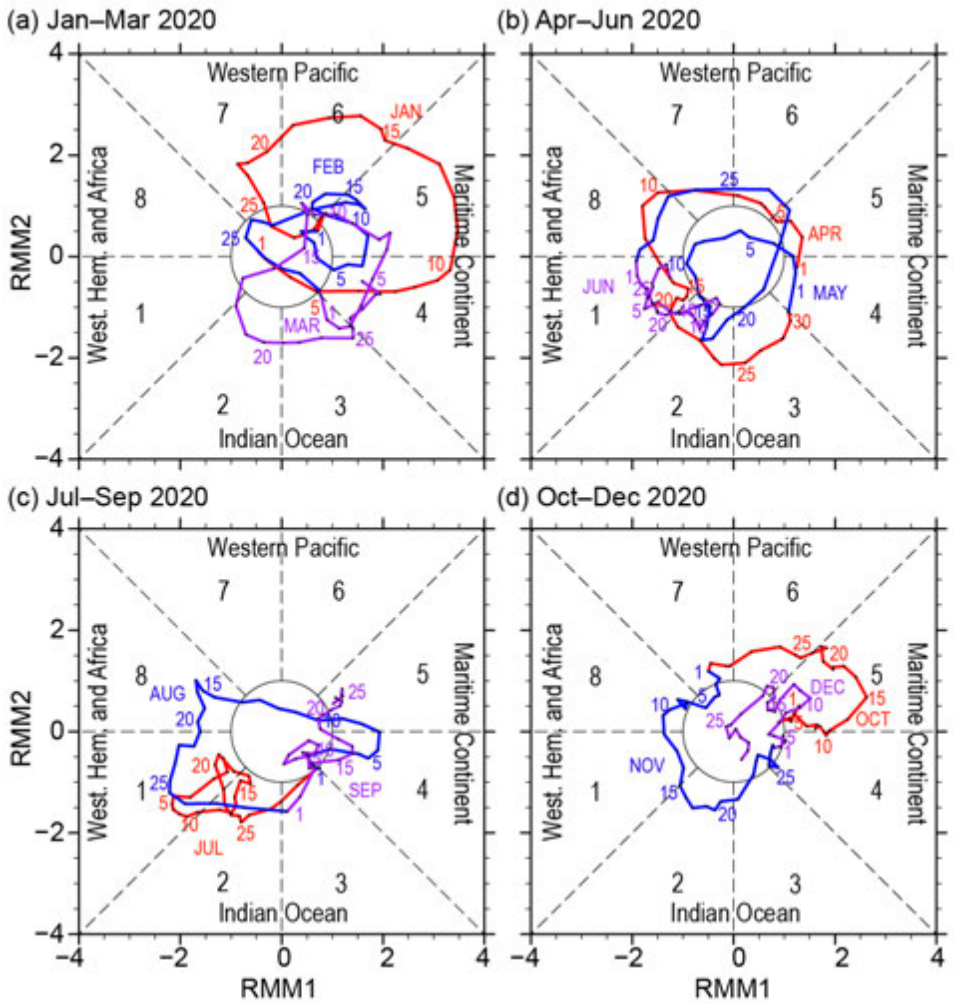

Fig. 4.8. Wheeler and Hendon (2004) RMM index for (a) Jan–Mar, (b) Apr–Jun, (c) Jul–Sep, and (d) Oct–Dec 2020. Each point represents the MJO amplitude and location on a given day, and the connecting lines illustrate its propagation. Amplitude is indicated by distance from the origin, with points inside the circle representing weak or no MJO. The eight phases around the origin identify the region experiencing enhanced convection, and counter-clockwise movement is consistent with eastward propagation.

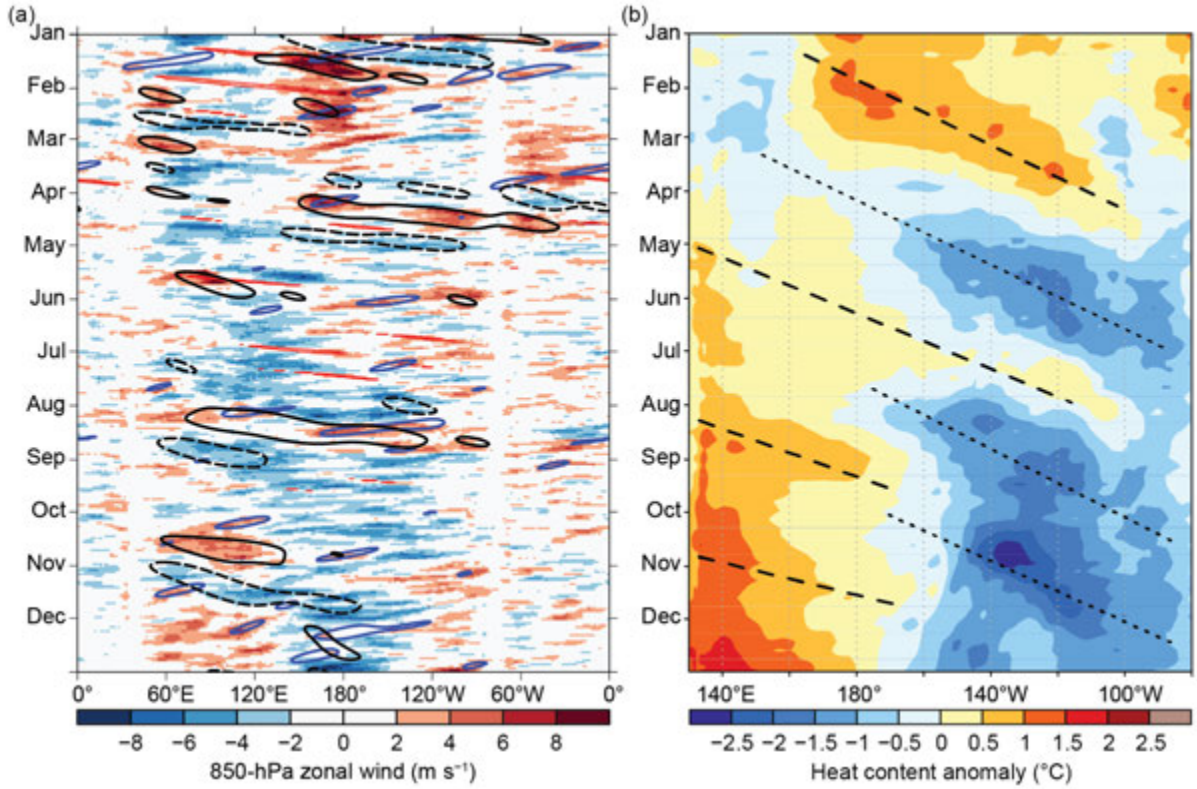

Fig. 4.9. (a) Time–longitude section for 2020 of anomalous 850-hPa zonal wind (m s^{-1}) averaged for 10°N to 10°S. Contours identify anomalies filtered for the MJO (black), atmospheric Kelvin waves (red), and equatorial Rossby waves (blue). Significant WWBS and trade wind surges over the equatorial Pacific that resulted in notable downwelling and upwelling oceanic Kelvin waves are dashed and dotted respectively. (b) Time–longitude section for 2020 of the anomalous equatorial Pacific Ocean heat content (°C), calculated as the mean temperature anomaly between 0–300-m depth. Yellow/red (blue) shading indicates above- (below-) average heat content. Relative warming (dashed lines) and cooling (dotted lines) due to downwelling and upwelling equatorial oceanic Kelvin waves are indicated. Anomalies are departures from the 1981–2010 base period pentad means. Data in (b) are derived from an analysis system that assimilates oceanic observations into an oceanic general circulation model (Behringer et al. 1998).

d. Intertropical convergence zones

1) Pacific—N. Fauchereau and B. Noll

Tropical Pacific rainfall patterns are dominated by two convergence zones, the Intertropical Convergence Zone (ITCZ; Schneider et al. 2014) north of the equator and the South Pacific Convergence Zone (SPCZ; Vincent 1994). Figure 4.10 summarizes the behavior for both convergence zones during 2020 using rainfall estimated from satellite microwave and infrared data in a product known as the Climate Prediction Center (CPC) Morphing Technique (CMORPH; Joyce et al. 2004). Rainfall transects over 30°S to 20°N are presented for each quarter of the year, averaged across successive 30-degree longitude bands, starting in the western Pacific at 150°E–180°. The 2020 seasonal variation is compared against the longer-term 1998–2019 CMORPH climatology.

Early in the year, the El Niño–Southern Oscillation (ENSO) phase was neutral, although an area of above-average ocean temperatures was located in the west-central Pacific, with a spatial signature somewhat similar to a weak, central Pacific El Niño (El Niño "Modoki"; see Ashok et al. 2007), although the Modoki condition is not a formal part of the ENSO section of this report (section 4b). The transects for January–March (Fig. 4.10a) for the western and central Pacific (150°W–150°E, especially 150°E to the date line) show that the SPCZ mean signature was shifted northeast of its climatological position, while the ITCZ appears to have been displaced slightly equatorward compared to normal. These anomalies were weak, but somewhat consistent with typical Modoki patterns (Ashok et al. 2007).

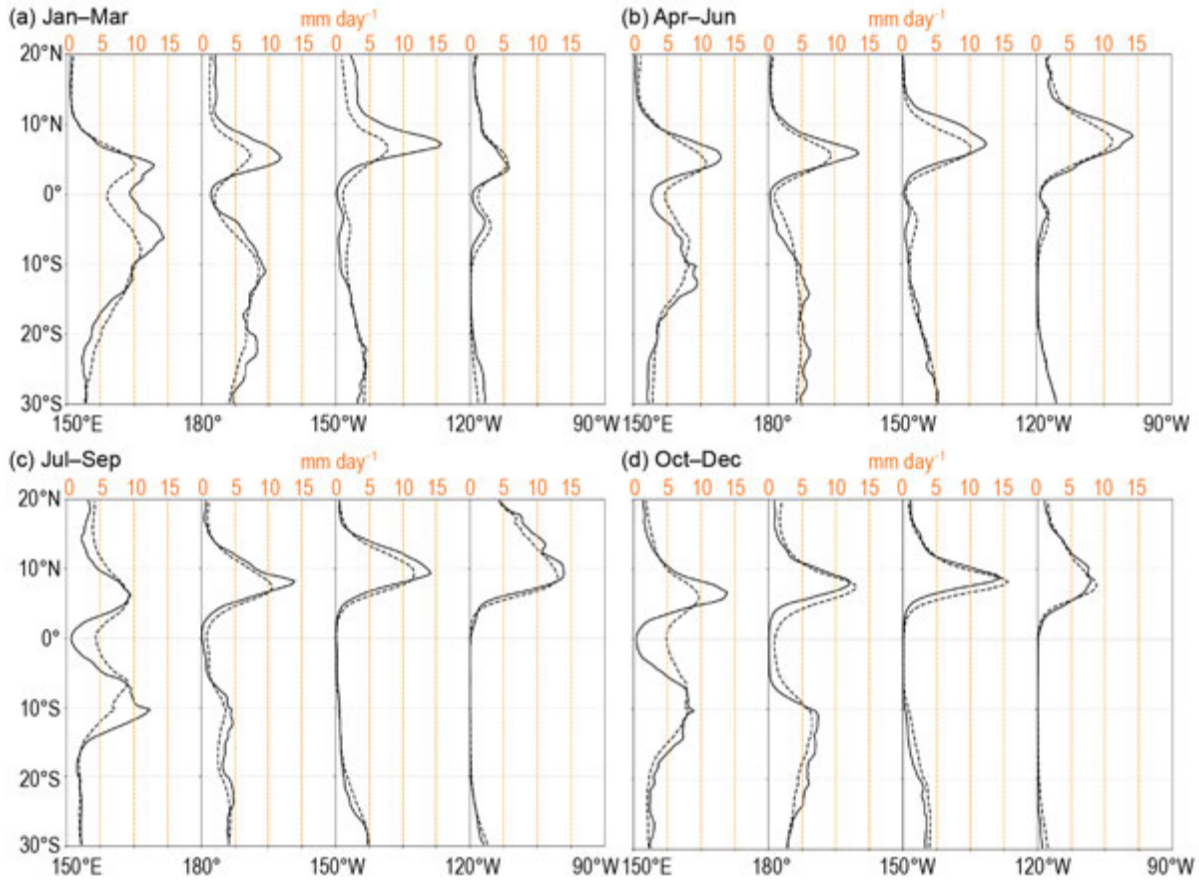

Fig. 4.10. Rainfall rate (mm day^{-1}) from the CMORPH analysis for (a) Jan–Mar, (b) Apr–Jun, (c) Jul–Sep, and (d) Oct–Dec of 2020. The separate panels for each quarter show the rainfall cross-section between 30°S and 20°N (solid line) and the 1998–2019 climatology (dotted line), separately for four 30° sectors from 150°E–180° to 120°–90°W.

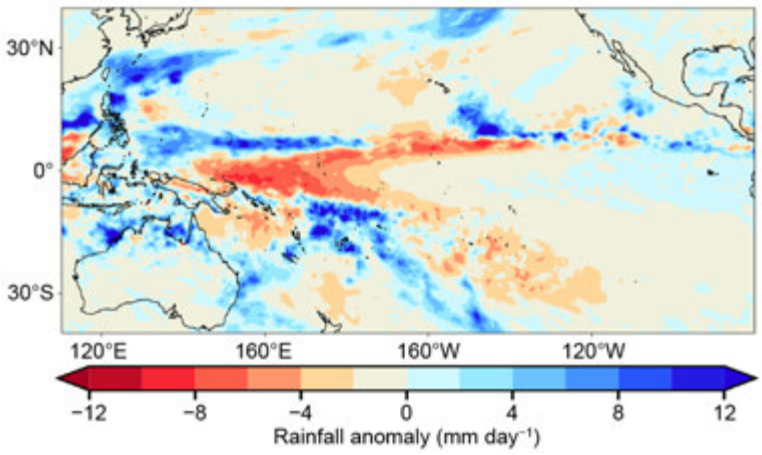

Fig. 4.11. Rainfall anomalies (mm day^{-1}) from CMORPH analysis for Dec 2020. The anomalies are calculated with respect to the 1998–2019 climatology.

During boreal summer, an increase in tropical trade winds contributed to cooling ocean temperatures across the equatorial central and eastern Pacific. At the end of 2020, it became more apparent that the La Niña was of the non-traditional central Pacific flavor, with the coolest sea surface temperatures (SSTs) located toward the central Pacific. Cooling SSTs across the central and eastern Pacific were accompanied with distinct shifts in the ITCZ position and intensity: from April to June, all sectors of the Pacific (see Fig. 4.10b) showed an ITCZ shifted north of its climatological position, with rainfall rates within the convergence zone exceeding climatological values. The ITCZ remained to the north of its usual position throughout the remainder of 2020, a pattern broadly consistent with La Niña conditions.

Meanwhile, the position and intensity of the SPCZ showed large month-to-month variability. During La Niña years, the SPCZ tends to be displaced to the southwest of its climatological position and, conversely, the SPCZ northeast of its climatological position during El Niño years. The SPCZ followed this pattern in the last quarter of 2020, as exemplified by anomalies recorded in December (Fig. 4.11).

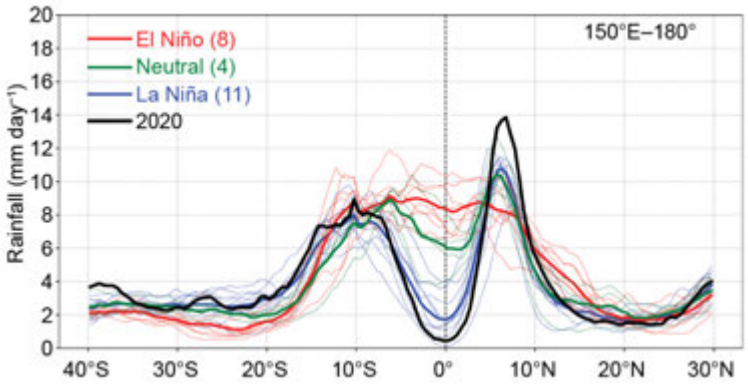

Fig. 4.12. CMORPH rainfall rate (mm day^{-1}) for Oct–Dec, for each year 1998 to 2019, averaged over the longitude sector 150°W–180°. The cross-sections are color-coded according to NOAA's ONI, except 2020, which is shown in black. Dotted lines are individual years and solid lines are the average over all years in each ENSO phase. Inset legend indicates how many years went into each composite.

Figure 4.12 shows a more detailed comparison of the western Pacific (150°E–180°) CMORPH rainfall transects for all years from 1998 to 2020. In 2020, October–December (OND) has a relatively clear La Niña signal. The ITCZ intensified and was shifted north of its climatological position, with the strongest positive anomalous precipitation rates on record between about 7°N and 9°N. Conversely, rainfall rates along the equator were among the lowest on record, which was consistent with La Niña conditions (blue line on Fig. 4.12). Farther south, the SPCZ position and intensity in OND 2020 was close to the composite average during La Niña years.

2) Atlantic—A. B. Pezza and C. A. S. Coelho

The Atlantic ITCZ is a well-organized convective band that oscillates between approximately 5°–12°N during July–November and 5°S–5°N during January–May (Waliser and Gautier 1993; Nobre and Shukla 1996). Equatorial atmospheric Kelvin waves can modulate ITCZ intraseasonal variability (Guo et al. 2014). ENSO and the Southern Annular Mode (SAM) can also influence the ITCZ on interannual time scales (Münnich and Neelin 2005). The SAM, also known as the Antarctic Oscillation, describes the north–south movement of the westerly wind belt that encircles Antarctica. A negative SAM event reflects an expansion of the westerly winds belt toward the equator, with more abundant midlatitude precipitation in general (see Fig. 6.2c for monthly SAM values in 2020).

A relatively persistent pattern dominated the main South American climate signals for 2020. For most of the year, the South Atlantic was warmer than normal, characterized by moist westerly wind bursts near the equator, affecting the Atlantic ITCZ. Significant anomalies in low-pressure systems dominated the 60°S latitude belt to the southwest of South America, with a corresponding weak South Atlantic anticyclone (Fig. 4.13a). A mostly positive SAM pattern, later reinforced by a rapid transition into La Niña from June onward, further reinforced the pattern above. As a result of this persistence, a large portion of inland Brazil experienced severe precipitation deficits and remarkable anomalous warmth, which escalated from September onward.

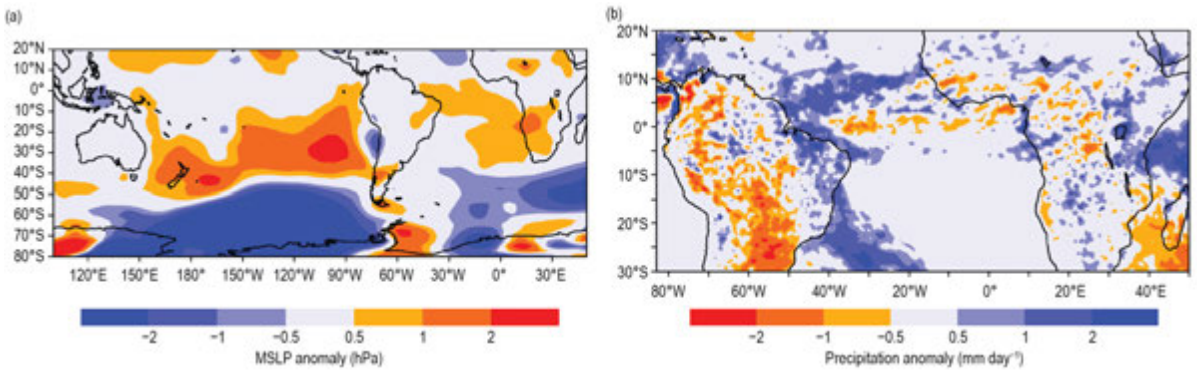

Fig. 4.13. Observed (a) tropical and SH MSLP anomaly (hPa) and (b) precipitation anomaly (mm day^{-1}) for tropical and subtropical South America and Africa for Jan–Dec 2020. MSLP anomalies are calculated with respect to a 1981–2010 climatology derived from the NCEP/NCAR Reanalysis (Kalnay et al. 1996). Precipitation anomalies calculated with respect to a 1998–2019 climatology are derived from CMORPH (Joyce et al. 2004).

In contrast, the Atlantic ITCZ experienced mildly enhanced convective activity south of the equator, with positive rainfall anomalies contrasting with the pattern for the tropics and subtropics (Fig. 4.13b). The ITCZ itself remained centered slightly north of its climatological position for most of the southern rainy season. The Atlantic Index (Pezza and Coelho 2019), as defined by the SST south of the equator minus the SST north of the equator over key areas of influence for the ITCZ, reflected the role of the north–south gradient mechanism for 2020, with the ITCZ tending to shift toward the warmer side of this gradient (Figs. 4.14a,b).

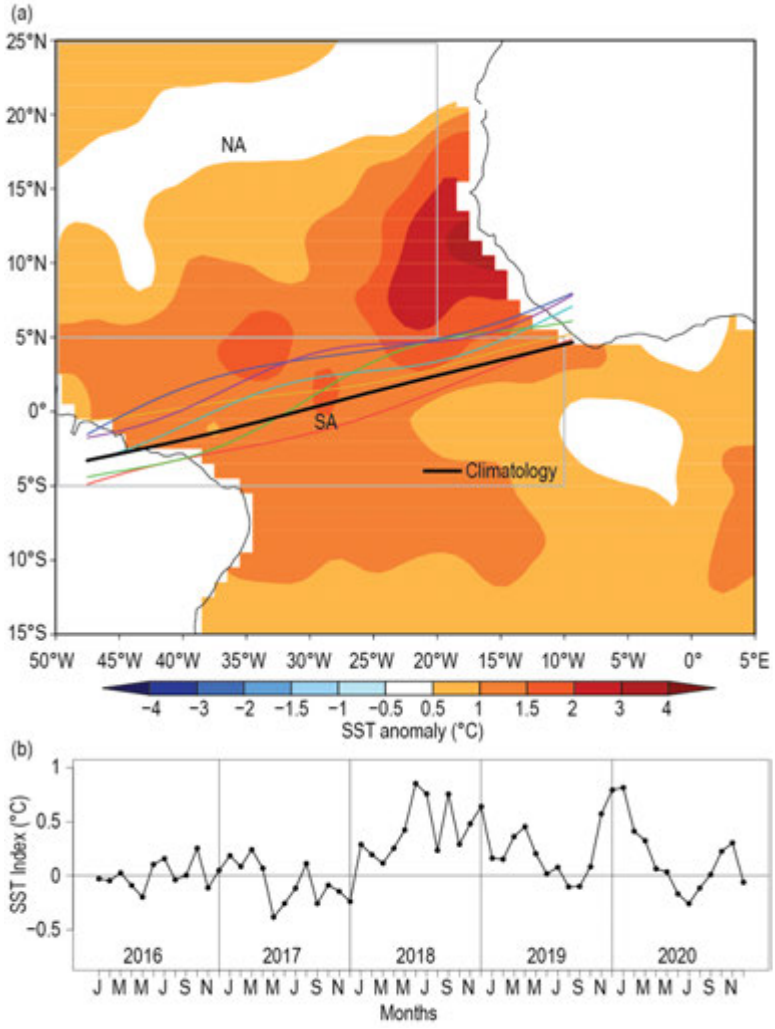

Fig. 4.14. (a) Atlantic ITCZ position inferred from OLR (Liebmann and Smith 1996) during Mar 2020. The colored thin lines indicate the approximate position for the six pentads of the month. The black thick line indicates the Atlantic ITCZ climatological position for Mar. The SST anomalies for Mar 2020 calculated with respect to the 1982–2019 climatology are shaded (°C). The two boxes indicate the areas used for the calculation of the Atlantic index in panel (b), which shows monthly OISST (Smith et al. 2008) anomaly time series averaged over the South Atlantic sector (SA region, 5°S–5°N, 10°–50°W) minus the SST anomaly time series averaged over the North Atlantic sector (NA region, 5°–25°N, 20°–50°W) for the period 2016–20, forming the Atlantic index. The positive phase of the index indicates favorable conditions for enhanced Atlantic ITCZ activity south of the equator.

e. Global monsoon summary—B. Wang and Q. He

The global monsoon is the dominant mode of annual precipitation and circulation variability and is a critical feature of Earth's climate system. The tropical monsoon rainfall domain was first defined by Wang (1994), who showed that a monsoon characterized by a rainy summer and dry winter distinguishes an arid climate (without a rainy season) from equatorial regions where rainfall lacks a significant seasonal cycle. The monsoon domain defined using precipitation characteristics is shown in Fig. 4.15, and consists of eight regional monsoons (Table 4.1). Figure 4.15 also shows global summer precipitation anomalies in the Southern Hemisphere (SH) during November 2019–April 2020 and the Northern Hemisphere (NH) during May–October 2020. Figure 4.16 shows temporal variations of summer monsoon precipitation and low-level circulation indices for each of the eight regional monsoons. The precipitation indices represent the anomalous precipitation rate averaged over the rectangular box regions, including both land and ocean areas shown in Fig. 4.15. Note that the precipitation averaged in each box well represents the precipitation averaged over the corresponding entire regional monsoon domain (r > 0.90). The

Table 4.1. Definition of the regional summer monsoon circulation indices and their Pearson correlation coefficients (r) with the corresponding regional summer monsoon precipitation indices for 1979/80–2019/20. All circulation indices are defined by the meridional shear of the zonal wind at 850 hPa (or 700 hPa in highland southern Africa), which measures the intensity (relative vorticity) of the monsoon troughs except for northern African (NAF) and East Asian (EA). The NAF monsoon circulation index is defined by the westerly monsoon strength. The EASM circulation index is defined by the meridional wind strength, which reflects the east–west thermal contrast between the Asian continent and the western North Pacific. The precipitation indices are defined by the areal mean precipitation over the blue box regions shown in Fig. 4.16. The correlation coefficients were computed using monthly time series (164 summer months; June–September in NH [1980–2020] and December–March in SH [1979/80–2019/20]). Bolded numbers represent significance at the 99% confidence level. (Adapted from Yim et al. 2014).

Regional monsoon	Definition of the circulation index	r
Indian (ISM)	U850 (5° –15°N, 40°–80°E) minus U850 (25°–35°N, 70°–90°E)	0.70
Western North Pacific (WNPSM)	U850 (5°–15°N, 100°–130°E) minus U850 (20°–35°N, 110°–140°E)	0.82
East Asian (EASM)	V850 (20°–40°N, 120°–140°E)	0.66
North American (NASM)	U850 (5°–15°N, 130°–100°W) minus U850 (20°–30°N, 110°–80°W)	0.85
Northern African (NAFSM)	U850 (0°–15°N, 60°–10°W)	0.68
South American (SASM)	U850 (20°–5°S, 70°–40°W) minus U850 (35°–20°S, 70°–40°W)	0.81
Southern African (SAFSM)	U700 (15°S-0°, 10°–40°E) minus U700 (25°–10°S, 40°–70°E)	0.63
Australian (AUSSM)	U850 (15°S–0°, 90°–130°E) minus U850 (30°–20°S, 100°–140°E)	0.89

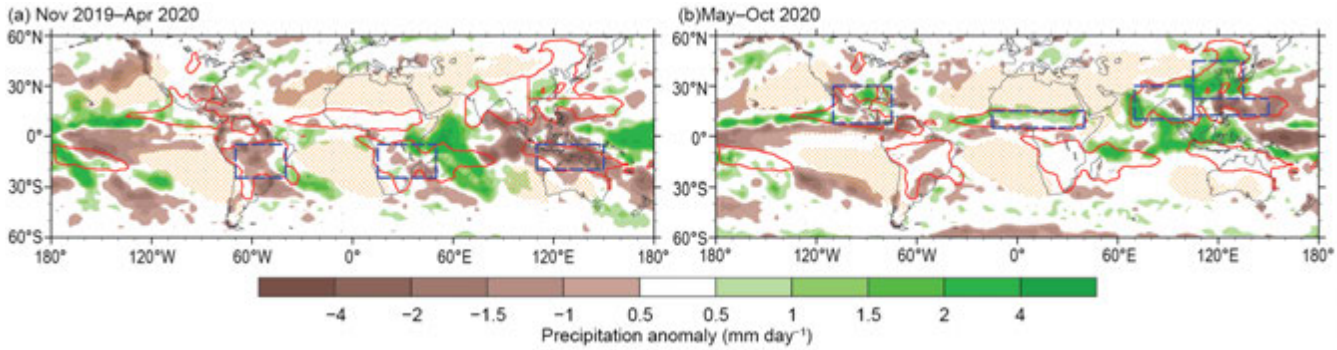

Fig. 4.15. Seasonal mean precipitation anomalies (mm day^{-1}) for (a) the SH summer monsoon season: Nov 2019–Apr 2020 and (b) the NH summer monsoon season: May–Oct 2020. Red lines outline the global monsoon precipitation domain. The monsoon domain is defined by (1) the annual range (local summer minus winter) where precipitation exceeds 300 mm and (2) the summer mean precipitation is >55% of the total annual precipitation amount, where summer is defined to be May–Sep for the NH and Nov–Mar for the SH (Wang and Ding 2008). The dotted area represents the dry region where the local summer precipitation rate is below 1 mm day^{-1}. Precipitation indices for each regional monsoon are defined by the areal mean precipitation in the corresponding rectangular regions (dashed blue), which are highly correlated with the precipitation averaged over the corresponding real regional monsoon domains. Rainfall data were taken from the GPCP (Huffman et al. 2009).

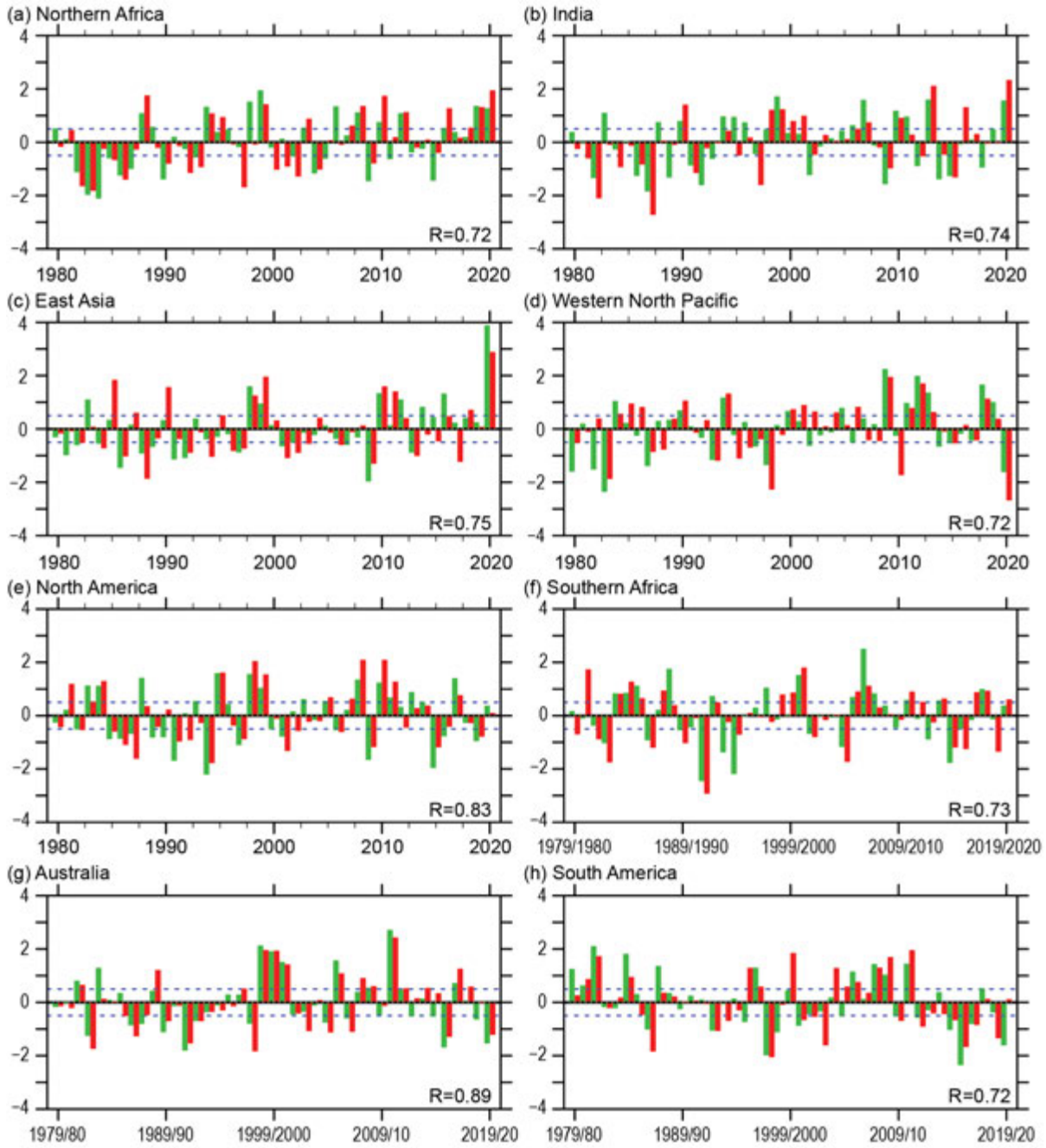

Fig. 4.16. (a)–(h) Normalized summer mean precipitation (green) and circulation (red) indices for each of the eight regional monsoons (Table 4.1). Indices were normalized by their corresponding standard deviation. Numbers shown in each panel's bottom right denote the correlation coefficient between the seasonal mean precipitation and circulation indices (sample size: 41). Dashed lines indicate ±0.5 std. dev. The monsoon seasons are May–Oct for the NH and Nov–Apr for the SH. (Data source: GPCP for precipitation and ERA-5 [Hersbach et al. 2020] for circulation.)

definitions of the circulation indices for each monsoon region are provided in Table 4.1. The precipitation and circulation indices are well-correlated in most regional monsoons, with correlation coefficients ranging from 0.63 to 0.89 with a sample size of 164 summer months (Table 4.1). The precipitation and circulation indices together provide consistent measurements of the strength of each regional monsoon system.

Total seasonal rainfall over the NH monsoon region over land was the highest since the start of the record in 1980 (Fig. 4.17). It was largely driven by the 2020 East Asian summer monsoon (EASM), which was nearly 4 standard deviations above average (Fig. 4.16c). The Meiyu season (July–August), a typical rainy season over the Yangtze and Huaihe River Valleys (YHRV) of China, doubled its climatological mean duration by 2 months in 2020. The May–October

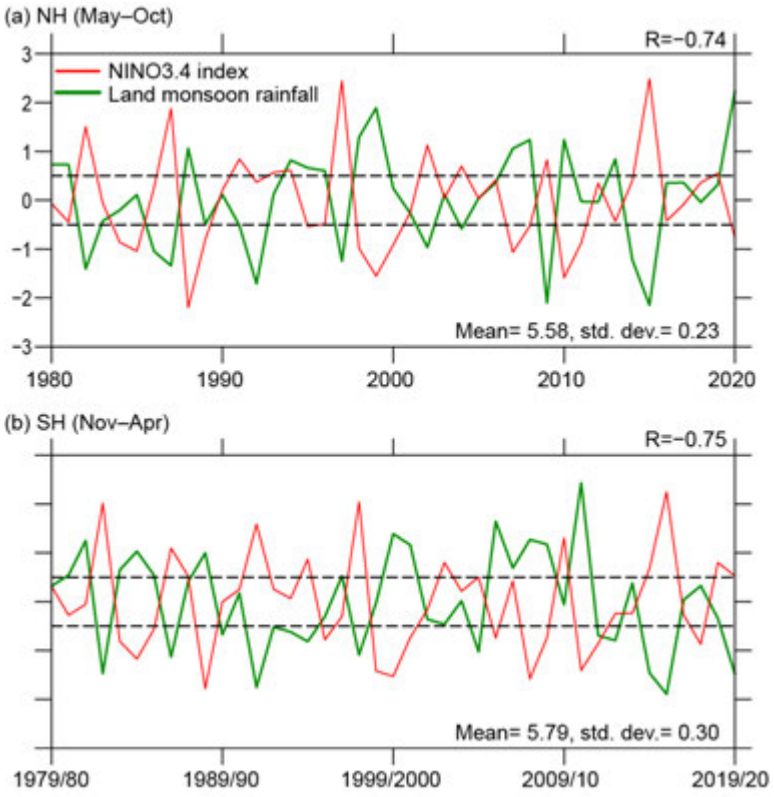

Fig. 4.17. (a) NH summer (May–Oct) land monsoon precipitation anomaly (green) normalized by its standard deviation. The climatological mean NH summer land monsoon precipitation (Mean) and standard deviation (SD) are shown in the lower right panel (mm day^{-1}). Numbers shown in each panel's top right denote the correlation coefficient between the seasonal mean precipitation anomaly and the simultaneous Niño-3.4 index (red). Dashed lines indicate ±0.5. (b) As in (a) except for the SH summer (Nov–Apr). Note that the land monsoon precipitation excludes the monsoon rainfall over the oceanic monsoon domain. (Data source: GPCP for precipitation, HadISST and ERSSTv5 for SST.)

accumulated rainfall averaged over the YHRV exceeded 750 mm, the most since the start of the record in 1961 (Qiao et al. 2021). Associated severe flooding affected about 45.5 million people and caused a direct economic loss of more than 100 billion Chinese Yuan ($15.5 billion [U.S. dollars]; Wei et al. 2020; see section 7g for more details).

During the 2019/20 SH summer monsoon season (November–April), precipitation over the Maritime Continent–Australian and South American monsoon regions was substantially suppressed, while rainfall in the equatorial central Pacific and the western Indian Ocean was markedly enhanced (Fig. 4.15a). This contrast is due to the anomalous Walker circulation associated with the warm Central Pacific sea surface temperature (SST) anomalies even though they did not reach the thresholds for El Niño. The Indian Ocean rainfall anomalies were also driven by a positive phase of the Indian Ocean dipole (IOD; Saji et al. 1999) SST anomaly, which was +1.8°C during SH summer. The Australian summer monsoon produced precipitation 1.5 standard deviations below normal, with an associated reduced circulation intensity (Fig. 4.16g). The South American monsoon region also received precipitation 1.5 standard deviations below normal, although the corresponding circulation's strength was near normal (Fig. 4.16h). Southern African summer monsoon precipitation and circulation intensity were normal (Fig. 4.16f) due to a dipolar structure in eastern Africa (increased rainfall in equatorial East Africa and decreased rainfall near Madagascar). The increased eastern African rainfall was largely caused by the positive phase of the IOD SST anomaly experienced from November 2019 to April 2020. During November 2019–April 2020, the IOD index is 1.82 standard deviations or 0.34°C (not shown). In fact, November 2019–April 2020 was the second-highest such period of the IOD index. Overall, the SH summer monsoon showed a consistent reduction of precipitation and weakening of the monsoon circulation, although there were various degrees of weakening in the three SH regional monsoons.

During the 2020 NH summer monsoon season (May–October), precipitation over the Maritime Continent was significantly above normal due to the rapidly developing La Niña, while there was a noticeable reduction of precipitation in the equatorial Pacific Ocean and the Philippine Sea (Fig. 4.15b). In addition to the unprecedented EASM strength, the summer precipitation over both the Indian and northern African monsoon regions were also ~1.5 standard deviations above normal, and the corresponding circulation intensity was >2 standard deviations above average (Figs. 4.16a,b). The North American monsoon was characterized by near-normal precipitation and circulation intensity (Fig. 4.16e), and the western North Pacific monsoon precipitation, which is generally out of phase with the EASM, was about 1.5 standard deviations below normal (Fig. 4.16d).

Monsoon rainfall over land has more significant socio-economic impacts than monsoon rainfall over the ocean. Therefore, we specifically examine land monsoon rainfall. Global land monsoon precipitation is strongly influenced by tropical SST anomalies, especially related to El Niño–Southern Oscillation (ENSO; Wang et al. 2012). Figure 4.17 highlights that both NH and SH land summer monsoon precipitation are well correlated with the simultaneous Niño-3.4, suggesting that ENSO explains about 50% of their variance. Figure 4.17 shows that the total amount of 2020 NH land monsoon precipitation was the highest of any monsoon season in the record that dates to 1980, whereas the 2019/20 SH land monsoon precipitation was below normal. However, the 2020 La Niña cannot fully explain the record high NH land monsoon precipitation nor the EASM extreme. Further study of the causes is warranted.

f. Indian Ocean dipole and unique Indian Ocean basin warming in 2020—L. Chen and J.-J. Luo

Year-to-year climate variability in the tropical Indian Ocean (IO), which is largely driven by local air–sea interactions and the El Niño–Southern Oscillation in the tropical Pacific, exerts great influence on weather and climate in the regions surrounding the IO (e.g., Saji et al. 1999; Luo et al. 2010; Xie et al. 2016). Among them, the Indian Ocean dipole (IOD; Saji et al. 1999) is an inherent air–sea coupled mode in the tropical IO. The IOD usually starts to grow in boreal summer, peaks in autumn, and terminates rapidly in early boreal winter in connection with the reversal of monsoonal winds along the west coast of Sumatra. As shown in Figs. 4.18a,b, a strong positive IOD event, with anomalously warm waters to the west and anomalously cool waters to the east, occurred in 2019 and was of an extreme intensity in the boreal fall of 2019 (Chen et al. 2020).

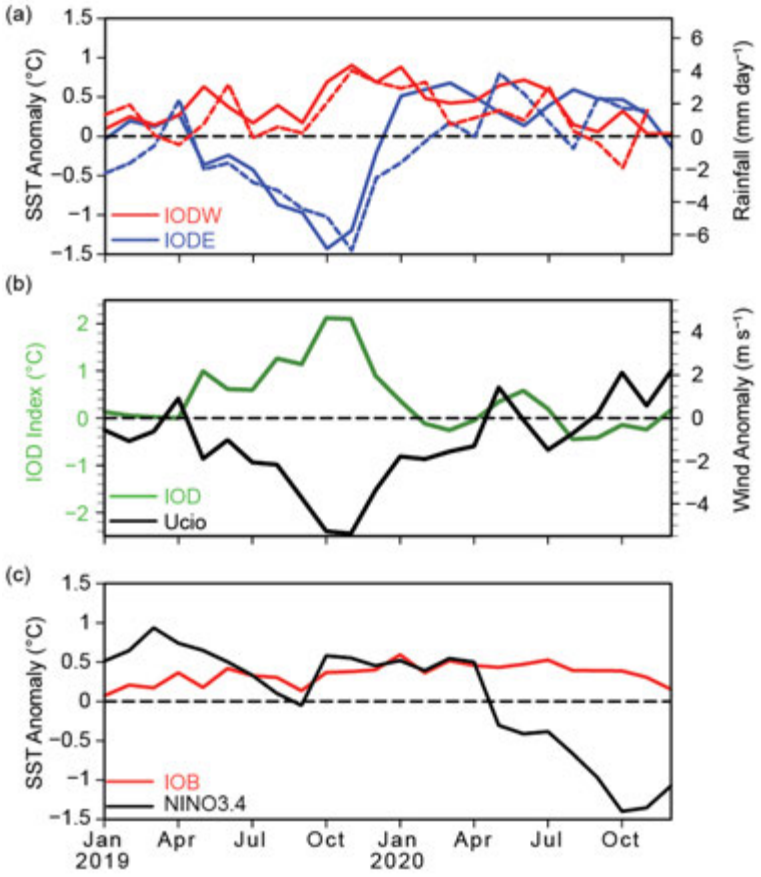

Fig. 4.18. (a) Monthly anomalies of SST (°C; solid lines) and precipitation (mm day^{-1}; dashed lines) for the eastern pole (IODE; 10°S–0°, 90°–110°E; blue lines) and the western pole (IODW; 10°S–10°N, 50°–70°E; red lines) of the IOD. (b) As in (a), but for the IOD index (measured by the SST difference between the IODW and IODE, green line) and surface zonal wind anomaly (m s^{-1}) in the central equatorial IO (Ucio; 5°S–5°N, 70°–90°E; black line). (c) As in (a), but for SST anomalies in the Niño-3.4 region (5°S–5°N, 170°–120°W; black line) and the tropical IO (IOB; 20°S–20°N, 40°–100°E; red line). Anomalies are relative to the 1982–2020 base period. (Sources: NOAA OISST [Reynolds et al. 2002]; monthly GPCP precipitation analysis [available at http://precip.gsfc.nasa.gov/]; and JRA-55 atmospheric reanalysis [Ebita et al. 2011].)

Throughout 2020, the IOD index (also known as the Dipole Mode Index) was near zero, indicating a neutral IOD status in 2020 (Fig. 4.18b). In the tropical IO, the most remarkable feature was that sea surface temperatures (SSTs) exhibited warm anomalies over the entire tropical IO throughout 2020 (Fig. 4.18c, Figs. 4.19a–d). Following the early boreal winter of 2019/20, the extreme positive IOD event rapidly terminated and then the tropical IO turned into an Indian Ocean basin (IOB) mode (Figs. 4.18b,c). The IOB, characterized by a basin-wide warming or cooling, is one of two dominant modes of SST anomalies in the tropical IO, and the other is IOD. In March–May 2020, above-average SST anomalies were observed over the tropical IO, and positive precipitation anomalies dominated the

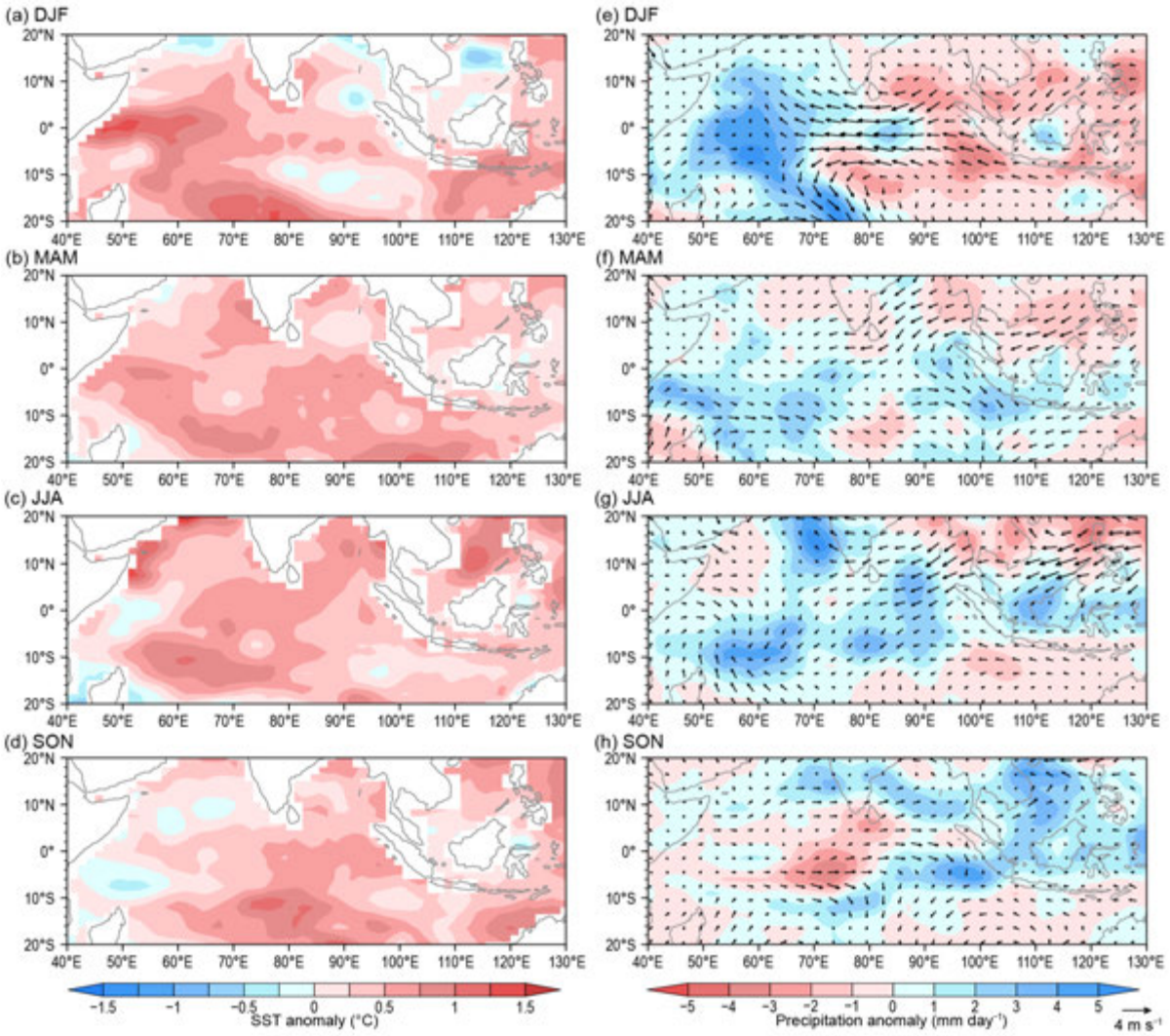

Fig. 4.19. (a)–(d) SST (°C, colored scales) anomalies during (a) Dec–Feb 2019/20, (b) Mar–May 2020, (c) Jun–Aug 2020, and (d) Sep–Nov 2020. (e)–(h) As in (a)–(d), but for precipitation (mm day^{-1}; °C, colored scales) and surface wind anomalies (vector). Anomalies were calculated relative to the climatology over the period 1982–2020. (Sources: NOAA OISST [Reynolds et al. 2002]; monthly GPCP precipitation analysis [available at http://precip.gsfc.nasa.gov/]; and JRA-55 atmospheric reanalysis [Ebita et al. 2011].)

equatorial IO (Figs. 4.19b,f). Given that there was more above-average precipitation occurring in the Southern Hemisphere compared to the Northern Hemisphere, the central and eastern equatorial IO were dominated by anomalous cross-equatorial northerly winds (Fig. 4.19f). During June–August, the above-average SSTs and above-average precipitation persisted in the tropical IO, and easterly anomalies occurred in the central and eastern equatorial IO (Figs. 4.19c,g). During September–November (SON), the above-average SSTs continued over the entire tropical IO, but there was a weak zonal gradient with larger SST anomalies in the eastern equatorial IO and smaller SST anomalies in the western equatorial IO (Figs. 4.19d,h). This weak zonal gradient of SST anomalies corresponded to a marginally negative value of IOD index in SON 2020 (Fig. 4.18b). Concurrently, the precipitation anomalies exhibited a dipole pattern with dry conditions in the western equatorial IO and wet conditions in the eastern equatorial IO. These conditions corresponded with westerly wind anomalies in the central equatorial IO (Fig. 4.19h).

On the other hand, the tropical Pacific had a prolonged weak El Niño-like warming status from winter 2018/19 to winter 2019/20 (Fig. 4.18c). The weakly positive Niño-3.4 index declined as SSTs cooled and became negative in May 2020. Then, a La Niña event rapidly developed throughout the remainder of 2020, maturing to a moderate status by the end of the year. Previous studies have suggested that in response to a preceding El Niño event, the IO tends to exhibit anomalous

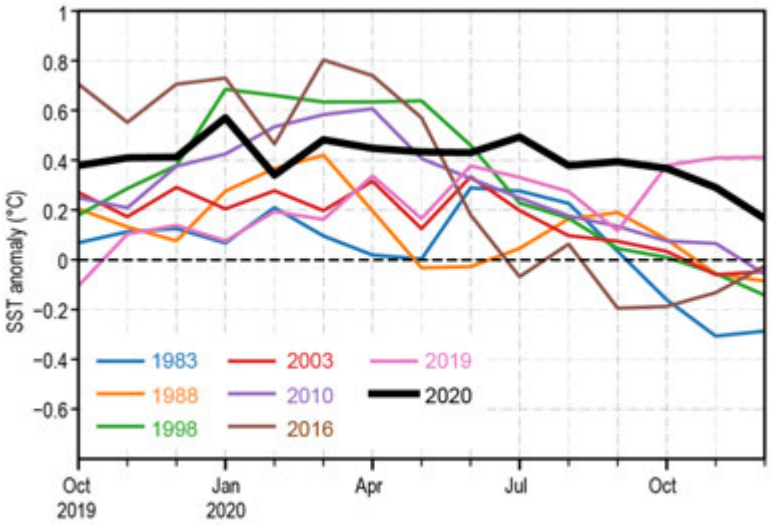

Fig. 4.20. Evolution of monthly SST anomalies averaged in the tropical IO (IOB; 20°S–20°N, 40°–100°E). The bold black curve indicates the IOB event in 2020 and the other curves indicate the other positive IOB events since 1980. (Source: NOAA OISST [Reynolds et al. 2002].)

basin-wide warming in the following year (Yang et al. 2007; Xie et al. 2016). However, there is not robust evidence to determine whether the weak El Niño in 2019/20 winter made a contribution to the long-lasting IOB mode in 2020.

The IO basin-wide anomalous warmth that dominated throughout 2020 differs from the majority of positive IOB events. The typical IOB event usually peaks in late boreal winter and early spring, and persists through boreal summer (Yang et al. 2007). The evolution of all of the positive IOB events since 1980 are displayed in Fig. 4.20. Most of the positive IOB events tend to peak in the first half of the year, then rapidly decay in the second half. In contrast, the basin-wide warming in 2020 did not begin declining until November, presenting a unique, long-lasting IOB event in 2020. Such a unique event in 2020 may be traced back to the continuous enhancement of the tropical IO warming trend during recent decades (Luo et al. 2012).

In summary, the IOD index exhibited a neutral status in 2020. A marked basin-wide anomalously warm SST pattern persisted throughout 2020, indicating that the IOB mode dominated in 2020. This unique IOB event in 2020 differed from most of the past positive IOB events, indicating that the long-lasting IO basin-wide warming of 2020 may be attributed to the long-term warming trend of SST in the IO (Luo et al. 2012).

g. Tropical cyclones

1) Overview—H. J. Diamond and C. J. Schreck

The International Best Track Archive for Climate Stewardship (IBTrACS) dataset comprises historical tropical cyclone (TC) best-track data from numerous sources around the globe, including all of the World Meteorological Organization (WMO) Regional Specialized Meteorological Centers (RSMCs; Knapp et al. 2010). This dataset represents the most complete compilation of global TC data. From these data, Schreck et al. (2014) compiled 1981–2010 climatological values of TC activity for each basin using statistics from both the WMO RSMCs and the Joint Typhoon Warning Center (JTWC). These values are referenced in each subsection.

Tallying the global TC numbers is challenging and involves more than simply adding up basin totals, because some storms cross TC basin boundaries, some TC basins overlap, and multiple agencies track and categorize TCs. Global metrics and Northern Hemisphere (NH) basins are typically measured from January to December while Southern Hemisphere (SH) basins are typically measured from July to June. Compiling the activity using preliminary data from NOAA's National Hurricane Center and the JTWC over all seven TC basins as archived in IBTrACS (Fig. 4.21), the 2020 calendar year had 102 (per Table 4.2) named storms (sustained wind speeds ≥ 34 kt or 17 m s–1), which is six more than last season (2019; Diamond and Schreck 2020) and well above the 1981–2010 average of 85 (Schreck et al. 2014). This year also featured 46 hurricanes/typhoons/cyclones (HTCs; sustained wind speeds ≥ 64 kt or 33 m s^{-1}), which is equal to the climatological average (Schreck et al. 2014). During 2020, 22 storms reached major HTC status (sustained wind speeds ≥ 96 kt or 49 m s^{-1}), which is just above the long-term average of 21 and 10 fewer than the 2019 season (Diamond and Schreck 2020). The Accumulated Cyclone Energy (ACE) for the season

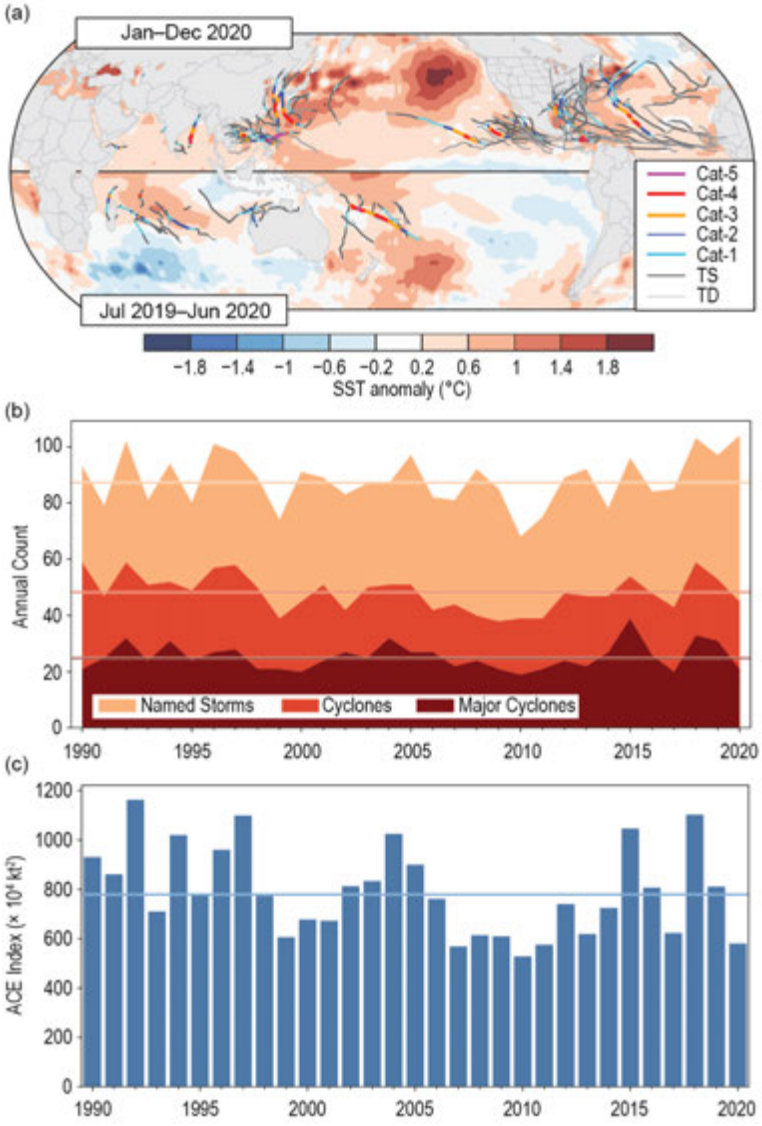

Fig. 4.21. (a) Global summary of TC tracks overlaid on associated OISST anomalies (°C; Reynolds et al. 2002) for the 2020 season relative to 1982–2010; (b) global TC counts; and (c) global ACE values. Horizontal lines on (b) and (c) are 1981–2010 normals.

was 574 × 10^4 kt^2, which would put it in the lowest 10% of years from 1981–2010 and considerably less than the value of 795 × 10^4 kt^2 in 2019 (Diamond and Schreck, 2019).

In sections 4g2–4g8, 2019/20 (SH) and 2020 (NH) seasonal TC activity is described and compared to the historical record for each of the seven WMO-defined TC basins. For simplicity, all counts are broken down by the U.S. Saffir-Simpson Hurricane Wind Scale (SSHWS). The overall picture of global TCs during 2020 is shown in Fig. 4.21. Actual counts by category are documented in Table 4.2.

Globally, three storms during the year reached SSHWS Category 5 strength (sustained wind speeds ≥ 137 kt or 70.5 m s^{-1}). This was three fewer than recorded in 2016 (Diamond and Schreck 2017), and two less than recorded in 2017 and 2019 (Diamond and Schreck 2018; 2020). The all-time record of 12 Category 5 global TCs was set in 1997 (Schreck et al. 2014),[3] while 11 Category 5 global TCs were recorded in 2018.

The three Category 5 storms in 2020 were: Super Typhoon Goni in the western North Pacific, Cyclone Amphan in the North Indian Ocean, and Tropical Cyclone Harold in the southwest Pacific. Despite only reaching Category 4 status, Iota caused devastating damage to the nations of Central America, especially Nicaragua and Honduras, that was exacerbated by the landfall of Category 4 Eta only 2 weeks prior to Iota in essentially the same area. Super Typhoon Goni was the strongest TC to make landfall in the historical record and led to almost 1 million people being evacuated from its path and thousands of homes destroyed. Super Cyclone Amphan caused $13.9 billion (U.S. dollars) in damage and resulted in over 100 fatalities, primarily in India. Harold had major impacts in the southwest Pacific, particularly in Vanuatu and the Solomon Islands. Of note, a fourth Category 5 storm, Yasa, formed in the Southwest Pacific in December 2020. While forming in 2020, this storm is part of the July–June 2020/21 tropical cyclone season and thus will be discussed in detail in next year's report. Sidebar 4.1 details the record-setting and devastating local impacts of Category 4 Hurricane Laura in Louisiana.

Finally, and while not an official TC basin, three significant TC-like storms or "medicanes" were recorded within the Mediterranean Sea in September, November, and December, affecting Greece, Tunisia, and Syria/Lebanon, respectively. Sidebar 4.2 focuses on these storms.

[3] SSHWS is based on 1-minute averaged winds, and the categories are defined at: https://www.weather.gov/mfl/saffirsimpson; the Australian category scale is based on 10-minute averaged winds, and those categories are defined at: https://australiasevereweather.com/cyclones/tropical_cyclone_intensity_scale.htm

Table 4.2. Global counts of TC activity by basin for 2020. "+" denotes top tercile; "++" is top 10%; "-" is bottom tercile; "--" is bottom 10% (all relative to 1981–2010). "+++" denotes record values for the entire IBTrACS period of record. (Note that some inconsistencies between Table 4.2 and the text of the various basin write-ups in section g exist and are unavoidable, as tallying global TC numbers is challenging and involves more than simply adding up basin totals, because some storms cross TC basin boundaries, some TC basins overlap, and multiple agencies are involved in tracking and categorizing TCs.)

Basin	TCs	HTCs	Major HTCs	SS Cat 5	ACE ($\times 10^4$ kt^2)
North Atlantic	30 +++	14 ++	7 ++	0	180 +
Eastern Pacific	17	4 −−	3	0	77 −
Western Pacific	23 −	12 −	7 −	1	150 −−
North Indian	5 +	4 ++	2 ++	1 ++	27 +
South Indian	11 +	6	3	0	54 −
Australia	10	3 −	0	0	31 −
Southwest Pacific	9	5 +	1	1 ++	56
Global Totals	**102** ++	**48**	**23**	**3**	**574** −−

2) Atlantic basin—G. D. Bell, M. Rosencrans, E. S. Blake, C. W. Landsea, H. Wang, S. B. Goldenberg, and R. J. Pasch

(I) 2020 SEASONAL ACTIVITY

The 2020 Atlantic hurricane season produced 30 named storms, of which 14 became hurricanes and seven of those became major hurricanes (Fig. 4.22a). The Hurricane Database 2 (HURDAT2; Landsea and Franklin, 2013) 1981–2010 seasonal averages (included in IBTrACS) are 12.1 named storms, 6.4 hurricanes, and 2.7 major hurricanes (Landsea and Franklin 2013). The 30 named storms during 2020 surpasses the previous record of 28 set in 2005. The 14 hurricanes during 2020 are the second most on record behind 15 observed in 2005, seven major hurricanes tied with 2005 for the most on record.

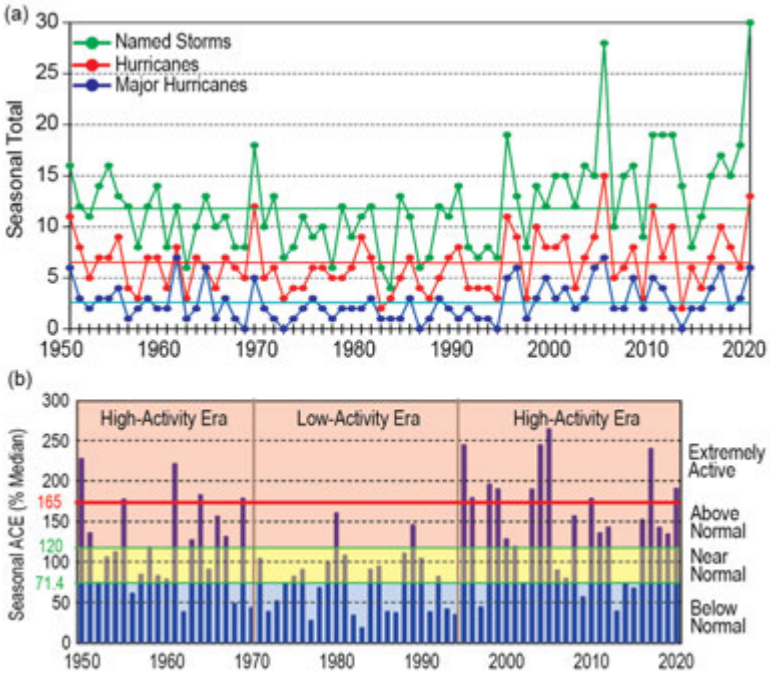

Fig. 4.22. Seasonal North Atlantic hurricane activity during 1950–2020. (a) Numbers of named storms (green), hurricanes (red), and major hurricanes (blue). (b) The ACE index expressed as percent of the 1981–2010 median value. ACE is calculated by summing the squares of the 6-hourly maximum sustained surface wind speed (kt) for all periods while the storm is at least tropical storm strength. Red, yellow, and blue shadings correspond to NOAA's classifications for above-, near-, and below-normal seasons, respectively (http://www.cpc.ncep.noaa.gov/products/outlooks/background_information.shtml). The thick red horizontal line at 165% of the median ACE value denotes NOAA's threshold for an extremely active season. Vertical brown lines separate high- and low-activity eras. Note that there is a low bias in activity during the 1950s to the early 1970s due to the lack of satellite imagery and a technique (Dvorak) to interpret tropical cyclone intensity for systems over the open ocean. (Source: HURDAT2 [Landsea and Franklin 2013].)

Nine of 30 named storms during 2020 were short-lived (≤2 days). There has been a large artificial increase (approximately five per year) in these "shorties" since 2000 (Landsea et al. 2010). These increased counts primarily reflect new observational capabilities such as scatterometers, Advanced Microwave Sounding Units, and the Advanced Dvorak Technique, and have no association with any known climate variability (Villarini et al. 2011).

The 2020 seasonal ACE value (Bell et al. 2000) was 191.5% of the 1981–2010 median (which is 92.4×10^4 kt^2; Fig. 4.22b). This value is the sixth largest since 1970 and is above NOAA's threshold for both an above-normal (120%) and an extremely active (165%) season. There have now been a record five consecutive above-normal seasons, which surpasses the previous record of four set in 1998–2001. Since the current Atlantic high-activity era began in 1995 (Goldenberg et al. 2001; Bell et al. 2019, 2020), there have been 18 above-normal seasons, with 10 being classified as extremely active. By comparison, the preceding 24-year low-activity era of 1971–94 had only two above-normal seasons, and none were extremely active.

(II) STORM FORMATION TIMES, REGIONS, AND LANDFALLS

Substantial TC activity occurred throughout the 2020 hurricane season (Fig. 4.23a). May–July saw a record nine named storms. Seven of those, of which four were "shorties," formed in the extratropics from pre-existing extratropical disturbances. On average, 1–2 named storms form per year during this period.

August–October (ASO), typically the most active part of the hurricane season, featured 18 named storms during 2020, with a record 10 forming in September. Ten of the 18 named storms became hurricanes, and four of those became major hurricanes. Most of these storms (13 of 18) formed in the Main Development Region (MDR, green box in Fig. 4.23c), which is also typical of an above-normal season. The MDR spans the tropical North Atlantic Ocean and Caribbean Sea between 9.5°N and 21.5°N (Goldenberg and Shapiro 1996; Goldenberg et al. 2001; Bell and Chelliah 2006; Bell et al. 2017, 2018, 2019). November 2020 saw three named storms, with two becoming major hurricanes over the western Caribbean Sea and striking Nicaragua as Category 4 storms, and generated the second-most Atlantic ACE on record (36×10^4 kt^2), trailing only 1932 (71×10^4 kt^2). On average, November sees only one named storm every other year. Only five major hurricanes have occurred in November in the previous 70 years (1950–2019), and 2020 had two.

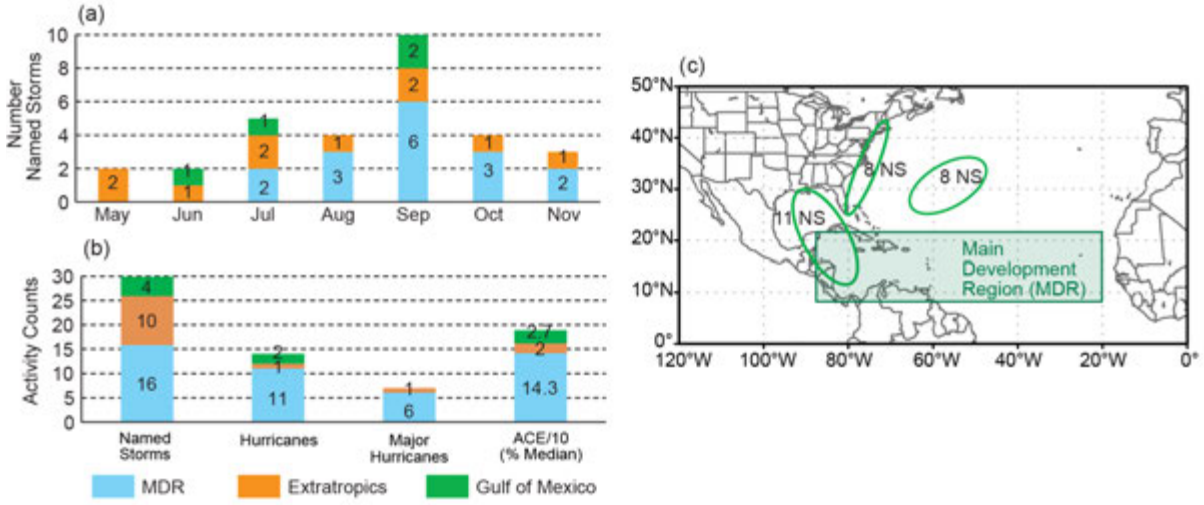

Fig. 4.23. Atlantic TC activity in 2020: (a, b) Storm counts and (c) areas of increased track density. In (a), named storm counts are shown for the month and region the storm was first named. In (b), total seasonal counts for the three storm classifications and ACE are shown for each region where the storm was first named. ACE reflects the entire storm ACE and is attributed to the region in which the storm was first named. Regions in (a, b) are indicated by the color bar below panel (b). In (c), areas of increased track density are shown by green ovals, and the number of named storms that passed through each region are indicated. The Atlantic MDR is shown by the green box. The "extratropics" includes all regions except for the MDR and Gulf of Mexico. (Source: HURDAT2 [Landsea and Franklin 2013].)

Historically, above-normal seasons result from a sharp increase in the number, intensity, and duration of storms that develop in the MDR. During the 2020 season, 16 of the 30 named storms formed in the MDR (Fig. 4.23b) and accounted for 10 of the season's 14 hurricanes and five of the season's seven major hurricanes. The associated MDR-related ACE value was 143% of the median and far exceeds the ACE of 27% associated with storms first named over the Gulf of Mexico and 20% for storms from the extratropics. This MDR-related ACE value was comparable to the 1981–2010 MDR average for above-normal seasons of 155% of the median. These values are roughly 10 times higher than the MDR average of 15.8% for below-normal seasons (Bell et al 2011).

The actual storm tracks during 2020 (not shown) showed three main regions of exceptionally high track density (Fig. 4.23c). One region extended from the western Caribbean Sea to the central U.S. Gulf Coast experiencing 11 named storms with nine as hurricanes and four of those as major hurricanes. Another region extended along the U.S. Atlantic Coast, with eight named storms, one of which became a hurricane. A third region covered the west-central North Atlantic, also with eight named storms, three of which became hurricanes and two of those became major hurricanes.

The season's storm tracks resulted in a record 12 landfalling storms in the continental United States. Six struck as hurricanes, including five as Category 1–2 storms and one as a Category 4 major hurricane (Hurricane Laura in Louisiana). Regionally, nine named storms (including four Category 1–2 hurricanes and Hurricane Laura) made landfall along the Gulf Coast. Louisiana alone experienced a record five landfalling storms, with two striking as Category 1–2 hurricanes (Delta and Zeta) and Category 4 Hurricane Laura. The U.S Atlantic Coast experienced three landfalling storms, including Category 1 Hurricane Isaias. Elsewhere, two hurricanes (Delta and Zeta) made landfall in Mexico, two major hurricanes (Eta and Iota) made landfall in Nicaragua, and one hurricane (Nana) made landfall in Belize.

(III) SEA SURFACE TEMPERATURES

Four main sea surface temperature (SST) signals were present during ASO 2020 (Fig. 4.24). First, SSTs were above average throughout the MDR (Fig. 4.24a), and the area-averaged SST anomaly was +0.6°C (Fig. 4.24b). The largest anomalies were observed throughout the Caribbean Sea and ranged from +0.5° to +1.0°C. Second, the area-averaged SST anomaly in the MDR was also higher (by 0.35°C) than that of the remainder of the global tropics (Fig. 4.24c). This signal typifies the warm phase of the Atlantic Multi-decadal Oscillation (AMO; Enfield and Mestas-Nuñez 1999; Bell and Chelliah 2006) and is a ubiquitous characteristic of Atlantic high-activity eras such as 1950–70 and 1995–present (Goldenberg et al. 2001; Vecchi and Soden 2007; Bell et al. 2018).

The third SST signal during ASO 2020 reflected above-average temperatures across most of the North Atlantic Ocean. Outside of the MDR, the largest anomalies (exceeding +1.5°C) occupied the western and portions of the central North Atlantic (Fig. 4.24a), where numerous tropical storms and hurricanes tracked across this region. The area-averaged SST anomaly in the western North Atlantic (red box, Fig. 4.24a) was +0.91°C and reflected a continuation of exceptional warmth that began in 2014 (Fig. 4.24d).

The fourth SST signal during ASO 2020 was the development of La Niña (section 4b). As discussed below, La Niña contributed to the extensive hurricane activity from September onward.

(IV) ATMOSPHERIC CONDITIONS

Climatologically, the ASO peak in Atlantic hurricane activity largely reflects the June–September peak in the West African monsoon. The inter-related circulation features of an enhanced monsoon increase hurricane activity, while those of an anomalously weak monsoon suppress it (Gray 1990; Hastenrath 1990; Landsea et al. 1992; Bell and Chelliah 2006; Bell et al. 2018, 2020). The association on multi-decadal time scales between the AMO and Atlantic hurricane activity largely exists because of their common relationship with the West African monsoon (Bell and Chelliah 2006).

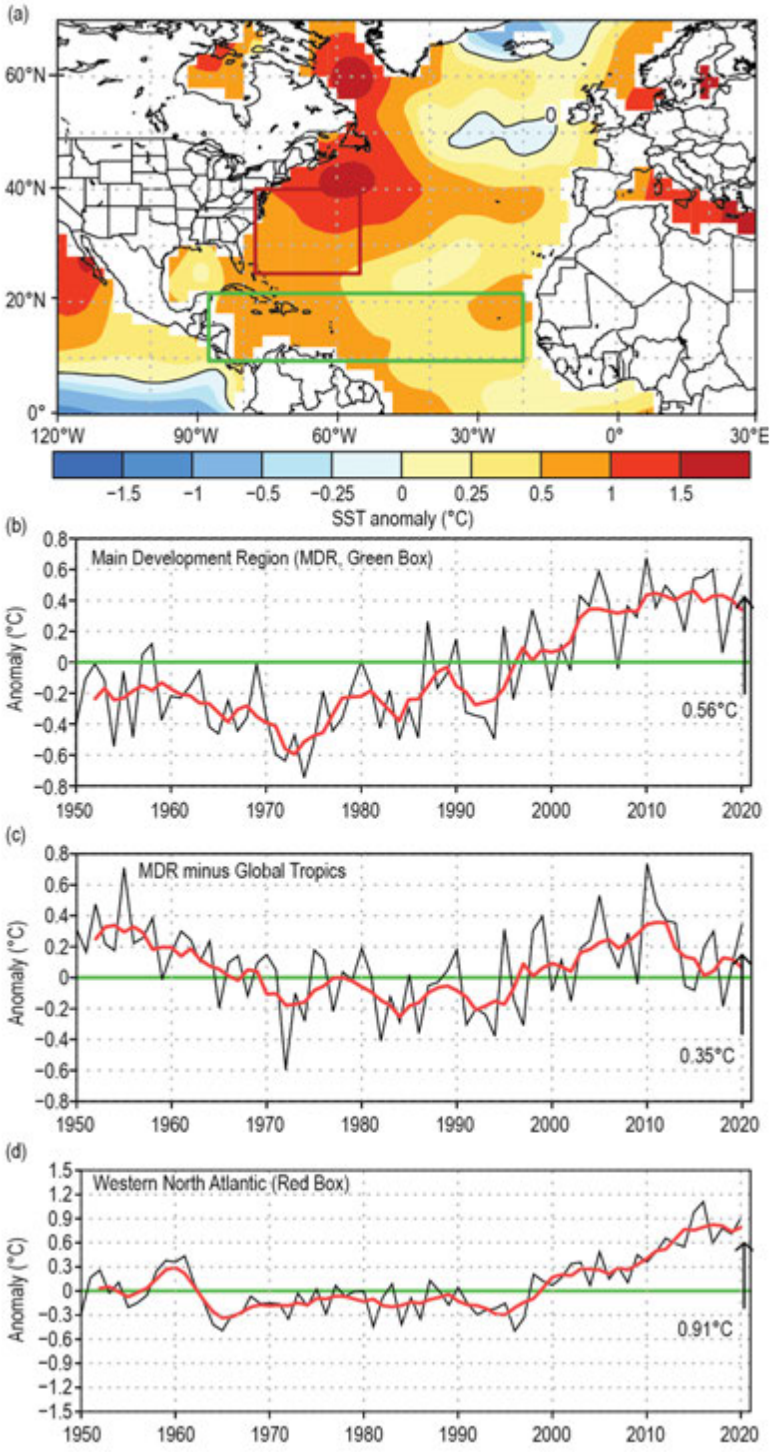

Fig. 4.24. (a) Aug–Oct 2020 SST anomalies (°C). (b)–(d) Time series of Aug–Oct area-averaged SST anomalies (black) and 5-point running mean of the time series (red), (b) in the MDR (green box in (a) spanning 20°–87.5°W and 9.5°–21.5°N), (c) difference between the MDR and the global tropics (20°S–20°N), and (d) in the western North Atlantic (red box in (a) spanning 55°–77.5°W and 25°–40°N). Anomalies are departures from the 1981–2010 period means. (Source: ERSST-v5 [Huang et al. 2017].)

The West African monsoon was enhanced during July–September 2020, as indicated by negative outgoing longwave radiation (OLR) anomalies across the African Sahel (red box, Fig. 4.25a). Total OLR values in this region averaged 234 W m^{-2} (Fig. 4.25b), with values less than 240 W m^{-2}, indicating deep tropical convection. Consistent with these conditions, the larger-scale divergent circulation at 200-hPa featured an extensive area of anomalous divergence and a core of negative velocity potential anomalies across subtropical northern Africa (Fig. 4.25c). The OLR time series shows that an enhanced monsoon has largely prevailed throughout the current Atlantic high-activity era and warm AMO of 1995–present (Fig. 4.25b). By contrast, a much weaker monsoon with OLR values well above 240 W m^{-2} in the Sahel region was typical of the low-activity and cool AMO period of the 1980s and early 1990s.

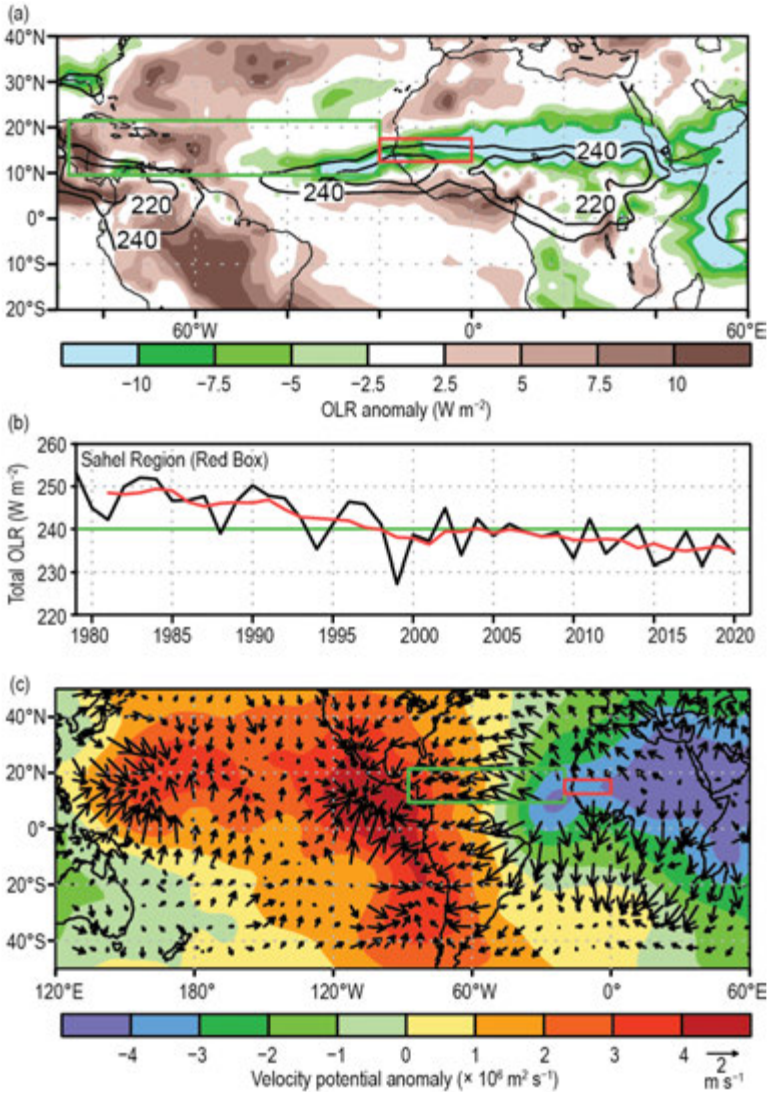

Fig. 4.25. (a) Jul–Sep 2020 anomalous OLR (W m^{-2}), with negative (positive) values indicating enhanced (suppressed) convection. (b) Time series of Jul–Sep total OLR (black) and 5-point running mean of the time series (red) averaged over the African Sahel region (red box in (a), (c) spanning 20°W–0° and 12.5°–17.5°N). (c) Jul–Sep 2020 anomalous 200-hPa velocity potential (× 10^6 m^2 s^{-1}) and divergent wind vectors (m s^{-1}). In (a), contours show total OLR values of 220 W m^{-2} and 240 W m^{-2}. In (a), (c), the green box denotes the Atlantic MDR. Anomalies are departures from the 1981–2010 means. (Source: NCEP/NCAR Reanalysis [Kalnay et al. 1996] for velocity potential and wind, and Liebmann and Smith [1996] for OLR.)

During ASO 2020, core atmospheric conditions within the MDR reflected a combination of the enhanced West African monsoon and La Niña. At 200 hPa, one monsoon-related feature was amplified subtropical ridges (indicated by anticyclonic streamfunction anomalies) across the Atlantic Ocean and Africa in both hemispheres (Fig. 4.26a). La Niña impacts in that field (Bell and Chelliah 2006) included cyclonic streamfunction anomalies in both hemispheres of the western and central subtropical Pacific, along with a contribution to the anticyclonic anomalies across the Caribbean Sea and MDR. This combination resulted in a zonal wave-1 anomaly pattern in both hemispheres (green ovals in Fig. 4.26a) that is a classic signal for an extremely active Atlantic hurricane season (Bell and Chelliah 2006; Landsea et al. 1998; Bell et al. 2011).

Within the MDR, this anomaly pattern also reflected a weaker tropical upper-tropospheric trough (indicated by anomalous easterly winds in Fig. 4.26b). Other monsoon-related features were present in the lower troposphere, including lower sea level pressure and weaker easterly and northeasterly trade winds (indicated by westerly and southwesterly anomalies) across the southern half of the central and eastern MDR (Fig. 4.26c).

The resulting combination of anomalous low-level westerlies and upper-level easterlies produced an extensive area of weak vertical wind shear across the tropical Atlantic, western Caribbean Sea, and southern Gulf of Mexico (Figs. 4.27a,b). The area-averaged magnitude of the vertical

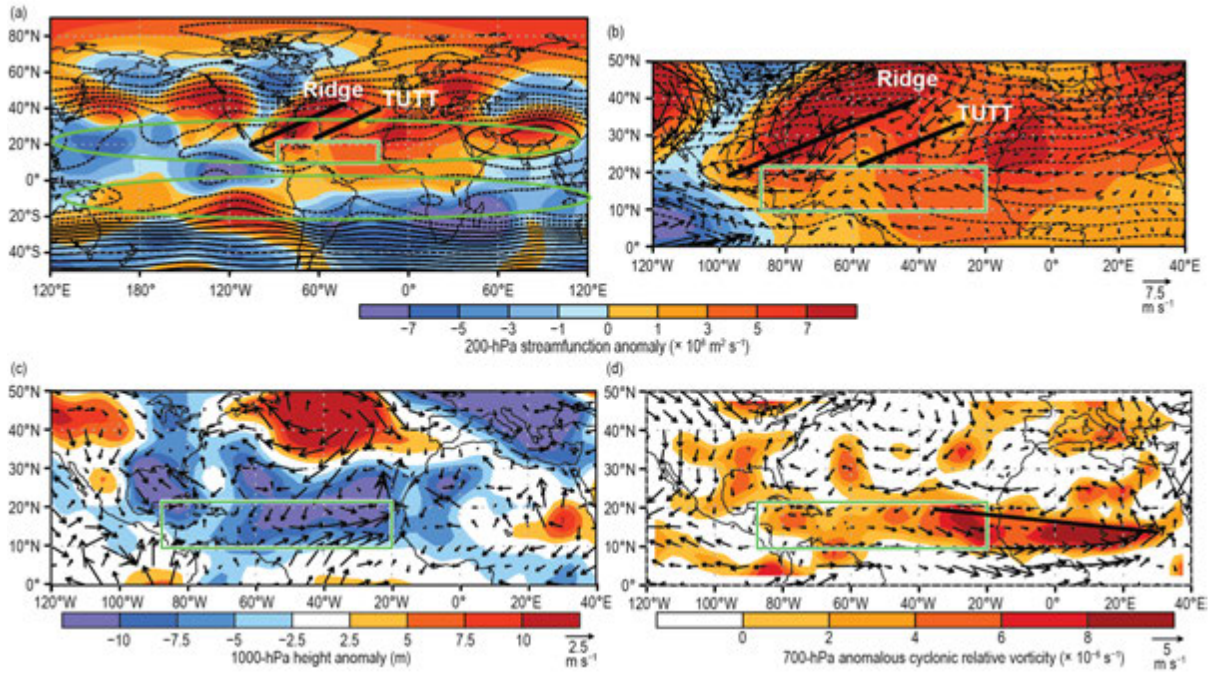

Fig. 4.26. Aug–Oct 2020: (a), (b) 200-hPa streamfunction (contours, interval is 5 × 10^6 m^2 s^{-1}) and anomalies (shaded), with anomalous vector winds (m s^{-1}) also shown in (b); (c) anomalous 1000-hPa heights (shaded, m) and vector winds; and (d) anomalous 700-hPa cyclonic relative vorticity (shaded, × 10^{-6} s^{-1}) and vector winds. In (a), (b) the upper-level ridge and TUTT discussed in the text are labeled and denoted by thick black lines. In (a), green ovals highlight the zonal wave-1 pattern discussed in the text. In (d), the thick solid line indicates the axis of the mean African Easterly Jet, which was hand-drawn based on total seasonal wind speeds (not shown). Vector scales differ for each panel and are below right of color bar. The green box denotes the MDR. Anomalies are departures from the 1981–2010 means. (Source: NCEP/NCAR Reanalysis [Kalnay et al. 1996].)

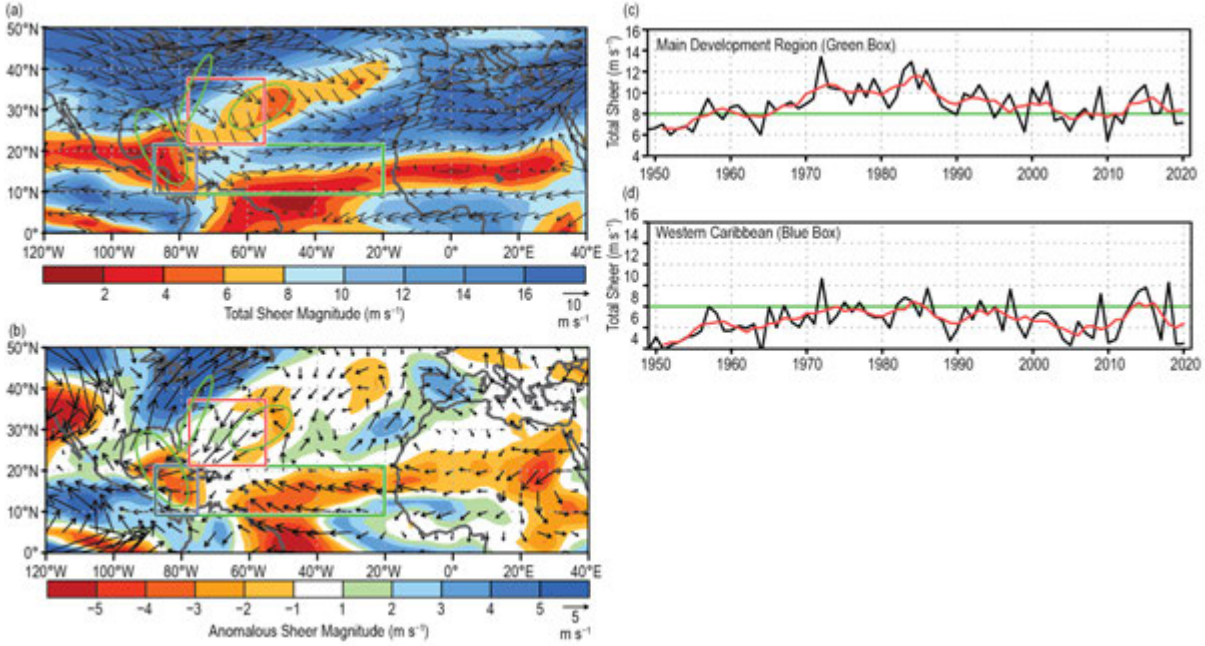

Fig. 4.27. Aug–Oct (ASO) magnitude of the 200–850 hPa vertical wind shear (m s^{-1}): 2020 (a) total magnitude and vector and (b) anomalous magnitude and vector. (c), (d) Time series of ASO vertical shear magnitude (black) and 5-point running mean of the time series (red) averaged over (c) the MDR (green box in (a),(b) spanning 20°–87.5°W and 9.5°–21.5°N), and (d) the western Caribbean Sea (blue box in (a),(b) spanning 87.5°–75°W and 9.5°–21.5°N). Regions with increased track density are shown by green ovals copied from Fig. 4.23c. Anomalies are departures from the 1981–2010 means. (Source: NCEP/NCAR Reanalysis [Kalnay et al. 1996].)

wind shear for the entire MDR was 7.2 m s^{-1} (Fig. 4.27c) and for the western Caribbean Sea was an exceptionally low 4.5 m s^{-1} (Fig. 4.27d). Both of these values are well below the upper threshold of 8 m s^{-1} considered conducive to hurricane formation on monthly time scales (Bell et al. 2017).

The anomalous low-level circulation also reflected an extensive flow of deep tropical moisture into the southern half of the central and eastern MDR. This moisture not only helps feed the monsoon, but also favors increased Atlantic hurricane activity. This situation contrasts with the drier and cooler air that normally accompanies enhanced northeasterly trade winds when the monsoon is weak.

Another aspect of the enhanced West African monsoon system during ASO 2020 was an upward extension of the easterly wind anomalies over the eastern half of the MDR to at least the 700-hPa level (Fig. 4.26d), which is the approximate level of the African Easterly Jet (AEJ). This anomaly pattern contributed to a deep layer of anomalous cyclonic relative vorticity (i.e., increased horizontal cyclonic shear) along the equatorward flank of the AEJ. These conditions are known to favor increased TC activity by helping African easterly waves to be better maintained and by providing an inherent cyclonic rotation to their embedded convective cells (Bell et al. 2004, 2006, 2017, 2018, 2020; Landsea et al. 1998).

The above conditions typified the many above-normal and extremely active seasons seen during the current Atlantic high-activity era; however, interannual signals were also in play during 2020. One of those was La Niña, which supported increased Atlantic hurricane activity over the Caribbean Sea and southern Gulf of Mexico in response to its contribution to weaker vertical wind shear. Another interannual signal was a strong ridge over the western North Atlantic (Figs. 4.26a,b). This ridge contributed to the weak vertical wind shear (Fig. 4.27a), exceptionally warm SSTs over the western North Atlantic (Fig. 4.24d), and to the development of several hurricanes north of the MDR. It also contributed to a highly anomalous steering current (Fig. 4.28), which not only helped focus the storm tracks (Fig. 4.23c), but also contributed to the development of several hurricanes north of the MDR.

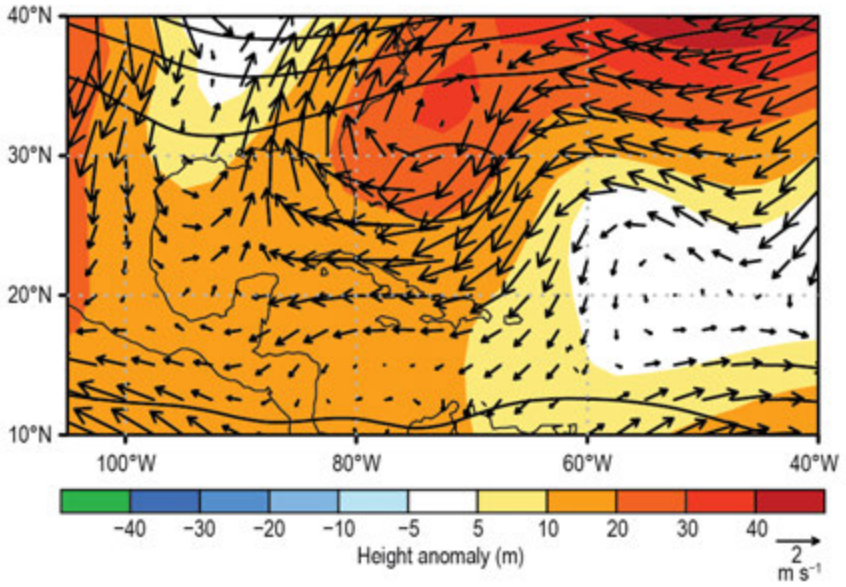

Fig. 4.28. Aug–Oct (ASO) vertically averaged anomalous wind vector between 850 and 200 hPa, along with 500-hPa heights (contours) and anomalies (shaded). (Source: NCEP/NCAR Reanalysis [Kalnay et al. 1996].)

Sidebar 4.1: Hurricane Laura: A record-setting hurricane for southwest Louisiana—

P. J. KLOTZBACH AND R. E. TRUCHELUT

The 2020 Atlantic hurricane season was extremely active, setting the record for most named storms observed in a single season with 30, breaking the old record of 28 set in 2005. The 2020 season also broke the record for most continental United States named storm landfalls in a single season with 11, breaking the old record of nine set in 1916. Of these 11 named storm landfalls, Hurricane Laura was the strongest, making landfall near Cameron, Louisiana, with maximum sustained winds of 130 kt (67 m s^{-1}) on 27 August 2020. Laura caused tremendous damage in Lake Charles and other smaller communities in southwest Louisiana. Laura was the third of four named storms that would make landfall in Louisiana in 2020, tying the old record of four Louisiana named storm landfalls set in 2002.

Fig. SB4.1. GeoColor satellite image of Category 4 Hurricane Laura on 26 Aug at 2050 UTC.

Here, the meteorological history of Laura will be summarized, along with some of the notable records that the system set. Historical landfall records from 1851–present are taken from the National Hurricane Center/Atlantic Oceanographic and Meteorological Laboratory archive located at: http://www.aoml.noaa.gov/hrd/hurdat/All_U.S._Hurricanes.html. Laura's observed values are taken from Pasch et al. (2021). All times are listed in hours UTC.

Laura became a tropical depression on 20 August in the central tropical Atlantic and slowly intensified to a tropical storm the following day. Westerly shear and dry air entrainment caused persistent displacement of the mid- and low-level circulation centers, and Laura remained a low-end tropical storm as it tracked just south of Puerto Rico on 22 August. Vertical wind shear decreased as Laura crossed the southern portion of the Dominican Republic and Haiti on 23 August. This allowed for better vortex alignment, and maximum sustained winds increased to 55 kt (28 m s^{-1}) before weakening slightly due to both an increase in northerly shear and land interaction with Cuba on 24 August.

Once Laura emerged from the west coast of Cuba, the storm entered a more favorable environment of relatively low wind shear, high sea surface temperatures (~30°C), and increased levels of mid-level moisture. Laura intensified slowly at first, reaching hurricane strength at 1200 UTC on 25 August over the south-central Gulf of Mexico. By early on 26 August, the environment became even more conducive for strengthening, and Laura rapidly intensified from a 75-kt (39-m s^{-1}) Category 1 hurricane at 00 UTC on 26 August to a 130-kt (67-m s^{-1}) Category 4 hurricane at 00 UTC on 27 August (Fig. SB4.1). This 55-kt (28-m s^{-1}) intensification in 24 hours was the fastest intensification rate for an Atlantic named storm in the Gulf of Mexico since Hurricane Karl in 2010, which also intensified by 55 kt (28 m s^{-1}) in 24 hours. Around 6 hours after ending its rapid intensification, Laura made landfall in southwest Louisiana at its peak intensity (i.e., 130 kt [67 m s^{-1}]). Following landfall, Laura rapidly weakened to a tropical storm later on 27 August and then to a tropical depression on 28 August as it tracked north into Arkansas, dissipating early on 29 August over the Ohio Valley.

Fig. SB4.2. Heavily damaged National Weather Service Lake Charles radar following Hurricane Laura. (Image courtesy of Brett Adair, Live Storms Media.)

Hurricane Laura caused tremendous damage in southwestern Louisiana, with a current estimated cost of $19 billion (U.S. dollars). Laura was responsible for seven direct and 34 indirect fatalities in the United States, with 31 additional fatalities occurring in Haiti and nine in the Dominican Republic. About 4 to 6 m of storm surge occurred to the east of Laura's landfall near Creole and Grand Chenier, Louisiana. Lake Charles, Louisiana, suffered extreme wind damage from gusts exceeding 115 kt (59 m s^{-1}), including the destruction of the Lake Charles' Weather Forecast Office's WSR-88D doppler radar (Fig. SB4.2). Laura's track was slightly farther east than anticipated just before landfall, thus sparing Lake Charles a much more significant storm surge.

The 130 kt (67 m s^{-1}) maximum sustained winds at the time of Laura's landfall were the strongest for a Louisiana hurricane since the Last Island Hurricane of 1856 and tied for the fifth strongest on record in the continental United States. Laura's landfall pressure of 939 hPa was the fourth lowest for a Louisiana hurricane on record, trailing Katrina in 2005 (920 hPa), the Last Island Hurricane in 1856 (934 hPa), and Rita in 2005 (937 hPa). Laura also rapidly intensified prior to landfall, defined to be an intensification of ≥30 kt in 24 hours (≥15 m s^{-1} in 24 hours). This was one of three hurricanes in 2020 to rapidly intensify in the 24 hours before its continental U.S. landfall, with the others being Hurricanes Hanna and Zeta. Like Laura, Zeta also rapidly intensified in the 24 hours prior to its landfall in Louisiana. Laura's 40 kt (21 m s^{-1}) of intensification in its final 24 hours prior to landfall in the continental United States are tied with Hurricanes Michael (2018) and Charley (2020) for the second highest in the last two decades, trailing only Zeta, which intensified by 45 kt in the 24 hours before its landfall in Louisiana in late October 2020.

3) Eastern North Pacific and Central North Pacific basins—K. M. Wood and C. J. Schreck

(I) SEASONAL ACTIVITY

This section combines statistics from the two agencies responsible for issuing advisories and warnings in the eastern North Pacific (ENP) basin: NOAA's National Hurricane Center in Miami, Florida (from the Pacific coast of North America to 140°W), and NOAA's Central Pacific Hurricane Center in Honolulu, Hawaii (between 140°W and the date line, the Central North Pacific [CNP]).

A total of 17 named storms formed in the combined ENP/CNP basin in 2020 (Fig. 4.29a), four of which became hurricanes and three became major hurricanes. This activity is near normal for named storms but below normal for hurricanes: the 1981–2010 IBTrACS seasonal averages are 16.5 named storms, 8.5 hurricanes, and 4.0 major hurricanes (Schreck et al. 2014). All named storms occurred between the official hurricane season start date of 15 May and end date of 30 November; however, the first tropical depression formed at 1200 UTC on 25 April, marking the earliest ENP tropical cyclone (TC) formation since the start of the satellite record in 1966 (Cangialosi 2020). That depression did not reach tropical storm intensity; the first to do so was Tropical Storm Amanda on 31 May. The final named storm, Tropical Storm Polo, dissipated on 19 November. Sixteen named storms were classified operationally and post-season analysis revealed the season's seventh tropical depression was, in fact, a short-lived tropical storm (Brown 2020). No named storms formed within the CNP, but one (Douglas) entered the region from the east, placing 2020 well below the 1981–2010 IBTrACS seasonal average of 4.7 for the CNP.

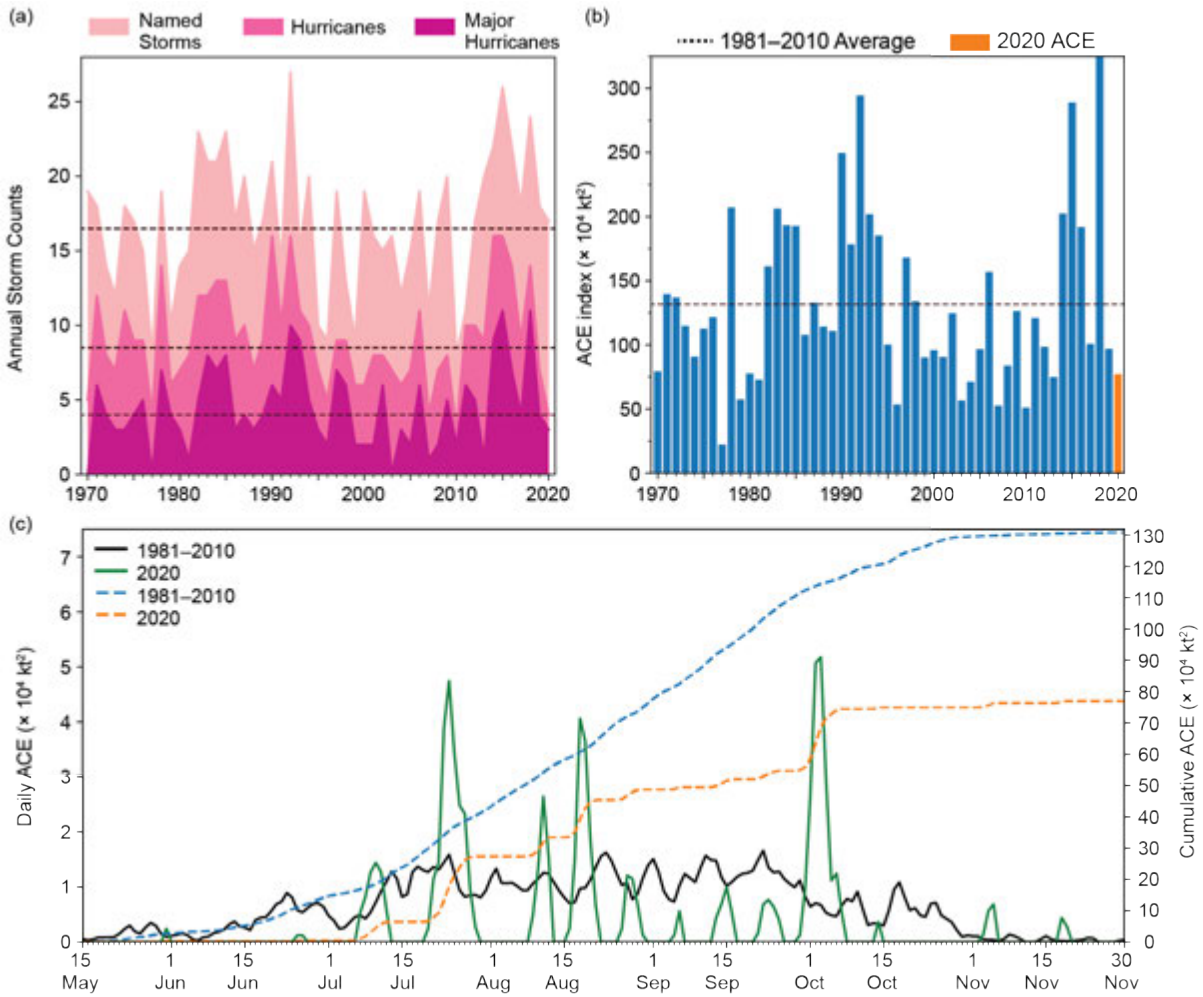

Fig. 4.29. (a) Annual storm counts by category during 1970–2020, with the 1981–2010 average by category denoted by each dashed line. (b) Annual ACE during 1970–2020, with 2020 highlighted in orange and the 1981–2010 average denoted by the dashed line. (c) Daily ACE during 1981–2010 (solid black) and during 2020 (solid green); accumulated daily ACE during 1981–2010 (dashed blue) and during 2020 (dashed orange).

The 2020 seasonal ACE index was 77 × 10^4 kt^2, or 58% of the 1981–2010 mean of 132 × 10^4 kt^2 (Figs. 4.29b,c; Bell et al. 2000; Schreck et al. 2014). The bulk of 2020 TC activity, including three hurricanes and two major hurricanes, was confined to July and August (comprising 63% of the season's ACE). Only tropical storms formed in September, and the season's final major hurricane (Marie) occurred in early October.

As in 2019 (Wood and Schreck 2020), three 2020 ENP TCs contributed more than half of the season's total ACE, with each reaching Category 4 intensity (113–136 kt; 58–70 m s^{-1}) on the SSHWS. In addition, all three TCs underwent rapid intensification (≥30 kt or 15.4 m s^{-1} in 24 hours) prior to peak intensity and later rapidly weakened while over open ocean (≤–30 kt or –15.4 m s^{-1} in 24 hours; Wood and Ritchie 2015). Hurricane Genevieve (16–21 August) exhibited the fastest 24-hour intensification rate of 50 kt (26 m s^{-1}). The fastest 24-hour intensification rate for Hurricane Douglas (21–29 July) was 45 kt (23 m s^{-1}), and Hurricane Marie (29 September–6 October) intensified 40 kt (21 m s^{-1}) in 24 hours. Despite achieving the most rapid 24-hour intensification rate, Genevieve spent the least amount of time at its peak intensity, which lasted only 6 hours before it began weakening. Conversely, Marie maintained ≥115-kt maximum winds for 30 hours.

(II) ENVIRONMENTAL INFLUENCES ON THE 2020 SEASON

Negative SST anomalies were observed over much of the equatorial eastern Pacific during the 2020 ENP hurricane season, a signature of the developing La Niña event (section 4b), although season-averaged SSTs were generally above normal where most TCs formed (Fig. 4.30a). Pronounced positive anomalies persisted at higher latitudes, particularly north of Hawaii, and these warmer-than-normal waters may have contributed to the long track of Douglas near Hawaii in July.

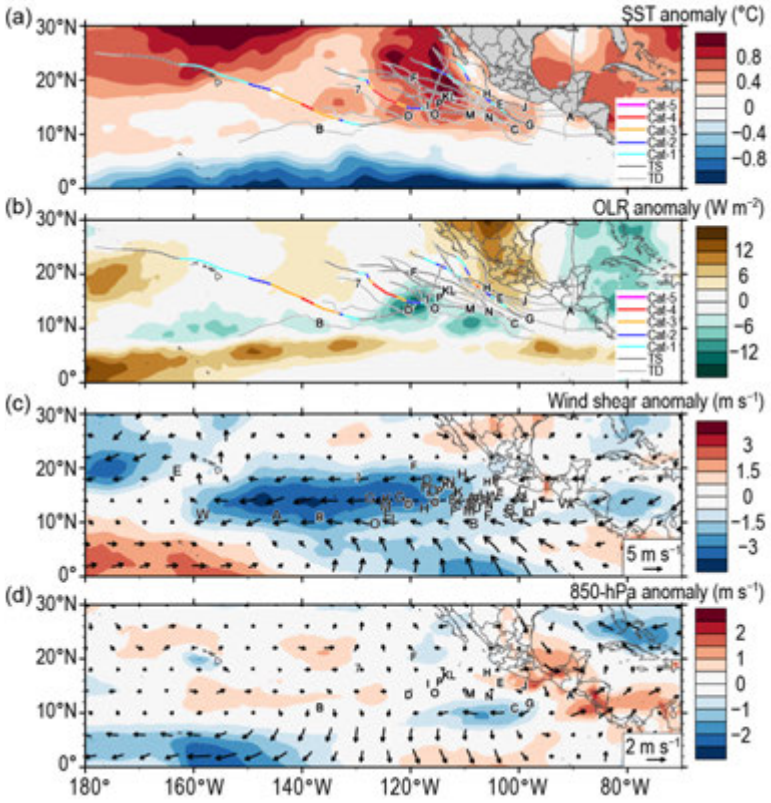

Fig. 4.30. 15 May–30 Nov 2020 anomaly maps of (a) SST (°C; Banzon and Reynolds 2013), (b) OLR (W m^{-2}; Schreck et al. 2018), (c) 200–850-hPa vertical wind shear (m s^{-1}) vector (arrows) and scalar (shading) anomalies, and (d) 850-hPa wind (m s^{-1}, arrows) and zonal wind (shading) anomalies. Anomalies are relative to the annual cycle from 1981–2010, except for SST, which is relative to 1982–2010 due to data availability. Letters denote where each TC attained tropical storm intensity; "7" represents the unnamed tropical storm revealed in post-season analysis. Wind data are obtained from CFSR (Saha et al. 2014).

Most TC activity was confined to the eastern part of the basin, where OLR anomalies were near or below normal and co-located with below-normal vertical wind shear (Figs. 4.30b,c); however, only two TCs tracked west of 120°W where the shear was most anomalously below normal. As in recent ENP seasons, 2020 was again marked by enhanced 850-hPa easterly flow near Central America, which may have limited activity by reducing the available low-level cyclonic vorticity (Fig. 4.30d).

Tropical cyclone activity in the ENP, especially cyclogenesis, can be affected by the Madden-Julian Oscillation (MJO) as well as convectively coupled Kelvin waves (e.g., Maloney and Hartmann 2001; Aiyyer and Molinari 2008; Schreck and Molinari 2011; Ventrice et al. 2012a,b; Schreck 2015, 2016). Although the MJO signal was weak within the ENP for much of the hurricane season, the enhanced convective phase in August may have supported the development of Elida, Fausto, and Genevieve (Fig. 4.31; see Kiladis et al. 2005, 2009 for methodology). The convectively enhanced phase of Kelvin waves likely contributed to the formation of Amanda, Boris, Cristina, Douglas, Iselle, and Lowell. Easterly wave activity can be inferred from Fig. 4.31 as westward-moving negative (green) anomalies; such waves were particularly active during the genesis of Cristina, Elida, Genevieve, Hernan, Karina, Lowell, Marie, Odalys, and Polo.

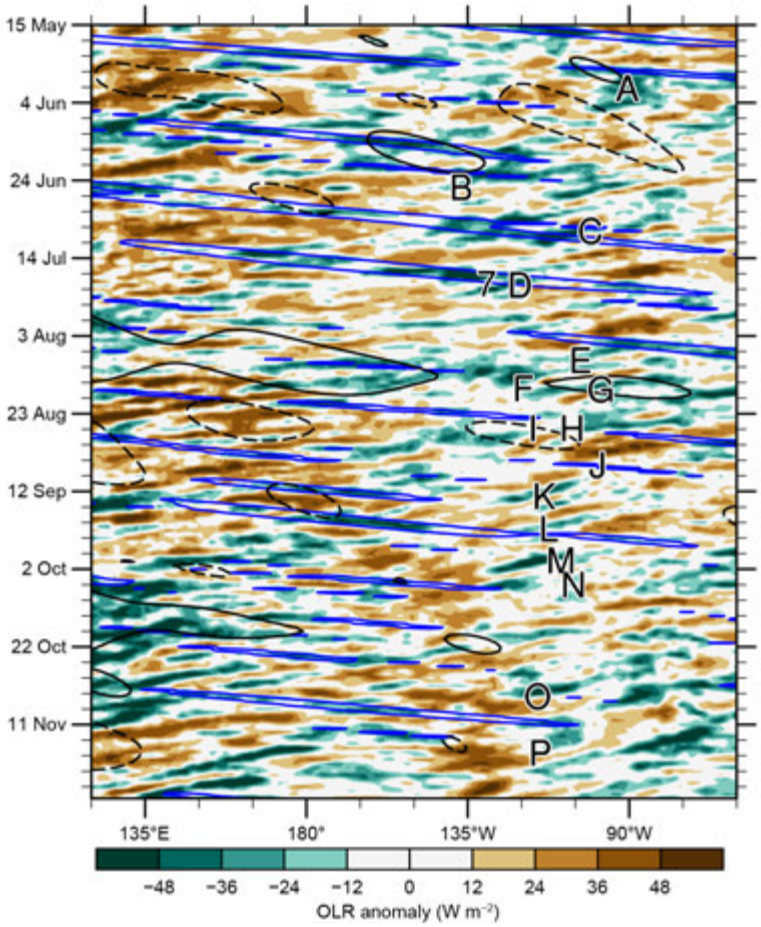

Fig. 4.31. Longitude–time Hovmöller diagram of 15°–5°N average OLR (W m^{-2}; Schreck et al. 2018). Unfiltered anomalies from a daily climatology are shaded. Negative anomalies (green) indicate enhanced convection. Anomalies filtered for Kelvin waves are contoured in blue at –10 W m^{-2} and MJO-filtered anomalies are contoured in black at ±10 W m^{-2} (dashed for positive, solid for negative). Letters denote the longitude and time when each TC attained tropical storm intensity; "7" represents the unnamed tropical storm revealed in post-season analysis.

(III) TROPICAL CYCLONE IMPACTS

One ENP TC made landfall while at least at tropical storm strength, yet five TCs (Amanda, Genevieve, Hernan, Iselle, and Douglas) produced impacts in 2020. Tropical Storm Amanda (30–31 May) became the second known Pacific TC to make landfall in Guatemala, with the first being Tropical Storm Agatha in 2010 (Berg 2020). Amanda contributed to excessive rainfall, widespread flooding, and numerous mudslides in Central America. The other contributors were Atlantic Tropical Storm Cristobal (which formed in part from Amanda's remnants) and a Central American gyre in the region as described by Papin (2014). These impacts resulted in 40 deaths, affected over 100,000 people, and damaged or destroyed over 3000 ha of crops (Berg 2020).

On average, 1.8 ENP TCs make landfall in Mexico each year (Raga et al. 2013), but no TCs made landfall in 2020. Nonetheless, Hurricane Genevieve tracked close to Baja California Sur, bringing heavy rain and strong winds to the peninsula as it weakened while encountering decreasing SSTs and dry air. Short-lived Tropical Storm Hernan (26–28 August) also impacted Baja California Sur, although it also did not make landfall. Shortly after Hernan dissipated, Tropical Storm Iselle (26–30 August) approached Baja California but weakened to a remnant low well offshore.

Hurricane Douglas, one of three Category 4 ENP hurricanes in 2020 and the only named storm to reach the CNP portion of the basin, passed within 50 nautical miles (93 km) of multiple Hawaiian Islands while at hurricane intensity (Latto 2020). Although the TC did not make landfall, its circulation crossed several of the northwestern Hawaiian Islands as a tropical storm. In line with its close proximity to land, there was some minor damage in Hawaii—mainly nuisance flooding and some downed trees, but no casualties were reported due to Douglas (see https://weather.com/safety/hurricane/news/2020-07-27-hawaii-hurricane-douglas).

4) Western North Pacific basin—S. J. Camargo

(I) OVERVIEW

The 2020 TC season in the western North Pacific (WNP) was below normal by most measures of TC activity. The data used here are primarily from the JTWC best-track data for 1945–2019 and preliminary operational data for 2020. All statistics are based on the 1981–2010 climatological period unless otherwise noted.

According to the JTWC, a total of 23 TCs (bottom quartile ≤ 23) reached tropical storm intensity in 2020. From these, 12 reached typhoon intensity (bottom quartile ≤ 15), with two reaching super typhoon status (≥130 kt, bottom quartile ≤ 2). There were also three tropical depressions (median = 3.5); however, Krovanh was considered a tropical storm by the Japan Meteorological Agency (JMA). Only 52% of the tropical storms intensified into typhoons (bottom quartile ≤ 59%) and only 17% of the typhoons reached super typhoon intensities (median = 25%). Figure 4.32a shows the number of storms in each category for 1945–2020.

The JMA total for 2020 was also 23 TCs (bottom quartile ≤ 23). While this is the same number of storms that reached tropical storm intensity for JTWC, there were differences between the agencies.[4] In addition to Krovanh, Tropical Storm Six was not included among the JMA 2020 storms, and Mekkhala and Kujira were considered typhoons by JTWC, but were only considered tropical storms by JMA. Of the 23 JMA TCs, eight were tropical storms (top quartile ≥ 7), five were severe tropical storms (median = 5), and 10 were typhoons (bottom quartile ≤ 13). Only 44% of the storms reached typhoon intensity (bottom quartile ≤ 50%). The number of all TCs (1951–1976) and tropical storms, severe tropical storms and typhoons (1977–2020) according to the JMA are shown in Fig. 4.32b. The Philippine Atmospheric, Geophysical and Astronomical Services Administration (PAGASA) named 22 TCs that entered its area of responsibility, including Tropical Depressions Carina, Gener (corresponding to JTWC Tropical Storm Six), and Ofel, which were not named by JMA.

[4] It is well known that there are systematic differences between the JMA and the JTWC datasets. These differences have been extensively documented in the literature (e.g., Knapp et al. 2013; Schreck et al. 2014).

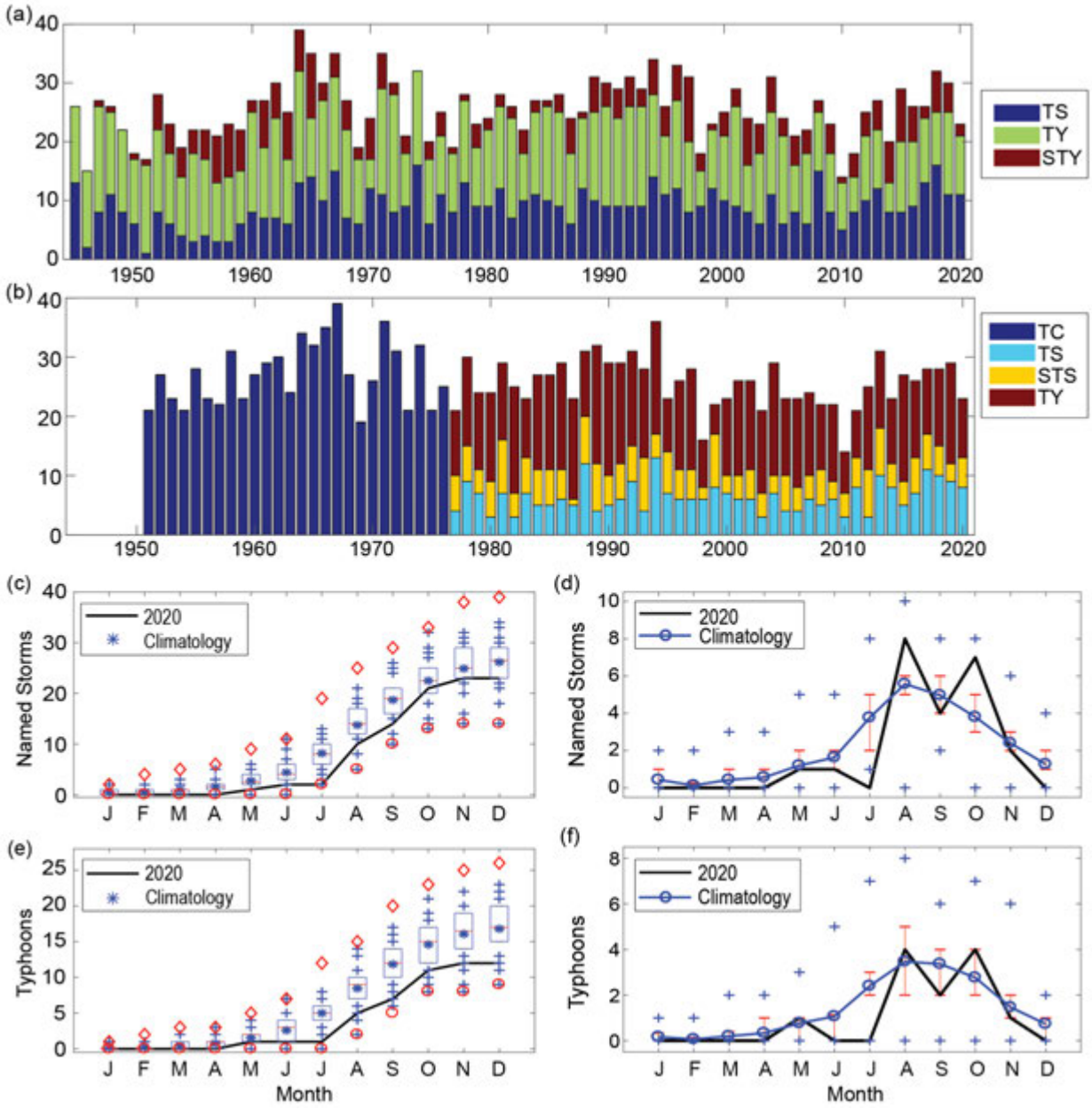

Fig. 4.32. (a) Number of tropical storms (TSs), typhoons (TYs) and super typhoons (STYs) per year in the WNP for the period 1945–2020 based on JTWC data. (b) Number of tropical cyclones (TCs; all storms that reach TS intensity or higher) from 1951 to 1976; number of TSs, severe tropical storms (STSs) and TYs from 1977 to 2020 based on JMA data. Panel (c) shows the cumulative number of tropical cyclones with TS intensity or higher (named storms) per month in the WNP in 2020 (black line), and climatology (1981–2010) as box plots (interquartile range: box; median: red line; mean: blue asterisk; values in the top or bottom quartile: blue crosses; high [low] records in the 1945–2019 period: red diamonds [circles]). Panel (e) is similar to panel (c) but for the number of TYs. Panels (d) and (f) show the number of named storms and TYs per month in 2020 (black line) and the climatological mean (blue line), the blue "+" signs denote the maximum and minimum monthly historical records, and the red error bars show the climatological interquartile range for each month (in the case of no error bars, the upper and/or lower percentiles coincide with the median). (Sources: 1945–2019 JTWC best-track dataset, 2020 JTWC preliminary operational track data for panels (a), (c), (d), (e), and (f); 1951–2020 RSMC-Tokyo, Japan Meteorological Agency (JMA) best-track dataset for panel (b).)

(II) SEASONAL ACTIVITY

No active storms were present from January to April, and therefore the season started with Typhoon Vongfong in May. Only Tropical Storm Nuri was active in June and none were active in July. Therefore, it was a below-normal early typhoon season (January–June) with only two named storms (bottom quartile ≤ 3), including only one typhoon (bottom quartile ≤ 1). The lack of storms during January–April was not unusual. Climatologically, the percentage of the years with an active TC (typhoon) during January, February, March, and April is 40% (16.7%), 13.3% (6.7%), 33.3% (16.7%), and 46.7% (30%), respectively; however, this was the first time in the historical record that no named storms occurred in July (Fig. 4.32d) and previously only four other years had no typhoons that month (1947, 1975, 1998, and 2019; Fig. 4.32f). Furthermore, there were also no typhoons in June, which climatologically has at least one active typhoon in 63% of the years.

By contrast with July, August was a busy month with eight named storms (top quartile ≥ 6), including four tropical storms (Sinlaku, Jangmi, Six, and Higos) and four typhoons (Hagupit, Mekkhala, Bavi, and Maysak; median = 3) active during that month. Super Typhoon Haishen formed on 31 August and was mostly active during September, and thus is considered a September storm in this analysis. There were four named storms active in September: Tropical Storms Noul and Dolphin (bottom quartile ≤ 4) and Super Typhoon Haishen and Typhoon Kujira (bottom quartile ≤ 2). Tropical Depression Twelve also formed in September. Similar to August, October was a busy month with one tropical depression (Twenty) and seven named storms (top quartile ≥ 5), including three tropical storms (Linfa, Nangka, and Atsani) and four typhoons (top quartile ≥ 4; Chan-Hom, Saudel, Molave, and Super Typhoon Goni).

The season ended with two storms in November (bottom quartile ≤ 2), Tropical Storm Etau and Typhoon Vamco (median = 1), and Tropical Depression Krovanh in December. As shown in Figs. 4.32c–e, the early season (January–June) activity level was below normal. These quiet months were followed by an average peak season (July–October), with 19 named storms (median = 17), including 10 typhoons (median = 12). The late season (November–December) was also quiet with two named storms (bottom quartile ≤ 3), including only one typhoon (bottom quartile ≤ 1). The below-normal activity in the early and late seasons led to a below-normal season overall, even with near-normal levels of activity during the peak season, including 2 months (August and October) with above-normal activity.

The total seasonal ACE in 2020 (Fig. 4.33a) was in the bottom quartile of the climatological distribution—the fifth lowest in the historical record. In most months, the ACE value was in the bottom quartile of the climatological distribution. Only May, October, and November ACE values reached the below-normal quartile (25%–50%; Fig. 4.33b). Of particular note is July 2020, which was the first July in the historical record (JTWC records began in 1945) with zero ACE. In contrast, a zero ACE value is not as rare an event in June, having happened 13 times before. Low ACE values are typical of La Niña in the western North Pacific (Camargo and Sobel 2005).

Furthermore, WNP ACE in 2020 had a sharp peak in October, while climatologically the WNP ACE peak is flatter and spread almost equally from August to October (Fig. 4.33b). The months from August to November corresponded approximately to 95% of the total ACE in 2020, which is much higher than the climatological median percentage of 68%. The ACE of three storms in 2020 were each in the top quartile of the ACE per storm climatology: Super Typhoons Goni and Haishen and Typhoon Maisak. Together these three storms contributed to 45% of the seasonal ACE (17%, 16%, and 12%, respectively).

The mean genesis location in 2020 was 17.8°N and 129.5°E, northwest of the climatological mean of 13.2°N, 142.8°E (std. dev. of 1.9° latitude and 5.6° longitude). The mean track position in 2020 was 20.1°N, 127.5°E, similarly northwest of the climatological mean of 17.3°N, 136.6°E (std. dev. of 1.4° latitude and 4.7° longitude). There is a well-known connection between genesis and track shifts in the WNP basin and El Niño/La Niña, with La Niña favoring a northwestward shift in TC genesis and track (Chia and Ropelewski 2002; Camargo and Sobel 2005; Camargo et al. 2007a).

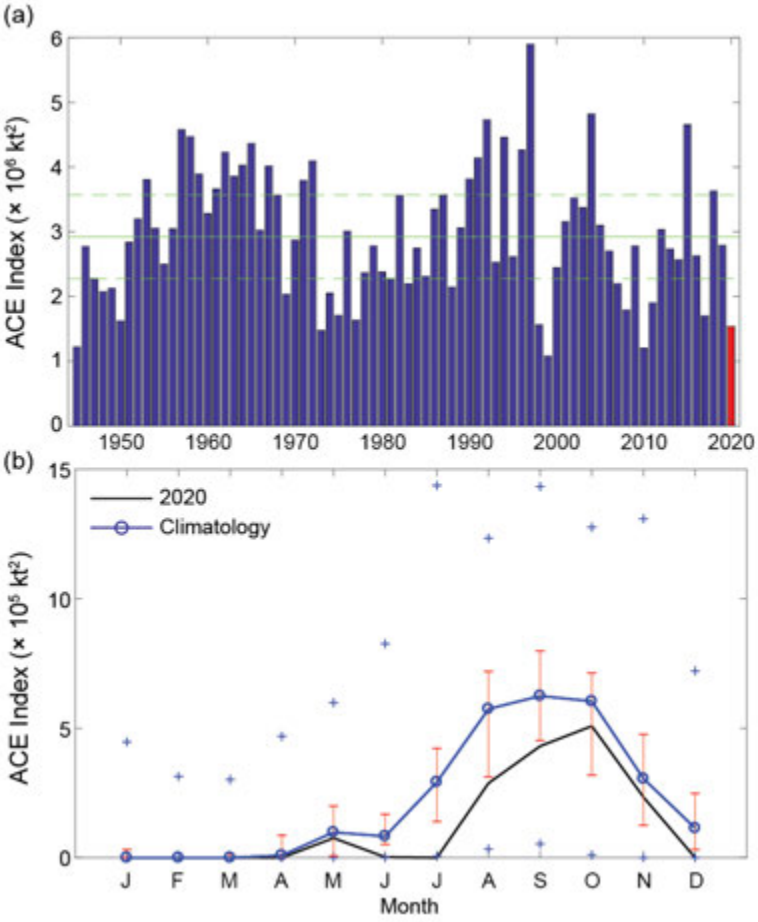

Fig. 4.33. (a) ACE per year in the WNP for 1945–2020. The solid green line indicates the climatological median (1981–2010), and the dashed lines show the climatological 25th and 75th percentiles. (b) ACE per month in 2020 (black line) and the median during 1981–2010 (blue line), with the red error bars indicating the 25th and 75th percentiles. In case of no error bars, the upper and/or lower percentiles coincide with the median. The blue "+" signs denote the maximum and minimum values during the 1945–2019. (Source: 1945–2019 JTWC best-track dataset; 2020 JTWC preliminary operational track data.)

The northwestward shift observed in 2020 is typical of La Niña seasons (genesis mean for La Niña events is 15.5°N, 136.1°E).

There were 70.25 days with active tropical storms and typhoons (bottom quartile ≤ 92.75). From these active days, 30.5 had typhoons (bottom quartile ≤ 49.5) and 10 days had major typhoons (Saffir–Simpson Categories 3–5; bottom quartile ≤ 15.75). The percentage of active days with typhoons and intense typhoons was 34% (bottom quartile ≤ 33%) and 11% (bottom quartile ≤ 10%), respectively. The median lifetime for TCs reaching tropical storm intensity was 5.0 days (bottom quartile ≤ 6.25 days) and for those reaching typhoon intensity was 6.4 days (bottom quartile ≤ 7.75 days).

The longest-lived storm in 2020 was Typhoon Chan-Hom (11.25 days), which was the only storm in the top quartile of the distribution (≥10.5 days). From the 23 named storms, only five had lifetimes above the median (7.75 days). These short-lived storms are another characteristic of La Niña in the WNP (Camargo and Sobel 2005; Camargo et al. 2007a). The maximum number of TCs active simultaneously in 2020 was three and occurred on 10 August (Tropical Storms Sinlaku, Jangmi, and Six), while two typhoons (Maysak and Haishen) were active on 2 September. The historical record is six active TCs (14–15 August 1996).

Including tropical depressions, 17 storms made landfall in 2020 (median = 17, 1951–2010 climatology). Landfall here is defined when a TC track is over land, and the previous TC location was over the ocean. In order to include landfall over small islands, tracks were interpolated from 6-hourly to 15-minutes intervals, and a high-resolution land mask was used. In cases of multiple landfalls, we considered the landfall with the highest intensity for each storm. Two storms made landfall as tropical depressions (below normal: 1–2 TDs), eight as tropical storms (top quartile ≥ 8), and five as typhoons Categories 1–2 (median = 5). Typhoon Vongfong and Super Typhoon Goni made landfall as major typhoons (Category 3–5; median = 2). Vongfong (named Ambo by PAGASA) made multiple landfalls in the Philippines, with the first and most intense landfall at San Policarpo in Eastern Samar. In late October, Typhoon Molave made landfall in both the Philippines and Vietnam and was followed in early November by Super Typhoon Goni (named Rolly by PAGASA), which made landfall in the same countries. Early estimates considered the Category 5 intensity of Goni at landfall at Catanduanes in the Philippines to be the strongest TC landfall ever recorded.

(III) ENVIRONMENTAL CONDITIONS

Figure 4.34 shows the environmental conditions associated with the 2020 typhoon season (June–October). The La Niña event was present for most of the typhoon season, with La Niña conditions developing in August 2020 (see section 4b). The SST anomaly pattern during the peak typhoon season (July–October [JASO]; Figs. 4.2c,d) was dominated by the standard eastern Pacific La Niña pattern, which includes above-normal SSTs in the western North Pacific. The genesis potential index (GPI; Fig. 4.34a; Emanuel and Nolan 2004; Camargo et al. 2007b) in JASO was characterized by two large regions of positive anomalies: the first near the Philippines and the second a large zonal band centered around 30°N. The first position of the storms formed during those months is also shown in Fig. 4.34a (black asterisks), and they are located around those two positive anomaly bands. The potential intensity (Emanuel 1988) anomalies (Fig. 4.34b) mostly reflect the SST anomalies, with positive anomalies in a horseshoe pattern in most of the WNP and negative anomalies close to the equator in the eastern part of the basin. With the exception of two bands of 600-hPa relative humidity anomalies (Fig. 4.34c) in the equatorial region (positive to the west, negative to the east), mid-level relative humidity was close to climatological conditions.

The extent of the monsoon trough, defined by 850-hPa zonal winds (Fig. 4.34d), was restricted from the South China Sea to the Philippines, as is typical in La Niña events. Many storms formed in this region during 2020 (Fig. 4.34a). Given the record lack of TCs in July, the conditions in that month are shown in Fig. 4.34e (GPI) and Fig. 4.34f (vertical wind shear). GPI anomalies in July (Fig. 4.34e) were negative in most of the basin, and the location of these negative anomalies coincided with regions of stronger-than-normal vertical wind shear (Fig. 4.34f). Comparing the GPI anomalies in July with the other components of the index (not shown: vorticity, potential intensity,

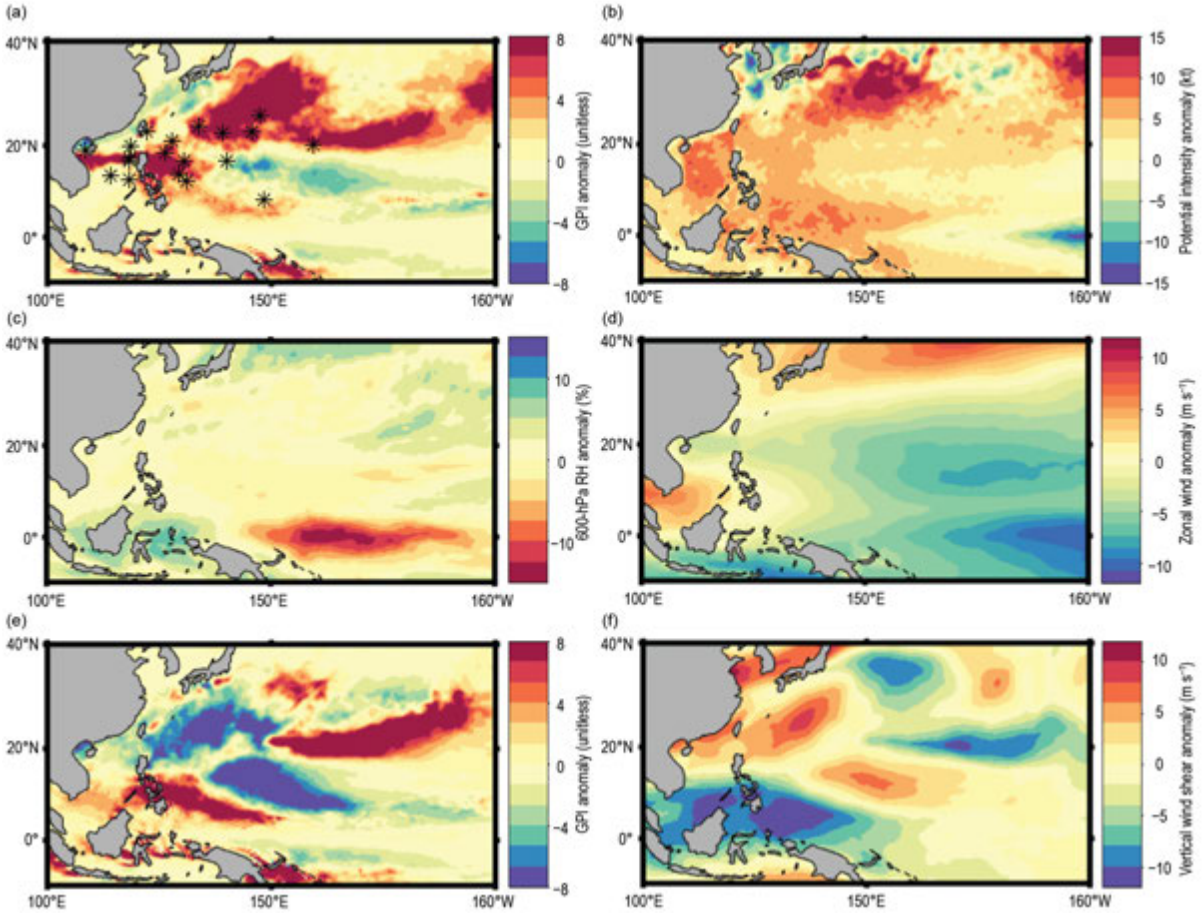

Fig. 4.34. (a) GPI anomalies in JASO 2020. First position of storms in JASO 2020 is marked with an asterisk, (b) potential intensity anomalies in JASO 2020, (c) 600-hPa relative humidity anomalies (%) in JASO 2020, (d) 850-hPa zonal winds (m s^{-1}) in JASO 2020, (e) GPI anomalies for Jul 2020, and (f) vertical wind shear magnitude anomalies for Jul 2020. (Source: ERA5 reanalysis [Hersbach et al. 2020].)

and relative humidity), it is clear that vertical wind shear anomalies were the main cause of the unfavorable GPI values during July. In addition to these unfavorable conditions, the MJO in July was active over the North Indian Ocean and suppressed over the WNP (Fig. 4.7), which likely contributed to the lack of storms that month.

(IV) TROPICAL CYCLONE IMPACTS

Many storms had social and economic impacts in Asia in 2020, in particular Typhoons Molave, Goni, and Vamco. Typhoon Molave mainly affected the Philippines and central Vietnam, where the storm caused widespread destruction and was one of the strongest storms to hit the country in the past 20 years according to the Vietnam Meteorological and Hydrological Administration. Molave was one of seven typhoons that affected Vietnam in 2020, and the combination of the monsoonal rains with these storms led to severe flooding in that country.

Super Typhoon Goni was the strongest TC to make landfall in the historical record and led to the evacuation of almost 1 million people from its path, with thousands of homes destroyed. Typhoon Vamco affected the same region of the Philippines just a few days later. This led to an emergency situation in the Philippines, with the National Disaster Risk Reduction and Management Council declaring a "state of calamity" for the island of Luzon. Local authorities reported the worst floods there in 45 years.

5) North Indian Ocean basin—A. D. Magee and C. J. Schreck

(I) SEASONAL ACTIVITY

The North Indian Ocean (NIO) TC season typically occurs between April and December, with two peaks of activity: May–June and October–December, due to the presence of the monsoon trough over tropical waters of the NIO during these periods. Tropical cyclone genesis typically occurs in the Arabian Sea and the Bay of Bengal between 8°N and 15°N. The Bay of Bengal, on average, experiences four times more TCs than the Arabian Sea (Dube et al. 1997).

The 2020 NIO TC season was the costliest season in recorded history, with damages amounting to ~$16 billion (U.S. dollars), the majority of which was driven from impacts associated with Super Cyclone Amphan ($13.9 billion [U.S. dollars]). In total, five named storms, four cyclones, and two major cyclones occurred in the region. While the number of named storms matched the IBTrACS–JTWC 1981–2010 climatology of 5.0, the numbers of both cyclones and major cyclones were tied for the third most since 1981 and were both more than double their climatological values (1.6 and 0.7, respectively; Fig. 4.35). Two major cyclone events occurred in the 2020 NIO TC season: Super Cyclone Amphan and Very Severe Cyclonic Storm Gati.

Above-average ACE index values were also recorded. The 2020 seasonal ACE index was 26.6 × 10^4 kt^2, over three times less than the record-shattering ACE generated during the 2019 NIO season, but above the 1981–2010 climatology of 19.1 × 10^4 kt^2. Indian Ocean dipole (IOD) conditions, as measured by the Dipole Mode Index, were neutral for the majority of the 2020 NIO TC

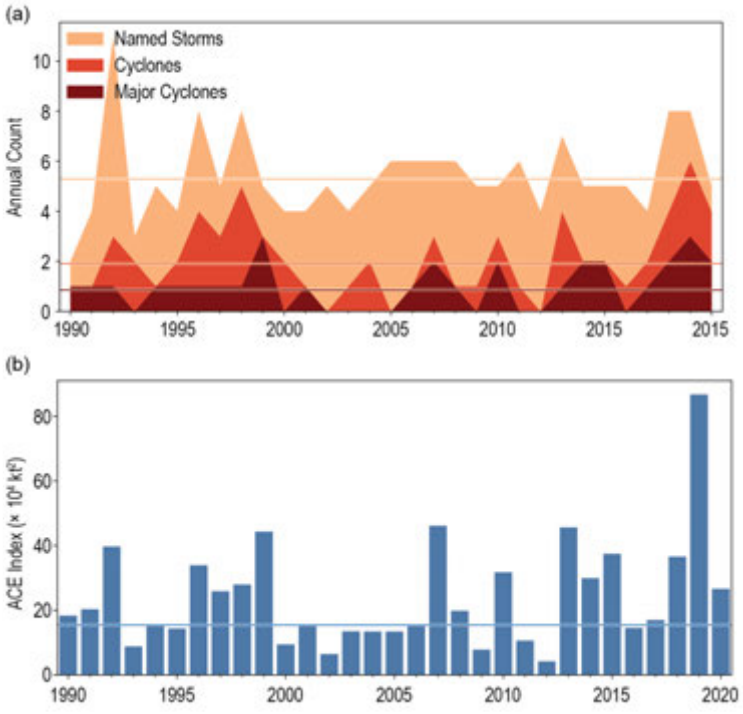

Fig. 4.35. Annual TC statistics for the NIO for 1990–2020: (a) number of named storms, cyclones, and major cyclones and (b) ACE (× 10^4 kt^2). Horizontal lines represent the 1981–2010 climatology.

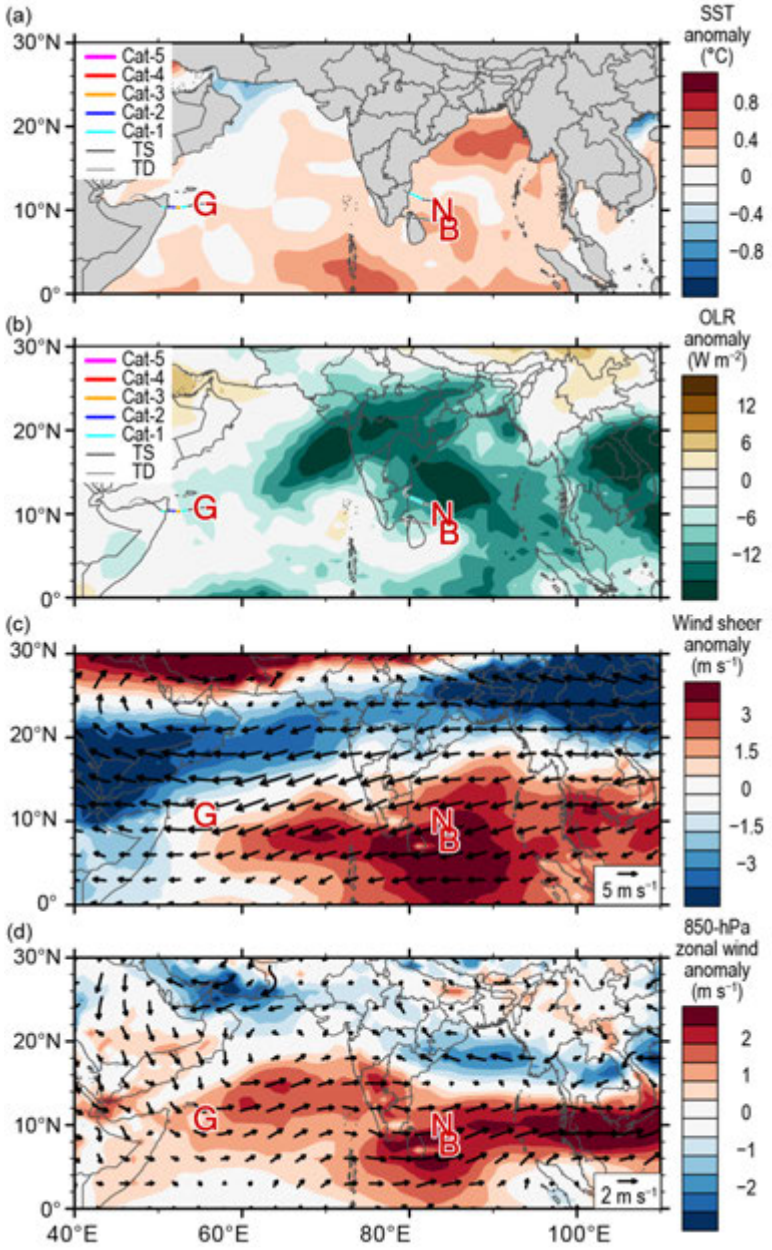

Fig. 4.36. 15 Sep–15 Dec 2020 NIO anomaly maps of (a) SST (°C; Banzon and Reynolds 2013), (b) OLR (W m $^{-2}$; Schreck et al. 2018), (c) 200–850-hPa vertical wind shear (m s^{-1}) vector (arrows) and scalar anomalies (shading), and (d) 850-hPa winds (m s^{-1} arrows) and zonal wind anomalies (shading). Anomalies are relative to the annual cycle from 1981–2010, except for SST, which is relative to 1982–2010. Letter symbols denote where each NIO TC attained its initial tropical storm intensity. (Source: Wind data from CFSR [Saha et al. 2014].)

season. Environmental conditions between 15 September and 15 December 2020 were characterized by average to above-average SSTs (Fig. 4.36a) and enhanced convection (Fig. 4.36b) in the region of cyclogenesis. Less favorable wind shear anomalies (>3 m s^{-1}), particularly in the Bay of Bengal, were present around the area of cyclogenesis around Cyclones Nivar and Burevi. Low-level westerly wind anomalies were present around 10°N (Fig. 4.36d).

(II) INDIVIDUAL TROPICAL CYCLONES AND IMPACTS

The first cyclone of the 2020 NIO cyclone season, Super Cyclone Amphan (16–21 May), was the first super cyclonic storm to form (winds ≥120 kt; ≥62 m s^{-1}) over the Bay of Bengal since Cyclone Odisha in 1999 (India Meteorological Department 2021b). Amphan originated from an area of low pressure in the southeastern Bay of Bengal, approximately 1000 km to the southeast of Andhra Pradesh, India. Exceptionally high SSTs

(30°–31°C) and low vertical wind shear (5–7 m s^{-1}) enabled Amphan to intensify from 50 kt (26 m s^{-1}) at 0600 UTC 17 May to 130 kt (67 m s^{-1}) at 2100 UTC 18 May. Amphan reached a maximum intensity of 145 kt (74 m s^{-1}) and a minimum central pressure of 901 hPa, equivalent to an SSHWS Category 5 system before crossing the West Bengal–Bangladesh coastline as a very severe cyclonic storm near Sundarbans with maximum sustained wind speed of 85 kt (44 m s^{-1}). Amphan maintained cyclonic storm intensity (winds ≥ 34 kt; 17 m s^{-1}) for almost 15 hours postlandfall. Damage associated with Amphan was estimated to be at $13.9 billion (U.S. dollars), the costliest cyclone recorded in the basin. In India alone, 98 deaths were reported, along with other fatalities in Bangladesh and Sri Lanka. The Indian state of West Bengal was most impacted by Amphan. In June, the Indian Red Cross Society reported that 2.9 million houses in the state were damaged or destroyed. A 24-hour accumulated rainfall of 240 mm was recorded at Alipore, and storm surge of approximately 15 feet inundated low-lying areas of West Bengal. Bhutan was also affected by flash flooding.

Cyclone Nisarga (2–3 June), originated as a depression in the Arabian Sea and developed into severe cyclonic storm Nisarga on 2 June, aided by an active pulse of the MJO that supported the enhancement of convective activity over the western Arabian Sea (India Meteorological Department 2021a). After recurving toward the northeast, Nisarga intensified into a Severe Cyclonic Storm on 3 June. With a peak intensity of 75 kt (38 m s^{-1}) and a minimum central pressure of 975 hPa, Nisarga made landfall along the Maharashtra coastline, approximately 100 km south of Mumbai, with reported maximum sustained winds of up to 65 kt (33 m s^{-1}). Nisarga maintained cyclonic storm intensity for approximately 7 hours after landfall, tracking toward the northeast throughout Maharashtra and Madhya Pradesh and dissipating quickly thereafter. Nisarga resulted in six fatalities and damage of over $800 million (U.S. dollars) was reported. Farmers living along the coast of Raigad and Ratnagiri suffered devastating losses, and crops including coconut, betel, and mango were destroyed. Significant rainfall (190 mm) was reported at Mahabaleshwar (Maharashtra), and up to 130 mm was reported at Mormugao (Goa) by the Indian Meteorological Department.

After 5 months of inactivity, Very Severe Cyclonic Storm Gati (21–25 November) made landfall across Somalia and was the first very severe cyclonic storm (winds ≥ 64 kt; 33 m s^{-1}) to do so since the start of the satellite era (India Meteorological Department 2020b). Gati originated from a low-pressure area that formed over the central part of the southern Arabian Sea. The MJO, favorable SSTs (29°–30°C), and low wind shear favored the development of Gati, which was defined as a "Midget System" with a compact core and eyewall. Its small size allowed it to undergo rapid intensification, reaching a maximum intensity of 100 kt (51 m s^{-1}) and a minimum central pressure of 967 hPa—a Category 3 SSHWS equivalent system. Gati made landfall near Hafun, with an estimated wind speed of 75 kt (39 m s^{-1}) and maintained cyclonic storm intensity for 15 hours after making landfall. Gati claimed the lives of nine people and brought heavy rainfall, particularly for northern Somalia. Over a 24-hour period, 128 mm of rainfall fell at Bosaso, exceeding the city's average annual rainfall total for the region of 100 mm. Flash flooding was also reported in Socotra Island, Yemen.

Cyclone Nivar (23–25 November) formed in the Bay of Bengal and tracked toward the west-northwest, passing to the northeast of Sri Lanka (India Meteorological Department 2020c). Nivar reached a maximum intensity of 70 kt (36 m s^{-1}) and a minimum central pressure of 981 hPa. On 25 November, Nivar made landfall crossing the Tamil Nadu and Puducherry coasts with recorded wind speeds of 65 kt (33 m s^{-1}). Nivar reportedly resulted in 14 deaths and damage of around $600 million (U.S. dollars). Intense rainfall of 310 mm in a 24-hour period was recorded at Tambaram (Tamil Nadu) and up to 250 mm was recorded at Kodur (Andhra Pradesh), causing flooding around many low-lying regions along the Adyar River. Flooding also closed a number of roads in greater Chennai.

The fifth and final cyclone of the season, Cyclone Burevi (1–5 December), was a relatively weak cyclone that developed from a low-pressure system that formed off the west coast of Aceh (India

Meteorological Department 2020a). Moving west-northwestward, Burevi reached a maximum intensity of 45 kt (23 m s^{-1}) and a minimum central pressure of 999 hPa, before making landfall on the coast of Sri Lanka north of Trincomalee. After passing across northern Sri Lanka, Burevi emerged into the Gulf of Mannar where, due to a lack of middle and upper tropospheric steering winds, it remained stationary close to the coastline of the Ramanathapuram district of India for around 18 hours, before weakening. The recent occurrence of Nivar caused upwelling of cooler waters and a relative cooling of SSTs, thus limiting the intensification of Burevi. Burevi affected Sri Lanka and the Indian states of Tamil Nadu and Keralam, with 11 deaths and five missing persons reported. Intense rainfall occurred, particularly over northern Tamil Nadu and Puducherry, with 360 mm recorded in Kollidam over a 24-hour period. Flooding isolated many rural villages from Chennai and resulted in widespread power outages across Puducherry.

6) South Indian Ocean basin—A. D. Magee and C. J. Schreck

(I) SEASONAL ACTIVITY

The South Indian Ocean TC basin extends south of the equator and from the African coastline to 90°E. While the SIO TC season extends year-round, from July to June, the majority of activity typically occurs between November and April when the Intertropical Convergence Zone is located in the SH. The 2019/20 season includes TCs that occurred from July 2019 to June 2020. Landfalling TCs typically impact Madagascar, Mozambique, and the Mascarene Islands, including Mauritius and Réunion Island; however, impacts can be felt in other locations within the region. The RSMC on La Réunion is the official monitoring agency for TC activity within the SIO basin.

The 2019/20 SIO season had 11 named storms, six cyclones, and three major cyclones, which nearly matches the IBTrACS-JTWC 1981–2010 mean of 10.5, 6.0, and 3.0, respectively (Fig. 4.37). December 2019 was a particularly active month, with three named cyclones (Belna, Ambali, and Calvinia) occurring within the basin. The 2019/20 seasonal ACE index was 53.6 × 10^4 kt^2, which is well below the 1981–2010 climatology of 92.7 × 10^4 kt^2. Cyclone-favorable conditions including anomalously warm SSTs (Fig. 4.38a) likely driven by the strongly positive IOD event of 2019 (Chen

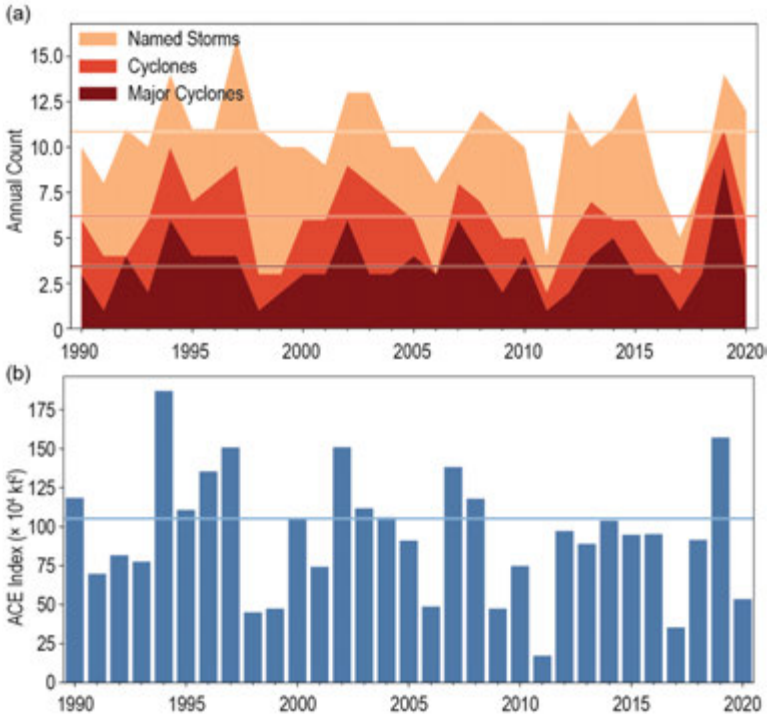

Fig. 4.37. Annual TC statistics for the SIO for 1990–2020: (a) number of named storms, cyclones, and major cyclones and (b) ACE (× 10^4 kt^2). Horizontal lines represent the 1981–2010 climatology.

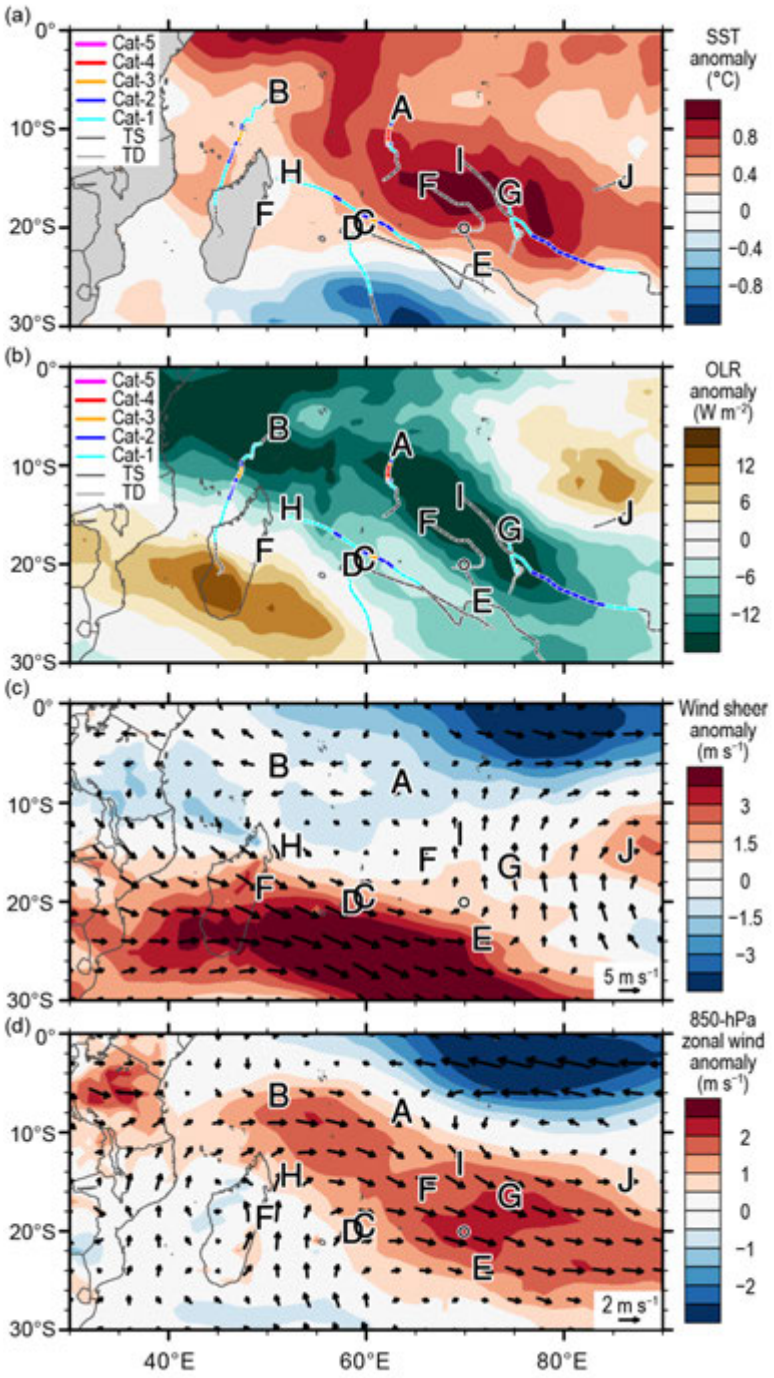

Fig. 4.38. Dec 2019–May 2020 SIO anomaly maps of (a) SST (°C; Banzon and Reynolds 2013), (b) OLR (W m^{-2}; Schreck et al. 2018); (c) 200–850-hPa vertical wind shear (m s^{-1}) vector (arrows) and scalar anomalies (shading), and (d) 850-hPa winds (m s^{-1} arrows) and zonal wind anomalies (shading). Anomalies are relative to the annual cycle from 1981–2010, except for SST, which is relative to 1982–2010. Letter symbols denote where each SIO TC attained its initial tropical storm intensity. (Source: Wind data from CFSR [Saha et al. 2014].)

et al. 2020), large areas of enhanced convection (<–12 W m^{-2}; Fig. 4.38b), and anomalously weak wind shear (Fig. 4.38c) were present in the main development region. Low-level westerly and northwesterly anomalies between ~10°–25°S, extending as far east as 90°E, provided enhanced cyclonic vorticity for many systems (Fig. 4.38d).

(II) NOTEWORTHY TROPICAL CYCLONES AND IMPACTS

The first named cyclone of the season, Cyclone Belna, initially started as a tropical disturbance to the west of the Seychelles. While tracking toward the west, Belna intensified over 24 hours and reached a peak intensity of 100 kt (51 m s^{-1}) and a minimum central pressure of 959 hPa, a Category 3 equivalent system on the SSHWS. After fluctuating in intensity, Belna reintensified as the system approached the Soalala district and made landfall along the northwestern coast of Madagascar, maintaining a southerly track over Madagascar before weakening and recurving to the southeast. Nine deaths were reported, with damages estimated to exceed $25 million (U.S. dollars). The primary hospital in Soalala was damaged by flooding, and significant power outages and a shortage of safe drinking water were reported in the region.

The second named cyclone of the season, Cyclone Ambali, developed from a trough between the Seychelles and the Chagos Archipelago (the same extended trough that resulted in Cyclone Belna). Anomalously high SSTs (29°–30°C) promoted rapid intensification of 110 kt (51 m s^{-1}), the most rapid intensification for an SH cyclone in a 24-hour period since 1980. On 6 December, Ambali reached a maximum intensity of 135 kt (69 m s^{-1}) and with a minimum central pressure of 929 hPa, was rated as a Category 4 equivalent system on the SSHWS. Within a few hours of reaching peak intensity, Ambali weakened due to unfavorable vertical wind shear. No significant damage was reported as a result of Ambali.

Cyclone Calvinia formed from a disturbance first observed by JTWC on 16 December. Calvinia initially tracked toward the south before turning southwest toward Mauritius, slowing down as it did so. At its closest point, Calvinia was approximately 60 km off the coast of Mauritius on 31 December and was tropical storm strength. A precyclonic alert was issued in advance for all three Mascarene Islands, which subsequently closed the Sir Seewoosagur Ramgoolam International Airport and Port Louis Harbour. Calvinia resulted in flooding and power outages for both Mauritius and southern Réunion. In southern Réunion, 325 mm of rainfall was recorded at Dimitile, along with a maximum wind gust of 64 kt (34 m s^{-1}). While tracking south away from Mauritius, Calvinia reintensified and reached peak intensity of 70 kt (36 m s^{-1}) and a minimum central pressure of 973 hPa—a Category 1 equivalent system on the SSHWS.

After a number of systems that achieved tropical storm strength including Diana, Esami, and Francisco, Cyclone Gabekile formed around 1200 km to the northeast of the island of Rodrigues and tracked southward, influenced by a subtropical ridge to the east. On 16 February, Gabekile reached its maximum intensity of 75 kt (39 m s^{-1}) and a minimum central pressure of 978 hPa—a Category 1 equivalent system on the SSHWS. Gabekile did not make landfall and continued to track southward before weakening.

Cyclone Herold formed off the northeastern coast of Madagascar where it remained almost stationary (<100 km from the coastline) for ~24 hours. During this time, Herold continued to intensify, but its slow-moving nature diminished the ocean heat content in the vicinity of the system, resulting in a slight weakening of the system. Herold then tracked to the southeast between the islands of Port Louis and Rodrigues, where it reached a peak intensity of 100 kt (51 m s^{-1}) and a minimum central pressure of 963—a Category 3 equivalent system on the SSHWS. It then tracked toward the southeast and rapidly weakened. Herold claimed the lives of five people and affected areas of Madagascar, Mauritius, and Rodrigues. On 13 March, 95 mm of rainfall was recorded in Sambava (northeastern Madagascar), and riverine flooding was reported from the Andranofosty River. Water levels were reported to be around 2 m, destroying homes, schools, and other essential services. In the Mascarene Islands, maximum sustained winds of 100 kt (51 m s^{-1}) were reported.

The last cyclone of the season, Cyclone Irondro was named approximately 1800 km to the east of Port Louis. On 4 April, Irondro reached a peak intensity of 95 kt (49 m s^{-1}) and minimum central pressure of 958 hPa—a Category 2 system on the SSHWS. Irondro continued to track toward the southeast where it weakened the following day due to unfavorable wind shear and lower SSTs.

7) Australian basin—B.C. Trewin and S. Bond

(I) SEASONAL ACTIVITY

The 2019/20 TC season was below normal in the broader Australian basin (areas south of the equator and between 90°E and 160°E, which includes Australian, Papua New Guinea, and Indonesian areas of responsibility); the Australian Bureau of Meteorology's warning area overlaps both the southern Indian Ocean and southwest Pacific. The season produced eight TCs, below the 1983/84–2010/11 average (1983/84 is the start of consistent satellite coverage over the region) of 10.8, in a season with a strong positive phase of the IOD, and warm waters in the central equatorial Pacific (although below the threshold for a formal El Niño declaration). The 1981–2010 IBTrACS Bureau of Meteorology seasonal averages for the basin are 9.9 named storms, 7.5 TCs, and 4.0 severe (or major) TCs (based on the Australian TC Intensity Scale unless noted otherwise), which compares with the 2019/20 IBTrACS counts of 10, six, and two, respectively (Fig. 4.39).

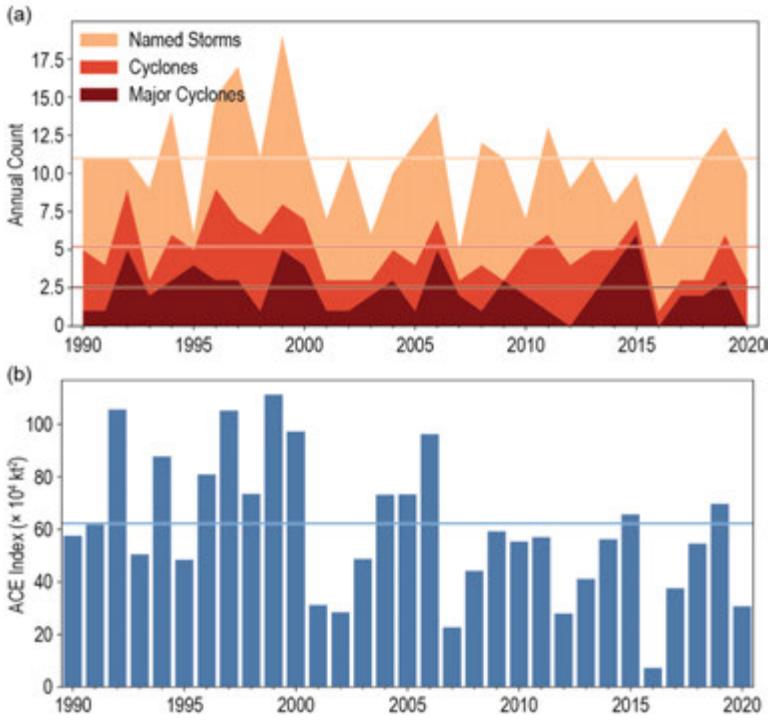

Fig. 4.39. Annual TC statistics for the Australian basin for 1990–2020: (a) number of named storms, cyclones, and major cyclones and (b) ACE (× 10^4 kt^2). The 1981–2010 means (horizontal lines) are included in both (a) and (b).

There were five TCs in the western sector[5] of the broader Australian region during 2019/20, two in the northern sector, and three in the eastern sector. (Esther passed through both the northern and eastern sectors, and Claudia passed through both the northern and western sectors.) Three systems made landfall in Australia as TCs, two in Western Australia and one in the Gulf of Carpentaria, while Tropical Cyclone Harold had major impacts in the southwest Pacific, particularly Vanuatu and the Solomon Islands, after leaving the Australian region (section 4g8).

(II) LANDFALLING AND OTHER SIGNIFICANT TROPICAL CYCLONES[6]

The most significant landfall of the season in the Australian region was Damien. Its precursor low moved west over the Kimberley region of northern Western Australia for several days in early February before emerging over water on 5 February. The low intensified and was named at 0600 UTC on 6 February near 17°S, 120°E. Further intensification took place as Damien turned southwest and then south, moving toward the Pilbara coast, and it reached Category 3 intensity,

[5] The western sector covers areas between 90°E and 125°E. The eastern sector covers areas east of the eastern Australian coast to 160°E, as well as the eastern half of the Gulf of Carpentaria. The northern sector covers areas from 125°E east to the western half of the Gulf of Carpentaria. The western sector incorporates the Indonesian area of responsibility, while the Papua New Guinea area of responsibility is incorporated in the eastern sector.

[6] The Australian TC Intensity Scale is used in this section except as noted otherwise.

with a central pressure of 955 hPa and maximum 10-minute sustained winds of 80 kt (42 m s^{-1}), on the evening of 7 February about 250 km north of Karratha. Damien continued to move south and made landfall near Karratha at close-to-peak intensity at about 0730 UTC on 8 February. It continued to move south over land and weakened below cyclone intensity on 9 February.

Damien caused widespread minor-to-moderate wind damage around Karratha, with a peak wind gust of 105 kt (54 m s^{-1}) at Karratha Airport. The Australian Bureau of Meteorology's radar at Dampier was badly damaged. Heavy rain caused some flooding along the cyclone's path. Both Karratha and Roebourne recorded 235 mm of rain in the 48 hours to 0900 local time on 9 February, with event totals above 100 mm extending south to near Meekatharra.

The other two landfalls of the season were both Category 1 cyclones: Blake in Western Australia and Esther in the Gulf of Carpentaria. Flooding was the main impact for both cyclones. Blake made its first landfall north of Broome on 6 January, then moved out to sea and tracked along the coast before a second landfall near Wallal Downs late on 7 January. Esther only briefly reached TC intensity as it made landfall near the Northern Territory–Queensland border on 24 February. Daily rainfall totals associated with Blake included 153 mm at Derby and 148 mm at Broome on 7 January, but the heaviest rainfall occurred in the interior of Western Australia as a result of moisture from Blake's remnant low; Carnegie received at least 270 mm (amount recorded before the gauge overflowed) on 10 January, the heaviest daily total on record in the Interior district of Western Australia. There was significant flooding in the west Kimberley, with Broome isolated by floodwaters, and in interior regions. Esther's remnant low drifted across the northern parts of the Northern Territory and northern Western Australia for more than a week, with numerous 48-hour rainfall totals in excess of 200 mm in both regions that caused significant flooding.

Claudia and Ferdinand reached severe (or major) cyclone intensity off the Western Australian coast in January and February, respectively. Ferdinand had maximum 10-minute sustained winds of 85 kt (43 m s^{-1}) and a minimum central pressure of 960 hPa, while Claudia reached 75 kt (39 m s^{-1}) and 969 hPa, respectively. Neither system was at cyclone intensity over land, although Claudia's precursor low produced extreme local rainfalls west of Darwin on 11 January. Dum In Mirrie Airstrip had a daily total of 562 mm, a record for the Northern Territory, while nearby Wagait Beach had 515 mm, although impacts were confined to localized flash flooding. Uesi was not a tropical cyclone within the Australian region, but after becoming subtropical it moved into the region, passing close to Lord Howe Island on 14 February, with a wind gust of 83 kt (43 m s^{-1}) at Windy Point. Some wind damage was reported. Gretel and Mangga both remained offshore in the Australian region and had no significant impacts on land.

8) Southwest Pacific basin—J.-M. Woolley, A. Magee, A. M. Lorrey, and H. J. Diamond

(I) SEASONAL ACTIVITY

The 2019/20 Southwest Pacific TC season officially began in November 2019 and ended in April 2020. Storm track data for 2019/20 were gathered from the Fiji Meteorological Service, Australian Bureau of Meteorology, and New Zealand MetService, Ltd. The Southwest Pacific basin (defined by Diamond et al. [2012] as 135°E–120°W) had nine TCs (based on the Australian TC Intensity Scale unless noted otherwise), including three severe (or major) TCs (based on the Australian TC intensity scale). As noted in section 4f1, Fig. 4.40 shows the standardized TC distribution based on the basin spanning the area from 160°E–120°W to avoid overlaps with the Australian basin that could result in double counting of storms; however, it is important to use the climatological definition of the Southwest Pacific basin (Diamond et al. 2012), instead of a political boundary.

The 1981–2010 South Pacific Enhanced Archive of Tropical Cyclones (SPEArTC; Diamond et al. 2012) indicates a seasonal average of 10.4 named TCs including 4.3 severe (or major) TCs. The 2019/20 TC season, therefore, had near-normal activity with nine named tropical cyclones, of which three were severe (Category 3 or above). Severe TCs accounted for one-third of the total number of TCs which is 11% less than last season.

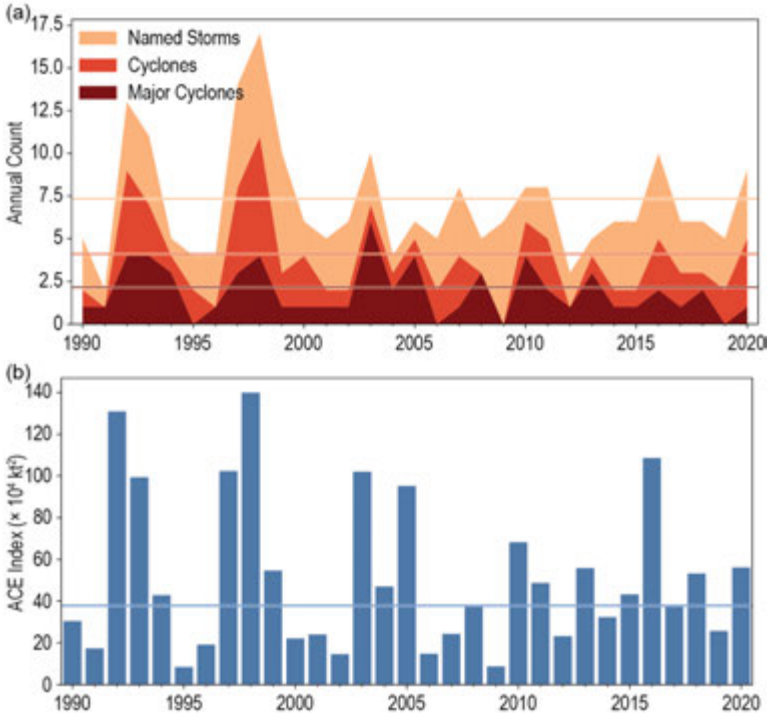

Fig. 4.40. Annual TC statistics for the Southwest Pacific for 1990–2020: (a) number of named storms, cyclones, and major cyclones and (b) ACE (× 10^4 kt^2). The 1981–2010 means (horizontal lines) are included in both (a) and (b).

(II) STORM TRACKS, LANDFALLS, AND IMPACTS

Tropical Cyclone Sarai formed from a southward tracking tropical depression (TD), located west of Tuvalu, which intensified into a Category 1 TC on 26 December while located approximately 100 km west of Rotuma. The storm reached Category 2 intensity on 27 December while it was 220 km west of Nadi in Fiji. The system tracked south and then turned east, passing south of Fiji and delivering heavy wind and rainfall on 27 December. More than 2000 people were evacuated to higher grounds, with two deaths reported. Damage to road infrastructure reached $5 million Fiji dollars ($2.5 million U.S. dollars). TC Sarai weakened to Category 1 intensity on 30 December and passed near Nuku'alofa on 31 December before rapidly deteriorating. Sarai's peak 10-minute sustained winds were 61 kt (31 m s^{-1}), and its minimum central pressure was 975 hPa.

Severe TC Tino was first noted as a tropical disturbance on 11 January to the southeast of Honiara in the Solomon Islands. The system tracked east between the Solomon Islands and Vanuatu and was classified as a Category 1 TC on 16 January before reaching Fiji. Tracking southeast, Tino strengthened to Category 2 intensity on 17 January near Vanua Levu and peaked as a Category 3 severe TC later that day with peak 10-minute sustained winds of 65 kt (33 m s^{-1}) and a minimum central pressure of 964 hPa. Tino passed over several of Tonga's Ha'apai islands on 18 January and gradually weakened as it tracked away to the southeast. By 19 January TC Tino had fully transitioned to an extratropical cyclone.

Severe TC Tino and its precursor tropical disturbance directly impacted the Solomon Islands, Vanuatu, Wallis and Futuna, Fiji, Tonga, and Niue, with the farthest geographic effects also reaching Samoa, American Samoa, Tuvalu, and the Cook Islands. In Tuvalu (500 km north of the storm track), waves up to 8 m combined with a king tide—an exceptionally high tide that occurs during a new or full moon—to cause catastrophic damage, including coastal erosion and flooding. Strong winds also blew roofs off buildings and uprooted trees and crops. In Fiji, over 3000 displaced people were housed across 78 evacuation centers. In Tonga, estimated gusts of 97 kt (50 m s^{-1}) were experienced across the Vava'u and Ha'apai island groups. Storm surge resulted in

damage to crops and main roads, including the causeway connecting the islands of Lifuka and Foa, contributing significantly to power outages in the area (~3000 people were affected overall). In Samoa, trees and billboards were toppled, disrupting power lines and blocking roads; power outages also affected several communities. Despite being 400 km away from Tino's center, strong winds tore off the upper layer of the Niue wharf.

Severe TC Uesi reached Category 1 TC intensity on 9 February while tracking south and positioned approximately 380 km west of Espiritu Santo in Vanuatu. Uesi intensified into a Category 3 TC the following day. On 11 February, Uesi passed west of New Caledonia, resulting in flooding that blocked several bridges and roads. There were also significant power outages and transportation delays. TC Uesi took a south-southwest trajectory and weakened to a Category 2 TC on 12 February. On 14 February, the system began to track to the south-southeast, transitioning to an extratropical storm over the Tasman Sea by the next day. TC Uesi's peak 10-minute sustained winds were 70 kt (36 m s^{-1}) with a minimum central pressure of 975 hPa.

TC Vicky developed from an east-southeast tracking TD that passed near Samoa and just south of Tutuila in American Samoa on 20 February before strengthening into a Category 1 TC later that day. The system then tracked southeast, passing just east of Niue on 21–22 February and weakened as it continued farther south. Vicky's peak 10-minute sustained winds were 40 kt (21 m s^{-1}), and its minimum central pressure was 996 hPa.

TC Wasi developed from a southeast-tracking TD and reached Category 1 TC intensity on 21 February while approximately 125 km north of the Wallis and Futuna Islands. The system strengthened to Category 2 intensity later that day as it tracked toward Samoa but became increasingly disorganized and weakened after passing south of the Samoan Islands. By 23 February, while positioned northwest of Niue, TC Wasi had weakened to below tropical cyclone strength. TC Wasi's peak 10-minute sustained winds were 60 kt (31 m s^{-1}), and its minimum central pressure was 975 hPa.

Tropical Cyclones Vicky and Wasi passed close to Samoa and American Samoa within 2 days of each other. River flooding was reported on the islands of Savai'i and Upolu, and brief power outages occurred in some locations.

Tropical Cyclone Gretel began as a tropical low that was located over the Arafura Sea on 10 March. The system intensified into a Category 1 storm on 14 March after tracking east-southeast, passing over Cape York Peninsula and across much of the Coral Sea. TC Gretel continued to strengthen and reached Category 2 TC intensity on 15 March before passing just south of New Caledonia, resulting in port closures and public transportation cancellations. The system transitioned into an extratropical cyclone on 16 March, while located well north of New Zealand. Gretel's peak 10-minute sustained winds were 54 kt (28 m s^{-1}) with a minimum central pressure of 971 hPa.

Severe TC Harold originated as a tropical low developing within a trough to the east of Papua New Guinea on 1 April and organized into a TC on 2 April near Honiara in the Solomon Islands. Tracking southeast, the system rapidly intensified, reaching SSHWS Category 5 intensity on 5 April. Harold made landfall as an SSHWS Category 5 storm on Espiritu Santo in Vanuatu on 6 April, and then on Pentecost later that day before reemerging over the South Pacific Ocean on an east-southeast trajectory. The system tracked just south of Viti Levu in Fiji, passing over the Kadavu islands early on 8 April before passing 115 km south of Nuku'alofa later that day. The storm weakened over the following days while tracking southeastward and was declared an extratropical TC on 10 April. Harold's peak 10-minute sustained winds were 124 kt (64 m s^{-1}) and its minimum central pressure was 912 hPa.

TC Harold impacted the Solomon Islands as a Category 1 TC, destroying or damaging dozens of homes. Twenty-eight passengers aboard a ferry from Honiara to Malaita Province were washed overboard by large waves caused by the storm, with all but one presumed dead. Harold passed directly over Vanuatu as an SSHWS Category 5 severe TC, the second-strongest TC on

record to make landfall across Vanuatu. Wind gusts exceeding 147 kt (76 m s^{-1}), rainfall totals of 250–450 mm, and a storm surge of up to 0.8 m contributed to torrential rain and flooding, with widespread telecommunication disruptions and a blackout. Significant damage occurred on Espiritu Santo upon Harold's initial landfall, destroying at least half of the buildings in the city of Luganville, with some areas experiencing damage to all structures.

Sidebar 4.2: "Medicanes" (Mediterranean tropical-like cyclones) in 2020—S.H. YOUNG

The traditional areas for tropical cyclone (TC) development in the Northern Hemisphere extend from the Atlantic African coast west across the Atlantic and Pacific Oceans, and the Indian Ocean to the eastern African coast. In the Southern Hemisphere, the eastern limit is around 120°W and extends east from there to the east African coast (Gray 1968). However, the March 2004 formation of Hurricane Catarina in the South Atlantic introduced the concept of tropical development in non-traditional areas (McTaggart-Cowan et.al. 2006).

The Mediterranean basin is another area not considered as an area for tropical development. Many cyclones in this basin are baroclinic synoptic-scale systems, but some are observed to resemble TCs, with an eyewall, an axisymmetric cloud pattern, and a warm core (Emanuel 2005). The fact that an eye feature develops is consistent with tropical development and can occur when winds reach 50 kt (36 m s^{-1}; Vigh et.al. 2012). These Mediterranean tropical-like systems are sometimes referred to as "medicanes," although their classification as TCs or subtropical cyclones are still the subject of debate.

These systems tend to develop under a mid-upper level cold low, often cut off from the westerlies, and where strong thermal gradients exist (Fita 2007). Another reason the Mediterranean is not considered suitable to support tropical development is the existence of low sea surface temperatures, below the 26.5°C often considered to be the minimum threshold for tropical development. McTaggart-Cowen et.al (2015) discuss how development and tropical transition can occur at lower temperatures.

Determining the climatology of medicanes is difficult as there is no formal definition of these systems, and many are identified based on satellite presentation. Cavicchia et al. (2014) used an algorithm that included the cyclone phase space (Hart 2003) to derive a frequency of 1.57 ± 1.30 events per season (maximum sustained wind > 56 kt (29 m s^{-1}), and between 0 and 5 events detected annually over the period 1948–2011. These systems are shown to usually form between September and April.

In 2020, there were three significant medicanes observed in the Mediterranean Sea, with one reportedly reaching hurricane strength of 65 kt (33 m s^{-1}; Fig. SB4.3; USDC 2020), while two displayed eye-like features. The first and strongest of the systems formed north of Libya on 15 September (Fig. SB4.4). Drifting northward, an eye feature developed on 17 September. The publication *Weekly Weather and Crop Bulletin* (USDC 2020) referred to the system as a "hurricane," with reported rainfall of up to 142 mm and likely higher on the windward-facing mountainous terrain. Following landfall, the residual low drifted southward and was last noted west of Crete. Shortly after this

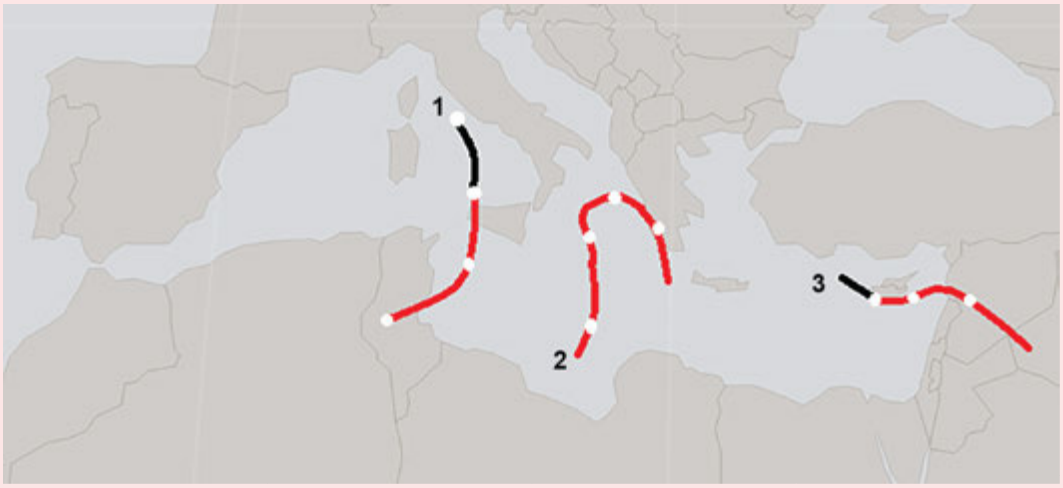

Fig. SB4.3. Tracks of medicanes derived from NCEP/NCAR Reanalysis (Kalnay et al. 1996) and satellite imagery. System #1, 16–19 Sep 2020; System #2, 20–23 Nov 2020; System #3, 14–17 Dec 2020. Black segments of track represent extratropical stage of the system.

system developed, Subtropical Storm Alpha developed in the eastern North Atlantic basin. The upper air aspects of the two systems were similar with cold core cut-off low precursors analyzed at the 700-hPa and 500-hPa levels, a feature that has been previously associated with tropical transition (TT; Pantillon et al. 2013).

The second system (Fig. SB4.4) developed on 20 November from an extratropical system between Italy and Sardinia, and underwent TT prior to crossing the western tip of Sicily (TT of baroclinic systems has been documented as a contributing factor to the development of medicanes [Mazza et al. 2017]). An eye-like feature then developed on 22 November prior to landfall in Tunisia. Maximum winds were estimated to have reached 40 kt (20 m s^{-1}) during the tropical phase.

The last system (Fig. SB4.4) developed south of Turkey on 14 December following the TT of a precursor system, then traveled east along the southern Cypriot coastline. A second landfall occurred along the Syrian coast while the remnant cloud mass tracked to near the Syria-Iraq border. Maximum winds were estimated around 45 kt (23 m s^{-1}). So, while the medicane is an area still open for debate in the tropical cyclone community, it is still an interesting feature, and to have three fairly significant such storms during the 2020 season was a topic considered as sufficiently interesting to highlight in this year's report.

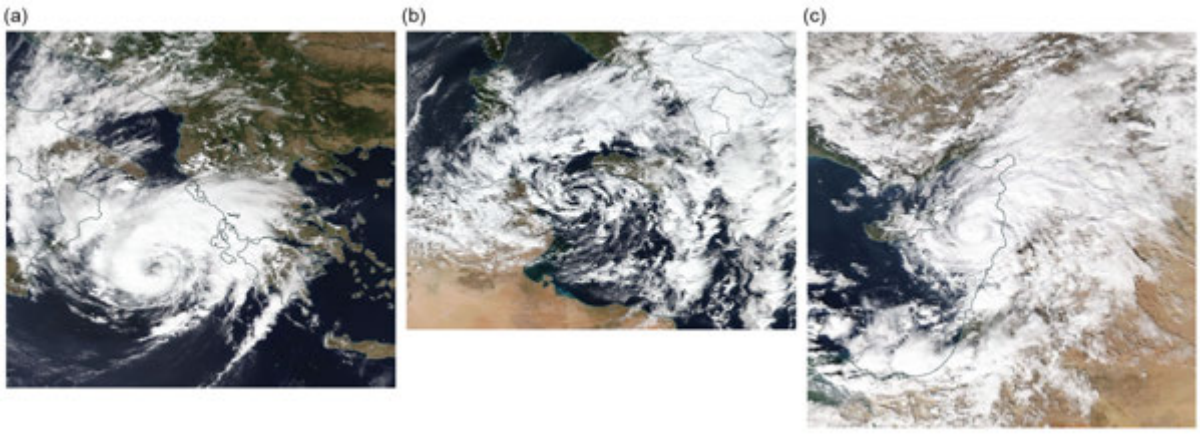

Fig. SB4.4. System #1, 17 Sep (NOAA 20); System #2, 21 Nov (*Aqua*); and System #3, 16 Dec (*Aqua*). Imagery courtesy of NASA Worldview.

h. Tropical cyclone heat potential—R. Domingues, G. J. Goni, J. A. Knaff, I-I Lin, and F. Bringas

In this section, upper-ocean heat content conditions based on the tropical cyclone heat potential (TCHP; e.g., Goni et al. 2009; 2017) are described as anomalies with respect to the long-term mean (1993–2019) and differences to conditions observed in 2019. TCHP quantifies the excess heat content between the sea surface and the depth of the 26°C isotherm (D26, the minimum temperature required for genesis and intensification; Leipper and Volgenau 1972; Dare and McBride 2011) and provides information about the amount of heat stored in the upper ocean and available to fuel TC intensification. As in this section, TCHP is often used as a convenient guide of pre-TC ocean thermal conditions because it carries information about the integrated upper-ocean thermal profile (from sea surface temperature [SST] to D26). High TCHP before a TC usually leads to a smaller amount of SST cooling during a TC, and hence higher enthalpy fluxes from the ocean into the storm, favoring intensification (e.g., Lin et al. 2013). Similarly, upper-ocean salinity is another condition of relevance for TC intensification because freshwater-induced barrier layers may also modulate the upper ocean mixing and cooling during a TC, and hence the air–sea fluxes (e.g., Balaguru 2012; Domingues et al. 2015). Areas in the ocean with pre-TC TCHP values above 50 kJ cm^{-2} have been associated with TC intensification (e.g., Shay et al. 2000; Mainelli et al. 2008; Lin et al. 2014, Knaff et al. 2018), provided that atmospheric conditions are also favorable.

TCHP seasonal anomalies (Fig. 4.41) are calculated as departures from the long-term mean (1993–2019) for the primary months of TC activity in each hemisphere: June–November 2020 in the Northern Hemisphere (NH) and November 2019–April 2020 in the Southern Hemisphere (SH). Differences between the 2020 and 2019 seasons are also analyzed (Fig. 4.42). In any of the regions highlighted in Fig. 4.41 in which TCs are known to form and intensify, TCHP anomalies generally exhibit large spatial and temporal variability due to mesoscale features and short- to long-term modes of variability (e.g., El Niño–Southern Oscillation [ENSO]) and trends.

The 2020 TC season exhibited above the mean 1993–2019 TCHP values in most of the tropical cyclone basins (Fig. 4.41), suggesting that conditions for TC development and intensification were generally favorable in terms of upper-ocean heat content. Notable anomalies with values as large as 30 kJ cm^{-2} above the long-term mean were observed in the North Indian, South Indian, and West Pacific basins, and in the western Caribbean Sea and parts of the Gulf of Mexico. Compared to 2019, TCHP values also increased in all basins (Fig. 4.42), with the exception of the East Pacific, where lower TCHP values observed in 2020 were associated with an ongoing La Niña event (additional details below).

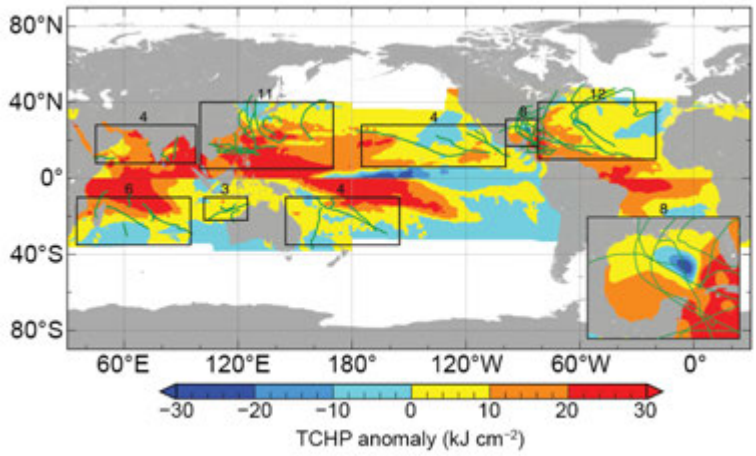

Fig. 4.41. Global anomalies of TCHP during 2020 computed as described in the text. The boxes indicate the seven regions where TCs occur: from left to right, southwest Indian, North Indian, west North Pacific, southeast Indian, southwest Pacific, east Pacific, and North Atlantic (shown as Gulf of Mexico and tropical Atlantic separately). The green lines indicate the trajectories of all tropical cyclones reaching at least Category 1 strength (≥ 64 kt, 34 m s^{-1}) and above during Jun–Nov 2020 in the NH and Nov 2019–Apr 2020 in the SH. The numbers above each box correspond to the number of Category 1 and above cyclones that traveled within each box. The Gulf of Mexico conditions are shown in the inset in the lower right corner.

In the SH, TCHP was anomalously elevated in the southwest Indian Ocean (IO) and beyond the date line during the TC season, and was near normal elsewhere (Fig. 4.41). The observed TC activity was slightly elevated in the southwest IO, which included TC Herold that skirted north of Mauritius. Harold formed near the Solomon Islands and later rapidly intensified before making landfall on Espiritu Santo and Pentecost Islands, Vanuatu, at Category 5 intensity. See section 4g8 for details of this storm.

In the IO, as indicated earlier, all three TC basins exhibited above-normal TCHP conditions (Fig. 4.41), with anomalies up to ~30 kJ cm^{-2} above the long-term average in the North IO basin inside the Bay of Bengal and in the southwest IO basin. All three basins also exhibited notable warming of 20 kJ cm^{-2} compared to values observed in 2019 (Fig. 4.42). In fact, the 2020 TCHP values were generally within the 80–100 kJ cm^{-2} range in the Bay of Bengal and southwest IO basin. Associated with these upper-ocean conditions, the North IO basin exhibited above-average TC activity, the southwest IO basin exhibited slightly above-normal

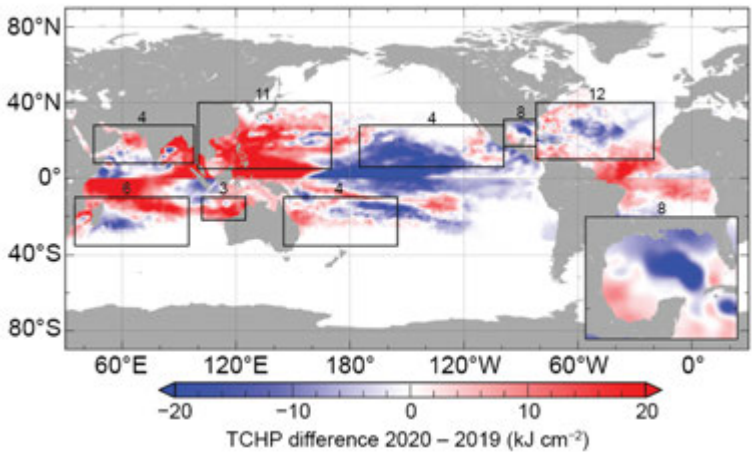

Fig. 4.42. TCHP anomaly difference (kg cm^{-2}) between the 2020 and 2019 tropical cyclone seasons (Jun–Nov in the NH and Nov 2019–Apr 2020 in the SH).

TC activity, and the southeast IO basin exhibited normal activity. With the above-average activity observed in the North IO basin, the 2020 TC season was also the costliest on record, largely due to Cyclone Amphan (16–21 May), which underwent rapid intensification over the anomalously large TCHP in the Bay of Bengal. Similarly, TC Gati, which was the most intense (100 kt, 51 m s^{-1}) to make landfall in Somalia since at least the start of the satellite era, rapidly and unexpectedly intensified over warm TCHP anomalies before striking land.

In the North Pacific, the ENSO state generally plays a large role in defining the large-scale upper-ocean thermal conditions that can impact both the eastern and western North Pacific basins (e.g., Lin et al. 2014, 2020; Zheng et al. 2015). In early 2020, ENSO transitioned from a weak positive phase to a negative phase by mid-year. La Niña conditions developed in August and persisted throughout the entire 2020 TC season. Associated with this ENSO state, TCHP values increased by over 20 kJ cm^{-2} in the western North Pacific and decreased by 20 kJ cm^{-2} in the eastern North Pacific basins with respect to conditions seen in 2019 (Fig. 4.42). Despite these changes, TCHP values were still 10–20 kJ cm^{-2} and 30 kJ cm^{-2} above the long-term mean in the eastern North Pacific and western North Pacific basins, respectively.

While upper-ocean conditions were warmer than normal, which is generally conducive for TC genesis and intensification, TC frequency in the western North Pacific basin was below average in 2020, as often found in La Niña years (Lin et al. 2020). This is because TC frequency in this basin is primarily controlled by atmospheric dynamics (Lin and Chan 2015) rather than by upper-ocean conditions. Despite the overall lower TC activity, large TCHP values likely contributed to the significant intensification of several storms in this basin, as also observed in previous La Niña or La Niña-like years (e.g., TC Megi in 2010, TC Haiyan in 2013; Lin et al. 2014). Among those, Super Typhoon Goni was a notable example. Goni developed south of Guam and followed a similar track to TC Haiyan in 2013 in the southwestern North Pacific main development region (Lin et al. 2014; i.e., east of the Philippines between 5°N and 20°N). As it traveled over areas characterized by high SSTs and high TCHP values (not shown), it experienced a very rapid intensification of 80 kt (41 m s^{-1}) during a 24-hour window, surpassing Haiyan's 60-kt intensification. Goni eventually reached the same record intensity of 170 kt (87 m s^{-1}) as Haiyan in 2013 before making landfall in the Philippines.

In the eastern North Pacific basin, there was an average number of TCs but a below-average number of hurricanes. The La Niña conditions observed in the North Pacific, which were associated with negative SST anomalies (not shown) and lower TCHP values compared to 2019 (Fig. 4.42), likely contributed to the reduced hurricane activity in this basin during the 2020 season.

The North Atlantic basin exhibited TCHP values 10–20 kJ cm^{-2} above the long-term mean in most areas within this basin (Fig. 4.41). Compared with conditions recorded in 2019, TCHP values were also approximately 10 kJ cm^{-2} larger in value for 2020 within the western Caribbean Sea, southern Gulf of Mexico, and along the southeast U.S. coast. A notable increase in TCHP values was observed in the western Caribbean Sea, where TCHP was approximately 30 kJ cm^{-2} larger-than-average conditions, with absolute values typically above 100 kJ cm^{-2} and as large as 140 kJ cm^{-2} (not shown). Associated with these conditions, the North Atlantic basin recorded unprecedented levels of TC activity (section 4g2). From the 14 TCs that reached Category 1 intensity, eight traveled through the open North Atlantic, Caribbean Sea, and Gulf of Mexico (Fig. 4.41). Hurricane Hanna (23–27 July) was the only system to develop and intensify strictly within the Gulf of Mexico. The positive TCHP anomalies observed in 2020 provided the favorable ocean conditions that likely contributed to this very intense TC activity, especially in the western Caribbean Sea, where Category 4 Hurricanes Delta (5–12 October), Eta (31 October–14 November), and Category 4 Hurricane Iota (13–18 November) reached their peak intensity. Iota, for example, rapidly intensified into a Category 5 hurricane over extremely anomalously high TCHP values for November.

In summary, the 2020 TC season exhibited positive TCHP anomalies in most of the TC basins (Fig. 4.41), with notable increases in the upper-ocean heat content in the North Indian, South Indian, and western North Pacific basins, and the western Caribbean and southern Gulf of Mexico. While this could suggest that upper-ocean conditions conducive for TC development and intensification were anomalously favorable in these basins in terms of upper-ocean heat content, in fact, global TC activity in terms of ACE was below normal in association with the La Niña conditions in place. In fact, some of the notable TCs of 2020 highlighted above, such as Cyclone Amphan in the North Indian Ocean, Super Typhoon Goni in the West Pacific, and Hurricane Iota in the Atlantic, underwent rapid intensification while traveling over areas with large TCHP values. In the Pacific Ocean, upper-ocean thermal conditions and TC activity were largely modulated by an ongoing La Niña, which likely caused below-normal TC activity in both the eastern and western North Pacific basins. In the Atlantic, a record number of named TCs were observed, with several major hurricanes reaching their peak intensity while traveling over the anomalously warm western Caribbean Sea. The 2020 season also featured the development of three hurricane-like cyclones or "medicanes" that were recorded within the Mediterranean Sea and were associated with positive SST anomalies.

Chapter 4 – Acronyms

ACE	accumulated cyclone energy
AEJ	African Easterly Jet
AMO	Atlantic Multi-decadal Oscillation
ASO	August–October
CMORPH	CPC Morphing Technique
CNP	central North Pacific
CPC	Climate Prediction Center
DJF	December–February
EASM	East Asian summer monsoon
ENP	East Asian summer monsoon
ENP	eastern North Pacific
ENSO	El Niño–Southern Oscillation
GPCP	Global Precipitation Climatology Project
GPI	genesis potential index
HTCs	hurricanes/typhoons/cyclones
IBTrACS	International Best Track Archive for Climate Stewardship
IO	Indian Ocean
IOB	Indian Ocean basin
IOD	Indian Ocean dipole
ITCZ	Intertropical Convergence Zone
JAS	July–September
JASO	July–October
JJA	June–August
JMA	Japan Meteorological Agency
JTWC	Joint Typhoon Warning Center
MAM	March–May
MDR	main development region
MJO	Madden-Julian Oscillation
NDJ	November–January
NAF	northern Africa
NH	Northern Hemisphere
NIO	North Indian Ocean
OLR	outgoing longwave radiation
OND	October–December
ONI	Oceanic Niño Index
PAGASA	Philippine Atmospheric, Geophysical and Astronomical Services Administration
RMM	Real-time Multivariate MJO
RSMCs	Regional Specialized Meteorological Centers
SAM	Southern Annular Mode
SH	Southern Hemisphere
SON	September–November
SPCZ	South Pacific Convergence Zone
SPEArTC	South Pacific Enhanced Archive of Tropical Cyclones
SSHWS	Saffir-Simpson Hurricane Wind Scale
SST	sea surface temperature

TC	tropical cyclone
TCHP	tropical cyclone heat potential
TD	tropical depression
TT	tropical transition
TUTT	tropical upper-tropospheric trough
WMO	World Meteorological Organization
WNP	western North Pacific
WWBs	westerly wind bursts
YHRV	Yangtze and Huaihe River Valleys

References

Aiyyer, A., and J. Molinari, 2008: MJO and tropical cyclogenesis in the Gulf of Mexico and eastern Pacific: Case study and idealized numerical modeling. *J. Atmos. Sci.*, **65**, 2691–2704, https://doi.org/10.1175/2007JAS2348.1.

Ashok, K., S. K. Behera, S. A. Rao, H. Weng, and T. Yamagata, 2007: El Nino Modoki and its possible teleconnection. *J. Geophys. Res.*, **112**, C11007, https://doi.org/10.1029/2006JC003798.

Balaguru, K., P. Chang, R. Saravanan, L. R. Leung, Z. Xu, M. Li, and J. S. Hsieh, 2012: Ocean barrier layers' effect on tropical cyclone intensification. *Proc. Natl. Acad. Sci. USA*, **109**, 14 343–14 347, https://doi.org/10.1073/pnas.1201364109.

Banzon, V. F., and R. W. Reynolds, 2013: Use of WindSat to extend a microwave-based daily optimum interpolation sea surface temperature time series. *J. Climate*, **26**, 2557–2562, https://doi.org/10.1175/JCLI-D-12-00628.1.

Baxter, S., S. Weaver, J. Gottschalck, and Y. Xue, 2014: Pentad evolution of wintertime impacts of the Madden–Julian oscillation over the contiguous United States. *J. Climate*, **27**, 7356–7367, https://doi.org/10.1175/JCLI-D-14-00105.1.

Behringer, D. W., M. Ji, and A. Leetmaa, 1998: An improved coupled model for ENSO prediction and implications for ocean initialization. Part I: The ocean data assimilation system. *Mon. Wea. Rev.*, **126**, 1013–1021, https://doi.org/10.1175/1520-0493(1998)126<1013:AICMFE>2.0.CO;2.

Bell, G. D., and M. Chelliah, 2006: Leading tropical modes associated with interannual and multi-decadal fluctuations in North Atlantic hurricane activity. *J. Climate*, **19**, 590–612, https://doi.org/10.1175/JCLI3659.1.

——, and Coauthors, 2000: The 1999 North Atlantic Hurricane season [in "Climate Assessment for 1999"]. Bull. Amer. Meteor. Soc., 81 (6), S19–S22, https://doi.org/10.1175/1520-0477(2000)81[s1:CAF]2.0.CO;2.

——, S. Goldenberg, C. Landsea, E. Blake, R. Pasch, M. Chelliah, and K. Mo, 2004: Atlantic hurricane season [in "State of the Climate in 2003"]. *Bull. Amer. Meteor. Soc.*, **85** (6), S20–S24, https://doi.org/10.1175/1520-0477-85.6s.S1.

——, E. Blake, K. C. Mo, C. W. Landsea, R. Pasch, M. Chelliah, and S. B. Goldenberg, 2006: Atlantic Basin [in "State of the Climate in 2005"]. *Bull. Amer. Meteor. Soc.*, **87** (6), S33–S37, https://doi.org/10.1175/1520-0477-87.6.S1.

——, ——, T. B. Kimberlain, C. W. Landsea, J. Schemm, R. J. Pasch, and S. B. Goldenberg, 2011: Atlantic Basin [in "State of the Climate in 2010"]. *Bull. Amer. Meteor. Soc.*, **92**, S115–S121, https://doi.org/10.1175/1520-0477-92.6.S1.

——, ——, C. W. Landsea, C. Wang, J. Schemm, T. Kimberlain, R. J. Pasch, and S. B. Goldenberg, 2017: Atlantic basin [in "State of the Climate in 2016"]. *Bull. Amer. Meteor. Soc.*, **98** (8), S108–S112, https://doi.org/10.1175/2017BAMSStateoftheClimate.1.

——, ——, ——, S. B. Goldenberg, and R. J. Pasch, 2018: Atlantic basin [in "State of the Climate in 2017"]. *Bull. Amer. Meteor. Soc.*, **99** (8), S114–S118, https://doi.org/10.1175/2018BAMSStateoftheClimate.1.

——, M. S. Halpert, and M. L'Heureux, 2019: ENSO and the tropical Pacific [in "State of the Climate in 2018"]. *Bull. Amer. Meteor. Soc.*, **100** (9), S101–S104, https://doi.org/10.1175/2019BAMSStateoftheClimate.1.

——, E. S. Blake, C. W. Landsea, M. Rosencrans, H. Wang, S. B. Goldenberg, and R. J. Pasch, 2020: Atlantic basin [in "State of the Climate in 2019"]. *Bull. Amer. Meteor. Soc.*, **101** (7), S204–S212, https://doi.org/10.1175/BAMS-D-20-0077.1.

Berg, R., 2020: Tropical Storm Amanda (EP022020). National Hurricane Center Tropical Cyclone Rep., 18 pp. https://www.nhc.noaa.gov/data/tcr/EP022020_Amanda.pdf.

Bjerknes, J., 1969: Atmospheric teleconnections from the equatorial Pacific. *Mon. Wea. Rev.*, **97**, 163–172, https://doi.org/10.1175/1520-0493(1969)097<0163:ATFTEP>2.3.CO;2.

Brown, D. P., 2020: Unnamed Tropical Storm (formerly Tropical Depression Seven-E) (EP072020). National Hurricane Center Tropical Cyclone Rep., 9 pp. https://www.nhc.noaa.gov/data/tcr/EP072020_Unnamed.pdf.

Camargo, S. J., and A. H. Sobel, 2005: Western North Pacific tropical cyclone intensity and ENSO. *J. Climate*, **18**, 2996–3006, https://doi.org/10.1175/JCLI3457.1.

——, A. W. Robertson, S. J. Gaffney, P. Smyth, and M. Ghil, 2007a: Cluster analysis of typhoon tracks: Part II: Large-scale circulation and ENSO. *J. Climate*, **20**, 3654–3676, https://doi.org/10.1175/JCLI4203.1.

——, K. A. Emanuel, and A. H. Sobel, 2007b: Use of a genesis potential index to diagnose ENSO effects on tropical cyclone genesis. *J. Climate*, **20**, 4819–4834, https://doi.org/10.1175/JCLI4282.1.

——, M. C. Wheeler, and A. H. Sobel, 2009: Diagnosis of the MJO modulation of tropical cyclogenesis using an empirical index. *J. Atmos. Sci.*, **66**, 3061–3074, https://doi.org/10.1175/2009JAS3101.1.

Cangialosi, J. P., 2020: Tropical Depression One-E (EP012020). National Hurricane Center Tropical Cyclone Rep., 7 pp. https://www.nhc.noaa.gov/data/tcr/EP012020_One-E.pdf.

Cassou, C., 2008: Intraseasonal interaction between the Madden Julian Oscillation and the North Atlantic Oscillation. *Nature*, **455**, 523–527, https://doi.org/10.1038/nature07286.

Cavicchia, L., H. von Storch, and S. Gualdi, 2014: A long-term climatology of medicanes. *Climate Dyn.*, **43**, 1183–1195, https://doi.org/10.1007/s00382-013-1893-7.

Chen, L., J.-J. Luo, and A. D. Magee, 2020: Indian Ocean dipole [in "State of the Climate in 2019"]. *Bull. Amer. Meteor. Soc.*, **100** (9), S229–S232, https://doi.org/10.1175/BAMS-D-20-0077.1.

Chia, H. H., and C. F. Ropelewski, 2002: The interannual variability in the genesis location of tropical cyclones in the northwest Pacific. *J. Climate*, **15**, 2934–2944, https://doi.org/10.1175/1520-0442(2002)015<2934:TIVITG>2.0.CO;2.

Clarke, A. J., 2010: Analytical theory for the quasi-steady and low-frequency equatorial ocean response to wind forcing: The "tilt" and "warm water volume" modes. *J. Phys. Oceanogr.*, **40**, 121–137, https://doi.org/10.1175/2009JPO4263.1.

CNN, 2020: Cyclone Amphan caused an estimated $13.2 billion in damage in India's West Bengal: Government source. 22 May, accessed 10 January 2021, https://edition.cnn.com/2020/05/22/weather/cyclone-amphan-damage-intl-hnk/index.html.

Dare, R. A., and J. L. McBride, 2011: Sea surface temperature response to tropical cyclones. *Mon. Wea. Rev.*, **139**, 3798–3808, https://doi.org/10.1175/MWR-D-10-05019.1.

Diamond, H. J., and J. A. Renwick, 2015: The climatological relationship between tropical cyclones in the southwest pacific and the Madden–Julian Oscillation. *Int. J. Climatol.*, **35**, 676–686, https://doi.org/10.1002/joc.4012.

——, and C. J. Schreck III, Eds., 2017: The tropics [in "State of the Climate in 2016"]. *Bull. Amer. Meteor. Soc.*, **98** (8), S93–S128, https://doi.org/10.1175/2017BAMSStateoftheClimate.1.

——, and ——, Eds., 2018: The tropics [in "State of the Climate in 2017"]. *Bull. Amer. Meteor. Soc.*, **99** (8), S101–S141, https://doi.org/10.1175/2018BAMSStateoftheClimate.1.

——, and ——, Eds., 2019: The tropics [in "State of the Climate in 2018"]. *Bull. Amer. Meteor. Soc.*, **100** (9), S101–S140, https://doi.org/10.1175/2019BAMSStateoftheClimate.1.

——, and ——, Eds., 2020: The tropics [in "State of the Climate in 2019"]. *Bull. Amer. Meteor. Soc.*, **100** (8), S185–S238, https://doi.org/10.1175/BAMS-D-20-0077.1.

——, A. M. Lorrey, K. R. Knapp, and D. H. Levinson, 2012: Development of an enhanced tropical cyclone tracks database for the southwest Pacific from 1840 to 2011. *Int. J. Climatol.*, **32**, 2240–2250, https://doi.org/10.1002/joc.2412.

Domingues, R., and Coauthors, 2015: Upper ocean response to Hurricane Gonzalo (2014): Salinity effects revealed by targeted and sustained underwater glider observations. *Geophys. Res. Lett.*, **42**, 7131–7138, https://doi.org/10.1002/2015GL065378.

Dube, S. K., D. Rao, P. C. Sinha, T. S. Murty, and N. Bahuluyan, 1997: Storm surge in the Bay of Bengal and Arabian Sea: The problem and its prediction. *Mausam* **48**, 288–304.

Ebita, A., and Coauthors, 2011: The Japanese 55-year reanalysis "JRA-55": An interim report. *Sci. Online Lett. Atmos.*, **7**, 149–152, https://doi.org/10.2151/sola.2011-038.

Emanuel, K. A., 1988: The maximum intensity of hurricanes. *J. Atmos. Sci.*, **45**, 1143–1155, https://doi.org/10.1175/1520-0469(1988)045<1143:TMIOH>2.0.CO;2.

——, 2005: Genesis and maintenance of "Mediterranean Hurricanes." *Adv. Geosci.*, **2**, 217–220, https://doi.org/10.5194/adgeo-2-217-2005.

——, and D. S. Nolan, 2004: Tropical cyclone activity and the global climate system. 26th Conf. on Hurricanes and Tropical Meteorology, Miami, FL, Amer. Meteor. Soc., 10A.2, https://ams.confex.com/ams/26HURR/techprogram/paper_75463.htm.

Enfield, D. B., and A. M. Mestas-Nuñez, 1999: Multiscale variabilities in global sea surface temperatures and their relationships with tropospheric climate patterns. *J. Climate*, **12**, 2719–2733, https://doi.org/10.1175/1520-0442(1999)012<2719:MVIGSS>2.0.CO;2.

Fita, L., R. Romero, A. Luque, K. Emanuel, and C. Ramis, 2007: Analysis of the environments of seven Mediterranean tropical-like storms using an axisymmetric, nonhydrostatic, cloud resolving model. *Nat. Hazards Earth Syst. Sci.*, **7**, 41–56, https://doi.org/10.5194/nhess-7-41-2007.

Frank, W. M., and P. E. Roundy, 2006: The role of tropical waves in tropical cyclogenesis. *Mon. Wea. Rev.*, **134**, 2397–2417, https://doi.org/10.1175/MWR3204.1.

Goldenberg, S. B., and L. J. Shapiro, 1996: Physical mechanisms for the association of El Niño and West African rainfall with Atlantic major hurricane activity. *J. Climate*, **9**, 1169–1187, https://doi.org/10.1175/1520-0442(1996)009<1169:PMFTAO>2.0.CO;2.

——, C. W. Landsea, A. M. Mestas-Nuñez, and W. M. Gray, 2001: The recent increase in Atlantic hurricane activity: Causes and implications. *Science*, **293**, 474–479, https://doi.org/10.1126/science.1060040.

Goni, G. J., and Coauthors, 2009: Applications of satellite-derived ocean measurements to tropical cyclone intensity forecasting. *Oceanography*, **22**, 176–183, https://doi.org/10.5670/oceanog.2009.78.

——, and Coauthors, 2017: Autonomous and Lagrangian Ocean observations for Atlantic tropical cyclone studies and forecasts. *Oceanography*, **30**, 92–103, https://doi.org/10.5670/oceanog.2017.227.

Gray, W., 1968: Global view of the origin of tropical disturbances and storms. *Mon. Wea. Rev.*, **96**, 669–700, https://doi.org/10.1175/1520-0493(1968)096<0669:GVOTOO>2.0.CO;2.

——, 1990: Strong association between West African rainfall and U.S. landfall of intense hurricanes. *Science*, **249**, 1251–1256, https://doi.org/10.1126/science.249.4974.1251.

Guo, Y., X. Jiang, and D. E. Waliser, 2014: Modulation of the convectively coupled Kelvin waves over South America and the tropical Atlantic Ocean in association with the Madden–Julian oscillation. *J. Atmos. Sci.*, **71**, 1371–1388, https://doi.org/10.1175/JAS-D-13-0215.1.

Halpert, M. S., and C. F. Ropelewski, 1992: Surface temperature patterns associated with the southern oscillation. *J. Climate*, **5**, 577–593, https://doi.org/10.1175/1520-0442(1992)005<0577:STPAWT>2.0.CO;2.

Hart, R. E., 2003: A cyclone phase space derived from thermal wind and thermal asymmetry. *Mon. Wea. Rev.*, **131**, 585–616, https://doi.org/10.1175/1520-0493(2003)131<0585:ACPSDF>2.0.CO;2.

Hastenrath, S., 1990: Decadal-scale changes of the circulation in the tropical Atlantic sector associated with Sahel drought. *Int. J. Climatol.*, **10**, 459–472, https://doi.org/10.1002/joc.3370100504.

Hendon, H., C. Zhang, and J. Glick, 1999: Interannual variation of the Madden–Julian oscillation during austral summer. *J. Climate*, **12**, 2538–2550, https://doi.org/10.1175/1520-0442(1999)012<2538:IVOTMJ>2.0.CO;2.

Hersbach, H., and Coauthors, 2020: The ERA5 global reanalysis. *Quart. J. Roy. Meteor. Soc.*, **146**, 1999–2049, https://doi.org/10.1002/qj.3803.

Huang, B., and Coauthors, 2017: Extended reconstructed sea surface temperature, version 5 (ERSSTv5): Upgrades, validations, and intercomparisons. *J. Climate*, **30**, 8179–8205, https://doi.org/10.1175/JCLI-D-16-0836.1.

Huffman, G. J., R. F. Adler, D. T. Bolvin, and G. Gu, 2009: Improving the global precipitation record: GPCP Version 2.1. *Geophys. Res. Lett.*, **36**, L17808, https://doi.org/10.1029/2009GL040000.

India Meteorological Department, 2020a: Cyclonic storm 'BUREVI' over the Bay of Bengal (30th November - 5th December 2020): A preliminary report. 20 pp., https://static.pib.gov.in/WriteReadData/userfiles/Summary-BUREVI_12122020.pdf.

——, 2020b: Very severe cyclonic storm 'GATI' over the Arabian Sea (21-24 November 2020): A report. 33 pp., http://rsmcnewdelhi.imd.gov.in/uploads/report/26/26_fd784d_gati.pdf.

——, 2020c: Very severe cyclonic storm 'NIVAR' over the Bay of Bengal (22nd-27th November 2020): A report. 42 pp., http://www.rsmcnewdelhi.imd.gov.in/uploads/report/26/26_891f5a_NIVAR.pdf.

——, 2020d: Severe cyclonic storm "NISARGA" over the Arabian Sea (01-04 June 2020): Summary. 35 pp., http://www.rsmcnewdelhi.imd.gov.in/images/pdf/publications/preliminary-report/nisarga.pdf.

——, 2021: Super cyclonic storm "AMPHAN" over Southeast Bay of Bengal (16 May - 21 May 2020): A report. 73 pp., http://www.rsmcnewdelhi.imd.gov.in/uploads/report/26/26_936e63_amphan.pdf.

Island Climate Update, 2020: The island climate update. National Institute of Water and Atmospheric Research, New Zealand, https://niwa.co.nz/climate/island-climate-update.

Joyce, R. J., J. E. Janowiak, P. A. Arkin, and P. Xie, 2004: CMORPH: A method that produces global precipitation estimates from passive microwave and infrared data at high spatial and temporal resolution. *J. Hydrometeor.*, **5**, 487–503, https://doi.org/10.1175/1525-7541(2004)005<0487:CAMTPG>2.0.CO;2.

Kalnay, E., and Coauthors, 1996: The NCEP/NCAR 40-Year Reanalysis Project. *Bull. Amer. Meteor. Soc.*, **77**, 437–471, https://doi.org/10.1175/1520-0477(1996)077<0437:TNYRP>2.0.CO;2.

Kayano, M., and V. Kousky, 1999: Intraseasonal (30-60 day) variability in the global tropics: Principal modes and their evolution. *Tellus*, **51**, 373–386, https://doi.org/10.3402/tellusa.v51i3.13459.

Kiladis, G. N., and K. M. Weickmann, 1992: Circulation anomalies associated with tropical convection during northern winter. *Mon. Wea. Rev.*, **120**, 1900–1923, https://doi.org/10.1175/1520-0493(1992)120<1900:CAAWTC>2.0.CO;2.

——, K. H. Straub, and P. T. Haertel, 2005: Zonal and vertical structure of the Madden–Julian oscillation. *J. Atmos. Sci.*, **62**, 2790–2809, https://doi.org/10.1175/JAS3520.1.

——, M. C. Wheeler, P. T. Haertel, K. H. Straub, and P. E. Roundy, 2009: Convectively coupled equatorial waves. *Rev. Geophys.*, **47**, RG2003, https://doi.org/10.1029/2008RG000266.

Klotzbach, P. J., 2010: On the Madden–Julian oscillation–Atlantic hurricane relationship. *J. Climate*, **23**, 282–293, https://doi.org/10.1175/2009JCLI2978.1.

Knaff, J. A., C. R. Sampson, and K. D. Musgrave, 2018: An operational rapid intensification prediction aid for the western North Pacific. *Wea. Forecasting*, **33**, 799–811, https://doi.org/10.1175/WAF-D-18-0012.1.

Knapp, K. R., M. C. Kruk, D. H. Levinson, H. J. Diamond, and C. J. Neumann, 2010: The International Best Track Archive for Climate Stewardship (IBTrACS): Unifying tropical cyclone data. *Bull. Amer. Meteor. Soc.*, **91**, 363–376, https://doi.org/10.1175/2009BAMS2755.1.

——, J. A. Knaff, C. R. Sampson, G. M. Riggio, and A. D. Schnapp, 2013: A pressure-based analysis of the historical western North Pacific tropical cyclone intensity record. *Mon. Wea. Rev.*, **141**, 2611–2631, https://doi.org/10.1175/MWR-D-12-00323.1.

Knutson, T. R., and K. M. Weickmann, 1987: 30–60 day atmospheric oscillations: Composite life cycles of convection and circulation anomalies. *Mon. Wea. Rev.*, **115**, 1407–1436, https://doi.org/10.1175/1520-0493(1987)115<1407:DAOCLC>2.0.CO;2.

Kousky, V. E., and M. T. Kayano, 1994: Principal modes of outgoing longwave radiation and 250-mb circulation for the South American sector. *J. Climate*, **7**, 1131–1143, https://doi.org/10.1175/1520-0442(1994)007<1131:PMOOLR>2.0.CO;2.

Krishnamurti, T. N., and D. Subrahmanyam, 1982: The 30–50 day mode at 850 mb during MONEX. *J. Atmos. Sci.*, **39**, 2088–2095, https://doi.org/10.1175/1520-0469(1982)039<2088:TDMAMD>2.0.CO;2.

Kruk, M. C., and C. J. Schreck, 2019: Eastern North Pacific basin [in "State of the Climate in 2018"]. *Bull. Amer. Meteor. Soc.*, **100**, S121–S124, https://doi.org/10.1175/2019BAMSStateoftheClimate.1.

Kumar, A., and Z.-Z. Hu, 2014: Interannual and interdecadal variability of ocean temperature along the equatorial Pacific in conjunction with ENSO. *Climate Dyn.*, **42**, 1243–1258, https://doi.org/10.1007/s00382-013-1721-0.

Landsea, C. W., and J. L. Franklin, 2013: Atlantic hurricane database uncertainty and presentation of a new database format. *Mon. Wea. Rev.*, **141**, 3576–3592, https://doi.org/10.1175/MWR-D-12-00254.1.

——, W. M. Gray, P. W. Mielke, and K. J. Berry, 1992: Long-term variations of western Sahelian monsoon rainfall and intense U.S. landfalling hurricanes. *J. Climate*, **5**, 1528–1534, https://doi.org/10.1175/1520-0442(1992)005<1528:LTVOWS>2.0.CO;2.

——, G. D. Bell, W. M. Gray, and S. B. Goldenberg, 1998: The extremely active 1995 Atlantic hurricane season: Environmental conditions and verification of seasonal forecasts. *Mon. Wea. Rev.*, **126**, 1174–1193, https://doi.org/10.1175/1520-0493(1998)126<1174:TEAAHS>2.0.CO;2.

——, G. A. Vecchi, L. Bengtsson, and T. R. Knutson, 2010: Impact of duration thresholds on Atlantic tropical cyclone counts. *J. Climate*, **23**, 2508–2519, https://doi.org/10.1175/2009JCLI3034.1.

Latto, A., 2020: Hurricane Douglas (EP082020). National Hurricane Center Tropical Cyclone Rep., 14 pp. https://www.nhc.noaa.gov/data/tcr/EP082020_Douglas.pdf.

Lau, W. K.-M., and D. E. Waliser, 2012: Intraseasonal Variability in the Atmosphere-Ocean Climate System. Springer, 642 pp.

Leipper, D. F., and D. Volgenau, 1972: Hurricane heat potential of the Gulf of Mexico. *J. Phys. Oceanogr.*, **2**, 218–224, https://doi.org/10.1175/1520-0485(1972)002<0218:HHPOTG>2.0.CO;2.

Liebmann, B., and C. A. Smith, 1996: Description of a complete (interpolated) outgoing longwave radiation dataset. *Bull. Amer. Meteor. Soc.*, **77**, 1275–1277, https://doi.org/10.1175/1520-0477-77.6.1274.

Lin, H., G. Brunet, and J. Derome, 2009: An observed connection between the North Atlantic oscillation and the Madden–Julian oscillation. *J. Climate*, **22**, 364–380, https://doi.org/10.1175/2008JCLI2515.1.

Lin, I. I., and J. Chan, 2015: Recent decrease in typhoon destructive potential and global warming implications. *Nat. Commun.*, **6**, 7182, https://doi.org/10.1038/ncomms8182.

——, and Coauthors, 2013: An ocean coupling potential intensity index for tropical cyclones. *Geophys. Res. Lett.*, **40**, 1878–1882, https://doi.org/10.1002/grl.50091.

——, I.-F. Pun, and C.-C. Lien, 2014: "Category-6" Supertyphoon Haiyan in global warming hiatus: Contribution from subsurface ocean warming. *Geophys. Res. Lett.*, **41**, 8547–8553, https://doi.org/10.1002/2014GL061281.

——, and Coauthors, 2020: ENSO and tropical cyclones. *El Niño Southern Oscillation in a Changing Climate*, *Geophys. Monogr.*, Vol. 253, Amer. Geophys. Union, 377–408, https://doi.org/10.1002/9781119548164.ch17.

Juo, J. J., R. Zhang, S. K. Behera, Y. Masumoto, F.-F. Jin, R. Lukas, and T. Yamagata, 2010: Interaction between El Niño and extreme Indian Ocean dipole. *J. Climate*, **23**, 726–742, https://doi.org/10.1175/2009JCLI3104.1.

——, W. Sasaki, and Y. Masumoto, 2012: Indian Ocean warming modulates Pacific climate change. *Proc. Natl. Acad. Sci. USA*, **109**, 18 701–18 706, https://doi.org/10.1073/pnas.1210239109.

Madden, R., and P. Julian, 1971: Detection of a 40–50 day oscillation in the zonal wind in the tropical Pacific. *J. Atmos. Sci.*, **28**, 702–708, https://doi.org/10.1175/1520-0469(1971)028<0702:DOADOI>2.0.CO;2.

—., and ——, 1972: Description of global-scale circulation cells in the tropics with a 40–50 day period. *J. Atmos. Sci.*, **29**, 1109–1123, https://doi.org/10.1175/1520-0469(1972)029<1109:DOGSCC>2.0.CO;2.

——, and ——, 1994: Observations of the 40–50-day tropical oscillation: A review. *Mon. Wea. Rev.*, **122**, 814–837, https://doi.org/10.1175/1520-0493(1994)122<0814:OOTDTO>2.0.CO;2.

Mainelli, M., M. DeMaria, L. Shay, and G. Goni, 2008: Application of oceanic heat content estimation to operational forecasting of recent Atlantic category 5 hurricanes. *Wea. Forecasting*, **23**, 3–16, https://doi.org/10.1175/2007WAF2006111.1.

Maloney, E. D., and D. L. Hartmann, 2001: The Madden–Julian oscillation, barotropic dynamics, and North Pacific tropical cyclone formation. Part I: Observations. *J. Atmos. Sci.*, **58**, 2545–2558, https://doi.org/10.1175/1520-0469(2001)058<2545:TMJOBD>2.0.CO;2.

Matthews, A. J., 2008: Primary and successive events in the Madden–Julian Oscillation. *Quart. J. Roy. Meteor. Soc.*, **134**, 439–453, https://doi.org/10.1002/qj.224.

Mazza, E., U. Ulbrich, and R. Klein, 2017: The tropical transition of the October 1996 medicane in the western Mediterranean Sea: A warm seclusion event. *Mon. Wea. Rev.*, **145**, 2575–2595, https://doi.org/10.1175/MWR-D-16-0474.1.

McTaggart-Cowan, R., L. F. Bosart, C. A. Davis, E. H. Atallah, J. R. Gyakum, and K. A. Emanuel, 2006: Analysis of Hurricane Catarina (2004). *Mon. Wea. Rev.*, **134**, 3029–3053, https://doi.org/10.1175/MWR3330.1.

McTaggart-Cowan, R., E. L. Davies, J. G. Fairman Jr., T. J. Galarneau Jr., and D. M. Schultz, 2015: Revisiting the 26.5°C sea surface temperature threshold for tropical cyclone development. *Bull. Amer. Meteor. Soc.*, **96**, 1929–1943, https://doi.org/10.1175/BAMS-D-13-00254.1.

Mo, K. C., 2000: The association between intraseasonal oscillations and tropical storms in the Atlantic Basin. *Mon. Wea. Rev.*, **128**, 4097–4107, https://doi.org/10.1175/1520-0493(2000)129<4097:TABIOA>2.0.CO;2.

Mo, K. C., and V. E. Kousky, 1993: Further analysis of the relationship between circulation anomaly patterns and tropical convection. *J. Geophys. Res.*, **98**, 5103–5113, https://doi.org/10.1029/92JD02952.

——, and R. W. Higgins, 1998: The Pacific–South American modes and tropical convection during the Southern Hemisphere winter. *Mon. Wea. Rev.*, **126**, 1581–1596, https://doi.org/10.1175/1520-0493(1998)126<1581:TPSAMA>2.0.CO;2.

Münnich, M., and J. D. Neelin, 2005: Seasonal influence of ENSO on the Atlantic ITCZ and equatorial South America. *Geophys. Res. Lett.*, **32**, L21709, https://doi.org/10.1029/2005GL023900.

Nobre, P., and J. Shukla, 1996: Variations of sea surface temperature, wind stress and rainfall over the tropical Atlantic and South America. *J. Climate*, **9**, 2464–2479, https://doi.org/10.1175/1520-0442(1996)009<2464:VOSSTW>2.0.CO;2.

Pantillon, F., J.-P. Chaboureau, P. J. Mascart, and C. Lac, 2013: Predictability of a Mediterranean tropical-like storm downstream of the extratropical transition of Hurricane Helene (2006). *Mon. Wea. Rev.*, **141**, 1943–1962, https://doi.org/10.1175/MWR-D-12-00164.1.

Papin, P. P., L. F. Bosart, and R. D. Torn, 2017: A climatology of Central American gyres. *Mon. Wea. Rev.*, **145**, 1983–2000, https://doi.org/10.1175/MWR-D-16-0411.1.

Pasch, R. J., R. Berg, D. P. Roberts, and P. P. Papin, 2021: Hurricane Laura (AL132020). National Hurricane Center Tropical Cyclone Rep., 75 pp, https://www.nhc.noaa.gov/data/tcr/AL132020_Laura.pdf.

Penland, C., and P. D. Sardeshmukh, 1995: The optimal growth of tropical sea surface temperature anomalies. *J. Climate*, **8**, 1999–2024, https://doi.org/10.1175/1520-0442(1995)008<1999:TOGOTS>2.0.CO;2.

Pezza, A. B., and A. S. Coelho, 2019: Atlantic [in "State of the Climate in 2018"]. *Bull. Amer. Meteor. Soc.*, **100** (9), S109–S110, https://doi.org/10.1175/2019BAMSStateoftheClimate.1.

Qiao, S., and Coauthors, 2021: The longest 2020 Meiyu season over the past 60 years: Subseasonal perspective and its predictions. *Geophys. Res. Lett.*, **48**, e2021GL093596, https://doi.org/10.1029/2021GL093596.

Raga, G. B., B. Bracamontes-Ceballos, L. Farfán, and R. Romero-Centeno, 2013: Landfalling tropical cyclones on the Pacific coast of Mexico: 1850–2010. *Atmósfera*, **26**, 209–220, https://doi.org/10.1016/S0187-6236(13)71072-5.

Reynolds, R. W., N. A. Rayner, T. M. Smith, D. C. Stokes, and W. Wang, 2002: An improved in situ and satellite SST analysis for climate. *J. Climate*, **15**, 1609–1625, https://doi.org/10.1175/1520-0442(2002)015<1609:AIISAS>2.0.CO;2.

Riddle, E., M. Stoner, N. Johnson, M. L'Heureux, D. Collins, and S. Feldstein, 2012: The impact of the MJO on clusters of wintertime circulation anomalies over the North American region. *Climate Dyn.*, **40**, 1749–1766, https://doi.org/10.1007/s00382-012-1493-y .

Ropelewski, C. F., and M. S. Halpert, 1989: Precipitation patterns associated with the high index phase of the southern oscillation. *J. Climate*, **2**, 268–284, https://doi.org/10.1175/1520-0442(1989)002<0268:PPAWTH>2.0.CO;2.

Rui, H., and B. Wang, 1990: Development characteristics and dynamic structure of tropical intraseasonal convection anomalies. *J. Atmos. Sci.*, **47**, 357–379, https://doi.org/10.1175/1520-0469(1990)047<0357:DCADSO>2.0.CO;2.

Saha, S., and Coauthors, 2014: The NCEP Climate Forecast System version 2. *J. Climate*, **27**, 2185–2208, https://doi.org/10.1175/JCLI-D-12-00823.1.

Saji, N. H., B. N. Goswami, P. N. Vinayachandran, and T. Yamagata, 1999: A dipole mode in the tropical Indian ocean. *Nature*, **401**, 360–363, https://doi.org/10.1038/43854.

Schneider, T., T. Bischoff, and G. H. Haug, 2014: Migrations and dynamics of the intertropical convergence zone. *Nature*, **513**, 45–53, https://doi.org/10.1038/nature13636.

Schreck, C. J., 2015: Kelvin waves and tropical cyclogenesis: A global survey. *Mon. Wea. Rev.*, **143**, 3996–4011, https://doi.org/10.1175/MWR-D-15-0111.1.

Schreck, C. J., 2016: Convectively coupled Kelvin waves and tropical cyclogenesis in a semi-Lagrangian framework. *Mon. Wea. Rev.*, **144**, 4131–4139, https://doi.org/10.1175/MWR-D-16-0237.1.

Schreck, C. J., and J. Molinari, 2011: Tropical cyclogenesis associated with Kelvin waves and the Madden–Julian oscillation. *Mon. Wea. Rev.*, **139**, 2723–2734, https://doi.org/10.1175/MWR-D-10-05060.1.

Schreck, C. J., J. Molinari, and A. Aiyyer, 2012: A global view of equatorial waves and tropical cyclogenesis. *Mon. Wea. Rev.*, **140**, 774–788, https://doi.org/10.1175/MWR-D-11-00110.1.

Schreck, C. J., J. M. Cordeira, and D. Margolin, 2013: Which MJO events affect North American temperatures? *Mon. Wea. Rev.*, **141**, 3840–3850, https://doi.org/10.1175/MWR-D-13-00118.1.

Schreck, C. J., K. R. Knapp, and J. P. Kossin, 2014: The impact of best track discrepancies on global tropical cyclone climatologies using IBTrACS. *Mon. Wea. Rev.*, **142**, 3881–3899, https://doi.org/10.1175/MWR-D-14-00021.1.

Schreck, C. J., H.-T. Lee, and K. R. Knapp, 2018: HIRS outgoing longwave radiation—Daily climate data record: Application toward identifying tropical subseasonal variability. *Remote Sens.*, **10**, 1325, https://doi.org/10.3390/rs10091325.

Shay, L. K., G. J. Goni, and P. G. Black, 2000: Effects of a warm oceanic feature on Hurricane Opal. *Mon. Wea. Rev.*, **128**, 1366–1383, https://doi.org/10.1175/1520-0493(2000)128<1366:EOAWOF>2.0.CO;2.

Smith, T. M., R. W. Reynolds, T. C. Peterson, and J. Lawrimore, 2008: Improvements to NOAA's historical merged land–ocean surface temperature analysis (1880–2006). *J. Climate*, **21**, 2283–2296, https://doi.org/10.1175/2007JCLI2100.1.

Stewart, S. R., 2019: Tropical Storm Priscilla (EP192019). National Hurricane Center Tropical Cyclone Rep., 9 pp. https://www.nhc.noaa.gov/data/tcr/EP192019_Priscilla.pdf.

Straub, K. H., 2013: MJO initiation in the real-time multivariate MJO index. *J. Climate*, **26**, 1130–1151, https://doi.org/10.1175/JCLI-D-12-00074.1.

USDC, 2020: Weekly Weather and Crop Bulletin. Vol 107, No. 38, U.S. Dept. of Commerce, 40 pp., https://usda.library.cornell.edu/concern/publications/cj82k728n?locale=en .

Vecchi, G. A., and B. J. Soden, 2007: Effect of remote sea surface temperature change on tropical cyclone potential intensity. *Science*, **450**, 1066–1071, https://usda.library.cornell.edu/concern/publications/cj82k728n?locale=en.

Ventrice, M. J., C. D. Thorncroft, and M. A. Janiga, 2012a: Atlantic tropical cyclogenesis: A three-way interaction between an African easterly wave, diurnally varying convection, and a convectively coupled atmospheric Kelvin wave. *Mon. Wea. Rev.*, **140**, 1108–1124, https://doi.org/10.1175/MWR-D-11-00122.1.

Ventrice, M. J., C. D. Thorncroft, and C. J. Schreck, 2012b: Impacts of convectively coupled Kelvin waves on environmental conditions for Atlantic tropical cyclogenesis. *Mon. Wea. Rev.*, **140**, 2198–2214, https://doi.org/10.1175/MWR-D-11-00305.1.

Vigh, J. L., J. A. Knaff, and W. H. Schubert, 2012: A climatology of Hurricane eye formation. *Mon. Wea. Rev.*, **140**, 1405–1426, https://doi.org/10.1175/MWR-D-11-00108.1.

Villarini, G., G. A. Vecchi, T. R. Knutson, and J. A. Smith, 2011: Is the recorded increase in short duration North Atlantic tropical storms spurious? *J. Geophys. Res.*, **116**, D10114, https://doi.org/10.1029/2010JD015493.

Vincent, D. G., 1994: The South Pacific Convergence Zone (SPCZ): A review. *Mon. Wea. Rev.*, **122**, 1949–1970, https://doi.org/10.1175/1520-0493(1994)122<1949:TSPCZA>2.0.CO;2.

Waliser, D. E., and C. Gautier, 1993: A satellite-derived climatology of the ITCZ. *J. Climate*, **6**, 2162–2174, https://doi.org/10.1175/1520-0442(1993)006<2162:ASDCOT>2.0.CO;2.

Wang, B., 1994: Climatic regimes of tropical convection and rainfall. *J. Climate*, **7**, 1109–1118, https://doi.org/10.1175/1520-0442(1994)007<1109:CROTCA>2.0.CO;2.

Wang, B., and Q. Ding, 2008: Global monsoon: Dominant mode of annual variation in the tropics. *Dyn. Atmos. Oceans*, **44**, 165–183, https://doi.org/10.1016/j.dynatmoce.2007.05.002.

Wang, B., J. Liu, H. J. Kim, P. J. Webster, and S. Y. Yim, 2012: Recent change of the global monsoon precipitation (1979-2008). *Climate Dyn.*, **39**, 1123–1135, https://doi.org/10.1007/s00382-011-1266-z.

Wei, K., C. Ouyang, H. Duan, Y. Li, and S. Zhou, 2020: Reflections on the catastrophic 2020 Yangtze River Basin flooding in southern China. *Innovation*, **1**, 100038, https://doi.org/10.1016/j.xinn.2020.100038.

Wheeler, M., and G. N. Kiladis, 1999: Convectively coupled equatorial waves: Analysis of clouds and temperature in the wavenumber-frequency domain. *J. Atmos. Sci.*, **56**, 374–399, https://doi.org/10.1175/1520-0469(1999)056<0374:CCEWAO>2.0.CO;2.

Wheeler, M. C., and H. H. Hendon, 2004: An all-season real-time multivariate MJO index: Development of an index for monitoring and prediction. *Mon. Wea. Rev.*, **132**, 1917–1932, https://doi.org/10.1175/1520-0493(2004)132<1917:AARMMI>2.0.CO;2.

Wood, K. M., and E. A. Ritchie, 2015: A definition for rapid weakening in the North Atlantic and eastern North Pacific. *Geophys. Res. Lett.*, **42**, 10 091–10 097, https://doi.org/10.1002/2015GL066697.

Wood, K. M., and C. J. Schreck, 2020: Eastern North Pacific and central North Pacific basins [in "State of the Climate in 2019"]. *Bull. Amer. Meteor. Soc.*, **101** (8), S212–S214, https://doi.org/10.1175/BAMS-D-20-0077.1.

Xie, S.-P., K. Yu, Y. Du, K. Hu, J. S. Chowdary, and G. Huang, 2016: Indo-Western Pacific Ocean capacitor and coherent climate anomalies in post-ENSO summer: A review. *Adv. Atmos. Sci.*, **33**, 411–432, https://doi.org/10.1007/s00376-015-5192-6.

Yang, J., Q. Liu, S.-P. Xie, Z. Liu, and L. Wu, 2007: Impact of the Indian Ocean SST basin mode on the Asian summer monsoon. *Geophys. Res. Lett.*, **34**, L02708, https://doi.org/10.1029/2006GL028571.

Yim, S. Y., B. Wang, J. Liu, and Z. W. Wu, 2014: A comparison of regional monsoon variability using monsoon indices. *Climate Dyn.*, **43**, 1423–1437, https://doi.org/10.1007/s00382-013-1956-9.

Yuan, J., and J. Cao, 2012: North Indian Ocean tropical cyclone activities influenced by the Indian Ocean dipole mode. *Sci. China Earth Sci.*, **56**, 855–865, https://doi.org/10.1007/s11430-012-4559-0.

Zhang, C., 2005: Madden–Julian oscillation. *Rev. Geophys.*, **43**, RG2003, https://doi.org/10.1029/2004RG000158.

Zhang, C., and J. Gottschalck, 2002: SST anomalies of ENSO and the Madden–Julian oscillation in the equatorial Pacific. *J. Climate*, **15**, 2429–2445, https://doi.org/10.1175/1520-0442(2002)015<2429:SAOEAT>2.0.CO;2.

Zheng, Z.-W., 2015: A long neglected damper in the El Nino–typhoon relationship: A 'Gaia-like' process. *Sci. Rep.*, **5**, 11103, https://doi.org/10.1038/srep11103.

STATE OF THE CLIMATE IN 2020

THE ARCTIC

M. L. Druckenmiller, T. Moon, and R. Thoman, Eds.

Special Online Supplement to the *Bulletin of the American Meteorological Society* Vol.102, No. 8, August, 2021

https://doi.org/10.1175/BAMS-D-21-0086.1

Corresponding author: Matthew L. Druckenmiller / druckenmiller@colorado.edu

STATE OF THE CLIMATE IN 2020

The Arctic

Editors

Jessica Blunden
Tim Boyer

Chapter Editors

Freya Aldred
Peter Bissolli
Howard J. Diamond
Matthew L. Druckenmiller
Robert J. H. Dunn
Catherine Ganter
Nadine Gobron
Gregory C. Johnson
Rick Lumpkin
Tim Li
Ademe Mekonnen
John B. Miller
Twila A. Moon
Ahira Sánchez-Lugo
Ted A. Scambos
Carl J. Schreck III
Sharon Stammerjohn
Richard L. Thoman
Kate M. Willett

Technical Editor

Andrea Andersen

***BAMS* Special Editor for Climate**

Michael A. Alexander

American Meteorological Society

Cover credit:
Stefan Hendricks / Alfred Wegener Institute CC-BY 4.0
Date: 2019-10-16-Location: Arctic Ocean, 84.765482°N, 133.905373°E
The crew of the research icebreaker Polarstern inspects the ice anchors after a sea ice fracturing event at the early stages of the Multidisciplinary drifting Observatory for the Study of Arctic Climate (MOSAiC) experiment.

The Arctic is one chapter from the *State of the Climate in 2020* annual report and is available from https://doi.org/10.1175/BAMS-D-21-0086.1. Compiled by NOAA's National Centers for Environmental Information, *State of the Climate in 2020* is based on contributions from scientists from around the world. It provides a detailed update on global climate indicators, notable weather events, and other data collected by environmental monitoring stations and instruments located on land, water, ice, and in space.
The full report is available from https://doi.org/10.1175/2021BAMSStateoftheClimate.1.

How to cite this document:

Citing the complete report:
Blunden, J. and T. Boyer, Eds., 2021: "State of the Climate in 2020". *Bull. Amer. Meteor. Soc.*, **102** (8), Si–S475, https://doi.org/10.1175/2021BAMSStateoftheClimate.1

Citing this chapter:
Druckenmiller, M. L., T. Moon, and R. Thoman, Eds., 2021: The Arctic [in "State of the Climate in 2020"]. *Bull. Amer. Meteor. Soc.*, **102** (8), S263–S315, https://doi.org/10.1175/BAMS-D-21-0086.1

Citing a section (example):
Holmes, R. M., A. I. Shiklomanov, A. Suslova, M. Tretiakov, J. W. McClelland, L. Scott, R. G. M. Spencer, and S. E. Tank, 2021: River discharge [in "State of the Climate in 2020"]. *Bull. Amer. Meteor. Soc.*, **102** (8), S290–S292, https://doi.org/10.1175/BAMS-D-21-0086.1.

Editor and Author Affiliations (alphabetical by name)

Ballinger, Thomas J., International Arctic Research Center, University of Alaska Fairbanks, Fairbanks, Alaska
Berner, Logan T., School of Informatics, Computing, and Cyber Systems, Northern Arizona University, Flagstaff, Arizona
Bernhard, Germar H., Biospherical Instruments Inc., San Diego, California
Bhatt, Uma S., Geophysical Institute, University of Alaska Fairbanks, Fairbanks, Alaska
Bjerke, Jarle W., Norwegian Institute for Nature Research, FRAM – High North Research Centre for Climate and the Environment, Tromsø, Norway
Box, Jason E., Geological Survey of Denmark and Greenland, Copenhagen, Denmark
Brown, R., Climate Research Division, Environment and Climate Change Canada, Montréal, Quebec, Canada
Cappelen, John, Danish Meteorological Institute, Copenhagen, Denmark
Christiansen, Hanne H., Geology Department, University Centre in Svalbard, The University Center in Svalbard, Longyearbyen, Norway
Decharme, B., Centre National de Recherches Météorologiques, Toulouse, France
Derksen, C., Climate Research Division, Environment and Climate Change Canada, Downsview, Ontario, Canada
Divine, Dmitry, Norwegian Polar Institute, Fram Centre, Tromsø, Norway
Drozdov, D. S., Earth Cryosphere Institute, and Tyumen State University, Tyumen, Russia
Druckenmiller, Matthew L., National Snow and Ice Data Center, Cooperative Institute for Research in Environmental Sciences at the University of Colorado, Boulder, Colorado
Elias Chereque, A., Department of Physics, University of Toronto, Toronto, Canada.
Epstein, Howard E., Department of Environmental Sciences, University of Virginia, Charlottesville, Virginia
Farquharson, L. M., Geophysical Institute, University of Alaska Fairbanks, Fairbanks, Alaska
Farrell, Sinead L., Department of Geographical Sciences, University of Maryland, College Park, Maryland
Fausto, Robert S., Geological Survey of Denmark and Greenland, Copenhagen, Denmark
Fettweis, Xavier, SPHERES research unit, University of Liège, Liège, Belgium
Fioletov, Vitali E., Environment and Climate Change Canada, Toronto, Ontario, Canada
Forbes, Bruce C., Arctic Centre, University of Lapland, Rovaniemi, Finland
Frost, Gerald V., ABR, Inc. Environmental Research & Services, Fairbanks, Alaska
Gargulinski, Emily, National Institute of Aerospace, Resident at NASA LaRC, Hampton, Virginia
Gerland, Sebastian, Norwegian Polar Institute, Fram Centre, Tromsø, Norway
Goetz, Scott J., School of Informatics, Computing, and Cyber Systems, Northern Arizona University, Flagstaff, Arizona
Grabinski, Z., Alaska Fire Science Consortium, International Arctic Research Center, University of Alaska, Fairbanks, Alaska
Grooß, Jens-Uwe, Forschungszentrum Jülich, Jülich, Germany
Haas, Christian, Alfred Wegener Institute, Helmholtz Centre for Polar and Marine Research, Bremerhaven, Germany
Hanna, Edward, School of Geography and Lincoln Centre for Water and Planetary Health, University of Lincoln, Lincoln, United Kingdom
Hanssen-Bauer, Inger, Norwegian Meteorological Institute, Blindern, Oslo, Norway
Hendricks, Stefan, Alfred Wegener Institute, Helmholtz Centre for Polar and Marine Research, Bremerhaven, Germany
Holmes, Robert M., Woodwell Climate Research Center, Falmouth, Massachusetts
Ialongo, Iolanda, Finnish Meteorological Institute, Helsinki, Finland
Isaksen, K., Norwegian Meteorlogical Institute, Blindern, Oslo, Norway
Jain, Piyush, Natural Resources Canada, Canadian Forest Service, Northern Forestry Centre, Edmonton, Alberta, Canada
Johnsen, Bjørn, Norwegian Radiation and Nuclear Safety, Østerås, Norway
Kaleschke, L., Alfred Wegener Institute, Helmholtz Centre for Polar and Marine Research, Bremerhaven, Germany
Kholodov, A. L., Earth Cryosphere Institute, Tyumen Science Center, Tyumen, Russia
Kim, Seong-Joong, Korea Polar Research Institute, Incheon, Republic of Korea
Korsgaard, Niels J., Geological Survey of Denmark and Greenland, Copenhagen, Denmark
Labe, Zachary, Colorado State University, Fort Collins, Colorado
Lakkala, Kaisa, Finnish Meteorological Institute, Sodankylä, Finland
Lara, Mark J., Department of Plant Biology, University of Illinois at Urbana-Champaign, Urbana, Illinois
Loomis, Bryant, NASA Goddard Space Flight Center, Greenbelt, Maryland
Luojus, K., Arctic Research Centre, Finnish Meteorological Institute, Helsinki, Finland
Macander, Matthew J., ABR, Inc. Environmental Research & Services, Fairbanks, Alaska
Malkova, G. V., Earth Cryosphere Institute, Tyumen Science Center, Tyumen, Russia
Mankoff, Kenneth D., Geological Survey of Denmark and Greenland, Copenhagen, Denmark
Manney, Gloria L., NorthWest Research Associates, Socorro, New Mexico
McClelland, James W., University of Texas at Austin, Marine Science Institute, Port Aransas, Texas
Meier, Walter N., National Snow and Ice Data Center, Cooperative Institute for Research in Environment Sciences at the University of Colorado, Boulder, Colorado
Moon, Twila A., National Snow and Ice Data Center, Cooperative Institute for Research in Environmental Sciences at the University of Colorado, Boulder, Colorado
Mote, Thomas, Department of Geography, University of Georgia, Athens, Georgia
Mudryk, L., Climate Research Division, Environment and Climate Change Canada, Downsview, Ontario, Canada
Müller, Rolf, Forschungszentrum Jülich, Jülich, Germany
Nyland, K. E., Department of Geography, George Washington University, Washington, D.C.
Overland, James E., NOAA/OAR Pacific Marine Environmental Laboratory, Seattle, Washington
Park, T., NASA Ames Research Center, Mountain View, California, and Bay Area Environmental Research Institute, Moffett Field, California
Pavlova, Olga, Norwegian Polar Institute, Fram Centre, Tromsø, Norway
Perovich, Don, Thayer School of Engineering, Dartmouth College, Hanover, New Hampshire
Petty, Alek, NASA Goddard Space Flight Center, Greenbelt, Maryland
Phoenix, Gareth K., Department of Animal and Plant Sciences, University of Sheffield, Sheffield, United Kingdom
Raynolds, Martha K., Institute of Arctic Biology, University of Alaska, Fairbanks, Alaska
Reijmer, C. H., Institute for Marine and Atmospheric Research Utrecht, Utrecht University, Utrecht, The Netherlands
Richter-Menge, Jacqueline, University of Alaska Fairbanks, Institute of Northern Engineering, Fairbanks, Alaska
Ricker, Robert, Alfred Wegener Institute, Helmholtz Centre for Polar and Marine Research, Bremerhaven, Germany

Editor and Author Affiliations (alphabetical by name)

Romanovsky, Vladimir E., Geophysical Institute, University of Alaska Fairbanks, Fairbanks, Alaska; Earth Cryosphere Institute, Tyumen Science Center, Tyumen, Russia

Scott, Lindsay, Woodwell Climate Research Center, Falmouth, Massachusetts

Shapiro, Hazel, Arctic Research Consortium of the United States, Fairbanks, Alaska

Shiklomanov, Alexander I., University of New Hampshire, Durham, New Hampshire; Arctic and Antarctic Research Institute, St. Petersburg, Russia

Shiklomanov, Nikolai I., Department of Geography, George Washington University, Washington, D.C.

Smeets, C. J. P. P., Institute for Marine and Atmospheric Research Utrecht, Utrecht University, Utrecht, The Netherlands

Smith, Sharon L., Geological Survey of Canada, Natural Resources Canada, Ottawa, Ontario, Canada

Soja, Amber, National Institute of Aerospace, Resident at NASA LaRC, Hampton, Virginia

Spencer, Robert G. M., Florida State University, Tallahassee, Florida

Starkweather, Sandy, Cooperative Institute for Research in Environmental Sciences, University of Colorado Boulder and Earth System Research Laboratory, NOAA, Boulder, Colorado

Streletskiy, Dimitri A., Department of Geography, George Washington University, Washington, D.C.

Suslova, Anya, Woodwell Climate Research Center, Falmouth, Massachusetts

Svendby, Tove, NILU-Norwegian Institute for Air Research, Kjeller, Norway

Tank, Suzanne E., University of Alberta, Edmonton, Alberta, Canada

Tedesco, Marco, Lamont Doherty Earth Observatory, Columbia University, Palisades, New York, and NASA Goddard Institute of Space Studies, New York, New York

Thoman, Richard L., International Arctic Research Center, University of Alaska Fairbanks, Fairbanks, Alaska

Tian-Kunze, X., Alfred Wegener Institute, Helmholtz Centre for Polar and Marine Research, Bremerhaven, Germany

Timmermans, Mary-Louise, Yale University, New Haven, Connecticut

Tømmervik, Hans, Norwegian Institute for Nature Research, FRAM and High North Research Centre for Climate and the Environment, Tromsø, Norway

Tretiakov, Mikhail, Arctic and Antarctic Research Institute, St. Petersburg, Russia

Tschudi, Mark, Aerospace Engineering Sciences, University of Colorado, Boulder, Colorado

Vakhutinsky, Sofia, National Snow and Ice Data Center, Cooperative Institute for Research in Environmental Sciences at the University of Colorado, Boulder, Colorado

van As, Dirk, Geological Survey of Denmark and Greenland, Copenhagen, Denmark

van de Wal, R. S. W., Institute for Marine and Atmospheric Research Utrecht and Department of Physical Geography, Utrecht University, Utrecht, The Netherlands

Veraverbeke, Sander, Faculty of Science, Vrije Universiteit Amsterdam, The Netherlands

Walker, Donald A., Institute of Arctic Biology, University of Alaska Fairbanks, Fairbanks, Alaska

Walsh, John E., International Arctic Research Center, University of Alaska Fairbanks, Fairbanks, Alaska

Wang, Muyin, NOAA/OAR Pacific Marine Environmental Laboratory, and Cooperative Institute for Climate, Ocean, and Ecosystem Studies, University of Washington, Seattle, Washington

Webster, Melinda, Geophysical Institute, University of Alaska Fairbanks, Fairbanks, Alaska

Winton, Øyvind, Geological Survey of Denmark and Greenland, Copenhagen, Denmark

Wood, K., NOAA, Pacific Marine Environmental Laboratory, Seattle, Washington

York, Alison, Alaska Fire Science Consortium, International Arctic Research Center, University of Alaska, Fairbanks, Alaska

Ziel, Robert, Alaska Fire Science Consortium, International Arctic Research Center, University of Alaska, Fairbanks, Alaska

Editoral and Production Team

Allen, Jessicca, Graphics Support, Cooperative Institute for Satellite Earth System Studies, North Carolina State University, Asheville, North Carolina

Andersen, Andrea, Technical Editor, Innovative Consulting and Management Services, LLC, NOAA/NESDIS National Centers for Environmental Information, Asheville, North Carolina

Hammer, Gregory, Content Team Lead, Communications and Outreach, NOAA/NESDIS National Centers for Environmental Information, Asheville, North Carolina

Love-Brotak, S. Elizabeth, Lead Graphics Production, NOAA/NESDIS National Centers for Environmental Information, Asheville, North Carolina

Misch, Deborah J., Graphics Support, Innovative Consulting and Management Services, LLC, NOAA/NESDIS National Centers for Environmental Information, Asheville, North Carolina

Riddle, Deborah B., Graphics Support, NOAA/NESDIS National Centers for Environmental Information, Asheville, North Carolina

Veasey, Sara W., Visual Communications Team Lead, Communications and Outreach, NOAA/NESDIS National Centers for Environmental Information, Asheville, North Carolina

5. Table of Contents

*Please refer to Chapter 8 (Relevant datasets and sources) for a list of all climate variables and datasets used in this chapter for analyses, along with their websites for more information and access to the data.

5. THE ARCTIC

M. L. Druckenmiller, T. Moon, and R. Thoman, Eds.

a. Overview—M. L. Druckenmiller, T. Moon, J. Richter-Menge, and R. Thoman

The Arctic in 2020 was exceptionally warm. The annual mean surface air temperature (SAT) anomaly for land areas poleward of 60°N was 2.1°C above the 1981–2010 average, marking the highest observed SAT anomaly for the terrestrial Arctic since at least 1900. It was also the seventh consecutive year with SAT anomalies of more than +1°C higher than the 1981–2010 average. This continued increase in Arctic SAT is the primary driver for many of the changes observed on a pan-Arctic scale and enhanced regionally in any given year. During 2020, for example, warm SAT anomalies persisted from winter into summer across the Eurasian Arctic, contributing to early and widespread wildfire activity across the region and to the near-record sea ice retreat and warm summer and autumn sea surface temperatures (SSTs) in the Laptev and Kara Seas.

Arctic sea ice conditions in both winter and summer 2020 are consistent with a continued long-term transformation toward less sea ice across the Arctic, with reductions in extent and thickness. Most notably, the minimum summer ice extent was the second lowest in the 42-year satellite record, behind only 2012. Satellite-derived sea ice observations during the 2019/20 winter growth season revealed a near-record low ice volume since the collection of this data began in 2010. Observations of ice age, which are a proxy for ice thickness, confirm a longer-term substantial loss of Arctic sea ice volume, with the percentage of ice less than 3 years old in March shrinking from roughly a third to less than 10% of the entire ice cover since 1985. This shift toward younger, and thus thinner, sea ice results in an Arctic-wide ice cover that is more responsive to transient and seasonal scale atmospheric conditions and more vulnerable to melting out in summer.

As high-albedo (brighter, more reflective) sea ice is replaced by a low-albedo (darker, less reflective) open-water surface, incoming solar radiation is absorbed in the surface water rather than being reflected back to space. This ice-albedo feedback mechanism remains a dominant feature of accelerated Arctic climate and environmental change and is strongly indicated by sustained warming in summer SSTs. Elevated SSTs closely track with Arctic waters experiencing sea ice loss in early summer and also play a role in delaying autumn freeze-up and increasing ocean heat storage into the following year. Over much of the Arctic Ocean, mean SSTs in August 2020 were consistent with statistically significant warming trends up to +0.1°C yr^{-1} from 1982 to 2020. Within the Arctic Ocean's marginal seas, mean August 2020 SSTs were around 1°–3°C warmer than the 1982–2010 mean. The Laptev and Kara Seas, in particular, experienced the largest SST anomalies, up to +5.5°C above the 1982–2010 August mean, due to the region's exceptionally low summer sea ice extents.

On land, Arctic observations from 2020 also point to the transformative role of increasing Arctic surface air temperatures across terrestrial and freshwater systems. Prominent spring warming over Eurasia contributed to regional snow cover extent (SCE) anomalies that were the fourth lowest and record lowest in May and June, respectively, for the 54-year record. While relatively less extreme, SCE anomalies over North America were also below average in both May and June (eighth and 10th lowest, respectively). Together with surface air temperatures and precipitation patterns, snow cover characteristics influence a range of surface and ecological processes, including the ground thermal regime, vegetation dynamics, and freshwater budgets. For the majority of permafrost monitoring sites across the Arctic, reported temperatures in 2020 were the highest on

record, continuing a long-term trend toward warming ground temperatures in all regions. While the productivity of Arctic tundra vegetation experiences considerable regional variability across years, the overall circumpolar trend in "greening" has remained positive since observations began in the early 1980s, with nine of the last 10 growing seasons exceeding the mean of the last 21 years of observations. Arctic river discharge observations from 2020 continue to reveal the intensification of the Arctic hydrologic cycle, with Eurasian and North American Arctic average annual river discharge increasing by 4.4 and 1.0 $km^3 yr^{-1}$, respectively, since 1976. The combined river discharge in 2020 from the eight largest Arctic rivers was ~12% greater than the 1981–2010 reference period, owing 44% of this increase to the anomalously high discharge from the two largest North American rivers—the Mackenzie and Yukon.

For the Greenland ice sheet, which holds the equivalent of 7.4 m of potential sea level rise, various observations track the rate and extent of ice melt and overall mass loss. Using satellite-based measurements of gravity anomalies, indirect measurements of total mass loss since 2002 reveal a mean loss rate of –268 ± 14 Gt yr^{-1}, which accounts for ~0.8 mm yr^{-1} of global mean sea level rise. In 2020, an overall ice loss of –293 ± 66 Gt was only moderately more than the 2002–19 mean. The moderate rate of ice loss was due in part to both summer atmospheric circulation patterns that promoted near- to below-mean air temperatures in the ice sheet interior and the absence of unusually large melt events, even though the cumulative summer melt-day extent was 28% higher than the 1981–2010 mean.

Throughout this chapter, sustained and long-term observations illuminate the rapid pace and persistence of Arctic change and its far-reaching societal and ecological implications (Thoman et al. 2020). The value of long-term observation is revealed not only in the context of prominent surface processes that are transforming the cryosphere, but also for the entire Arctic system and its global connections. For example, Arctic stratospheric ozone concentrations from February through May 2020 were the lowest in the corresponding satellite record, which began in 2004, drawing attention to the human health and environment effects of increasing ultraviolet radiation reaching the Earth's surface. Arctic observations are also often marked by regional differences (e.g., continental scale differences in snow cover and terrestrial greening), indicating a complex and variable system that requires local and regional observing strategies that feed into and complement Arctic-wide assessments.

b. Surface air temperature—T. J. Ballinger, J. E. Overland, M. Wang, M. A. Webster, U. S. Bhatt, E. Hanna, I. Hanssen-Bauer, S.-J. Kim, R. L. Thoman, and J. E. Walsh

Surface air temperatures (SAT), generally measured at a height of 2 m, are one of the foremost Arctic change indicators (Box et al. 2019), with ongoing boreal warming effects felt across the global climate system (Moon et al. 2019). While terrestrial Arctic SAT patterns vary seasonally and interannually, the overall trend has been positive since the 1970s (Fig. 5.1). This warming

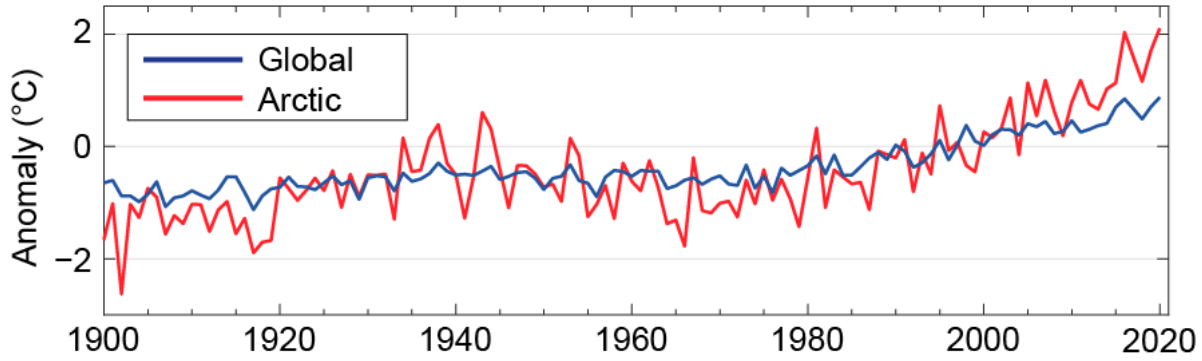

Fig. 5.1. Mean annual (Jan–Dec) SAT anomalies (°C) for terrestrial weather stations located in the Arctic (60°–90°N; red line) and globally (blue line) for the 1900–2020 period. Both time series are presented with respect to their 1981–2010 mean SAT values. (Source: CRUTEM4; Jones et al. 2012.)

has dramatically impacted the Arctic system, most notably through the decline of sea ice extent and thickness (Stroeve and Notz 2018; section 5d), decrease in snow cover (Cohen et al. 2020; section 5f), loss of glacial ice (Hanna et al. 2020; section 5e), and increase in permafrost thaw (Biskaborn et al. 2019; section 5h). Arctic ecosystems are also highly sensitive to SAT trends and extreme temperature events. For example, increased trends in terrestrial vegetation productivity and "greening" of the Arctic tundra (section 5i) are closely linked with Arctic SAT warming (Myers-Smith et al. 2020).

Intense Arctic temperature anomalies characterized 2020, as evidenced by the highest mean annual terrestrial SAT anomaly since the start of the record in 1900 (Fig. 5.1). In northern Eurasia—beginning in winter and continuing into spring and summer—the region's persistent warm anomalies were underscored by the late June heat wave in north-central Siberia (Overland and Wang 2021; section 7g2). Sustained abnormal temperatures played a major role in the region's vigorous wildfire activity, as detailed in Sidebar 5.1, and the near-record summertime sea ice melt and warm sea surface temperatures (SSTs) in the Laptev and Kara Seas (section 5c). Continued warm anomalies atop the Barents and Kara Seas during autumn were associated with an upper-level ridge of high pressure and an Arctic–midlatitude linkage event in December that brought widespread cold to eastern Asia and the North Pacific.

1) Mean annual surface air temperature over the terrestrial Arctic

In 2020, the Arctic annual mean SAT anomaly for terrestrial areas poleward of 60°N was 2.1°C above the 1981–2010 average (Fig. 5.1). This marked the highest-observed SAT anomaly for the terrestrial Arctic since at least 1900 and continued a pattern of seven consecutive years (and 8 of the last 10 years) where SAT anomalies were more than 1°C higher than the 1981–2010 average. Arctic warming has consistently outpaced global air temperature warming since 2000 (Fig. 5.1) due to Arctic amplification, a phenomenon driven by multiple processes that operate on different space and time scales (Overland et al. 2021). For example, seasonally variable mechanisms within the Arctic, such as ice-albedo and cloud-radiative feedbacks, play a critical role in modifying air temperatures (Cohen et al. 2020).

2) Seasonal air temperature patterns

Seasonal patterns of near-surface air temperature anomalies are shown for the winter (January–March), spring (April–June), summer (July–September), and autumn (October–December) of 2020 (Fig. 5.2). These seasonal divisions roughly coincide with annual cycles of the Arctic cryosphere, such as the onset of snowmelt and sea ice retreat during spring and their advances during autumn.

Winter was characterized by above-average temperatures stretching from eastern Europe to central Siberia. An extensive area of +3° to +5°C air temperature anomalies occurred in north-central Siberia (Fig. 5.2a). In contrast, areas extending eastward from Alaska to Greenland and Svalbard showed abnormally cold air temperatures.

Aligned with the highest winter Arctic Oscillation since records began in 1950 (Ballinger et al. 2020), a zonal polar jet stream in 2020 yielded westerly winds, stormy weather, and relatively mild northern Eurasian temperatures, while constraining colder-than-normal air over Alaska and portions of northern Canada (Fig. 5.3a). Frequent warm air intrusions into Eurasia were the product of anomalous cyclone activity, with records set for above-average winter storm occurrence and intensity over the Kara Sea and adjacent terrestrial areas (Figs. 5.4a,b). The anomalous atmospheric circulation pattern and storminess impacted the Multidisciplinary drifting Observatory for the Study of Arctic Climate (MOSAiC) Expedition, accelerating the icebreaker's drift across the central Arctic Ocean (approximately three times faster than Nansen's historic Fram expedition in the 1890s along a similar route; Shupe et al. 2020).

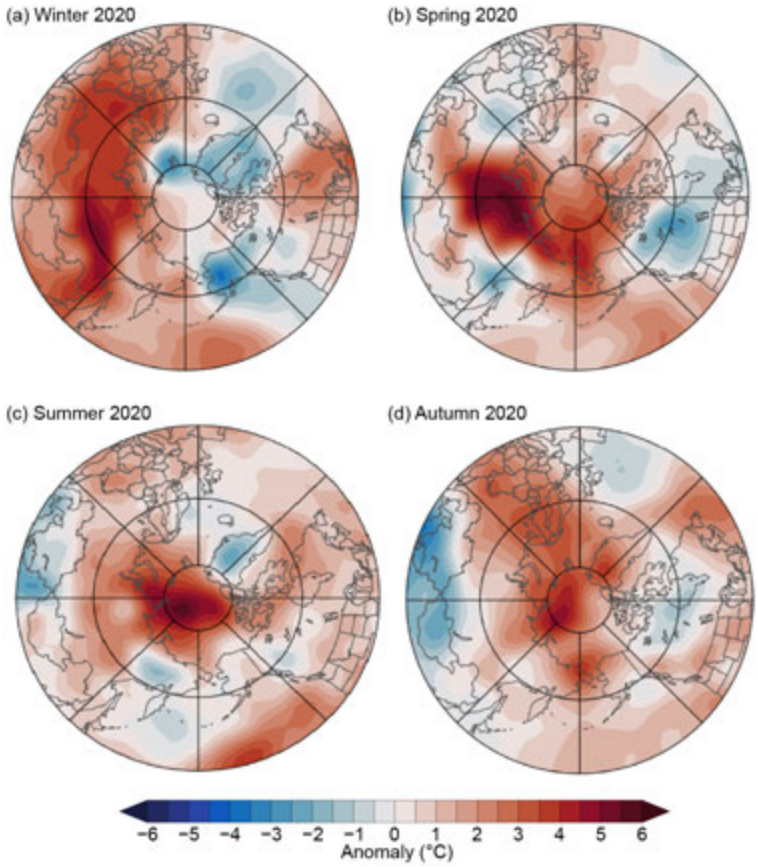

Fig. 5.2. Near-surface (925-hPa) seasonal air temperature anomalies (°C) for 2020 relative to the 1981–2010 base period for (a) winter, (b) spring, (c) summer, and (d) autumn. The 925-hPa layer is used to emphasize large spatial temperature patterns, rather than local surface features. (Source: NCEP/NCAR Reanalysis; Kalnay et al. 1996.)

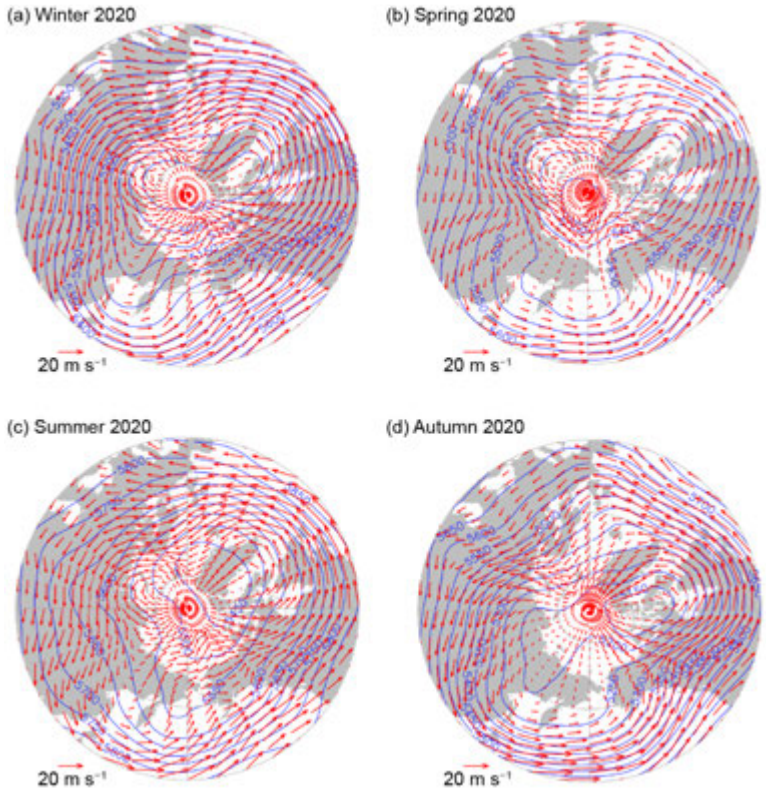

Fig. 5.3. Atmospheric circulation patterns described by 500-hPa geopotential heights (GPH; m, blue contours) and 500-hPa winds (red vectors) for (a) winter, (b) spring, (c) summer, and (d) autumn of 2020. The wind vector scale indicates winds of 20 m s^{-1}. (Source: NCEP/NCAR Reanalysis; Kalnay et al. 1996.)

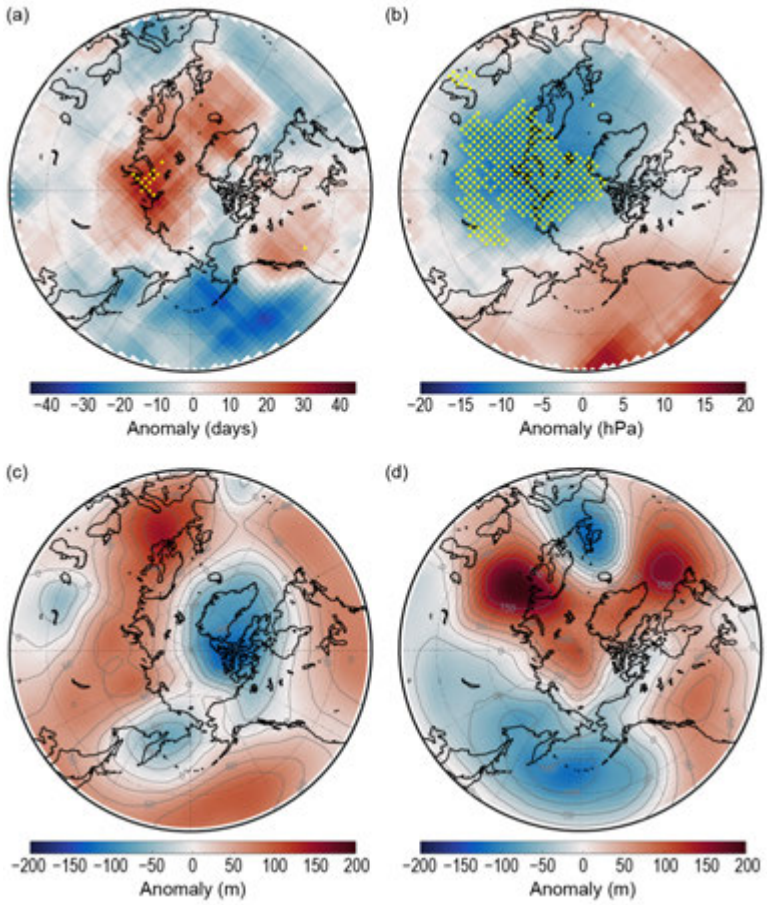

Fig. 5.4. Arctic atmospheric extremes during 2020. (a) Winter cyclone count (number of days with cyclone activity) anomalies and (b) cyclone intensity (minimum cyclone sea-level pressure [SLP], hPa) anomalies, relative to their respective 1981–2010 means. Yellow dots mark areas with the highest cyclone counts and the lowest seasonal average of minimum SLP within cyclones, respectively, during winter 2020. (Source: ERA5 SLP data is from Hersbach et al. 2020, and the cyclone methods are described in Webster et al. 2019.) (c) November and (d) December 500-hPa geopotential height anomalies (m), relative to the 1981–2010 mean, provide a snapshot of the evolving autumn meridional jet stream pattern that caused a cold outbreak over East Asia and the North Pacific in December 2020. (Source: ERA5 Reanalysis; Hersbach et al. 2020.)

Warm air temperature anomaly patterns covered much of the Arctic Ocean and coastal areas during spring (Fig. 5.2b). At +5°C, north-central Siberian air temperature anomalies remained far above normal. Late June was especially warm in the region, with a new record high station SAT (since 1885) of 38°C observed at Verkhoyansk, Russia, on 20 June (Overland and Wang 2021). Northward warm air advection fed by an upstream trough of low pressure over Europe (Fig. 5.3b) led to record low Eurasian Arctic spring snow cover extent (section 5f) and a sea ice melt season that began nearly 1 month earlier than the 1981–2010 mean in the Kara and Laptev Seas (http://nsidc.org/arcticseaicenews/2020/08/steep-decline-sputters-out/).

Summer air temperatures were relatively high for the central Arctic Ocean (4°–5°C above average) and dissipated toward the terrestrial Arctic (Fig. 5.2c). Although warm anomalies over north-central Siberia were not as intense as in winter and spring, the strength of the summertime warm anomaly increased toward the coastal areas and into the Kara and Laptev Seas. The North Atlantic Arctic, including Svalbard and Novaya Zemlya, also remained relatively warm through summer. Despite below-normal air temperatures in the interior of the Greenland ice sheet, above-average, but well below record, ice sheet melt ensued (section 5e). High-pressure ridging atop the Siberian coast (Fig. 5.3c) steered warm air off the continent, across the Kara and Laptev Seas, and toward the central Arctic, contributing to above-average SST anomalies and near-record sea ice losses during late-summer (see sections 5c and 5d).

The Eurasian Arctic warm temperature anomaly continued into autumn, particularly along the coast, highlighted by air temperatures ~4°C above normal in the Laptev Sea (Fig. 5.2d). Local temperature anomaly maxima were also found over northern Greenland and the Chukchi Sea, stretching into Chukotka and northern Alaska. Amidst a wavy polar jet stream, ridging and southerly winds atop these areas supported above-average air temperatures (Fig. 5.3d).

An Arctic-midlatitude linkage event also emerged from this meridional jet stream configuration. During November, a wide swath of upper-level high pressure developed over warm northern Eurasia (Fig. 5.4c). As with previous late autumn/early winter linkage cases documented by Overland et al. (2021), the associated ridge continued to build into December across the Ural Mountains and Barents-Kara Seas region, while a trough developed downstream that brought extreme cold air to eastern Asia and the North Pacific (Fig. 5.4d).

Sidebar 5.1: Wildland fires in the high northern latitudes—A. YORK, U. S. BHATT, E. GARGULINSKI, Z. GRABINSKI, P. JAIN, A. SOJA, R. THOMAN, S. VERAVERBEKE, AND R. ZIEL

Despite the low annual temperatures and short growing seasons that characterize high northern latitudes (HNL), wildland fire is the dominant ecological disturbance within the region's boreal forest, the world's largest terrestrial biome. The boreal forest, also known as taiga, is the band of mostly coniferous trees stretching across the area north of the July 13°C isotherm in North America and Eurasia. Wildland fires also impact tundra regions bordering the taiga. This sidebar summarizes variability and trends in fire disturbance in HNL and outlines how climate and subseasonal fire weather conditions in HNL influence the extent of area burned.

Variability and trends

Most area burned in HNL occurs during sporadic episodes of large fire growth, preceded by extended periods of drying and accompanied by anomalously hot and dry conditions (Flannigan et al. 2009). For example, 50% of the area burned in Alaska from 2002 to 2010 was consumed in just 36 days (Barrett et al. 2016). Significant weather events, including prolonged warm dry weather associated with blocking high-pressure systems (Hayasaka et al. 2016) and convective lightning storms (Veraverbeke et al. 2017), are responsible for much of the variability in HNL fire history. In both Alaska and Canada, lightning-caused fires are responsible for the majority of area burned since at least 1980 when reliable records began (AICC data; Hanes et al. 2019), in part because lightning-ignited fires are more likely to be remote and subject to lower levels of suppression compared to human-caused fires.

Long-term data on burned area have been compiled for Alaska and Canada but are more limited in Eurasia and Arctic tundra regions. These records show considerable interannual variability and that large fire years in the most fire-prone HNL regions are not temporally coincident (York et al. 2020). Figure SB5.1 shows cumulative satellite-derived fire detections across HNL from 2012 to 2020 from both the MODIS (*Terra* and *Aqua*) and VIIRS SNPP instruments (Giglio et al. 2018; Schroeder et al. 2014). These data are the best available proxy for burned area in the absence of a current satellite-derived high-latitude burned area product.

Within the Arctic Circle (>66.5°N), 2020 and 2019 stand out as extreme fire years that began unusually early in the season (Fig. SB5.1a). The majority of the fire activity in these years was in the republic of Sakha in northeastern Siberia, where fires burned primarily in montane ecosystems across landscapes underlain by permafrost, with some fires burning only about 11 km from the Chukchi Sea. The 2020 late winter, early spring, and summer temperature anomalies in this region were remarkable (see section 5b), while precipitation anomalies were below normal, and snowmelt was the earliest recorded since 1967 (Thoman et al. 2020; section 5f). Satellite imagery suggests that a large number of overwintering fires (Scholten et al. 2021) from 2019 jumpstarted the 2020 fire season in the region (Wheeling 2020). Including lower latitudes in fire detection analysis (Figs. SB5.1b,c) decreases the interannual variability and alters the years of maximum fire detections, with 2019 as a consistently exceptional fire year across HNL.

Climatological influences

Climate is a dominant control of fire activity on interannual and decadal scales. The relationship between climate and fire is strongly nonlinear in both boreal and tundra ecosystems, with likelihood of fire occurrence within a 30-year period much higher where mean July temperatures exceed 13.4°C (Young et al. 2017). HNL fire regimes appear to be responding

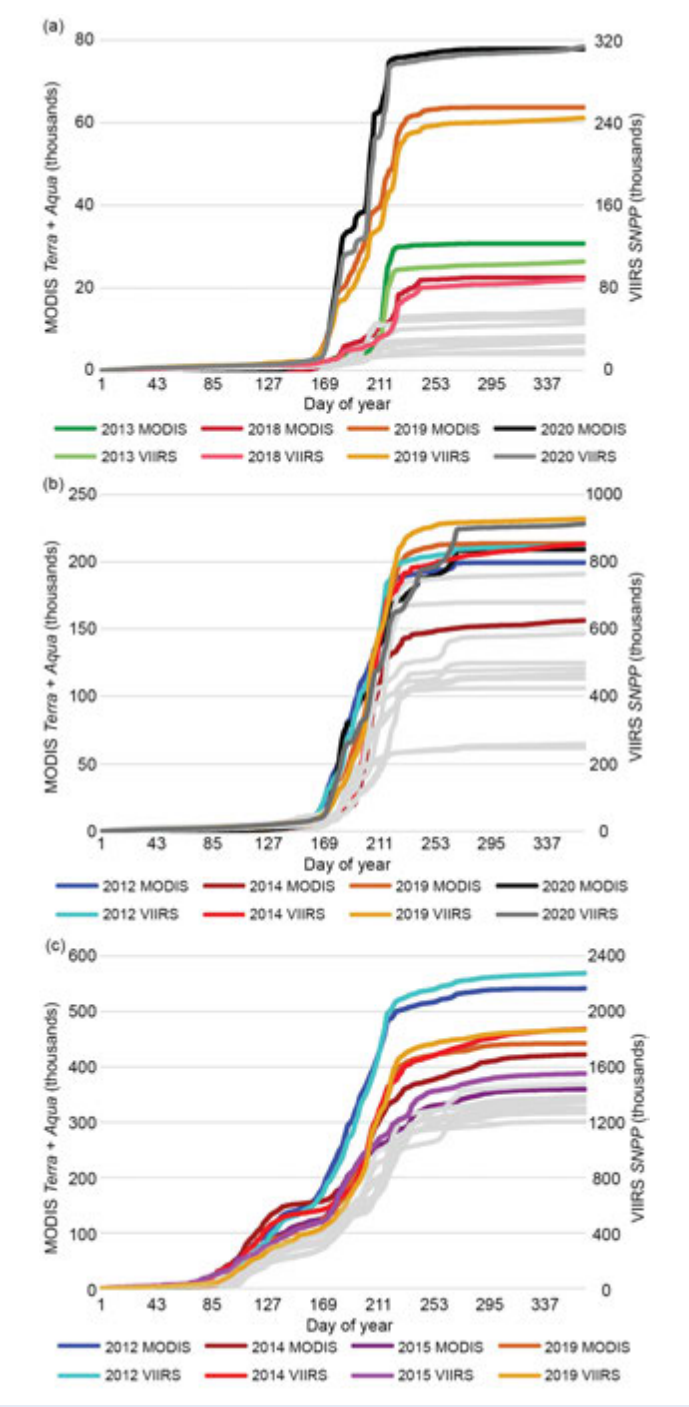

Fig. SB5.1. Cumulative satellite-derived active-fire detections across HNL for 2012–20 from both the 1-km MODIS (*Terra* and *Aqua*) and 375-m VIIRS (*Suomi NPP*) instruments (Giglio et al. 2018; Schroeder et al. 2014) for latitudes (a) >66.5°N (within the Arctic Circle), (b) >60°N, and (c) >50°N. The 4 years with the highest detections are listed and shown in color within each panel; within each year, colors are distinct. Other years with relatively lower detections are shown in gray. VIIRS detections, shown on the right axis, are consistently an order of magnitude greater than MODIS detections due to the higher resolution of the VIIRS instrument.

to environmental changes associated with warming climate (Hanes et al. 2019). Although highly variable, burned area has increased over the past several decades in much, but not all, of boreal North America (Hanes et al. 2019; York et al. 2020, and references therein), and lightning ignitions have increased in the same region (Veraverbeke et al. 2017; Bieniek et al. 2020). Partain et al. (2016) found that anthropogenically-driven climate change increased the likelihood of the extremely dry fuel conditions seen in Alaska in 2015 by 34%–60%. South-central Alaska experienced extreme late-season wildfire activity in 2019, accompanied by exceptionally dry summer conditions, observed as the lowest cumulative June–August (ERA5) Standardized Precipitation-Evapotranspiration Index (SPEI) since 1979, as determined by reanalysis (ERA5; Bhatt et al. 2021). A separate analysis of the 2019 Alaska fire season attributed Alaska's extreme fire activity in July to anthropogenic activity, primarily through an increase in anthropogenic ignition and secondarily through climate-induced biomass abundance (Yu et al. 2021).

Reflecting the importance of cumulative drying on fuelbed flammability, the Canadian Forest Fire Danger Rating System (CFFDRS) uses its Buildup Index (BUI; Wotton 2009) as a numerical rating of fuel availability for consumption. The BUI is derived from daily accounting of surface air temperature, relative humidity, and 24-hour rainfall totals. In boreal and arctic systems, BUI reflects the flammability of duff fuels (i.e., accumulated layers of partially decomposed moss and organic material) below the surface (York et al. 2020). As BUI crosses significant thresholds, fires can burn more intensely, spread more aggressively, and pose more problems for suppression.

Figure SB5.2 shows total 2-m air temperature and BUI changes and time series for boreal and tundra regions of Eurasia and North America in June for the 42-year period of record (1979–2020), calculated using ERA5 data (McElhinny et al. 2020). Widespread increases in temperature and BUI in both June and July (data not shown) and on both continents, particularly Eurasia, suggest that conditions are becoming generally more favorable for fire growth, with increases in cumulative drying and flammability likely to result in more intense burning, more fire growth episodes, and greater consumption of fuels. Despite this general trend, considerable interannual variability remains, exemplified by the near-record low June 2020 BUI in North America (Fig. SB5.2d).

These observations of area burned, BUI, and temperature are consistent with analyses projecting significant increases (up to fourfold) in burned area in HNL ecosystems by the end of the twenty-first century under a range of climate change scenarios (Young et al. 2017; Yue et al. 2015, and references therein). Because specific fire events depend on multiple interacting factors, the resulting changes in HNL fire regimes will vary greatly over space and time. However, all evidence indicates that northern ecosystems are increasingly vulnerable to wildland fire and its impacts.

(Text in this essay was drawn from a longer 2020 Arctic Report Card essay [York et al. 2020].)

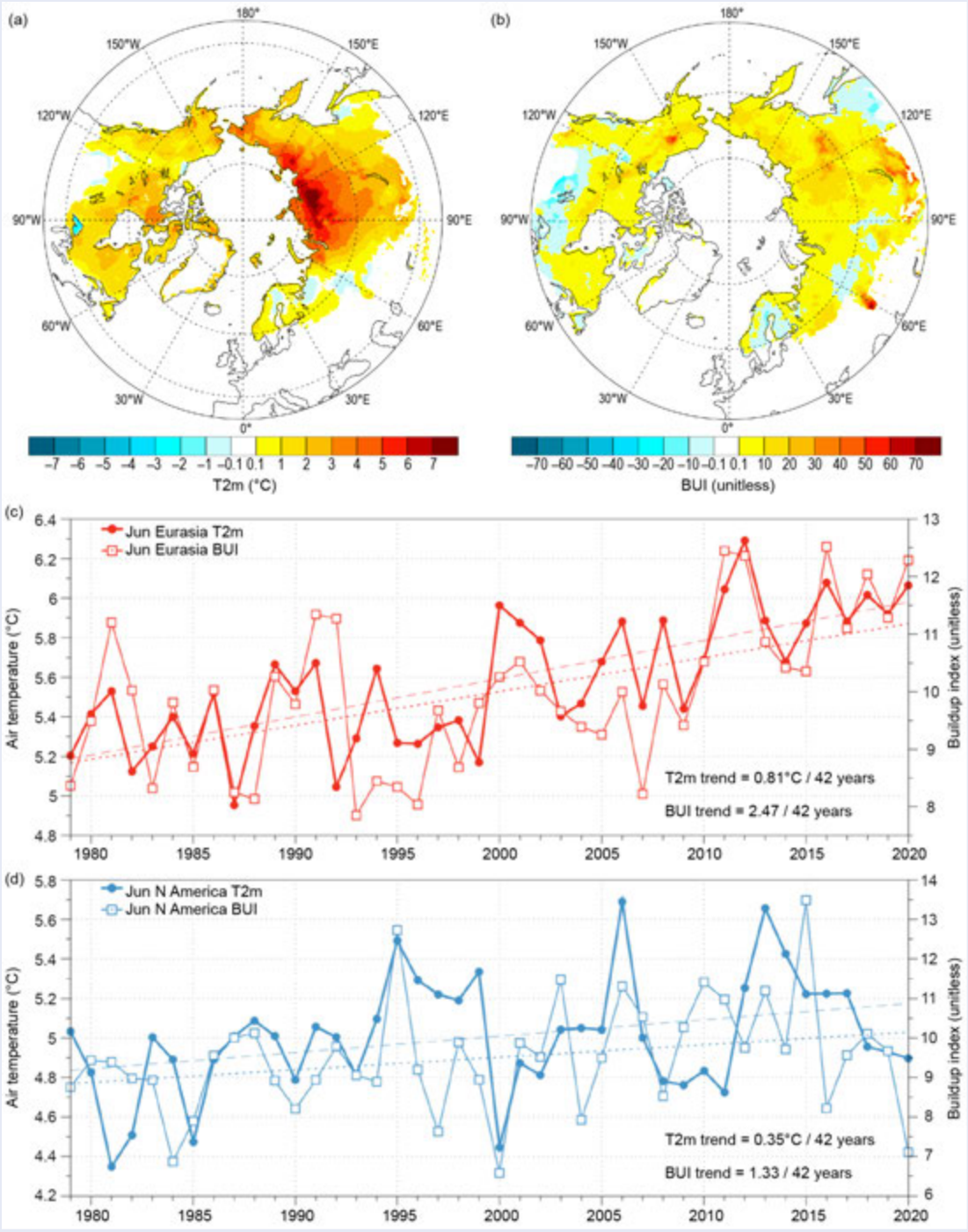

Fig. SB5.2. Change in Jun boreal and tundra (a) 2-m air temperature (*T*2m, in °C) and (b) BUI (unitless) from 1979 to 2020, from ERA5 data. Jun T2m and BUI time series for boreal and tundra areas of (c) Eurasia and (d) North America. Linear-fit trends over 1979–2020 (dashed for T2m and dotted for BUI) are significant for Eurasia at the 99% confidence level and for North America at the 95% confidence level using a t-test.

c. Sea surface temperature—M.-L. Timmermans and Z. Labe

Summer sea surface temperatures (SSTs) in the Arctic Ocean are driven mainly by the amount of incoming solar radiation absorbed by the sea surface. Solar warming of the Arctic surface ocean is influenced by the distribution of sea ice (with greater warming occurring in ice-free regions), cloud cover, and upper-ocean stratification. Discharge of relatively warm Arctic river waters can provide an additional source of heat to the surface of marginal seas. In the Barents and Chukchi Seas, there is also a contribution to ocean heat by the advection of warm waters from the North Atlantic and North Pacific Oceans, respectively.

Arctic SST is an essential indicator of the role of the ice–albedo feedback mechanism in any given summer sea ice melt season. As the area of sea ice cover decreases, more incoming solar radiation is absorbed by the ocean and, in turn, the warmer ocean melts more sea ice. In addition, higher SSTs are associated with delayed autumn freeze-up and increased ocean heat storage throughout the year. Marine ecosystems are influenced by SSTs, which affect the timing and development of primary and secondary production cycles, as well as available habitat for upper-trophic and temperature-sensitive species. Finally, with respect to carbon cycling, warmer SSTs are associated with reduced ocean uptake of CO_2 from the atmosphere, and thus represent another positive feedback loop to a changing climate.

The SST data presented here are a blend of in situ and satellite measurements from August 1982 to August 2020, taken from the monthly mean NOAA Optimum Interpolation (OI) SST Version 2 product (OISSTv2; Reynolds et al. 2002, 2007). Compared to purely in situ temperature measurements, the OISSTv2 product explains about 80% of the variance, with an overall cold bias via its tendency to underestimate SST by 0.02°C (Stroh et al. 2015). The OISSTv2 product uses a linear relationship with sea ice concentration to infer SST, with SST constrained to –1.8°C (the freezing point of seawater with a salinity of 33 g kg^{-1} at the sea surface) where ice concentration is 100% (Reynolds et al. 2007). Variations in freezing temperature as a result of variations in sea surface salinity (not accounted for in the algorithm) imply that OISSTv2 SSTs under sea ice can be too cool by up to 0.2°C, with the highest errors in the fresher surface waters of the Canada Basin. August mean SSTs provide the most appropriate representation of Arctic Ocean summer SSTs because they are not affected by the cooling and subsequent sea ice growth that typically takes place in the latter half of September. The period 1982–2010 is used as the climatological reference for the August mean.

August 2020 mean SSTs ranged from 7° to 10°C in the southern Chukchi and Barents Seas to approximately 1° to 3°C in the other Arctic Ocean marginal seas that are ice-free in August (Fig. 5.5a). Mean SSTs in August 2020 were consistent with sustained mean August SST warming trends from 1982 to 2020 over much of the Arctic Ocean, with statistically significant (at the 95% confidence interval) linear warming trends of up to +0.1°C yr^{-1} (Fig. 5.5b). Mean August SSTs for the entire Arctic (the Arctic Ocean and marginal seas north of 67°N) exhibit a linear warming trend of 0.03 ± 0.01°C yr^{-1}. The cooling trend in mean August SSTs in the northern Barents Sea region remains a notable exception (see Timmermans et al. 2020) and remains under study.

August 2020 mean SSTs were around 1°–3°C warmer than the 1982–2010 August mean over most of the Arctic Ocean's marginal seas (Fig. 5.6a). The largest anomalies were observed in the Laptev and Kara Seas, with values up to +5.5°C (Fig. 5.6a). Conversely, similar to August 2019 conditions, the northern Barents Sea region was marked by anomalously cool SSTs in August 2020 with temperatures up to –1.5°C below the mean (Fig. 5.6), contributing further to the region's long-term cooling trend. Relative to August 2019, August 2020 SSTs were up to 4°C cooler in the Chukchi and Beaufort Seas and a few degrees warmer overall in the Kara and Laptev Seas (Fig. 5.6). The strong interannual variability in spatial patterns of SST bear a close relationship to early summer sea ice concentrations (section 5d), with direct solar heating of the exposed surface waters likely driving an active ice–albedo feedback.

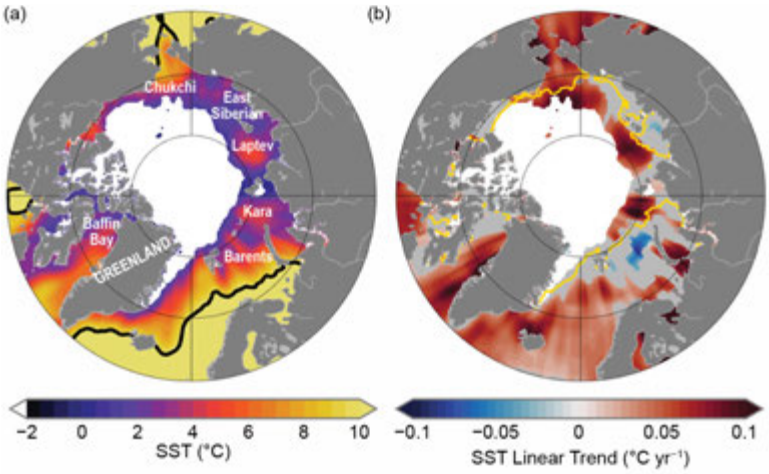

Fig. 5.5. (a) Mean sea surface temperature (SST; °C) in Aug 2020. White shading is the Aug 2020 mean sea ice extent, and black contours indicate the 10°C SST isotherm. (b) Linear SST trend (°C yr^{-1}) for Aug of each year from 1982 to 2020. The trend is only shown for values that are statistically significant at the 95% confidence interval; the region is shaded gray otherwise. White shading is the Aug 2020 mean sea ice extent, and the yellow line indicates the median ice edge for Aug 1982–2010. (Sources: SST data are from the NOAA OISSTv2; sea ice extent and ice edge data are from NOAA/NSIDC Climate Data Record of Passive Microwave Sea Ice Concentration, Version 3; Peng et al. 2013; Meier et al. 2017.)

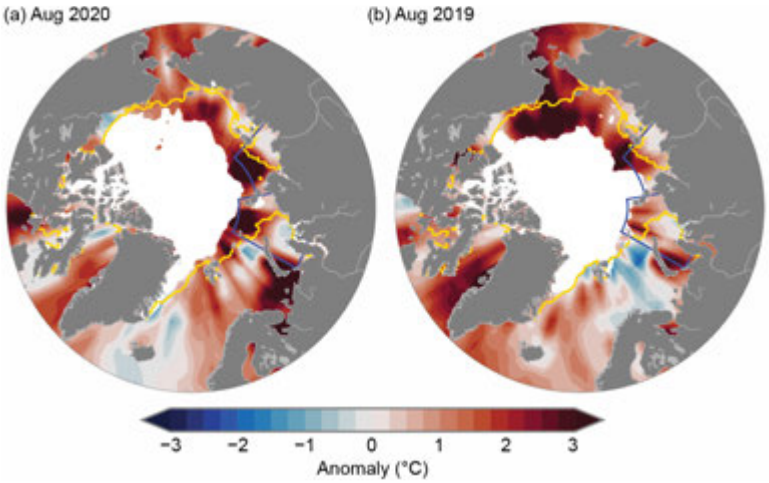

Fig. 5.6. Sea surface temperature (SST) anomalies (°C) in (a) Aug 2020 and (b) Aug 2019 relative to the Aug 1982–2010 mean. The yellow line indicates the median ice edge for Aug 1982–2010 and white shading indicates the mean sea ice extent in (a) Aug 2020 and (b) Aug 2019. The two regions marked by blue boxes indicate the Kara and Laptev Seas and relate to data presented in Fig. 5.7. (Sources: SST data are from the NOAA OISSTv2; sea ice extent and ice-edge data are from NOAA/NSIDC Climate Data Record of Passive Microwave Sea Ice Concentration, Version 3; Peng et al. 2013; Meier et al. 2017.)

Anomalously warm SSTs in the Laptev and Kara Seas distinguished the August 2020 SST field. Overall, Kara Sea SSTs are becoming warmer in August with a linear warming trend over 1982–2020 of 0.03 ± 0.01°C yr^{-1} (Fig. 5.7a). Although not statistically significant, Laptev Sea August mean SSTs also appear to be warming, with a linear trend of 0.02 ± 0.02°C yr^{-1} (Fig. 5.7b). The interplay between regional sea ice cover and solar absorption is evident in the low sea ice extents in August 2020 in these seas (Figs. 5.7c,d). Both regions also saw exceptionally low sea ice extents in July 2020, with Laptev Sea ice extent showing a record minimum for July. A similar pattern of SST anomalies in these regions extended through October 2020.

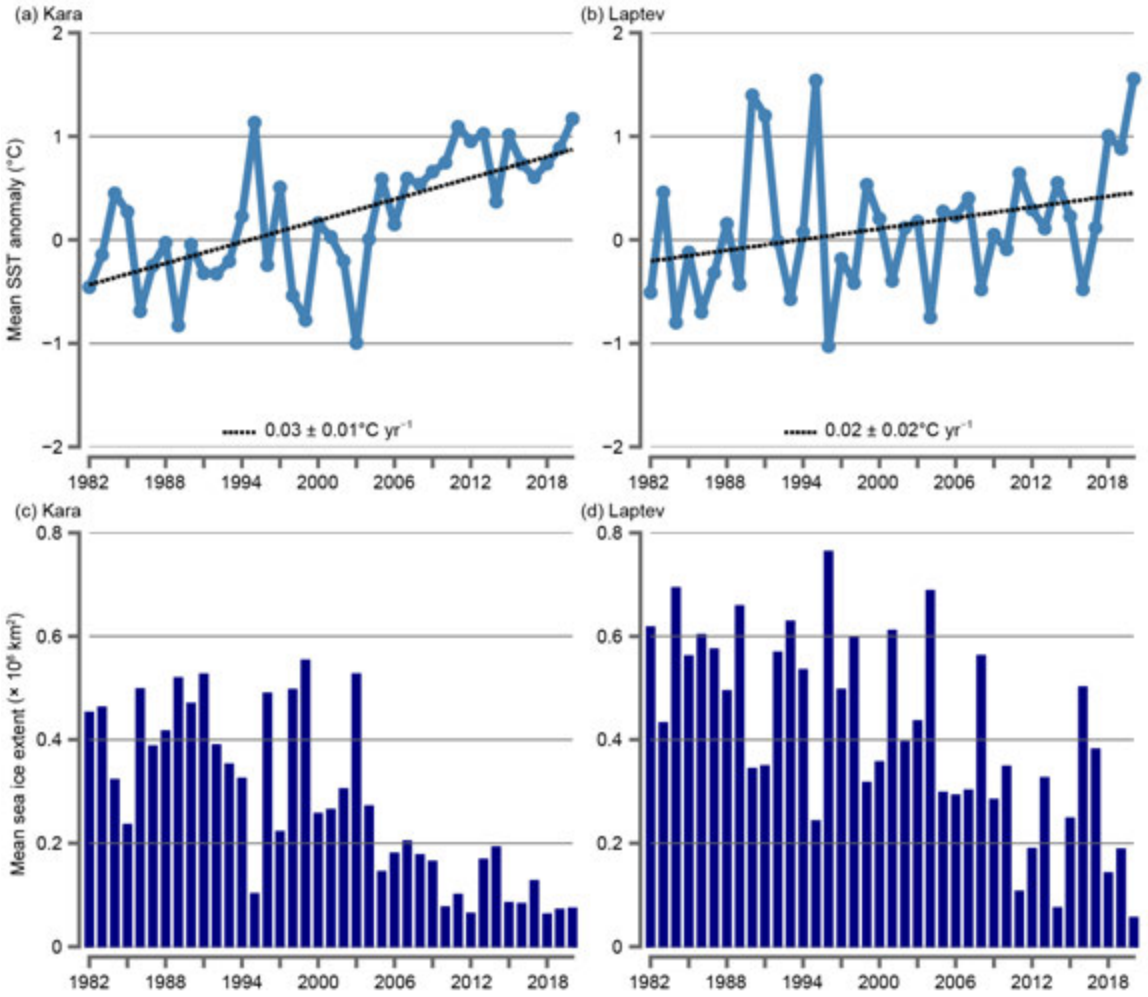

Fig. 5.7. Area-averaged sea surface temperature (SST) anomalies (°C) for Aug of each year (1982–2020) relative to the 1982–2010 Aug mean for the (a) Kara and (b) Laptev Sea regions, shown by blue boxes in Fig. 5.6. The dotted lines show the linear SST anomaly trends over the period shown and numbers in the legends indicate the trends in °C yr^{-1} (with 95% confidence intervals). Aug sea ice extents calculated over the (c) Kara and (d) Laptev Sea regions. (Sources: SST data are from the NOAA OISSTv2; sea ice extent data are from the NSIDC Sea Ice Index, Version 3 (Fetterer et al. 2017) using a regional mask introduced by Meier et al. 2007.)

d. Sea ice—W. Meier, D. Perovich, S. Farrell, C. Haas, S. Hendricks, L. Kaleschke, A. Petty, M. Tschudi, M. Webster, D. Divine, S. Gerland, O. Pavlova, R. Ricker, X. Tian-Kunze, and K. Wood

1) Sea ice extent

Sea ice is an important component of the Arctic climate system. It reflects much of the incoming solar energy due to its high albedo, or surface reflectivity, and acts as a physical barrier between the ocean and atmosphere, limiting sensible and latent heat transfer. It also serves as an important habitat for flora and fauna and it is a critical element of Indigenous culture (e.g., Gearheard et al. 2013). The long-term decline of Arctic sea ice extent from the now >40-year passive microwave satellite record (1979 to present) has become one of the most iconic indicators of global climate change. Here we use extent values from the National Snow and Ice Data Center (NSIDC) Sea Ice Index (Fetterer et al. 2017). The Sea Ice Index trends and anomalies are generally consistent with other extent products (e.g., the Ocean and Sea Ice Satellite Application Facility Climate Change Initiative [OSI SAF CCI; Lavergne et al. 2019]).

March is the typical month of the maximum annual sea ice extent. In 2020, March extent was 14.79 million km^2 (Fig. 5.8a), with the daily annual maximum extent reached on 5 March, at 15.05 million km^2—the 11th-lowest daily maximum extent in the satellite record and the highest

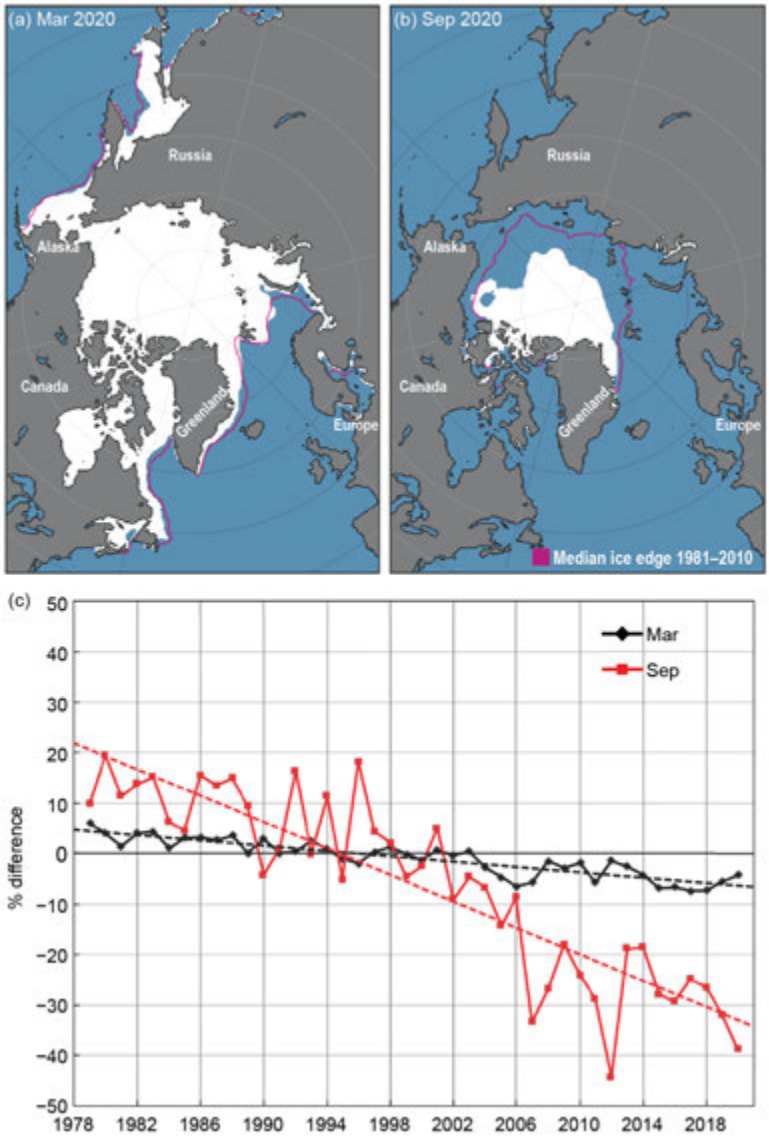

Fig. 5.8. Sea ice extent maps for (a) Mar 2020 and (b) Sep 2020, with ice concentration >15% in white; the magenta contour indicates the median extent for 1981–2010. (c) Percent anomaly of Mar (black) and Sep (red) extent for 1979–2020 relative to the 1981–2010 average; the dashed lines indicate the linear trend.

since 2013. The somewhat higher maximum relative to recent years does not account for changes in thickness (discussed below). Also, interannual variability is expected and does not negate the multi-decadal decline in winter ice cover. Overall, March has experienced a significant long-term (1979–2020) trend loss of –40,400 km^2 ice extent per year (–2.6 % per decade relative to the 1981–2010 average; Fig. 5.8c).

The summer of 2020 was marked by an early retreat and late freeze-up of sea ice, particularly in the Laptev Sea, leading to daily record lows in the region for much of mid-June through mid-November. As a result, the Northern Sea Route along the Siberian coast was open for about 2.5 months (late July through mid-October), compared to less than a month that was typical in the past. Another notable feature was an unconsolidated ice pack during late summer in the eastern Arctic. This loose ice pack with broken ice floes separated by open water allowed the German icebreaker RV Polarstern to easily reach the North Pole in August as part of the Multidisciplinary Drifting Observatory for the Study of Arctic Climate (MOSAiC).

September is the month when the minimum annual sea ice extent occurs. In 2020, this average monthly ice extent was 3.92 million km^2 (Fig. 5.8b), the second lowest monthly extent in the 42-year satellite record. On 15 September, the annual minimum Arctic sea ice extent of 3.74 million km^2 was reached; this was also the second lowest on record. The September monthly

extent has been decreasing at an average rate of –82,700 km^2 per year since 1979 (–13.1% per decade relative to the 1981–2010 average; Fig. 5.8c).

2) Sea ice thickness and volume

While ice extent provides an easily quantifiable long-term metric of sea ice conditions, the ice thickness and volume provide crucial additional insight into the state of the ice pack. In the past decade, satellite altimetry has provided new estimates of thickness and volume over the entire Arctic basin, beginning with the ESA CryoSat-2 radar altimeter, launched in 2010. The NASA Ice, Cloud, and land Elevation 2 (ICESat-2) laser altimeter, launched in 2018, now provides a second, independent source of thickness estimates.

Because radar altimeter measurements have higher relative errors for thin ice, a product has been developed (Ricker et al. 2017) that combines CryoSat-2 data with estimates of thin ice from the ESA Soil Moisture Ocean Salinity (SMOS) passive microwave radiometer. By combining thickness with sea ice concentration, a seasonal record of sea ice volume can be produced.

The time series of CryoSat-2/SMOS sea ice volume, spanning October 2019 to April 2020, shows that Northern Hemisphere (NH) sea ice volume grew by ~13,400 km^3 during the winter 2019/20 season, but it was consistently below the 10-year average through the winter to the beginning of the melt season in April (Figure 5.9a). A spatial map of thickness shows a typical pattern of

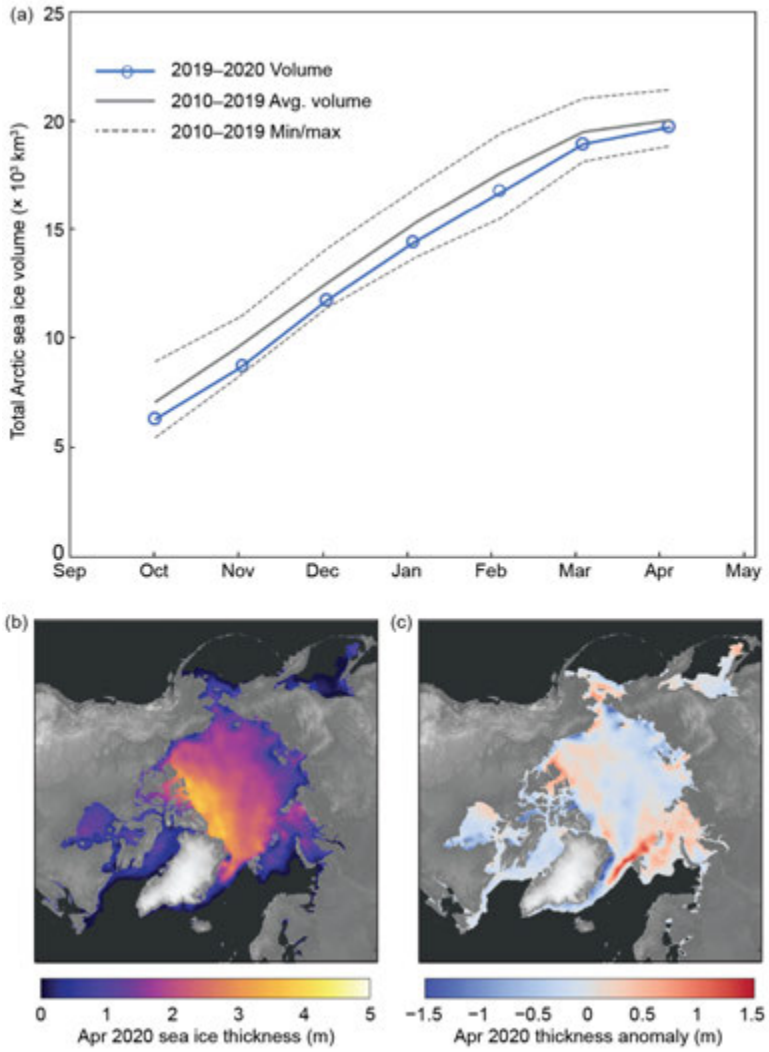

Fig. 5.9. (a) Time series of monthly Northern Hemisphere (NH) sea ice volume (× 10^3 km^3) from CryoSat-2/SMOS in winter 2019/20, spanning Oct 2019 to Apr 2020 (blue line with blue circles) compared to the 10-year average (solid gray line) for winter 2010/11 through winter 2018/19, and the lowest (min) and highest (max) sea ice volume (dashed gray lines) for the same 10 years; (b) CryoSat-2/SMOS Apr 2020 sea ice thickness (m) and (c) thickness anomaly (m).

thicker ice toward Greenland and the Canadian Archipelago (Figure 5.9b). The below-average (relative to the 2010–19 average) total sea ice volume in April 2020 was characterized by wide areas of below-average ice thickness in the central Arctic basin and on the Russian continental shelves (Figure 5.9c). However, ice thickness in April 2020 was above average in the Beaufort, Barents, and Greenland Seas and north of Svalbard, likely caused by an increase in southward advection of thicker multiyear sea ice.

The CryoSat-2/SMOS estimates are consistent with sea ice thickness estimates derived from ICESat-2 release 3 freeboards (not shown), updated from Petty et al. (2020) using NESOSIM v1.1 (Petty et al. 2018) snow loading. These thickness estimates within an inner Arctic Ocean domain also indicate a slightly thinner winter ice cover for much of 2019/20 compared to 2018/19, with an April 2020 mean thickness of 2.0 ± 0.3 m (compared to 2.1 ± 0.3 m in April 2019).

3) Ice age

The age of sea ice is another key descriptor of the state of the sea ice cover, and older ice tends to be thicker and thus more resilient to changes in short-term atmospheric and oceanic variations compared to younger (thinner) ice. Sea ice age derived from Lagrangian tracking of ice parcels (Tschudi et al. 2019, 2020) indicates a significant loss of older ice types. In the mid-1980s, ice >3 years old was the dominant type of ice within the Arctic Ocean region, comprising roughly a third of the ice in March (Fig. 5.10). In March 2020, less than 10% of the Arctic Ocean ice cover was older than 3 years. The dominant ice type is now first-year ice (0–1 years old), which comprised about 70% of the March 2020 Arctic Ocean ice cover. The median ice age dropped from 2–3 years old in the mid-1980s to less than 1 year old by 2020. The total extent of the oldest ice (>4 years old) declined from 2.50 million km^2 in March 1985 to 0.34 million km^2 in March 2020.

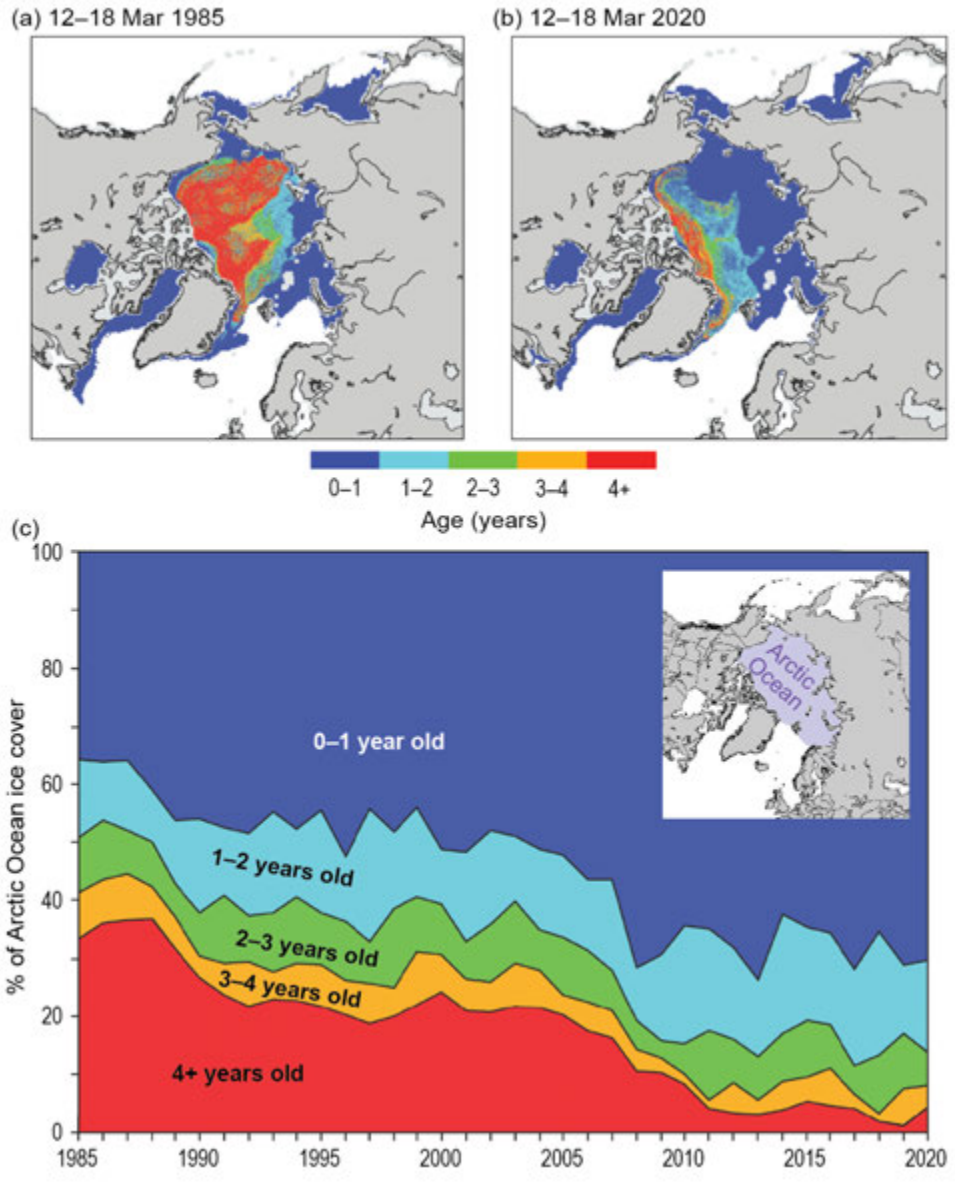

Fig. 5.10. Late winter sea ice age coverage map for the week of (a) 12–18 Mar 1985 and (b) 12–18 Mar 2020. (c) Sea ice age percentage within the Arctic Ocean (purple shaded region in bottom inset) for the week of 12–18 Mar from 1985 to 2020. (Source: Data are from NSIDC and University of Colorado [Tschudi et al. 2019, 2020].)

e. Greenland ice sheet—T. A. Moon, M. Tedesco, K. D. Mankoff, J. E. Box, J. Cappelen, R. S. Fausto, X. Fettweis, N. J. Korsgaard, B. Loomis, T. Mote, C. H. Reijmer, C. J. P. P. Smeets, D. van As, R. S. W. van de Wal, and Ø. A. Winton

The Greenland ice sheet holds an estimated 7.4 m of potential sea level rise (Morlighem et al. 2017). Following a period of relative stability from the 1970s to early 1990s, the ice sheet began losing ice at an accelerating rate (Mouginot et al. 2019). The two largest annual mass losses since regular monitoring began in the 1950s occurred in 2012 and 2019, with losses of −464 ± 62 Gt and −532 ± 58 Gt, respectively (Sasgen et al. 2020; estimates including all Greenland glaciers and peripheral ice caps). Total ice loss in 2020 was −293 ± 66 Gt, slightly above the 2002–19 average. These annual losses are equivalent to ~1.3 mm (2012: −464 Gt); ~1.5 mm (2019: −532 Gt); and ~0.8 mm (2020: −293 Gt) of global mean sea level rise. For comparison, 1993–2018 total global mean sea level rise was ~3.3 mm yr^{-1} (Frederikse et al. 2020).

Total annual ice loss reflects the annual cycle of snow accumulation (gain) and ice/snow ablation (loss), known as the ice mass balance. To capture this cycle, Greenland measurements are compiled from September through August. The seasons are autumn (September–November), winter (December–February), spring (March–May) and summer (June–August), and anomalies are relative to the 1981–2010 mean unless noted otherwise. The Greenland ice mass budget is determined by the total of two components: surface mass balance (SMB)—the total annual surface mass change (usually positive) that is particularly linked to atmospheric and ice sheet surface conditions—and dynamic ice loss from the calving of icebergs (solid ice discharge) into the ocean (always negative).

Turning first to SMB, results from the Modèle Atmosphérique Régional (MAR; e.g. Tedesco et al. 2013) using the ECMWF Re-Analysis 5 (ERA5) indicate a SMB anomaly of −68 ± 40 Gt yr^{-1} over September 2019–August 2020 with respect to the 1981–2010 mean of 343 ± 100 Gt yr^{-1} (2020 anomaly shown in Fig. 5.11a; note that 1 km^3 water equivalent is equal to 1 Gt). Abnormal cyclonic circulation promoted near- to below-average summer air temperatures in the interior and east, while warmer-than-average conditions impacted the southern, northern, and most coastal regions. In situ temperature measurements at 20 Danish Meteorological Institute (DMI) weather stations and eight Programme for Monitoring of the Greenland Ice Sheet (PROMICE) weather station transects were also near- to above-average during autumn 2019 and spring 2020, consistent with concurrent net ablation measurements (Fig. 5.11b; Fausto and van As 2019). Winter 2019/20 temperatures were near to below average at almost all DMI stations and substantially lower than average at Summit Station in the ice sheet interior.

Atmospheric and ice sheet surface conditions influence snow microphysical properties, especially albedo, the fraction of surface reflected sunlight. A high albedo (bright surface) means more sunlight is reflected, while a low albedo (dark surface) leads to greater sunlight absorption. The 2020 overall summer ice-sheet-wide albedo (0.808) was +1.3 standard deviations above the 2000–20 mean (0.791; Fig. 5.12c), with positive and negative regional anomalies (Fig. 5.12a, using 2000–09 reference period; after Box et al. 2017).

Surface melt duration and extent, measured via daily satellite observations from the Special Sensor Microwave Imager/Sounder (SSMIS) passive microwave radiometer (e.g., Mote 2007; Tedesco et al. 2013) also varied regionally. The overall number of melt days in 2020 was greater than the 1981–2010 mean (80% of June–August days had a melt extent that was greater than the median melt extent for that day; Fig. 5.12d), with regionally varying anomalies (Fig. 5.12b). Though the 2020 maximum daily melt extent (33.8% of the ice sheet surface) was lower than the mean maximum daily extent (39.8%), the cumulative summer melt-day extent (summing melt extent across all days) was 28% higher than the 1981–2010 mean. In synthesis, there were not many days with very large melt extents, but many days that exceeded the average.

Melt duration patterns generally correspond with albedo and surface air temperature anomalies. In 2020, discrepancies between the melt duration (Fig. 5.12b) and SMB anomalies (Fig. 5.11a)

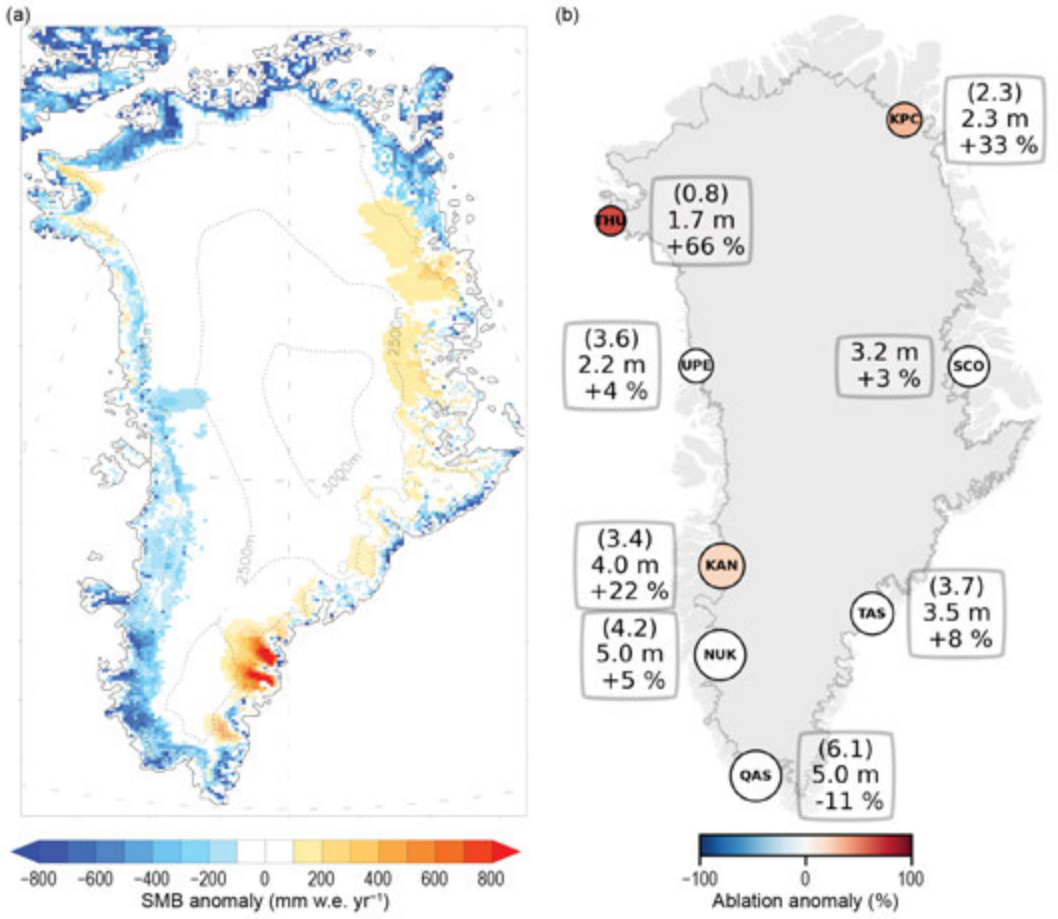

Fig. 5.11. (a) Surface mass balance anomaly for Sep 2019 to Aug 2020 (mm water equivalent yr^{-1}) produced by MAR using reference period 1981–2010. (b) Net ablation for 2020 (covering the end of the 2019 melt season to the end of the 2020 melt season in m of ice yr^{-1}) from two sources: 1) estimated by MAR (in parentheses at top of inset boxes) and 2) measured via in situ observation at PROMICE weather stations (in parentheses at center of inset box) along the Greenland ice sheet margin. Using PROMICE measurements, circle size is scaled to ice ablation and color indicates anomaly (%; in parentheses at bottom of inset box), referenced to the 1981–2010 base period following Van As et al. (2016). White circles indicate anomaly values not exceeding methodological and measurement uncertainty.

occurred along the east central margin; summer snowfall increased the surface albedo, while atmospheric conditions such as surface air temperature supported relatively high melt duration.

Turning to solid ice discharge, the 1981–2010 mean total discharge was −460 ± 46 Gt yr^{-1}, while mean discharge during 2010–19 was −487 ± 49 Gt yr^{-1} (Fig. 5.13a; Mankoff et al. 2020). Solid ice discharge for September 2019 to August 2020 totaled −503 ± 50 Gt yr^{-1}, with the largest contribution from the southeast region (Figs. 5.13a,c). Associated net glacier surface area loss due to glacier front retreat was −55.4 km^2 for 47 Greenland tidewater glaciers selected to provide regional coverage and include major glaciers (Fig. 5.13b), considerably lower than the mean annual loss of −99.5 km^2 for these glaciers since 2002 (Andersen et al. 2019).

Finally, the total mass change of the ice sheet, combining SMB and solid ice discharge, reflects annual contributions to sea level rise. The GRACE (Gravity Recovery and Climate Experiment, 2002–17) and GRACE-FO (Follow On, 2018–present) satellite missions indirectly measure total mass change by detecting gravity anomalies. Over the full span of both missions, the mean rate of mass loss for the Greenland ice sheet is −268 ± 14 Gt yr^{-1} (2-model fit uncertainties reported; Fig. 5.14, GRACE data). GRACE-FO data show that the September 2019 to August 2020 annual mass loss was −293 ± 66 Gt (against an average for the period 1980–2010 of −75 ± 145 Gt yr^{-1}), equivalent to ~0.8 mm global sea level rise, and the results align with several other methods (Fig. 5.14). Over the 2018/19 season, a new record annual mass loss of −532 ± 58 Gt was observed (Sasgen et al.

2020), marking a dramatic change from the decreased annual mass losses of about –100 Gt yr^{-1} over 2017/18. While mass loss for 2020 exceeds the 2002–19 mean, it is substantially lower than the record 2019 ice loss.

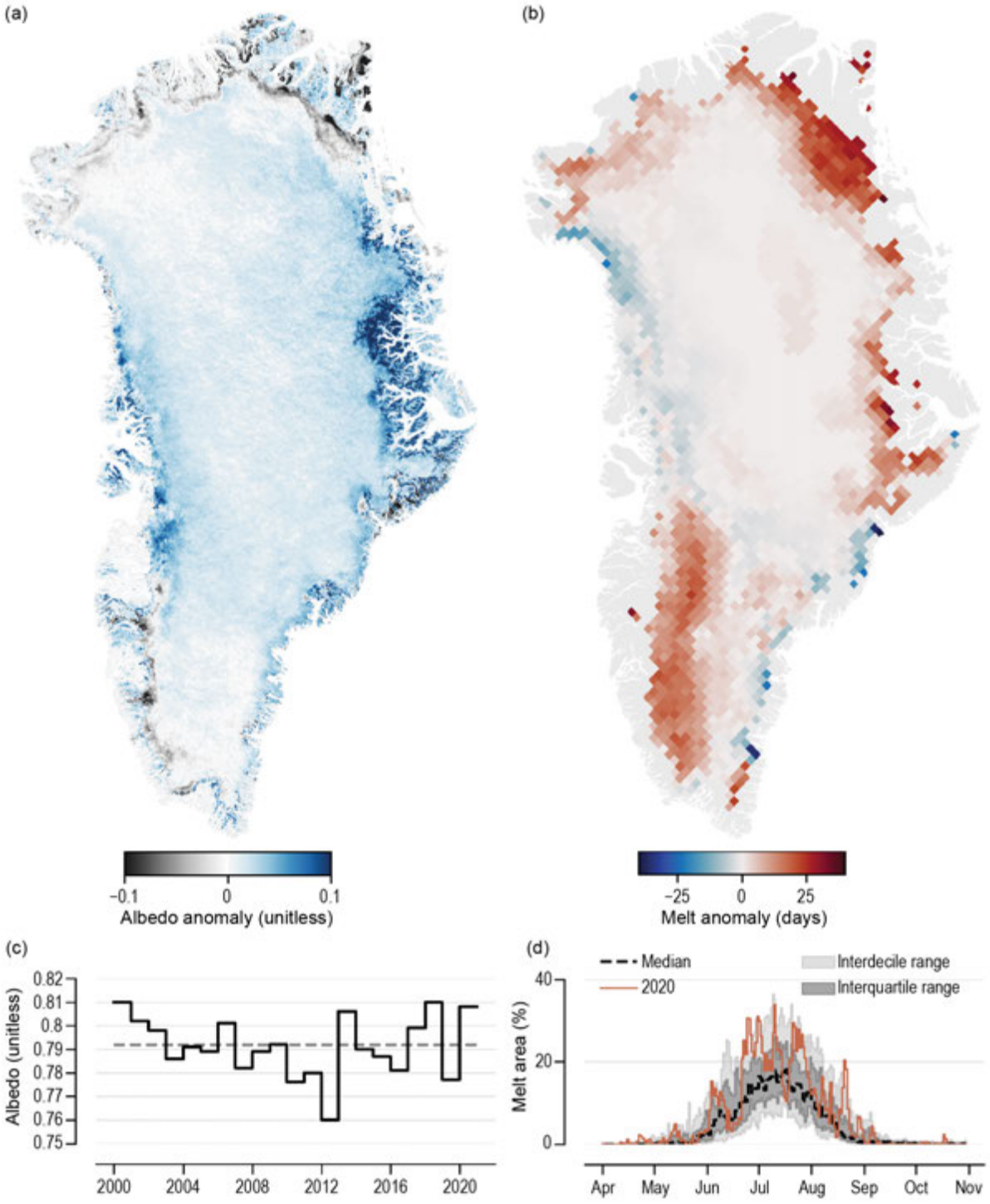

Fig. 5.12. (a) Albedo anomaly for summer 2020, relative to a 2000–09 reference period. (b) Melt anomaly (in number of melting days) for summer 2020 with respect to the 1981–2010 reference period and estimated from spaceborne passive microwave observations. (c) Time series for summer albedo of Greenland ice sheet surface. (d) SSMIS-derived surface melt extent as a percentage of the ice sheet area during 2020 (solid red).

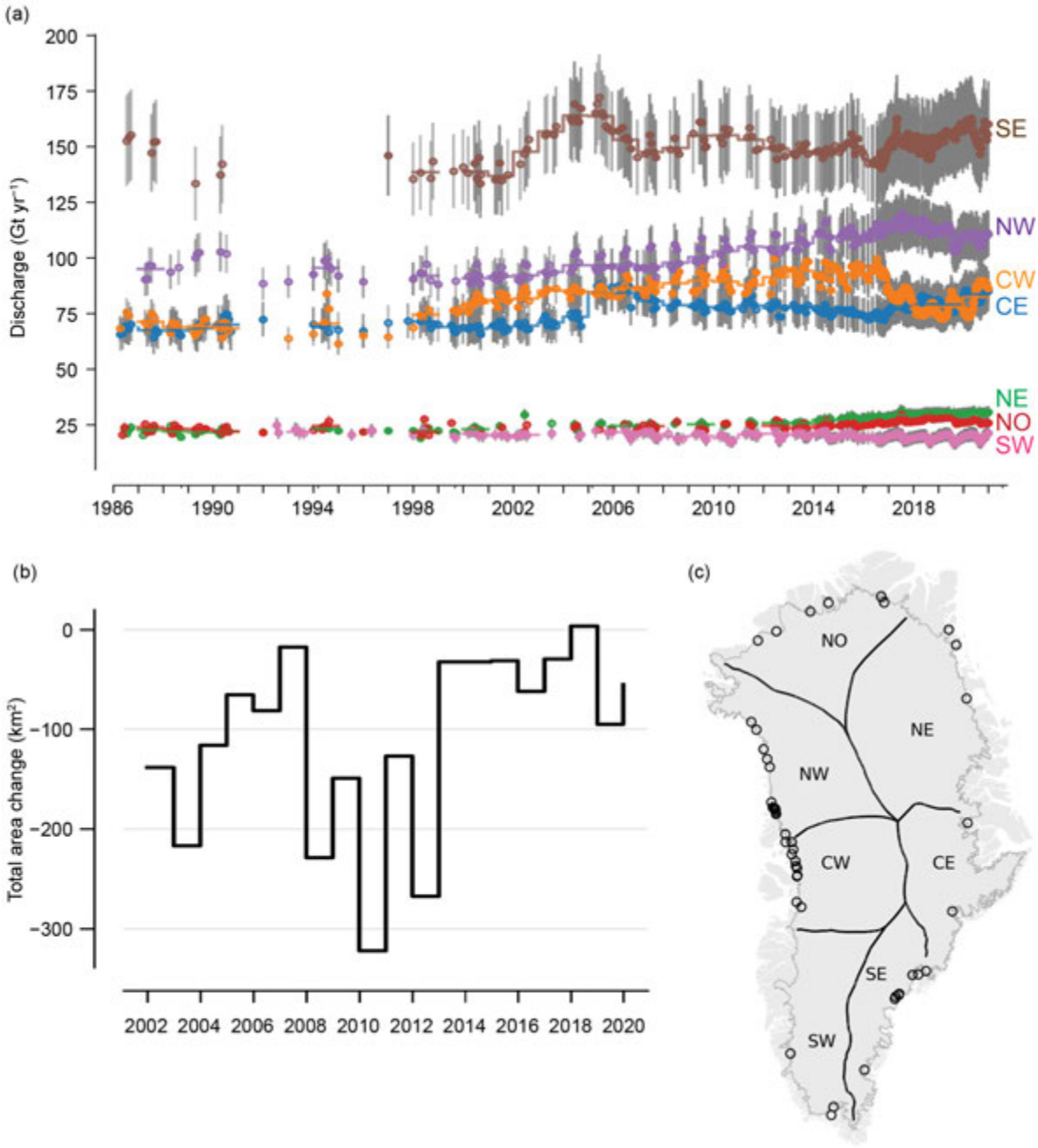

Fig. 5.13. (a) Time series of solid ice discharge (Gt yr^{-1}) from the Greenland ice sheet. Dots represent when observations occurred, and gray bars show ±10% uncertainty range. (b) Total annual area changes (km^2) at 47 major Greenland tidewater glaciers. (c) Boundaries for regions included in (a): north (NO), northeast (NE), central east (CE), southeast (SE), southwest (SW), central west (CW), and northwest (NW), and sampled glaciers for (b) indicated with open circles.

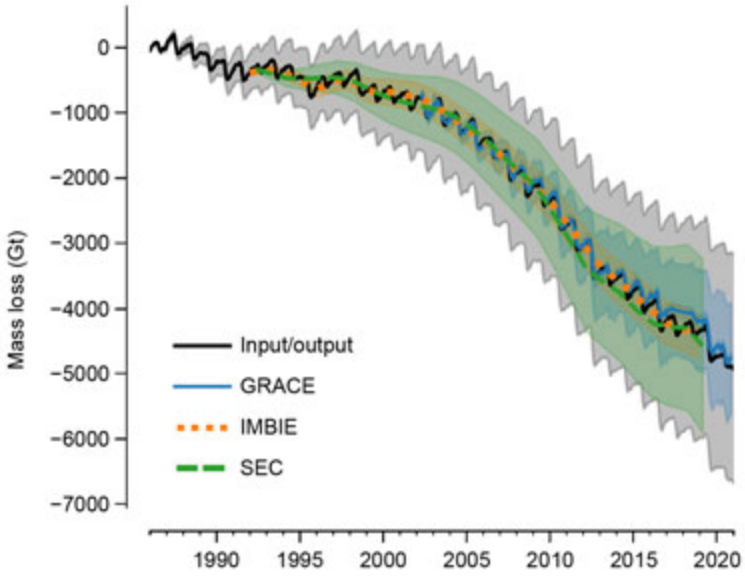

Fig. 5.14. Comparison of results using four total mass balance measurement datasets. IMBIE results are from Shepherd et al. (2020). SEC is from Simonsen et al. (2021, data: 10.11583/DTU.13353062.v1). The input/output method is the mean of MAR, RACMO, and HIRHAM/HARMONIE regional climate models minus discharge from Mankoff (2020, data: https://doi.org/10.22008/promice/data/ice_discharge/d/v02). GRACE (2002–17) and GRACE–FO (2018–present) data and technical notes are hosted at https://podaac-tools.jpl.nasa.gov/drive/files/allData. GRACE data are scaled by 0.84 to account for peripheral glaciers.

f. Terrestrial snow cover—L. Mudryk, A. Elias Chereque, R. Brown, C. Derksen, K. Luojus, and B. Decharme

Snow covers the Arctic terrestrial surface (areas north of 60°N) for up to 9 months each year and influences the surface energy budget, ground thermal regime, and freshwater budget of the Arctic (Brown et al. 2017). Snow also interacts with vegetation, affects biogeochemical activity, and impacts terrestrial and aquatic ecosystems including migration and access to forage for wildlife (Callaghan et al. 2011). Pan-Arctic monitoring of snow cover extent (SCE), duration, depth, and water equivalent provides a suite of indicators broadly relevant across these physical and ecological systems. All of these indicators exhibit negative trends over long time periods (i.e., 3 decades or more), albeit with varying levels of interannual variability, consistent with a strong response to increasing temperatures (Mudryk et al. 2020a).

SCE anomalies (relative to the 1981–2010 climatology) for spring 2020 were computed separately for the North American and Eurasian terrestrial sectors of the Arctic. Anomalies were derived from the NOAA snow chart climate data record, which extends from 1967 to present (Fig. 5.15). The SCE anomalies over the Eurasian Arctic were well below normal in May (fourth lowest). Additional melt through June associated with a Siberian heat wave resulted in the lowest Eurasian June SCE in the entire 54-year record. North American Arctic spring SCE anomalies were below average in both May and June (eighth and 10th lowest, respectively).

Snow cover duration (SCD) anomalies across the Arctic region for the 2019/20 snow season (Figs. 5.16a,b) were derived from the NOAA daily Interactive Multisensor Snow and Ice Mapping System (IMS) snow cover product. Anomalies in the total number of days with snow cover were computed separately for each half of the snow season: August 2019 to January 2020, referred to as "onset period," and February to July 2020, referred to as "melt period." The SCD during the onset period (Fig. 5.16a) was close to normal over much of the Arctic, with values reflecting a slightly later start over the eastern Canadian Arctic (Baffin Island and Northern Quebec) and slightly earlier-than-normal onset to the snow season over coastal eastern Siberia and the Scandinavian Peninsula. The marked difference between Arctic and sub-Arctic Europe is linked to atmospheric variability associated with above-average surface temperatures across central Europe. The SCD during the melt period (Fig. 5.16b) over the North American Arctic indicates a combination of late and early melt with more persistent snow occurring in southern Nunavut and early snowmelt

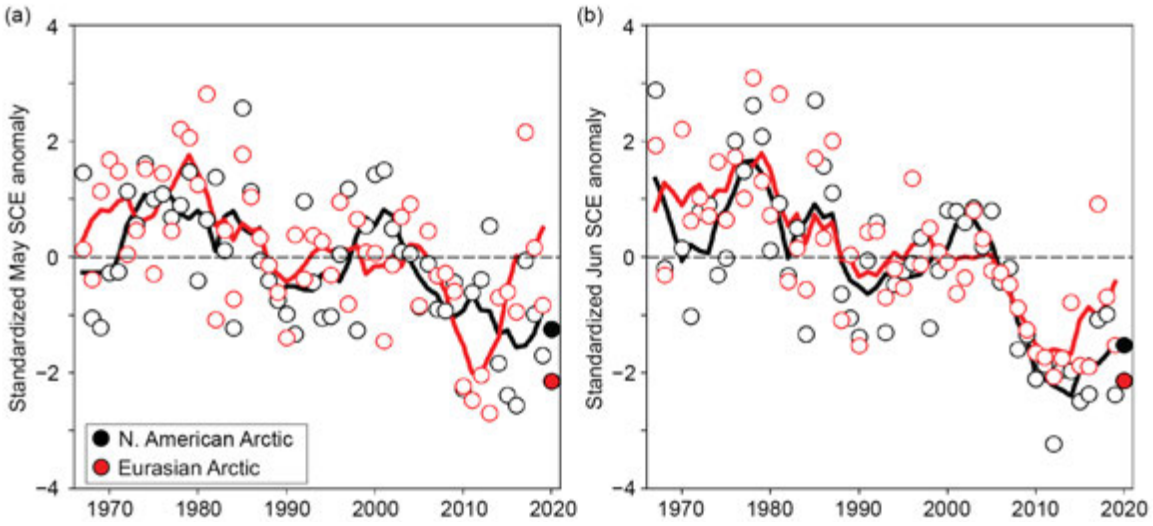

Fig. 5.15. Monthly snow cover exent (SCE) anomalies for Arctic terrestrial areas (>60°N) for (a) May and (b) Jun from 1967 to 2020. Anomalies are relative to the 1981–2010 average and standardized (each observation differenced from the mean and divided by the standard deviation, and thus unitless). Solid black and red lines depict 5-yr centered running means for North America and Eurasia, respectively, computed with 1968–69 values mirrored before 1967 and 2018–19 values mirrored after 2020. Filled circles are used to highlight 2020 anomalies. (Source: Estilow et al. 2015; Robinson et al. 2012.)

occurring across most of the Canadian Arctic Archipelago and parts of Alaska and Yukon Territory. Over Eurasia, later-than-normal snowmelt occurred over the Scandinavian peninsula, likely due to larger-than-normal snow accumulation (Fig. 5.16c), consistent with an earlier start to the snow season and above-normal winter precipitation. In marked contrast, and despite the larger-than-normal accumulation of snow through March (Fig. 5.16c), springtime temperatures averaging more than +5°C above normal (see section 5b) resulted in complete snowmelt up to a month early across extensive areas of central Siberia.

Snow depth anomalies (Figs. 5.16c,d) were derived from the Canadian Meteorological Centre (CMC) daily gridded global snow depth analysis, which combines air temperature and precipitation analyses with the assimilation of surface snow depth observations. Snow accumulation over the 2019/20 season resulted in above-average March snow depth across the Arctic (Fig. 5.16c). In parts of the North American Arctic, deep snow persisted throughout the spring into June (Fig. 5.16d). Across central Siberia, changes in monthly snow depth from April to June signified strong melt, which led to below-average June snow depths (Fig. 5.16d) and the lowest Eurasian Arctic June snow extent in the full observational record, despite the anomalously deep March snowpack.

Four products were used to generate a multi-dataset snow water equivalent (SWE) anomaly time series (1981–2020) for April (Fig. 5.17): (1) the Modern-Era Retrospective Analysis for Research and Applications version 2 (MERRA-2); (2) a simple temperature index model driven by ERA-interim meteorology described in Brown et al. (2003); (3) the physical snowpack model, Crocus (Brun et al. 2013), also driven by ERA-Interim meteorology; and (4) the European Space Agency GlobSnow product derived through a combination of satellite passive microwave data and climate station observations. Note that Crocus data were not available for 2019 or 2020 and that ERA5 meteorology was used to provide a 2020 SWE estimate from the temperature index model (ERA-interim production ceased in mid 2019). The use of multiple SWE products allows for the determination of inter-product spread through the time series (though the calculated spread may be reduced for 2019/20 owing to the use of three products in place of four). The SWE estimates for April 2020 indicate above-normal snow accumulation over both the Eurasian and North American Arctic, consistent with deeper-than-normal March snow depths shown in Fig. 5.16c.

In summary, snow accumulation during the 2019/20 winter was above normal across nearly the entire Arctic. Nonetheless, above-average springtime temperatures over central Siberia were extreme enough to drive rapid snowmelt that produced the lowest Eurasian June SCE documented across the 54-year observational record. Springtime anomalies of SCE over North America were more moderate, though still negative, due to a combination of regions with deeper, more persistent snow and regions that experienced early melt.

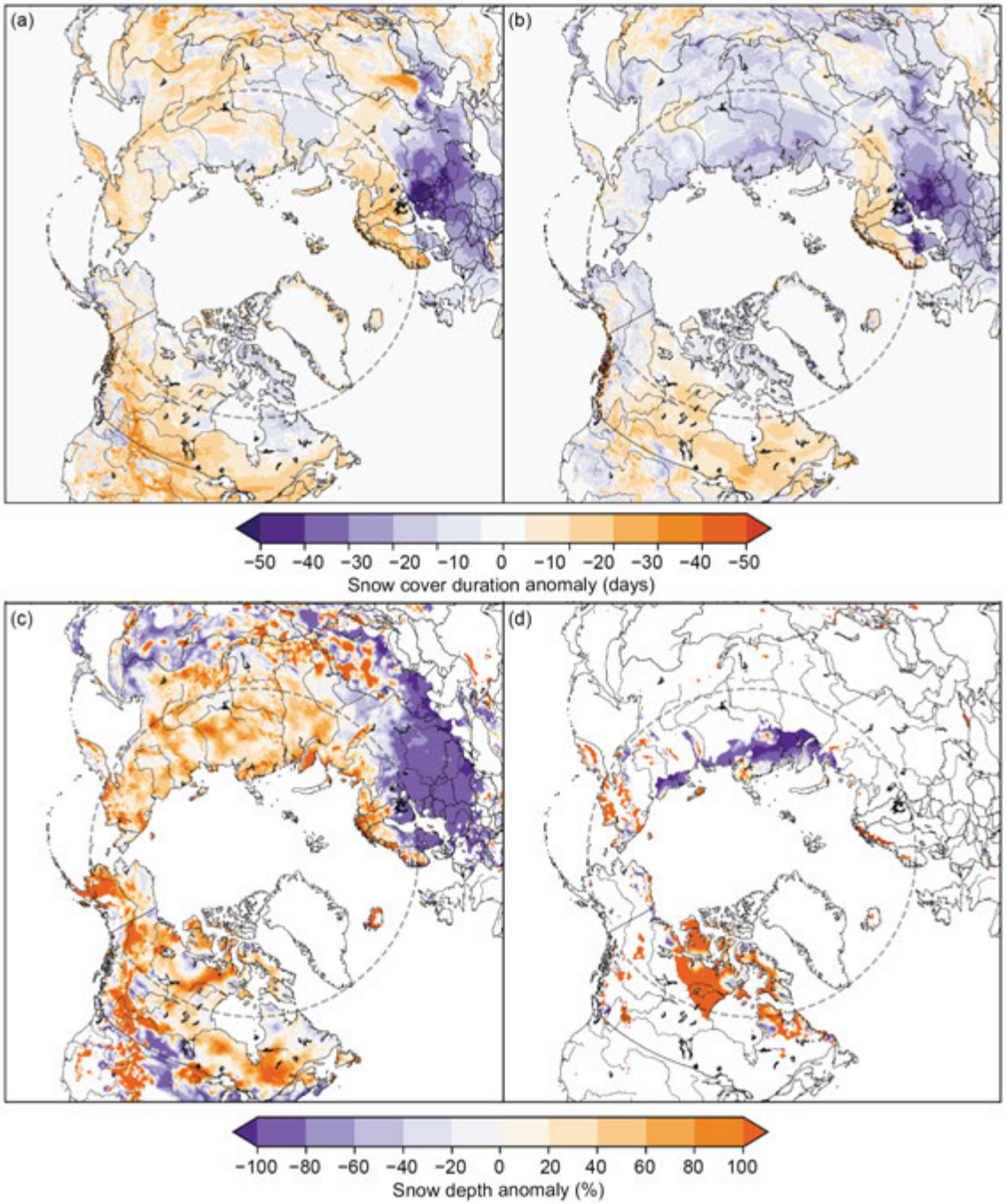

Fig. 5.16. Snow cover duration (SCD) anomalies (days; difference from 1998–2018 mean; purple denotes shorter SCD than average; orange denotes longer SCD than average) across the (a) snow onset period (Aug 2019–Jan 2020) and (b) snowmelt period (Feb–Jul 2020). Snow depth anomalies (% of the 1999–2018 average; purple denotes shallower snow than average; orange denotes deeper snow than average) in 2020 for (c) Mar and (d) Jun. The latitude 60°N is marked by a gray dashed circle; land north of this circle defines Arctic terrestrial areas considered in this study. (Source: [a and b] Helfrich et al. 2007; U.S. National Ice Center 2008. [c] and [d] Brasnett 1999; Brown and Brasnett 2010.)

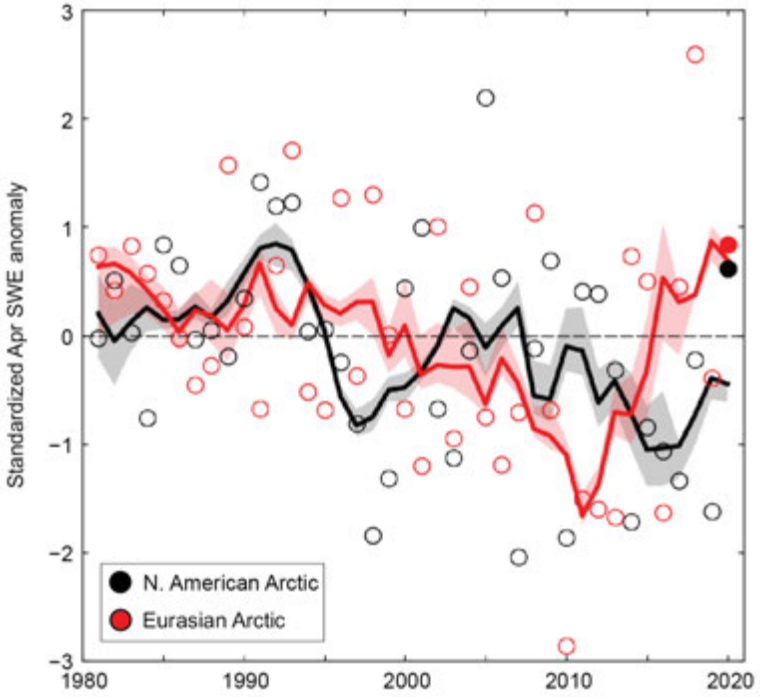

Fig. 5.17. Mean April snow water equivalent (SWE) anomalies for Arctic terrestrial areas calculated for North American (black) and Eurasian (red) sectors of the Arctic. Anomalies are relative to the 1981–2010 average and standardized (each observation differenced from the mean and divided by the standard deviation, and thus unitless). Filled circles are used to highlight 2020 anomalies. Solid black and red lines depict 5-year centered running means for North America and Eurasia, respectively, computed with 1982-83 values mirrored before 1981 and 2018-19 values mirrored after 2020. Spread among the running means for individual datasets is shown in shading. (Sources: MERRA2: Gelaro et al. 2017; GMAO 2015; temperature index model: Brown et al. 2003; Crocus: Brun et al. 2013; GlobSnow: Takala et al. 2011; www.globsnow.info.)

g. River discharge—R. M. Holmes, A. I. Shiklomanov, A. Suslova, M. Tretiakov, J. W. McClelland, L. Scott, R. G. M. Spencer, and S. E. Tank

The Arctic Ocean makes up approximately 1% of the global ocean by volume but receives more than 10% of global riverine discharge (McClelland et al. 2012). Consequently, terrestrial influences via river inputs are more pronounced in the Arctic Ocean than in other ocean basins. The rapid environmental change occurring in the Arctic is altering land-ocean interactions, which is also impacting coastal and ocean physics, chemistry, and biology. Because rivers naturally integrate the processes that are occurring throughout their watersheds, trends in the discharge and chemistry of Arctic rivers can also signal widespread terrestrial change including permafrost thaw and the amount or seasonality of precipitation (Rawlins et al. 2010; Holmes et al. 2013).

A long-term increase in Arctic river discharge has been well documented by time series data dating to the 1930s, providing compelling evidence of intensification of the Arctic hydrologic cycle (Peterson et al. 2002; McClelland et al. 2006). While there is still some uncertainty about what is driving this trend, increased atmospheric moisture transport may contribute to precipitation increases in some seasons (Zhang et al. 2013; Vihma et al. 2016). For example, there is a tendency toward increasing snowfall during autumn and early winter in western Siberia (Wegmann et al. 2015) and in the Canadian Arctic (Kopec et al. 2016). The changes in winter precipitation and correspondingly in snow accumulation can partly explain increases in spring river flows, which are mainly due to snowmelt (Shiklomanov et al. 2021). However, aggregated over the pan-Arctic and large river basins, annual precipitation, which is typically the most important water balance component for runoff generation, does not show a large enough change to support the observed increasing trend in annual river discharge (Shiklomanov et al. 2021).

River discharge was last included in the 2018 *State of the Climate* report. In the present report, river discharge values for 2020 and 2019 are presented to directly compare recent behavior in the

eight largest Arctic rivers. River data used in this analysis are available through the Arctic Great Rivers Observatory (arcticgreatrivers.org). Six of the rivers lie in Eurasia and two are in North America. Collectively, the watersheds of these eight rivers cover approximately 70% of pan-Arctic drainage area and account for the majority of river water inputs to the Arctic Ocean (Fig. 5.18). Discharge measurements for the six Russian rivers began in 1936, whereas discharge measurements did not begin until 1973 for the Mackenzie River and 1976 for the Yukon River in North America. These time series are used to establish a reference period (1981–2010) to compare and contextualize recent observations. Years are presented as "water years," 1 October–30 September, to more closely align with the annual cycle of hydrologic processes such that precipitation and runoff occur during the same time period. Thus, water year 2020 covers the period 1 October 2019 through 30 September 2020.

In 2020, the combined discharge of the eight largest Arctic rivers was 2625 km^3, which is 277 km^3 (~12%) greater than the 1981–2010 average (Table 5.1). Discharge from the two North American rivers combined was ~25% greater than their average, while discharge from the six Eurasian rivers combined was ~8% greater. Overall, 44% of the increase above the reference period for the eight rivers came from the two North American rivers, with the Mackenzie River being the largest contributor.

Fig. 5.18. Watersheds of the eight largest Arctic rivers that are featured in this analysis. Collectively, these rivers cover approximately 70% of the 16.8 million km^2 pan-Arctic watershed (indicated by the red boundary line). The red dots show the location of the discharge monitoring stations.

Table 5.1. Annual discharge (km^3) for the eight largest Arctic rivers for 2020 and 2019, compared to the 1981–2010 reference period. Red values indicate provisional data and are subject to modification until official data are published.

Year[1]	Yukon	Mackenzie	Pechora	S. Dvina	Ob'	Yenisey	Lena	Kolyma	Total
	North America		Eurasia						
2020	259	356	120	166	472	596	596	58	**2625**
2019	208	222	143	104	429	552	488	64	**2210**
Average (1981–2010)	**205**	**288**	**114**	**104**	**398**	**612**	**557**	**70**	**2348**

[1] Year refers to Water Year (1 October of the previous year to 30 September of the noted year)

High May–September discharge was largely responsible for the high annual discharge for the North American rivers in 2020 (Fig. 5.19). This can be explained by high snow accumulation and spring flood volume due to record high precipitation in February–April in the Mackenzie River basin and the wettest summer since 1985 based on analysis of precipitation aggregated over the Mackenzie and Yukon watersheds (Hersbach et al. 2020). For the Eurasian rivers, extraordinarily high May discharge (+3.1 std. dev. above average) was followed by extraordinarily low June discharge (–2.3 std. dev. below average; Fig. 5.19). The pattern observed for the Eurasian rivers is consistent with the observed high terrestrial snow cover and snow water equivalent during winter 2019/20, followed by a remarkably warm spring in 2020 (see sections 5b and 5f). This led to an early snowmelt, shifting more of the runoff period from June to May.

In contrast to 2020, 2019 was a relatively low-discharge year. The combined discharge of the eight largest Arctic rivers was 2210 km^3, which is 138 km^3 (~6%) less than the 1981–2010 average (Table 5.1). Discharge from the two North American rivers and the six Eurasian rivers was ~13% and ~4% less than average, respectively. Overall, 46% of the decrease below average came from the two North American rivers, with Mackenzie River discharge being well-below average and the Yukon River being slightly above. The remaining 54% of the decrease came from the six Eurasian rivers, with the Yenisey and Lena being the largest contributors. Relatively low 2019 Arctic river discharge is consistent with the observations of below-average snow water equivalent in April 2019 in both the Eurasian and North American Arctic (Mudryk et al. 2020b).

The 85-year time series available for the Eurasian Arctic rivers demonstrates an increase in their combined discharge. The positive linear trend across this entire time series indicates that the average annual discharge of Eurasian Arctic rivers is increasing by 2.5 km^3 per year. When data are considered from 1976 through 2020 (the length of the period of record for North American rivers), the average annual increase in discharge is 4.4 km^3 per year (Fig. 5.20). For the North American Arctic rivers, the average increase over the period of record is 1.0 km^3 per year. These observations indicate that Arctic river discharge continues to trend upward, providing powerful evidence for the intensification of the Arctic hydrologic cycle.

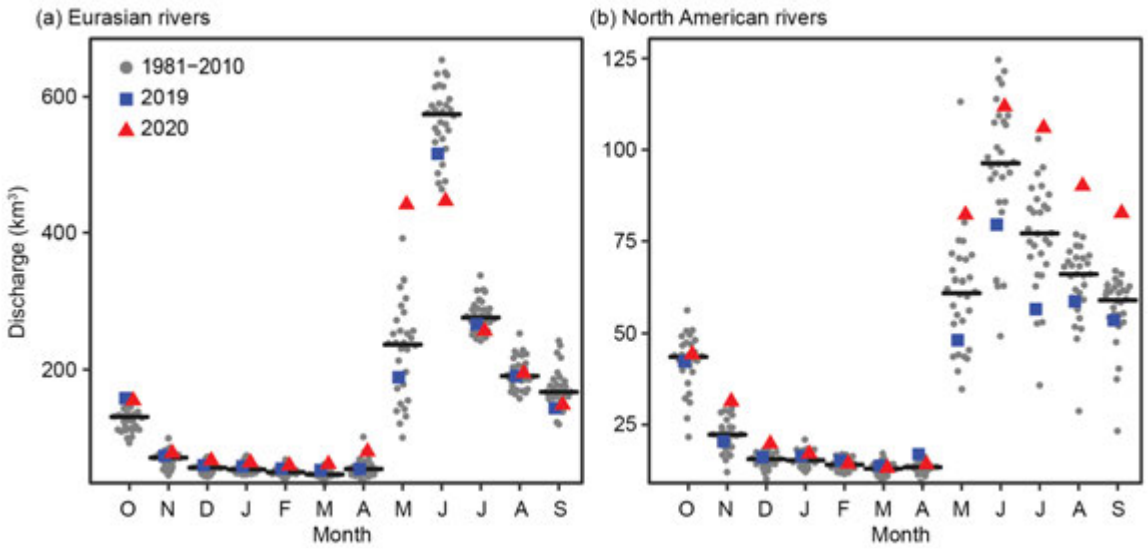

Fig. 5.19. Monthly discharge (km^3) in (a) Eurasian and (b) North American rivers for 2020 and 2019 compared to monthly discharge throughout the 1981–2010 reference period. The black bars indicate the average monthly discharge during the reference period.

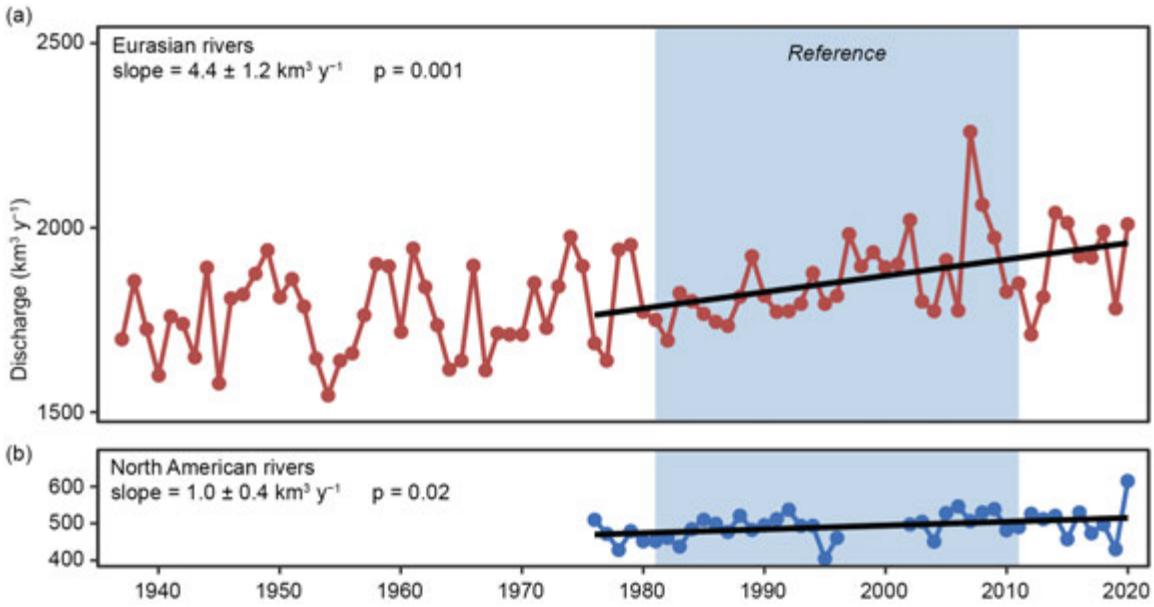

Fig. 5.20. Long-term trends in annual discharge ($km^3\ yr^{-1}$) for (a) Eurasian and (b) North American Arctic rivers. Gaps in the North American rivers time series span from 1996 through 2001 due to missing Yukon data from 1996 to 2001 and missing Mackenzie measurements in 1997 and 1998. Reported slopes are for the period 1976–2020. Note the different scales for the (a) Eurasian and (b) North American river discharge.

h. Permafrost—S. L. Smith, V. E. Romanovsky, K. Isaksen, K. E. Nyland, A. L. Kholodov, N. I. Shiklomanov, D. A. Streletskiy, L. M. Farquharson, D. S. Drozdov, G. V. Malkova, and H. H. Christiansen

Permafrost refers to Earth materials (e.g., bedrock, mineral soil, organic matter) that remain at or below 0°C for 2 years or longer and underlies extensive regions of the high-latitude landscape (Brown et al. 1997). Overlying the permafrost is the active layer, which thaws and refreezes annually. Permafrost, especially where it contains large volumes of ice, can play a critical role in the stability of Arctic landscapes. Warming of permafrost, active layer thickening, and ground ice melt cause changes in surface topography, hydrology, and landscape stability, thus having implications for the integrity of the Arctic infrastructure and ecosystems (Romanovsky et al. 2017; Bjella 2019). Changes in permafrost conditions can also affect the rate of release of carbon dioxide and methane to the atmosphere, with the potential to accelerate global warming (Schuur 2020).

Permafrost conditions respond to shifts in the surface energy balance through a combination of interrelated changes in ground temperature and active layer thickness (ALT). Ground temperatures fluctuate seasonally near the surface, while below the depth of seasonal temperature variation, ground temperature reflects longer-term changes in climate. Long-term changes in permafrost temperatures are driven by changes in air temperature (Romanovsky et al. 2017); however, permafrost temperature trends show local variability due to other important influences such as snow cover, vegetation characteristics, and soil moisture. Monitoring sites across the Arctic (Fig. 5.21) have been recording ground temperature in the upper 30 m for up to 5 decades, providing critical data on changes in permafrost stability. Observed changes in ALT relate to shorter-term (year-to-year) fluctuations in climate and are especially sensitive to changes in summer air temperature and precipitation.

Travel restrictions in 2020 due to COVID-19 limited data collection in some regions. For boreholes that have data loggers, the lack of site visits may only delay data acquisition with little impact on record continuity. For data collected manually, including ALT, there is a loss of data for 2020.

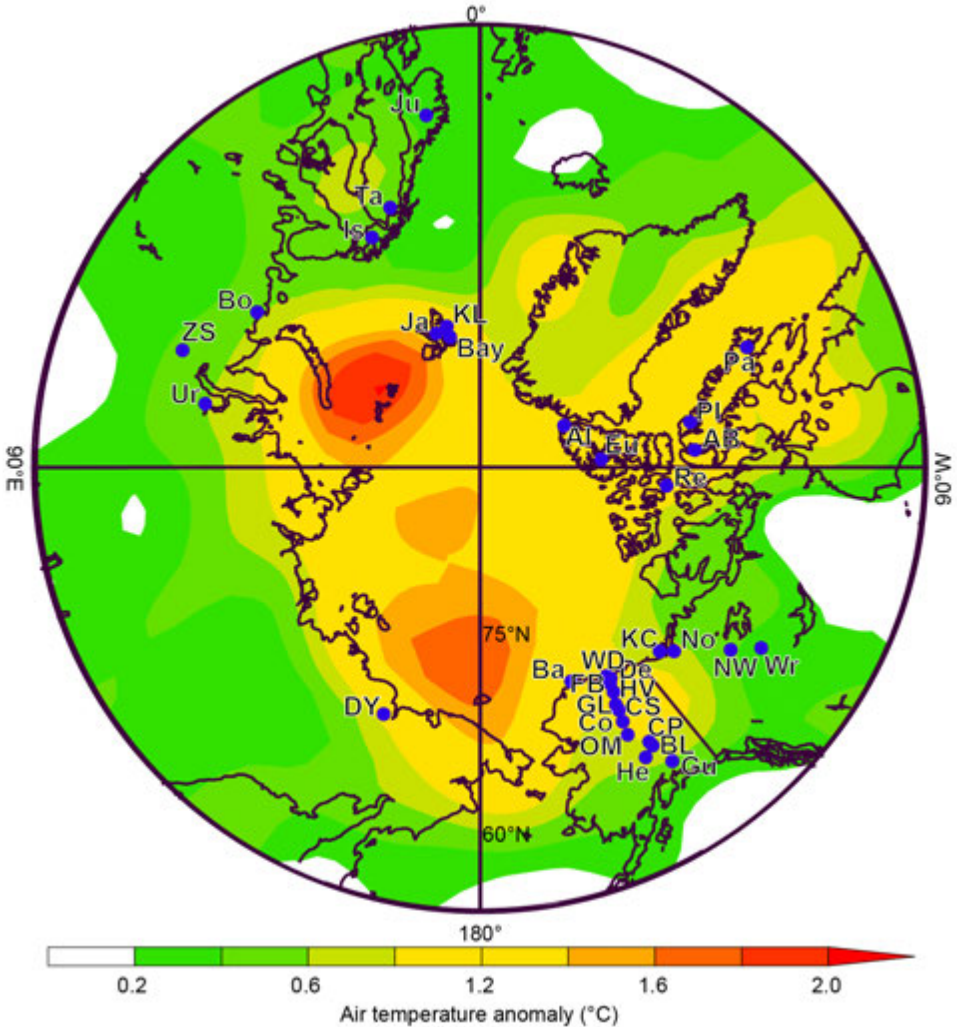

Fig. 5.21. Location of the permafrost temperature monitoring sites (for which data are shown in Fig. 5.22), superimposed on average surface air temperature anomalies (°C) during 2000–20 (with respect to the 1981–2020 mean) from the NCEP-reanalysis (Kalnay et al. 1996). Reanalysis data provided by the NOAA/ESRL Physical Sciences Division, Boulder Colorado (www.esrl.noaa.gov/psd/). See Table 5.2 for site names. Information about these sites is available at http://gtnpdatabase.org/, http://permafrost.gi.alaska.edu/sites_map, and https://www2.gwu.edu/~calm/.

1) Permafrost temperatures

Observed increases in permafrost temperatures since the 1980s were generally greater in colder permafrost at higher latitudes, where the largest increases in air temperature were observed (Figs. 5.21, 5.22). Permafrost temperatures in 2020 (where available) were higher than those observed in 2019 (except some sites in the Barents region) and the highest on record at a majority of the observation sites (Fig. 5.22; Table 5.2). In northern Alaska, for example, temperatures in 2020 were up to 0.1°C higher than in 2019 and in the Alaskan interior the 2020 temperature at one site (Old Man) was >0.1°C higher than in 2019, about 1.4°C higher than in 1985 (Figs. 5.22a,b). At Alert in the Canadian High Arctic, permafrost temperatures were also higher in 2020, and 1.4°C higher than at the start of monitoring in 1978 (Fig. 5.22c).

At some sites, recent increases in the rate of permafrost warming have also been observed (Fig. 5.22; Table 5.2). In the Canadian High Arctic, warming rates for 2000–20 were greater than that for the entire 40-year record (Fig. 5.22c; Table 5.2). Throughout the Arctic, the response of permafrost with temperatures close to 0°C (i.e., warm permafrost sites) is slower (generally <0.3°C decade^{-1}) due to latent heat effects related to melting ground ice. Warming at some sites with cold continuous permafrost, however, has been more rapid. For example, in the Beaufort-Chukchi region, permafrost temperatures in northern Alaska have increased by 0.35° to 0.81°C decade^{-1}

(Fig. 5.22a; Table 5.2). Over a shorter record in northeastern Siberia, permafrost temperatures have increased by 0.4°C decade^{-1}, similar to the twenty-first century rate for northern Alaska (0.4° to 0.7°C decade^{-1}).

In the Nordic region, permafrost warming reported by Isaksen et al. (2011) and Etzelmüller et al. (2020) is continuing (Fig. 5.22d). The longest records in high-Arctic Svalbard (Janssonhaugen) and in the discontinuous permafrost regions of Scandinavia (Juvvasshøe) indicate ground temperatures during 2020 were the highest measured since the late 1990s. The highest warming rate is observed on Svalbard at the Janssonhaugen site (Table 5.2), where cold permafrost has warmed by 0.7°C per decade since 1998, similar to the higher latitude sites in other regions. Lower warming rates are observed in the warm discontinuous permafrost of Scandinavia (e.g., Iskoras), similar to warm permafrost in Russia (e.g., Bolvansky #56) and northwestern North America (Figs. 5.22b,d).

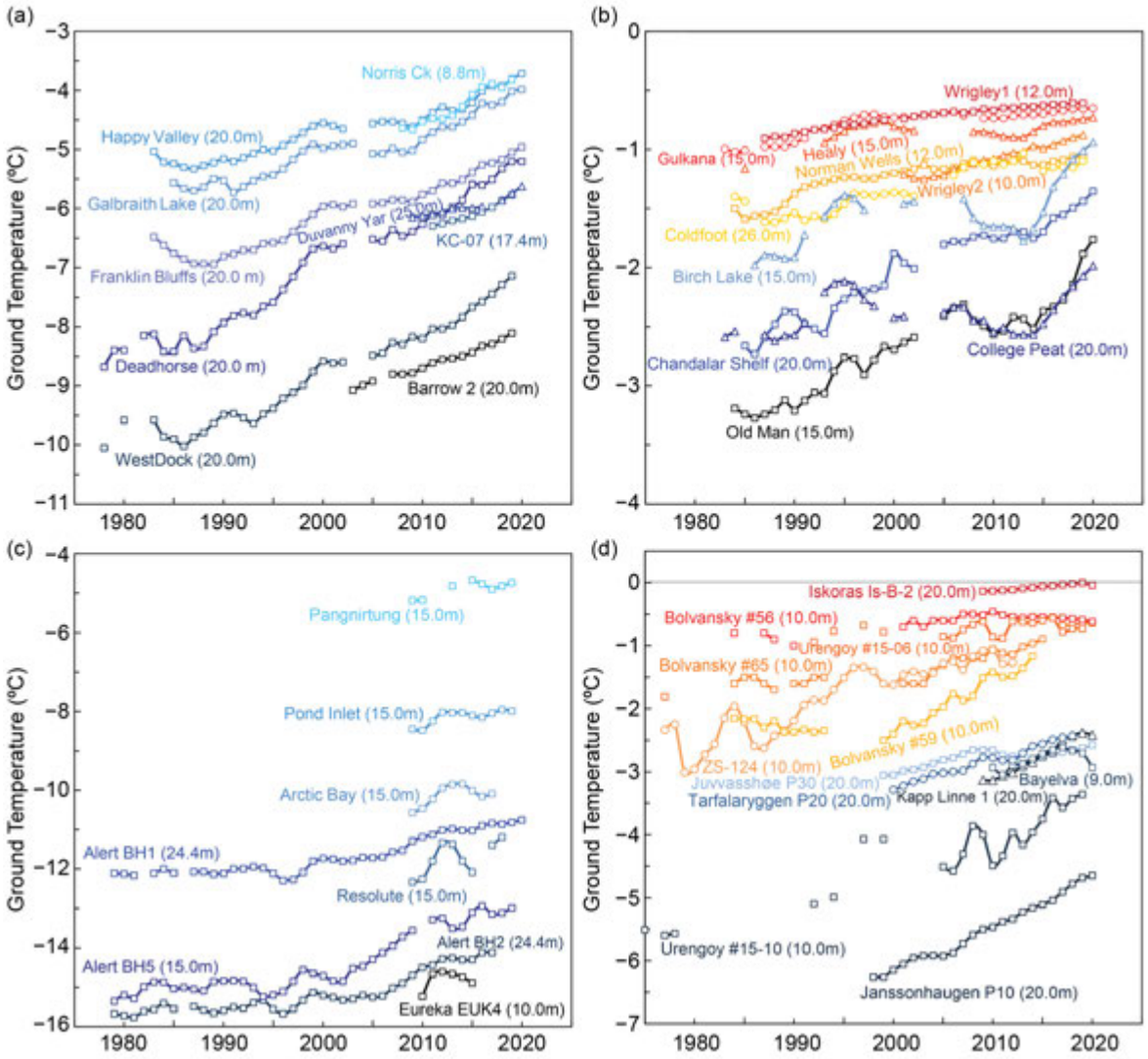

Fig. 5.22. Time series of mean annual ground temperature (°C) at depths of 9–26 m below the surface at selected measurement sites that fall roughly into priority regions of the Adaptation Actions for a Changing Arctic Project (see Romanovsky et al. 2017): (a) cold continuous permafrost of northwestern North America and northeastern East Siberia (Beaufort–Chukchi region); (b) discontinuous permafrost in Alaska and northwestern Canada; (c) cold continuous permafrost of eastern and High Arctic Canada (Baffin Davis Strait); (d) continuous to discontinuous permafrost in Scandinavia, Svalbard, and Russia/Siberia (Barents region). Temperatures are measured at or near the depth of zero annual amplitude where the seasonal variations of ground temperature are less than 0.1°C. Note differences in *y*-axis value range. Borehole locations are shown in Fig. 5.21. Data are updated from Christiansen et al. 2010; Romanovksy et al. 2020; Smith et al. 2019; Ednie and Smith 2015; Boike et al. 2018.

Table 5.2. Rate of change in mean annual ground temperature (°C decade^{-1}) for permafrost monitoring sites shown in Fig. 5.21. For sites where measurements began prior to 2000, the rate of change for the entire available record and the period after 2000 are provided. The periods of record are shown in parenthesis below the rates of change. The names of the stations with record high temperatures in 2020 are shown in red. * denotes sites not reporting in 2020.

Subregions	Sites	Entire Record	Since 2000
Beaufort-Chukchi Region			
North of East Siberia	Duvany Yar (DY)	NA	+0.44 (2009–20)
Alaskan Arctic plain	West Dock (WD)*, Deadhorse (De), Franklin Bluffs (FB), Barrow (Ba)*	+0.40 to +0.81 (1978– 2020)	+0.49 to +0.74 (2000–20)
Northern foothills of the Brooks Range, Alaska	Happy Valley (HV), Galbraith Lake (GL)	+0.35 to +0.44 (1983–2020)	+0.44 to +0.48 (2000–20)
Northern Mackenzie Valley	Norris Ck (No)*, KC-07(KC)*	NA	+0.6 to +0.8 (2008–19)
Discontinuous Permafrost Alaska and NW Canada			
Southern foothills of the Brooks Range, Alaska	Coldfoot (Co)*, Chandalar Shelf (CS), Old Man (OM)	+0.08 to +0.39 (1983–2020)	+0.14 to +0.41 (2000–20)
Interior Alaska	College Peat (CP), Birch Lake (BL), Gulkana (Gu), Healy (He)	+0.09 to +0.30 (1983–2020)	+0.04 to +0.26 (2000–20)
Central Mackenzie Valley	Norman Wells (NW)*, Wrigley (Wr)*	Up to +0.1 (1984–2019)	<+0.1 to +0.2 (2000–19)
Baffin Davis Strait Region			
Baffin Island	Pangnirtung (Pa)*, Pond Inlet (PI)*	NA	+0.4 (2009–19)
High Canadian Arctic	Resolute (Re)*	NA	+0.7 (2009–18)
High Canadian Arctic	Alert (Al) @15m* Alert (Al) @24m	+0.6 +0.4 (1979 – 2020)	+1.1 +0.6 (2000–20)
Barents Region			
North of West Siberia	Urengoy 15-06* and 15-08 (Ur)*	+0.20 to +0.48 (1974–2019)	+0.08 to +0.77 (2005–19)
Russian European North	Bolvansky 56, and 65 (Bo)	+0.05 to +0.26 (1984–2020)	+0.04 to +0.48 (2001–20)
Svalbard	Janssonhaugen (Ja), Bayelva (Bay), Kapp Linne 1 (KL)	+0.7 (1998–2020)	+0.6 to +0.8 (2000–20)
Northern Scandinavia	Tarfalarggen (Ta), Iskoras Is-B-2 (Is)	NA	+0.1 to +0.5 (2000–20)
Southern Norway	Juvvasshøe (Ju)	+0.2 (1999–2020)	+0.2 (2000–20)

2) Active layer thickness

With the exception of the Mackenzie Valley in northwest Canada (at which thaw tubes are used), active layer data reported here were measured by mechanical probing across grids varying from 1 ha to 1 km^2 in size and representative of regional landscapes (Shiklomanov et al. 2012). Increases in ALT are observed over the period of record in some regions but for other regions trends are less evident.

The average ALT (0.46 m) for 12 North Slope of Alaska sites reporting in 2020 was 0.015 m below the 2003–12 mean for the same 12 sites and 0.06 m lower than in 2019 (Fig. 5.23). Observers from local communities were able to make measurements so that some 2020 ALT data were collected. Interior Alaska continues to exhibit pronounced ALT increases over the last 25 years, with a new record average of 0.92 m in 2020.

Sites in Svalbard displayed similar ALT values to the two previous years, values that were approximately 0.13 m above the 2003–12 mean (Fig. 5.23). ALT for Greenland in 2020 was similar to that in 2019, 0.08 m above the 2003–12 mean (Strand et al. 2020).

Sites in West and East Siberia reported increased ALT in 2020, continuing the general trend, with the average ALT (1.46 m) for West Siberia being a new record maximum for the observation period (Fig. 5.23). Significant ALT reduction was reported in 2020 for sites in the Russian European North and Chukotka, but these values are based on fewer sites and may not be representative of regional trends previously reported (Abramov et al. 2019; Vasiliev et al. 2020).

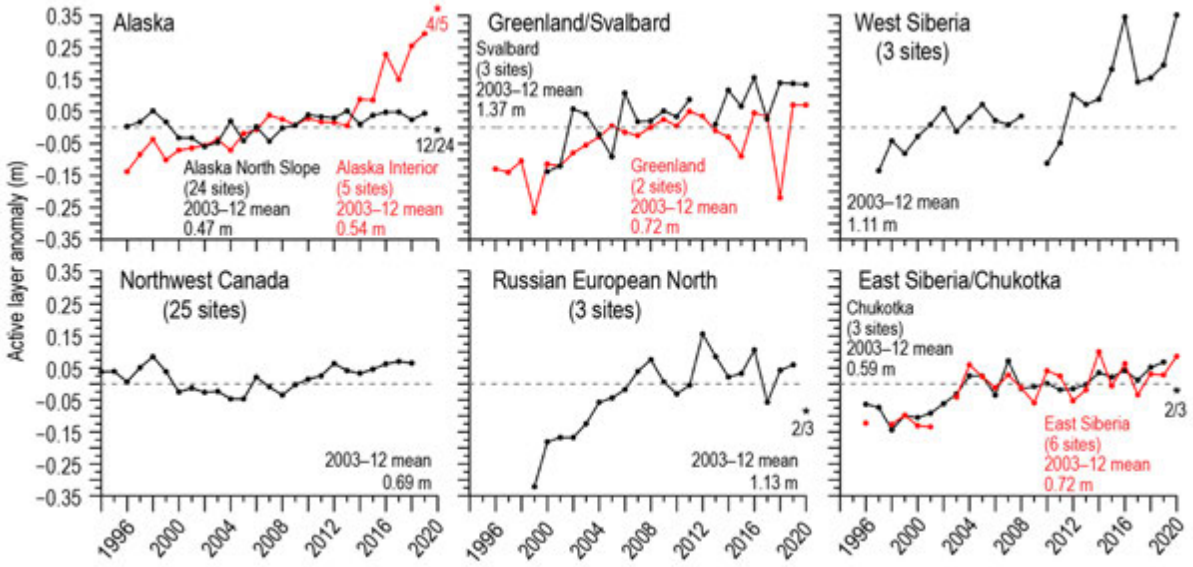

Fig. 5.23. Long-term active layer thickness anomalies in six different Arctic regions as observed by the Circumpolar Active Layer Monitoring (CALM) program. The data are shown as annual anomalies (m) relative to the mean value for the reference period 2003–12. Positive and negative anomaly values indicate the active layer is thicker or thinner than the 10-year mean values, respectively. The number of sites varies by region (numbers provided on figure), because only sites with >20 years of continuous thaw depth observations from the end of the thaw season were included. Asterisks on the figure represent 2020 data, as observations from fewer sites (number provided beside asterisks) were possible due to pandemic-related restrictions. Site-specific data are available at www2.gwu.edu/~calm/.

i. Tundra greenness—G. V. Frost, M. J. Macander, U. S. Bhatt, H. E. Epstein, L. T. Berner, J. W. Bjerke, B. C. Forbes, S. J. Goetz, M. J. Lara, T. Park, G. K. Phoenix, M. K. Raynolds, H. Tømmervik, and D. A. Walker

Occupying Earth's northernmost lands, the Arctic tundra biome is a focal point of global environmental change because vegetation and underlying permafrost soils are strongly influenced by warming air temperatures and interactions with sea ice loss in the adjacent Arctic Ocean (Lawrence et al. 2008; Bhatt et al. 2010; Serreze and Barry 2011; sections 5b–d). One of the most striking consequences of the Arctic's warming climate has been an increase in the productivity ("greenness") of tundra vegetation, which is largely governed by summer temperature (Berner et al. 2020; Bjorkman et al. 2020). Tundra greenness has been monitored by Earth-observing satellites since 1982 and a growing constellation of spaceborne sensors provide increasingly detailed observations of Arctic ecosystems.

The spaceborne record of global vegetation productivity began in late 1981 using the Advanced Very High Resolution Radiometer (AVHRR), a sensor that collects daily observations and continues to operate onboard polar-orbiting satellites today. The long-term dataset reported here is the Global Inventory Modeling and Mapping Studies 3g V1.2 dataset (GIMMS-3g+), which is based on corrected and calibrated AVHRR data with a spatial resolution of about 8 km (Pinzon and Tucker 2014). At the time of this writing, however, processed GIMMS-3g+ data are available only through the 2019 growing season. Therefore, we also report observations from the Moderate Resolution

Imaging Spectroradiometer (MODIS), a more modern sensor with a higher spatial resolution of 500 m that became operational in 2000. Both AVHRR and MODIS monitor vegetation productivity using the Normalized Difference Vegetation Index (NDVI), a spectral dimensionless metric of vegetation productivity that exploits the unique way in which green vegetation reflects light in the red and near-infrared wavelengths. Here we summarize the GIMMS-3g+ and MODIS records for Maximum NDVI (MaxNDVI), the peak yearly value that is strongly correlated with the biomass of aboveground vegetation during midsummer (Raynolds et al. 2012). For MODIS, we computed MaxNDVI from daily Nadir Bidirectional Reflectance Distribution Function Adjusted Reflectance data (MCD43A4, version 6; Schaaf 2020).

The GIMMS-3g+ and MODIS records both indicate that MaxNDVI has increased across most of the circumpolar Arctic during 1982–2019 and 2000–20, respectively (Figs. 5.24a,b). Although the two datasets consider different periods, several Arctic regions stand out as change "hotspots" in both records. In North America, greening has been strongest in northern Alaska and mainland Canada, while trends have been flat or negative ("browning") in parts of the Canadian Arctic Archipelago. In Eurasia, strong greening has occurred in the Russian Far East (Chukotka), but browning is evident in the East Siberian Sea sector and portions of the Taymyr Peninsula. Trends in northwestern Siberia and the European Arctic, however, are somewhat mixed for both time periods. Regional differences in Arctic greenness highlight that ecosystem responses to climate change are also influenced by the local properties of sea ice, permafrost, seasonal snow, soil composition and moisture, disturbance processes, wildlife, and human activities (Buchwal et al. 2020; Skarin et al. 2020; Epstein et al. 2021; Kemppinen et al. 2021; Kropp et al. 2021).

The MODIS MCD43A4 record complements the GIMMS-3g+ dataset for the 21-year period since 2000 and provides observations for the 2020 growing season. The mean circumpolar MaxNDVI value in 2020 was by far the highest in the MODIS record (3.4% higher than the previous high set in 2012). Circumpolar MaxNDVI increased 4.0% from the 2019 value; increases from the previous year were larger for the North American Arctic (5.6%) than for Eurasia (2.0%). The overall trend in circumpolar MaxNDVI remains strongly positive and circumpolar values have exceeded the 21-year mean in nine of the last 10 growing seasons (Fig. 5.25). The GIMMS-3g+ record also indicates increasing mean circumpolar MaxNDVI for both the full record (1982–2019) and the period of overlap with MODIS (2000–2019).

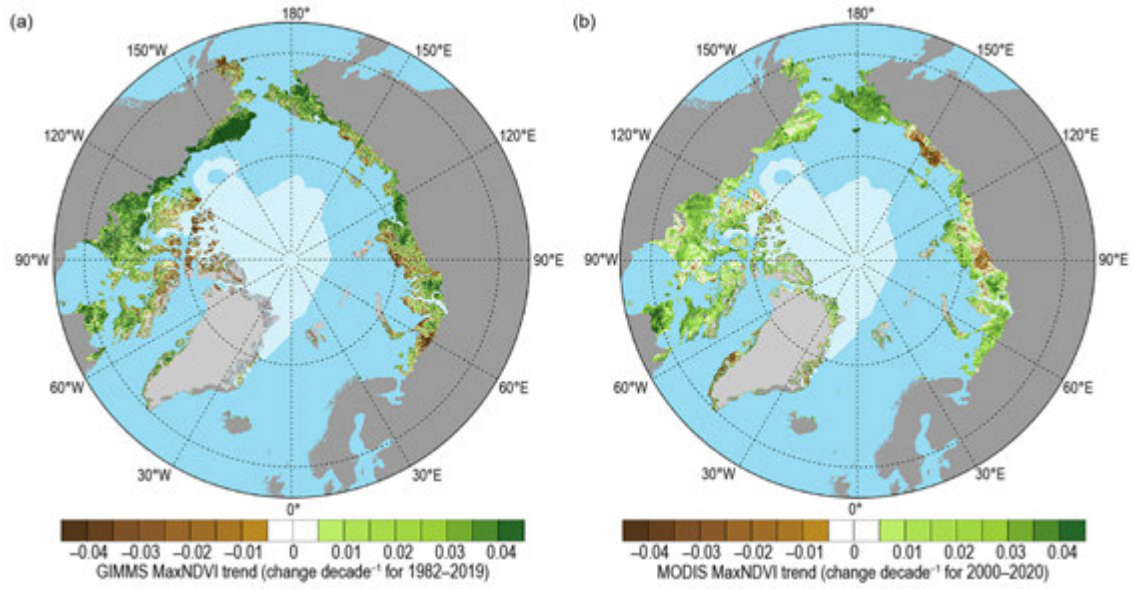

Fig. 5.24. Magnitude of the MaxNDVI trend calculated as the change decade^{-1} over a least squares, linear fit trend line for (a) 1982–2019 based on the GIMMS-3g+ dataset, and (b) 2000–20 based on the MODIS MCD43A4 dataset. GIMMS-3g+ data for 2020 were not available for this report due to data-processing requirements.

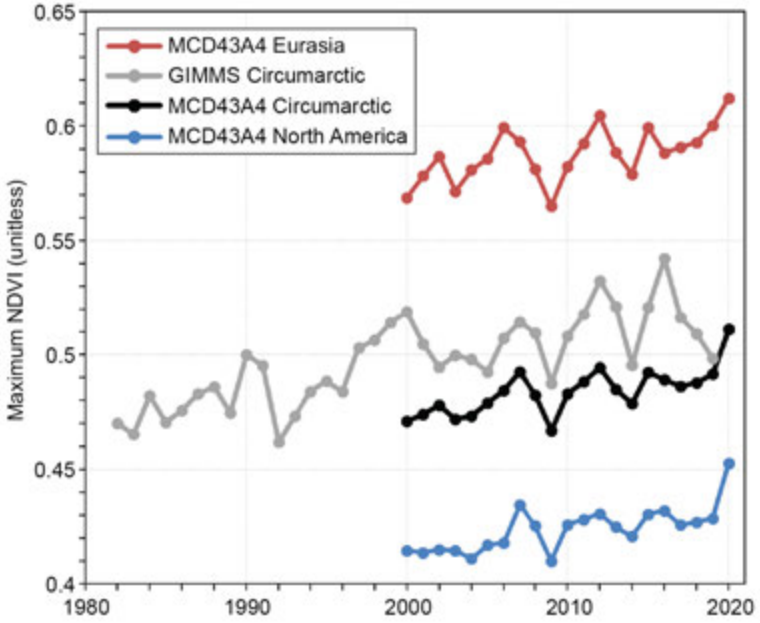

Fig. 5.25. Time series of MaxNDVI from the MODIS MCD43A4 (2000–20) dataset for the Eurasian Arctic (red), North American Arctic (blue), and the circumpolar Arctic (black), and from the long-term GIMMS-3g+ (1982–2019) dataset for the circumpolar Arctic (in gray).

Recent remote sensing- and field-based studies provide context for understanding changes in vegetation and ground conditions that correlate with MaxNDVI trends. Many site-specific studies have detected increased growth and expansion of tundra shrubs, such as birches (*Betula*), willows (*Salix*), and alders (*Alnus*; Andreu-Hayles et al. 2020; Liljedahl et al. 2020; Shevtsova et al. 2020). Spaceborne observations also indicate changes in growing season length and the timing of phenological events such as spring snowmelt (section 5f), vegetation green-up, and autumn senescence. For example, a recent analysis of vegetation phenology using MODIS NDVI data revealed that the 2020 Arctic growing season began and ended on average over 5 days earlier and 2 days later, respectively, relative to the 2000–10 baseline (section 2h4). The start of the 2020 growing season was particularly early in the Eurasian Arctic, where green-up occurred about 9 days earlier than average due to warm spring temperatures and early snowmelt. In Svalbard, Vickers et al. (2020) evaluated snow cover using MODIS data and concluded that the length of the growing season increased by 4.2 days decade^{-1} since 2000. Moreover, a study of MaxNDVI over central Svalbard from 1986 to 2015 linked local greening to increasing temperature; however, the pace of greening was slower during the second half of the study period, which may be attributed to more frequent extreme winter warming events that can damage vegetation (Vickers et al. 2016).

Die-back or removal of vegetation can also be caused by landscape disturbances, including wildfire (Heim et al. 2021; Sidebar 5.1) and permafrost thaw (Verdonen et al. 2020; Chen et al. 2021; Swanson 2021; section 5h), as well as herbivore and pest outbreaks (Lund et al. 2017; Prendin et al. 2020). Severe event-driven browning has led to major reductions in carbon dioxide uptake by tundra plants in the European Arctic (Treharne et al. 2020). While Arctic warming is likely to continue to drive greening, drivers of browning are also increasing in frequency (Landrum and Holland 2020; Myers-Smith et al. 2020; Wu et al. 2020), highlighting the emergence of increased variability as a component of Arctic climate change.

j. Ozone and ultraviolet radiation—G. H. Bernhard, V. E. Fioletov, J.-U. Grooß, I. Ialongo, B. Johnsen, K. Lakkala, G. L. Manney, R. Müller, and T. Svendby

Past emissions of man-made chlorine-containing substances have caused substantial chemical depletion of ozone in the stratosphere (WMO 2018). The resulting ozone loss led to increases of ultraviolet (UV) radiation at Earth's surface with adverse effects on human health and the

environment (EEAP 2019; Neale et al. 2021). The chemical destruction of polar ozone occurs within a cold stratospheric cyclone known as the polar vortex, which forms over the North Pole every year during winter (WMO 2018). The polar vortex between December 2019 and March 2020 was the strongest on record since the start of satellite observations in 1979/80 (Lawrence et al. 2020) and affected stratospheric ozone concentrations in the Northern Hemisphere (NH) until August 2020.

1) Ozone

Chemical processes that drive ozone depletion in the polar stratosphere are initiated at temperatures below about 195 K (–78°C) at altitudes of approximately 15 to 25 km. These low temperatures lead to the formation of polar stratospheric clouds (PSCs), which act as a catalyst to transform inactive forms of chlorine-containing substances into active, ozone-destroying chlorine species. Temperatures were low enough for PSC formation by mid-November 2019, earlier than in any previous year since the start of observations by the *Aura* Microwave Limb Sounder (MLS) in 2004 (Manney et al. 2020; DeLand et al. 2020). Temperatures in the lower stratosphere remained conducive to PSC existence until 25 March 2020, which is about 1 month longer than typical (Lawrence et al. 2020). The number of days with temperatures low enough for sustaining PSCs was the highest since at least 1980 (Lawrence et al. 2020).

Because of the exceptionally strong, cold, and persistent stratospheric polar vortex, the potential for chemical ozone depletion was the highest since at least 2004. The MLS measurements near 16 km (the approximate altitude where most ozone loss typically occurs) show chlorine activation starting in mid-November 2019 and ozone declining by December (Fig. 5.26). From February 2020 onward, ozone concentrations were the lowest in the MLS record and remained below past measurements (2004–19) until May, exceeding the ozone loss observed in the previous record years of 2010/11 and 2015/16.

The low ozone concentrations in the lower stratosphere during winter/spring 2019/20 led to exceptionally small Arctic total ozone columns (TOC; i.e., ozone amounts integrated from the surface to the top of the atmosphere) between January and July 2020. The TOCs in February, March, and April 2020 averaged over the polar cap (latitudes ≥63°N) were the lowest of the satellite record starting in 1979 (Lawrence et al. 2020), with near-record lows also for January, May,

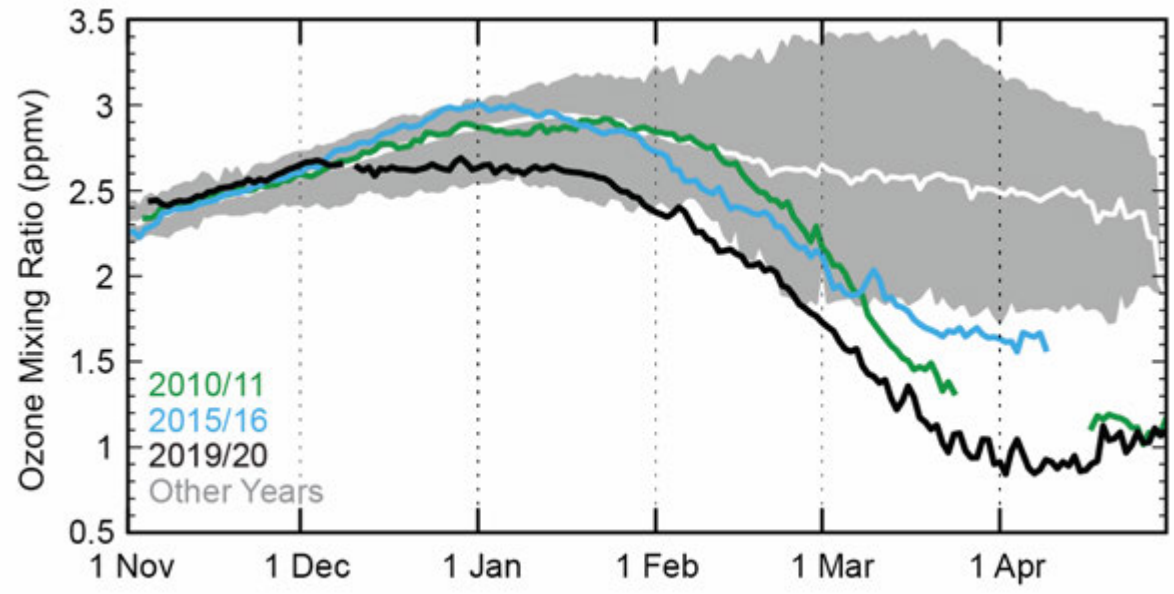

Fig. 5.26. Average ozone concentrations (expressed as ozone mixing ratio in ppmv) at an altitude of ~16 km for the area bounded by the polar vortex measured by *Aura* MLS. Data from 2019/20 (black), 2010/11 (green), and 2015/16 (cyan) are compared with the average (solid white) and minimum/maximum range (gray shading) from 2004/05 to 2018/19, excluding 2010/11 and 2015/16. The gap in the 2010/11 record is due to missing data; the 2015/16 record is foreshortened by the early vortex breakup that year (Manney and Lawrence 2016).

June, and July. While chemical ozone destruction ceased at the beginning of April 2020, TOCs over the NH remained depressed between May and August as ozone-depleted polar air mixed with air from midlatitudes.

Figure 5.27 focuses on the variation in TOC between 1979 and 2020 for March alone because March is the month with the largest potential for chemical ozone depletion in the Arctic (WMO 2018). Instead of illustrating the mean polar cap TOC discussed above, Fig. 5.27 shows the March minimum of the daily mean TOC within an area that encloses the polar vortex and is surrounded by the 63°N contour of "equivalent latitude" (Butchart and Remsberg 1986). In March 2020, the minimum Arctic daily TOC was 295 Dobson units (DU), which was the lowest value since the start of satellite observations in 1979 and 21% (79 DU) below the average of the observational record (374 DU).

Spatial deviations of monthly average TOCs from past (2005–19) averages (Fig. 5.28a) were estimated from Ozone Monitoring Instrument (OMI) measurements. In March 2020, TOC anomalies as large as –40% and exceeding 3 standard deviations were measured over northern Canada and the adjacent Arctic Ocean. In April, TOC anomalies up to –35% and exceeding 3 standard deviations were observed for virtually all areas north of 60°N. During the breakup of the polar vortex in May (Manney et al. 2020), areas with abnormally low (>3 std. dev.) TOCs still persisted over Siberia.

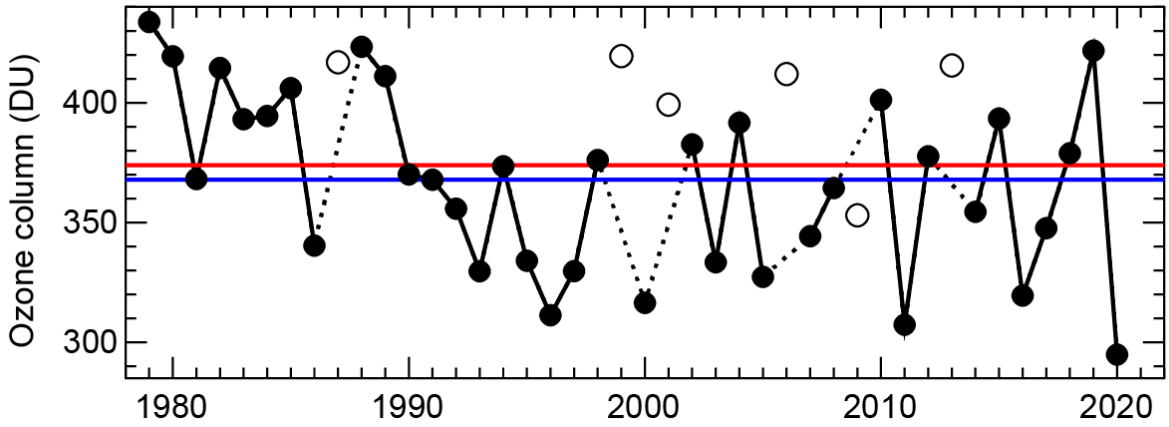

Fig. 5.27. Minimum of the daily average total ozone column (Dobson units, DU) for Mar poleward of 63°N equivalent latitude (Butchart and Remsberg 1986). Open circles represent years in which the polar vortex was not well-defined in Mar, resulting in relatively high values owing to mixing with lower latitude air masses and a lack of significant chemical ozone depletion. Red and blue lines indicate the average total ozone column for 1979–2019 and 2005–19, respectively. Ozone data for 1979–2016 are based on the combined total column ozone database version 3.4 produced by Bodeker Scientific (www.bodekerscientific.com/data/total-column-ozone). Ozone data for 2017–20 are from the OMI. The graph is adapted from Müller et al. (2008) and WMO (2018), updated using ERA5 reanalysis data (Hersbach et al. 2020) for determining equivalent latitude.

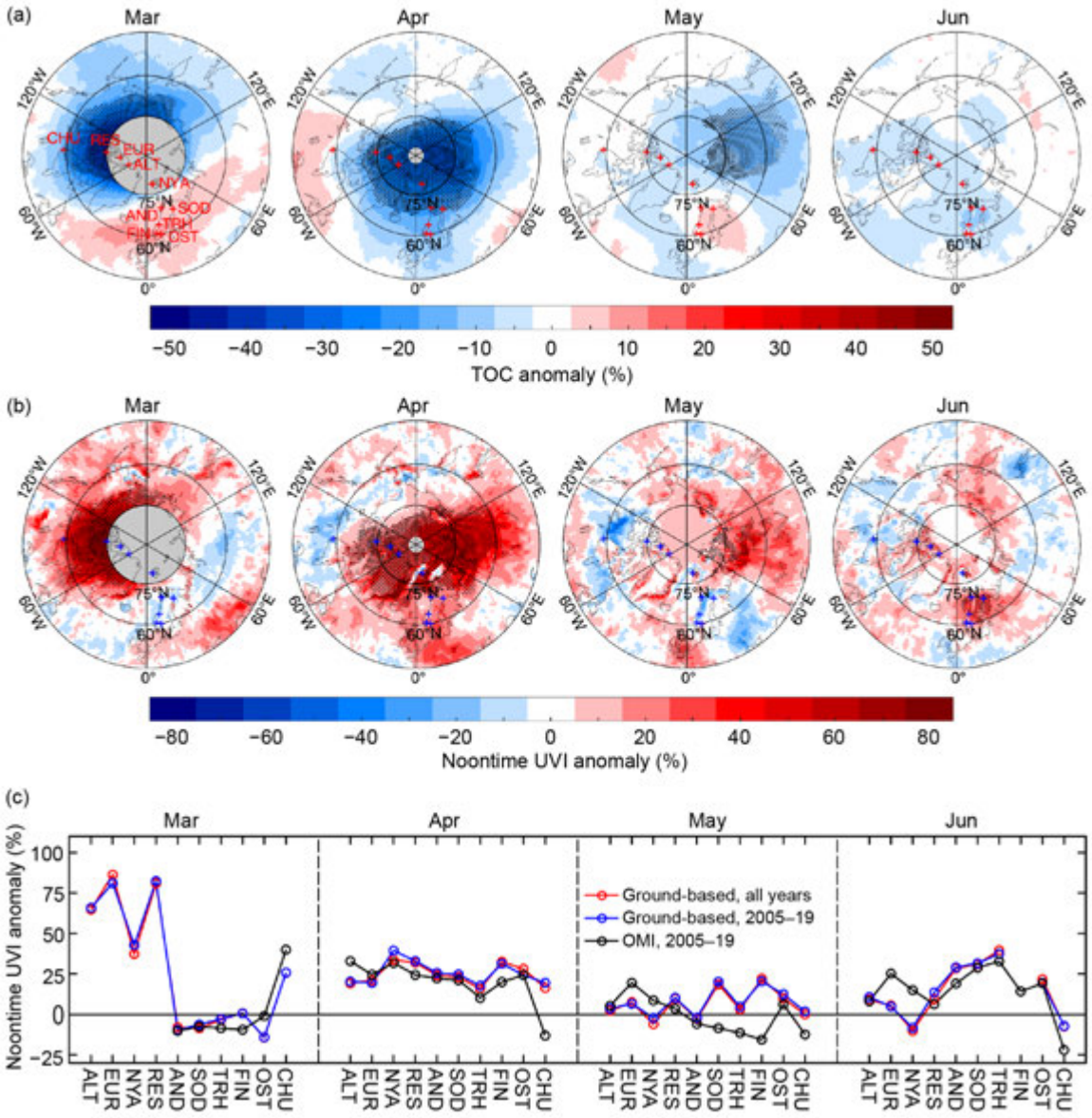

Fig. 5.28. Monthly mean anomaly maps of (a) total ozone column (%) and (b) noontime UV index (%) for Mar, Apr, May, and Jun 2020 relative to 2005–19 means. Stippling indicates pixels where anomalies exceed 3 std dev. Gray-shaded areas centered at the North Pole in the maps for Mar and Apr indicate latitudes where no Ozone Monitoring Instrument (OMI) data are available because of polar darkness. Locations of ground stations are indicated by crosses in every map, with labels added to the first map. Maps are based on the OMTO3 Level 3 total ozone product (Bhartia and Wellemeyer 2002). (c) Anomalies of monthly means of the noontime UV index (%) for 2020 derived from measurements at 10 ground stations (north to south along *x*-axis) relative to all years with available data (red) and 2005–19 (blue). The black datasets indicate anomalies for the same stations derived from OMI measurements (b) relative to 2005–19. Site acronyms are ALT: Alert (83°N); EUR: Eureka (80°N); NYA: Ny-Ålesund (79°N); RES: Resolute (75°N); AND: Andøya (69°N); SOD: Sodankylä (67°N); TRH: Trondheim (63°N); FIN: Finse (61°N); OST: Østerås (60°N); and CHU: Churchill (59°N). Figure adapted from Bernhard et al. (2020).

2) Ultraviolet radiation

UV radiation is quantified with the UV index (UVI), which measures the ability of UV radiation to cause erythema (sunburn) in human skin (WHO 2002). In addition to its dependence on TOC, the UVI depends on the sun angle, clouds, aerosols, and surface albedo (Weatherhead et al. 2005). In the Arctic, the UVI scale ranges from 0 to about 7; UVI values north of 80°N remain below 3.

On several days in 2020, UVIs observed by ground-based radiometers at 10 sites distributed across northern Canada and Europe exceeded historical (2005–19) means by more than 75% (Bernhard et al. 2020). At the Canadian sites, these means were surpassed by more than 6 standard deviations. Monthly mean UVIs were 75% higher than normal in northern Canada in March

2020 and elevated by about 25% at all sites in April 2020 (Bernhard et al. 2020). These large relative anomalies occurred early in the year when the Sun is still low in the sky. Therefore, UVI increases remained small in absolute terms and did not exceed typical summertime UVI values under clear skies.

Figure 5.28b quantifies spatial differences in monthly average noontime UVIs from past (2005–19) averages based on measurements by OMI. Areas with high UVIs roughly match areas with low TOCs (Fig. 5.28a), but UVI anomalies have larger spatial variability because of their added dependence on clouds. In March 2020, monthly average UVI anomalies over the Canadian Arctic and the adjacent Arctic Ocean ranged between 30% and 70%, often exceeding 3 standard deviations. In April 2020, UVI anomalies were positive over a vast area, including northern Canada, Greenland, northern Europe, and Siberia. The maximum anomaly was 78% and anomalies exceeded 3 standard deviations almost everywhere north of 70°N. In May 2020, UVI anomalies of up to 60% and exceeding 3 standard deviations were measured over Siberia. The UVIs in June were elevated by up to 30% over parts of Norway, Sweden, and Finland, resulting from a combination of negative TOC anomalies (Fig. 5.28a) and unusually fair weather with several cloudless days (Bernhard et al. 2020). Ground-based measurements generally confirm UVI anomalies derived from satellite data (Fig. 5.28c).

Sidebar 5.2: Assessing 15 years of Arctic Observing Network contributions to tracking key Arctic climate variables—H. SHAPIRO, S. STARKWEATHER, S. VAKHUTINSKY, AND M.L. DRUCKENMILLER

Introduction and methods

Western science and Indigenous observations in the Arctic have revealed dramatic environmental changes, with potentially catastrophic consequences to Arctic and global ecosystems and society (e.g., Thoman et al. 2020; Slats et al. 2019). However, gaps and structural challenges in observing systems have hampered scientific understanding of these changes (Lee et al. 2019; Murray et al. 2018; AOS EOC 2018). Among other factors, Arctic observing systems face extreme physical conditions, limited regional infrastructure, and a patchwork of jurisdiction and policy approaches across eight Arctic nations and other observing partners. These challenges, coupled with urgent societal and scientific needs, led to the vision of an internationally-coordinated Arctic Observing Network (AON; NRC 2006) with sustained, integrated observations targeting the most critical aspects of a rapidly changing Arctic. Tracking, evaluating, and continuously improving the AON is a critical effort. Annual Arctic Report Card (ARC; https://arctic.noaa.gov/Report-Card/) assessments provide a 15-year record (2006–20) of shifting Arctic conditions with consistent studies on seven key variables, identified since 2007 as "Vital Signs" reports (topics listed in Table SB5.1; Thoman et al. 2020). These Vital Signs are annually mirrored in the BAMS *State of the Climate* Arctic Chapter's headings and provide a substantial foundation for a retrospective analysis exploring how the AON's support of Arctic indicator variables has changed during 2007 to 2020.

This study examines the quality of the observation and model-derived data products used for each ARC Vital Sign report to establish the annual status of key variables (e.g., terrestrial snow cover extent) in the context of their long-term trends. Authors from each Vital Sign validated the catalog of data products and independently rated their performance. A value tree assessment (VTA) was used to systematically link observational inputs (i.e., satellite or in situ measurements) to the value-added data product and application outputs they support and assess their performance (IDA 2017). The VTA methodology weighs the relative contributions of individual observing systems and data products, while revealing linkages throughout the system. VTA can also reveal where value is limited or terminates due to technical hurdles. VTA provides funders and policymakers with evidence to strategically fill observing gaps and remove impediments to value propagation. For example, these methodologies were employed in the national assessment of civil earth observations called for by Congress (OSTP 2014) and are related to methods used within USGS, NOAA, and other agencies to evaluate existing observing systems and identify needs (USGS 2019).

Findings

Since 2007, reports on these ARC Vital Sign indicators employed more than 100 different data products to support key findings of Arctic change. In 2020, the 27 data products employed were derived from gridded products based on satellite or blended analyses (14), modeled products (8), and in situ networks (5). Reanalyses and other model products depend on a complex set of observational inputs, the full accounting of which exceeds the scope of this analysis. The need for multinational and interagency support for the systems that underpin Arctic indicator reports is evident in the mix of products, which are developed for both operational (8) and research (19) purposes and supported by the United States, Canada, Japan, and European nations. To support transparency around the key findings of the 2020 ARC, a searchable online catalog of the 2020 data products is now available on the NSF Arctic Data Center website (https://arcticdata.io/catalog/portals/reportcard).

The VTA revealed the diverse observing and data inputs required to develop the annual status of key Arctic variables (Fig. SB5.3 and Acronyms section). The most widely used observing systems are the Passive Microwave (PM) satellite (currently DMSP/SSMIS), NASA's Moderate Resolution Imaging Spectroradiometer (MODIS) satellite instrument, and in situ automated weather stations (AWS). With persistent atmospheric reanalysis and satellite retrieval issues near the surface in high latitudes, AWS networks continue to provide critical insights. The PM provides high utility for cryospheric observations, even under cloudy conditions, making it a good fit for the Arctic. The dependence of five indicators on the PM (four shown in Fig. SB5.3; a fifth, Ocean Primary Productivity, did not meet the threshold for inclusion in the graphic, which only displays the most critical observations and data products in each category) reveals an important vulnerability given that the last satellite is beyond its planned life without a replacement scheduled (Lavergne et al. 2019). This contrasts with the Normalized Difference Vegetation

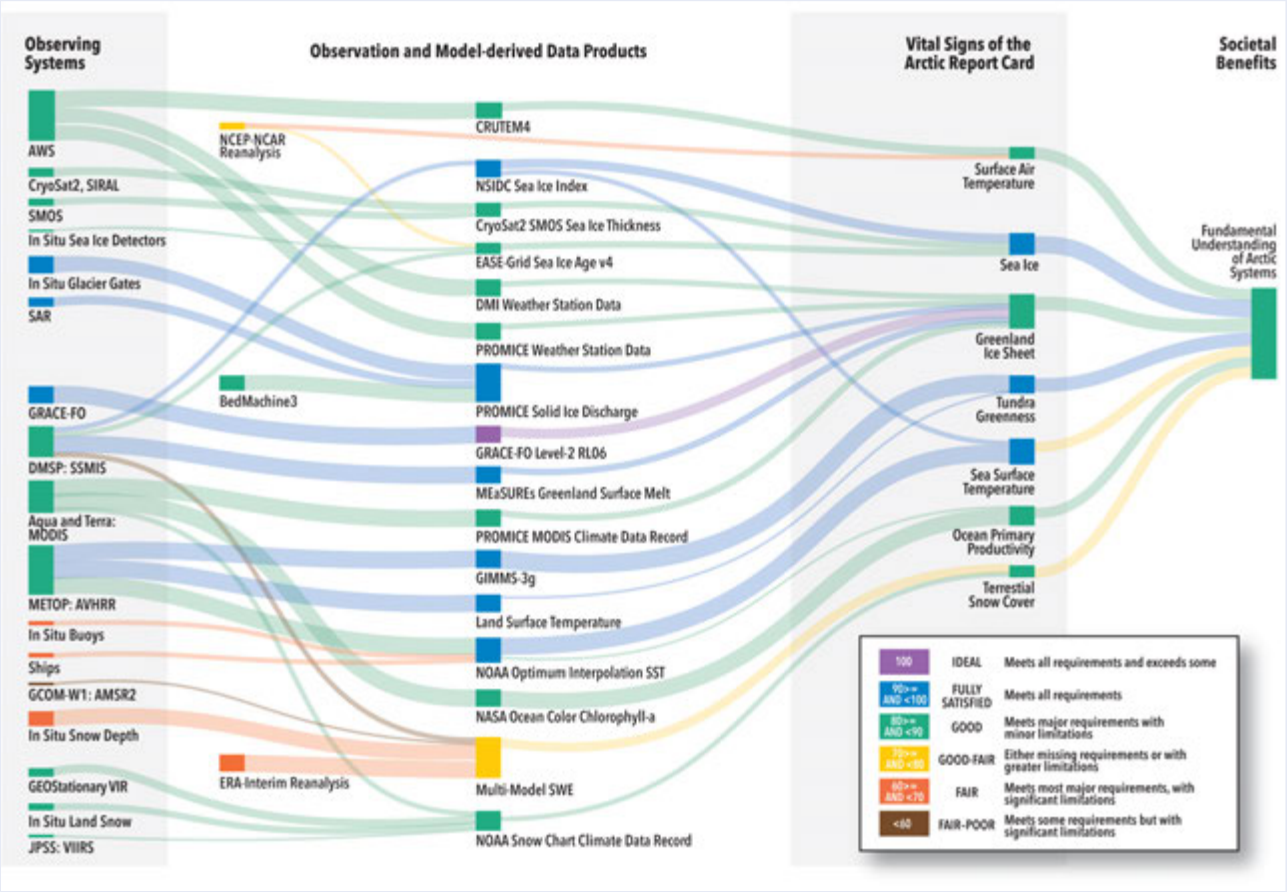

Fig. SB5.3. Value tree assessment (VTA) for the ARC2020. Observing system value in support of the seven ARC Vital Signs propagates forward (left to right) through observation and model-derived data products, then Vital Signs to societal benefit. In this VTA, the primary benefit to society is increased scientific understanding of Arctic systems. Color coding indicates a performance score for nodes (see insert) averaged across all uses; links are weighted (indicated by line thickness) based on their criticality to downstream value. See Acronyms list.

Index (NDVI, section 5i) that is supported by multiple systems (MODIS, AVHRR, and LandSat). Authors choose to work with AVHRR, despite its lower spatial resolution, because the longer record (compared to MODIS) and comprehensive coverage (compared to LandSat) better supports the goals of the ARC.

For the value tree reanalysis, authors rated the performance of their report (i.e., how well the essay conveys long-term trends in the subject of interest) and how it has changed since it first appeared in the ARC (Table SB5.1). Over the last 15 years, five of seven indicators have seen moderate (+10) to large (+40) performance improvements. Taken as a composite across all indicator topics, the quality of the AON and its data products has risen from a performance score of 61 to 84, or from "Fair" to "Good" (see Key in Fig. SB5.3). These ratings are specific to the ARC itself and not reflective of the performance of the AON across all applications. While these improvements are encouraging, there are still significant gaps in the AON of relevance to key Arctic indicators, with the most pronounced gaps noted in Table SB5.1. These gaps also indicate opportunities for targeted improvements of the AON and its data products.

Conclusions

Through this VTA, we see that the data products and observing systems that underlie key indicators of Arctic change, specifically the ARC Vital Signs (mirrored in this chapter), have matured since 2007 due to sponsorship of new observations, focused improvements to existing data products, and a growing scientific understanding of Arctic processes. While the improvements are encouraging, the results of this analysis are focused only on Western science observations and are biased, as the ARC preferentially reports variables that are consistently possible to observe in the Arctic. The AON's quality is a critical indicator that should be monitored; VTA methods provide a starting point for such comprehensive analyses.

Table SB5.1. 2007 and 2020 Performance Ratings and Context, provided by Vital Sign authors and using scale as presented in Key of Fig. SB5.3. In this context, performance is defined as the Vital Sign's ability to convey the long-term trend with high confidence.

Vital Sign	Performance Rating, 2007 or first year in the ARC	Performance Rating, 2020	What accounts for positive changes in the ratings? (+) What is limiting better performance? (–)
Surface air temperature	60	70	+ Improvements in high latitude models and datasets + Additional monitoring sites (AWS sites in Alaska and coastal Greenland and on the Greenland Ice Sheet) – Need for improved accuracy in Arctic reanalyses
Terrestrial snow cover	40	80	+ Longer data records + Additional reference data sets analyzed for comparison – Satellite capabilities, such as Ku-band radar, are needed, especially in mountainous areas – Limited snow water equivalent observations
Greenland Ice Sheet	50	80	+ Longer data records + Additional monitoring sites + Increased understanding of natural processes + New satellite capabilities (e.g., GRACE comprehensive mass balance, ICESat-2, Sentinel-1 ice velocities) + Expanded field of researchers – Limited regional model data – Data limited due to clouds and polar night – Continued sparse in situ observations due to region size
Sea ice	60	80	+ Longer data records + Ice thickness estimates provided in new satellite capabilities (CryoSat-2 and ICESat-2) – Low spatial resolution of datasets, especially in coastal zone – Time-lag in data delivery for snow depth and melt ponding over sea ice, melt-onset, and freeze-up date – Limited capabilities for some parameters during summer melt season
Sea surface temperature	90	90	+ Improved spatial coverage, accuracy, and reliability in datasets – Low spatial resolution of datasets, especially in coastal zone
Ocean primary productivity	80	80	+ Longer data records – Accuracy of chlorophyll-*a* concentrations in Arctic waters – Limited efficacy of remote sensing technology due to cloudy and ice-covered Arctic conditions
Tundra greenness	50	90	+ Longer data records + Improvements in high latitude models and datasets – Limited efficacy of remote sensing technology due to cloudy and snowy Arctic conditions – Joint needs of record length and fine-scale temporal and spatial resolution not met by existing datasets – Lack of consistency across different coarse-resolution NDVI datasets

Acknowledgments

The editors thank Dr. Jackie Richter-Menge (University of Alaska Fairbanks), who served as a senior editorial advisor for this chapter, drawing on her many years of experience as this chapter's lead editor. The editors also thank Florence Fetterer (National Snow and Ice Data Center) and Dr. John Walsh (International Arctic Research Center, University of Alaska Fairbanks) for providing an initial review of the full chapter. Their careful read and thoughtful input improved each of the sections and, importantly, led to better coherency between the sections.

a. Overview

- Matthew Druckenmiller and Twila Moon appreciate support from NOAA's Arctic Research Office.

b. Surface air temperature

- Thomas Ballinger was supported by the Experimental Arctic Prediction Initiative at the University of Alaska Fairbanks.
- Melinda Webster was supported by NASA's Weather and Atmospheric Dynamics program under 80NSSC20K0922.

d. Sea ice

- Walt Meier's contribution was supported by the NASA Snow and Ice Distributed Active Archive Center (DAAC) at NSIDC, part of the NASA Earth Science Data and Information System (ESDIS) Project.

e. Greenland ice sheet

- Data from the Programme for Monitoring of the Greenland Ice Sheet (PROMICE) were provided by the Geological Survey of Denmark and Greenland (GEUS) at http://www.promice.dk.
- Twila Moon was supported by the University of Colorado Boulder Cooperative Institute for Research in Environmental Sciences.
- Marco Tedesco was supported by National Science Foundation ANS #1713072, National Science Foundation PLR-1603331, NASA MAP #80NSSC17K0351, NASA #NNX17AH04G, and the Heising-Simons foundation.
- Thomas Mote was supported by National Science Foundation #1900324.

g. River discharge

- Max Holmes and coauthors acknowledge National Science Foundation support for the Arctic Great Rivers Observatory (NSF 1913888, 1914081, 1914215, 1913962).
- Shiklomanov and Tretiakov acknowledge support from the Russian Foundation for Basic Research (grants 18-05-60192 and 18-05-60240).

i. Tundra greenness

- The authors thank Jorge Pinzon at NASA's Goddard Space Flight Center for developing and maintaining the AVHRR GIMMS-3g+ dataset for NDVI.

j. Ozone and ultraviolet radiation

- Germar Bernhard and coauthors acknowledge the support of Biospherical Instruments, San Diego; the Research Council of Norway through its Centres of Excellence funding scheme, project number 223268/F50; the Academy of Finland for supporting UV measurements through the FARPOCC, SAARA, and CHAMPS (grant no. 329225) projects; the European Space Agency for supporting the DACES project; the Norwegian Environment Agency for funding UV measurements at Andøya and Ny-Ålesund; and the European Union for supporting e-shape. The authors also thank the Microwave Limb Sounder team at NASA's Jet Propulsion Laboratory for data-processing and analysis support, and Juha M. Karhu, Tomi Karppinen, and Markku Ahponen from the Finnish Meteorological Institute for operating the Brewer UV spectroradiometer at Sodankylä.

Sidebar 5.1 Wildland fires in the high northern latitudes

- The material is based upon work supported in part by the National Science Foundation award #OIA-1753748, by the State of Alaska, by the Joint Fire Science Program award #20-3-01-1, by the NOAA Climate Program Office through Grant NA16OAR4310162 with the Alaska Center for Climate Assessment and Policy at the University of Alaska at Fairbanks, and by the NASA Weather and Data Analysis program.

Sidebar 5.2 Assessing 15 years of Arctic Observing Network contributions to tracking key Arctic climate variables

- Hazel Shapiro was supported by the Interagency Arctic Research Policy Committee and the Arctic Research Consortium of the United States (NSF grant #PLR-1928794).
- Sandy Starkweather appreciates support from NOAA's Arctic Research Program.
- All the authors appreciate the support of the subject matter experts who contributed their time and expertise, and the Arctic Data Center for their partnership in creating a searchable online catalog of the 2020 data products referenced in this study.

Chapter 5 – Acronyms

ALT	active layer thickness
AON	Arctic Observing Network
ARC	Arctic Report Card
AVHRR	Advanced Very High Resolution radiometer
AWS	automated weather stations
BUI	Buildup Index
CALM	Circumpolar Active Layer Monitoring
CFFDRS	Canadian Forest Fire Danger Rating System
CMC	Canadian Meteorological Centre
DMI	Danish Meteorological Institute
DU	Dobson units
GIMMS-3g+	Global Inventory Modeling and Mapping Studies 3g V1.2
GRACE	Gravity Recovery and Climate Experiment
GRACE-FO	GRACE Follow-On
HNL	high northern latitudes
ICESat-2	Ice, Cloud, and land Elevation 2
IMS	Interactive Multisensor Snow and Ice Mapping System
MAR	Modèle Atmosphérique Régional
MaxNDVI	maximum NDVI
MCD43A4	Nadir Bidirectional Reflectance Distribution Function Adjusted Reflectance
MERRA-2	Modern-Era Retrospective Analysis for Research and Applications version 2
MLS	Microwave Limb Sounder
MODIS	Moderate Resolution Imaging Spectroradiometer
MOSAiC	Multidisciplinary drifting Observatory for the Study of Arctic Climate
NDVI	Normalized Difference Vegetation Index
NH	Northern Hemisphere
NSIDC	National Snow and Ice Data Center
OISSTv2	Optimum Interpolation Sea Surface Temperature version 2
OMI	Ozone Monitoring Instrument
OSI SAF CCI	Ocean and Sea Ice Satellite Application Facility Climate Change Initiative
PM	Passive Microwave
PROMICE	Programme for Monitoring of the Greenland Ice Sheet
PSCs	polar stratospheric clouds
SAT	surface air temperature
SCD	snow cover duration
SCE	snow cover extent
SLP	sea-level pressure
SMB	surface mass balance
SMOS	Soil Moisture Ocean Salinity
SPEI	Standardized Precipitation-Evapotranspiration Index
SSMIS	Special Sensor Microwave Imager/Sounder

SSTs	sea surface temperatures
SWE	snow water equivalent
TOC	total ozone column
UV	ultraviolet
UVI	ultraviolet index
VTA	value tree assessment

References

Abramov, A., and Coauthors, 2021: Two decades of active layer thickness monitoring in northeastern Asia. *Polar Geogr.*, https://doi.org/10.1080/1088937X.2019.1648581, in press.

AICC, 2020: Alaska fire history data. Alaska Interagency Coordination Center, accessed 10 September 2020, https://fire.ak.blm.gov/predsvcs/intel.php.

Andersen, J. K., and Coauthors, 2019: Update of annual calving front lines for 47 marine terminating outlet glaciers in Greenland (1999–2018). *Geol. Surv. Denmark Greenl. Bull.*, **43**, e2019430202, https://doi.org/10.34194/GEUSB-201943-02-02.

Andreu-Hayles, L., B. V. Gaglioti, L. T. Berner, M. Levesque, K. J. Anchukaitis, S. J. Goetz, and R. D'Arrigo, 2020: A narrow window of summer temperatures associated with shrub growth in Arctic Alaska. *Environ. Res. Lett.*, **15**, 105012, https://doi.org/10.1088/1748-9326/ab897f.

AOS EOC, 2018: Report of the 4th Arctic observing summit: AOS 2018, Davos, Switzerland, 24-26 June 2018. International Study of Arctic Change (ISAC) Program Office, Arctic Institute of North America, 17 pp., www.arcticobservingsummit.org/sites/default/files/Report%20on%20the%20AOS%202018_FINAL_March2019_0.pdf.

Ballinger, T. J., and Coauthors, 2020: Surface air temperature. NOAA Arctic Report Card 2020, R. L. Thoman, J. Richter-Menge, and M. L. Druckenmiller, Eds., NOAA, https://doi.org/10.25923/gcw8-2z06.

Barrett, K., T. Loboda, A. D. McGuire, H. Genet, E. Hoy, and E. Kasischke, 2016: Static and dynamic controls on fire activity at moderate spatial and temporal scales in the Alaskan boreal forest. *Ecosphere*, **7**, e01572, https://doi.org/10.1002/ecs2.1572.

Berner, L. T., and Coauthors, 2020: Summer warming explains widespread but not uniform greening in the Arctic tundra biome. *Nat. Commun.*, **11**, 4621, https://doi.org/10.1038/s41467-020-18479-5.

Bernhard, G., and Coauthors, 2020: Record-breaking increases in Arctic solar ultraviolet radiation caused by exceptionally large ozone depletion in 2020. *Geophys. Res. Lett.*, **47**, e2020GL090844, https://doi.org/10.1029/2020GL090844.

Bhartia, P. K., and C. W. Wellemeyer, 2002: TOMS-V8 total O3 algorithm. OMI Algorithm Theoretical Basis Document Volume II, NASA Goddard Space Flight Center Tech. Doc. ATBD-OMI-02, 15–31, http://eospso.nasa.gov/sites/default/files/atbd/ATBD-OMI-02.pdf.

Bhatt, U. S., and Coauthors, 2010: Circumpolar Arctic tundra vegetation change is linked to sea ice decline. *Earth Interact.*, **14**, https://doi.org/10.1175/2010EI315.1.

——, and Coauthors, 2021: Emerging anthropogenic influences on the South-central Alaska temperature and precipitation extremes and related fires in 2019. *Land*, **10**, 82, https://doi.org/10.3390/land10010082.

Bieniek, P. A., and Coauthors, 2020: Lightning variability in dynamically downscaled simulations of Alaska's present and future summer climate. *J. Appl. Meteor. Climatol.*, **59**, 1139–1152, https://doi.org/10.1175/JAMC-D-19-0209.1.

Biskaborn, B. K., and Coauthors, 2019: Permafrost is warming at a global scale. *Nat. Commun.*, **10**, 264, https://doi.org/10.1038/s41467-018-08240-4.

Bjella, K., 2019: Warming and thawing permafrost and impacts on infrastructure [in "State of the Climate in 2018"]. *Bull. Amer. Meteor. Soc.*, **100** (9), S157–S159, 10.1175/2019BAMSStateoftheClimate.1.

Bjorkman, A. D., and Coauthors, 2020: Status and trends in Arctic vegetation: Evidence from experimental warming and long-term monitoring. *Ambio*, **49**, 678–692, https://doi.org/10.1007/s13280-019-01161-6.

Boike, J., and Coauthors, 2018: A 20-year record (1998–2017) of permafrost, active layer, and meteorological conditions at a high Arctic permafrost research site (Bayelva, Spitsbergen). *Earth Syst. Sci. Data*, **10**, 355–390, https://doi.org/10.5194/essd-10-355-2018.

Box, J. E., D. van As, and K. Steffen, 2017: Greenland, Canadian and Icelandic land ice albedo grids (2000-2016). *Geol. Surv. Denmark Greenl. Bull.*, **38**, 53–56, https://doi.org/10.34194/geusb.v38.4414.

——, and Coauthors, 2019: Key indicators of Arctic climate change: 1971–2017. *Environ. Res. Lett.*, **14**, 045010, https://doi.org/10.1088/1748-9326/aafc1b.

Brasnett, B., 1999: A global analysis of snow depth for numerical weather prediction. *J. Appl. Meteor.*, **38**, 726–740, https://doi.org/10.1175/1520-0450(1999)038<0726:AGAOSD>2.0.CO;2.

Brown, J., O. J. Ferrians Jr., J. A. Heginbottom, and E. S. Melnikov, 1997: Circum-Arctic map of permafrost and ground-ice conditions. U.S. Geological Survey Circum-Pacific Map CP-45, https://doi.org/10.3133/cp45.

Brown, R. D., and B. Brasnett, 2010: Canadian Meteorological Centre (CMC) Daily Snow Depth Analysis Data, Version 1. NASA National Snow and Ice Data Center Distributed Active Archive Center, accessed 27 July 2020, https://doi.org/10.5067/W9FOYWH0EQZ3.

——, B. Brasnett, and D. Robinson, 2003: Gridded North American monthly snow depth and snow water equivalent for GCM evaluation. *Atmos.–Ocean*, **41**, 1–14, https://doi.org/10.3137/ao.410101.

——, D. Vikhamar Schuler, O. Bulygina, C. Derksen, K. Luojus, L. Mudryk, L. Wang, and D. Yang, 2017: Arctic terrestrial snow cover. *Snow, Water, Ice and Permafrost in the Arctic (SWIPA) 2017*, Arctic Monitoring and Assessment Programme, 25–64.

Brun, E., V. Vionnet, A. Boone, B. Decharme, Y. Peings, R. Valette, F. Karbou, and S. Morin, 2013: Simulation of Northern Eurasian local snow depth, mass, and density using a detailed snowpack model and meteorological reanalyses. *J. Hydrometeor.*, **14**, 203–219, https://doi.org/10.1175/JHM-D-12-012.1.

Buchwal, A., and Coauthors, 2020: Divergence of Arctic shrub growth associated with sea ice decline. *Proc. Natl. Acad. Sci. USA*, **117**, 33 334–33 344, https://doi.org/10.1073/pnas.2013311117.

Butchart, N., and E. E. Remsberg, 1986: The area of the stratospheric polar vortex as a diagnostic for tracer transport on an isentropic surface. *J. Atmos. Sci.*, **43**, 1319–1339, https://doi.org/10.1175/1520-0469(1986)043<1319:TAOTSP>2.0.CO;2.

Callaghan, T., and Coauthors, 2011: The changing face of Arctic snow cover: A synthesis of observed and projected changes. *Ambio*, **40**, 17–31, https://doi.org/10.1007/s13280-011-0212-y.

Chen, Y., F. S. Hu, and M. J. Lara, 2021: Divergent shrub-cover responses driven by climate, wildfire, and permafrost interactions in Arctic tundra ecosystems. *Global Change Biol.*, **27**, 652–663, https://doi.org/10.1111/gcb.15451.

Christiansen, H., and Coauthors, 2010: The thermal state of permafrost in the Nordic area during the International Polar Year 2007–2009. *Permafrost Periglacial Processes*, **21**, 156–181, https://doi.org/10.1002/ppp.687.

Cohen, J., and Coauthors, 2020: Divergent consensuses on Arctic amplification influence on mid-latitude severe winter weather. *Nat. Climate Change*, **10**, 20–29, https://doi.org/10.1038/s41558-019-0662-y.

DeLand, M. T., P. K. Bhartia, N. Kramarova, and Z. Chen, 2020: OMPS LP observations of PSC variability during the NH 2019–2020 season. *Geophys. Res. Lett.*, **47**, e2020GL090216, https://doi.org/10.1029/2020GL090216.

Ednie, M., and S. L. Smith, 2015: Permafrost temperature data 2008-2014 from community based monitoring sites in Nunavut. Geological Survey of Canada Open File 7784, 18 pp., https://doi.org/10.4095/296705.

EEAP, 2019: Environmental Effects and Interactions of Stratospheric Ozone Depletion, UV Radiation, and Climate Change: 2018 Assessment Report. Environmental Effects Assessment Panel, United Nations Environment Programme, 390 pp. https://ozone.unep.org/sites/default/files/2019-04/EEAP_assessment-report-2018%20%282%29.pdf.

Epstein, H. E., and Coauthors, 2021: Spatial patterns of arctic tundra vegetation properties on different soils along the Eurasia Arctic Transect, and insights for a changing Arctic. *Environ. Res. Lett.*, **16**, 014008, https://doi.org/10.1088/1748-9326/abc9e3.

Estilow, T. W., A. H. Young, and D. A. Robinson, 2015: A long-term Northern Hemisphere snow cover extent data record for climate studies and monitoring. *Earth Syst. Sci. Data*, **7**, 137–142, https://doi.org/10.5194/essd-7-137-2015.

Etzelmüller, B., and Coauthors, 2020: Twenty years of European mountain permafrost dynamics—The PACE legacy. *Environ. Res. Lett.*, **15**, 104070, https://doi.org/10.1088/1748-9326/abae9d.

Fausto, R.S. and D. van As, 2019: Programme for monitoring of the Greenland Ice Sheet (PROMICE): Automatic weather station data, version: v03. Geological Survey of Denmark and Greenland, accessed 14 September 2020, https://doi.org/10.22008/promice/data/aws.

Fetterer, F., K. Knowles, W. N. Meier, M. Savoie, and A. K. Windnagel, 2017: Sea Ice Index, Version 3. Subset: Regional Daily Data (updated daily), National Snow and Ice Data Center, accessed 15 February 2021, https://doi.org/10.7265/N5K072F8.

Flannigan, M., B. Stocks, M. Turetsky, and M. Wotton, 2009: Impacts of climate change on fire activity and fire management in the circumboreal forest. *Global Change Biol.*, **15**, 549–560, https://doi.org/10.1111/j.1365-2486.2008.01660.x.

Frederikse, T., and Coauthors, 2020: The causes of sea-level rise since 1900. *Nature*, **584**, 393–397, https://doi.org/10.1038/s41586-020-2591-3.

Gearheard, S., L. K. Holm, H. Huntington, J. M. Leavitt, and A. R. Mahoney, Eds., 2013: *The Meaning of Ice: People and Sea Ice in Three Arctic Communities*. International Polar Institute, 336 pp.

Gelaro, R., and Coauthors, 2017: The Modern-Era Retrospective Analysis for Research and Applications, version 2 (MERRA-2). *J. Climate*, **30**, 5419–5454, https://doi.org/10.1175/JCLI-D-16-0758.1.

Giglio, L., L. Boschetti, D. P. Roy, M. L. Humber, and C. O. Justice, 2018: The Collection 6 MODIS burned area mapping algorithm and product. *Remote Sens. Environ.*, **217**, 72–85, https://doi.org/10.1016/j.rse.2018.08.005.

GMAO, 2015: MERRA-2tavg1_2d_lnd_Nx:2d, 1-Hourly, Time-Averaged, Single-Level, Assimilation, Land Surface Diagnostics V5.12.4. Goddard Earth Sciences Data and Information Services Center, accessed 26 August 2020, https://doi.org/10.5067/RKPHT8KC1Y1T.

Hanes, C. C., X. Wang, P. Jain, M. A. Parisien, J. M. Little, and M. D. Flannigan, 2019: Fire-regime changes in Canada over the last half century. *Can. J. For. Res.*, **49**, 256–269, https://doi.org/10.1139/cjfr-2018-0293.

Hanna, E., and Coauthors, 2020: Mass balance of the ice sheets and glaciers—Progress since AR5 and challenges. *Earth-Sci. Rev.*, **201**, 102976, https://doi.org/10.1016/j.earscirev.2019.102976.

Hayasaka, H., H. L. Tanaka, and P. A. Bieniek, 2016: Synoptic-scale fire weather conditions in Alaska. *Polar Sci.*, **10**, 217–226, https://doi.org/10.1016/j.polar.2016.05.001.

Heim, R. J., A. Bucharova, L. Brodt, J. Kamp, D. Rieker, A. V. Soromotin, A. Yurtaev, and N. Hölzel, 2021: Post-fire vegetation succession in the Siberian subarctic tundra over 45 years. *Sci. Total Environ.*, **760**, 143425, https://doi.org/10.1016/j.scitotenv.2020.143425.

Helfrich, S., D. McNamara, B. Ramsay, T. Baldwin, and T. Kasheta, 2007: Enhancements to, and forthcoming developments in the Interactive Multisensor Snow and Ice Mapping System (IMS). *Hydrol. Processes*, **21**, 1576–1586, https://doi.org/10.1002/hyp.6720.

Hersbach, H., and Coauthors, 2020: The ERA5 global reanalysis. *Quart. J. Roy. Meteor. Soc.*, **146**, 1999–2049, https://doi.org/10.1002/qj.3803.

Holmes, R. M., and Coauthors, 2013: Climate change impacts on the hydrology and biogeochemistry of Arctic rivers. *Global Impacts of Climate Change on Inland Waters*, C. R. Goldman, M. Kumagai, and R. D. Robarts, Eds., Wiley, 3–26.

IDA, 2017: International Arctic Observations Assessment Framework. IDA Science and Technology Policy Institute, 73 pp., www.arcticobserving.org/news/268-international-arctic-observations-assessment-framework-released.

Isaksen, K., and Coauthors, 2011: Degrading mountain permafrost in southern Norway: Spatial and temporal variability of mean ground temperatures, 1999–2009. *Permafrost Periglacial Processes*, **22**, 361–377, https://doi.org/10.1002/ppp.728.

Jones, P. D., D. H. Lister, T. J. Osborn, C. Harpham, M. Salmon, and C. P. Morice, 2012: Hemispheric and large-scale land-surface air temperature variations: An extensive revision and an update to 2010. *J. Geophys. Res.*, **117**, D05127, https://doi.org/10.1029/2011JD017139.

Kalnay, E., and Coauthors, 1996: The NCEP/NCAR 40-Year Reanalysis Project. *Bull. Amer. Meteor. Soc.*, **77**, 437–471, https://doi.org/10.1175/1520-0477(1996)077<0437:TNYRP>2.0.CO;2.

Kemppinen, J., P. Niittynen, A.-M. Virkkala, K. Happonen, H. Riihimäki, J. Aalto, and M. Luoto, 2021: Dwarf shrubs impact tundra soils: Drier, colder, and less organic carbon. *Ecosystems*, https://doi.org/10.1007/s10021-020-00589-2, in press.

Kopec, B., X. Feng, F. A. Michel, and E. Posmentier, 2016: Influence of sea ice on Arctic precipitation. *Proc. Natl. Acad. Sci. USA*, **113**, 46–51, https://doi.org/10.1073/pnas.1504633113.

Kropp, H., and Coauthors, 2021: Shallow soils are warmer under trees and tall shrubs across Arctic and boreal ecosystems. *Environ. Res. Lett.*, **16**, 015001, https://doi.org/10.1088/1748-9326/abc994.

Landrum, L., and M. M. Holland, 2020: Extremes become routine in an emerging new Arctic. *Nat. Climate Change*, **10**, 1108–1115, https://doi.org/10.1038/s41558-020-0892-z.

Lavergne, T., and Coauthors, 2019: Version 2 of the EUMETSAT OSI SAF and ESA CCI sea-ice concentration climate data records. *Cryosphere*, **13**, 49–78, https://doi.org/10.5194/tc-13-49-2019.

Lawrence, D. M., A. G. Slater, R. A. Tomas, M. M. Holland, and C. Deser, 2008: Accelerated Arctic land warming and permafrost degradation during rapid sea ice loss. *Geophys. Res. Lett.*, **35**, L11506, https://doi.org/10.1029/2008GL033985.

Lawrence, Z. D., J. Perlwitz, A. H. Butler, G. L. Manney, P. A. Newman, S.H. Lee, and E. R. Nash, 2020: The remarkably strong Arctic stratospheric polar vortex of winter 2020: Links to record-breaking Arctic oscillation and ozone loss. *J. Geophys Res. Atmos.*, **125**, e2020JD033271, https://doi.org/10.1029/2020JD033271.

Lee, C. M., and Coauthors, 2019: A framework for the development, design and implementation of a sustained Arctic ocean observing system. *Front. Mar. Sci.*, **6**, 451, https://doi.org/10.3389/fmars.2019.00451.

Liljedahl, A. K., I. Timling, G. V. Frost, and R. P. Daanen, 2020: Arctic riparian shrub expansion indicates a shift from streams gaining water to those that lose flow. *Commun. Earth Environ.*, **1**, 50, https://doi.org/10.1038/s43247-020-00050-1.

Lund, M., K. Raundrup, A. Westergaard-Nielsen, E. López-Blanco, J. Nymand, and P. Aastrup, 2017: Larval outbreaks in West Greenland: Instant and subsequent effects on tundra ecosystem productivity and CO2 exchange. *Ambio*, **46**, 26–38, https://doi.org/10.1007/s13280-016-0863-9.

Mankoff, K. D., A. Solgaard, W. Colgan, A. P. Ahlstrøm, S. A. Khan, and R. S. Fausto, 2020: Greenland ice sheet solid ice discharge from 1986 through March 2020. *Earth Syst. Sci. Data*, **12**, 1367–1383, https://doi.org/10.5194/essd-12-1367-2020.

Manney, G. L., and Z. D. Lawrence, 2016: The major stratospheric final warming in 2016: Dispersal of vortex air and termination of Arctic chemical ozone loss. *Atmos. Chem. Phys.*, **16**, 15 371–15 396, https://doi.org/10.5194/acp-16-15371-2016.

Manney, G. L., and Coauthors, 2020: Record-low Arctic stratospheric ozone in 2020: MLS observations of chemical processes and comparisons with previous extreme winters, *Geophys. Res. Lett.*, **47**, e2020GL089063, https://doi.org/10.1029/2020GL089063.

McClelland, J. W., S. J. Deìry, B. J. Peterson, R. M. Holmes, and E. F. Wood, 2006: A pan-arctic evaluation of changes in river discharge during the latter half of the 20th century. *Geophys. Res. Lett.*, **33**, L06715, https://doi.org/10.1029/2006GL025753.

——, R. M. Holmes, K. H. Dunton, and R. Macdonald, 2012: The Arctic Ocean estuary. *Estuaries Coasts*, **35**, 353–368, https://doi.org/10.1007/s12237-010-9357-3.

McElhinny, M., J. F., Beckers, C. Hanes, M. Flannigan, and P. Jain, 2020: A high-resolution reanalysis of global fire weather from 1979 to 2018—Overwintering the drought code. *Earth Syst. Sci. Data*, **12**, 1823–1833, https://doi.org/10.5194/essd-2019-248.

Meier, W., J. Stroeve, and F. Fetterer, 2007: Whither Arctic sea ice? A clear signal of decline regionally, seasonally and extending beyond the satellite record. *Ann. Glaciol.*, **46**, 428–434, https://doi.org/10.3189/172756407782871170.

——, F. Fetterer, M. Savoie, S. Mallory, R. Duerr, and J. Stroeve, 2017: NOAA/NSIDC Climate Data Record of Passive Microwave Sea Ice Concentration, Version 3. National Snow and Ice Data Center, accessed 1 January 2020, https://doi.org/10.7265/N59P2ZTG.

Moon, T. A., and Coauthors, 2019: The expanding footprint of rapid Arctic change. *Earth's Future*, **7**, 212–218, https://doi.org/10.1029/2018EF001088.

Morlighem, M., and Coauthors, 2017: BedMachine v3: Complete bed topography and ocean bathymetry mapping of Greenland from multibeam echo sounding combined with mass conservation. *Geophys. Res. Lett.*, **44**, 11 051–11 061, https://doi.org/10.1002/2017GL074954.

Mote, T., 2007: Greenland surface melt trends 1973–2007: Evidence of a large increase in 2007. *Geophys. Res. Lett.*, **34**, L22507, https://doi.org/10.1029/2007GL031976.

Mouginot, J., and Coauthors, 2019: Forty-six years of Greenland ice sheet mass balance from 1972 to 2018. *Proc. Natl. Acad. Sci. USA*, **116**, 9239–9244, https://doi.org/10.1073/pnas.1904242116.

Mudryk, L., M. Santolaria-Otín, G. Krinner, M. Ménégoz, C. Derksen, C. Brutel-Vuilmet, M. Brady, and R. Essery, 2020a: Historical Northern Hemisphere snow cover trends and projected changes in the CMIP-6 multi-model ensemble. *Cryosphere*, **14**, 2495–2514, https://doi.org/10.5194/tc-14-2495-2020.

——, R. Brown, C. Derksen, K. Luojus, and B. Decharme, 2020b: Terrestrial snow cover [in "State of the Climate in 2019"]. *Bull. Amer. Meteor. Soc.*, **101** (8), S263–S265, https://doi.org/10.1175/BAMS-D-20-0086.1.

Müller, R., J.-U. Grooß, C. Lemmen, D. Heinze, M. Dameris, and G. Bodeker, 2008: Simple measures of ozone depletion in the polar stratosphere. *Atmos. Chem. Phys.*, **8**, 251–264, https://doi.org/10.5194/acp-8-251-2008.

Murray, M. S., R. D. Sankar, and G. Ibarguchi, 2018: The Arctic observing summit, background and synthesis of outcomes 2013-2016. International Study of Arctic Change Program Office, Arctic Institute of North America, 8 pp., www.arcticobservingsummit.org/sites/default/files/AOS_Synthesis_FinalReport.pdf.

Myers-Smith, I. H., and Coauthors, 2020: Complexity revealed in the greening of the Arctic. *Nat. Climate Change*, **10**, 106–117, https://doi.org/10.1038/s41558-019-0688-1.

NRC, 2006: *Toward an Integrated Arctic Observing Network*. The National Academies Press, 128 pp., https://doi.org/10.17226/11607.

Neale, R. E., and Coauthors, 2021: Environmental effects of stratospheric ozone depletion, UV radiation, and interactions with climate: UNEP Environmental Effects Assessment Panel, Update 2020. *Photochem. Photobiol. Sci.*, **20**, 1–67, https://doi.org/10.1007/s43630-020-00001-x.

OSTP, 2014: National Plan for Civil Earth Observations. National Science and Technology Council, 71 pp., https://obamawhitehouse.archives.gov/sites/default/files/microsites/ostp/NSTC/2014_national_plan_for_civil_earth_observations.pdf.

Overland, J. E., and M. Wang, 2021: The 2020 Siberian heat wave. *Int. J. Climatol.*, **41**, E2341–E2346, https://doi.org/10.1002/joc.6850.

——, and Coauthors, 2021: How do intermittency and simultaneous processes obfuscate the Arctic influence on midlatitude winter extreme weather events? *Environ. Res. Lett.*, **16**, 043002, https://doi.org/10.1088/1748-9326/abdb5d.

Partain, J. L., and Coauthors, 2016: An assessment of the role of anthropogenic climate change in the Alaska fire season of 2015 [in "Explaining Extremes of 2015 from a Climate Perspective"]. *Bull. Amer. Meteor. Soc.*, **97** (12), S14–S18, https://doi.org/10.1175/BAMS-D-16-0149.1.

Peltier, W. R., D. F. Argus, and R. Drummond, 2018: Comment on "An assessment of the ICE-6G_C (VM5a) glacial isostatic adjustment model" by Purcell et al. *J. Geophys. Res. Solid Earth*, **123**, 2019–2018, https://doi.org/10.1002/2016JB013844.

Peng, G., W. N. Meier, D. J. Scott, and M. H. Savoie, 2013: A long-term and reproducible passive microwave sea ice concentration data record for climate studies and monitoring. *Earth Syst. Sci. Data*, **5**, 311–318, https://doi.org/10.5194/essd-5-311-2013.

Peterson, B. J., R. M. Holmes, J. W. McClelland, C. J. Vorosmarty, R. B. Lammers, A. I. Shiklomanov, I. A. Shiklomanov, and S. Rahmstorf, 2002: Increasing river discharge to the Arctic Ocean. *Science*, **298**, 2171–2173, https://doi.org/10.1126/science.1077445.

Petty, A. A., M. Webster, L. Boisvert, and T. Markus, 2018: The NASA Eulerian Snow on Sea Ice Model (NESOSIM) v1.0: Initial model development and analysis. *Geosci. Model Dev.*, **11**, 4577–4602, https://doi.org/10.5194/gmd-11-4577-2018.

——, N. T. Kurtz, R. Kwok, T. Markus, T. A. Neumann, 2020. Winter Arctic sea ice thickness from ICESat-2 freeboards. *J. Geophys. Res. Oceans*, **125**, e2019JC015764. https://doi.org/10.1029/2019JC015764.

Pinzon, J., and C. Tucker, 2014: A non-stationary 1981–2012 AVHRR NDVI3g time series. *Remote Sens.*, **6**, 6929–6960, https://doi.org/10.3390/rs6086929.

Prendin, A. L., and Coauthors, 2020: Immediate and carry-over effects of insect outbreaks on vegetation growth in West Greenland assessed from cells to satellite. *J. Biogeogr.*, **47**, 87–100, https://doi.org/10.1111/jbi.13644.

Rawlins, M. A., and Coauthors, 2010: Analysis of the arctic system freshwater cycle intensification: observations and expectations. *J. Climate*, **23**, 5715–5737, https://doi.org/10.1175/2010JCLI3421.1.

Raynolds, M. K., D. A. Walker, H. E. Epstein, J. E. Pinzon, and C. J. Tucker, 2012: A new estimate of tundra-biome phytomass from trans-Arctic field data and AVHRR NDVI. *Remote Sens. Lett.*, **3**, 403–411, https://doi.org/10.1080/01431161.2011.609188.

Reynolds, R. W., N. A. Rayner, T. M. Smith, D. C. Stokes, and W. Wang, 2002: An improved in situ and satellite SST analysis for climate. *J. Climate*, **15**, 1609–1625, https://doi.org/10.1175/1520-0442(2002)015<1609:AIISAS>2.0.CO;2.

——, T. M. Smith, C. Liu, D. B. Chelton, K. S. Casey, and M. G. Schlax, 2007: Daily high-resolution-blended analyses for sea surface temperature. *J. Climate*, **20**, 5473–5496, https://doi.org/10.1175/2007JCLI1824.1.

Ricker, R., S. Hendricks, L. Kaleschke, X. Tian-Kunze, J. King, and C. Haas, 2017: A weekly Arctic sea-ice thickness data record from merged CryoSat-2 and SMOS satellite data. *Cryosphere*, **11**, 1607–1623, https://doi.org/10.5194/tc-11-1607-2017.

Robinson, D. A., T. W. Estilow, and NOAA CDR Program, 2012: NOAA Climate Data Record (CDR) of Northern Hemisphere (NH) Snow Cover Extent (SCE), Version 1 [r01]. NOAA National Centers for Environmental Information, accessed 27 July 2020, https://doi.org/10.7289/V5N014G9.

Romanovsky, V., and Coauthors, 2017: Changing permafrost and its impacts. Snow, Water, Ice and Permafrost in the Arctic (SWIPA) 2017, Arctic Monitoring and Assessment Programme, 65–102.

——, and Coauthors, 2020: Terrestrial permafrost [in "State of the Climate in 2019"]. *Bull. Amer. Meteor. Soc.*, **101**(8), S265–S269, https://doi.org/10.1175/BAMS-D-20-0086.1

Sasgen, I., and Coauthors, 2020: Return to rapid ice loss in Greenland and record loss in 2019 detected by the GRACE-FO satellites. *Commun. Earth. Environ.*, **1**, 8, https://doi.org/10.1038/s43247-020-0010-1.

Schaaf, C. B., and Z. Wang, 2015: MCD43A4 MODIS/Terra+Aqua BRDF/Albedo Nadir BRDF Adjusted Ref Daily L3 Global - 500m V006. NASA EOSDIS Land Processes DAAC, accessed 21 February 2021, https://doi.org/10.5067/MODIS/MCD43A4.006.

Scholten, R., R. Jandt, E. A. Miller, B. M. Rogers, and S. Veraverbeke, 2021: Overwintering fires in boreal forests. *Nature*, **593**, 399–404, https://doi.org/10.1038/s41586-021-03437-y.

Schroeder, W., P. Oliva, L. Giglio, and I. A. Csiszar, 2014: The new VIIRS 375m active fire detection data product: Algorithm description and initial assessment. *Remote Sens. Environ.*, **143**, 85–96, https://doi.org/10.1016/j.rse.2013.12.008.

Schuur, E. A. G., 2020: Permafrost carbon [in "State of the Climate in 2019"]. *Bull. Amer. Meteor. Soc.*, **101** (8), S270–S271, https://doi.org/10.1175/BAMS-D-20-0086.1.

Serreze, M. C., and R. G. Barry, 2011: Processes and impacts of Arctic amplification: A research synthesis. *Global Planet. Change*, **77**, 85–96, https://doi.org/10.1016/j.gloplacha.2011.03.004.

Shevtsova, I., B. Heim, S. Kruse, J. Schröder, E. I. Troeva, L. A. Pestryakova, E. S. Zakharov, and U. Herzschuh, 2020: Strong shrub expansion in tundra-taiga, tree infilling in taiga and stable tundra in central Chukotka (north-eastern Siberia) between 2000 and 2017. *Environ. Res. Lett.*, **15**, 085006, https://doi.org/10.1088/1748-9326/ab9059.

Shiklomanov, N. I., D. A. Streletskiy, and F. E. Nelson, 2012: Northern Hemisphere component of the global Circumpolar Active Layer Monitoring (CALM) program. *Proc. 10th Int. Conf. on Permafrost*, Vol. 1, Salekhard, Russia, Tyumen Oil and Gas University, 377–382.

Shiklomanov, A. I., S. J. Deìry, M. V. Tretiakov, D. Yang, D. Magritsky, A. Georgiadi, and W. Tang, 2021: River freshwater flux to the Arctic Ocean. Arctic Hydrology, *Permafrost and Ecosystem*, Y. Daqing and K. Douglas, Eds., Springer, 703–738.

Shupe, M. D., and Coauthors, 2020: The MOSAiC expedition: A year drifting with the Arctic sea ice. NOAA Arctic Report Card 2020, R.L. Thoman, J. Richter-Menge, and M. L. Druckenmiller, Eds., NOAA, https://doi.org/10.25923/9g3v-xh92.

Simonsen, S. B., V. R. Barletta, W. T. Colgan, and L. S. Sørensen, 2021: Greenland Ice Sheet mass balance (1992–2020) from calibrated radar altimetry. *Geophys. Res. Lett.*, **48**, 105–110, https://doi.org/10.1029/2020GL091216.

Skarin, A., M. Verdonen, T. Kumpula, M. Macias-Fauria, M. Alam, J. T. Kerby, and B. C. Forbes, 2020: Reindeer use of low Arctic tundra correlates with landscape structure. *Environ. Res. Lett.*, **15**, 115012, https://doi.org/10.1088/1748-9326/abbf15.

Slats, R., and Coauthors, 2019: Voices from the front lines of a Changing Bering Sea: An indigenous perspective for the 2019 Arctic Report Card. Arctic Report Card 2019, J. Richter-Menge, M. L. Druckenmiller, and M. Jeffries, Eds., NOAA, www.arctic.noaa.gov/Report-Card/Report-Card-2019.

Smith, S. L., C. Duchesne, and A. G. Lewkowicz, 2019: Tracking changes in permafrost thermal state in Northern Canada. *Cold Regions Engineering 2019*, J.-P. Bilodeau et al., Eds., American Society of Civil Engineers, 670–677, https://doi.org/10.1061/9780784482599.077.

Strand, S., H. Christiansen, M. Johansson, J. Akerman, and O. Humlum, 2020: Active layer thickening and controls on interannual variability in the Nordic Arctic compared to the circum-Arctic. *Permafrost Periglacial Processes*, **32**, 47–58, https://doi.org/10.1002/ppp.2088.

Stroeve, J., and D. Notz, 2018: Changing state of Arctic sea ice across all seasons. *Environ. Res. Lett.*, **13**, 1–23, https://doi.org/10.1088/1748-9326/aade56.

Stroh, J. N., G. Panteleev, S. Kirillov, M. Makhotin, and N. Shakhova, 2015: Sea-surface temperature and salinity product comparison against external in situ data in the Arctic Ocean. *J. Geophys. Res. Oceans*, **120**, 7223–7236, https://doi.org/10.1002/2015JC011005.

Swanson, D. K., 2021: Permafrost thaw-related slope failures in Alaska's Arctic National Parks, c. 1980–2019. *Permafrost Periglacial Processes*, https://doi.org/10.1002/ppp.2098, in press.

Takala, M., K. Luojus, J. Pulliainen, C. Derksen, J. Lemmetyinen, J.-P. Kärnä, and J. Koskinen, 2011: Estimating northern hemisphere snow water equivalent for climate research through assimilation of space-borne radiometer data and ground-based measurements. *Remote Sens. Environ.*, **115**, 3517–3529, https://doi.org/10.1016/j.rse.2011.08.014.

Tedesco, M., X. Fettweis, T. Mote, J. Wahr, P. Alexander, J. Box, and B. Wouters, 2013: Evidence and analysis of 2012 Greenland records from spaceborne observations, a regional climate model and reanalysis data. *Cryosphere*, **7**, 615–630, https://doi.org/10.5194/tc-7-615-2013.

The IMBIE Team, 2020: Mass balance of the Greenland Ice Sheet from 1992 to 2018. *Nature*, 579, 233–239, https://doi.org/10.1038/s41586-019-1855-2.

Thoman, R. L., J. Richter-Menge, and M. L. Druckenmiller, Eds., 2020: Arctic Report Card 2020. NOAA, 143 pp., https://doi.org/10.25923/mn5p-t549.

Timmermans, M.-L., Z. Labe, and C. Ladd, 2020: Sea surface temperature [in "State of the Climate in 2019"]. *Bull. Amer. Meteor. Soc.*, **101** (8), S249–S251, https://doi.org/10.1175/BAMS-D-20-0086.1.

Treharne, R., J. W. Bjerke, H. Tømmervik, and G. K. Phoenix, 2020: Extreme event impacts on CO2 fluxes across a range of high latitude, shrub-dominated ecosystems. *Environ. Res. Lett.*, **15**, 104084, https://doi.org/10.1088/1748-9326/abb0b1.

Tschudi, M., W. N. Meier, J. S. Stewart, C. Fowler, and J. Maslanik, 2019: EASE-Grid Sea Ice Age, Version 4. NASA National Snow and Ice Data Center Distributed Active Archive Center, accessed 15 February 2021, https://doi.org/10.5067/UTAV7490FEPB.

——, ——, and ——, 2020: An enhancement to sea ice motion and age products at the National Snow and Ice Data Center (NSIDC). *Cryosphere*, **14**, 1519–1536, https://doi.org/10.5194/tc-14-1519-2020.

USGS, 2019: Demonstrating the Value of Earth Observations—Methods, Practical Applications, and Solutions—Group on Earth Observations Side Event Proceedings. USGS Open-File Rep. 2019-1033, 33 pp., https://pubs.usgs.gov/of/2019/1033/ofr20191033.pdf.

U.S. National Ice Center, 2008: IMS Daily Northern Hemisphere Snow and Ice Analysis at 1 km, 4 km, and 24 km Resolutions, Version 1. National Snow and Ice Data Center, accessed 27 July 2020, https://doi.org/10.7265/N52R3PMC. .

van As, D., R. S. Fausto, J. Cappelen, R. S. van de Wal, R. J. Braithwaite, and H. Machguth, 2016: Placing Greenland ice sheet ablation measurements in a multi-decadal context. *Geol. Surv. Denmark Greenl. Bull.*, **35**, 71–74, https://doi.org/10.34194/geusb.v35.4942.

Vasiliev, A. A., D. S. Drozdov, A. G. Gravis, G. V. Malkova, K. E. Nyland, and D. A. Streletskiy, 2020: Permafrost degradation in the western Russian Arctic. *Environ. Res. Lett.*, **15**, 045001, https://doi.org/10.1088/1748-9326/ab6f12.

Veraverbeke, S., B. M. Rogers, M. L. Goulden, R. R. Jandt, C. E. Miller, E. B. Wiggins, and J. T. Randerson, 2017: Lightning as a major driver of recent large fire years in North American boreal forests. *Nat. Climate Change*, **7**, 529534, https://doi.org/10.1038/nclimate3329.

Verdonen, M., L. T. Berner, B. C. Forbes, and T. Kumpula, 2020: Periglacial vegetation dynamics in Arctic Russia: decadal analysis of tundra regeneration on landslides with time series satellite imagery. *Environ. Res. Lett.*, **15**, 105020, https://doi.org/10.1088/1748-9326/abb500.

Vickers, H., K. A. Høgda, S. Solbø, S. R. Karlsen, H. Tømmervik, R. Aanes, and B. B. Hansen, 2016: Changes in greening in the high Arctic: insights from a 30 year AVHRR max NDVI dataset for Svalbard. *Environ. Res. Lett.*, **11**, 105004, https://doi.org/10.1088/1748-9326/11/10/105004.

——, S. R. Karlsen, and E. Malnes, 2020: A 20-year MODIS-based snow cover dataset for Svalbard and its link to phenological timing and sea ice variability. *Remote Sens.*, **12**, 1123, https://doi.org/10.3390/rs12071123.

Vihma, T., and Coauthors, 2016: The atmospheric role in the Arctic water cycle: A review on processes, past and future changes, and their impacts. *J. Geophys. Res. Biogeosci.*, **121**, 586–620, https://doi.org/10.1002/2015JG003132.

Weatherhead, B., A. Tanskanen, and A. Stevermer, 2005: Ozone and ultraviolet radiation. Arctic Climate Impact Assessment, Cambridge University Press, 152–182, www.amap.no/documents/download/1086/inline.

Webster, M. A., C. Parker, L. Boisvert, and R. Kwok, 2019: The role of cyclone activity in snow accumulation on Arctic sea ice. *Nat. Commun.*, **10**, 5285, https://doi.org/10.1038/s41467-019-13299-8.

Wegmann, M., and Coauthors, 2015: Arctic moisture source for Eurasian snow cover variations in autumn. *Environ. Res. Lett.*, **10**, 054015, https://doi.org/10.1088/1748-9326/10/5/054015.

Wheeling, K., 2020: The rise of zombie fires. *Eos,* **101**, https://doi.org/10.1029/2020EO146119.

WHO, 2002: Global solar UV index: A practical guide. WHO/SDE/OEH/02.2, 28 pp., www.who.int/uv/publications/en/GlobalUVI.pdf.

WMO, 2018: Scientific Assessment of Ozone Depletion: 2018. World Meteorological Organization, Global Ozone Research and Monitoring Project Rep. 58, 588 pp., https://csl.noaa.gov/assessments/ozone/2018/.

Wotton, B. M., 2009: Interpreting and using outputs from the Canadian forest fire danger rating system in research applications. *Environ. Ecol. Stat.*, **16**, 107–131, https://doi.org/10.1007/s10651-007-0084-2.

Wu, W., X. Sun, H. Epstein, X. Xu, and X. Li, 2020: Spatial heterogeneity of climate variation and vegetation response for Arctic and high-elevation regions from 2001–2018. *Environ. Res. Commun.*, **2**, 011007, https://doi.org/10.1088/2515-7620/ab6369.

York, A., U. S. Bhatt, E. Gargulinski, Z. Grabinski, P. Jain, A. Soja, R. L. Thoman, and R. Ziel, 2020: Wildland fire in high Northern latitudes. Arctic Report Card 2020, R. L. Thoman, J. Richter-Menge, and M. L. Druckenmiller, Eds., NOAA, https://doi.org/10.25923/2gef-3964.

Young, A. M., P. E. Higuera, P. A. Duffy, and F. S. Hu, 2017: Climatic thresholds shape northern highlatitude fire regimes and imply vulnerability to future climate change. *Ecography*, **40**, 606617, https://doi.org/10.1111/ecog.02205.

Yu, Y., J. P. Dunne, E. Sheviakova, P. Ginoux, S. Malyshev, J. G. John, and J. P. Krasting, 2021: Increased risk of the 2019 Alaskan July fires due to anthropogenic activity [in "Explaining Extreme Events of 2019 from a Climate Perspective"]. Bull. Amer. Meteor. Soc., 102 (1), S1–S7, https://doi.org/10.1175/BAMS-D-20-0154.1.

Yue, X., L. J. Mickley, J. A. Logan, R. C. Hudman, M. V. Martin, and R. M. Yantosca, 2015: Impact of 2050 climate change on North American wildfire: Consequences for ozone air quality. *Atmos. Chem. Phys.*, **15**, 1003310055, https://doi.org/10.5194/acp-15-10033-2015.

Zhang, X., J. He, J. Zhang, I. Polyakov, R. Gerdes, J. Inoue, and P. Wu, 2013: Enhanced poleward moisture transport and amplified northern high-latitude wetting trend. *Nat. Climate Change*, **3**, 47–51, https://doi.org/10.1038/nclimate1631.

STATE OF THE CLIMATE IN 2020

ANTARCTICA AND THE SOUTHERN OCEAN

S. Stammerjohn and T. Scambos, Eds.

Special Online Supplement to the *Bulletin of the American Meteorological Society* Vol.102, No. 8, August, 2021

https://doi.org/10.1175/BAMS-D-21-0081.1

Corresponding author: Sharon Stammerjohn / Sharon.Stammerjohn@colorado.edu

STATE OF THE CLIMATE IN 2020

Antarctica and the Southern Ocean

Editors

Jessica Blunden
Tim Boyer

Chapter Editors

Freya Aldred
Peter Bissolli
Howard J. Diamond
Matthew L. Druckenmiller
Robert J. H. Dunn
Catherine Ganter
Nadine Gobron
Gregory C. Johnson
Tim Li
Rick Lumpkin
Ademe Mekonnen
John B. Miller
Twila A. Moon
Ahira Sánchez-Lugo
Ted A. Scambos
Carl J. Schreck III
Sharon Stammerjohn
Richard L. Thoman
Kate M. Willett

Technical Editor

Andrea Andersen

***BAMS* Special Editor for Climate**

Michael A. Alexander

American Meteorological Society

Cover credit:
Scientists acquiring measurements of East Antarctic sea ice and snow cover thickness and properties during the 2003 Australian-led ARISE multi-disciplinary field experiment. The photo was taken by Rob Massom (Australian Antarctic Division) on 10 October 2003.

Antarctica and the Southern Ocean is one chapter from the *State of the Climate in 2020* annual report and is available from https://doi.org/10.1175/BAMS-D-21-0081.1. Compiled by NOAA's National Centers for Environmental Information, *State of the Climate in 2020* is based on contributions from scientists from around the world. It provides a detailed update on global climate indicators, notable weather events, and other data collected by environmental monitoring stations and instruments located on land, water, ice, and in space. The full report is available from https://doi.org/10.1175/2021BAMSStateoftheClimate.1.

How to cite this document:

Citing the complete report:
Blunden, J. and T. Boyer, Eds., 2021: "State of the Climate in 2020". *Bull. Amer. Meteor. Soc.,* **102** (8), Si–S475, https://doi.org/10.1175/2021BAMSStateoftheClimate.1

Citing this chapter:
Stammerjohn, S. and T. Scambos, Eds., 2021: Antarctica and the Southern Ocean [in "State of the Climate in 2020"]. *Bull. Amer. Meteor. Soc.*, **102** (8), S317–S355, https://doi.org/10.1175/BAMS-D-21-0081.1.

Citing a section (example):
Kramarova, N., P. A. Newman, E. R. Nash, S. E. Strahan, C. S. Long, B. Johnson, M. Pitts, M. L. Santee, I. Petropavlovskikh, L. Coy, J. de Laat, G. H. Bernhard, S. Stierle, and K. Lakkala, 2021: 2020 Antarctic ozone hole [in "State of the Climate in 2020"]. *Bull. Amer. Meteor. Soc.*, **102** (8), S345–S349, https://doi.org/10.1175/BAMS-D-21-0081.1.

Editor and Author Affiliations (alphabetical by name)

Adusumilli, Susheel, Scripps Institution of Oceanography, University of California San Diego, La Jolla, California
Barreira, Sandra, Argentine Naval Hydrographic Service, Buenos Aires, Argentina
Bernhard, Germar H., Biospherical Instruments Inc., San Diego, California
Bozkurt, Deniz, Department of Meteorology, University of Valparaíso, Valparaíso and Center for Climate and Resilience Research (CR)2, Santiago, Chile
Bushinsky, Seth M., University of Hawaii at Mānoa, Honolulu, Hawaii
Clem, Kyle R., School of Geography, Environment and Earth Sciences, Victoria University of Wellington, Wellington, New Zealand
Colwell, Steve, British Antarctic Survey, Cambridge, United Kingdom
Coy, Lawrence, Science Systems and Applications, Inc., NASA Goddard Space Flight Center, Greenbelt, Maryland
De Laat, Jos, Royal Netherlands Meteorological Institute (KNMI), DeBilt, Netherlands
du Plessis, Marcel D., Department of Marine Sciences, University of Gothenburg, Gothenburg, Sweden
Fogt, Ryan L., Department of Geography, Ohio University, Athens, Ohio
Foppert, Annie, Australian Antarctic Program Partnership, Hobart, Tasmania, Australia
Fricker, Helen Amanda, Scripps Institution of Oceanography, University of California San Diego, La Jolla, California
Gardner, Alex S., Jet Propulsion Laboratory, California Institute of Technology, Pasedena, California
Gille, Sarah T., Climate, Atmospheric Science and Physical Oceanography, Scripps Institution of Oceanography, University of California, San Diego, La Jolla, California
Gorte, Tessa, Department of Atmospheric and Oceanic Sciences, University of Colorado Boulder, Boulder, Colorado
Johnson, Bryan, NOAA/OAR Earth System Research Laboratory, Global Monitoring Division, and University of Colorado, Boulder, Colorado
Keenan, Eric, Department of Atmospheric and Oceanic Sciences, University of Colorado Boulder, Boulder, Colorado
Kennett, Daemon, School of Geography, Environment and Earth Sciences, Victoria University of Wellington, Wellington, New Zealand
Keller, Linda M., Department of Atmospheric and Oceanic Sciences, University of Wisconsin-Madison, Madison, Wisconsin
Kramarova, Natalya A., NASA Goddard Space Flight Center, Greenbelt, Maryland
Lakkala, Kaisa, Finnish Meteorological Institute, Helsinki, Finland
Lazzara, Matthew A., Department of Physical Sciences, School of Arts and Sciences, Madison Area Technical College, and Space Science and Engineering Center, University of Wisconsin-Madison, Madison, Wisconsin
Lenaerts, Jan T. M., Department of Atmospheric and Oceanic Sciences, University of Colorado Boulder, Boulder, Colorado
Lieser, Jan L., Australian Bureau of Meteorology, Hobart, TAS, Australia, and Institute for Marine and Antarctic Studies, University of Tasmania, Hobart, Tasmania, Australia
Li, Zhi, Climate Change Research Centre, University of New South Wales, Sydney, New South Wales, Australia
Liu, Hongxing, Department of Geography, University of Cincinnati, Cincinnati, Ohio
Long, Craig S., NOAA/NWS National Center for Environmental Prediction, College Park, Maryland
MacFerrin, Michael, Earth Science and Observation Center, CIRES, University of Colorado, Boulder, Colorado
Maclennan, Michelle L., Department of Atmospheric and Oceanic Sciences, University of Colorado Boulder, Boulder, Colorado
Massom, Robert A., Australian Antarctic Division and Australian Antarctic Program Partnership (AAPP), Hobart, Tasmania, Australia
Mikolajczyk, David, Space Science and Engineering Center, University of Wisconsin-Madison, Madison, Wisconsin
Montgomery, Lynn, Department of Atmospheric and Oceanic Sciences, University of Colorado Boulder, Boulder, Colorado
Mote, Thomas L., Department of Geography, University of Georgia
Nash, Eric R., Science Systems and Applications, Inc.; NASA Goddard Space Flight Center, Greenbelt, Maryland
Newman, Paul A., NASA Goddard Space Flight Center, Greenbelt, Maryland
Petropavlovskikh, Irina, Cooperative Institute for Research in Environmental Sciences, University of Colorado Boulder, and NOAA/OAR Earth System Research Laboratory, Boulder, Colorado
Pitts, Michael, NASA Langley Research Center, Hampton, Virginia
Reid, Phillip, Australian Bureau of Meteorology and Australian Antarctic Program Partnership (AAPP), Hobart, Tasmania, Australia
Rintoul, Steven R., CSIRO Oceans and Atmosphere, Hobart, Tasmania, Australia, Centre for Southern Hemisphere Oceans Research, Hobart, Tasmania, Australia, Australian Antarctic Program Partnership, Hobart, Tasmania, Australia
Santee, Michelle L., NASA Jet Propulsion Laboratory, California Institute of Technology, Pasadena, California
Scambos, Ted A., Earth Science and Observation Center, CIRES, University of Colorado, Boulder, Colorado
Shadwick, Elizabeth H., CSIRO Oceans & Atmosphere, Hobart, Tasmania, Australia Centre for Southern Hemisphere Oceans Research, Hobart, Tasmania, Australia, Australian Antarctic Program Partnership, Hobart, Tasmania, Australia
Silvano, Alessandro, Ocean and Earth Science, National Oceanography Centre, University of Southampton, Southampton, United Kingdom
Stammerjohn, Sharon, Institute of Arctic and Alpine Research, University of Colorado, Boulder, Colorado
Stierle, Scott, NOAA/OAR Global Monitoring Laboratory, Boulder, Colorado; CIRES, University of Colorado, Boulder, Colorado
Strahan, Susan, Universities Space Research Association, NASA Goddard Space Flight Center, Greenbelt, Maryland
Sutton, Adrienne J., Pacific Marine Environmental Laboratory, NOAA, Seattle Washington
Swart, Sebastiaan, Department of Marine Sciences, University of Gothenburg, Gothenburg, Sweden, and Department of Oceanography, University of Cape Town, Rondebosch, South Africa
Tamsitt, Veronica, Climate Change Research Centre, University of New South Wales, Sydney, NSW, Australia, and Centre for Southern Hemisphere Oceans Research, Hobart, Tasmania, Australia; College of Marine Science, University of South Florida, St. Petersburg, Florida
Tilbrook, Bronte, CSIRO Oceans & Atmosphere, Hobart, Tasmania, Australia, and Australian Antarctic Program Partnership, Hobart, Tasmania, Australia
Wang, Lei, Department of Geography and Anthropology, Louisiana State University, Baton Rouge, Louisiana
Williams, Nancy L., College of Marine Science, University of South Florida, St. Petersburg, Florida
Yuan, Xiaojun, Lamont-Doherty Earth Observatory of Columbia University, Palisades, New York

Editorial and Production Team

Allen, Jessicca, Graphics Support, Cooperative Institute for Satellite Earth System Studies, North Carolina State University, Asheville, North Carolina

Andersen, Andrea, Technical Editor, Innovative Consulting Management Services, LLC, NOAA/NESDIS National Centers for Environmental Information, Asheville, North Carolina

Hammer, Gregory, Content Team Lead, Communications and Outreach, NOAA/NESDIS National Centers for Environmental Information, Asheville, North Carolina

Love-Brotak, S. Elizabeth, Lead Graphics Production, NOAA/NESDIS National Centers for Environmental Information, Asheville, North Carolina

Misch, Deborah J., Graphics Support, Innovative Consulting Management Services, LLC, NOAA/NESDIS National Centers for Environmental Information, Asheville, North Carolina

Riddle, Deborah B., Graphics Support, NOAA/NESDIS National Centers for Environmental Information, Asheville, North Carolina

Veasey, Sara W., Visual Communications Team Lead, Communications and Outreach, NOAA/NESDIS National Centers for Environmental Information, Asheville, North Carolina

6. Table of Contents

*Please refer to Chapter 8 (Relevant datasets and sources) for a list of all climate variables and datasets used in this chapter for analyses, along with their websites for more information and access to the data.

6. ANTARCTICA AND THE SOUTHERN OCEAN

S. Stammerjohn and T. Scambos, Eds.

a. Overview—S. Stammerjohn and T. Scambos

Antarctic and Southern Ocean climate for 2020 was marked by several mid-year shifts, including reversals from generally warmer to cooler temperatures on the continent, weaker to stronger westerlies over the ocean, greater to lesser precipitation on the West Antarctic ice sheet, a warmer to colder stratosphere, and lesser to greater circumpolar sea ice extent. The year was also marked by several records, including the highest air temperature ever recorded on the continent (18.3°C, Francelino et al. 2021) that was observed on the northeastern tip of the Antarctic Peninsula on 6 February 2020. This temperature record was accompanied by the largest late-summer surface melt event yet recorded in the satellite data (since 1978) that affected more than 50% of the Antarctic Peninsula and reached elevations exceeding 1700 m. As described in Sidebar 6.1, the record warming and melting were caused by an exceptional atmospheric circulation pattern (an "atmospheric river") that delivered extreme warmth and moisture from sub-tropical and middle latitudes to the West Antarctic region.

Later in the year, another record was broken with the longest-lived (and 12th-largest) ozone hole yet observed over the last 41 years. Below-average stratospheric temperatures were observed in winter and persisted well into spring 2020. These low austral spring temperatures stood in stark contrast to the year before when a dramatic stratospheric warming event occurred in September 2019. Both of these events had lasting effects on the climate: the 2020 event led to unusually high levels of ultraviolet radiation in the spring and summer of 2020/21 (section 6h), while the 2019 stratospheric warming event led to strong surface warming in spring and summer of 2019/20, particularly across Queen Maud Land (Clem et al. 2020a; Newman et al. 2020).

The shift from negative to positive net daily sea ice extent (SIE) anomalies in early August 2020 was particularly noteworthy as it marked the end of a long run of daily negative SIE anomalies that had persisted since the austral spring of 2016. This shift coincided with a strengthening and expansion of the Amundsen Sea Low during the latter half of 2020 in response to an evolving La Niña in the tropical Pacific. As discussed in Sidebar 6.2, responses to such perturbations emanating from the tropics, when extreme, have the potential to be "disruption events" at high southern latitudes and are associated with large shifts in the Antarctic climate system.

In the Southern Ocean, the most prominent anomalies observed during 2020 were a significant shoaling, freshening, and warming of two Subantarctic Mode Water production areas in the southeast Pacific and Indian Oceans, significant because these are key areas for global ocean uptake of heat and carbon. Deeper down, however, 2020 marks the continued reversal (since ~2014) of freshening and warming of Antarctic Bottom Water that had been previously observed over the last half century. On the continent, negative ice sheet mass anomalies, particularly on the Antarctic Peninsula and the Amundsen sector of the West Antarctic ice sheet, outweighed the small positive gains elsewhere.

More details on Antarctica's climate, weather, ice, ocean, and ozone are presented below for 2020. In most sections, and as for previous years, the 2020 anomalies are derived through comparison with the 1981–2010 climatology if sufficient data are available (and when not, other date ranges are given). Place names mentioned throughout the chapter are provided in Fig. 6.1.

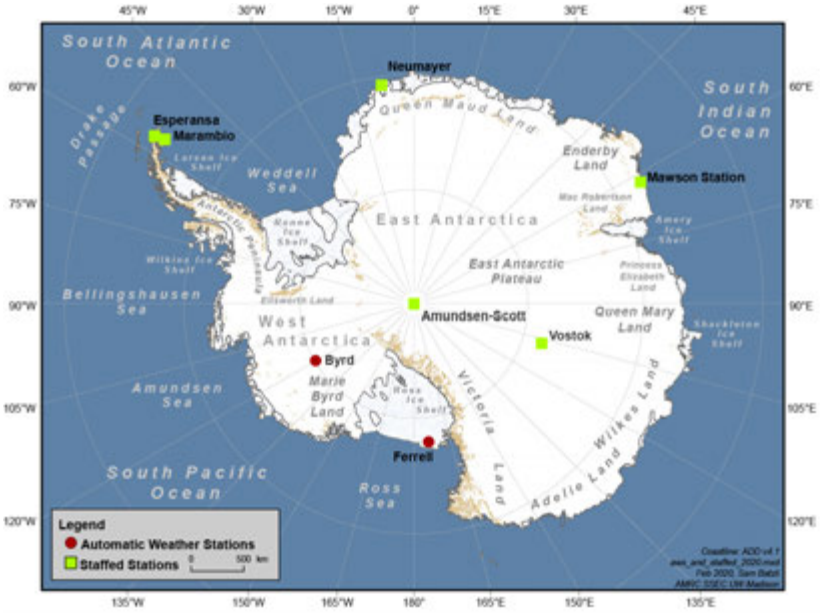

Fig. 6.1. Map of stations and other regions discussed in this chapter.

b. Atmospheric circulation and surface observations—K. R. Clem, S. Barreira, R. L. Fogt, S. Colwell, L. M. Keller, M. A. Lazzara, and D. Mikolajczyk

The 2020 Antarctic atmospheric circulation exhibited anomalous seasonal variability with large temperature swings on the continent and in the Weddell and Ross Sea sectors in particular. Meanwhile, East Antarctica experienced persistently warm conditions throughout much of the year. In the lower stratosphere and down through the troposphere, the year began with anomalously warm conditions associated with the late 2019 stratospheric warming event (Newman et al. 2020), while in contrast, 2020 finished with anomalously cold conditions in the stratosphere tied to an unusually large and deep ozone hole that developed during spring (see section 6h for more details).

The Antarctic atmospheric circulation anomalies were examined using the European Centre for Medium-Range Weather Forecasts fifth-generation atmospheric reanalysis (ERA5). Figure 6.2 shows the monthly geopotential height (Fig. 6.2a) and temperature (Fig. 6.2b) anomalies averaged over the polar cap (60°–90°S) and the monthly circumpolar zonal wind anomalies (Fig. 6.2c) averaged over 50°–70°S. The anomalies (contoured) and standard deviations (shaded) are relative to the 1981–2010 climatology. To summarize the surface climate anomalies, the year was split into four groups based on periods of relatively persistent surface pressure and temperature anomaly patterns: January–March, April–June, July–October, and November–December. The surface pressure and temperature anomalies (contours) and standard deviations (shaded) are averaged for each group relative to their 1981–2010 climatology (Fig. 6.3). Monthly temperature and pressure anomaly time series are also shown for select Antarctic staffed (Marambio, Neumayer, Mawson, Vostok) and automated (Ferrell AWS, Byrd AWS) weather stations (Fig. 6.4).

From January to March, geopotential height near the surface (Fig. 6.2a) and surface pressure (Fig. 6.3a) steadily decreased across the Antarctic continent while the midlatitudes were dominated by positive pressure anomalies. By March, tropospheric geopotential heights over the polar cap were more than 25 m (–1.5 std. dev.) below average, and surface pressure at all six weather stations ranged from –3 to –12 hPa below average. Concurrently, stronger-than-average circumpolar westerlies, peaking around +2 m s^{-1} (+1.5 std. dev.), developed through the troposphere and stratosphere, and the Southern Annular Mode (SAM) index reached its highest value of the year (+2.05) during March (Fig. 6.2c). Locally deep pressure anomalies were centered over Marie Byrd Land, the Ross Ice Shelf, and Wilkes Land (Fig. 6.3a, noting this shows a 3-month average). These cyclonic anomalies (particularly in February) produced warm northerly flow and positive surface air temperature anomalies of +1° to +2°C (+2 std. dev.) across the Antarctic Peninsula and Ross Ice Shelf during January–March, resulting

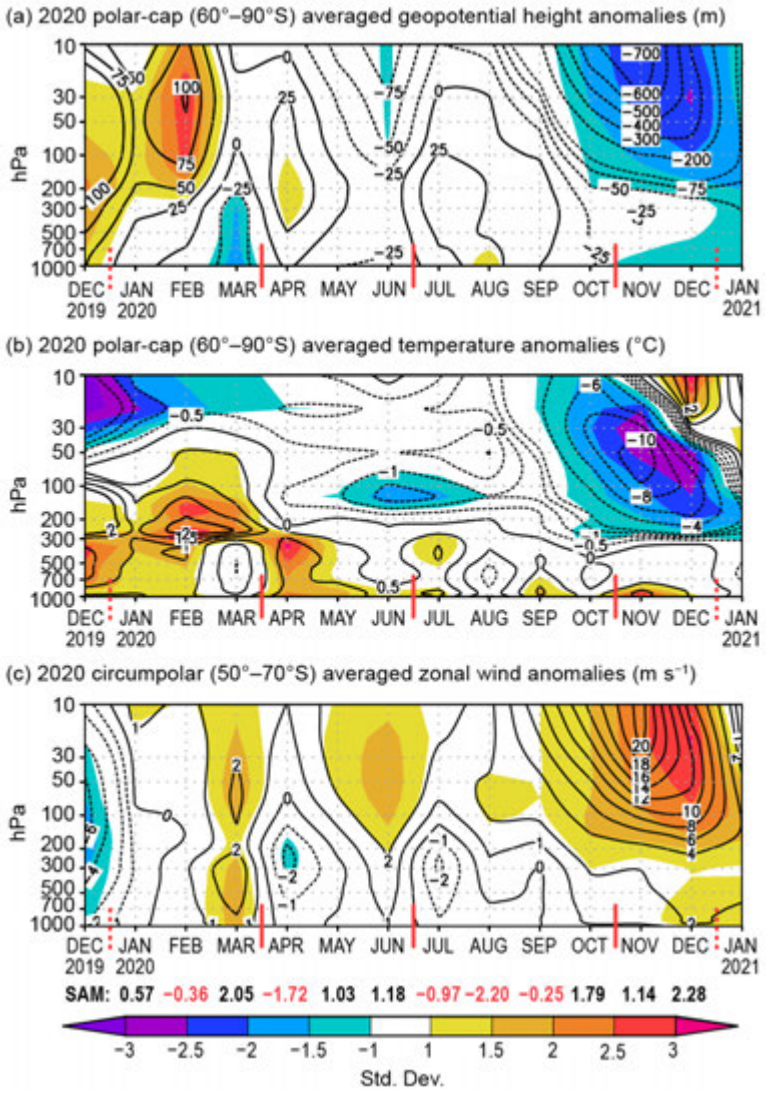

Fig. 6.2. Area-averaged (weighted by cosine of latitude) monthly anomalies over the southern polar region in 2020 relative to 1981–2010: (a) polar cap (60°–90°S) averaged geopotential height anomalies (contour interval is 25 m up to ±100 m and 100 m after ±100 m); (b) polar cap averaged temperature anomalies (contour interval is 0.5°C up to ±2°C and 2°C after ±2°C); (c) circumpolar (50°–70°S) averaged zonal wind anomalies (contour interval is 2 m s^{-1} with an additional contour at ±1 m s^{-1}). Shading depicts std. dev. of monthly anomalies from the 1981–2010 climatological average as indicated by color bar at bottom. Red vertical bars indicate the four climate periods used for compositing in Fig. 6.3; the dashed lines near Dec 2019 and Dec 2020 indicate circulation anomalies wrapping around the calendar year. Values from the Marshall (2003) SAM index are shown below (c) in black (positive values) and red (negative values). (Source: ERA5 reanalysis.)

in a new record high monthly mean temperature at Ferrell AWS of –10.7°C (+3.8°C above average) in February (Fig. 6.4e). Esperanza Station, on the northeastern side of the Antarctic Peninsula, recorded a temperature of +18.3°C on 6 February, the highest temperature recorded to date on the Antarctic continent replace with (Francelino et al. 2021). The causes of this record warming of the Antarctic Peninsula region are detailed in Sidebar 6.1.

Negative surface pressure anomalies of –4 to –6 hPa (–1 to –2 std. dev.) persisted across the Ross Ice Shelf and Marie Byrd Land from April through June (Figs. 6.3b, 6.4e,f), allowing anomalously warm conditions (+2° to +3°C) to continue across the Antarctic Peninsula and adjacent Ellsworth Land through early winter. The warming also spread inland across the plateau during April–June (Figs. 6.3f, 6.4d) and polar cap averaged temperature anomalies were +0.5° to +1°C (+1.5 to +2.5 std. dev.) from April to June (Fig. 6.2b).

During July–October, the persistent low-pressure anomaly over the Ross Ice Shelf shifted northward into the Ross Sea (Fig. 6.3c). The broader surface pressure anomaly composite during this period (Fig. 6.3c) was consistent with a developing La Niña/Pacific–South American pattern (Yuan 2004), with high pressure east of New Zealand, low pressure over the Ross Sea, and high pressure in the Weddell Sea. Associated with this pattern in the South Atlantic region, Neumayer Station set a new record high monthly mean pressure of 995.7 hPa (+10.9 hPa above average) in August (Fig. 6.4b). The high-pressure anomaly in the Weddell Sea produced strong negative surface temperature anomalies of –7° to –9°C (>–3 std. dev.) across the Ronne Ice Shelf and the adjacent Filchner Ice Shelf to the east (Fig. 6.3g) from July through October, extending eastward along the coast to Neumayer Station, where a monthly temperature anomaly of –8.2°C was observed during August, coinciding with its record high pressure (Fig. 6.4b). The high-pressure anomaly in the Weddell Sea also ended the warm conditions on the Peninsula, and Marambio Station recorded its coldest August on record (–21.8°C, –8.7°C below average; Fig. 6.4a).

In contrast to the large fluctuations in the South Atlantic sector of Antarctica, surface pressures were near average to slightly above average over the remainder of the continent from April

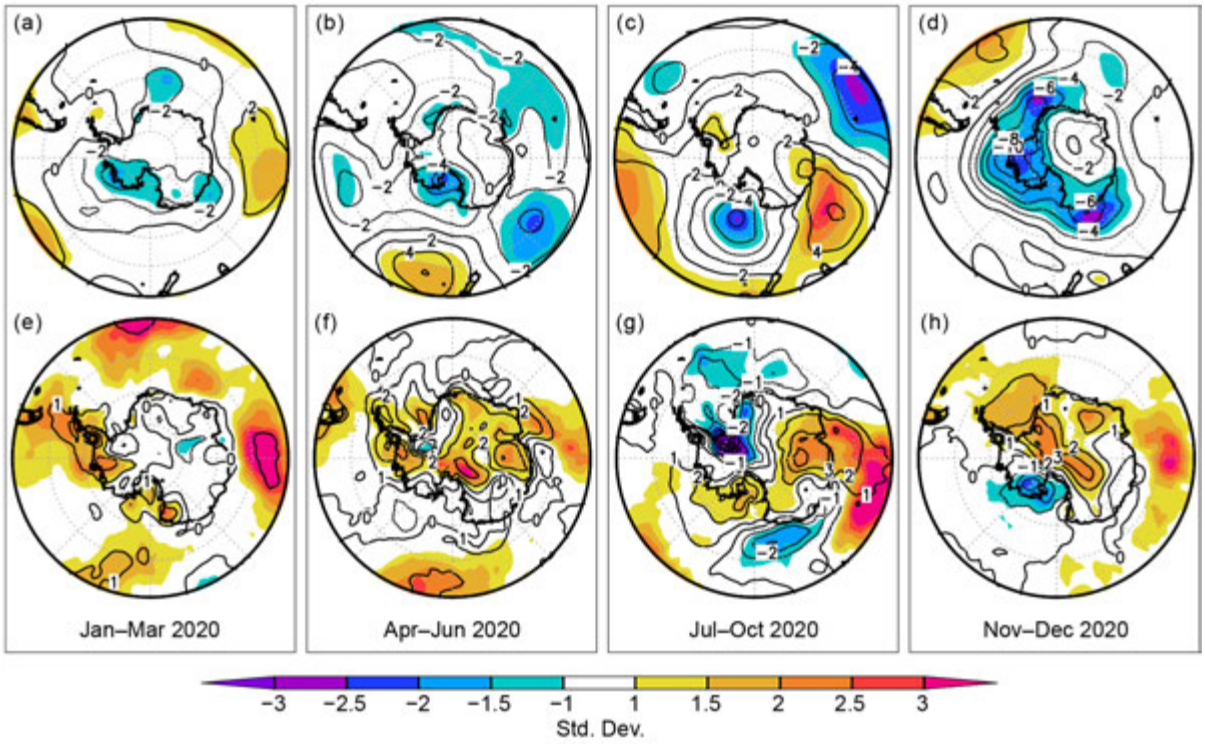

Fig. 6.3. (top) Surface pressure and (bottom) 2-m temperature anomalies relative to 1981–2010 for (a),(e) Jan–Mar 2020; (b),(f) Apr–Jun 2020; (c),(g) Jul–Oct 2020; (d),(h) Nov–Dec 2020. Contour interval is 2 hPa for surface pressure anomalies and 1°C for 2-m temperature anomalies. Shading depicts standard deviation of anomalies. (Source: ERA5 reanalysis.)

through October, extending upward through the troposphere (Figs. 6.2a, 6.3b,c, 6.4). In addition, a strong positive pressure anomaly developed just offshore of East Antarctica from 90° to 135°E during July–October (Fig. 6.3c), which produced positive surface temperature anomalies of +2° to +4°C (+2 std. dev.) across the Amery Ice Shelf and portions of the plateau (Fig. 6.3g). While no monthly record high temperatures were set here during this period, Mawson and Vostok stations observed persistently above-average temperature anomalies of +2° to +6°C from April to October (Figs. 6.4c,d), and Vostok Station experienced its warmest spring (September–November) on record (not shown).

The surface circulation underwent a dramatic shift during November and December, losing its La Niña-like wave train characteristics (Fig. 6.3d) and transitioning to a more zonally symmetric positive SAM pattern with below-average pressure over much of the continent and a deepened Amundsen Sea Low (Sidebar 6.2). However, the surface expression was not typical of most concurrent La Niña and positive SAM phases (Fogt et al. 2011). The strongest negative pressure anomalies were located over and near West Antarctica, where Byrd AWS recorded its lowest monthly pressure on record for October, November, and December (Fig. 6.4f), and Ferrell AWS (Fig. 6.4e) recorded its lowest pressure on record for December (both around –10 to –12 hPa). Concurrently, pressures over much of East Antarctica were near average. The regional low pressure over West Antarctica combined with relatively high pressures over East Antarctica produced anomalously warm conditions across the Weddell Sea and throughout much of the interior (Fig. 6.3h), where surface air temperatures were generally +2° to +3°C (+2 std. dev.) above normal; both Marambio (+3.8°C) and Vostok (+4°C) recorded their warmest Novembers on record (Figs. 6.4a,d). Below-average temperatures were found only across Marie Byrd Land and the Ross Ice Shelf during November and December, where southerly flow developed on the western side of the low pressure, marking a switch from the above-average temperatures that previously persisted here for much of the year.

In the stratosphere, strong negative geopotential height and temperature anomalies developed in October (Figs. 6.2a,b), associated with the anomalously large and deep ozone hole (section 6h). The geopotential height and temperature anomalies peaked in November at –700 m (–2 std. dev.)

and –10°C (–2.5 std. dev.), respectively. These anomalies strengthened the north–south pressure gradient and resulted in a strengthened stratospheric polar vortex of around 20 m s^{-1} in November (Fig. 6.2c). These strong anomalies in geopotential height, temperature, and winds persisted in the stratosphere through December, while much weaker anomalies characterized the troposphere. Whether the atypical regional nature of the surface circulation anomalies contributed to the unusually persistent ozone hole (section 6h), perhaps through a lack of planetary scale waves propagating from the troposphere to the stratosphere, remains an open question.

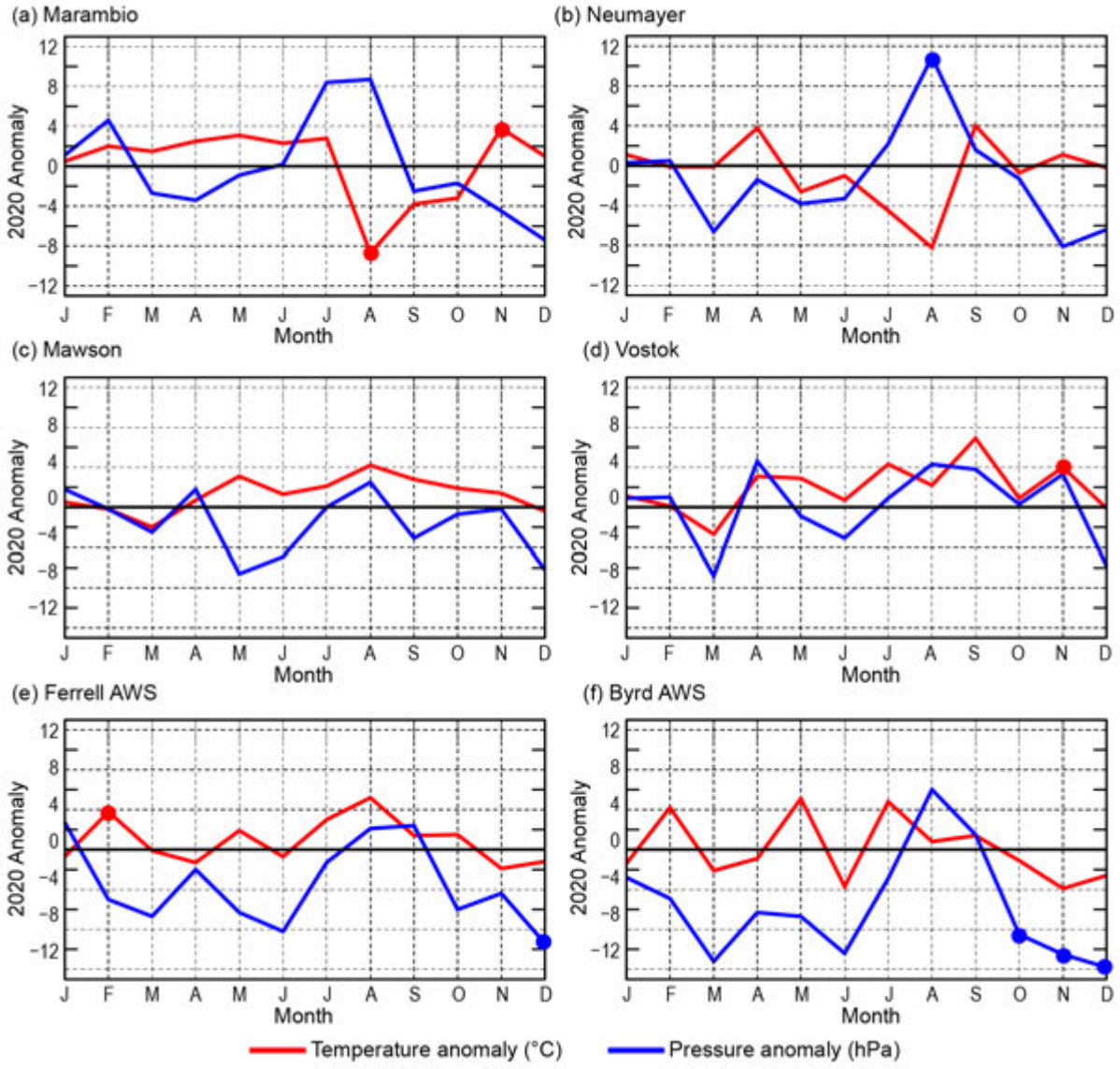

Fig. 6.4. Monthly Antarctic climate anomalies during 2020 at six representative stations [four staffed (a)–(d), and two automatic (e),(f)]. Anomalies for temperature (°C) are shown in red and MSLP/surface pressure (hPa) are shown in blue, with filled circles denoting monthly mean records set for each station in 2020. All anomalies are based on differences from the monthly 1981–2010 averages. Observational data used to calculate records start in 1970 for Marambio, 1981 for Neumayer and Ferrell AWS, 1954 for Mawson, 1958 for Vostok, and 1980 for Byrd AWS.

Sidebar 6.1: Record warmth and surface melt on the Antarctic Peninsula in February 2020—K. R. CLEM, M. MACFERRIN, D. KENNETT, D. BOZKURT, AND T. SCAMBOS

On 6 February 2020, the Argentine research base, Esperanza, located on the northeast tip of the Antarctic Peninsula (AP; 63.4°S, 57.0°W, elevation 13 m a.s.l.), measured a 2-m temperature of 18.3°C (Francelino et al. 2021), which is the highest temperature ever recorded on the Antarctic continent, surpassing the previous record of 17.5°C (also at Esperanza) set on 24 March 2015. The AP also experienced its largest early-February surface melt extent on record, affecting more than 50% of the region and reaching elevations exceeding 1700 m a.s.l. on the Peninsula's southwestern side. As detailed below, these record events were tied to an exceptional atmospheric circulation pattern that brought extreme heat and moisture from sub-tropical and middle latitudes to the entire West Antarctic region, with surface warming on the eastern Peninsula being further intensified by the Foehn wind effect.

Figure SB6.1a shows the three-hourly surface synoptic conditions observed at Esperanza over the 5–7 February period (obtained from the Global Telecommunications System). Eighteen hours prior to the record, temperatures were steady around 0°C with high relative humidity between 80% and 90% and light and variable winds. Temperatures began increasing steadily between 0600 and 1200 UTC on 6 February and then increased rapidly during the 1200–1500 UTC period from 6.3°C (1200 UTC) to 18.3°C (1500 UTC). Coinciding with the sharp rise in temperature, relative humidity dropped to 27% and winds increased in speed while shifting from the northeast to the southwest. The synoptic conditions indicate the sudden rise in temperature was due to Foehn-related warming, which is common on the eastern Peninsula and characterized by a spike in temperature, a drop in relative humidity, and persistent westerly winds (Cape et al. 2015). Temperatures remained warm following the main spike with winds remaining strong out of the southwest, including 15.7°C observed 3 hours later (1800 UTC) and 17.3°C observed 6 hours later (2100 UTC), indicating a relatively long-duration Foehn event.

Foehn events are typically associated with high levels of moisture convergence on an upstream windward slope, which aids the rapid saturation of air as it ascends the slope (the western Peninsula). This causes the air to cool more slowly at about –5°C 1000 m^{-1} (the saturated adiabat) than if it were not saturated. With less cooling, air crossing the ridge is far warmer than usual, allowing higher temperatures to be reached as the air descends the leeward slope (the eastern Peninsula) where it warms at about +10°C 1000 m^{-1} (the dry adiabat). Indeed, the remarkable increase in temperature at Esperanza occurred shortly after landfall of an "atmospheric river" (AR; outlined in green in Fig. SB6.1b) on the western Peninsula, which occurred at 0600 UTC on 6 February, 9 hours prior to the record temperature. Atmospheric rivers are long, narrow corridors of extremely high moisture flux (>85th percentile; Guan and Waliser 2015). Landfalling ARs in West Antarctica are unusual, with only around 12 events per year, but they are responsible for 40%–80% of surface melting in the region (Wille et al. 2019). The 6 February AR developed between a broad, double-barrel, low-pressure complex over the South Pacific (contours in Fig. SB6.1b), with a 960-hPa low in the western Amundsen Sea and a second 976-hPa low to its northeast near 50°S, and an area of strong (1024 hPa) high pressure centered over southern South America. Together, these features rapidly transported unusually warm, moist air sourced from 35°–40°S latitude poleward and eastward toward the AP, steered along the southern edge of the South America high-pressure cell.

The circulation pattern responsible for the 6 February AR was also remarkable. Figure SB6.1c shows averaged anomalies for the 4–10 February 2020 period of mean sea level pressure (MSLP, contours), surface air temperature (SAT, color), and surface wind (vectors) relative to the 1981–2010 4–10 February climatology. Along the northwest Peninsula and over Drake Passage, MSLP was more than 15 hPa (+2.5 std. dev.) above average. The exceptional nature of this high-pressure anomaly was even more apparent through the middle troposphere, where 4–10 February geopotential height along the northwest Peninsula from the 850-hPa to 500-hPa level was the highest on record (since 1979), including a 500-hPa geopotential height of 5505 m that was 296 m (+4 std. dev.) above average, shattering the previous record of 5357 m (148 m above average) set in 1998. Meanwhile, the low-pressure center in the Amundsen Sea was more than 12 hPa below average and the low pressure northeast of this region near 50°S was more than 6 hPa below average.

These strong circulation anomalies also advected extremely warm air into the region, producing positive SAT anomalies of more than 6°C across nearly all of West Antarctica and the AP. These anomalously warm temperatures, further enhanced by Foehn effect warming on the eastern Peninsula, caused anomalously large surface melt extents across the AP during a 7-day span from 6 to 12 February (Fig. SB6.1d). While the median melt extent from 1989 to 2020 is just 1%–2% for those dates, on 8 February 2020, surface melt reached 49.4% of the AP, breaking the previous satellite-measured record of 31.0% set on 8 February 1996. The next day on 9 February, surface melt reached 53.8% of the Peninsula, also a daily record, and

remained at record high levels (for the satellite record) through 12 February.

Similar circulation anomalies were seen during the previous record high Antarctic temperature on 24 March 2015 at Esperanza (Rondanelli et al. 2019), which also accompanied an AR that made landfall on the western Peninsula. Therefore, the anomalous circulation pattern described here appears exceptionally favorable for the development of ARs and is a key driver of extreme warmth and surface melt on the AP. Previously it was shown that the 24 March 2015 circulation anomalies were forced by tropical convection (Rondanelli et al. 2019), with 6 February 2020 also exhibiting a pattern forced by tropical convection in the South Pacific Convergence Zone (Clem et al. 2019). Projections of future climate and surface melt extremes on the Peninsula will need to account for the occurrence and tropical linkages of this atmospheric circulation pattern, including a climate-driven tendency for increased Foehn frequency and intensity (Cape et al. 2015).

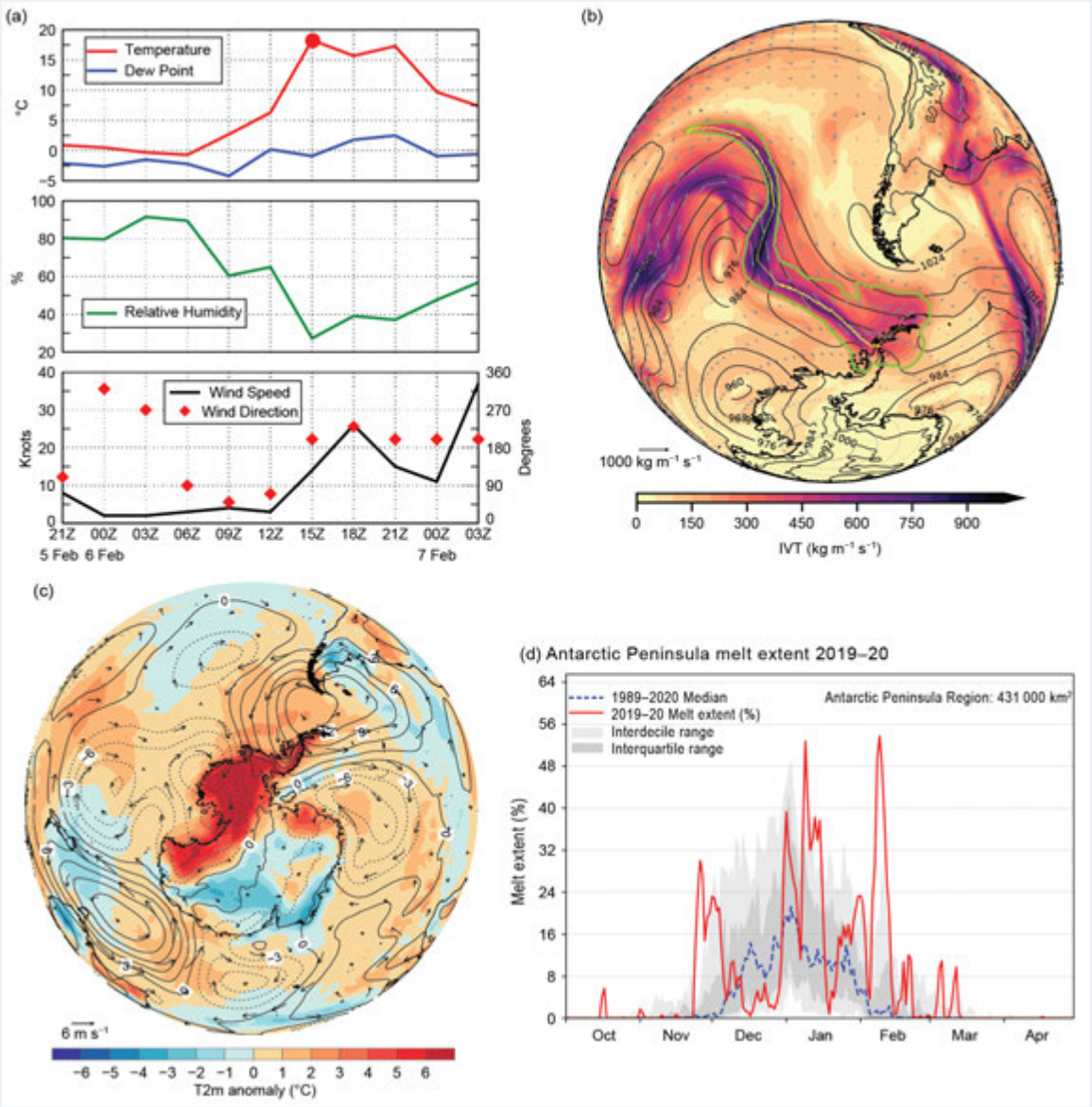

Fig. SB6.1. (a) Observed Esperanza synoptic conditions during 5–7 Feb 2020: (top) 2-m temperature and dew point (°C, the red filled circle denotes the 18.3°C temperature record), (middle) 2-m relative humidity (%), and (bottom) 10-m wind speed (kt) and direction. (b) The atmospheric river (AR) that made landfall on the Antarctic Peninsula (AP) on 6 Feb 2020 at 0600 UTC: ERA5 integrated water vapor transport (IVT, kg m^{-1} s^{-1}; shaded/vectors), outline of AR/IVT exceeding 85th percentile for Jan–Mar 2020 (green contour) and ERA5 MSLP (hPa, black contours). The AR axis (yellow) denotes the pathway of maximum water vapor flux. (c) 4–10 February 2020 ERA5 MSLP (hPa, contour), 2-m temperature (°C, shaded), and 10-m wind (m s^{-1}, vectors) anomalies relative to 1981–2010. (d) Daily totals of melt extent (%) over the AP (red line) from 1 Oct 2019 to 30 Apr 2020 from passive-microwave measurements (Meier et al. 2019). Daily median (dashed blue line), inter-quartile (dark gray shading), and inter-decile (light gray shading) ranges are included for the baseline period of Oct 1989 through Apr 2020.

c. Ice sheet surface mass balance—J. Lenaerts, E. Keenan, M. Maclennan, and T. Gorte

The grounded portion of the Antarctic ice sheet (AIS) is characterized by a frigid continental climate. Even in peak summer, atmospheric temperatures on the continent are low enough to prevent widespread surface melt (section 6d) or liquid precipitation, unlike the Greenland ice sheet (see section 5e). With few exceptions (e.g., the northern Antarctic Peninsula [AP]), any meltwater that is produced refreezes locally in the firn (compacted snow older than 1 year), making meltwater runoff negligible on the AIS. On the other hand, sublimation is a significant component of AIS surface mass balance (SMB; Lenaerts and Van Den Broeke 2012; Agosta et al. 2019; Mottram et al. 2021), especially in summer and on the flanks of the ice sheet where dry downsloping winds and blowing snow occur frequently (blowing snow >50% of the time; Palm et al. 2018). By far, the dominant contributor to AIS SMB, with a magnitude of about +2300 Gt (Gt = Gigatons = 10^{12} kg) yr^{-1} over grounded ice areas, is solid precipitation, i.e., snowfall.

Atmospheric reanalysis products are important tools for analyzing in near-real time AIS SMB and its two dominant components, snowfall and sublimation. Here we use reanalysis data from MERRA-2 at 0.5° × 0.625° horizontal resolution (Gelaro et al. 2017) and ERA-5 at 0.28° horizontal resolution (Copernicus Climate Change Service [C3S] 2017) to analyze the 2020 AIS SMB, its spatial and seasonal characteristics, and its comparison to the climatological base period (1981–2010). Based on recent work comparing reanalysis products with in situ observations on Antarctica, MERRA-2 and ERA-5 were the best performing (Wang et al. 2016; Gossart et al. 2019; Medley and Thomas 2019); however, important biases remain that are associated with the relatively low spatial resolution of the reanalysis products and poor or no representation of important SMB processes (e.g., blowing snow, clear-sky precipitation).

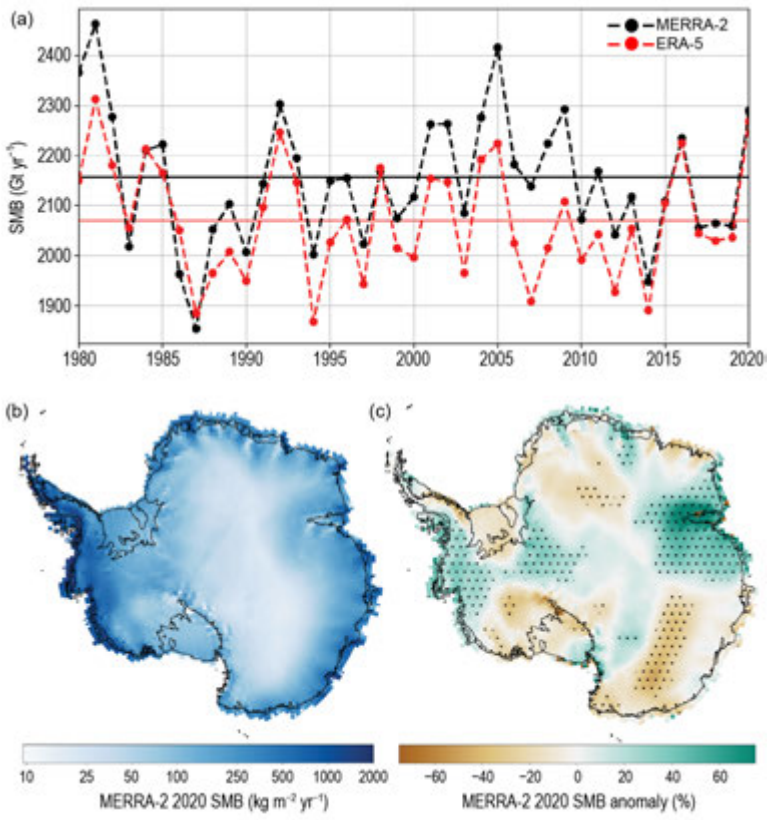

Fig. 6.5. Antarctic surface mass balance (SMB) in 2020. (a) Time series of annual Antarctic ice sheet integrated surface mass balance (Gt yr^{-1}) from 1980 to 2020, according to MERRA-2 (black) and ERA-5 (red) for the grounded portion of the ice sheet; horizontal lines are 1981–2010 means respectively. (b) and (c) 2020 SMB and SMB (kg m^{-2} yr^{-1}) anomaly(%) relative to 1981–2010 according to MERRA-2. In (c), 2020 SMB anomaly is higher than the 1981–2010 std. dev. in the stippled areas.

A time series of AIS SMB from 1980 to 2020 is provided, based on these two reanalysis products (Fig. 6.5a). The climatological (1981–2010) mean SMB is 2157 ± 131 Gt yr^{-1} in MERRA-2 and 2070 ± 113 Gt yr^{-1} in ERA-5. While both time series show comparable interannual variations, with year-to-year SMB differences of >300 Gt yr^{-1} between dry and wet years, neither of the reanalyses indicates a significant long-term trend in SMB. Furthermore, there is no significant trend in the difference between MERRA-2 and ERA-5 over the entire 1980–2020 period (p = 0.58), although there are periods when the two estimates agree more closely.

The 2020 SMB total and SMB anomaly were 2290 Gt and 133 Gt, respectively, for MERRA-2, falling outside the 1 standard deviation range in total SMB. Although 2020 AIS SMB was significantly higher than the 1981–2010 mean, 5 of the previous 40 years had a higher SMB, suggesting that 2020 was still within historical variability. As both reanalysis datasets produce similar results, we use MERRA-2 hereafter to focus on spatial and seasonal

characteristics of the 2020 SMB. As described in many past studies, annual coastal AIS SMB is relatively high, e.g., >500 mm water equivalent (w.e.) in the western AP and coastal West Antarctic ice sheet (WAIS), decreasing sharply inland and with elevation on the ice sheet, e.g., <50 mm w.e. in the East Antarctic ice sheet (EAIS) interior (Fig. 6.5b). The year 2020 was no exception.

Our MERRA-2 results indicate substantial spatial variability in the 2020 anomaly relative to the 1981–2010 mean (Fig. 6.5c). In particular, 2020 SMB was substantially higher than climatology (>25%) along the areas of WAIS bordering the eastern Amundsen and Bellingshausen Seas, as well as the Amery Ice Shelf region on the EAIS, thus helping to offset part of the ice dynamic-based mass loss that is ongoing in West Antarctica (section 6e; Adusumili et al. 2021). On the other hand, 2020 SMB was low compared with the climatology (<–15%) in western Queen Maud Land and Wilkes Land, marking a brief reversal of recent high-accumulation years there (Lenaerts et al. 2013). Additionally, 2020 SMB was significantly below average in Marie Byrd Land, which, along with the positive SMB anomaly farther east, is remarkably consistent with the observed long-term SMB trends in West Antarctica (Medley and Thomas 2019).

Seasonally, the climatological (1981–2010) AIS SMB varies considerably (Fig. 6.6), with a minimum in austral summer (less than 140 Gt month^{-1}) and maximum in austral autumn and winter (more than 200 Gt month^{-1}). For 2020, the first 3 months (January–March) and last 3 months (October–December) were well within the 1 standard deviation range (gray shading) relative to the 1981–2010 period. Comparing the 2020 anomaly with the long-term mean and standard deviation (Fig. 6.6, black line and gray shading) indicates that the high SMB values in April, May, and July, as well as the low SMB values in August, were statistically significant (>1 std. dev.). The drastic difference between the July and August total SMB values reflects anomalously high and low snowfall in those 2 months, respectively, in the West Antarctic region bordering the eastern Amundsen and Bellingshausen Seas. The high snowfall in July was associated with a juxtaposition of strong positive pressure anomalies over the AP and strong negative pressure anomalies over the eastern Ross Sea (see Fig. SB6.3a) that funneled warm moisture-laden air over the West Antarctic coastal region. The positive pressure anomaly shifted east of the AP in August, the atmospheric circulation became more zonal west of the AP (Fig. SB6.3b), and the delivery of warm moisture-laden air from the north sharply decreased to this area (see also section 6f and Sidebar 6.2 for the corresponding sea ice response).

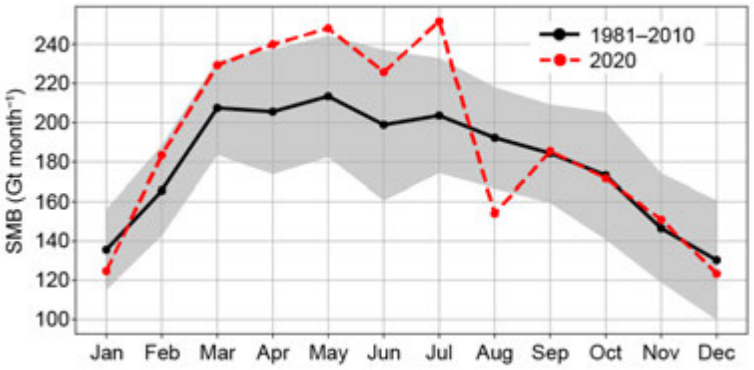

Fig. 6.6. Seasonal cycle of (grounded) AIS-integrated SMB according to MERRA-2 for 2020 (red) and 1981–2010 climatology (black line shows the mean, gray shading is ± 1 std. dev.).

d. Ice sheet seasonal melt extent and duration—M. MacFerrin, T. Mote, L. Wang, H. Liu, L. Montgomery, and T. Scambos

Surface melt on the Antarctic Ice Sheet (AIS) occurs primarily on the coastal margins, especially on the Antarctic Peninsula (AP) and Antarctic ice shelves. It is generally not a large component of Antarctica's net surface mass balance because few areas have significant runoff of meltwater. However, surface melt has a major effect on the density of the underlying glacial firn (compacted snow older than 1 year) and can induce crevasse deepening, calving, or glacier acceleration through hydrofracture and input of water to the ice–bed interface. Because the austral melt season (defined here as 1 October through 30 April) spans two calendar years, we focus here on the 2019/20 melt season. (Next year's report will discuss the 2020/21 melt season.) The season bounded by October

2019 through April 2020 had well-above-average melt anomalies in several regions when compared to their long-term average (here, 1989–2020). The AP had an especially strong melt season (Banwell et al. 2021).

Daily surface melt was mapped using satellite passive microwave brightness temperature data, obtained as daily-composited polar stereographic products from the National Snow and Ice Data Center (products NSIDC-0001 and NSIDC-0007; Meier et al. 2019; Gloerson 2006) spanning 1979–present. Daily passive microwave brightness temperatures using the 37 GHz horizontal polarization channel have been acquired by the SMMR, SSM/I, and SSMIS sensors aboard the NOAA Nimbus-7 and DMSP F8, F11, F13, F17, and F18 satellites. Surface melt was determined by brightness temperatures that exceed a dynamically established threshold using a simple microwave emission model of the expected presence of liquid water in near-surface layers of ice and snowpack. The method used here was first developed to track Greenland's ice sheet surface melting on a daily basis (Mote and Anderson 1995, 2007, 2014). However, large seasonal fluctuations in brightness temperature from areas of dry polar firn in Antarctica can create false positive melt in an unmodified version of the Greenland algorithm. False positives were identified by filtering cells that have a negative 18V minus 37V GHz frequency gradient (SMMR) or 19V minus 37V GHz frequency gradient (SSM/I), and were removed if the measured brightness temperature only marginally exceeded the modeled melt threshold (<10 Kelvin).

During the SMMR sensor period (1979–87), passive microwave composite data are only available every other day. To address the daily temporal gaps, melt extent totals are interpolated between days, or if longer temporal gaps are present, the gaps are filled with the long-term mean value. For error assessment however, the SSMI sensor period (1989–2020) is used as the baseline given the higher quality (i.e., not interpolated) SSMI-derived melt data (e.g., Figs. 6.7b, SB6.1d). An ice extent mask of 25-km grid cells for the AIS was developed from the Quantarctica v3.0 Detailed Basemap dataset (Norwegian Polar Institute 2018). All 25-km cells that contained ≥50% land ice or ice shelf were included, while coastal cells that contained a large fraction of sea ice or open ocean were excluded. We divided the AIS into seven regions that comprise the main drainage basins (following Shepherd et al. 2012; Fig. 6.7).

Figure 6.7a shows the AIS melt extent and total number of melt days for the 2019/20 melt season. More than 60% of the total AIS surface melt occurred on the AP, which had large melt events in November, January, and February (Fig. SB6.1d). These large melt events were caused by warm atmospheric rivers from the southern Pacific Ocean and record high temperatures on the

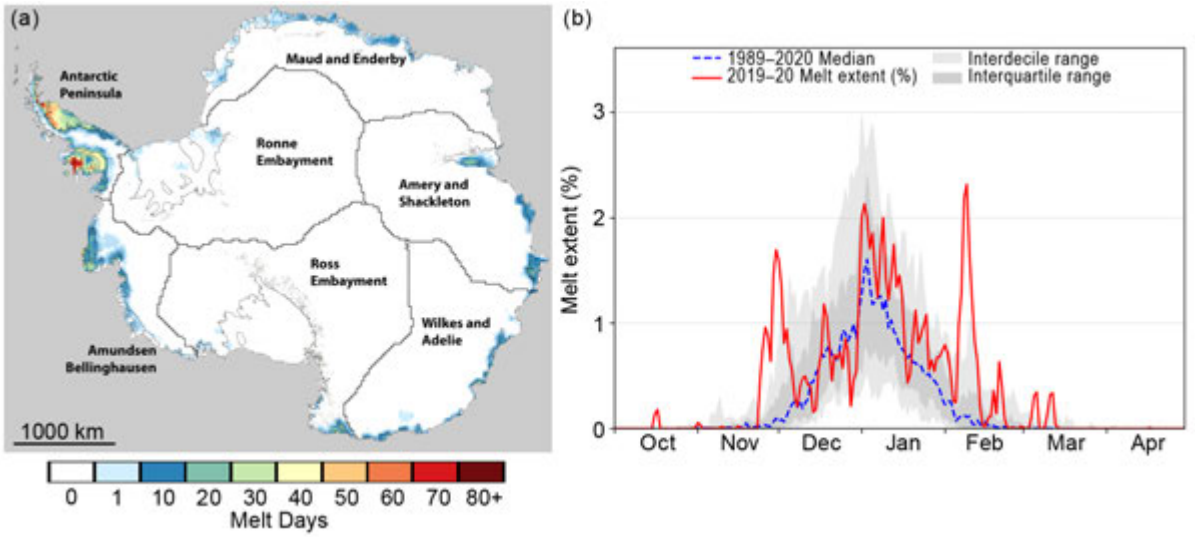

Fig. 6.7. Surface melt across the Antarctic ice sheet as detected from passive microwave satellites. (a) Map of the sum of melt days from 1 Oct 2019 to 30 Apr 2020, with Antarctic sub-regions outlined and labeled. (b) Time series of melt (%) for all of Antarctica (red) compared to median daily values (blue), inter-quartile ranges (dark gray), and inter-decile ranges (light gray) from the 1989–2020 base period.

Peninsula (Sidebar 6.1; Clem et al. 2019). The February 2020 melt event set a late-season record for the 1979–2020 period, for both the AP region (Fig. SB6.1d) and for the entire ice sheet (Fig. 6.7b). The Amery and Shackleton ice shelves, most of the coast of Wilkes Land in East Antarctica, and the Amundsen-Bellinghausen region in West Antarctica also saw above-average melt in 2019/20, although not as pronounced as the melt events on the Peninsula. Comparatively, the Ronne and Ross ice shelves experienced lower-than-average melt conditions.

Long-term trends in annual melt index (the sum of daily melt extent [10^6 km^2 · days] for each year; Zwally and Fiegles 1994; Liu et al. 2006) show general declines in surface melt during the 42-year satellite record for the AIS (Fig. 6.8a), dominated by the decline in melt on the AP (Fig. 6.8b).

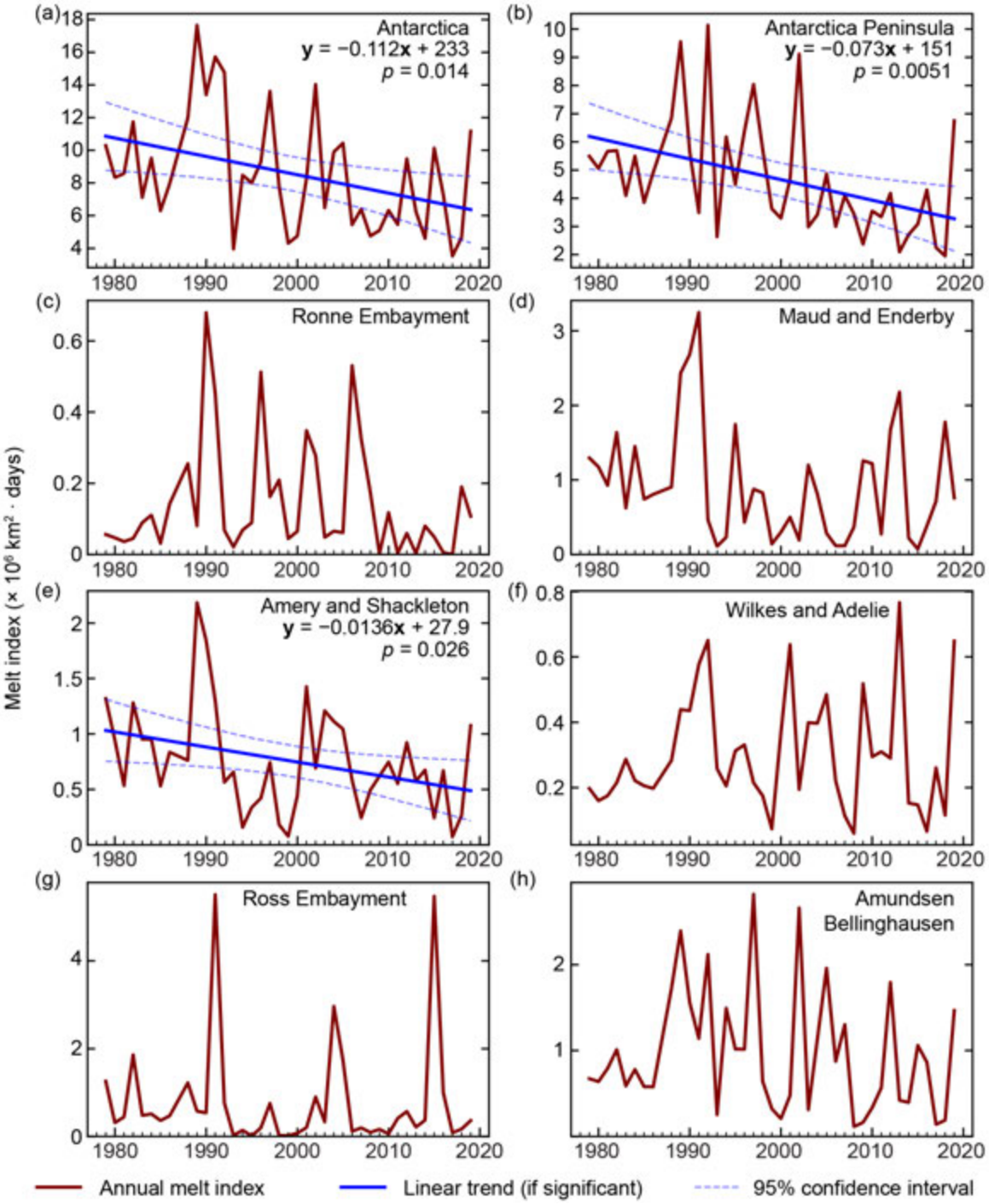

Fig. 6.8. Long-term time series of annual melt index (× 10^6 km^2 · days) for the 1979–2020 satellite record for (a) all of Antarctica and (b)–(h) each sub-region labeled in Fig. 6.7a. Trend lines and 95% trend confidence intervals are outlined in blue where the *p*-values of the slopes are statistically significant ($p \leq 0.05$). Due to a 41-day gap in satellite observations from Dec 1987–Jan 1988, the 1987 melt season is omitted from these time series.

This negative trend is consistent with previous studies of satellite-observed melt since the late 1970s (Liu et al. 2006; Tedesco 2009; Barrand et al. 2013; Oliva et al. 2017), but contrasts with a warming of West Antarctica (including the Peninsula) since the mid-twentieth century that then leveled off at the start of the twenty-first century (Turner et al. 2016). A statistically significant reduction in surface melt was also observed for the Amery-Shackleton region of East Antarctica (Fig. 6.8e), but the trend accounts for only 12% of the continent-wide signal, as opposed to 65% from the AP. Other regions of the AIS show large interannual variability in surface melt but no statistically significant trends over the satellite record.

A recent study (Montgomery et al. 2020) reported on a newly identified firn aquifer in Antarctica located on the Wilkins Ice Shelf to the southwest of the AP (Fig. 6.1). Because firn aquifers are hydrological features in ice sheets or ice shelves that can store large amounts of surface meltwater in the subsurface firn, identifying firn aquifers is relevant for assessing the impacts of Antarctic surface melt. Firn aquifers form in areas of high melt and high snow accumulation, where large volumes of meltwater percolate several meters into firn pore spaces and where meltwater can be stored through winter without refreezing (Kuipers-Munneke et al. 2014). Previously, firn aquifers were only observed in mountain glaciers and in the Greenland ice sheet (Fountain and Walder 1998; Forster et al. 2014). The recent study by Montgomery et al. (2020) shows that the Wilkins Ice Shelf firn aquifer is highly permeable, based on assessments of borehole permeability at the level of the aquifer and on observed drawdown of the water table in a nearby rift. Previously, very rapid calving events were observed on the Wilkins Ice Shelf (Scambos et al. 2009) and were likely a result of hydrofracture, driven by the extensive aquifer (Montgomery et al. 2020). Another recent study using modeling shows favorable conditions for aquifers on other AP ice shelves, such as the remnants of the Wordie Ice Shelf (van Wessem et al. 2020), and indeed additional aquifers have been identified in the field near the Wilkins Ice Shelf (MacDonnell et al. 2021). Given the key role firn aquifers play in ice shelf and ice sheet stability and the ongoing efforts in mapping of their distributions, we will continue to report on aquifer research in the coming years.

e. Ice sheet changes from satellite observations—A. Gardner, S. Adusumilli, and H. A. Fricker

The Antarctic ice sheet (AIS) gains mass through accumulation (total snowfall minus melt runoff and sublimation; see section 6c) and loses mass primarily by processes occurring at the coasts: seaward ice flow and iceberg calving (which generally has an episodic, multidecadal cycle) and basal melt of floating ice (continuous, but time-varying with ocean heat flux; Depoorter et al. 2013). For any given time period, the net mass balance of the competing loss and gain terms depends on interactions between ice, ocean, and atmosphere. Averaged over long-time scales, ice loss from calving and basal melt are approximately equal (Rignot et al. 2013) and seasonal effects are minimized. If the AIS were in steady-state, their sum would offset the mass gain from net accumulation. In the *State of the Climate in 2019* report, we reviewed long-term changes in AIS mass over the period 1992–2019 and discussed the processes to which they are attributed (Fricker and Gardner 2020). Over that period, the AIS experienced a rapid increase in ice discharge to the ocean and inland dynamic thinning (elevation lowering), largely driven by increased rates of ice sheet thinning and grounding-line retreat concentrated along the Amundsen Sea coast.

A recent, and more precise, estimate of decadal change in AIS mass comes from Smith et al. (2020) and is based on high-accuracy laser altimetry data acquired by NASA's ICESat (2003–09) and ICESat-2 (2018–19). The Smith et al. study corroborated the scale and location of previously reported (e.g., Shepherd et al. 2018) ice sheet mass losses in West Antarctica that were partially offset by mass gains in parts of East Antarctica, with a net grounded ice mass loss of 118 Gt yr^{-1}, adding an estimated total of 5.5 mm to sea level over the 2003–19 period. ICESat-2 data can now be used to show changes on shorter timescales that reveal drivers of elevation changes over shorter intervals, such as accumulation events and/or firn compaction (i.e., compacted snow older than 1 year). For example, ICESat-2 data revealed increases in ice sheet surface elevation in West Antarctica between April 2019 and June 2020 (Adusumilli et al. 2021); 41% of these height

changes were due to extreme precipitation, and half of this precipitation occurred as a result of "atmospheric rivers," strong frontal systems that transported large amounts of water (here, primarily as snow) from lower latitudes to the Antarctic continental interior (section 6c; Sidebar 6.1; Lenaerts et al. 2020).

For this report we derived estimates of ice sheet surface height from NASA's ICESat-2 laser altimeter over the period November 2019 to November 2020, as well as mass anomalies over this same period from NASA's satellite gravimeter (GRACE-FO; Wiese et al. 2019). Conversion of height differences to mass differences requires a firn density model (e.g., Ligtenberg et al. 2011) to establish the relationship between height and mass, but this model was not available for this report. The derived ice sheet surface height estimates are from the ATLAS/ICESat-2 L3A Land Ice Height, Version 3 data product (Smith et al. 2021; https://nsidc.org/data/ATL06/versions/2) that provides precise estimates of height along ground tracks. Height changes were determined by differencing two, 3-month averages centered on November 2019 and November 2020 (Fig. 6.9a), smoothed using a 30-km Gaussian filter. Surface mass anomalies were derived from JPL GRACE and GRACE-FO (Wiese et al. 2019; https://podaac.jpl.nasa.gov/dataset/TELLUS_GRAC-GRFO_MASCON_CRI_GRID_RL06_V2), which solve for mass anomalies from the satellite gravimeters and were determined on 300-km diameter spherical caps (Wiese et al. 2019). For the November 2019 to November 2020 period, the annual analysis included estimates derived from GRACE-FO data only, and the gravity-derived mass anomalies were calculated for the same period as the altimetry, using the same 3-month averaging. To determine ice sheet mass anomalies in units of ice equivalent height changes (Fig. 6.9b), we identified all grids (or mass concentration blocks, i.e., mascons) located within the provided land mask that contain more than 10,000 km^2 of land. We then interpolated area-averaged rates of change using natural neighbor interpolation according to the location of the land-weighted mascon centroid. We excluded all non-land areas inclusive of ice shelves, noting that GRACE is insensitive to changes in ice shelf mass.

Our maps (Fig. 6.9) show ongoing losses in West Antarctica, specifically in the Antarctic Peninsula and the Amundsen Sea sector, and in East Antarctica, specifically Enderby, Wilkes (Totten Glacier), and Oates Lands (Cook Glacier). Many of the increases in height around Antarctica correspond well with positive surface mass balance anomalies reported for 2020 (Fig. 6.5c), which suggests a major contribution of surface processes in driving sub-annual height and mass changes during this period. The exception was the Amundsen Sea sector, which experienced net mass loss due to grounded ice discharge and surface lowering outweighing the positive surface mass balance anomaly (Fig. 6.5c).

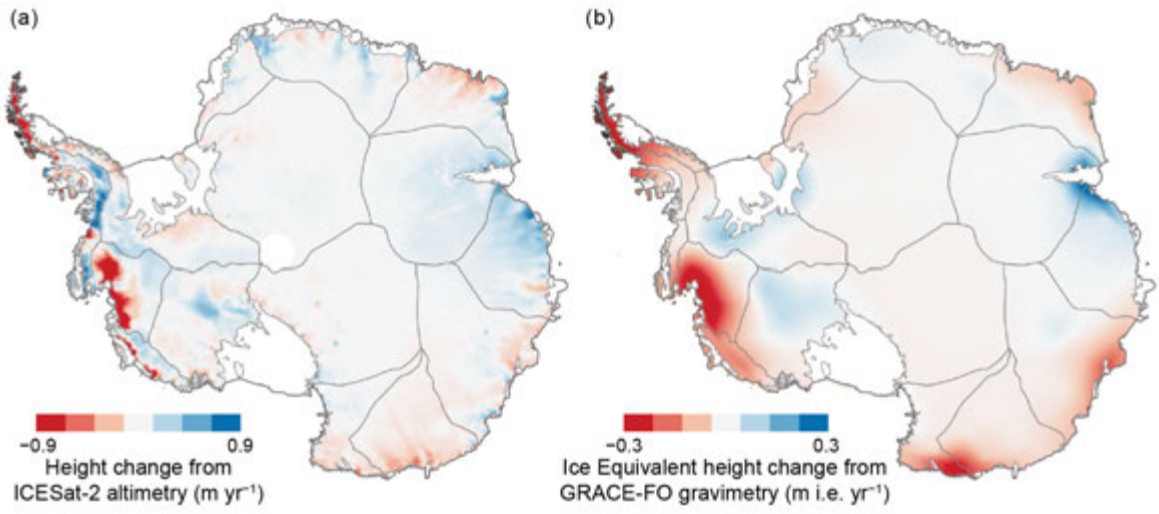

Fig. 6.9. (a) Height change (m yr^{-1}) from ICESat-2 and (b) ice equivalent (i.e.) height change (m i.e. yr^{-1}) from GRACE-FO for the period Nov 2019 to Nov 2020.

There were no major calving events from the large ice shelves in 2020, unlike 2019 with the calving of iceberg D-28 from the Amery Ice Shelf (Walker et al. 2021; Francis et al. 2021). However, the ice front of Pine Island Ice Shelf, a rapidly thinning ice shelf in the Amundsen Sea sector (Paolo et al. 2015), retreated to its most landward location observed in recent decades following a small calving event (~200 km^2) in February 2020 (Lhermitte et al. 2020).

f. Sea ice extent, concentration, and seasonality—P. Reid, S. Stammerjohn, R. A. Massom, S. Barreira, T. Scambos, and J. L. Lieser

Antarctic sea ice plays a crucial role in the global climate system and is highly sensitive to climate change and variability (Walsh 1983; Liu et al. 2002; Roach et al. 2020). Sea ice seasonally covers a vast area of the high-latitude Southern Ocean each year, expanding its extent from ~3×10^6 km^2 in summer to 19–20×10^6 km^2 in winter (Parkinson 2019). This seasonal cycle is driven by large-scale atmospheric and oceanic circulations and temperature, but on shorter time scales is highly sensitive to the frequent occurrence of high wind and wave events, and also serves as a physical buffer for those ice shelves vulnerable to the destructive effects of ocean swells (Massom et al. 2018). As a highly reflective, insulative blanket, the sea ice and its snow cover strongly modify ocean–atmosphere fluxes and interactions (Bourassa et al. 2013). In turn, sea ice processes are of high importance to the physical and chemical properties and dynamics of the high-latitude ocean and atmosphere, including global ocean overturning (thermohaline) circulation (Meredith and Brandon 2017). The modification of ocean salinity and stratification by sea ice growth/melt processes moderates climate change by regulating the Southern Ocean's capacity to take up and store anthropogenic heat and carbon from the atmosphere (Frölicher et al. 2015), while more locally these same sea ice processes modify warm ocean-water incursions to Antarctic outlet glaciers and ice shelves and thus basal melt rates (Timmermann and Hellmer 2013). Sea ice also forms a key habitat for a myriad of biota—ranging from micro-organisms to whales (Thomas 2017)—that are highly adapted to (and dependent on) its presence and seasonal changes (Massom and Stammerjohn 2010). Human activities around Antarctica such as the resupply of research stations and field experiments are also strongly affected by sea ice (COMNAP 2015). Given these factors, changes and variability in Antarctic sea ice have important ramifications.

Based on past assessments of the satellite passive microwave record, net Antarctic sea ice extent (SIE) had a small positive trend of 1.0% ± 0.5% per decade from 1979 to 2018 (Parkinson 2019) that consisted of contrasting regional and seasonal contributions (Stammerjohn and Maksym 2017). In the past decade, however, Antarctic sea ice coverage transitioned from persistently positive daily SIE anomalies and record highs during 2012 to mid-2015 (Reid and Massom 2015) to persistently negative daily SIE anomalies and record lows during late 2016 to early 2020 (Reid et al. 2020).

Now in 2020, after three and a half years of persistently negative net SIE anomalies, SIE rebounded close to the 1981–2010 average both in March and June and then remained above the long-term average from mid-August through mid-December (Fig. 6.10a). Annual minimum SIE in 2020 occurred on 19 February (2.71×10^6 km^2, slightly below average), and the maximum on 25 September (19.06×10^6 km^2, slightly above average). Sea surface temperatures to the north of the sea ice were generally above average earlier in the year, before transitioning to below or near average later in the year (e.g., Figs. 6.10c,d; see also section 6g, Fig. 6.12f). Large-scale atmospheric circulation patterns around Antarctica varied quite strongly during 2020 (section 6b, Fig. 6.3), greatly influencing the regional distribution of sea ice. Hence, the following description of the seasonal and regional evolution of sea ice closely follows the four climate periods described in section 6b.

Early 2020 was characterized by weakened westerly winds and a negative Southern Annular Mode (SAM) index value that was accompanied by a strengthening of westerly winds and positive SAM value in March (Fig. 6.2c). Westerly winds generally cause ice divergence away from the continent (Hall and Visbeck 2002), such that the strengthened westerly winds in early 2020 contributed to a rebound of summer SIE from persistently negative in January–February

to near-average in March, particularly in the western Weddell Sea (Fig. 6.10c). There was also a slightly stronger-than-normal Amundsen Sea Low (ASL) in early 2020 located at ~170°W (Fig. 6.3a) that contributed to decreased SIE in the eastern (~140°–160°W) Ross Sea and slightly increased SIE in the western (~150°–170°E) Ross Sea (Fig. 6.10b). The central Weddell Sea region (~20°–40°W) also had much lower-than-normal SIE (Fig. 6.10b), a summer anomaly pattern that has persisted since 2017 (Turner et al. 2020).

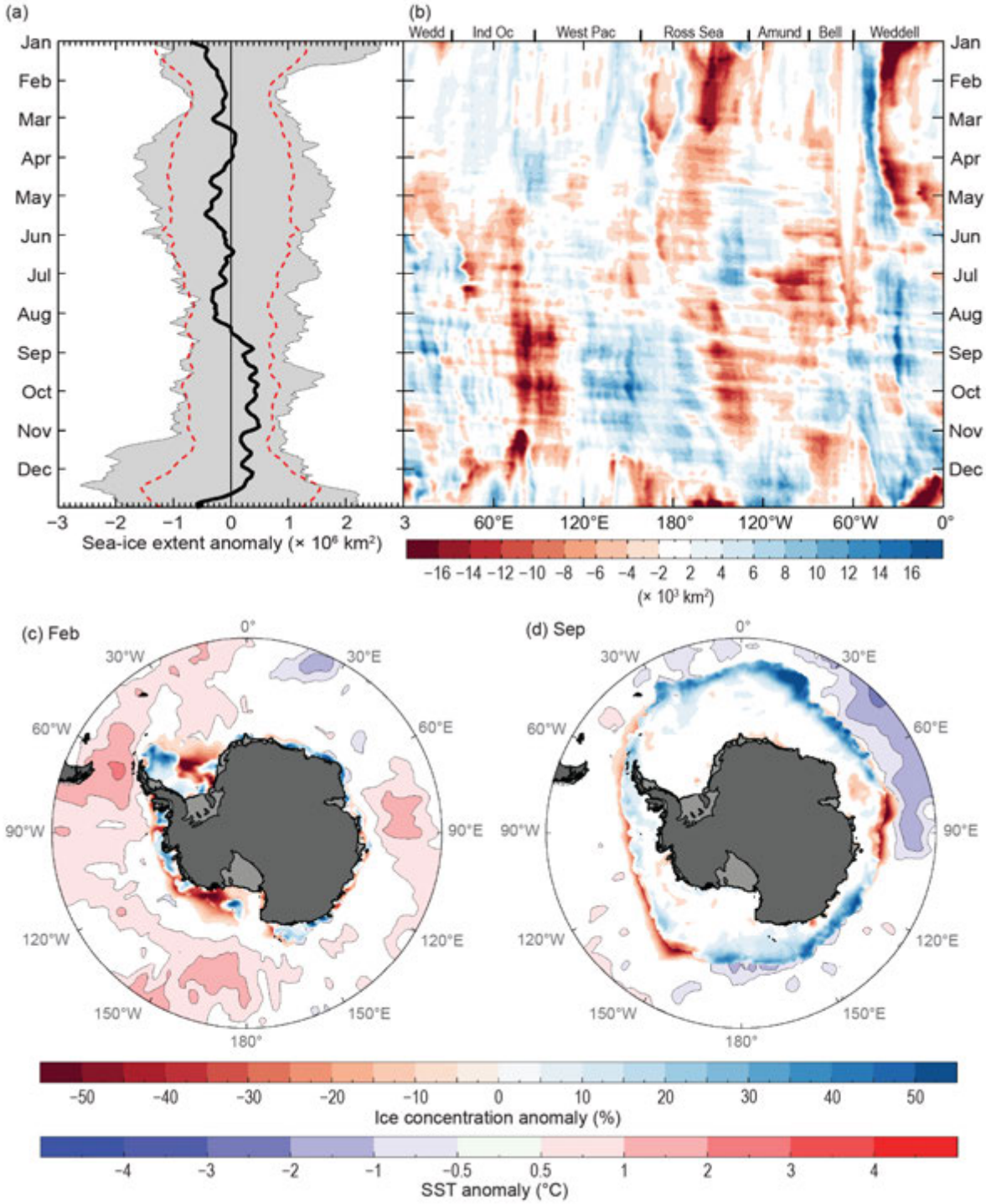

Fig. 6.10. (a) Time series of net daily sea ice extent (SIE) anomalies (× 10^6 km^2) for 2020 (solid black line) relative to 1981–2010. The gray shading represents historical (1979–2018) daily SIE anomalies; dotted red contours are the ± 1 std. dev. (b) Hovmöller (time–longitude) representation of daily SIE anomalies (× 10^3 km^2 per degree of longitude) for 2020. Maps of sea ice concentration anomalies (%) and sea surface temperature anomalies (°C; Reynolds et al. 2002; Smith et al. 2008) for (c) Feb and (d) Sep 2020. Sea ice concentration is based on satellite passive microwave ice concentration data (Cavalieri et al. 1996, updated yearly, for climatology and Maslanik and Stroeve 1999, for the 2020 sea ice concentration). See Fig. 6.1 for relevant place names.

In April, circumpolar surface westerly winds weakened again (Fig. 6.2c), and the net SIE anomaly became more negative (Fig. 6.10a), followed by the development in May of a zonal wave-3 pattern in the longitudinal distribution of SIE (Fig. 6.10b). The zonal wave-3 pattern was caused by atmospheric low-pressure systems centered at ~130°W, ~70°E, and ~140°E that led to contrasting SIE anomalies to the east/west of these three low-pressure centers. The zonal wave-3 pattern also resulted in corresponding early/late regional anomalies in the timing of ice-edge advance (Fig. 6.11a).

The austral winter of 2020 was characterized by a transition to persistently positive net SIE anomalies starting in August in association with a developing (but relatively weak at the time) La Niña that initially resulted in a strengthened ASL at ~160°W that thereafter expanded toward ~140°W during September–November (Sidebar 6.2; Stammerjohn et al. 2008; Yuan 2004). The ASL in August also comprised a zonal wave-2 atmospheric pattern, with an additional negative pressure anomaly at ~70°E, separated by a high-pressure ridge at ~140°E (Figs. 6.3e, SB6.3b). This zonal wave-2 pattern resulted in increased/decreased SIE in the Ross Sea/Amundsen-western Bellingshausen Seas (Figs. 6.10b,d), somewhat characteristic of La Niña periods (Sidebar 6.2). During September, SIE was also more extensive (positive anomaly) from the western Weddell Sea to the Indian Ocean sector (~30°W to ~70°E) and the eastern Pacific region through to the Ross Sea sector (~120°E to ~160°W), with reductions (negative SIE anomalies) elsewhere (Figs. 6.10b,d). From September through October, negative SIE anomalies were prevalent between ~160°W and 90°W, in conjunction with warm northerly winds along the eastern limb of the expansive low-pressure anomaly. Interestingly, there was late-season sea ice growth in the eastern Bellingshausen Sea region from ~60° to 80°W, i.e., just outside (eastward) of the low-pressure anomaly region, influenced by the ASL as described above.

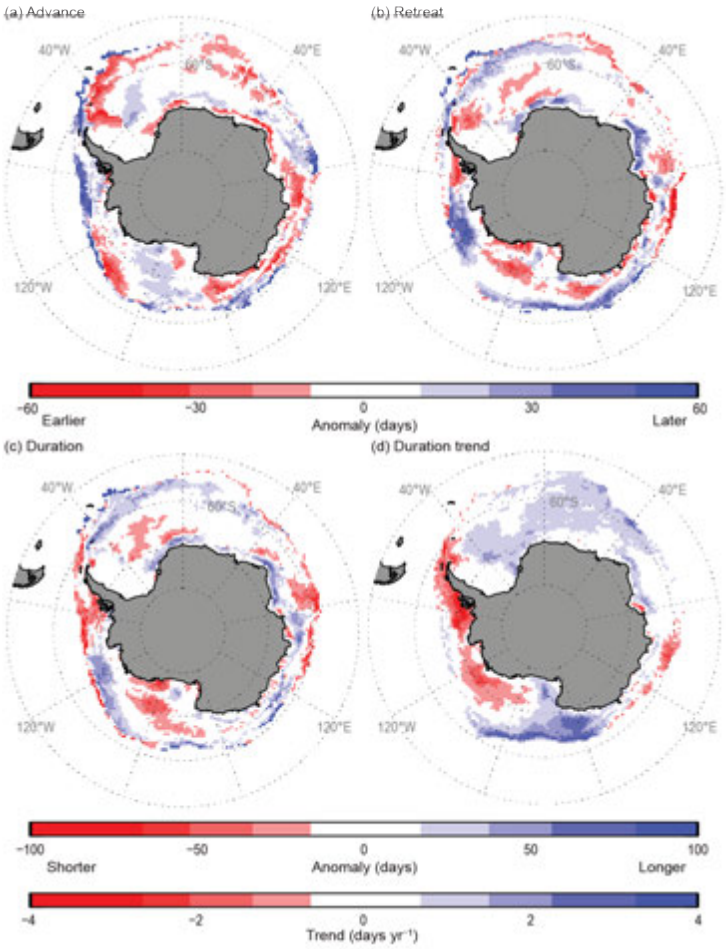

Fig. 6.11. Seasonal sea ice anomalies (days) in 2020 of (a) advance and (b) retreat; (c) total duration and (d) duration trend (Stammerjohn et al. 2008). Both the climatology (for computing the anomalies) and trend are based on 1981/82 to 2010/11 data (Cavalieri et al. 1996, updated yearly), while the 2020/21 duration-year data are from the NASA Team NRTSI dataset (Maslanik and Stroeve 1999).

From November through the end of the year, the ASL began to weaken, the circumpolar atmospheric trough deepened southward, and the SAM index became positive again. The enhanced circum-Antarctic cyclonic activity altered the regionality of sea ice coverage as the annual retreat season progressed. In most regions (except for the Amundsen Sea region) and during December, net SIE decreased sharply (Fig. 6.10a), particularly within the two major gyre embayments of the Ross and Weddell Seas (Figs. 6.10b, 6.11b), as often happens in late spring in response to the southward deepening of the circumpolar trough (e.g., Watkins and Simmonds 1999). Seasonally, the net result was a longer ice season in most of the outer pack (except for the Bellingshausen Sea and eastern Indian Ocean areas), contrasted against a shorter ice season in the inner pack (Fig. 6.11c). In further contrast, the ice season in the Bellingshausen Sea in 2020 was anomalously short but in-line with the long-term trend in that region (Fig. 6.11d).

Sidebar 6.2. "Disruption events" and large shifts in sea ice anomalies: a tropical–high latitude tango—P. REID, R. FOGT, AND X. YUAN

While there are some quite distinct cryospheric processes and features that influence Antarctic weather and climate variability (e.g., atmosphere–ocean–sea ice–ice sheet interactions, shallow stable atmospheric boundary layers, and strong horizontal atmospheric moisture gradients), the sensitivity of the Antarctic climate to tropical variability underscores the important role of strong tropical teleconnections (e.g., Yuan et al. 2018). On a year-to-year basis, variability in the tropics, driven by interactions between the ocean and atmosphere, often results in large-scale modes of climate variability such as the El Niño–Southern Oscillation (ENSO), Indian Ocean dipole, Atlantic Multidecadal Oscillation, and Madden-Julian Oscillation (MJO). The original tropical signal may manifest itself in the form of atmospheric Rossby waves that travel southward and influence the position and strength of the upper-tropospheric jet streams through poleward fluxes of momentum and heat (Yuan et al. 2018). In turn, the anomalous position of the jet streams alters the position of cyclogenesis around Antarctica (Riehl and Teweles 1953; Vederman 1954; Raphael et al. 2016), most frequently changing the depth of the atmospheric phenomenon known as the Amundsen Sea Low (ASL; Li et al. 2015; Raphael et al. 2016; Yuan et al. 2018) and the strength of the westerly winds and the Southern Annular Mode (SAM; Fogt and Marshall 2020). Variations in the convective zone of the southeast Pacific (the South Pacific Convergence Zone) also alter West Antarctic climate through Rossby wave interaction (Clem et al. 2020b; Stammerjohn and Scambos 2020).

The high-latitude atmospheric response to tropical teleconnections, as described above, can induce large sea ice extent (SIE) anomalies, particularly if local atmospheric phenomena (e.g., ASL, SAM) amplify or abruptly change the regional distribution of the SIE anomaly. In some cases the anomalous SIE response may be considered a "disruption event" (e.g., Hirota et al. 2018) such that the SIE anomaly is not only at, or near, record-breaking magnitude, but also exhibits a strong shift in sign. To further exemplify what we mean by disruption events, we give two examples below.

As discussed in section 6f, net SIE in 2020 increased from generally below average early in the year to, quite rapidly (1–2 weeks), above average from August through mid-December (Fig. SB6.2, red line). The main contributor to this sudden increase in SIE was the development of a strong ASL in August that continued to deepen in September (Figs. SB6.3b,c). The strong ASL resulted from Rossby wave activity associated with a developing La Niña (and associated changes in the Walker Circulation, as measured by the Southern Oscillation Index), which is typical for this phase of ENSO (Yuan 2004). The result of the strong ASL was above-average SIE within the Ross Sea and below-average SIE in the Amundsen–Bellinghausen Seas region (Figs. SB6.3b, 6.10b; Stammerjohn et al. 2008). The relationship between the variability of the ASL and the resultant sea ice distribution is complex (Raphael et al. 2016) and is discussed in more detail in section 6f with respect to 2020. However, the timing of the SIE anomaly reversal is also important: August, when the La Niña began to intensify, is toward the end of the sea ice advance season and, as described in section 6f, led to persistently positive net SIE anomalies through mid-December 2020 (Fig. SB6.2, red line). This SIE anomaly reversal in early August 2020 is particularly noteworthy as a disruption event because prior to 2020, net circumpolar SIE had been anomalously and persistently negative for more than 3 years (since the austral spring of 2016; Reid et al. 2020), thus it took an event of this scale to shift the net SIE anomaly from persistently negative to positive (for at least four consecutive months).

When a disruption event happens early in the sea ice advance season (or conversely later in the ice retreat season), the magnitude of the SIE anomaly reversal can be even larger, as occurred in 1980. In contrast to 2020, a positive anomaly of the ASL—a high-latitude blocking high—developed during early 1980

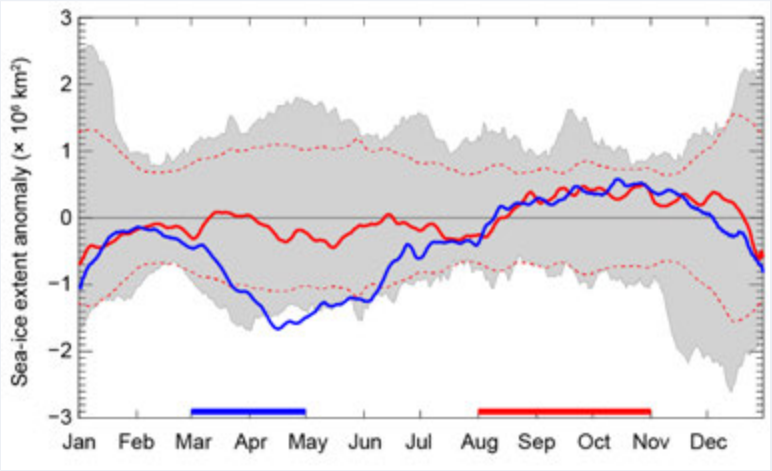

Fig. SB6.2. Time series of net (total) sea ice extent anomaly (× 10^6 km^2; 1981–2010 base period) for 2020 (red line) and 1980 (blue line). The gray shading represents historical (1981–2020) SIE anomalies; dotted red contours are the ± 1 std. dev. The blue horizontal line represents the period of high-latitude blocking high in 1980. The red horizontal line represents the period of deep Amundsen Sea Low in 2020.

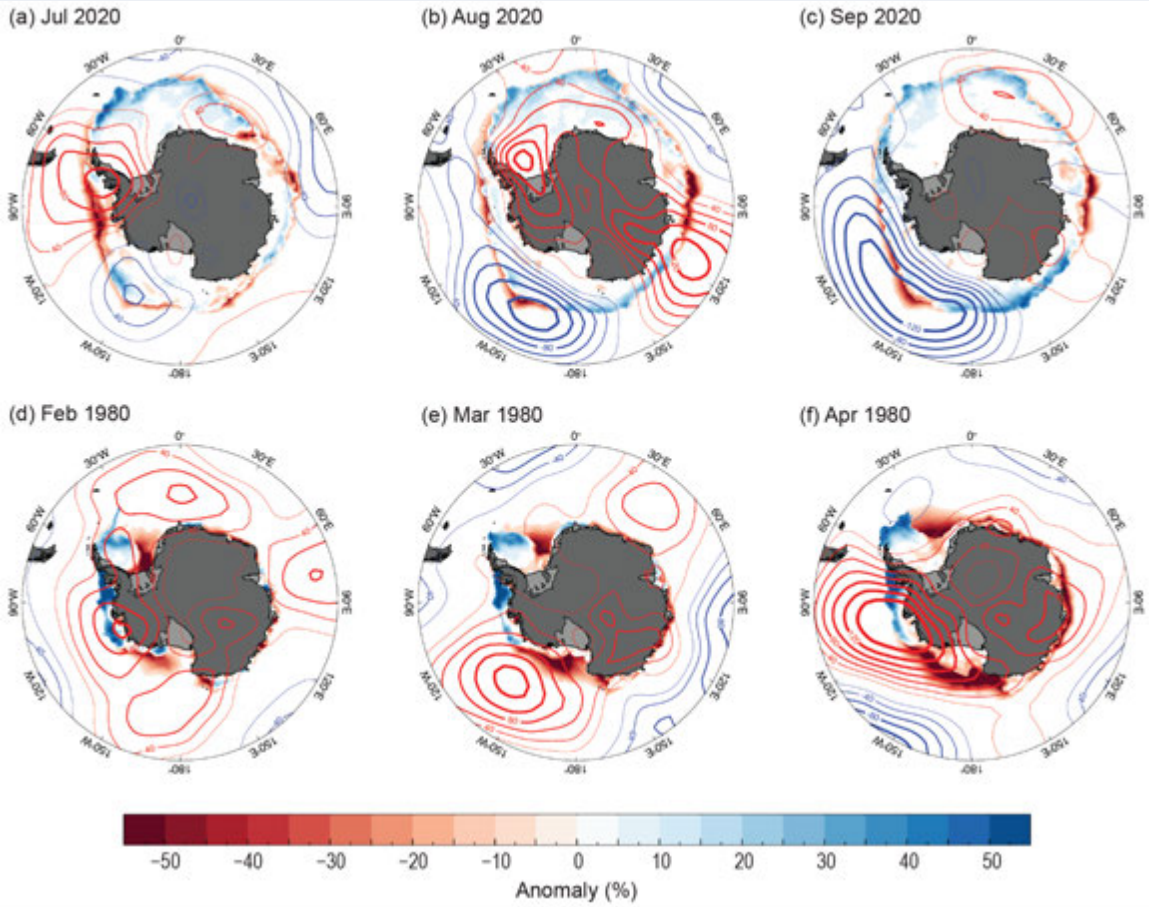

Fig. SB6.3. Anomalies of monthly mean sea ice concentration (%) and 850-hPa geopotential height (hPa) over Antarctica for (a) Jul 2020, (b) Aug 2020, (c) Sep 2020, (d) Feb 1980, (e) Mar 1980, and (f) Apr 1980. Anomalies are based on the 1981–2010 climatology.

(Figs. SB6.3d–f) and produced a strong but opposite response in sea ice distribution, e.g., strongly negative versus positive SIE anomalies in the Ross Sea. This response was associated with a weakening El Niño combined with MJO activity in the west and central Pacific (based on the MJO index of Wheeler and Hendon 2004) 200-hPa zonal wind, and satellite-observed outgoing longwave radiation (OLR). In this region (west/central Pacific), MJO activity is often associated with a high-latitude blocking high within the central and eastern Ross Sea (Lee and Seo 2019). The response in sea ice distribution was strong, with the net SIE reaching record daily lows (Fig. SB6.2, blue line). Many of those daily lows that occurred in April and early May 1980 are still records, even 40 years later. During March and April 1980, SIE expanded by only ~4.3×10^6 km^2, the lowest rate of expansion on record for those months and over 2 standard deviations below average (~5.4×10^6 km^2). The record daily low SIE in late April to early May 1980 was largely the result of strong northerly winds focused on the Ross Sea (Figs. SB6.3e,f), i.e., on-ice winds that kept the ice edge southward. Elsewhere, weakened westerly winds in association with a strong negative SAM index also contributed to negative SIE anomalies through weakened Ekman transport of the ice edge northward. By June, however, the SIE began to rapidly expand in association with strengthened westerly winds and increased Ekman transport northward; these favorable conditions were sustained through mid-December, promoting positive SIE anomalies from mid-August to mid-December 1980 (Fig. SB6.2).

There is a wide body of scientific literature examining how the tropics modulate Antarctic SIE and when amplified locally, the SIE anomalous response can be extreme in terms of magnitude and sign reversal (and thus a disruption event). But equally important is how Antarctic sea ice variability, particularly during disruption events, might influence extrapolar regions of the Southern Hemisphere, a topic much less studied. In the high wind and wave environment of the Southern Ocean, sea ice amplifies variability from both the atmosphere and ocean through its constraint on atmosphere–ocean fluxes. The 2 years discussed above, 1980 and 2020, are examples of amplified Antarctic SIE variability, and within that context, the following questions arise:

1. Does the regional distribution of sea ice play a passive or active role in modulating the tropical–high latitude connection, particularly during disruption events?
2. Conversely, what impact does the regional distribution of sea ice have on the midlatitude and tropical weather/climate systems?

The second question has been examined on a climate-scale scenario for both the Arctic and Antarctic, most recently using fully coupled global models (England et al. 2020). This work suggests that ice loss in the Antarctic region causes an oceanic and atmospheric northward heat transport, with the ocean signal dominating on climate time scales of a century or more. For the Arctic, coupling an ice–ocean model to an atmospheric model has shown an improvement in tropical cyclone forecast guidance (Smith et al. 2018).

In posing these questions we must remember that the tropical–high latitude interaction is not the only forcing influencing sea ice distributions. Other factors such as stratospheric ozone and Southern Ocean variability also play significant roles (NAS 2017). While much progress has been made toward better understanding the drivers of Antarctic climate variations, many exciting research opportunities still remain.

g. Southern Ocean—V. Tamsitt, S. Bushinsky, Z. Li, M. du Plessis, A. Foppert, S. Gille, S. Rintoul, E. Shadwick, A. Silvano, A. Sutton, S. Swart, B. Tilbrook, and N. L. Williams

The Southern Ocean (SO) plays a unique role in the climate system and is responsible for 40% of oceanic anthropogenic carbon dioxide (CO_2) uptake and 75% of the ocean's uptake of heat from the atmosphere (Frölicher et al. 2015). The relatively recent increases in deployments of biogeochemical floats (Claustre et al. 2020), Saildrone Uncrewed Surface Vehicles (USVs; Sutton et al. 2021), and Deep Argo (Roemmich et al. 2019) have provided novel insights into seasonal and interannual variability in SO properties and fluxes. Here, we present 2020 anomalies of SO air–sea heat and CO_2 fluxes and show recent changes in mixed layer (ML) and Antarctic Bottom Water (AABW) properties.

1) Air–sea heat flux

We use the ERA5 reanalysis to evaluate the annual and 1981–2010 climatological state of the surface net heat flux for the SO (all ocean data points south of 40°S, with means area-weighted; positive values indicate ocean heat gain). The SO annual mean heat flux anomalies varied between positive (maximum: 1.31 W m^{-2}) and negative (minimum: –1.28 W m^{-2}) values with a 5–10 year period (Fig. 6.12a). The 2020 SO annual heat flux anomaly was moderately positive (+0.20 ± 0.12 W m^{-2}) and followed other positive heat flux anomalies over 2014–19 (excepting 2018). However, we note that the 2020 positive SO annual heat flux anomaly is an average of both large positive and negative regional anomalies. The multi-year (1979–2020) mean heat flux anomaly was –0.01 W m^{-2} compared to the 1981–2010 climatology, emphasizing that the 1981–2010 time series begins and ends with a phase of negative heat flux anomalies. We note that the time series of net heat flux anomalies differs in the magnitude and range from that presented in *State of the Climate in 2019* (Queste et al. 2020), which is due to a switch in reanalysis products from NCEP to ERA5, as ERA5 heat fluxes were deemed more reliable (Tamsitt et al. 2020).

The SO annual mean net heat flux for 2020 and climatology show broad spatial agreement in the sign of the heat flux (Figs. 6.12b,c). Within the open ocean (40°S to the sea ice edge) and particularly within the Antarctic Circumpolar Current (ACC) domains, there was widespread heat gain in the South Atlantic and Indian Oceans, and heat loss in the South Pacific Ocean. Within the sea ice sector, heat loss was generally found nearer to the Antarctic coast, with heat gain toward the winter sea ice edge (except in portions of the Indian Ocean at 60°E, Ross Sea at 180°E, and Amundsen Sea at 120°W, where heat loss extended to the winter ice edge).

The difference between 2020 and the climatology (Fig. 6.12d) reveals mostly positive heat flux anomalies in the sea ice sector in 2020, with a mean of +0.23 ± 0.01 W m^{-2}, where the uncertainty is the standard error of the mean. In the open ocean (40°S to the sea ice edge), the mean heat flux anomaly was +0.19 ± 0.02 W m^{-2}, with the positive anomalies in the Pacific Ocean and north of

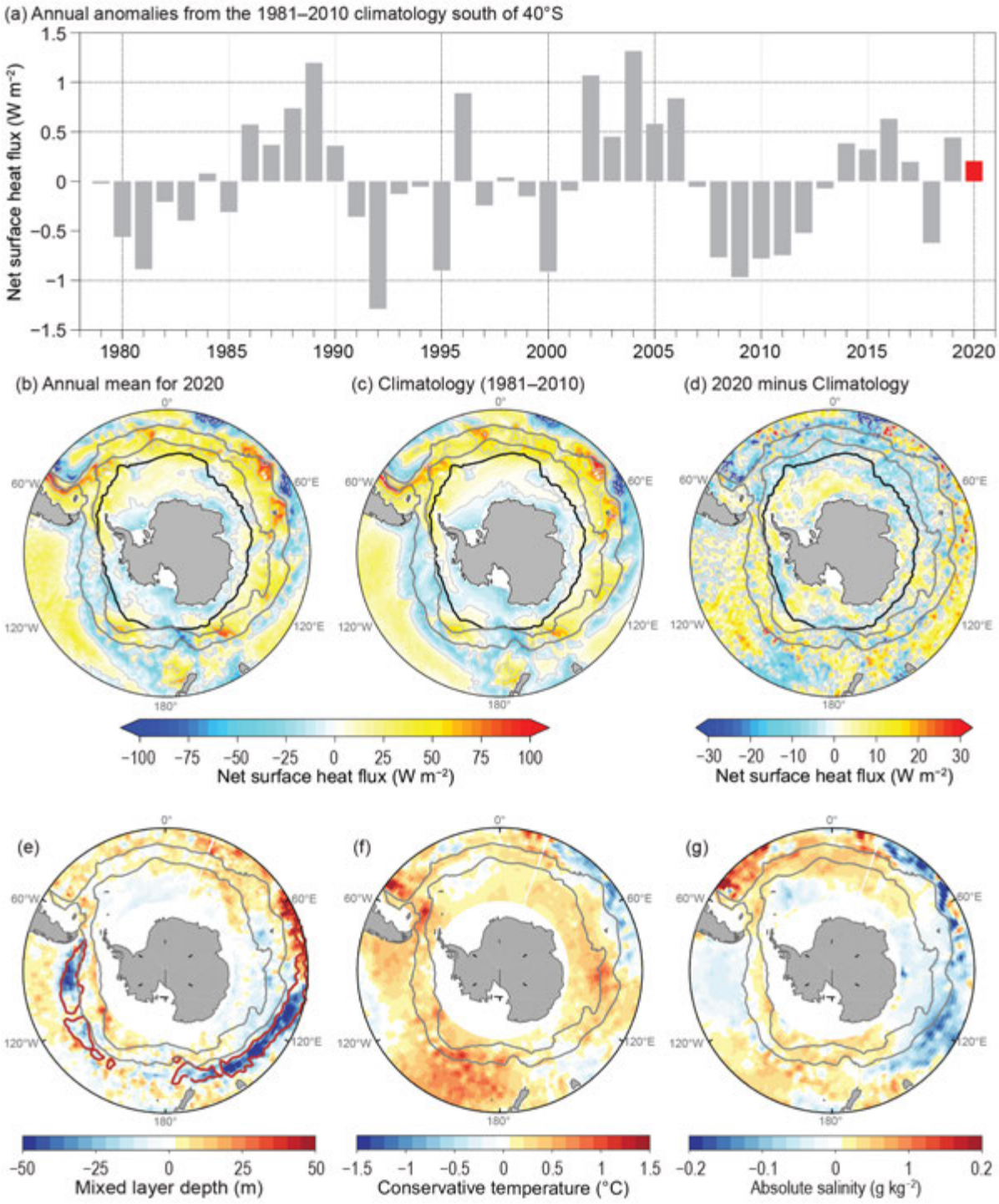

Fig. 6.12. 2020 anomalies of net air–sea heat flux and mixed layer (ML) properties. (a) Time series of ERA5 net air–sea heat flux annual mean anomalies (W m^{-2}) from the 1981–2010 mean for the entire Southern Ocean south of 40°S. The 2020 anomaly is highlighted in red. Maps of ERA5 mean net air–sea heat flux (W m^{-2}) for (b) 2020, (c) climatology (1981–2010), and (d) 2020 minus climatology. Maps of gridded Argo 2020 annual mean anomalies relative to 2004–10 mean of (e) ML depth (m), (f) ML conservative temperature (°C), and (g) ML absolute salinity (g kg^{-1}). MLD is defined using a density threshold following de Boyer Montégut et al. 2004. Gray contours in (b)–(g) show the mean position of the Subantarctic and Polar Fronts from Sokolov and Rintoul (2009). Black contours in (b)–(d) indicate the Sep 2020 mean 15% sea ice concentration from the University of Bremen AMSR2 daily 6.25-km gridded sea ice product and light gray contours in (b)–(d) are the zero net heat flux line. Red contours in (e) indicate a maximum MLD of 300 m. On all maps the outer latitude is 40°S.

the ACC outweighing the mostly negative anomalies in the Atlantic and Indian Oceans. Strong negative heat flux anomalies are attributed to the Agulhas and Falklands Western Boundary Currents, while eddy-like features between 40°S and 45°S can be identified by the large heat gain and loss anomalies, which are averaged out in the long-term mean.

2) Mixed layer properties

Anomalies of mixed layer depth (MLD) and ML conservative temperature (i.e., temperature proportional to potential enthalpy to better represent heat content) and absolute salinity in 2020 were computed relative to the climatological (2004–10) seasonal cycle (Figs. 6.12e–g) using monthly gridded Argo data (Roemmich and Gilson 2009).

In 2020, the most significant observation is the shallower MLs (Fig. 6.12e) occurring in the deepest wintertime ML regions, particularly in the southeast Pacific and southeast Indian Subantarctic Mode Water (SAMW) formation regions, where the annual mean MLD was >50 m shallower than climatology. This contrasts with a deeper ML in the central Indian SAMW formation region. The negative MLD anomaly corresponds to the location of positive air–sea heat flux anomaly (i.e., weaker heat loss; Fig. 6.12d). As a consequence of the anomalous heat gain, a warmer ML was found in the Pacific and southeast Indian sectors, while a colder ML was observed in the central Indian Ocean (Fig. 6.12f). A less saline ML was also observed in the warming ML region of the southeast Indian and southwest Pacific Oceans, contributing to the ML shoaling. Anomalies in the MLD induce anomalies in the subduction and volume of SAMW (Sallée et al. 2010; Li et al. 2021) and thus anomalies in the oceanic uptake of anthropogenic heat and carbon.

3) Air–sea CO_2 flux

Recent technological advancements in making direct measurements of air and surface seawater pCO_2 and wind speed autonomously from USV have reduced observational uncertainties in the Southern Ocean carbon budget by targeting gaps in the observing system (Sabine et al. 2020). The novel USV data, an example of which is shown for 2019 (Fig. 6.13a), can be used to estimate potential error in different CO_2 flux estimates. Once the air–sea gradient in CO_2 is determined, different satellite-based wind speed products and sampling frequencies have the largest impact on CO_2 flux uncertainty with biases ranging from −4% to +20% (Sutton et al. 2021).

Biogeochemical profiling floats deployed by the Southern Ocean Carbon and Climate Observations and Modeling project (SOCCOM) also complement the shipboard underway measurements that underpin air–sea CO_2 flux estimates (Figs. 6.13b–d). Unlike earlier studies, USV-, ship-, and float-based estimates of CO_2 flux were found to be in good agreement in 2019 (Sutton et al. 2021). Float-based flux estimates have greater uncertainty compared to ship and USV estimates, yet yield new information about seasonal cycles and interannual variations. Nonetheless, anomalously strong winter outgassing in the Antarctic Zone (AZ), the area between the Polar Front and the seasonally ice-covered ocean (see also Fig. 6.13a), was consistently indicated (Fig. 6.13d), both as estimated from floats (Gray et al. 2018) and float-derived products (Bushinsky et al. 2019) for 2014–17 and for the 2014–20 float-only AZ annual average flux (+0.18 ± 0.11 Pg C yr^{-1}) relative to the 1982–2010 mean ship-derived AZ fluxes (e.g., Landschützer et al. 2016, +0.01 ± 0.035 Pg C yr^{-1}; Rödenbeck et al. 2013, +0.01 ± 0.038 Pg C yr^{-1}). These float-estimated anomalies reinforce the need to utilize all ship-, USV-, and float-based pCO_2 measurements in order to form a fully resolved seasonal, spatial, and interannual picture of SO carbon uptake.

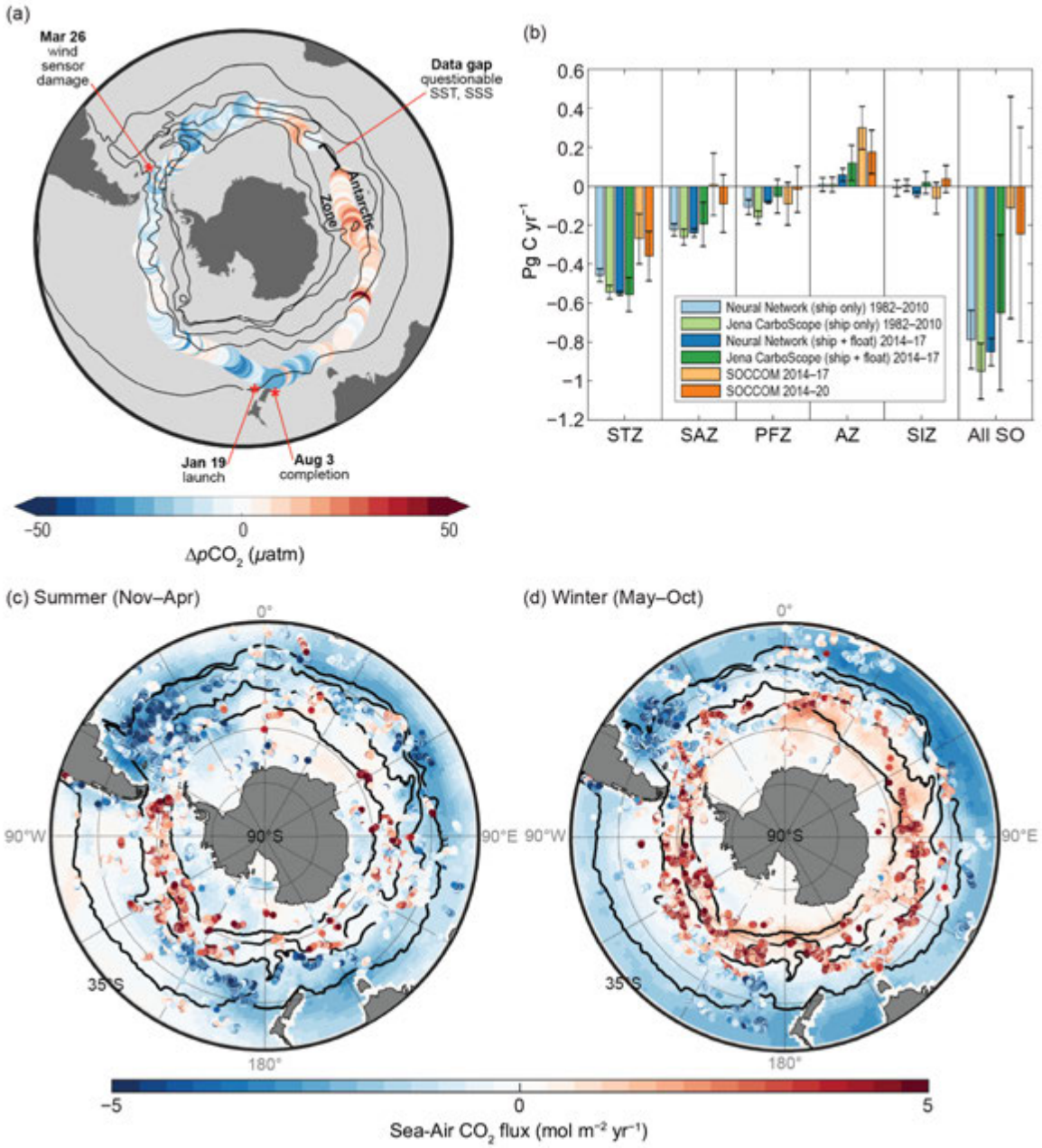

Fig. 6.13. Sea–air fluxes of CO_2. (a) Uncrewed Surface Vehicles-measured ΔpCO_2 (seawater–air; µatm) in the Southern Ocean in 2019. Black lines indicate climatological locations of the major fronts as described in Sutton et al. (2021). (b) Annual mean fluxes (Pg C yr^{-1}) for long-term ship-derived averages, 2014–17 combined ship and float averages, and float-derived 2014–17 estimates from Bushinsky et al. (2019), and float-derived estimates from 2014–20. A 2014–20 average for float estimates is presented instead of 2020 data alone as year-to-year variations in float data coverage make unmapped interannual variability difficult to determine at current float densities. (c) Summer (Nov–Apr) fluxes (mol m^{-2} yr^{-1}) showing 1982–2010 mean (base map) from Landschützer et al. (2016) and float-derived instantaneous fluxes from 2014–20 SOCCOM biogeochemical profiling floats (colored circles). Note the difference in temporal averaging between the base map (6-month) and float data (6-hourly). Black lines represent the Subtropical Front, Subantarctic Front, Polar Front, and seasonal ice extent (Gray et al. 2018), from north to south, delineating the Subtropical Zone, Subantarctic Zone, Polar-Frontal Zone, Antarctic Zone, and Seasonal Ice Zone. (d) Same as (c) but for winter (May–Oct) months. In all plots, positive is a flux to the atmosphere.

4) Recent recovery of Antarctic Bottom Water formation

Observations during the past half century showed a sustained warming, freshening, and decrease in volume of AABW (Johnson 2008; Purkey and Johnson 2013; van Wijk and Rintoul 2014; Menezes et al. 2017; Aoki et al. 2020). These changes have been linked to increased melting of the Antarctic Ice Sheet (AIS; Jacobs and Giulivi 2010; Jullion et al. 2013).

More recent ship and Deep Argo observations have revealed a rebound in AABW properties. AABW volume and salinity in the Ross Sea have increased since 2014 (Castagno et al. 2019; Silvano et al. 2020; Thomas et al. 2020; Bowen et al. 2021), and in the Weddell Sea AABW volume increased between 2014 and 2018 (Abrahamsen et al. 2019). In the Ross Sea, renewal of AABW formation has been attributed to an unusual combination of positive Southern Annular Mode and extreme El Niño conditions between 2015 and 2018 that produced anomalies in coastal winds that in turn drove increased sea ice formation, shelf water salinity increases, and a larger volume of dense AABW (Silvano et al. 2020). In the Weddell Sea, the causes of the recent AABW rebound are less clear (Abrahamsen et al. 2019; Gordon et al. 2020). While the projected increase in melt of the AIS will likely continue to drive a reduction in AABW formation, recent reversals of this trend underscore the sensitivity of the coupled ocean–cryosphere system to climate modes, teleconnections, and episodic events (e.g., iceberg calving; Shadwick et al. 2013).

h. 2020 Antarctic ozone hole—N. Kramarova, P. A. Newman, E. R. Nash, S. E. Strahan, C. S. Long, B. Johnson, M. Pitts, M. L. Santee, I. Petropavlovskikh, L. Coy, J. de Laat, G. H. Bernhard, S. Stierle, and K. Lakkala

The 2020 ozone hole was the 12th largest since the start of the NASA satellite observational record in 1979 at 23.5 Mkm^2 (the average area for 7 September to 13 October), with a minimum total ozone column of 94 Dobson units (DU). The 2020 austral spring was marked by a lack of planetary wave activity that resulted in a cold and stable polar stratospheric vortex, creating favorable conditions for ozone depletion. Due to the weaker-than-usual planetary-scale wave activity from September to December—waves that propagate from the troposphere into the stratosphere that force warming of the stratosphere and deceleration of the westerly polar night jet—the winter-to-summer circulation transition was delayed by several weeks, leading to the longest-lived ozone hole in the observational record. Record low ozone values in late austral spring and early summer led to unusually high levels of ultraviolet (UV) radiation in the Antarctic region (the area nominally south of 60°S).

Persistently low temperatures were observed in the Antarctic lower stratospheric vortex during winter and spring 2020 (Fig. 6.14a). Low temperatures supported formation of polar stratospheric clouds (PSCs), whose combined volume was above average in July and August (Fig. 6.14b). These clouds provide surfaces for heterogeneous chemical reactions that release chlorine (Cl_2), which is converted to active, ozone-destroying chlorine species after sunlight returns to polar latitudes in late August and September. In September, the key month for ozone depletion, vortex-averaged temperatures on the 440 K isentropic surface (~60 hPa or ~19 km) were consistently near or below the 2005–18 average, sustaining the PSC volume at near-average levels (Figs. 6.14a,b). Chlorine monoxide (ClO) concentrations (Fig. 6.14c) were near average until mid-September and above average in early October, similar to 2015. The 2020 vortex-mean ozone concentrations on the 440 K isentropic surface were close to average throughout the entire season (Fig. 6.14d) and reached a minimum in early October. The ozone hole area—the area with the total ozone column below 220 DU—peaked on 20 September (Fig. 6.14e). The partial ozone column between 12 km and 20 km derived from ozone sonde observations at the South Pole (Fig. 6.14f) declined rapidly in September and measured 6.1 DU on 15 October, the third lowest since sonde observations began in 1986. The lowest 2020 total ozone column of 94 DU was observed on 6 October (Fig. 6.14g).

In most years, planetary wave activity increases in September and October, decelerating the circumpolar winds and increasing lower stratospheric temperatures. This wave activity forces poleward and downward transport of ozone-rich air to the Antarctic lower stratosphere. This strong austral spring advection replenishes ozone in the depleted Antarctic region during the

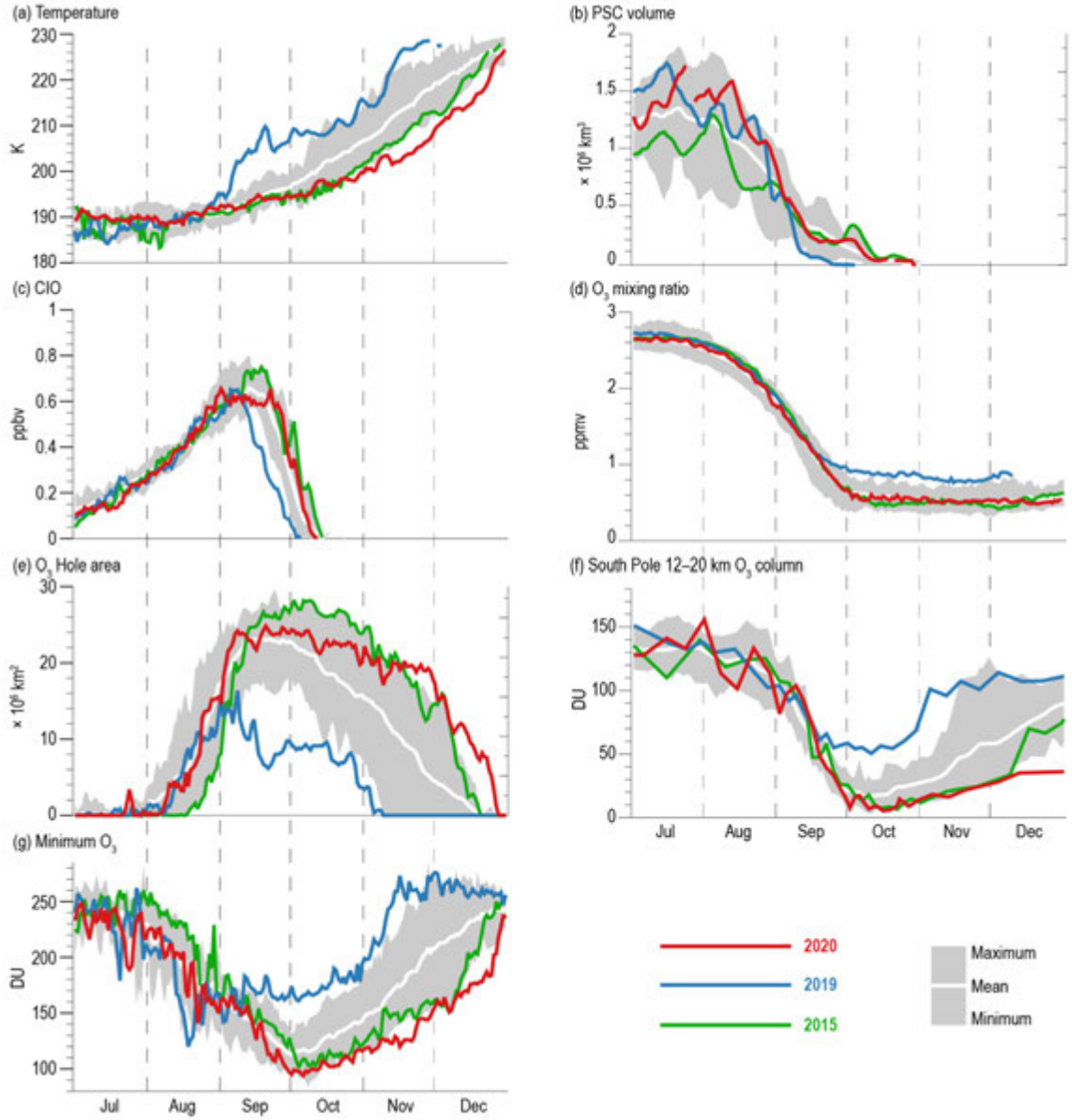

Fig. 6.14. Antarctic values of (a) vortex-averaged MERRA-2 temperature (K), (b) CALIPSO PSC volume (× 10^6 km^3; updated from Pitts et al. 2018), (c), (d) vortex-averaged ClO (ppbv) and O_3 (ppmv) measured by the *Aura* Microwave Limb Sounder (MLS; updated from Manney et al. 2011), (e) Antarctic ozone hole area (× 10^6 km^2; area with ozone total column less than 220 Dobson units [DU]) measured by the *Aura* Ozone Monitoring Instrument (OMI) and Suomi National Polar-orbiting Partnership/Ozone Mapping and Profiler (SNPP OMPS), (f) lower stratospheric ozone column (12–20 km, DU) based on sonde measurements at South Pole, and (g) minimum total column ozone (DU) over 60°–90°S from OMI/OMPS. MERRA-2 temperature and MLS averages are made inside the polar vortex on the 440 K potential temperature surface (~19 km or 60 hPa). Gray shading shows the range of daily Antarctic values for 2005 (for all but (b), which starts in 2006) through 2018. The white curve indicates the 2005–18 mean.

October–November period. Conditions in 2020 diverged from this typical behavior. Wave activity was weaker than average in August and September and at record low levels in October and November, resulting in a cold and stable polar vortex that persisted through December. Starting in late October, the Antarctic lower stratosphere saw a number of low-temperature records (Fig. 6.14a). The November-mean temperature at 50 hPa hit a record low of 213.2 K, 12.9 K below the November mean for the entire observational period (1980–2019).

The weak wave activity throughout the austral spring slowed the winter-to-summer transition, resulting in the longest-lived ozone hole in the observational record. The minimum total column ozone (Fig. 6.14g) reached record low values in November and December 2020. The 12–20 km ozone

column values at the South Pole were consistently below average since late September, breaking a number of daily records from late-October to December (Fig. 6.14f). Recent model-based studies (e.g., Müller et al. 2018) demonstrated that when the vortex remains cold and stable, as it did in 2020, near-complete lower stratospheric ozone destruction can still occur at the current levels of chlorine and bromine, even though they are 12.4% lower than their peak in 2000.

Monthly mean ozone hole areas in November and December 2020 were the largest on record at 19.5 Mkm^2 and 8.9 Mkm^2, respectively; in most other years the ozone hole disappeared by December. Similarly, the year 2015 exhibited weak wave activity that led to a persistently large hole and low ozone minima in October–December (Nash et al. 2016; green lines in Fig. 6.14). In both years, ozone depletion ceased by mid-October (Fig. 6.14d) because the volume of PSCs and ClO concentration dropped to near zero (Figs. 6.14b,c). Ozone column values (Figs. 6.14f,g) then remained seasonally low for the rest of the year due to the stable vortex and lack of poleward and downward transports of ozone-rich air.

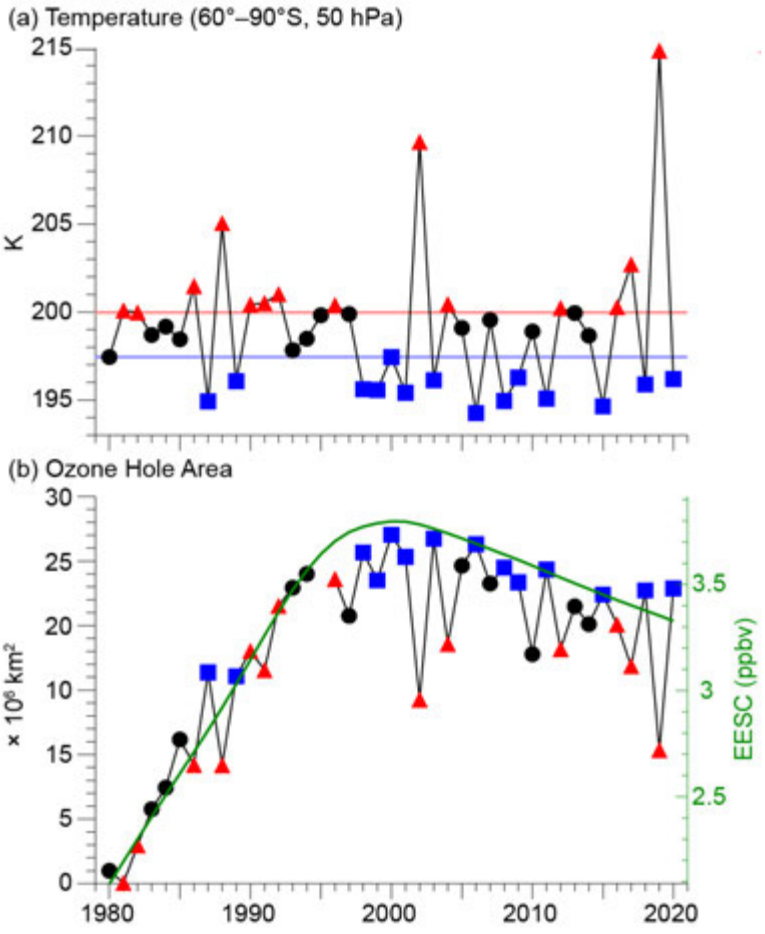

Fig. 6.15. (a) MERRA-2 50-hPa Sep mean temperature (K) averaged over 60°–90°S and (b) Sep mean Antarctic ozone hole area (× 10^6 km^2). Years with temperatures in the lowest (highest) third are shown as blue squares (red triangles). The horizontal blue and red lines indicate temperature levels with ±1 std. dev. from the 1980–2020 mean (33rd and 66th percentiles). The green curve (and right vertical axis) in (b) shows the NASA-estimated EESC level in the Antarctic lower stratosphere modeled with the assumption of a 5.2 mean age of air (Newman et al. 2007). Ozone data in (b) for 1979–1992 are from the TOMS Nimbus-7, 1993–94 are from TOMS Meteor-3, 1996–2004 are from Earth Probe TOMS, 2005–15 are from *Aura* OMI, and 2016–20 are from SNPP OMPS. There were no satellite total ozone observations for 1995.

The significant ozone loss in 2020 represents a dramatic turnabout from the 2019 ozone depletion season, when a stratospheric warming event in September terminated ozone loss cycles and ended depletion early. Lower stratospheric temperatures in 2019 increased in mid-August, and the September-mean temperature was 16 K above the long-term average (blue line in Fig. 6.14a). The ClO concentrations rapidly declined in early September, and ozone levels were 13%–55% above the average in mid-September–October 2019 (blue lines in Figs. 6.14d,f,g). The 2019 warming event also enabled transport of ozone into the polar region, reducing the severity of the ozone hole, which grew to only 16.4 Mkm^2 in early September and vanished by early November (Fig. 6.14e).

September is the most critical month for ozone depletion (Solomon et al. 2016; Strahan et al. 2019). In this month, polar vortex temperatures are typically low and less variable than in October, and sunlight returns to polar latitudes, activating photochemical reactions that catalytically destroy ozone. The ozone hole area in September (Fig. 6.15b) is controlled by two main factors: stratospheric chlorine and bromine loading and meteorological variability. To estimate the concentration of human-produced and natural chlorine and bromine compounds in the stratosphere, we use a metric called effective equivalent stratospheric chlorine (EESC; Newman et al. 2007). The stratospheric EESC concentration maximum was reached around 2000; it declined

thereafter due to actions prompted by the 1987 Montreal Protocol and following amendments. The 2020 EESC levels are 12.4% below the peak (green line in Fig. 6.15b).

Year-to-year variations in the lower stratospheric temperature (Fig. 6.15a) also affect the severity of ozone depletion. The area of the ozone hole is larger in colder years and smaller in warmer years. To isolate the effects of declining EESC on ozone recovery, we focus on years with similarly cold meteorological conditions (blue points in Fig. 6.15). We estimate that EESC has declined by 469 ppt, from 3797 ppt to 3328 ppt, since 2000. Strahan et al. (2014) derived a linear relationship of 125 ppt EESC Mkm^{-2} between the observed ozone hole area and EESC during the coldest years. Therefore, we expect the hole area to decline at a long-term average rate of 0.19 $Mkm^2\ yr^{-1}$. Using the blue points in Fig. 6.15b that identify years with September lower stratospheric temperatures at least 1 standard deviation below the long-term mean, we calculate a downward trend in the September average ozone hole area of 0.21 ± 0.11 $Mkm^2\ yr^{-1}$ since 2000, in good agreement with the expected trend. These results are consistent with the emergence of ozone recovery due to the Montreal Protocol despite large interannual fluctuations in the stratospheric dynamics over Antarctica (Solomon et al. 2016).

The persistence of the 2020 ozone hole until early austral summer resulted in record-breaking high UV radiation across the Antarctic region. Surface UV radiation depends on solar elevation, total ozone column, clouds, aerosols, and surface reflectivity (e.g., Bais et al. 2019). Ultraviolet radiation is quantified here with the UV Index (UVI), which is a measure of erythema (sunburn) UV radiation for human skin (WHO 2002). The UVI at the South Pole Station (Fig. 6.16a) and Arrival Heights, a coastal site near McMurdo research station (78°S, 167°E; Fig. 6.16b), was consistently above the 1990–2019 average during October–December 2020 (red lines in Fig. 6.16), in sharp contrast to 2019 (blue lines in Fig. 6.16), when total ozone column values were on average 100 DU larger than in 2020.

As the sun's elevation approached its seasonal peak, the UVI at the South Pole reached 4.0 on 15 December. This value tied within the measurement uncertainty with the record highs in 1998 and 2015. At Arrival Heights, the UVI reached a new all-time record of 7.8 on 23 December, exceeding the previous record for this day by 2.5 units. At Marambio (Fig. 6.16c), a research station located on the Antarctic Peninsula, the daily maximum UVI exceeded 12 on several days in late November and early December 2020 when the ozone hole extended toward South America. The UVI exceeded 15 on 29 November and 1 December 2020. A UVI greater than 11 is considered extreme, and typically such high UVI values are only observed in the tropics or at high mountain elevations. The record high 2020 UVI values in the Antarctic region dramatically contrast with the low 2019 values (blue lines in Fig. 6.16 for UVI and Fig. 6.14 for ozone), illustrating how year-to-year dynamically driven ozone variability impacts surface UV radiation.

Despite persistently cold temperatures and a stable vortex, the ozone depletion in 2020 was not as severe as in the early 2000s, when the concentration of ozone-depleting substances was close to its maximum. The recovery of the Antarctic ozone hole, due to the Montreal Protocol, is becoming evident despite large interannual variability in stratospheric dynamics. Weaker-than-average wave activity during austral spring led to the delayed transition from the winter-to-summer circulation, sustaining low ozone values over Antarctica until late December and resulting in unusually high levels of UV radiation.

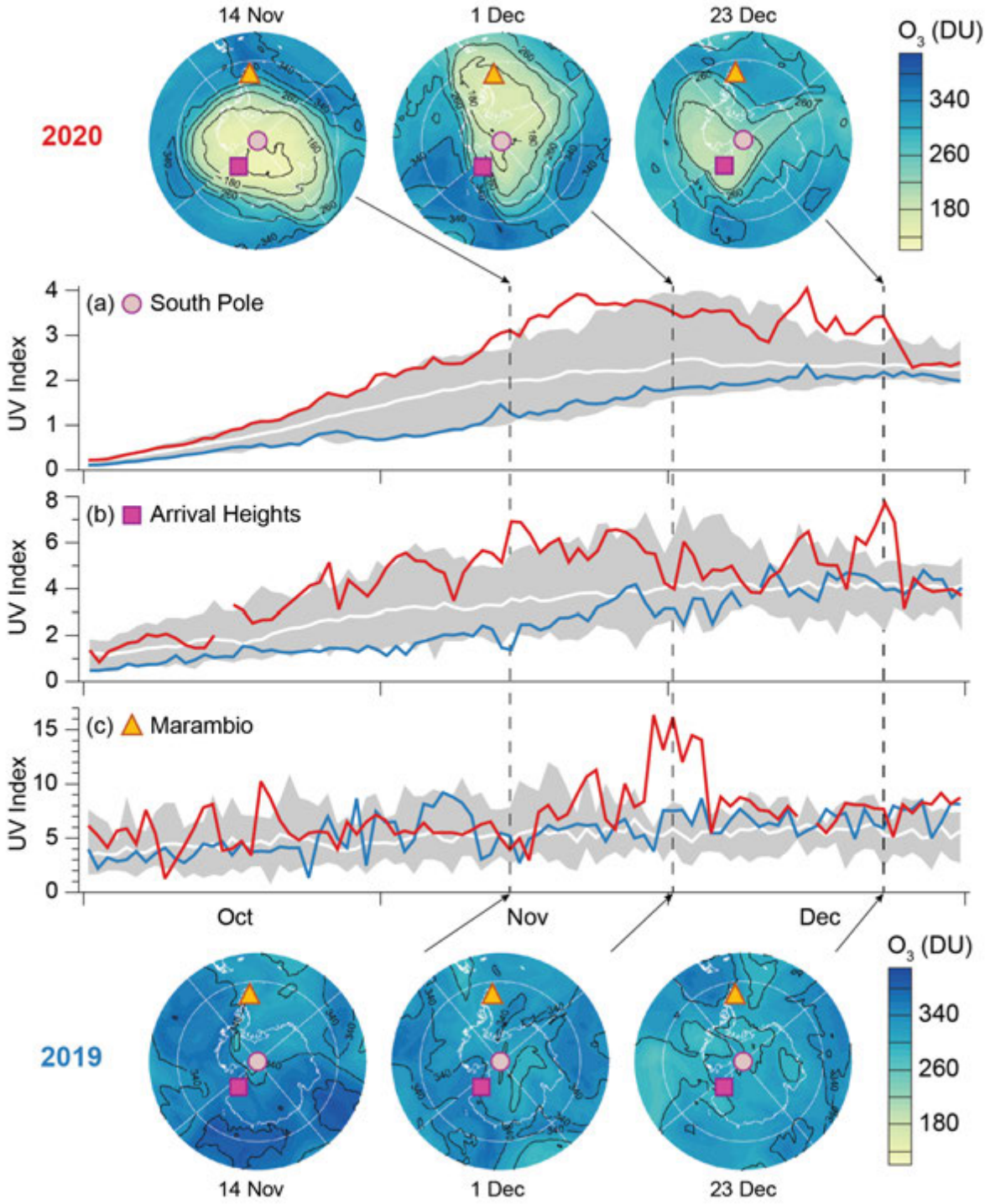

Fig. 6.16. Daily maximum UVI measured at three Antarctic stations: (a) South Pole (90°S), (b) Arrival Heights (near McMurdo Station; 78°S, 167°E), and (c) Marambio (64°S, 56°E). Colored lines show values for 2019 (blue line) and 2020 (red line), compared with each station's long-term mean (white line) and min/max range (gray shading) of similar observations between 1990 and 2018, except for Marambio, where there is a gap in data between 2011 and 2016. Data from 2019 and 2020 are preliminary and are expected to agree with final data to within ±5% (Aun et al. 2020; Lakkala et al. 2020). Marambio data for 2000–10 are from the Antarctic NILU-UV network (Lakkala et al. 2018). Data at South Pole and Arrival Heights up to 2009 are from the National Science Foundation's UV monitoring network (Booth et al. 1994; Bernhard et al. 2004); later data are from the NOAA Antarctic UV Monitoring Network (https://www.esrl.noaa.gov/gmd/grad/antuv/) and are corrected for small drifts in the calibration scale (Bernhard and Stierle 2020). Maps on the top and bottom show OMPS total ozone column values for 3 days in 2020 and 2019, respectively. Black lines indicate ozone contours.

Acknowledgments

Phil Reid and Jan Lieser were supported through the Australian Bureau of Meteorology, and Rob Massom by the Australian Antarctic Division. The work of Phil Reid and Rob Massom was also supported by the Australian Government's Australian Antarctic Partnership Program and contributes to AAS Project 4116.

Sharon Stammerjohn was supported under NSF PLR 1440435; she also thanks the Institute of Arctic and Alpine Research and the National Snow and Ice Data Center, both at the University of Colorado Boulder, for institutional and data support.

Sandra Barreira was supported by the Argentine Naval Hydrographic Service.

Ted Scambos was supported under NASA grant NNX14AM54G, the Arctic Sea Ice News and Analysis project and NSF ANT 1738992, the NSF-NERC International Thwaites Glacier Collaboration TARSAN project.

Work at the Jet Propulsion Laboratory, California Institute of Technology, was done under contract with the National Aeronautics and Space Administration (NASA). The authors would like to acknowledge Margit Aun from University of Tartu, Servicio Meteorológico Nacional (SMN) in Argentina, Spanish Agencia Estatal de Meteorología (AEMET), Argentinian Dirección Nacional del Antártico-Instituto Antártico Argentino (DNA-IAA), and Academy of Finland's projects FARPOCC and SAARA for Marambio data. Kaisa Lakkala is supported by the CHAMPS project (grant no. 329225) of the Academy of Finland under the CLIHE programme. We are indebted to the many NOAA Corps Officers and GML technical personnel who spend the winters at the South Pole Station to obtain the ongoing balloon and ground-based datasets. We also acknowledge the logistics support in Antarctica provided by the National Science Foundation Office of Polar Programs.

Veronica Tamsitt acknowledges support of CSHOR; CSHOR is a joint research Centre for Southern Hemisphere Ocean Research between QNLM and CSIRO. Air–sea heat flux data and code used in section 6g can be accessed online from doi:10.5281/zenodo.4595930. This is PMEL contribution number 5218.

Chapter 6 – Acronyms

AABW	Antarctic Bottom Water
ACC	Antarctic Circumpolar Current
AIS	Antarctic ice sheet
AMO	Atlantic Multidecadal Oscillation
AP	Antarctic Peninsula
AR	atmospheric river
ASL	Amundsen Sea Low
AWS	automated weather stations
AZ	Antarctic Zone
C3S	Copernicus Climate Change Service
CL_2	chlorine
ClO	chlorine monoxide
CO_2	carbon dioxide
DU	Dobson units
EAIS	East Antarctic ice sheet
EESC	equivalent stratospheric chlorine
ENSO	El Niño–Southern Oscillation
IVT	integrated water vapor transport
MJO	Madden-Julian Oscillation
ML	mixed layer
MLD	mixed layer depth
MLS	Microwave Limb Sounder
MSLP	mean sea level pressure
NSIDC	National Snow and Ice Data Center
OMI	ozone monitoring instrument
PSC	polar stratospheric cloud
SAM	Southern Annular Mode
SAMW	Subantarctic Mode Water
SAT	surface air temperature
SIE	sea ice extent
SMB	surface mass balance
SNPP OMPS	Suomi National Polar-orbiting Partnership/Ozone Mapping and Profiler
SO	Southern Ocean
SOCCOM	Southern Ocean Carbon Climate Observations and Modeling
USVs	uncrewed surface vehicles
UV	ultraviolet
UVI	ultraviolet index
w.e.	water equivalent
WAIS	West Antarctic ice sheet

References

Abrahamsen, E. P., and Coauthors, 2019: Stabilization of dense Antarctic water supply to the Atlantic Ocean overturning circulation. *Nat. Climate Change*, **9**, 742–746, https://doi.org/10.1038/s41558-019-0561-2.

Adusumilli, S., M. Fish, H. A. Fricker, and B. M. Medley, 2021: Atmospheric river precipitation contributed to rapid increases in surface height of the west Antarctic ice sheet in 2019. *Geophys. Res. Lett.*, **48**, e2020GL091076, https://doi.org/10.1029/2020GL091076.

Agosta, C., and Coauthors, 2019: Estimation of the Antarctic surface mass balance using the regional climate model MAR (1979-2015) and identification of dominant processes. *Cryosphere*, **13**, 281–296, https://doi.org/10.5194/tc-13-281-2019.

Aoki, S., and Coauthors, 2020: Freshening of Antarctic Bottom Water off Cape Darnley, East Antarctica. *J. Geophys. Res. Oceans*, **125**, e2020JC016374, https://doi.org/10.1029/2020JC016374.

Aun, M., and Coauthors, 2020: Solar UV radiation measurements in Marambio, Antarctica, during years 2017–2019. *Atmos. Chem. Phys.*, **20**, 6037–6054, https://doi.org/10.5194/acp-20-6037-2020.

Bais, A. F., G. Bernhard, R. L. McKenzie, P. J. Aucamp, P. J. Young, M. Ilyas, P. Jöckel, and M. Deushi, 2019: Ozone-climate interactions and effects on solar ultraviolet radiation. *Photochem. Photobiol. Sci.*, **18**, 602–640, https://doi.org/10.1039/C8PP90059K.

Banwell, A. F., R. T. Datta, R.L. Dell, M. Moussavi, L. Brucker, G. Picard, C. A. Shuman, and L. A. Stevens, 2021: The 32-year record-high surface melt in 2019/2020 on the northern George VI Ice Shelf, Antarctic Peninsula. *Cryosphere*, **15**, 909–925, https://doi.org/10.5194/tc-15-909-2021.

Barrand, N. E., D. G. Vaughan, N. Steiner, M. Tedesco, P. Kuipers Munneke, M. R. van den Broeke, and J. S. Hosking, 2013: Trends in Antarctic Peninsula surface melting conditions from observations and regional climate modeling. *J. Geophys. Res. Earth Surf.*, **118**, 315–330, https://doi.org/10.1029/2012JF002559.

Bernhard, G., and S. Stierle, 2020: Trends of UV radiation in Antarctica. *Atmosphere*, **11**, 795, https://doi.org/10.3390/atmos11080795.

——, C. R. Booth, and J. C. Ehramjian, 2004: Version 2 data of the National Science Foundation's ultraviolet radiation monitoring network: South Pole. *J. Geophys. Res.*, **109**, D21207, https://doi.org/10.1029/2004JD004937.

Booth, C. R., T. B. Lucas, J. H. Morrow, C. S. Weiler, and P. A. Penhale, 1994: The United States National Science Foundation's polar network for monitoring ultraviolet radiation. *Ultraviolet Radiation in Antarctica: Measurements and Biological Effects*, C. S. Weiler and P. A. Penhale, Eds., Antarctica Research Series, Vol. 62, Amer. Geophys. Union, 17–37.

Bourassa, M. A., and Coauthors, 2013: High-latitude ocean and sea ice surface fluxes: Challenges for climate research. *Bull. Amer. Meteor. Soc.*, **94**, 403–423, https://doi.org/10.1175/BAMS-D-11-00244.1.

Bowen, M. M., D. Fernandez, A. Forcen-Vazquez, A. L. Gordon, B. Huber, P. Castagno, and P. Falco, 2021: The role of tides in bottom water export from the western Ross Sea. *Sci. Rep.*, **11**, 2246, https://doi.org/10.1038/s41598-021-81793-5.

Bushinsky, S. M., and Coauthors, 2019: Reassessing Southern Ocean air-sea CO2 flux estimates with the addition of biogeochemical float observations. *Global Biogeochem. Cycles*, **33**, 1370–1388, https://doi.org/10.1029/2019GB006176.

Cape, M. R., M. Vernet, P. Skvarca, S. Marinsek, T. Scambos, and E. Domack, 2015: Foehn winds link climate-driven warming to ice shelf evolution in Antarctica. *J. Geophys. Res. Atmos.*, **120**, 11 037–11 057, https://doi.org/10.1002/2015JD023465.

Castagno, P., V. Capozzi, G. R. DiTullio, P. Falco, G. Fusco, S. R. Rintoul, G. Spezie, and G. Budillon, 2019: Rebound of shelf water salinity in the Ross Sea. *Nat. Commun.*, **10**, 5441, https://doi.org/10.1038/s41467-019-13083-8.

Cavalieri, D. J., C. L. Parkinson, P. Gloersen, and H. J. Zwally, 1996: Sea ice concentrations from Nimbus-7 SMMR and DMSP SSM/I-SSMIS passive microwave data, version 1. NSIDC, accessed 10 February 2021, https://doi.org/10.5067/8GQ8LZQVL0VL.

Claustre, H., K. S. Johnson, and Y. Takeshita, 2020: Observing the global ocean with biogeochemical-Argo. *Annu. Rev. Mar. Sci.*, **12**, 23–48, https://doi.org/10.1146/annurev-marine-010419-010956.

Clem, K. R., B. R. Lintner, A. J. Broccoli, and J. R. Miller, 2019: Role of the south Pacific convergence zone in west Antarctic decadal climate variability. *Geophys. Res. Lett.*, **46**, 6900–6909, https://doi.org/10.1029/2019GL082108.

——, S. Barreira, R. L. Fogt, S. Colwell, L. M. Keller, M. A. Lazzara, and D. Mikolajczyk, 2020a: Atmospheric circulation and surface observations [in "State of the Climate in 2019"]. *Bull. Amer. Meteor. Soc.*, **101** (8), S293–S296, https://doi.org/10.1175/BAMS-D-20-0090.1.

——, R. L. Fogt, J. Turner, B. R. Lintner, G. J. Marshall, J. R. Miller, and J. A. Renwick, 2020b: Record warming at the South Pole during the past three decades. *Nat. Climate Change*, **10**, 762–770, https://doi.org/10.1038/s41558-020-0815-z.

COMNAP, 2015: Sea ice challenges workshop report. COMNAP, 37 pp., https://www.comnap.aq/publications/symposiums-workshops-reports.

C3S, 2017: ERA5: Fifth generation of ECMWF atmospheric reanalyses of the global climate. Copernicus Climate Change Service Climate Data Store (CDS), accessed 4 May 2018, https://cds.climate.copernicus.eu/cdsapp#!/dataset/reanalysis-era5-single-levels-monthly-means?tab=overview.

de Boyer Montégut, C., G. Madec, A. S. Fischer, A. Lazar, and D. Iudicone, 2004: Mixed layer depth over the global ocean: An examination of profile data and a profile-based climatology. *J. Geophys. Res.*, **109**, C12003, https://doi.org/10.1029/2004JC002378.

Depoorter, M. A., J. L. Bamber, J. A. Griggs, J. T. M. Lenaerts, S. R. M. Ligtenberg, M. R. van den Broeke, and G. Moholdt, 2013: Calving fluxes and basal melt rates of Antarctic ice shelves. *Nature*, **502**, 89–92, https://doi.org/10.1038/nature12567.

England, M. R., L. M. Polvani, L. Sun, and C. Deser, 2020: Tropical climate responses to projected Arctic and Antarctic Sea ice loss. *Nat. Geosci.*, **13**, 275–281, https://doi.org/10.1038/s41561-020-0546-9.

Fogt, R. L., and G. J. Marshall, 2020: The Southern Annular Mode: Variability, trends, and climate impacts across the Southern Hemisphere. *Wiley Interdiscip. Rev.: Climate Change*, **11**, 1–24, https://doi.org/10.1002/wcc.652.

——, D. H. Bromwich, and K. M. Hines, 2011: Understanding the SAM influence on the South Pacific ENSO teleconnection. *Climate Dyn.*, **36**, 1555–1576, https://doi.org/10.1007/s00382-010-0905-0.

Forster, R. R., and Coauthors, 2014: Extensive liquid meltwater storage in firn within the Greenland ice sheet. *Nat. Geosci.*, **7**, 95–98, https://doi.org/10.1038/ngeo2043.

Fountain, A. G., and J. S. Walder, 1998: Water flow through temperate glaciers. *Rev. Geophys.*, **36**, 299–328, https://doi.org/10.1029/97RG03579.

Francelino, M. R. and Coauthors, 2021: WMO evaluation of two extreme high temperatures occurring in February 2020 for the Antarctic Peninsula region. *Bull. Amer. Meteor. Soc.*, https://doi.org/10.1175/BAMS-D-21-0040.1, in press.

Francis, D., K. S. Mattingly, S. Lhermitte, M. Temimi, and P. Heil, 2021: Atmospheric extremes triggered the biggest calving event in more than 50 years at the Amery Ice shelf in September 2019. *Cryosphere*, **15**, 2147–2165, https://doi.org/10.5194/tc-15-2147-2021.

Fricker, H. A., and A. Gardner, 2020: Recent Changes in the Antarctic Ice Sheet [in "State of the Climate in 2019"]. *Bull. Amer. Meteor. Soc.*, **101** (8), S304–S306, https://doi.org/10.1175/BAMS-D-20-0090.1.

Frölicher, T. L., J. L. Sarmiento, D. J. Paynter, J. P. Dunne, J. P. Krasting, and M. Winton, 2015: Dominance of the Southern Ocean in anthropogenic carbon and heat uptake in CMIP5 models. *J. Climate*, **28**, 862–886, https://doi.org/10.1175/JCLI-D-14-00117.1.

Gelaro, R., and Coauthors, 2017: The Modern-Era Retrospective Analysis for Research and Applications, version 2 (MERRA-2). *J. Climate*, **30**, 5419–5454, https://doi.org/10.1175/JCLI-D-16-0758.1.

Gloersen, P., 2006: Nimbus-7 SMMR polar gridded radiances and sea ice concentrations, Version 1. Subset: 37 & 19 GHz, h-polarization, 25 km grid, Oct 1979–April 1987. NASA National Snow and Ice Data Center Distributed Active Archive Center, accessed 5 May 2020, https://doi.org/10.5067/QOZIVYV3V9JP.

Gordon, A. L., B. A. Huber, and E. P. Abrahamsen, 2020: Interannual variability of the outflow of Weddell Sea Bottom Water. *Geophys. Res. Lett.*, **47**, e2020GL087014, https://doi.org/10.1029/2020GL087014.

Gossart, A., S. Helsen, J. T. M. Lenaerts, S. Vanden Broucke, N. P. M. van Lipzig, and N. Souverijns, 2019: An evaluation of surface climatology in state-of-the-art reanalyses over the Antarctic ice sheet. *J. Climate*, **32**, 6899–6915, https://doi.org/10.1175/JCLI-D-19-0030.1.

Gray, A. R., and Coauthors, 2018: Autonomous biogeochemical floats detect significant carbon dioxide outgassing in the high-latitude Southern Ocean. *Geophys. Res. Lett.*, **45**, 9049–9057, https://doi.org/10.1029/2018GL078013.

Guan, B., and D. E. Waliser, 2015: Detection of atmospheric rivers: Evaluation and application of an algorithm for global studies. *J. Geophys. Res. Atmos.*, **120**, 12 514–12 535, https://doi.org/10.1002/2015JD024257.

Hall, A., and M. Visbeck, 2002: Synchronous variability in the Southern Hemisphere atmosphere, sea ice, and ocean resulting from the annular mode. *J. Climate*, **15**, 3043–3057, https://doi.org/10.1175/1520-0442(2002)015<3043:SVITSH>2.0.CO;2.

Hirota, N., H. Shiogama, H. Akiyoshi, T. Ogura, M. Takahashi, Y. Kawatani, M. Kimoto, and M. Mori, 2018: The influences of El Nino and Arctic sea-ice on the QBO disruption in February 2016. *Climate Atmos. Sci.*, **1**, 10, https://doi.org/10.1038/s41612-018-0020-1.

Jacobs, S. S., and C. F. Giulivi, 2010: Large multidecadal salinity trends near the Pacific–Antarctic continental margin. *J. Climate*, **23**, 4508–4524, https://doi.org/10.1175/2010JCLI3284.1.

Johnson, G. C., 2008: Quantifying Antarctic Bottom Water and North Atlantic Deep Water volumes. *J. Geophys. Res.*, **113**, C05027, https://doi.org/10.1029/2007JC004477.

Jullion, L., A. C. Naveira Garabato, M. P. Meredith, P. R. Holland, P. Courtois, and B. A. King, 2013: Decadal freshening of the Antarctic Bottom Water exported from the Weddell Sea. *J. Climate*, **26**, 8111–8125, https://doi.org/10.1175/JCLI-D-12-00765.1.

Kuipers Munneke, P., S. R. M. Ligtenberg, M. R. van den Broeke, J. H. van Angelen, and R. R. Forster, 2014: Explaining the presence of perennial liquid water bodies in the firn of the Greenland ice sheet. *Geophys. Res. Lett.*, **41**, 476–483, https://doi.org/10.1002/2013GL058389.

Lakkala, K., and Coauthors, 2018: UV measurements at Marambio and Ushuaia during 2000–2010. *Atmos. Chem. Phys.*, **18**, 16 019–16 031, https://doi.org/10.5194/acp-18-16019-2018.

——, and Coauthors, 2020: New continuous total ozone, UV, VIS and PAR measurements at Marambio, 64° S, Antarctica. *Earth Syst. Sci. Data*, **12**, 947–960, https://doi.org/10.5194/essd-12-947-2020.

Landschützer, P., N. Gruber, and D. C. E. Bakker, 2016: Decadal variations and trends of the global ocean carbon sink. *Global Biogeochem. Cycles*, **30**, 1396–1417, https://doi.org/10.1002/2015GB005359.

Lee, H. J., and K. H. Seo, 2019: Impact of the Madden-Julian oscillation on Antarctic sea ice and its dynamical mechanism. *Sci. Rep.*, **9**, 10761, https://doi.org/10.1038/s41598-019-47150-3.

Lenaerts, J. T. M., and M. R. van den Broeke, 2012: Modeling drifting snow in Antarctica with a regional climate model: 2. Results. *J. Geophys. Res.*, **117**, D05109, https://doi.org/10.1029/2010JD015419.

——, E. van Meijgaard, M. R. van den Broeke, S. R. M. Ligtenberg, M. Horwath, and E. Isaksson, 2013: Recent snowfall anomalies in Dronning Maud Land, East Antarctica, in a historical and future climate perspective. *Geophys. Res. Lett.*, **40**, 2684–2688, https://doi.org/10.1002/grl.50559.

——, E. Keenan, M. Maclennan, and T. Gorte, 2020: Surface mass balance of the ice sheet [in "State of the Climate in 2019"]. *Bull. Amer. Meteor. Soc.*, **101** (8), S298–S300, https://doi.org/10.1175/2020BAMSStateoftheClimate.1.

Lhermitte, S., and Coauthors, 2020: Damage accelerates ice shelf instability and mass loss in Amundsen Sea Embayment. *Proc. Natl. Acad. Sci. USA*, 117, 24 735–24 741, https://doi.org/10.1073/pnas.1912890117.

Li, X., E. P. Gerber, D. M. Holland, and C. Yoo, 2015: A Rossby wave bridge from the tropical Atlantic to west Antarctica. *J. Climate*, **28**, 2256–2273, https://doi.org/10.1175/JCLI-D-14-00450.1.

Li, Z., M. H. England, S. Groeskamp, I. Cerovečki, and Y. Luo, 2021: The origin and fate of Subantarctic Mode Water in the Southern Ocean. *J. Phys. Oceanogr.*, https://doi.org/10.1175/JPO-D-20-0174.1, in press.

Ligtenberg, S. R. M., M. M. Helsen, and M. R. van den Broeke, 2011: An improved semi-empirical model for the densification of Antarctic firn. *Cryosphere*, **5**, 809–819, https://doi.org/10.5194/tc-5-809-2011.

Liu, H., L. Wang, and K. C. Jezek, 2006: Spatiotemporal variations of snowmelt in Antarctica derived from satellite scanning multichannel microwave radiometer and Special Sensor Microwave Imager data (1978–2004). *J. Geophys. Res. Earth Surf.*, **111**, F01003, https://doi.org/10.1029/2005JF000318.

Liu, J., D. G. Martinson, X. Yuan, and D. Rind, 2002: Evaluating Antarctic sea ice variability and its teleconnections in global climate models. *Int. J. Climatol.*, **22**, 885–900, https://doi.org/10.1002/joc.770.

MacDonell, S., F. Fernandoy, P. Villar, and A. Hammann, 2021: Stratigraphic analysis of firn cores from an Antarctic ice shelf firn aquifer. *Water*, **13**, 731, https://doi.org/10.3390/w13050731.

Manney, G. L., and Coauthors, 2011: Unprecedented Arctic ozone loss in 2011. *Nature*, **478**, 469–475, https://doi.org/10.1038/nature10556.

Marshall, G. J., 2003: Trends in the southern annular mode from observations and reanalyses. *J. Climate*, **16**, 4134–4143, https://doi.org/10.1175/1520-0442(2003)016%3C4134:TITSAM%3E2.0.CO;2.

Maslanik, J., and J. Stroeve, 1999: Near-real-time DMSP SSM/I-SSMIS daily polar gridded sea ice concentrations. National Snow and Ice Data Center, accessed February 2021, https://doi.org/10.5067/U8C09DWVX9LM.

Massom, R. A., and S. E. Stammerjohn, 2010: Antarctic sea ice change and variability - Physical and ecological implications. *Polar Sci.*, **4**, 149–186, https://doi.org/10.1016/j.polar.2010.05.001.

——, T. A. Scambos, L. G. Bennetts, P. Reid, V. A. Squire, and S. E. Stammerjohn, 2018: Antarctic ice shelf disintegration triggered by sea ice loss and ocean swell. *Nature*, **558**, 383–389, https://doi.org/10.1038/s41586-018-0212-1.

Medley, B., and E. R. Thomas, 2019: Increased snowfall over the Antarctic ice sheet mitigated twentieth-century sea-level rise. *Nat. Climate Change*, **9**, 34–39, https://doi.org/10.1038/s41558-018-0356-x.

Meier, W. N., H. Wilcox, M. A. Hardman, and J. S. Stewart, 2019: DMSP SSM/I-SSMIS daily polar gridded brightness temperatures, version 5. Subset: 37 & 19 GHz, h-polarization, 25 km grid, Oct 1987–April 2020. NASA National Snow and Ice Data Center Distributed Active Archive Center, accessed 11 February 2021, https://doi.org/10.5067/QU2UYQ6T0B3P.

Menezes, V. V., A. M. Macdonald, and C. Schatzman, 2017: Accelerated freshening of Antarctic Bottom Water over the last decade in the Southern Indian Ocean. *Sci. Adv.*, **3**, e1601426, https://doi.org/10.1126/sciadv.1601426.

Meredith, M. P., and M. A. Brandon, 2017: Oceanography and sea ice in the Southern Ocean. Sea Ice, D. N. Thomas, Ed., Wiley-Blackwell, 216–238, https://doi.org/10.1002/9781118778371.ch8.

Montgomery, L., and Coauthors, 2020: Hydrologic properties of a highly permeable firn aquifer in the Wilkins Ice Shelf, Antarctica. *Geophys. Res. Lett.*, **47**, e2020GL089552, https://doi.org/10.1029/2020GL089552.

Mote, T. L., 2007: Greenland surface melt trends 1973–2007: Evidence of a large increase in 2007. *Geophys. Res. Lett.*, **34**, L22507, https://doi.org/10.1029/2007GL031976.

——, 2014: MEaSUREs Greenland surface melt daily 25km EASE-Grid 2.0, Version 1. NASA National Snow and Ice Data Center Distributed Active Archive Center, accessed 10 February 2021, https://doi.org/10.5067/MEASURES/CRYOSPHERE/nsidc-0533.001.

——, and M. R. Anderson, 1995: Variations in snowpack melt on the Greenland ice sheet based on passive microwave measurements. *J. Glaciol.*, **41**, 51–60, https://doi.org/10.3189/S0022143000017755.

Mottram, R., and Coauthors, 2020: What is the surface mass balance of Antarctica? An intercomparison of regional climate model estimates. *Cryosphere Discuss.*, https://doi.org/10.5194/tc-2019-333.

Müller, R., J.-U., Grooß, A. M. Zafar, S. Robrecht, and R. Lehmann, 2018: The maintenance of elevated active chlorine levels in the Antarctic lower stratosphere through HCl null cycles. *Atmos. Chem. Phys.*, **18**, 2985–2997, https://doi.org/10.5194/acp-18-2985-2018.

NAS (National Academies of Sciences, Engineering, and Medicine), 2017: *Antarctic Sea Ice Variability in the Southern Ocean-Climate System: Proceedings of a Workshop.* The National Academies Press, 82 pp., https://doi.org/10.17226/24696.

Nash, E., and Coauthors, 2016: Antarctic ozone hole [in "State of the Climate in 2015"]. *Bull. Amer. Meteor. Soc.*, **97** (8), S168–S172, https://doi.org/10.1175/2016BAMSStateoftheClimate.1.

Newman, P., E. R. Nash, N. Kramarova, and A. Butler, 2020: Sidebar 6-1: The 2019 southern stratospheric warming [in "State of the Climate in 2019"]. *Bull. Amer. Meteor. Soc.*, **101** (8), S297–S298, https://doi.org/10.1175/BAMS-D-20-0090.1.

——, J. S. Daniel, D. W. Waugh, and E. R. Nash, 2007: A new formulation of Equivalent Effective Stratospheric Chlorine (EESC). *Atmos. Chem. Phys.*, **7**, 4537–4552, https://doi.org/10.5194/acp-7-4537-2007.

Norwegian Polar Institute, 2018: Quantarctica v3.0, detailed basemap. www.npolar.no/quantarctica/.

Oliva, M., F. Navarro, F. Hrbáček, A. Hernandéz, D. Nývlt, P. Pereira, J. Ruiz-Fernandéz, and R. Trigo, 2017: Recent regional climate cooling on the Antarctic Peninsula and associated impacts on the cryosphere. *Sci. Total Environ.*, **580**, 210–223, https://doi.org/10.1016/j.scitotenv.201 6-12.030.

Palm, S. P., V. Kayetha, and Y. Yang, 2018: Toward a satellite-derived climatology of blowing snow over Antarctica. *J. Geophys. Res. Atmos.*, **123**, 10301–10313, https://doi.org/10.1029/2018JD028632.

Paolo, F. S., H. A. Fricker, and L. Padman, 2015: Volume loss from Antarctic ice shelves is accelerating. *Science*, **348**, 327–331, https://doi.org/10.1126/science.aaa0940.

Parkinson, C. L., 2019: A 40-y record reveals gradual Antarctic sea ice increases followed by decreases at rates far exceeding the rates seen in the Arctic. *Proc. Natl. Acad. Sci. USA*, **116**, 14414–14423, https://doi.org/10.1073/pnas.1906556116.

Pitts, M. C., L. R. Poole, and R. Gonzalez, 2018: Polar stratospheric cloud climatology based on CALIPSO spaceborne lidar measurements from 2006 to 2017. *Atmos. Chem. Phys.*, **18**, 10881–10913, https://doi.org/10.5194/acp-18-10881-2018.

Purkey, S. G., and G. C. Johnson, 2013: Antarctic Bottom Water warming and freshening: Contributions to sea level rise, ocean freshwater budgets, and global heat gain. *J. Climate*, **26**, 6105–6122, https://doi.org/10.1175/JCLI-D-12-00834.1.

Queste, B. Y., and Coauthors, 2020: Southern Ocean [in "State of the Climate in 2019"]. *Bull. Amer. Meteor. Soc.*, **101** (8), S307–S309, https://doi.org/10.1175/BAMS-D-20-0090.1.

Raphael, M. N., and Coauthors, 2016: The Amundsen Sea low: Variability, change, and impact on Antarctic climate. *Bull. Amer. Meteor. Soc.*, **97**, 111–121, https://doi.org/10.1175/BAMS-D-14-00018.1.

Reid, P. A., and R. A. Massom, 2015: Successive Antarctic Sea ice extent records during 2012, 2013 & 2014 [in "State of the Climate in 2014"]. *Bull. Amer. Meteor. Soc.*, **96** (7), S163–S164, https://doi.org/10.1175/2015BAMSStateoftheClimate.1.

——, S. Stammerjohn, R. A. Massom, S. Barreira, T. Scambos, and J. L. Lieser, 2020: Sea ice extent, concentration, and seasonality [in "State of the Climate in 2019"]. *Bull. Amer. Meteor. Soc.*, **101**, S304–S306, https://doi.org/10.1175/BAMS-D-20-0090.1.

Reynolds, R. W., N. A. Rayner, T. M. Smith, D. C. Stokes, and W. Wang, 2002: An improved in situ and satellite SST analysis for climate. *J. Climate*, **15**, 1609–1625, https://doi.org/10.1175/1520-0442(2002)015<1609:AIISAS>2.0.CO;2.

Riehl, H., and S. Teweles, 1953: A further study on the relation between the jet stream and cyclone formation. *Tellus*, **5**, 66–79, https://doi.org/10.3402/tellusa.v5i1.8561.

Rignot, E., S. Jacobs, J. Mouginot, and B. Scheuchl, 2013: Ice-shelf melting around Antarctica. *Science*, **341**, 266–270, https://doi.org/10.1126/science.1235798.

Roach, L. A., and Coauthors, 2020: Antarctic sea ice area in CMIP6. *Geophys. Res. Lett.*, **47**, e2019GL086729, https://doi.org/10.1029/2019GL086729.

Rödenbeck, C., and Coauthors, 2013: Global surface-ocean pCO2 and sea-air CO2 flux variability from an observation-driven ocean mixed-layer scheme. *Ocean Sci.*, **9**, 193–216, https://doi.org/10.5194/os-9-193-2013.

Roemmich, D., and J. Gilson, 2009: The 2004–2008 mean and annual cycle of temperature, salinity, and steric height in the global ocean from the Argo Program. *Prog. Oceanogr.*, **82**, 81–100, https://doi.org/10.1016/j.pocean.2009.03.004.

——, and Coauthors, 2019: On the future of Argo: A global, full-depth, multi-disciplinary array. *Front. Mar. Sci.*, **6**, 439, https://doi.org/10.3389/fmars.2019.00439.

Rondanelli, R., B. Hatchett, J. Rutllant, D. Bozkurt, and R. Garreaud, 2019: Strongest MJO on record triggers extreme Atacama rainfall and warmth in Antarctica. *Geophys. Res. Lett.*, **46**, 3482–3491, https://doi.org/10.1029/2018GL081475.

Sabine, C., and Coauthors, 2020: Evaluation of a new carbon dioxide system for autonomous surface vehicles. *J. Atmos. Oceanic Technol.*, **37**, 1305–1317, https://doi.org/10.1175/JTECH-D-20-0010.1.

Sallée, J. B., K. Speer, S. R. Rintoul, and S. Wijffels, 2010: Southern Ocean thermocline ventilation. *J. Phys. Oceanogr.*, **40**, 509–529, https://doi.org/10.1175/2009JPO4291.1.

Scambos, T., and Coauthors, 2009: Ice shelf disintegration by plate bending and hydro-fracture: satellite observations and model results of the 2008 Wilkins ice shelf break-ups. *Earth and Planet. Sci. Lett.*, **280**, 51–60, https://doi.org/10.1016/j.epsl.2008.12.027.

Shadwick, E., and Coauthors, 2013: Glacier tongue calving reduced dense water formation and enhanced carbon uptake. *Geophys. Res. Lett.*, **40**, 904–909, https://doi.org/10.1002/grl.50178.

Shepherd, A., and Coauthors, 2018: Mass balance of the Antarctic ice sheet from 1992 to 2017. *Nature*, **558**, 219–222, https://doi.org/10.1038/s41586-018-0179-y.

Shepherd, A., and Coauthors, 2012: A reconciled estimate of ice-sheet mass balance, Science, 338, 1183–1189, https://doi.org/10.1126/science.1228102.

Silvano, A., and Coauthors, 2020: Recent recovery of Antarctic Bottom Water formation in the Ross Sea driven by climate anomalies. *Nat. Geosci.*, **13**, 780–786, https://doi.org/10.1038/s41561-020-00655-3.

Smith, B., H. A. Fricker, A. S. Gardner, B. Medley, J. Nilsson, F. S. Paolo, N. Holschuh, S. Adusumilli, K. Brunt, B. Csatho, K. Harbeck, T. Markus, T. Neumann, M. R. Siegfried, and H. J. Zwally, 2020: Pervasive ice sheet mass loss reflects competing ocean and atmosphere processes. *Science*, **368**, https://doi.org/10.1126/science.aaz5845.

——, ——, ——, M. R. Siegfried, S. Adusumilli, B. M. Csathó, N. Holschuh, J. Nilsson, F. S. Paolo, and the ICESat-2 Science Team, 2021: ATLAS/ICESat-2 L3A Land Ice Height, Version 4, version 4. NASA National Snow and Ice Data Center Distributed Active Archive Center, accessed 20 February 2021, https://doi.org/10.5067/ATLAS/ATL06.003..

Smith, G. C., and Coauthors, 2018: Impact of coupling with an ice-ocean model on global medium-range NWP forecast skill. *Mon. Wea. Rev.*, **146**, 1157–1180, https://doi.org/10.1175/MWR-D-17-0157.1.

Smith, T. M., R. W. Reynolds, T. C. Peterson, and J. Lawrimore, 2008: Improvements to NOAA's historical merged land–ocean surface temperature analysis (1880–2006). *J. Climate*, **21**, 2283–2296, https://doi.org/10.1175/2007JCLI2100.1.

Sokolov, S., and S. R. Rintoul, 2009: Circumpolar structure and distribution of the Antarctic circumpolar current fronts: 1. Mean circumpolar paths. *J. Geophys. Res.*, **114**, C11018, https://doi.org/10.1029/2008JC005108.

Solomon, S., D. J. Ivy, D. Kinnison, M. J. Mills, R. R. Neely, and A. Schmidt, 2016: Emergence of healing in the Antarctic ozone layer. *Science*, **353**, 269–274, https://doi.org/10.1126/science.aae0061.

Stammerjohn, S., and T. Maksym, 2017: Gaining (and losing) Antarctic sea ice: Variability, trends and mechanisms. *Sea Ice*, D. N. Thomas, Ed., Wiley-Blackwell, 261–289, https://doi.org/10.1002/9781118778371.ch10.

——, and T. A. Scambos, 2020: Warming reaches the South Pole. *Nat. Climate Change*, **10**, 710–711, https://doi.org/10.1038/s41558-020-0827-8.

——, D. G. Martinson, R. C. Smith, X. Yuan, and D. Rind, 2008: Trends in Antarctic annual sea ice retreat and advance and their relation to El Niño–Southern Oscillation and Southern Annular Mode variability. *J. Geophys. Res.*, **113**, C03S90, https://doi.org/10.1029/2007JC004269.

Strahan, S. E., A. R. Douglass, P. A. Newman, and S. D. Steenrod, 2014: Inorganic chlorine variability in the Antarctic vortex and implications for ozone recovery. *J. Geophys. Res. Atmos.*, **119**, 14098–14109, https://doi.org/10.1002/2014JD022295.

——, A. R. Douglass, and M. R. Damon, 2019: Why do Antarctic ozone recovery trends vary? *J. Geophys. Res. Atmos.*, **124**, 8837–8850, https://doi.org/10.1029/2019JD030996.

Sutton, A. J., N. L. Williams, and B. Tilbrook, 2021: Constraining Southern Ocean CO2 flux uncertainty using uncrewed surface vehicle observations. *Geophys. Res. Lett.*, **48**, e2020GL091748, https://doi.org/10.1029/2020GL091748.

Tamsitt, V., I. Cerovečki, S. A. Josey, S. T. Gille, and E. Schulz, 2020: Mooring observations of air–sea heat fluxes in two Subantarctic Mode Water formation regions. *J. Climate*, **33**, 2757–2777, https://doi.org/10.1175/JCLI-D-19-0653.1.

Tedesco, M., 2009: Assessment and development of snowmelt retrieval algorithms over Antarctica from K-band spaceborne brightness temperature (1979–2008). *Remote Sens. Environ.*, **113**, 979–997, https://doi.org/10.1016/j.rse.2009.01.009.

Thomas, D. N., Ed., 2017: *Sea Ice*. 3rd ed. Wiley-Blackwell, 664 pp.

Thomas, G., S. G. Purkey, D. Roemmich, A. Foppert, and S. R. Rintoul, 2020: Spatial variability of Antarctic Bottom Water in the Australian Antarctic Basin from 2018–2020 captured by Deep Argo. *Geophys. Res. Lett.*, **47**, e2020GL089467, https://doi.org/10.1029/2020GL089467.

Timmermann, R., and H. H. Hellmer, 2013: Southern Ocean warming and increased ice shelf basal melting in the twenty-first and twenty-second centuries based on coupled ice-ocean finite-element modelling. *Ocean Dyn.*, **63**, 1011–1026, https://doi.org/10.1007/s10236-013-0642-0.

Turner, J., and Coauthors, 2016: Absence of 21st century warming on Antarctic Peninsula consistent with natural variability. *Nature*, **535**, 411–415, https://doi.org/10.1038/nature18645.

——, and Coauthors, 2020: Recent decrease of summer sea ice in the Weddell Sea, Antarctica. *Geophys. Res. Lett.*, **47**, e2020GL087127, https://doi.org/10.1029/2020GL087127.

van Wessem, J. M., C. R. Steger, N. Wever, and M. R. van den Broeke, 2021: An exploratory modelling study of perennial firn aquifers in the Antarctic Peninsula for the period 1979–2016. *Cryosphere*, **15**, 695–714, https://doi.org/10.5194/tc-15-695-2021.

van Wijk, E. M., and S. R. Rintoul, 2014: Freshening drives contraction of Antarctic Bottom Water in the Australian Antarctic Basin. *Geophys. Res. Lett.*, **41**, 1657–1664, https://doi.org/10.1002/2013GL058921.

Vederman, J., 1954: The life cycles of jet streams and extratropical cyclones. *Bull. Amer. Meteor. Soc.*, **35**, 239–244, https://doi.org/10.1175/1520-0477-35.6-239.

Walsh, J. E., 1983: The role of sea ice in climatic variability: Theories and evidence. *Atmos. Ocean*, **21**, 229–242, https://doi.org/10.1080/07055900.1983.9649166.

Wang, Y., and Coauthors, 2016: A comparison of Antarctic Ice Sheet surface mass balance from atmospheric climate models and in situ observations. *J. Climate*, **29**, 5317–5337, https://doi.org/10.1175/JCLI-D-15-0642.1.

Watkins, A. B., and I. Simmonds, 1999: A late spring surge in the open water of the Antarctic sea ice pack. *Geophys. Res. Lett.*, **26**, 1481–1484, https://doi.org/10.1029/1999GL900292.

Wheeler, M. C., and H. H. Hendon, 2004: An all-season real-time multivariate MJO index: Development of an index for monitoring and prediction. *Mon. Wea. Rev.*, **132**, 1917–1932, https://doi.org/10.1175/1520-0493(2004)132<1917:AARMMI>2.0.CO;2.

WHO, 2002: Global solar UV index: A practical guide. World Health Organization, 28 pp., www.who.int/uv/publications/en/GlobalUVI.pdf.

Walker, C. C., M. K. Becker, and H. A. Fricker, 2021: A high resolution, three-dimensional view of the D-28 calving event from Amery Ice Shelf with ICESat-2 and satellite imagery. *Geophy. Res. Lett.*, **48**, https://doi.org/https://doi.org/10.1029/2020GL091200.

Wiese, D. N., D.-N. Yuan, C. Boening, F. W. Landerer, and M. M. Watkins, 2019: JPL GRACE Mascon Ocean, Ice, and Hydrology Equivalent Water Height RL06 CRI Filtered Version 02, version 2. PO.DAAC, accessed 20 February 2021, https://doi.org/10.5067/TEMSC-3JC62.

Wille, J. D., V. Favier, A. Dufour, I. V. Gorodetskaya, J. Turner, C. Agosta, and F. Codron, 2019: West Antarctic surface melt triggered by atmospheric rivers. *Nat. Geosci.*, **12**, 911–916, https://doi.org/10.1038/s41561-019-0460-1.

Yuan, X., 2004: ENSO-related impacts on Antarctic sea ice: A synthesis of phenomenon and mechanisms. *Antarct. Sci.*, **16**, 415–425, https://doi.org/10.1017/S0954102004002238.

——, M. R. Kaplan, and M. A. Cane, 2018: The interconnected global climate system-a review of tropical-polar teleconnections. *J. Climate*, **31**, 5765–5792, https://doi.org/10.1175/JCLI-D-16-0637.1.

Zwally, H. J., and S. Fiegles, 1994: Extent and duration of Antarctic surface melting. *J. Glaciol.*, **40**, 463–475, https://doi.org/10.3189/S0022143000012338.

STATE OF THE CLIMATE IN 2020

7. REGIONAL CLIMATES

P. Bissolli, C. Ganter, T. Li, A. Mekonnen, and A. Sánchez-Lugo, Eds.

Special Online Supplement to the *Bulletin of the American Meteorological Society* Vol.102, No. 8, August, 2021

https://doi.org/10.1175/2021BAMSStateoftheClimate_Chapter7.1
Corresponding authors:
North America: Ahira Sánchez-Lugo / Ahira.Sanchez-Lugo@noaa.gov.
Central America and the Caribbean: Ahira Sánchez-Lugo / Ahira.Sanchez-Lugo@noaa.gov
South America: Ahira Sánchez-Lugo / Ahira.Sanchez-Lugo@noaa.gov
Africa: Ademe Mekonnen / amekonne@ncat.edu
Europe: Peter Bissolli / Peter.Bissolli@dwd.de
Asia: Tim Li / timli@hawaii.edu
Oceania: Catherine Ganter / Catherine.Ganter@bom.gov.au

STATE OF THE CLIMATE IN 2020
Regional Climates

Editors

Jessica Blunden
Tim Boyer

Chapter Editors

Freya Aldred
Peter Bissolli
Howard J. Diamond
Matthew L. Druckenmiller
Robert J. H. Dunn
Catherine Ganter
Nadine Gobron
Gregory C. Johnson
Rick Lumpkin
Tim Li
Ademe Mekonnen
John B. Miller
Twila A. Moon
Ahira Sánchez-Lugo
Ted A. Scambos
Carl J. Schreck III
Sharon Stammerjohn
Richard L. Thoman
Kate M. Willett

Technical Editor

Andrea Andersen

***BAMS* Special Editor for Climate**

Michael A. Alexander

American Meteorological Society

Cover credit:
Rights Managed Photo by STR/AFP via ©Getty Images
Flooded buildings are seen in Nanjing, in China's eastern Jiangsu province on 19 July 2020.
Vast swaths of China were inundated by the worst flooding in decades along the Yangtze River.

Regional Climates is one chapter from the *State of the Climate in 2020* annual report. Compiled by NOAA's National Centers for Environmental Information, *State of the Climate in 2020* is based on contributions from scientists from around the world. It provides a detailed update on global climate indicators, notable weather events, and other data collected by environmental monitoring stations and instruments located on land, water, ice, and in space. The full report is available from https://doi.org/10.1175/2021BAMSStateoftheClimate.1.

How to cite this document:

Citing the complete report:
Blunden, J. and T. Boyer, Eds., 2021: "State of the Climate in 2020". *Bull. Amer. Meteor. Soc*, **102** (8), Si–S475, https://doi.org/10.1175/2021BAMSStateoftheClimate.1

Citing this chapter:
Bissolli, P., C. Ganter, T. Li, A. Mekonnen, and A. Sánchez-Lugo, Eds., 2021: Regional Climates [in "State of the Climate in 2020"]. *Bull. Amer. Meteor. Soc.*, **102** (8), S357–S463, https://doi.org/10.1175/2021BAMSStateoftheClimate_Chapter7.1.

Citing a section (example):
Thiaw, W. M., P.-H. Kamsu-Tamo, M. F. Zaheer, and B. Pugh, 2021: Central Asia [in "State of the Climate in 2020"]. *Bull. Amer. Meteor. Soc.*, **102** (8), S441–S445, https://doi.org/10.1175/2021BAMSStateoftheClimate_Chapter7.1

Editor and Author Affiliations (alphabetical by name)

Alfaro, Eric J., Center for Geophysical Research and School of Physics, University of Costa Rica, San José, Costa Rica
Alves, Lincoln M., Centro de Ciencia do Sistema Terrestre/Instituto Nacional de Pesquisas Espaciais, Sao Paulo, Brazil
Amador, Jorge A., Center for Geophysical Research and School of Physics, University of Costa Rica, San José, Costa Rica
Andrade, B., Seychelles Meteorological Authority, Mahe, Seychelles
Argeñalso, Francisco, Centro Nacional de Estudios Atmosféricos, Oceanográficos y Sísmicos, Tegucigalpa, Honduras
Asgarzadeh, P., National Center for Climate and Drought Crisis Management, Islamic Republic of Iranian Meteorological Organization, Iran
Baez, Julian, Universidad Católica Nuestra Senora de la Asunción, Asunción, Paraguay
Barakiza, Reuben, Burundi Hydrometeorological Department, Bujumbura, Burundi
Bardin, M. Yu., Yu. A. Izrael Institute of Global Climate and Ecology; Institute of Geography, Russian Academy of Sciences, Russia
Bardin, Mikhail, Institute of Global Climate and Ecology, Moscow, Russia
Bissolli, Peter, Deutscher Wetterdienst, WMO RA VI Regional Climate Centre Network, Offenbach, Germany
Bochníček, Oliver, Slovak Hydrometeorological Institute, Slovakia
Bukunt, Brandon, NOAA/NWS Weather Forecast Office, Guam
Calderón, Blanca, Center for Geophysical Research, University of Costa Rica, San José, Costa Rica
Campbell, Jayaka D., Department of Physics, The University of the West Indies, Jamaica
Chandler, Elise, Bureau of Meteorology, Melbourne, Victoria, Australia
Chang'a, Ladislaus, Tanzania Meteorological Authority, Dar es Salaam, Tanzania
Cheng, Vincent Y. S., Environment and Climate Change Canada, Toronto, Ontario, Canada
Clarke, Leonardo A., Department of Physics, The University of the West Indies, Jamaica
Correa, Kris, Servicio Nacional de Meteorología e Hidrología del Perú, Lima, Perú
Cortés, Catalina, Dirección de Meteorológica de Chile, Santiago de Chile, Chile
Costa, Felipe, International Centre for Research on El Niño, Guayaqui, Ecuador
Cunha, A.P.M.A., Centro Nacional de Monitoramento e Alertas de Desastres Naturais CEMADEN, Sao Paulo, Brazil
Demircan, Mesut, Turkish State Meteorological Service, Ankara, Turkey
Dhurmea, K. R., Mauritius Meteorological Service, Vacoas, Mauritius
Diawara, A., NOAA/NWS National Centers for Environmental Prediction, Climate Prediction Center, College Park, Maryland
Diouf, Sarah, NOAA/NWS National Centers for Environmental Prediction, Climate Prediction Center, College Park, Maryland
Dulamsuren, Dashkhuu, Climate change and resource research section, Information and Research, Institute of Meteorology, Hydrology and Environment, National Agency for Meteorology, Hydrology and Environmental Monitoring, Ulaanbaatar, Mongolia
ElKharrim, M., Direction de la Météorologie Nationale Maroc, Rabat, Morocco
Espinoza, Jhan-Carlo, Université Grenoble Alpes, Institut des Géosciences de l'Environnement, IRD, CNRS, Grenoble INP, Grenoble, France
Fazl-Kazem, A., National Center for Drought Monitoring and Crisis Management, Islamic Republic of Iranian Meteorological Organization, Iran
Fenimore, Chris, NOAA/NESDIS National Centers for Environmental Information, Asheville, North Carolina
Fuhrman, Steven, NOAA/NWS National Centers for Environmental Prediction, Climate Prediction Center, College Park, Maryland
Ganter, Catherine, Bureau of Meteorology, Melbourne, Victoria, Australia
Gleason, Karin, NOAA/NESDIS National Centers for Environmental Information, Asheville, North Carolina
Guard, Charles "Chip" P., Tropical Weather Sciences, Sinajana, Guam
Hagos, Samson, Pacific Northwest National Laboratory, Department of Energy, Richland, Washington
Hanafusa, Mizuki, Tokyo Climate Center, Japan Meteorological Agency, Japan
Hasannezhad, H. R., National Center for Climate and Drought Crisis Management, Islamic Republic of Iranian Meteorological Organization, Iran
Heim, Jr., Richard R., NOAA/NESDIS National Centers for Environmental Information, Asheville, North Carolina
Hidalgo, Hugo G., Center for Geophysical Research and School of Physics, University of Costa Rica, San José, Costa Rica
Ijampy, J. A., Nigerian Meteorological Agency, Abuja, Nigeria
Im, Gyo Soon, Climate Change Monitoring Division, Korea Meteorological Administration, South Korea
Joseph, Annie C., Dominica Meteorological Service, Canefield, Dominica
Jumaux, G., Météo France, Direction Interrégionale pour l'Océan Indien, Réunion
Kabidi, K. R., Direction de la Météorologie Nationale Maroc, Rabat, Morocco
Kamsu-Tamo, P-H., NOAA/NWS National Centers for Environmental Prediction, Climate Prediction Center, College Park, Maryland
Kennedy, John, Met Office Hadley Centre, Exeter, United Kingdom
Khan, Valentina, Hydrometeorological Research Center of the Russian Federation/A.M. Obukhov Institute of Atmospheric Physics, Russian Academy of Sciences, Moscow, Russia
Khiem, Mai Van, Viet Nam National Center of Hydro-Meteorology Forecasting, Viet Nam Meteorology Hydrology Administration, Viet Nam
King'uza, Philemon, Tanzania Meteorological Authority, Dar es Salaam, Tanzania
Korshunova, Natalia N., All-Russian Research Institute of Hydrometeorological Information - World Data Center, Obninsk, Russia
Kruger, A. C., Climate Service, South African Weather Service, Pretoria, South Africa Lakatos, Mónika, Climatology Unit, Hungarian Meteorological Service, Budapest, Hungary
Lam, Hoang Phuc, Viet Nam National Center of Hydro-Meteorology Forecasting, Viet Nam Meteorology Hydrology Administration, Viet Nam
Lander, Mark A., University of Guam, Mangilao, Guam
Lavado-Casimiro, Waldo, Servicio Nacional de Meteorología e Hidrología del Perú, Lima, Perú
Lee, Tsz-Cheung, Hong Kong Observatory, Hong Kong, China
Leung, Kinson H. Y., Environment and Climate Change Canada, Toronto, Ontario, Canada
Li, Tim, Department of Atmospheric Sciences, University of Hawaii, Honolulu, Hawaii, USA
Macara, Gregor, National Institute of Water and Atmospheric Research, Ltd., Auckland, New Zealand
Mamen, Jostein, Climate Division, Norwegian Meteorological Institute, Oslo, Norway
Marengo, José A., Centro Nacional de Monitoramento e Alertas de Desastres Naturais CEMADEN, Sao Paulo, Brazil
McBride, Charlotte, Climate Service, South African Weather Service, Pretoria, South Africa
Mekonnen, Ademe, Department of Physics, North Carolina A & T University, Greensboro, North Carolina
Misevicius, Noelia, Instituto Uruguayo de Meteorología, Montevideo, Uruguay
Moise, Aurel, Centre for Climate Research Singapore, Meteorological Service, Singapore

Editor and Author Affiliations (alphabetical by name)

Molina-Carpio, Jorge, Universidad Mayor de San Andrés, La Paz, Bolivia
Mora, Natali, Center for Geophysical Research, University of Costa Rica, San José, Costa Rica
Mostafa, Awatif E., Department of Seasonal Forecast and Climate Research, Cairo Numerical Weather Prediction, Egyptian Meteorological Authority, Cairo, Egypt
Mtongori, Habiba, Tanzania Meteorological Authority, Dar es Salaam, Tanzania
Mutai, Charles, Kenya Meteorological Department, Nairobi, Kenya
Ndiaye, O., Senegalese Meteorological Service, Dakar, Senegal
Nieto, Juan José, International Centre for Research on El Niño, Guayaqui, Ecuador
Nyembo, Latifa, Tanzania Meteorological Authority, Dar es Salaam, Tanzania
Nying'uro, Patricia, Kenya Meteorological Department, Nairobi, Kenya
Pan, Xiao, Nanjing University of Information Science and Technology, China
Pascual Ramírez, Reynaldo, National Meteorological Service of Mexico, Mexico City, Mexico
Phillips, David, Environment and Climate Change Canada, Toronto, Ontario, Canada
Pugh, Brad, NOAA/NWS National Centers for Environmental Prediction, Climate Prediction Center, College Park, Maryland
Rajeevan, Madhavan, Earth System Science Organization, Ministry of Earth Sciences, New Delhi, India
Rakotonirina, M. L., Madagascar Meteorological Service, Madagascar
Ramos, Andrea M., Instituto Nacional de Meteorologia, Brasilia, Brazil
Robjhon, M., NOAA/NWS National Centers for Environmental Prediction, Climate Prediction Center, College Park, Maryland
Rodriguez Camino, Ernesto, Agencia Estatal de Meteorología, Madrid, Spain
Rodriguez Guisado, Esteban, Agencia Estatal de Meteorología, Madrid, Spain
Ronchail, Josyane, Laboratoire LOCEAN-IPSL, Paris, France
Rösner, Benjamin, Laboratory for Climatology and Remote Sensing, Faculty of Geography, University of Marburg, Marburg, Germany
Salinas, Roberto, Dirección de Meteorología e Hidrología/Dirección Nacional de Aeronáutica Civil, Asunción, Paraguay
Sánchez-Lugo, Ahira, NOAA/NESDIS National Centers for Environmental Information, Asheville, North Carolina
Sato, Hirotaka, Tokyo Climate Center, Japan Meteorological Agency, Japan
Sato, Hitoshi, Tokyo Climate Center, Japan Meteorological Agency, Japan
Sayouri, Amal, Direction de la Météorologie Nationale Maroc, Rabat, Morocco
Sebaziga, Joseph, Rwanda Meteorology Agency, Kigali, Rwanda
Sensoy, Serhat, Turkish State Meteorological Service, Ankara, Turkey
Spillane, Sandra, Met Éireann, Dublin, Ireland
Trachte, Katja, Brandenburg University of Technology, Cottbus, Germany
van der Schrier, Gerard, Royal Netherlands Meteorological Institute, De Bilt, Netherlands
Sima, F., Division of Meteorology, Department of Water Resources, Banjul, The Gambia
Smith, Adam, NOAA/NESDIS National Centers for Environmental Information, Asheville, North Carolina
Spence, Jacqueline M., Meteorological Service, Jamaica, Kingston, Jamaica
Sreejith, O. P., India Meteorological Department, Pune, India
Srivastava, A. K., India Meteorological Department, Pune, India
Stella, José L., Servicio Meteorológico Nacional, Buenos Aires, Argentina
Stephenson, Kimberly A., Department of Life Sciences, The University of the West Indies, Jamaica
Stephenson, Tannecia S., Department of Physics, The University of the West Indies, Jamaica
Supari, S., Division for Climate Variability Analysis, Center for Climate Change Information, BMKG, Indonesia
Tajbakhsh-Mosalman, Sahar, Islamic Republic of Iranian Meteorological Organization, Iran
Tamar, Gerard, Grenada Meteorological Office, St. George, Grenada
Taylor, Michael A., Department of Physics, The University of the West Indies, Jamaica
Teshome, Asaminew, Ethiopia Meteorological Agency, Addis Ababa, Ethiopia
Thiaw, Wassila M., NOAA/NWS National Centers for Environmental Prediction, Climate Prediction Center, College Park, Maryland
Tobin, Skie, Bureau of Meteorology, Melbourne, Victoria, Australia
Trotman, Adrian R., Caribbean Institute for Meteorology and Hydrology, Bridgetown, Barbados
Van Meerbeeck, Cedric J., Caribbean Institute for Meteorology and Hydrology, Bridgetown, Barbados
Vazifeh, A., National Center for Drought Monitoring and Crisis Management, Islamic Republic of Iranian Meteorological Organization, Iran
Wakamatsu, Shunya, Tokyo Climate Center, Japan Meteorological Agency, Japan
Wang, Wei, Minhang Meteorological Bureau, Shanghai, China
Xin, Fei, Shanghai Climate Center, Shanghai, China
Zeng, F., Pacific Northwest National Laboratory, Department of Energy, Richland, Washington
Zhang, Peiqun, Beijing Climate Center, Beijing, China
Zhu, Zhiwei, Nanjing University of Information Science and Technology, China

Editorial and Production Team

Allen, Jessicca, Graphics Support, Cooperative Institute for Satellite Earth System Studies, North Carolina State University, Asheville, North Carolina
Andersen, Andrea, Technical Editor, Innovative Consulting Management Services, LLC, NOAA/NESDIS National Centers for Environmental Information, Asheville, North Carolina
Hammer, Gregory, Content Team Lead, Communications and Outreach, NOAA/NESDIS National Centers for Environmental Information, Asheville, North Carolina
Love-Brotak, S. Elizabeth, Lead Graphics Production, NOAA/NESDIS National Centers for Environmental Information, Asheville, North Carolina
Misch, Deborah J., Graphics Support, Innovative Consulting Management Services, LLC, NOAA/NESDIS National Centers for Environmental Information, Asheville, North Carolina
Riddle, Deborah B., Graphics Support, NOAA/NESDIS National Centers for Environmental Information, Asheville, North Carolina
Veasey, Sara W., Visual Communications Team Lead, Communications and Outreach, NOAA/NESDIS National Centers for Environmental Information, Asheville, North Carolina

7. Table of Contents

7. Table of Contents

*Please refer to Chapter 8 (Relevant datasets and sources) for a list of all climate variables and datasets used in this chapter for analyses, along with their websites for more information and access to the data.

7. REGIONAL CLIMATES

P. Bissolli, C. Ganter, T. Li, A. Mekonnen, and A. Sánchez-Lugo, Eds.

a. Overview

This chapter provides summaries of the 2020 temperature and precipitation conditions across seven broad regions: North America, Central America and the Caribbean, South America, Africa, Europe and the Middle East, Asia, and Oceania. In most cases, summaries of notable weather events are also included. Local scientists provided the annual summary for their respective regions and, unless otherwise noted, the source of the data used is typically the agency affiliated with the authors. The primary base period used for these analyses is 1981–2010. However, please note that on occasion different nations, even within the same section, may use unique periods to define their normals. Section introductions typically define the prevailing practices for that section, and exceptions will be noted within the text. Similarly, many contributing authors use languages other than English as their primary professional language. To minimize additional loss of fidelity through re-interpretation after translation, editors have been conservative and careful to preserve the voice of the author. In some cases, this may result in abrupt transitions in style from section to section.

b. North America—A. Sánchez-Lugo, Ed.

1) Canada—K. H. Y. Leung, V. Y. S. Cheng, and D. Phillips

In Canada, 2020 was characterized by a warmer-than-average winter in most of southern Canada and southern Nunavut and by a cooler-than-average spring in most of Canada, with the exception of the northern parts of Yukon, Northwest Territories, and Nunavut. The country also experienced a warmer-than-average summer over most of Nunavut and eastern Canada and a warmer-than-average autumn in northern Nunavut. Autumn was cooler than-average across most of western and southern parts of northern Canada.

(I) TEMPERATURE

The 2020 annual average temperature for Canada was 0.3°C above the 1981–2010 average and the 14th-warmest year since nationwide records began in 1948 (Fig. 7.1). Four of the 10 warmest years have occurred during the last decade, with 2010 the warmest year on record (2.2°C above average). The national annual average temperature record has increased 1.8°C over the past 73 years. Spatially, annual anomalies above +0.5°C were recorded in far northern and parts of eastern Canada. Annual anomalies below −0.5°C were observed mainly in the southern areas of Yukon, Northwest

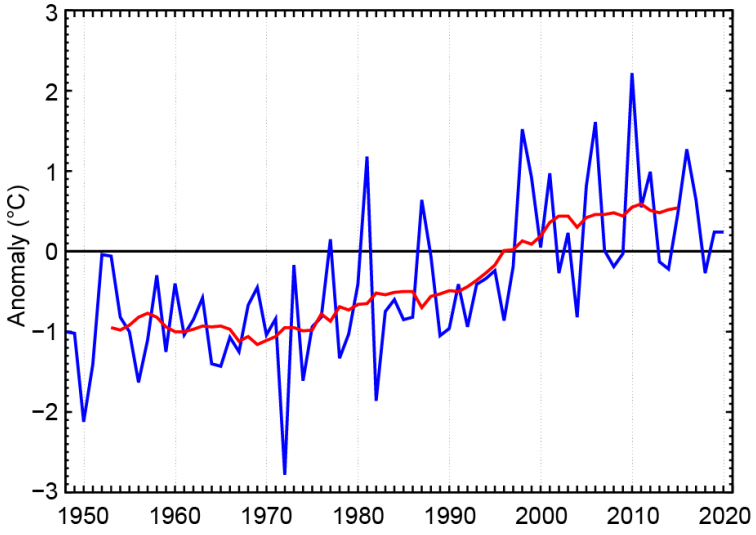

Fig. 7.1. Annual average temperature anomalies (°C; 1981–2010 base period) in Canada for 1948–2020. Red line is the 11-year running mean. (Source: Environment and Climate Change Canada.)

Territories, Nunavut, interior British Columbia, and the Prairie regions (Fig. 7.2). Four provinces/territories (Nova Scotia, New Brunswick, Prince Edward Island, and Quebec) recorded an average annual temperature among their 10 warmest on record.

Seasonally, the nationally averaged winter (December–February) 2019/20 temperature was 0.7°C above average—the 17th-warmest winter on record. Winter anomalies more than 2.0°C above average were recorded over Ontario, Manitoba, most of Saskatchewan, parts of southern Nunavut, and western Quebec. Ontario and Manitoba reported their seventh- and eighth-warmest winters on record, respectively. The majority of Yukon and Northwest Territories, and some areas in the northern parts of Nunavut and Newfoundland experienced below-average winter temperatures. The national average temperature for the winter season has increased by 3.3°C over the past 73 years, the most of any season.

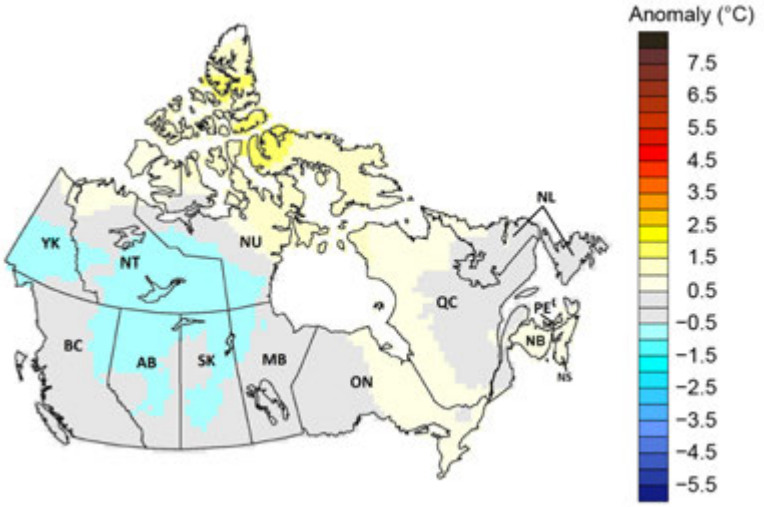

Fig. 7.2. Annual average temperature anomalies (°C; 1981–2010 base period) in Canada for 2020. (Source: Environment and Climate Change Canada.)

The national average temperature for spring (March–May) 2020 was 0.7°C below average and the 31st lowest in the 73-year record. Below-average temperatures were recorded over most of Canada, with temperatures anomalies of –3.0°C observed in the northern Prairies region. Above-average conditions were observed only over parts of northern Canada, with departures from average more than +1.5°C in some areas. No province or territory experienced an average spring temperature among its 10 highest or lowest. The national average spring temperature has increased by 1.6°C over the past 73 years.

The national average summer (June–August) temperature was 0.6°C above average and the sixth highest since 1948. Central Nunavut and northern Quebec experienced anomalies more than +1.5°C, with Nunavut, New Brunswick, and Prince Edward Island all observing their fifth-warmest summer on record. Other provinces also had an average summer temperature among their 10 warmest: Ontario (sixth warmest), Quebec (seventh warmest), Nova Scotia (seventh warmest), and Newfoundland (ninth warmest). Areas from the interior of British Columbia to southern Yukon and Northwest Territories, along with a small region in southern Saskatchewan, experienced below-average summer temperatures. The national average summer temperature has increased by 1.5°C over the past 73 years.

The national average temperature for autumn (September–November) 2020 was 0.1°C above average and the 36th warmest since 1948. Temperatures anomalies above +2.5°C were observed across northern Nunavut. Autumn anomalies of –1°C or below were reported in southern areas of Yukon, Northwest Territories, and Nunavut, and most of the prairies provinces to northwestern Ontario. The national autumn temperature has increased by 1.6°C over the past 73 years.

(II) PRECIPITATION

Over the past decade, precipitation monitoring technology has evolved, and Environment and Climate Change Canada (ECCC) and its partners implemented a transition from manual observations to the use of automatic precipitation gauges. Extensive data integration is required to link the current precipitation observations to the long-term historical manual observations. The update and reporting of historical adjusted precipitation trends and variations will be on temporary hiatus pending an extensive data reconciliation and resumed thereafter. ECCC remains committed

to providing credible climate data to inform adaptation decision making, while ensuring the necessary data reconciliation occurs as monitoring technology evolves.

(III) NOTABLE EVENTS AND IMPACTS

On 16 January, a deep low-pressure system situated over western New York tracked through the northeastern United States to Newfoundland's Avalon Peninsula (a normal track for a mid-winter storm). As the storm deepened and strengthened, its central pressure dropped more than 54 hPa in 48 hours. Intense snow began falling early on 17 January, and blizzard conditions prevailed for 18 straight hours, with visibility decreasing to 200 m or less. The historical daily snowfall record was broken at St. John's International Airport, with over 75 cm recorded. Nearby, Mount Pearl and Paradise, Newfoundland, reported 90 cm of snow over a 28-hour period. An average snowfall intensity of 10 cm per hour was also recorded in St. John's and the surrounding regions. The last time St. John's experienced close to 75 cm of snowfall in a single day was in April 1999. Wind speeds during the blizzard reached hurricane force at 160 km h^{-1} along the coast and 125 km h^{-1} at St. John's International Airport. The deep low and strong winds also generated a significant storm surge with a wave height of 8.7 m on 18 January, damaging docks and boats. This storm contributed to the snowiest January on record for St. John's.

On 13 June, warm and humid air over Alberta generated multiple rounds of severe thunderstorm cells. With colliding winds at various heights over southern Alberta, the wind shear helped fuel large, long-lived thunderstorms. That same day, a severe thunderstorm cell with a hail core passed over northeastern Calgary, producing tennis-ball size hail and wind speeds up to 70 km h^{-1} (~20 m s^{-1}). The violent hailstorm shook houses, broke windows, damaged vehicles, and downed trees, which led to power outages to more than 10,000 customers and hail almost 10 cm deep piled up along roads. The damage incurred from this storm was Canada's costliest and the fourth-most expensive insured natural disaster in Canadian history, with Canadian insurers estimating at about $1.3 billion (Canadian dollars; $1 billion [U.S. dollars]) in losses. This value excludes crop losses.

On 2 August, the warm front of a low-pressure system brought significant tropical-sourced moisture (50–70 mm) eastward from Windsor to the Greater Toronto Area and Niagara region and along the north shore of Lake Ontario. Rainfall in the city of Barrie totaled between 80–90 mm, its highest August 1-day rainfall total on record and highest 1-day total for any month in the past 25 years. The same storm system also spawned four tornadoes with winds estimated between 130 and 190 km h^{-1} (EF-0 to EF-2 on the Enhanced Fujita Scale) in southern Ontario.

During 6–7 August, a low-pressure system from Alberta moved eastward toward Manitoba and generated many severe thunderstorm cells that produced large hail, powerful winds, and torrential downpours. On 7 August, an EF-3 tornado touched down near Scarth in western Manitoba, 13 km south of Virden. Wind speeds associated with the deadly tornado exceeded 200 km h^{-1} for between 10–15 minutes and reached wind speeds estimated as high as 260 km h^{-1}. The tornado left a 9-km long path of destruction and caused two fatalities.

2) United States—K. Gleason, C. Fenimore, R. R. Heim Jr., and A. Smith

The annual average temperature for the contiguous United States (CONUS) in 2020 was 12.4°C, which was 0.9°C above the 1981–2010 average and was the fifth-warmest year in the 126-year record, with the five warmest years all occurring since 2012 (Fig. 7.3a). Much of the country experienced temperature anomalies at least +1°C or more above average (Fig. 7.4a). Exceptions to this warmth occurred across parts of the Plains, Midwest, and Northwest. Based on a linear regression of data from 1895 to 2020, the annual CONUS temperature over the 126-year record is increasing at an average rate of 0.09°C $decade^{-1}$ (0.27°C $decade^{-1}$ since 1970). Across Alaska, the average annual temperature in 2020 was 0.11°C above average and was the coldest year since 2012.

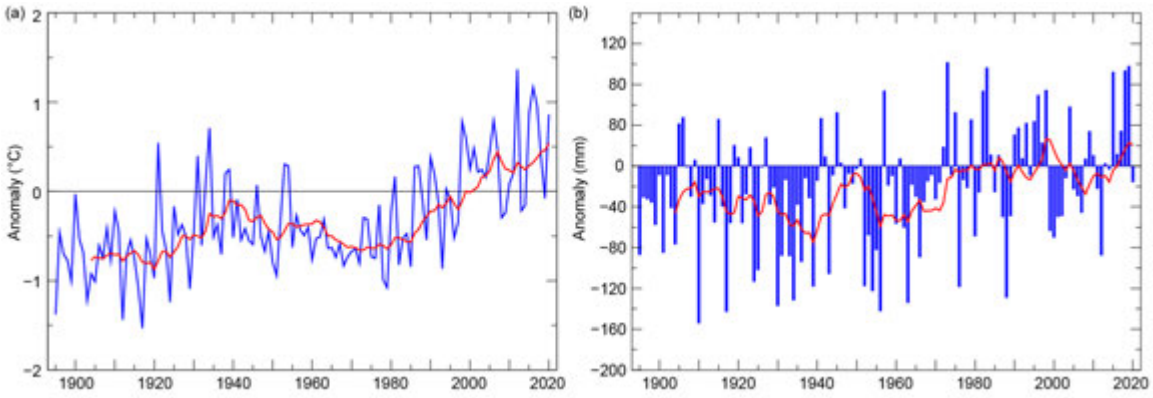

Fig. 7.3. Annual (a) mean temperature anomalies (°C) and (b) precipitation anomalies (mm) for the CONUS during 1895–2020 (1981–2010 base period). Red line is the lagged 10-year running mean. (Source: NOAA/NCEI.)

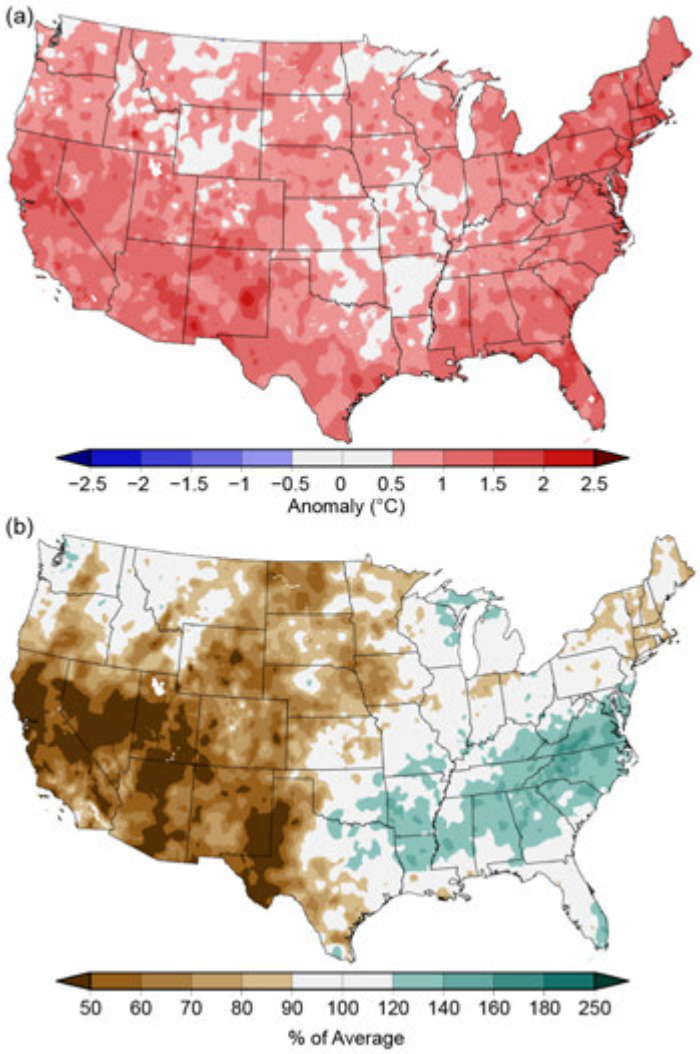

Fig. 7.4. Annual (a) average temperature anomalies (°C) and (b) total precipitation (% of average) in the CONUS for 2020 (1981–2010 base period). (Source: NOAA/NCEI.)

The annual temperature for Alaska over the 96-year record is increasing at an average rate of 0.17°C decade^{-1} (0.50°C decade^{-1} since 1970).

Average precipitation across the CONUS totaled 769 mm, which was 98% of the 1981–2010 average (Fig. 7.3b). Overall, the annual precipitation total has been increasing at an average rate of 5 mm decade^{-1} (4 mm decade^{-1} since 1970).

(l) TEMPERATURE

The winter (December–February) 2019/20 CONUS temperature was 1.4°C above average and was sixth warmest on record. Above-average warmth was present from coast-to-coast with near-record temperatures observed from portions of the Ohio Valley to New England. The CONUS spring (March–May) temperature was 0.5°C above average, ranking in the highest third of the record. Above-average temperatures were observed across the West, South, Great Lakes, and along the East Coast, with Florida experiencing its second-warmest spring on record. Near-average spring temperatures spanned from the Northern Rockies and Plains to the Tennessee Valley, with pockets of below-average temperatures observed across portions of the northern tier. The summer (June–August) CONUS temperature was 0.9°C above average, the fourth highest in the 126-year record. Arizona in the West and Connecticut, Massachusetts, and Rhode Island in the East each had their warmest summer on record. Below-average temperatures were observed in portions of the lower Mississippi Valley. The autumn (September–November) CONUS temperature was 0.8°C above average, the 11th warmest on record. Above-average temperatures were present across much of the western, southern, and eastern United States. California and Arizona in the West and Florida in the Southeast were each

record warm. The central United States experienced near-average temperatures with small areas of below-average temperatures spread through the regions.

(II) PRECIPITATION

The primary weather pattern for 2020 can be characterized by a ridge of high pressure that dominated the western United States and a trough of low pressure across the East. This pattern brought warm, dry air to much of the West throughout the year, while an active storm track impacted the weather from the lower Mississippi Valley to the Mid-Atlantic. North Carolina and Virginia had their second- and third-wettest year on record, respectively. Conversely, Nevada and Utah each had their driest year on record, with five other western states ranking 2020 among their five driest years (Fig. 7.4b). The absence of the North American Monsoon during 2020 contributed to the lack of precipitation received across the western United States.

Winter precipitation across the CONUS was 114% of average and ranked in the wettest third of the historical record. Above-average precipitation fell across much of the Great Lakes, central Plains, and Southeast. Precipitation totals across Alabama and Georgia were second highest on record during this three-month period. Below-average precipitation occurred across parts of the West, Gulf Coast, northern Rockies, and Plains. Spring 2020 precipitation was 105% of average and ranked in the wettest third of the record. Above-average precipitation occurred across portions of the West Coast, Southern Plains, Great Lakes, Ohio Valley, and Southeast. Precipitation was below average across parts of the Pacific Northwest, central Rockies, and northern Plains. Summer precipitation was 95% of average across the CONUS, with above-average wetness occurring across the Great Lakes, the middle and lower Mississippi River Valley, and the Mid-Atlantic. Conditions were dry across much of the West, Central Plains, and Northeast. Precipitation totals for Arizona and New Mexico were the lowest and second lowest on record, respectively. The autumn CONUS precipitation total was 87% of average. Above-average precipitation extended from the Gulf of Mexico into the Mid-Atlantic and across parts of the Deep South, Great Lakes, and Northwest. Drier-than-average conditions were present across much of the West, Northern and Central Plains, as well as parts of the Northeast. Precipitation across Arizona was record low for the autumn season, while in Virginia it was fourth lowest.

As 2020 progressed, both the CONUS drought footprint and intensity steadily grew. Minimum drought coverage for the year was 9.6% in mid-February, and the maximum extent was nearly 50% near the end of December. Drought early in the year was primarily confined to portions of the West and Texas. Over the first 3 months of the year, drought expanded across the West and also emerged in Florida. Above-average temperatures across the western United States exacerbated drought intensity and extent moving into the summer months. Flash drought, or the rapid onset of drought, developed across New England during the late summer and autumn as the region experienced below-average precipitation and record to near-record temperatures. At the peak of the drought coverage in December, more than 22% of the CONUS experienced extreme and exceptional drought—the two worst categories—from the West to the Northern Plains.

(III) NOTABLE EVENTS AND IMPACTS

There were 22 weather and climate events across the United States during 2020 with losses each exceeding $1 billion (U.S. dollars): seven tropical cyclone events, 13 severe storm events, one drought, and one major wildfire event (Fig. 7.5). This shatters the previous annual record of 16 events that occurred in both 2011 and 2017. The year's loss total of $95 billion (U.S. dollars) was the fourth-highest cost on record. The most costly events of the year include Hurricane Laura (see Sidebar 4.1 for details), the Western Wildfires, and the Midwest Derecho, which, together, accounted for nearly half of the U.S. cost total during 2020. The Western Wildfires consumed almost 4.2 million ha from California to Colorado and was the largest area consumed across the CONUS since at least 2000. The Midwest Derecho damaged infrastructure and crops from South

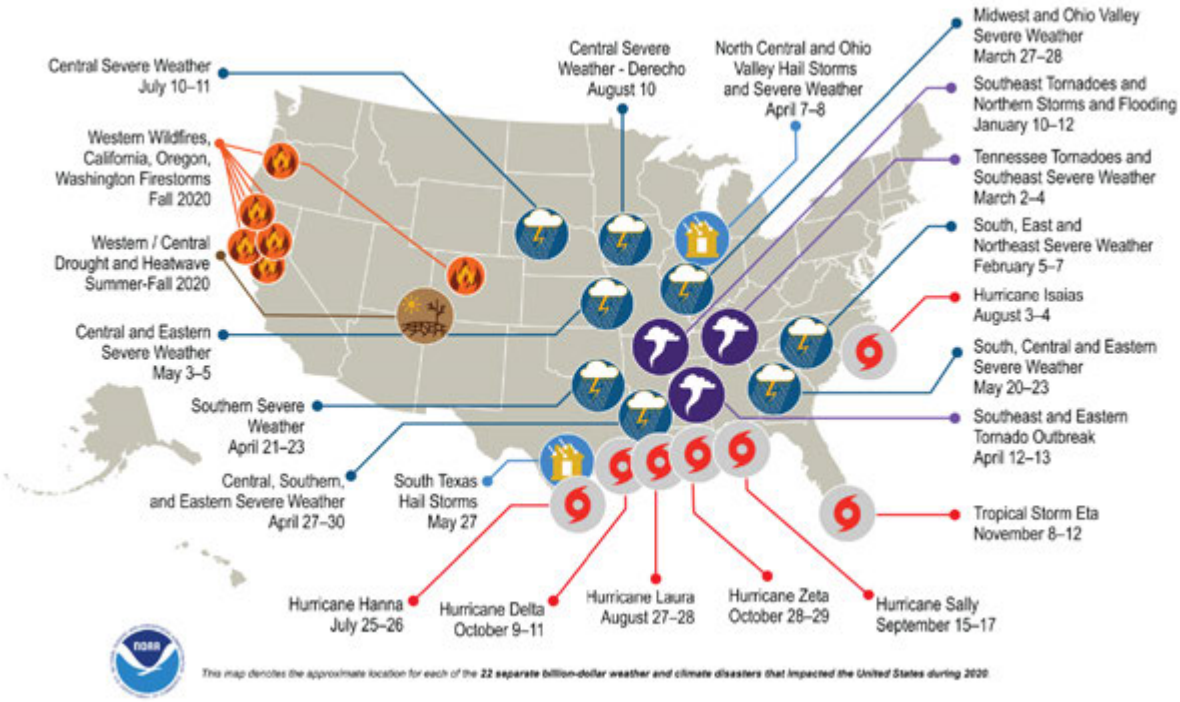

Fig. 7.5. Map depicting date, approximate location, and type of the 22 weather and climate disasters in the United States in 2020, with losses for each exceeding $1 billion (U.S. dollars). (Source: NOAA/NCEI.)

Dakota to Ohio with the most damage occurring across Iowa. The total cost of U.S. billion-dollar disasters over the last five years (2016–20) exceeds a record $600 billion (U.S. dollars; Smith 2020).

Record- to near-record sea surface temperatures across parts of the central Pacific Ocean contributed to the warmest year on record for both Kahului and Hilo, Hawaii, for 2020.

Preliminary reports for 2020 indicate that there were 1075 tornadoes across the CONUS. This was slightly below the 1991–2010 annual average of 1251 tornadoes. This included the 12–13 April tornado outbreak that produced 140 tornadoes from Texas to Maryland and 32 related fatalities. This was the deadliest tornado outbreak since April 2014.

3) Mexico—R. Pascual Ramírez

Temperatures across Mexico were above average during most of 2020, with the annual national mean temperature of 22.4°C tying with 2017 and 2019 as the warmest year on record. (Fig. 7.6). The 2020 precipitation total for Mexico was near average at 97% of normal. Most of the country, with the exception of the Yucatan Peninsula, the northeastern parts of the country, and the coast of Jalisco, had below-average rainfall for the year (Fig. 7.7b). Above-average precipitation on the Yucatan Peninsula was associated with tropical cyclones that impacted the region.

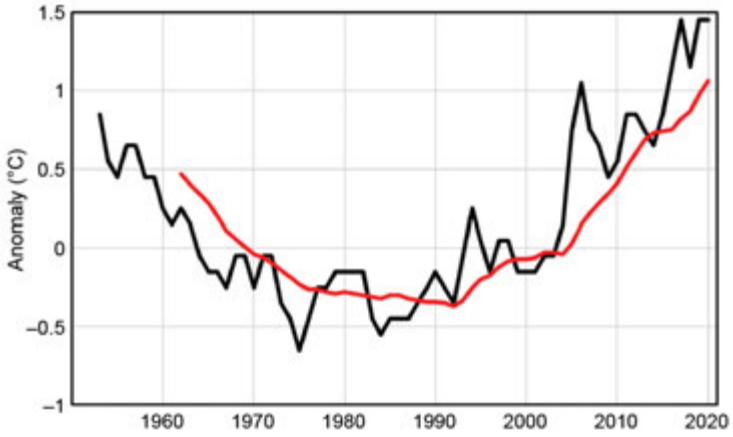

Fig. 7.6. Annual (a) mean temperature anomalies (°C, black line; 1981–2010 base period) and (b) precipitation anomalies for Mexico. Red line depicts the lagged 10-year running mean. (Source: National Meteorological Service for Mexico.)

(I) TEMPERATURE

The 2020 national mean temperature was 1.5°C above the 1981–2010 average (Fig. 7.6). In addition to tying with 2017 and 2019 for the warmest year since temperature records began in 1953, this marked the 16th consecutive year with the annual average temperature at least nominally above average. The months of January through November were all warmer than average, with

March, April, May, July, and November each record warm for their respective month. Seasonally, winter (January–March) ranked among the five warmest such periods on record. The summer period of July–September was the second warmest on record, behind 2019.

The 2020 mean temperature was above average across much of the country, with a few locations across the north, northwest, northern Baja California, and parts of the central and South Pacific that experienced below-average annual temperatures (Fig. 7.7a). Two states (Puebla and Yucatan) had their warmest year on record, and 10 had their second-warmest year on record. No state had a below-average annual temperature.

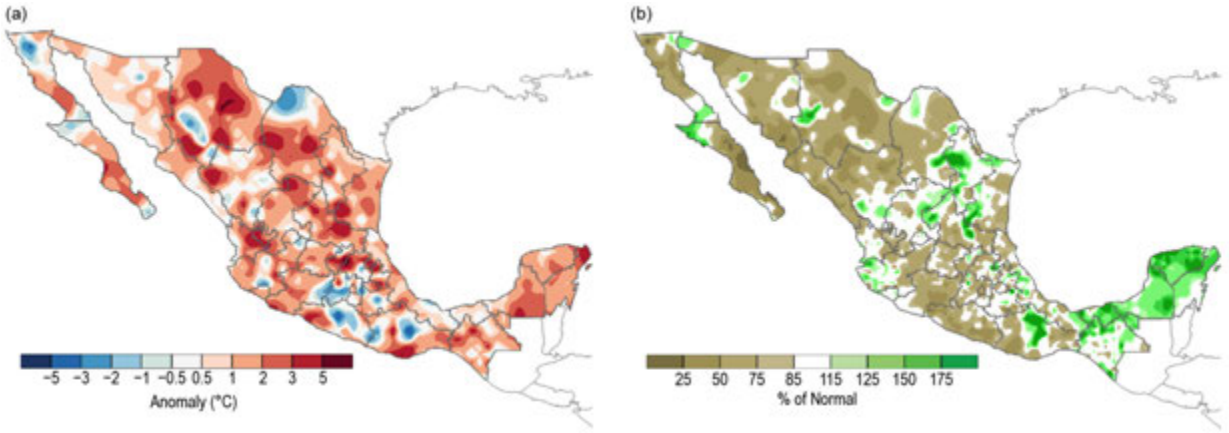

Fig. 7.7. 2020 annual mean (a) temperature anomalies (°C) and (b) precipitation anomalies (% of normal) over Mexico (1981–2010 base period). (Source: National Meteorological Service of Mexico.)

(II) PRECIPITATION

Rainfall distribution varied regionally (Fig. 7.7b), with above-normal precipitation across southern areas, especially notable in the Yucatan Peninsula where the state of Yucatan observed its wettest year on record. Other regions with above-average rainfall included the northeast, specifically in central Nuevo León and southwestern Tamaulipas, along with small areas across the central-west region. The rest of the country had below-average precipitation, with the greatest deficits in the north and northwest states and states along the South Pacific coast.

With no impact from tropical cyclones on the Mexican Pacific side and a late onset and weak North American Monsoon, dryness and drought conditions were a constant concern throughout the year for the northwest, central-west, and southern Pacific states. In contrast, southern states and the Yucatan Peninsula received beneficial rainfall between June and October from Tropical Storms Cristobal and Gamma, along with Hurricanes Hanna, Delta, and Zeta.

Climatologically, September is the rainiest month of the year, contributing 18.4% of the annual rainfall. September 2020 was indeed the rainiest month of the year, but contributed a slightly lesser percentage of the annual rainfall (17.7%). One reason for the below-average amount could be, as noted above, the lack of rainfall from reduced tropical cyclone activity near the country typically has occurred in September in past years. Climatologically, March is the driest month of the year, contributing 1.8% to the annual rainfall. However, in 2020, April, which typically contributes 2.5% of the annual rainfall, was the driest month of the year, contributing only 1.9% of the total annual rainfall.

(III) NOTABLE EVENTS AND IMPACTS

Five tropical cyclones affected Mexico during 2020, all from the Caribbean or the Atlantic basin (see section 4g2 for details), with no tropical cyclones affecting Mexico from the Pacific side (see section 4g3). Five storms is near the long-term average. In 2005, seven tropical cyclones affected the country—the highest number on record.

Tropical Storm Cristobal, the first tropical cyclone to affect the country during 2020, brought significant rainfall to southern Mexico and the Yucatan Peninsula, causing flooding over the Yucatan Peninsula during 1–4 June. Hurricane Hanna impacted northeastern Mexico on 26–27 July, and Tropical Storm Gamma and Hurricanes Delta and Zeta tracked over the Yucatan Peninsula in October (see section 4g2 for details).

Drought majorly impacted the northern states of Chihuahua and Sonora throughout the year. At the end of 2020, Mexico's federal government issued a Drought Disaster Declaration for both states. With the declaration, these states were given access to resources to mitigate their losses; most of the losses reported were on rain-fed crops and livestock.

c. Central America and the Caribbean—A. Sánchez-Lugo, Ed.

1) Central America—J. A. Amador, H. G. Hidalgo, E. J. Alfaro, B. Calderón, and N. Mora

For this region, nine stations from five countries were analyzed (see Fig. 7.8 for data and station list). The station distribution covers the relevant intraseasonal regimes of precipitation (Amador 1998; Magaña et al. 1999; Amador et al. 2016a,b), wind (Amador 2008), and temperature (Hidalgo et al. 2019) on the Caribbean and Pacific slopes of Central America (CA). Precipitation and temperature records for the stations analyzed and regional wind were provided either by CA National Weather Services (CA-NWS), NOAA, or the University of Costa Rica. Anomalies are reported using a 1981–2010 base period and were calculated using CA-NWS data. The methodologies used for all variables can be found in Amador et al. (2011).

(I) TEMPERATURE

The mean temperature (Tm) pentad frequency distributions in 2020, as well as the climatology, for the nine stations analyzed are shown in Fig. 7.8. During 2020, most stations had near- to cooler-than-normal conditions. The 2020 mean temperature for Liberia, Costa Rica (Tm7), was at least 3°C below average. Meanwhile, Puerto Barrios, Guatemala (Tm2), observed an annual temperature that was 2°C above average, the highest departure among the stations. Puerto Limón, Costa Rica (Tm4), had a below-average annual temperature with respect to its climatological normal, while Puerto San José, Guatemala (Tm9), observed an above-average temperature. Philip Goldson International Airport (Tm1) recorded slightly above-average annual temperature for 2020. A comparison between the climatology and the 2020 pentad distributions shows that seven of the nine stations presented different statistical distributions (exceptions were Puerto Lempira [Tm3] and David [Tm6]), suggesting that Tm was distributed significantly different from the climatology in 2020. Puerto Barrios (Tm2), Puerto Limón (Tm4), Tocumen International Airport (Tm5), Liberia (Tm7), Choluteca (Tm8), and Puerto San José (Tm9) showed significantly different means than climatology.

(II) PRECIPITATION

The accumulated pentad precipitation (P) time series for the nine stations in Central America are presented in Fig. 7.8. Puerto Barrios (P2), Puerto Lempira (P3), Puerto Limón (P4), and Tocumen International Airport (P5) showed different 2020 statistical distributions from that of the base period, while the remainder of the stations showed no significant differences from climatology. Puerto Limón observed drier-than-normal conditions during most of the year, while Liberia (P7) was wetter than normal (after pentad 60, approximately mid-October), ending the year with a rainfall surplus. These conditions in Liberia and Limón are consistent with a characteristic teleconnection pattern associated with La Niña, the cold phase of the El Niño–Southern Oscillation (ENSO; Hidalgo et al. 2019). General wet conditions were also registered in Puerto Barrios and Puerto Lempira after pentad 60. For Tocumen International Airport (P5) and David (P6), both in Panamá, precipitation totals were near normal. Puerto San José (P9) began the year with above-normal rainfall, but below-normal precipitation rates were registered around mid-September and

the year ended drier than normal. Philip Goldson International Airport (P1) and Choluteca (P8) showed the opposite pattern: the year began drier than average but increased precipitation rates around pentad 60 led to wetter-than-normal conditions by the end of 2020.

Low-level circulation anomalies in the westernmost Caribbean Sea and Pacific regions show slightly weaker winds in the trade wind system during July (vectors in Fig. 7.8), but the relationship of precipitation distribution associated with the emergence of La Niña during summer did not follow the normal pattern (Amador 2008). During a typical La Niña episode, below-normal winds are usually associated with slightly below-normal precipitation along the Caribbean slopes and above-normal precipitation on the Pacific slopes during summer. In 2020, only Puerto Limón showed that expected behavior with below-normal precipitation. The anomalously active hurricane season may be responsible for this anomaly (see Sidebar 7.1).

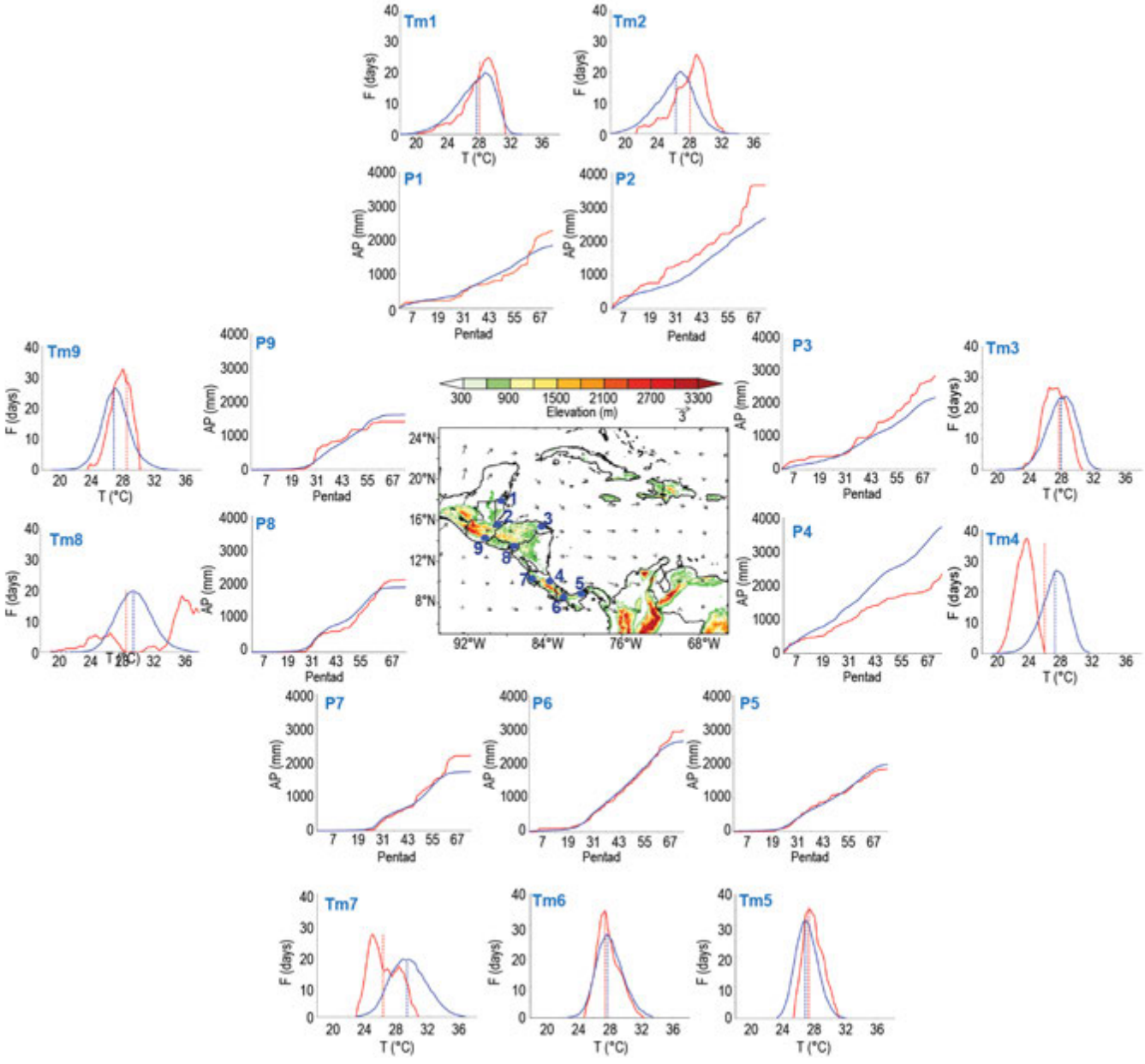

Fig. 7.8. Mean surface temperature (Tm; °C) frequency (F; days), and accumulated pentad precipitation (P; mm) time series are shown for nine stations (blue dots) in Central America: (1) Philip Goldson International Airport, Belize; (2) Puerto Barrios, Guatemala; (3) Puerto Lempira, Honduras; (4) Puerto Limón, Costa Rica; (5) Tocumen International Airport, Panamá; (6) David, Panamá; (7) Liberia, Costa Rica; (8) Choluteca, Honduras; and (9) Puerto San José, Guatemala. The blue solid line represents the 1981–2010 average values and the red solid line shows 2020 values. Vertical dashed lines show the mean temperature for 2020 (red) and the 1981–2010 period (blue). Vectors indicate July wind anomalies at 925 hPa (1981–2010 base period). Shading depicts regional elevation (m). (Sources: NOAA/NCEI and CA-NWS.)

(III) NOTABLE EVENTS AND IMPACTS

In the eastern tropical Pacific Ocean, Tropical Storm Amanda made landfall along the Guatemala–El Salvador border on 31 May, becoming the only named storm of the season to make landfall in that region. From the remnants of this storm, Tropical Storm Cristóbal (1–12 June) formed in the Gulf of Campeche (Mexico), affecting northern Central America and causing more than 30 fatalities in the region. In the Caribbean basin, tropical cyclone activity during 2020 was extremely active with 10 named storms, five hurricanes, and three major hurricanes (Category 3 or higher on the Saffir-Simpson Hurricane Wind Scale). The three major hurricanes were Delta (5–10 October, Category 4); Eta (31 October–13 November, Category 4, landfall over Nicaragua and Honduras on 3–5 November); and Iota (13–18 November, Category 4). Eta and Iota made landfall near the same location between the northeastern coast of Nicaragua and southern coast of Honduras as major hurricanes and were associated with severe impacts over the isthmus. As seen in Table 7.1, the season resulted in a total of 237 fatalities due to hydrometeorological events and 16 deaths by lightning strikes.

Table 7.1. Number of fatalities in several Central American countries due to tropical storms and lightning strikes. Some countries reported fatalities for two storms. (Data sources: Central American National Weather Services, National Emergency Committees communications and regional newspapers.)

Country	Amanda	Christóbal	Eta	Iota	Lightning Strikes
Panamá	—	—	**19**	—	3
Costa Rica	—	—	2	—	1
Nicaragua	—	—	2	16	7
El Salvador	27		1	1	1
Honduras	4		77	22	1
Guatemala	2	3	53	8	3
Totals	**33**	**3**	**154**	**47**	**16**

2) Caribbean—T. S. Stephenson, M. A. Taylor, A. R. Trotman, C. J. Van Meerbeeck, K. A. Stephenson, L.A. Clarke, G. Tamar, J. M. Spence, Annie C. Joseph, and J. D. Campbell

(I) TEMPERATURE

In 2020, the Caribbean experienced above-average and record temperatures, with annual mean temperatures anomalies ranging from +0.25°C to +2.50°C above the 1981–2010 average. Anomalies were highest over the northwestern Caribbean (Jamaica, Cuba, and the Bahamas) and over Trinidad and Barbados in the east (Fig. 7.9a). The annual average temperature anomaly over the domain was approximately 0.85°C above average, the second highest since the start of the record in 1891 (Fig. 7.10a). Region-wide, the month of September was particularly hot, with 26 Caribbean locations (out of 28 with an up-to-date historical record of daily maximum temperature spanning at least 30 years) recording an above-average number of hot days—that is, days with a maximum temperature exceeding the 90th percentile as calculated from a 1985–2014 climatological period—between 8 and 28 hot days. Annual average maximum temperatures were record high for Freeport, The Bahamas (29.9°C; since 1971), for Canefield, Dominica (31.9°C; since 1982), and for Crown Point, Tobago, Trinidad and Tobago (31.3°C; since 1971), while Lamentin, Martinique (31.3°C), and Sint Maarten (31.1°C) reported their second-highest maximum temperatures since 1971 and 1983, respectively, and Hewannora, Saint Lucia (31.0°C), reported its third highest since 1979. Record high monthly average maximum temperatures for any month were observed in Aruba (34.3°C in September), Martinique (32.9°C in September in Lamentin), and Saint Lucia (32.4°C in September at Hewanorra), since 1985, 1975, and 1986, respectively. Record daily maximum temperatures were observed in September relative to the entire historical records for the countries

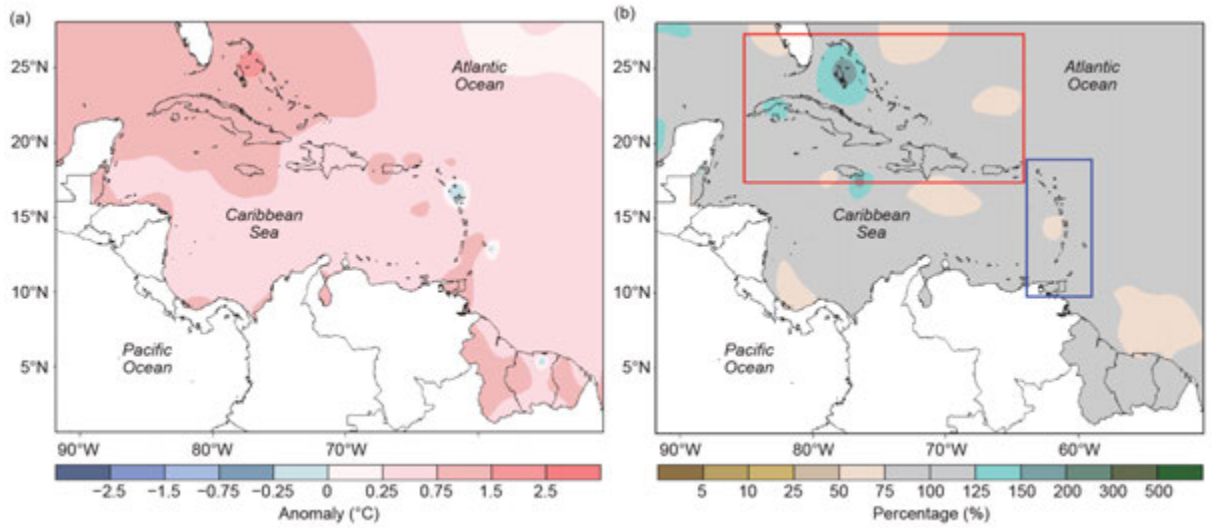

Fig. 7.9. Annual (a) mean temperature anomalies (°C) and (b) total precipitation anomalies (% of normal) relative to 1981–2010. Red (Blue) rectangle encloses northern (eastern) Caribbean. (Source: Caribbean Climate Outlook Forum [CariCOF] and the Caribbean Institute for Meteorology and Hydrology.)

of Dominica (35.7°C at Canefield Airport on 15 September) and Grenada (34.0°C at Point Salines on 16 September), with records starting in 1975 and 1986, respectively.

(II) PRECIPITATION

In 2020, the Caribbean experienced near-normal to slightly above-normal daily precipitation, averaging 0.28 mm day^{-1} above the 1981–2010 normal (Fig. 7.10b). The eastern and northern Caribbean subdomains had anomalies of +0.18 mm day^{-1} and +0.09 mm day^{-1}, respectively, according to Global Precipitation Climatology Centre (GPCC) satellite analyses. Station data further suggest that the northern countries over the eastern Caribbean (e.g., Anguilla, Sint Maarten, Guadeloupe, St. Kitts, and St. Thomas) experienced normal rainfall, with drier-than-normal conditions observed over some southern countries (e.g., St. Vincent, St. Lucia, and Martinique). Some northern Caribbean locations (e.g., The Bahamas, western Cuba, and eastern Jamaica) showed above-normal precipitation compared to the rest of the region (Fig. 7.9b), likely linked to storms and hurricanes traversing (near) these locations. New Providence, Bahamas (2206.3 mm), and Port-au-Prince, Haiti (1715.6 mm), each recorded their wettest year on record since 1970 and 1982, respectively when observations commenced. Conversely, Monte Cristi, Dominican Republic (265.2 mm), recorded its driest year on record since 1972 when its record began.

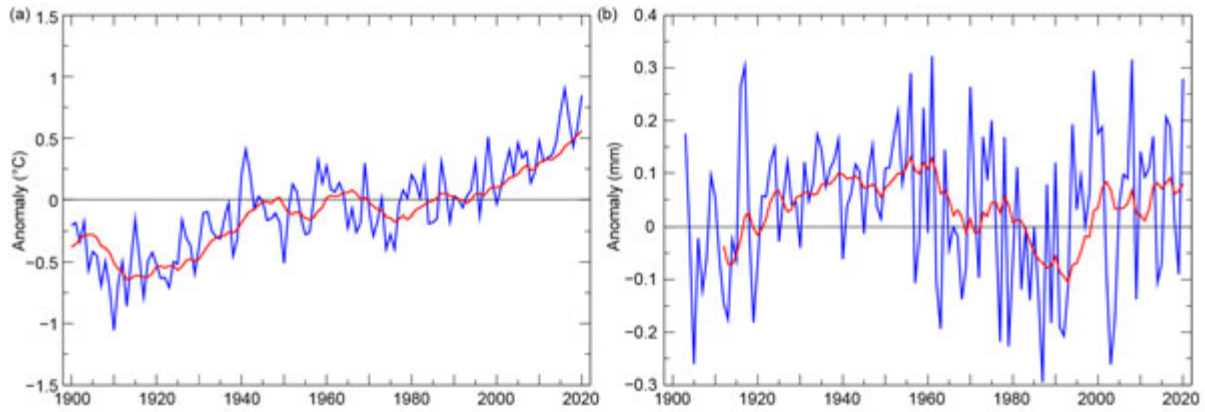

Fig. 7.10. Annual average (a) temperature anomalies (°C) and (b) daily rainfall anomalies (mm day^{-1}) for the Caribbean (9°–27°N; 58°–90°W) for 1903–2020 relative to the 1981–2010 average. The red line is the 10-year running mean. (Sources: NOAA/NCEI and GPCC from the KNMI Climate Explorer.)

The transition from ENSO-neutral conditions in January to La Niña by August was an important driver for how rainfall patterns emerged over the region. La Niña conditions are generally associated with above-normal late season Caribbean rainfall (e.g., Taylor et al. 2002). Initially, drier conditions were observed over most of the region during the first 6 months of the year, persisting from October 2019. The exception was over eastern Dominican Republic and southward to Dominica where very wet conditions were observed during January–March. October–December was characterized by recurrent extreme rainfall related to La Niña conditions and above-average storm activity, causing flooding across many Caribbean countries.

(III) NOTABLE EVENTS AND IMPACTS

A Sahara dust event in June 2020 impacted the Caribbean. The haze was visible in a number of islands with Guadeloupe, Martinique, and Puerto Rico classifying air quality levels as hazardous. Puerto Rico recorded concentrations of PM10 (particulate matter that can penetrate into the lungs causing respiratory problems and disease) higher than 500 μg m^{-3}, the highest observed in the last 20 years of data (WMO 2020).

Hurricane Isaias impacted the Caribbean from 28 July to 1 August, bringing heavy rains to the eastern Caribbean, which led to flash floods, landslides, and damage to electricity, infrastructure, and water supply in Puerto Rico, along with two reported deaths and widespread flooding in the Dominican Republic. The impact of Hurricane Isaias to The Bahamas was pronounced, including damage to homes even as the country was still recovering from the losses from Hurricane Dorian in 2019. Some residents were left homeless in Cuba due to severe flooding, and Haiti experienced damage to crops and homes.

In August, Hurricane Laura impacted the Caribbean as a tropical storm and caused 24 fatalities. The impact was particularly devastating in Haiti where flash flooding and landslides in Port-au-Prince killed at least 21 people. Laura also caused three deaths in the Dominican Republic. Both Jamaica and Cuba experienced landslides, flooding, and damage to critical infrastructure. See section 4g2 and Sidebar 4.1 for more details about Hurricane Laura.

An extended drought impacted the insular Caribbean from October 2019 to mid-2020, causing water scarcity, bush fires, and agricultural losses. In St. Vincent and the Grenadines, the 2020 drought was considered the worst in 50 years (Nurse 2020).

Sidebar 7.1: **Record-breaking hurricane landfalls in Central America**—S. DIOUF, S. FUHRMAN, W. M. THIAW, AND F. ARGEÑALSO

In less than 1 month, Central America was impacted by two powerful hurricanes between 1 and 18 November 2020: Category 4 Hurricanes Eta and Iota. These two close events caused massive devastation and destruction in the region, leaving little respite to the population.

Hurricane Eta

Tropical Storm Eta became the 28th named storm of the 2020 Atlantic Hurricane season (see section 4g2) on 1 November, tying the record number of storms set in 2005. For the second time since the start of the storm naming convention in 1950, the Greek alphabet was used to name the tropical system, because the designated list of 21 names for the 2020 season was exhausted. This was also the first time that the name Eta was used in the Atlantic basin.

After remaining a tropical storm for several hours, Eta intensified explosively on 2 November to reach peak intensity as a strong Category 4 hurricane, with maximum sustained winds of 240 km h^{-1} and its lowest recorded pressure of 923 hPa. Eta was the 12th hurricane and the fifth major hurricane of this Atlantic hurricane season.

After approaching the northeastern Nicaragua coast, the eye of Hurricane Eta made an impactful landfall in Nicaragua, about 25 km south of Puerto Cabezas, on 3 November (Fig. SB7.1). The Puerto Cabezas airport measured sustained winds of 172 km h^{-1} and a gust of 217 km h^{-1} during a 2-hour period. Winds were so strong that they uprooted trees and ripped roofs from homes.

The storm drenched neighboring Honduras, where widespread flooding and landslides caused damage across the country. The Honduras emergency management agency reported the rescue of over 20 people and the displacement of at least 559 people due to significant flooding.

On 4 November, Hurricane Eta was downgraded to a tropical storm with sustained maximum winds of near 110 km h^{-1} and a minimum central pressure of 990 hPa. As it moved over land and entered eastern Honduras, it continued to weaken into a tropical depression by the evening, while still spreading very heavy rain. Many roads and bridges were destroyed or temporarily made inaccessible, and power lines were knocked down, leaving the population cut off from assistance. The impacts of the hurricane reached far beyond the areas directly hit by Eta. Storm totals in excess of 100 mm were measured as widely as David, Panama, and Belize City, Belize. Torrential rains led to severe flooding that occurred in the central and southern regions of Belize, affecting around 60,000 people.

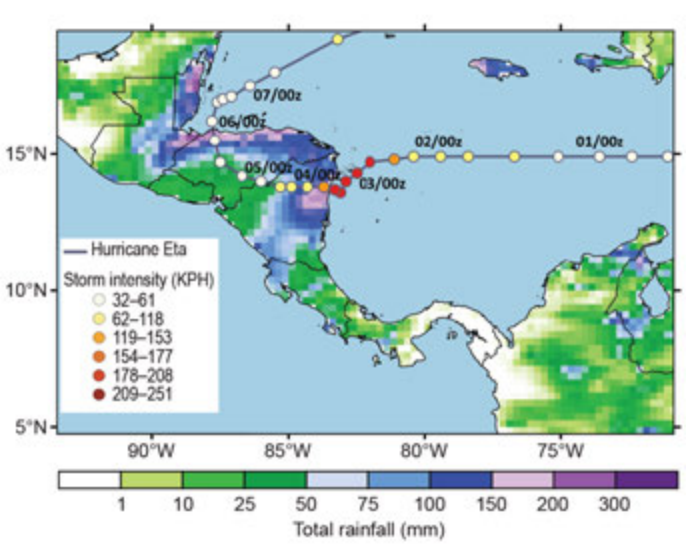

Fig. SB7.1. Hurricane Eta National Hurricane Center (NHC) best track overlaid with associated cumulative satellite estimated rainfall (mm; CMORPH) for 2–7 Nov 2020. (Source: NOAA/NCEP.)

The following day, Eta entered northeastern Guatemala. It generated accumulated precipitation totals of more than 200 mm in 24 hours, especially notable in northern Guatemala. The excessive rainfall led to a landslide that killed eight people and injured four others in the village of Quejà, San Cristobal Verapaz. In addition, 88 people disappeared in the Agua Caliente neighborhood. On 6 November, Eta's circulation turned northeastward over the Caribbean Sea and exited the region.

Hurricane Iota

While residents were still coping with the aftermath of Hurricane Eta, another major storm was approaching, threatening to compound destruction and inflict additional damages for the same hard-hit areas in Central America.

On 14 November, Tropical Storm Iota became the 30th named storm of the season. By 15 November, Iota reached hurricane status as it approached Central America, becoming the 13th hurricane of this unusually busy hurricane season.

On 16 November, Iota intensified into a Category 3 storm, becoming the sixth major hurricane of the season. For the first time on record, the Atlantic basin experienced two major hurricanes during the month of November. As the hurricane approached Central America, its pressure fell from 945 hPa to 935 hPa in a little over an hour. Additionally, intense lightning was present in the southwestern quadrant of the eyewall, along with hail that is unusual for a tropical system. This contributed to the

extraordinary characteristics of the hurricane. Iota strengthened to become an extremely dangerous Category 4 storm, with maximum sustained winds reaching 260 km h^{-1} and its minimum central pressure estimated at 917 hPa.

On 17 November, Iota made destructive landfall along the eastern coast of Nicaragua, notably near the town of Haulover situated south of Puerto Cabezas, which was soaked and lashed by Category 4 Eta earlier in the month. In Haulover, around 1750 residents, mostly indigenous people, were impacted by the devastating rains measured in excess of 150 mm, according to NOAA's CPC Morphing Technique (CMORPH) estimates (Fig. SB7.2). Iota was the strongest hurricane to impact Nicaragua on record.

A few hours later, Iota was downgraded to a tropical storm, while still dropping very heavy rains on Nicaragua, with rivers overflowing and trees and electricity poles felled by unceasing winds. The storm degraded to a tropical depression as it headed into El Salvador on 18 November and finally dissipated a few hours later. For the second time in 2 weeks, Ramón Villeda Morales International Airport in Honduras was engulfed by floodwaters.

The widespread flooding from Iota was exacerbated by the antecedent ground saturation after Hurricane Eta. Together, the two storms dumped an enormous amount of rain on a large part of the region. According to satellite rainfall estimates, more than 300 mm of rain fell over much of eastern Nicaragua, northern Honduras, parts of eastern Guatemala, and Belize. CMORPH climatology indicates about 100–200 mm of rain typically during the month of November in that region.

Impacts

According to the United Nations Office for the Coordination of Humanitarian Affairs, Eta and Iota affected more than 7.3 million people in all Central American countries, especially Honduras, Nicaragua, and Guatemala. In Honduras, more than 2.9 million people were impacted by Hurricane Eta, and this number increased to 3.8 million after the passage of Iota. The two hurricanes and their aftermaths claimed the lives of 98 people, destroyed more than 61,000 homes, and damaged more than 700 roads across Honduras. One month after Iota, 95,000 people were still living in shelters. The Nicaraguan government estimated that damages and economic losses attributed to both events were $738 million (US dollars; 6.2% of the Gross Domestic Product).

Relentless rainfall and winds from both hurricanes also resulted in decreased yield for the *Segunda/Postrera* agricultural season that typically starts with planting in August and September and concludes with harvest in December. According to the Ministry of Agriculture and Livestock of Honduras, more than 8000 ha of maize and more than 12,000 ha of beans were destroyed in 10 departments of Honduras. Banana, African palm, and sugar cane were also severely affected. In Nicaragua, bean crops, which account for 25% of the national production, significantly suffered from both storms, especially in the northern part of the country. In Guatemala, the Ministry of Agriculture, Livestock and Food estimated a total of 164,000 ha of crop areas suffered damage. The eastern part of the country, which is an important bean-producing area, lost 50%–60% of bean crops. These important agricultural losses, combined with the economic effects of the COVID-19 pandemic across Central America, led to a decline in annual income and worsened food insecurity for a large number of people in the region.

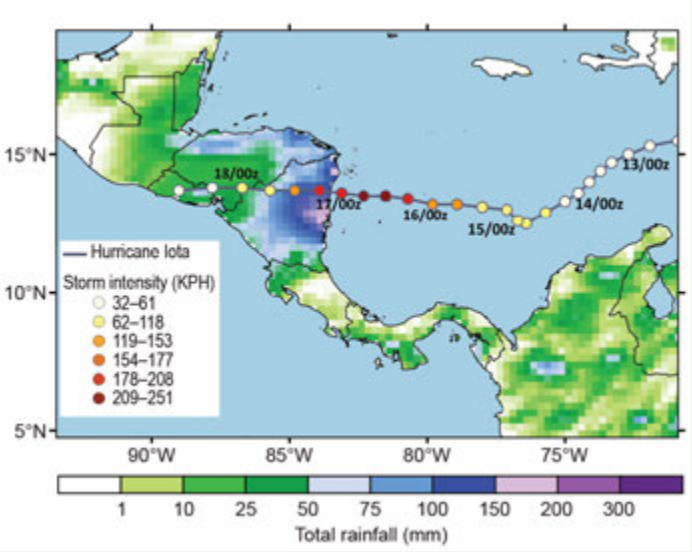

Fig. SB7.2. Hurricane Iota NHC best track overlaid with associated cumulative satellite estimated rainfall (mm; CMORPH) for 16–18 Nov 2020. (Source: NOAA/NCEP.)

d. South America—A. Sánchez-Lugo, Ed.

With the exception of northeastern Brazil and most of Colombia, most of South America had above-average temperatures during the year. The most notable maximum temperatures were reported in central South America and southwestern Brazil, where temperature anomalies were at least +1.5°C. Below-average minimum temperatures were observed in Colombia, northeastern Argentina, and eastern Brazil. During the year, wetter-than-normal conditions were observed in eastern Colombia and northern and northeastern Brazil. Below-average conditions were mainly observed in Chile, eastern Ecuador, northern Peru, eastern Bolivia, southern Brazil, and most of Uruguay, Paraguay, and northwestern Argentina. Anomalies in this section are all based on the 1981–2010 average, unless otherwise noted.

1) NORTHERN SOUTH AMERICA—J. J. Nieto and F. Costa

This section includes Colombia, Ecuador, Guyana, Suriname, and Venezuela.

(I) TEMPERATURE

Annual temperature departures of at least +0.5°C above the 1981–2010 average were observed across much of northern South America. Mean monthly temperatures were above normal for most of the year throughout the region despite a La Niña that developed and prevailed in the eastern tropical Pacific for much of the second half of 2020.

On the cool side, Colombia observed an annual maximum temperature anomaly of −0.8°C below normal, and conversely, Venezuela had an annual maximum temperature anomaly of +1.5°C above normal. During April, July, and October, several locations across Venezuela had a maximum temperature anomaly close to +2.5°C, while much of Ecuador had an annual maximum temperature anomaly of +0.3°C (Fig. 7.11a). Most of northern South America observed annual minimum temperature anomalies between +0.5°C and +1.5°C, although some Andean regions of southern Ecuador and central Colombia reported below-normal minimum temperature anomalies of about −0.5°C (Fig. 7.11b).

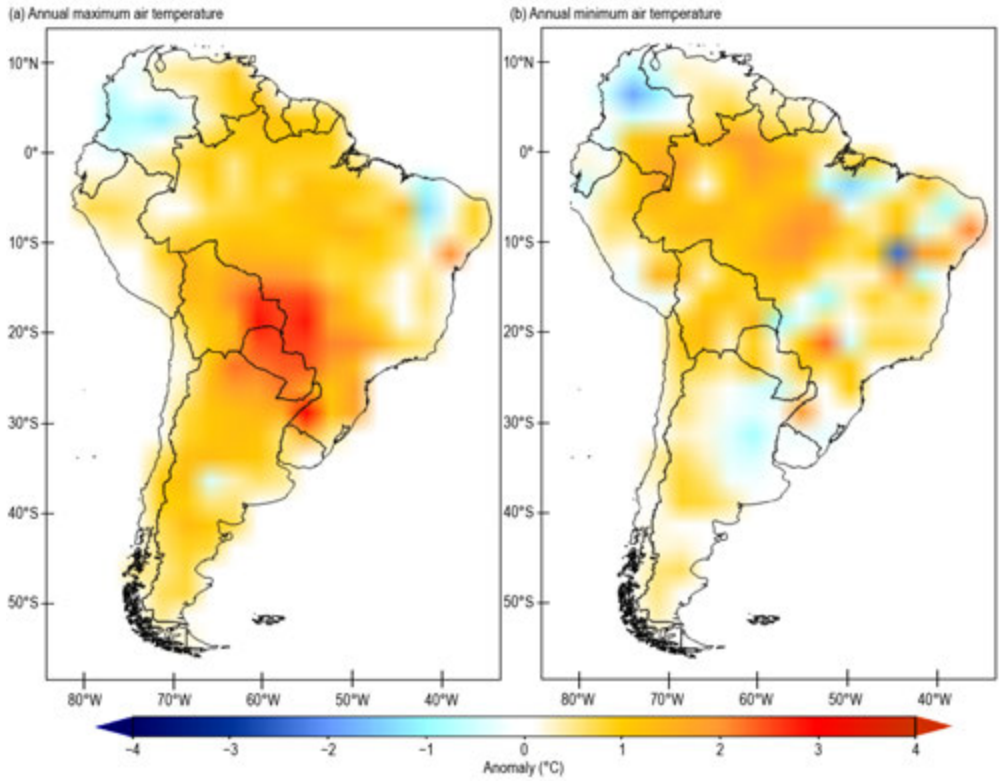

Fig. 7.11. Annual (a) maximum and (b) minimum temperature anomalies (°C; 1981–2010 base period). (Source: Data from NMHSs of Argentina, Colombia, Chile, Brazil, Ecuador, Paraguay, Peru, Suriname, and Venezuela; processed by CIIFEN.)

(II) PRECIPITATION

Parts of northern South America, particularly Venezuela, had 50%–60% above-normal rainfall during September and October. Rainfall in central and eastern Colombia was 20%–30% above normal during October and November. Above-normal rainfall in the north of northern South America was associated with two major hurricanes: Eta and Iota (see Sidebar 7.1 for details), in addition to the effects of La Niña, which is usually associated with increased rainfall in the region. Western (coastal region) and eastern (Amazon region) Ecuador reported 20%–40% and 60%–80%, respectively, below-normal rainfall for the year, with the second half of the year contributing to much of the deficit. The northern Andean region of Ecuador had 30%–40% above-normal annual rainfall, with September–November particularly wet (Fig. 7.12).

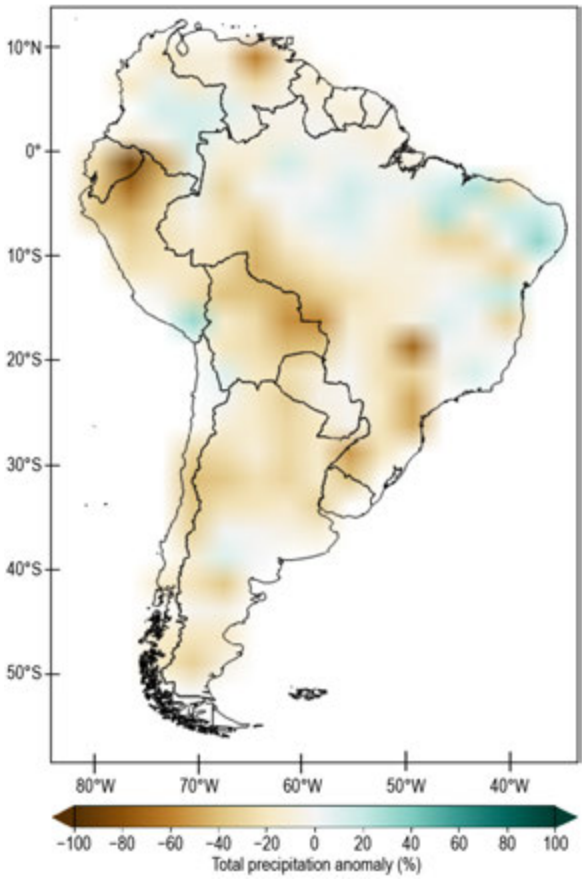

Fig. 7.12. Annual precipitation anomalies (%; 1981–2010 base period). (Source: data from NMHSs of Argentina, Colombia, Chile, Brazil, Ecuador, Paraguay, Peru, Suriname, and Venezuela; processed by CIIFEN.)

(III) NOTABLE EVENTS AND IMPACTS

Intense rainfall occurred during August, with a cumulative 446 mm recorded at the Rancho Grande (10.3°N, 67.6°W) hydrometeorological station (62% above its climatological average), contributing to a landslide in the upper basin of the state of Aragua in northern Venezuela in September. The detached mass was deposited on a nearby populated area. Tributaries of the El Limón River also suddenly overflowed. As a result of this event, more than 1400 people were affected, with eight serious injuries reported. Additionally, more than 400 homes, 120 commercial properties, and dozens of vehicles were damaged, and electric and water system outages were reported.

Also in the state of Aragua, heavy rainfall in October caused flashfloods. During this event, a 1-hour precipitation total of 85 mm was recorded. As a result of the rains, increased flows of the Turmero, Madre Vieja, Caño Colorado, El Manguito, Corral de Piedra, and La Trinidad Rivers were observed. Nearly 20,000 people were affected, including one reported fatality, and nearly 5000 structures and vehicles were damaged or destroyed.

In late October and early November, floods were reported over a 2-week period in Guyana due to heavy rainfall, affecting more than 1600 households across five regions. In Georgetown, where the highest level of rainfall was observed, during 3–4 November, the accumulated total was 120.3 mm. The rains, combined with high tides, affected the infrastructure of maritime and river defenses, which protect people, assets, livelihood, and the environment.

On 16 November, the passage of Hurricane Iota was recorded in the San Andres and Providencia Department, two island groups in the Caribbean Sea about 775 km northwest of mainland Colombia. Within 4 hours, Iota intensified from a Category 3 to a powerful Category 4 storm, with maximum wind speeds of more than 230 km h^{-1}. The impacts of Iota in the region included downed power lines, damaged and destroyed homes, uprooted trees, floods, and strong winds (see Sidebar 7.1 and section 4g2 for more details about the storm).

During the first 2 weeks of November, heavy rain fell in the Bogotá region of Colombia, exceeding 190 mm. Resulting landslides affected the road infrastructure of the region and, consequently,

the traffic. The above-normal rainfall was associated with the ongoing La Niña that developed in August, which typically increases rainfall in the Colombian highlands.

During Ecuador's rainy season, which extends from January to April, both the coastal and Amazon region registered hundreds of extreme events, including 594 landslides, 234 floods, and 125 structural collapses. For the Pichilingue (1.1°S, 79.5°W) meteorological station, the 24-hour precipitation total on 9 February was 156.4 mm, a 25-year return period. On 7 March, the Milagro (2.1°S, 79.6°W) meteorological station registered 156.3 mm, also a 25-year return period. In total, more than 72,000 people were affected, with 73 deaths and injuries reported. Over 4500 homes and 3330 ha of crops were damaged or destroyed.

2) CENTRAL SOUTH AMERICA—J. A. Marengo, J. C. Espinoza, L. M. Alves, J. Ronchail, A. P Cunha, A. M. Ramos, J. Molina-Carpio, K. Correa, W. Lavado-Casimiro, J. Baez, and R. Salinas

This region includes Brazil, Peru, Paraguay, and Bolivia.

(I) TEMPERATURE

The 2020 temperature for central South America was +0.8°C above normal and was the second highest for the region since 1960 (Fig. 7.13). Only 2015 had a higher temperature departure, which was mainly due to the influence of the warm-phase El Niño that was present in the tropical Pacific Ocean at the end of the year. In 2020, a moderate cool-phase La Niña was present in the tropical Pacific Ocean. The annual mean temperature for 2020 was 0.5°–1.0°C above normal across most of Peru, northern Paraguay, and the eastern Bolivian lowlands. In February and March, temperatures departures from average of +3°C were observed across the northern Peruvian coast.

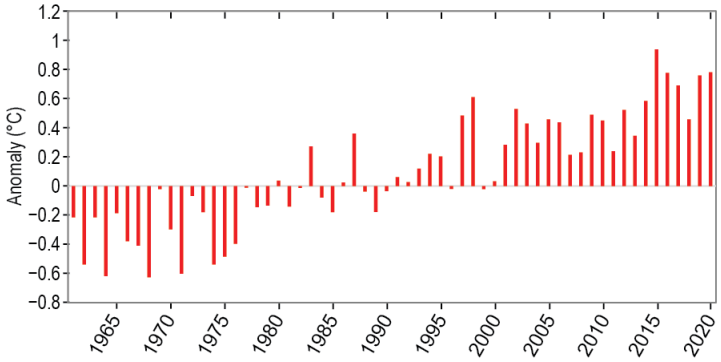

Fig. 7.13. Time series of mean annual regional air temperature anomalies (°C) from 1961 to 2020 for central South America (Brazil, Bolivia, Paraguay, and Peru). Anomalies are relative to 1981–2010 base period. (Source: HadCRUT4.)

(II) PRECIPITATION

Annual precipitation was below normal across most of central South America, including the central Andes, the Amazon, the Pantanal regions, and southeastern South America. The austral summer was characterized by below-normal rainfall in Amazonia and southern Brazil. Above-normal rainfall was observed across the semiarid area of northeastern Brazil during March–May, ending a 6-year drought in that region. In Peru, there were several episodes of extreme rainfall in the Andes during the austral summer, while drought was reported along the northern Peruvian coast (see *Notable events and impacts*).

Dry conditions spanned from May to November across most of the central Andes, with several stations recording less than half of their normal precipitation. This resulted in a delayed onset of the rainy season by at least 10 days, which affected crop production. During September–November, the Bolivian lowlands suffered one of its most severe droughts on record, depleting soil water storage and favoring wildfire development. As indicated by the Integrated Drought Index (IDI; Cunha et al 2019), droughts also spanned the Paraguayan Chaco, the Pantanal, and southern

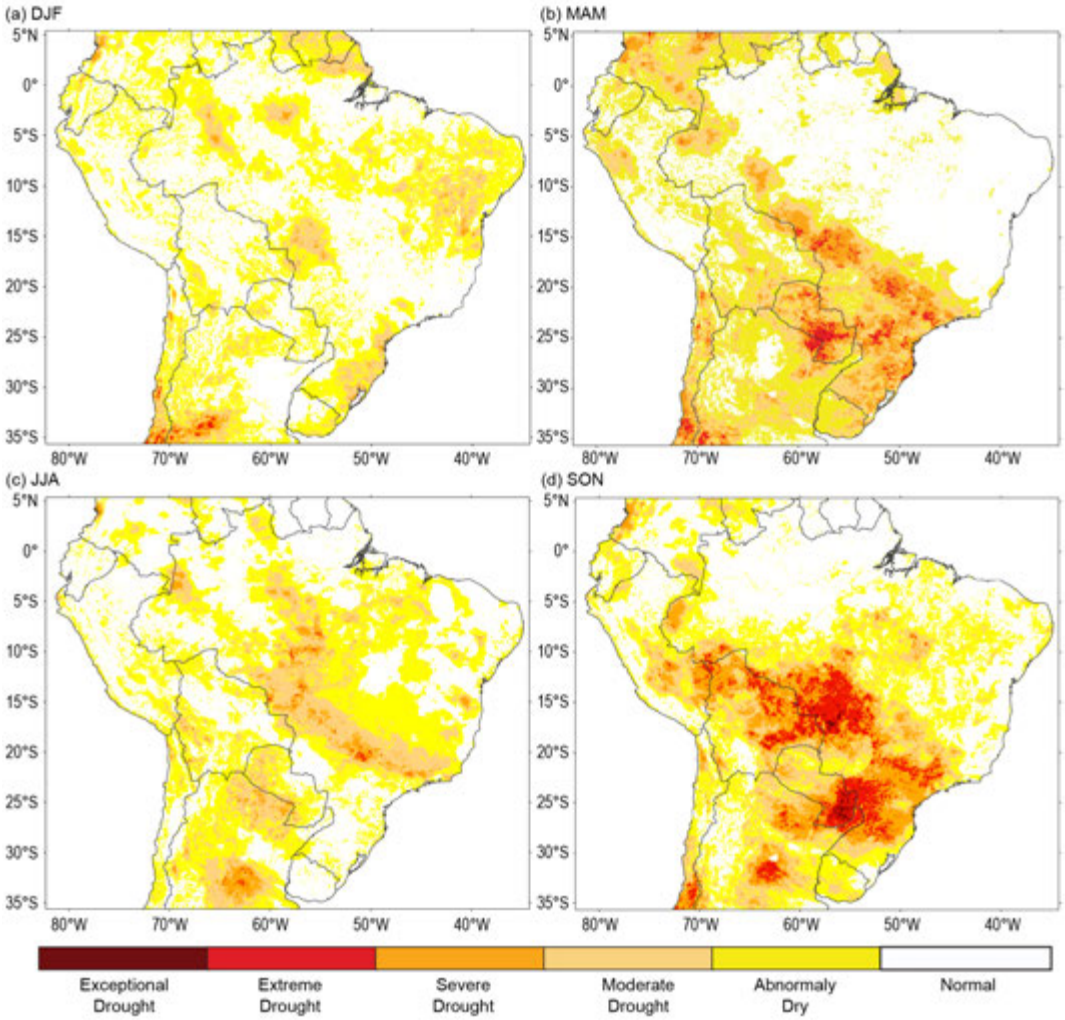

Fig. 7.14. Integrated Drought Index (IDI) maps for central South America during (a) DJF 2019/20, (b) MAM 2020, (c) JJA 2020, and (d) SON 2020. (Source: CEMADEN.).

Brazil during the same period (Figs. 7.14a–d). The IDI combines a meteorological-based drought index and remote sensing-based index to assess drought events (Cunha et al. 2019). The Paraguay River shrank to its lowest levels in half a century, resulting in potable water accessibility issues and limited river traffic (see *Notable events and impacts*).

(III) NOTABLE EVENTS AND IMPACTS

Several significant weather and climate extreme events occurred across central South America during the year that are depicted in Fig. 7.15. Some of the events described below are included in this figure.

On 8–9 January and again on 10 February, heavy rainfall affected the city of São Paulo, Brazil, triggering landslides and flash floods that left 24 dead and 5150 homeless. In Belo Horizonte (Minas Gerais), on 16–17 February, flash floods left 61 people dead and more than 3000 homeless.

During January–March heavy rain triggered floods and landslides that affected most of the Peruvian coastal and Andean regions. On 22–23 January, the southern coast of Peru received record-breaking rainfall of 13 mm day^{-1} in regions where it normally does not rain. On 21–22 February, exceptional rainfall was reported along the southern coast of Peru; landslides and overflows damaged four districts of the Tacna region, where three people died. The Chili River (Arequipa) flow rate reached 81.7 m^3 s^{-1}, which is 68.7 m^3 s^{-1} above normal, producing floods that damaged over 470 houses.

In La Paz and other Andean departments of Bolivia, severe weather during January and February affected over 11,600 families and 5300 ha of agricultural crops, and caused 18 fatalities. Later

in the year, record-breaking precipitation was received on 20 August (136.8 mm, the highest daily record for August), following several days of heavy rainfall; several zones of Santa Cruz city were flooded. Rainfall during August 2020 was also a record for the month with a total of 312.7 mm, more than 800% of average (41 mm).

During 30 June–1 July, an intense extratropical cyclone reached southern Brazil. On 30 June, the mean sea level pressure at the core of the system was 1004 hPa, dropping to 972 hPa on 1 July within 24 hours, bringing tornadoes, hail, and wind gusts exceeding 130 km h^{-1}. The storm caused 18 fatalities in southern Brazil due to falling trees and structures, affected 229 municipalities, and left 2600 people homeless. About 639,000 people in Rio Grande do Sul and 1.5 million in Santa Catarina were left without electricity.

A severe cold wave affected the southern Peruvian Andes in early July, with temperatures dropping as low as –22.6°C in Mazocruz (Puno) on 3 July, 9.6°C below the average minimum temperature for July. Lima, Peru, had two unusual cold episodes with temperatures below 10°C on 18 July (9.6°C, average is 13.9°C) and 13 August (9.5°C, average is 13.8°C). These two episodes brought the lowest minimum temperatures since 1985. During 21–23 August, a cold air outbreak affected southeastern Brazil in Curitiba and São Paulo. The cold wave reached the lower Chaco region of Paraguay and also affected the western Amazonia of Brazil and the city of Iquitos in the northern Peruvian Amazon.

A strong heat wave episode (15 days with maximum temperature above the 90th percentile) affected southeastern and central-western Brazil, Bolivia, and Paraguay during the first half of October. During that time, the city of São Paulo recorded four of its five highest daily maximum temperatures on record (for example, 37.5°C on 2 October, highest temperature in 77 years; average is 24.8°C). Several locations across the Bolivian lowlands and in Paraguay also had their highest maximum temperature on record (Fig. 7.15). Of note, Sao José de Chiquitos recorded a maximum temperature of 43.4°C on 8 October (average is 33.9°C) and Concepción in Paraguay registered 42.6°C on 2 October (average is 33.4°C).

A weak summertime rainy season in the Pantanal started in 2019 and continued in 2020. Between January and August, rainfall was 50% below normal in the Brazilian Pantanal (up to 300 mm $month^{-1}$ below normal) and the Upper Parana basin. The number of fires registered by

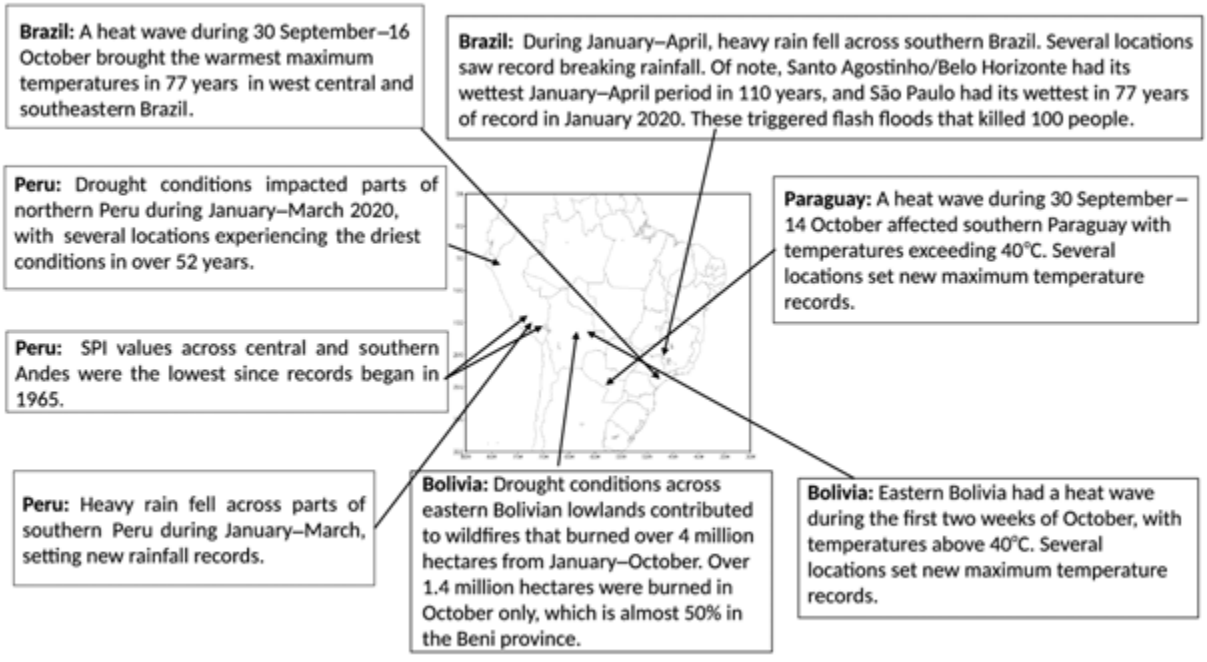

Fig. 7.15. Map depicting date, approximate location, and type of selected notable extreme weather events across central South America. (Sources of data: Peru: SENAMHI; Bolivia: SENAMHI, FAN; Paraguay: DMH; Brazil: INMET, CEMADEN, Climatempo, INPE; International: UN OCHA, Web Relief.)

National Institute for Space Research (INPE) in the Brazilian Pantanal exceeded last year's value by 241% (Marengo et al 2021). The levels of the Paraguay River at Ladário were below average since 2018 and continued to drop into 2020. The drought and anomalous warm weather in these regions spread devastation and increased the fire risk in agricultural land and protected areas and affected population and goods transportation along the Paraguay River (Marengo et al 2021).

Most of northern Peru experienced rainfall deficits between 15%–100% during its austral summer. By March, the discharge of the Chicama River was 38.81 $m^3 s^{-1}$, which is about 70% less than its normal rate. The low levels of the main reservoirs (Gallito Ciego, Tinajones, and Poechos) affected water supply for agriculture in the irrigated region.

3) Southern South America—J. L. Stella, N. Misevicius, and C. Cortés

This region includes Argentina, Chile, and Uruguay.

(I) TEMPERATURE

Above-normal temperatures were observed across most of southern South America (SSA) during 2020, with annual mean anomalies between +0.5°C and +2.0°C in large areas. A small region, including Uruguay and adjacent areas of Argentina, recorded near-normal temperatures. The 2020 national mean temperature anomalies for Argentina (+0.63°C) and Chile (+0.83°C) were the second and third highest, respectively, since national records began in 1961, while Uruguay had a temperature anomaly (+0.08°C) that was near normal. The decadal mean temperature for 2011–20 was the highest on record for Argentina, with a significant positive trend since 2001 (Fig. 7.16).

Summer 2019/20 was characterized by normal to above-normal temperatures across the region, with pronounced sub-seasonal variability over the eastern part. Western provinces of Argentina were affected by several heat waves (defined as minimum and maximum temperature surpassing the 90th percentile for three or more consecutive days) during the latter part of January. An 11-day heat wave record was set in both the cities of San Rafael and Malargüe.

Autumn was extremely warm over most parts of SSA. Both Atlantic and Pacific high-pressure systems weakened during this season, favoring a high-pressure blocking pattern over the continent, which discouraged the normal cold front passages such that sunny and warmer-than-average days prevailed during the season. March was extremely hot over the region and several locations broke historical records. The national mean monthly temperature anomaly for Argentina was +2.0°C, breaking the previous record set in March 1980 (+1.8°C). Uruguay had its second-warmest March since records began in 1961 (+1.7°C). A late heat wave during the first half of the month affected parts of central and northern Argentina and Uruguay. The city of Artigas reported a maximum temperature of 40.2°C on 13 March, tying the national temperature record that was set in the city of Treinta y Tres in March 1970.

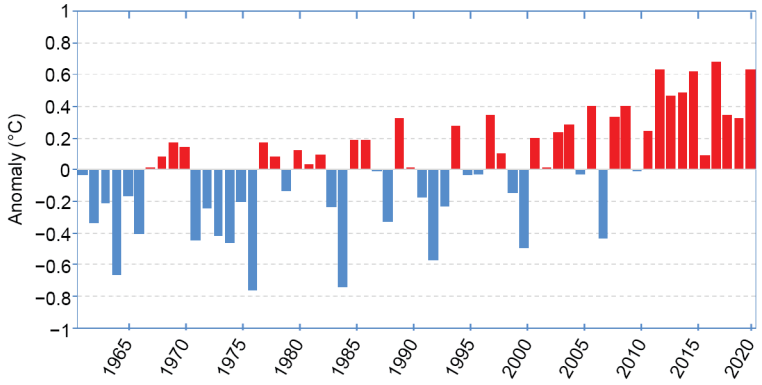

Fig. 7.16. Annual mean temperature anomaly (°C; 1981–2010 base period) time series from 1961 to 2020 for Argentina.

Austral winter had near-normal temperatures across most of SSA, with the exception of the extreme north and extreme south regions, where above-normal and below-normal temperatures, respectively, prevailed. Sub-seasonal variability was predominant during the season. The end of June through July was particularly cold over southern Argentina and Chile. Extreme cold waves (defined as when the minimum and maximum temperatures are below the 10th percentile for three or more consecutive days) affected this region. Daily temperatures were as low as –20°C in Perito Moreno, Argentina, on 27 June. Puerto Natales, in Chile, reported its lowest temperature on record (–13.1°C) on 28 June. The extreme low temperatures caused lakes, seas, and soil to freeze near Puerto Natales and Río Grande.

Spring was characterized by above-normal temperatures over most parts of Argentina and Chile, while Uruguay had near-normal conditions. Maximum temperatures were extremely high in the north in part due to severe drought conditions that prevailed during most of the year. An unusual extreme hot spell affected the region from 25 September to 2 October. Temperatures rose well above 40°C for several days and some local all-time maximum temperature records were broken (43.5°C in Corrientes; 40.0°C in Oberá). For the first time since records began, a temperature above 40°C was observed in Iguazú (40.1°C).

(II) PRECIPITATION

Much of SSA had below-average annual rainfall during 2020. Rainfall deficits were 20%–60% below average north of 35°S and south of 40°S. A small area in the central part of SSA recorded near-normal precipitation. The year was characterized by a severe drought that impacted most of La Plata Basin (see *Notable events and impacts*). Argentina had its driest year since 1995 and fifth driest since national records began in 1961. The central-southern region of Chile reported its 11th consecutive year with a rainfall deficit. This period is known as a "Mega-drought." For Uruguay, 2020 was the third-driest year since 1981.

Below-normal rainfall dominated all Uruguay and Chile and much of Argentina during austral summer 2019/20. However, intense precipitation affected parts of Argentina during 4–15 February, especially in the provinces of Tucuman, Salta, Jujuy, Chaco, Santiago del Estero, and Córdoba, with daily rainfall totals up to 175 mm. Thunderstorms with intense precipitation affected the Atacama Region of northern Chile during the last week of January. The rainfall over the mountains triggered landslides and river floods in populated locations, causing severe damage.

Autumn was extremely dry across the region. Precipitation anomalies were 20%–60% below average over northern Argentina, central Chile, and Uruguay. At the end of the season, the first significant snowfall took place in the northwest Chubut province in Argentina. The city of Esquel reported a 15 cm snowfall total during 27–29 May.

Drought conditions worsened in northeastern Argentina and northern Uruguay, triggering several bushfires that severely affected Cordoba province and the Delta del Paraná region in Argentina. Meanwhile, southern Argentina and southern Chile were affected by heavy snowfall and rainfall several times during June and July (see *Notable events and impacts*). Southern Uruguay had above-normal precipitation, particularly due to heavy rainfall in June.

During spring, dry conditions persisted in SSA. In combination with high temperatures, the occurrence of severe bush fires extended to many other regions across Argentina. Precipitation anomalies were 40%–80% below normal in northeastern Argentina, its driest spring on record.

(III) NOTABLE EVENTS AND IMPACTS

Northern and central Argentina and Uruguay were severely affected by one of the worst droughts ever recorded in the region. The drought, which began in 2019, continued during 2020 after a weak summertime rainy season. Rainfall deficits of up to 300 mm month^{-1} below normal were detected over the Upper Parana River basin. By the end of spring, the drought worsened north of 35°S. Dry and warm conditions favored the development of fires, affecting human activities

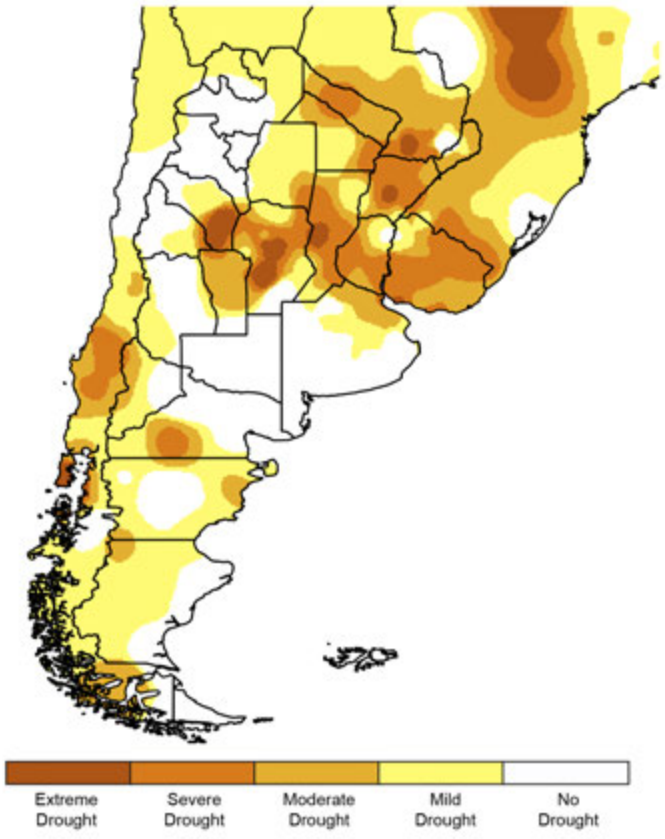

Fig. 7.17. SPI map for the 12-month period Jan–Dec 2020 for southern South America.

and biodiversity. For the year, the Standardized Precipitation Index indicated a classification of severe drought for several locations in Argentina, Uruguay, and also in Chile (Fig. 7.17).

A snowy winter was observed in southern Argentina. Major snowfalls occurred between the end of June and during July, reaching the plateau as well as the coast. Some locations were affected by blocked roads and power outages, among other impacts. According to estimated satellite measurements, the snow cover extent during May–October for central and southern Patagonia was the highest since 2000 (Fig. 7.18).

e. Africa—A. Mekonnen, Ed.

Analyses in this section are based on observational records from meteorological and hydrological services across Africa. Additionally, rainfall data from the Global Precipitation Climatology Project (GPCP) and temperature reanalysis data from the National Centers for Environmental Prediction/National Center for Atmospheric Research (NCEP/NCAR) were also used. Notable events are based on reports from government agencies, research/Early Warning organizations, and United

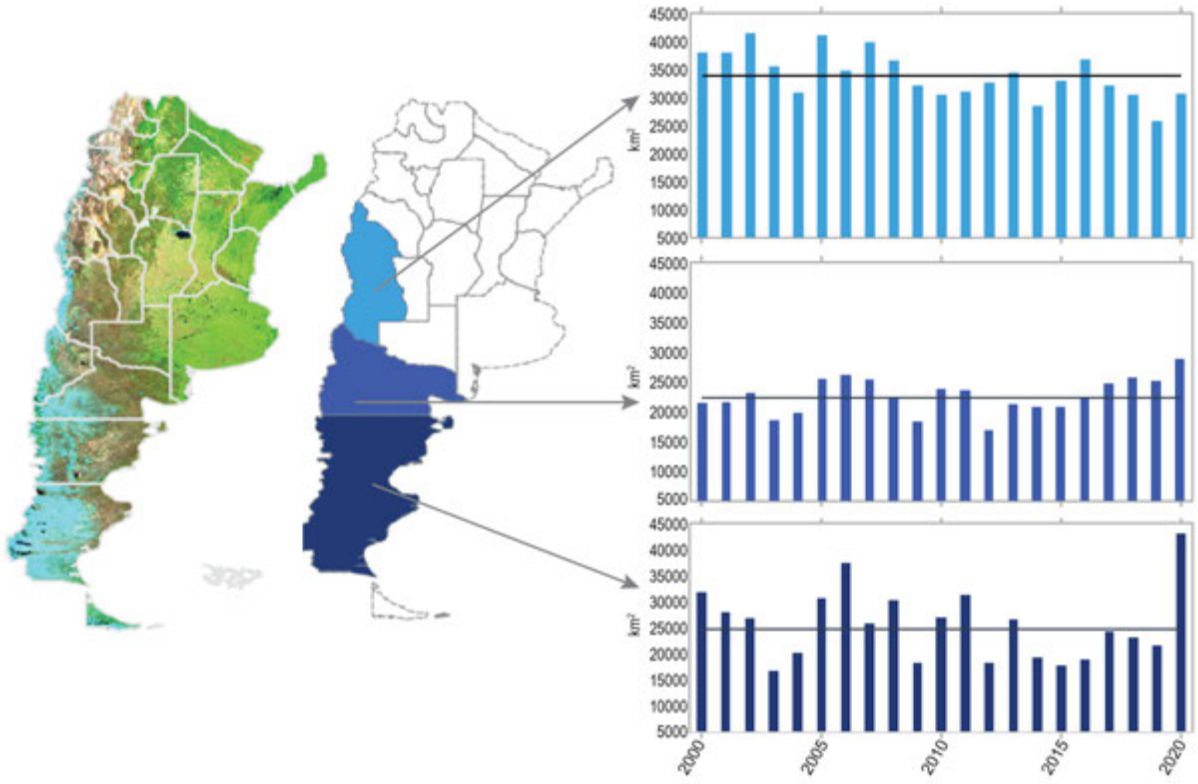

Fig. 7.18. (left) Satellite measurements (MODIS) of snow cover extent (km^2; light blue in left-side map) during May–Oct 2020 over central and southern Patagonia. (right) May–Oct snow cover extent (km^2) shown in time series for the period 2001–20 for three regions, as depicted on the right-side map.

Nations (UN)-based agencies. The climatological base period used is 1981–2010. Here, temperature and precipitation base periods are referred to interchangeably as average or normal.

In 2020, large parts of northern and equatorial Africa observed above-normal temperatures, while an area centered around the borders between northern Nigeria, southern Niger, and southwestern Chad experienced temperatures up to 1.5°C below normal. Most of South Africa, Namibia, and southern Angola also had below-normal annual temperatures (Fig. 7.19a).

Annual rainfall over the Sahel and eastern Africa, including border areas between Congo and the Democratic Republic of Congo, was above normal. The southern coast of West Africa south of 10°N and most of southern Africa (south of 10°S) received below-normal annual rainfall (Fig. 7.19b).

Extreme weather events and high climate variability were reported across the continent. These include heavy rainfall, extreme flooding, locust infestations, and land-falling tropical cyclones.

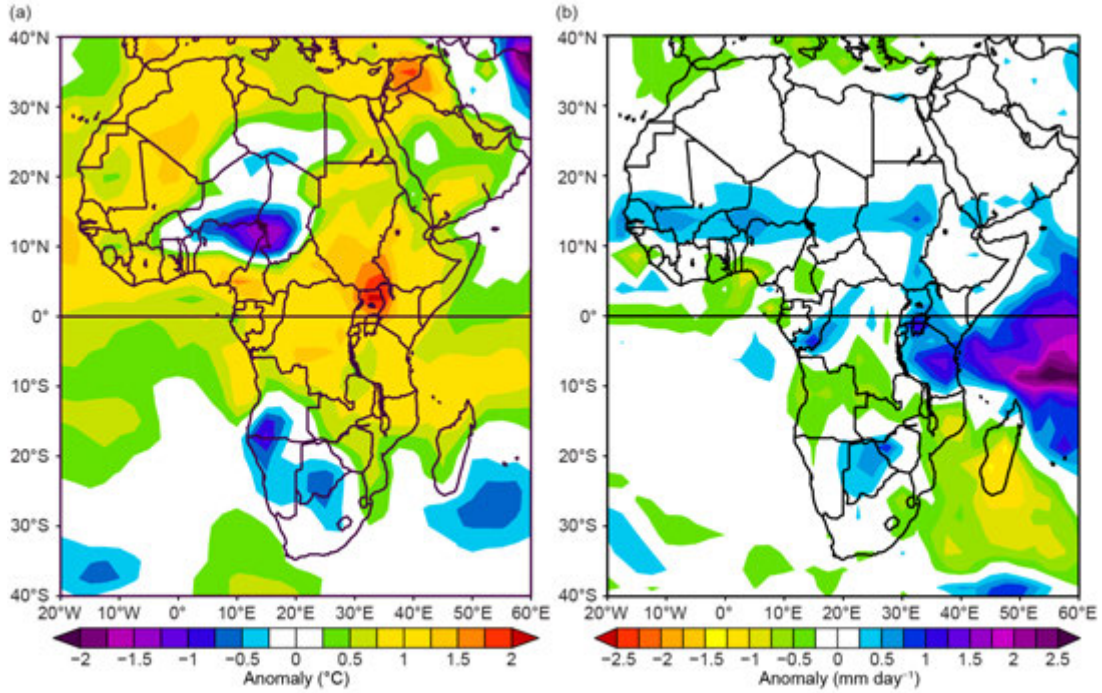

Fig. 7.19. Annual (a) temperature anomalies (°C) and rainfall anomalies (mm day^{-1}) 1981–2010 base period. (Sources: NCEP/NCAR and GPCP.)

1) North Africa—K. Kabidi, A. Sayouri, M. ElKharrim, and A. E. Mostafa

This region, which includes Morocco, Algeria, Tunisia, Libya, Mauritania, and Egypt, is characterized by arid and semi-arid climate. Precipitation over the region is highly variable both in space and time. Rainfall over western North Africa (comprising Morocco and northern and western Algeria) is generally of a short duration but at times intense. Mauritania in the south is characterized by arid to desert climate.

In 2020, above-normal annual mean temperatures dominated most of Mauritania, Morocco, Algeria, and Egypt, while southern Libya observed below-normal temperatures. Moroccan records show that annual temperatures across the country were about 1.2°C above normal, and precipitation was 32% below normal.

(I) TEMPERATURE

Winter (December–February) 2019/20 temperatures were above normal over most of Morocco (+0.9°C), northern Algeria, and Tunisia. Below-normal temperatures were observed over southern Morocco, Mauritania, southern Algeria, Libya, and Egypt (Fig. 7.20a). Temperatures of 1.5° to 2°C below normal dominated southern Libya and southwestern Egypt. Egyptian meteorological

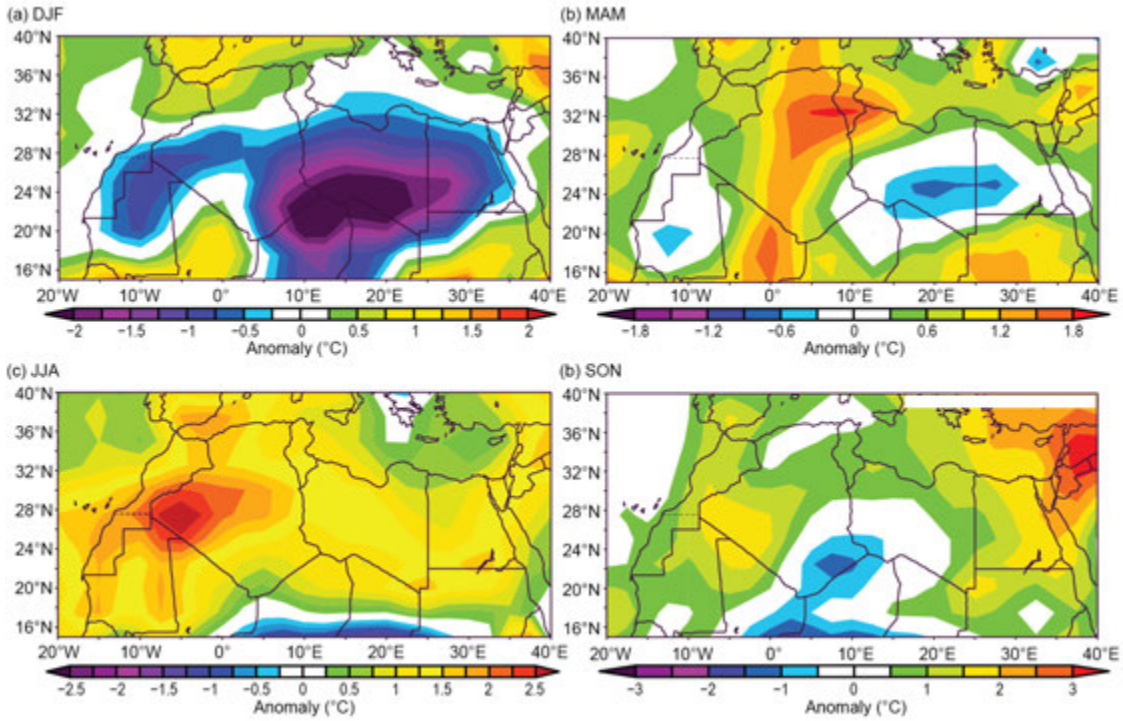

Fig. 7.20. North Africa seasonally averaged mean temperature anomalies (°C; 1981–2010 base period) for (a) DJF 2019/20, (b) MAM 2020, (c) JJA 2020, and (d) SON 2020. (Source: NOAA/NCEP.)

records show above-normal temperatures over the north of the country in December, but January temperatures were as much as 2°C below normal, particularly notable over the southern half. Still, warmth prevailed for the season: a new February temperature record of 3.8°C above normal was recorded at Port Said in northeastern Egypt.

In spring (March–May), temperature anomalies varied across the region (Fig. 7.20b). Above-normal temperatures were observed from northern Mali northward through Algeria, the northern half of Morocco, and Tunisia, while below-normal temperatures were observed to both the west and east of this region (Fig. 7.20b). Stations in the northern mountainous area of Morocco reported monthly maximum temperatures up to 6°C above normal in May (not shown). In Egypt, May was also exceptionally warm, with some stations reporting monthly average temperatures up to 4°C above normal.

Summer (June–August) was warmer than normal throughout the region (Fig. 7.20c). Southeastern Morocco, southwestern Algeria, and northern Mauritania exhibited mean temperature anomalies greater than +2°C. Temperatures exceeding 40°C were reported from Morocco during July and August. High daytime temperatures were also reported from Egypt. For example, 46°C was recorded at Kharga in central Egypt on 31 July. A continuation of above-normal temperatures across Algeria, Morocco, Mauritania, and the eastern half of Egypt (Fig. 7.20d) was observed in autumn (September–November); however, minimum temperatures over Morocco were below normal. Southwestern Libya and southeastern Algeria had mainly below-normal temperatures in autumn.

(II) PRECIPITATION

Generally, precipitation in 2020 was below normal with marked variability across the region and over time. Strong deficits, as much as 90% below normal, were reported from the Saharan region of Morocco. In winter, precipitation was below normal over most of the region (Fig. 7.21a). Morocco reported an overall precipitation deficit up to 56% below normal. Despite an overall winter rainfall deficit, some stations in Egypt reported heavy downpours in January.

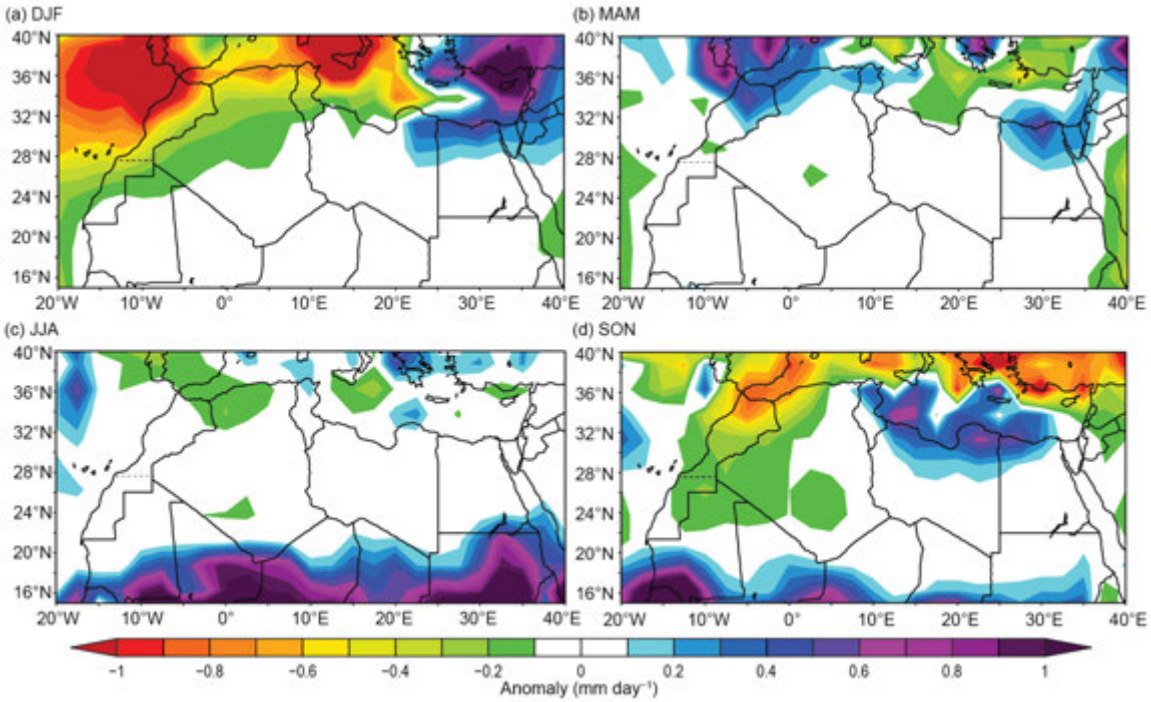

Fig. 7.21. North Africa seasonally averaged rainfall anomalies (mm day^{-1}; 1981–2010 base period) for (a) DJF 2019/20, (b) MAM 2020, (c) JJA 2020, and (d) SON 2020. (Source: NOAA/NCEP.)

Most of northern Morocco, northern Algeria, Tunisia, and Egypt received above-normal rainfall during spring, while the remainder of the region was near normal (Fig. 7.21b). Rainfall in April varied widely across Morocco, with stations reporting between 23% and 265% of normal. In May, Morocco reported 75% above-normal precipitation.

Summer is typically a dry season for North Africa, and the seasonal rainfall was near normal across the region (Fig. 7.21c). In contrast, above-normal rainfall was observed over most of the region during autumn (Fig. 7.21d). Rainfall between 20% and 100% of normal was reported in November from southern and central Morocco. Cairo, Egypt, reported 71 mm of rainfall on 14 November, the highest 24-hour total on record.

(III) NOTABLE EVENTS AND IMPACTS

Reports from Morocco indicated severe flood occurrences during March and November 2020 that caused property damage and cost human lives. Morocco also reported significant damages caused by forest fires that were associated with high summer temperatures, some of which exceeded 40°C in July and August. Similarly high temperatures were observed in Algeria. In Egypt, temperatures reached as high as 46°C at Luxor in the southeast.

2) West Africa—S. Hagos, W. M. Thiaw, Z. Feng, J. A. Ijampy, F. Sima O. Ndiaye, P-H. Kamsu-Tamo, A. Diawara, and S. Diouf

West Africa extends from the Guinea coast to about 20°N and from the eastern Atlantic coast to Niger. Climatologically, it consists of two distinct but inherently linked sub-regions: (1) The Sahel to the north from about 12°N to 17°N, spanning countries from Senegal and The Gambia in the west to Niger in the east and (2) the Gulf of Guinea to the south from about 4°N to 10°N encompassing the Guineas to the west along the east Atlantic coast and Nigeria and Cameroon to the east. The Sahel is semi-arid, while the Coast of Guinea region has a wet tropical climate. The West African monsoon season is associated with the latitudinal movement of a section of the active convective zone associated with the Saharan heat low in the north and its northerly reach limited by Harmattan winds from the northeast. The wet period runs from June through September.

Interannual variations of this seasonal rainfall are controlled by sea surface temperature (SST) fluctuations across the Gulf of Guinea the Mediterranean Sea, and the equatorial east Pacific. At longer timescales, the Atlantic multidecadal oscillation (Martin and Thorncroft 2014) and tropical Indian Ocean SSTs (Giannini et al. 2003) are known to modulate Sahel precipitation. Through most of summer 2020, El Niño–Southern Oscillation (ENSO) conditions were neutral and trending toward La Niña, while the Gulf of Guinea was slightly cooler than normal, both of which typically favor wet conditions over the Sahel region (Janicot et al. 2001; Zhang et al. 2021).

(l) TEMPERATURE

The highest mean annual temperatures, between 27°C and 30°C, were observed over the central and western Sahel, encompassing Senegal, southern Mauritania, Mali, and Burkina Faso (Fig. 7.22a). The area along the border of northeastern Senegal and Mauritania recorded mean annual temperatures exceeding 32°C. Mean annual temperatures were lower over the Gulf of Guinea region, between 24°C and 26°C, over the central areas from Guinea to Benin and much of Nigeria. Mean annual temperatures were about 27°C along the Gulf of Guinea coast and over the northern areas of Cote d'Ivoire, Ghana, Togo, and Benin, extending into northwestern and northeastern Nigeria. Maximum temperatures between 40°C and 46°C were reported from stations in Nigeria between March and June. About 80 days of maximum temperatures exceeding 40°C were reported from Nuguru, Nigeria, surpassing its previous record of 77 days in 2019.

Mean annual temperatures were above normal over much of the western and central Sahel and along the Guinea coast, with departures of about +0.5° to +1°C (Fig. 7.22b). Western Mali, southeastern Senegal, western Guinea, and coastal Gulf of Guinea registered mean annual temperatures above their 90th percentiles (not shown). Mean annual temperatures were below normal over northern Benin and Nigeria and in southern Niger by as much as –1.5°C (Fig. 7.22b), with the lowest temperatures in the past 30 years recorded in northeastern Nigeria. Annual maximum temperatures were overall below normal across the Sahel but exceeded 38°C in southern Mauritania, central Mali, and portions of northwestern and northeastern Niger (not shown). In the Gulf of Guinea, annual maximum temperatures ranged from 24° to 30°C (+1° to +3°C above normal). Annual minimum temperatures were above normal in much of West Africa, with the highest departures from the mean about +2° to +3°C over eastern Senegal and western Mali (not shown).

In 2020, April, May, and June were the warmest months in the Sahel, with readings exceeding 37°C in northern Mali and southern Mauritania, which was +1° to +2°C above normal for Mali and +3°C for southern Mauritania. Mean maximum temperatures exceeded 42°C in northern

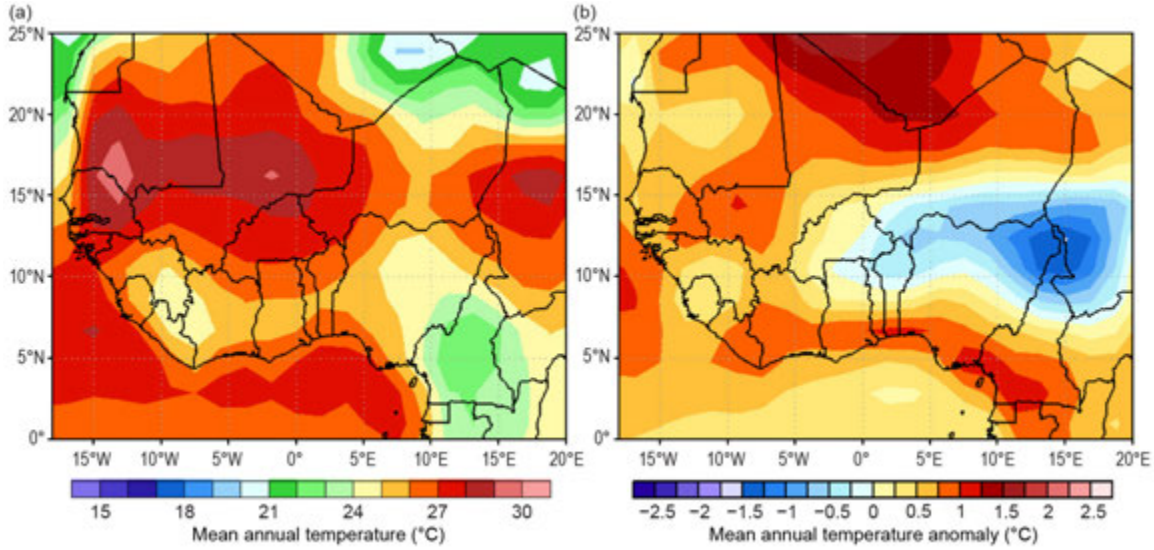

Fig. 7.22. Mean annual (a) temperature and (b) temperature anomalies (°C; 1981–2010 base period) for West Africa in 2020. (Source: NOAA/NCEP.)

Sahel during this time, while mean minimum temperatures were 22° to 26°C. Temperatures were also significantly above normal across West Africa during December 2020, with departures from the mean averaging +2° to +4°C across southeastern Senegal and the western areas of Mali and Burkina Faso. This was due to both elevated maximum and minimum temperatures during the month. Mean monthly temperatures were below normal over the central Sahel, including Burkina Faso, southern Niger, and northern Nigeria during July–September, with temperatures 24° to 26°C, about –1° to –2°C below the mean. The border between Niger and Nigeria observed its lowest mean July temperatures over the past 30 years.

(II) PRECIPITATION

Annual rainfall ranged between 1000 mm and 2000 mm over the Gulf of Guinea region with the areas of maximum rainfall along the western Guinea coast and over southeastern Nigeria (Fig. 7.23a). Rainfall decreased northward, ranging from 300 to 1000 mm in the southern and central Sahel. The climatologically dry areas of the Sahel registered rainfall between 50 mm and 300 mm (Fig. 7.23a). Consistent with the trend of the last 2 decades and the prominence of the Atlantic Multidecadal Oscillation featuring a warm tropical North Atlantic, annual rainfall was once again above normal across the Sahel (Fig. 7.23b; e.g., Mohino et al. 2011), with surpluses of 100–150 mm from Senegal eastward to Niger and exceeding 150 mm over the western areas of Mali and Niger (Fig. 7.23b). These large rainfall departures placed much of the Sahel above its 90th percentile, with west central Senegal and southern Niger recording rainfall above the 95th percentile. Departures of +50 to +100 mm above normal were observed across the northern Sahel.

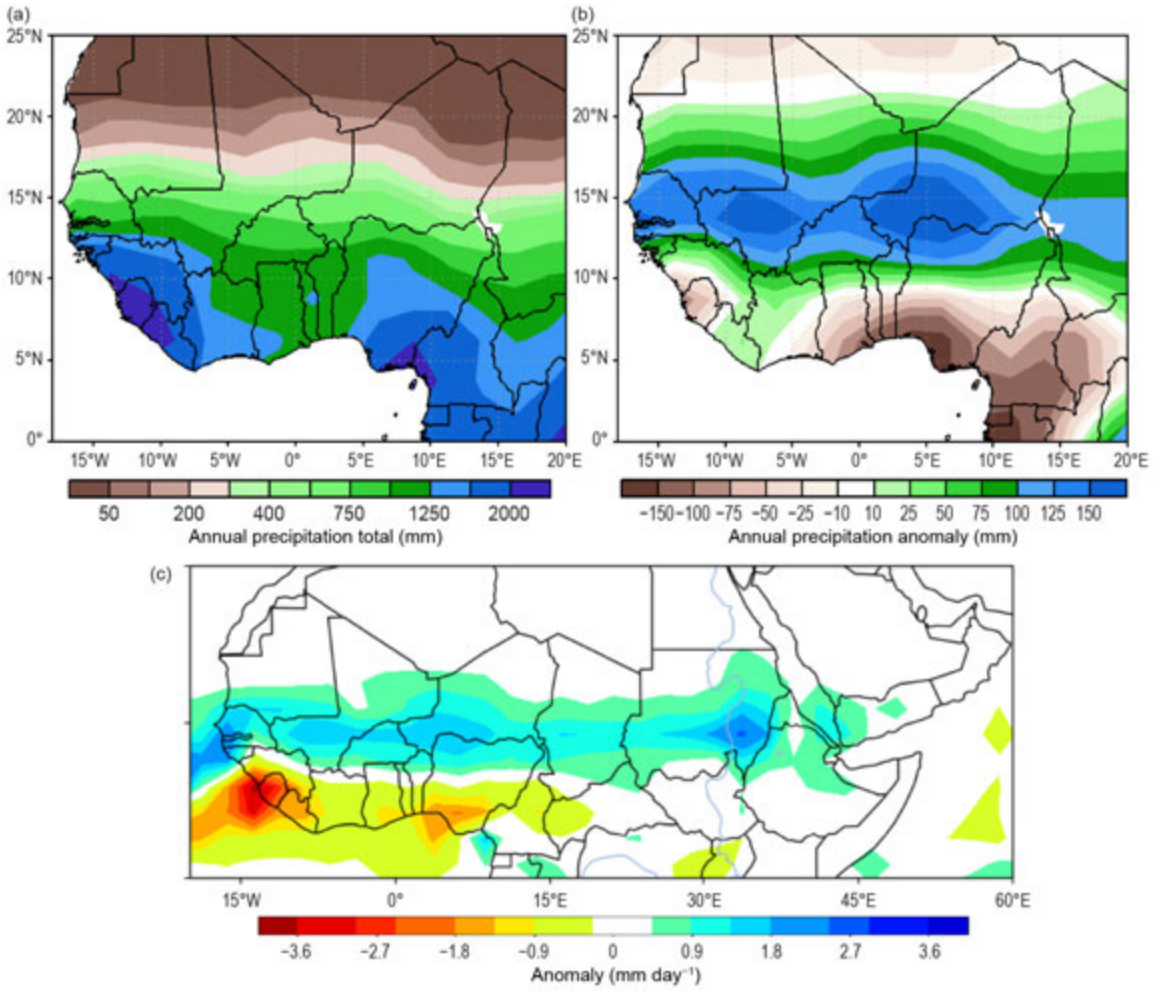

Fig. 7.23. Cumulative annual (a) precipitation totals (mm), (b) annual precipitation anomalies (mm), and (c) Jun–Sep precipitation anomalies (mm day^{-1}) for West Africa in 2020. (Source: NOAA/NCEP and GPCP.)

Over the Gulf of Guinea region, annual rainfall was much below normal along the eastern Guinea coast, with deficits as much as 150 mm below the mean along coastal Nigeria (Fig. 7.23b). Rainfall deficits were 50–150 mm farther inland in the southern areas of Ghana, Togo, Benin, and Nigeria. Mean annual rainfall was slightly below normal over southern Guinea and Sierra Leone and was slightly above normal over Liberia and the northern Gulf of Guinea region.

In the Sahel, rainfall during June–September accounts for much of its annual cumulative rainfall. Totals ranged from 100 to 500 mm in the northern Sahel (just north of 15°N) to 500–1000 mm in the central areas (12°–15°N) to over 1200 mm in the areas of maximum precipitation, including the western Guinean coast. These amounts corresponded to above-normal rainfall across the Sahel, with moisture surpluses exceeding 200 mm across the southern Sahel from Senegal eastward to Niger. The western areas of Niger and Senegal registered rainfall above their 95th percentiles during July–September. Precipitation was significantly below normal over the Sahel in June when much of the precipitation was limited to coastal regions. The situation improved and wetter conditions were observed through the rest of the season for much of West Africa with somewhat drier-than-normal conditions along the Guinean coast (Fig. 7.23c). In Nigeria, 1-day rainfall totals of at least 100 mm were observed in different parts of the country. The city of Yelwa recorded the highest daily rainfall value of 176.2 mm in August followed by Ilorin (160.0 mm), Lafia (152.0 mm), Jalingo (148.4 mm), Bauchi (133.2 mm), and Ibadan (132.0 mm). The month of September contributed significantly to rainfall surpluses in the western Sahel, with over 300 mm (100 mm above the mean) over Senegal, following a drier-than-normal August.

In the Gulf of Guinea region, rainfall was significantly above normal along the western Guinea coast during March–May and October–December, with surpluses of about 100 mm and 200 mm, respectively. In contrast, July–September departures were about 200 mm below the mean in the southern areas and reached 400 mm below the mean over Sierra Leone and Liberia.

(III) NOTABLE EVENTS AND IMPACTS

Extremely heavy rains in West Africa caused many of the countries to face their most devastating floods in recent history. Heavy downpours with accumulations near 100 mm in June soaked southern Niger, resulting in floods across the sub-region. The towns of Maradi and Tahoua were the hardest hit, with 13,667 and 4173 people affected, respectively, according to the Ministry of Humanitarian Action and Disaster Management. As of 21 July, there were 14 fatalities and more than 35,000 people affected and over 3400 houses destroyed, with loss of livestock and crops. Sustained torrential rains in August and September (the station at Gaya in southwestern Niger recorded 130 mm from 23–29 August) caused the Niger River to overflow, shutting down the capital, Niamey. An additional 170 mm between 31 August and 17 September worsened the flood situation as the Niger River rose to approximately 8 m, well above the 6.2-m alert level. According to the government of Niger, as of the end of September, the floods affected about 400,000 people, caused 65 deaths, and severely damaged or destroyed 32,000 houses and 6000 ha of farmland. On 24 August, floods killed three people and displaced 1500 residents in N'Djamena, Chad, according to the International Organization for Migration.

Exceptionally heavy rains across northern and southern Nigeria in late September and early October resulted in widespread floods, compounding the risks to human health and food security. The Benue and Niger Rivers overflowed and caused severe floods in many states, including Kebbi, Niger, Kwara, Kogi, Edo, Anambra, Delta, Kano, Jigawa, Rivers, Bayelsa, and Adamawa. According to the Red Cross, these floods were a result of heavy rainfall in river catchments, coupled with the release of dams in the neighboring countries of Niger, Cameroon, and Benin, which all experienced flooding. In Nigeria, at least 40 people lost their lives. Jigawa State had its worst flood in 32 years, according to the Jigawa State Emergency Management Agency and the International Federation of the Red Cross and Red Crescent Societies (http://floodlist.com/africa/nigeria-floods-october-2020).

On 8 June, a windstorm and heavy rainfall affected parts of Borno State in northeastern Nigeria, causing damage to shelters in several Internally Displaced People's (IDP) camps, according to the International Organization for Migration. The severe weather also affected around 1200 people and damaged a total of 240 shelters in IDP camps in Jere, Damboa, Konduga, and Maiduguri. The heaviest rainfall occurred in Damboa, Konduga, and Maiduguri, resulting in damage to about 60 shelters (Floodlist, 11 June 2020). Yobe state was also affected by the windstorm.

In early June, torrential rain in Accra, Ghana, led to major flooding and two fatalities, according to the National Disaster Management Organization of Ghana. On 18 June, heavy rains in Abidjan and environs, Ivory Coast, caused flash flooding and landslides that killed 13 people, according to National Office Civil Protection of Ivory Coast.

In Burkina Faso, the northeastern town of Dori registered 298 mm between 30 July and 11 August, resulting in eight fatalities, according to the government of Burkina Faso. The floods were so widespread between July and September that the government declared a state of emergency and released $9 million (U.S. dollars) to help flood victims and repair damaged public infrastructure.

In Mali, persistent heavy rains in June and July caused massive flooding in the south. The towns of Mopti and Sikasso were among the hardest hit, with Sikasso receiving cumulative rainfall of 259 and 230 mm in June and July, respectively. Mopti registered 390 mm in July, including 145 mm during 3–5 July and 78 mm during 30–31 July. According to the UN Office for the Coordination of Humanitarian Affairs, the floods affected more than 13,000 people.

In Senegal, the northern town of Linguere—a climatologically dry area—registered 237 mm during 1–9 September. The rains were widespread across the country, forcing the government to declare a state of emergency on 5 September. The Senegalese Red Cross Society indicated that the unprecedented rains decimated homes and flooded streets, especially in the capital city of Dakar, with more than 3000 people affected.

In The Gambia, as in the rest of the Sahel region, monsoon rains started late but persisted well past the climatological end of the season. The Gambia experienced its heaviest downpour in October. According to The Gambia Red Cross Society and the National Disaster Management Agency, severe flooding occurred in some parts of the country following heavy downpours on 13 October, especially notable within the Kanifing Municipality and West Coast Region. The floods caused major property damage and destruction, displacement, and health hazards associated with flooding. Some farmlands were washed away by the rains, particularly in the North Bank Region. The rainy season was also marked by significant high winds that caused major damage to homes.

3) Central Africa—W. M. Thiaw and P-H. Kamsu-Tamo

Central Africa features a unique climate system marked by a strong spatial variability as it spans a wide area of Africa across both the Northern and Southern Hemisphere (NH; SH). The region analyzed in this section extends from the southern tip of the Democratic Republic of Congo (DRC) northward into central Chad. Longitudinally, the region extends from about 5°E to about 35°E. This analysis includes Cameroon, Chad, Central Africa Republic (CAR), DRC, Congo, Gabon, Equatorial Guinea, and São Tomé and Príncipe.

(I) TEMPERATURE

The mean annual temperature was between 21°C and 25°C across much of the region, except for southern Chad, where temperatures approached 27°C and maximum temperatures were up to 35°C. However, the relatively high temperatures were 2° to 3°C below normal in some localities in southern Chad. Mean temperatures along coastal Gabon and Congo and over northeastern DRC averaged about +0.5° to +1°C above the mean, placing the temperatures in the 90th percentile. Temperatures in local areas in central DRC ranked as high as the 99th percentile (Fig. 7.24a). The months of March–May were the warmest in the northern sector of the region. Mean temperatures

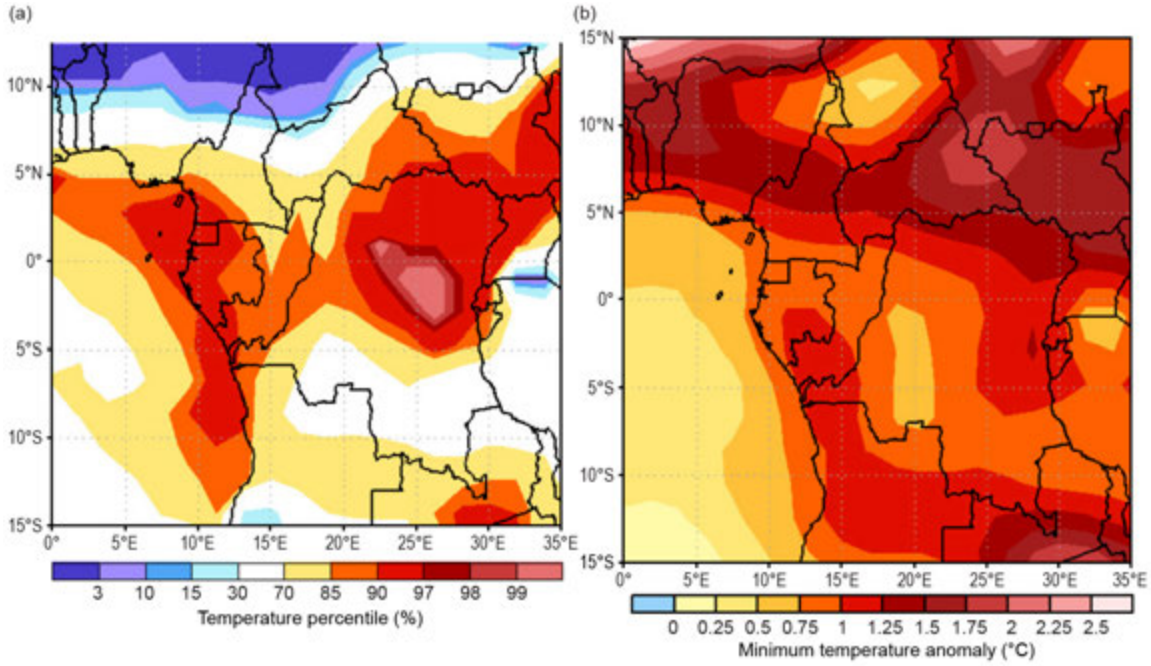

Fig. 7.24. Annual (a) temperature percentiles (%) and (b) minimum temperature anomalies (°C) for Central Africa in 2020. 1981–2010 base period. (Source: NOAA/NCEP.)

were 28° to 30°C across CAR and northern Cameroon. While the temperature exceeded 35°C in some localities in southern Chad in April, this was still about –1°C below the mean. Temperature departures were also –1° to –2°C below the mean in northern Cameroon. Though mean temperatures were relatively low in northern Cameroon and CAR in December, around 20° to 25°C, this area had the highest positive anomalies of about +2° to +3°C above the December mean, placing this month in the 99th percentile. Maximum temperatures for this region in December exceeded 30°C, more than +2°C above the mean and in the 95th percentile. Northern DRC also had maximum temperatures in the 99th percentile during December. Annual minimum temperatures were above normal across the region (Fig. 7.24b). Departures from normal were highest in northeastern DRC, CAR, and northern Cameroon. Minimum temperatures were above normal from January to May, above the 95th percentile in most areas, and were generally normal to below normal from June through November. In December, minimum temperatures were +2° to +3°C above normal in the northern sector encompassing CAR, Cameroon, and southern Chad to end the year.

(II) PRECIPITATION

The climate of Central Africa exhibits seasonality at both the north and south ends of the region. The rainfall pattern is closely related to the north–south movement of the peak convective zone. Rainfall is unimodal in the northern areas of the region and marked with dry conditions during the NH autumn, winter, and spring months of November through April and a return to the rains during the NH summer. The southern areas of the region are dry during the NH summer months and wet during the NH autumn through winter and early spring seasons. The central areas of the region around the equator receive rainfall year-round. The area of maximum annual rainfall is located along coastal Cameroon, with totals exceeding 2000 mm. On average, rainfall amounts range from 1200 mm over the southern tip of DRC and the southern areas of CAR and Cameroon to 2000 mm across much of DRC, Congo, Gabon, and southern Cameroon (Fig. 7.25a). Annual rainfall totals are generally lower over southern Chad with a steep north–south gradient indicated by about 200 mm rainfall amounts in the central areas of Chad to about 1000 mm in the southern tip (Fig. 7.25a).

During 2020, three areas of maximum annual rainfall over southwestern Cameroon and north-central DRC emerged with totals exceeding 2000 mm (Fig. 7.25a). Most areas in northern DRC received rainfall near 2000 mm, while totals ranged from 500 to 1500 mm in the south–north

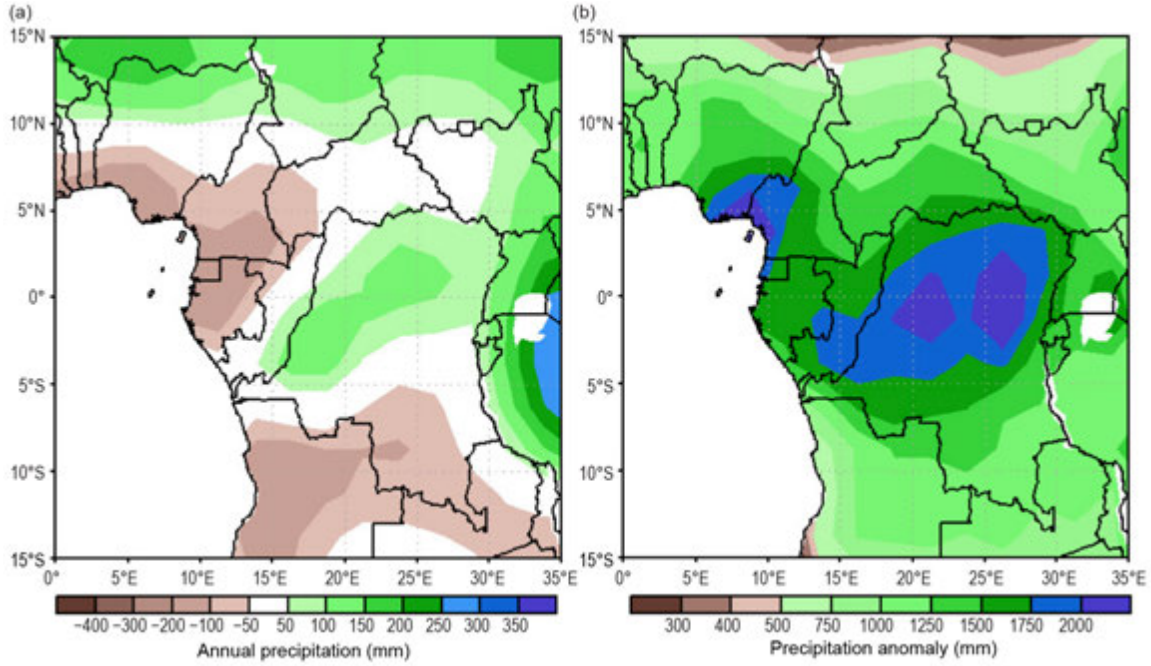

Fig. 7.25. Annual (a) cumulative precipitation (mm) and (b) precipitation anomalies (mm) for Central Africa. 1981–2010 base period. (Source: NOAA/NCEP.)

direction from southern to northern DRC and in the north–south direction from southern Chad to northern DRC and Congo. Rainfall was below normal over western CAR, the southern half of Cameroon, Equatorial Guinea, and much of Gabon, with deficits of 100 to 200 mm (Fig. 7.25b). Annual totals ranked below the 5th percentile along the border between CAR and Cameroon, making 2020 the third-driest year since the start of the record in 1979. Part of the northern DRC observed rainfall about 100–200 mm above normal, placing this area above the 70th percentile. Tshopo Province in northern DRC recorded its second-highest rainfall amount since 1979.

Rainfall was significantly below normal over much of Cameroon and western CAR during the NH summer, with deficits reaching 150 mm in August, in the 5th percentile, making August 2020 one of the driest in this area on record. Rainfall was also below normal over the southern areas of DRC during the NH winter with a 5th-percentile ranking for the January–March period. Totals averaged 300–500 mm, with rainfall deficits more than 150 mm below the mean. Rainfall was much above normal in Chad during July–September, with departures from the mean exceeding 150 mm and above the 80th percentile. A similar pattern prevailed in the central sector of the region during the NH autumn, with areas in east central DRC near the Rwandan border registering about 1000 mm during October–December. The month of November contributed about 500 mm, ~150 mm above the mean and in the 95th percentile, making this month one of the wettest Novembers in the historical record.

(III) NOTABLE EVENTS AND IMPACTS

Heavy rainfall exceeded 135 mm in the South Kivu Province, eastern DRC, during 16–17 April according to the NOAA/CPC satellite rainfall estimates version 2 (RFE2). This deluge triggered extensive flooding, affecting nearly 75,000 people with 40 fatalities and 6000 households displaced, according to the U.S. Agency for International Development.

About 100 mm of rain on 1 October soaked the town of Sake near Lake Kivu in the North Kivu Province of eastern DRC, causing severe flooding and overflowing banks of the Mutahyo River. The provincial government reported at least 11 fatalities, with houses washed away and school and health buildings damaged. Bridges were destroyed and roads washed out, cutting connections between Sake and the provincial capital, Goma.

Heavy rainfall exceeding 120 mm, accompanied by strong winds, on 30 November led to severe flooding in the city of Mbanza-Ngungu in Kongo-Central Province in DRC, causing 13 fatalities and several more injuries, along with destroyed or severely damaged homes.

4) East Africa—L. Chang'a, E. Bekele, W. M. Thiaw, C. Mutai, A. Teshome, P. Nying'uro, J. Sebaziga, H. Mtongori, R. Barakiza, P. King'uza, and L. Nyembo.

East Africa, or the Greater Horn of Africa (GHA), spans the equator and extends between 10°S–20°N and 20°–50°E. Its northern sector comprises Sudan, South Sudan, Ethiopia, Eritrea, Djibouti, and the northern two-thirds of Somalia. Southern Somalia, Kenya, northern Tanzania, Uganda, Rwanda, and Burundi are in its equatorial sector, while the southern sector encompasses central and southern Tanzania. The region has a complex terrain, with elevation ranging from about 160 m below sea level at Ethiopia's northern exit of the Rift Valley to more than 5000 m above sea level at glaciated Mount Kilimanjaro. The complex topographical features of the region are further typified by the presence of large lakes (e.g., Lake Victoria). The complex topography coupled with large-scale forcing factors including the peak moist convective zone (traditionally referred to as the intertropical convergence zone), ENSO, and Indian Ocean dipole are largely responsible for stronger spatial and temporal variability of climate patterns. The lower-latitude regions, including Kenya, Uganda, southern Ethiopia, and southern parts of Somalia and northern Tanzania, experience two rainy seasons during March–May (MAM) and October–December (OND). Central, western, and northern Ethiopia, Sudan, and South Sudan have a single dominant rainy season during June–September (JJAS). Central and southern Tanzania experiences a single dominant rainy season during November–April.

(I) TEMPERATURE

Annual mean temperatures over much of the Sudan, Somalia, Djibouti, Eritrea, and parts of eastern Ethiopia exceeded 30°C, while annual mean temperatures over most of central Ethiopia were less than 22°C (Fig. 7.26a). However, anomalously higher mean annual temperatures were observed western Ethiopia, Kenya, and Uganda (Fig. 7.26a). Annual mean maximum temperatures reached 42°C locally in eastern Sudan and ranged between 35°C and 40°C in other parts of the country. Eastern Kenya and much of Somalia, Djibouti, and Eritrea had annually averaged maximum temperatures between 35°C and 38°C, while it was less than 30°C over western Ethiopia and in the Lake Victoria region.

Meteorological station data indicate that most of the region experienced above-normal temperatures; Addis Ababa Bole International Airport in Ethiopia, for example, reported an annual temperature that was 1.3°C above normal (Fig. 7.26b). Overall, the mean annual temperature for East Africa exhibits a warming trend, with 2020 tied with 2017 as the third-warmest year on record (Fig. 7.26c). Spatially, the annual mean temperature was among the top 5% warmest since 1981 over several locations, including South Sudan, much of Ethiopia, Uganda, and Kenya (Fig. 7.26b).

Anomalously warm temperatures were observed across most of the region between March and December 2020, being most pronounced in central and northern Ethiopia. During December–February (DJF) 2019/20 and JJAS, mean temperatures were below normal over southern Sudan, northern South Sudan, and northeastern and southeastern Ethiopia. Temperatures were above normal in western Ethiopia extending southward into the Lake Victoria region, including western Kenya, Uganda, Rwanda, Burundi, and western Tanzania. Temperatures were above normal over much of East Africa during MAM and OND. These observations indicate a non-uniform temperature dynamic in the region during 2020 that may be driven in part by complex and diverse topographical features.

Maximum temperatures were above normal over much of the region, with the highest anomalies located over western areas of Ethiopia and Kenya along the borders of Uganda, South Sudan, and Sudan. The lowest annual mean minimum temperatures (Tmin) of 2020 were observed over

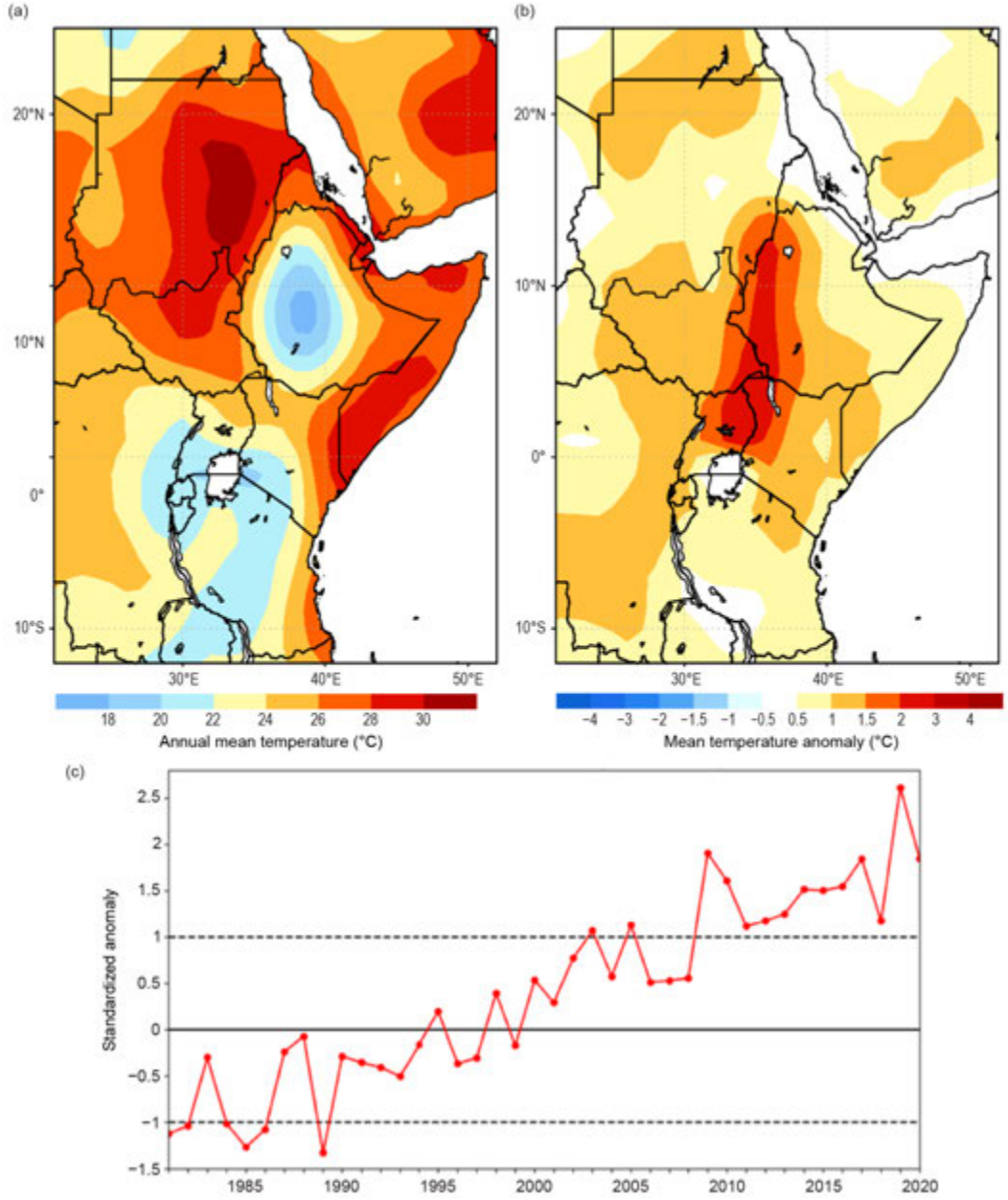

Fig. 7.26. Annual (a) mean temperature (°C) and (b) mean temperature anomalies (°C) for East Africa. 1981–2010 base period. (c) Annual standardized temperature anomaly time series for the period 1981–2020. (Sources: NOAA/NCEP and NOAA CPC.)

western Ethiopia (<8°C) and were between 10°C and 20°C across much of the rest of Ethiopia, southern Uganda and Kenya, and much of Tanzania, except for the coastline (not shown). Mean Tmin were 20°–25°C over much of eastern Sudan, South Sudan, and Somalia. Overall, the Tmin was above normal across the region.

(II) PRECIPITATION

Annual rainfall surpassed 1000 mm across western Ethiopia, portions of South Sudan, much of Uganda, Rwanda, Burundi, western Kenya, and much of Tanzania (Fig. 7.27a). Central and eastern Kenya, central Ethiopia, southern Sudan, and northern South Sudan received rainfall between 600 mm and 1000 mm. Totals were less over northern Sudan, Eritrea, Djibouti, and northern Somalia, with rainfall estimates ranging between 50 mm and 600 mm. Rainfall was significantly above normal over eastern Tanzania, southwestern Kenya, where surpluses exceeded 300 mm (Fig. 7.27b). Rainfall was above normal over much of southern and northwestern Kenya and portions of east central Sudan, with totals averaging 150–300 mm above the mean in eastern

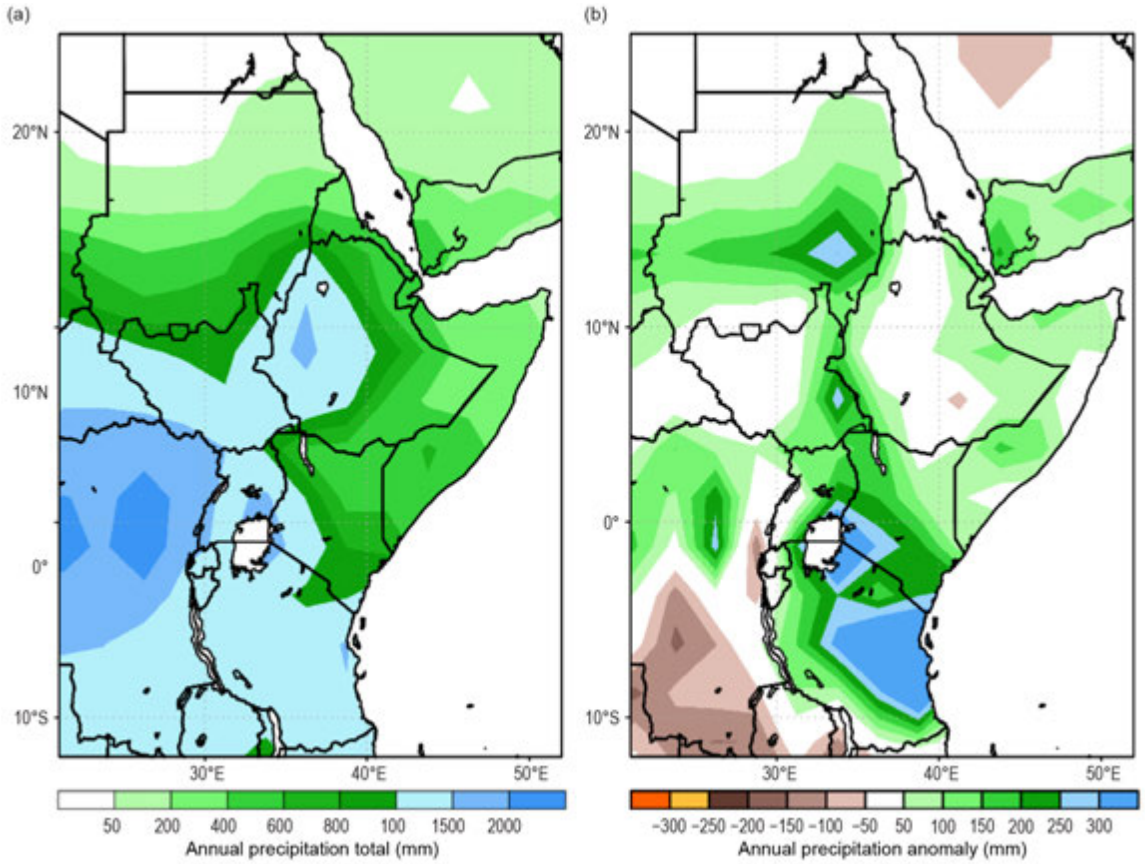

Fig. 7.27. Annual (a) cumulative precipitation (mm) and (b) precipitation anomalies (mm) for East Africa in 2020. 1981–2010 base period; GPCP data. (Source: NOAA/NCEP.)

Uganda and southeastern Sudan. The climatologically drier areas of Somalia, Djibouti, eastern Eritrea, and northern Sudan registered 50–100 mm above the mean. Annual rainfall amount exceeded the 90th percentile over central Tanzania, southwestern Kenya, and much of Sudan. Overall, 2020 was the wettest in the historical record since 1981 in the Lake Victoria region, with totals exceeding 1.5 standard deviations above the mean.

Most of the region recorded normal to above-normal rainfall during all seasons; excessive rainfall was more pronounced during MAM over Burundi, Kenya, Rwanda, Uganda, and Tanzania (not shown). Most of Burundi and Kenya recorded 125%–150% of their long-term means during MAM, while Addis Ababa Bole (Ethiopia) recorded 140% of its normal. Some parts of northwestern Kenya, particularly around Turkana County, recorded more than 200% of its long-term mean precipitation. In Rwanda, both MAM and OND rainfall seasons were relatively higher than the long-term average for most observing stations. In Tanzania, observed rainfall was 150%–175% of normal during November–April and 125%–150% of normal during MAM. Higher rainfall totals exceeding 175% of the long-term average were observed over central and some parts of southwestern Tanzania. Rainfall was also much above normal over Sudan during JJAS, with anomalies exceeding 200 mm locally in the southeast near the border with Ethiopia; rainfall totals across the eastern and central sectors of the Sudan were among their highest (top 5%) since the start of the record in 1981 (Fig. 7.27b).

(III) NOTABLE EVENTS AND IMPACTS

On 23 March, 122.5 mm of rainfall was recorded at the Kilwa meteorological station in Tanzania, the highest on record in this station for the month of March and second highest on record since its record began in 2005. Nearly all dams that supply hydroelectric power in Tanzania were flooded beyond their water-holding capacity such that they were forced to discharge.

April brought extremely heavy rains to East Africa. The most severe downpours occurred during 14–20 April and triggered widespread flooding and landslides in Ethiopia, Somalia, Rwanda, and Burundi. According to NOAA/CPC satellite RFE2, rainfall totals exceeded 160 mm in portions of Rwanda and Burundi during this 7-day period, with more than 200 mm recorded over northern Rwanda. The U.S. Embassy in both countries declared a state of emergency. According to U.S. Agency for International Development and the Government of Rwanda Ministry of Emergency Management, the floods destroyed more than 2000 houses and more than 3500 ha of crops. An estimated 62,300 people were in need of immediate food assistance. There were 113 fatalities and more than 100 injuries due to the extreme rains. In western Burundi, the floods resulted in an overflow of the Ruzizi River, affecting an estimated 45,000 people. Over southern Ethiopia and southern Somalia, rainfall totals during the same period exceeded 200 mm, resulting in flooding with eight fatalities and infrastructural damage, especially in the Gamo region of southern Ethiopia.

On 27 April, 80 mm of rain led to flash flooding that swept through the city of Qardho (also known as Gardo) in the northeastern Bari region of Somalia. At least six fatalities were reported, while hundreds of families lost their homes.

During 2020, extreme events including floods, heavy rainfall, and landslides led to a total of 341 fatalities and more than 13,500 damaged houses in Rwanda, while 7000 houses were damaged and more than 50,000 people were displaced in Burundi. During the OND rainy season in Kenya, there were approximately 300 fatalities and more than 150,000 households were affected due to heavy rainfall and flooding. During the JJAS rainfall season in Ethiopia, more than one million people were affected and nearly 300,000 were displaced due to flooding. In Tanzania, 40 deaths and the destruction of more than 2450 houses were reported due to heavy rainfall and flooding. Similarly, the overflow of the Nile River in Khartoum and the surrounding areas in the Sudan caused extensive damage in property and loss of lives. Elagib et al. (2021) reported that the 2020 floods in the Sudan caused the loss of 417 human lives and affected up to two million people. The flood was associated with heavy rainfall over Ethiopia and upstream Nile basin countries (Elagib et al. 2021).

A widespread desert locust infestation from 2019 into 2020 impacted the equatorial and northern sectors of East Africa, as heavy rains and prevailing winds were favorable for breeding and movement across the region. A large swarm of locusts spread across 14 Kenyan counties and later spread into Ethiopia, northeastern Somalia, Uganda, and South Sudan, while some groups reached parts of northern Tanzania. The massive infestation resulted in significant crop damage across eastern Africa. According to an early assessment by the UN Food and Agriculture Organization, desert locusts caused the destruction of nearly 200,000 ha of cropland and more than 1.2 million ha of pasturelands, as well as the loss of more than 350,000 metric tons of cereal, resulting in one million people in need of food aid in Ethiopia. The World Bank estimated that locust-related losses, including damage to crops, livestock, and other assets, may be as much as $8.5 billion (U.S. dollars) for the East Africa region and Yemen.

5) Southern Africa—A. C. Kruger, C. McBride, M. Robjhon, and W. M. Thiaw

Southern Africa comprises the sub-region located to the south of 5°S and includes Angola, Namibia, Zambia, Botswana, Zimbabwe, Malawi, South Africa, Lesotho, Eswatini, and Mozambique. The region has two main seasons—the wet season, which spans from November of the previous year to April, and the dry season, which lasts from May to October.

(I) TEMPERATURE

Annual mean temperatures were above normal over the northeastern region, with anomalies of about +0.5° to +1°C across eastern Zambia, northern Zimbabwe, Malawi, and northern Mozambique. According to the historical record since 1979, annual temperatures ranked above the 90th percentile in central Zambia, northern Zimbabwe, and northern Mozambique. In contrast,

near- to below-normal temperatures dominated the western and central sectors, including southern Angola, northern Namibia, Botswana, and parts of central South Africa. Southern Angola and northwestern Namibia reported negative anomalies between –1°C and –2°C; this was below the 5th percentile in northwestern Namibia.

Annual maximum temperatures were above normal over northeastern Angola, Zambia, Malawi, northern Mozambique, and parts of western South Africa and southern Mozambique (Fig. 7.28a), while the annual minimum temperature was 0.5° to 2.5°C below normal over southern Angola and northern Namibia (Fig. 7.28b). South Africa reported its fifth-warmest year in the 70-year record, about 0.5°C above normal, based on the data of 26 climate stations (Fig. 7.28c). South Africa is warming at an average rate of +0.16°C per decade, statistically significant at the 5% level.

During DJF 2019/20, mean temperatures were above normal over northern Angola, central Zambia, Zimbabwe, northeastern South Africa, and western and southern Mozambique (not shown). Below-normal temperatures were observed over Botswana and central South Africa. While the average maximum temperature was well below normal over Botswana and central South Africa, it was above normal over a wide area extending from Angola and eastern Namibia eastward to Mozambique.

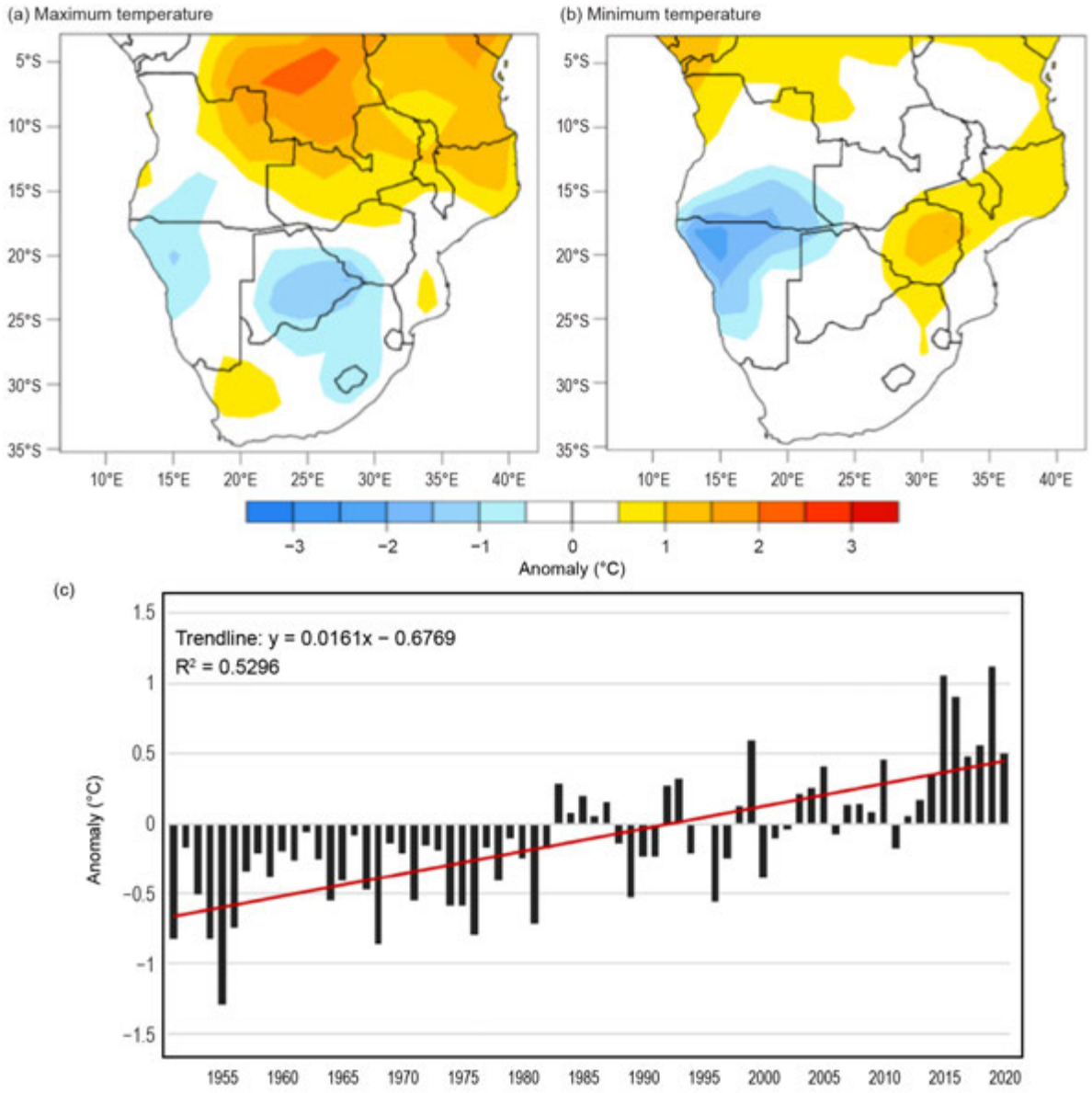

Fig. 7.28. Annual (a) maximum and (b) minimum temperature anomalies (°C; CDAS data). (c) Annual temperature anomaly time series (°C) for the period 1951–2020. Red line indicates linear trend. (Sources: NOAA/NCEP and South African Weather Service.)

During MAM, above-normal temperatures persisted over northern Angola, Zambia, eastern Zimbabwe, Malawi, and parts of northern and southern Mozambique (not shown). During the dry and cold season of JJA, mean temperatures averaged well below normal, with negative anomalies of more than –1.5°C across Angola, northern Namibia, and central South Africa (not shown).

Early during September–November (SON) season, well above-normal temperatures returned over eastern Zambia, Malawi, northern Zimbabwe, and northern Mozambique, while below-normal temperatures lingered in southern Angola and western Namibia (not shown). Maximum temperatures ranked above the 99th percentile over southeastern Zambia, Malawi, and northern Mozambique.

(II) PRECIPITATION

Annual rainfall totals near or above 1000 mm were reported over the northern sector, while accumulations of less than 600 mm were observed across the western region during 2020 (Fig. 7.29a). Rainfall for the year was below normal across much of southern Africa, including Angola, central Zambia, Malawi, northern Mozambique, and western and eastern South Africa, Eswatini, and southernmost Mozambique (Fig. 7.29b). In contrast, annual rainfall was above normal over the central sector, including Botswana, Zimbabwe, and central South Africa. Large rainfall deficits exceeding 250 mm were observed over northeastern Mozambique (Fig. 7.29b). Conversely, surpluses surpassed 250 mm over northeastern Botswana and western Zimbabwe, ranking between the 95th and 99th percentiles, based on the 42-year record.

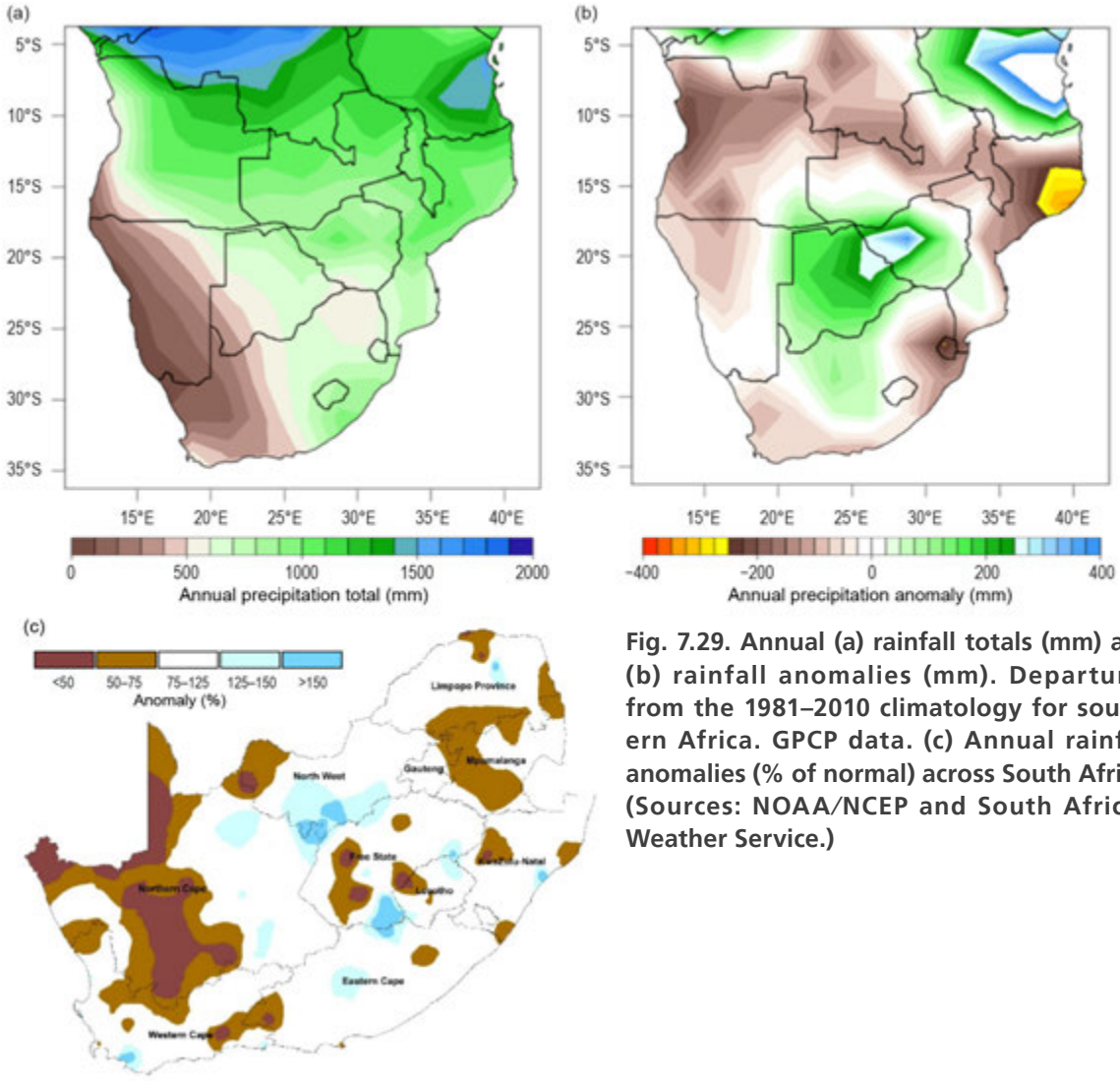

Fig. 7.29. Annual (a) rainfall totals (mm) and (b) rainfall anomalies (mm). Departures from the 1981–2010 climatology for southern Africa. GPCP data. (c) Annual rainfall anomalies (% of normal) across South Africa. (Sources: NOAA/NCEP and South African Weather Service.)

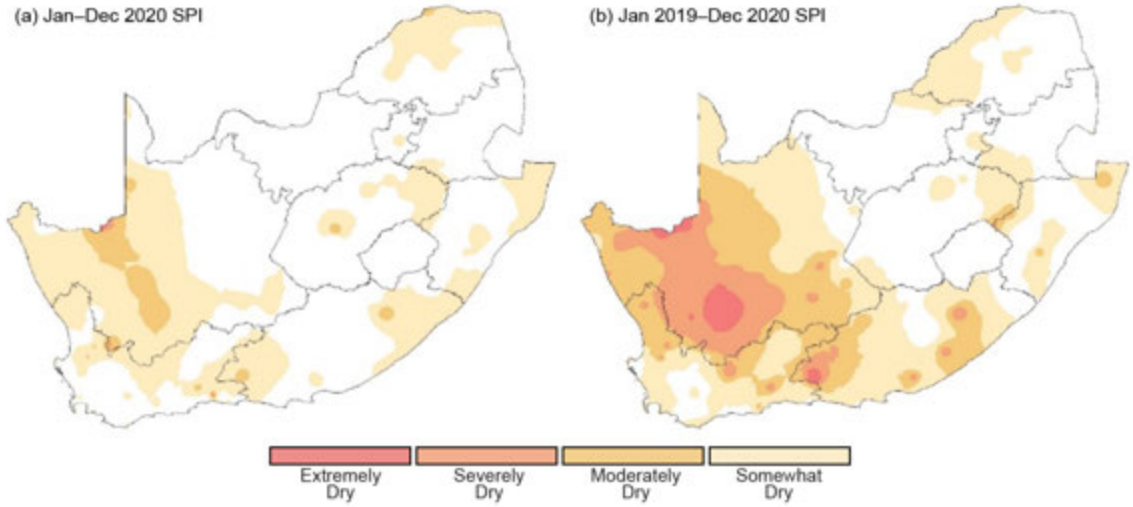

Fig. 7.30. (a) 12-month and (b) 24-month SPI maps for South Africa ending Dec 2020 (Source: South African Weather Service).

The most significant feature of the rainfall during 2020 in South Africa was the persisting dry conditions in western South Africa, with a substantial region receiving less than 50% of its normal precipitation (Fig. 7.29c; see also *Notable events and impacts*). The central interior also shows isolated areas that remained dry. However, the area of South Africa experiencing drought decreased over the year, where some regions received adequate precipitation in the early austral summer rainy season of 2020/21. The remainder of the country received near-normal rainfall. No significant area of the country received substantially above-normal rainfall, except for southern parts of the North–West Province. The 12-month standardized precipitation index (SPI; Fig. 7.30a) for South Africa ending December 2020 indicates that the western interior was somewhat to moderately dry in places; however, the 24-month SPI (Fig. 7.30b) shows that the long-term effects of the drought persist, with extensive regions showing moderate to severely dry conditions over the last 2 years.

During DJF, wetter-than-normal conditions were experienced over western Angola, Botswana, central and northern South Africa, Malawi, and northern Mozambique (not shown), while below-normal rainfall extended over Zambia and northern Zimbabwe to central Mozambique.

During MAM, wetter-than-normal conditions persisted over Botswana, western Zimbabwe, and central South Africa. In contrast, drier-than-normal conditions developed over Angola, Malawi, and Mozambique (not shown). Seasonal accumulation was so low over Malawi and northern Mozambique that rainfall totals were below the fifth percentile.

During the dry season of June–August, rainfall was near normal over much of the region; however, below-normal rainfall was received over Lesotho and southeastern South Africa (not shown). Seasonal rainfall ranked between the fifth and 10th percentiles across central and southern South Africa, suggesting that midlatitude systems likely failed to bring winter moisture into the region. By SON, while near-normal rainfall dominated over much of southern Africa, above-normal rainfall returned over Botswana, southeastern Angola, and southwestern Zambia (not shown). Total rainfall ranked between the 90th and 95th percentiles in northwestern Botswana and southeastern Angola. Conversely, below-normal rainfall re-emerged over southeastern Zambia, northern Zimbabwe, southern Malawi, northern Mozambique, eastern South Africa, Eswatini, and southernmost Mozambique.

(iii) NOTABLE EVENTS AND IMPACTS

Dry conditions persisted over large parts of western South Africa during 2020 including some areas where dryness has prevailed for about 7 years. The year began with dry conditions persisting in most parts of the western interior, with above-normal temperatures in the central parts exacerbating the dryness. The Northern Cape was declared a disaster area after drought impacted

the province. A total of 200 million rand (~$14 million U.S. dollars) was set aside to help address the crisis. KwaZulu-Natal Province was also impacted by a shorter-term drought, accompanied by high temperatures, that affected 256 towns and surrounding communities. The most impacted areas include Uthukela, Umzinyathi, Amajuba, Zululand, Uthungulu, and Umgungundlovu districts. Adequate rain fell in the southern and northeastern parts of the country, although some associated severe storms caused extensive damage to infrastructure. By February, above-normal rainfall spread to the central and southeastern interior, but the late-summer rainfall ended abruptly, followed by drier conditions in March. Severe storms were reported in February with extensive damage, especially in the Gauteng and Eastern Cape Provinces. In April some areas received more than twice their normal amounts over the eastern half of South Africa. Localized flooding was reported in several places. Many flooding events occurred during austral summer and autumn. Based on NOAA's CPC RFE2, Gauteng Province received 100–300 mm of precipitation during 4–10 December 2019, which led to flooding in many parts of the Province on 11 December, affecting 3500 people with two fatalities reported, according to the Emergency Events Database (EM-DAT). During 7–10 February, RFE2 estimated 90 mm of precipitation, again in Gauteng, that caused flash floods, leading to three fatalities and affecting 200 people.

According to the Southern African Science Service Centre for Climate Change and Adaptive Land Management, upstream areas, such as Onjiva in southern Angola, recorded cumulative rainfall totals of 263 mm from 26 February to 3 March, which triggered floods over many areas downstream of northern Namibia, including the Oshana, Oshikoto, Omusati, and Ohangwena Regions on 6 March, affecting 1000 people.

During 16–22 March, up to 150 mm of rain fell across northern Zambia, with the largest totals over the Luapula and parts of the Northern Provinces. These large rainfall totals resulted in flooding across 28 districts over the Northwestern, Copperbelt, Luapula, Northern, Muchinga, Eastern, Western, and Lusaka Provinces of Zambia, with an estimated 700,000 people affected, according to the Disaster Management and Mitigation Unit. During the same period, rainfall estimates approached 100 mm over southwest-central Angola, causing flooding and damages and affecting over 2000 families over the Cuanza Sul, Malanje, Lunda Sul, and Cunene Provinces of Angola, based on report from the Agência Angola Press.

Tropical Storm Chalane made landfall over the Muanza District in the Sofala Province of central Mozambique on 30 December, causing at least two fatalities and affecting nearly 11,000 people, according to the United Nations Office for the Coordination of Humanitarian Affairs. The impact was smaller over Zimbabwe as the system weakened into a tropical depression, with about 600 people displaced and minor infrastructure damages reported. In contrast, drought caused food shortage over Lesotho by the end of the year, affecting 766,000 residents, according to EM-DAT.

6) Western Indian Ocean island countries—G. Jumaux, M. Robjhon, W.M. Thiaw, R. Dhurmea, M. L. Rakotonirina, and B. Andrade

The Western Indian Ocean island countries consist of Madagascar, Seychelles, Comoros, Mayotte (France), Réunion (France), Mauritius, and Rodrigues (Mauritius). With two distinct main seasons, western Indian Ocean islands generally experience a warm and wet period during November of the antecedent year to April and a cold and dry season during May–October. Overall, 2020 was warmer than normal (Fig. 7.31). Annual rainfall was above normal in Seychelles and Madagascar and below normal over the rest of the island countries (Fig. 7.31).

(l) TEMPERATURE

The annual mean temperature over Réunion Island (based on three stations) was 0.24°C above normal, the 15th highest since record keeping began in 1968. March and October, both +0.8°C above normal (Fig. 7.32), were among the six warmest for their respective months, while the

January maximum temperature and November minimum temperature were among the 10 coldest, at −0.5°C below normal. The lowest minimum temperature (–2.3°C) was recorded in the highlands at Plaine-des-Chicots on 11 August.

In Mauritius, the annual mean temperature (based on two stations at Vacoas and Plaisance) was slightly above normal for 2020 (+0.51°C). Maximum temperatures were close to normal (+0.18°C) while minimum temperatures were above normal (+0.86°C). Mean temperatures were near normal for most of the austral summer months (anomaly < +0.5°C; Fig. 7.32), except March (+0.7°C). Above-normal mean temperatures prevailed during the winter months from July to October. Mauritius experienced above-normal maximum and minimum temperatures in October, making this the warmest October since 1960.

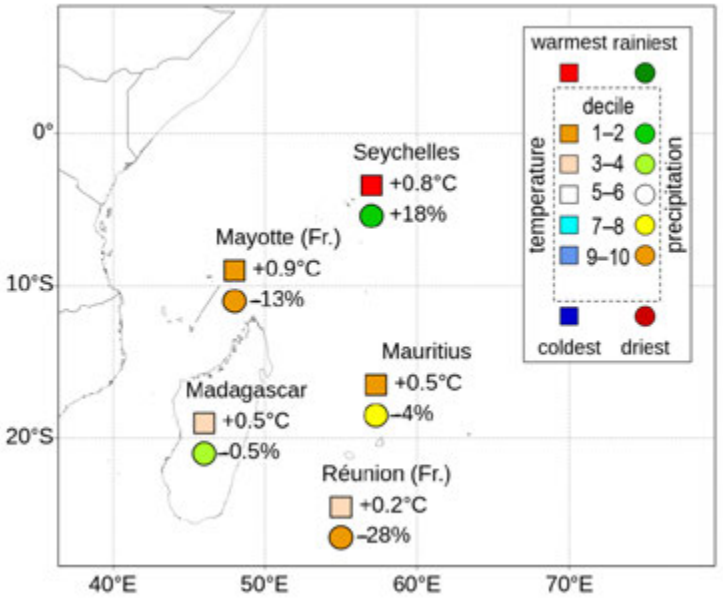

Fig. 7.31. Mean annual temperature anomalies (°C, squares), annual rainfall anomalies (% of normal, circles), and their respective deciles for the Western Indian Ocean island countries in 2020. 1981–2010 base period. (Sources: Météo France; and Meteorological Services of Mauritius, Seychelles, and Madagascar.)

In Madagascar, the mean temperature for 2020 (based on 18 stations) was 23.9°C, which was 0.5°C above normal and the 10th-warmest year since 1980. The mean annual minimum and maximum temperatures were 19.3°C and 28.5°C, respectively, +0.6°C and +0.4°C above normal. The cold settled and was marked in the central highlands. The minimum absolute temperature recorded was 2.0°C (–4°C below normal) at Antsirabe on 28 July. The absolute maximum temperature of 42.9°C was recorded at Bezaha on 9 November 2020, +7.9°C above the monthly average.

In Mayotte (Pamandzi Airport), the annual temperature was the second highest in the 60-year record, with an average temperature of 27.7°C (+0.9°C above normal and 0.3°C below the record set the previous year in 2019). Seven consecutive months from January to July (Fig. 7.32) were each among their three warmest on record.

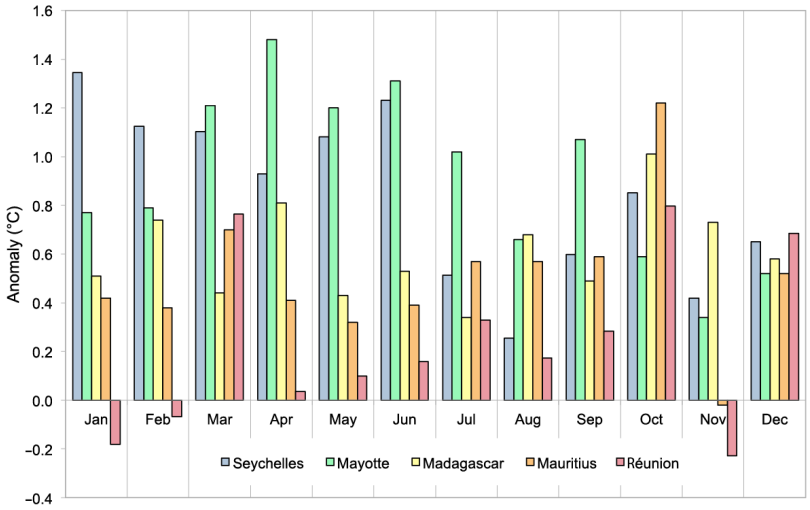

Fig. 7.32. Monthly mean temperature anomalies (°C; 1981–2010 base period) for the Western Indian Ocean island countries in 2020. (Sources: Météo France; and Meteorological Services of Mauritius, Seychelles, and Madagascar.)

At Seychelles International Airport, the annual mean temperature anomaly for 2020 was +0.8°C above normal, which is the highest since records began in 1972, surpassing 2019 (Fig. 7.33). All months were above normal; January, March, and May each were the warmest on record. February, April, June, September, and October were each among their three warmest.

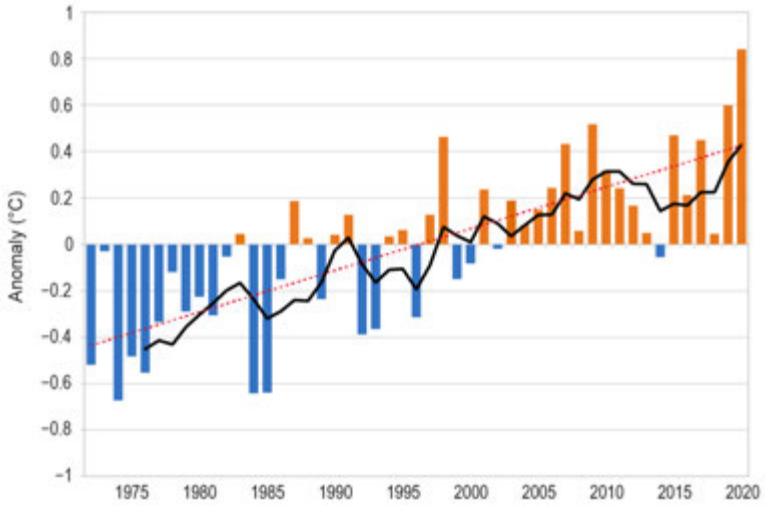

Fig. 7.33. Annual mean temperature anomaly time series (°C; 1981–2010 base period) in Seychelles for the period 1972–2020. Black line is the 5-yr running mean and red line represents the linear trend. (Source: Seychelles Meteorological Service.)

(II) PRECIPITATION

The annual rainfall total over Réunion Island was 72% of normal, making 2020 the third-driest year since 1972. North Réunion Island experienced deficits during the rainy season (December–April), while the rainfall over South Réunion Island was adequate (except in February). The South received rainfall associated with Tropical Storms Calvinia in December 2019 and Diane in January 2020 (see section 4g6). The dry season (May–November) was the second driest on record, with 60% of normal precipitation, causing drought in 21 out of 24 localities. Some stations recorded their lowest annual rainfall since records began, notably in the towns of Saint-Denis, Le Port, and Salazie.

In Mauritius, the mean annual rainfall total was 1921 mm, which was 96% of normal (average rainfall is 1999 mm). Marked variability in rainfall from month to month (Fig. 7.34) was observed during (austral) summer, while all austral winter months had deficient rainfall except June. Winter 2020 tied with 2018 as the sixth-driest such season since the start of the record in 1904 and the second driest of the last decade.

Total annual rainfall in Madagascar (average of 18 stations) was 1698 mm, which is 99.5% of normal. Spatially, however, the northern part of the island was wetter than normal while the southern part was drier (Fig. 7.35). January was the wettest month of the year. The highest annual amount compared to normal was observed in Antsohihy in the northwest, at 189% of its normal precipitation. Associated with the evolution of Tropical Cyclone Herold (see section 4g6), the highest accumulated precipitation total within a 24-hour period in 2020 was 205.6 mm recorded in Sambava in the northeast on 17 March.

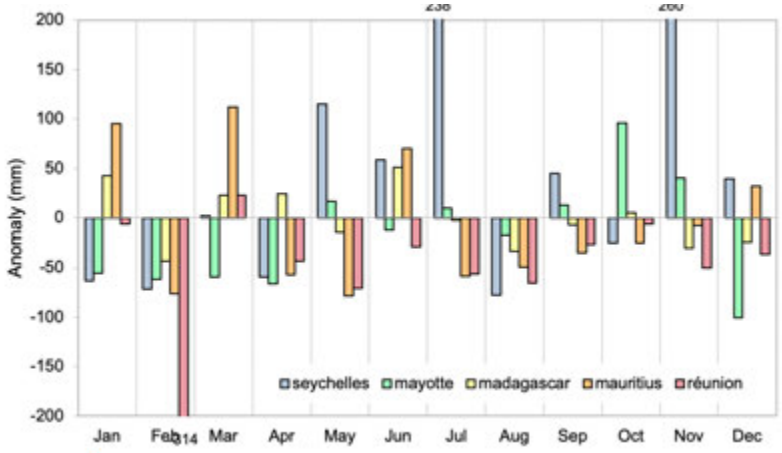

Fig. 7.34. Monthly rainfall anomalies (mm; 1981–2010 base period) in the Western Indian Ocean island countries in 2020. (Sources: Météo France; and Meteorological Services of Mauritius, Seychelles, and Madagascar.)

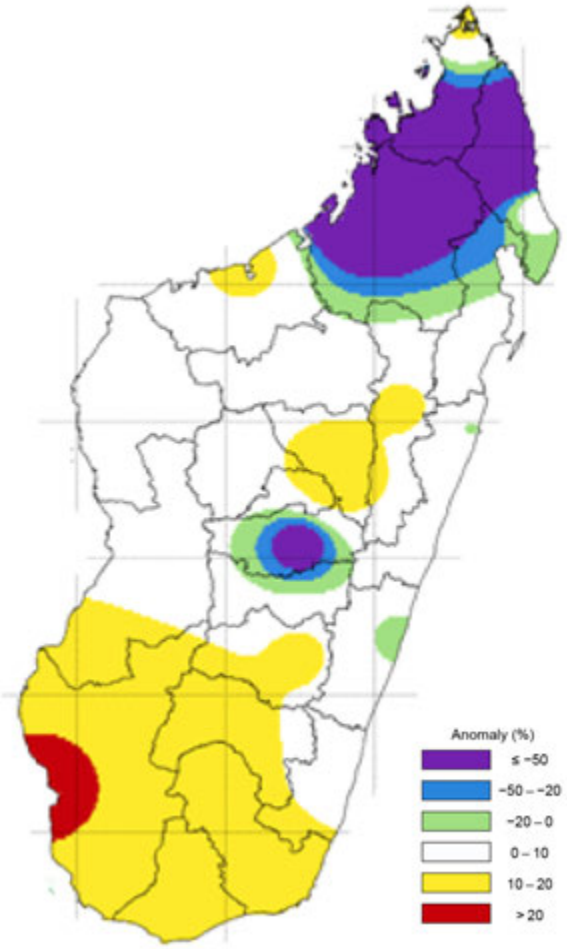

Fig. 7.35. Annual rainfall anomalies (%; 1981–2010 base period) across Madagascar in 2020. (Source: Madagascar Meteorological Service.)

For Mayotte, the total annual rainfall (average of two stations) was 1288 mm, which was 87% of normal. The total rainfall during the first half of the year was 77% of normal, the sixth driest of the 60-year record for this period, and 109% of normal during the second half. April and August were among their five driest on record, while October was the third wettest.

In Seychelles, the annual rainfall total (2803 mm) was 118% of normal, making 2020 the sixth-wettest year since the start of the record in 1972. July and November were each their wettest on record, contributing to the annual surplus.

(III) NOTABLE EVENTS AND IMPACTS

During November–April 2019/20, the southwest Indian Ocean basin experienced 10 tropical storms, of which six developed into tropical cyclones. Seven tropical cyclones and tropical storms made landfall and impacted the region. Five of these tropical systems affected Madagascar. Tropical Cyclone Belna made landfall in the Soalala District in the Boeny Region of western Madagascar on 9 December 2019, affecting about 3000 people, according to the National Office for Risk and Disaster Management (BNGRC). Tropical Storm Diane began as an incipient weather disturbance over the Mozambique Channel and tracked eastward to traverse Madagascar on 23 January. Portions of the Boeny and Sofia regions of western Madagascar received 1-day rainfall totals over 140 mm, according to the RFE2.0. The BNGRC reported widespread flooding across the Alaotra Mangoro, Analamanga, Betsiboka, Boeny, Melaky, and Sofia regions. Reports indicate that 31 people were killed and more than 107,000 affected. The system intensified and was officially named as a tropical storm when it passed near Mauritius on 24 January. Tropical Storm Francisco made landfall in Mahanoro in eastern Madagascar on 15 February after moving near Mauritius as

a deepening low-pressure system on 11 February. Tropical Cyclone Herold meandered near northeastern Madagascar on 14 March, bringing 1-day estimated precipitation totals of 120–140 mm over portions of Sambava and Antalaha. Herold caused severe flooding, with floodwaters up to 2 m in some areas, resulting in four deaths and over 3000 affected people across the Maroantsetra, Sambava, and Antalaha Districts, according to the disaster authorities. Toward the end of the year, Tropical Storm Chalane made landfall over the city of Fenoarivo Atsinanana in eastern Madagascar on 27 December. Although Toamasina station, located about 100 km farther south, recorded 351 mm of rainfall on 26 December, rains from Chalane resulted in localized flooding and minor damages only in the city, based on reports.

Over Mauritius, Tropical Cyclone Calvinia hugged right to the east of the island on 30 December 2019, closing the island's main airport and businesses. Tropical Storm Esami formed as a tropical depression to the east-southeast of Port Louis and moved eastward across the island with peak sustained winds at 83 km h^{-1} on 23 January.

f. Europe and the Middle East—P. Bissolli, Ed.

Throughout this section, 1981–2010 is the base period used for both temperature anomalies and precipitation percentages, unless otherwise specified. European countries conform to different standards applied by their individual national weather services. All seasons mentioned in this section refer to the Northern Hemisphere. More detailed information can be found in the *Monthly and Annual Bulletin on the Climate* in RA VI – European and the Middle East, provided by WMO RA VI Regional Climate Centre on Climate Monitoring (RCC-CM; http://www.dwd.de/rcc-cm). Anomaly information has been taken from Figs. 7.37–7.40 and aggregations of CLIMAT station data when national reports are not available. Appendix Table A7.1 at the end of this chapter provides a list of included countries and their lengths of record for both temperature and precipitation.

1) Overview

Based on the Global Historical Climate Network (GHCN) v4.0.1 dataset (Menne et al. 2018), Europe (36°–72°N, 23°W–60°E) experienced its warmest year in the history of measurements with an anomaly of +1.9°C (Fig. 7.36). Overall, the year was exceptionally warm and almost all of Europe reported temperatures higher than normal (Fig. 7.37). With the exception of Portugal, southern Spain, most of Italy, Ireland, and the northern United Kingdom, all of Europe observed anomalies well above +1.0°C. For many countries, the year proved to be the warmest or second warmest on record (warmest: Latvia, +2.4°C above normal; Netherlands, +1.6°C; Belgium, +1.9°C; France and Switzerland, +1.5°C; Belarus, +2.3°C; European Russia, +2.9°C [1961–90 base period]; Estonia, +2.4°C; Finland, +2.4°C; Lithuania, +2.3°C; Luxembourg, +2.1°C; Poland, +1.9°C; Kazakhstan, +2.2°C; Spain, +1.2°C; Sweden, +2.0°C; Norway, +1.9°C; Ukraine, +2.8°C [1961–90]; second warmest: Germany, +1.6°C; Denmark, +1.5°C; Romania, +1.7°C); third warmest: Turkey, +1.4°C).

For central and southern European Russia, the eastern part of Ukraine, Turkey, Georgia in the South Caucasus, most of the Baltic states, and Greece, the year was characterized by a precipitation deficit. It was as low as 20%–60% of normal in wide regions around the Black Sea (Fig. 7.38). Germany, Switzerland, and most of France (except the most western parts) also received below-normal precipitation, as low as 60%–80% of normal across wide parts of Germany. Northern Europe, on the other hand, received above-normal precipitation, mostly around 125% of normal. Similarly, the eastern Iberian Peninsula, some regions of Italy, and many countries east of Germany reported above-normal precipitation.

Winter was very warm in all of Europe with anomalies from +1° to +3°C on the Iberian Peninsula to +5°C and above in the northeast of the region (Fig. 7.39). Only southern Greece, western Turkey, and the Middle East reported winter anomalies partly below +1°C. Between intense low pressure over Iceland and the northern North Atlantic and an Azores high extending to the

western Mediterranean, a warm airflow from the North Atlantic prevailed. Anomalies within the high-pressure area were lower due to cold clear nights. In February, almost no areas in Europe observed anomalies below +3°C. Precipitation during winter (Fig. 7.40) was above normal for most countries north of the Alps due to frequent North Atlantic pressure systems, as well as for Turkey and the Middle East, where Mediterranean cyclones developed occasionally. These regions received precipitation mostly around 125% of normal but more than 167% of normal in localized areas. The western Iberian Peninsula, the Mediterranean, and the Balkan states received below-normal precipitation due to the influence of prevailing high-pressure systems.

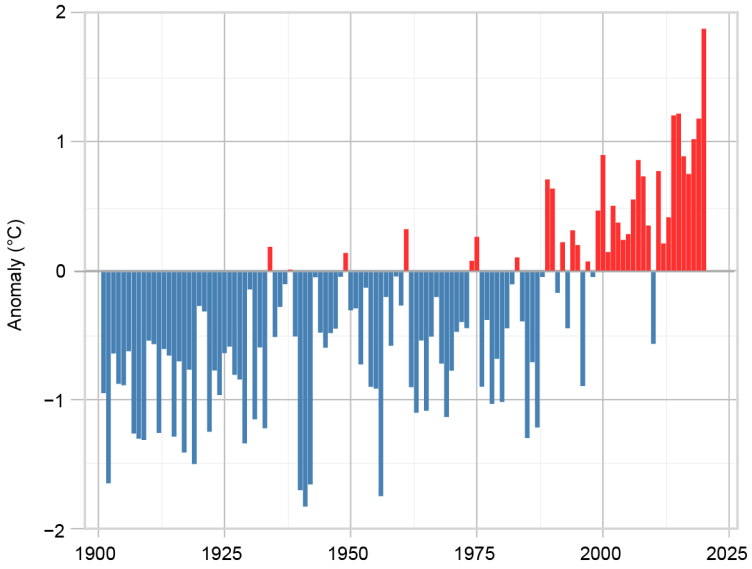

Fig. 7.36. Annual average land surface air temperature anomalies for 1900–2020 for Europe (36°–72°N, 10°W–60°E) relative to the 1981–2010 base period. (Source: GHCN version 4.0.1 dataset [Menne et al. 2018].)

Spring was warmer than usual in western Europe, where a high-pressure ridge dominated, with anomalies of +1° to +3°C, while central Europe had near-normal temperatures. The season started out warmer than usual in March for eastern and northern Europe with anomalies from +1°C east of Germany to above +5°C in European Russia. For western Europe, anomalies were below +1°C. During April, anomalies dropped below normal across eastern Europe, while in central and western Europe, anomalies ranged from just above normal in the southern and western Iberian Peninsula to +5°C in central France under the influence of high pressure. During May, temperatures continued to be above normal for western Europe, the Mediterranean, and the Middle East, while temperatures for central, northern, and eastern Europe were below normal with anomalies of –2° to –3°C for large parts of Poland, Belarus, and the Ukraine. Spring was wetter than normal for eastern Europe due to Arctic troughs extending into that area, with many areas receiving precipitation well above 167% of normal. Conversely, the Nordic and Baltic states, Germany, the BeNeLux countries (Belgium, Netherlands, and Luxembourg), Switzerland, many areas of France, the United Kingdom, as well as the central Mediterranean, were drier than normal, due to more high-pressure influence that contributed to a third successive spring precipitation deficit after 2018 and 2019. Northwestern Germany, the BeNeLux, and the southern United Kingdom received precipitation as low as 20% of normal. During this season, April was notably drier than normal in western, central, and eastern Europe (except for Russia), with widespread precipitation of 20%–60% of normal and some areas even below 20%.

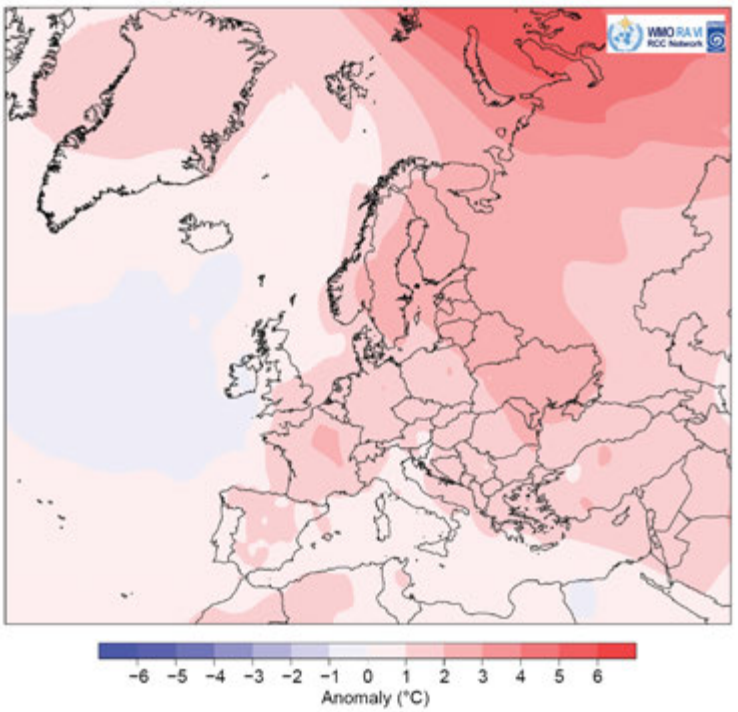

Fig. 7.37. Annual mean air temperature anomalies (°C; 1981–2010 base period) in 2020. (Source: interpolated climate station data, Deutscher Wetterdienst [DWD].

The year continued with above-normal temperatures during summer. Anomalies for the season were around +1°C for many countries. Lower-than-normal pressure in southwestern Europe and higher-than-normal pressure in the northeast led to an increased flow of subtropical warm air. Distribution of precipitation during the summer months was very inhomogeneous. South central Europe and the Balkan states, the United Kingdom, northwestern France, the northwestern parts of the Iberian Peninsula, and central Spain, which were in the low-pressure area, received above-normal precipitation. Northern Europe and the Baltic states, influenced by higher-than-normal pressure, as well as the southern parts of the Iberian Peninsula, which were strongly influenced by dry subtropical air from northern Africa, were drier than normal (20%–60% of normal) for the season. For many areas north of the Black Sea, precipitation was well below 60% of normal.

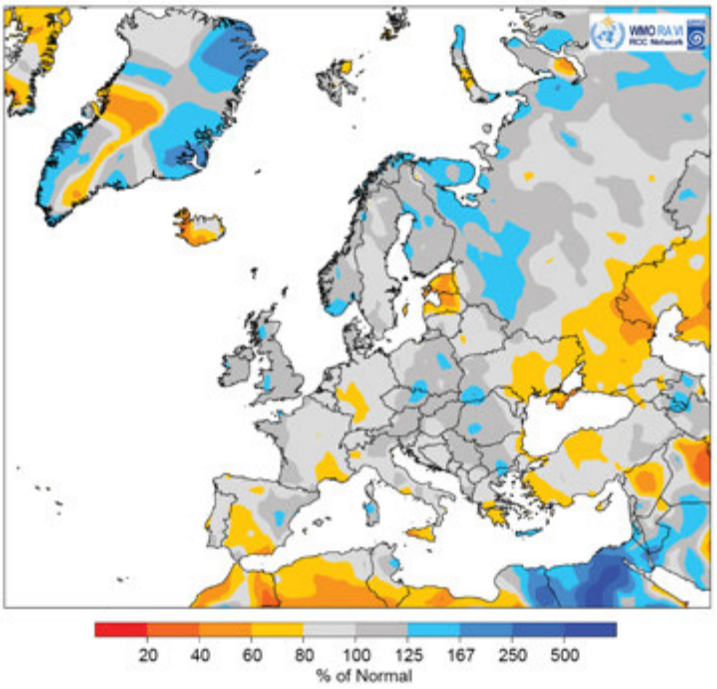

Fig. 7.38. European precipitation totals (% of 1981–2010 average) for 2020. (Source: GPCC, created by DWD.)

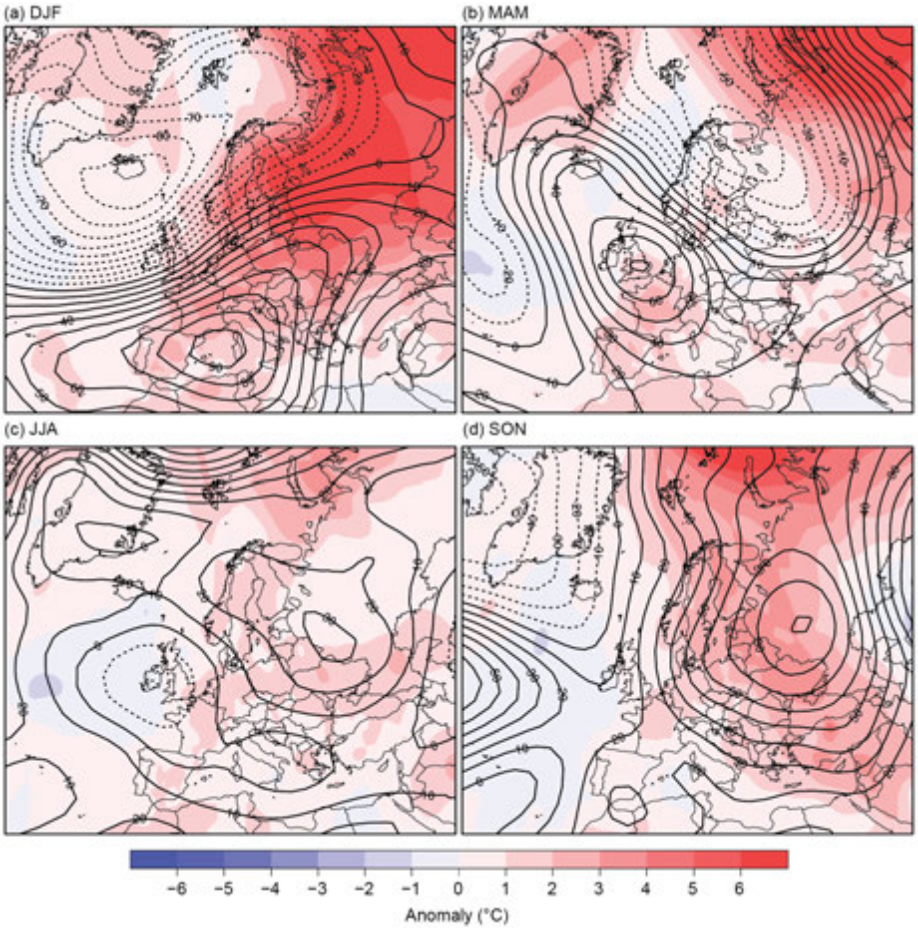

Fig. 7.39. Seasonal anomalies (1981–2010 base period) of 500-hPa geopotential height (contour; m) and surface air temperature (shading; °C) using data from the NCEP/NCAR reanalysis and DWD, respectively, for (a) DJF 2019/20, (b) MAM 2020, (c) JJA 2020, and (d) SON 2020.

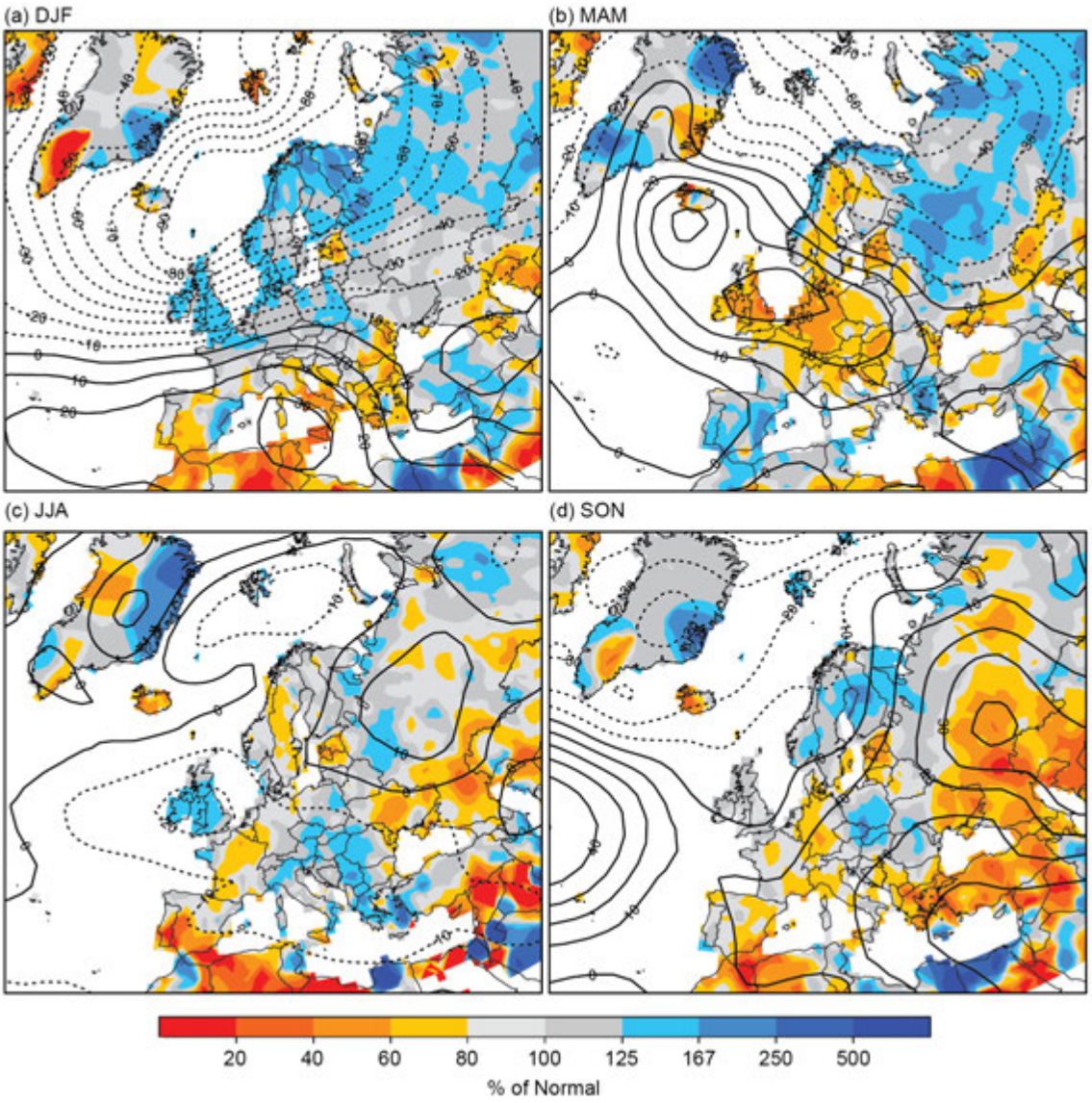

Fig. 7.40. Seasonal anomalies for 2020 (1981–2010 base period) of sea level pressure (hPa) from NCAR/NCEP reanalysis (contours) for (a) DJF 2019/20, (b) MAM 2020, (c) JJA 2020, and (d) SON 2020. Colored shading represents the percentage of seasonal mean precipitation for 2020 compared with the 1981–2010 mean from GPCC (Schneider et al. 2018).

Autumn was warmer than normal across Europe, except for areas on the Iberian Peninsula and Ireland. The Russian high was expanded to the west into Europe, and warm air from the Middle East reached much of the European continent. In most of western and central Europe, anomalies were between +1°C and +2°C, while eastern Europe and the Baltic states observed anomalies of +3° to +4°C due to higher warm air advection from the subtropics. Autumn precipitation was close to normal or slightly wetter than normal for Ireland, the United Kingdom, the BeNeLux, and the Scandinavian countries. In contrast, Germany, France, Switzerland, Italy, and the Iberian Peninsula received precipitation of around 80% of normal. Eastern Ukraine, southern European Russia, Turkey, and the South Caucasus, where high-pressure influence was strong, were even drier for the season, with precipitation mostly 40%–60% of normal.

December 2020 was again a warm month in Europe, except for Ireland in the west und parts of European Russia in the east. It was wetter than normal in December across much of western Europe, parts of northern Europe, and the central Mediterranean region, but very dry for the season in southern Iberia, parts of central Europe, much of eastern Europe, Turkey, and the Middle East.

2) Western Europe

This region includes Ireland, the United Kingdom, Belgium, the Netherlands, Luxembourg, and France.

(I) TEMPERATURE

Except for the United Kingdom (third warmest with anomaly of +0.8°C) and Ireland (close to normal), all western European countries reported a record warm year (France: +1.5°C; Netherlands, +1.6°C; Belgium, + 1.9°C; Luxembourg +2.1°C).

Winter was warmer than normal, and many countries reported average temperatures among their three warmest on record (anomalies: France, +2.7°C [warmest]; Luxembourg, +3.0°C [second warmest]; Netherlands, +3.1°C [second warmest]; Belgium, +2.7°C [second warmest]). Except for Ireland and the United Kingdom, every country reported anomalies of well above +2.0°C for all three months. For February, anomalies between +3.4° and +3.9°C were reported by France, the Netherlands, Belgium, and Luxembourg, making February 2020 one of the five warmest Februaries for each of these countries (second warmest for France).

Spring was very warm for France, Belgium, and Luxembourg (anomalies of +1.7°C, +1.2°C, and +2.0°C, respectively), ranking second warmest for France and third warmest for Belgium and Luxembourg. Anomalies for Ireland, the United Kingdom, and the Netherlands were below +0.9°C. April was notably warm: France reported its third-warmest April with an anomaly of +3.0°C as did Luxembourg (+4.2°C). The United Kingdom and the Netherlands had their fifth- (+1.7°C) and sixth- (+1.9°C) warmest April on record, respectively. May was fifth warmest (+1.5°C) for France, while Ireland, Belgium, and Luxembourg reported anomalies of around +0.7°C. The United Kingdom and the Netherlands temperatures were near normal.

Summer temperatures ranged from +1.0°C above average in France to +1.6°C in Luxembourg and was among the 10 warmest on record. Temperatures were only slightly above normal for the United Kingdom, and Ireland reported slightly below-normal temperatures. During July, both the United Kingdom and Ireland recorded temperature anomalies more than below –1.0°C below average.

During autumn, temperatures again were very different on the isles from the mainland. While the United Kingdom and Ireland had temperatures near normal, Belgium, Luxembourg, and the Netherlands reported their fourth-warmest autumn (anomalies of +1.4°C, +1.7°C, +1.2°C, respectively) and France its fifth warmest (+1.1°C).

(II) PRECIPITATION

Precipitation for the year was close to normal in the region. Winter was wetter than normal for all countries, from 104% of normal in Belgium to 143% for the United Kingdom. Only southern France received slightly less-than-normal precipitation. The individual months of the season were wetter than normal except for January for the region and February for southern France, both of which were drier than normal. February was the wettest on record for the United Kingdom as well as for the Netherlands with 237% and 267% of normal, respectively, and second wettest for Luxembourg (237% of normal).

Spring was drier than normal, with 40%–60% of normal precipitation for most of the region. The United Kingdom reported its fifth-driest May with only 47% of normal precipitation, contributing to one of its five driest springs on record.

Summer rainfall was between 66% and 85% of normal, except for the United Kingdom and Ireland, which received above-normal precipitation of around 135% of normal, and the Netherlands with near-normal precipitation. July was very dry for Belgium with 33% of normal precipitation (fifth driest on record), Luxembourg 12% of normal (second driest), and France 30% of normal (record driest).

During autumn, precipitation was near normal for Ireland, the United Kingdom, and Belgium, while Luxembourg, the Netherlands, and France reported slightly below-normal precipitation, between 84% and 90% of normal.

(III) NOTABLE EVENTS AND IMPACTS

During 19–20 January, western Europe experienced exceptionally high pressure. At Heathrow Airport (London) 1049.6 hPa was measured, which was the highest atmospheric sea level pressure recorded in the United Kingdom in more than 300 years. The same value was measured in Cherbourg (France), which broke the previous record set on 3 March 1990. The station Findel Airport (Luxembourg) and De Bilt (Netherlands) measured 1048 hPa. A consequence of the high-pressure levels was record high sunshine duration in many places.

During February, two storms passing over northwestern Europe led to extensive traffic disruptions. Storm Ciara (9–11 February) reached strengths up to hurricane force (12 on the Beaufort Wind Scale); at exposed places in the United Kingdom and France, wind gusts surpassed 200 km h^{-1} and reached 120 km h^{-1} in lowland areas on 10 February. The central pressure of the low dipped below 940 hPa, and pressure differences between northern and southern Europe reached up to 80 hPa. Daily precipitation in some areas reached almost 75% of the monthly normal (e.g., 180 mm at Lake District, northern England), leading to record high river levels and flooding. In the United Kingdom, the Netherlands, Belgium, and France, public transport experienced major disruptions due to delays and cancellations of train, flight, and ferry connections. While the extremely low air pressure in northern Europe was a risk to flying, mainly due to increased turbulence, some non-cancelled flights even profited from this special situation resulting in a new record for crossing the Atlantic in under five hours set by a British Airways aircraft due to higher wind speeds. Since soils were already saturated by rainfall brought by Storm Ciara, the heavy rain brought by the second storm, Dennis (15–16 February), caused record river levels and widespread flooding in the United Kingdom and Ireland. In south Wales at the Crai Reservoir in Powys, 157.6 mm of precipitation was measured in 48 hours, which is more than the normal total for February.

The high-pressure influence from the Azores and continued southwesterly winds resulted in unusually warm temperatures in February across Europe. In southern France, record temperatures for February were set. Never before it has been so warm so early in the year and new records were set at multiple stations; for example, Biarritz reported 26.6°C, which is higher than the monthly mean for July and August, and Cambo-les-Bains reached 27.8°C. In Bastia on Corsica, the temperature did not drop below 21.9°C on 10–11 February, making it the first tropical night (minimum temperature >20°C) ever during the winter season at this location.

During a heat wave from 6 to 13 August, exceptionally high temperatures were measured. Much of England experienced temperatures above 30°C on the 7th and 9th. Heathrow and Kew Garden reported a maximum of 36.4°C. The Netherlands counted a record of eight consecutive tropical days with daily maximum temperatures above 30°C. At station De Bilt (the Netherlands), a new weekly average maximum temperature record of 33.2°C was set. Large parts of France experienced temperatures around 30°C.

On 3 October, southeastern France experienced extreme precipitation. Mons (west of Nice) reported 571 mm in 24 hours; in Saint-Martin-Vésubie (same region), a new daily record was set with a 24-hour total of 500 mm. On the same day, due to storm Alex which remained quasi-stationary that day, many weather stations in southern central England and eastern Scotland reported their wettest October day on record. The United Kingdom area average for this day was 31.7 mm, which made it the wettest day on record (series starting in 1891).

3) Central Europe

This region includes Germany, Switzerland, Austria, Poland, Czechia, Slovakia, and Hungary.

(I) TEMPERATURE

Annual temperatures ranged from +1.0° to +1.9°C above normal in central Europe. Switzerland and Poland reported their warmest year on record (anomalies of +1.5°C and +1.9°C, respectively) and Germany reported its second (+1.6°C). The winter season was especially warm. It was the warmest winter on record for Switzerland and Poland with anomalies of +2.9° and +4.1°C, respectively, and second warmest for Germany (+3.3°C), Austria (+2.7°C), and Czechia (+3.3°C). Hungary and Slovakia each observed one of their five warmest winters, with anomalies of +2.6° and +2.8°C. All winter months were warmer than usual, but February temperatures were near-record high. It was the second-warmest February for Germany (+4.4°C), Switzerland (+3.9°C), Austria (+4.1°C), Poland (+4.7°C), and Czechia (+4.7°C).

During spring, temperature anomalies were below +1.0°C, except for Switzerland, which reported +1.8°C above normal, its third-warmest spring. Germany and Austria reported spring anomalies of +0.6° and +0.8°C, while Poland, Czechia, Slovakia, and Hungary observed near-normal temperatures.

Summer was about +1.0°C above normal for the region. In June, anomalies for Germany and Poland were above +1.0°C, while the rest of the region was cooler than normal. Except for Switzerland (anomaly +1.2°C), temperatures were near normal in July. The season ended with a warmer-than-normal August: anomalies were above +1.0°C for all countries in the region. Poland, Hungary, and Germany observed anomalies of +2.0°C and above, with Germany reporting its second-warmest August.

For autumn, temperatures were mostly +1.0° to +1.4°C above normal, except for Poland (+2.0°C) and Austria (+0.7°C). In September, anomalies were well above +1.0°C for the whole region, but in October, Austria reported normal temperatures and Switzerland was slightly colder than normal. On the other hand, Switzerland reported its fourth-warmest November, with an anomaly of +2.5°C. Germany reported an anomaly of +1.8°C, while Poland was +2.5°C above average, making this one of its five warmest Novembers on record.

(II) PRECIPITATION

Precipitation was close to normal (86%–116%) in the region for the year. Winter was slightly wetter than normal, with 100%–120% of normal precipitation. In January, only Poland received above-normal precipitation even though rain mostly fell in the north. All other countries reported 40%–60% of normal precipitation. Winter ended with a considerably wetter-than-normal February, with most of the countries receiving well above 160% of their normal precipitation. Germany reported 228% of its normal precipitation, its second-wettest February. Only Hungary observed near-normal precipitation.

In spring, only some local areas received above 80% of normal precipitation. Germany and Hungary reported countrywide precipitation slightly below 60% of normal. Except for Hungary and Slovakia, which received close-to-normal precipitation, the season started drier than normal for the region. April was notably dry. Countrywide precipitation did not exceed 60% of normal anywhere and was even below 40% of normal for multiple countries. Germany reported 33% of its normal precipitation, Poland 23%, Hungary 25%, Slovakia 20%, and Czechia 39%. While May continued to be drier than normal for Switzerland, Hungary, and especially Germany, which reported 54% of normal precipitation, Poland, Czechia, and Austria reported slightly above-normal precipitation. Overall, this was the third-driest spring (following 2018 and 2019) for much of central Europe. However, this did not continue into summer.

During the summer season, Germany and Switzerland received near-normal precipitation. For the other countries in the region, precipitation ranged from around 110% of normal in Poland

to around 140% of normal in Austria, Hungary, and Czechia. With the exception of July, when countrywide precipitation was below normal for Switzerland, Germany, Czechia, and Poland, precipitation was above normal in central Europe during all of summer.

Autumn was drier than normal for Switzerland and Germany, with 76% of normal precipitation while the rest of the region received above-normal precipitation. For Germany, Switzerland, and Hungary, the season started with a drier-than-normal September (60%–80% of normal precipitation). Poland, Slovakia, Czechia, and Austria received above-normal precipitation, up to 150% of normal. October was wetter than normal for all countries in the region; precipitation ranged from 124% of normal in Germany to above 200% for Hungary and Czechia. Parts of Slovakia reported precipitation close to 300% of normal. The season ended with a very dry November; precipitation did not exceed 60% of normal across the region. Germany, Austria, Switzerland, and Hungary reported only around 30% of their normal precipitation.

(III) NOTABLE EVENTS AND IMPACTS

Between 9 and 11 February, Storm Sabine (Storm Ciara in Western Europe, as noted earlier) caused wind speeds up to hurricane force (12 on the Beaufort Wind Scale) in central Europe. At the station Feldberg in Germany, gusts up to 177 km h^{-1} were measured on 10 February. In Andermatt (Switzerland) and Sniezka (Poland), gusts of 202 km h^{-1} and 198 km h^{-1} were measured, respectively. In Germany, daily precipitation totals around 40 mm were reported, which led to local flooding, for example at the fish market in Hamburg. Additionally, a record amount of wind power—equivalent to 44 nuclear power plants—was produced. The ongoing warm airflow from the southwest caused record high temperatures. On 3 February new daily minimum temperature records of 10.6°C at the University of Pécs (Hungary), 9.2°C in Budapest, and 12.5°C in Payerne (Switzerland) were set. A new daily maximum record for February (23.9°C) was observed the same day in Magadino/Cadenazzo (southern Switzerland). On 16 February, a new daily high-temperature record of 18.2°C was set in Czechia. Germany reported a new monthly record of 19.4°C at the station in Worms. The exceptional warmth even reached high up into the Alps, leading to new February maximum temperature records at several mountain stations; for example, a temperature of 3.9°C was measured at the station Sonnblick Mountain in Austria (3106-m a.s.l.), the highest since 1886.

During 12–19 June, as a result of an almost stationary low-pressure system, central Europe experienced thunderstorms accompanied by sometimes heavy precipitation. Some areas in Germany received daily precipitation amounts of more than 60 mm. Locally, in combination with hail, 1-hour totals of 20 to 40 mm were measured. The highest daily sum of 133 mm occurred at station Bottmersdorf (southwest of Magdeburg). In Slovakia, a 1-day precipitation total of 129.1 mm was recorded on 19 June at the border of the central and eastern part of Slovakia at Muráň, causing flooding in this area.

During 26–29 June, Poland, Hungary, and Slovakia received exceptional amounts of localized precipitation during thunderstorms that caused flooding. Several areas in Poland received above 50 mm of rain in 24 hours. At the station Jaslo (Podkarpackie, foreland of Carpathian Mountains), 100 mm fell in 5 hours, and 1-hour totals of 30 to 40 mm were recorded. Wind with gusts up to 90 km h^{-1} and hail up to 4 cm in diameter were reported in Szczecinek (Middle Pomerania, western Poland). River water levels rose by more than 3 m in 1 day. The provinces Masovia (including Warsaw), Lesser Poland, and Podkarpackie were most affected. On 28 June at the station Muránská Huta–Predná Hora in eastern central Slovakia, 102 mm of rain fell in 1 hour and a 24-hour total of 132 mm was measured, raising the nearby Zdychava River water level by 0.75 m in 1 hour and 15 minutes. In Hungary, 24-hour totals up to 95 mm were reported, of which most was received within half an hour.

4) The Nordic and Baltic countries

This section includes Iceland, Norway, Denmark, Sweden, Finland, Estonia, Latvia, and Lithuania.

(I) TEMPERATURE

It was a record warm year for many of the Nordic and the Baltic countries: Latvia (anomaly of +2.4°C), Lithuania (+2.5°C), Norway (+1.9°C), Estonia (+2.9°C), and Sweden (+2.0°C). Denmark observed its second-warmest year, at +1.5°C. In Iceland, temperatures were near normal.

Winter was exceptionally warm, with anomalies well above +4.0°C across the region and close to +6.0°C for most of the Baltic countries. Norway, Finland, Denmark, Estonia, Latvia, and Lithuania all reported their warmest winter on record. While all winter months were warmer than normal and often ranked among their five warmest in the various countries, January was particularly notable as it was the warmest on record for all countries of the Nordic and Baltic regions with widespread anomalies of around +5.0°C and above.

Spring was slightly warmer than normal as anomalies were up to +0.6°C. March was warmer than usual and temperatures ranged from around +2.0°C above normal in Norway to around +3.0°C above normal in the Baltic countries. In April, only Denmark, southern Sweden, and southern Norway reported above-normal temperatures, while Finland, Estonia, Latvia, and Lithuania were near to slightly colder than normal. The season ended with below-normal temperatures in May across the entire region (except Iceland), close to –2.0°C below normal in the Baltic countries.

Summer again was slightly warmer than normal, with anomalies of +0.7° to +1.3°C. Temperatures in Iceland were near normal. June was the warmest month of the season; many countries reported anomalies close to or above +3.0°C. Only Iceland reported a lower, but still positive, anomaly of +0.9°C. July was colder than normal everywhere, with anomalies from –1.0° to –1.7°C (Iceland –0.7°C). During August, temperatures were once again above normal, but only Denmark and Sweden reported monthly anomalies above +1.0°C.

Autumn was exceptionally warm and the warmest on record for Lithuania, Latvia, Estonia, and Finland with anomalies of around +3.0°C. In Denmark, Norway, and Sweden, anomalies were +1.5° to +2.3°C, making this the fourth-warmest autumn for these countries. October and November were record warm for some countries. Lithuania reported its warmest October (+3.0°C above normal) as did Latvia (+3.2°C). November was the warmest for Estonia (anomaly of +4.0°C), Finland (+4.5°C), and Latvia (+4.0°C), second warmest for Denmark (+2.6°C), and third warmest for Lithuania (+3.5°C). For Iceland, with the exception of October with a slightly above average anomaly of +1.0°C, temperatures were near normal.

(II) PRECIPITATION

For most countries of the region, precipitation was near normal for the year. Norway reported above-normal precipitation (120% of normal), making 2020 its second-wettest year on record. Denmark reported 104% of its normal precipitation. Latvia and Estonia received only around 60% of normal precipitation, with lesser amounts in some areas.

Winter was wetter than normal with precipitation ranging from 108% of normal in Latvia to 155% of normal in Norway. For Norway, this was its wettest winter on record and second wettest for Denmark (155%). Except for January in Latvia and Estonia, all months of the season were wetter than normal in the region. In February, Denmark received a record high precipitation total of 284% of normal, making this its wettest February on record.

Spring was drier than normal for Sweden, Denmark, Latvia, and Estonia with precipitation between 66% and 80% of normal. Finland, Iceland, and Lithuania reported near-normal precipitation. Only Norway saw a wetter-than-average spring, with 130% of normal precipitation. During March, most countries reported near- to slightly-above-normal precipitation. Only Denmark was

dry, reporting 71% of normal precipitation. April was also drier than normal for Denmark (63% of normal), along with Latvia (53% of normal) and Lithuania (26%). Norway and Estonia, however, received 130% and around 116% of their normal precipitation, respectively. With the exception of Latvia, Lithuania, and Norway, where precipitation was close to normal, the end of the spring was drier than normal, with countrywide precipitation reported between 50% and 80% of normal.

During summer, overall precipitation was near to slightly above normal for all countries of the region, except for Estonia, where the dry spring evolved into a summer drought. June was drier than normal in Sweden, northern Norway, and Estonia, with many areas receiving only 40%–80% of normal precipitation. Other countries reported around 120% of their normal precipitation. In July, many areas received around 120% of normal precipitation; however, Estonia received only 80% of its normal precipitation. The season ended dry across the region. While Denmark and Lithuania reported around 90% of normal precipitation in August, other countries reported only 60%–80%.

For autumn, Denmark and the Baltic states reported 80%–90% of normal precipitation while Scandinavian countries received precipitation around 120% of normal. September was drier than normal, with around 50% of normal precipitation in Denmark and Lithuania and around 80% of normal precipitation for Latvia and Estonia. Norway and Finland each reported above-normal precipitation around 120% of normal. In October, Sweden received close to 200% of its normal precipitation. While the national average in Finland was around 125% of normal, some northern areas received more than 160% of normal precipitation. For the other countries in the region, October was close to normal. Only Iceland reported below-normal precipitation, around 75% of normal. The season ended with a wetter-than-normal November across the Scandinavian countries with around 120% of normal precipitation. Lithuania, Latvia, Estonia, and Iceland received 80%–90% of normal precipitation during the month. Denmark reported only 68% of its normal.

(III) NOTABLE EVENTS AND IMPACTS

In January, strong westerlies brought warm and dry air to Scandinavia that caused record high temperatures. On 2 January, the station Sunndalsøra in western central Norway (located near the western coast) measured 19.0°C, which was the highest temperature ever recorded during winter in Scandinavia. Many other stations in Norway recorded temperatures of 15°–18°C. New records were also set in Sweden. At station Oskarshamn (Småland, located at the Baltic Sea coast of Sweden), 12.1°C was reported, which tied the previous January record set in 2007. South of Norrland (mainly central Sweden), January temperatures were the highest for the last 50 years. On 8 January, a new record of 10.5°C was set at station Orebro (southern Sweden) where measurements started in 1858. Temperatures remained high and further records were set on 20 and 21 January when daily maximum temperatures exceeded 10.0°C at many stations in Norway and Sweden.

On 14 April, record-breaking snowfall was measured in northern and central Finland. The station Tahtela at Sodankylä reported 1.25 m of new snow, breaking the old record of 1.19 m from 6 April 2000. Additional extreme snowfall was observed in Norway, where daily snow accumulation of up to 1.2 m occurred locally around Tromsö. During 4–5 April, a blizzard with wind gusts up to 111 km h^{-1} brought up to 1.5 m of snow in 24 hours in Iceland. Roads were closed and flights cancelled.

During May, several towns were threatened by flooding due to melting of the exceptional amount of snow accumulated during winter in northern Sweden and Finland (Lapland received the most in the last 60 years). On 31 May, the station Kittilä's Poka (Finnish Lapland) still measured 45 cm of snow, which is a new record for the 49-year-long series.

From 14 to 27 June, Scandinavia experienced a heat wave with high temperatures exceeding 30°C in many places. In Norway, a record high number of 11 days with daily maximum temperature surpassing 30°C occurred in June in several locations. New records were set at 36 stations in Norway. The highest temperature of 34.3°C was reached in Trondheim on 27 June. In Sweden,

the highest June temperature in Sweden since 1970 (34.0°C), was measured at Skelleftea Airport (Västerbotten Province, at the northern Baltic Sea coast) on 25 June.

During November many new temperature records were set in Scandinavia as warm air flowed north on the east side of ex-hurricane Zeta at the beginning of the month. In Norway, three new county records were recorded on 6 November: In Oslo, Blindern measured 16.1°C; in Viken, Råde–Tomb recorded 17.6°C; and in Vestfold and Telemark, Melsom recorded 17.4°C. On 18 November, a temperature of 15.1°C was measured at the Swedish stations Norrköping and Oskarshamn. This was the highest temperature ever observed in Sweden so late in the course of a year.

5) Iberian Peninsula

This region includes Spain, Portugal (1971–2000 base period), and Andorra.

(I) TEMPERATURE

The Iberian Peninsula observed its warmest year on record. Spain and Portugal reported temperature anomalies of +1.1° and +1.0°C, respectively.

Winter was warmer than usual. Spain and Portugal each reported their second-warmest winter with anomalies of +1.8° and +1.5°C. During February, when the Iberian Peninsula was under extensive high pressure, temperatures were higher than normal and resulted in a record warm month for Spain (tied with 1990) with an anomaly of +3.0°C and +2.5°C for Portugal.

Spring anomalies were +1.5°C for Spain (fourth warmest) as well as for Portugal. Blocking high pressure over the British Islands (Fig. 7.39b) led to exceptionally above-normal temperatures and made May the warmest on record for both Spain (+2.7°C above normal) and Portugal (+3.3°C).

Summer started with a near-normal June, but was followed by the warmest July on record for Portugal (anomaly +4.6°C) and third warmest for Spain (+2.0°C). August concluded the season with near-normal temperatures for Portugal and slightly above-normal temperatures for Spain.

Autumn temperatures were slightly above normal, but with variations between months. While October was colder than normal with anomalies just above –1.0°C, the season ended with a very warm November, the third warmest for Spain (+2.0°C above normal).

(II) PRECIPITATION

The Iberian Peninsula received near-normal precipitation during the year, at least on areal average. During winter, precipitation was near-normal for Spain on average, but distributed inhomogeneously; eastern Spain received above-normal precipitation while the rest of the country received below-normal precipitation. Portugal reported slightly below-normal precipitation. February was extremely dry; most of Spain received less than 25% of its normal precipitation and Portugal received less than 40% of its normal.

In spring, above-normal precipitation for both March and April (both well above 125% of normal) was followed by a drier-than-normal May. Overall, spring was wetter than normal, with 137% and 114% of normal precipitation for Spain and Portugal, respectively.

Summer precipitation was close to normal for much of Spain, while Portugal reported only 45% of normal and its spatial distribution was very inhomogeneous. During autumn, an opposite pattern emerged, and Portugal received near-normal precipitation while Spain observed only 86% of its normal. September was drier than normal almost everywhere on the Iberian Peninsula except for the center of Spain. During October, southern Spain was very dry with precipitation as low as 25% of normal, while northern Spain and Portugal received above-normal precipitation. The season ended wetter than normal in November for southern Portugal as well as eastern Spain; northern Spain received less than 60% of its normal precipitation.

(III) NOTABLE EVENTS AND IMPACTS

On 18–25 January, Storm Gloria impacted Spain, bringing abundant precipitation to the Mediterranean coast and the Balearic Islands, with more than 100 mm totals over an extensive coastal strip between Catalonia and Alicante and surpassing 400 mm at many stations within this strip.

Between 31 March and 1 April, the coastal region of Valencia in eastern Spain was hit by torrential rainfall, which led to flash floods. Between 34 mm and 39 mm of rainfall was measured, which is about four times the normal for these two days. Locally, station Castellon recorded 150 mm of daily precipitation, which was its highest total since 1976. The municipality of La Pobla Tornesa registered 197.6 mm of rain in 24 hours.

From 19 to 31 May, a heat wave affected Portugal and western Spain. Highest daily temperatures exceeded 37°C, for example, 37.3°C in Pinhảo (Portugal) on 28 May.

During the summer of 2020, there were several significant warm episodes, with two heat waves observed in mainland Spain and the Balearic Islands in July and August. A major heat wave occurred from 25 July to 2 August, with temperatures exceeding 40°C across much of the southwest quadrant of the Iberian Peninsula and in parts of the southeast, the interior of Ebro Valley, eastern Cantabrian, and the island of Mallorca.

During 4–5 November, a low-pressure system led to heavy rain and thunderstorms. The region around Valencia recorded 48-hour totals of up to 500 mm (e.g., 502 mm in Sueca/Muntanyeta dels Sants). In Ardales, a 24-hour total of 148 mm was recorded, which is almost 50% higher than the November monthly average of 100 mm. Roads were closed as a consequence of flash floods and landslides. Damaged tracks on the route Algeciras-Madrid led to a derailed train in Teba.

6) Central Mediterranean region

This region includes Italy (1961–90 base period), Monaco, Malta, Slovenia, Croatia, Serbia, Montenegro, Bosnia and Herzegovina, Albania, Macedonia, Greece, and Bulgaria.

(I) TEMPERATURE

The year was warmer than normal for the central Mediterranean, with anomalies between +0.9°C and +1.9°C. Italy reported its third-warmest year on record (+1.6°C above normal) and Slovenia its fifth warmest (+1.3°C).

During winter, anomalies ranged from around +1.0°C in Greece to above +3.0°C in Slovenia. It was the second-warmest winter for Italy (+2.3°C above normal) and third warmest for Slovenia (+3.1°C). During January, only Italy, Slovenia, and Bulgaria reported temperatures more than +1.0°C above normal. Temperatures were close to normal in Greece while the rest of the region reported anomalies between +0.4° and +0.9°C. February was exceptionally warm for Greece; in Malta anomalies were less than +2.0°C. The highest nationwide anomaly for the region was reported by Slovenia (+4.5°C above normal), its second-warmest February on record. Anomalies well above +3.0°C were reported by Bosnia and Herzegovina, Bulgaria, Croatia, and Serbia.

Spring was slightly warmer than normal for most of the region, with temperatures mostly ranging from +0.2°C above normal in North Macedonia to +0.8°C above normal in Slovenia; only Italy and Albania reported higher anomalies of +1.5°C. March temperatures ranged from +1.0°C above normal in Italy and Slovenia to +1.3°C for most of the Balkans; however, in Bulgaria, anomalies were above +2.0°C. During April, Italy, Slovenia, and Croatia all reported +1.5°C anomalies, while temperatures were near normal in Greece, North Macedonia, and Bulgaria. The season ended near to slightly colder than normal (anomalies up to −0.5°C) for most of the region in May, with the exception of Italy and Greece, which had positive anomalies of +1.9° and +1.0°C.

During summer, temperatures were around +0.5°C above normal for most of the region. Only Italy, Albania, and Greece reported temperatures above +1.0°C of normal. Summer started with near- to slightly below-normal temperatures for the whole region during June. July was near

normal in the north of the Balkans and warmer than normal in the south; Greece and Albania reported anomalies between +1.0° and +2.0°C. With temperatures +1.0° to +1.5°C above normal, the season ended with a warmer-than-normal August for the whole region.

Autumn temperatures were +1.0° to +2.0°C above normal for the Balkan Peninsula, while most of Italy and Slovenia reported anomalies below +1.0°C. September was the warmest month of the season. Italy and Slovenia reported anomalies of +1.7° and +1.4°C, respectively, and on the Balkan Peninsula, temperatures were between +2.0°C and +3.0°C above normal. For Italy and Malta, October was colder than normal by −0.7°C. Slovenia and Croatia reported near-normal temperatures. In Serbia, Bosnia and Herzegovina, and Greece, anomalies were +1.0° to +1.5°C. Temperature anomalies exceeded +2.0°C in Bulgaria. The season ended with anomalies around +2.0°C for Italy, Albania, and Montenegro in November. In Slovenia, Croatia, Bosnia and Herzegovina, Bulgaria, Greece, and Malta, anomalies did not exceed +0.6°C.

(II) PRECIPITATION

Overall, annual precipitation in the region was 80% to slightly above 100% of normal. Seasonally, winter was drier than normal in central and southern Italy, Malta, North Macedonia, most of Greece, and some parts of Bulgaria, Croatia, and Bosnia and Herzegovina with mostly 60%–80% of normal precipitation. In Sicily (Italy) and Malta, precipitation was only around 30% of normal. January was drier than normal for the whole region; with some local exceptions, precipitation did not exceed 60% of normal. For central and southern Italy, Malta, most of Greece, and some parts of Bulgaria and Croatia, rainfall was below 20% of normal. The season ended wetter than normal for Bulgaria and Serbia, while drought conditions, severe in some places, prevailed in most of Italy and Greece, where precipitation was just 20% and 40% of normal in February. Sicily and Malta received less than 20% of their normal precipitation. Overall, February was the driest on record for Malta and second driest for Italy.

Spring was wetter than normal for Bulgaria, Greece, North Macedonia, and Albania, with some areas receiving around 160% of their normal precipitation. Slovenia, Croatia, Bosnia and Herzegovina, and Italy, in contrast, reported precipitation around 80% of normal. In March, only Croatia and Bosnia and Herzegovina received below-normal precipitation (60%–80%), while the rest of the region had near- to slightly above-normal precipitation. April was drier across the region (20%–60% of normal), except for Greece, North Macedonia, and southern Bulgaria, where some areas received more than 170% of normal precipitation. May was drier than normal over western Greece, North Macedonia, Albania, and Italy, with around 80% of normal precipitation. For Bulgaria and Serbia, spring ended slightly wetter than normal.

During summer, nationally averaged precipitation was 110%–130% of normal across the whole region. Only Sicily and eastern Bulgaria received below-normal rainfall. The season started with a wetter-than-normal June for most of the region, with precipitation 122%–160% of normal; Albania and North Macedonia reported below-normal precipitation (70%–80% of normal). In July, the distribution of precipitation was inhomogeneous. Italy and North Macedonia reported near-normal precipitation. For Serbia and Albania, the month was drier than normal, with only 50%–60% of normal rainfall, while Slovenia reported 128% of its normal precipitation. With the exception of eastern Bulgaria, summer ended wetter than normal for the Balkan Peninsula in August. Nationally averaged precipitation ranged from 110% of normal in Slovenia to above 380% in North Macedonia (its wettest summer on record).

Precipitation was near normal for Slovenia, Croatia, Italy, and Malta during autumn, while it was drier than normal for Serbia, North Macedonia, Albania, Montenegro, Bosnia and Herzegovina, and Bulgaria. Most of Serbia, Albania, North Macedonia, and Greece received only 40%–80% of their normal precipitation. September was drier than normal in Bulgaria and North Macedonia with 60%–80% of normal precipitation. Italy, Slovenia, and Serbia reported slightly above normal (111%–118%) precipitation. Montenegro, Albania, and the southwestern parts of Greece received

130%–170% of normal precipitation. October was wetter than normal for most countries of the region, with precipitation 120%–160% of normal. However, it was drier than normal in Malta (33% of normal), North Macedonia (44%), and large parts of Greece (40%–80%). The season ended with an exceptionally dry November for the region. In many areas, rainfall did not exceed 50% of normal. Serbia reported only 14% of its normal precipitation, and Albania and Macedonia received less than 5%. For North Macedonia, it was the driest November on record. While Italy reported countrywide precipitation of 50% of normal, it was especially dry in the north where rainfall was well below 20% of normal. Slovenia reported 34% of its normal precipitation.

(III) NOTABLE EVENTS AND IMPACTS

On 2 and 3 March, the western Mediterranean and the Balkans experienced unusually high maximum temperatures due to warm air inflow east of a deep trough. Italy, Albania, and Greece recorded temperatures around 23°–25°C (normal March maxima are about 15–16°C in that area).

Between 12 and 22 May, Italy and the southern Balkans experienced an extreme heat wave. In southern Italy, temperatures around 40°C were recorded. Temperatures in the southern Balkans were between 33°C and 38°C. Some of the reported temperatures were the highest since 1945 for that time of year. Following the end of the heat wave, heavy thunderstorms with hail occurred over the Balkans. Walnut-sized hail, which caused damage to agriculture, buildings, and cars, was reported in Serbia.

After thunderstorms accompanied by heavy rain, Serbia and Bosnia experienced heavy flooding during 21–23 June. Some municipalities in central and western Serbia declared a state of emergency after overflowing rivers caused widespread damage to bridges, roads, power lines, and around 700 homes. The station Loznica recorded a daily precipitation of 210 mm on 23 June (weekly total was 304 mm). Bosnia reported flooding, landslides, blocked roads, and damage to roads, bridges, and houses in the region between Tuzla and Sarajevo. On 16 June, a heavy hailstorm caused flooding in the region of Drama in northern Greece. The storm lasted for more than half an hour and in some areas, the hail layer reached a thickness of 30–40 cm.

After a storm during the night of the 6–7 July, large parts of the city of Sofia (Bulgaria) were flooded. Many Metro stations, buildings, and underpasses were submerged.

On 29 July, a supercell caused an extreme hailstorm, with hail reaching diameters of 10 cm over central Slovenia. This caused extensive damage in the area from the towns of Vodice to Domzale in central Slovenia. The city of Palermo (Sicily) was hit by a thunderstorm, which brought more than 100 mm of rain in 3 hours. Severe flooding overwhelmed the sewer system and cars were swept away. The weather station at the astronomical observatory in Palermo recorded a new July daily precipitation record of 74 mm in a series reaching back to 1794.

Thunderstorms accompanied by heavy rain caused flash flooding on the island of Evia in central Greece on 8–9 August. Within a few hours, 200–300 mm were recorded on parts of the island, which is about 80% of its annual precipitation. At least seven people lost their lives.

At least four people were killed during a heavy thunderstorm accompanied by egg-sized hail on 29 and 31 August in northern Italy.

During 17–18 September, the medicane "Udine" ("Ianos" in Greece) caused heavy damage to roads, ports, and the power grid, as well as flooding in the Ionian Sea and mainland Greece. Precipitation estimates based on satellite, station, and model data were 186 mm over the Ionian Sea and 123 mm over western Greece mainland in 32 hours. (See Sidebar 4.2 for more information on medicanes in 2020).

On 9–10 November, more than 150 mm fell in 24 hours over some areas on Crete Island (Greece), causing flash flooding. Vehicles, roads, and houses were damaged. At least 79 people had to be rescued. After more than 450 mm of rain fell during 20–22 November in southern Italy, a state of emergency was declared in the Calabria region due to severe flooding that caused widespread damage.

7) Eastern Europe

This region includes European part of Russia, Belarus, Ukraine (1961–90 base period), Moldova and Romania, and west Kazakhstan.

(I) TEMPERATURE

The year was exceptionally warm for eastern Europe, with temperatures more than +2.0°C above average for most countries. It was the warmest year on record for the European part of Russia (+2.9°C), Belarus (+2.3°C), Ukraine (+2.2°C), Moldova (+2.0°C), and Kazakhstan (+2.3°C). Romania reported its second-warmest year (+1.7°C). During winter, anomalies were well above +3.0°C; Romania reported the lowest monthly anomaly of +1.7°C for the whole region and season in January. It was the warmest winter on record for European Russia (+5.4°C above normal), Belarus (+5.1°C), Ukraine (+4.0°C), Moldova (+3.8°C), and Kazakhstan (+5.4°C), while it was second warmest for Romania (+3.1°C).

Spring started with a warmer-than-normal March. Anomalies ranged from +2.6°C in Romania to above +6.2°C in Kazakhstan. It was the warmest March on record in European Russia (+5.9°C anomaly, 1961–90 base period). During April, only Moldova and Romania reported above-normal temperatures, while the other countries reported temperatures ranging from −0.8°C below normal in Belarus to near normal in Ukraine. The season closed with a colder-than-normal May for most of the region, except for Kazakhstan (+2.0°C above normal) and some eastern parts of European Russia. Anomalies in Belarus, Ukraine, and Moldova were around −2.2°C, while Romania reported −1.3°C below normal.

During summer, the entire region experienced temperatures +1.0° to +1.3°C above normal. For most of the region, June was the warmest of the summer months; only Romania reported an anomaly lower than +1.0°C. During July, temperatures were below normal for Belarus (anomaly of −0.6°C) and some areas of northwestern Russia. In the Ukraine, Moldova and Romania temperature anomalies were +0.5° to +0.8°C. In Kazakhstan, temperatures were +3.2°C above normal. August was colder than normal in Kazakhstan, at −1.2°C below normal while Belarus and Ukraine reported anomalies around +1.0°C. For Romania and Moldova, temperatures were +1.6° and +1.7°C above normal, respectively.

With the exception of Kazakhstan, the entire region experienced an unusually warm autumn. For Belarus, Romania, and the Ukraine it was the warmest September on record, with reported anomalies of +2.6°, +3.2°, and +3.5°C, respectively. In Moldova, temperature anomalies were above +4.0°C. The warmth continued in October; Romania observed its second-warmest October on record (+2.8°C above normal), while European Russia was record warm (+3.4°C, 1961–90 base period). Belarus reported temperatures +3.8°C above normal, and in the Ukraine and Moldova, anomalies reached above +4.0°C, each ranking October 2020 among their five warmest Octobers on record.

(II) PRECIPITATION

The year was slightly drier than normal across the region, with 86%–96% of normal precipitation; Kazakhstan reported a lower value of 72% of normal. The areas around the Black Sea, southern Russia, and Kazakhstan received the least precipitation.

During winter, the Ukraine and Belarus received near-normal precipitation. Moldova and Romania reported below-normal precipitation of 50% and 80% of normal, respectively. Except for Russia, which reported normal precipitation, January was drier than normal. Belarus and Kazakhstan received 80%–90% of their normal precipitation and the Ukraine 55% of its normal. For Moldova and Romania, January ranked as the second and third driest on record, with only 23% and 30% of normal precipitation, respectively. In February, most of the region received around 150% of normal precipitation. Only Belarus reported near-normal precipitation.

Spring was slightly wetter than normal for European Russia and near normal for the Ukraine. Belarus, Romania, Moldova, and Kazakhstan received 70%–80% of their normal precipitation. During March, only some areas in the southwest of Romania and most of northern Russia received above-normal precipitation. Belarus reported around 70%, the Ukraine 68%, Romania 110%, and Kazakhstan and Moldova each 50% of normal precipitation. For Belarus, the Ukraine, Moldova, and Romania, April was very dry with nationally averaged precipitation below 40% of normal, and even less in localized areas. Romania reported its driest April on record. Spring ended with a wetter-than-normal May for most of the region, with countrywide precipitation 110%–174% of normal. The Ukraine had its second-wettest May, with 174% of normal precipitation.

Summer was drier than normal for the Ukraine and Moldova, with 80% of normal precipitation. Many areas in southern Russia and Kazakhstan received only 40%–80% of their normal precipitation. Although some areas received above-normal precipitation, June and July were drier than normal for Russia and Kazakhstan. Most of Kazakhstan received less than 20%–40% of normal precipitation in June; however, for Belarus, Moldova, and Romania, precipitation was 120%–155% of normal. While some eastern areas in the Ukraine received below-normal rainfall, overall precipitation was slightly above normal for the country. July rainfall was near normal for Romania and drier than normal for Belarus, the Ukraine, and Moldova with 60%–90% of normal precipitation. Summer ended with above-normal precipitation for Kazakhstan (around 130% of normal) and some parts of Russia in August. Meanwhile, the Ukraine reported only 43% of normal precipitation and Romania received 70%, marking its third-driest August on record.

The Ukraine and Romania reported near-normal rainfall for autumn. Belarus received around 80% of its normal precipitation. For most of Kazakhstan and many areas of European Russia, precipitation was 40%–60% of normal. The season started with near-normal precipitation in September for the Ukraine and Romania, while Belarus received around 70% of its normal. While overall Russia received 80% of normal precipitation, it was especially dry in southern European Russia where large areas received less than 20% of normal precipitation. October was wetter than normal for the western countries of the region: Belarus, the Ukraine, Moldova, and Romania received 110%–170% of normal precipitation. In Kazakhstan, rainfall was very low—around 20% of normal. While overall Russia received around 70% of normal precipitation, the south was very dry again with around 20% of normal precipitation in some areas. The season concluded with below-normal rainfall across most of the region, with nationally averaged precipitation of 40%–80% of normal in November.

(III) NOTABLE EVENTS AND IMPACTS

Due to manmade grass burning and favorable dry conditions together with strong winds, on 4 April wildfires broke out in areas heavily contaminated by the Chernobyl nuclear accident. The fires reached the Exclusion Zone about 1 km from the power plant, where radioactive contamination is the highest. The fire was taken under control only after 10 days and an area of at least 20,000 ha burned. Due to the fire, significantly elevated levels of cesium 137 were measured in the air in Kiev, which, according to the Institute for Radiological Protection and Nuclear Safety (IRSN), posed no risk to health.

Between 8 and 17 June, extremely high temperatures were measured in Russia up to the Arctic circle. Many stations reported temperatures up to 32°C, which is around +20°C above normal. On 9 June, the station Nizhnyaya Pesha located at 66.7°N measured a temperature of 30.3°C. A new daily maximum record of 31.4°C was set in Moscow on 17 June.

Following heavy rain on 22–23 June, overflowing rivers damaged roads, bridges, and power lines in western Ukraine. Approximately 7500 homes were flooded, over 470 people were displaced, and three people were killed.

A combination of significantly above-average temperatures and precipitation deficits (60%–75% of normal) during autumn in European Russia resulted in significant below-average winter grain crop moisture (relative to 2000–19) in the Southern Federal District, in certain regions of the Central Federal District, and the Volga Federal Districts of Russia.

8) Middle East

This region includes Israel, Cyprus, Jordan, Lebanon, and Syria.

(I) TEMPERATURE

Overall, the year was warmer than usual across the Middle East, with temperatures +1.1° to +1.5°C above normal. It was the third-warmest year on record for Cyprus and Jordan and the fourth warmest for Syria.

Winter was slightly warmer than normal for the region, except for Cyprus where the anomaly was close to +1.0°C. January had temperatures that were near to slightly below normal. The season ended with February anomalies close to +1.0°C across the region, except for Syria, which reported near-normal temperatures.

Spring started with a warmer-than-usual March, with anomalies close to +1.5°C for all countries of the region. April was near normal, but in May, anomalies were above +1.5°C, except in Syria (+0.5°C above normal). Cyprus and Israel each reported their third-warmest May on record (anomalies of +2.5°C and +1.8°C, respectively).

Summer temperatures ranged from +0.6°C above average in Syria to +1.0°C in Jordan. June was near to below normal for most of the region. Except for Jordan (anomaly +0.6°C), anomalies ranged from −0.3°C (Syria) to +0.2°C (Israel). July was the warmest month of the season; anomalies for Cyprus and Israel were +1.0°C. Jordan and Syria reported their third-warmest July with anomalies of +3.0° and +1.6°C, respectively. August temperatures were a little more than +1.0°C higher than normal for Cyprus and Israel, while the anomaly for Syria was close to +0.5°C. August was slightly cooler than normal for Jordan.

Autumn was exceptionally warm for the entire Middle East; most countries observed temperatures more than +2.0°C above normal. Cyprus and Syria each reported their warmest autumn on record, with anomalies of +2.6° and +2.5°C, while it was second warmest for Israel and Jordan, at +2.1° and +2.8°C, respectively. September was the warmest on record for all countries in the region and October was warmest on record for all except Israel (third warmest). September anomalies ranged from +2.8°C in Israel to +4.3°C in Jordan. During October, anomalies were not quite as high but still well above +2.0°C (Cyprus +3.0°C; Syria +2.5°C; Israel +2.2°C; Jordan +3.4°C). For Cyprus, the November temperature was nearly +2.0°C above normal, while anomalies were close to +1.0°C across the rest of the region.

(II) PRECIPITATION

During the year, except for Syria, the Middle East received above-normal precipitation. For Cyprus and Israel, precipitation was around 160% of normal and for Jordan it was 120% of normal. For Syria, the year was wetter than normal in the west and drier than normal in the east.

Winter was wetter than normal; many areas received precipitation above 125% of normal and above 167% of normal in localized areas. During January, the northern and western parts of the region were wetter than normal. In February, southern Israel and many parts of Jordan were wetter than normal, while many parts of Syria received only 20%–60% of normal precipitation (even less in central Syria).

While spring was wetter than normal overall (except for large areas in central Syria and northern Jordan), precipitation was distributed very inhomogeneously over the months. After a wetter-than-normal season start in March, large areas of the Middle East received well below 20% of normal precipitation in April. For the most western parts of Syria, Lebanon, and Israel,

precipitation was around 125% of normal. Localized areas in southern Jordan received above-normal precipitation of around 500%. In May, only northern Israel, northwestern Jordan, and Lebanon received above-normal precipitation; only 20%–60% of normal was received elsewhere.

Summer was especially dry. Large parts of Israel and Syria received almost no precipitation at all during their dry season. In Cyprus, precipitation was around 80% of normal. Most of Jordan, especially the north, received little precipitation. For Cyprus, Syria, Lebanon, and Israel all summer months were drier than normal with precipitation totals of mostly 0%–30% of normal. Precipitation was above normal for Jordan, southern Israel, and southeastern Syria in July.

At the beginning of autumn, only localized areas observed some precipitation in northern Jordan, otherwise the Middle East received precipitation well below 20% of normal or none at all. The dry September was followed by an extremely dry October, with most of the area receiving no precipitation, which led to the whole Middle East experiencing an extreme drought. November was wetter for most of the region, where precipitation ranged from 125%–250% above normal (except for northwestern Syria).

(III) NOTABLE EVENTS AND IMPACTS

From 25 December 2019 to 10 January 2020, storm activity with exceptionally high precipitation led to flooding, heavy damage to property, and casualties in Cyprus, Syria, Lebanon, and Israel. On 4 January, 74 mm of precipitation was measured within 2 hours in Tel Aviv, which is around 20% of the annual rainfall. On 8 January, a daily total of 97 mm was measured in Haifa. The Haifa Center Hashoma railway station was completely flooded after the area received a downpour of 50 mm in less than 2 hours. Within 24 hours, the Sea of Galilee rose by 23 cm. Overall, during this period, average rainfall totals of 350–400 mm occurred (550 mm in localized areas). This was the highest 2-week total since January 1969 and the third highest in the last 80 years. For some areas in the south, precipitation surpassed monthly and seasonal normals and broke a 76-year old record. In Cyprus, some of the largest water reservoirs were completely filled and even overflowing the dam walls (an all-time record) after heavy rain between 6 and 8 January. Following these events, Syria and Lebanon experienced snowstorms due to cold air inflow, with Lebanon measuring snow depth of 130 cm in Kfardebian (1900-m altitude) on 10 January.

On 18 February an extreme cold spell with temperatures as low as –11°C, accompanied by heavy snow and ice storms, made living conditions for over 80,000 displaced people difficult. At least seven children including one baby froze to death.

After heavy precipitation between 9 and 11 April, the water level of the Sea of Galilee rose up to only 6–21 cm below maximum capacity and thus close to completely full for the first time since 1992. The abundant rainfall that started in January increased the water levels by 3.12 m. All of Israel had received more than its normal annual precipitation totals by this time.

At the beginning of May, intense and unusual thunderstorms were observed across Israel (typically, the dry season has already begun around this time of year). On 5 May, 828 lightning strikes were observed (monthly normal is 30). Heavy rain and hail led to flooding and highway blockages. During 23 and 24 May, unusually late snow was observed on Mount Hermon (2814 m a.s.l.).

During an exceptional heat wave at the beginning of September, many countries in the Middle East reported new maximum temperature records; in Hassakah (Syria) 47.0°C was measured on 3 and 4 September; Houche-Al-Oumara (Lebanon) 44.3°C on 3 September; Gecitkale (Cyprus) 45.8°C on 4 September; and 48.5°C at Aqaba Airport (Jordan) on 5 September. Eilat (south Israel) reached 48.9°C on 4 September, setting both a monthly and an all-time maximum temperature over the 70 year-long record. On 3 September, two new monthly records were broken in Jerusalem; a new maximum temperature of 41.2°C was measured for the 118-year-long record, and the temperature did not drop below 31°C the following night. In Kefar Blum, a maximum temperature above 40°C occurred on eight consecutive days.

Following an October with no precipitation at all for Israel, exceptionally intense rain during 20–22 November caused severe flooding of houses, roads, and cars. Around Mount Carmel, 24-hour totals of 230 mm (the highest since 1998) were measured. Other areas of the country received 100–150 mm of rainfall during this time, which was more than double the monthly normal.

9) Turkey and South Caucasus

This region includes Turkey, Armenia, Georgia, and Azerbaijan.

(I) TEMPERATURE

Overall, the year was warmer than normal for the region with annual temperatures +1.0° to +1.6°C above normal. The year started with a warmer-than-normal winter. Turkey observed temperatures that were +1.4°C above normal, while anomalies for Armenia, Georgia, and Azerbaijan were around +2.0°C. Armenia reported its second-warmest January and February on record.

Spring started with an exceptionally warm March, with temperatures more than +4.0°C above normal almost everywhere in eastern Turkey and the South Caucasus. After a colder-than-normal April for the South Caucasus (anomalies between –1.0°C and –2.0°C) and near normal for Turkey, May was warmer than normal, with temperatures about +1.0°C above normal.

For most of the region, summer was only slightly warmer than normal, with anomalies of around +0.6°C; Georgia and some parts of northern Turkey observed anomalies above +1.0°C. For Turkey, the season started with a near-normal June while in the South Caucasus anomalies were well above +2.0°C. July temperatures were around +1.3°C above normal, except in Georgia with around +2.0°C anomalies. August was colder than normal in eastern Turkey and the South Caucasus. Anomalies were slightly below –2.0°C in Armenia and Azerbaijan.

Due to a very warm September and October, autumn was exceptionally warm, especially for Turkey, which reported its warmest autumn on record (+2.5°C above normal). Georgia and Armenia also reported anomalies of +2.0°C, while in Azerbaijan it was close to +1.0°C above normal. Both Georgia and Armenia reported September and October monthly anomalies above +2.5°C. In most of Turkey, temperature anomalies were well above +3.0°C and even higher in localized areas, making both September and October the warmest on record.

(II) PRECIPITATION

Annual precipitation was distributed inhomogeneously for Turkey and Armenia during 2020, but were close to normal on balance: the southern parts of the region and also some parts of Turkey (Mersin, Giresun, Trabzon, Şirnak, Adiyaman, Diyarbakir, Hakkari, Batman Kirklareli) received above -normal precipitation while the northern parts were drier than normal. Overall, precipitation for Turkey was 87% of its annual normal. Georgia received only 80% of its normal precipitation. For Azerbaijan, the year was slightly wetter than normal.

During winter, Turkey received above-normal precipitation of about 110%, even though precipitation was below normal in the east and west. Georgia and Armenia reported precipitation totals that were 75% of normal. The distribution of precipitation in January was inhomogeneous in Turkey, with some parts in the east and west receiving 40%–80% of normal while precipitation was above normal in other areas. Armenia reported 43% of its normal and Georgia overall received near-normal precipitation. Winter ended with near-normal precipitation in February for most of the South Caucasus and slightly wetter than normal for Turkey (115% of normal).

During spring, the region received around 115% above-normal precipitation except in western Turkey where precipitation was below normal (locally as low as 80% of normal). Except for western and central Turkey in March and April, all months were slightly wetter than normal in most of the region but up to 170% of normal in localized areas.

Summer was drier than normal for both Georgia and Armenia with only 90% of normal precipitation. Azerbaijan received around 115% of its normal precipitation. While some southern regions

in Turkey were drier than normal, nationally averaged precipitation was slightly above normal. For the South Caucasus, only June was drier than normal, while it was wetter than normal for Turkey. During July and August, western and central Turkey received below-normal precipitation, as low as 20% of normal in some places.

During autumn, precipitation was between 40%–60% of normal almost everywhere in the region. September and October were notably dry. Only some local areas in western Turkey received above-normal precipitation during those months. September precipitation was 40% of normal on average. During October, rainfall totals were even lower in many areas. Eastern Turkey received less than 20% of its normal precipitation and Georgia received around 30% of its normal. On average, November precipitation was around 80% of normal for the region, although some parts of eastern Turkey received precipitation up to 169% of normal.

(III) NOTABLE EVENTS AND IMPACTS

During 6–7 January, heavy winds, rain, and snow affected large areas of Turkey. The southern province of Mersin received around 165 mm of precipitation in 24 hours, causing heavy flooding and landslides. At least two people were killed. In some parts of Istanbul, more than 110 mm of precipitation fell in 24 hours and wind gusts over 104 km h^{-1} were measured. Flooding caused traffic disruptions and strong winds damaged over 100 buildings.

In February, Turkey experienced an extensive cold spell with snowstorms, blizzards, and extremely cold temperatures. Roads were blocked by snow or closed due to risk of avalanches. During the night of 9–10 February, a new local record low temperature of −40°C was recorded in Gole (Ardahan Province, northeastern Turkey). On 21 February, a blizzard hit southeastern Turkey and buried a village under about 6 m of snow. Seventy villages were isolated and electricity and water supplies were disrupted.

On 29 July, heavy precipitation caused flooding in western Georgia (upper Racha province). Floods and mudslides caused heavy damage to roads and bridges, which isolated over 2000 people. The water and electricity supply was disrupted for 400 homes. In the Guria area at the Black Sea coast, agriculture fields, roads, and power lines were damaged.

g. Asia—T. Li, Ed.

Throughout this section the base periods used vary by region. The current standard is the 1981–2010 average for both temperature and precipitation, but earlier base periods are still used in several countries. All seasons mentioned in this section refer to those of the Northern Hemisphere (NH), with winter referring to December–February 2019/20, unless otherwise noted.

1) Overview—T. Li, Z. Zhu, P. Zhang, T. C. Lee, S. Supari, M. Hanafusa, Hir. Sato, S. Wakamatsu, G. S. Im, D. Dulamsuren, A. Moise, M-V. Khiem, and H-P. Lam

Annual mean surface air temperatures during January–December 2020 were above normal across most of Asia, with dominating positive anomalies above +3.0°C in Siberia and other positive anomalies exceeding 1.0°C from the eastern part of East Asia to the Indochina Peninsula (Fig. 7.41). Annual precipitation totals were above normal (>120%) from western to central Siberia, in the eastern part of East Asia, from western India to Pakistan, and southeast of Arabian Peninsula, and below normal (<80%) in western Central Asia and western China (Fig. 7.42).

In winter, positive temperature anomalies dominated Siberia and much of Asia, except from western China to northern India (Fig. 7.43a). Seasonal precipitation was below normal across much of Southeast Asia (Fig. 7.43b) and much above normal in northeast China. In spring, dominating positive temperature anomalies continued across much of Siberia (Fig. 7.43c). In summer, positive temperature anomalies were observed in northern Siberia, from Japan to the Korean Peninsula, and from southeastern China to the Indochina peninsula (Fig. 7.43e). The eastern part of East Asia experienced above-normal precipitation (Fig. 7.43f). In autumn, much-above-normal

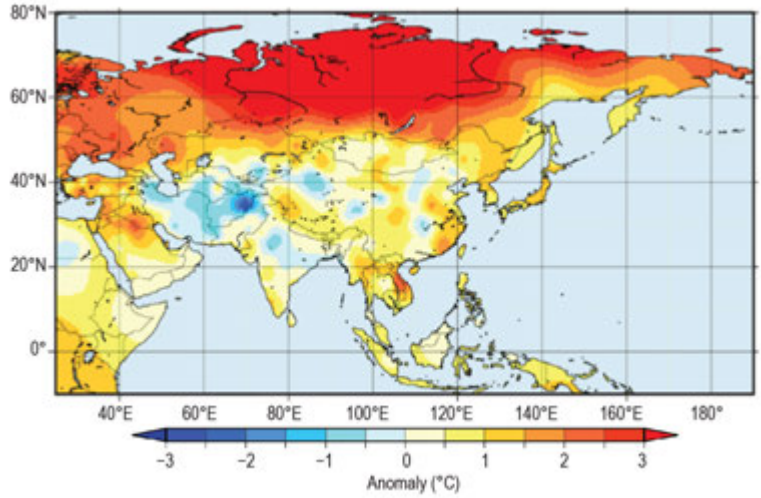

Fig. 7.41. Annual mean surface temperature anomalies (°C; 1981–2010 base period) over Asia in 2020. (Source: Japan Meteorological Agency.)

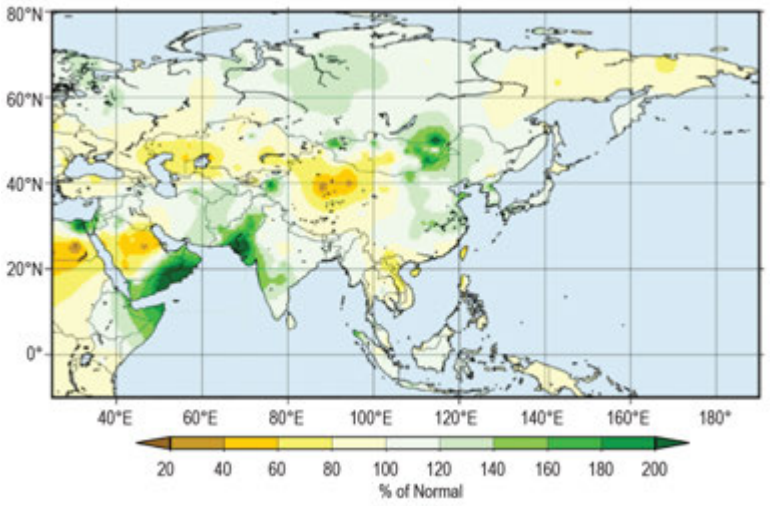

Fig. 7.42. Annual precipitation (% of normal; 1981–2010 base period) over Asia in 2020. (Source: Japan Meteorological Agency.)

temperatures prevailed in Siberia, while temperatures were below normal from northwestern China to Central Asia (Fig. 7.43g). The seasonal precipitation total was above normal in and around southern India due to late withdrawal of the monsoon season (Fig. 7.43h) and above normal in northeast China.

In winter, positive 500-hPa geopotential height anomalies and 850-hPa temperature anomalies occurred from Siberia to East Asia (Fig. 7.44a) and notably continued over a wide area of Siberia during spring (Fig. 7.44b). Also in spring, convective activity was suppressed over the South China Sea (Fig. 7.45b), which was accompanied by the southward shift of the subtropical jet stream over Eurasia. In summer, lower-tropospheric anti-cyclonic circulation anomalies straddling the equator were present over the western tropical Pacific; these anomalies were associated with enhanced convection over the western Indian Ocean and suppressed convection over the western Pacific, respectively (Fig. 7.45c). In autumn, convective activity was enhanced from the northern Indian Ocean to the Maritime Continent, and suppressed to the west of the date line in the equatorial Pacific (Fig. 7.45d). In the 500-hPa height field, a wavy anomaly pattern was seen over Eurasia with negative anomalies over Central Asia (Fig. 7.44d).

2) Russia—M. Yu. Bardin and N. N. Korshunova

Estimates of climate features for Russia are obtained from hydrometeorological observations of the Roshydromet Observation Network. Anomalies are relative to the 1961–90 base period, and national rankings and percentiles reflect the 1936–2020 period of record. Note that the temperature database was extended significantly, which in some cases changed previous ranking. The boundary between Asian Russia and European Russia is considered to be 60°E.

(I) TEMPERATURE

The year 2020 in Russia was record warm, with the annual mean temperature 3.2°C above normal (Fig. 7.46), exceeding the previous record of 2007 (2.2°C above normal) by a full 1°C. Both Asian and European Russia were record warmest. Anomalies above the 95th percentile were observed at most stations across the country, except for some coastal regions of the northern Far East. Over vast territories in northern Siberia, annual mean temperatures exceeded the climatology by more than 5°C (more than 6°C in the Taimyr Peninsula). Seasonally, winter, spring, and autumn each were warmest on record for Russia; summer 2020 was fifth warmest.

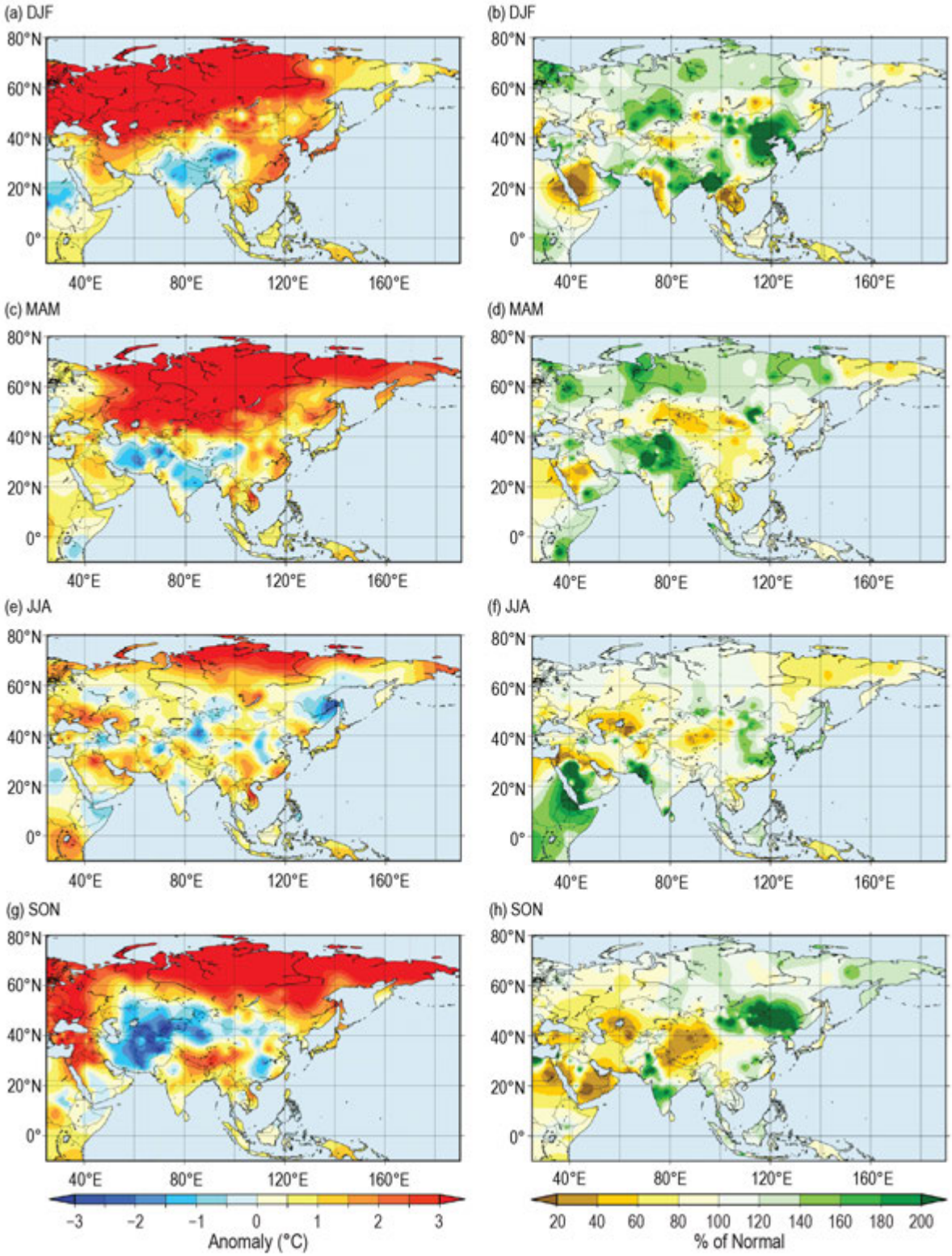

Fig. 7.43. Seasonal mean surface temperature anomalies (°C, left column) and seasonal precipitation (% of normal, right column) over Asia in 2020 for (a,b) winter; (c,d) spring; (e,f) summer; and (g,h) autumn. All relative to 1981–2010. (Source: Japan Meteorological Agency.)

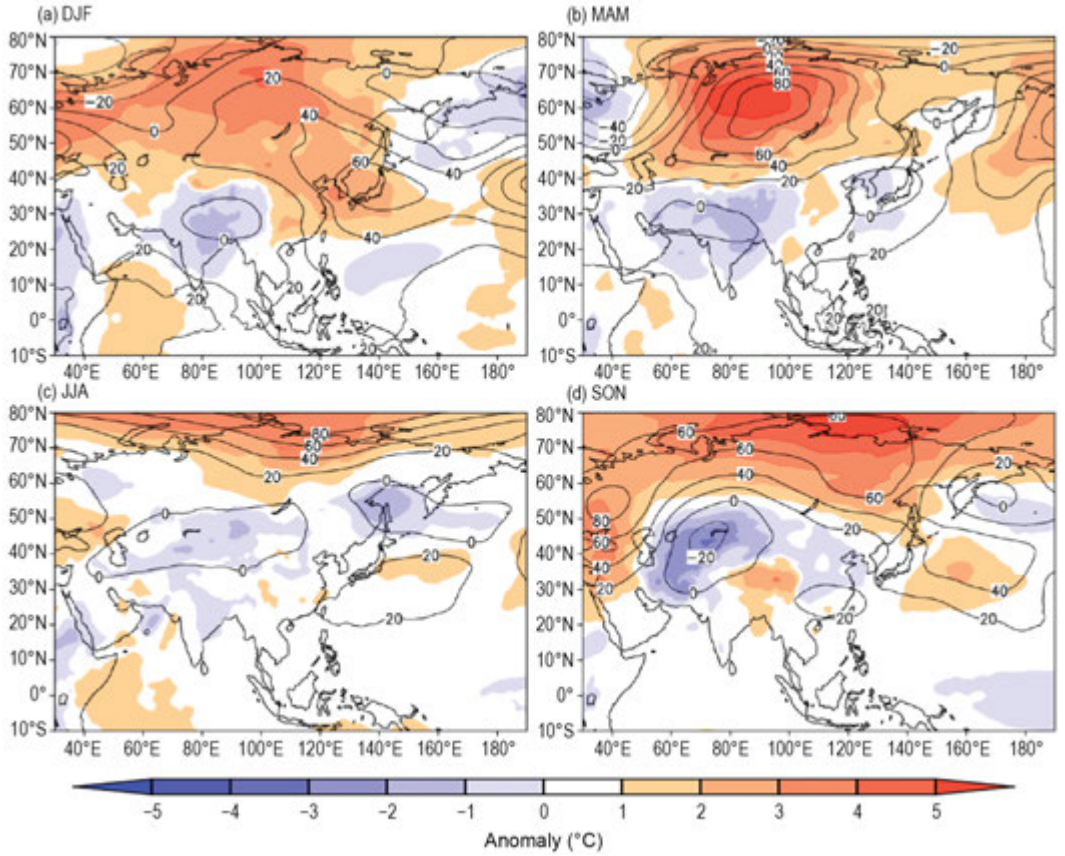

Fig. 7.44. Seasonal mean anomalies of 500-hPa geopotential height (contour, gpm) and 850-hPa temperature (shading, °C) in 2020 for (a) winter, (b) spring, (c) summer, and (d) autumn, using data from the JRA-55 reanalysis. The base period is 1981–2010. (Source: Japan Meteorological Agency.)

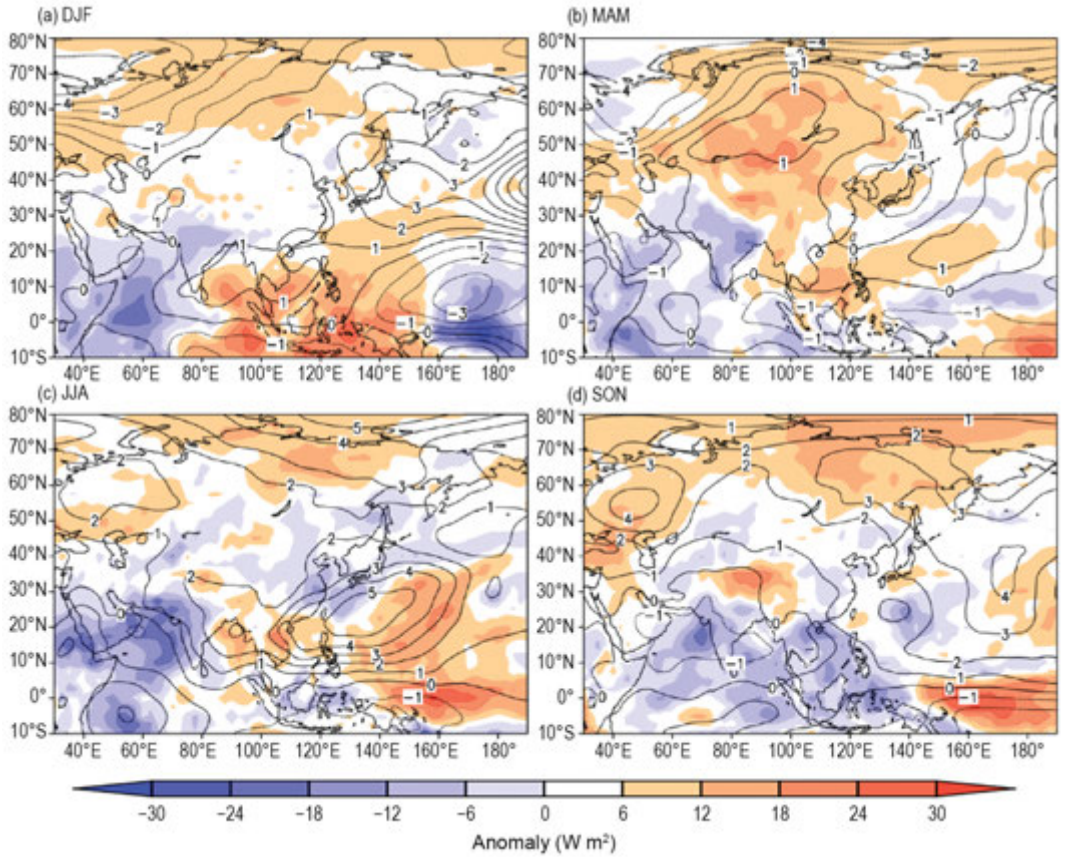

Fig. 7.45. Seasonal mean anomalies of 850-hPa stream function (contour, 1×10^6 m^2 s^{-1}) using data from the JRA-55 reanalysis and OLR (shading, W m^{-2}) using data originally provided by NOAA in 2020 for (a) winter, (b) spring, (c) summer, and (d) autumn. The base period is 1981–2010. (Source: Japan Meteorological Agency.)

Winter 2019/20 was warmest on record for both Asian and European Russia. For Russia as a whole, the mean temperature was 5°C above normal, 1.5°C above the previous warmest winter of 2014/15. European Russia was especially warm (6.8°C above normal; 2.5°C above the warmest winter of 2015/16) as was Western Siberia, where temperatures were more than 7°C above normal almost everywhere. Only the northern Far East was near normal. January was abnormally warm across the country, except in the Chukotka region (Fig. 7.47). Intense westerlies brought European Russia warm air from the Atlantic, and large areas with temperatures 8°–12°C above normal were observed in its northwestern and central parts. Many stations observed new record high temperatures on 15–17 January. Another strong warm center formed in the Irkutsk and Krasnoyarsk regions of Siberia.

It was a record warm spring for Asian Russia (4.61°C above normal). It was especially warm in Western Siberia with temperature anomalies exceeding +6°C everywhere, including the eastern part, where temperatures were 9°C above normal. Most stations in the Urals and Siberia reported temperatures above their 95th percentile. March, April, and May were each among their three warmest months on record for both Russia as a whole and for Asian Russia, with May being the warmest month on record. In European Russia, following an abnormally warm winter, March

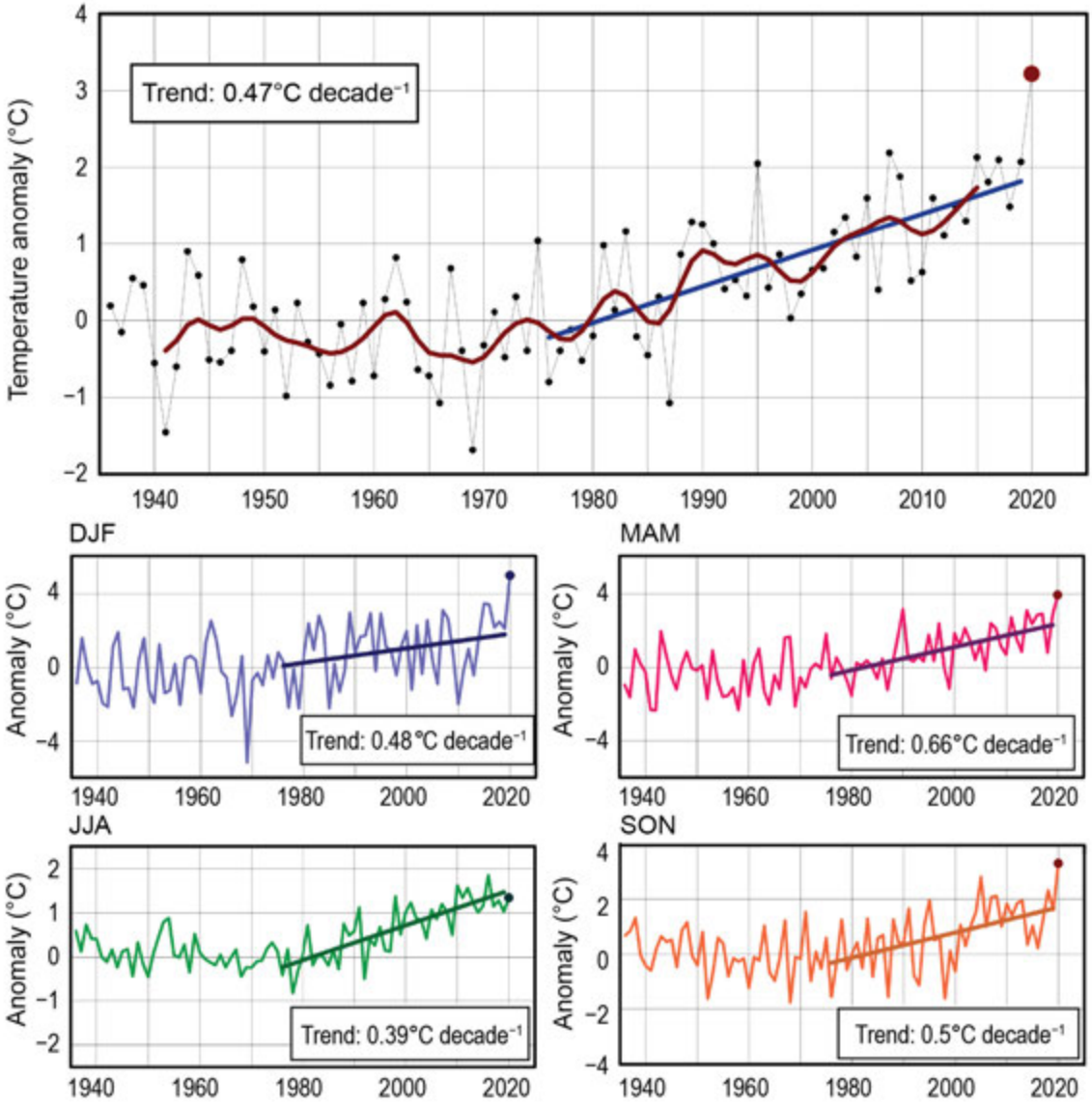

Fig. 7.46. Annual and seasonal mean temperature anomalies (°C; 1961–90 base period) averaged over the territory of Russia for the period 1936–2020. The bold red line on the annual mean time series is an 11-point binomial filter. Linear trend (°C decade^{-1}) is calculated for the period 1976–2020.

was the warmest on record with an average temperature 5.9°C above normal. It was also very warm in Western Siberia, especially around the Ob' River estuary, where monthly temperatures were more than 8°C above normal.

Summer was the fifth warmest on record, with an overall temperature 1.34°C above normal. It was Asian Russia's seventh-warmest summer, also 1.34°C above normal. European Russia observed its 13th warmest, at +1.35°C. The highest departures from average occurred in the polar

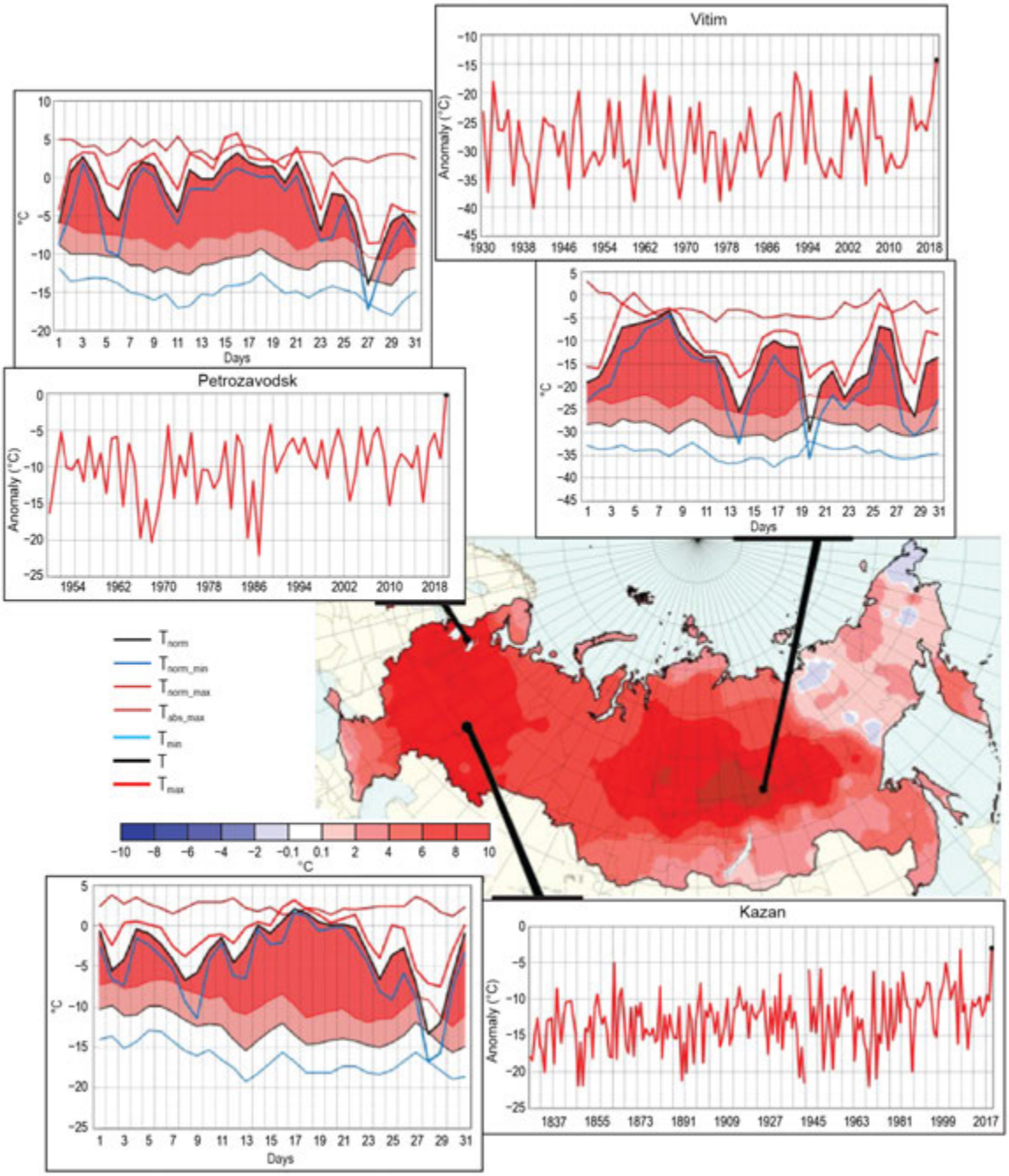

Fig. 7.47. Temperature anomalies across Russia (shading, contour interval is 2°C) in Jan 2020. Insets: Mean monthly and mean, minimum, and maximum daily temperatures (°C) in Jan 2020 at meteorological stations Petrozavodsk (upper left), Vitim (upper right), and Kazan (bottom). $T_{61\text{-}90}$ on plots of monthly temperatures is 1961–90 mean. Plots of daily temperature show observed daily mean (T, black line), daily minimum (Tmin, blue line), and daily maximum (Tmax, red line) temperatures along with their climatological values (three lowermost curves: Tnorm, black; Tnorm_min, blue; Tnorm_max, red) and absolute maximum temperature (Tabs_max, dark red); the area between the normal daily mean curve Tnorm and the observed daily mean curve is shaded pink where T > Tnorm, and is shaded red if T was above normal daily maximum Tnorm_max. Starting years of records vary.

zone of Siberia (temperature anomalies of about +5°C observed at the Kara coast). July had the highest departure from average among the summer months and was the fifth-warmest July on record, at 1.46°C above normal.

Autumn in Russia was record warm, 3.29°C above average, due to record warmth in September and November (2.49°C and 5.44°C above normal, respectively) in Asian Russia and in October in European Russia (3.42°C above normal). In the second half of November, warm air transported by Atlantic cyclones resulted in the formation of a vast warm area in northern and central Siberia, with temperatures 10°–12°C above normal.

All seasons in Russia have warmed since the mid-1970s. Annual and seasonal trends are statistically significant at 1%, except winter. Winters cooled after the mid-1990s, then began to warm again after 2010 (Fig. 7.46). The anomalously warm seasons of 2020 resulted in changes of trend estimates, notably winter and autumn estimates for 1976–2020 are +0.48°C and +0.50°C decade^{-1}, respectively, while 1976–2019 estimates are +0.39°C and +0.43°C decade^{-1}.

(II) PRECIPITATION

Across Russia as a whole, 2020 was among its 15 wettest years on record, with total precipitation about 106% of normal (Fig. 7.48). Asian Russia was sixth wettest (109% of normal), while European Russia was near normal (101%). Overall, winter and spring were wet while summer and autumn were near normal. Southern European Russia experienced precipitation deficits throughout the year, notably in summer and autumn.

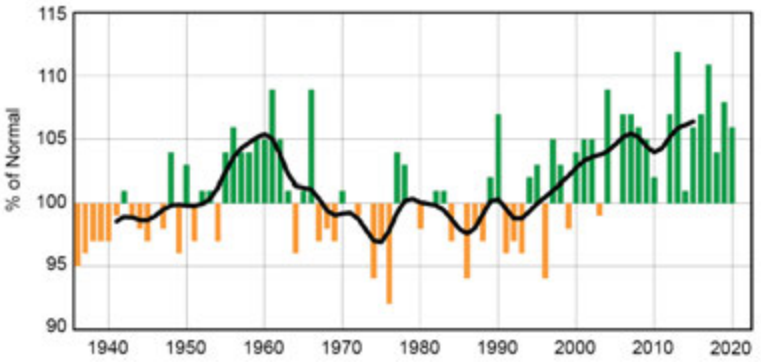

Fig. 7.48. Annual precipitation (% of normal; 1961–90 base period) averaged over the Russian territory for 1936–2020. The smoothed time series (11-point binomial filter) is shown as a bold line.

Across all of Russia, winter 2019/20 was the third wettest on record, with 120% of normal precipitation. Asian Russia received 119% of its normal precipitation (fourth wettest on record), while European Russia received 120% (tied as eighth wettest). Precipitation above 120% of normal was observed in Western Siberia and southern Yakutia (Sakha). In northern European Russia, the Northwestern Federal District precipitation was record high at 149% of normal.

It was Russia's fourth-wettest spring on record, with precipitation 121% of normal; Asian Russia had 119% of normal precipitation (tied for third wettest), while precipitation in European Russia was 123% of normal (tied for seventh wettest). The wettest regions were central European Russia (144%, third wettest on record) and the Urals Federal District (152%, record wettest). It was the second-wettest March in Asian Russia (169% of normal), notably wet in central parts of Siberia, Chukotka, and Kamchatka with precipitation above 200% of normal and above 300%–400% at many stations. April was dry in Asian Russia east of 80°E (below 40% of normal over large areas) and southern European Russia. May was the second wettest on record for the month for Russia as a whole, at 129% of normal.

In summer, precipitation was less than 70% of normal in many regions, including southern European Russia, Yakutia (Sakha), and Chukotka. August was dry across Asian Russia east of 80°E (with the exception of the narrow belt along the southern boundary).

Autumn was dry over large areas in Siberia and in the central and southern regions of European Russia: 54% of normal precipitation in the Southern Federal District, marking its third driest autumn on record. Northern European Russia, Baikal, and Amur had a wetter-than-normal autumn.

(III) NOTABLE EVENTS AND IMPACTS

On 4 February, heavy rainfall caused flooding on the Pshish River (0.2 m above hazardous level) in the town of Khadyzhensk in the Krasnodar Territory. Flooding inundated and washed out roads, damaged 80 buildings, 22 households, and two pedestrian bridges.

On 13 March, strong winds, as high as 26 m s^{-1}, caused substantial damage to infrastructure in Moscow and the Moscow Region. Eleven people were injured and one person was killed.

On 28–30 March, a heavy snowstorm with wind speeds reaching 30–33 m s^{-1} raged for 18 hours in the Pevek settlement, Chukotka Autonomous District. Wind gusts at the coast attained 44–50 m s^{-1}.

During 24 April–16 July, 333 and 731 fire incidents were recorded in Buryatia and the Trans-Baikal Territory, covering 54,663 and 298,393 ha, respectively.

On 27 June, strong winds up to 24–28 m s^{-1} in the Nizhniy Novgorod Region caused power to be cut off in 92 settlements and also damaged roofs and cars.

On 28 July, 48 mm of rain in Moscow inundated underground stations and roads and injured two people.

On 16–17 September, during flooding on the Amur River due to heavy rainfall, the water level around the Leninskoe settlement in the Jewish Autonomous Region rose to 9.68 m, above the danger level of 8.50 m. Two settlements, Leninskoe and Kukelevo, were inundated; 97 people were evacuated.

On 29–30 September, the rainfall flood crest on the Amur River reached the city of Komsomolsk; the water level was 7.04 m, surpassing the danger level of 6.5 m. Basements in four kindergartens, the city theatre, and 50 high rise buildings were inundated, with water levels more than 1 m in places.

3) East and Southeast Asia—P. Zhang, T. C. Lee, S. Supari, M. Hanafusa, Hir. Sato, S. Wakamatsu, G. S. Im, D. Dulamsuren, A. Moise, M-V. Khiem, and H-P. Lam

Countries/places considered in this section include China, Hong Kong (China), Indonesia, Japan, Korea, Mongolia, Singapore, and Vietnam. Unless otherwise noted, anomalies refer to a normal period of 1981–2010.

(I) TEMPERATURE

Annual mean temperatures for 2020 across East and Southeast Asia are shown in Fig. 7.41. The annual mean air temperature for China was 0.7°C above the 1981–2010 normal, the eighth highest since the start of the record in 1951. Temperatures were above normal in all seasons, especially winter (December 2019–February 2020; +1.2°C) and spring (+1.1°C). Hong Kong, China, experienced its second-warmest year on record since 1884, with an annual mean temperature of 24.4°C, 1.1°C above normal.

Annual mean temperatures were significantly above normal across Japan. Eastern Japan's annual temperature anomaly was +1.2°C, the highest since records began in 1946. South Korea's annual mean temperature was 13.2°C (+0.7°C above average; fifth highest since national records began in 1973). In January and June, the monthly mean temperatures were 2.8°C (+3.8°C above normal) and 22.8°C (+1.6°C above normal), respectively, which were record high for those months. The annual mean temperature over Mongolia was 1.1°C (+1.0°C; sixth highest since 1940); the country observed its third-warmest April on record with an average temperature 3.3°C above normal in the range of 0.1° to 5.1°C. Mongolia experienced its greatest negative monthly anomaly of the year in December, –3.0°C below normal (mean temperature of –21.2°C).

At +0.94°C, the annual mean temperature for Indonesia was second highest since the start of the record in 1981 (behind 2016). Only two out of the 83 reporting stations observed negative temperature anomalies. The highest temperature recorded during the year was 38.4°C on 4 November in East Nusa Tenggara. Singapore's annual mean temperature in 2020 was 28.0°C (+0.5°C above

normal; eighth highest on record). Four of the past 6 years are among the country's 10 warmest years since 1929, when records began. Above-average monthly temperatures were recorded for the first five months of 2020, peaking in May at 28.9°C. June 2020 was the second-coolest June in the past 20 years (28.1°C; −0.2°C below average). September 2020 tied the record with 2013 for the coolest September in the last 10 years (27.5°C; −0.1° below average).

There were 13 large-scale heat waves in Vietnam during 2020. In June, the daily maximum temperature exceeded 35°C in most parts of the country, with an average monthly temperature +1.5° to +2.5°C above average. In the Northern Delta and North Central regions, the monthly temperature anomalies reached approximately +3°C: Hanoi (+3.0°C), Bac Ninh (+3.0°C), Ha Nam (+2.9°C), and Hung Yen (+2.8°C).

(II) PRECIPITATION

Figure 7.42 shows the 2020 annual precipitation as a percentage of normal over East and Southeast Asia. The annual mean precipitation total for China was 694.8 mm, 110.3% of normal and the fourth highest since 1951. The annual total precipitation for river basins was above normal in the Songhua River (138%), Huaihe River (124%) Yangtze River (122%, highest since start of record in 1961), Yellow River (116%), Liaohe River (112%), and Haihe River (112%), and below average in the Pearl River (95%). In 2020, the annual total rainfall of Hong Kong, China, was 2395.0 mm, near the average of 2398.5 mm.

In Japan, annual precipitation amounts were significantly above average on the Sea of Japan side of western Japan and above average on the Sea of Japan side of northern Japan, on the Pacific side of eastern and western Japan, and in Okinawa/Amami. Annual total precipitation in South Korea was 1591.2 mm (121.7% of normal; sixth wettest since national records began in 1973). From June to August, South Korea received its third-highest precipitation total on record for June–August (1007.0 mm). Although Mongolia's annual total precipitation was near normal at 251.3 mm, April 2020 was the driest April since 1940 at 32.4% of normal.

In Indonesia, annual rainfall was generally above normal with 23 of 83 weather stations recording more than 120% of normal precipitation, likely associated with the development of the 2020/21 La Niña event. The spatial average of 2713 mm makes 2020 the third-wettest year since the start of the record in 1981, behind 2010 and 1998, both of which were strong La Niña years. The largest rainfall anomaly, approximately 209% of normal, was recorded in Kerinci, Sumatra. In Singapore, annual total rainfall was near average over most of the island-wide rainfall stations. However, the Changi climate station recorded its eighth-lowest annual total rainfall over the past 30 years (1886.6 mm; 87% of normal). The driest period in 2020 was January–March, with less than 70% of average precipitation observed during each month. In contrast, the 2020 Southwest Monsoon season (June–September) was the wettest since 1981 (30% above normal), coinciding with the emergence of La Niña. Singapore also experienced 6 days with rainfall rates above 70 mm hr^{-1} (the highest recorded since 2013).

In Vietnam, there was a prolonged heavy rainfall period during October and the first half of November with total rainfall of 1000+ mm in many places, including: Ha Tinh City (Ha Tinh): 2521 mm; Khe Sanh (Quang Tri): 2894 mm; A Luoi (Thua Thien Hue): 4526 mm; Tra My (Quang Nam): 2813 mm; and Ba To (Quang Ngai): 2292 mm. The daily rainfall amounts were exceptionally high in Huong Linh (Quang Tri): 763 mm day^{-1}; Thuong Nhat (Thua Thien Hue): 719 mm day^{-1}; Ky Thuong (Ha Tinh): 809 mm day^{-1}; and Ha Tinh city (Ha Tinh): 884 mm day^{-1}.

(III) NOTABLE EVENTS AND IMPACTS

In China, typhoon-related disaster damage in 2020 was significantly less than that of the past 10 years (2010–19), with eight people dead or missing and approximately $4.7 billion (U.S. dollars) in direct economic losses. During March–April, drought occurred in the southwestern province of Yunnan due to both below-average precipitation (20%–50% of normal over most of

the region) and above-average temperatures (+1° to +2°C). In mid-April, an area encompassing 195,000 km^2 was classified in the middle category and higher, according to the meteorological drought composite index. Conversely, the Meiyu/Baiu/Changma season, which started earlier and ended later than normal, was the wettest such season since 1961 (see Sidebar 7.2 for a discussion of this event). During summer 2020, the Yangtze River basin experienced its most severe flooding since 1998, due to heavy rain.

Hong Kong, China, experienced its hottest summer (June–August) on record with a mean temperature of 29.6°C (1.2°C above normal). With a record-breaking mean temperature of 30.2°C, July 2020 was the hottest of any month in Hong Kong, China, since records began in 1884. Hong Kong, China, reported 50 Hot Nights (daily minimum temperature ≥ 28.0°C) and 47 Very Hot Days (daily maximum temperature ≥ 33.0°C) in 2020, with both breaking the highest annual record. Packing high winds and heavy rain, the strike of Typhoon Higos to the Pearl River Estuary necessitated the issuance of the Increasing Gale or Storm Signal No. 9 in Hong Kong, China, on 19 August.

In July, long-term heavy rain events occurred mainly in eastern and western Japan due to the active Baiu front. As a result, there was record heavy rainfall and lack of sunshine in these regions. The end of rainy season was later than normal nationwide, except in the Okinawa region.

South Korea experienced its second-highest total precipitation (693.4 mm) since 1973 during Changma, the monsoon season. In early September, Typhoon Maysak made landfall in the southeastern part of South Korea, and record high precipitation of 1037.5 mm was observed at Mt. Halla on Jeju island from 2 to 3 September.

In Mongolia, a total of 90 hydrometeorological extreme events were reported during 2020. During the summer, convection-related extreme events such as flood, hail, and lightning occurred more often than usual, with lightning frequency setting a record for the year. Together, these extreme events caused 15 fatalities and about $2.7 million (U.S. dollars) in economic losses.

On 1 January, Jakarta, Indonesia, experienced extremely heavy rainfall, with daily rainfall totals of more than 200 mm at many observation points. The highest total was 377 mm, recorded at Halim Airport in southeastern Jakarta. This marked the highest daily rainfall in Jakarta since 1996. The extreme precipitation triggered floods that affected large areas of this capital city and disrupted public transportation.

In Singapore, intense heavy rainfall events occurred more frequently in 2020, with total hourly rainfall exceeding 70 mm on 6 days (the top 1% of all heavy rainfall events recorded in Singapore), causing flash floods at various locations across the island. The highest hourly rainfall total of 2020 was 106.1 mm recorded in August at Bedok South; the record high hourly rainfall total of 130.7 mm was recorded at Ulu Pandan in July 2007.

Of 15 tropical cyclones that occurred in the South China Sea in 2020, eight directly affected Vietnam. Typhoon Molave was one of the most intense storms to reach Vietnam in the past 20 years. Binh Chau (Quang Ngai) recorded average wind speeds of 34 m s^{-1} and gusts of 42 m s^{-1}. Ly Son stations (Quang Ngai) observed average wind speeds of 31 m s^{-1} and gusts of 41 m s^{-1}.

Sidebar 7.2: **Extreme floods along the Meiyu/Baiu/Changma front in summer 2020**—

W. WANG, F. XIN, X. PAN, T. LI, HIT. SATO, AND Z. ZHU

Exceptionally strong and prolonged precipitation occurred along the Meiyu/Baiu/Changma front, extending from central China to southern Japan, in June–July 2020 (Fig. SB7.3a). The accumulated rainfall total over the Yangtze River Valley (YRV) during that 2-month period was the largest for the past 60 years. Historically, floods have occurred over the YRV and along the Meiyu/Baiu/Changma front during the decaying phase of a strong eastern Pacific (EP) El Niño (e.g., in 1983, 1998, and 2016; Chang et al. 2000a,b; Li and Wang 2005). Summer 2020 was preceded only by a moderate central Pacific (CP) El Niño (termed by China Meteorological Administration). What caused the exceptionally strong flood?

The most notable feature of the anomalous circulation in June–July (JJ) 2020 is a large-scale, low-level anticyclone in the tropical western North Pacific (WNP) south of the Meiyu/Baiu/Changma front (Fig. SB7.3a). Southerly anomalies west of the anticyclone advected warm and moist air northward, converging into the front. The occurrence of the low-level anomalous anticyclone signifies a southwestward shift of the Western Pacific Subtropical High.

During the prolonged period of heavy rainfall, the upper-tropospheric circulation anomaly was characterized by a quasi-stationary Rossby wave train pattern (Fig. SB7.3b) elongated along the subtropical jet stream in Eurasia. The Rossby wave train is known as the Silk Road teleconnection pattern (Enomoto et al. 2003).

Another notable feature is a cold surface temperature anomaly north of the Meiyu front (Fig. SB7.4c). The cold anomaly resulted from cold advection by northeasterly anomalies in northeastern Asia (Fig. SB7.4a). A dipole pattern appeared in the anomalous temperature advection field. This dipole pattern strengthened the meridional temperature gradient and led to a persistent and strong front.

A similar dipole pattern appeared in the anomalous moisture advection field, as seen in Fig. SB7.4b. As a result, abnormally dry air appeared north of the Meiyu/Baiu/Changma front, while the moisture increased along the front. A remarkable north–south contrast between a dry/cold condition to the north and a wet/warm condition to the south can be clearly seen in the low-level moist static energy (MSE) anomaly field (Fig. SB7.4d). A positive MSE anomaly appeared south of 30°N in East Asia, whereas a negative MSE anomaly occurred north of 30°N. The separation line was tilted slightly toward the northeast. The placement of the high MSE air to the south and the low MSE air to the north persisted for the 2-month period, leading to a stationary Meiyu/Baiu/Changma front (Fig. SB7.3a).

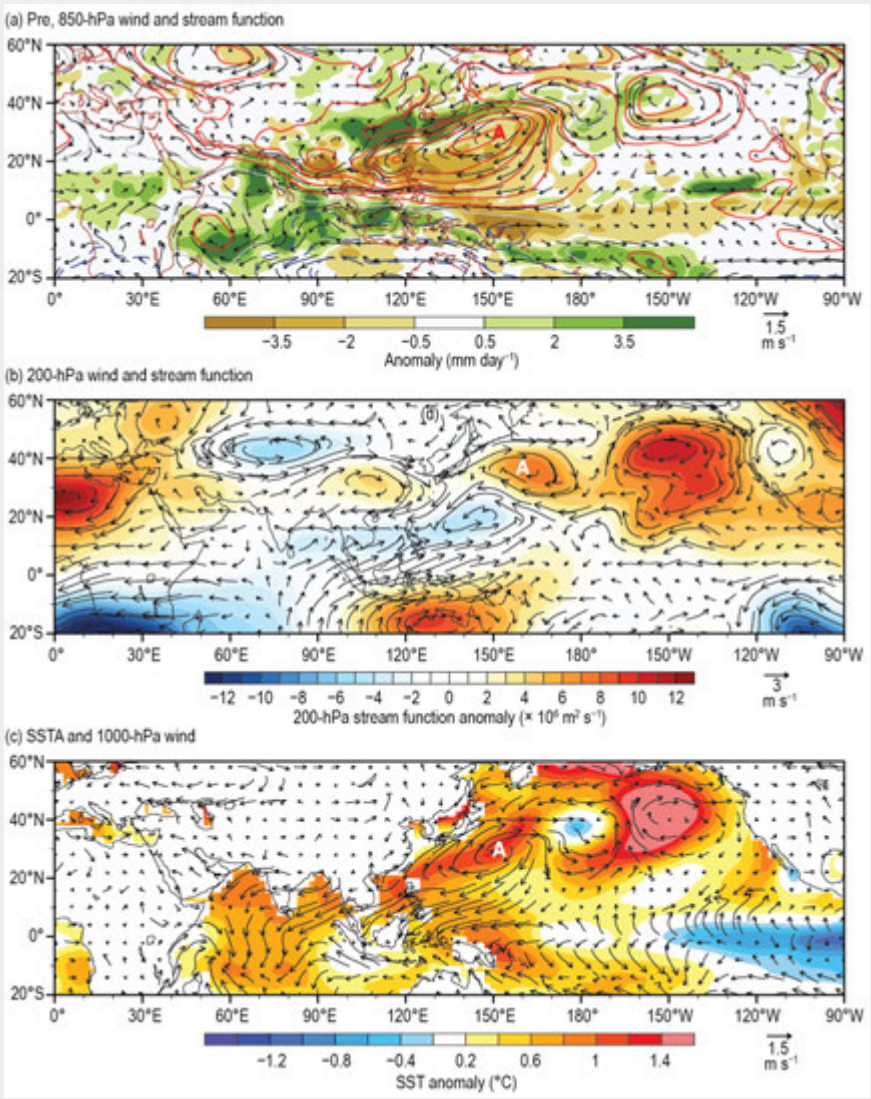

Fig. SB7.3. The horizontal patterns of (a) anomalous precipitation (shading, mm day^{-1}) and wind (vector, ms^{-1}) and stream function (contour 10^6 m^{2}s^{-1}) anomalies at 850 hPa, (b) anomalous wind (vector, ms^{-1}) and stream function (contour 10^6 m^{2}s^{-1}) at 200 hPa, and (c) anomalous SST (shading, °C) and wind at 1000 hPa (vector, ms^{-1}) averaged in Jun–Jul (JJ) 2020. The baseline for the mean climatology is 1979–2020. Letter "A" denotes the anomalous anticyclonic center in the WNP.

Typically, the Meiyu rainband remains over the YRV for a relatively short period (~2–3 weeks) and then moves northward. Why did the anomalous circulation and rainband persist. Why did the anomalous circulation and rainband persist for a 2-month period during JJ 2020? Given that the atmospheric circulation does not have such a long memory, it is important to examine the oceanic forcing (Wang et al. 2003). As seen in Fig. SB7.3c, a La Niña-like sea surface temperature anomaly (SSTA) pattern appeared in the equatorial Pacific in June–July (JJ) 2020. Meanwhile, a warm SSTA occurred over the tropical Indian Ocean (IO).

Idealized numerical model (ECHAM4) experiments confirmed the roles of the La Niña-like SSTA pattern in the Pacific and the warming in the IO in maintaining the WNP anticyclone in JJ 2020. Typically, a CP El Niño is characterized by a slow SSTA transition in the equatorial Pacific (Li and Hsu 2017); however, the 2019/20 CP El Niño was an exception. A quick phase transition occurred in early 2020, and by JJ a cold SSTA appeared in the equatorial Pacific. The cold SSTA induced a negative precipitation anomaly in the equatorial CP, leading to an anomalous anticyclone response to its northwest (Gill 1980).

A moderate warming in the tropical IO is often observed during the decaying phase of a CP El Niño. The exceptionally strong IO warming in JJ 2020 was attributed to the combination of the interannual variation and the interdecadal fluctuation/long-term trend. The strong IO warming induced a Kelvin wave response to its east and maintained the WNP anticyclone through the Kelvin wave-induced anticyclonic shear mechanism (Wu et al. 2009; Li et al. 2017).

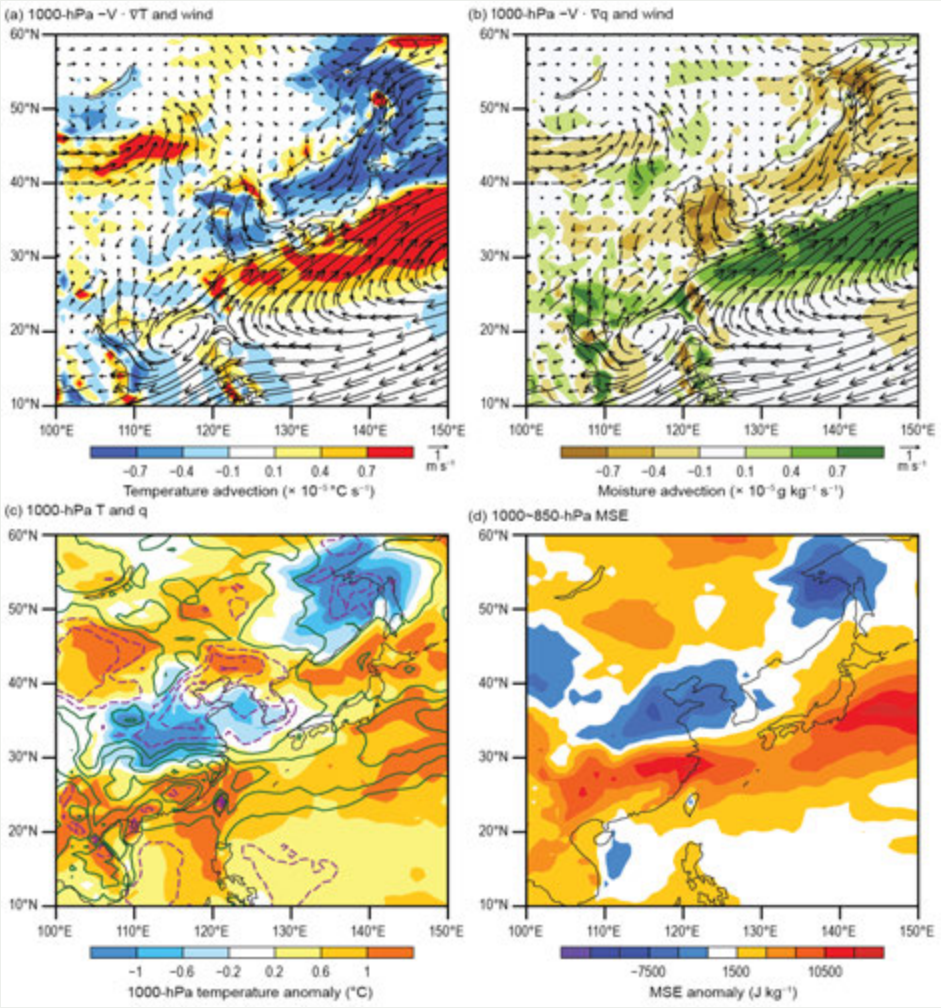

Fig. SB7.4 The horizontal patterns of (a) advection of mean temperature by anomalous wind at 1000 hPa (shading, × 10^{-5} °C s^{-1}) superposed by 1000-hPa wind anomaly vector (m s^{-1}), (b) advection of mean moisture by anomalous wind (shading, × 10^{-5} g kg^{-1} s^{-1}) superposed by the anomalous wind vector at 1000 hPa (m s^{-1}), (c) anomalous temperature (shading, °C) and specific humidity (contour, g kg^{-1}) at 1000 hPa, and (d) moist static energy (shading, J kg^{-1}) anomaly integrated from 1000 hPa to 850 hPa averaged in JJ 2020.

The observational analysis above reminds us that caution is needed in predicting El Niño impacts based on composite results alone. A more detailed tracking of the SSTA evolution, such as a slow or quick phase transition, is critical. One needs also to consider the impact of the interdecadal change and long-term warming trend. Finally, it is important to consider that there is always inherent variability in the climate system that can influence atmospheric circulation patterns in any given year and thus alter expected ENSO impacts in a variety of ways.

4) South Asia—O. P. Sreejith, A. K. Srivastava, and M. Rajeevan

Countries in this section include Bangladesh, India, Pakistan, and Sri Lanka. Unless otherwise noted, climate anomalies are relative to the 1981–2010 base period.

(I) TEMPERATURE

In 2020, South Asia generally experienced above-normal temperatures. The annual mean temperature averaged over India was 0.29°C above the 1981–2010 average, making 2020 the eighth-warmest year since nationwide records began in 1901 (Fig. 7.49). India's average seasonal mean temperatures were above normal for all of the seasons except the pre-monsoon season (March–May), when it was slightly below normal. India's average seasonal mean temperature anomalies during the monsoon season (June–September, +0.43°C) and the post-monsoon season (October–December, +0.53°C) largely accounted for the above-normal annual temperature for the year. The warmest year on record is 2016 (0.71°C above average).

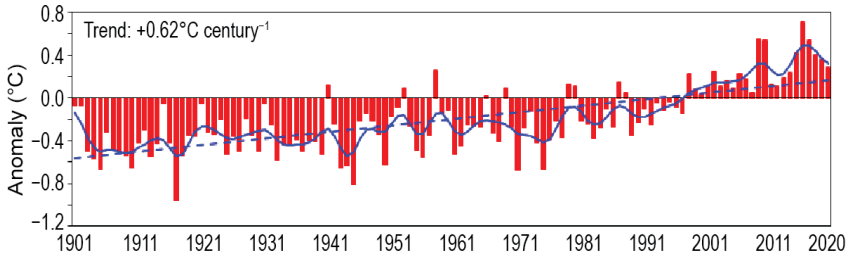

Fig. 7.49. Annual mean temperature anomalies (°C; 1981–2010 base period) averaged over India for the period 1901–2020. The smoothed time series (9-point binomial filter) is shown as a continuous blue curve.

(II) PRECIPITATION

The summer monsoon season (June–September) contributes about 75% of the annual precipitation over South Asia. The 2020 summer monsoon season set in over Kerala (southwestern parts of peninsular India) on its climatological normal date (1 June) and covered the entire country on 26 June, 12 days ahead of its normal date.

For India, the Long Term Average (LTA) value of the summer monsoon rainfall, calculated using all data from 1961 to 2010, is 880 mm. The standard deviation of Indian summer monsoon rainfall (ISMR) is around 10% of the LTA; however, over smaller regions, the natural variability of the monsoon (standard deviation) is large—around 19%. As such, the ISMR exceeding 110% of the LTA in a year is considered excess rainfall, while the ISMR less than 90% of the LTA in a year is considered deficient rainfall.

During 2020, the ISMR averaged over the country as a whole was 109% of its LTA value, high but within the normal range. In general, rainfall was fairly well distributed over most parts of the country. The seasonal rainfall over the homogeneous regions of Northwest India, Central India, South Peninsula, and East/Northeast India was 84%, 115%, 129%, and 106% of their LTA, respectively. The homogeneous region of Northwest India received comparatively less rainfall (84% of LTA; Fig. 7.50). At the monthly scale, rainfall for the country as a whole was above normal during June and August (118% and 127% of LTA, respectively) and normal during July and September (90% and 104% of LTA, respectively). For the country as a whole, average rainfall was above or near normal on most of the days during the season (Fig. 7.51). Table 7.2 lists 24-hour rainfall records during the 2020 ISMR season.

During winter (January–February) 2020, rainfall over India was normal (99% of LTA). It was above normal (121% of LTA) during the pre-monsoon season (March–May), while during the post-monsoon season (October–December), it was normal (101% of LTA).

Pakistan, located at the western edge of the pluvial region of the South Asian monsoon, receives 60%–70% of its annual rainfall during its summer monsoon season (July–September). The climatological summer monsoon sets over eastern parts of Pakistan around 1 July with a standard deviation of 5 days; in 2020 onset occurred on 26 June. The summer monsoon rainfall over Pakistan for the season was above normal (141% of LTA). Rainfall was below normal in July (66% of LTA),

normal during August (108%), and significantly above normal during September (189%). Spatially, rainfall was generally above normal over most of the country except some parts of the west central and northwestern regions. Sindh and Baluchistan provinces received exceptionally high rainfall during the monsoon season (463% and 371% of their LTA, respectively). During the summer monsoon season in Bangladesh and Sri Lanka (May–September), Bangladesh received normal rainfall and Sri Lanka received above-normal rainfall.

The northeast monsoon (NEM) sets in over southern peninsular India during October and over Sri Lanka in late November. The NEM contributes 30%–50% of the annual rainfall over southern peninsular India and Sri Lanka as a whole. In 2020, the NEM set in over southern peninsular India on 28 October. The 2020 NEM seasonal rainfall over south peninsular India was normal (110% of LTA); NEM rainfall activity over Sri Lanka during October to December 2020 was also normal.

(III) NOTABLE EVENTS AND IMPACTS

Cold wave conditions prevailed over central parts of India, notably during January, and caused the deaths of about 150 people. Of these deaths, 88 were from the northern Indian state of Uttar Pradesh, 45 from Bihar (all reported on a single day, 1 January), and 16 from the state of Jharkhand.

Heavy rainfall and flood-related incidents claimed more than 600 lives from different parts of India during the pre-monsoon, monsoon, and post-monsoon seasons. On 7 August, in the Munnar and Idukki districts of Kerala, 65 people were killed during landslides triggered by heavy rainfall activity.

Thunderstorms and lightning, along with associated flash floods, hail, and strong winds, claimed 815 lives from different parts of India. Among these, 280 deaths were reported in Bihar, 220 in Uttar Pradesh, 122 in Jharkhand, 72 in Madhya Pradesh, 23 in Maharashtra, and 20 in Andhra Pradesh. Severe thunderstorms and lightning on 26 February and 14 March resulted in approximately 200 deaths in different parts of Uttar Pradesh, Bihar, and Jharkhand (northern/eastern parts of India).

In Bangladesh, continuous heavy rains from late June through much of July caused one of the most severe floods in decades, affecting one-third of the country. Approximately 50 people died and more than 1.5 million people were affected by this flooding. In addition, there was widespread loss of crops and houses.

Across Pakistan, heavy rains and floods killed about 400 people during the monsoon season. Karachi, the most populous city in Pakistan, received record rainfall during August, mainly due to continuous heavy rains during the last week of the month. On 28 August, one station in Karachi Faisal reported the highest ever recorded 24-hour rainfall: 231.0 mm. With the excess rainfall, Karachi flooded in the last week of August, killing approximately 50 people.

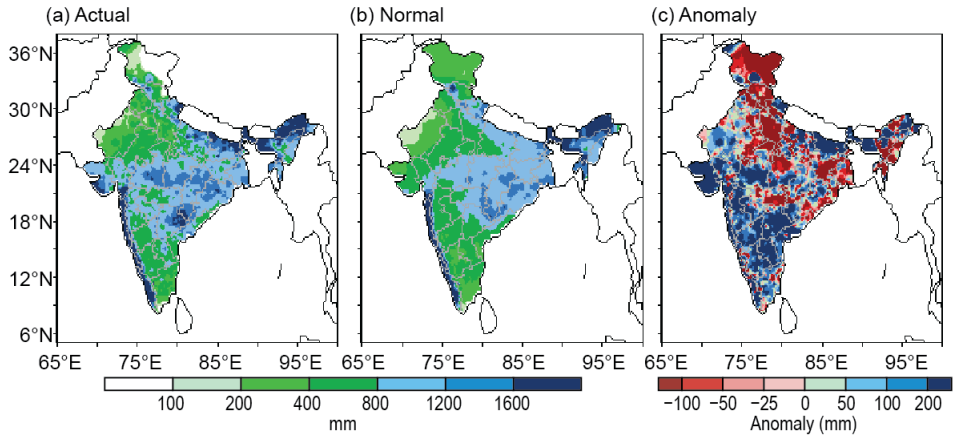

Fig. 7.50. Spatial distribution of (a) actual, (b) normal, and (c) anomalous monsoon seasonal (Jun–Sep) rainfall (mm) over India in 2020.

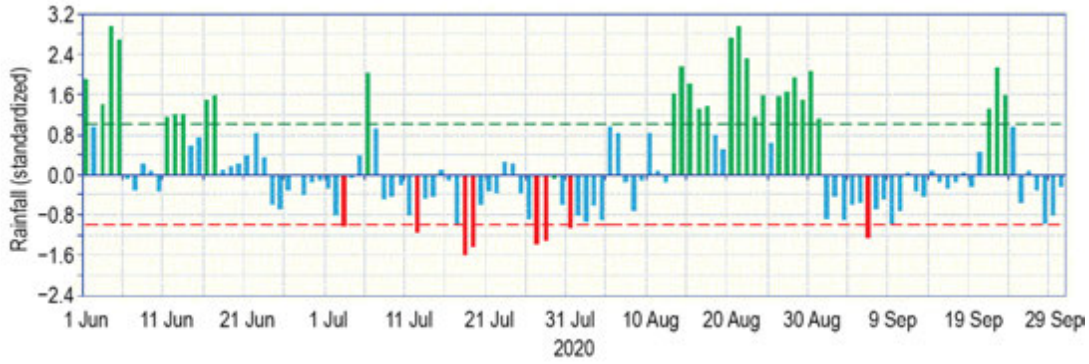

Fig. 7.51. Daily standardized rainfall time series averaged over the core monsoon zone of India (1 Jun–30 Sep 2020). The horizontal dashed lines delineate anomalies greater than ±1 std. dev. The green, red, and blue color bars indicate days with active, suppressed, and normal monsoon conditions, respectively.

Table 7.2. Record 24-hour rainfall totals in India during the 2020 southwest monsoon season.

Station	24-hour rainfall (mm)	Date	Previous record (mm)	Date of record	Year of record
Jun 2020					
Ozar (Nashik AP)	144.2	4	103.2	27	2002
K. Paramathy	84.0	2	57.6	1	2000
Jul 2020					
Okha	476.7	8	330.5	27	2010
Mahbubnagar	131.6	3	106.6	23	2005
Nandyal	145.8	30	143.2	11	2010
Chennai AP	115.4	10	85.8	16	1978
Aug 2020					
Indore	263.4	22	212.6	10	1981
Mumbai (Colaba)	331.8	6	287	3	1881
Dahanu	383.1	5	353.3	14	1945
Hanamkonda	212.2	15	190.5	26	1924
Pamban	121.8	9	73.9	31	1937
Sep 2020					
Mangalore AP	251.8	11	159.8	24	2010
Panambur	229.6	11	125.2	24	2010
Belgaum (Sambra) AP	168.1	10	150	24	2010

In 2020, five tropical cyclones formed over the North Indian Ocean: Super Cyclonic Storm Amphan, Very Severe Cyclonic Storm Nivar, and Cyclonic Storm Burevi developed in the Bay of Bengal, while Severe Cyclonic Storm Nisarga and Very Severe Cyclonic Storm Gati formed over the Arabian Sea. Amphan formed during the pre-monsoon season and crossed the coast of the northeastern Indian state of West Bengal over Sundarbans on 20 May. The storm claimed 90 lives and about 4000 livestock, mainly from West Bengal. Nisarga, which formed early in the monsoon season, crossed the coast of the western Indian state of Maharashtra on 3 June. The remaining three cyclones, Nivar, Burevi, and Gati, formed during the post-monsoon season. Nivar crossed the coast of the south Indian state of Tamil Nadu close to Puducherry, killing 12 people and more than 10,800 livestock from the states of Tamil Nadu and Andhra Pradesh. In Tamil Nadu, Burevi killed nine people and 200 livestock. Additionally, from 1 to 3 December, Burevi brought heavy rainfall to the northern and eastern districts of Sri Lanka, which resulted in severe floods in the region during the first 2 weeks of December. Although more than 90,000 people were affected

by the flooding, there were few casualties and house collapses. Gati moved westward, making landfall over the Somalia coast. Please refer to section 4g5 for more details about the 2020 North Indian Ocean tropical cyclone season.

5) Southwest Asia—A. Vazifeh, A. Fazl-Kazem, H. R. Hasannezhad, P. Asgarzadeh, and S. Tajbakhsh-Mosalman

This section covers only Iran. Turkey is included in the Europe subsection, 7f. Climate anomalies are relative to a 1984–2019 base period for temperature and precipitation.

(I) TEMPERATURE

Generally, Iran experienced above-average mean temperatures (Fig. 7.52) throughout all four seasons, with some areas reporting a seasonal mean temperature that was +3°C above the normal range. For the most part, during spring and autumn, the eastern half of the country was in the normal-to-below normal temperature range; the western half of Iran was in the above-normal temperature range throughout all of 2020.

(II) PRECIPITATION

In general, spring was wetter than normal in the southeast provinces and central regions, and autumn was wetter than normal in the southwest (Figs. 7.53b,d). In spring, Iran received below-normal precipitation across most of the country except in the south-southeast. The season was relatively dry with below-normal precipitation, and, in particular, the shortage of rainfall in western mountainous regions was considerable (with normal annual range being 450–650 mm).

In summer, rain is generally limited to northern provinces in the southern coastal regions of the Caspian Sea, through migrating summertime midlatitude cyclonic activity and lake effect-induced rain by the Caspian Sea influence, and in southeast Iran through monsoonal activity and westward movement of mid-tropospheric inverted troughs that suppresses subsidence and the region favors afternoon/early night scattered thunderstorms. Summer 2020 was drier (wetter) than normal in north (southeast) of the country (Fig. 7.53c).

As shown in Fig. 7.54, in 2020, Iran in general received below-normal precipitation for the year. As such, most of the country was drier than normal, especially in the mountainous regions, namely the Zagross in the west and the Alborz in the north and south of the Caspian Sea. Most of the comparatively rainy areas in the subtropical highland country are in northern and western Iran. These areas received below-normal annual precipitation, especially during spring and summer, whereas southeastern Iran, where the annual normal range of precipitation is low (100–150 mm), had normal-to-above normal precipitation.

(III) NOTABLE EVENTS AND IMPACTS

Heavy rain in southern Iran caused flooding in the Hormozgan Province (north of the Hormoz Strait) on 11 February. The region's Rudan station recorded its highest observed 24-hour accumulated rainfall total of 174 mm.

On 23 March, a strong thunderstorm caused flooding in southern Iran. An accumulated rainfall total of 141 mm was recorded at the Kahnuj station of Kerman province in southeast Iran—the highest 24-hour amount recorded in the area.

For 3 days in December, low-level easterly currents were coupled with the easterly movement of midlatitude cyclonic activity across a southeastern Mediterranean–Middle East track, triggering heavy rains in the region and over the western windward faces of the Zagross Mountains and flooding the Khuzestan Province plains in the southwest. The 24-hour accumulated rain on 6 December in the region was exceptionally severe, and heavy rain flooded the Khuzestan and north of the Bushehr Provinces on the northwest side of the Persian Gulf. In the city of Ahwaz, the provincial capital, all streets and houses along the Karoon River banks were flooded, killing five people and causing heavy damage to homes and governmental buildings.

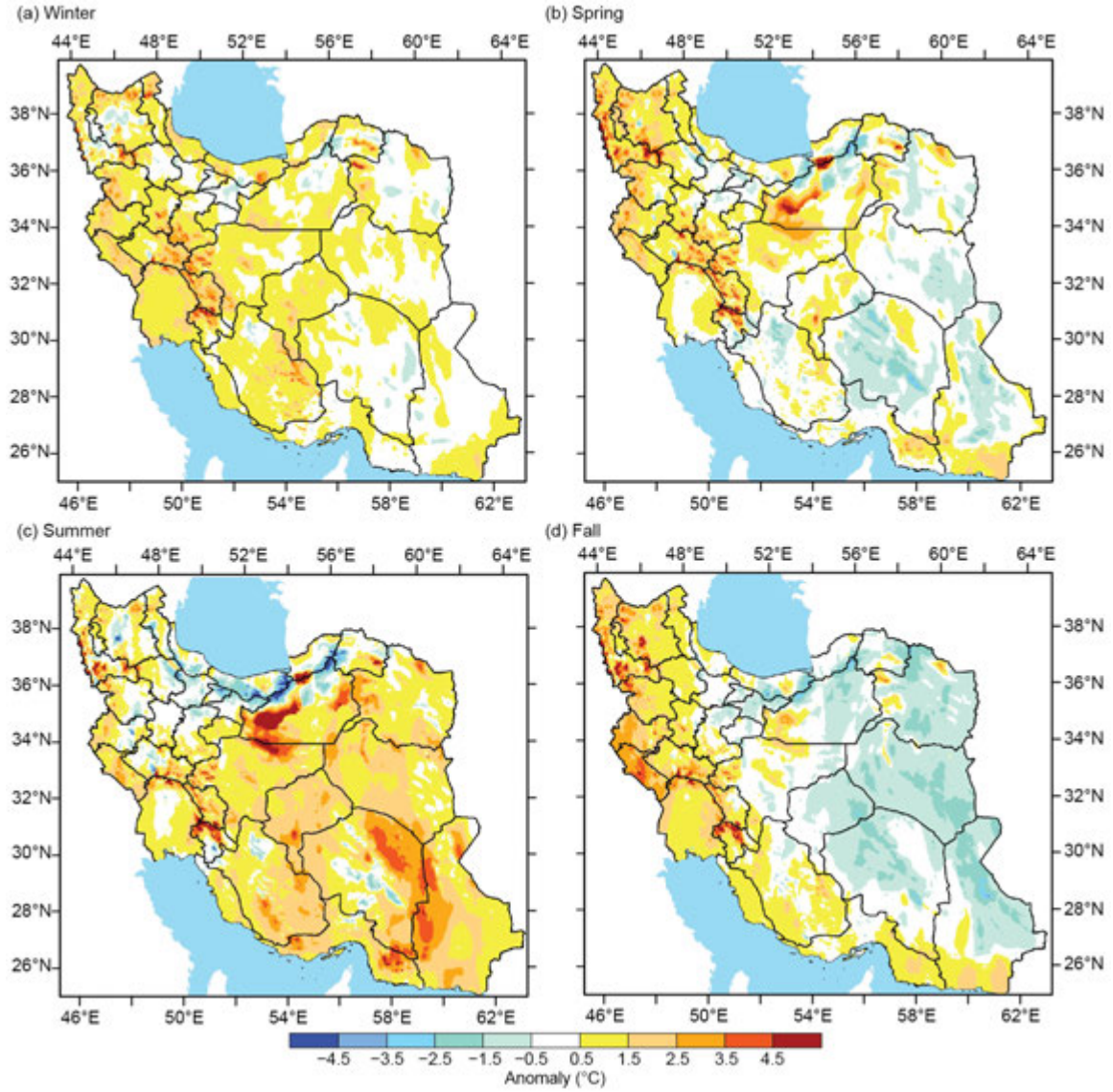

Fig. 7.52. Seasonal surface (2 m) temperature anomalies (°C) over Iran in (a) winter (top left), (b) spring (top right), (c) summer (bottom left), and (d) autumn (bottom right) 2020. (Source: I. R. of Iran Meteorological Organization.)

Temperatures in the western half of Iran were above normal during November–December and heat waves (five or more days with temperatures +5°C above normal) were recorded at more than 92 stations in that region.

6) Central Asia—W. M. Thiaw, P.-H. Kamsu-Tamo, M. F. Zaheer, and B. Pugh

Central Asia is a landlocked, semi-arid region spanning a wide latitudinal area that extends from the northern temperate zone with Russia at its northern border to the southern subtropics. It exhibits a complex topography ranging from vast plains to high mountains, with the Caspian Sea at its western edge. Its climate is quite diverse and is influenced by the strong inhomogeneity of the terrain. For the purpose of this analysis, Central Asia is defined as the region encompassing the countries of Afghanistan to the south; from east to west, Turkmenistan, Uzbekistan, Tajikistan, and Kyrgyzstan in the central part of the region; and Kazakhstan to the north. Unless otherwise specified, the base period is 1981–2010.

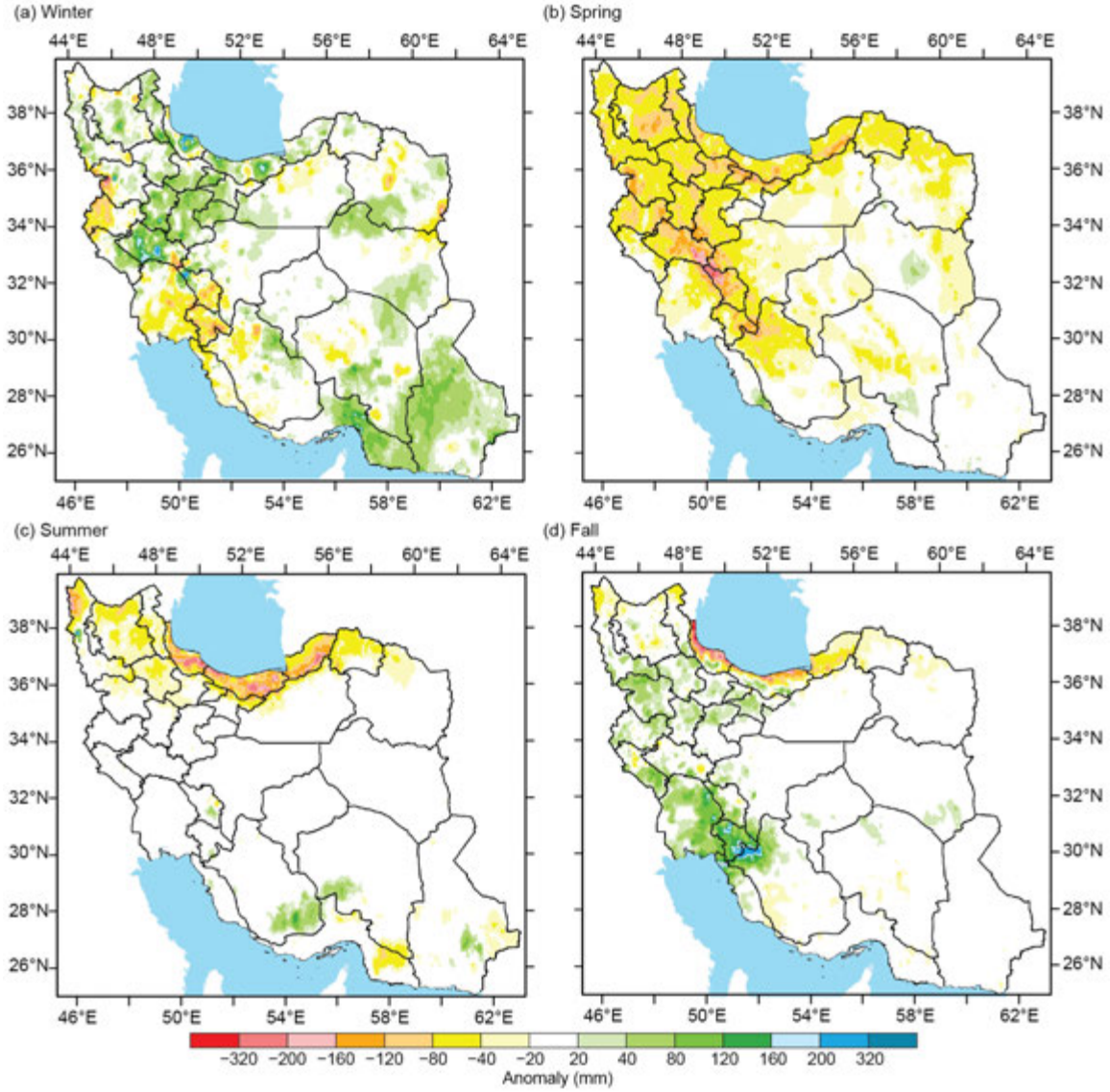

Fig. 7.53. Seasonal precipitation anomalies (mm; 1984–2019 base period) over Iran in (a) winter (top left), (b) spring (top right), (c) summer (bottom left), and (d) autumn (bottom right) 2020. (Source: I. R. of Iran Meteorological Organization.)

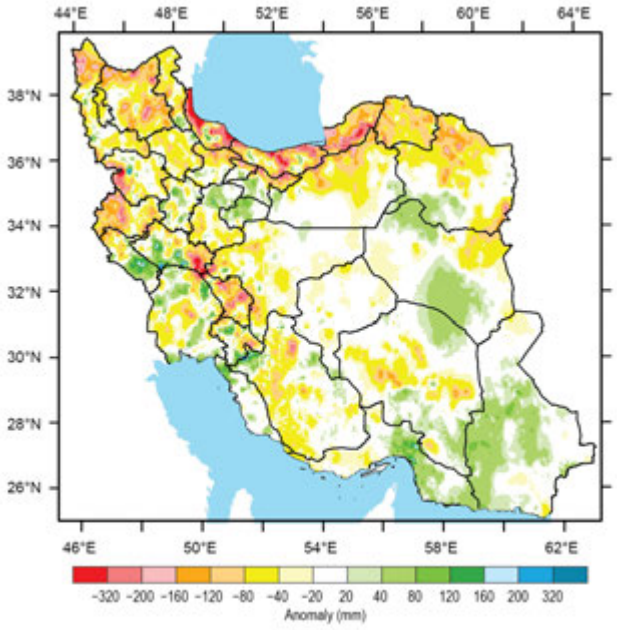

Fig. 7.54. Annual precipitation anomalies (mm; 1984–2019 base period) across Iran in 2020.

(I) TEMPERATURE

Climatologically, mean annual temperatures are lower (0°–10°C) over the northern and east central areas of the region encompassing northern Kazakhstan, Kyrgyzstan, and Tajikistan, and northeastern Afghanistan. They are higher (15°–20°C) over Uzbekistan, Turkmenistan, and western Afghanistan. During 2020, the mean annual temperature was between 15°C and 20°C over western Afghanistan, much of Turkmenistan, Uzbekistan, and portions of western Kazakhstan (Fig. 7.55a). Temperatures were lower over northern Afghanistan, Kyrgyzstan, and the northern two-thirds of Kazakhstan, where they averaged between 2°C and 8°C, reaching 0°C in western Tajikistan and into below-freezing temperatures in the west. These temperatures were overall below normal across the region, with the lowest temperature anomalies of

about –1° to –2°C in the central areas, encompassing much of Afghanistan, western Turkmenistan and Uzbekistan, eastern Tajikistan, Kyrgyzstan, and southern Kazakhstan (Fig. 7.55b). Temperature departures from average reached –3°C in local areas in northwestern Afghanistan, the far western areas of Turkmenistan and Uzbekistan, and western Tajikistan, making 2020 one of the coldest years in these localities based on the 1981–2010 climatology. Temperatures were slightly above normal over northern Kazakhstan, where anomalies averaged +0.5° to +1.5°C, with the most elevated temperatures at the 90th percentile rank observed over portions of the northwest and northeast.

An analysis of temperature throughout the year suggests that December was extremely cold in much of Central Asia, with temperatures hovering around –15°C in much of Kazakhstan, and approaching –20°C in some locales in the north, about 5°–10°C below the mean. Over central and southern Central Asia, mean temperatures averaged about –10°C (5°–10°C below the mean) in December 2020. Mean temperatures were milder early in the year in January and February, ranging between –10°C and –15°C (5°–10°C above the mean) over much of Kazakhstan, placing February in the upper 95th percentile rank for this region. They were about –5° to 10°C in January and February 2020 in the southern and central areas of Central Asia. During the spring and summer months, temperatures soared and exceeded 30°C in July over much of Central Asia including western Afghanistan, Turkmenistan, Uzbekistan, and southwestern Kazakhstan. Temperatures were lower in northern Kazakhstan, Tajikistan, and Kyrgyzstan, where they averaged about 20°C in July. Temperatures were generally 1°–3°C below the mean in much of Central Asia during the summer, except for northwestern Kazakhstan in July, where temperatures were about 2°–3°C above the mean. The spring months of March–May 2020 were also generally 2°–10°C colder than normal, with the highest departures observed over central Afghanistan.

Annual maximum temperatures (T_{max}) featured a steep north–south temperature gradient with the lowest maximum temperatures (about 4°C) registered in northern Kazakhstan and the highest temperatures (about 15°–20°C) observed in Uzbekistan, Turkmenistan, and southern Afghanistan. Afghanistan registered T_{max} as high as 25°C in its southern tip. However, annual T_{max} was generally below the mean over much of the region, with anomalies –1° to –3°C over much of Kazakhstan, the western areas of Turkmenistan and Uzbekistan, and Kyrgyzstan, reaching and exceeding –5°C over much of Afghanistan and Tajikistan. The lowest T_{max} values (about –15°C;

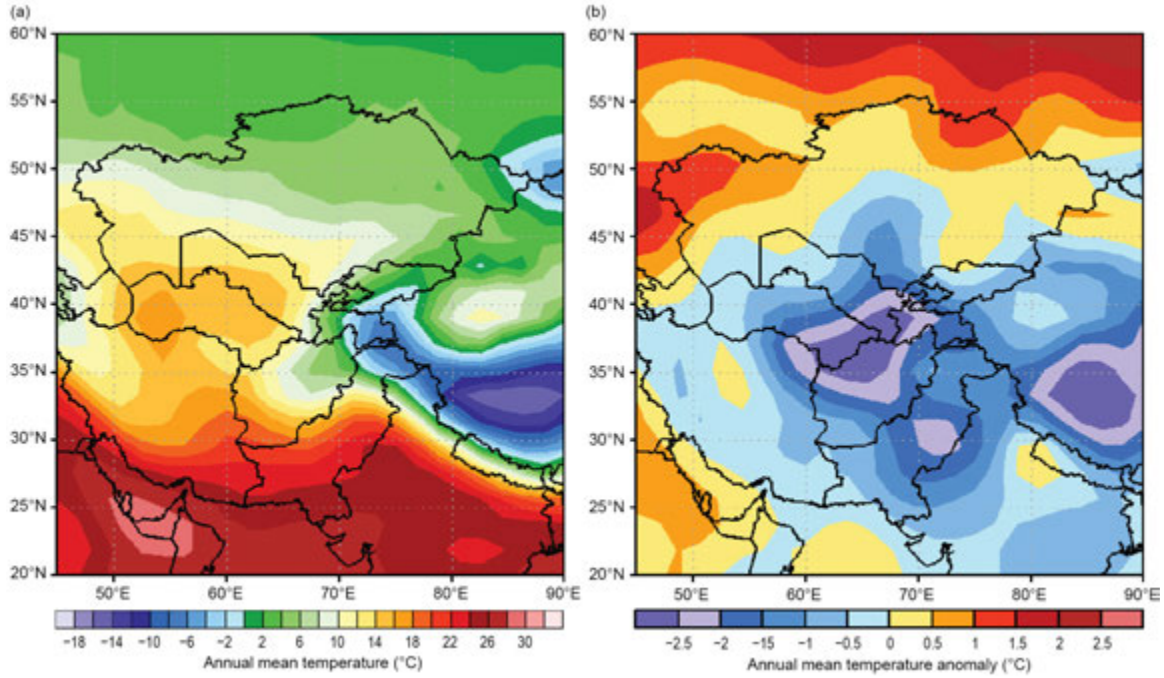

Fig. 7.55. Annual (a) mean temperature (°C) and (b) mean temperature anomalies (°C, 1981–2010 base period) for Central Asia. (Source: NOAA/NCEP.)

5°–10°C below the mean) were observed in northern Kazakhstan in December and the highest T_{max} (about 42°C; 3°–5°C above the mean) in far western Afghanistan, Turkmenistan, and Tajikistan, and southwestern Kazakhstan in July.

Annual minimum temperatures (T_{min}) ranged between 0°C and 5°C in northern Afghanistan and much of Kazakhstan. They averaged 10°–15°C over the western areas of Turkmenistan and southwestern Kazakhstan and –5° to –10°C over eastern Tajikistan and southern Kyrgyzstan. T_{min} dipped below –20°C (5°–10°C below the mean) in much of Kazakhstan in December, with some locales in the central areas registering their coldest T_{min} on record. However, in July, T_{min} approached 25°C (1°–2°C above the mean) in Turkmenistan, Uzbekistan, and southwestern Kazakhstan.

(II) PRECIPITATION

The mean annual precipitation is quite variable across Central Asia and ranges from less than 200 mm over southwestern Afghanistan and the central areas of Turkmenistan and Uzbekistan to 200–400 mm over central Afghanistan, the western areas of Turkmenistan and Uzbekistan, eastern Kyrgyzstan, and the southern two-thirds of Kazakhstan. Precipitation is generally higher and about 400–700 mm over northeastern Afghanistan, much of Tajikistan, western Kyrgyzstan, and northern Kazakhstan. Typically, the winter and spring seasons bring the highest precipitation (rain and snow) amounts in the southern and central areas of the region, while the summer months tend to be drier. Precipitation tends to be equally distributed throughout the year over northern Kazakhstan.

The precipitation patterns in 2020 resembled climatology, with average precipitation observed over northern Kazakhstan, Kyrgyzstan, Tajikistan, and northeastern Afghanistan, where totals ranged between 500 mm and 600 mm, or 80%–120% of normal (Fig. 7.56a). Annual totals were lower (200–500 mm) across much of central and southeastern Kazakhstan, Kyrgyzstan, central Afghanistan, much of Turkmenistan, and western Uzbekistan. Precipitation was less than 200 mm over the southern tip of Afghanistan, northern Turkmenistan, central Uzbekistan, and local areas in southwestern Kazakhstan. However, precipitation was significantly above average, with surpluses exceeding 100 mm of normal (120%–150% of normal; Fig. 7.56b) over central and southern Afghanistan and eastern Turkmenistan, where totals ranged between 100 mm and 500 mm, placing some of these localities in the upper 95th percentile rank. Precipitation was below average, about 50–100 mm deficits (50%–80% of normal) in western and eastern Kazakhstan.

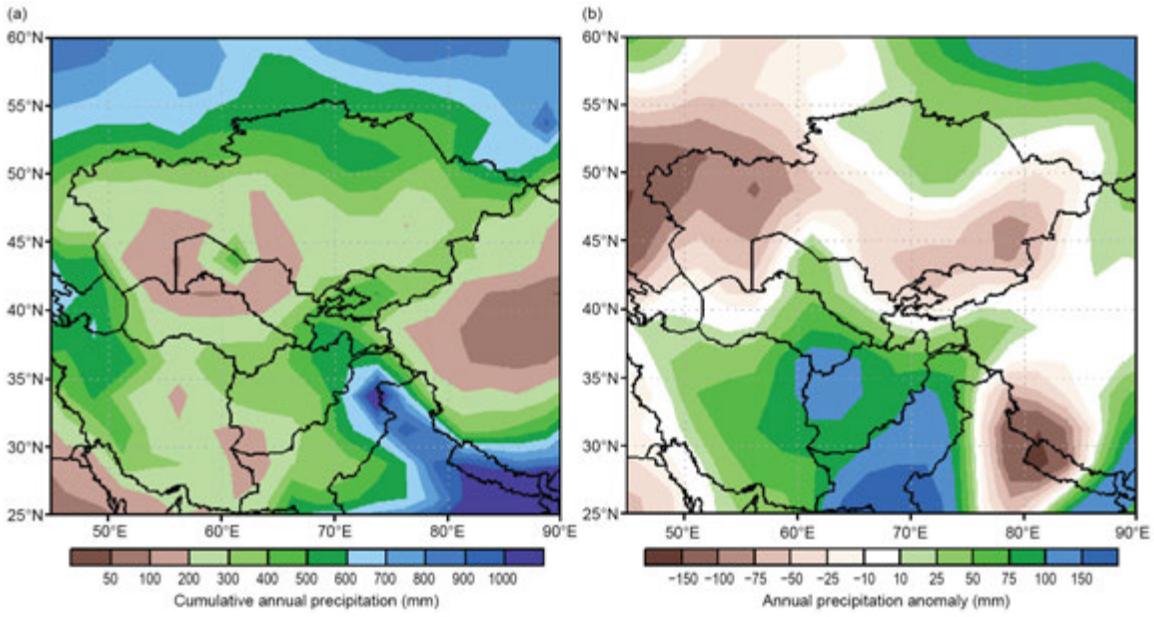

Fig. 7.56. Cumulative annual (a) precipitation (mm) and (b) annual precipitation anomalies (mm; 1981–2010 base period) for Central Asia. (Source: NOAA/NCEP GPCP data.)

An analysis of precipitation throughout the year reveals surpluses ranging between 30 mm and 60 mm (120%–150% of normal) over much of northern Kazakhstan during January, February, and April. Surpluses were also evident over much of Afghanistan in April and November, exceeding 100 mm or 200% of normal precipitation in some locales.

(III) NOTABLE EVENTS AND IMPACTS

According to the International Federation of Red Cross and Red Crescent, heavy snowfall, flooding, and a large number of avalanches occurred over many parts of Afghanistan between 12 and 15 January, affecting several provinces including Kandahar, Helmand, and Zabul, with casualties and significant damage to homes and livelihoods. The event caused mass destruction of houses and shelters, loss of lives and public facilities, and displacement of people from their homes. According to the NOAA CPC Satellite Rainfall Estimates version 2 (RFE2), widespread and sustained moderate-to-heavy rain fell across Afghanistan from 20 March to 14 April, with daily estimates exceeding 50 mm in some locales, resulting in sustained flooding across Afghanistan, Kyrgyzstan, Tajikistan, and the southern areas of Turkmenistan and Uzbekistan. Northern and western Afghanistan received more than 100 mm of precipitation over this period. The cumulative effect of this precipitation and rapid snowmelt caused severe flooding in more than a dozen provinces of Afghanistan. According to the Afghanistan Natural Disaster Management Authority, about 288 houses were destroyed and an additional 400 were damaged. About 500 ha of land were also damaged, 15 people injured, and 11 fatalities. According to the United Nations, as of April 2020, more than 17,000 people suffered from heavy rains and floods across Afghanistan, with nearly 2000 homes destroyed. Deluge in the Greater Kabul area with rainfall estimates exceeding 100 mm on 25 and 26 August resulted in a deadly flash floods. According to the Afghan Red Crescent Society Emergency Operations Center, there were 95 casualties, about 140 people injured, 800 houses damaged, and 150 livestock perished.

h. Oceania—C. Ganter, Ed.

1) Overview—C. Ganter

The region of Oceania began 2020 with the El Niño–Southern Oscillation (ENSO) in a neutral state, although La Niña emerged in the second half of the year. This was a welcome change for the Australian region, with La Niña contributing to increased rainfall over the continent, after a very significant 2019/20 fire season. Some Southwest Pacific islands observed dry conditions due to La Niña, and the Northwest Pacific and Micronesia region saw a distinct absence of typhoon activity, a classic La Niña signature (see Sidebar 7.3). Parts of New Zealand experienced meteorological drought in early 2020; La Niña conditions contributed to higher temperatures in the latter part of the year.

2) Northwest Pacific and Micronesia—M. A. Lander, C. P. Guard, and B. Bukunt

This assessment covers the area from the date line west to 130°E, between the equator and 20°N. It includes the U.S.-Affiliated Islands of Micronesia, but excludes the western islands of Kiribati and nearby northeastern islands of Indonesia. The analyses are based on station data and anomalies are provided with respect to the 1981–2010 base period.

For much of Micronesia, the weather and climate of 2020 will be remembered for being relatively free of any extremes of wind, waves, or rainfall. Most locations were drier than average during the first half of the year, with an uptick in rainfall (with respect to average) at all locations in the second half of the year. Two locations (Kapingamarangi and Saipan) observed near-record low annual rainfall totals while Kosrae had a record wet year. No typhoons passed through the region during a cyclone season that was remarkably quiet throughout the whole basin (see section 4g7).

Table 7.3. Average 6-month (Jan–Jun and Jul–Dec) temperature anomalies (°C) and 6-month and annual rainfall (mm, totals and percent of average) for selected Micronesia locations during 2020. The average values (AVG) are for the 1981–2010 base period. Latitudes and longitudes are approximate. "Kapinga" stands for Kapingamarangi Atoll in Pohnpei State, Federated States of Micronesia. The color fill of the boxes indicates: pink for above-average temperature and blue for below average; green for above-average rainfall and yellow for below average.

Location	Max Temp Min Temp		Rainfall (mm)							
	Jan–Jun	Jul–Dec	Jan–Jun	Jan–Jun	Jan–Jun	Jul–Dec	Jul–Dec	Jul–Dec	Jan–Dec	Jan–Dec
	°C	°C	AVG	2020	%	AVG	2020	%	2020	%
Saipan 15°N, 146°E	+1.35 +0.86	+1.35 +0.90	499.1	233.4	52.0	1322.8	1140.7	86.2	1771.9	77.6
Guam 13°N, 145°E	+0.33 +0.33	+0.28 +0.38	691.6	562.36	81.3	1788.4	1701.8	95.2	2264.2	91.3
Yap 9°N, 138°E	−0.09 +0.54	−0.46 −0.22	1169.7	943.9	80.7	1901.9	1937.3	101.9	2881.1	93.8
Palau 7°N, 134°E	−0.08 −0.19	+0.03 −0.99	1798.1	1684.8	93.7	2279.4	2170.2	95.2	4077.5	94.5
Chuuk 7°N, 152°E	+0.54 +1.33	+0.80 +0.79	1584.2	1245.9	78.6	1833.1	2135.4	116.5	3381.2	99.0
Pohnpei 7°N, 158°E	−0.56 +2.13	−0.62 +1.79	2266.4	2143.0	94.6	2336.6	2771.4	116.5	4914.4	106.8
Kapinga 1°N, 155°E	n/a	n/a	1750.8	1367.0	78.1	1510.5	436.4	28.9	1803.4	55.3
Kosrae 5°N, 163°E	+0.19 +0.12	−0.21 +0.36	2567.9	3119.4	121.5	2342.9	2882.1	123.0	6001.5	122.2
Majuro 7°N, 171°E	0.00 +0.94	−0.06 +1.25	1368.3	1676.4	122.5	1868.2	2238.2	119.8	3914.6	121.0
Kwajalein 9°N, 168°E	+0.68 +0.74	+0.58 +0.56	801.4	738.4	92.1	1579.1	1579.4	100.0	2317.8	97.4

Approximately two-thirds of locations experienced above-average temperatures. The average 6-month maximum and minimum temperature anomalies and the 6-month and annual rainfall values for select locations across Micronesia are summarized in Table 7.3.

(I) TEMPERATURE

Across Micronesia, above-average temperatures outweighed below-average temperatures at a ratio of about 60:40 throughout the year. Abnormally clear and dry conditions during the first half of 2020 likely contributed to widespread above-average warmth. Increased cloudiness and rainfall during the second half of 2020 accompanied cooler temperatures with respect to average at some stations. Very warm temperatures are typically experienced in the Micronesian islands when skies are clear and winds are light; cooler temperatures occur when conditions are unusually cloudy, wet, and windy.

(II) PRECIPITATION

There were two major characteristics of the Micronesian regional precipitation during 2020. Widespread dryness was a major feature of the first half of 2020; however, at most locations the dry conditions were not exceptional. Impacts on crops and water supply were minimal, with the exception of those associated with severe drought on Kapingamarangi (see later discussion).

Additionally, there were only a few isolated extreme daily rainfall events across the region. On 28 August a thunderstorm over southern Guam produced 150–200 mm of rainfall in about 2 hours over a small area, which resulted in a flash flood of the Umatac River. This flood damaged a few homes and other property, and nearly inundated the Umatac River Bridge, which has a 2.4 m clearance over the base flow. The Army Base at Kwajalein Atoll reported two separate days in September with nearly 125 mm of rain. Pohnpei and Kosrae received monthly rainfall in excess of 500 mm for 4 and 5 months of the year, respectively. There were reports of minor flooding of streams and roadways from these two locations.

(III) NOTABLE EVENTS AND IMPACTS

Historically, most of the islands of Micronesia are dry in years when the climate system is moving toward the cool ENSO phase of La Niña (i.e., the Oceanic Niño Index [ONI] is negative and trending colder) and are wet when the climate system is moving toward the warm phase of El Niño (i.e., the ONI is positive and trending warmer; Table 7.4). Conditions are driest when the ONI starts the year very warm and rapidly cools (i.e., a typical post-El Niño year), and wettest of all when the ONI starts the year cold and rapidly warms (i.e., a typical El Niño onset year). During 2020, the ONI at the beginning of the year was on the warm side of ENSO-neutral and then steadily cooled to La Niña conditions by the boreal autumn. The drier conditions across most of Micronesia in 2020 are likely associated the anomalous cooling of sea surface temperatures (SSTs) in the eastern and central Pacific with the developing La Niña, as indicated by the ONI. Indeed, this was the case for seven of the 10 island locations shown in Table 7.3. Wetter conditions in the second half of the year were not quite sufficient to erase deeper and more widespread dryness in the first half of 2020.

Exceptional dryness was observed in two locations in Micronesia during 2020: Saipan (in the Northern Mariana Islands) and Kapingamarangi (along the equator to the south of Pohnpei Island). Saipan's annual rainfall total of 1172 mm was the lowest since 1998 (a post-El Niño year). Kapingamarangi's annual rainfall total of 1803 mm was the second-lowest 12-month sum in its historical record. Saipan's dryness was somewhat isolated as nearby islands such as Guam and Rota had near-average annual totals. The dryness at Kapingamarangi was typical for the onset of La Niña and was well-forecast several months in advance. Impacts of low rainfall on Saipan were minimal during 2020, but on Kapingamarangi, there were severe shortages of potable water in the latter half of 2020, requiring delivery of water supplies by ship.

Table 7.4. NOAA's monthly ONI for 2015–20. Red numbers are at-or-exceeding the El Niño threshold (≥ 0.5) for a minimum of five overlapping consecutive seasons to indicate El Niño, blue numbers are at-or-exceeding the La Niña threshold (≤ –0.5) for a minimum of five overlapping consecutive seasons to indicate La Niña, and black numbers are ENSO-neutral. Both 2015 and 2018 (shaded green) were El Niño onset years and behaved as such in Micronesia, with widespread abundant rainfall and enhanced tropical cyclone activity. The years 2016 and 2019 (yellow shading) were both post-El Niño years and behaved as such in Micronesia, with widespread dry conditions in the first half of both of those years and with reduced tropical cyclone activity (especially during 2016). During 2017, the climate system was mostly in a state of ENSO-neutral and the weather across Micronesia was unremarkable. During 2020, the climate system transitioned from ENSO-neutral to La Niña over the course of the year. With a cooling ONI, 2020 was predictably dry, but with an unforeseen remarkable reduction in tropical cyclone activity. Up and down arrows indicate the trend of the ONI during the each of the years.

Year	JFM	FMA	MAM	AMJ	MJJ	JJA	JAS	ASO	SON	OND	NDJ	DJF	
2015	0.5	0.5	0.5	0.7	0.9	1.2	1.5	1.9	2.2	2.4	2.6	2.6	↑
2016	2.5	2.1	1.6	0.9	0.4	–0.1	–0.4	–0.5	–0.6	–0.7	–0.7	–0.6	↓
2017	–0.3	–0.2	0.1	0.2	0.3	0.3	0.1	–0.1	–0.4	–0.7	–0.8	–1.0	↓
2018	–0.9	–0.9	–0.7	–0.5	–0.2	0.0	0.1	0.2	0.5	0.8	0.9	0.8	↑
2019	0.7	0.7	0.7	0.7	0.5	0.5	0.3	0.1	0.2	0.3	0.5	0.5	↓
2020	0.5	0.5	0.4	0.2	–0.1	–0.3	–0.4	–0.6	–0.9	–1.2	–1.3	–1.2	↓

Conversely, heavy rainfall was noted in two locations: Majuro (in the Republic of the Marshall Islands) and at Kosrae (the easternmost island of the Federated States of Micronesia). Kosrae received 6002 mm of annual rainfall, its highest annual total with records dating to 1986. Majuro Atoll also had high monthly rainfall throughout 2020, with an annual total of 3915 mm. This was the 17th-highest amount in the station's 67-year historical record. With La Niña becoming stronger through the end of the year, the east–west cloud band commonly identified as the Intertropical Convergence Zone (ITCZ) was persistent and continually confined to a narrow latitudinal band that encompassed Kosrae (5.3°N) and Majuro (7.1°N), but strayed only infrequently to islands farther north (e.g., Kwajalein, Guam, and Saipan) or islands farther south (e.g., Kapingamarangi). Heavy rainfall is generally not a problem for atolls—in fact, it is welcome—where it rapidly and harmlessly finds its way to the sea. Kosrae is a high island and can experience unwanted flooding, but given that the annual average rainfall there is near 5000 mm, residents are accustomed to extreme rainfall and have adapted accordingly.

Sidebar 7.3: **Clear La Niña signal in Micronesian typhoon tracks of 2020**—M. A. LANDER, C. P. GUARD, AND B. BUKUNT

The year 2020 is a classic example of the effect that La Niña can have on typhoon tracks across the Micronesia region. Almost no tropical cyclone (TC) activity occurred near the islands of Micronesia, apart from a few showery days as the precursor disturbances to a few of the western North Pacific basin's named storms harmlessly passed by.

In general, El Niño years are associated with an eastward displacement of TC activity and La Niña years are associated with a westward displacement of TC activity in the western North Pacific, with a dramatic effect on the distribution of TCs in Micronesia. Figure SB7.5 shows a comparison of the tropical cyclone tracks during opposite phases: 2015 (El Niño) and 2020 (La Niña).

During 2020, the Joint Typhoon Warning Center (JTWC) observed 26 tropical cyclones in the western North Pacific basin that included 12 typhoons, 12 tropical storms, and two tropical depressions. The JTWC average annual counts of typhoons, tropical storms, and tropical depressions are 18, 10, and three, respectively. The Japan Meteorological Agency named 23 storms, which included only eight typhoons and 15 tropical storms. There was a large westward displacement to the genesis locations and tracks of the 2020 TCs, which is the primary reason for the notable absence of TCs in Micronesia. Conversely, the east coast of China, Vietnam, and Korea experienced the brunt of the impacts from the tropical cyclones of 2020 (see sections 4g4 and 7g4 for more details).

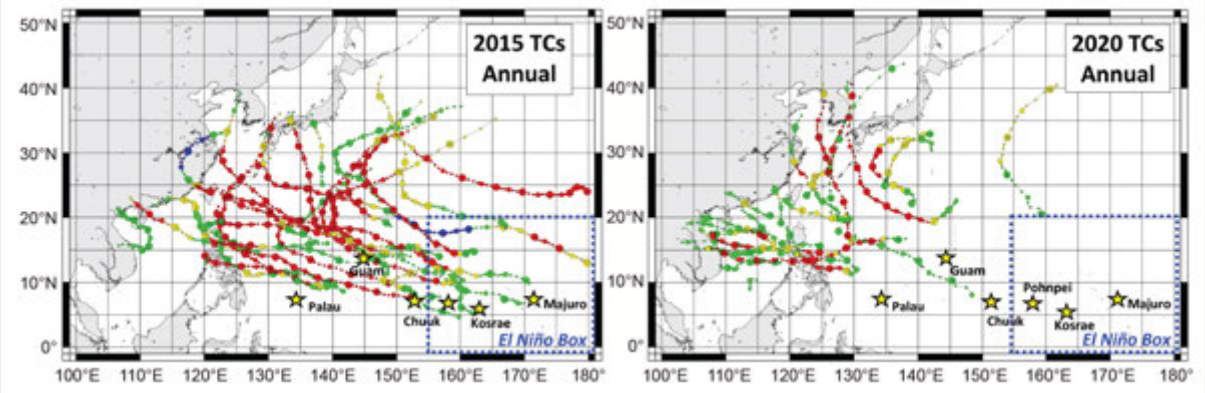

Fig. SB7.5. The typhoon tracks of 2015 (strong El Niño) and of 2020 (La Niña onset) are shown to illustrate the dramatic changes that can occur to the distribution of TCs in the western North Pacific from the state of ENSO. The islands of Micronesia (yellow stars) are profoundly affected, with TCs occurring in the "El Niño Box" almost exclusively during El Niño years. These typhoon track charts were adapted from the output of the plotting utility on the "digital typhoon" web site: http://agora.ex.nii.ac.jp/digital-typhoon/. Dot colors indicate the following: tropical storm (green), severe tropical storm (yellow), typhoon (red), and subtropical (blue).

3) Southwest Pacific—E. Chandler

Countries considered in this section include American Samoa, Cook Islands, Fiji, French Polynesia, Kiribati, New Caledonia, Niue, Papua New Guinea (PNG), Samoa, Solomon Islands, Tonga, Tuvalu, Vanuatu, and Wallis and Futuna. The temperature analysis is based on the Climate Anomaly Monitoring System (CAMS) monthly surface air temperature anomalies (https://iridl.ldeo.columbia.edu/maproom/Global/Atm_Temp/Anomaly.html). Anomalies are with respect to the 1971–2000 base period. The precipitation analysis is based on monthly analyses presented in the Climate and Oceans Support Program in the Pacific (COSPPac) Monthly Bulletin (https://www.pacificmet.net/products-and-services/climate-bulletin) and COSPPac Online Climate Outlook Forum (https://www.pacificmet.net/products-and-services/online-climate-outlook-forum). The base period for precipitation is 1979–95.

The year began in an ENSO-neutral state, which persisted until the middle of 2020 before transitioning to La Niña conditions (see section 4b for details). SSTs were persistently warm across the equatorial Pacific through the first half of 2020 before retracting to the west later in the year as the equatorial water cooled. Atmospheric indicators of the developing La Niña event became evident in the middle of the year, with strengthening equatorial trade winds and a reduction in cloud and rainfall near the date line. Precipitation was below normal for most of the year along the equator, with the strongest suppression of rainfall in the western Pacific in the later part of the year. Air temperatures were close to normal for most of the year, but became below average along the equator as La Niña strengthened toward the end of the year.

(I) TEMPERATURE

Air temperatures were near normal across most of the southwest Pacific during the first quarter of 2020 (Fig. 7.57a), apart from +1° to +2°C positive anomalies in a region centered on the equator and stretching from north of PNG to the Line Islands in Kiribati. By March, the warm anomalies extended southward, covering eastern PNG, the Solomon Islands, and northern Vanuatu. This region of above-normal air temperatures was associated with the above-normal equatorial SSTs in the same region.

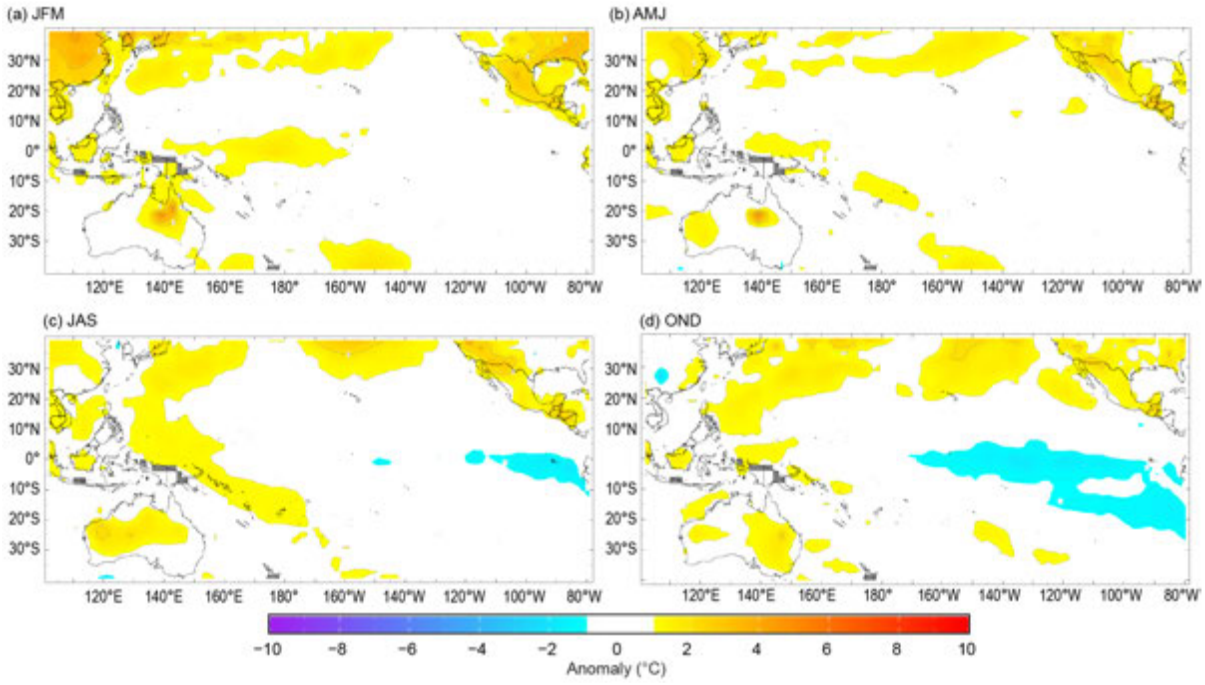

Fig. 7.57. Global seasonal temperature anomalies (°C) for (a) JFM, (b) AMJ, (c) JAS, and (d) OND. (Source: CAMS.)

Warm equatorial anomalies weakened in the second quarter of the year (Fig. 7.57b), with temperature anomalies of +1° to +2°C persisting only in the far western Pacific near PNG by June. Small regions of positive anomalies occurred later in the quarter over the Solomon Islands and across a region extending southeast to include Niue, Tonga, and the southern Cook Islands.

In July, August, and September (Fig. 7.57c) the area of positive anomalies expanded to encompass a broad region stretching from northern PNG in a southeast direction to Fiji and Tonga, with anomalies in the +1° to +2°C range. In contrast, the emerging La Niña was associated with negative anomalies developing off the South American coast and along the eastern equatorial Pacific. Small regions of –1° to –2°C anomalies extended west as far as eastern Kiribati.

The positive anomalies that previously extended southeast from PNG receded during October–December (OND), though some smaller regions remained warmer than average, associated with persistently warm ocean temperatures in the far western South Pacific. Negative anomalies expanded westward along the equator through the last quarter of 2020 as La Niña strengthened, with air temperatures 1°–2°C below normal across Tokelau, eastern Kiribati, northern Cook Islands, and French Polynesia (Fig. 7.57d). However, by December 2020 these cool anomalies had begun to contract both in spatial extent and strength of the departure from normal.

In summary, temperatures during 2020 were close to normal across much of the southwest Pacific, with the notable exception of a large region of +1° to +2°C anomalies occurring southeast from PNG through Fiji for much of the year. The warmth was most extensive during the middle of the year. In the second half of the year, the developing La Niña was associated with below-normal temperatures extending from South America along the equator to eastern Kiribati. These negative anomalies were most extensive during October–December.

(II) PRECIPITATION

Typical of a neutral-ENSO state, the region experienced a mixed rainfall pattern in the first quarter of 2020. The South Pacific Convergence Zone (SPCZ) was located on or shifted slightly to the north of its long-term position in January and February before shifting southward to the east of the Solomon Islands in March, bringing it close to Vanuatu and Fiji (Figs. 7.58a–c). Located on the date line, a region of above-average rainfall stretched eastward along the equator during January and February. As a result, rainfall above the 90th percentile for January–March (JFM) was recorded in western Kiribati, Samoa, and Tuvalu, while Savusavu Airport on Vanua Levu, Fiji, recorded its driest JFM in 59 years of record (359 mm).

The SPCZ was south of its long-term average position east of the Solomon Islands during April, while during May and June, the SPCZ was largely suppressed (Figs. 7.58d–f). Rainfall for the April–June (AMJ) quarter was reduced along the equator in early signs of the developing La Niña, with the strongest negative anomalies on and to the west of the date line. Conversely, rainfall was enhanced from northern Vanuatu eastward to Niue and Samoa during April and again during June. Rainfall for AMJ was above the 90th percentile in southern Fiji, Niue, Samoa, Tonga, and Vanuatu. Two stations in Vanuatu recorded their highest AMJ rainfall on record: Sola (1895 mm, 46-year record) and Pekoa (1517 mm, 50-year record). In contrast, rainfall below the 10th percentile was observed in the Gilbert Island group of Kiribati and the northern PNG Islands.

During July–September (JAS), the ocean surface cooled along the equator, as expected with the developing La Niña. Rainfall continued to be suppressed in this region, with the largest anomalies to the north of PNG and the Solomon Islands. Western Kiribati received JAS rainfall below the 10th percentile. Meanwhile, the SPCZ was displaced south of its normal position over the Solomon Islands (Figs. 7.58g–i), contributing to rainfall above the 90th percentile in northern Fiji, Samoa, Solomon Islands, Tonga, and, particularly due to heavy rainfall during July, in a large region extending from the Solomon Islands to southern French Polynesia. Auki in the eastern Solomon Islands recorded its wettest JAS in its 58-year record (1101 mm).

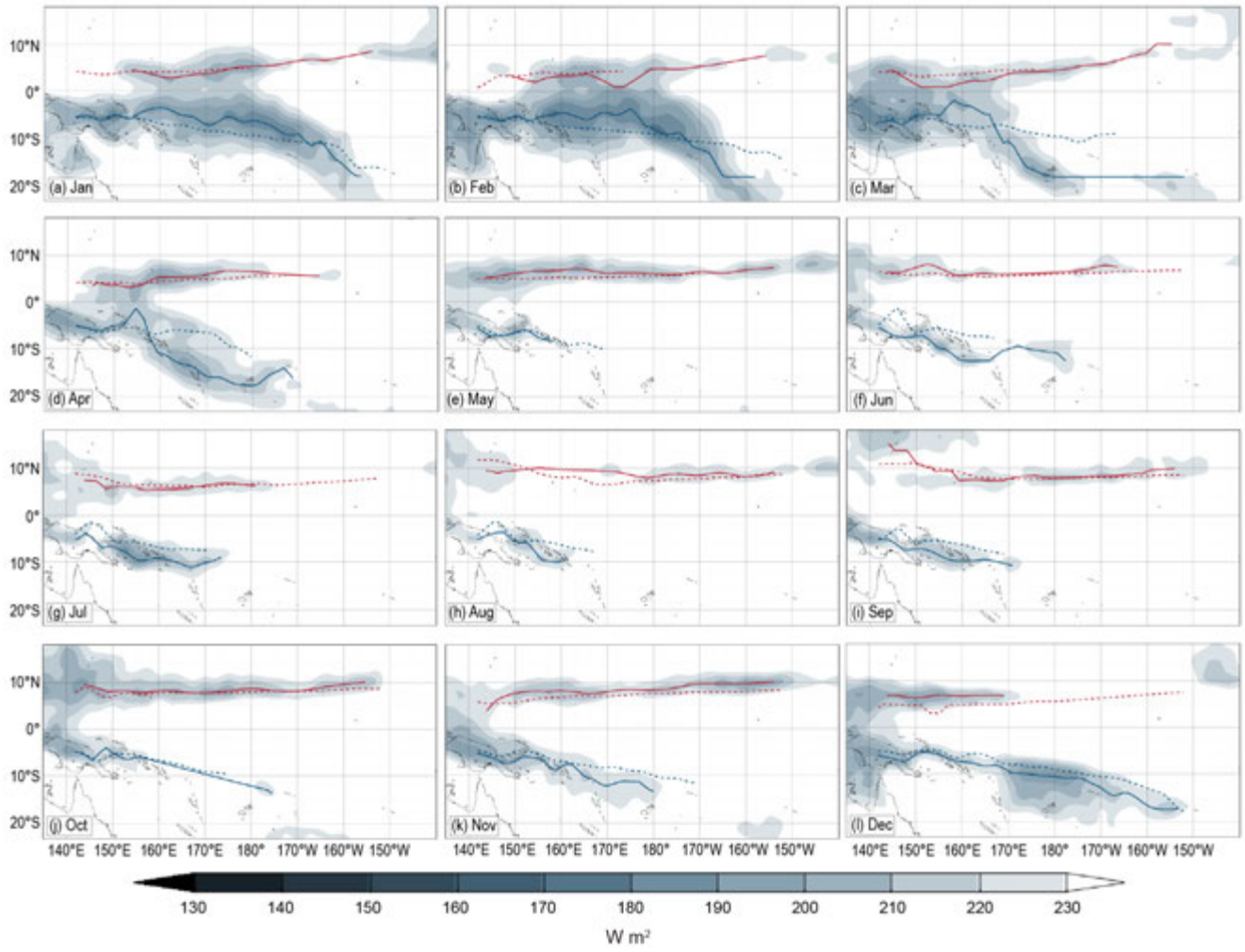

Fig. 7.58. Monthly South Pacific Convergence Zone (SPCZ) locations determined by OLR measurement for 2020. The blue line indicates SPCZ and the red line indicates the ITCZ, with dashed lines indicating the respective 1981–2010 climatological positions. (Source: Australian Bureau of Meteorology.)

Rainfall patterns during the last quarter of 2020 reflected an established La Niña. The SPCZ continued to be suppressed during October, then became active during November and December (Figs. 7.58j–l). The active SPCZ near the date line in December was associated with enhanced rainfall and tropical cyclone activity (see *Notable events and impacts*). Overall, there was a broad region near the equator with suppressed rainfall. Regions that recorded rainfall below the 10th percentile include the northern Cook Islands, western Kiribati, the northern Solomon Islands, and Tuvalu. Beru (Kiribati) recorded its second-driest OND in its 62-year record (12 mm). Conversely, there was also a broad band of enhanced rainfall in the South Pacific near the date line during this period, with totals above the 90th percentile recorded in several areas, including Fiji, northwestern PNG, Samoa, and Tonga. Faleolo (Samoa) recorded its third-wettest OND in the 58-year record (1135 mm).

In summary, rainfall in the southwest Pacific in 2020 was suppressed along the equator from April onward, associated with the transition from ENSO-neutral to La Niña. Below-normal rainfall was particularly evident in the western South Pacific later in the year, with strong suppression of rainfall in a broad region to the north of PNG and the Solomon Islands. Many South Pacific Islands experienced a wetter-than-normal start to the dry season. Numerous locations on and to the east of the date line that are influenced by the SPCZ observed enhanced rainfall toward the end of the year, including that associated with two cyclones that formed in December (see *Notable events and impacts*).

(III) NOTABLE EVENTS AND IMPACTS

Severe tropical cyclone Harold formed east of PNG in early April and moved southeast toward the Solomon Islands. By 4 April, Harold had reached Category 4 status, strengthening to Category 5 the next day before making landfall on 6 April over Espiritu Santo in southern Vanuatu. At Harold's peak there were 10-minute sustained winds of 230 km h^{-1} as the storm moved east away from Pentecost, Vanuatu. On 7 April Harold approached Suva, Fiji, before continuing southeast across the Tongan island of Tongatapu and to the south of its capital Nuku'alofa. The impacts from Harold were felt across several countries: in the Solomon Islands, 27 people drowned when they were washed overboard from a ship. There were two fatalities on Malo Island, Vanatu, while one person died and another 26 reported injuries across Fiji. Extensive damage occurred in the Solomon Islands, Vanuatu, Fiji, and Tonga, including ships washed ashore, buildings, houses, and bridges destroyed or damaged by wind as well as coastal and river inundation. There was also a loss of telecommunications and electricity, and water shortages were experienced in many areas. Several villages were evacuated due to flash flooding and inundation, and localized crop damage was reported. See section 4g8 for more details.

On 13 December, Tropical Cyclones Yasa and Zazu were both named after two tropical disturbances reached TC thresholds. Yasa was the most intense tropical cyclone of 2020, with a minimum barometric pressure of 899 hPa and maximum 10-minute sustained winds of 250 km h^{-1}. Yasa formed to the east of Vanuatu and moved in a southeasterly direction. The storm quickly intensified to Category 5 on 14 December, making it the earliest date on record that a Category 5 cyclone formed in the southwest Pacific. Yasa passed over Vanua Levu, Fiji, bringing wind gusts of up to 345 km h^{-1}, causing widespread destruction of buildings and crops; four people died. There was localized flooding and high rainfall over many highly populated areas, resulting in the loss of power, water supply, roads, and phone connections. Zazu, in comparison, formed near Niue and reached a Category 2 status on 15 December. The storm brought high rainfall and heavy surf that damaged Niue's wharf, before tracking to the south and away from populated areas.

4) Australia—S. Tobin

For this section, monthly area-averaged temperatures are based on the ACORN-SAT dataset v2.1 (Trewin 2018), which begins in 1910. Daily temperatures and mapped temperature analyses are based on the Australian Water Availability Project (AWAP) dataset (Jones et al. 2009), which begins in 1910 for temperature. Area-averaged rainfall values and mapped analyses use the new Australian Gridded Climate Data (AGCD) dataset (Evans et al. 2020), which begins in 1900.

(I) TEMPERATURE

The year 2020 was Australia's fourth-warmest year in its 111-year record. The area-averaged annual mean temperature was 0.76°C above the 1981–2010 average. The warmest year on record was 2019 (+1.13°C). The annual nationwide mean maximum temperature (Fig. 7.59) was the

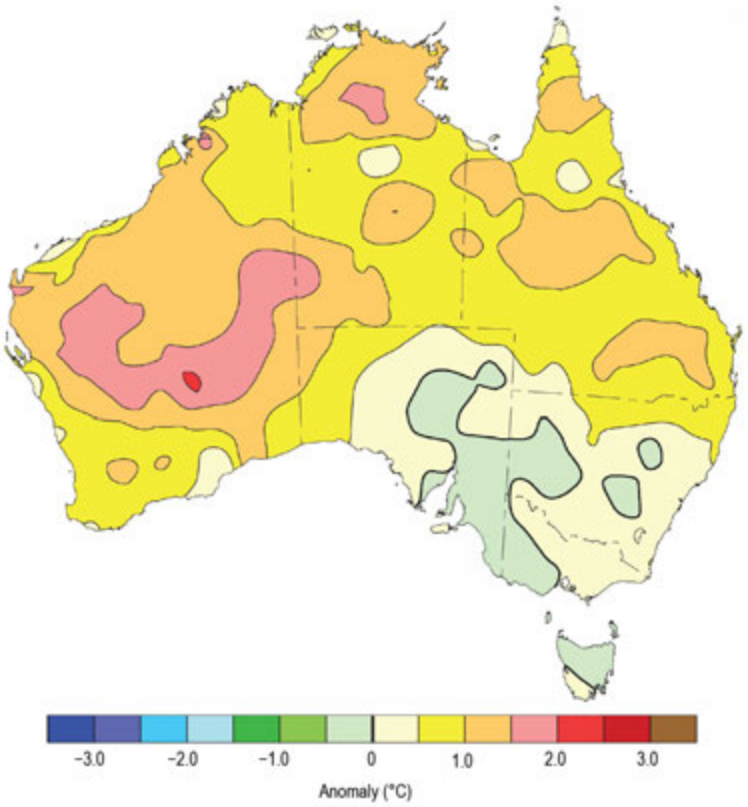

Fig. 7.59. Maximum temperature anomalies (°C) for Australia, averaged over 2020, relative to a 1981–2010 base period. (Source: Australian Bureau of Meteorology.)

eighth highest on record at 0.86°C above average. The mean minimum temperature (Fig. 7.60) was 0.67°C above average, the fourth highest on record.

Annual mean temperatures were above or very much-above average for most of Australia and in the highest 10% of historical observations for most of Western Australia, the Northern Territory, Queensland, and along the coast of New South Wales and far eastern Victoria.

Mean maximum temperatures were well-above average across most of Australia, but close to average for much of the inland southeast away from the east coast. They were in the highest 10% of historical observations for most of Western Australia, the Northern Territory, and Queensland away from the southwest.

Mean minimum temperatures were above average for much of the country, but close to average for eastern South Australia, northwestern Victoria, and southwestern New South Wales. Annual mean minima were in the highest 10% of historical observations for most of Western Australia, western South Australia, much of the Northern Territory and Queensland, and along the east coast.

Warmth was widespread and persistent through the year—the national mean temperature was among the 10 highest on record for seven of the 12 months of the year. Both November and spring as a whole had record high temperatures.

An increased diurnal temperature range is common in inland eastern Australia when rainfall is low during the cooler months of the year. Minimum temperatures during the middle months of 2020 were below average over much of southeastern Australia while mean maximum temperatures were above or well-above average over most of Australia.

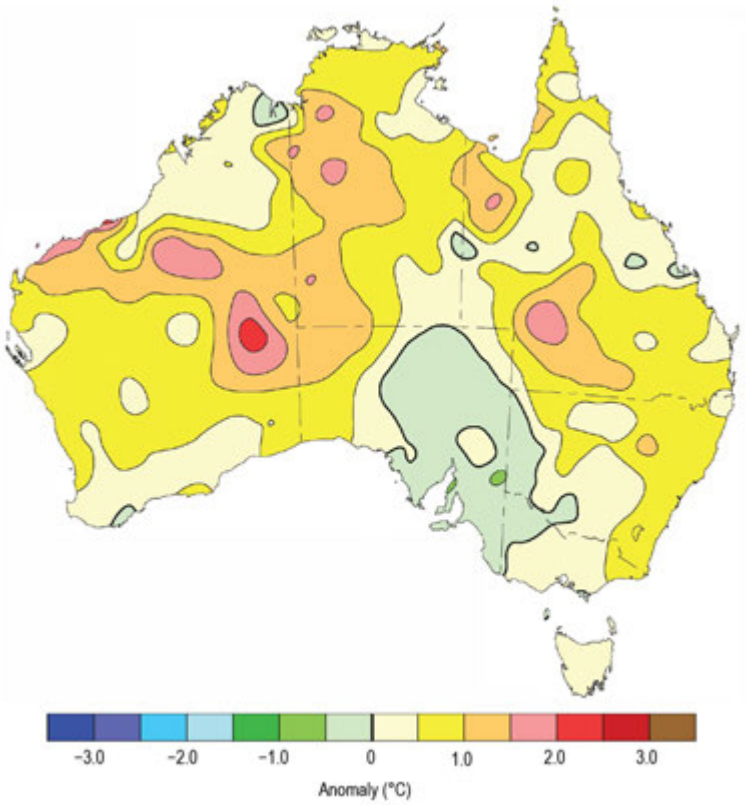

Fig. 7.60. Minimum temperature anomalies (°C) for Australia, averaged over 2020, relative to a 1981–2010 base period. (Source: Australian Bureau of Meteorology.)

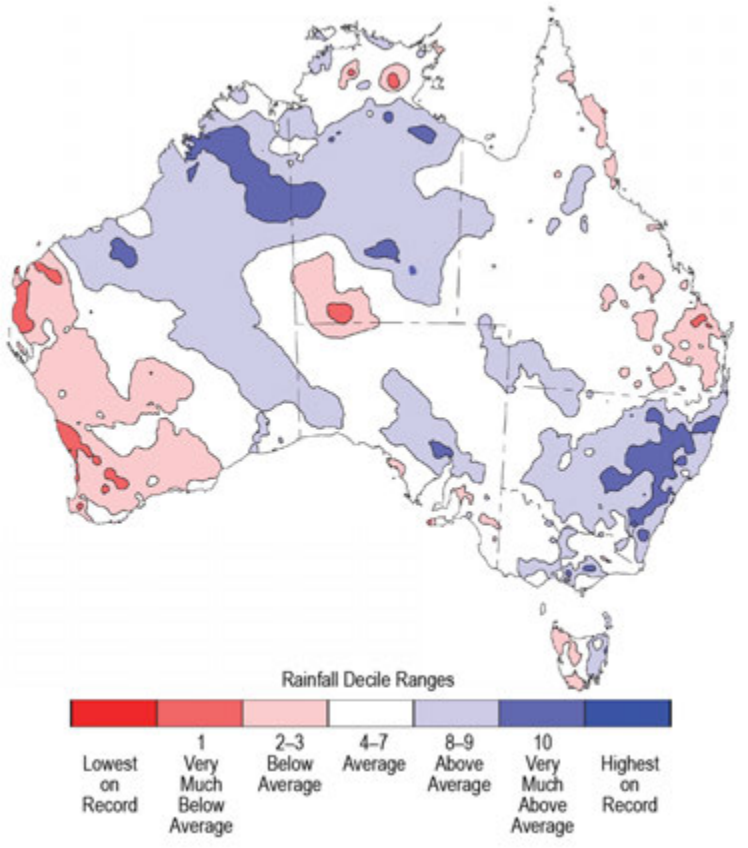

Fig. 7.61. Rainfall deciles for Australia for 2020, based on the 1900–2020 distribution. (Source: Australian Bureau of Meteorology.)

(II) PRECIPITATION

Averaged across Australia, rainfall for 2020 was 485.5 mm, very close to the 1981–2010 average of 481.6 mm. Compared to the 1900–2020 distribution, annual rainfall was below average for parts of southeastern and east coast Queensland, the west and

southwest of Western Australia, and western Tasmania (Fig. 7.61). Annual rainfall was above average across large parts of New South Wales, much of northern and eastern Western Australia, and much of the Northern Territory.

Above-average rainfall in the northwest was largely a result of tropical systems during December, whereas in New South Wales, contributions were spread across the year, mostly during February–April, August–October, and December.

Rainfall was above average for large parts of eastern Australia during February–April. The middle of the year was notably drier, with May–July rainfall being below or well-below average across much of the southern half of Australia. For the southern Australian region (south of 26°S), May–July rainfall was the seventh lowest in the 121-year record.

During late winter to early spring, both the developing La Niña and negative Indian Ocean dipole-like state of the Indian Ocean (see section 4f for details of the Indian Ocean dipole) favored above-average rainfall over eastern and southern Australia. A temporary weakening of La Niña during November brought below- or very-much-below-average rainfall to much of the eastern two-thirds of Australia, while tropical lows in the north and a slow-moving low and coastal trough in the east contributed to Australia's fourth-wettest December on record.

Following Australia's driest year on record in 2019, and protSracted widespread low rainfall since late 2016, there were significant rainfall deficiencies in place across much of Australia at the start of 2020. While water storages in the southern Murray–Darling Basin saw significant increases during 2020, storage levels in the northern Basin remained low at the end of the year.

Farther west, large areas of Western Australia saw very little rain from April to July, and short-term rainfall deficiencies emerged in the southwest in addition to existing multi-year rainfall deficiencies in the region where climatologically May, June, and July are the wettest 3 months of the year.

(III) NOTABLE EVENTS AND IMPACTS

The last days of 2019 and first days of 2020 saw particularly hazardous fire weather. Extremely high temperatures across parts of southeastern Australia and northerly winds driven by a cold front and trough contributed to significant increases in the number and size of active fires in eastern Australia (BoM 2020) where multiple fires had been burning since austral spring 2019. Extreme heat again affected southeastern Australia at the end of January and beginning of February.

Severe storms affected southeast Australia during mid-to-late January including heavy rainfall, hail up to 6 cm in diameter, and damaging winds. One of the most severe hailstorms on record in Canberra occurred on 20 January. Estimates of insured losses across Canberra, Melbourne, and Sydney reached $320 million Australian dollars (~$240 million U.S. dollars).

Accumulation of heat in the ocean waters east of Queensland during February and into March led to coral bleaching across the Great Barrier Reef. This was the third mass-bleaching event to affect the reef in 5 years.

Widespread heavy rainfall during the first half of February across much of Queensland and along the east coast of Australia contributed to both riverine and flash flooding in parts of southeast, southern, and inland Queensland and eastern New South Wales. Renewed heavy rainfall at the end of February and early March, partly associated with the remnants of Tropical Cyclone Esther (see section 4g7), led to further widespread flooding in Queensland and heavy rainfall as far south as Victoria.

Heat built in northwestern Australia during August, with records set at a large number of stations in northern Western Australia during the last week of the month. Some stations broke their previous August record multiple times during the event.

Heat waves also affected large areas in November, including much of northwest to southeast Queensland around the middle of the month and much of southeast and eastern Australia toward

the end of the month. Large areas experienced daily maximum temperatures more than 10°C above average over a number of days. Extreme heat continued into the first days of December.

A slow-moving low-pressure system and coastal trough resulted in very heavy rainfall and flooding for parts of northeastern New South Wales and southeastern Queensland during mid-December.

For further detail on these and other significant events, please see Special Climate Statements, Monthly Weather Reviews, and the Annual Climate Statement at http://www.bom.gov.au/climate/current.

5) Aotearoa New Zealand—Gregor Macara

In the following discussion, the base period is 1981–2010. The nationwide average temperature is based upon the National Institute of Water and Atmospheric Research (NIWA) seven-station temperature series that began in 1909 (see https://www.niwa.co.nz/our-science/climate/information-and-resources/nz-temp-record/seven-station-series-temperature-data). The precipitation and temperature anomaly maps were generated using interpolation of observed data from New Zealand's climate monitoring network.

(I) TEMPERATURE

The year 2020 was Aotearoa New Zealand's seventh-warmest year since records began in 1909. The nationwide average temperature was 13.24°C, 0.63°C above the 1981–2010 normal. Annual mean temperatures were above average (+0.51° to +1.20°C) across much of the North Island and many parts of the South Island. Near-average (within 0.50°C of average) temperatures occurred in much of Southland, eastern and inland Otago, coastal Canterbury, West Coast, Marlborough, coastal parts of the southern North Island, and the Central Plateau (Fig. 7.62a). Air flow anomalies over New Zealand transitioned to northeasterly during winter, which persisted over the North

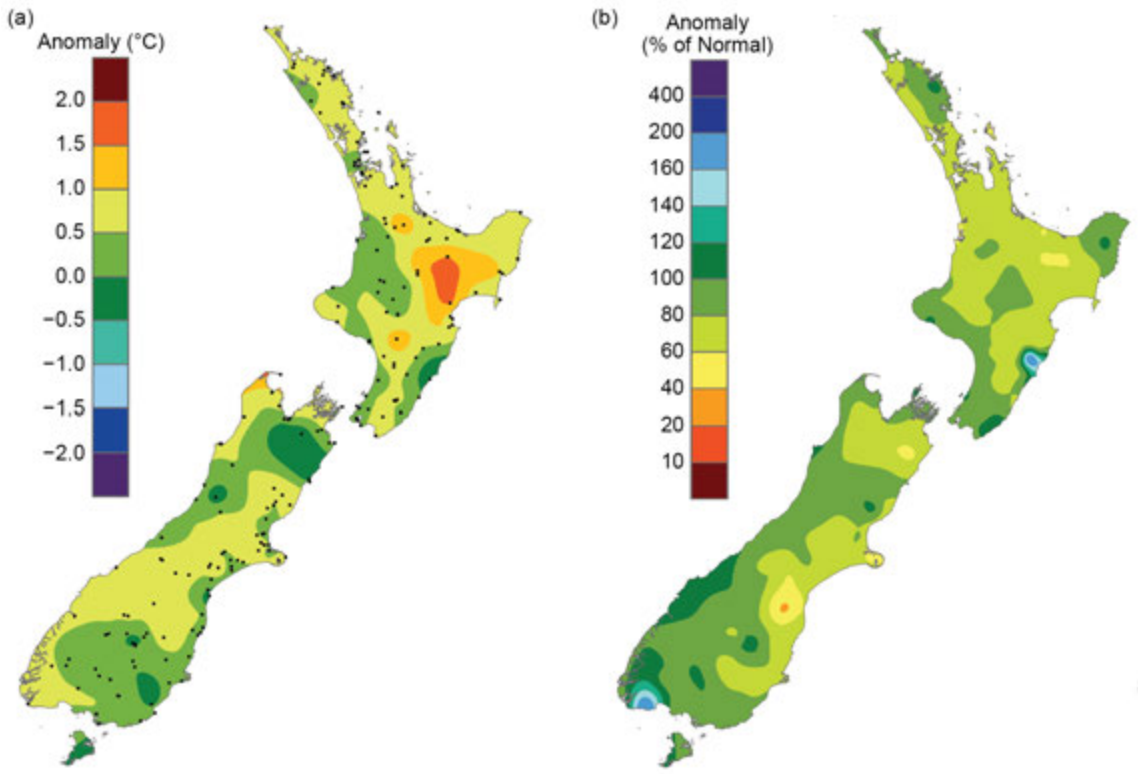

Fig. 7.62. Annual (a) average temperature anomaly (°C) and (b) total rainfall (%) for 2020, relative to the 1981–2010 base period. The dots on (a) represent the locations of climate stations used to create both the temperature and rainfall maps. (Source: NIWA.)

Island through spring; this is a traditional hallmark of La Niña, which contributed to the observed above-average temperatures. Relatively hot conditions occurred during the end of January and early in March, with four locations across the northern North Island experiencing their highest daily temperature on record. The highest temperature of 2020 was recorded on 31 January at Gisborne (38.2°C), which was New Zealand's fifth-highest January temperature on record and tied as the 19th-hottest temperature on record for all months. This heat contributed to the warmest winter on record for the country, with a nationwide average temperature of 9.6°C, 1.1°C above average. The lowest air temperature of the year was –12.3°C, recorded at Middlemarch (Otago, South Island) on 14 June.

(II) PRECIPITATION

Annual rainfall totals for 2020 were below normal (50%–79% of normal) across many northern, eastern, and inland parts of the North Island and parts of Marlborough, Canterbury, and eastern Otago on the South Island. Fourteen locations observed record low or near-record low rainfall totals. Rainfall was near normal (80%–119% of normal) for most of the remaining areas of the country including eastern parts of Northland, the Central Plateau, western and southern parts of the North Island, Nelson, West Coast, inland Otago, and Southland (Fig. 7.62b). Hamilton (Waikato, North Island) observed its driest year since records began in 1905. Of the regularly reporting rainfall gauges, the wettest location in 2020 was Cropp River in the Hokitika River catchment (West Coast, South Island, 975 m above sea level), with an annual rainfall total of 11,532 mm. The driest of the regularly reporting rainfall sites in 2020 was Hakataramea Valley (inland South Canterbury), which recorded 205 mm of rainfall.

(III) NOTABLE EVENTS AND IMPACTS

Figure 7.63 provides a schematic of notable events across New Zealand during 2020. Significant smoke and haze from Australian bushfires affected New Zealand for several days starting 1 January. The smoke and dust associated with this event contributed to the deposition of a particulate layer over parts of the Southern Alps, causing an unusual brown discoloration of the snow that persisted for several months.

From late-December 2019 through until February 2020, several locations across New Zealand observed record or near-record dry spells (defined here as 15 consecutive days or more with less than 1 mm of rain on any one day), with much of the North Island and northern South Island affected by meteorological drought. Most notably, a 64-day dry spell was recorded in Blenheim, making it the longest dry spell on record for the town.

From 1 to 4 February, very heavy rain fell in Southland and Otago. During this period, Milford Sound (Southland, South Island) recorded 1104 mm of rainfall (equivalent to 243% of its average February rainfall). A State of Emergency was declared, with 380 people stranded due to damaged roads. Approximately 4000 people were evacuated from their homes in Gore and Mataura due to flooding.

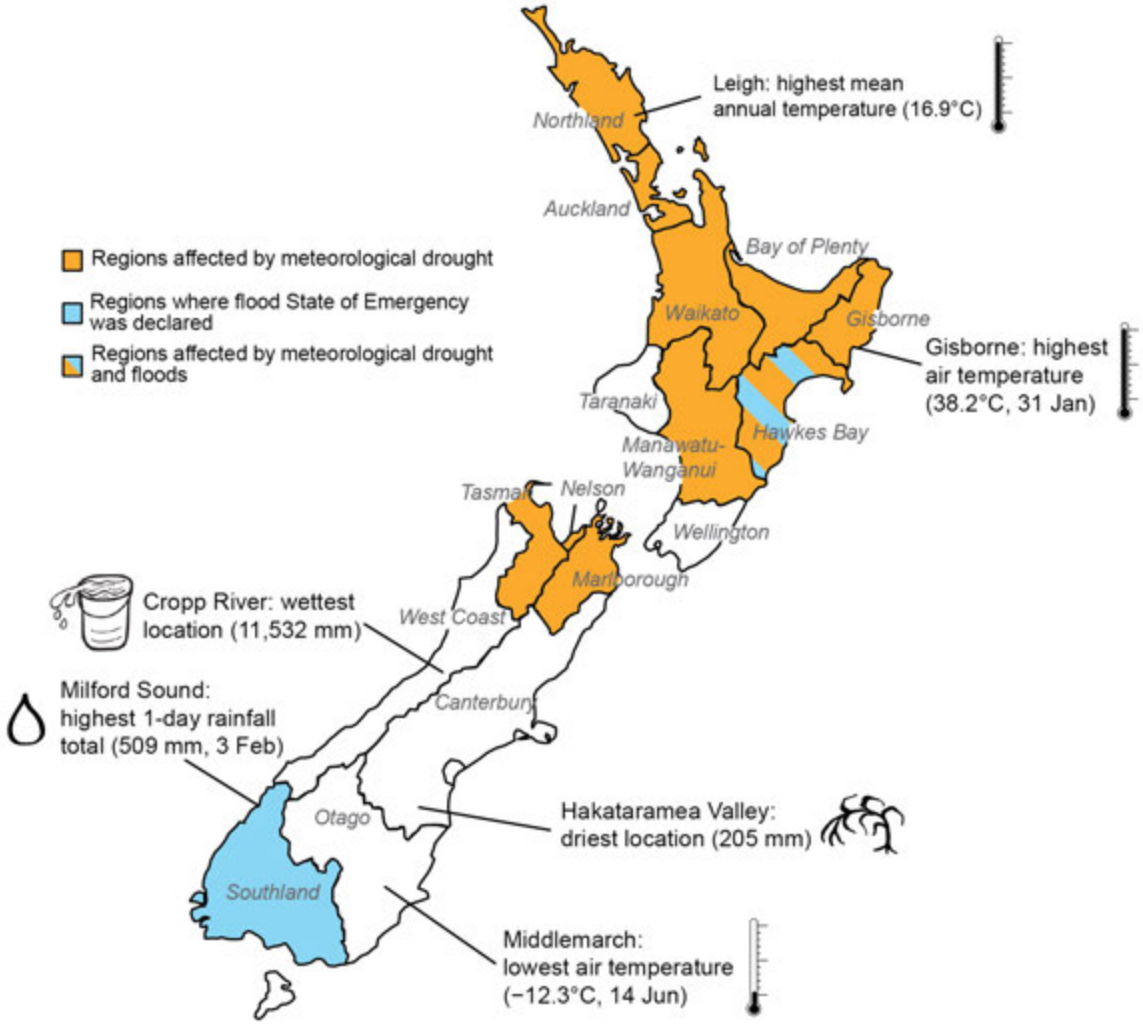

Fig. 7.63. Notable weather events and climate extremes for New Zealand in 2020. (Source: NIWA, https://niwa.co.nz/climate/summaries/annual-climate-summary-2020.)

On 9 November, a low-pressure system situated east of New Zealand brought heavy rainfall to the eastern North Island. Napier (Hawke's Bay) recorded 242 mm of rainfall (equivalent to 31% of its average annual rainfall), resulting in landslides, power outages, road closures, and the declaration of a State of Emergency. It was the city's second-highest daily rainfall total since records began in 1870.

Acknowledgments

The editors thank the numerous National Meteorological and Hydrological Services for collecting and providing data for this report. Special thanks to all the authors in this chapter for their timely contributions, and the thoughtful and constructive comments from internal and external reviewers, and the document editors.

Africa

We would like to acknowledge the national and/or hydrometeorological services/bureaus of Morocco, Algeria, Egypt, Senegal (National Aviation and Meteorology Agency), Nigeria, Ethiopia, Kenya, Tanzania, Burundi, Rwanda, South Africa, Madagascar, Seychelles, Comoros Mayotte (France), Reunion (France), and Mauritius.

- We acknowledge support by the NOAA-CPC International Desk. Global data sets from NCEP./NCAR and GPCP are acknowledged.
- Samson Hagos and Zhe Feng are supported by the U.S. Department of Energy Office of Science Biological and Environmental Research as part of the Atmospheric Systems Research (ASR) Program.

Europe

- Valuable climate information was provided by National Meteorological and Hydrological Services of the WMO RA VI Region, either by direct submission to the authors or via the web.
- Valentina Khan acknowledges the support of Ministry of Science and Higher Education of the Russian Federation (Agreement No.075-15-2021-577 with A.M. Obukhov Institute of Atmospheric Physics RAS).

Asia

- The following grants (China National Key R&D Program 2018YFC1505806 and 2018YFA0605604, NSF AGS-2006553, and NOAA grant NA18OAR4310298) are acknowledged.

APPENDIX 1: Chapter 7 – Acronyms

AGCD	Australian gridded climate data
AMJ	April–June
AWAP	Australian Water Availability Project
BNGRC	National Office for Risk and Disaster Management
CA	Central America
CAMS	Climate Anomaly Monitoring System
CA-NWS	Central America National Weather Services
CAR	Central Africa republic
CMORPH	CPC Morphing Technique
CONUS	contiguous United States
COSPPac	Climate and Oceans Support Program in the Pacific
CP	central Pacific
CPC	Climate Prediction Center
DJF	December–February
DRC	Democratic Republic of Congo
ECCC	Environment and Climate Change Canada
EM-DAT	Emergency Events Database
ENSO	El Niño–Southern Oscillation
EP	eastern Pacific
GHA	Greater Horn of Africa
GHCN	Global Historical Climate Network
GPCC	Global Precipitation Climatology Centre
IDI	Integrated Drought Index
IDP	Internally Displaced People
INPE	National Institute for Space Research
IO	Indian Ocean
ISMR	Indian summer monsoon rainfall
ITCZ	intertropical Convergence Zone
JAS	July–September
JFM	January–March
JJ	June–July
JJAS	June–September
JTWC	Joint Typhoon Warning Center
LTA	long-term average
MAM	March–May
MSE	moist static energy
NCEP/NCAR	National Centers for Environmental Prediction/National Center for Atmospheric Research
NEM	Northeast monsoon
NH	Northern Hemisphere
NIWA	National Institute of Water and Atmospheric Research
OND	October–December
ONI	Oceanic Niño Index
PNG	Papua New Guinea
RCC-CM	Regional Climate Centre on Climate Monitoring
RFE2	rainfall estimates version 2

SH	Southern Hemisphere
SON	September–November
SPCZ	South Pacific Convergence Zone
SPI	standardized precipitation index
SSA	Southern South America
SST	sea surface temperature
SSTA	sea surface temperature anomaly
TC	tropical cyclone
UN	United Nations
WNP	western North Pacific
YRV	Yangtze River Valley

APPENDIX 2: Supplemental Materials

Table A7.1. Temporal coverage of nationally averaged temperature and precipitation in situ observations for Europe/WMO RA VI Region. For some countries, only one station (preferably with long time series) has been used (name of the location in brackets). All records extend to the present.

Nation	Temperature start of record	Precipitation start of record	Source
European average	1950	1950	GHCN[1] data
Albania (Korce)	1963	1963	CLIMAT[2]
Andorra	1950	1950	NMHS[3]
Armenia	1935	1935	NMHS
Austria	1767	1858	NMHS
Azerbaijan (Astara)	1991	1991	CLIMAT
Belarus	1881	1945	NMHS
Belgium	1981	1981	NMHS
Bosnia & Herzegovina (Banja Luka)	1955	1955	CLIMAT
Bulgaria	1930	1954 (Burgas)	NMHS/CLIMAT
Croatia (Split/Marjan)	1949	1949	CLIMAT
Cyprus (Nicosia)	1899	1899	NMHS
Czechia	1961	1961	NMHS
Denmark	1873	1874	NMHS
Estonia	1961	1961	NMHS
Finland (Helsinki)	1900	1961	NMHS
France	1900	1959	NMHS
Georgia	1956	1881 (Tbilisi)	NMHS
Germany	1881	1881	NMHS
Greece	1960	1949 (Athens)	NMHS/CLIMAT
Hungary	1901	1901	NMHS
Iceland (Stykkishólmur)	1900	1856	NMHS
Ireland	1900	1900	NMHS
Israel	1951	1935 (Deganya)	NMHS
Italy	1961	1949 (Alghero)	NMHS/CLIMAT
Jordan (Amman)	1981	1981	NMHS
Kazakhstan	1941	1941	NMHS
Latvia	1924	1924	NMHS
Lebanon (Beirut)	1949	1949	CLIMAT
Lithuania	1961	1887 (Vilnius)	NMHS
Luxembourg (Findel)	1947	1947	NMHS
Malta (Luqa)	1923	1949	NMHS/CLIMAT
Moldova (Chisinau)	1886	1891	NMHS
Monaco	not available	not available	—
Montenegro (Plevlja)	1955	1955	CLIMAT
Netherlands	1901	1901	NMHS
North Macedonia (Bitola)	1955	1955	CLIMAT

(cont.) Table A7.1. Temporal coverage of nationally-averaged temperature and precipitation in situ observations for Europe/WMO RA VI Region. For some countries, only one station (preferably with long time series) has been used (name of the location in brackets). All records extend to the present.

Nation	Temperature start of record	Precipitation start of record	Source
Norway	1900	1900	NMHS
Poland	1951	1951	NMHS
Portugal	1931	1931	NMHS
Romania	1961	1954 (Bistrita)	NMHS/CLIMAT
Russia, European part	1936	1936	NMHS
Serbia	1951	1951	NMHS
Slovakia	1951	1961	NMHS
Slovenia	1961	1961	NMHS
Spain	1965	1965	NMHS
Sweden	1860	1860	NMHS
Switzerland	1864	1864	NMHS
Syrian Arab Republic (Aleppo)	1960	1960	CLIMAT
Turkey	1971	1949 (Adana)	NMHS
Ukraine	1891	1891	NMHS
United Kingdom	1884	1862	NMHS

[1]GHCN = Global Historical Climatology Network (Menne et al. 2018)
[2]CLIMAT station data as reported worldwide via the WMO Global Telecommunication System
[3]NMHS = National Meteorological and Hydrological Service; for individual names of NMHSs see https://public.wmo.int/en/about-us/members

References

Amador, J. A., 1998: A climatic feature of the tropical Americas: The trade wind easterly jet. *Top. Meteor. Oceanogr.*, **5**, 91–102.

—, 2008. The Intra-Americas Seas Low-Level Jet (IALLJ): Overview and future research. *Ann. N. Y. Acad. Sci.*, **1146**, 153–188, https://doi.org/10.1196/annals.1446.012.

—, E. J. Alfaro, H. G. Hidalgo, and B. Calderón, 2011: Central America [in "State of the Climate in 2010"]. *Bull. Amer. Meteor. Soc.*, **92**, S182–S183, https://doi.org/10.1175/1520-0477-92.6.S1.

—, E. R. Rivera, A. M. Durán-Quesada, G. Mora, F. Sáenz, B. Calderón, and N. Mora, 2016a: The easternmost tropical Pacific. Part I: A climate review. *Int. J. Trop. Biol.*, **64**, S1–S22.

——, A. M. Durán-Quesada, E. R. Rivera, G. Mora, F. Sáenz, B. Calderón, and N. Mora, 2016b: The easternmost tropical Pacific. Part II: Seasonal and intraseasonal modes of atmospheric variability. *Int. J. Trop. Biol.*, **64**, S3–S57.

BoM, 2020: Special Climate Statement 73—Extreme heat and fire weather in December 2019 and January 2020. Bureau of Meteorology, 17 pp., http://www.bom.gov.au/climate/current/statements/scs73.pdf.

Caribbean Institute for Meteorology and Hydrology, 2020: Caribbean Drought Bulletin Vol VI – VII, CIMH CRCC, accessed 27 January 2021, https://rcc.cimh.edu.bb/drought-bulletin-archive/.

Chang, C. P., Y. S. Zhang, and T. Li, 2000a: Interannual and interdecadal variations of the East Asian summer monsoon and tropical Pacific SSTs. Part I: Roles of the subtropical ridge. *J. Climate*, **13**, 4310–4325, https://doi.org/10.1175/1520-0442(2000)013<4310:IAIVOT>2.0.CO;2.

——, ——, and ——, 2000b: Interannual and interdecadal variations of the East Asian summer monsoon and tropical Pacific SSTs. Part II: Meridional structure of the monsoon. *J. Climate*, **13**, 4326–4340, https://doi.org/10.1175/1520-0442(2000)013<4326:IAIVOT>2.0.CO;2.

Cuhna, A. P., and Coauthors, 2019: Extreme drought events in over Brazil from 2011 to 2019. *Atmosphere*, **10**, 642, https://doi.org/10.3390/atmos10110642

Elagib, N. A., I. S. Al Zayed, S. A. G. Saad, M. I. Mahmood, M. Basheer, and A. H. Fink, 2021: Debilitating floods in the Sahel are becoming frequent. *J. Hydrol.*, **599**, 126362, https://doi.org/10.1016/j.jhydrol.2021.126362.

Enomoto, T., B. J. Hoskins, and Y. Matsuda, 2003: The formation mechanism of the Bonin high in August. *Quart. J. Roy. Meteor. Soc.*, **129**, 157–178, https://doi.org/10.1256/qj.01.211.

Evans, A., D. A. Jones, R. Smalley, and S. Lellyett, 2020: An enhanced gridded rainfall analysis scheme for Australia. Bureau Research Rep. 041, Bureau of Meteorology, 39 pp., http://www.bom.gov.au/research/publications/researchreports/BRR-041.pdf.

FAN, 2020: Incendios forestales en Bolivia 2019–2020. Accessed 25 January 2021, http://incendios.fan-bo.org/Satrifo/?p=3987.

Giannini, A., R. Saravanan, and P. Chang, 2003: Oceanic forcing of Sahel rainfall on interannual to interdecadal time scale. *Science*, **302**, 1027–1030, https://doi.org/10.1126/science.1089357.

Gill, A. E., 1980: Some simple solutions for heat-induced tropical circulation. *Quart. J. Roy. Meteor. Soc.*, **106**, 447–462, https://doi.org/10.1002/qj.49710644905.

Hidalgo, H. G., E. J. Alfaro, J. A. Amador, and A. Bastidas, 2019: Precursors of quasi-decadal dry-spells in the Central America Dry Corridor. *Climate Dyn.*, **53**, 1307–1322, https://doi.org/10.1007/s00382-019-04638-y.

Janicot, S., S. Trzaska, and I. Poccard, 2001: Summer Sahel–ENSO teleconnection and decadal time scale SST variations. *Climate Dyn.*, **18**, 303–320, https://doi.org/10.1007/s003820100172.

Jones, D. A., W. Wang, and R. Fawcett, 2009: High-quality spatial climate datasets for Australia. *Aust. Meteor. Oceanogr. J.*, **58**, 233–248, https://doi.org/10.22499/2.5804.003.

Li, T., and B. Wang, 2005: A review on the western North Pacific monsoon: Synoptic-to-interannual variabilities. *Terr. Atmos. Ocean. Sci.*, **16**, 285–314, https://doi.org/10.3319/TAO.2005.16.2.285(A).

——, and P.-C. Hsu, 2017: *Fundamentals of Tropical Climate Dynamics*. Springer, 239 pp.

——, B. Wang, B. Wu, T. J. Zhou, C. P. Chang, and R. H. Zhang, 2017: Theories on formation of an anomalous anticyclone in western North Pacific during El Niño: A review. *J. Meteor. Res.*, **31**, 987–1006, https://doi.org/10.1007/s13351-017-7147-6.

Magaña, V., J. A. Amador, and S. Medina, 1999: The midsummer drought over Mexico and Central America. *J. Climate*, **12**, 1577–1588, https://doi.org/10.1175/1520-0442(1999)012<1577:TMDOMA>2.0.CO;2.

Marengo, J. A., and Coauthors, 2021: Extreme drought in the Brazilian Pantanal in 2019–2020: Characterization, causes, and impacts. *Front. Water*, **3**, 639204, https://doi.org/10.3389/frwa.2021.639204.

Martin, E. R., and C. D. Thorncroft, 2014: The impact of the AMO on the West African monsoon annual cycle. *Quart. J. Roy. Meteor. Soc.*, **140**, 31–46, https://doi.org/10.1002/qj.2107.

Mohino, E., S. Janicot, and J. Bader, 2011: Sahel rainfall and decadal to multi-decadal sea surface temperature variability. *Climate Dyn.*, **37**, 419–440, https://doi.org/10.1007/s00382-010-0867-2.

Nurse, M., 2020: Droughts, hurricanes, pandemic, and hope: Current realities impacting Caribbean agriculture. CARICOM Today, 5 June, accessed 19 March 2021, https://today.caricom.org/2020/06/03/droughts-hurricanes-pandemic-and-hope-current-realities-impacting-caribbean-agriculture/.

SENAMHI, 2020: Datos preliminares, boletines agroclimáticos y reportes hidrológicos 2020. Accessed 25 January 2021, www.senamhi.gob.bo/boletines.

Taylor, M., D. Enfield, and A. Chen, 2002: Influence of the tropical Atlantic versus the tropical Pacific on Caribbean rainfall. *J. Geophys. Res.*, **107**, 3127, https://doi.org/10.1029/2001JC001097.

Trewin, B., 2018: The Australian Climate Observations Reference Network – Surface Air Temperature (ACORN-SAT) version 2. Bureau Research Rep. 032, Bureau of Meteorology, 57 pp., http://www.bom.gov.au/climate/change/acorn-sat/documents/BRR-032.pdf.

Wang, B., R. G. Wu, and T. Li, 2003: Atmosphere–warm ocean interaction and its impacts on Asian–Australian monsoon variation. *J. Climate*, **16**, 1195–1211, https://doi.org/10.1175/1520-0442(2003)16<1195:AOIAII>2.0.CO;2.

WMO, 2020: WMO issues airborne dust bulletin as historic event hits Caribbean. WMO News, 26 June, accessed 19 March 2021, https://public.wmo.int/en/media/news/wmo-issues-airborne-dust-bulletin-historic-event-hits-caribbean.

Wu, B., T. Zhou, and T. Li, 2009: Seasonally evolving dominant interannual variability mode over the East Asia. *J. Climate*, **22**, 2992–3005, https://doi.org/10.1175/2008JCLI2710.1.

Zhang, Q., and Coauthors, 2021: Understanding the variability of the rainfall dipole in West Africa using the EC-Earth last millennium simulation. *Climate Dyn.*, **57**, 93–107, https://doi.org/10.1007/s00382-021-05696-x.

STATE OF THE CLIMATE IN 2020

RELAVENT DATASETS AND SOURCES

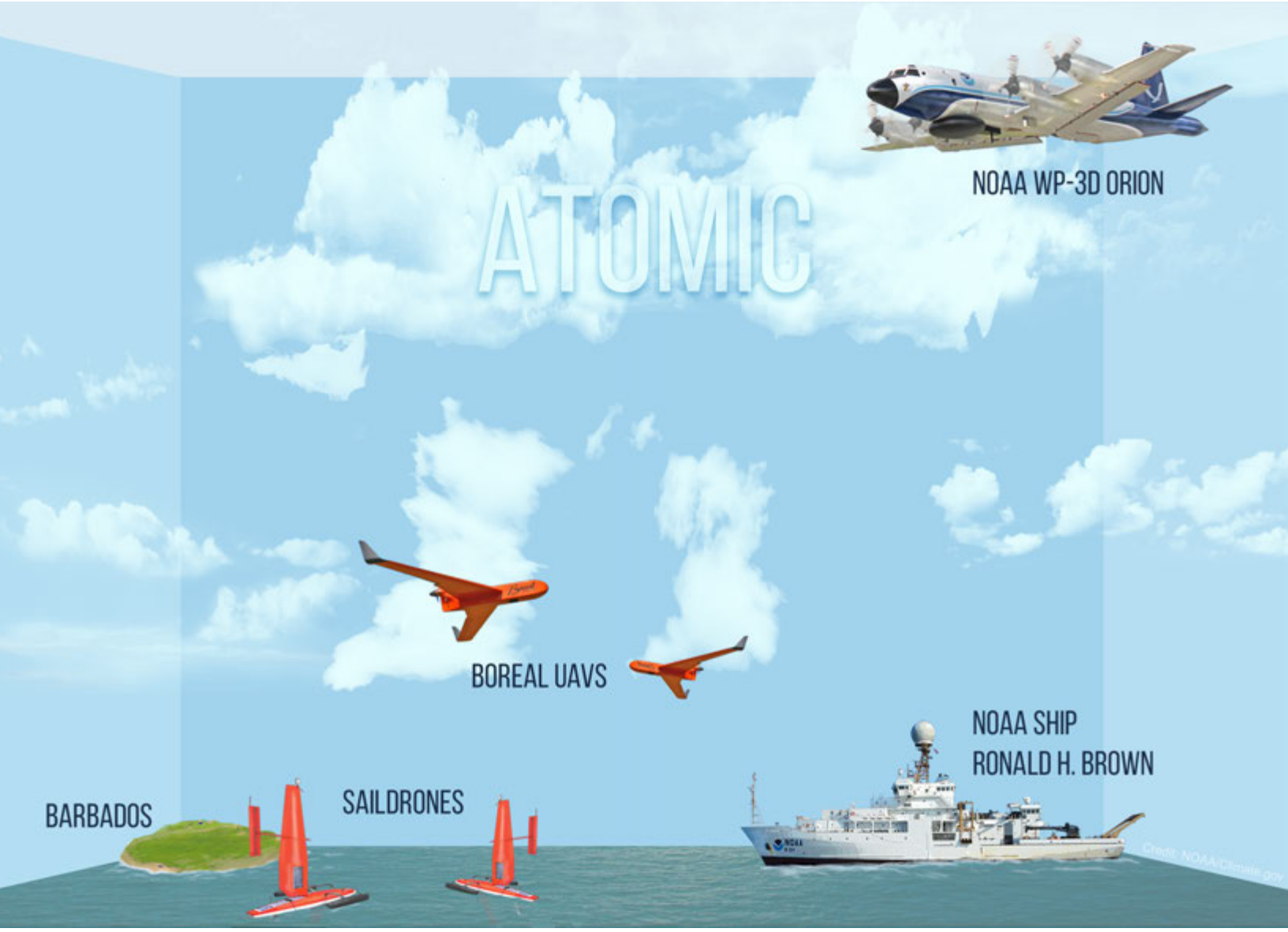

See Chapter 1 (Introduction) for information about the ATOMIC field campaign. Image credit:NOAA/Climate.gov

Special Online Supplement to the *Bulletin of the American Meteorological Society* Vol.102, No. 8, August, 2021

10.1175/2021BAMSStateoftheClimate_Chapter8.1
Corresponding author: Jessica Blunden / Jessica.Blunden@noaa.gov

8: RELEVANT DATASETS AND SOURCES

General Variable or Phenomenon	Specific dataset or variable	Source	Section
Aerosols	CAMS Reanalysis	https://ads.atmosphere.copernicus.eu/cdsapp#!/dataset/cams-global-radiative-forcing-auxilliary-variables?tab=overview	2g3
	MODIS Aerosol	https://modis.gsfc.nasa.gov/data/dataprod/mod04.php	2g3
	AATSR	https://earth.esa.int/eogateway/instruments/aatsr	2g3
Air-sea fluxes	CERES Energy Balanced and Filled	https://ceres.larc.nasa.gov/data/	3e4
	CERES FLASHflux	https://ceres.larc.nasa.gov/data/	3e1
	ERA5	https://www.ecmwf.int/en/forecasts/datasets/reanalysis-datasets/era5	6g1
	Woods Hole Oceanographic Institute OAFlux	http://oaflux.whoi.edu	3e1, 3e2, 3e3
Albedo	MODIS	https://doi.org/10.5067/MODIS/MCD43C3.006	2h1
	MODIS (Greenland)	https://doi.org/10.22008/promice/data/modis_greenland_albedo	5e
Biomass, Greenness or Burning	GFAS v1.4	ftp://ftp.mpic.de/GFAS/sc17 (special reprocessing)	2h3
	Global Inventory Modeling and Mapping Studies (GIMMS) 3gv1	https://iridl.ldeo.columbia.edu/SOURCES/.NASA/.ARC/.ECOCAST/.GIMMS/.NDVI3g/.v1p0/index.html?Set-Language=en	5i
	MODIS MCD43A4	https://lpdaac.usgs.gov/products/mcd43a4v006/	5i
	MODIS fire	https://modis.gsfc.nasa.gov/data/dataprod/mod14.php	5SB.1
	VIIRS SNPP	https://oceancolor.gsfc.nasa.gov/data/viirs-snpp/	5SB.1
Cloud Properties	Aqua MODIS C6	http://dx.doi.org/10.5067/MODIS/MYD08_M3.006	2d7, 2h3
	Terra MODIS C6	http://dx.doi.org/10.5067/MODIS/MOD08_M3.006	2d7
	MODIS 08_L3	https://modis.gsfc.nasa.gov/data/dataprod/mod08.php	2d7
	CALIPSO	http://www-calipso.larc.nasa.gov	2d7, 6h
	CERES MODIS	https://ceres.larc.nasa.gov/data/general-product-info/	2d7
	CLARA-A2	https://www.cmsaf.eu/EN/Home/home_node.html	2d7
	CLOUD_CCI	www.esa-cloud-cci.org	2d7
	HIRS	https://www.ncei.noaa.gov/access/metadata/landing-page/bin/iso?id=gov.noaa.ncdc:C00951	2d7
	MISR	https://l0dup05.larc.nasa.gov/L3Web/	2d7
	PATMOS-x/AVHRR	www.ncdc.noaa.gov/cdr/atmospheric/avhrr-cloud-properties-patmos-x	2d7
	PATMOS-x/MODIS C6	http://ladsweb.nascom.nasa.gov	2d7
	SatCORPS	No public archive	2d7
Drought	CRU TS 4.05	https://crudata.uea.ac.uk/cru/data/hrg/cru_ts_4.05/	2d11
Land Evaporation	GLEAM	www.gleam.eu/	2d12
FAPAR	MERIS	https://earth.esa.int/eogateway/	2h2
	MODIS-TIP	http://ladsweb.nascom.nasa.gov/	2h2
	SeaWiFS FAPAR	http://fapar.jrc.ec.europa.eu/	2h2
Geopotential Height	ERA5	https://www.ecmwf.int/en/forecasts/datasets/reanalysis-datasets/era5	6b
	NCEP/NCAR Reanalysis 1: Pressure	https://psl.noaa.gov/data/gridded/data.ncep.reanalysis.pressure.html	4d2, 4f2

(cont.) Relevant datasets and sources

General Variable or Phenomenon	Specific dataset or variable	Source	Section
Glacier Mass, Area or Volume	GRACE / GRACE-FO	https://grace.jpl.nasa.gov/data/get-data/	5e, 5f, 6e
	World Glacier Monitoring Service	http://dx.doi.org/10.5904/wgms-fog-2020-08	2c3
	Glacier Front Line (Greenland)	https://doi.org/10.22008/promice/data/calving_front_lines	e3
Groundwater and terrestrial water storage	GRACE / GRACE-FO	https://grace.jpl.nasa.gov/data/get-data/	2d9
Humidity, [Near] Surface	ERA5	https://www.ecmwf.int/en/forecasts/datasets/reanalysis-datasets/era5	2d1
	HadISDH	www.metoffice.gov.uk/hadobs/hadisdh	2d1
	MERRA-2	https://gmao.gsfc.nasa.gov/reanalysis/MERRA-2/	2d1
	JRA-55 Atmospheric Reanalysis	http://jra.kishou.go.jp/JRA-55/index_en.html	2d1
Humidity, Upper Atmosphere	ERA5	https://www.ecmwf.int/en/forecasts/datasets/reanalysis-datasets/era5	2d3
	HIRS	www.ncdc.noaa.gov/cdr/fundamental/hirs-ch12-brightness-temperature	2d3
	UTH, Microwave	by email to Viju.John@eumetsat.int	2d3
Ice Sheet Characteristics	DMSP-SSMIS	https://nsidc.org/data/nsidc-0001	6d
	ERA5	https://www.ecmwf.int/en/forecasts/datasets/reanalysis-datasets/era5	6c
	ICESat, ICESat-2	https://icesat-2.gsfc.nasa.gov/	5d2, 6e
	Cryosat-2	https://earth.esa.int/eogateway/missions/cryosat	5d2
	SMOS	https://earth.esa.int/eogateway/missions/smos	5d2
	MERRA-2	https://gmao.gsfc.nasa.gov/reanalysis/MERRA-2/	6c, 6h
	Modèle Atmosphérique Régionale surface mass	https://mar.cnrs.fr/	5e
	PROMICE (Greenland)	https://doi.org/10.22008/promice/data/aws	5e
	DMI Weather Stations	http://polarportal.dk/en/weather/historisk-vejr/#:~:text=DMI%20has%20a%20number%20of,go%20back%20almost%20250%20years.&text=One%20cannot%20expect%20that%20temperature%20observations%20spanning%20centuries%20are%20homogeneous	5e
	ICE_6G_D	https://www.atmosp.physics.utoronto.ca/~peltier/data.php	5e
	Ice Discharge (Greenland)	https://doi.org/10.22008/promice/data/ice_discharge/d/v02	5e
Lake Ice	Global Lake and River Ice Phenology Database, Version 1	https://doi.org/10.7265/N5W66HP8	2c4
	Great Lakes Ice	www.glerl.noaa.gov/data/ice	2c4
	ERA5	https://www.ecmwf.int/en/forecasts/datasets/reanalysis-datasets/era5	2c4

(cont.) Relevant datasets and sources

General Variable or Phenomenon	Specific dataset or variable	Source	Section
Lake Temperature	ERA5	https://www.ecmwf.int/en/forecasts/datasets/reanalysis-datasets/era5	2b3
	NERC Globolakes, Copernicus Climate Service	https://cds.climate.copernicus.eu/cdsapp#!/dataset/satellite-lake-water-temperature?tab=overview	2b3
	MetOp A & B ATSR and AVHRR	https://www.eumetsat.int/website/home/Satellites/CurrentSatellites/Metop/index.html	2b3
	Sentinel 3 SLSTR	https://sentinel.esa.int/web/sentinel/user-guides/sentinel-3-slstr/overview	2b3
Lake Water Levels	Hydroweb	http://hydroweb.theia-land.fr/	2b3
Modes of Variability	Arctic Oscillation (AO)	www.cpc.ncep.noaa.gov/products/precip/CWlink/daily_ao_index/teleconnections.shtml	2e1
	Indian Ocean Dipole Mode Index	https://psl.noaa.gov/gcos_wgsp/Timeseries/DMI/	4f, 4h
	Madden-Julian Oscillation (MJO) - Real-time Multivariate MJO	www.bom.gov.au/climate/mjo/graphics/rmm.74toRealtime.txt	4c
	North Atlantic Oscillation (NAO)	https://climatedataguide.ucar.edu/climate-data/hurrell-north-atlantic-oscillation-nao-index-station-based	2e1
	Oceanic Nino Index (ONI)	www.cpc.ncep.noaa.gov/products/analysis_monitoring/ensostuff/ensoyears.shtml	4b
	Southern Annular Mode (SAM)	www.antarctica.ac.uk/met/gjma/sam.html	6b
	Southern Annular Mode (SAM, AAO)	www.cpc.ncep.noaa.gov/products/precip/CWlink/daily_ao_index/aao/aao.shtml	2e1
	Multivariate El Nino Index (MEI)	https://psl.noaa.gov/enso/mei/	3i
	Southern Oscillation Index (SOI)	ftp://ftp.bom.gov.au/anon/home/ncc/www/sco/soi/soiplaintext.html	2e1
Rock Glacier Kinematics	Austria: V. Kaufmann and A. Kellerer-Pirklbauer, France: X. Bodin and E. Thibert, Switzerland: R. Delaloye, J. Noetzli and C. Pellet	availabe from authors upon request	2SB.2
Ocean Carbon	fCO_2	www.socat.info	3j2
	Takahashi LDEO fCO_2	https://www.ncei.noaa.gov/access/ocean-carbon-data-system/oceans/LDEO_Underway_Database/	3j2
	Global Ocean Ship-Based Hydrographic Investigations Program	www.go-ship.org	3j3
	Saildrone	https://data.saildrone.com/	6g3
	SOCCOM profiling float	https://soccom.princeton.edu/content/data-access	6g3

(cont.) Relevant datasets and sources

General Variable or Phenomenon	Specific dataset or variable	Source	Section
Ocean Heat Content	CLIVAR and Carbon Hydrographic Data Office	https://cchdo.ucsd.edu/	3c
	CSIRO/ACE CRC/IMAS-UTAS estimate	www.cmar.csiro.au/sealevel/thermal_expansion_ocean_heat_timeseries.html	3c
	IAP/CAS	https://climatedataguide.ucar.edu/climate-data/ocean-temperature-analysis-and-heat-content-estimate-institute-atmospheric-physics	3c
	PMEL/JPL/JIMAR	http://oceans.pmel.noaa.gov	3c
	MRI/JMA	https://www.data.jma.go.jp/gmd/kaiyou/english/ohc/ohc_data_en.html	3c
	NCEI	https://www.ncei.noaa.gov/access/global-ocean-heat-content/	3c
	UK Met Office EN4.0.2	www.metoffice.gov.uk/hadobs/en4/download-en4-0-2-l09.html	3c
	Argo monthly climatology	https://sio-argo.ucsd.edu/RG_Climatology.html	3SB1, 6g2
	Argo	https://usgodae.org/argo/argo.html	3c
Ocean Mass	GRACE	https://grace.jpl.nasa.gov/data/get-data	3f
Ocean Salinity	Aquarius V3.0	http://podaac.jpl.nasa.gov/aquarius	3d2
	Argo	https://usgodae.org/argo/argo.html	3d2
	Blended Analysis for Surface Salinity	ftp://ftp.cpc.ncep.noaa.gov/precip/BASS	3d2
	SMAP	https://podaac.jpl.nasa.gov/SMAP	3d2
	SMOS	https://earth.esa.int/eogateway/missions/smos	3d2
	World Ocean Atlas 2013	www.nodc.noaa.gov/OC5/woa13/	3d2, 3d3
	World Ocean Atlas 2018	https://www.ncei.noaa.gov/products/world-ocean-atlas	2d8
	NCEI	https://www.ncei.noaa.gov/access/global-ocean-heat-content/	3d3
Outgoing Longwave Radiation	AVHRR	https://psl.noaa.gov/data/gridded/data.interp_OLR.html	4d2, 4g2
	Daily OLR	www.ncdc.noaa.gov/cdr/atmospheric/outgoing-longwave-radiation-daily	4b2, 4b3, 4c, 4g3, 4g5, 4g6

(cont.) Relevant datasets and sources

General Variable or Phenomenon	Specific dataset or variable	Source	Section
Ozone, Total Column and Stratospheric	GOME/SCIAMACHY/GOME2 (GSG) Merged Total Ozone	http://www.iup.uni-bremen.de/UVSAT/datasets/merged-wfdoas-total-ozone	2g4
	GOME/SCIAMACHY/GOME2 (GTO) Merged Total Ozone	https://atmos.eoc.dlr.de/gto-ecv	2g4
	GOZCARDS ozone profiles	https://gozcards.jpl.nasa.gov	2g4
	Aura OMI/MLS	https://disc.sci.gsfc.nasa.gov/Aura/data-holdings/MLS ftp://toms.gsfc.nasa.gov/pub/omi/data/ozone/ (for years 2013-2017) https://disc.gsfc.nasa.gov/datasets/OMTO3d_003/summary https://disc.gsfc.nasa.gov/datasets/OMUVBd_003/summary	5j1, 6h
	Multi Sensor Reanalysis (MSR-2) of total ozone	http://www.temis.nl/protocols/O3global.html	2g4
	NASA BUV/SBUV v8.6 (MOD v8.6) Merged Ozone	http://acdb-ext.gsfc.nasa.gov/Data_services/merged	2g4
	NOAA BUV/SBUV v8.6 (MOD v8.6) Merged Ozone	ftp://ftp.cpc.ncep.noaa.gov/SBUV_CDR	2g4
	Bodeker Scientific	http://www.bodekerscientific.com/data/total-column-ozone	5j1
	Ozone Mapping & Profiler Suite (OMPS)	https://ozoneaq.gsfc.nasa.gov/omps/	6h
	Ozonesonde	www.esrl.noaa.gov/gmd/dv/spo_oz	6h
	SAGE II/OSIRIS	dataset linked to Bourassa et al. (2018) doi:10.5194/amt-11-489-2018	2g4
	SAGE-SCIA-OMPS	dataset linked to Arosio et al., (2018) doi:10.5194/amt-2018-275	2g4
	SWOOSH	www.esrl.noaa.gov/csd/groups/csd8/swoosh/	2g4
	WOUDC Ground-based Ozone	ftp.tor.ec.gc.ca cd /pub/woudc/Projects Campaigns/ZonalMeans	2g4
	Antarctic UV monitoring network	https://gml.noaa.gov/grad/antuv/	6h
	NDACC lidar, microwave and FTIR	ftp://ftp.cpc.ncep.noaa.gov/ndacc	2g4
Ozone, Tropospheric	Aura OMI/MLS	http://acd-ext.gsfc.nasa.gov/Data_services/cloud_slice/new_data.html	2g6
	NOAA Observatory Data	ftp://aftp.cmdl.noaa.gov/data/ozwv/SurfaceOzone/	2g6
Permafrost	Active Layer Thickness	www2.gwu.edu/~calm/	2c1, 5h2
	GTN-P global mean annual ground temperature data for permafrost	https://doi.org/10.1594/PANGAEA.884711	2c1
	Global Terrestrial Network for Permafrost (GTN-P)	http://gtnpdatabase.org/	2c1, 5h1
	Permafrost Temperature	http://permafrost.gi.alaska.edu/sites_map	5h1
	Permafrost Temperature at Chinese (QTP) sites	https://nsidc.org/data/GGD700/versions/1	2c1
	Permafrost Temperature at French sites	permafrance.osug.fr	2c1
	Permafrost Temperature at Norwegian sites	www.tspnorway.com	2c1
	Permafrost Temperature at Swiss sites (PERMOS)	www.permos.ch	2c1

(cont.) Relevant datasets and sources

General Variable or Phenomenon	Specific dataset or variable	Source	Section
Phenology	NDVI	https://modis.gsfc.nasa.gov/data/dataprod/mod13.php	2h4
	PhenoCam	http://phenocam.sr.unh.edu	2h4
	Harvard Forest	https://harvardforest1.fas.harvard.edu/exist/apps/datasets/showData.html?id=hf003	2h4
	Natures Calendar	https://naturescalendar.woodlandtrust.org.uk/	2h4
Vegetation Optical Depth	VODCA	https://zenodo.org/record/2575599	2SB.3
	ESA CCI Biomass	https://catalogue.ceda.ac.uk/uuid/bedc59f37c9545c981a839eb552e4084	2SB.3
	MODIS MOD15A2H LAI	https://earthexplorer.usgs.gov/	2SB.3
Phytoplankton, Ocean Color	MODIS-Aqua	https://oceancolor.gsfc.nasa.gov/data/aqua/	3i
	SeaWiFS	https://oceancolor.gsfc.nasa.gov/data/seawifs/	3i
Precipitation	Climate Extremes Index	https://www.ncdc.noaa.gov/extremes/cei/	2d5
	CMORPH	www.cpc.ncep.noaa.gov/products/janowiak/cmorph_description.html	4d1
	ERA5	https://www.ecmwf.int/en/forecasts/datasets/reanalysis-datasets/era5	2d5
	GHCN v4	www.ncdc.noaa.gov/temp-and-precip/ghcn-gridded-products/precipitation	2d5
	GHCNDEX	www.climdex.org/datasets.html	2d5
	GPCP v2.3	https://psl.noaa.gov/data/gridded/data.gpcp.html	3e2, 4e, 4f, 4h
	GPCC	www.dwd.de/EN/ourservices/gpcc/gpcc.html	2d5
	MERRA-2	http://gmao.gsfc.nasa.gov/reanalysis/MERRA-2/	2d5
	European Climate & Assessment & Dataset	https://www.ecad.eu/	2d5
Pressure, Sea Level or Near-Surface	ERA5	https://www.ecmwf.int/en/forecasts/datasets/reanalysis-datasets/era5	5b2, 6b, 6SB.1
	HadSLP2r	http://hadobs.metoffice.com/hadslp2/	2e1
	NCEP/NCAR Reanalysis	www.esrl.noaa.gov/psd/data/gridded/data.ncep.reanalysis.html	4f2
	ERA5	https://www.ecmwf.int/en/forecasts/datasets/reanalysis-datasets/era5	5f
River Discharge	CaMA Flood	http://hydro.iis.u-tokyo.ac.jp/~yamadai/cama-flood/	
	ELSE	offline	
	DDM30	https://www.uni-frankfurt.de/45218101/DDM30	
Sea Ice Age	EASE-Grid v3	http://nsidc.org/data/nsidc-0611/	5d3
Sea Ice Duration	Near-Real-Time DMSP SSM/I-SSMIS Daily Polar Gridded	http://nsidc.org/data/nsidc-0081.html	5d3, 6f
	Nimbus-7 SMMR and DMSP SSM/I (Bootstrap)	http://nsidc.org/data/nsidc-0079.html	6f

(cont.) Relevant datasets and sources

General Variable or Phenomenon	Specific dataset or variable	Source	Section
Sea Ice Extent / Area / Concentration	Nimbus-7 SMMR and DMSP SSM/I (Bootstrap)	http://nsidc.org/data/seaice_index/	5c, 5d1, SB6.2
	Nimbus-7 SMMR Sea Ice Concentration	https://nsidc.org/data/nsidc-0007	6d
	NSIDC Passive Microwave Sea Ice Concentration	https://nsidc.org/data/G02202	5c
	Passive Microwave melt data (Greenland)	https://nsidc.org/greenland-today/	5e
	NSIDC Sea Ice Extent	https://nsidc.org/data/g02135	5c, 5d1
	OSI SAF CCI : OSI-401-b	http://osisaf.met.no/p/ice/ice_conc_reprocessed.html	5d1
	GRACE technical notes T13, T14	TN-13: https://podaac-tools.jpl.nasa.gov/drive/files /allData/gracefo/docs/TN-13_GEOC_JPL_RL06.txt TN-14: https://podaac-tools.jpl.nasa.gov/drive/files /allData/gracefo/docs/TN-14_C30_C20_GSFC_SLR.txt	5e
	AMSR-E	https://soccom.princeton.edu/content/data-access	6g3
Sea Level / Sea Surface Height	GRACE / GRACE-FO	https://grace.jpl.nasa.gov/data/get-data/	3f
	NOAA/NESDIS/STAR	www.star.nesdis.noaa.gov/sod/lsa/SeaLevelRise /LSA_SLR_timeseries.php	3f
	CMEMS	http://marine.copernicus.eu/services-portfolio/access -to-products/?option=com_csw&view=details&product _id=SEALEVEL_GLO_PHY_L4_NRT _OBSERVATIONS_008_046	3f
	Argo	https://usgodae.org/argo/argo.html	3f
	Tide Gauge	http://uhslc.soest.hawaii.edu/	3f
	AVISO	https://www.aviso.altimetry.fr/en/data.html	3g, 3h
ocean currents	AOML climate indices	https://www.aoml.noaa.gov/phod/indexes/index.php	3g
	Ocean Surface Current Analysis - Real time (OSCAR)	https://podaac.jpl.nasa.gov/dataset/OSCAR_L4_OC_ third-deg	3g
	Global Drifter Program	https://www.aoml.noaa.gov/phod/gdp/	3g
	Atlantic Ship of Opportunity XBT	https://www.aoml.noaa.gov/phod/goos/xbt_network/	3h
	RAPID array	https://rapid.ac.uk/rapidmoc/	3h
	MOVE array	http://www.oceansites.org/tma/move.html	3h
	OSNAP	https://www.o-snap.org/	3h
	SAMBA	http://www.oceansites.org/tma/samba.html	3h
	Florida Current transport	https://www.aoml.noaa.gov/phod/floridacurrent /data_access.php	3h
Sea Surface Temperature	ERSSTv5	https://doi.org/10.7289/V5T72FNM	3b, 4b, 4e, 4g2
	HadSST3.1.1	www.metoffice.gov.uk/hadobs/hadsst3	3b, 4e
	HadSST4	https://www.metoffice.gov.uk/hadobs/hadsst4/	2SB.1, 3b
	NOAA Optimum Interpolation SST (OISST) v2	http://apdrc.soest.hawaii.edu/dods/public_data /NOAA_SST/OISST/monthly	4b1, 4d2, 4f
	NOAA Optimum Interpolation SST (OISST) v2	https://www.ncdc.noaa.gov/oisst	2b3, 3b, 4g3, 4g5, 4g6, 4h, 5c

(cont.) Relevant datasets and sources

General Variable or Phenomenon	Specific dataset or variable	Source	Section
Snow Properties	Canadian Meteorological Centre Daily Snow Depth Analysis v1	https://nsidc.org/data/NSIDC-0447	5f
	Crocus Snowpack Model	http://www.umr-cnrm.fr/spip.php?article265	5f
	GlobSnow 2	https://nsidc.org/data/NSIDC-0595/versions/2	5f
	NOAA Interactive Multi-sensor Snow and Ice Mapping System (Snow Cover Duration)	https://usicecenter.gov/Products/ImsHome	5f
	NOAA Snow Chart Data Record (Snow Cover Extent)	www.snowcover.org	2c2, 5f
	Northern Hemisphere (NH) Snow Cover Extent (SCE), Version 1	doi:10.7289/V5N014G9	2c2, 5f
	MERRA-2	http://gmao.gsfc.nasa.gov/reanalysis/MERRA-2/	5f
Soil Moisture	ESA CCI SM	www.esa-soilmoisture-cci.org/index.php	2d10
Temperature, [Near] Surface	Antarctic Meteorological Research Center (AMRC) AWS	http://amrc.ssec.wisc.edu/data	6b
	CRUTEM4	www.metoffice.gov.uk/hadobs/crutem4	5b1
	ERA5	https://www.ecmwf.int/en/forecasts/datasets/reanalysis-datasets/era5	2b1, 2b3, 2SB.1, 5SB.1, 6b
	GHCNDEX	www.climdex.org/	2b3
	HadCRUT5 Global Temperature	https://www.metoffice.gov.uk/hadobs/hadcrut5/	2b1
	JRA-55 Atmospheric Reanalysis	http://jra.kishou.go.jp/JRA-55/index_en.html	2b1, 4f
	MERRA-2	http://gmao.gsfc.nasa.gov/reanalysis/MERRA-2/	2b3
	MERRA-2 monthly	https://goldsmr4.gesdisc.eosdis.nasa.gov/data/MERRA2_MONTHLY/M2TMNXLND.5.12.4	2h4
	NASA/GISS Global Temperature	https://data.giss.nasa.gov/gistemp/	2b1
	NCEP/NCAR Reanalysis	https://psl.noaa.gov/data/gridded/data.ncep.reanalysis.html	5b2, 5f
	ERA-Interim	www.ecmwf.int/en/research/climate-reanalysis/era-interim	5f
	NOAA/NCEI NOAAGlobalTemp	www.ncdc.noaa.gov/data-access/marineocean-data/noaa-global-surface-temperature-noaaglobaltemp	2b1

(cont.) Relevant datasets and sources

General Variable or Phenomenon	Specific dataset or variable	Source	Section
Temperature, Upper Atmosphere	ERA5	https://www.ecmwf.int/en/forecasts/datasets/reanalysis-datasets/era5	2b4, 2b5, 6b, 6h
	JRA-55 Atmospheric Reanalysis	http://jra.kishou.go.jp/JRA-55/index_en.html	2b4, 2b5
	MERRA-2	http://gmao.gsfc.nasa.gov/reanalysis/MERRA-2/	2b4, 2b5, 6h
	NOAA merged SSU+AMSU satellite data	https://www.star.nesdis.noaa.gov/smcd/emb/mscat/index.php	2b5
	RAOBCORE, RICH	www.univie.ac.at/theoret-met/research/raobcore (get version 1.7 fro Leo Haimberger)	2b4,2b5
	RATPAC A2	www.ncdc.noaa.gov/data-access/weather-balloon/radiosonde-atmospheric-temperature-products-accessing-climate/ratpac-a	2b4
	RSS v4.0	www.remss.com	2b4, 2b5
	NOAA/NESDIS/STAR MSU v4.1	ftp://ftp.star.nesdis.noaa.gov/pub/smcd/emb/mscat/data/MSU_AMSU_v4.1	2b4
	UW MSU v1.0	https://pochedls.github.io/#!data.md	2b4
	UAH MSU v6.0	https://www.nsstc.uah.edu/public/msu/	2b4, 2b5
	NCAR merged SSU+MLS satellite data	ftp://ftp.acom.ucar.edu/user/randel/SSUdata	2b5
	Stratospheric QBO data	https://acd-ext.gsfc.nasa.gov/Data_services/met/qbo/qbo.html	2b5
	CLASSnmat	https://catalogue.ceda.ac.uk/uuid/9058edd550624de69a8b2a882d11b65c	2SB.1
	UAHNMAT	https://www.nsstc.uah.edu/climate/	2SB.1
TOA Earth Radiation Budget	CERES EBAF Ed4.1	https://ceres-tool.larc.nasa.gov/ord-tool/jsp/EBAF41Selection.jsp	2f1
	TSIS TIM Level 3 Total Solar Irradiance 24-hour Means	doi:10.5067/TSIS/TIM/DATA306	2f1
Solar Transmission, Apparent	Mauna Loa Observatory	https://www.esrl.noaa.gov/gmd/webdata/grad/mloapt/mauna_loa_transmission.dat	2f2
Trace Gases	Atmospheric Greenhouse Gas Index (AGGI)	www.esrl.noaa.gov/gmd/aggi	2g1
	Atmospheric Gas trends	www.esrl.noaa.gov/gmd/ccgg/trends	2g1
	CAMS Reanalysis (Carbon Monoxide)	https://ads.atmosphere.copernicus.eu/cdsapp#!/dataset/cams-global-radiative-forcing-auxilliary-variables?tab=overview	2g7
	Nitrous Oxide	www.esrl.noaa.gov/gmd/hats/combined/N2O.html	2g1
	Ozone-Depleting Gas Index (ODGI)	www.esrl.noaa.gov/gmd/odgi	2g2
Tropical Cyclone Data	HURDAT2	www.aoml.noaa.gov/hrd/hurdat/Data_Storm.html	4g2
	International Best Track Archive for Climate Stewardship (IBTrACS)	www.ncdc.noaa.gov/ibtracs/	4g1, 4g3, 4g5, 4g6, 4g7
	JTWC Best-track Dataset	https://www.metoc.navy.mil/jtwc/jtwc.html?best-tracks	4g4,4g5
	RSMC-Tokyo, JMA best-track data	www.jma.go.jp/jma/jma-eng/jma-center/rsmc-hp-pub-eg/besttrack.html	4g4
	Southwest Pacific Enhanced Archive of Tropical Cyclones (SPEArTC)	http://apdrc.soest.hawaii.edu/projects/speartc	4g8
	HURDAT US Hurricanes	http://www.aoml.noaa.gov/hrd/hurdat/All_U.S._Hurricanes.html	4SB.1

(cont.) Relevant datasets and sources

General Variable or Phenomenon	Specific dataset or variable	Source	Section
UV Radation Data	Canadian sites	ftp://exp-studies.tor.ec.gc.ca/pub/uvdata /Preliminary/MSC	5j2
	Greenland site	http://uv.biospherical.com/Version2/data.asp	5j2
	Norwegian sites	https://github.com/uvnrpa/Minute_Data	5j2
	OMI	https://disc.gsfc.nasa.gov/ datasets?page=1&source=AURA%20OMI	5j2
	NASA Aura Microwave Limb Sounder	https://mls.jpl.nasa.gov/products/h2o_product.php	2g5
Water Vapor, Total Column	COSMIC	https://cdaac-www.cosmic.ucar.edu/	2d2
	ERA5	https://www.ecmwf.int/en/forecasts/datasets /reanalysis-datasets/era5	2d2, 6SB.1
	GNSS Ground-Based Total Column Water Vapor	https://doi.org/10.25326/18	2d2
	JRA-55 Atmospheric Reanalysis	http://jra.kishou.go.jp/JRA-55/index_en.html	2d2
	METOP A B C	https://www.eumetsat.int/our-satellites/metop-series	2d2
	RSS SSM/I -AMSR-E Ocean Total Column Water Vapor	www.remss.com	2d2
Wind, [Near] Surface	ERA5	https://www.ecmwf.int/en/forecasts/datasets /reanalysis-datasets/era5	2e2, 4g4
	HadISD3.1.1	www.metoffice.gov.uk/hadobs/hadisd/	2e2
	JRA-55 Atmospheric Reanalysis	http://jra.kishou.go.jp/JRA-55/index_en.html	4h
	MERRA-2	http://gmao.gsfc.nasa.gov/reanalysis/MERRA-2/	2e2
	RSS Radiometer winds	www.remss.com/measurements/wind	2e2
Wind, Upper Atmosphere	Climate Forecast System Reanalysis	www.ncdc.noaa.gov/data-access/model-data /model-datasets/climate-forecast-system-version2-cfsv2	4g3, 4g5, 4g6
	ERA5	https://www.ecmwf.int/en/forecasts/datasets /reanalysis-datasets/era5	2e3,4e,6b
	ERA-Interim	www.ecmwf.int/en/research/climate-reanalysis /era-interim	2e3
	JRA-55 Atmospheric Reanalysis	http://jra.kishou.go.jp/JRA-55/index_en.html	2e3
	MERRA-2	http://gmao.gsfc.nasa.gov/reanalysis/MERRA-2/	2 e3
	NCEP/NCAR Reanalysis	https://psl.noaa.gov/data/gridded/data.ncep .reanalysis.html	4b2, 4b3, 4c, 4g2, 4g3
	QBO	https://www.geo.fu-berlin.de/met/ag/strat/produkte /qbo/index.html	2 e3